BROOKHAVEN NATIONAL LABORATORY

Jefferson Lab

Electron-Ion Collider

at Brookhaven National Laboratory

Conceptual Design Report

2021

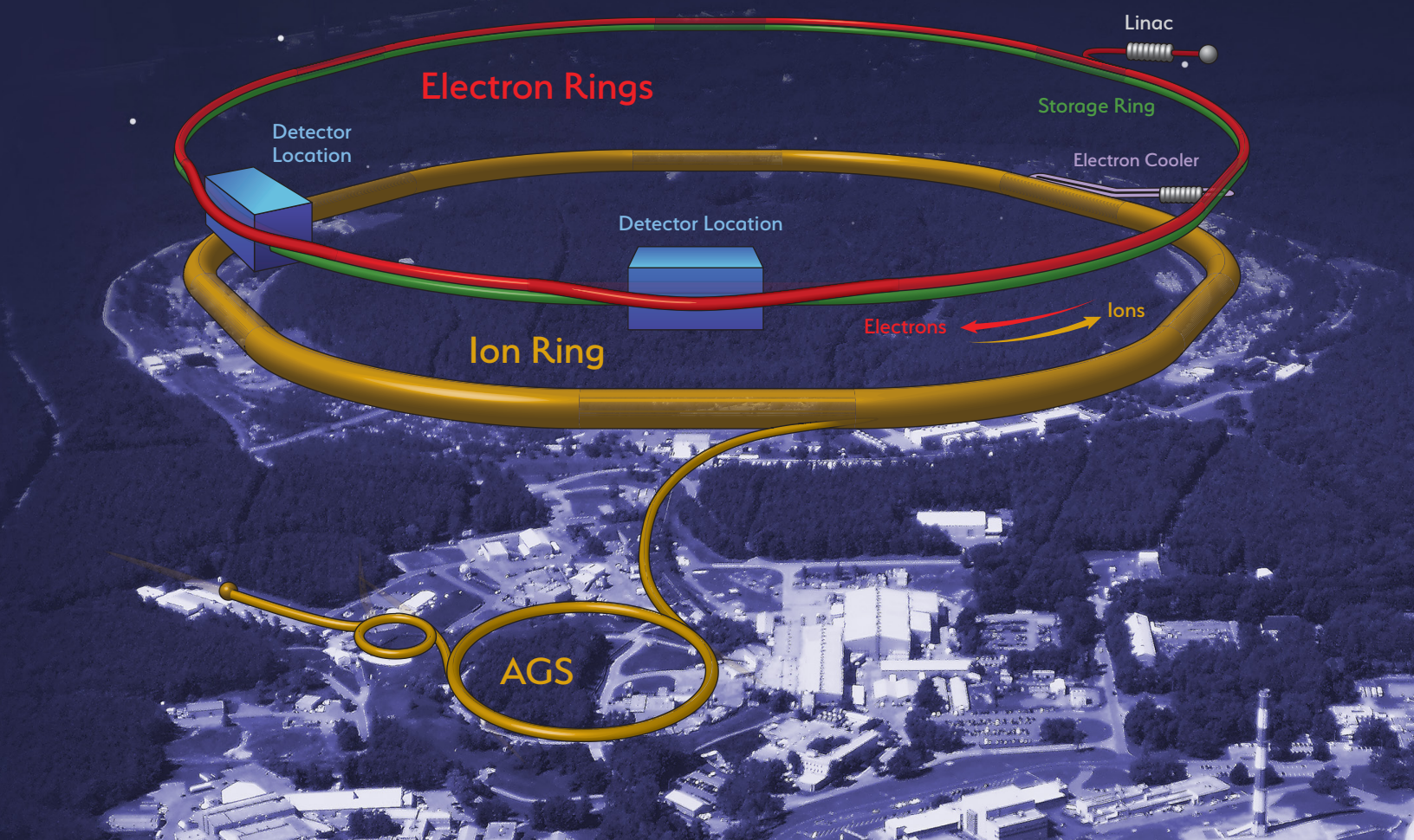

EIC CDR

February, 2021

Electron Ion Collider
Conceptual Design Report

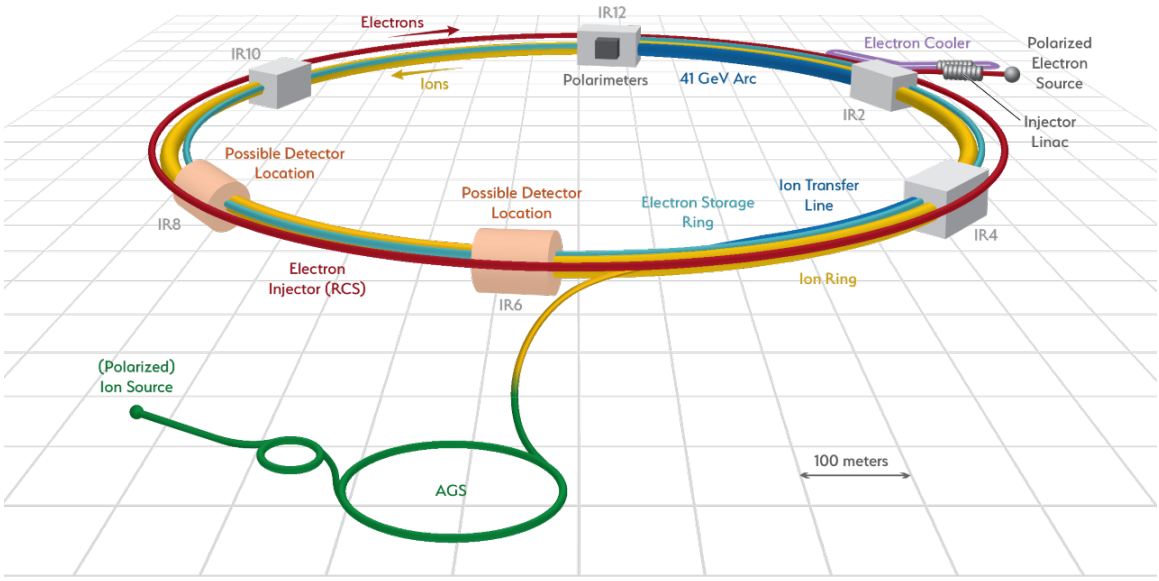

Disclaimer

Editor:

J. Beebe-Wang[1]

Contributors:

J. Adam[1], W. Akers[2], A. Arno[1], E-C. Aschenauer[1], K. Bane[3], F. Barbosa[2], G. Bassi[1], P. Baxevanisi[1], E. Beebe[1], J. Beebe-Wang[1], Y. Belyavina[1], S. Benson[2], I. Ben-Zvi[1], J.S. Berg[1], M. Blaskiewicz[1], A. Blednykh[1], S. Binello[1], J.M. Brennan[1], A. Bressan[4], S. Brooks[1], K. Brown[1], M. Bruker[2], Y. Cai[3], C.M. Camacho[5], K. Chen[1], W. Cheng[1], W. Christie[1], Z. Conway[1], F. Craner[1], S. Dalla Torre[4] K. Dehmelt[6], K. Deitrick[7], J. Delayen[8], S. Derbenev[2], A. Deshpande[6], S. De Silva[8], K. Dixon[2], T. D'Ottavio[1], K.A. Drees[1], J. Dunlop[1], L. Elouadhriri[2], R. Ent[2], J. Epstein[1], O. Evdokimov[9], M. Fallier[1], S. Fazio[1], A. Fedotov[1], N. Feege[12], P.K. Feng[1], W. Fischer[1], A. Flores[1], C. Folz[1], N. Franco[1], Y. Furletova[2], B.R.P. Gamage[2], M. Gaowei[1], D. Gaskell[2], C.J. Gardner[1], D. Gassner[1], E. Gianfelice-Wendt[10], J. Grames[2], X. Gu[1], C. Gulliford[7], J. Guo[2], W. Guo[1], F. Hannon[2], Y. Hao[1], D. Hatton[1], A. Hershcovitch[1], C. Hetzel[1], D. Holmes[1], T. Horn[11], D. Hseuh[1], H. Huang[1], J. Huang[1], R. Hulsart[1], A. Hutton[2], P. Inacker[1], W. Jackson[1], J. Jamilkowski[1], A. Jentsch[1], F. Karl[1], C. Keppel[2], J. Kewisch[1], A. Kiselev[1], P. Kolb[1], M. Kostin[2], G. Krafft[2], R. Lambiase[1], R. Li[2], Y. Li[1], Z. Li[3], C-J. Liaw[1], F. Lin[2], C. Liu[1], W. Liu[1], H. Lovelace III[1], T. Ludlam[1], Y. Luo[1], M. Mapes[1], F. Marhauser[2], I. Marneris[1], B. Martin[1], A. Marusic[1], D. Marx[1], G. McIntyre[1], E. McSweeney[1], F. Méot[1], J-L. Mi[1], T. Michalski[2], R. Michnoff[1], T. Miller[1], J. Mills[1], M. Minty[1], C. Montag[1], V. Morozov[2], D. Morrison[1], J. Morris[1], A. Mule[7], M. Musgrave[12], S. Nayak[1], C. Mayes[13], E. Nissen[2], Y. Nosochkov[3], S. Nemesure[1], D. Padrazo[1], B. Page[1], R.B. Palmer[1], M. Paniccia[1], H. Park[2], B. Parker[1], S. Peggs[1], A. Petrone[1], B. Podobedov[1], S. Polizzo[1], J. Preble[2], V. Ptitsyn[1], J. Qiang[14], O. Rahman[1], R. Rajput-Ghoshal[1], V. Ranjbar[1], D. Raparia[1], J. Reich[1], R. Rimmer[2], J. Ritter[1], G. Robert-Demolaize[1], Y. Roblin[2], P. Rossi[1], P. Sampson[1], J. Sandberg[1], M. Sangroula[1], T. Satogata[2], J. Scaduto[1], W.B. Schmidke[1], R. Seidl[15], S. Seletskiy[1], A. Seryi[2], T. Shaftan[1], J. Skaritka[1], V. Smalyuk[1], K. Smith[1], M. Spata[2], G. Stupakov[3], A. Sy[2], N. Taylor[13], S. Tepikian[1], R. Than[1], C. Theisen[1], P. Thieberger[1], D. Trbojevic[1], N. Tsoupas[1], J. Tuozzolo[1], T. Ullrich[1], R. Venugopalan[1], S. Verdú-Andrés[1], E. Wang[1], G. Wang[1], G-M. Wang[1], H. Wang[2], S. Wang[2], D. Weiss[1], W-T. Weng[1], F. Willeke[1], M. Wiseman[2], H. Witte[1], W. Wittmer[2], Q. Wu[1], A. Wund[1], B. Xiao[1], T. Xin[1], D. Xu[1], W. Xu[1], W. Yu[1], A. Zaltsman[1], A. Zelenski[1], H. Zhang[2], W. Zhang[1], Y. Zhang[2], Z.Q. Zhang[1], Z. Zhao[1], B. Zihlman[2]

---

[1]Brookhaven National Laboratory, USA
[2]Thomas Jefferson National Accelerator Facility, USA
[3]SLAC National Accelerator Laboratory, USA
[4]University of Trieste and INFN at Trieste, Italy
[5]Institut de Physique Nucléaire at Orsay, France
[6]The Massachusetts Institute of Technology, USA
[7]Cornell University, USA
[8]Old Dominion University, USA
[9]University of Illinois at Chicago, USA
[10]Fermi National Accelerator Laboratory, USA
[11]Catholic University of America, USA
[12]Stony Brook University, USA
[13]Xelera Research LLC, Ithaca, NY, USA
[14]Lawrence Berkeley National Laboratory, USA
[15]RIKEN Nishina Center for Accelerator-Based Science, Japan

Executive Summary

In January 2020, U.S. Secretary of Energy Dan Brouillette announced the decision to build an Electron Ion Collider (EIC) at Brookhaven National Laboratory (BNL), stating "The EIC promises to keep America in the forefront of nuclear physics and particle accelerator technology, critical components of the overall U.S. leadership in science."

While advancing the state of the art of particle colliders, the EIC will enable the U.S. nuclear physics community, with world-wide participation, to take a giant step forward in the centuries-old quest to understand the nature of matter at its most fundamental level, providing the clearest picture yet of how the elemental quarks and gluons interact to form the basic structure of atoms and nuclei.

The Conceptual Design Report (CDR) provides the technical reference design for the EIC. It demonstrates the capability of the new facility to meet the performance goals required to deliver the full scientific program recommended by the Department of Energy's Nuclear Science Advisory Committee and the National Research Council of the National Academies of Sciences, Engineering, and Medicine. Specifically, the design meets the following key requirements:

- Center-of-mass energy range from $\sim$ 20 to 100 GeV, upgradable to $\sim$ 140 GeV,
- Ion beams from deuterons to the heaviest stable nuclei,
- High luminosity, up to $10^{34}\,\mathrm{cm}^{-2}\,\mathrm{s}^{-1}$ for electron-proton collisions,
- Highly spin-polarized electron, proton, and light-ion beams, and
- An interaction region and integrated detector capable of nearly 100% kinematic coverage, with the capability of incorporating a second such interaction region as needed.

This CDR has evolved from the Preliminary Conceptual Design Report for an EIC prepared by BNL in 2019. Since then the design of the accelerator systems has been

further developed and refined in a joint effort of teams from BNL and Thomas Jefferson National Accelerator Facility (TJNAF). TJNAF will be a major partner in realizing the EIC.

In the meantime, the international EIC Users Group has organized a set of study groups and a year-long series of workshops (the "Yellow Report Initiative") to develop requirements and concepts for the design of experimental equipment optimized for the EIC science goals. The CDR explicitly incorporates input from this on-going study.

In summary, this CDR, the product of fully engaged national laboratory teams and an active scientific user community, represents the technical basis for the next major EIC project milestone, DOE Critical Decision 1 (CD-1).

This CDR is one of several documents prepared to meet the CD-1 requirements. Together they define the EIC project. In Appendix C we briefly summarize some of the project-defining elements that are not explicitly discussed in the CDR but are detailed elsewhere in the submitted documentation.

Contents

Chapter 1

EIC Overview

1.1 Physics Case of the Electron-Ion Collider

In the decades since the discovery of quarks, experiments in nuclear and particle physics have led to a fundamental theory of strong interactions — quantum chromodynamics (QCD) — that describes an extraordinary richness of nature at the subatomic level. The visible mass of matter in our universe the atoms and molecules that constitute the galaxies, planets, and life itself is made up of a dynamic substructure of quarks bound together by force-carrying gluons in complex systems internal to the protons and neutrons of atomic nuclei. An understanding of how the properties of matter originate from the deeply fundamental constituents of QCD is the primary goal of nuclear physics and the central motivation for polarized electron-proton and electron-ion collisions at the Electron-Ion Collider (EIC).

To date, a global program of precision measurements with high energy spin-polarized particle beams has begun to quantify how the intrinsic spins and orbital momenta of quarks, anti-quarks, and gluons each contribute to the characteristic spins of observed particles, but the mechanism by which this complex system results in the characteristic spin $\frac{1}{2}$ of the nucleon is not yet understood. The EIC is designed with the capability to answer this question.

Neutrons and protons bound inside atomic nuclei exhibit collective behavior that reveals the QCD substructure under extreme conditions. We now know, through laboratory experiments with high energy heavy ion collisions at RHIC [1] and the CERN Large Hadron Collider (LHC) [2], that at temperatures and densities similar to those of the nascent universe moments after the Big Bang, nuclear matter is transformed into a plasma of quarks and gluons. The strongly coupled "perfect fluid" property of this quark-gluon plasma [3] came as a remarkable surprise, and has brought widespread interest to the study of nuclear matter dominated by the strong force, and the understanding that the formation and evolution of this extreme phase of QCD matter is dominated by the properties of gluons at high density.

The most energetic nuclear collisions, including electron-proton collisions at HERA [4], established the dominance of gluons in the structure of nuclear matter when probed at high energies. This arises from the property that gluons, unlike their electromagnetic analogue (the photon), can interact directly with each other. Like quarks, gluons can interact through a "color" charge. The energy of self-interaction among the gluons accounts for a significant fraction of the nucleon mass. In collisions at higher and higher energies the density of gluons seen in the nucleon increases rapidly and without apparent limit. While this rise must saturate at some point, this saturation of the gluon density has not been observed yet, and its mechanism is of fundamental interest. It is widely conjectured that such a saturated gluonic state may have universal properties for all strongly interacting particles in nature. The EIC, through high energy collisions of electrons with heavy nuclei, is expected to enable detailed studies of this extraordinary state of matter.

In the last two decades, nuclear physicists have developed new phenomenological tools to enable remarkable tomographic images of the quarks and gluons inside protons and neutrons. These tools are being utilized and will be further enhanced at the upgraded 12 GeV CEBAF [5] at TJNAF and the COMPASS [6] experiment at CERN. Applying these new tools to study the transition of matter from being dominated by quarks to being governed by gluons will require the higher energy and beam polarization of an EIC.

In light of these advances and discoveries, a worldwide community of scientists has come together at many international conferences and workshops over the past several years to articulate the key science questions for a next-generation facility, the EIC, and to broadly specify its performance requirements. Following an intensive ten-week workshop held at the University of Washington's Institute for Nuclear Theory (INT) in 2011, a summary White Paper, published initially in 2014 and updated in 2016 [7] presents the science case for an EIC, including some "golden measurements" and the accelerator and detector concepts required to achieve them.

The Department of Energy's Nuclear Science Advisory Committee has addressed these studies. Its 2015 Long Range Plan for U.S. Nuclear Physics [8], acknowledged the "qualitative leap in technical capabilities" required for the EIC, and identified an EIC as "the highest priority new facility construction following the completion of FRIB". In 2018 this program was endorsed by the National Academies of Sciences Committee on U.S. Based Electron Ion Collider Science Assessment [9], stating:

"An EIC can uniquely address three profound questions about nucleons — neutrons and protons, and how they are assembled to form the nuclei of atoms:

- How does the mass of the nucleon arise?
- How does the spin of the nucleon arise?
- What are the emergent properties of dense systems of gluons?"

These questions call for an EIC with capabilities that far exceed any current or past colliding beam accelerator facility:

- A collider with a range of center-of-mass energies E_{CM} from 20–140 GeV will enable a kinematic reach well into the gluon-dominated regime;
- Highly polarized ($\approx$70%) electron, proton, and light nuclear ion beams (for example, deuterons, or ^{3}He) are planned for a comprehensive study of the nucleon structure including their spin: The electron beam brings to bear the unmatched precision of the electromagnetic interaction as a probe, while polarized nucleon beams are needed to determine the correlations of sea quark and gluon distributions with the nucleon's spin. High values of polarization reduce the uncertainties in determination of these correlations;
- High collision luminosity 10^{33} to $10^{34}\,\mathrm{cm}^{-2}\,\mathrm{s}^{-1}$ over a broad range in E_{CM} will enable precise determination of the confined momentum and spatial distributions of sea quarks and gluons in nucleons and nuclei;
- Ion beams from deuteron to the heaviest nuclei (gold or uranium) of the EIC will provide access to the regime of saturated gluon densities and to understand how color propagates through nuclear matter.

In this document we present the plan for realizing the EIC. The EIC proposal provides a design that fully utilizes the existing RHIC facility to produce hadron beams, including high-intensity polarized proton beams, and takes advantage of recent technical advances to provide a powerful, cost-effective new facility that fully meets the requirements for a compelling and lasting research program, with high potential for new discovery, as spelled out in the EIC White Paper [7] and described below in Section 2.3.

1.2 Overview of the Electron Ion Collider

The EIC takes advantage of the entire existing Relativistic Heavy Ion Collider (RHIC) facility with only a few modifications at a relatively small cost on the scale of the project. The well-established beam parameters of the present RHIC facility are close to what is required for the highest performance of the EIC, with the exception of the total hadron beam current which will be increased by a factor of approximately three by increasing the number of bunches. The addition of an electron storage ring (ESR) inside the present RHIC tunnel will provide polarized electron beams up to 18 GeV for collisions with the polarized protons or the heavy ions of RHIC.

The EIC design must satisfy the requirements of the science program while having acceptable technical risk, reasonable cost, and a clear path to achieving design performance after a period of initial operations. The present EIC design is the result of a design strategy which takes all these requirements into account.

The storage ring-based design meets or even exceeds the requirements referenced in the Long Range Plan [8], including the upgraded energy reach:

- Center-of-mass energy (E_{CM}) of 20 to 140 GeV.

- A luminosity of up to $10^{34}\,\mathrm{cm}^{-2}\,\mathrm{s}^{-1}$; the long range plan requires 10^{33} to $10^{34}\,\mathrm{cm}^{-2}\,\mathrm{s}^{-1}$.
- High polarization of electron and light ion beams with arbitrary spin patterns, with time-averaged polarization of ≈70%, as required by the Long Range Plan.
- Beam divergences at the interaction point and apertures of the interaction region magnets that are compatible with the acceptance requirements of the colliding beam detector.
- Collisions of electrons with a large range of light to heavy ions (protons to uranium ions); the long range plan requires ions as heavy as uranium.
- Up to two interaction regions.

The RHIC tunnel incorporates two large experimental halls with infrastructure for two major colliding beam detectors. These are at the 6 o'clock position[1], where the RHIC STAR detector [10] is currently operating, and the 8 o'clock position, home of the RHIC sPHENIX detector [11] (see Figure 1.1). The design described here supports two EIC detectors, but the project scope includes only one interaction region and one detector. In this report, we describe in detail the interaction region (IR) configuration for a large, general-purpose detector in one of these areas (likely the 6 o'clock area), which fulfills the requirements for the full range of EIC science questions described above and in Chapter 2. Our plans for the EIC include the capability for two such detectors.

The scientific requirements, calling for high luminosity and near-complete angular coverage by the detector, result in an IR lattice that produces a significant degree of chromaticity (energy sensitivity of the beam optics). The nonlinear sextupole fields needed to compensate for this effect generally limit the dynamic aperture and must be well optimized to provide sufficient beam lifetime. Calculations motivated by experience at HERA [12] indicate that adding an identical second IR can be achieved without further reduction of the dynamic aperture (see Section 4.6.4). We thus plan to allow for detectors at both the IR6 and IR8 positions. The forces acting on the particles in each beam, which are introduced by the collective charges of the opposing beam, respectively; these dynamical implications are called beam-beam effects. To avoid unacceptably large beam-beam effects in the case of two experiments, the collider would operate in a mode where each of the two experiments sees one-half of the bunch crossings; i.e., each experiment receives half of the total luminosity (see Section 4.6.4).

The highest luminosities can only be achieved by implementing strong cooling of the hadron beams to counteract emittance growth by Intrabeam Scattering (IBS) [13] associated with the corresponding small beam emittances. Cooling of hadron beams with energies up to 275 GeV requires a novel cooling technique that is being developed and tested in a BNL R&D program [14].

[1] RHIC is composed of six sextants separated by six 200 m long straight sections, with each straight section having a potential collision point in the center. These six straight sections are denoted as 2, 4, 6, 8, 10, and 12 o'clock, or IR2 to IR12, with IR12 being the Northern-most IR.

The luminosity is proportional to the electron beam current. At energies of 10 GeV and higher, the electron beam current is limited by the RF power installed to replace the synchrotron radiation power emitted by the electron beam. The installed RF power of 10 MW is not a hard limit, but a design choice to limit construction and operations costs.

The design satisfies all requirements without exceeding fundamental beam dynamics limits. In particular, the design parameters remain within the limits for maximum beam-beam tune shift parameters (hadrons: $\xi_p \leq 0.015$; electrons: $\xi_e \leq 0.1$) and space charge parameter (≤ 0.06), as well as beam intensity limitations and IR chromaticity contributions. The EIC is composed of one of the present RHIC superconducting accelerator rings, an ESR with a similar circumference in the same tunnel, and an injector ring for on-energy injection of polarized electron bunches. The hadron and the electron beams collide in one (and possibly two) interaction point(s). The outline for the EIC is shown in Figure 1.1.

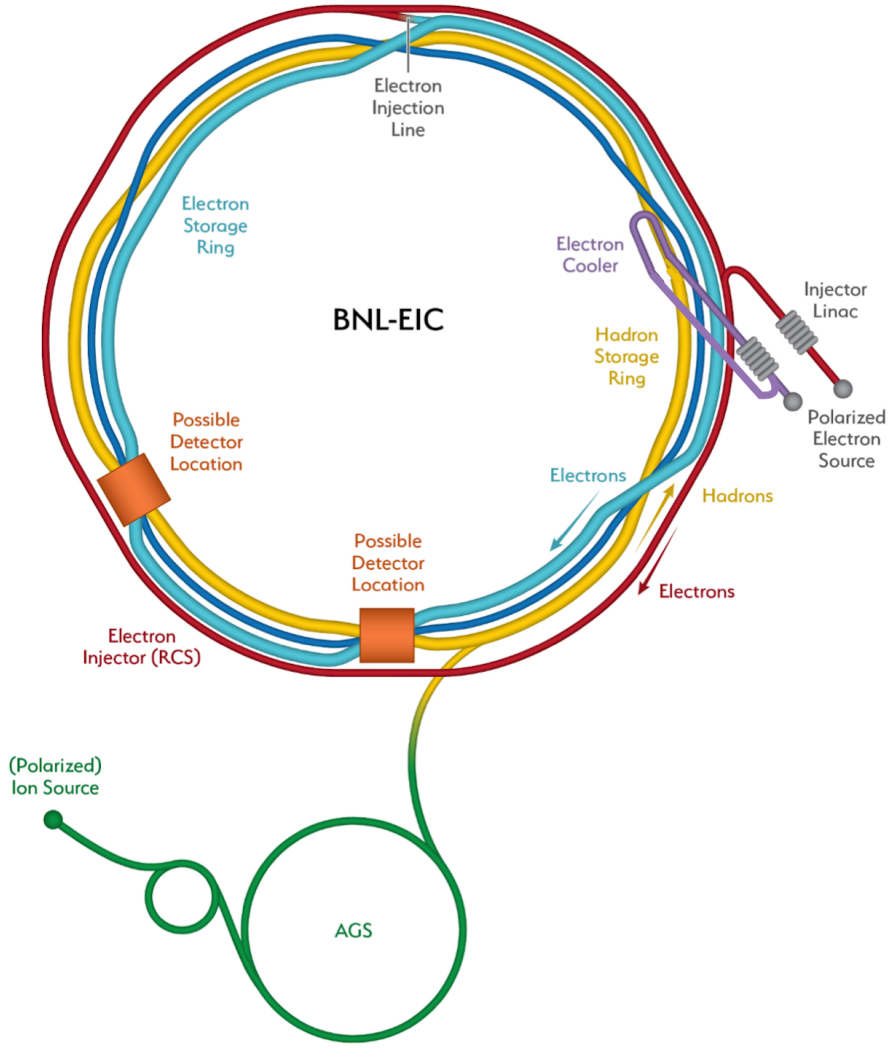

Figure 1.1: Schematic diagram of the EIC layout.

Polarized electron bunches carrying a charge of 7 nC are generated in a state-of-the-art polarized electron source. The beam is then accelerated to 400 MeV by the electron injection LINAC and injected into the rapid cycling synchrotron (RCS) that is also located in the RHIC tunnel. Two batches of four of these 7 nC bunches are injected into adjacent RCS RF buckets, and subsequently merged into two 28 nC electron bunches. Once per second, the two new electron bunches are accelerated to a beam energy of up to 18 GeV, and injected into the ESR, where they are brought into collisions with the hadron beam.

Half of the bunches will have polarization anti-parallel to the magnetic guide field, the other half parallel. The Sokolov-Ternov effect [15] tends to polarize the electron beam in the direction anti-parallel to the main dipole field, upwards in the ESR. The asymptotic value, which results from the balance with spin diffusion [16], depends in practice upon how well the machine is aligned and corrected. The time constant is energy dependent, larger at lower energy.

To maintain high spin polarization, each of the bunches with their spins parallel or anti-parallel to the main dipole field is replaced every one to three minutes depending on the polarization direction with respect to the magnetic guide field. The polarization lifetime is larger at lower beam energies and bunch replacements are therefore needed less frequently.

The highest luminosity of $L = 1 \times 10^{34}\,\mathrm{cm}^{-2}\,\mathrm{s}^{-1}$ is achieved with 10 GeV electrons colliding with 275 GeV protons (E_{CM} =105 GeV). The high luminosity is achieved due to large beam-beam parameters, a flat shape (or large aspect ratio σ_x/σ_y) of the electron and hadron bunches at the collision point, and the large circulating electron and proton beam currents distributed over as many as 1160 bunches. Table 1.1 lists the main design parameters for the beam energies with the highest peak luminosity.

At lower center-of-mass energies, the collision parameters must be re-optimized to remain within the limitations already discussed, which tends to result in lower luminosity. At a higher center-of-mass energy, achieved by increasing the electron energy to 18 GeV, the electron beam intensity must be reduced to prevent the synchrotron radiation power loss from exceeding 10 MW. Figure 1.2 shows the peak luminosity versus center-of-mass energy that will be achieved in the EIC. In the case of collisions between electrons and ions, the electron-nucleon luminosity is lower, but event rates comparable to the electron-proton case will be achieved.

The electron and hadron beams must be quickly separated after collisions to avoid parasitic crossings without introducing separator magnets, and to avoid the associated generation of synchrotron radiation in the detector region. The beams therefore collide with a crossing angle of 25 mrad. Collisions with a crossing angle reduce the overlap region of the colliding bunches, which reduces the luminosity by an order of magnitude for 25 mrad. In addition, with a crossing angle, the transverse beam-beam forces depend strongly on the longitudinal position of individual particles in the bunch. These forces generate strong synchro-betatron coupling and strong resonances that affect the beam lifetime and stability. These crossing angle effects are avoided by employing crab crossing [18], using crab cavities. Compensation of the crossing angle with crab cavities is a technology demonstrated in the electron-positron collider KEKB [19], and crab cavities are part of the high

Table 1.1: Maximum luminosity parameters.

Parameter	hadron	electron
Center-of-mass energy [GeV]	104.9	
Energy [GeV]	275	10
Number of bunches	1160	
Particles per bunch [10^{10}]	6.9	17.2
Beam current [A]	1.0	2.5
Horizontal emittance [nm]	11.3	20.0
Vertical emittance [nm]	1.0	1.3
Horizontal β-function at IP β_x^* [cm]	80	45
Vertical β-function at IP β_y^* [cm]	7.2	5.6
Horizontal/Vertical fractional betatron tunes	0.228/0.210	0.08/0.06
Horizontal divergence at IP $\sigma_{x'}^*$ [mrad]	0.119	0.211
Vertical divergence at IP $\sigma_{y'}^*$ [mrad]	0.119	0.152
Horizontal beam-beam parameter ξ_x	0.012	0.072
Vertical beam-beam parameter ξ_y	0.012	0.1
IBS growth time longitudinal/horizontal [hr]	2.9/2.0	-
Synchrotron radiation power [MW]	-	9.0
Bunch length [cm]	6	0.7
Hourglass and crab reduction factor [17]	0.94	
Luminosity [$10^{34}\,\mathrm{cm}^{-2}\,\mathrm{s}^{-1}$]	1.0	

luminosity upgrade of the LHC.

The main elements of the EIC that have to be added to the existing RHIC complex are:

- A low frequency photo-cathode electron source delivering up to 10 nC bunches of polarized electrons at 1 Hz.
- A 400 MeV normal-conducting S-band injector LINAC.
- A 400 MeV to 18 GeV spin-transparent rapid-cycling synchrotron (RCS) in the RHIC tunnel.
- A high-intensity ESR in the RHIC tunnel, with up to 18 GeV beam energy using superconducting RF cavities.
- A high luminosity interaction region with 25 mrad crossing angle, crab cavities and spin rotators that allows for a full acceptance detector; a second interaction region is possible and feasible, but not included in the project.

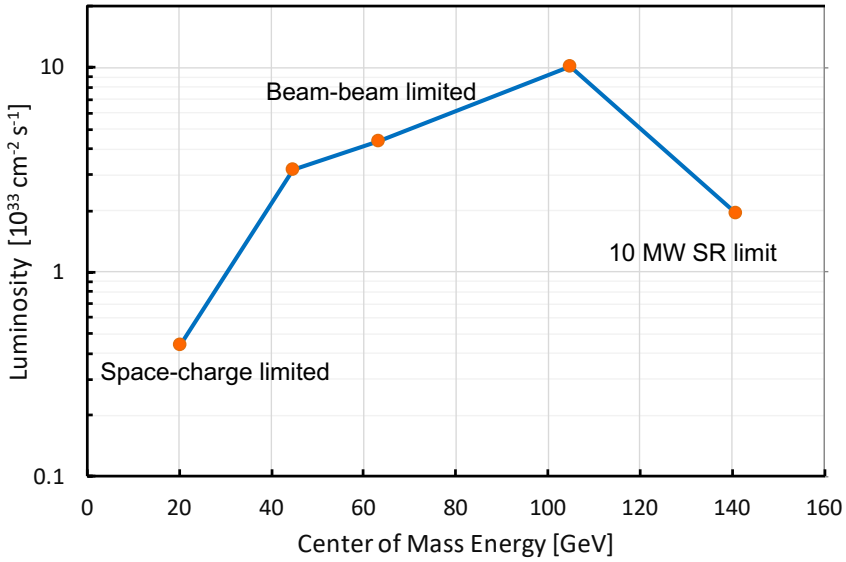

Figure 1.2: EIC electron-proton peak luminosity versus center-of-mass energy (E_{CM}). The luminosity for low E_{CM} is limited by space charge, for intermediate E_{CM} by the beam-beam interaction, and for high E_{CM} by the electron beam intensity and the total synchrotron radiation power. (Solid lines connecting the dots are inserted to guide the eye.)

- A 149 MeV energy recovery LINAC that provides continuous electron beams for strong hadron cooling.
- A small number of additional buildings. The most important ones will house additional RF power stations, pulsed magnet systems, and the electron injector complex.

The ESR design is using established and existing technologies which were previously implemented at high intensity ESRs such as the B-factories of KEK [19] and SLAC [20], as well as at modern synchrotron light sources.

1.3 EIC Design Concept

The EIC conceptual design provides a path towards a machine with a nominal luminosity of up to $10^{34}\,\mathrm{cm}^{-2}\,\mathrm{s}^{-1}$. The overall concept is to base the design, to a large extent, on existing technologies which will greatly reduce the technical risk. This is expected to result in reduced project costs and rapid commissioning, and will provide usable physics data soon after project completion.

Here we describe the parameters for the maximum performance, referred to as the nominal parameters (note: the discussion refers mainly to electron proton collisions, however, most of the statements are valid for electron ion collisions as well):

- The design peak luminosity reaches up to $1.0 \times 10^{34}\,\mathrm{cm}^{-2}\,\mathrm{s}^{-1}$, depending on the center-of-mass energy (see Figure 1.2). The electron energy and the luminosity at energies $E_e \geq 10\,\mathrm{GeV}$ is limited by the installed RF power to compensate the power of the synchrotron radiated by the beam. This supports a beam current of 2.5 A at an energy of 10 GeV. At a beam energy of 18 GeV, a luminosity of $0.15 \times 10^{34}\,\mathrm{cm}^{-2}\,\mathrm{s}^{-1}$ is still achievable.

- The center-of-mass energy range from 20 to 140 GeV is realized by proton energies that range from 41 to 275 GeV, and by electron energies up to 18 GeV. The maximum energy of 275 GeV is greater than the present maximum energy of RHIC (255 GeV), which is limited by a few interaction region magnets that will be removed. The lowest EIC proton energy is 41 GeV, limited by the need to synchronize the proton and electron beam revolution frequencies.

- Both electron and hadron beams will be spin polarized with flexible spin patterns. Proton polarization is part of the present RHIC program and can be carried over as-is to the EIC. The capability of light ion polarization (^{3}He and deuterons) will be added by installing additional ion sources and Siberian snakes (a set of magnets to suppress spin-depolarizing resonances first described in Reference [21]), and by improved polarimetry. The electron beam polarization will be enabled by full-energy injection of polarized electron bunches with the desired spin direction (up or down) and frequent electron bunch replacement to ensure a high degree of polarization.

- The EIC physics program requires detection of forward scattered hadrons with high efficiency. A transverse momentum detection acceptance for scattered protons from 200 MeV/c to 1.3 GeV/c in at least one transverse plane is realized by limiting the angular divergence of the proton beam at the interaction point (IP). Proton β-functions at the IP are chosen such that 50% of all scattered protons with a transverse momentum of 200 MeV/c can be detected by forward detectors close to the beam ("Roman Pots"). This limits the achievable luminosity in this configuration. As the cross section increases steeply with decreasing scattering angle, it will be sufficient to operate in this mode for only a short amount of time ($\approx$10%), which then has only a correspondingly small impact on integrated luminosity. For the nominal parameters, this lower limit of detectable transverse momentum is higher, which allows us to decrease the horizontal β-function at the IP substantially, thus increasing the maximum luminosity by a factor of two or more.

The design which supports these performance requirements is based on the concept of using one of the existing RHIC rings with minimum change to operate it as the Hadron Storage Ring (HSR). As much as possible of the RHIC infrastructure is used for the new collider. In particular, the existing RHIC tunnel is able to accommodate the additional accelerator rings. The parameters are chosen to provide the best conditions for beam stability with the envisioned luminosity goal. These basic concepts translate into the following design assumptions:

- The revolution frequencies of electron ring and hadron ring need to be identical for

stable collider operation. To minimize civil engineering efforts, the electron ring is installed in the existing RHIC tunnel.

- The electron and hadron beams have the same beam sizes just before collision at the interaction point. The beams are flat, with the horizontal beam size being larger than the vertical beam size. At the interaction point, the two beams intersect at a full crossing angle of 25 mrad in the horizontal plane. The resulting luminosity loss will be largely restored by rotating the bunches around the vertical axis at the IP (perpendicular to the crossing plane) by half the crossing angle using transversely deflecting RF resonators, or crab cavities, in both the hadron and electron rings.

- Hadron beam parameters are a modest extrapolation of those achieved at RHIC, with two exceptions. The number of bunches is increased from 111 to a maximum of 1160. The total proton current, however, is only increased by a factor of three. Injection and acceleration will be performed with 290 bunches. At the maximum beam energy in storage mode, the bunches will be adiabatically split into 1160 bunches in two steps. The required proton emittance is considerably smaller than present RHIC proton emittances. This requires strong hadron cooling to reduce the emittance and control emittance growth due to intrabeam scattering (IBS). A powerful cooling scheme has been developed in the form of coherent electron cooling, which is incorporated in the design. Because this is a novel concept which constitutes a performance risk, a lower-risk alternative solution that makes use of the existing second available RHIC superconducting ring has been developed. In this scenario the second ring will operate as a frequent on-energy injector. With this injector and in conjunction with bunched beam electron cooling at injection energy [22], peak and average luminosity are close to the nominal operating parameters achievable with strong hadron cooling. This option is described in [23].

- The maximum electron beam-beam parameter does not exceed $\xi_e = 0.1$, a level that has been routinely achieved at the B-factories KEKB [19] and PEP-II [20]. The electron ring will operate near the integer betatron resonance to enhance the luminosity with the pinch effect, while simultaneously minimizing the impact of systematic depolarizing spin resonances.

- The maximum synchrotron radiation power emitted by the beam is 8.8 MW. This needs to be continuously replaced by the RF system. Taking into account other loss mechanisms like higher order modes or transmission losses, the required RF power is 13 MW. The 8.8 MW synchrotron radiation loss corresponds to a linear synchrotron radiation power load of 3 kW/m on average, equivalent to 16 W/mm^2 in the arcs. This linear load is less than half of the corresponding value for KEKB [19] and PEP-II [20]. All machine components, such as vacuum chamber cooling capacity, are designed for a maximum synchrotron radiation power of 10 MW, thus providing sufficient margin.

- The layout described here supports two interaction regions (IR) and two interaction points (IP). However the second interaction region is not part of the scope of this

conceptual design. Preliminary considerations of second IR luminosity and beam dynamic challenges are described in Appendix refsec-2ndIR.

1.4 Beam Parameters and Luminosity

The EIC luminosity is maximized for a center of mass energy of $E_{\rm CM}$ =105 GeV. The luminosity will be lower over most of the $E_{\rm CM}$ range of 20–140 GeV, but still above 10^{33} cm^{-2}s^{-1}. Note that parameters in this section are for electron-proton collisions. Electron ion collisions will be described later.

The luminosity is proportional to the beam currents of electrons and hadrons, or the number of colliding particles per unit of time. Maximizing the total beam currents in both collider rings is a basic concept of maximizing luminosity. As already discussed, the planned electron beam current is 2.5 A, limited by the planned power of the RF system needed to replace synchrotron radiation losses at 10 GeV. This beam current is high but not unprecedented as both PEP-II and KEKB operated with that current. The 1 A beam current for the hadron ring is a reasonable extrapolation of RHIC which runs with 300 mA protons.

The bunch spacing must be sufficiently large to ensure high physics data quality that requires bunch-by-bunch luminosity measurements and bunch-by-bunch polarimetry. The bunch spacing in present RHIC (and in HERA) is approximately 100 ns. With state-of-the-art detector technology a bunch spacing of 10 ns is, while being challenging, feasible without disadvantages for electron-ion collision physics data quality.

The next consideration for bunch spacing concerns the maximum bunch intensity that should not exceed the thresholds of collective single bunch instabilities. Electron bunches with $N_e = 1.7 \times 10^{11}$ particles per bunch are close to single bunch intensity limits but are still stable assuming an achievable vacuum chamber impedance. Proton bunches of $N_p = 0.7 \times 10^{11}$ are well within previously achieved performance. Given the maximum electron beam current of 2.5 A, the resulting number of bunches is 1160 with a bunch spacing of 10 ns and a 1 µs abort or ion clearing gap.

Finally, the bunch spacing and thus the number of bunches determines the optimum value for the beam emittance. The smaller the bunch spacing, the smaller the number of particles per bunch for any given total beam current, which reduces the beam-beam tune shift. The beam-beam tune shift characterizes the strength of the forces on the individual particles in a bunch by the electromagnetic field of the oncoming colliding bunch. It is proportional to the number of particles in the oncoming bunch divided by its beam emittance $\varepsilon_{e,p}$, $\xi_{e,p} \propto N_{e,p}/\varepsilon_{p,e}$. Note that we require equal beam sizes for hadron and electrons at the IP to minimize detrimental beam-beam effects. Maximizing the beam-beam tune shift will maximize the luminosity. The maximum values, $\xi_p \leq 0.015$ for hadrons and $\xi_e \leq 0.10$, are suggested by previous performance and confirmed by extensive beam-beam simulations. Thus a smaller bunch spacing with more bunches and less particles per bunch offers the opportunity to work with smaller beam emittances.

The smaller beam emittance reduces the aperture requirements, and implies smaller values

of the beam divergence at the IP, which is advantageous for detection of forward-scattered particles. However, this can only be exploited with strong cooling of the hadron beam emittance to balance IBS.

A larger bunch spacing with a large number of particles per bunch would require that the emittance be intentionally increased to remain within beam-beam tune shift limits. This will reduce or eliminate the need for strong hadron cooling but will be limited by single bunch intensity limitations due to single bunch collective instabilities. A larger emittance would make detection of forward-scattered particles more challenging.

A small beam cross section is the other ingredient of maximum luminosity. There are two factors that determine the horizontal and vertical beam size $\sigma_{x,y}$, strong local focusing and small beam emittance, as $\sigma^*_{x,y} = \sqrt{\beta_{x,y} \times \varepsilon_{x,y}}$.

The beam focusing is characterized by the β-function at the IP, referred to as β^*. There are a number of practical limitations for β^*.

The hourglass effect is one such limitation. A small β^* implies rapid growth of nearby β, as $\beta(s) = \beta^* + s^2/\beta^*$ where s is the drift distance from the IP. The increase of luminosity due to strong focusing saturates if the β-function becomes smaller than the hadron bunch length.

Furthermore, the unwanted side effects of strong focusing — large beam size in the final focus quadrupoles and strong nonlinear chromaticity — increase as β^* is reduced. Strong nonlinear chromaticity must be compensated by strong sextupole fields, which reduce the dynamic aperture.

Large beam size requires large beam aperture in the final focus quadrupoles which has technological limits. These limitations are complicated by the large acceptance requirements of the colliding beam detector, which require that a section of $\pm 4.5\,\mathrm{m}$ distance from the IP be kept free from accelerator elements.

Finally, a small hadron β^* implies large hadron beam divergence which limits the acceptance of forward scattered hadrons.

The design strategy is to choose the bunch spacing such that the luminosity goal of $L = 10^{34}\,\mathrm{cm}^{-2}\,\mathrm{s}^{-1}$ can be reached with a small emittance that requires only a moderate cooling rate of $0.5\,\mathrm{h}^{-1}$ but still allows for bunch-by-bunch measurement of polarization, luminosity and other parameter relevant for physics. β^* functions are chosen such that chromaticity can be corrected and final focus magnets can be implemented with available technologies.

To increase the luminosity even further, the cross sections of the beams are chosen to be elliptical with an aspect ratio or flatness of $\sigma^*_y/\sigma^*_x = 0.09$. This value is optimized by beam-beam simulation studies. The beam-beam tune shift is reduced for flat beams, so a smaller value of emittance can be chosen to increase the luminosity.

In summary, the collider luminosity is maximized by

- running with the highest beam currents,

- at a center-of-mass energy in the middle of the energy range,
- using flat beams, low emittances, and small β-functions at the IP, with focusing magnets installed as close as possible to the IP but leaving a ± 4.5 m region around the IP free of accelerator elements,
- beam currents distributed over many, closely spaced bunches, while ensuring that the bunch currents are stable,
- acceptable hadron beam cooling requirements.

These choices lead to a crossing angle collision geometry of 25 mrad, and result in the parameter set shown in Table 1.1 in Section 1.2.

Maximum luminosity is achieved with an electron beam energy of 10 GeV and a proton beam energy of 275 GeV, which corresponds to a center-of-mass energy of 105 GeV. The synchrotron radiation power increases rapidly as it scales with the electron energy to the 4^{th} power, $P \propto E_e^4$. This means that the electron current must be reduced by the same factor to keep the total synchrotron radiation power below the limit of 10 MW. At the highest electron energy of 18 GeV, the electron current is only 0.26 A — about ten times smaller than the maximum value. The loss in luminosity is mitigated by decreasing the number of bunches by a factor of four and adjusting the transverse beam parameters. The increase of the electron beam emittance, which scales as E_e^2, is compensated by increasing the phase advance in the arcs from 60° per FODO cell[2] to 90° per FODO cell. The overall result is that the luminosity is reduced by only a factor of five compared with the maximum value achieved at 10 GeV electron energy.

These considerations result in the luminosity versus center-of-mass energy as shown in Figure 1.2. The parameters shown in Table 1.1 are derived under the assumption that the proton beam emittances will remain constant during the store at the small values of $\varepsilon_x = 11.3$ nm and $\varepsilon_y = 1.0$ nm. However, the dense hadron beam is subject to substantial emittance growth due to IBS. IBS must be counterbalanced by strong cooling of the hadron beam to maintain emittances and bunch length during the store. The store duration must be much larger than the time it takes to replace a depleted hadron beam to obtain a high average luminosity. We have worked out a strong hadron cooling scheme called micro-bunched coherent electron cooling, an extrapolation of stochastic cooling to high bandwidth. This scheme has been demonstrated theoretically and with detailed simulations. A conceptual layout has been worked out with technical details of its major components. A coherent electron cooling setup is being tested experimentally [24] at RHIC. Strong cooling is discussed further in Section 1.9.6. For a detailed description of the strong hadron cooling design see Section 3.9.

As already mentioned in Section 1.3, the design must enable detection of scattered protons with a minimum transverse momentum of $p_t = 200$ MeV/c, which at a hadron beam energy of 275 GeV corresponds to a scattering angle of 730 µrad in the horizontal plane. The

[2] A FODO cell is a lattice structure with alternating gradient quadrupole magnets between the bending magnets.

RMS divergence of the proton beam at the IP must not exceed one tenth of this minimum scattering angle, $\sigma' \leq 73\,\mu\text{rad}$. However, this requirement may be violated in the vertical plane, provided the beam divergence in the horizontal plane meets the requirement. A horizontal RMS beam divergence of 56 µrad allows detection of 50% of all scattered protons with a transverse momentum of 200 MeV/c. The EIC will be operated for a short time, say 10% of the time, with a large β_x^* that results in this low divergence and thus provides high acceptance at the expense of reduced luminosity. For about 90% of the time, the EIC will operate at small β_x^* for high luminosity but with a divergence angle exceeding 73 µrad. Because of the large cross section for small p_t, a large amount of data can be collected in a short amount of time so there is eventually an equal amount of data at all p_t values from 200 MeV/c to 1.3 GeV/c. This scenario substantially increases the effective luminosity of the facility.

So far we have only discussed electron-proton collisions. Most of the considerations discussed in this section apply to ions with only a few exceptions which are addressed below. Ions are characterized by the number of nucleons, A, and the electrical charge Ze, with $A \approx 2.5Z$ for heavy ions. The maximum beam-beam tune shift of the electrons is proportional to Z (for protons $Z = 1$). The number of ions per bunch, N_i, must be reduced by a factor Z to maintain the electron tune shift value in collisions with ions. The beam-beam tune shift for the hadrons is also proportional to Z but is inversely proportional to A. Thus the ion beam-beam tune shift is reduced approximately by a factor of 2.5 for a constant number of electrons. In conclusion, the electron-ion luminosity is reduced by a factor of Z. However, most of the cross sections in electron-ion collisions will increase by a factor of A compared to electron-proton cross sections, so the data rate is increased by a factor of about 2.5 for ions compared with protons. A full luminosity parameter table is shown in Section 3.1.1. Note that heavy ion beams will be unpolarized.

1.5 Beam-Beam Dynamics

The EIC approach to achieving stable beam-beam interactions is similar to the HERA approach. Each beam is assumed to reach the same beam-beam tune shift values as in collisions with a beam of the same species. The beam-beam tune shift, discussed in Section 1.4, is an established measure of the strength of the highly nonlinear interaction of the two colliding beams. Previous experience provides an excellent starting point for the maximum tolerable beam-beam tune shift of electrons and hadrons, but stability of beams in collisions must be also assessed by simulation. Simulation codes and methods are whenever possible compared and benchmarked with experiments and previous performance, in particular with RHIC and HERA experience. There are two simulation methods. The first is strong-strong interaction simulations that model both beams with macro-particles. This method is characterized by high noise levels due to artificial Schottky-noise as a consequence of the relatively small number of macro-particles. The other method, called "weak-strong", represents the fields of one beam by continuous, quasi-static functions. This method cannot simulate effects that involves the full dynamics of both beams. There are also hybrid solutions which attempt to mitigate issues of the two methods.

The challenge of the beam-beam interaction in the EIC is the stability of the hadron beam, which lacks any intrinsic damping.

Coherent beam-beam instabilities for the EIC have been assessed by strong-strong simulations using the codes BBSS [25] and BeamBeam3D [26]. The simulations confirmed coherent beam-beam instabilities in the EIC. This instability was infrequently observed in HERA. As discussed in more detail in this report, the EIC intensity threshold for this instability was found to be a factor of two above the planned beam intensity. Thus, we do not expect issues with coherent beam-beam instabilities with the present beam parameters in the EIC. The assessment of slow emittance growth due to real physical noise is more difficult. Strong-strong simulation results exhibit large emittance growth. There are clear indications that this growth is due to artificial Schottky noise, as shown by analysis, and confirmed in comparison of simulations with beam measurements. This shows that the emittance growth observed in simulations is artificial, but does not provide information on hidden dynamical effects which might cause real emittance growth.

A number of methods have been developed to minimize these difficulties, such as running the strong-strong simulation for a short time until the electron beam distribution has settled, and using strong-strong simulations only where they give trustworthy results, such as for coherent instabilities and resonances not seen in weak-strong simulations. Other simulation efforts continue with weak-strong simulations, using the equilibrium electron distribution found from strong-strong simulations.

A number of critical effects have been identified this way. The curvature of crabbed beams due to the sinusoidal waveform of the crab cavities results in separation of the hadron bunch head and tail from the electron beam center in collisions, which drives synchro-betatron resonances. These can be avoided by proper choice of tunes. The beam flatness, σ_y/σ_x, is another critical parameter which if chosen too small, leads to unacceptable growth of the vertical hadron emittance. Simulation studies concluded that the optimum beam flatness for EIC is 0.09.

1.6 Layout of the Interaction Region

The layout of the interaction region (IR) fulfills the following requirements:

- Beams must be strongly focused to β^* of a few centimeters at the interaction point by final focus quadrupoles.
- The final focus quadrupoles must have sufficient aperture for the large beam size associated with the small β^*.
- Contributions to the IR chromaticity must be minimized, as they must be compensated by nonlinear sextupole fields, which limit the dynamic aperture.
- Provide a large acceptance for hadrons scattered at very small angles from the collision point with transverse momenta as small as p_t =200 MeV/c. Consequently,

the final focus quadrupole magnets must have a large aperture so scattered hadrons and neutrons can be detected by detector elements placed further downstream. The beam divergence, and therefore the minimum β^*, is restricted so these particles are outside the 10σ proton beam envelope.

- The beams collide with a crossing angle of 25 mrad to separate the electron and proton beams quickly, to avoid parasitic collisions. This provides space for a neutron detector in the forward hadron direction, and for the luminosity detector in the forward electron direction. The crossing angle would strongly reduce luminosity and cause severe beam stability issues if it was not compensated by crab cavities (transverse RF cavities that kick the head and the tail of the proton and electron bunches in opposite directions in the plane of the crossing angle, so the bunches collide head-on). These RF cavities are placed at a horizontal betatron phase advance of $\pi/2$ from the interaction point (IP) on both the rear and the forward side, forming a 180° bump. This causes the bunches to be tilted at the IP so the bunches are aligned when colliding with each other. Crab cavities thus restore head-on collisions and prevent damaging beam dynamics effects.

- Strong synchrotron radiation generated by the electron beam can destroy sensitive detector equipment and make data taking impossible. Dipole magnets on the forward side must be avoided, and control of synchrotron radiation in the quadrupole magnets is an important consideration in the design of the beam optics. Synchrotron radiation generated in the forward region must be absorbed on the rear side of the IR as far as possible from the detector.

- Proton and electron beams are spin polarized. Additional light hadron beams (deuteron and ^{3}He) can be spin polarized with further development. Spin rotator magnets rotate the vertical spin direction in the arcs into the longitudinal direction (helical spin) at the IP. The IR design requires two pairs of spin rotators. Spin rotators for the hadrons already exist in RHIC; new spin rotators are required for the electron beam. The beam optics between the rotators must be spin transparent, or spin matched, to avoid depolarizing effects (no spin rotation dependence of betatron amplitudes and phases and momentum deviation).

Figure 1.3 shows a schematic of the top-view of the IR with a 25 mrad beam crossing angle which satisfies all these conditions. For high luminosities, the β-functions at the IP are required to be as small as possible. In the case of 10 GeV electrons colliding with 275 GeV hadrons, the β-functions are $\beta^*_{x,e} = 45\,\text{cm}$, $\beta^*_{y,e} = 5.6\,\text{cm}$, $\beta^*_{x,p} = 80\,\text{cm}$, and $\beta^*_{y,p} = 7.2\,\text{cm}$ (see Table 1.1).

The first magnet on the forward side is a superconducting spectrometer magnet with a very large aperture. An electron quadrupole is located inside the warm aperture of the spectrometer magnet, shielded from the dipole field by an anti-dipole magnet. Further downstream, the electron beam is shielded from the strong fields of the superconducting hadron quadrupoles by return yokes with designated cut-out regions which provide a field-free region for the electron beam. A strong dipole magnet is required on this side of the IP to steer the hadron beam away from the path of neutrons that are detected in the

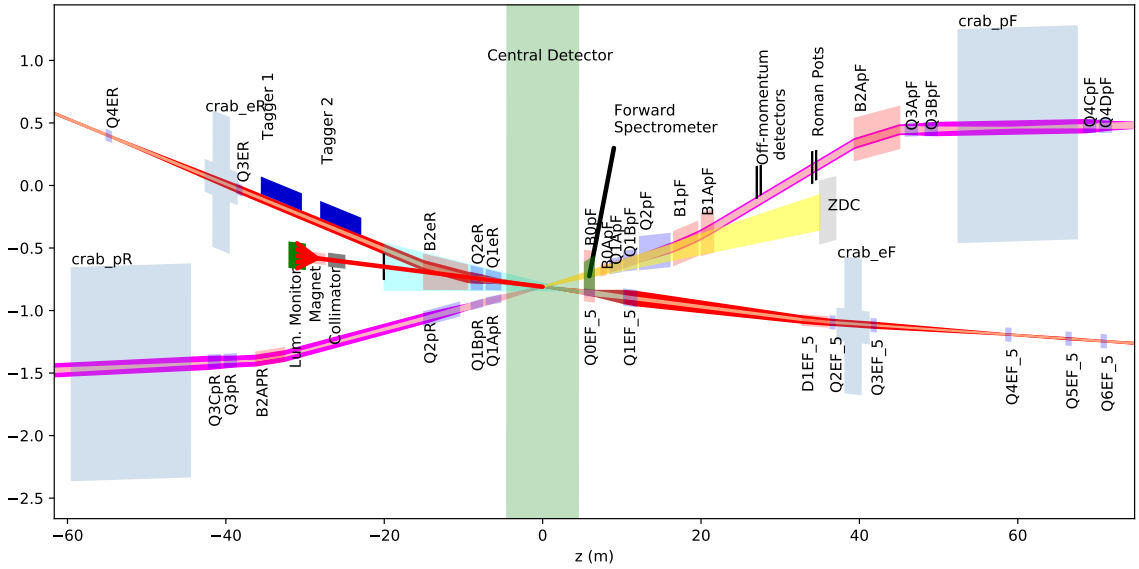

Figure 1.3: Schematic layout of the interaction region (top view, as shown for high divergence, no cooling). Beams cross at an angle of 25 mrad. Note the length scales for the horizontal and vertical axis are very different. The IR design integrates focusing magnets for both beams, luminosity and neutron detectors, electron taggers, spectrometer magnets, near-beam detectors (Roman pots for hadrons), crab cavities, and spin rotators for both beams. The two beams are focused by quadrupole doublets. Final focus quadrupoles for hadrons and electrons share common cryostats. On the hadron-forward side, there are separate focusing magnets which are partially longitudinally interleaved. The first quadrupole magnet for electrons is integrated into a hadron spectrometer dipole. On the rear side, hadrons and electrons are focused by quadrupoles which are installed side-by-side in the same cryostat. The maximum β-functions in the IR for hadrons of 2000 m are within the operating range of RHIC, while the maximum β-functions for electrons are below 925 m.

downstream neutron detector. The apertures for the hadron magnets on the forward side are considerably larger than required by the circulating hadron beam to provide sufficient clearance for scattered hadrons from the IP to be detected further downstream. For further details of IR magnet properties see Section 3.2.1.

On the rear side, the superconducting focusing magnets for electrons and hadrons are installed side-by-side in the same cryostat. Electron quadrupoles have an extra large aperture to provide sufficient space for the synchrotron radiation fan that is generated by the forward-side quadrupoles, which must be absorbed further downstream, far from sensitive detector components. The electron beam is steered away from the path of γ-radiation created by electron-hadron scattering (Bethe-Heitler), which is used to measure luminosity. The bending magnet acts as a spectrometer magnet for scattered electrons.

The maximum β-functions in the low-β quadrupoles for hadrons are $\hat{\beta}_{x,p} = 910\,\text{m}$ and $\hat{\beta}_{y,p} = 1970\,\text{m}$, respectively. For electrons the corresponding numbers are $\hat{\beta}_{x,e} = 925\,\text{m}$ and $\hat{\beta}_{y,e} = 620\,\text{m}$.

1.7 Spin Rotators

The spin polarization direction of electron and hadron beams is preserved during beam storage if the spin orientation in the arcs of the accelerator is vertical. In collision, both electron and hadron spins are required to be in the longitudinal direction. To rotate the electron spin from the vertical direction in the arcs to the longitudinal direction, a set of magnets called spin rotators are required that need to be integrated into the interaction region. A second spin rotator, which rotates the spin back into the stable vertical direction, is required after the beam passes the interaction point. Spin rotators are an integral part of the interaction region and are associated with a number of beam optics conditions as discussed below.

The ends of the arcs on either side of the detectors in IR8 and IR6 provide space to accommodate the spin rotators. A spin rotator consists of two pairs of 7 Tesla solenoid magnets and associated dipoles, plus a set of quadrupoles for coupling compensation.

The proton spin rotators are identical to those used in RHIC, which are based on helical dipole magnets.

1.8 Electron Storage Ring Design

1.8.1 Electron Storage Ring Overview

The ESR is located in the existing RHIC tunnel, in the same plane as the ion ring, and has a circumference of 3833.940 m that matches the proton revolution time at 133 GeV (with a well centered orbit). Like the ion ring, it consists of three inner and three outer arcs (six arcs in total) to have the same revolution time as the ion ring. Figure 1.4 is a 3D rendering of an EIC arc tunnel section.

The ring is organized as follows:

- Straight section IR 6 is foreseen for a colliding beam detector, with hadron/electron low-β section, spin rotators, and crab cavities.
- Straight section IR 10: superconducting RF systems, hadron beam abort.
- Straight section IR 12: polarimetry, damper systems, special instrumentation, electron injection and extraction.
- Straight section IR 2: electron source and pre-injector LINAC, electron injection, strong hadron cooler facility.
- Straight section IR 4: hadron injection, warm hadron RF.

The average arc radius is 380 m, with a dipole bending radius of ρ =290 m. The lattice in the arcs and the non-colliding utility straights is composed of FODO cells. Each of the

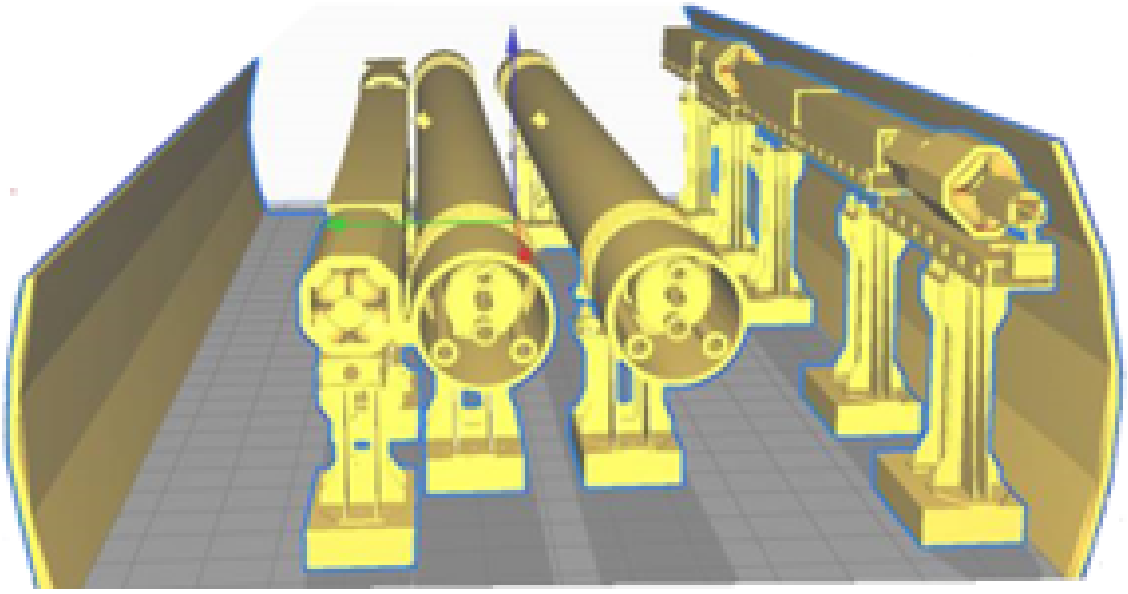

Figure 1.4: 3D rendering of an EIC arc tunnel section. The two segments in the center are the dipoles of the Blue and Yellow RHIC rings; one of them is part of the EIC collider. On the far left are a quadrupole and a dipole magnet of the ESR in the same plane as the hadron magnets; on the far right is a half cell of the rapid cycling synchrotron that is elevated by 50 cm with respect to the collider magnets.

bends in the arcs consists of three individual magnets, a short, 0.594 m long magnet in the center, the field of which can be reversed, between two longer (l =3.253 m) magnets, thus forming super-bends. This ensures sufficient synchrotron radiation and radiation damping for all beam energies between 5–18 GeV, with sufficient damping decrements for the anticipated strong beam-beam parameters of $\xi_{x,y} \leq 0.1$. In addition, the split magnets produce the desired beam emittance at all beam energies from 5–10 GeV. Each arc of the electron ring is composed of 16 identical FODO cells with dipole, quadrupole, sextupole and corrector magnets. A missing-magnet scheme matches the dispersion into the dispersion-free straight sections.

The horizontal emittances required at different energies are realized by a combination of FODO cell phase advances in the arc and using the super-bends, while the vertical emittance is controlled by applying a local skew-quadrupole bumps. At a beam energy of 18 GeV, the phase advance per arc FODO cell is set to 90°, while at 5 and 10 GeV it is reduced to 60°. The vertical phase advance is set to the same value of 60° to maximize the dynamic aperture. These different phase advances require a flexible chromaticity correction scheme, based on four families per arc for a FODO cell phase advance of 90°, and on six families per arc for a 60° phase advance lattice.

1.8.2 Electron Spin Polarization in the Storage Ring

The collision of longitudinally polarized electrons is a key requirement of the electron-ion collider. High spin polarization of the electron beam during collision operation is a design feature of the ESR. The evolution of beam polarization in electron storage rings is governed by two processes related to synchrotron radiation:

- The Sokolov-Ternov self-polarization [15] occurs due to the fact that spin flips from parallel to anti-parallel spin with respect to the magnetic guide field are more likely than the inverse process.
- There is depolarization caused by synchrotron radiation quantum emission and corresponding fluctuations of the closed orbit of individual electrons, as first described by Derbenev and Kondratenko [16].

The self-polarization process in conjunction with stochastic depolarization leads to a slow buildup of electron polarization in the direction opposite to the vertical guiding field, up to a maximum level of 92.4% in an accelerator without spin rotators and with sufficiently weak spin resonances. However, the presence of spin rotators, super-bends, and strong spin resonances as well as imperfections of the beam orbit and the beam optics reduces the equilibrium polarization level. An important quantity is also the self-polarization time, resulting from the two competing processes, both of which depend strongly on beam energy. Note that the self-polarization can increase or decrease the polarization of the electron bunches, depending whether the spins are parallel or anti-parallel to the magnetic field. The self-polarization time is quite long over the entire electron operational energy range ($\geq$ 30 min), but still demands a full-energy polarized electron injector, so the electron beam is injected into the storage ring with high polarization ($\approx$85%). One benefit of the long self-polarization time is that spin patterns containing bunches of opposite polarization orientation can be efficiently used.

The plans for high electron polarization operation in the EIC are based on the successful HERA spin program. [27]. As in HERA, the EIC polarization has a reasonably high equilibrium polarization of (30 to 50%), which results in a fairly slow decay of high initial polarization towards equilibrium polarization. This implies that beam energies must be chosen far from spin resonance conditions. Depolarizing effects are dominated by spin diffusion caused by the quantum nature of synchrotron radiation emission. The strength of depolarizing effects generally increases with a high power of the electron beam energy, E^7, thus making it more difficult to maintain high polarization in storage rings at higher energies. With a high polarization of the injected electron beam of 85% and for given depolarization times, the required average polarization of 70% in the storage ring determines the time each electron bunch be replaced by a fresh bunch. This time is on average 2 minutes in the worst case at 18 GeV, differs for the spin directions parallel or anti-parallel to the vertical magnetic guiding field.

This replacement time defines the repetition time of the rapid cycling injector synchrotron (RCS).

The accelerator technology used to achieve high polarization at high energies includes highly efficient orbit correction, beam-based alignment of beam position monitors relative to quadrupole field centers, and harmonic spin matching [28]. Control of betatron coupling is also essential to maintain high levels of polarization. These tools mitigate the effects of imperfection spin resonances and their synchrotron sidebands. In addition, the intrinsic resonances must be narrow enough to preserve high polarization, at least at energies far enough away from spin resonance conditions.

As discussed earlier, the EIC storage ring uses split dipoles to increase the damping decrement at lower energies. Such enhanced synchrotron radiation increases the spin diffusion rate. Thus, careful attention has been paid to the possibility of enhanced depolarization at lower energies.

Polarization tuning to eliminate imperfection resonances is expected to be easier in the EIC than it was in HERA. A much more efficient polarimeter design and the frequent injection of fully polarized bunches is expected to speed up the tuning process by a factor 10 to 100 compared to HERA.

1.8.3 Electron Storage Ring Dynamic Aperture

The dynamic aperture of the ESR is critical. With maximum β-functions of 925 m, a single interaction region contributes approximately 30% to the natural chromaticity. A phase advance of 90° per FODO cell is required to achieve the desired horizontal beam emittance of 20 nm for 18 GeV beam energy. At 10 GeV, where the highest luminosity is achieved, the optimum betatron phase advance in the arcs is 60° per FODO cell. The total natural chromaticity including one IR is $\xi_{x,y} \approx -100$. At 18 GeV, the interaction region contributes chromaticities of $\xi_{x,y}^{\mathrm{IR}} \approx -30$. The dynamic aperture for on-momentum particles is maximized by using a two-family sextupole correction scheme to set the chromaticities to $\xi_{x,y} = +1.$. Non-uniform distribution of sextupole fields with high peak values of the sextupole field reduce dynamic aperture. The large off-momentum β-beat generated by the low-β quadrupole magnets (or final focus magnets) in the interaction region(s) causes a large nonlinear chromaticity. This deteriorates the off-momentum dynamic aperture, since strong nonlinear resonances that affect electrons with large momentum offset cannot be avoided. The strategy to recover off-momentum dynamic aperture is two-fold:

- Achieve as much intrinsic compensation of $(\Delta\beta_{x,y}/\beta_{x,y})/(\Delta p/p)$ by optimized betatron phase advances between the sources of chromaticity. However, this is constrained by the spin matching conditions and the special phase advances between the crab cavities and the IP.
- Arrange the sextupoles in the arcs in families which are tuned to create an off-momentum β-beat that cancels the off-momentum β-beat from the IR, while avoiding the generation of nonlinear resonance driving terms.

In addition, sextupoles in the dispersion-free straight sections, called "geometric sextupoles," may be used to minimize residual contributions to driving terms of nonlinear

resonances or tune shift with amplitude.

The six EIC arcs consist of 16 regular periodic FODO cells and have, at each end, three FODO cells for dispersion matching, which are not identical to the regular cells. For the 60° optics for a beam energy of 10 GeV, a scheme with a structure of 32 sextupole magnets (16 horizontally focusing and 16 vertically focusing ones) per arc is applied. They are powered in three horizontal and three vertical families. Vertically focusing sextupoles are interleaved with the horizontal ones. Sextupoles belonging to the same family appear in pairs with 180° betatron phase advance. This implies that driving terms for off-momentum β-beat accumulate over the sextupoles of the same family and thereby maximize the potential for compensation of the off-momentum β-beat from the IR. The contributions to nonlinear driving terms from sextupoles of the same family, however, cancel, so nonlinear effects are only created in higher order. In case of the 60° lattice, the β-wave generated in the IR arrives at each arc with a different phase and the sextupole families need to be re-optimized in each individual arc.

This scheme produces an on-momentum dynamic aperture of $\pm 20\sigma_x$ and provides a momentum aperture of $8\sigma_{\mathrm{p}}$. These estimates include magnetic imperfections and effects of misalignment. The number of sextupoles per arc and plane should be a multiple of six to achieve intrinsic cancellation of the third order resonance, which is not the case with $n_{sextupoles} = 16$). An additional margin is provided by non-chromatic sextupoles in the straight sections for cancellation of nonlinear resonances which have not yet been optimized. Figure 1.5 shows the dynamic aperture for different values of the relative momentum offset $\Delta p/p$ in the (x, y) plane.

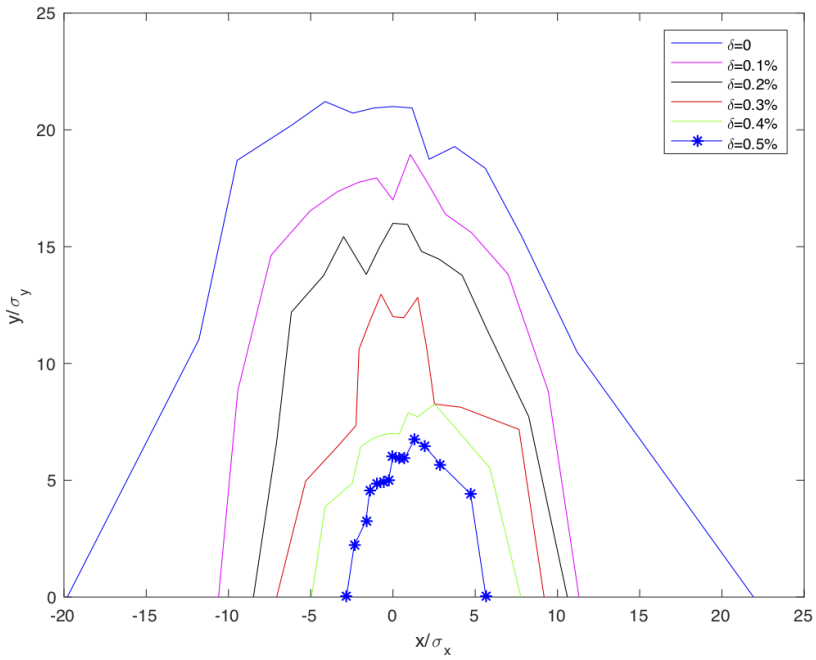

Figure 1.5: Dynamic aperture in the (x, y) plane for different values of the momentum offset $\Delta p/p$ for 60°-lattice. Results are obtained with 6-D particle tracking for one damping time.

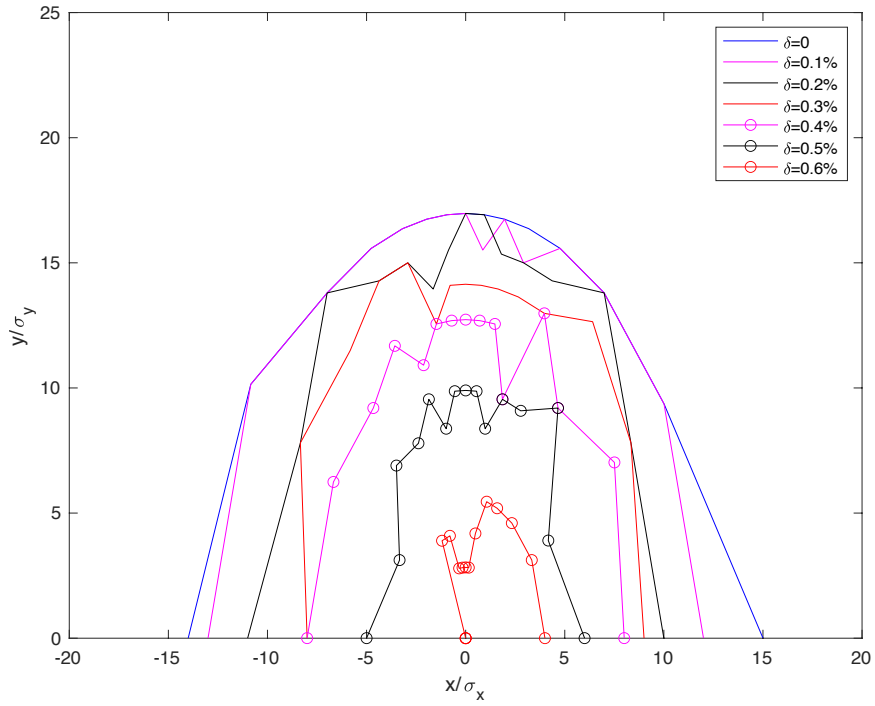

Figure 1.6: Dynamic aperture in the (x, y) plane for different values of the momentum offset $\Delta p/p$ for the 18 GeV, 90° lattice. Results are obtained with 6-D particle tracking for one damping time.

For the 90° lattice, the beam optics in the interaction region is designed such that the first sextupole in each arc occurs at $\simeq (2k+1)(90°$ distance from the IP. With a phase advance of 90°, two sextupoles in neighboring cells (horizontally focusing or vertically focusing, respectively) will generate an off-momentum β-beat if the two strengths are different. Sextupoles in successive pairs with the same strengths will add to this β-beat. This scheme implies that sextupoles are arranged in pairs spaced by $180° = 2 \times 90°$ so the contributions to third order resonances are intrinsically compensated.

Acceptable dynamic aperture is achieved by compensating the off-momentum β-beat which arises from the final focus magnets in the adjacent arcs, see Figure 1.6.

An option for further improvement of the dynamic aperture is to optimize the betatron phase advance between the six arcs to enable all sextupoles for correction of second order chromaticity to act coherently, thereby minimizing peak sextupole strengths.

With sixteen sextupole-pairs in each sextant, the 90° sextupole scheme provides intrinsic compensation of 3rd order resonances.

1.8.4 Collective Effects in the ESR

Coherent instabilities, intrabeam scattering, and Touschek scattering have been considered in the design of the ESR. Emittance growth times due to intrabeam scattering in the electron storage ring are of order minutes, much longer than the 50 ms radiation damping times. Touschek lifetimes are hours — much longer than the bunch replacement time required to compensate polarization loss. Coherent instabilities in the electron ring have been studied using a modified version of TRANFT [29], which was used during the design of NSLS-II. The code has evolved to simulate both single bunch and coupled bunch instabilities by tracking typically five bunches and assuming a uniform fill pattern. This allows use of a few times 10^5 simulation particles per bunch when doing coupled bunch calculations.

Numerically obtained wakefields have been obtained for preliminary models of vacuum chamber components. The strongest long-range transverse wake is assumed to be due to resistive wall. For design parameters, Landau damping provides transverse stability. There is head room at 10 GeV and higher. For 5 GeV the beam is stable but near threshold. The narrow band longitudinal impedance is due to RF cavities which are still being designed. Taking a pessimistic case we find a transverse damper with gain $Im(Q_s) = 0.001$ will suppress coupled bunch longitudinal oscillations. Such a damper should have no significant impact on hadron beam emittance coupled through the beam-beam force [30].

The fast-ion instability is a challenging two-stream instability for high-intensity electron machines. This instability can be suppressed sufficiently in the EIC if vacuum pressures can be kept at low, but achievable, values. A coupled bunch feedback system with special attention paid to low-noise implementation will be included for mitigation. A simulation has also been written to study this instability, and, as with impedance-driven instabilities, the beam-beam force is the dominant transverse damping mechanism. The code has been bench-marked against analytic estimates, ELEGANT, and experimental data.

1.9 Hadron Ring Design

1.9.1 Lattice Design

RHIC and its injector complex will remain, for the most part, unchanged. The arcs with their superconducting magnet structure will remain the same; other modifications are necessary or may be desirable. EIC hadrons will circulate in the "Yellow" ring, and the "Blue" ring will remain in place. The sextant between IR6 and IR4 of the Blue ring will serve as a transfer line and the beam will be injected in IR4, where injection kickers with faster rise time will be installed. Some modification of the RF system is necessary to accommodate the 290 bunches at injection and to accomplish the splitting into 1160 bunches. Space for more RF cavities will be provided in IR4 and IR10. The non-colliding straight

sections (utility straights) will be simplified by removing the DX magnets[3], to simplify the geometry and provide space for the electron ring crossover from inner to outer arcs and vice versa. This measure also enables the highest proton beam energy to be raised from 255 GeV to 275 GeV. The sextant between IR2 and IR12 of the Blue ring will be used as a bypass to circulate low energy hadrons at 41 GeV, which then have the same revolution time as electrons despite their reduced velocity. The magnet current in this sextant must be reversed for this mode of operation. However, the superconducting magnets of RHIC can operate without the protection of cold diodes at the low fields corresponding to a 41 GeV proton beam energy.

1.9.2 Hadron Ring Dynamic Aperture

The strong focusing of the hadrons at the collision point causes maximum β-functions in the low-β quadrupoles of $\beta_x = 910\,\mathrm{m}$ and $\beta_y = 1970\,\mathrm{m}$. The contribution to the natural chromaticity generated in one IR amounts to $\xi_x = -30$ and $\xi_y = -40$, which is 20% of the contributions from the arcs. This implies that a large contribution of the chromaticity generated in the interaction region must be compensated by sextupoles in the arcs to confine the tune footprint of the hadron beam within the space between nonlinear resonance lines. The strong sextupoles increase the strengths of nonlinear resonances, so the resonance-free space in the tune diagram shrinks. There is a maximum amount of IR chromaticity and corresponding tune footprint which can be accepted. As the hadron lattice has a 90° betatron phase advance per FODO cell, the phase advance between the IP and the first regular sextupole in the arc must also be 90° to compensate the nonlinear chromaticity with four sextupole families (two horizontal and two vertical families).The dynamic aperture of the hadron ring has been determined under these conditions by particle tracking, and benchmarked with similar calculations for RHIC data. The simulations demonstrate that the hadron beam will have sufficient dynamic aperture.

1.9.3 Electron Cloud Effects

Electron clouds are a serious concern for the ion ring with 1160 bunches and 6×10^{10} particles per bunch. Electrons produced in the beam vacuum chamber by ionization of the residual gas by the beam may get accelerated by the following bunches and hit the vacuum chamber wall, thereby releasing more electrons from the wall. This mechanism can create an electron avalanche that builds up rapidly as the bunch train passes by. The consequences include high cryogenic losses and beam instabilities. In addition to beam current and bunch parameters, the key parameter that determines the seriousness of the electron cloud effect is the secondary emission yield (SEY, number of emitted electrons from the surface per incident electron) of the vacuum chamber material. We plan to insert copper plated screens in the RHIC arc beam pipes that are coated with amorphous carbon. This

[3]DX separator dipoles on each side of each IP put the two hadron beams of present RHIC onto the common head-on collision orbits. The D0 dipoles at the entrance of the quadrupole triplets put the two RHIC beams on near-parallel orbits.

will reduce both the heat load due to the beam image current and will reduce the secondary electron emission coefficient sufficiently so the electron cloud instability is suppressed (see Section 1.11.3).

1.9.4 Intrabeam Scattering

Intrabeam scattering (IBS) is the effect of multiple Coulomb scattering of charged particles off each other inside a bunched beam, taking into account the Lorentz boost. IBS causes emittance growth in all oscillation planes of the beam. It limits the beam density needed for high luminosities, and affects the luminosity lifetime and the average luminosity. Beam parameters must be chosen to achieve an IBS growth time of several hours (given the beam setup time of typically one hour) unless the emittance growth can be overcome by strong cooling. Table 1.2 lists the beam parameters and calculated IBS growth times for the EIC design parameters of protons at 41 GeV, 100 GeV, and 275 GeV.

Table 1.2: EIC proton beam parameters.

Parameter	41 GeV	100 GeV	275 GeV
Bunch intensity [10^{10}]	2.6	6.9	6.9
RMS Horizontal normalized emittance [mm mrad]	1.9	4.0	2.8
RMS Vertical normalized emittance [mm mrad]	0.45	0.22	0.45
Longitudinal bunch area [eV s]	0.2	0.4	0.7
RF frequency [MHz]	197	591	591
RF voltage [MV]	10.5	16.1	28
RMS momentum spread [10^{-4}]	10.4	9.0	6.6
RMS bunch length [cm]	7.5	7	6
Longitudinal emittance IBS growth time [hours]	3.8	2.	3.4
Horizontal emittance IBS growth time [hours] (without coupling)	3.4	2.3	2.0

For the high luminosity parameters listed in Table 1.2, beam size growth due to IBS is significant, and strong cooling is required to maintain the beam density and the luminosity over a reasonable store time of at least several hours.

The parameters in Table 1.2 are based on reuse of the existing 197 MHz RHIC RF system, and the addition of a new 591 MHz RF system for the hadron ring. The results are based on a complete decoupling of the horizontal and vertical betatron motion, which is essential to maintain unequal emittances in the horizontal and vertical plane. Very good vertical orbit control is also mandatory to avoid any significant vertical dispersion. With strongly suppressed vertical dispersion, there will be no significant emittance growth due to IBS in the vertical plane.

1.9.5 Instabilities in the Hadron Storage Ring

Instabilities in the HSR have been studied using the same techniques as were used for the ESR. It is assumed that instabilities during injection and ramping can be handled, possibly requiring active feedback. Studies focused on conditions at store. The broad band transverse and longitudinal impedances have been measured [31, 32]. The narrow band longitudinal impedance due to the higher order modes in the 197 MHz RF cavities are assumed to dominate. The narrow band transverse impedance is due to higher order modes in the crab cavities. An important parameter is the beta function at the crab cavity. For 275 GeV, voltage limitations require $\beta_{crab} = 1300$ m. At 100 GeV, $\beta_{crab} = 500$ m was assumed, well within the voltage limits.

The beam is stable at 100 and 275 GeV at nominal intensities. For both these cases the expected growth rate in the absence of damping is comparable to the maximum damping that is provided by the beam-beam interaction. At 41 GeV, even with $\beta_{crab} = 50$ m, a persistent instability with an e-folding time of 2 seconds remains. This is almost certainly due to the average space charge tune shift of $\Delta Q_{sc} = 0.013$. This value is significantly larger than the half width at base of the tune spread from beam beam, $\Delta Q_{BB}/4 \approx 0.004$. Hence the coherent tune is shifted outside the incoherent band and any resistive impedance can drive growth. It is assumed that such a slow instability will be actively damped.

1.9.6 Hadron Ring Strong Beam Cooling

The highest luminosity in the EIC can only be achieved by introducing a strong beam cooling mechanism that counteracts IBS in the hadron bunches, which would otherwise cause a rapid increase of hadron emittance and reduction of luminosity. Moreover, the hadrons with large transverse and longitudinal amplitudes due to IBS suffer a strong nonlinear beam-beam force from the electron beam, which enhances halo formation and experimental backgrounds. Thus, with the parameters required for a luminosity of $L = 10^{34}\,\mathrm{cm}^{-2}\,\mathrm{s}^{-1}$, the hadron beam would quickly become unusable without cooling and would have to be replaced frequently. As the turn-around time of superconducting magnets in RHIC is about 30-60 minutes, an increase of peak luminosity above a certain level of performance would result in reduction of average luminosity. In [23] an option of using the second RHIC superconducting ring as an accelerator ring and on-energy injector is discussed. Our nominal solution that has been adopted for the EIC project, however, is to introduce strong hadron cooling to generate and maintain high proton beam quality, as described in this section.

The EIC high luminosity parameters (see Tables 1.1 and 1.2) were selected to have an IBS growth time $\varepsilon/(\mathrm{d}\varepsilon/\mathrm{d}t)$ of no less than two hours to ease the requirements for the strong hadron cooling.

Stochastic cooling is a well established cooling mechanism for hadrons pioneered at RHIC for bunched ion beams. It is used successfully for cooling of gold beams in RHIC operations and has enhanced the luminosity significantly. The existing stochastic cooling sys-

tem of RHIC, with some upgrade of its amplifier power, will provide sufficient cooling for the EIC ion beams [33]. For protons, the cooling rates at typical intensities of EIC proton bunches fall short of the need by orders of magnitude because of bandwidth limitations of the system. Thus, the discussion in this section will focus on cooling of the proton beams. Electron cooling with a DC electron beam is a standard cooling mechanism for hadron beams that works well at low hadron energies up to a few GeV. For large multi-GeV hadron energies, however, this cooling method requires enormous electron beam currents as the cooling time scales strongly with the beam energy as $\gamma^{5/2}$, with γ being the relativistic Lorentz factor of the hadrons. Using bunched electron beams accelerated by an RF LINAC as recently demonstrated in RHIC [34] would mitigate this. However, electron beam currents in the order of several amperes would be needed to provide sufficient cooling at EIC energies.

For these reasons more advanced approaches for strong hadron cooling have been developed. A novel method of hadron cooling that promises to work at high hadron beam energies has been proposed [24]. This method, which is called "coherent electron cooling", uses an electron beam to pick up the longitudinal Schottky noise of the hadron beam, and subsequently amplifies the signal by sending the electron beam through a free electron laser or using alternative beam-dynamics effects. The micro-bunched electron beam is then merged with the hadron beam with the proper timing. The electron beam then acts as a kicker to reduce the energy spread of the hadron beam. A proof-of-principle experiment on a low energy RHIC ion beam is underway that aims at demonstrating coherent electron cooling.

For the EIC, a variant of this method has been developed. This variant achieves micro-bunching amplification by sending the beam through a chicane or a series of chicanes with optimized R_{56} [35], spaced by a quarter of the electron beam plasma wavelength.

Figure 1.7 shows the layout of the proposed coherent electron cooling system for the EIC, designed to support the storage of hadron beams required for luminosities in the range of $10^{34}\,\mathrm{cm}^{-2}\,\mathrm{s}^{-1}$. An electron beam generated by a superconducting RF gun is injected into an energy-recovery superconducting LINAC that provides an energy gain of 149 MeV. The fully accelerated electron beam of 150 MeV is injected onto an orbit that overlaps with the orbit of the EIC hadron beam in the straight section of IR2 over a distance of 40 m, which is called the "modulator section". After this first common section, the hadron beam propagates through a section with an appropriately tuned R_{56} to separate hadrons with positive and negative energy deviation by a longitudinal drift corresponding to the width of the micro-bunch peak of the electron beam. The hadron beam path length is increased by a chicane which extends over a large fraction of the straight section to match the path length of the electrons.

The electron beam is energy-modulated due to residual fluctuating space-charge forces from the hadron beam. The electron beam then passes through a chicane where the energy modulation caused by the hadron beam density fluctuation is transformed into a micro-bunching of the electron beam. The density modulation of the electron beam is then amplified by a mechanism exploiting plasma oscillations. An electron beam with a non-uniform longitudinal density distribution is subject to plasma oscillations. After one-

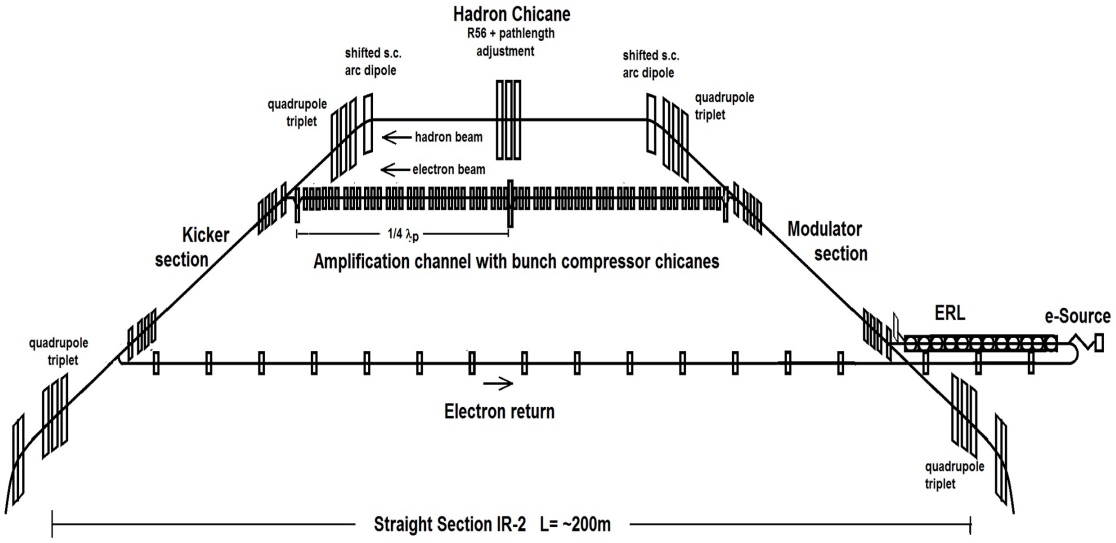

Figure 1.7: Schematic of the layout of the EIC strong hadron cooling facility. Note that the vertical scale has been stretched by a factor of $\simeq 50$.

quarter plasma oscillation wavelength of drift, the micro-bunching is transformed into a larger energy modulation which, after a second chicane, is turned into an amplified micro-bunching. Two such amplification stages produce a sufficiently strong electron density modulation to achieve a cooling time about one to two hours. The micro-bunched electron beam is again launched onto the hadron orbit, thereby overlapping with the hadron beam with carefully adjusted timing such that the density peak of the electrons is now in the center of the original density fluctuation of the hadrons. Hadrons with higher energy will be ahead of the electron micro-bunch and will be decelerated. Hadrons with lower energy will trail behind the electron micro-bunch and will be accelerated. The energy spread of the hadrons will thus be reduced after this "kicker" section. Cooling times of ≈ 100 minutes are envisioned. Table 1.3 summarizes the parameters of the EIC coherent cooling.

Coherent electron cooling of the transverse phase space is achieved by introducing a non-zero dispersion value in the modulator and kicker sections. In the presence of this dispersion, the ion energy modulation due to the space-charge forces between the ions and the electrons is converted into a transverse deflection (or kick), eventually resulting in a small change in the transverse emittance of the ions. By changing the value of the dispersion, the cooling can be distributed between the transverse and longitudinal degrees of freedom. The strong hadron cooling design is described in detail in Section 3.9.

Table 1.3: Parameters of the EIC coherent electron cooling.

Parameter	Value
Hadron energy range [GeV]	41-275
Electron beam energy [MeV]	22-150
Electron beam current [mA]	100
Electron charge per bunch [nC]	1
1st R_{56} [cm]	0.71
2nd R_{56} [cm]	0.71
3rd R_{56} [cm]	0.71
Plasma amplification stages	2
Length of the modulator section [m]	40
Length of the kicker section [m]	40
Cooling time [mins]	≈ 100

1.10 Electron Injection Complex

1.10.1 General Considerations

The requirements for the electron injector complex are driven by the need for polarized electrons in electron-ion collisions. The electron polarization should be close to 80% in the ESR.

The RCS injector will deliver electron bunches which are 85% spin polarized at beam energies up to 18 GeV. As described in Section 1.8.2, the polarization of the electron beam will decay towards the equilibrium polarization with a timescale of $\simeq 30$ min and must be replaced every few minutes to maintain high average polarization.

This is accomplished by fast kicker magnets which remove one electron bunch while a fresh electron bunch is injected simultaneously in its place.

In the storage ring, the highest bunch charge of 28 nC is required for operation at 10 GeV and below. For 18 GeV operation a bunch charge of 11.7 nC is sufficient. Two batches of four bunches of 7 nC (or 5 nC in case of 18 GeV operation) are injected into the RCS at the injection energy of 400 MeV, accelerated to an energy of 1 GeV, and subsequently merged first into two bunches, then into one bunch using RF systems with one half and one quarter of the main RF frequency. These bunch charge and rate requirements are sufficient for operation at all energies, as shown in Table 1.4.

The electron injection complex consists of the following elements:

- Electron gun with a Ga-As photo-cathode.

- Low energy transfer line (0.4 MeV).
- Electron S-band LINAC (400 MeV).
- Medium energy transfer line (400 MeV).
- Rapid Cycling Synchrotron (0.4 to 18 GeV) in the RHIC tunnel.
- High energy transfer line (up to 18 GeV).

Table 1.4: Requirements for the electron injector.

Parameter	5 GeV	10 GeV	18 GeV
Source kinetic energy E_k ($\gamma = 1.27$) [keV]		350	
LINAC energy gain [MeV]		400	
Repetition rate [Hz]		≤ 2	
Normalized electron emittance after LINAC [µm]	20	20	55
Emittances at RCS extraction $\varepsilon_x/\varepsilon_y$ [nm]	20/2	20/1.2	24/2
Bunch charge in storage ring [nC]	28	28.5	10
Number of bunches in storage ring	1160	1160	290
Bunch charge in source and RCS [nC]	5.5	5.5	11.7
Bunch replacement period [min]	48.5	48.5	2.4
Bunch replacement period (polar. req.) [min]	70	59	3.1

1.10.2 Polarized Electron Source

The polarized electron source must provide two batches of four bunches. Each bunch must have a total charge of 5-7 nC, normalized transverse emittance of 10-55 µm, and 85% polarization. The injector must have a repetition rate of 1 Hz. These requirements are sufficient for all collider operation modes.

Polarized electron beams are obtained from special photo-cathodes. The most common material used successfully in the last 30 years is Ga-As crystal. Strained Ga-As cathodes that are irradiated with UV laser light of 780 nm yield high polarization of the extracted electron beam and a high quantum efficiency ($QE \geq 1\%$) when coated with a mono-layer of Cs.

The polarized electron gun of the Stanford Linear Collider (SLC) was developed in the 1980s, and provided reliable performance, delivering up to 20 nC [36] of polarized electrons (70-75% polarization) at 120 Hz repetition rate. In principle, the EIC electron injector could be based on the SLC gun. However, to exploit the technical development which has occurred in the last three decades, a dedicated EIC gun is being developed which promises

higher beam energy, longer cathode lifetime, higher reliability, and higher polarization ($\geq 80\%$). A comparison of gun parameters is shown in Table 1.5.

Table 1.5: Electron source parameters.

Project	Bunch length σ_s [ps]	Bunch charge [nC]	Energy [MeV]	Emittance [µm]	$\Delta\gamma/\gamma$ [%]	Cathode material
SLC 5 mJ, 845 nm Laser	2000	$9-16$	0.12	15	1.5	Ga-As
EIC 5 mJ, 780 nm Laser	2000	7	0.35	$10-55$	2	Ga-As super lattice

A new gun geometry based on an "inverted gun" scheme has been designed; these designs have an inverted-geometry ceramic to minimize surface area available for breakdown. The design is optimized for a high extraction voltage of 300-350 keV and low electron beam loss. For good cathode lifetime and high reliability, excellent vacuum conditions are needed in the gun, the extraction line, and the tune-up beam dump. A prototype of this beam line has been built and tested. A load lock system for installation of prepared and activated cathodes into the gun has been designed. A prototype of this system is available and has been tested.

1.10.3 Rapid Cycling Synchrotron

Full energy injection of polarized electron bunches is accomplished by a Rapid Cycling Synchrotron (RCS) in the RHIC tunnel, which accelerates the electrons from the 400 MeV LINAC to up to 18 GeV for injection into the storage ring. The synchrotron has a repetition rate of up to 2 Hz and a total ramping time of 100 ms. The most important design feature of the synchrotron is spin transparency — the preservation of spin polarization during acceleration — up to the full energy of 18 GeV. This is accomplished by enforcing a high lattice periodicity P. The RHIC tunnel, however, only allows a lattice symmetry of six as it is composed of six arcs separated by six straight sections. The lattice design overcomes this constraint by configuring the straight section beam optics such that the transformation of beam coordinates through the straight section is an identity transformation. This also includes the electron spin. To suppress intrinsic depolarizing resonances, the periodicity P and the vertical betatron tune $Q_{y,\mathrm{arc}}$ (calculated only including the betatron phase advance in the arcs) must fulfill the conditions:

$$P - Q_{y,\mathrm{arc}} > a\gamma \tag{1.1}$$

and

$$Q_{y,\mathrm{arc}} > a\gamma \tag{1.2}$$

where $a\gamma = 40.849$ is the spin tune with $a = 1.16 \times 10^{-3}$ being the anomalous magnetic moment of the electrons. This leads to the choice of $Q_{y,\mathrm{arc}} \approx 50$ and $P = 96$, which is readily accomplished given the large arcs of RHIC. The lattice in the arcs is thus composed of 6×32 FODO cells, each with a betatron phase advance of 70°. A super-period consists of two FODO cells as there are two sextupole families per plane to compensate linear and nonlinear chromaticity. A special feature of one of the straight sections is that the rapid cycling synchrotron must pass around the colliding beam detector with a spin transparent chicane. At the peak energy of 18 GeV, the electrons suffer an energy loss of 36 MeV/turn due to synchrotron radiation. The acceleration and radiation loss compensation is done by 5-cell superconducting 591 MHz RF cavities.

The concept of spin transparent acceleration was extensively simulated. The amount of depolarization during the acceleration was found to be only about two percent. These simulations take into account an imperfect machine lattice. To obtain realistic estimates of the preservation of electron spin polarization, imperfections of quadrupole fields, typical betatron coupling, misalignment, and closed orbit errors, as well as sextupole fields for chromaticity corrections, have been introduced in the machine model.

Correction algorithms have been applied to adjust correction elements such as dipole correctors and tune correction quadrupoles. It is assumed that closed orbit excursions can be kept below 0.5 mm. It is further assumed that the betatron tunes during the ramp are kept within $|\Delta Q| \leq 0.01$ by applying tune feedback or pre-programmed time-dependent tune corrections. With this realistic machine model, simulations show that the polarization is robust and resilient against residual imperfections (see Figure 1.8). These good polarization results are consistently obtained for a number of statistical error seeds.

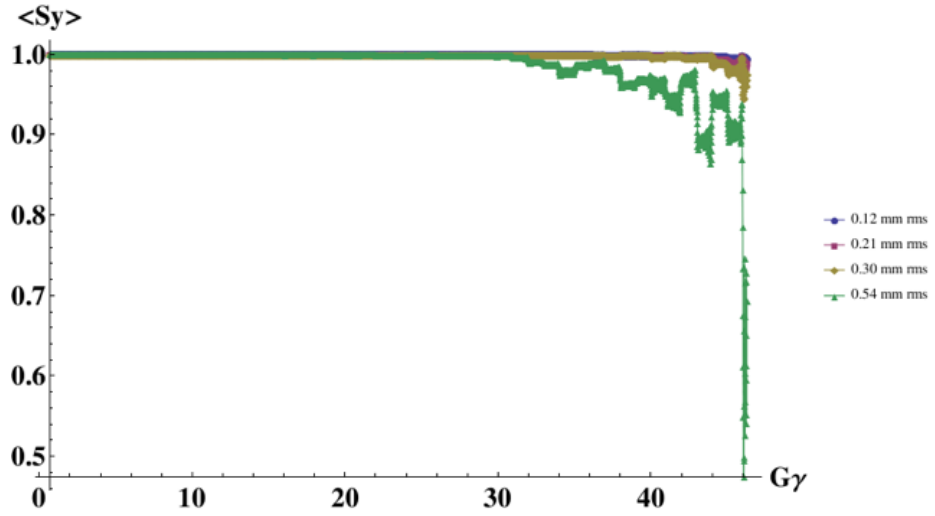

Figure 1.8: Electron spin polarization in the Rapid Cycling Synchrotron as a function of beam energy expressed in terms of spin tune $a\gamma$ during the ramp. Different colored curves indicate different RMS values of residual orbit distortions. Note the suppressed zero of the vertical scale.

The synchrotron accelerates two bunches each with a charge of up to 28 nC. With this amount of bunch charge, the electron beam remains below any collective instability threshold above beam energies of 1 GeV. Two batches of four bunches of 7 nC each are injected in four successive turns into four adjacent 591 MHz buckets at the injection energy of 400 MeV. The RCS is then ramped to 1 GeV and the four bunches are combined into one with two steps of pairwise merging using 295.5 MHz and 198.7 MHz RF systems, respectively.

1.10.4 Electron Injection from the RCS to the ESR

The requirements of high average polarization in the ESR greater than the natural equilibrium polarization, and spin up and spin down patterns in the ESR during collisions, necessitate regular bunch replacement. At an electron beam energy of 18 GeV, individual electron bunches will be replaced on average every two minutes.With 290 bunches, this corresponds to a 1 Hz injection cycle.The electron injection is accomplished by a combination of fast and slow kickers and a pulsed eddy current injection septum in the horizontal plane.

The slow kickers create a closed 360° bump. The first sine half-wave is used to extract a bunch with depleted polarization to create an empty bucket for the fresh bunch. This portion of the wave kicks a large fraction of the stored beam to transverse amplitudes close to the extraction septum. A fast kicker magnet, adjacent to the first slow bump kicker, kicks the bunch that will be extracted and replaced by a fresh injected bunch. The additional kick allows the selected bunch to enter the extraction septum.

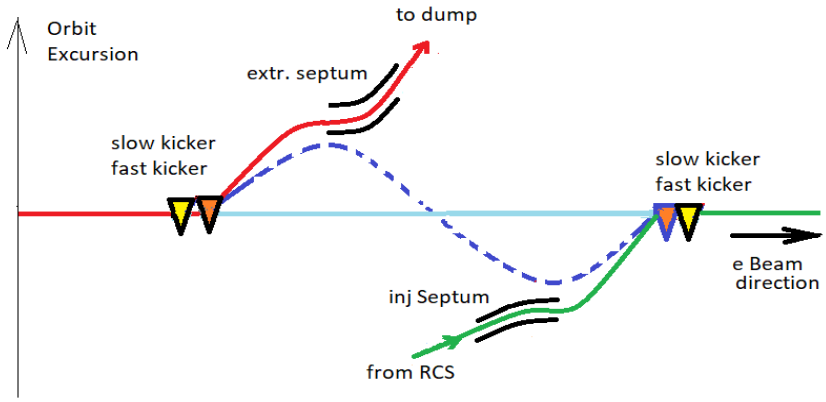

Figure 1.9: Electron injection and extraction scheme, based on one slow 360° kicker bump. The first sine half-wave is for extraction (left side) and the second one for injection (right side) which bring the stored beam within three horizontal RMS beam sizes ($\sigma_{\mathrm{RMS}} = \sqrt{\epsilon_x \beta_x + D_x^2 \sigma_e^2}$) to the injection and extraction septum, respectively. The bumps rise in 13 µs (one turn) and return to zero during the following 13 µs. Fast kicker magnets extract the used bunch and inject the fresh bunch from the injection septum onto the closed orbit respectively.

The second sine half-wave is for injection. The new bunch is extracted from the RCS and passes through the pulsed injection septum into the beam aperture. A fast kicker launches the injected bunch onto the closed orbit. This on-axis scheme results in injection without transverse oscillations. The fresh bunch is immediately on-axis for collisions with a corresponding hadron bunch at the IP. The scheme is illustrated in Figure 1.9.

1.11 Hardware Systems of the EIC

By far, the largest fraction of present-day RHIC will remain unchanged for the EIC. There are only a few technical components of the hadron storage ring that need some upgrade for EIC operations. These will be discussed in the following sections. Much of the hardware of the new electron rings is based on well known accelerator technologies such as room temperature magnets and magnet power supplies. Established electron beam instrumentation technology can be carried over to the EIC as well. Innovation is limited to critical systems such as RF systems, vacuum systems and IR magnets. Only these critical subsystems will be described in the following sections.

The total power consumption of the ESR magnet system is about 30% of the RF power (output power) and is thus a significant fraction of the increased operational power needs for the EIC as compared to RHIC. Figure 1.10 shows the power consumption of the EIC magnet systems.

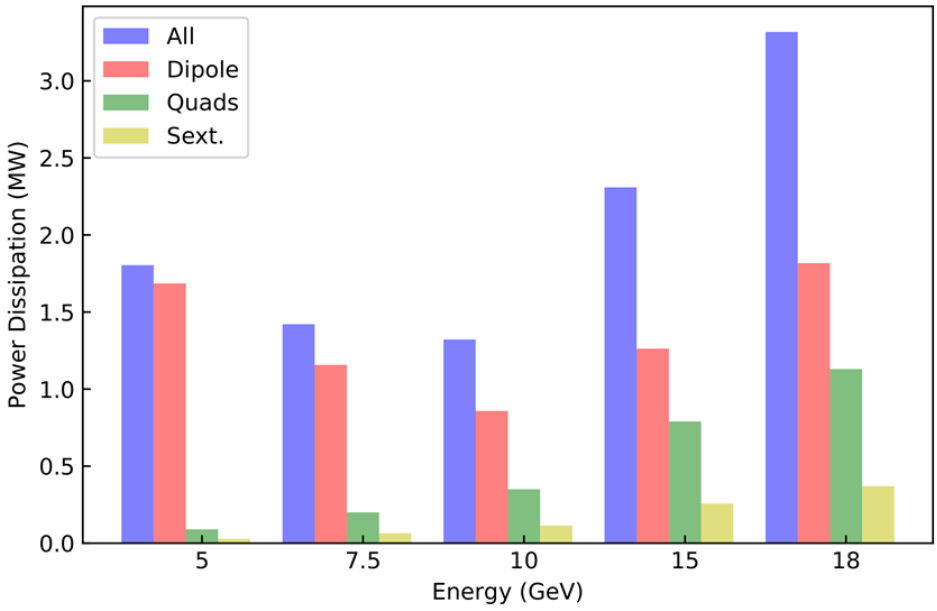

Figure 1.10: Power dissipation of storage ring magnets for operation energies 5 GeV to 18 GeV.

1.11.1 Hadron RF Systems

Hadron bunches extracted from the AGS will be received by the existing RF capture and acceleration system, modified from its RHIC operational frequency of 28 MHz to 24.6 MHz for the EIC. Bunch train formation for maximum luminosity operation requires adiabatic splitting of the hadron bunches into four bunches via a two-stage bunch splitting scheme. This requires new normal conducting bunch splitting cavities, two each at 49.3 MHz and 98.5 MHz.

The existing RHIC 197 MHz system will be used to further compress the bunches before they can be accepted and compressed to the final store bunch length in a 591 MHz storage cavity system. The 591 MHz RF system will be superconducting, employing cryomodules identical to the RCS 591 MHz RF system. Two 591 MHz cavities will be required to squeeze the bunches to 6 cm bunch length, which requires a total RF voltage of 28 MV.

1.11.2 Hadron Injection Kicker

A new injection kicker system will be required to support single bunch transfers with a bunching frequency of 24.6 MHz. This kicker system must provide rise, flattop and fall times which total no more than the 24.6 MHz bunching period, or 40.7 ns, compared to the current RHIC bunching frequency of 107 ns. Rise and fall times will need to be on the order of 10 ns, providing about 20 ns of flattop for the injected bunches. A total of 20 kicker units will span a length of $\approx$25 m. The new injection kickers will be placed in IR4. The corresponding changes to the magnetic elements in IR4 are minor.

1.11.3 Insertion of a Beam Screen in the Hadron Ring Beam Pipe

The high peak current of the EIC proton beam, with its large number of short, high intensity bunches circulating off-axis, results in unacceptably high dynamic heat load of the cold stainless steel beam pipes in the superconducting RHIC magnets. To reduce this heat load to levels below 0.5 W/m, within the budget of the 4.6 K RHIC cryogenic system, the resistive-wall impedance of the vacuum chamber must be decreased. This will be accomplished by inserting a beam screen with lower resistive-wall impedance into the entire hadron ring. The inner surface of the beam screen is copper, which has much lower electrical resistivity than stainless steel, especially at cryogenic temperatures.

To prevent electron cloud buildup due to the short bunch spacing, the secondary electron yield (SEY) of the vacuum chamber surface should be close to (or below) 1. A layer of amorphous carbon (aC) will be applied on top of the beam screen copper surface to reduce the SEY below the critical value.

A full description of the beam screen design is given in Section 6.4.4.

1.11.4 ESR Vacuum System

The ESR vacuum system consists of 3.8 km of vacuum chamber separated into 36 vacuum sections. Each of the arc vacuum sections is comprised of eight arc FODO cells. Each FODO cell has two 7.4 m long super-bends, each with a common vacuum chamber, and two 1.7 m long quadrupole chambers. The quadrupole chambers accommodate the quadrupole, sextupole and corrector magnets, the beam position monitors, synchrotron radiation masks, and pump ports. The individual chambers are separated by RF shielded bellows. There are also twelve vacuum sections for the 1.2 km of straight section and, in addition, twelve sections with specialized equipment, such as interaction region, RF-sections, and beam injection/extraction. The sections are separated by gate-valves that isolate the vacuum sections from each other.

The vacuum chambers are pumped by NEG-strips, titanium sublimation pumps and ion getter pumps. The vacuum system is designed for a pressure of 10 nTorr with full beam current of 2.5 A. The lifetime due to bremsstrahlung from scattering off the rest gas is greater than 20 hours for all beam energies from 5-18 GeV.

The thermal load from synchrotron radiation hitting the beam pipe is considerable. A total synchrotron radiation power of up to 10 MW can be accommodated by the water-cooled vacuum chamber. On average, the vacuum chamber is exposed to a linear power density of 4 kW/m if the electron beam energy is between 10-18 GeV.

With a horizontal aperture of 80 mm, the emitted synchrotron radiation travels, on average, five meters before it hits the vacuum chamber. With a horizontal beam emittance of $\varepsilon_x = 24$ nm and an emittance ratio of $\kappa = \varepsilon_y/\varepsilon_x \simeq 0.1$, the synchrotron radiation spot of the 18 GeV beam has a height of $h \simeq 180$ µm when it hits the vacuum chamber. This corresponds to an average power density of $\simeq 16\,\mathrm{W/mm^2}$. A material with good heat conductivity properties must be chosen, which has, at the same time, good vacuum properties, good mechanical stability, and will allow standard manufacturing processes such as extrusion, welding, or brazing. Such a material is OFS copper, which has a heat conductance close to that of pure copper, as well as excellent manufacturability. In addition, this material has excellent yield strength and it is less costly than materials with comparable properties. Figure 1.11 shows a cross section of the vacuum chamber.

With a cooling water velocity of 1.2 m/s, the maximum temperature on the inner surface of the dipole chamber is less than 100° C. The chamber profile will be fabricated as a copper extrusion. With current developments in the fabrication of copper profiles, it may be possible to produce the required profile in as a single cross section. This possibility will be investigated as part of the vacuum R&D program. If a single profile with all of the required features cannot be produced, the cross section will be fabricated out of 3 pieces e-beam welded together to preserve the properties of the bulk material by minimizing the heat effected zone. The highest surface temperature is obtained during 5 GeV operation, when the center dipole is reversed in field direction and increased to about twice the value required for 18 GeV operation. The gas load in the vacuum chamber is dominated by desorption of molecules from the chamber wall when it is hit by synchrotron radiation (Photon Stimulated Desorption — PSD). The photon flux at 10 GeV with a beam current of

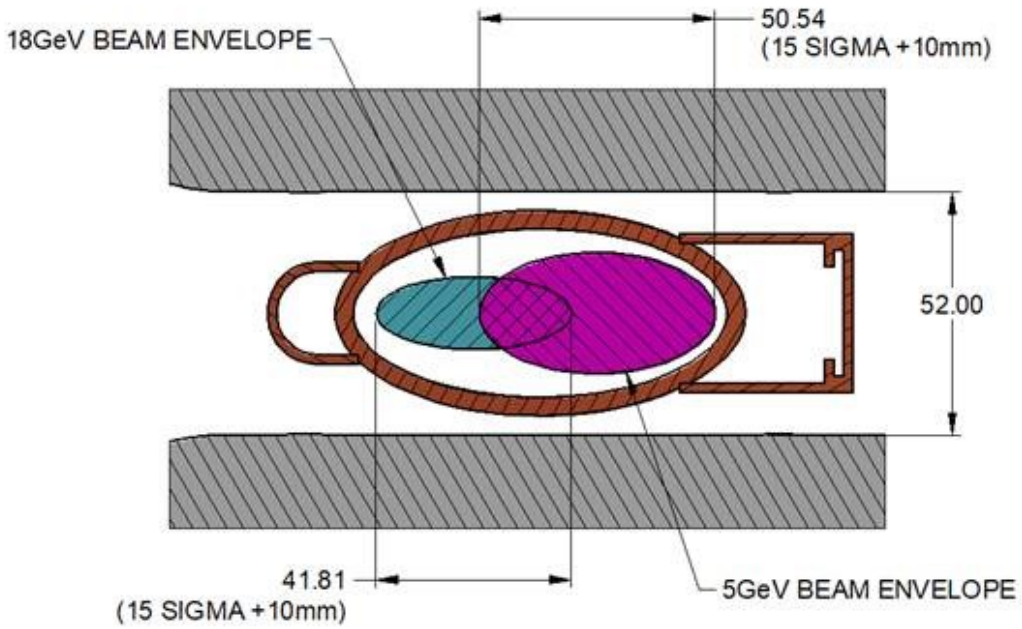

Figure 1.11: Cross section of storage ring vacuum chamber in dipole magnets.

2.5 A (worst case) is $8.08 \times 10^{17} \times E[\text{GeV}] \times I[\text{mA}] = 2 \times 10^{22}$ photons/sec. A desorption coefficient in the order of $\eta = 1 \times 10^{-6}$ molecules/photon is assumed to be achieved after 1000 A $\cdot$ *hrs* of beam conditioning. With this assumption, the desorbed gas load in the total arc length of 1521 m would be 1.3×10^{13} molecules/$(\text{s} \cdot \text{m})$ or 3×10^{-7} Torr $\cdot$ l/s $\cdot$ m. The linear pumping speed is designed to provide 100 l/s $\cdot$ m which results in an average pressure of approximately 3 nTorr. This capacity is achieved by pumping slots which provide a 10% opening between the antechamber and the beam channel. Near the location of the quadrupole magnets, large lumped TSP cartridges and ion getter pumps are foreseen.

Due to the high beam currents, the RF-shielded bellows are a critical element of the vacuum system design. The EIC will adapt the design that has been produced for the NSLS-II storage ring. The electrical contact is accomplished by fingers on the outside of the sleeve. (see Figure 1.12). Good contact is ensured by the use of spring fingers. The NSLS-II design has shorter and wider fingers compared to the bellows designed for the Advanced Photon Source. The gaps in-between fingers are minimized to avoid heating of the fingers by RF power leaking through the gaps.

Another critical element of the vacuum design is the RF seal of flange connections. The pre-conceptual design choice is to use soft RF springs. These require careful assembly and alignment to avoid steps and discontinuities in the vacuum chamber, which could lead to considerable impedance and beam heating.

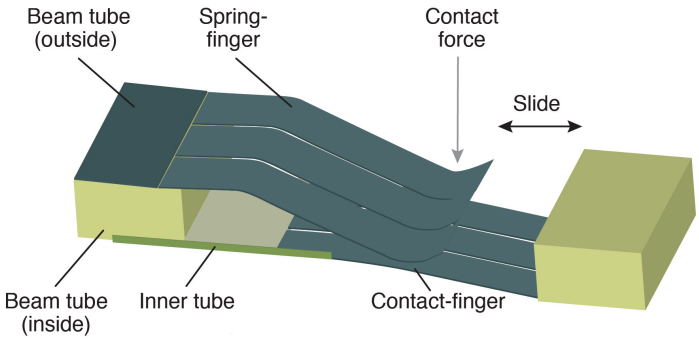

Figure 1.12: Schematic view of the bellow-finger concept.

1.11.5 ESR RF System

One parameter that by design choice limits the luminosity of the EIC is the RF power needed to compensate the synchrotron radiation loss in the ESR. Synchrotron radiation power is limited by design choice to 10 MW maximum in order to limit construction and operational cost. Current design parameters do not generate the full 10 MW at maximum luminosity, but the RF system is designed to accommodate it. The installed voltage requirement is determined by the maximum energy loss per turn at 18 GeV and the required bucket height. The current conceptual design calls for 17 1-cell, single cavity SRF cryomodules delivering a maximum of 4.0 MV each for 68 MV total installed voltage. Table 1.6 summarizes a few relevant parameters for 10 GeV and 18 GeV operations that determine the RF System.

Table 1.6: Summary of the EIC RF system requirements for 10 GeV and 18 GeV operations.

Parameter	10 GeV	18 GeV
Beam Current [A]	2.5	0.23
Energy Loss per Turn [MeV]	3.52	37.0
Synchrotron Radiation Power [MW]	8.4	8.8
Required RF Voltage [MV]	21.6	61.5

Superconducting RF cavities are chosen for several reasons:

- Operational cost saving. SRF requires negligible RF power for the cavities. A rough estimate of RF power required to drive NCRF cavities yields about 11 MW in addition to the 10 MW beam power, based on a 2-cell structure with a Q_0 of 3.0E4, a circuit (R/Q) of 100Ω per cell, and a voltage of 1 MV per cell. This doubles the overall CW RF power requirements compared with an SRF system, and adds an additional 11 MW of cooling load to the water system.

- SRF cavities have a much higher stored energy and are therefore much better suited to handle heavy beam loading conditions.
- The impedances which drive coupled bunch instabilities are much lower than they would be for a normal-conducting cavity system with the same RF voltage.
- The much higher operating gradient of superconducting cavities (16 MV/m vs. 2 MV/m for normal-conducting cavities) leads to an installed system requiring much less longitudinal space than normal-conducting cavities.

Superconducting RF systems are used in most light sources, and for example the Super KEKB electron-positron collider. Technical solutions for such cavity systems based on single-cell 500 MHz resonators exist. The designs are mature and the systems are in principle commercially available. The available systems are however, not optimized for high energy beam applications such as the EIC. While the systems would work technically, the solution would not be optimum from a cost point of view.

The ESR RF system is described in detail in Section 6.5 and summary parameters are shown here in Table 1.7

Table 1.7: EIC RF system parameters.

Parameter	Value
RF Frequency [MHz]	591
Number of cells per cavity	1
Number of cryostats	17
Maximum accelerating gradient [MV/m]	16
Total installed voltage [MV]	68
Maximum required RF voltage [MV]	62
Maximum operating power per input coupler [kW]	330
Number of input couplers per cryomodule	2
Total installed RF power [MW]	13.0
Number of RF power amplifier stations	34
HOM power per cryomodule [kW]	35
HOM absorber type	beam-pipe SiC
Beam pipe absorbers per cryostat	2

1.11.6 High Power RF Input Couplers and Power Amplifiers

The power delivered per cavity is very high and the choice was made to employ two power couplers per cavity rated for 400 kW CW operation. The coupler design is based on a high

power CW coupler originally designed and tested on the superconducting photo-cathode gun developed at BNL. The ESR coupler is a further development of this high power FPC. Operation at different electron beam currents and beam energies requires an optimized, variable coupling to avoid a large amount of reflected RF power. The optimum coupling varies by about a factor of 10 over the range of operating parameters. A "Reverse Phasing" of "RF Focus-Defocus (RF FODO)" operating mode has been studied and is under consideration. This mode, developed at KEK-B [37], is primarily aimed at reducing transient beam loading and optimal cavity detuning for reactive beam loading compensation. As such it has the beneficial side effect of reducing the required range of coupling and in principle could allow for fixed coupling to cover all operating scenarios depending on the overall optimization of system performance. This mode is discussed in both the RF Beam Dynamics and the ESR RF System sections of the CDR.

For the worst case beam loading scenario at 10 GeV, the expected maximum operating power of the couplers is about 330 kW each, traveling wave, with higher transient power resulting from the beam abort gap and other transient events. The couplers will be tested to 500 kW CW in full reflection. Figure 1.13 shows a 3D model of the ESR variable coupling high power input coupler.

RF power sources for the ESR cryomodules will be based on solid state power amplifiers (SSPAs). Solid state power has become very attractive in recent years with development spurred by the communication industry. It has become competitive in cost per watt and power density (when high voltage power supplies and other support systems for high power tube based systems are considered). The RF system includes a power margin of about 30% to allow for intentional non-optimal detuning (for stability), field regulation and transmission losses.

1.11.7 Crab Cavities

The EIC crab cavities, designed to operate at two frequencies, 197 MHz and 394 MHz, will be realized as superconducting Double Quarter Wave (DQW) or RF-dipole (RFD) Crab Cavities. These cavity types, designed and developed at the US (the DQW by BNL and the RFD by ODU, TJNAF and SLAC) and CERN for the LHC luminosity upgrade, have gone through a rigorous development program. While the frequency of the LHC crab cavity devices is 400 MHz, conveniently close to the 394 MHz EIC crab cavity frequency, the choice of 197 MHz frequency, as well as the tight EIC impedance budgets, brings design and engineering challenges.

At this time, a total of ten LHC-style crab cavities, five for DQW and five for RFD, have been built and tested with exceptionally good results. For each type, a proof-of-principle cavity built by Niowave Inc. and tested at BNL (DQW) and TJNAF (RFD), two prototype cavities built by Niowave through the LARP program and tested at TJNAF, and two prototype cavities of the same design built and tested at CERN.

While the superconducting crab cavity is the most critical element of the crabbing system, there are many other auxiliary subsystems that are challenging and critical for the

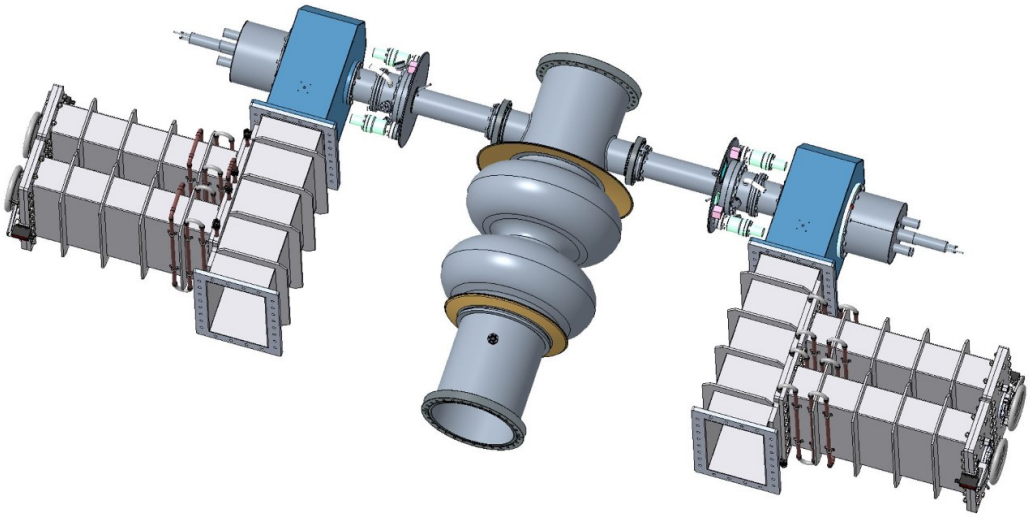

Figure 1.13: 3D model of the ESR 500 kW CW variable Q_{ext} power coupler. Two fixed coaxial couplers are shown attached to the cavity. The blue structures are the coax-waveguide doorknob transitions. These are attached to the waveguide tuner sections which are used to adjust the Q_{ext} of the couplers.

proper crabbing of the beam, including the liquid helium tank, HOM dampers, fundamental power and pickup couplers, mechanical cavity frequency tuner, as well as the crab cavity cryomodule. At this point all the subsystems mentioned have been built and successfully tested for the LHC DQW, and lessons learned from the LHC devices will be applied to the EIC design.

The ultimate test of any accelerator cavity is its performance in the presence of beam. This is particularly true for hadron crab cavities, since there has never been any previous implementation of crab cavities in hadron accelerators. For this reason, a complete system, including two fully dressed DQW with all the couplers and tuners in a cryomodule, has been installed at CERN in the SPS accelerator, as shown in Figure 1.14. Beam tests commenced in April 2018. During these tests no detrimental effects on the proton beam were observed. RFD cryomodule will be tested in SM18 (2022) and in the SPS (2023).

1.11.8 Civil Construction, Infrastructure, and Cryogenic System Upgrades

An important feature of the EIC is that, due to the significant existing RHIC infrastructure, a relatively small amount of new building square footage is required. There are 8 proposed new buildings, totaling 119,310 square feet. A new 42,130 square feet building in the IR10 location will house RF power amplifiers and supporting equipment for the ESR and the RCS. A new 29,560 square feet facility will be constructed in the IR2 straight section to house the electron pre-injection LINAC and the strong hadron cooling electron ERL with their associated laser systems and other support equipment at locally optimized points.

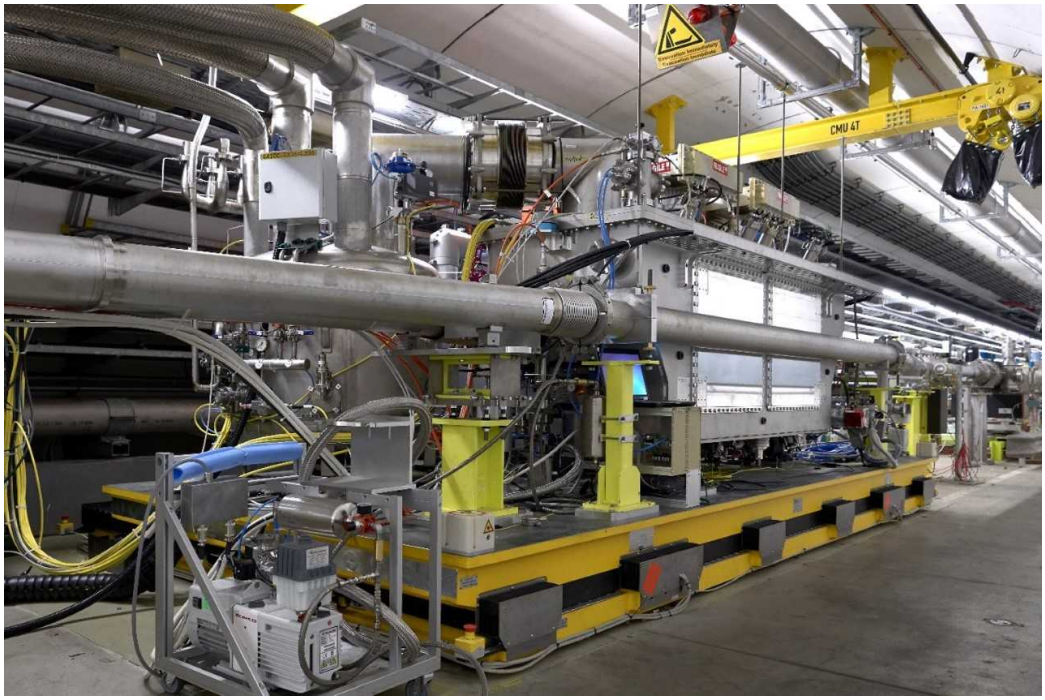

Figure 1.14: The LHC prototype twin DQWCC cryomodule installed in the SPS tunnel for beam tests (Photo Courtesy CERN).

The current operation of RHIC requires distributed cooling water systems located at (or near) the points of use. The EIC will however require a significant increase in cooling water capacity for the ESR vacuum chamber along with magnet and power supply cooling for the ESR and RCS. Each building will have HVAC requirements driven by the equipment and rack demand. The requirement for electron beam thermal stability will drive the design and installation of a new HVAC system for the tunnel. See Section 7.2 for details of buildings and utilities upgrades.

The existing central cryogenic plant will be used for cryogenic cooling for all of the EIC, but additional cryogenic support facilities will be required to support 2°K cooling of new superconducting RF equipment in IRs 2, 10, and 6. Cryogenic system upgrades are described in Section 6.10.

Existing site electrical power is currently sufficient for the needs of the EIC; however, the distribution system will require an upgrade to supply enough power to the new locations. A ”ring bus” style distribution is envisioned for the EIC, allowing for sections of the ring to be opened for maintenance operations without affecting downstream loads. A new 20 MVA main power transformer will be installed to support RF power demand. Backup power capacity will be installed in the form of diesel generators along with distributed UPS systems where required. Upgrades to the electrical utilities and systems are described in Section 7.3.

1.12 EIC Experimental Equipment

The EIC project scope includes a general purpose detector, and related equipment, capable of carrying out the core scientific measurements envisioned in the community White Paper [7] and subsequent studies. As described in Chapter 2 of this CDR, the detailed suite of measurements that comprise the experimental program place stringent requirements not only on accelerator performance but also on the detector configuration, which in turn is intimately connected to the design of the machine lattice in the interaction region, described in Section 2.5. A key requirement of such a detector is that it have very nearly complete angular coverage for outgoing particles (see Figure 1.15).

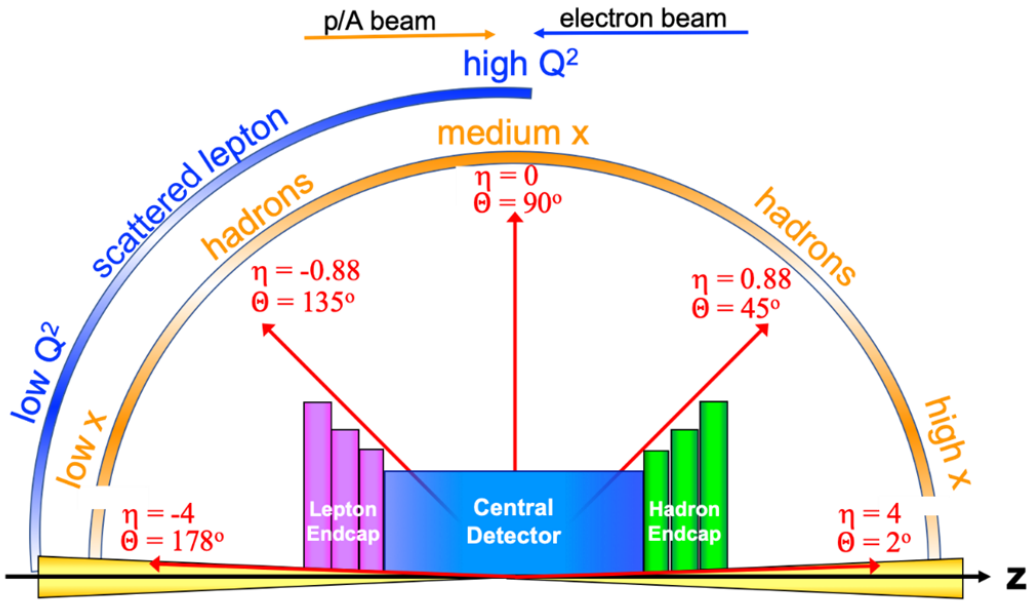

Figure 1.15: A schematic showing distributions of hadrons and the scattered leptons over kinematic regions of importance for detector coverage (See Section 2.5.1).

It is expected that the ultimate design of the detector will result from a proposal-driven community-wide effort, with a call for proposals expected in early 2021. In the meantime, the international EIC User Group (EICUG) has initiated a wide-ranging study of detector concepts and relevant technologies capable of meeting the EIC requirements. This activity will culminate in a "Yellow Report" whose completion is anticipated in January 2021 (http://www.eicug.org/web/content/yellow-report-initiative).

The on-going EICUG Yellow Report activity includes detailed simulations of the key electron-proton and electron-nucleus interaction processes, and relates current detector technologies and R&D efforts to the EIC requirements. This is seen as providing a basis and input for specific design proposals to come.

In Chapter 8 we draw upon this continuing work to outline in detail the design requirements for an EIC general purpose detector, taking account of the expected event geometries, collision rates, and corresponding backgrounds. A plausible "reference detector" is described, illustrating how components using current and developing technologies for particle sensors, readout, and data transfer might be configured to achieve the necessary measurement accuracy with the required statistical and systematic precision over the full kinematic range indicated in Figure 1.15. An isometric view of such a reference central detector is shown in Figure 1.16 (see Section 8.4 for detail). This reference detector is configured to match the IR design requirements outlined in Section 2.5, with the detailed IR design given in Section 3.2.

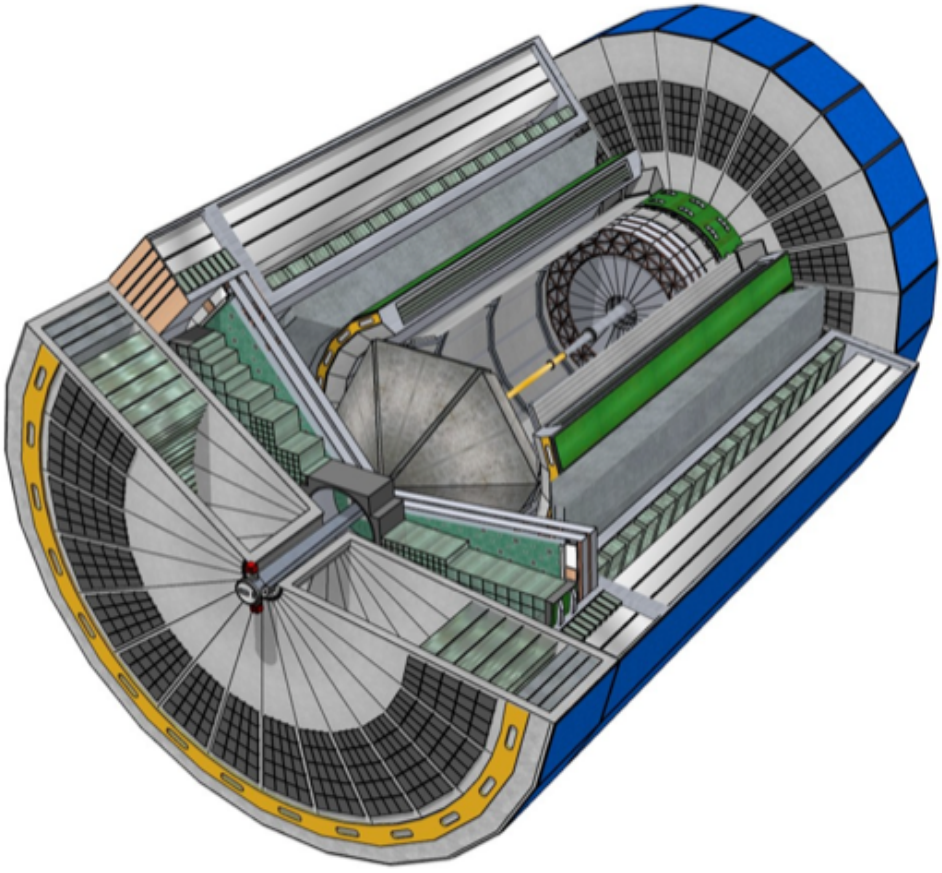

Figure 1.16: CAD drawing of the reference EIC central detector. The overall detector length is 9m ($\pm$4.5m). See Section 8.7.2.

Auxiliary detectors and procedures for lepton and hadron polarimetry are described, as well as the specific requirements for installation and maintenance of detector components in the existing experimental areas of the RHIC complex.

In keeping with the NSAC and NAS recommendations, the EIC is designed with the capa-

bility of having two intersection regions, with two detectors simultaneously taking data. While outside the present scope of the DOE-funded EIC project, there is considerable interest in the international scientific community for implementing a second detector whose capabilities would complement, in some way, those of the first. Appendix A describes a concept for a second IR design, optimized for maximum luminosity toward the lower end of the EIC range of collision energies.

1.13 Overview Summary

The EIC collider, as described in the conceptual design provides collisions of electron and hadron beams stored in two storage rings: the Yellow ring of the Relativistic Heavy Ion Collider (RHIC) and a new ESR with high luminosity of $L = 10^{34}\,\mathrm{cm}^{-2}\,\mathrm{s}^{-1}$ over a center-of-mass energy range from 20–140 GeV. The technical solution is based on accelerator physics and technology that is a moderate extrapolation of the state-of-the-art. Appendix B gives a detailed description of the hadron beams in the RHIC complex that are available for the EIC. The required modifications of RHIC are few and relatively inexpensive on the scale of the entire project. The challenge of the design lies in its implementation in an existing tunnel with existing infrastructure at a reasonable cost, which will require detailed planning. The final factor of two to three in luminosity requires strong hadron cooling, which will be realized by a novel scheme or by substantial extrapolation of existing technology. The main mitigation of the corresponding technical risk lies in the fact that a respectable luminosity of up to $4.3 \times 10^{33}\,\mathrm{cm}^{-2}\,\mathrm{s}^{-1}$ can be achieved without strong hadron cooling.

The electron injector complex consists of a polarized electron gun and 400 MeV S-band LINAC which will provide polarized electron bunches of 12 nC to the rapid cycling synchrotron in the RHIC tunnel. This large synchrotron is to be constructed with normal-conducting magnets and both SRF and NCRF systems. The critical requirement is high spin transparency for the polarized beam. This has been taken into account by special design features and has been tested by extensive simulations.

The anticipated performance of the collider has been addressed by a comprehensive accelerator physics design study. The design allows for two large-solid-angle detectors utilizing the existing experimental areas now occupied by the RHIC detectors STAR and sPHENIX. Final parameters are chosen such that the design values and values are less than the maximum values predicted from simulations and experiments. In that sense, the presented solution should be considered as robust and realistically achievable. While there are no components that require completely new technical concepts, several components are at state-of-the-art or slightly beyond present technology. The list of these components includes special superconducting magnets in the interaction regions with large apertures. Other advanced components are 2-cell superconducting cavities with 1 MW of input power and variable coupling of the forward power couplers. Strong hadron cooling requires a CW electron source which can reliably deliver 100 mA of beam current.

Chapter 2

EIC Science and Requirements for Machine Design

2.1 Introduction

The science mission of the Electron-Ion Collider is to provide us with an understanding of the internal structure of the proton and more complex atomic nuclei that is comparable to our knowledge of the electronic structure of atoms. Unlike the more familiar molecular and atomic structure, the interactions and structures are not well separated in protons and other forms of nuclear matter, but are inextricably mixed up, and the observed properties of nucleons and nuclei, such as mass and spin, emerge out of this complex system.

2.1.1 EIC Physics and Accelerator Requirements

A consensus study report of the National Academies of Sciences, published in 2018, on an **Assessment of U.S.-based Electron-Ion Collider Science** [9], recognized this and concluded "EIC science is compelling, timely and fundamental". The NAS study further found that "An EIC can uniquely address three profound questions about nucleons — neutrons and protons — and how they are assembled to form the nuclei of atoms:

- How does the mass of the nucleon arise?
- How does the spin of the nucleon arise?
- What are the emergent properties of dense systems of gluons?"

They also concluded that "These three high-priority science questions can be answered by an EIC with highly polarized beams of electrons and ions, with sufficiently high luminosity and sufficient, and variable, center-of-mass energy."

This reinforces the unique accelerator requirements of the Electron-Ion Collider, requiring a large luminosity, $10^{33--34}\,\mathrm{cm}^{-2}\mathrm{s}^{-1}$ over a large and variable range of center-of-mass energies, between 20 and 140 GeV, high electron and (light) ion beam polarizations of above 70%, and a large range of accessible ion beams, from deuterium to the heaviest nuclei (uranium or lead). It should be understood that the required electron polarization is longitudinal, whereas the polarization requirement for protons and light ions is for both longitudinal and transverse. Due to the broad science program foreseen at the Electron-Ion Collider, the possibility to have a second interaction region and associated detector was emphasized in the report.

As stated in the National Academy of Sciences Committee recommendations, "a central goal of modern nuclear physics is to understand the structure of the proton and neutron directly from the dynamics of their quarks and gluons, governed by the theory of their interactions, quantum chromodynamics (QCD), and how nuclear interactions between protons and neutrons emerge from these dynamics." The scientific program of the Electron-Ion Collider (EIC) is designed to make unprecedented progress towards this goal.

The EIC can be seen as a microscope to image the 3D QCD structure of protons, neutrons and other hadrons — composite systems of quarks and gluons, and their intrinsic dynamics and correlations that lead to mass, spin, and other emergent properties. The EIC would explore the QCD landscape over a large range of resolution (Q^2) and quark/gluon density ($1/x$), from the region where visible matter is (mostly) quark systems built from up, down and strange quarks to a gluon-dominated region. Heavy nuclei are critical to explore the high-density gluon matter.

2.1.2 Interaction Region and Detector Requirements

Beyond the unique accelerator requirements, EIC science also leads to a unique set of detector requirements, and a novel **fully** integrated detector and interaction region scheme. **All** final state particles carry information about the 3D QCD structure of nuclear matter and the emergent phenomena. Therefore, it is essential that the interaction region and the detector at the EIC are designed so all particles are identified and measured at as close to 100% acceptance as possible and with the necessary resolutions.

The basic physics process at the EIC is Deep Inelastic Scattering (DIS), which is represented in Fig. 2.1. An ion, composed of nucleons, which are in turn composed of partons (quarks and gluons), moves in one direction and collides with an electron moving in the other direction. The electron collides with a parton within the ion in a hard collision.

We qualitatively define three classes of particles in the final state:

- The scattered electron,
- Particles associated with the initial state ion, and
- Particles associated with the struck parton.

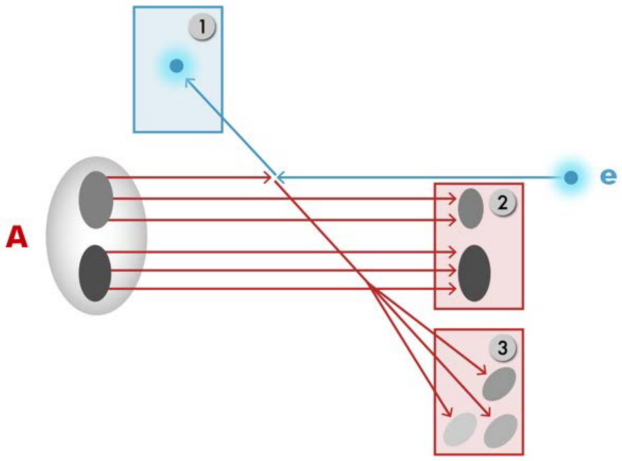

Figure 2.1: Classification of the final-state particles of a DIS process at the EIC: scattered electron (1), the particles associated with the initial state ion (2), and the struck parton (3).

The difficulty in achieving good acceptance in the forward regions at a collider has to do with the accelerator elements needed to deliver the colliding beams. To first order, the luminosity at the interaction point is inversely proportional to the distance between the nearest quadrupole magnets. On the other hand, the closer the beam elements are to the interaction point, the more they obstruct the acceptance at shallow angles with respect to the beam axis, and restrict the acceptance for forward particles. This complicates achieving close to 100% acceptance for all three types of particles, but especially the particles associated with the initial state ion.

This leads to a unique and novel integration of the detector in the interaction region, extending over a large region (± 40 m) beyond the main detector. It also should be pointed out that any change has impact on a wide variety of systems, from beam dynamics to accelerator performance to magnet engineering requirements to detection capability — the latter in terms of (gaps in) acceptance, particle identification and resolutions.

Further integration is required for ancillary measurements to deliver on the EIC science program, such as those to absolutely determine the longitudinal electron and longitudinal and/or transverse proton/light-ion polarizations with beam polarimeters, with good systematic (order 1%) understanding. For the electrons a transverse polarization measurement is not a requirement but often useful to underpin the systematic understanding of the spin direction. Further, the exact frequency of electron-ion collisions per second must be experimentally determined with luminosity monitors with again a goal of better than 1% understanding. Both of these goals are non-trivial, with beam dynamics potentially impacting long-time averaging methods.

The central detector region of the EIC is designed to measure those final state particles from the hard collision between the electron and the parton in the ion (particles of types 1 and 3 in Fig. 2.1) and is very much like the traditional collider detectors. The EIC central

detector needs to provide the measurements to determine Q^2 and x variables of the electron scattering kinematics (or, the resolution Q^2 and quark/gluon density $1/x$ of the QCD landscape). The central detector is divided into three sections, the Electron-endcap, the Hadron-endcap and the Barrel. The three different central detector sections correspond to different x and Q^2 regions for the scattered electron.

Beyond determination of x and Q^2, measurement of two transverse kinematics degrees of freedom (transverse momentum and impact parameter), as well as flavor identification of the partonic collision is central to the 3D QCD nucleon and nuclear structure program planned for the EIC. The energy scale of the transverse kinematics is $\sim$200 MeV/c. This means that identification and precise measurements of single hadrons among the particles associated with the scattered partons (Particles of type 3 in Fig. 2.1) are also needed in the central detector.

Crucial information on hadron structure is carried by particles that do not emerge from the beam envelope within the coverage of the central detector. Broadly speaking, there are two types of forward final state particles that need to be reconstructed. The first type of forward particles comes from interactions in which the beam particle receives a large transverse momentum kick and fragments into many parts. These particles typically retain a velocity similar in magnitude, but with significantly different kinematics, from that of the incident beam particle and may have very different charge-to-mass ratios. Such particles will separate relatively rapidly from the beam. An example of such a particle is a forward proton from a deuteron-electron DIS, a process that can give information on QCD neutron structure (inside a deuteron) comparable to QCD proton structure. Another example are forward neutrons.

The second type is a (hadron) beam particle that stays intact during the collision, only loses a small fraction of its longitudinal momentum, and acquires a small transverse momentum. These particles are for example protons or ions in non-dissociative diffractive interactions and will have a trajectory that is close to the proton (ion) beam. To map these types of forward final state particles, a highly-integrated extended ("far-forward") detector region is defined downstream of the ion beam, and after the beam final-focusing elements, covering about 30 m. The far-forward detector region together with the central detector provides essential near-complete coverage for final state particles associated with the incident ion beam particle.

Similarly, the "far-backward" detector region is highly integrated to capture a third type of measurements, those close to the beam line in the electron-beam direction. This allows to monitor the luminosity as well as to significantly increase the low-Q^2 coverage of the detector. Electron-ion collisions where the electron is scattered through a very shallow angle corresponds to the case where the exchanged photon is almost real. Such photoproduction processes are of interest in their own right but also can allow a program of spectroscopy.

The science program at the electron-ion collider (EIC) has the potential to revolutionize our understanding of 3D QCD nuclear and nucleon structure. It will also explore new states of QCD. In order to maximize the potential of an EIC, it is important to have a large (near-100%) acceptance not only in the central region, but also in the region that is

close to both the ion-beam and electron-beam direction — i.e. a total acceptance detector is needed. There has never been a collider detector that has both the central and forward (or backward) acceptances maximized in tandem, and this design is uniquely suited to the EIC physics program.

2.2 EIC Context and History

Half a century of investigations have revealed that the neutrons and protons (nucleons) that make up the atomic nucleus are composed of more basic constituents, the quarks and gluons, with their interactions mediated by the exchange of gluons. Their discovery has led to the development of the fundamental theory of strong interactions, quantum chromodynamics (QCD). QCD attributes the forces among quarks and gluons (collectively called partons) to their color charge. In contrast to quantum electrodynamics, where the force carriers (photons) are electrically neutral, gluons carry color charge and therefore do self-interact.

As a consequence of QCD, the internal structure of nucleons consists of a complex dynamical system of valence quarks immersed in a quantum sea of virtual quarks, antiquarks, and gluons, a system unlike any other heretofore observed in nature. The spin of the nucleon is not a simple sum of the spins of the valence quarks, but also includes significant contributions from this quantum sea. The mass of the nucleon is not the sum of its constituent partons (which is near zero), but emerges from interactions among the valence quarks, antiquarks, and gluons.

Understanding the structure of nucleons and nuclei, as well as their properties such as spin, mass, and nucleon-nucleon interactions from the properties and dynamics of quarks and gluons is a central goal of nuclear science. Decades of work in high energy physics and nuclear physics to probe the nature of matter at the QCD level has revealed a rich tapestry with many detailed answers, but the most fundamental questions remain unsolved, entailing many opportunities for new discoveries. The Electron Ion Collider (EIC) is conceived with unique capabilities to explore this new realm of discovery for understanding the fundamental role of QCD in the observed structure of matter.

The dynamical interactions between quarks and gluons have profound consequences, such as the generation of the nucleon mass. They also result in a little explored domain of matter where gluons dominate the nuclear wavefunction. Hints of this domain have been seen in nuclear collisions at RHIC and the LHC where the nuclei collide at nearly the speed of light. Similar hints have been obtained from prior electron-proton scattering at HERA. The corresponding strong color fields are at the heart of many poorly understood emergent phenomena in QCD, such as confinement, properties of the quark gluon plasma, and the origin of nucleon spin. A quantitative study of matter in this domain of gluon dominance is a central goal of the EIC.

In the last two decades, nuclear physicists have developed new phenomenological tools that show promise of realizing tomographic images of the quarks and gluons inside polar-

ized and unpolarized protons and neutrons. These tools are being utilized now and will be further refined in the next few years to study the valence quark and the start of the sea-quark region in the nucleon using the 12 GeV CEBAF at TJNAF and the COMPASS experiment at CERN, respectively. However, our knowledge of the nucleon will be far from complete without the investigation of the gluon dominated region within it. While high-energy polarized and unpolarized hadron-hadron collisions at RHIC and the LHC have initiated the exploration of this gluon-dominated regime, the EIC will complement these studies by simultaneously bringing the precision of the well-understood electromagnetic probe, polarized beams, and high energies to the study of the gluon dominated region. As one increases the energy of the electron-nucleon collision, the deep inelastic scattering process probes regions of progressively higher gluon densities. However, the density of gluons inside a nucleon must eventually saturate to avoid an indefinite rise in the strength of the nucleon-nucleon interaction. How this exactly happens in QCD is unknown. Unambiguous evidence of this saturated gluon density has so far eluded us, although tantalizing hints at RHIC and the LHC have been observed. Experimental design limitations of the past are being specifically addressed in the design of the EIC in order to study this remarkable form of matter; this will be facilitated by electron collisions with heavy nuclei, where coherent contributions from many nucleons effectively amplify the probed gluon density.

The scientific goals and the machine parameters of the EIC were first agreed upon in deliberations at a community-driven program held at the Institute for Nuclear Theory (INT) [38]. They were further refined and summarized in the EIC White Paper [7]. The EIC science goals were set by identifying critical questions in QCD that remain unanswered despite the significant experimental and theoretical progress made over the past decades, and would remain unanswered unless the EIC is realized. Those science goals and the consequent machine parameters for the EIC were supported in the 2015 NSAC Long Range Plan (LRP) [8] leading to the recommendation for the EIC as the "highest priority new facility" to be constructed in the US by DOE's Office of Nuclear Physics.

The EIC machine design presented in this document addresses all the scientific goals that were identified by the broader community [7, 8, 38, 39] as the most compelling questions in QCD that the future Electron Ion Collider must address. During 2017 an independent assessment of the science of EIC was conducted by a panel convened by the National Academies of Sciences, Engineering, and Medicine [9]. The report strongly endorses this program, noting that it addresses profound scientific questions central to nuclear physics research while also advancing U.S. leadership in accelerator science and technology.

In parallel to growing the science case addressed by the EIC, there has been a vibrant R&D program [40] developing the detector technologies needed for a state-of-the-art compact collider detector. Over the years several consortia have been established to address the challenges in tracking, calorimetry and particle identification detectors both at mid-, backward and forward rapidities. Following the trends from the Large-Hadron Collider (LHC) in data acquisition (DAQ) also at EIC one is investigating a free streaming DAQ, thus eliminating any trigger and providing a large potential for not yet anticipated physics ideas. In addition emphasis was given to integrate all the ancillary detectors along the lepton and hadron beamlines into the wider interaction region.

2.3 The Science Goals of the EIC and the Machine Parameters

In this section, we present a few selected topics among the set of compelling questions in QCD that led to the recommendation for construction of an EIC in the NSAC process, and summarize the machine parameters that are needed to address them.

The key scientific questions that the EIC could address are:

1. How are the sea quarks and gluons, and their spins, distributed in space and momentum inside the nucleon? How do nucleon properties emerge from them and their interactions?

2. How do color-charged quarks and gluons, and jets, interact with a nuclear medium? How do the confined hadronic states emerge from these quarks and gluons? How do the quark-gluon interactions create nuclear binding?

3. How does a dense nuclear environment affect the quarks and gluons, their correlations and their interactions? What happens to the gluon density in nuclei? Does it saturate at high energy, giving rise to a gluonic matter with universal properties in all nuclei and even nucleons?

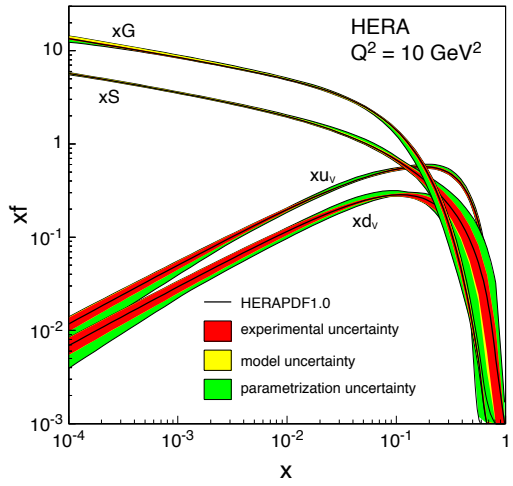

Figure 2.2: The gluon (xG), sea (xS) and valence quarks (x u_v and x d_v) distributions as extracted from the data collected at HERA along with their uncertainties. Domination of gluons at $x \leq 0.1$ is evident.

Figure 2.2 depicts the parton distribution functions extracted from *e+p* scattering data from the HERA collider at DESY. To leading order, these functions represent the probability density for finding a particle with a certain longitudinal momentum fraction x at resolution scale Q^2. The plots show the valence quark, sea quark, and gluon distributions extracted from the data. The most surprising feature of this result was the rapid rise of the gluon

distribution with decreasing x, indicating that gluons dominate the proton's wavefunction at high energies.

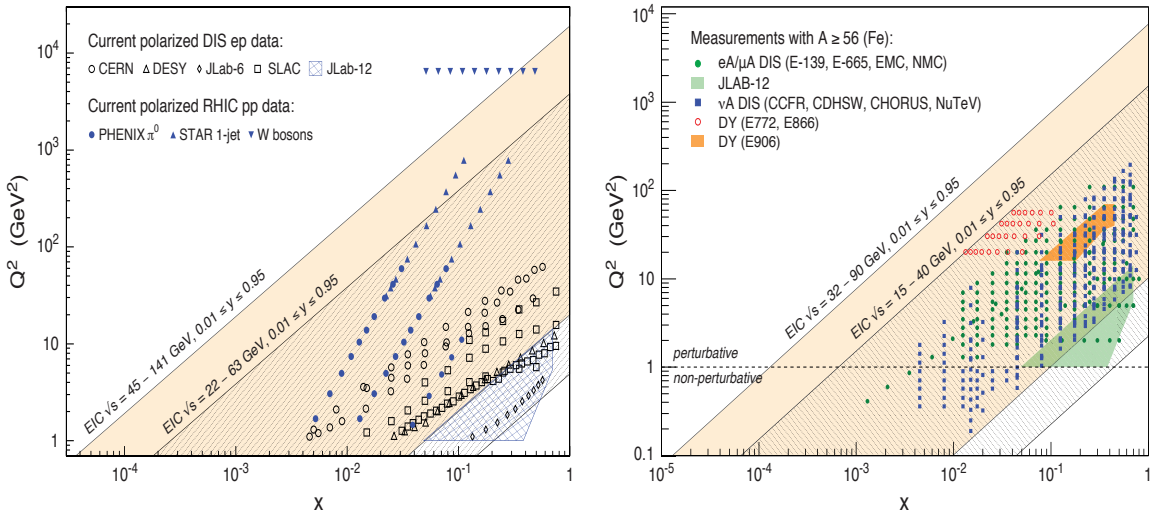

Figure 2.3: Left: The x-Q^2 range covered by the EIC with two different center-of-mass energy ranges in comparison with past and existing polarized e+p at CERN, DESY and SLAC and p+p experiments at RHIC. Right: the kinematic range in x-Q^2 for lepton-nucleus deep inelastic scattering and Drell-Yan (DY) experiments and future CEBAF 12 GeV experiments in comparison with the EIC.

The EIC design described in this document covers a center-of-mass energy range for the e+p collisions of $\sqrt{s}$ of 29 to 140 GeV. The kinematic reach in x and Q^2, the momentum transferred by the electron to the proton, is shown in Figure 2.3. The diagonal lines in each plot represent lines of constant *inelasticity*, y, which represents the ratio of the virtual photon's energy to the incoming electron's, in the target rest frame. The variables x, Q^2, y and s are related to each other by a simple equation $Q^2 = sxy$. Since the EIC is being designed to study the domain of gluon dominance in the proton, it has to have a substantial energy reach to access the low-x region ($x \propto 1/s$). The left figure shows the kinematic acceptance for polarized and unpolarized e+p collisions, and the right figure shows the acceptance for e+A collisions. Also shown for comparison is the reach of past and current fixed target facilities that acquire comparable data sets, and in case of the left plot, polarized p+p collisions from RHIC. Note that there are no data from past or current experiments in the region of $x < 5 \times 10^{-3}$. The two figures establish that the EIC would, for the first time, allow us to explore significantly lower values of x where the role of gluon degrees of freedom is enhanced.

The details of the science case for the EIC have been presented in the EIC White Paper [7]. In what follows, we describe, in greater detail, the compelling scientific questions outlined above, and motivate the requirements for the machine parameters that would help us address these questions.

2.3.1 Nucleon Spin and Imaging

Nucleon Spin

Understanding the nucleon spin in terms of its components, quarks, anti-quarks, gluons, and the dynamics resulting from color interactions, has been an important goal for nuclear scientists over the past five decades. The nucleon spin can be split into its components [41]:

$$\frac{1}{2} = \frac{1}{2}\Delta\Sigma(Q_f^2) + \Delta G(Q_f) + L_{Q+G}(Q_f) \tag{2.1}$$

where $\Delta\Sigma$, ΔG, and L are the contributions from quarks and anti-quarks, gluons, and their angular momentum to the nucleon spin. They are evaluated at a fixed scale Q_f and summed over the whole x range from 0 to 1. The discovery by the EMC experiment at CERN in the 1980s, that the quark and anti-quark spin alignment ($\Delta\Sigma$ in the equation above) could not explain the nucleon's spin, brought this fundamental issue into the limelight. Since then, numerous fixed target polarized electron/muon scattering experiments and polarized proton collisions at RHIC [42] have confirmed that the spin alignment of quarks+antiquarks, and gluons, in the covered kinematic region ($0.001 \leq x \leq 0.6$) does not explain the nucleon's spin, thus providing indirect evidence for a potential contribution from parton orbital angular momenta, L_{Q+G}. The largest uncertainties in $\Delta\Sigma$ and ΔG come from the unmeasured regions of $x < 5 \times 10^{-3}$, where no data exist. With measurements in this region, the EIC will provide precise measurements of $\Delta\Sigma$ and ΔG that will resolve the spin components of the proton [7, 39, 43].

Figure 2.4 illustrates the potential impact of the EIC on reducing the uncertainty in knowledge of the unmeasured region assuming the $\sqrt{s}$ range indicated in the figure. The EIC will significantly reduce the uncertainty in the knowledge of $\Delta\Sigma + \Delta G$ for $10^{-6} < x < 10^{-3}$ (y-axis), as well as in the contribution from orbital angular momentum in the range $10^{-3} < x < 1$ (x-axis). It is evident from this plot that the higher center-of-mass energy is required to make measurements for which the errors are much smaller than the individual contributions. For the EIC measurements of $\Delta\Sigma$ and ΔG inclusive DIS longitudinally polarized double spin asymmetries are necessary where the scale dependence of asymmetries measured at the same x but different Q^2 provides information to the gluon spin contribution.

In addition, the role of sea quark helicities and their contribution to the total spin has been only slightly addressed at moderate to high momentum fractions so far. In particular the role of strange quarks, an entire sea object, is still very unclear and has so far mostly been obtained via hyperon decay constants and the assumption of SU(3) flavor symmetry. Using those assumptions, a substantial negative contribution is found in global fits (reducing the contribution of $\Delta\Sigma$ to the proton spin) while no direct indication of such a behavior was seen in semi-inclusive DIS measurements so far. DIS measurements in which final-state hadrons are measured (in addition to the scattered electron), are commonly referred to as "Semi-Inclusive DIS" (SIDIS) measurements. Using SIDIS measurements at the EIC will enable the direct determination of the strange and other sea quark helicities with the help of fragmentation functions. Especially the fragmentation of partons into kaons, which

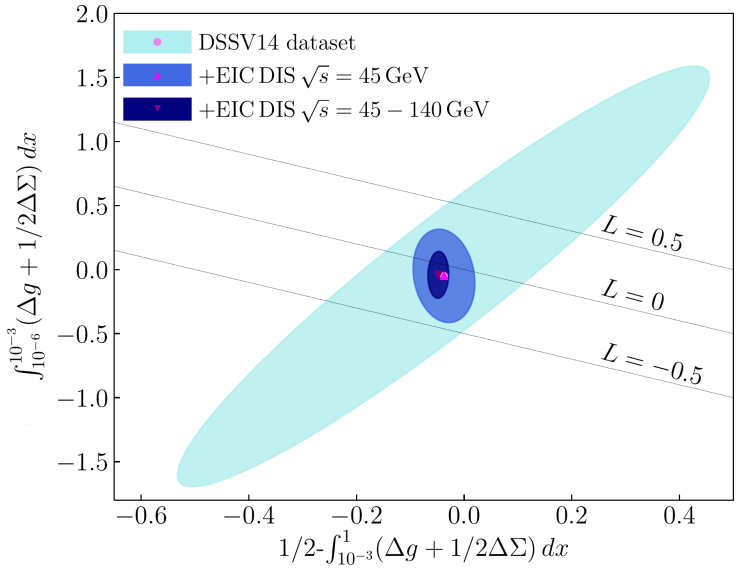

Figure 2.4: The impact of different center-of-mass energies on our knowledge of the sum of quark and gluons' helicity contributions in the range $10^{-6} < x < 10^{-3}$ (vertical axis) versus the contribution from the orbital angular motion in the range $10^{-3} < x < 1$ (horizontal axis). The calculations are shown at a fixed scale of $Q_f^2 = 10\,\text{GeV}^2$ [39].

contain a strange quark as valence flavor, enhances the sensitivity to the strange helicities. Figure 2.5 displays the expected uncertainties of various sea quark helicities as a function of x when not only including EIC DIS but also semi-inclusive DIS data. One can clearly see that the impact on the sea quark helicities greatly improves under the inclusion of SIDIS EIC data.

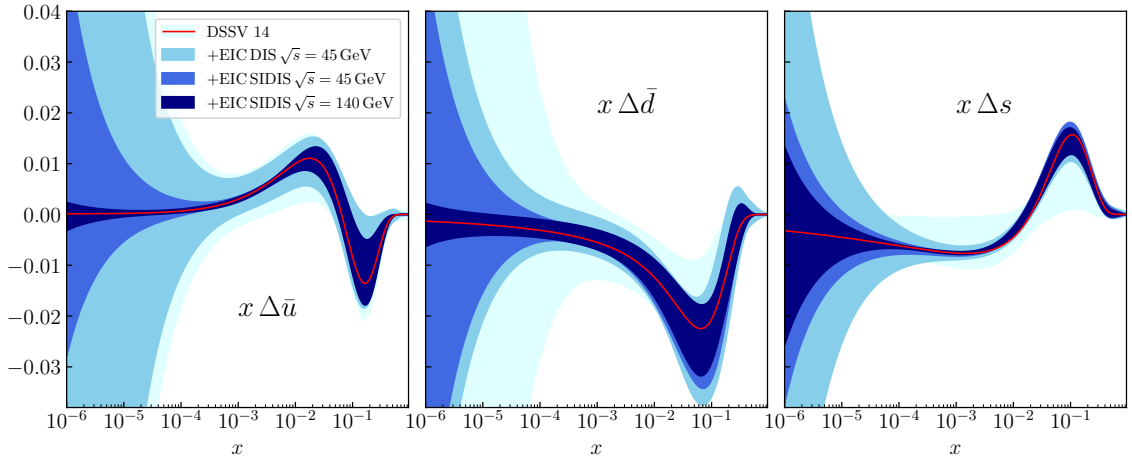

Figure 2.5: The impact of the EIC measurements on the sea quark helicity distributions as a function of x. From left to right, the anti u-quark, anti d-quark and strange quark helicities are displayed including their expected uncertainties. [44].

Machine and Detector Requirements For Polarized Inclusive and Semi-inclusive Deep Inelastic Scattering

Obtaining double longitudinal spin asymmetries require measuring inclusive deep inelastic scattering (DIS) with longitudinally polarized electrons off longitudinally polarized protons. Typically, 70% beam polarization was assumed in the conducted simulations. Most studies were performed assuming a data set with integrated luminosity $L = 10$ fb^{-1}, and it was shown in [39, 43] and references therein that the statistical uncertainties at this luminosity are considerably smaller than the current theoretical uncertainties. Experimental systematic uncertainties, coming from polarization measurements and other (time dependent, detector related) false asymmetries in measurements would then have to be constrained to a few percent [45]. Similar measurements using polarized ^{3}He or deuteron are needed to obtain full flavor separation of the spin structure. The machine requirements are similar to the ones discussed for the proton except for the need of neutron rich polarized nuclear beams. In addition, this science program will need high center-of-mass energies and an integrated luminosity of at least 10 fb^{-1}.

As will be discussed in more detail later, the scattered DIS leptons can be predominantly found in the backward endcap region, the central detector region and, at high x and Q^2, also the forward region. In the latter case using the total hadronic final state or combined methods are often required to determine the DIS kinematics well enough. Final state hadrons needed for the semi-inclusive measurements range from the forward regions with high momenta of up to 70 GeV at the higher collision energies to the backward endcap region and generally smaller momenta. For the flavor sensitivity to the sea quark helicities, pions and kaons need to be cleanly identified in the detector.

Imaging The Confined Motion Of Quarks

Experiments with collisions of electrons on transversely polarized protons, deuterons (D), or helium (^{3}He) targets, have measured single spin azimuthal asymmetries for various identified hadrons over a broad range of kinematics. Similar effects have been observed and studied in singly polarized p+p collisions. The commonly accepted origin of these asymmetries are the correlations between the transverse momentum of quarks and their spin, as well as the spin of the parent nucleons. Therefore a full picture of the nucleon has to include the transverse spin and momentum distribution of partons in addition to their longitudinal one.

SIDIS and polarized p+p measurements over the past decade, have allowed scientists to formulate a framework in which the measurements of single spin azimuthal asymmetries for different identified hadrons are connected to the transverse momentum distribution (TMD) of partons, *i.e.*, their confined motion inside the nucleon and to its transverse spin contribution. These TMDs incorporate the correlations between the motion of partons, their spin, and the spin of the parent nucleon. These correlations arise from spin-orbit coupling among the partons about which very little is known to-date. One can define eight types of TMDs [46] based on the different combinations of quark and nucleon spin

orientations, and a similar set of eight TMDs for gluons—all of which need to be mapped out if one is to gain full knowledge of the 3D momentum and spin structure of the nucleon. As these measurements mostly require hadrons in the final state, also similar sets of TMD fragmentation functions are involved in order to access these distributions.

The data sets used to constrain TMDs are currently more limited in x and Q^2 than the measurements shown in Figure 2.3 (left) used to constrain the helicity PDFs. With its polarized beams and high energy, the EIC will dramatically advance our knowledge of TMDs. One will be able to map out the 2+1 dimensional momentum structure of the different quark flavors and gluons inside nucleons over a wide region in x and Q^2 [7,47].

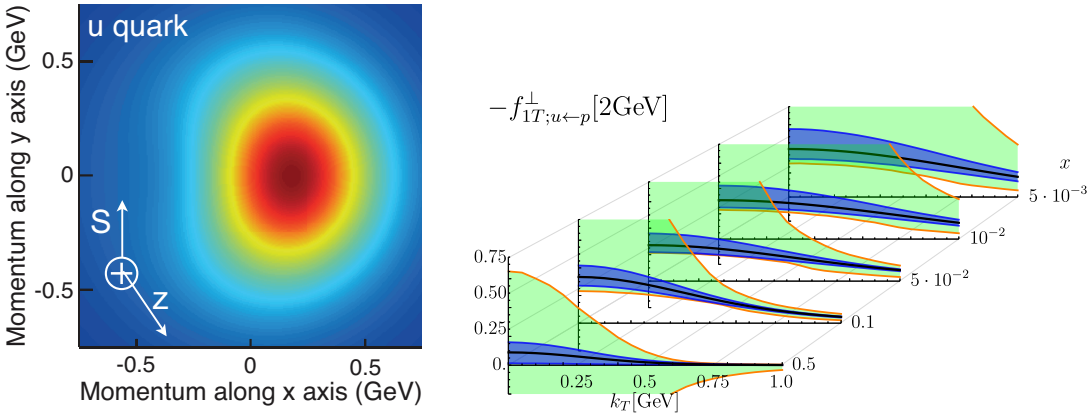

Figure 2.6: Left: The transverse momentum distribution of an up quark with longitudinal momentum fraction $x = 0.1$ in a transversely polarized proton moving in the z-direction, while polarized in the y-direction. The color code indicates the probability of finding the up quarks. Right: The transverse-momentum profile of the up quark Sivers function at five x values accessible to the EIC, and corresponding statistical uncertainties.

Figure 2.6 (left) depicts the transverse-momentum distribution of up quarks inside a proton moving in the z-direction (pointing out of the page) with its spin polarized in the positive y-direction. The colors represent the probability of finding the *up* quarks for the given momenta. The anisotropy in transverse momentum is described by the Sivers distribution function [7,48,49], which describes the correlation between the proton's spin direction and the motion of its quarks and gluons. While the figure is based on a preliminary extraction of this distribution from current, limited, experimental data and the expected precision at an EIC, nothing is known about the spin and momentum correlations of the gluons and sea quarks. The achievable statistical precision of the quark Sivers function from EIC kinematics assuming an integrated luminosity of 10 fb^{-1} is shown in Figure 2.6 (right). Currently no data exist for extracting such a picture in the gluon-dominated region in the proton or in light nuclei. For (sea)quark related Sivers function measurements semi-inclusive single spin asymmetries for certain azimuthal correlations of hadrons and nucleon spins around the virtual photon direction are required. To single out gluon processes to access the gluon Sivers function, nearly back-to-back pairs of jets or heavy flavor

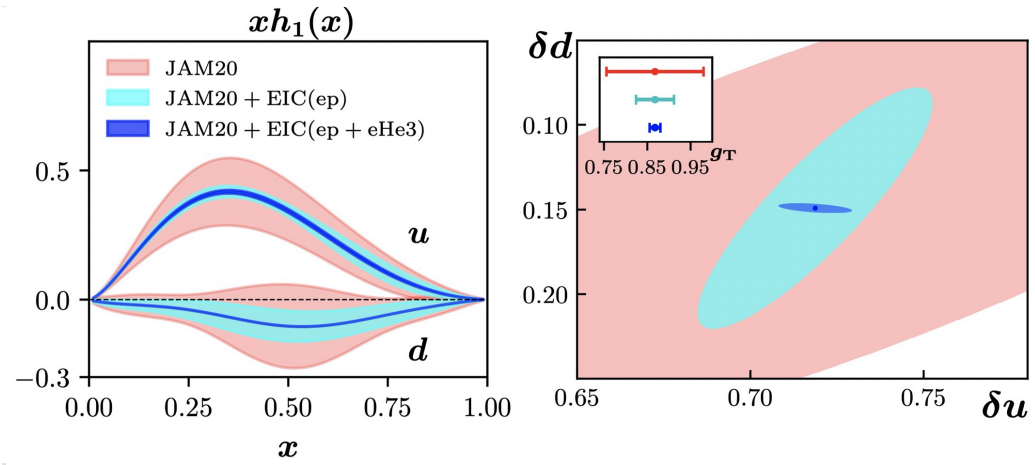

Figure 2.7: Expected up and down quark transversity distributions (left) and tensor charges (right) at an EIC in comparison to current extractions [50].

hadrons are required where the transverse spin dependent transverse momentum imbalance relates to the gluon Sivers function. The EIC will be crucial to realize such a program. Similarly important is the transverse spin distribution of quarks inside a transversely polarized nucleon which also requires the use of TMD or di-hadron fragmentation functions despite not being an explicitly transverse momentum dependent object itself. The integral over x is also called the tensor charge of the nucleon which may be connected to physics beyond the standard model. The current experimental precision is very limited and still requires various phenomenological assumptions, but the comparison of the tensor charges extracted from the EIC and from lattice QCD simulations may be sensitive to such physics. While the tensor charges are expected to be valence dominated, only the full integrals over a large range in x will remove the extrapolation uncertainties that current and future fixed-target measurements have and complement them. The expected precision on the transversity distributions and tensor charges for up and down quarks is shown in Figure. 2.7 in comparison to current extractions [50] with a precision that would exceed lattice calculations.

In addition to extracting the transverse spin and momentum picture of the nucleon, substantial theoretical interest lies in understanding the scale dependence of explicitly transverse momentum dependent functions. Unlike the collinear case that is well understood, there are plenty of open questions that can only be answered by a machine such as the EIC that has a large range of scales while covering transverse momenta from low, non-perturbative, to high, perturbative, regions.

Machine Requirements For TMD Measurements

Measurements of transverse momentum dependent distribution and fragmentation functions require longitudinally and transversely polarized hadron beams colliding with (un)polarized electrons. Simulations to investigate the degree to which the EIC can con-

strain the Sivers and other TMD functions assumed 70% transverse polarization of the proton beam [7]. As mentioned earlier, semi-inclusive DIS implies the identification of final state hadrons in coincidence with the scattered electrons. There is already experimental evidence for flavor dependence, namely, a dependence on the type of quark involved in the collision, of the different TMDs. These measurements require that the hadron type in the final state be identified, in order to tag the flavor of the parton as up quarks are more likely to fragment into positive pions, down quarks into a negative pion and strange quarks into kaons. To obtain a detailed understanding of the eight different quark and gluon TMDs, one needs to bin the experimental observables in multiple variables, such as x, Q^2, y, p_T, z and $\phi_{S,h}$ simultaneously, where p_T is the hadron transverse momentum and z is the momentum fraction of the final state hadron, both with respect to the virtual photon. $\phi_{S,h}$ are the azimuthal angles of the incoming nucleon spin and the outgoing hadron around the virtual photon direction evaluated relative to the lepton scattering plane. The smooth coverage of all azimuthal angles for the given other kinematic variables requires a homogeneous detector with as little gaps as possible. Mapping the TMDs in multiple dimensions will require larger statistics than for inclusive measurements. To fully disentangle the flavor dependence of the various TMDs, it is important to collect data with neutron rich transversely polarized beams, such as ^{3}He or D with equivalent experimental conditions. Each of these collider operating modes will need an integrated luminosity (or significant fraction) of 10 fb^{-1}. There is an obvious redundancy in the data sets. For example, unpolarized target conditions could be achieved by combining oppositely polarized longitudinal or transverse data sets, thus running the collider effectively for two physics programs simultaneously. However, despite such opportune simultaneity in data taking, it is anticipated that the systematic program of measurements essential for the complete mapping of TMDs will require large collective integrated luminosities (a couple of 10 fb^{-1}) at various collisions energies for different hadron beams and their spin orientation [7]. The wide range in $x - Q^2$ provided by the EIC is essential for mapping the TMDs. To explore gluon TMDs, access to the gluon dominated low-x region is critical and requires both high energy ($\sqrt{s} \geq 100\,\text{GeV}$) and a large luminosity [47, 51].

Imaging the Transverse Spatial Distribution of Partons

As in the case of the transverse momentum distribution of partons inside a hadron, we know little about what a hadron looks like in transverse spatial dimensions. Many of our expectations are solely based on models. In some cases, it is expected that at large-x, the quantum numbers of the hadrons come from the struck partons in the DIS measurement. As one goes to low-x, and gluon distribution begins to saturate, its an interesting question of how gluons and sea quarks clump together in the hadron. At some yet unknown low-x a very high density gluon saturated region is reached [7, 39].

It is now possible to measure the transverse spatial distributions experimentally. The study of the spatial distribution of quarks and gluons requires a special category of measurements, that of exclusive reactions. Examples are deeply virtual Compton scattering (DVCS) and deeply virtual vector meson (DVVM) production. In these, the proton remains intact after the electron has scattered off, and a photon or a vector meson is produced. Ex-

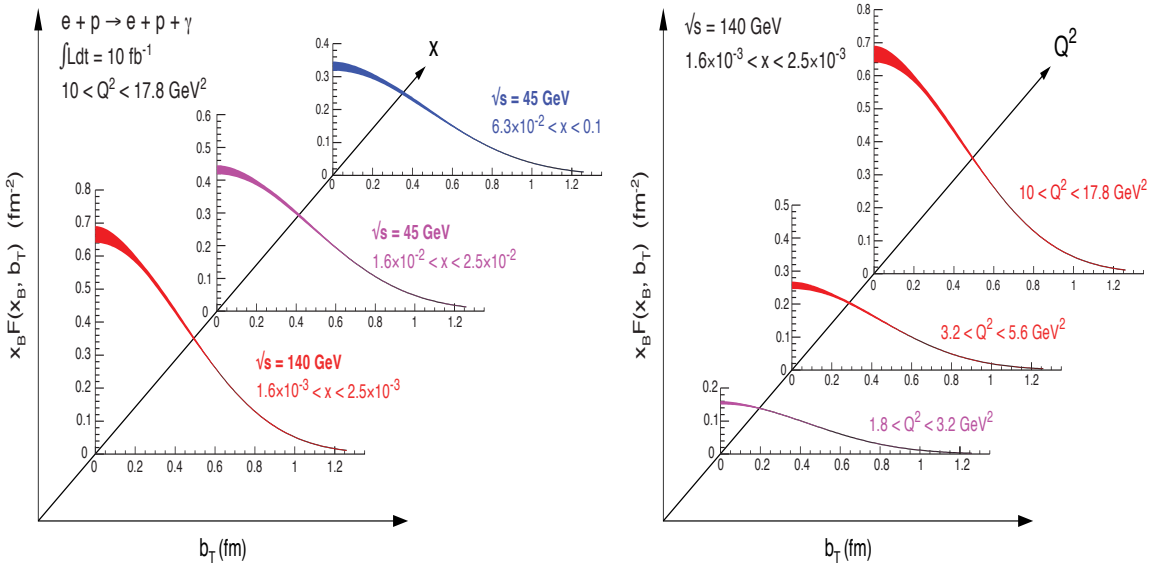

Figure 2.8: The projected precision of the transverse spatial distribution of partons obtained from the Fourier transform of the measurement of unpolarized DVCS cross section as a function of $|t|$ at the EIC for a targeted luminosity of $10\,\mathrm{fb}^{-1}$ at each center-of-mass energy. Impact parameter, b_T, is the distance from the center of the proton. Left: the evolution in x at a fixed Q^2 ($10 < Q^2 < 17.8\,\mathrm{GeV}^2$). Right: the evolution in Q^2 at a fixed x ($1.6 \times 10^{-3} < x < 2.5 \times 10^3$). The red and blue bands indicate extraction of spatial distribution only with high and low center-of-mass energies, respectively, while the purple band is accessible at both.

clusivity demands that all final state products are detected. This includes the scattered electron, the produced photon or vector meson, and the scattered proton. The spatial distribution of quarks and gluons in these experiments is extracted from the Fourier transform of the differential cross section with respect to the momentum transfer, t, between the incoming and the scattered proton. The non-perturbative quantities that encode the spatial distributions are called Generalized Parton Distributions (GPDs) [52–54]. They are interesting to nuclear scientists not only because of their fundamental importance in non-perturbative QCD, but also because the second moment of particular sets of quark and gluon GPDs will give us information about total quark and total angular momentum of quarks and gluons in the proton [55]. This spatial distribution yields a picture of the proton that is complementary to the one obtained from the transverse-momentum distribution of quarks and gluons.

Currently, our knowledge of GPDs from DVCS is limited and is based on fixed target experiments at intermediate to high-x or at low-x from the HERA collider measurements. The high-energy, high-luminosity EIC will make a very significant impact on these measurements. It is anticipated that measurements made for protons in the range $0.04 \lesssim t < 1.5\,\mathrm{GeV}^2$ will enable maps of parton distributions all the way down to 0.1 fm [39,56]. Such exclusive measurements performed on nuclei will enable us to gain a deeper understanding of the transverse quark and gluon distributions within.

Figure 2.8 shows the precision with which an EIC will provide transverse spatial distribution for quarks [39]. The red and blue bands are reachable only with high or low energy collider operations, respectively, while the purple band is reachable by both. To reach low-x and high-Q^2 the EIC needs to have the higher center-of-mass energy. The measurements were simulated using an integrated sample of 10 fb^{-1}. The uncertainties shown in this plot only account for statistics and experimental systematics, not for the systematic uncertainties associated with the extraction of these quantities from data. For more about the extraction of proton size, we refer to [7, 39, 56].

Machine Requirements for GPD Physics

GPD physics is one of the most demanding in terms of luminosity as it requires multi-dimensional binning of very low cross-section processes. While it has been shown that an integrated luminosity of 10 fb^{-1} is sufficient to get to precise unpolarized spatial distribution functions, transverse spin asymmetry measurements that are sensitive to GPD E require 100 fb^{-1}. This amount of integrated luminosity will be necessary at several center-of-mass energies in order to cover the physics program outlined in the EIC White Paper [7] and high Q^2 and high x measurements will need the highest luminosity possible in to achieve a statistical precision comparable to the systematics uncertainties of the measurements.

The continuous measurement of t from $\sim$ 0.02 to about 1.5 GeV^2 demands a careful design of the interaction region to detect the forward going protons scattered under small angles combined with a careful choice of the hadron beam parameters, *i.e.*, angular divergence and large acceptance magnets. A complete map of the spatial distributions of quarks and gluons including polarization effects, requires high polarization of hadron and lepton beams [7, 56].

Pion and Kaon Form Factors and Structure Functions

A recent addition to the physics program at the EIC originating from a series of workshops taking place since 2017 aims to study not only the sub-structure of the nucleon and nuclei, but extend it to the lightest bound states of the strong interaction, pions and kaons. As pions and kaons are unstable, their substructure could not be directly accessed via DIS and most of its limited information originates from secondary pion/kaon beam Drell-Yan measurements [57]. There is, however an opportunity to study their substructure using the Sullivan process [58, 59] where the lepton scatters not on the nucleon but on a virtual meson emitted from the initial nucleon and the remaining baryon is detected at very forward angles. The corresponding diagrams are displayed in Fig. 2.9 for elastic and deeply inelastic scattering on the meson.

The EIC allows to explore pion and kaon structure functions over a large QCD landscape in x and Q^2 to map the quark and gluon distributions in pions and kaons at a roughly similar level as for the proton when using only the HERA data. This would allow to give

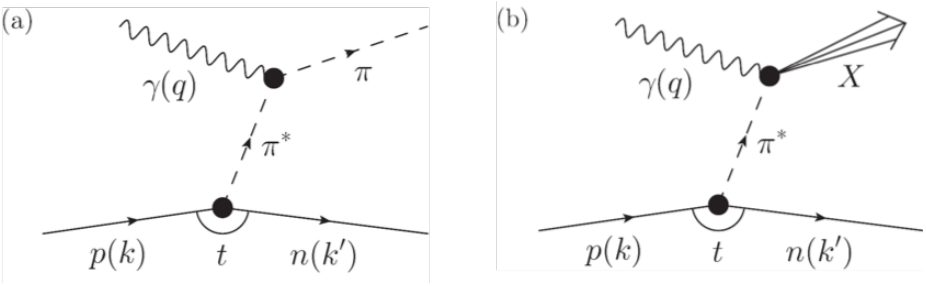

Figure 2.9: Diagrams depicting the scattering of the virtual photon on a virtual pion emitted from the nucleon a), elastically or b) deeply in-elastically.

crucial insights to the understanding of mass. The vast majority of the proton mass is emergent and due to quark-gluon interactions, and similar emergent-mass mechanisms must play a role in the pion and kaon. Yet the mass of the pion is only 140 MeV. This has led to speculation if the pion as viewed at high energies is full or empty of gluons. The EIC data will give unique insight in the emergent-mass mechanism and why the pion mass is so light. The kaon mass is ∼490 MeV and is at the boundary of the emergent- and Higgs-mass mechanisms, the latter responsible for the larger strange quark mass. Whether kaons viewed at high energies have less or more gluons in them than pions is unclear. The EIC will similarly allow access to the pion form factor to large values of Q^2 ∼35 GeV^2.

Machine Requirements for Pion/Kaon Substructure Measurements

The debris of the meson and the scattered lepton can be detected by the central detectors. In the case of the virtual meson of the Sullivan process being a π^+, the resulting baryon is a neutron that can be detected by zero-degree calorimeters. When studying the kaon structure via this process, the forward-going baryon becomes a Λ and decays either into a π^--proton pair or a π^0-neutron pair. Detecting the charged particles is quite challenging but the neutral particles can be detected by a finely segmented zero-degree calorimeter. Due to the long life-time of the Λ, the lower collision energies are slightly favored in ensuring the decay before the ZDC. However, the larger angular spread of the forward-going baryons at lower energies would require a larger ZDC which could possibly interfere with accelerator elements.

Since only a small fraction of the nucleons emit a virtual meson and only small momentum transfers from the nucleon to the resulting baryon allow the interpretation in terms of a real pion, the highest luminosities are necessary.

2.3.2 Physics with High-Energy Nuclear Beams at the EIC

The nucleus is a QCD molecule, with a complex structure corresponding to bound states of nucleons. Understanding the formation of nuclei in QCD is an ultimate long-term goal

of nuclear physics. With its wide kinematic reach, as shown in Fig. 2.10, the capability to probe a variety of nuclei in both inclusive and semi-inclusive DIS measurements, the EIC will be the first experimental facility capable of exploring the internal 3-dimensional sea quark and gluon structure of a fast-moving nucleus. Furthermore, the nucleus itself is a unique QCD laboratory for discovering the collective behavior of gluonic matter at an unprecedented occupation number of gluons, for studying the propagation of fast-moving color charges in a nuclear medium to shed light on the mystery of the hadronization process, and to study of the quark-gluon origin of short range nucleon-nucleon forces in the nuclei.

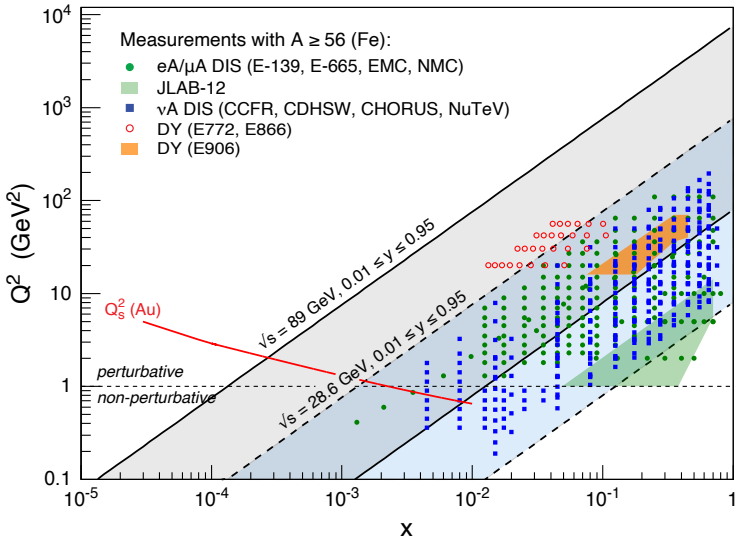

Figure 2.10: The range in the square of the transferred momentum by the electron to the nucleus, Q^2, versus the parton momentum fraction x accessible to the EIC in e+Au collisions is depicted for the highest and lowest center-of-mass energies available at an EIC. The data points reflect existing e+A data. The red curve illustrates the expected saturation scale $Q_s^2(x)$ for Au.

Study of High Gluon Density Matter

A key feature of gluon saturation is the emergence of a momentum scale Q_S, known as the saturation scale. If this scale is significantly larger than the QCD confinement scale Λ_{QCD}, the dynamics of strongly correlated gluons can be described using weak coupling many-body methods. The framework that enables such computations is called the Color Glass Condensate (CGC) [60]. The CGC predicts that $Q_S^2 \propto A^{1/3}$; thus, the novel domain of saturated gluon matter may be accessed sooner at a given energy in large nuclei (see Fig. 2.10). This regime of QCD is assumed to exist in all hadrons and nuclei when viewed at high energies where one is able to probe the low-x regime in full detail. Unambiguous establishment of this novel domain, and its detailed study, is one of the most important goals of the EIC.

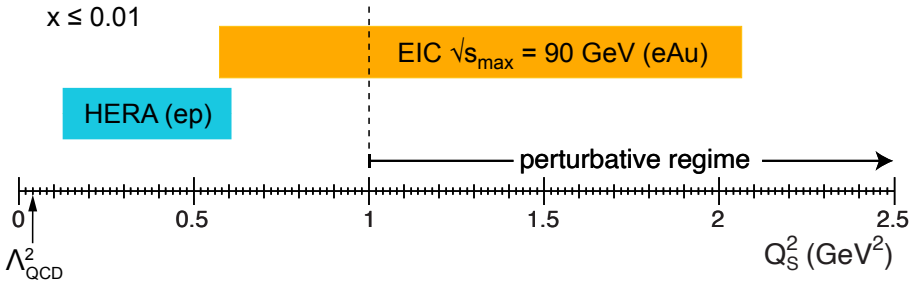

Figure 2.11: The accessible values of the saturation scale Q_S^2 at an EIC in e+A collisions compared to e+p collisions at HERA. In both cases maximum center-of-mass energies is assumed.

QCD predicts that the saturation of gluons is achieved precociously in large nuclei, *i.e.*, at larger values of x than in the proton since the saturation scale Q_S^2 is enhanced by approximately $A^{1/3}$. Figure 2.11 shows calculations for the saturation scales for the e+A collisions at maximum center-of-mass energies and for e+p collisions at HERA. Perturbative calculations can be performed reliably in the higher Q^2 region to the right of the dashed vertical line. It is in this region where $Q^2 > Q_S^2$ that DGLAP evolution can be reliably compared with the saturation calculations. Clearly, the saturation scales achievable at the EIC are significantly larger than those in e+p although the $\sqrt{s}$ energy for HERA was substantially larger. This enhancement of Q_s^2 in nuclei is a consequence of the high energy probe coupling coherently to all the partons along its path length in the nucleus. This figure makes the case that, to explore saturation phenomena reliably, one needs to have the largest nuclei at the highest possible center-of-mass energy.

While there are multiple experimental signatures of saturation discussed in the literature [7], we only use two in this section to motivate the requirement for the energy of the collider; these are dihadron suppression and diffraction in e+A collisions.

The dihadron correlation in the process $e + \mathrm{A} \rightarrow e' + h_1 + h_2 + X$ refers to the angular correlations between two hadrons h_1 and h_2. The angle between the two hadrons in the azimuthal plane is sensitive to the transverse momentum dependence of gluons as the parton shower develops, and to their interactions among themselves—the mechanism that leads to saturation. The experimental signature of saturation is a progressive suppression of the away-side ($\Delta\Phi = \pi$) correlations of hadrons with increasing atomic number A at a fixed value of x. A systematic comparison of the magnitudes and widths in the dihadron azimuthal distribution in e+p and e+A collisions at various energies should lead us to the appropriate conclusion about the existence of saturation [39,61]. In the left plot in Fig. 2.12 (for details see [39,61]), we plot the ratio of the correlations functions in e+Au to those in e+p for three energies. The suppression increases with increasing center-of-mass energy of 90 GeV. Since the typical uncertainties in saturation models are approximately equal to what would be a suppression of 20%, a significantly larger suppression ratio would be highly desirable, suggesting the highest possible center-of-mass energy is essential for establishing saturation unambiguously. The right plot in Fig. 2.12 depicts the corresponding

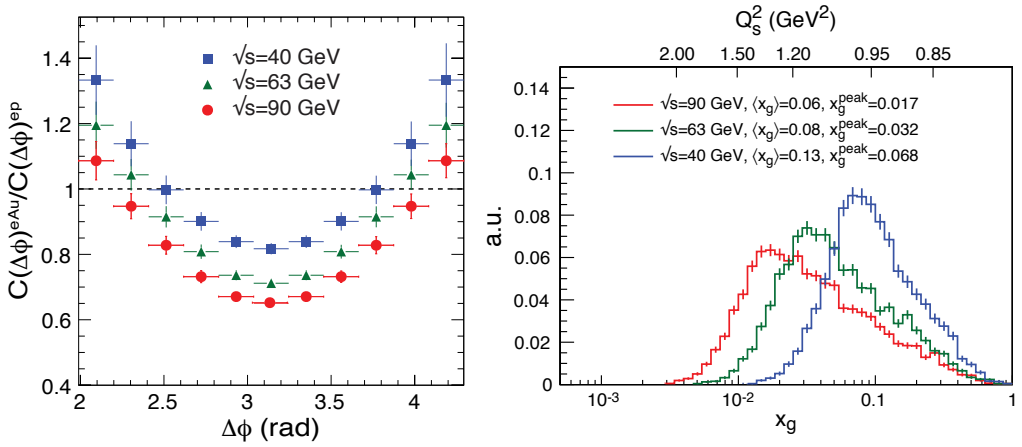

Figure 2.12: **Left:** Ratio of dihadron correlation functions in e+Au collisions to those in$e$+p collisions in a simulation study at three different center-of-mass energies. Ratio below 1 implies a suppression or disappearance of hadrons, which is statistically significant (and maximal) at $\Delta\phi = \pi$ radians. **Right:** x_g distributions probed by the correlated hadron pairs for the different center-of-mass energies in e+Au collisions. The average and peak values for the distributions are shown. The gluon saturation scales Q_s^2 corresponding to x_g values are displayed on top of the plot.

x_g distributions for dihadrons produced at the three different center-of-mass energies discussed. The larger the energy, the smaller the x_g values one can access, and the further we reach into the saturation regime. Since the saturation scale is a function of x_g alone, we also show the reference Q_s^2 values on the top of the plot.

Diffraction in e+A scattering is another promising avenue to establish the existence of saturation and study the underlying dynamics. Diffraction entails the exchange of a color neutral object between the virtual photon and the target. A consequence of this is a rapidity gap between the target remnant and the diffractively produced system. Conversely, if the exchanged particle is not color neutral, then in the detector one would observe a broad spray of final state hadrons filling up the rapidity gap. At HERA, these types of diffractive events made up a surprisingly large fraction of the total e+p cross section (10–15%). There are two explanations of such large diffraction cross-sections. One is the physics of saturation. The other is due to nonperturbatively shadowed diffractive structure functions that satisfy leading twist evolution equations. At EIC, the diffractive DIS off nuclei, saturation models predict that over 20% of the cross-section will be diffractive. In contrast, the perturbative QCD based leading twist shadowing (LTS) models do not predict any such enhancement. Since diffractive cross sections are proportional to the square of the nuclear gluon distribution, $\sigma \propto g(x, Q^2)^2$, they are very sensitive to the onset of gluon saturation, and are important for the study the gluon saturation.

Figure 2.13 illustrates this dramatic effects of gluon density saturation in e+A versus e+p collisions at an EIC. The plot considers coherent diffractive processes, defined to include all events in which the beam nucleus remains intact and feature a rapidity gap contain-

ing no produced particles. As shown in the figure, the fraction of such diffractive events are greatly enhanced by gluon saturation (the red points) in comparison with the predictions of shadowing model (the blue points). In all gluon saturation models, the coherent destructive multiple interaction among colored gluons suppresses both the coherent diffractive and total DIS cross-sections on nuclei compared to those on the proton, but, the suppression on the coherent diffractive events with the nucleus remained intact is much weaker than that of the total cross section leading to a dramatic enhancement in the double ratio as shown in Fig. 2.13. An early measurement of coherent diffraction in e+A collisions at the EIC would provide the first unambiguous evidence for gluon saturation.

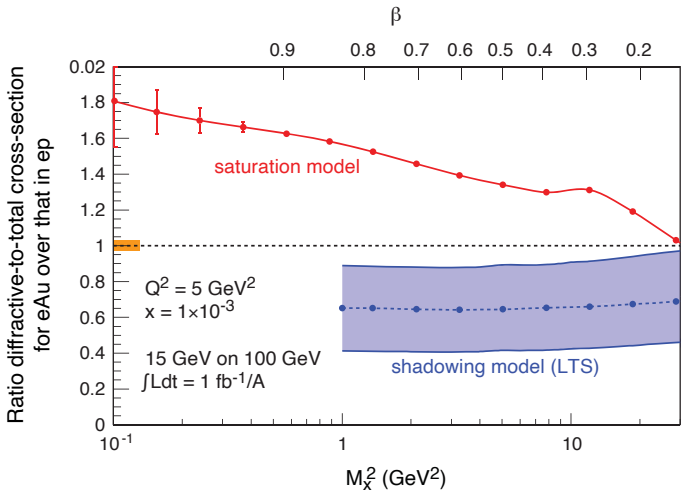

Figure 2.13: The ratio of diffractive over total cross-section for DIS on gold normalized to DIS on proton plotted for different values of M_X^2, the mass squared of hadrons produced in the collisions for models assuming saturation and non-saturation [7]. The statistical error bars are too small to depict and the projected systematic uncertainty for the measurements is shown by the orange bar. The theoretical uncertainty for the predictions of the LTS model is shown by the grey-blue band.

Machine Parameters For Studies of Gluon Saturation

Highest energy operation of the EIC with the heaviest nuclei will be an essential requirement for discovery of the gluon saturation. A detailed study of saturation beyond its discovery would require a systematic variation of the nuclear size and of $\sqrt{s}$ to see where the saturation sets in. Di-hadron correlation studies performed with an 10 fb^{-1}/A integrated luminosity are sufficient to get a clean signature. Such integrated data sets are also sufficient for many diffractive studies, and many of these measurements could be performed simultaneously for a particular nucleus. Some diffracting studies, like exclusive vector meson production will be more luminosity hungry since the require the measurement of multi-differential quantities. Running at the maximum energy is the most crucial requirement for this key EIC physics.

Nuclear Modifications of Parton Distribution Functions

When compared to our knowledge of parton distribution functions in the proton, our knowledge of nuclear PDFs (nPDF) is significantly more limited. Most of it comes from fixed target experiments in a region of intermediate to high-x as shown in Figure 2.10. Recently available data from the LHC have been included in nPDF extractions but have had limited impact on extracting nuclear PDFs [62]. High energy electron-nucleus collisions at the EIC will enable measurements of nuclear PDFs over a broad and continuous range in Q^2 all the way from photo-production ($Q^2 \sim 0$) to large Q^2 in the perturbative region. This will enable scientists to study the nPDFs with unprecedented precision. Precise knowledge of nPDFs will be crucial when searching for the transition between linear and non-linear evolution of the parton densities with change of the resolution scale of the probe. The latter saturation regime occurs at low-x and low interaction scale Q^2 where the gluon densities are highest and the recombination of low-x gluons becomes increasingly important. In e+A scattering such non-linearities are predicted to be more pronounced than in e+p interactions [63] due to an enhanced saturation scale Q_S^2.

Precision Measurements of Nuclear PDFs

Nuclear PDFs are dominantly determined through global fits to existing inclusive DIS data off nuclei using reduced cross-sections. The reduced cross section, σ_r, can be expressed in terms of the structure function F_2 and the longitudinal structure function F_L as:

$$\sigma_r = F_2(x, Q^2) - \frac{y^2}{1 + (1 - y)^2} \cdot F_L(x, Q^2) \tag{2.2}$$

While F_2 is sensitive to the momentum distributions of (anti)quarks and to gluons mainly through scaling violations, F_L has a larger direct contribution from gluons. An additional constraint on the gluon distribution at moderate to high-x comes from charm production driven by photon-gluon fusion. The fraction of charm production grows with the energy, reaching about ∼15% of the total cross section at the highest $\sqrt{s}$, thus permitting one to set a robust and independent constraint on the gluon distribution in nuclei at high-x [7, 39].

Figure 2.14 shows the reduced cross section for inclusive and charm production in e+A scattering. The data were simulated using three different center-of-mass energies, 31.6, 44.7, and 89.4 GeV. The blue shaded region indicates the existing data, and grey bands indicate the uncertainty in the EPPS16 parameterization [62], the most up-to-date nPDF. Note that the estimated experimental uncertainties on the data are very small compared to theory uncertainties, and the higher center-of-mass energy enables a broader range in (x, Q^2), particularly in the low-x region where gluons dominate. Higher energies are clearly advantageous, and 10 fb^{-1}/A combined for the data at all center-of-mass energies will be sufficient to make significant impact on our knowledge of nuclear PDFs.

Figure 2.15 shows F_L for inclusive (left) and for charm (right) calculations based on EPPS16 along with the uncertainties estimated at each energy. Note that the measurement of F_L

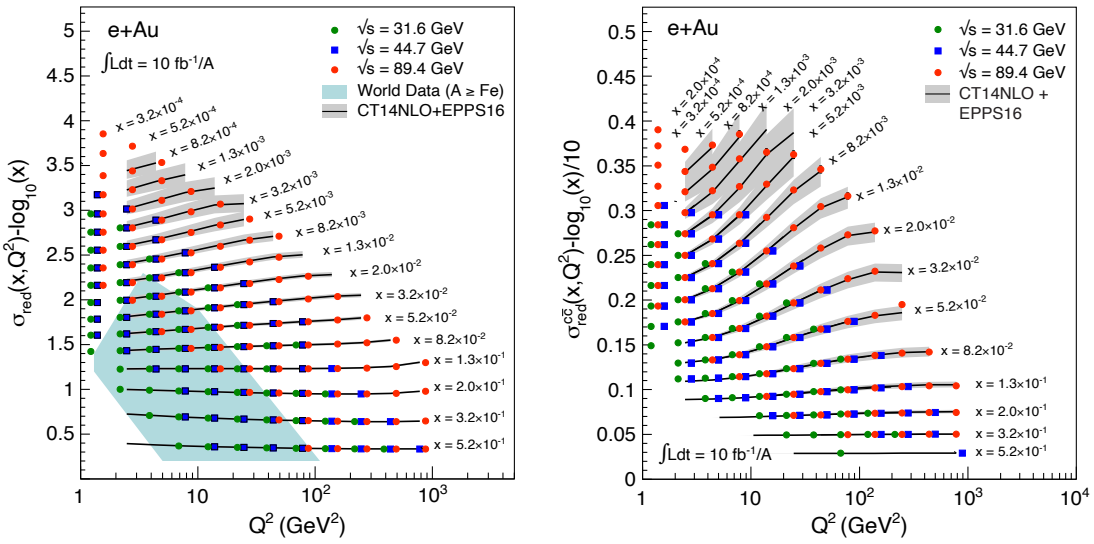

Figure 2.14: Reduced cross section for inclusive (left plot) and charm (right plot) plotted for x and Q^2 along with their uncertainties (shown in grey bands) from EPPS16 model. EIC simulated data [64] are shown for different center-of-mass energy combinations. The blue band in the left plot shows the currently available data.

requires one to operate the collider at several different center-of-mass energies. This simulation was performed with total of 10 fb^{-1} data over the combination of three center-of-mass energies [64]. The width of the gray bands reflects the current theoretical uncertainty in both cases and is wider than the statistical uncertainties from the simulations indicating that these uncertainty bands would be reduced significantly using future EIC data.

How parton distributions in nuclei are modified relative to those in the proton can be quantified by plotting their ratio normalized by the atomic number of the nucleus. The deviation of this ratio from unity is a clear demonstration that the nuclear parton distributions are not a simple convolutions of those in the proton. A depletion of this ratio is often called shadowing, while an enhancement is dubbed anti-shadowing. The reduced cross-sections of simulated EIC data was used together with existing world-data in a global fit to evaluate the level of improvements of gluon PDFs the EIC will provide [64]. The study allowed for additional flexibility in the fit function (EPPS16*) used to derive the gluon PDF in the nuclei in order to better evaluate the EICs impact. Figure 2.16 shows the ratio of gluon distribution in Pb to that in proton plotted at two different values of Q^2. The grey bands indicate the current uncertainties in the nuclear PDFs, orange bands indicate the improvement we could expect from the inclusive data sets, and the hatched band indicates the further improvement one expects from the inclusion of charm quark production in this analysis. Including charm quarks in the analysis helps significantly in the large-x region, where they are produced abundantly through the photon-gluon fusion process [39, 64].

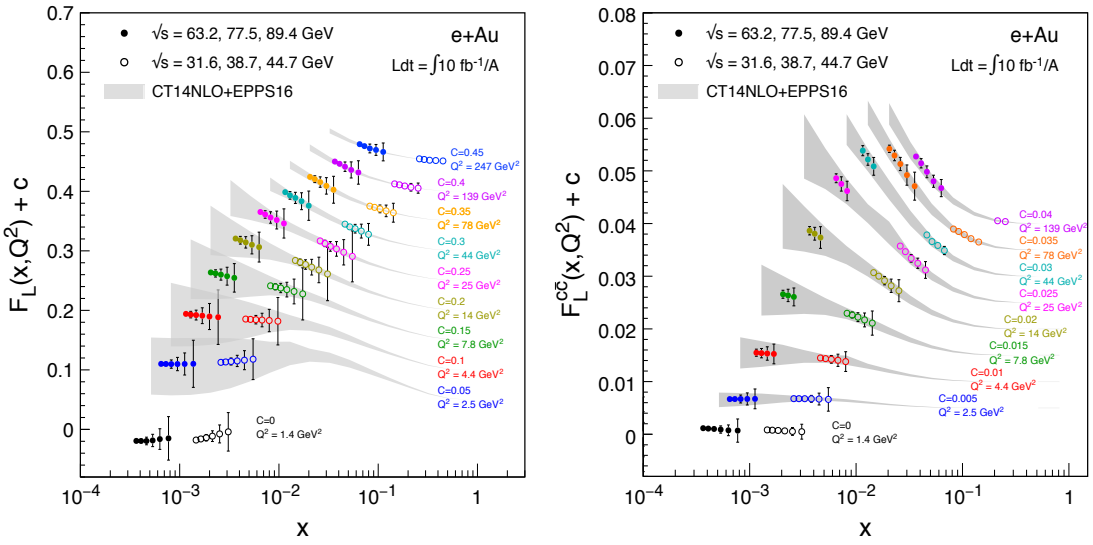

Figure 2.15: Inclusive F_L (left plot) and charm (right plot) $F_L^{c\bar{c}}$ simulated data [64] shown with the EPPS16 nuclear PDFs. Grey bands are uncertainties in the model, and the EIC data simulated with $10\,\mathrm{fb}^{-1}/\mathrm{A}$ are shown for three center-of-mass energies.

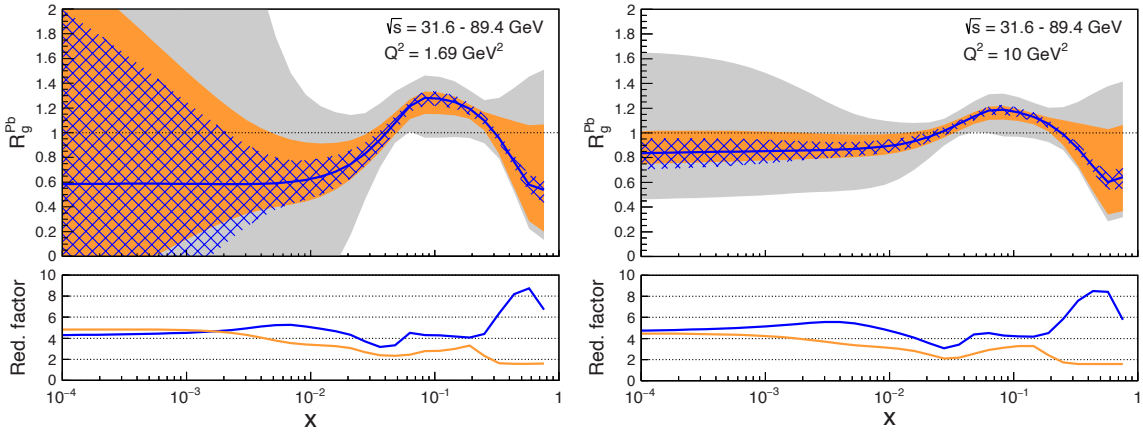

Figure 2.16: Nuclear PDFs improvements with the EIC. The ratio R_g^{Pb}, from EPPS16*, of gluon distributions in a lead nucleus relative to the proton at $Q^2 = 1.69\ \mathrm{GeV}^2$ (left) and $Q^2 = 10\ \mathrm{GeV}^2$ (right). The grey band represents the EPPS16* theoretical uncertainty. The orange (blue hatched) band includes the EIC simulated inclusive (charm quark) reduced cross-section data. The lower panel in each plot shows the reduction factor in the uncertainty with respect to the baseline fit.

Machine Parameters For Precision Nuclear PDF Measurements

Based on recent studies for inclusive DIS and charm cross section measurements [64], large $\sqrt{s}$ presents a significant advantage, as a wider x-Q^2 coverage can be explored and one reaches further in the region of gluon dominance. For precise high impact measurements an integrated luminosity of 10 fb^{-1}/A is sufficient. In fact, beyond a few fb^{-1}, these measurements become systematics dominated and more statistics will not affect the overall uncertainties.

2.3.3 Passage of Color Charge Through Cold QCD Matter

Figure 2.17 shows a schematic of an e+A scattering event. The virtual photon transmits the energy from the electron and interacts with a quark inside a nucleon in the nucleus. The struck quark will subsequently traverse the nucleus, interacting with the color charges inside the nucleus and continually lose energy. At some point, this quark will hadronize and form a color neutral hadron. Whether the hadronization process happens inside or outside the nucleus depends on the interplay between the energy of the quark and the atomic number of the nucleus.

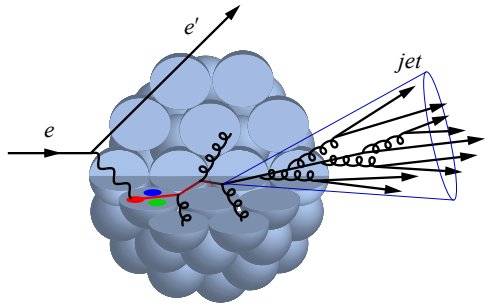

Figure 2.17: Schematic depiction of a struck parton propagating through cold nuclear matter resulting in the formation of a single jet.

If the virtual photon energy (in the nuclear rest frame) is large, the quark that is kicked will have a large energy and produces a jet. Measuring the jets experimentally gives several advantages in comparison to leading hadron studies. Reconstructed from multiple (ideally all) final state particles produced by hadronization of the scattered parton, jets are much closer proxies for the parton kinematics than any single particle observable. Using jets in many cases removes (or minimizes) hadronization uncertainties. On the other hand, jets are composite objects with rich internal substructure encoding shower evolution and hadronization details.

Jets are versatile tools for experimental studies at hadron-hadron and lepton-hadron colliders, addressing variety of physics topics from precision measurement of the Standard Model processes to searches beyond Standard Model and transport properties of quark

gluon plasma. The methodology of jet reconstruction and underlying background handling is rapidly developing at the modern collider facilities, on par with the progress in theoretical understanding of emerging jet data at the next-to-next-to-leading order for many channels. The experience thereby gathered can be gainfully applied to physics at the EIC, and without a doubt jets will be indispensable in the next chapter of collider experiments to be written there. At the EIC the jet will be an effective tool to be employed to measure and study the hadronic component in high energy photon structure [65] and gluons' helicity in polarized protons [39]. Jet measurements will also contribute to constraining polarized and unpolarized parton distribution functions, probing gluon transverse momentum dependent distributions, and most relevant for this section, to studies of QCD hadronization, shower evolution, and cold nuclear matter effects.

Several recent works [66, 67] detail the feasibility and applications of jet studies at the EIC. The jet kinematic distributions, including inclusive jet transverse momentum and pseudorapidity spectra, and dijet mass and pseudorapidity distributions, were quantified for a range of Q^2 values, processes, and beam energies. The energy contribution from underlying event activity was also studied as a function of jet energy [66], and while for energetic jets, the underlying event contributions are found small, at lower jet energies, these contributions are found to have a fractionally significant effect. Some of these studies are also incorporating expected detector performance. They show that the best jet reconstruction performance can only be achieved at sufficiently high energies, and thus high center-of-mass energy collisions are vital for jet studies.

Energetic jet born by scattered parton encodes the history of multiple interactions with the target nucleus, which generate p_T-broadening. Thus, a comparison of the cross-section in e+p and e+A collisions is expected to be sensitive to in-medium broadening effects. Several key measurements relying on jets were identified for their sensitivity to parton energy loss in the nucleus [67], together with developments of new tools for controlling hadronization effects. Among such measurements are several variables assessed via lepton-jet correlations, including the ratio of the electron to jet transverse momenta, and a relative azimuthal angle between the measured jet and electron. These measurements will allow constraining parton transport coefficient in the nuclei [68]. The lepton-jet correlations are measured in the lab-frame and could be compared directly to the similar measurements at RHIC and LHC elucidating the hot and cold nuclear matter effects on propagating parton.

It is expected that the variability of energy of the collider and the "dialing" of the nuclear size, both of which are possible with the EIC, will allow us to study the emergence of jets as a function of energy, and to study the internal spatial structure of jets systematically as an additional topic of high interest. Studying how jet substructure is modified between e+A and e+p collisions could provide additional information about details of how partons lose energy in the cold nuclear medium. A comparison of jet properties in e+A versus e+p collisions is thus a promising avenue to study a broad set of QCD phenomena related to the passage of color through cold QCD matter and the hadronization/fragmentation processes.

In addition to jet studies, identified hadron measurements will provide additional experimental avenue for detailed understanding of cold-QCD effects of color-charge. Parton

propagation through cold nuclear matter and its effects on hadronization have been previously studied by the HERMES collaboration in semi-inclusive deep-inelastic scattering on nuclei via relative hadron production cross-sections for various light-flavor particle species. These most precise measurements to date left room for different modeling of hadronization dynamics and in-medium attenuation. EIC experiments will be able to extend these light-flavor cross-section measurements into new kinematic domains and augment these studies with heavy flavor mesons. Recent theoretical works [69] highlighted the sensitivity of D- and B-meson production to the transport properties of cold nuclear medium. Studies of the medium-induced suppression patterns of heavy hadrons are shown to have high discriminating power for theoretical models of energy loss and hadronization in nuclear matter. In addition to inclusive hadron and jet production measurements, mapping the modification of heavy flavor production in reactions with nuclei of different sizes will provide an experimental handle for understanding transport properties of nuclear matter.

Machine Design Parameters for Jets Studies

Jets can only be produced and identified cleanly at high enough collider energies. High momentum jets feature higher hadron multiplicity and a more complex internal structure. As such, high center-of-mass energy is vital for jet studies. Nuclear size is an essential control variable in these experiments and a broad range from light to heavy nuclei would be desired for systematic studies of energy loss in a nuclear medium. It is imperative to have matching beam energies for e+p and e+A collisions to avoid extrapolation related uncertainties and deliver most precise measurements of nuclear effects.

2.4 Summary of Machine Design Parameters for the EIC Physics

Here we summarize the machine requirements that were motivated in the previous section through a set of key measurements that reflect the highlights of the EIC science program. The important machine design parameters were originally discussed in great detail in section 1.2 of the EIC White Paper [7]. The successful scientific outcome of the EIC depends critically on: (a) the luminosity, (b) the center-of-mass energy and its range, (c) the lepton and light ion beam polarization, and (d) the availability of ion beams from deuteron to the heaviest nuclei. Two interaction regions are desired to ensure a robust physics program with complementary detector systems.

Luminosity

In the discussion of each physics topic in the previous section we quoted the integrated luminosity needed to perform the corresponding measurements. The EIC is being designed to achieve peak luminosities between $10^{33--34}\text{cm}^{-2}\ \text{sec}^{-1}$. To put these numbers into context, note that a luminosity of $10^{33}\text{cm}^{-2}\text{s}^{-1}$ and strong hadron cooling ($L_{\text{peak}} = L_{\text{avg}}$) yields

an integrated luminosity of $1.5\,\mathrm{fb}^{-1}$ per month. Here we assume an 60% operations efficiency for the collider complex as routinely achieved by RHIC. Without strong hadron cooling for the same operations parameters, one would get a 30% reduction, as the average luminosity L_{avg} per fill is reduced to 70% of the peak luminosity L_{peak}. Most of the key physics topics discussed in the EIC White Paper [7] and summarized here are achievable with an integrated luminosity of 10 fb^{-1} corresponding to 30 weeks of operations. One notable exception is the study of the spatial distributions of quarks and gluons in the proton with polarized beams. These measurements require up to a integrated luminosity of $100\,\mathrm{fb}^{-1}$ and would therefore benefit from an increased luminosity of $10^{34}\mathrm{cm}^{-2}\,\mathrm{sec}^{-1}$. It should be noted that many measurements can be performed simultaneously by judiciously choosing beam species and their spin orientation appropriately.

Center-of-Mass Energy

To ensure a wide kinematic reach and large coverage of the phase space, the EIC requires a variable center-of-mass energy $\sqrt{s}$ in the range of $\sim 20 - -100$ GeV, upgradable to 140 GeV [7]. An energy of $\sqrt{s}_{eN} = 140\,\mathrm{GeV}$ is needed to provide sufficient kinematic reach into the gluon dominated regime. Some measurements require a variation in $\sqrt{s}$. The lower center-of-mass energy range is driven by the ability to measure well transverse quantities, which are of the order of 10–100 MeV. This is important for example for the accurate determination of quark TMDs at high values of Q^2.

Polarization of Beams

EIC Physics involves two types of asymmetries: (*i*) double spin asymmetries, requiring both electron and hadron beams to be polarized, and (*ii*) single spin asymmetries, requiring only one beam—typically the hadron beam—to be polarized. The statistical uncertainties for spin asymmetries are strongly affected by the degree of polarization achieved. For double spin asymmetries the dependence is $\delta A_{LL} \sim 1/\left[P_e P_p \sqrt{N}\right]$ and for single spin asymmetries $\delta A = 1/\left[P\sqrt{N}\right]$. Therefore, high beam polarizations are mandatory to reduce the statistical uncertainties. Measurements require longitudinal and transverse polarization orientation for protons, deuterons, ^{3}He and other polarizable light nuclei, as well as longitudinal polarization for the electron beam.

Nuclear Beams

Ion beams of the heaviest nuclei (Gold, Lead, or Uranium) combined with the highest $\sqrt{s}$, will provide precocious access to the domain of saturated gluon densities and to understand how color propagates through nuclear matter. Light ions are essential to study the A-dependence of gluon saturation and for precision studies of short range nuclear correlations.

2.5 Scientific Requirements for the Detectors and IRs

The physics program of an EIC, imposes several challenges on the design of a detector and, more globally the extended interaction region as it spans center-of-mass energies from 29 GeV to 141 GeV, different combinations of both beam energy and particle species, and several distinct physics processes. The EIC science program can be categorized in different general processes as shown in Table 2.1.

Table 2.1: Different categories of processes measured at an EIC.

Inclusive DIS: $e + p/\mathrm{A} \longrightarrow e' + X$; for this process, it is essential to detect the scattered electron, e', with high precision. All other final state particles (X) are ignored. The scattered electron is critical for all processes to determine the event kinematics.	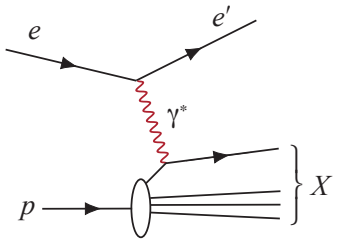
Semi-inclusive DIS: $e + p/\mathrm{A} \longrightarrow e' + h^{\pm,0} + X$, which requires detection of *at least one* hadron in coincidence with the scattered electron.	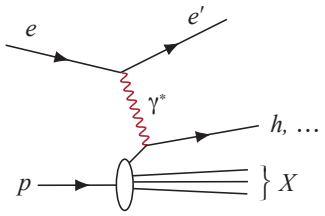
Exclusive DIS: $e + p/\mathrm{A} \longrightarrow e' + p'/A' + \gamma/h^{\pm,0}/VM$, which require the detection of *all* particles in the event with high precision.	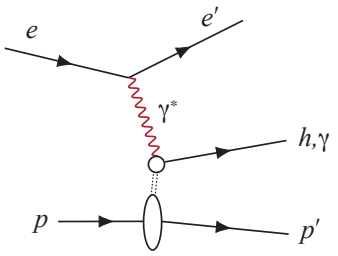
Electro-weak processes: $e + p/\mathrm{A} \longrightarrow \nu + X$; at high enough momentum transfer Q^2, the electron-quark interaction is mediated by the exchange of a $W^{\pm}$ gauge boson instead of the virtual photon. In this case the event kinematic cannot be reconstructed from the scattered electron, but needs to be reconstructed from the final state particles.	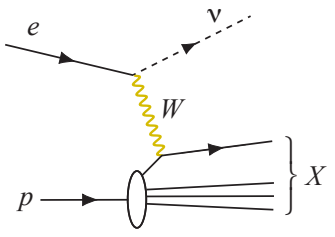

The directions of the beams are defined following the convention used at the HERA collider at DESY: the hadron beam travels in the positive z-direction/pseudo-rapidity and the electron beam travels in the negative z-direction/pseudo-rapidity. We call the hadron going direction the forward region and the electron going one the backward region.

2.5.1 Scientific Requirements for the Detectors

In this section we focus on the scientific requirements on a general purpose detector, which is fully optimized to address the full range of EIC physics. These requirements substantially affect the design of the interaction region. All the different physics processes to be measured at an EIC require having the event and particle kinematics $(x, Q^2, y, W, p_t, z, \Phi, \theta)$ reconstructed with high precision. The key variables x, Q^2, y, and W are either determined from the scattered electron or from the hadronic final state using the Jacquet-Blondel method [70]. In order to access the full $x - Q^2$ plane at different center-of-mass energies and for strongly asymmetric beam energy combinations, the detector must be able to reconstruct events over a wide span in rapidity and scattering angle. This imposes requirements on both detector acceptance and resolution. In contrast to symmetric energy colliders without good coverage of the rapidity range $|y| > 2$, where a significant fraction of the $x - Q^2$ phase space will be missed, this puts much more emphasis on the lepton and hadron endcap. Figure 2.18 illustrates the correlation between pseudo-rapidity (scattering angle) and the $x - Q^2$ phase space.

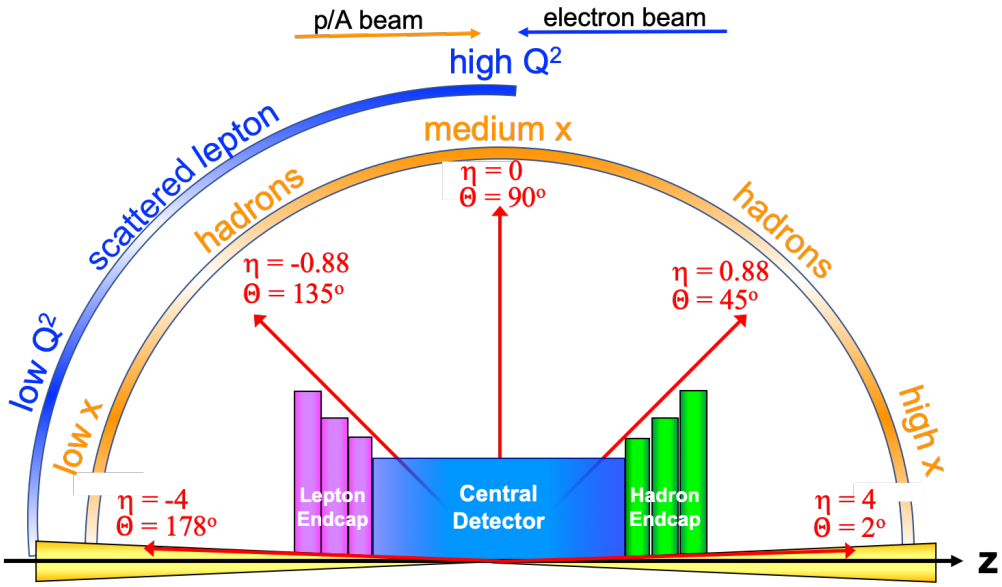

Figure 2.18: A schematics showing how hadrons and the scattered lepton for different $x - Q^2$ are distributed over the detector rapidity coverage.

Methods of Event Kinematic Reconstruction

It is common to reconstruct the event kinematic in DIS with different methods depending on the region of inelasticity y one is accessing. At large inelasticity y, where radiative corrections become large, as illustrated in Fig. 7.25 in [38] and the kinematics of the event is reconstructed from the scattered electron, there are two ways to address this: one is to calculate radiative corrections and correct for them; the other is to utilize the hadronic activity in the detector together with cuts on the invariant mass of the hadronic final state, which will reduce the impact of radiative corrections to a minimum. At small lepton scattering angles or correspondingly small inelasticity radiative corrections are small, but the momentum and scattering angle resolution for the scattered lepton deteriorates. This problem is addressed by re-constructing the lepton kinematics purely from the hadronic final state using the Jacquet-Blondel method or using a mixed method like the double angle method [70], which uses information from the scattered lepton and the hadronic final state. At HERA, these methods were successfully used down to y of 0.005. The main reason this hadronic method renders better resolution at low y follows from the equation $y_{JB} = (E - p_z^{had})/2E_e$, where $(E - p_z^{had})$ is the sum over the energy minus the longitudinal momentum of all hadronic final-state particles and E_e is the electron beam energy. This quantity has no degradation of resolution for $y < 0.1$ as compared to the electron method, where $y_e = 1 - (1 - cos\theta_e)E'e/2E_e$. To allow for efficient unfolding of measured quantities, i.e. cross sections and asymmetries, for smearing effects due to detector resolutions and radiative events and retain the statistical power it is important to have a survival probability in each kinematic bin of $\sim$80% or better. Typically, one can reach for a given center-of-mass energy squared, roughly a decade of Q^2 at fixed x when using only the electron method to determine the kinematics, and roughly two decades when including the hadronic or double angle method. If only using the electron method, one can increase the range in accessible Q^2 by lowering the center-of-mass energy. The coverage of each setting is given by the product of y times s. As lower y_{min} that can be reached, the fewer settings in s are needed. However, this is an important consideration for any measurement, which needs to separate the cross-section components due to longitudinal and transverse photon polarization, i.e. the measurement of F_L where one needs to have full y-coverage at all energies.

Inclusive and Semi-inclusive DIS

Scattered Lepton: To minimize the energy loss and multiple scattering of the scattered electron and not to degrade the resolution of the kinematic variables (x, Q^2, y, W) derived from the scattered electron, *the beam pipe needs to be as thin as possible and made from a low mass material, i.e. Beryllium.* As discussed in Section 2.3.2, the study of non-linear QCD effects at the largest gluon densities requires electron-nucleus (i.e. U, Pb, Au) collisions at the highest center-of-mass energies. At the EIC, this implies 18 GeV electrons colliding with heavy ion beams of 110 GeV to reach $Q^2 < Q_s^2$ ($\sim$1 GeV^2) at the lowest x possible. Figure 2.19 shows the relationship between Q^2 and pseudo-rapidity of the scattered electron. To reach $Q^2 \sim 1\,\text{GeV}^2$, the scattered electron needs to be detected down to a pseudo-rapidity of $\eta = -4$ corresponding to an angle of 2° off the beam line. The electron scattering angle

especially at low Q^2 is independent of the hadron beam energy.

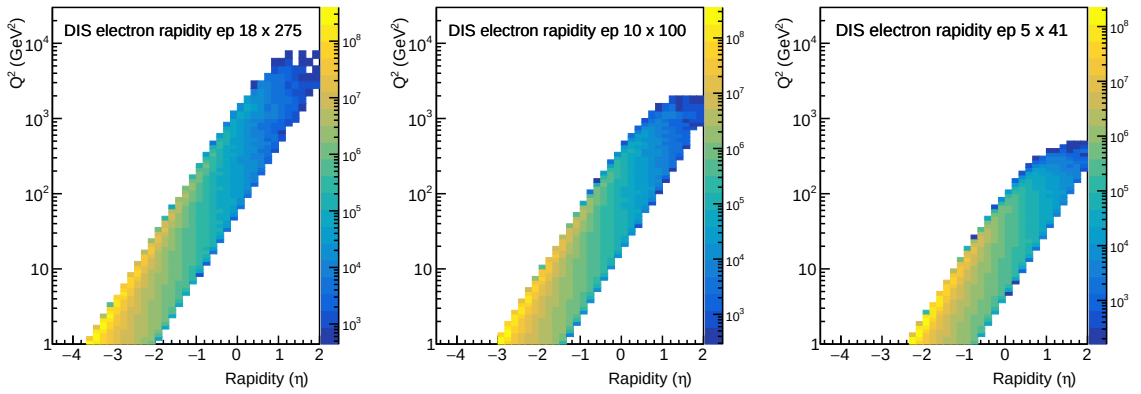

Figure 2.19: Q^2 vs. pseudo-rapidity in the laboratory frame for the scattered electron at different center-of-mass energies. The following cuts have been applied: $0.01 < y < 0.9$, with inelasticity, y, defined as the fraction of the electron's energy lost in the nucleon rest frame. The electron scattering angle especially at low Q^2 is independent of the hadron beam energy.

Figure 2.20 (upper row) illustrates the dependence between the momentum of the scattered lepton and its scattering angle for three different center-of-mass energies. It is clearly shown that as higher the center-of-mass energy the more the lepton goes in the original electron beam direction, corresponding to negative pseudo-rapidity and such very small scattering angles with respect to the beam axis. Varying the hadron beam energy for a fixed lepton beam energy has no influence on the scattered lepton pseudo-rapidity/scattering angle correlation. Several EIC physics topics require going to low x at low Q^2 such an EIC detector needs to have good electron identification and momentum/energy measurement at pseudo-rapidities < -2, which means detecting the scattered lepton 2° of the beam axis with an energy close to the lepton beam energy. *As such, no collider equipment can be installed inside the main detector volume and extend beyond* 1.5°.

Hadron Kinematics: Figure 2.20 (lower row) shows the momentum versus pseudo-rapidity (scattering angle) distributions in the laboratory frame for pions originating from semi-inclusive reactions for different lepton and proton beam energy combinations. For the lowest center-of-mass energy, pions are scattered in the forward (ion) direction. With increasing center-of-mass energy, the pions increasingly populate the central region of the detector. At the highest center-of-mass energy, pions are even largely produced going back-ward (i.e. in the lepton beam direction). For increasing hadron beam energies at fixed lepton beam energy the pseudo-rapidity distribution remains the same but the maximum hadron momentum increases at fixed pseudo-rapidity. The kinematic distributions for kaons and protons/anti-protons are essentially identical to those of the pions. The distributions for semi-inclusive events in electron-nucleus collisions may be slightly altered due to nuclear modification effects, but the global features will remain.

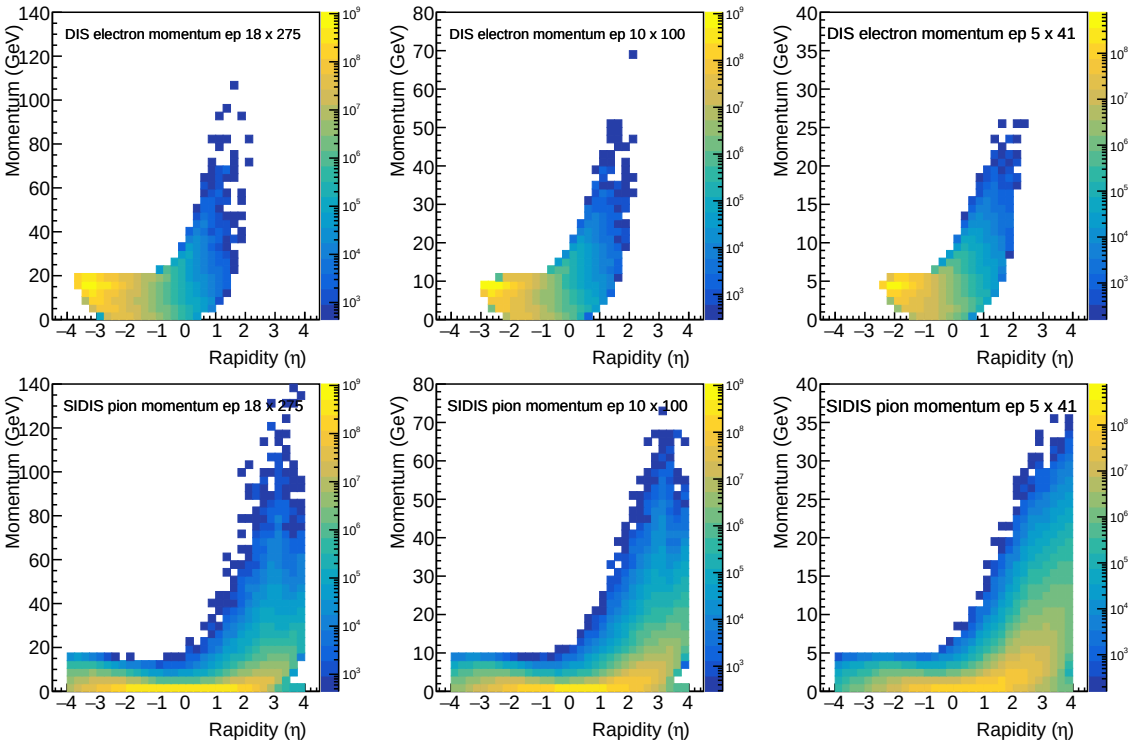

Figure 2.20: Top panel: Scattered DIS lepton momenta as a function of pseudorapidity from left to right for the highest energy collisions of 18 GeV electrons on 275 GeV protons, 10 GeV on 100 GeV and 5 GeV on 41 GeV. Bottom panel: SIDIS pion momenta as a function of pseudorapidity for the same three beam energy combinations. The following cuts have been applied: $0.01 < y < 0.9$, with inelasticity, y, momentum transfer $Q^2 > 1\,\text{GeV}$, and $W^2 > 10\,\text{GeV}^2$, as well as $0.05 < z < 0.95$ for the pions.

Figure 2.21 indicates the momentum/energy range of the scattered electron (black curve), photons (green), negative charged pions (blue) and kaons (cyan) as well as antiprotons (violet) and their sum (magenta) for a center-of-mass energy of 140 GeV (18 GeV on 275 GeV) as function of pseudo-rapidity. This plot provides on the one hand the needed information on the requirements for the scattered lepton identification as well as for identifying pions, kaons and protons. For the entire pseudo-rapidity ($-4 < \eta < 4$) negative pions, kaons and antiprotons show the same momentum distributions, with negative pions having a factor $\sim 3 - -5$ higher multiplicity as negative kaons and antiprotons. In the central detector region ($-1 < \eta < 1$) the momenta are of typically 0.1 GeV/c to 4 GeV/c with a maximum of about 10 GeV/c. Hadrons with higher momenta go typically in the forward (ion) direction for low lepton beam energies, and in the backward direction for higher lepton beam energies.

The hadrons need to be identified with a purity $> 95\%$ at preferably an efficiency of $> 90\%$ to measure identified hadron double spin asymmetries as small as 0.0001. Events with $Q^2 < 10\,\text{GeV}^2$ typically correspond to negative rapidities ($\eta < -2$) and $Q^2 > 10\,\text{GeV}^2$ correspond to rapidities $-2 < \eta < 1$. Depending on the center-of-mass energy the rapidity

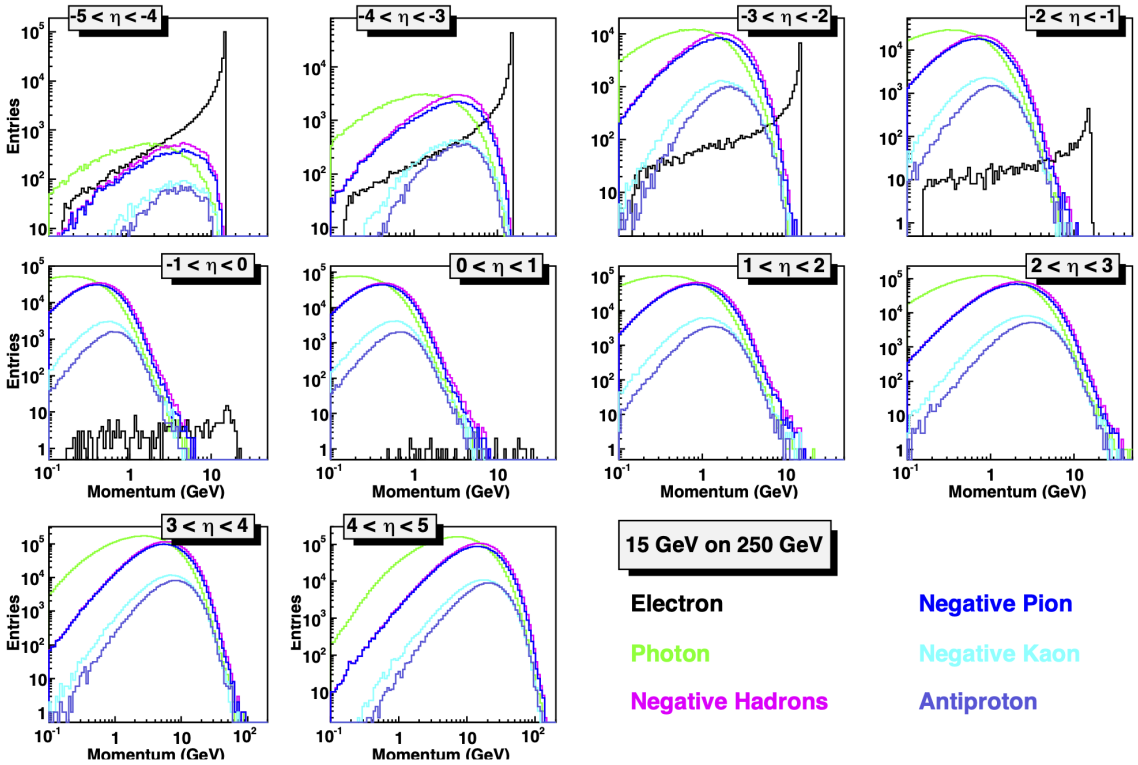

Figure 2.21: The momentum distribution for the scattered electrons (black), photons (greens), and negatively charged hadrons (magenta) for different pseudo-rapidity bins in the laboratory frame for beam energies of 18 GeV on 275 GeV. The distributions for negatively charged Pions (blue), Kaons (cyan) and antiprotons (violet) are shown as well. No kinematic cuts have been applied.

distributions for hadrons (both charged and neutral) and the scattered lepton can overlap and need to be disentangled. For $\eta < -3$ electron, photon and charged hadron rates vary from being comparable to a factor of 10 different. For the higher pseudo-rapidities electron rates are a factor of 100–1000 smaller than photon and charged hadron rates, and comparable at a 10 GeV/c total momentum. For very high Q^2-events a suppression factor of > 100 is needed. This adds another requirement to the detector: **excellent electron identification**. It is noted that the kinematic region in pseudo-rapidity over which hadrons and also photons need to be suppressed, typically by a factor of 10–1000, shifts to more negative pseudo-rapidity with increasing center-of-mass energy. Measuring the ratio of the energy and momentum of the scattered lepton, typically gives a reduction factor of $\sim$100 for hadrons. This requires the availability of both tracking detectors (to determine momentum) and electromagnetic calorimetry (to determine energy) over the same rapidity coverage. By combining information from these two detectors, one also immediately suppresses the misidentification of photons in the lepton sample. Having good tracking detectors with similar rapidity-coverage as electromagnetic calorimetry similarly aids the y-resolution at low y from the lepton method. The hadron suppression is further

improved by adding a Hadron Calorimeter and/or a Cerenkov detector to the electromagnetic calorimetry and/or having tracking detectors to provide good dE/dx. *The resulting lepton purities should be* $> 99\%$ *with preferable a detection efficiency of* $> 90\%$.

Exclusive Processes

Exclusive DIS and especially exclusive diffractive processes require a careful design of the detector and the IR in the outgoing proton/nucleus beam direction. Contrary to exclusive electron-proton events, for electron-nucleus collisions it is not possible to tag the outgoing intact scattered nucleus. Therefore, another technique needs to be realized to ensure exclusivity. One can require a "rapidity gap" in the detector, meaning that there is a region in the detector from the hadron beam towards the center of the detector in which there is no activity from the hadronic final state. The efficiency for detecting exclusive events and their purity therefore depends strongly on the rapidity coverage (hermiticity) of the detector. Simulations have shown that a rapidity coverage of -2 to 4 is required to have detection efficiencies $> 90\%$ and a purities $> 90\%$ for exclusive e+A events assuming a cross section ratio of Exclusive-to-DIS events of 10:90 as measured at HERA.

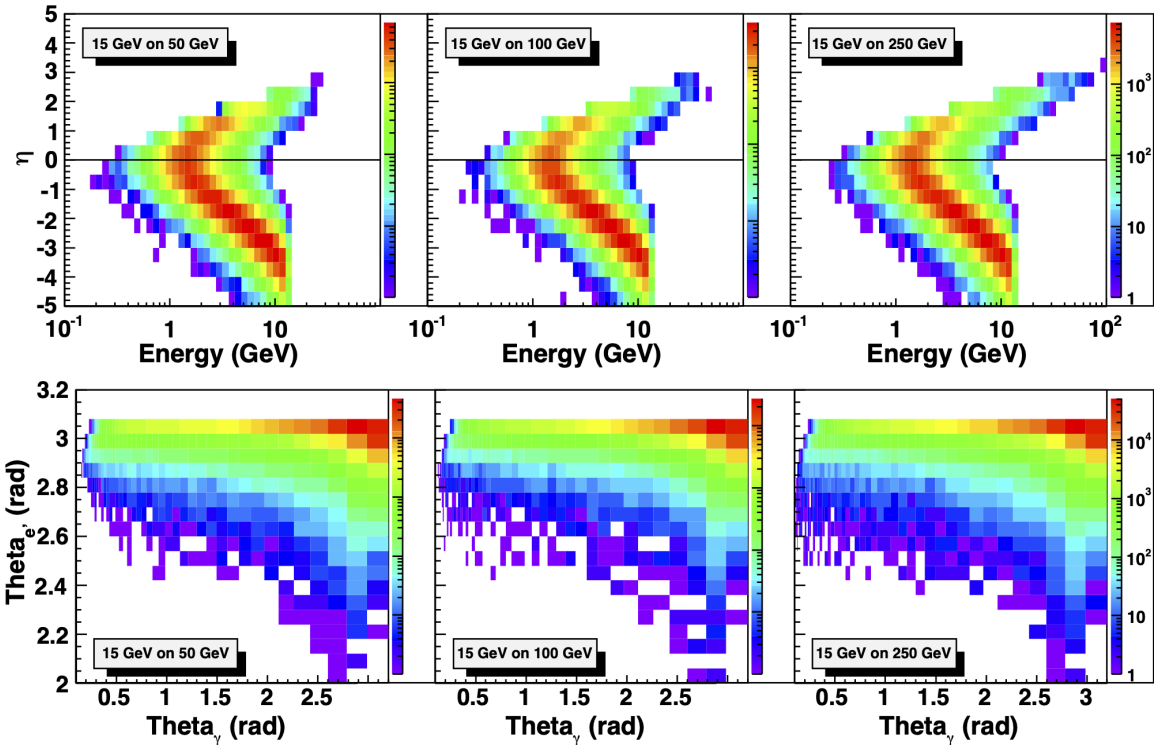

Figure 2.22: The energy vs. pseudo-rapidity in the laboratory frame for photons from DVCS (top) and the correlation between the scattering angle of the DVCS photon and the scattered lepton for three different center-of-mass energies. The following cuts have been applied: $Q^2 > 1\,\mathrm{GeV}^2$, $0.01 < y < 0.85$, and $-5 < \eta < 5$.

As a case example for an exclusive process, Figure 2.22 shows the energy vs. rapidity distributions for photons from deeply virtual Compton scattering, and the correlation between the scattering angle of the DVCS photon and the scattered lepton in the laboratory frame for different beam energy combinations. The general patterns follow the ones in Figure 2.20, but even at the low lepton beam energies the DVCS photons go more into the backward direction. To separate the DVCS events from their dominant background from Bethe-Heitler events it is important to measure the DVCS photon energy and the lepton momentum down to 1 GeV and to be able to resolve their scattering angle difference $(\theta_e - \theta_\gamma)$ down to below 1^o. The most challenging constraints on the detector design for exclusive reactions compared to semi-inclusive reactions are, however, not given by the final state particle, but to ensure the exclusivity of the event. Exclusivity can be achieved by different methods. In electron-proton scattering by detecting all reactions products, especially the scattered protons going forward under extremely small scattering angles or requiring a rapidity gap between the hadron beam and produced pseudo-scalar/vector mesons and jets. To make the rapidity gap method highly efficient a detector with an acceptance to high pseudo-rapidities is needed. In lepton-nucleus scattering exclusivity can be ensure by the rapidity gap method or by vetoing the nuclear breakup by requiring no decay neutrons in the zero-degree calorimeter. *Therefore no collider equipment can be installed inside the main detector volume and/or extend beyond* 1.5° *in order to not compromise the efficiency and purity of exclusive events that are detected through the rapidity-gap method.*

Detector Requirements

We conclude this section with a brief summary of the key detector requirements that are imposed by the rich physics program of an EIC.

- The EIC requires a *h*ermetic detector with *l*ow mass inner tracking.
- The main detector needs to cover the range of $-4 < \eta < 4$ for the measurement of electrons, photons, hadrons, and jets. It will need to be augmented by auxiliary detectors like low-Q^2 tagger in the far backward region and proton (Roman Pots) and neutron (ZDC) detection in the far forward region.
- The components of an EIC detector will have moderate occupancy as the event multiplicities are low. However, depending on the machine background level certain components close to the beamline might see higher occupancies. For details see Sec. 8.3.2.
- An EIC detector will have to cope with a data rate of up to $\sim$ 500 kHz at full luminosity.
- Compared to LHC detectors, the various subsystems of an EIC detector have moderate radiation hardness requirements.
- Excellent momentum resolution in the central detector ($\sigma_{p_T}/p_T(\%) = 0.05 p_T \oplus 0.5$).
- Good momentum resolution in the backward region with low multiple-scattering terms ($\sigma_{p_T}/p_T(\%) \approx 0.1 p_T \oplus 0.5$).

- Good momentum resolution at forward rapidities ($\sigma_{p_T}/p_T(\%) \approx 0.1 p_T \oplus 1 - -2$).
- Good impact parameter resolution for heavy flavor measurements ($\sigma \approx 5 \oplus 15/p \sin^{3/2}\theta$ (μm)).
- Good electromagnetic calorimeter resolution in the central detector ($\sigma(E)/E \approx 10\%/\sqrt{E}$).
- Excellent electromagnetic calorimeter resolution at forward rapidities ($\sigma(E)/E < 2\%/\sqrt{E}$).
- Good hadronic resolution in forward region ($\sigma(E)/E \approx 50\%/\sqrt{E}$).
- Excellent PID for 3 σ $\pi/K/p$ separation up to 45 GeV/c in forward region, up to 8 GeV/c in the central detector. and up to 7 GeV/c in the backward region.

2.5.2 Scientific Requirements for the Interaction Regions

To cover the physics program, as described in earlier sections, it is extremely important to integrate the detector into the interaction region *already during the early design stages* of the collider. In the following, the requirements will be discussed, categorized according to the processes described in Table 2.1.

Exclusive Processes

The detection of forward-going scattered protons from exclusive reactions, as well as of decay neutrons from the breakup of heavy ions in incoherent and non-diffractive reactions, is particularly challenging.

Electron-Proton Scattering: In general, for exclusive reactions, one wishes to map the four-momentum transfer, or Mandelstam variable $t = |p_{\text{in}} - p_{\text{out}}|^2$ of the hadronic system, and then obtain an image of the spatial partonic structure of the proton by a Fourier transform of the (un)polarized cross section as function of t Figure 2.23 shows what fraction of the beam momentum ($x_L = p'_L/p_{\text{Beam}}$) is carried by these scattered protons as measured by ZEUS at HERA [71] and the correlation between the proton scattering angle and its momentum. This illustrates that the remaining baryonic states go in the very forward proton-beam direction. Even at a proton energy of 50 GeV, the proton scattering angles only range to about 25 mrad. At proton energies of 250 GeV, this number is further reduced by a factor of five. In all cases, the scattering angles are small. As discussed earlier (see section 2.5.1), the main detector reaches down to a rapidity -4 to 4, corresponding to 35 mrad from the beam line. Therefore, these protons are not seen in the main detector and need a different technique to be detected, i.e. Roman Pots. Their acceptance strongly depends on the exact interaction region design.

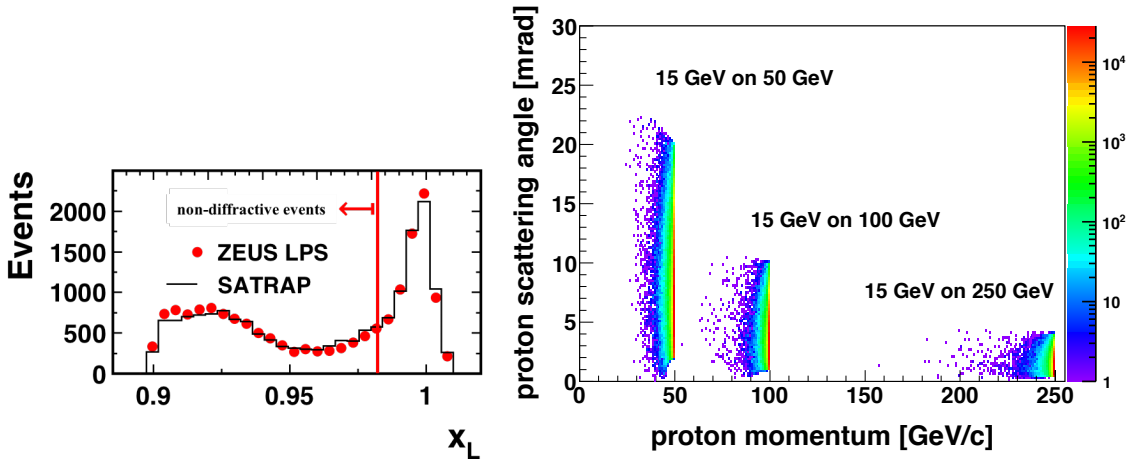

Figure 2.23: Left: Fraction of the beam momentum carried by the scattered protons as measured by ZEUS at HERA. Right: The scattered proton momentum vs. scattering angle in the laboratory frame for DVCS events with different beam energy combinations. The following cuts have been applied: $1\,\mathrm{GeV}^2 < Q^2 < 100\,\mathrm{GeV}^2, 0.01 < y < 0.85, 10^{-5} < x < 0.5$ and $0.01\,\mathrm{GeV}^2 < t < 1\,\mathrm{GeV}^2$. The angle of the recoiling hadronic system is directly and inversely correlated with the proton energy. It thus decreases with increasing proton energy.

Figure 2.24 (top) shows the cross section of exclusive real photon production (DVCS: $ep \longrightarrow e'p'\gamma$) as function of t. The red dots represent the measurements and their statistical precision as obtained at EIC for $\sqrt{s} = 141\,\mathrm{GeV}$ and an integrated luminosity of $10\,\mathrm{fb}^{-1}$ for $0.03\,\mathrm{GeV}^2 < |t| < 1.6\,\mathrm{GeV}^2$ corresponding to an acceptance in p_T of $0.18\,\mathrm{GeV/c} < p_T < 1.3\,\mathrm{GeV/c}$, which is the nominal requirement from the EIC White Paper. The blue curves represent an exponential fit to the measured points for different regions in t with the width of the band representing the uncertainty of the fit. The different rows show the result for different acceptances in p_T of the scattered protons. The lower row shows the impact parameter dependent PDF obtained from a Fourier transform of the cross section measurement with different p_T acceptances. The bands represent the parametric errors in the fit and the uncertainty from different extrapolations to the regions of unmeasured (very low and very high) p_T of the scattered protons. *Based on these studies and the EIC White Paper, protons with* $0.18\,\mathrm{GeV/c} < p_T < 1.3\,\mathrm{GeV/c}$ *need to be transported through the IR such that they can be detected as soon as they are separated from the core of the beam.*

To obtain a full picture of the (un)polarized spatial partonic imaging of the proton it is critical to have measurements of the (un)polarized diffractive cross sections of reactions with a charge exchange, like $e + p \rightarrow e' + n$. In this case the four-momentum transfer t is obtained from the forward scattered neutrons. Figure 2.25 shows the correlation of the scattering angle of the neutrons as function of t for two different beam energy combinations. Like for the protons, the neutrons are scattered at very small angles with respect to the outgoing proton beam. *These neutrons with an angular distribution from 9 mrad (at* $\sqrt{s} = 141\,\mathrm{GeV}$*) to 26 mrad (at* $\sqrt{s} = 32\,\mathrm{GeV}$*) from the hadron beam axis need to be transported through the IR to a zero-degree calorimeter.*

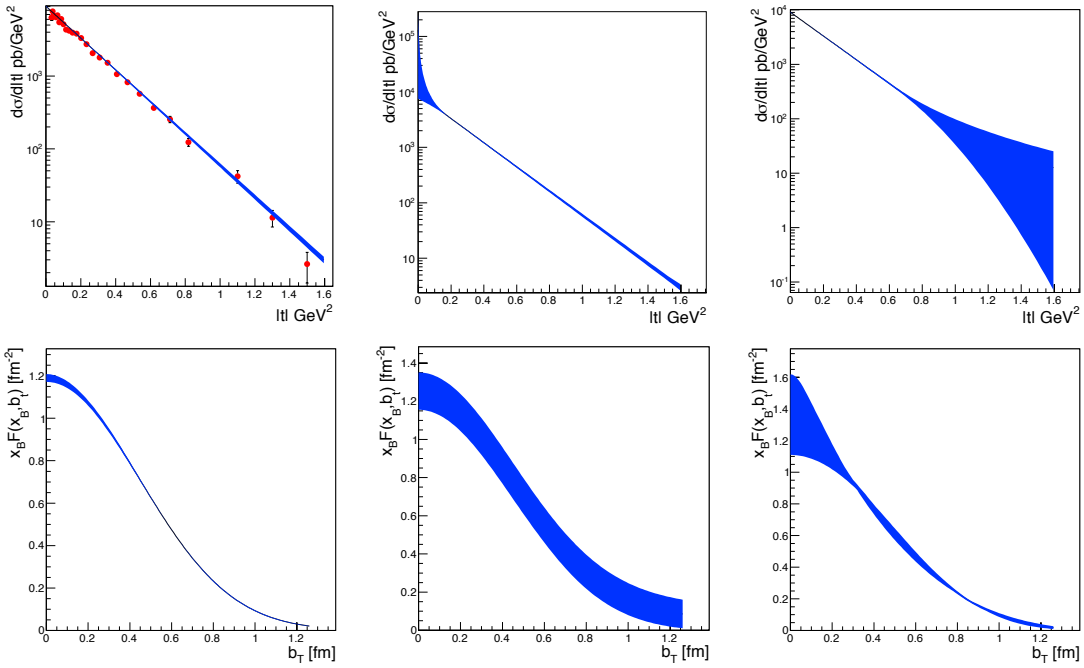

Figure 2.24: Top: The cross section as function of t. The red dots represent the measurements and their statistical precision as obtained at EIC for $\sqrt{s} = 141\,\text{GeV}$ and an integrated luminosity of $10\,\text{fb}^{-1}$. The blue curves represent an exponential fit to the measured points for different regions in t with the width of the band representing the uncertainty of the fit. The different rows show the result for different acceptances in p_T of the scattered protons. Bottom: The impact parameter dependent PDF obtained from a Fourier transform of the measured cross section with different p_T acceptances. The bands represent the parametric errors in the fit and the uncertainty from different extrapolations to the regions of unmeasured (very low and very high) p_T of the scattered protons. Left: $0.18\,\text{GeV/c} < p_T < 1.3\,\text{GeV/c}$, $0.03\,\text{GeV}^2 < |t| < 1.6\,\text{GeV}^2$; Middle: $0.44\,\text{GeV/c} < p_T < 1.3\,\text{GeV/c}$; Right: $0.18\,\text{GeV/c} < p_T < 0.8\,\text{GeV/c}$.

Electron-Nucleus Scattering: The only possible way to tag coherent diffractive exclusive electron-nucleus events for heavy nuclei is to veto nuclear breakup. For coherent diffractive events the intact nucleus is scattered under very small forward angles in the outgoing beam direction and mainly remains inside the beam envelope. Tagging exclusive events can be realized by requiring no neutrons and photons from the nuclear breakup in a zero-degree calorimeter. Figure 2.26 shows the breakup neutron momentum vs. scattering angle in the laboratory frame for different beam energies. *To achieve a very high tagging efficiency of* $\sim$ 100% *for coherent diffractive electron-nuclei scattering events one needs to transport neutrons and photons within a cone of four mrad to six mrad, depending on the beam energy, through the IR to a zero-degree calorimeter.*

For all the different processes, collision geometries in e+A (see Figure 2.27) can be determined by utilizing the ZDC. The number of forward neutrons produced and detected in the ZDC is expected to be sensitive to the path length d of the parton and fragmentation

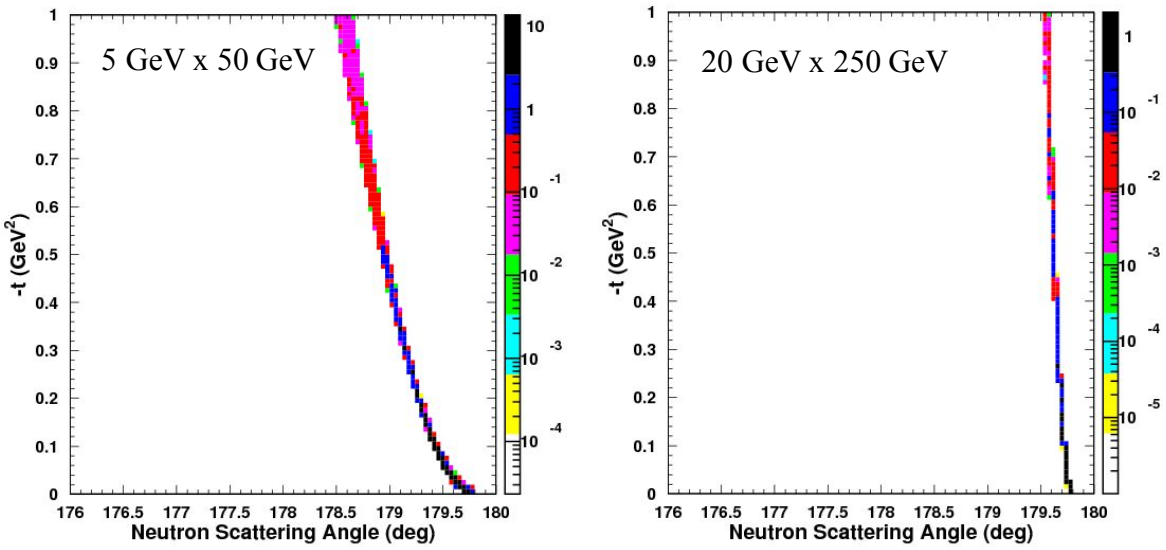

Figure 2.25: The neutron scattering angle as function of t in the laboratory frame for two different beam energy combinations. Note a scattering angle of 180° corresponds to the outgoing proton beam direction in this plot.

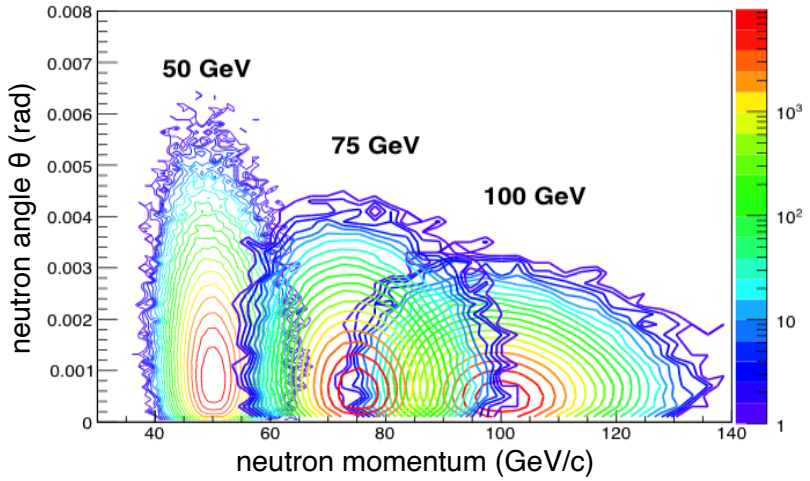

Figure 2.26: The scattered neutron momentum vs. scattering angle in the laboratory frame for different beam energies.

of the colliding nucleon along the virtual photon direction in the nucleus. See Figure 2.27 for the correlation between the number of forward scattered neutrons and the path length. The geometric information is an additional and useful gauge for investigating properties of partonic interactions in nuclei. While the impact parameter b has a correlation with the number of neutrons in the ZDC, the most "central" collision in e+A ($b \sim 0$) can be identified from events with the highest neutron multiplicity since the longest path length of the nucleon fragmentation in the nucleus is expected to be at $b = 0$. This will be an effective

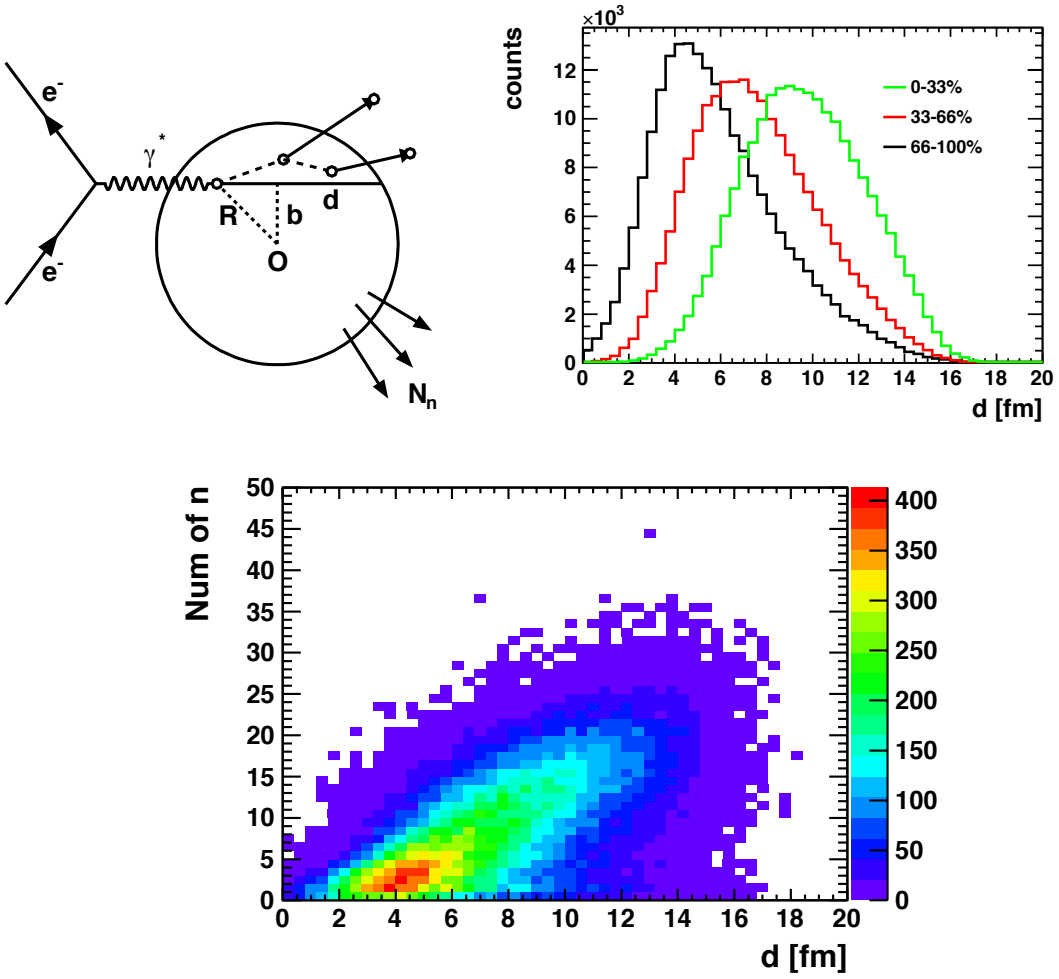

Figure 2.27: Top-left: Collision geometry of e+A, showing the path length d of the parton and fragmentation of the struck nucleon along the virtual photon direction. The impact parameter b is defined as the transverse distance between the center of the nucleon and the virtual photon. Top-right: Distribution of the path length as selected by the neutron multiplicity. The estimate done using DPMJet-III [72]. Bottom: Correlation between number of produced forward neutrons vs. path length of parton and fragmentation of the struck nucleon in the nucleus. All the forward neutrons can be detected in the ZDC.

tool for selecting events with maximized nuclear effects in SIDIS e+A collisions, like e.g., dihadron correlation studies [61,73].

Recent physics studies showed that selecting on the number of neutrons to reach a centrality of $> 5\%$ enhances the effective A in the reaction, which is crucial for any measurements of non-linear effects in QCD. This, and the requirement that the four-momentum transfer t in diffractive reactions with a charge exchange is obtained from the neutron, requires a ZDC with higher energy resolution ($\approx 30\%/\sqrt{E}$) than is currently achieved at RHIC ($65\%/\sqrt{E} + 15\%$ for a ZDC size of 10 cm $\times$ 10 cm $\times$ 60 cm). This requires more space in

x-y to integrate a ZDC in order to minimize shower leakages in the transverse direction at 30 m from the IR. The required space will depend on the exact detector technology chosen; for examples see [74,75]. The longitudinal size required would be around one meter.

Inclusive Processes

There are many physics topics beyond what was discussed in the EIC White Paper [7] that benefit from tagging the scattered electron at Q^2 values significantly below $1\,\mathrm{GeV}^2$. An example is the determination of the (un)polarized partonic structure of photons [65].

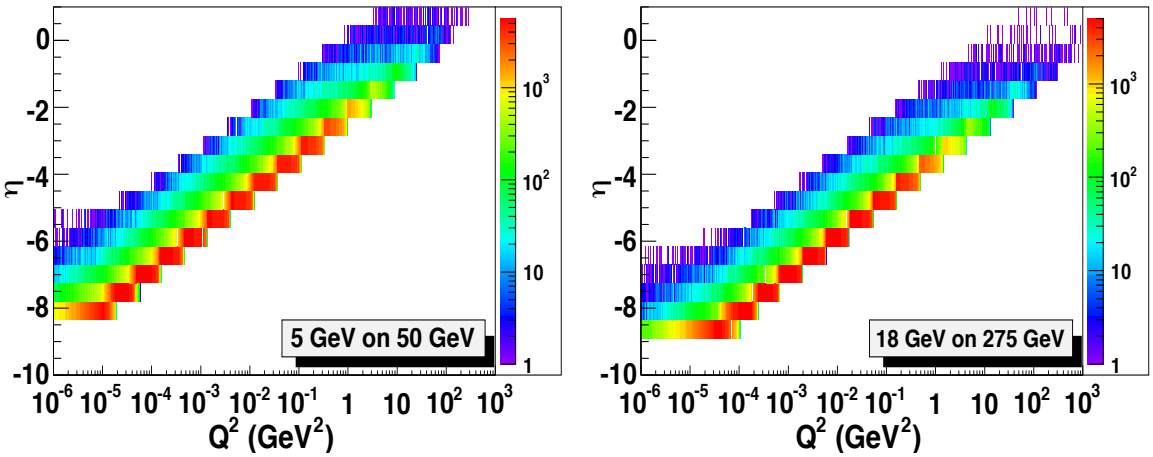

Figure 2.28: Relation between Q^2 of the scattered electron rapidity for 5 GeV and 18 GeV electron beam energy.

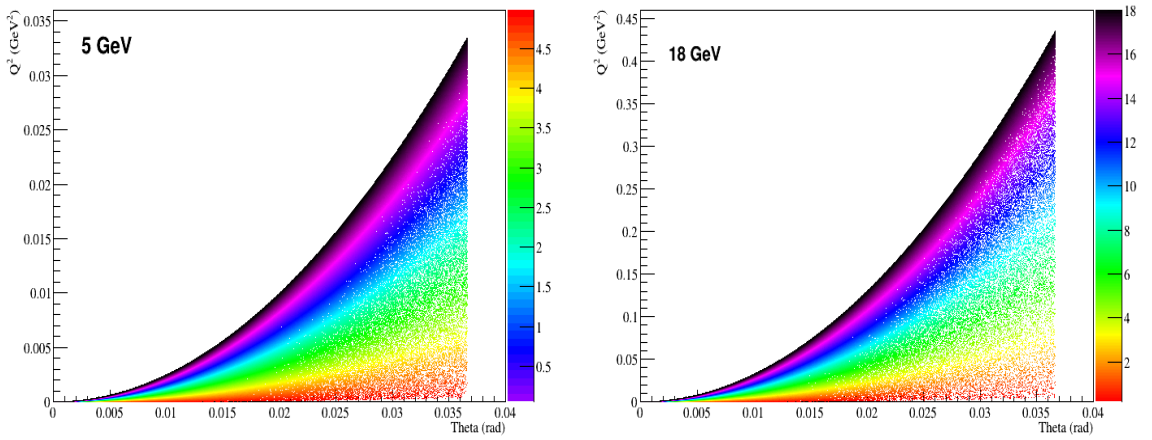

Figure 2.29: The relation between the electron scattering angle and Q^2 for 5 GeV and 18 GeV electron beam energy. The colors indicate the energy of the scattered electron.

Scattered electrons with a $Q^2 < 0.5\,\mathrm{GeV}^2$ cannot be detected in the main detector. Therefore, as was the case in all in HERA detectors, a special low-Q^2 tagger is needed. The scattered electrons will be detected in an electromagnetic calorimeter with several Si-tracking planes in front. Such a device needs to be well-integrated into the IR design and care needs to be taken to separate the scattered electrons from electrons from the bremsstrahlung process, which, due to their high cross-section and the high EIC luminosity will be dominant. Figures 2.28 and 2.29 show several kinematic relations for the scattered electron, i.e. Q^2 vs. rapidity, Q^2 as function of the electron scattering angle, and its energy.

Electron-Nucleus Scattering

The physics program of an EIC requires electron-(un)polarized proton and neutron collisions to allow full flavor separation of (un)polarized parton distribution functions. As polarized neutron beams are not feasible, (un)polarized ^{3}He and deuterium beams constitute effective proxy for a neutron beam. To ensure that the scattering really occurred on the neutron, the spectator proton(s) need to be detected. Figure 2.30 shows the correlation of momentum and scattering angle for the spectator protons from electron-deuteron and

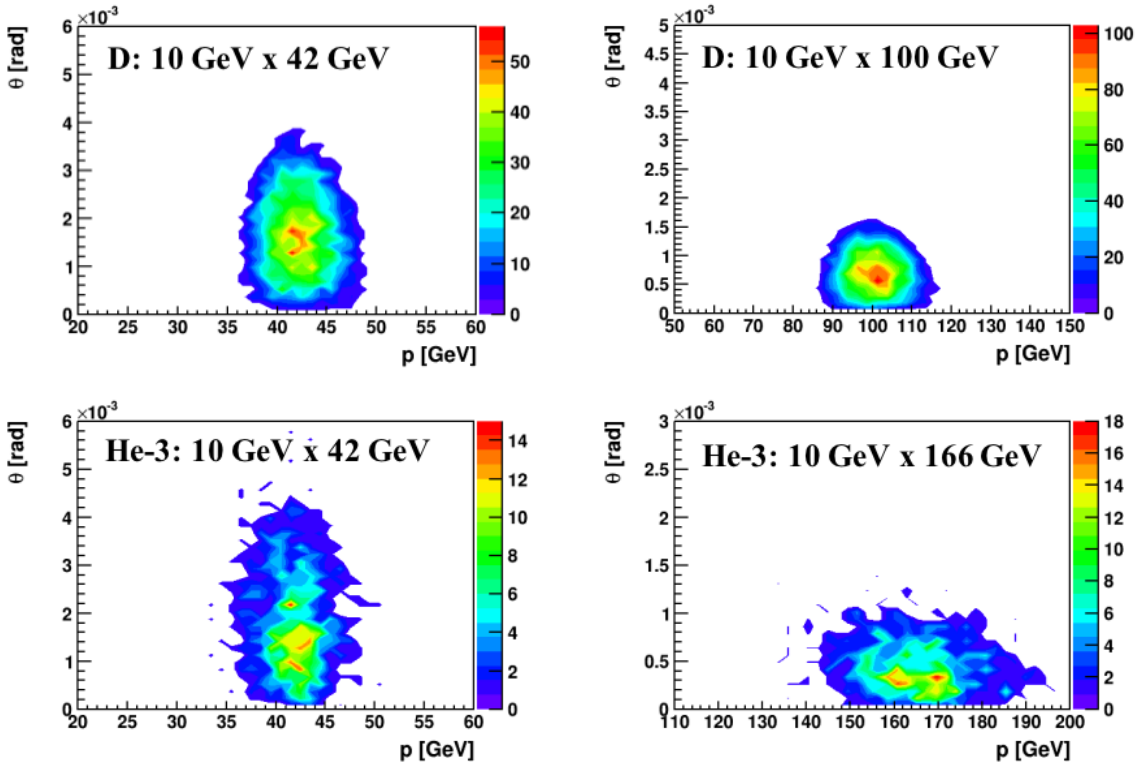

Figure 2.30: The correlation of momentum and scattering angle for the spectator proton in electron-deuteron and electron-^{3}He-scattering for two different values of $\sqrt{s}$.

electron-^{3}He scattering for two different values of $\sqrt{s}$. The detection of these spectator protons is challenging as they have small scattering angles and a different rigidity compared to the hadron beam, which leads to stronger bending in the magnets. The (un)polarized ^{3}He and deuterium beams do not only constitute effective neutron beams, but also provide the possibility to study how the proton structure is modified if bound in a nucleus. For this purpose, the spectator neutron needs to be tagged. These neutrons have the same distribution in scattering angle and momentum as the protons. Therefore, a ZDC with its acceptance optimized for break-up neutrons as described above (see Figure 2.26) will also have a high acceptance for these spectator neutrons.

Auxiliary Detectors

To utilize the full statistical power made possible by the high luminosity of 10^{33} to $10^{34}\,\mathrm{cm}^{-2}\mathrm{s}^{-1}$, it is indispensable to have high precision measurements of the electron and hadron beam polarizations and the luminosity. Doubly polarized electron-hadron colliders are the best way to unravel the internal structure of the nucleons and are the only tool, which will allow us to finally unravel how the spin of the proton is built by its quarks and gluons. Figure 7 in Ref. [45] shows, that for a high precision determination of the gluon contribution to the spin of the proton, the overall systematic uncertainty should be around two percent. An increase of the overall systematic uncertainty of five percent leads to a 30% increase in the uncertainty of the contribution of the gluons to the spin of the protons.

Luminosity The bremsstrahlung process $e + p \longrightarrow e + p + \gamma$ was used successfully for the measurement of luminosity by the HERA collider experiments [76–78]. It has the features of a precisely known large QED cross-section resulting in negligible statistical uncertainty. In contrast to HERA, where only the electron beam was polarized, both the electron and proton/light ion beams will be polarized in EIC. In this case the bremsstrahlung rate is sensitive to the polarization dependent term a in the cross section $\sigma_{\mathrm{brems}} = \sigma_0(1 + aP_eP_h)$. Thus, the polarization (P_e, P_h) and luminosity measurements are coupled, and the precision of the luminosity measurement is limited by the precision of the polarization measurement. This also limits the precision of the measurement of double spin asymmetries $A_{LL} = 1/(P_eP_h)(N^{++/--} - RN^{+-/-+})/(N^{++/--} + RN^{+-/-+})$ through the determination of the relative luminosity $R = L^{++/--}/L^{+-/-+}$. The precision needed for the relative luminosity measurement is driven by the magnitude of A_{LL} at low-x and Q^2, which is typically on the order of 10^{-4}. At RHIC levels of 2 to 4×10^{-4} have been achieved. A factor of 2 to 5 improvement is required for the EIC. As discussed earlier, due to the high luminosity it is critical to minimize the systematic uncertainties; the requirement for the systematic uncertainty is $\delta L/L < 1\%$. The straightforward method for measuring bremsstrahlung is to use a calorimeter at zero degrees in the electron direction counting the resulting photons, the distribution of which is strongly peaked in the forward direction. The calorimeter is also exposed to the direct synchrotron radiation fan and must be shielded, thus degrading the energy resolution. At peak HERA luminosities, the photon calorimeters were hit by 1–2 photons per HERA bunch crossing. At an EIC luminosity of $10^{33}\,\mathrm{cm}^{-2}\,\mathrm{s}^{-1}$, the mean num-

ber of photons per bunch crossing is over 20 for electron-proton scattering and increases with Z^2 of the target for nuclear beams. The distributions are broad, with a mean proportional to the number of photons per bunch crossing. The counting of bremsstrahlung photons thus is effectively an energy measurement in the photon calorimeter with all of the related systematic uncertainties (e.g. gain stability) of such a measurement. An alternative method to counting bremsstrahlung photons, used effectively by the ZEUS collaboration at HERA, employs a pair spectrometer. A small fraction of photons is converted into e^+e^- pairs in the vacuum chamber exit window. A dipole magnet splits the pairs and each particle hits a separate calorimeter adjacent to the unconverted photon direction. Further details about the luminosity monitor can be found in section 8.4.4.

Lepton and Hadron Polarimetry

Lepton Polarization: Compton back-scattering is the established method to measure electron beam polarization in *e+p* colliders. At HERA, there were two Compton back-scattering polarimeters [79], one measuring the transverse polarization (TPOL) of the beam through a position asymmetry, and another one measuring the longitudinal polarization (LPOL) of the beam through an energy asymmetry in Compton back-scattered photons. The TPOL and LPOL systematic uncertainties of HERA RUN-I were 3.5% and 1.6% and Run-II 1.9% and 2.0%, respectively. To balance the expected high luminosity at the EIC, these systematic uncertainties should be reduced to $\sim$ 1%. More details on EIC electron polarimetry can be found in Section 8.6.1.

Hadron Polarization: Measuring the hadron beam polarization is significantly more involved. Contrary to the electron case, there is no process that can be calculated from first principles. Therefore, a two-tier measurement is needed: one providing the absolute polarization, which normally has low statistical power, and a high statistical power measurement that measures the relative polarization. At RHIC [80], the single spin asymmetry A_N of the elastically scattered polarized proton beam on a polarized hydrogen jet is used to determine the absolute polarization. This measurement provides the average polarization per fill and for each proton beam with a statistical uncertainty on the order of $\approx$ 5% and a systematic uncertainty of 3.2%. High-statistics bunch-by-bunch relative polarization measurements are provided by measuring the single spin asymmetry A_N for scattering the polarized proton beam off a carbon fiber target. To obtain absolute measurements, the pC-measurements are cross-normalized to the absolute polarization measurements from the hydrogen-jet polarimeter. The pC-measurements provide the polarization lifetime and the polarization profile per fill with high statistical precision. The achieved total systematic uncertainty for single spin asymmetries until 2015 is 3.4%.

The same concept is currently planned for all polarized hadron beams in the EIC, namely proton, deuterium, and ^{3}He [81]. It is foreseen to continue to have the absolute and relative hadron polarimeters located at IP12 in EIC; therefore, no constraints need to be considered for the IR.

However, there is the requirement for a local polarimeter between the spin rotators to monitor the degree of spin rotation from transverse in the arcs to longitudinal at the experiments. This can be done by integrating a fast, high precision proton-carbon (pC) polarimeter into the extended IR. This pC polarimeter is based on very small angle polarized proton-carbon elastic scattering in the Coulomb-Nuclear Interference region. The analyzing power is maximum for transverse or radial hadron beam polarization and goes to zero for longitudinal polarized hadron beams. The requirements on the extended IR region are purely spatial ($\sim$ 0.5 to 0.8 m) to integrate the scattering chamber for the carbon target intercepting the beam and the Si-detectors to measure the elastically scattered carbons. More details on the EIC absolute and relative hadron beam polarimetry can be found in Section 8.6.2.

Summary of Requirements for the Interaction Regions

Table 2.2 summarizes the requirements for the overall interaction region design derived from the EIC physics discussed in the 2010 INT Report [38], the EIC White Paper [7], and the document assessing the energy dependence of key measurements [39].

Table 2.2: Summary of the requirements from the physics program on the overall IR design.

	Hadron	Lepton
Machine element free region	-4.5 m to $+5.0$ m main detector beam elements $< 1.5^\circ$ in main detector volume	
Beam Pipe	Low mass material, i.e. Beryllium	
Integration of detectors	Local Polarimeter	
Zero Degree Calorimeter	$60\,\text{cm} \times 60\,\text{cm} \times 2\,\text{m}$ @$s = 30\,\text{m}$	
scattered proton/neutron acc. all energies for e+p	Proton: $0.18\,\text{GeV/c} < p_T < 1.3\,\text{GeV/c}$ $0.5 < x_L < 1 (x_L = E'_p/E_{Beam})$ Neutron: $p_T < 1.3\,\text{GeV/c}$	
scattered proton/neutron acc. all energies for e+A	Proton and Neutron: $\theta < 6\,\text{mrad}$ (for $\sqrt{s} = 50\,\text{GeV}$) $\theta < 4\,\text{mrad}$ (for $\sqrt{s} = 100\,\text{GeV}$)	
Luminosity	Relative Luminosity: $R = L^{++/--}/L^{+-/-+} < 10^{-4}$	
		γ acceptance: ± 1 mrad $\rightarrow \delta L/L < 1\%$
Low Q^2-Tagger		Acceptance: $Q^2 < 0.1\,\text{GeV}$

Chapter 3

EIC Design

3.1 Beam Parameters, Luminosities and Complex Layout

3.1.1 Beam Parameters and Luminosities

Overview

The polarized Electron-Ion Collider EIC provides collisions of polarized electrons and polarized protons in the center-of-mass energy region from 20 to 141 GeV, and polarized electron-heavy ion collisions up to 89 GeV/n. This is accomplished by adding an electron storage ring with up to 18 GeV beam energy to the existing RHIC facility, and colliding those electrons with polarized protons or heavy ions stored in the hadron storage ring (HSR) operating at energies between 41 and 275 GeV (protons), or 41 to 110 GeV/nucleon (ions). The high electron energy requires a large bending radius of the electron storage ring, which will therefore be installed in the existing RHIC tunnel. Beams will be brought into collision in up to two interaction regions, namely in IR6 and IR8. Electron-proton luminosities reach $1.0 \times 10^{34}\,\mathrm{cm}^{-2}\mathrm{sec}^{-1}$. These high luminosities require strong hadron cooling to counteract emittance growth due to intrabeam scattering, which is very challenging. To mitigate the risk associated with strong hadron cooling, a scenario which uses a full-energy injector has been developed [23]. In this scheme, the entire hadron fill in the HSR is replaced approximately every two to three hours at collision energy, thus keeping the luminosity nearly constant. In addition to this mitigation, a moderate luminosity scenario has been worked out that reaches luminosities of up to $4.3 \times 10^{33}\,\mathrm{cm}^{-2}\mathrm{sec}^{-1}$ without cooling.

These high luminosities are achieved by increasing the number of bunches, from 110 in the present RHIC to 1160 (580 without cooling), and operating both the electron and the hadron storage rings at their respective beam-beam limits. The beam-beam limits assumed in the design are based on parameters achieved — or even slightly exceeded — at RHIC (hadrons) and the e^+e^- collider B-Factories PEP-II and KEKB (electrons). In addition, a maximum synchrotron radiation power of 10 MW is chosen to limit operational costs. It

is worthwhile mentioning that this is not a technical limitation; in KEKB, the synchrotron radiation power loss per unit length, which at 10 kW/meter is state-of-the art, is more than twice as high as the 4 kW/meter in the EIC.

Luminosity

The luminosity of an electron-ion collider is given as

$$\mathcal{L} = \frac{N_{\mathrm{e}} N_{\mathrm{h}}}{4\pi\sigma_x\sigma_y} H f_{\mathrm{rep}}, \tag{3.1}$$

with N_{e} and N_{h} being the electron and hadron bunch intensities, respectively, and σ_x and σ_y the horizontal and vertical RMS beam sizes at the interaction point (IP), which are assumed to be identical for the two beams. H is a factor reflecting the impact of the hourglass effect and the crossing angle; it is near unity if the RMS bunch lengths are smaller than the IP β-functions β_x^*, β_y^*, and the crossing angle is corrected using crab cavities. $f_{\mathrm{rep}} = N_b f_{\mathrm{rev}}$ denotes the bunch repetition rate, with N_b the number of bunches per ring and f_{rev} the revolution frequency of the collider rings.

The numbers of particles per bunch, N_{e} and N_{h} are constrained by the beam-beam parameters $\xi_{e,h,x,y}$ induced by each beam on the other, which are computed as

$$\begin{aligned} \xi_{e,h,x,y} &= \frac{r_{e,h}}{2\pi} \frac{N_{h,e}\beta^*_{e,h,x,y}}{\gamma_{e,h}\sigma_{h,e,x,y}(\sigma_{h,e,x} + \sigma_{h,e,y})} \\ &= \frac{r_{h,e}}{2\pi} \frac{N_{e,h}}{\gamma_{e,h}\epsilon_{h,e,x,y}} \frac{1}{1+K_{x,y}}, \end{aligned} \tag{3.2}$$

where we have used

$$\sigma_{x,y} = \sqrt{\epsilon_{h,x,y}\beta^*_{h,x,y}} = \sqrt{\epsilon_{e,x,y}\beta^*_{e,x,y}}. \tag{3.3}$$

$r_{h,e}$ are the classical radii of the hadrons or electrons, $K_x = \sigma_x/\sigma_y$, and $K_y = \sigma_y/\sigma_x$, while $\epsilon_{h,x,y}$ and $\epsilon_{e,x,y}$ denote the horizontal and vertical emittances of the hadron and electron beam, respectively.

Expressing the bunch populations through the beam currents,

$$I_{h,e} = N_{h,e} q f_{\mathrm{rep}}, \tag{3.4}$$

and combining Equations (3.1) to (3.4) we re-write the luminosity as

$$\mathcal{L} \propto H\sqrt{\gamma_e\gamma_h I_e I_h(1+K_x)(1+K_y)}\left(\frac{\xi_{h,x}\xi_{h,y}\xi_{e,x}\xi_{e,y}}{\beta^*_{h,x}\beta^*_{h,y}\beta^*_{e,x}\beta^*_{e,y}}\right)^{1/4}. \tag{3.5}$$

RHIC has achieved a beam-beam parameter of $\xi_p = 0.015$ in proton-proton collisions; we therefore base the EIC design on the same value. Beam-beam tune shift parameters in excess of $\xi_e = 0.1$ have been reached at the e^+e^- collider KEKB. The main parameters of that machine resemble the EIC electron ring as shown in Table 3.1, and can therefore serve as a reference for EIC.

Table 3.1: Key design parameters of CESR-B [82], PEP-II [83, 84], KEKB [85], and the EIC electron ring. The EIC numbers in parentheses correspond to the version without strong hadron cooling.

Parameter	CESR-B	PEP-II LER/HER	KEKB LER/HER	EIC
Circumference C [m]	768	2200	3000	3834
Number of bunches N_b	36	1588	1584	1160 (580)
Beam current I [A]	0.365	2.45/1.55	1.3/1.6	2.5
Bunch intensity N_e [10^{10}]	16.2	7.0/4.4	5.0/6.2	15 (30)
Beam-beam parameter ξ_e	0.062	0.064/0.055	0.12/0.1	0.1
Transv. damp. decr. δ [10^{-4}]	1.1	1.8/2	2.5	1.25

Taking into account all these constraints, the luminosity is maximized for flat beams with $K_x \gg 1$, as indicated by Equation (3.5). This is realized by both unequal β-functions, $\beta^*_x \gg \beta^*_y$, and unequal emittances, $\epsilon_x > \epsilon_y$. Electron storage rings naturally have a very small vertical emittance; betatron coupling and wigglers will be used to increase the electron beam vertical emittance to an appropriate level. Increasing the hadron horizontal emittance may also be performed with transverse injection mismatch or application of horizontal kicker noise.

The magnitudes of the hadron design emittances are chosen such that they can be achieved and maintained by the projected strong electron cooling facility, which must counterbalance the emittance growth rates due to IBS. Without hadron cooling peak luminosities reach up to $4.3 \times 10^{33}\,\mathrm{cm}^{-2}\mathrm{sec}^{-1}$ based on hadron beam emittances close to those achieved during current RHIC operations, which are listed in Table 3.2.

Table 3.2: Proton beam emittances and intensities achieved during regular RHIC operations.

Parameter	Value
Bunch intensity $[10^{10}]$	26
RMS normalized emittance, h/v [μm]	2.5/2.5
Longitudinal bunch area [eV-s]	1.6

To reach an electron beam-beam parameter $\xi_e = 0.1$, comparable to KEKB, sufficient synchrotron radiation damping is necessary. While the transverse synchrotron radiation damping decrement at KEKB was $\delta = 2.5 \times 10^{-4}$, simulation studies indicate that in EIC a transverse damping decrement of $\delta = 1.25 \times 10^{-4}$ is sufficient for stable operation at $\xi_e = 0.1$. This is consistent with the fact that the maximum beam-beam parameter at KEKB reached $\xi_e = 0.12$.

IP β-functions

The minimum achievable IP β-functions β^* are limited by a number of factors. The β-functions and therefore the transverse RMS beam sizes reach their maximum in the low-β quadrupoles which are located at a distance l^* from the interaction point (IP) according to

$$\beta(l^*) = \beta^* + \frac{(l^*)^2}{\beta^*}. \tag{3.6}$$

The EIC Physics program requires a machine-element free space of ± 4.5 m around the IP. In practice, due to required vacuum system elements such as warm-to-cold transitions and bellows, the first magnets cannot be installed closer to the IP than approximately at $l^* > 5$ m. The large β-functions resulting from small values of β^* require large apertures in those low-β magnets. As a consequence, for a given gradient requirement in those magnets, the peak field must increase accordingly. In order to reduce the risk and cost associated with building and operating those magnets, the maximum peak field for the EIC IR magnets is kept low enough for conventional NbTi technology. For an electron ion collider IR we must have coil structures that provide large magnetic fields in the hadron beam aperture while shielding the electron beam from these fields, and the EIC experimental physics program requires some hadron magnets to have very large apertures.

Large β-functions in the focusing quadrupoles result in large contributions to the chromaticity ζ of the machine lattice,

$$\zeta = \frac{1}{4\pi} \oint k(s)\beta(s)\,\mathrm{d}s, \tag{3.7}$$

where $k(s)$ denotes the quadrupole strength. This chromaticity must be compensated using sextupole magnets in the arcs. Due to the nonlinear nature of those magnets they limit the dynamic aperture of the machine. Experience at other colliders shows that sufficient dynamic aperture can be achieved as long as the chromatic contribution of the interaction region, ζ_{IR}, does not exceed approximately 1/3 of the chromaticity of the arcs,

$$\zeta_{\mathrm{IR}} < \frac{1}{3}\zeta_{\mathrm{arcs}}. \tag{3.8}$$

In the EIC electron storage ring (ESR), this condition is fulfilled as long as the maximum β-functions in the low-β quadrupoles do not exceed $\hat{\beta} \simeq 800\,\mathrm{m}$.

Small values of β^* in conjunction with long hadron bunches lead to a geometric reduction of the luminosity. Assuming Gaussian beams, this so-called hourglass effect can be expressed as

$$\begin{aligned} R(t_x, t_y) &= \frac{L}{L_0} \\ &= \int_{-\infty}^{\infty} \frac{\exp(-t^2)}{\sqrt{(1 + t^2/t_x^2)(1 + t^2/t_y^2)}} \frac{\mathrm{d}t}{\sqrt{\pi}}, \end{aligned} \tag{3.9}$$

with

$$t_x^2 = \frac{2({\sigma_{x,p}^*}^2 + {\sigma_{x,e}^*}^2)}{(\sigma_{z,p}^2 + \sigma_{z,e}^2)({\sigma_{x,p}^*}^2/{\beta_{x,p}^*}^2 + {\sigma_{x,e}^*}^2/{\beta_{x,e}^*}^2)}. \tag{3.10}$$

In addition, the finite EIC crossing angle of $\theta = 25$ mrad causes a further reduction of the luminosity despite the use of crab cavities due to the finite wavelength of the 197 MHz crab cavities, which causes a significant residual offset of the head and the tail of the long hadron bunch w.r.t. the electron bunch. In the limit of short electron bunch length and small crossing angle ($\sin\theta \approx \theta$), the luminosity can be expressed as

$$L = \frac{2 f_b N_p N_e}{\sigma_{z,p}(2\pi)^{3/2}} \int_{-\infty}^{\infty} \mathrm{d}z \frac{\exp\left\{-\frac{(\hat{x}\sin(2kz) - \theta z)^2}{2(\sigma_{x,e}^2 + \sigma_{x,p}^2)} - \frac{2z^2}{\sigma_{z,p}^2}\right\}}{\sqrt{(\sigma_{x,e}^2 + \sigma_{x,p}^2)(\sigma_{y,e}^2 + \sigma_{y,p}^2)}}, \tag{3.11}$$

where k is the crab cavity RF wavelength , $k = 2\pi f_{\mathrm{crab}}/c$, $\hat{x}$ is the maximum offset at the

IP due to the crab cavity, and the z dependence of the transverse beam sizes are included. The luminosity is close to maximum when $2k\hat{x} = \theta$. To limit the geometric luminosity loss due to the hourglass effect and the finite wavelength of the crab cavities, the lowest β^* values should not be significantly smaller than the RMS hadron bunch length. Taking $\sin x \approx x - x^3/6$ the two terms in the exponential of Equation (3.11) are equal at $z = \sigma_{z,p}$ when

$$2\hat{x}k^3\sigma_{z,p}^3 = 3\sqrt{\sigma_{x,p}^2 + \sigma_{x,e}^2}, \tag{3.12}$$

which can be used to judge the relative importance of bunch length and crab wave number as compared to transverse beam size. This puts an upper limit on the wave number of the crab cavity, though other effects, such as synchrobetatron resonances, impose additional constraints.

Lastly, the EIC physics program requires detection of protons with a transverse momentum as low as $p_\perp = 200\,\mathrm{MeV/c}$. At 275 GeV proton beam energy, for instance, this translates into a scattering angle of 0.72 mrad. In order to detect these scattered particles, the divergence angle of the proton beam itself at the IP must be smaller than this scattering angle, so the scattered particles travel outside the proton beam envelope where they can be intercepted by dedicated detectors. Experience at HERA has shown that such "Roman Pots" can be operated safely at a transverse distance of about $10\,\sigma$ from the beam center, where σ denotes the RMS beam size at the location of the Roman Pot. This restricts the RMS proton beam divergence at the IP to a tenth of the minimum scattering angle to be detected, $10\,\sigma' \leq 72\,\mathrm{mrad}$ in at least one transverse plane. For a given proton beam emittance this, in turn, limits the minimum β-function at the IP to

$$\beta^* \geq \epsilon/\sigma'^2 \tag{3.13}$$

The short hadron bunch lengths require small longitudinal emittances in order to limit the resulting momentum spread $\Delta p/p$ for a given bunch length, which would otherwise exceed the off-momentum dynamic aperture of the machine. In conjunction with high bunch intensities, these small hadron beam emittances, on the other hand, result in fast emittance growth rates of approximately 2 h due to intrabeam scattering (IBS) in the $10^{34}\,\mathrm{cm^{-2}sec^{-1}}$ luminosity version. This growth needs to be counteracted by strong hadron cooling to achieve typical store lengths of 10–12 hours. In the moderate luminosity scenario, minimum IBS growth times are 8 hours, which is comparable to present RHIC and therefore does not require cooling.

Beam Heating

While short, intense hadron bunches are desirable to maximize the luminosity, they cause a significant heat load to the 4.6 K cryogenic system due to the resistive wall impedance of the stainless steel beam pipes of the RHIC superconducting magnets, which scales as the

product of total beam current, I, and peak bunch current, $\hat{I}$,

$$P_{\text{cryo}} \propto I \cdot \hat{I}. \tag{3.14}$$

We will insert a beam screen with copper on its interior surface throughout the existing RHIC beam pipes to reduce the vacuum chamber resistivity and hence keep the dynamic heat load below 0.5 W/m.

The short bunch spacing of ≈ 10 ns together with the high bunch intensity may give rise to electron clouds in the hadron ring. The threshold for this instability depends strongly on the secondary electron yield (SEY) of the vacuum chamber surfaces. Simulations show that below an SEY of 1.2 the instability does not occur. To reduce the secondary electron emission in the hadron ring vacuum chambers to a sufficiently low value, a thin layer of amorphous carbon will be applied on top of the copper surface of the beam screen.

RF System

Together with the reduced longitudinal emittance achieved by bunch splitting, high RF voltages are required to reach the desired short bunch lengths. It is planned to upgrade the present RF system, which consists of 28 and 197 MHz cavities, with a 591 MHz RF system, thus limiting the required RF voltage due to the higher harmonic number.

The total electron beam current $I_e = e \cdot N_e \cdot f_b$, where e is the electron charge, is limited by the available RF power required to restore the synchrotron radiation losses. This radiated power can be expressed as

$$P\,[\text{kW}] = 88.46 \cdot \frac{E_e\,[\text{GeV}]^4}{r\,[\text{m}]} \cdot I_e\,[\text{A}]. \tag{3.15}$$

Here E_e is the electron beam energy, and r the dipole bending radius of the storage ring. To limit the required investment cost for the storage ring RF system as well as the operating cost, the synchrotron radiation power has been limited to 10 MW. The RF system in the electron storage ring consists of superconducting 591 MHz two-cell cavities. With a voltage of 3 MV per cell, a total of 24 cells are required to provide the necessary voltage at 18 GeV beam energy. The cavities are located in IR10. There is a plan to go to one cell per cavity and 18 cavities at 3.9 MV per cell but this does not significantly impact other systems.

Besides the RF power requirement the electron beam intensity is limited by collective effects, namely the coupled bunch instability (CBI) and the transverse mode coupling instability (TMCI). While the plan is to have a damper for longitudinal instabilities, the beam-beam tune spread is a potent source of transverse Landau damping. Any transverse damper would be designed to act only when beam-beam was either weak or absent.

Beam Polarization

Both the electron and the proton beam in the EIC require a high degree of polarization. Polarized protons with up to 65% polarization at energies up to 250 GeV have already been routinely achieved using two Siberian snakes in RHIC. Relocation of the two existing Siberian Snakes from the unused second RHIC ring to the hadron storage ring, and converting unused spin rotators into two additional Siberian Snakes for the HSR is expected to increase spin polarization to the 70% level. Additional improvements planned in the AGS will raise this level to 80%.

High polarization with arbitrary spin patterns in the electron ring is achieved by injecting bunches with the desired spin orientation at full collision energy. Bunches with their spin orientation parallel to the main dipole field of the storage ring will slowly reverse their polarization direction due to the Sokolov-Ternov effect. It is therefore necessary to replace entire bunches at a rate significantly faster than the Sokolov-Ternov time constant.

The shortest Sokolov-Ternov (de-)polarization time over the entire energy range of the electron storage ring occurs at 18 GeV, where it reaches $\tau_{S-T} = 28$ min. Replacing individual bunches after approximately 2 min ensures a high level of polarization in either spin orientation. The injection scheme uses "swap-out" injection and extraction with the rapid cycling synchrotron operating with two bunches and a 2 Hz repetition rate.

Electron bunches are generated in an SLC-type polarized electron gun. The SLC gun has routinely generated 16 nC electron bunches at a 120 Hz rate with over 80% polarization. This performance is sufficient for the EIC, which requires 10 nC at 1 Hz and similar polarization levels. After pre-acceleration in a 400 MeV normal-conducting S-band LINAC these bunches will be injected into a rapid-cycling synchrotron (RCS) in the RHIC tunnel to be accelerated to full collision energy of up to 18 GeV. The RCS is ramped once per second within 200 ms from 400 MeV to 18 GeV. Two electron bunch trains of up to four bunches each are injected using a mutiharmonic transverse deflecting cavity, pulsed during a single turn. This enables bunch injection in adjacent 591 MHz buckets. After acceleration to 1 or 1.5 GeV the bunches are merged pairwise to achieve the final required charge (see Section 3.6.5 for detail). Merging is then followed by acceleration and extraction.

In order to preserve polarization during acceleration, the RCS lattice has a high superperiodicity. Together with the appropriate choice of the betatron tune this ensures that no intrinsic spin resonances are encountered during the entire ramp to 18 GeV. This high superperiodicity is somewhat broken due to the required bypass around the EIC detector. However, spin tracking studies have shown that less than 2% of the initial polarization is lost during the ramp to 18 GeV even with an RMS orbit error of 1 mm. The RF system in the RCS is comprised of multi-cell superconducting 591 MHz cavities with a total voltage of 72 MV.

Polarized protons are injected from the existing AGS at 25.5 GeV, and accelerated to full storage energy in the EIC hadron storage ring. With the maximum design bunch intensity and longitudinal emittance being about half the values presently achieved in RHIC, the required values can be reached by longitudinal bunch splitting.

While the spin orientation in both the electron and the proton beam is vertical in the storage ring arcs, the experiments require longitudinally polarized beams. The necessary spin rotation is accomplished by the existing helical dipole rotators in the proton ring, and by solenoid-based spin rotators in the electron machine. Spin matching is required to preserve spin polarization in the presence of these solenoids.

Interaction Region

The beams are brought into collision in either one or two interaction regions (IRs), at 6 o'clock (present STAR location) and 8 o'clock (PHENIX/sPHENIX). The two beams collide at a total crossing angle of 25 mrad, which provides early beam separation to avoid parasitic collisions, and allows low-β quadrupoles for the two beams to be installed close to the interaction point, with the first magnet located just outside the ± 4.5 long detector. The crossing angle is compensated by sets of crab cavities in each beam. These 197 MHz double quarter-wave crab cavities are scaled versions of the 400 MHz HL-LHC prototype crab cavities.

Beam Parameters

The beam parameters with and without strong hadron cooling and the resulting luminosities of electron-proton collisions at different center-of-mass energies $\sqrt{s}$ are listed in Tables 3.3 and 3.4. The required bunch intensities and longitudinal emittances can be achieved by longitudinal splitting of bunches with parameters very similar to present RHIC (see Table 3.2), assuming a moderate increase of the bunch intensity listed in the Table from 26×10^{10} to 30×10^{10} protons/bunch. The horizontal design emittances with strong hadron cooling are very close to the ones already achieved, while the much smaller vertical emittances are achieved and maintained by cooling. Depending on the actual cooling scheme, this process may also affect the horizontal plane where cooling is not desirable. The details of how to overcome this conundrum still need to be worked out.

Without hadron cooling, the vertical design emittances are identical to the ones achieved in RHIC, except for the case of highest center-of-mass energy $\sqrt{s} = 141$ GeV, which requires a slightly smaller vertical emittance that can be achieved by scraping in the AGS. The horizontal emittances without cooling are about twice as large as in present RHIC and can be easily achieved by application of noise to a broadband kicker or a deliberate injection mismatch.

Table 3.5 shows parameters and luminosities for collisions of electrons with fully stripped gold ions ($Z = 79$, $A = 197$).

Table 3.3: EIC beam parameters for different center-of-mass energies $\sqrt{s}$, with strong hadron cooling. High divergence configuration.

Species	proton	electron	proton	electron	proton	electron	proton	electron	proton	electron
Energy [GeV]	275	18	275	10	100	10	100	5	41	5
CM energy [GeV]	140.7		104.9		63.2		44.7		28.6	
Bunch intensity [10^{10}]	19.1	6.2	6.9	17.2	6.9	17.2	4.8	17.2	2.6	13.3
No. of bunches	290		1160		1160		1160		1160	
Beam current [A]	0.69	0.227	1	2.5	1	2.5	0.69	2.5	0.38	1.93
RMS norm. emit., h/v [µm]	5.2/0.47	845/71	3.3/0.3	391/26	3.2/0.29	391/26	2.7/0.25	196/18	1.9/0.45	196/34
RMS emittance, h/v [nm]	18/1.6	24/2.0	11.3/1.0	20/1.3	30/2.7	20/1.3	26/2.3	20/1.8	44/10	20/3.5
β^*, h/v [cm]]	80/7.1	59/5.7	80/7.2	45/5.6	63/5.7	96/12	61/5.5	78/7.1	90/7.1	196/21.0
IP RMS beam size, h/v [µm]	119/11		95/8.5		138/12		125/11		198/27	
K_x	11.1		11.1		11.1		11.1		7.3	
RMS $\Delta\theta$, h/v [µrad]	150/150	202/187	119/119	211/152	220/220	145/105	206/206	160/160	220/380	101/129
BB parameter, h/v [10^{-3}]	3/3	93/100	12/12	72/100	12/12	72/100	14/14	100/100	15/9	53/42
RMS long. emittance [10^{-3}, eV·s]	36		36		21		21		11	
RMS bunch length [cm]	6	0.9	6	0.7	7	0.7	7	0.7	7.5	0.7
RMS $\Delta p/p$ [10^{-4}]	6.8	10.9	6.8	5.8	9.7	5.8	9.7	6.8	10.3	6.8
Max. space charge	0.007	neglig.	0.004	neglig.	0.026	neglig.	0.021	neglig.	0.05	neglig.
Piwinski angle [rad]	6.3	2.1	7.9	2.4	6.3	1.8	7.0	2.0	4.2	1.1
Long. IBS time [h]	2.0		2.9		2.5		3.1		3.8	
Transv. IBS time [h]	2.0		2		2.0/4.0		2.0/4.0		3.4/2.1	
Hourglass factor H	0.91		0.94		0.90		0.88		0.93	
Luminosity [10^{33}cm^{-2}s^{-1}]	1.54		10.00		4.48		3.68		0.44	

Table 3.4: EIC beam parameters for different center-of-mass energies $\sqrt{s}$, with strong hadron cooling. High acceptance configuration.

Species	proton	electron	proton	electron	proton	electron	proton	electron	proton	electron
Energy [GeV]	275	18	275	10	100	10	100	5	41	5
CM energy [GeV]	140.7		104.9		63.2		44.7		28.6	
Bunch intensity [10^{10}]	18.9	6.2	6.9	17.2	6.9	17.2	4.8	17.2	2.6	13.3
No. of bunches	290		1160		1160		1160		1160	
Beam current [A]	0.69	0.227	1	2.5	1	2.5	0.69	2.5	0.38	1.93
RMS norm. emit., h/v [µm]	5.2/0.46	845/70	3.3/0.3	391/26	3.2/0.29	391/26	2.7/0.25	196/18	1.9/0.45	196/34
RMS emittance, h/v [nm]	17.6/1.6	24.0/2.0	11/1.0	20/1.3	30/2.7	20/1.3	26/2.3	20/1.8	44/10	20/3.5
β^*, h/v [cm]]	417/38	306/30	265/24	149/19	94/8.5	143/18	80/7.2	103/9.2	90/7.1	196/21
IP RMS beam size, h/v [µm]	271/24		172/16		169/15		143/13		198/27	
K_x	11.1		11.1		11.1		11.1		7.3	
RMS $\Delta\theta$, h/v [µrad]	65/65	89/82	65/65	116/84	180/180	118/86	180/180	140/140	220/380	101/129
BB parameter, h/v [10^{-3}]	3/3	92/100	12/12	72/100	12/12	72/100	14/14	100/100	15/9	53/42
RMS long. emittance [10^{-3}, eV·s]	36		36		21		21		11	
RMS bunch length [cm]	6	0.9	6	0.7	7	0.7	7	0.7	7.5	0.7
RMS $\Delta p/p$ [10^{-4}]	6.8	10.9	6.8	5.8	9.7	5.8	9.7	6.8	10.3	6.8
Max. space charge	0.007	neglig.	0.004	neglig.	0.026	neglig.	0.021	neglig.	0.05	neglig.
Piwinski angle [rad]	2.8	0.9	4.3	1.4	5.2	1.5	6.1	1.7	4.2	1.1
Long. IBS time [h]	2.0		3.2		2.5		3.1		3.8	
Transv. IBS time [h]	2.0		2.0		2.0/4.0		2.0/4.0		3.4/2.1	
Hourglass factor H	0.99		0.98		0.94		0.91		0.93	
Luminosity [10^{33}cm^{-2}s^{-1}]	0.32		3.14		3.14		2.92		0.44	

Table 3.5: EIC beam parameters for e-Au operation for different center-of-mass energies $\sqrt{s}$, with strong hadron cooling.

Species	Au ion	electron	Au ion	electron	Au ion	electron	Au ion	electron
Energy [GeV]	110	18	110	10	110	5	41	5
CM energy [GeV]	89.0		66.3		46.9		28.6	
Bunch intensity [10^{10}]	0.08	6.2	0.05	17.2	0.05	17.2	0.036	17.2
No. of bunches	290		1160		1160		1160	
Beam current [A]	0.23	0.227	0.57	2.50	0.57	2.50	0.41	2.50
RMS norm. emit., h/v [µm]	5.1/0.7	705/20	5.0/0.4	391/20	5.0/0.4	196/20	3.0/0.3	196/20
RMS emittance, h/v [nm]	43.2/5.8	20.0/0.6	42.3/3.0	20.0/1.0	42.3/3.0	20.0/2.0	68.1/5.7	20.0/2.0
β^*, h/v [cm]]	91/4	196/41	91/4	193/12	91/4	193/6	90/4	307/11
IP RMS beam size, h/v [µm]	198/15		196/11		197/11		248/15	
K_x	0.077		0.057		0.056		0.061	
RMS $\Delta\theta$, h/v [µrad]	218/379	101/37	216/274	102/92	215/275	102/185	275/377	81/136
BB parameter, h/v [10^{-3}]	1/1	37/100	3/3	43/47	3/2	86/47	5/4	61/37
RMS long. emittance [10^{-3}, eV·s]	16		16		16		16	
RMS bunch length [cm]	7	0.9	7	0.7	7	0.7	11.6	0.7
RMS $\Delta p/p$ [10^{-4}]	6.2	10.9	6.2	5.8	6.2	6.8	10	6.8
Max. space charge	0.007	neglig.	0.008	neglig.	0.008	neglig.	0.038	neglig.
Piwinski angle [rad]	4.4	1.1	4.5	1.2	4.5	1.5	5.8	1.2
Long. IBS time [h]	0.33		0.36		0.36		0.85	
Transv. IBS time [h]	0.81		0.89		0.89		0.16	
Hourglass factor H	0.85		0.85		0.85		0.71	
Luminosity [10^{33}cm^{-2}s^{-1}]	0.52		4.76		4.77		1.67	

3.1.2 Layout of EIC Accelerator Systems

The EIC accelerator complex is composed of the existing systems that constitute present RHIC and some systems which have been added. The most important existing system is the two RHIC storage rings with their superconducting magnets inside the RHIC tunnel. Only one superconducting ring is needed for EIC as the hadron storage ring (HSR). The ring is composed of six sextants separated by straight sections. The straight sections are labeled as "2, 4, 6, 8, 10 and 12 o'clock", with 12 o'clock being in the northernmost part of the ring, or, alternatively, as IR2 to IR12. The ring complex also includes the hadron injector chain with the AGS synchrotron, the Booster synchrotron, the injector LINAC and the particle sources. Furthermore there is a large cryogenic 4 K liquid helium plant located near IR6 that feeds the superconducting magnets.

New systems are the electron beam complex consisting of the electron storage ring, the electron injector synchrotron, and the electron injector. The storage ring and the injection synchrotron are located in the RHIC tunnel. In addition there is a 150 MeV energy recovery LINAC which provides electrons for strong hadron cooling.

The utility space of the present RHIC complex is not sufficient to host the equipment. A number of new buildings is required. These are described in Sections 6.10 and 7.2.

Figure 3.1 provides an overview of the layout of the EIC facility. The diagram shows the RHIC tunnel and labels indicate which of the new systems are located at or near which straight section. The new systems are summarized as follows:

- IR6 and 8:
  IR6 and IR8 accommodate the EIC colliding beam detectors and the magnetic lattices required for the interaction regions. The interaction region straights also host the spin rotators for electron and hadron beams, and the crab cavities for both beams. For the hadron beam two times two crab cavities are required. The spin rotators of the hadrons are identical to present RHIC. The crab cavities require a small 2 K liquid He plant.

- IR4:
  The hadrons traveling from the injection line via the outer arc from IR6 to IR4 are injected in IR4 and the new fast injection kickers of 25 m total length are located there. This straight section also accommodates the room temperature RF for hadrons. The hadron storage RF system needs an upgrade for splitting each bunch into 4 bunches and to provide short bunches for collisions. These systems, consisting of 49 MHz and 98 MHz cavities for splitting, and 591 MHz storage cavities, are placed there as well.

- IR2:
  This straight section hosts instrumentation, feedback systems, the electron source, the 400 MeV S-band injector LINAC, the electron cooler, and the beam dumps.

- IR12:
  This straight section accommodates the polarimeters for both electron and hadron

beams. At this location a small 2 K liquid He plant is needed for the superconducting ERL.

- IR10:
  IR10 hosts the hadron beam abort and the electron RF systems for storage ring and rapid cycling synchrotron.

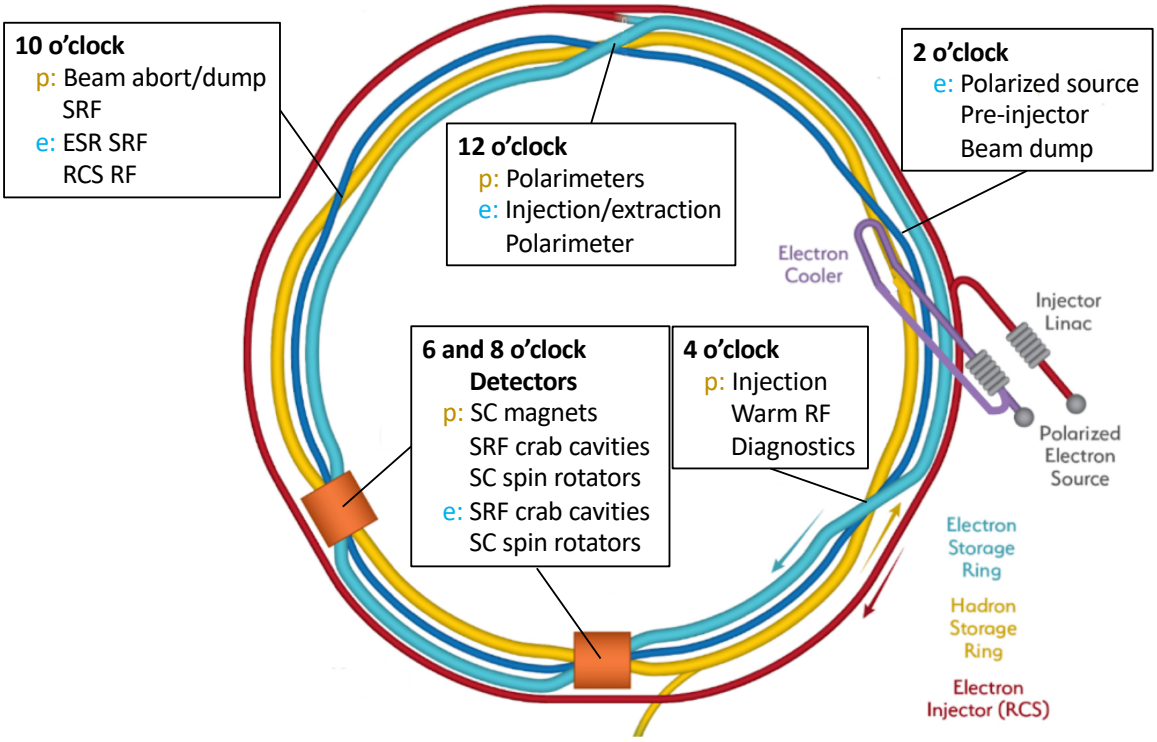

Figure 3.1: Schematic layout of locations of EIC Accelerator Hardware Systems. The yellow lines represent the "Yellow" ring for hadrons. The light blue line represents the electron storage ring, and the red line represents the rapid cycling injector synchrotron. The dark blue line is the unused part of the "Blue" ring which will stay in place. Note that the lattice and simulations described in this document are for the case of a single detector at the 6 o'clock area. Calculations with a second detector at the 8 o'clock area are in progress. Initial studies for the two-detector configuration are described in Sections 4.3 and 4.6.

3.2 Interaction Region Design

3.2.1 Interaction Region Design Concept

The design parameters of the EIC and their rationale have been discussed in Section 3.1.1. Some parameters relevant to the interaction region design are repeated in Table 3.6 for convenience.

Table 3.6: Key beam parameters at the energy point of highest luminosity relevant for the interaction region design.

	Proton	Electron	Proton	Electron	Proton	Electron
E_{CM} [GeV]	105		140		29	
Energy [GeV]	275	10	275	18	41	5
ϵ_x [nm]	11.3	20.0	18.	24.0	44	20.0
ϵ_y [nm]	1.0	1.3	1.6	2.0	10.	3.5
β_x^* [cm]	80	45	80	50	90	196
β_y^* [cm]	7.2	5.6	7.1	5.7	7.1	21.0

The purpose of the interaction region (IR) is to focus the beams to small spot sizes at the collision point and to separate them into their respective beam lines while providing the space and geometry required by the physics program for the detector. The separation is accomplished by a total crossing angle of 25 mrad between the two beams, which has the advantage of avoiding the introduction of separator dipoles in the detector vicinity that would generate a substantial amount of synchrotron radiation. The detrimental effects of this crossing angle on the luminosity and beam dynamics are compensated by a crab-crossing scheme. Figure 3.2 shows a zoom in of the rear and forward side of the IR.

The layout of the interaction region (IR) fulfills the following requirements:

- To achieve high luminosity, small beam cross sections are required. The beams are strongly focused at the interaction point (IP, small β^*) by low-β-quadrupole magnets (also referred to as final focusing quadrupoles).
- The final focusing quadrupoles must have sufficient aperture for the large beam size at their location.
- Large contributions to the chromaticity, which is a set of parameters characterizing the energy sensitivity of the beam optics, are generated in the low-β quadrupoles. Chromaticity needs to be compensated by nonlinear sextupole fields which, in turn, limit the dynamic aperture. The IR design balances small β^* and tolerable values of chromaticity.

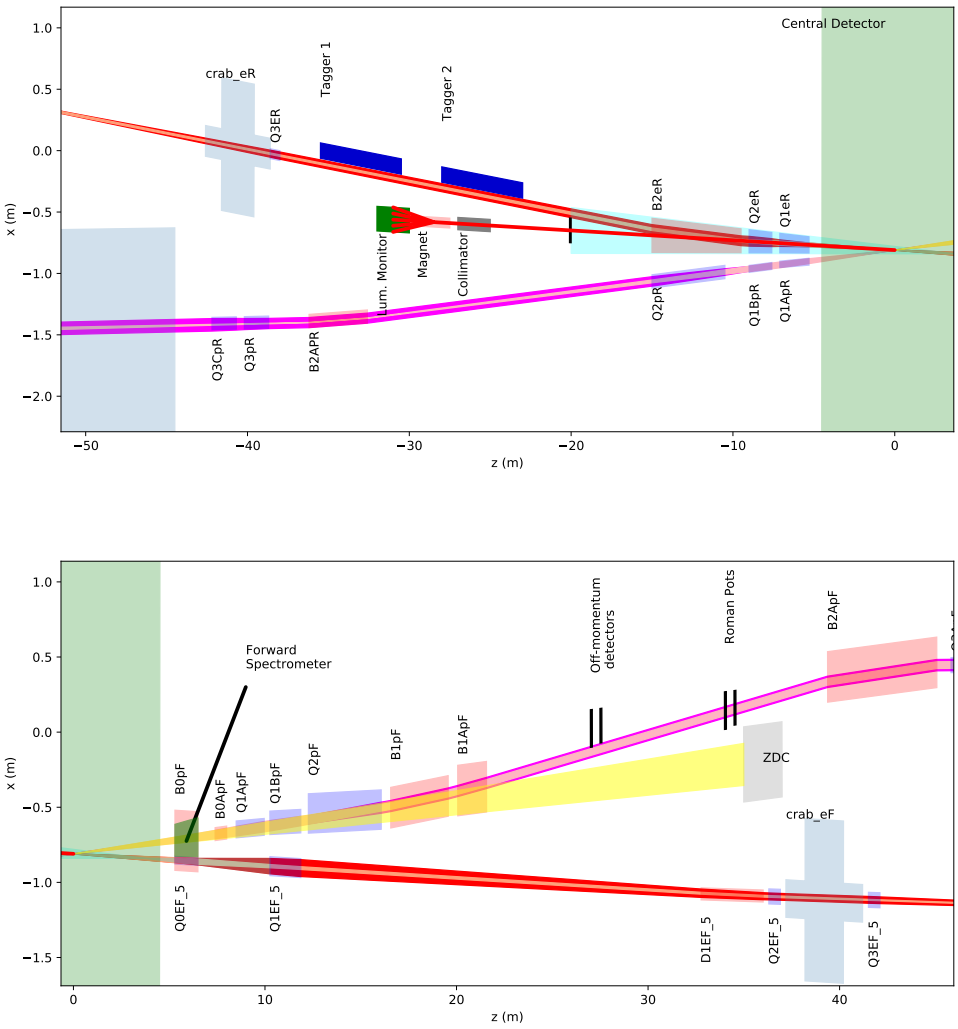

Figure 3.2: A zoom of the interaction region layout in the rear (top) and forward (bottom) directions.

- The colliding beam detector requires a large acceptance of protons scattered off the collision point. Therefore, we do not place accelerator components inside the detector ($\pm 4.5\,\mathrm{m}$ from the IP). Some of the low-β quadrupoles have even larger apertures so scattered protons and neutrons can be detected by detector elements placed further downstream.

- The beam divergence (and the minimum β^*) is restricted to enable detection of forward scattered protons with transverse momentum as small as $p_t = 200\,\mathrm{MeV/c}$. These particles are then outside the $10\,\sigma$ proton beam envelope and are detectable by near-beam-detectors, "Roman Pots", which are placed along the forward hadron beam pipe.

- The beams collide under a crossing angle of 25 mrad to provide immediate separation of the electron and proton beams, to avoid parasitic collisions and to provide space for a neutron detector at zero degree in the forward [1] direction and the luminosity detector in the rear side where the electron exit. An important factor is the large bunch frequency (up to 99 MHz, which corresponds to only 10 ns bunch spacing) required for high luminosity. The crossing angle effects (enlarged transverse beam size and excitation of synchro-betatron resonances) must be compensated for by using crab cavities, transverse RF resonators which kick the head and the tail of the proton (and electron) bunches in opposite directions in the plane of the crossing angle. These cavities are placed at a horizontal betatron phase advance of $\pi/2$ from the interaction point (IP) on both the rear and the forward sides, forming a 180° bump. This causes the bunches to be tilted in the horizontal plane by exactly half the crossing angle at the IP, and provides (ideally) the same collision geometry as head-on collisions and thereby avoids synchrobetatron coupling.

- Strong synchrotron radiation, which might be generated by the electron beam, can destroy sensitive detector equipment and make data-taking impossible. Therefore, we argue that the electron beam must not experience dipole fields in the interaction region (IR), and certainly not upstream of the IP (we use the term forward side). This is another strong reason why the two beams must collide at a crossing angle. Synchrotron radiation generated in the low-β quadrupoles on the rear-electron side should be absorbed on the rear side of the IR as far as possible from the detector so as to minimize backscattered photons. This requires an extra large aperture for the electron low-β quadrupole magnets on the downstream side of the IP.

- Both the light hadron and electron beams are spin polarized. Polarization is only stable if the polarization direction coincides with the direction of the guide field in the arc. In collisions, the spins of the electron beam are oriented longitudinally and the ones for the hadron beam either longitudinally or transverse. Thus the IR design accommodates pairs of spin rotators, which ensures longitudinal spin at the IP and vertical spin in the arcs. The spin rotators in the hadron ring already exist and are unchanged in this design. The spin rotators for the electron beam consist of two pairs of strong solenoids with quadrupole magnets in-between each pair which are tuned such that the x-y coupling by the two solenoids cancels. This set of four solenoids is required on both sides of the IP. The beam transport between the rotators is "spin transparent". This means that the magnetic fields in quadrupole magnets experienced by a particle performing betatron and synchrotron oscillations cancel between the spin rotators.

- The IR layout must provide room for a luminosity monitor on the rear side. This monitor detects hard γ-rays that are generated in the Bethe-Heitler process and exploited for luminosity measurement. The dipole magnet bending the electrons away from the path of the γ beam is at the same time a spectrometer magnet for the off-momentum electrons generated at low Q^2.

[1] The IP separates the IR into a forward and a rear side or direction. The forward side is the side of the proton beam coming from the IP and the rear side is the side of protons going to the IP.

- On the forward proton side, a neutron spectrometer is required. A dipole magnet bends the hadron beam away from the collision axis to provide space for this element. It also generates dispersion which helps to detect forward scattered protons in detectors that are integrated into the hadron beam pipe (called "Roman Pots").

The small β-functions at the IP necessitate focusing elements as close as possible to the IP. This is accomplished by a combination of dual-aperture magnets and single-aperture quadrupoles with field-free regions for the electron beam, as shown in Figures 3.3. Design magnet apertures are chosen such that a minimum aperture radius of 10σ for protons and 15σ for electrons is ensured in all operating modes. Tables 3.7 to 3.9 list the magnet parameters (with a starting Q,B nomenclature indicating quadrupole, dipole) in the electron and proton beam lines and their positions, beginning from the interaction point (IP).

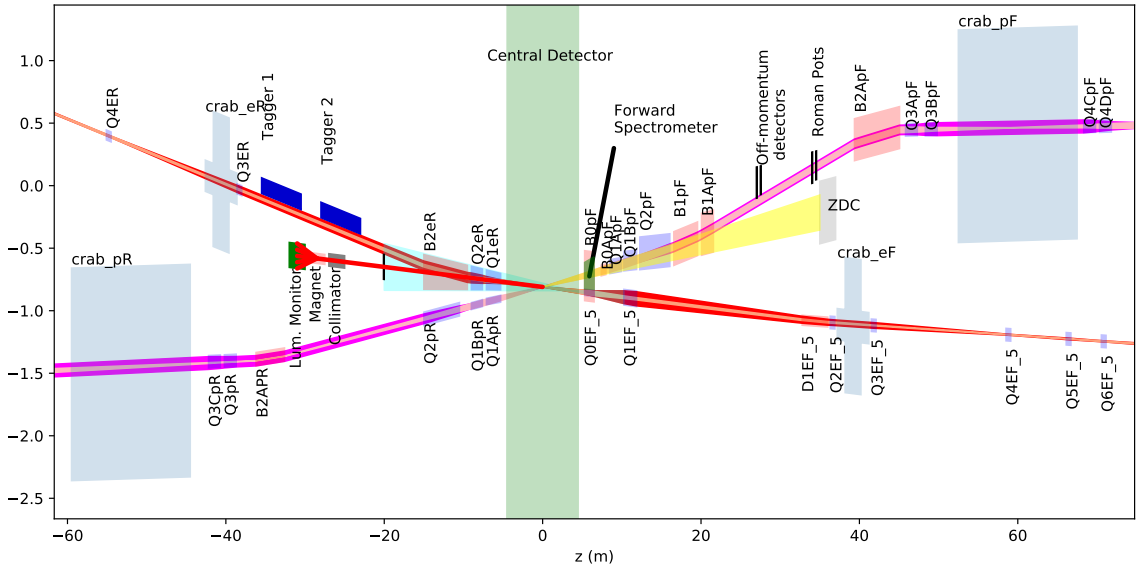

Figure 3.3: Schematic layout of the interaction region (top view, as simulated for high divergence, no cooling). Beams cross with a crossing angle of 25 mrad. Note the length scales for the horizontal and vertical axis are very different. The IR design integrates focusing magnets for both beams, luminosity and neutron detectors, electron taggers, spectrometer magnets, near-beam detectors (Roman pots for hadrons), crab cavities, and spin rotators for both beams. The two beams are both focused by quadrupole doublets. On the hadron-forward side, there are separate focusing magnets, which are longitudinally interleaved. The first quadrupole magnet for electrons is integrated into a hadron spectrometer dipole. On the rear side, hadrons and electrons are focused by quadrupoles, which are installed side-by-side in the same cryostat. The maximum β-functions in the IR for hadrons of 2000 m remain within the operating range of RHIC, while the maximum β-functions for electrons remain below 500 m.

Since for both beams the vertical IP β-function is much smaller than the horizontal one, $\beta_y^* \ll \beta_x^*$, the innermost quadrupoles on both beam lines are vertically focusing. In the hadron ring this limits the maximum vertical β-function in those magnets to about 1600 m

Table 3.7: Forward hadron magnets, the settings are for 275 GeV.

FORWARD DIRECTION	Hadron Magnets						
	B0PF	B0APF	Q1APF	Q1BPF	Q2PF	B1PF	B1APF
Center position [m]	5.9	7.7	9.23	11.065	14.170	18.070	20.820
Length [m]	1.2	0.6	1.46	1.6	3.8	3.0	1.5
Center position w.r.t. to x-axis [cm]	-1.50	5.5	1.40	2.38	4.07	3.90	8.00
Angle w.r.t. to z-axis [mrad]	-25.0	0.0	-5.5	-10.0	-10.2	9.0	0.0
Inner radius [cm]	20.0	4.3	5.6	7.8	13.1	13.5	16.8
Peak field [T]	-1.3	-3.3	0.0	0.0	0.0	-3.4	-2.7
Gradient [T/m]	0.0	0.0	-72.608	-66.180	40.737	0.0	0.0

Table 3.8: Forward electron magnets, the settings are for 18 GeV electron beam energy.

FORWARD DIRECTION	Electron Magnets		
	Q0eF	Q1eF	D1eF
Center position [m]	5.9	11.065	34.389
Length [m]	1.2	1.61	3.238
Angle w.r.t. to z-axis [mrad]	25.0	25.0	25.0
Inner radius [cm]	2.50	6.3	NA
Peak field [T]	0.0	0.0	0.067
Gradient [T/m]	-14.05	6.2624	

at a proton beam energy of 275 GeV, resulting in moderate contributions to the overall chromaticity of the machine. The horizontal β-function is intentionally increased to about 1300 m in the region of the crab cavities. This limits the required voltage of those devices, which scales as $1/\sqrt{\beta_x^* \beta_{\mathrm{crab},x}}$, to about $U_{\mathrm{crab}} = 12$ MV. At lower energies the IP β-functions are increased, resulting in lower β-functions in the low-β magnets as well as at the crab cavities. However, due to the lower beam rigidity the required crab cavity voltage does not exceed 14 MV at any energy.

The focusing scheme for the electrons is conceptually the same as for the hadrons. The vertical β-function reaches a maximum of about 500 m in the low-β quadrupoles, while the horizontal β is intentionally increased to about 200 m at the crab cavities to limit their required voltage.

The forward hadron magnet apertures are completely dominated by experimental acceptance requirements, and the $10\,\sigma$ outline shown for the circulating beam only uses the small central regions of the magnet apertures. This allows particles scattered at small angles to pass through the apertures of the innermost magnets so they can be detected by detectors which are integrated into the hadron beam vacuum system ("Roman Pots") further down

Table 3.9: Rear hadron and electron quadrupoles with their apertures tapered in proportion to their distance to the IP for 275 GeV and 18 GeV, respectively.

REARWARD DIRECTION	Hadron Magnets			Electron Magnets		
	Q1APR	Q1BPR	Q2PR	Q1eR	Q2eR	B2ER
Center position [m]	-6.2	-8.30	-12.75	-6.2	-8.30	-12.25
Length [m]	1.80	1.40	4.50	1.80	1.4	5.50
Angle w.r.t. to z-axis [mrad]	0.0	0.0	0.0	25.0	25.0	25.0
Entrance radius [cm]	2.00	2.80	5.40	6.60	8.30	9.70
Exit radius [cm]	1.00	1.00	1.00	1.00	1.00	1.00
Peak field [T]	0.0	0.0	0.0	0.0	0.0	-0.198
Gradient [T/m]	-78.375	-78.375	33.843	-13.980	14.100	0.0

the beamline.

Fig. 3.4 shows a schematic cutaway view, looking from the IP, of B0 the first forward side dual-function superconducting magnet where the electron beam pipe is on the left and hadron beam pipe on the right. The cross hatched region shown inside Fig. 3.4 indicates the warm space dedicated for experimental detectors placed outside the hadron beam pipe that cover an intermediate angle, 6–20 mrad, range for forward particles (that would not make it through the other forward hadron magnet to the Roman Pots and ZDC). The main B0 coils, denoted B0PF in the hadron lattice, consist of concentric quadrupole and dipole superconducting coils that provide a combined function, 1.3 T average, magnetic field over the detector instrumented region afford spectrometer functionality. However, the relative magnetic strengths of the B0PF quadrupole and dipole coils are carefully tuned to provide some quadrupole focusing, but most importantly zero dipole field, at the center of the electron beam pipe. In this manner we pass the electron beam close by the much larger magnitude spectrometer field needed for measuring the forward hadrons without generating excessive hard synchrotron radiation.

The purely quadrupole field at the electron beam axis also serves a useful purpose as the first focusing element for the electron beam on the forward side, denoted Q0EF in the electron lattice. In this way we have Q0EF as close as possible to the IP and this is useful to avoid overly large forward side electron Twiss beta functions and thus minimize the IR chromaticity impact on the storage ring optics. However, since we must be able to vary the electron and hadron beam energies independently, we provide for an additional much smaller diameter superconducting quadrupole coil for electron gradient tuning, i.e. either adding or subtracting from the main coil gradient. This electron gradient tuning coil shows as black on the 3D main coil field map plotted on Fig. 3.5. All of these coils will be wound using BNL Direct Wind coil production techniques with the main coils using 1 mm diameter seven-strand round cable and the gradient tuning coil using 0.33 mm single strand wire. The main quadrupole and dipole coils will be wound on independent support

tubes to give space for liquid helium to flow between these coils. Space for helium cooling and what is effectively a mini-cryostat is needed around the gradient adjustment coil. As is should be obvious from Fig. 3.4, this necessary structure around the electron beam will unavoidably cut a little bit into the hadron forward acceptance in the region between the two beams. Also, because the B0 zero-field axis is parallel to the common axis of the main quadrupole and dipole coils, the B0 magnet is aligned with the outgoing electron beam and the circulating hadron beam enters B0 with the full 25 mrad crossing angle as shown in Fig. 3.4.

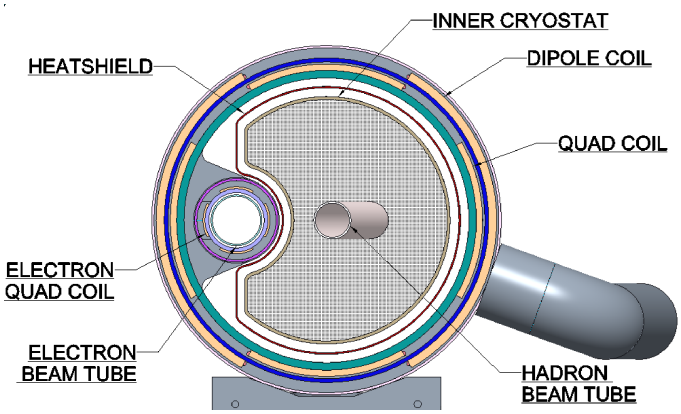

Figure 3.4: Cutaway view of the B0 spectrometer with warm space for detector elements highlighted in the cross hatch region. The view is from the IP end of the magnet with the electron beam pipe on the left and the hadron beam pipe on the right. As described in the text, B0 uses a combination of superconducting coils to provide pure focusing (with zero dipole field) at the electron beam and a 1.3 T average magnetic spectrometer field at the hadron beam.

The B1PF and B1APF dipoles separate the hadron beam from the outgoing 4 mrad neutron cone, and create dispersion at the Roman Pots to allow determination of the forward momentum of the scattered particles.

The last bending magnet on the electron forward side is located sufficiently far away to limit synchrotron radiation. Within this region the only source of synchrotron radiation is focusing in quadrupole magnets. The synchrotron radiation fan generated in the far arc dipoles can be easily collimated such that it is completely contained within the radiation fan produced by the quadrupoles in the straight. This fan has finite maximum divergences, collimated to 13 σ bounds, that are allowed to pass without interference through the beam pipe and following magnets, thus allowing for installation of detector components close to the beam. This is discussed in detail in Section 3.2.7.

On the rear side, no dipoles are introduced into the proton beam line, which allows placement of the low-β quadrupoles even closer to the IP than on the forward side. The electron beamline contains a bending magnet that bends the electrons away from the γ-beam generated by scattering of electrons at the hadrons (Bethe-Heitler process) which is used to measure luminosity in the luminosity monitor placed in this area. The bending magnet

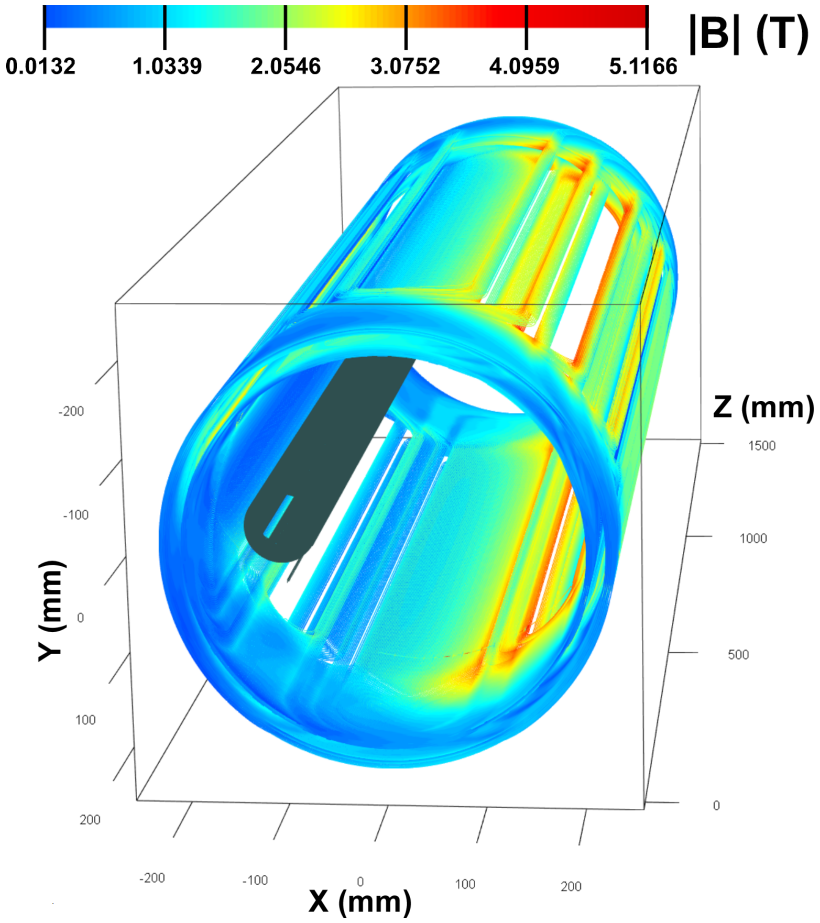

Figure 3.5: 3D perspective view of the Direct Wind B0 superconducting coil structure. Large diameter nested quadrupole and dipole coils provide the 1.3 T average magnetic field needed for spectrometer functionality, while their fields cancel to yield zero dipole field at the offset location of the electron beam. The smaller coil, used to adjust the net electron focusing gradient, is indicated here in black.

also serves as a spectrometer to tag scattered electrons that lost energy in the Bethe-Heitler process, but most importantly for the scattered electrons with low Q^2. However, since this magnet is introduced downstream of the main detector, the associated synchrotron radiation fan does not pass through the experiment.

The vertically focusing low-β quadrupoles Q1ER and Q1APR as well as Q2ER and Q1BPR are realized as superconducting dual-aperture magnets sharing the same iron yoke, as shown in Figure 3.6 (left). The apertures for both beams are tapered and angled with respect to each other, following the divergent hadron beam and synchrotron radiation fan as they emerge from the central detector, as depicted in Figure 3.6 (right). The tapering is needed to minimize the initial magnet apertures and to allow enough iron between the beams in order to limit the magnetic fields for each of them effecting the other section.

The required horizontal aperture radius x_{synch} to accommodate the synchrotron radiation

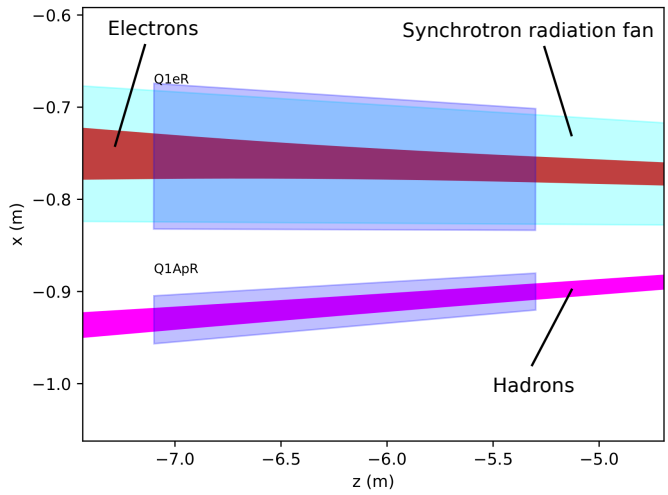

Figure 3.6: Cross section and top view of the first rear quadrupoles Q1ER and Q1APR, sharing the same iron yoke. The apertures are tapered around the synchrotron radiation fan and the hadron beam envelope, respectively.

fan from the 12.5σ electron beam at distance s from the IP is parameterized as

$$x_{\text{synch}}(s) = 6.75 \times 10^{-3}(s + 3.5) \tag{3.16}$$

This was used for the initial design of the magnets, where it was found that using masks can substantially reduce the rear electron magnet aperture size, as shown in section 3.2.7.

The vertical size of the synchrotron radiation fan y_{synch} is significantly smaller than the horizontal one. The horizontally focusing quadrupoles Q2ER (tapered) and Q2PR (not tapered) are conceptually similar to Q1ER and Q1APR. With these apertures, the entire synchrotron radiation fan is transported safely through the interaction region until it hits a dedicated absorber 23 m from the IP. Recently much more detailed simulations based with the SYNRAD code have been done and are described in section 3.2.7.

It is noted that the EIC has the capability of having two interaction regions (IRs). There is complementarity in the design of the two IRs with respect to the center-of-mass energy range where the 2nd IR is optimized to have the highest luminosity and detection capabilities alternative to the 1st IR. Appendix A discusses implementation of the 2nd IR consistent with nuclear physics, accelerator and engineering requirements. These include the operation of both IRs over the entire energy range of 29 GeV to 140 GeV center of mass. Consistent with user demands and the complementarity approach, the 2nd IR is optimized to provide the highest luminosity at a lower CM that the 1st IR, between ≈45 GeV and ≈80 GeV. This allows one to level the luminosity curve of the EIC as a whole at a higher level over a wider energy range. It can also provide a different acceptance coverage than the 1st IR described in this chapter.

3.2.2 Experiment Solenoid Coupling Compensation

Solenoid Strengths and Coupling Parameters

The *characteristic angle* associated with a detector solenoid of integrated field strength B_sL is

$$\theta \;=\; \frac{B_sL}{2(B\rho)} \tag{3.17}$$

The *coupling strength* that measures the influence of a solenoid in a particular lattice is the closest approach of the eigentunes, a positive-definite quantity given by

$$\Delta Q_{min} \;=\; \frac{g|\theta|}{2\pi} \tag{3.18}$$

when it is caused by the solenoid alone. The *weight factor*

$$g \;=\; \left(\gamma_x\beta_y + \gamma_y\beta_x + 2(1-\alpha_x\alpha_y)\right)^{1/2} \tag{3.19}$$

depends on the Twiss function values at the collision point inside the solenoid. If

$$\alpha_x^* \;=\; \alpha_y^* \;=\; 0 \tag{3.20}$$

as is usually the case, then

$$g \;=\; \left(\frac{\beta_x^*}{\beta_y^*} + \frac{\beta_y^*}{\beta_x^*} + 2\right)^{1/2} \tag{3.21}$$

with a minimum of $g = 2$ when the optics are round, with $\beta_x^* = \beta_y^*$. The weight factor approaches 10 in flat optics when $\beta_x^* \gg \beta_y^*$.

The coupling strength needs to be

$$\Delta Q_{min} \ll 1 \tag{3.22}$$

for unconstrained beam operations, for example with a goal value of $\Delta Q_{min} \approx 0.001$ after linear coupling corrections which can be performed locally (using skew quadrupoles and perhaps anti-solenoids near the collision point) or globally (using skew quadrupoles around the entire ring).

Table 3.10 lists characteristic angles and coupling strengths for detector solenoids in the EIC and in a selection of other collider rings. Figure 3.7 shows the HSR uncorrected coupling strength ΔQ_{min} as a function of the 4 m experiment solenoid field. Figure 3.8 shows the HSR coupling matrix as a function of s for a 4 m experiment solenoid field of 1.5 T.

Other Accelerators

Before 1981:

1. SPEAR, PEP and CESR used half-strength anti-solenoids before the first quadrupole

Table 3.10: Detector solenoid strengths at relevant storage rings. See [86] for CESR values, [87] for RHIC values, [88] for JLEIC values, and Table 3.3 of [89] for EIC values.

Ring	e/p	Total E [GeV]	Rigidity $(B\rho)$ [Tm]	Twiss β_x^* [m]	Twiss β_y^* [m]	Weight g	Strength B_sL [Tm]	Strength θ [rad]	$\Delta Q_{\min}$ Predict	$\Delta Q_{\min}$ Simulate
CESR	e	5	16.68	6.28	.041	12.5	4.68	.140	.279	
RHIC	p	250	833.90	–	–	2	5	.003	.001	
JLEIC	e	5	16.68	0.10	.020	2.68	12	.360	.154	
	p	100	333.55	[a]	[a]	2[a]	12	.018	.006[a]	
ESR	e	5	16.68	1.96	.210	3.38	6	.180	.097	
	e	10	33.36	1.67	.064	5.30	6	.090	.076	.0466
	e	18	60.04	0.59	.050	3.73	6	.050	.030	.025[a]
HCR	p	41	136.76	0.90	.071	3.84	6	.022	.013	
	p	100	333.55	0.90	.040	4.95	6	.009	.007	
	p	275	917.30	0.90	.040	4.797	6	.00308	.00243	.00250

[a] TBD

2. PETRA partially decoupled by judiciously choosing the polarities of the 3 detector solenoids

3. LEP was designed to use 4 pairs of skew quadrupoles, anti-symmetrically power around the IP.

In CESR 3 pairs of skew quadrupoles were used on either side of the CLEO detector solenoid in the local correction scheme implemented in 1981 to combat the unusually large value of $\Delta Q_{min} = 0.279$ [91]. The two innermost pairs were driven by mechanically rolling the doublet quadrupoles closes to the IP. Only two pairs of anti-symmetrically powered skew quadrupoles were necessary to reduce ΔQ_{min} to zero. However, a third pair (but not a fourth) was found necessary in order to avoid losing luminosity to beam-beam effects. It's quite likely that the EIC will need a similar correction scheme in the electron storage ring (ESR), due to the low energy parameters that are very similar to those in CESR. Three or four skew quadrupoles on each side of the IP?

The STAR solenoid in RHIC has a coupling strength of only $\Delta Q_{min} = 0.001$ (at maximum rigidity). This value is so small that its correction is handled by the global decoupling system that also takes care of quadrupole roll misalignments around the entire ring. RHIC has no special IR skew quadrupoles or anti-solenoids. Things are a bit different in the HSR because of the partially flat beams, but the conclusion could well be the same – linear coupling may not need local correction.

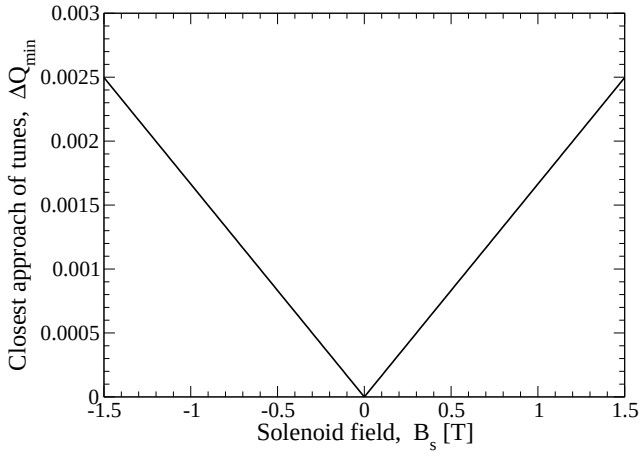

Figure 3.7: The coupling strength ΔQ_{min} simulated by BMAD in the HSR as a function of the field of a 4 m long solenoid detector. In this simulation the total proton energy is E = 275 GeV/c for a rigidity of $B\rho = 917.30$ [Tm], and the collision point Twiss functions are $(\beta_x^*\,[\mathrm{m}], \alpha_x^*, \beta_y^*\,[\mathrm{m}], \alpha_y^*) = (0.90, 0.00, 0.04, 0.00)$ for $g = 4.797$. The simulated value of $\Delta Q_{min} = 0.00250$ is in good agreement with the predicted value of 0.00243.

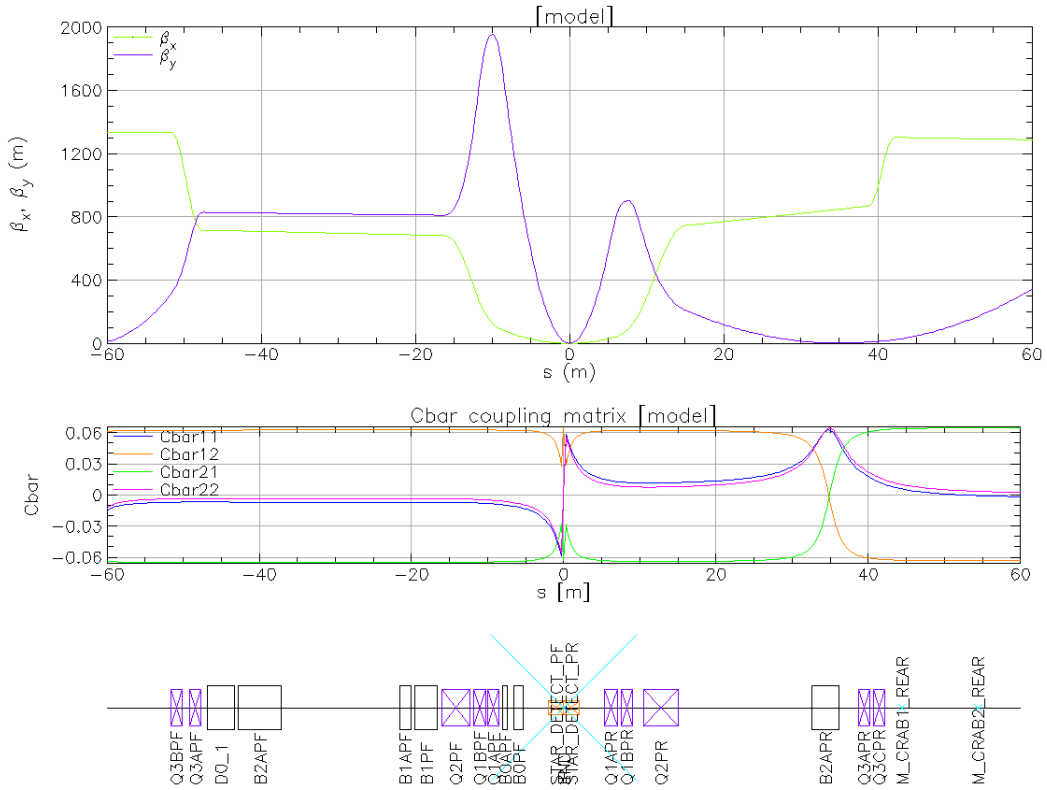

Figure 3.8: The coupling matrix [90] in the HSR as a function of the azimuthal co-ordinate s (which increases in the clockwise direction) when the field in the 4 m detector solenoid is $B_s = 1.5$ T. The collision point IP6 is at $s = 0$.

Discussion of the Solenoid Integration Issues

To integrate the detector solenoid into the detector region, one must resolve the following issues [88, 92–95]

1. Closed orbit distortion. Since the electron beam moves along the solenoid axis, this problem is unique to the ion beam. To produce the 25 mrad beam crossing angle, the ion beam must pass the solenoid at the same angle with respect to the solenoid axis. Due to this angle, the ion beam sees transverse, mostly radial magnetic field, which produces a mostly vertical kick. Since the area before the first forward final focusing quad is densely occupied by detector components, there is essentially no space for orbit correctors in that area and the beam must pass with an offset through the forward final focusing quadrupoles. This raises the question of the necessary field quality at the offset orbit and therefore of the dynamic aperture. However, the forward quadrupoles are designed with a large angular acceptance for detection purposes so even an offset beam stays within a good field region typically defined to be within 2/3 of the aperture radius. Thus, one can use a conventional correction scheme as discussed below.

2. Transverse beam focusing. This effect is small for both beams and can be easily accounted for by final focusing quadrupoles.

3. Polarization effect. Since the electron beam needs to only have longitudinal polarization at the IP and the beam passes the solenoid along its axis, the solenoid only causes a small coherent spin tune shift but does not change the polarization orientation. If necessary the spin tune shift must be accounted for by the spin rotators or an anti-solenoid. The ion polarization dynamics is less trivial. The spin experiences transverse and longitudinal fields along a spiral orbit inside the solenoid. The orbit is then corrected by dipole kickers, which have spin effects themselves. Therefore, one must consider the entire section where the orbit is perturbed with all of its elements to determine the net spin effect. The most straightforward way to do it is by a numerical simulation. If necessary the additional rotation and spin tune shift must be accounted for by the ion spin rotators.

4. Rotation of the crabbing planes of both beams. Without correction, the crabbed bunches arrive tilted at the IP. This reduces their overlap and therefore the luminosity. Moreover, the crabbing plane is then also rotated at the compensating set of the crab cavities. The crabbing kick does not get completely compensated and is no longer localized. This may lead to emittance growth. The crab cavities are located next to the final focusing quadrupoles. There is very little space for any coupling correction elements such as skew quadrupoles and anti-solenoid. How this issue is addressed is one of the factors determining the choice of the coupling correction scheme.

5. Transverse coupling. It is essential to precisely compensate coupling of the electron beam as locally as possible. In addition, the compensation must be done in a way

that does generate vertical dispersion outside of the coupled section. Uncontrolled coupling and vertical dispersion cause vertical emittance growth and deteriorate polarization lifetime. To the contrary, localization of coupling compensation is less critical for ions. It can be done globally as long as the necessary flatness of the ion beam is maintained. Vertical dispersion is acceptable as long as it is small enough to meet various beam dynamics requirements such as vertical IBS rate, chromatic effects, and smallness of the dispersion at the crab cavities. Due to the flatness and crabbing of both beams, both of them must be locally decoupled at the IP unless controlled coupling is introduced to adjust the aspect ratio of the beam spot size. The controlled coupling is relevant to the electron beam.

Vertical Closed Orbit Correction in the Hadron Ring

The EIC electron and hadron beams collide at the longitudinal center of the detector solenoid with a total crossing angle of $\psi = 25$ mrad. This is illustrated in Figure 3.9, which also shows a preliminary arrangement of dipole correctors around IP6. The central axis of the solenoid is the design trajectory of the electron beam, and so the hadron beam encounters a solenoid that has been deliberately yawed by ψ around a vertical axis at the IP. This causes horizontal displacements of Δx_E and Δx_W at the East and West fringe fields of the solenoid, where

$$\Delta x_E = -\Delta x_W = \frac{\psi L}{2} \tag{3.23}$$

and $L = 4$ m is the magnetic length of the solenoid. The hadron beam experiences systematic vertical angular kicks at the fringes, with strengths

$$\Delta y'_E = \theta \frac{\Delta x_E}{L} = \frac{1}{2}\theta\psi$$

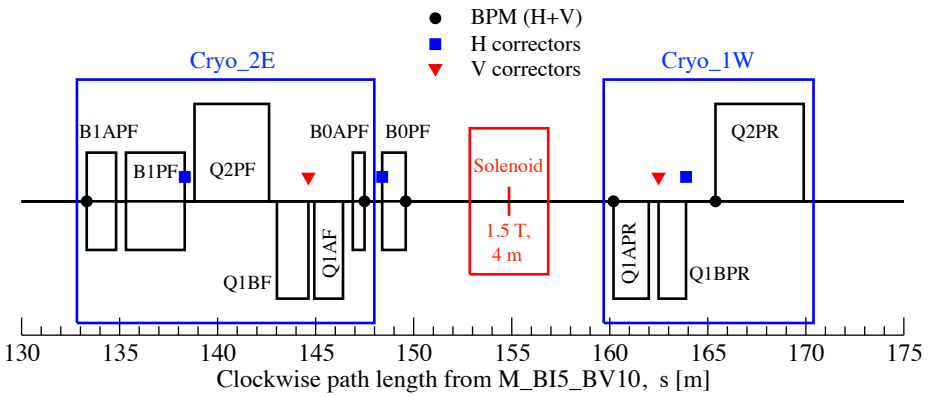

Figure 3.9: Preliminary conceptual layout of optical components in the HSR near the collision point IP6.

$$\Delta y'_W = -\theta \frac{\Delta x_W}{L} \;=\; \frac{1}{2}\theta\psi \tag{3.24}$$

which are equal. Outside the solenoid, the vertical closed orbit is distorted as if there is a single angular kick of strength

$$\Delta y'^{*}_{equivalent} \;=\; \theta\psi \tag{3.25}$$

at the collision point. The global closed orbit correction system can be used to correct for these effects, mostly driving the vertical correctors nearest to the IP. Inside the solenoid, the vertical hadron closed orbit has an angle but no displacement

$$\begin{aligned} \Delta y^{*}_{CO} &= 0 \\ \Delta y'^{*}_{CO} &= \frac{1}{2}\theta\psi. \end{aligned} \tag{3.26}$$

At the West end of the solenoid, the displacement and angle of the vertical closed orbit are

$$\begin{aligned} \Delta y^{W}_{CO} &= \frac{L}{2}\theta\psi \\ \Delta y'^{W}_{CO} &= \theta\psi. \end{aligned} \tag{3.27}$$

These statements about the vertical closed orbit are only true to first order in θ. They are consistent with the fact that the solenoid matrix can be written *exactly* (assuming only thin fringe fields) as

$$N_{solenoid} \;=\; F\,R(\theta) \tag{3.28}$$

where R is the 4×4 rotation matrix

$$R(\theta) \;=\; \left(\begin{array}{c|c} \cos(\theta)\, I_2 & \sin(\theta)\, I_2 \\ \hline -\sin(\theta)\, I_2 & \cos(\theta)\, I_2 \end{array}\right) \tag{3.29}$$

and

$$F \;=\; \left(\begin{array}{c|c} D & 0 \\ \hline 0 & D \end{array}\right) \tag{3.30}$$

where

$$D \;=\; \begin{pmatrix} \cos(\theta) & \sin(\theta)\,(L/\theta) \\ -\sin(\theta)\,(\theta/L) & \cos(\theta) \end{pmatrix} \tag{3.31}$$

Note that the matrix

$$D(L,\theta^2) \;\approx\; \begin{pmatrix} 1 & L \\ 0 & 1 \end{pmatrix} \;+\; \mathcal{O}(\theta^2) \tag{3.32}$$

is just a drift, to first order in θ.

We choose an orbit correction scheme that minimizes the size and extent of the orbit excursion given the spacial constraints for corrector placement. Since there is no orbit displacement at the IP and the orbit excursion is primarily vertical, the majority of the correction is done by two vertical correctors with non-trivial vertical betatron phase advance between

them located downstream of the IP. The optimal phase advance between the correctors is $\pi/2$. However, it can be smaller at the expense of the corrector strengths. The 1st vertical corrector y_1^{ds} is placed as close to the detector solenoid as possible to minimize the size of the closed orbit excursion. It is integrated into the $B0A$ dipole. The second vertical corrector y_2^{ds} is placed at the next available location after a set of quadrupoles and dipoles. Figure 3.10 indicates the corrector locations and shows the corrected orbit at 275 GeV. The correction in Figure 3.10 is done with a 4 m long solenoid set at 3 T, which is the highest field the solenoid is planned to be run at. As expected, y_1^{ds} and y_2^{ds} are the strongest correctors with integrated fields of -65 and 81 mTm, respectively. The rest of the correctors are used to account for higher-order orbital effects of the solenoid and are also needed to correct for imperfections and control the orbit position at the IP. They are much weaker with field integrals of under 1 mTm. Note that x_1^{ds} is implemented by adjustment of the $B0A$ dipole's field. The solenoid and the orbit excursion caused by it have little effect on the linear optics as illustrated in Figure 3.11.

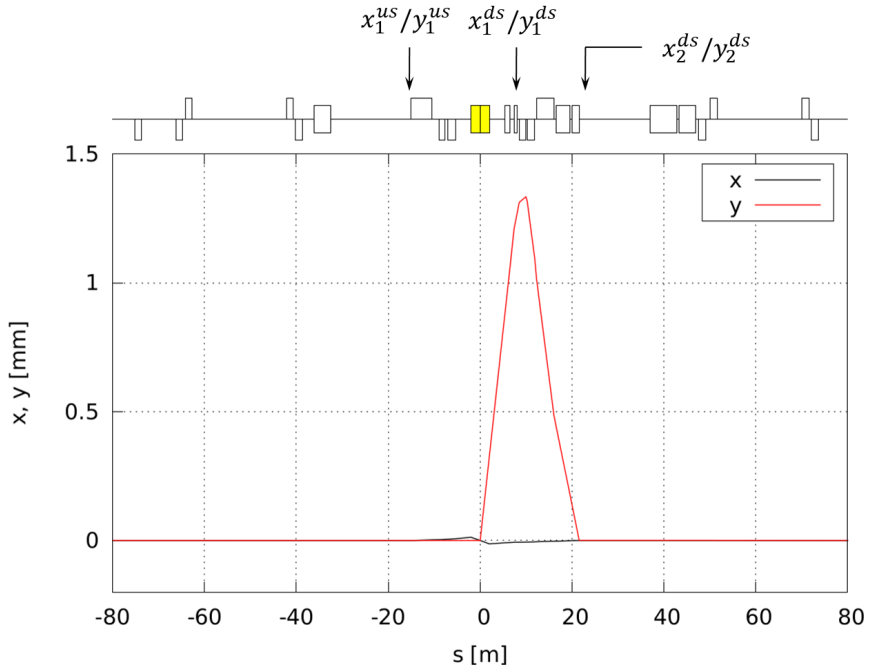

Figure 3.10: Corrected ion orbit at 275 GeV. The corrector location are indicated.

At a fixed field of the detector solenoid, its normalized strength is inversely proportional to the beam energy. What is relevant for the optical effect of the solenoid is its normalized strength. Thus, it has the strongest impact at the lowest collider energy of 41 GeV. In the scenario when the beam is accelerated in the HSR, the solenoid strength cannot be ramped together with the beam. Therefore, the beam is injected with the solenoid at full strength. Thus, we consider orbit correction with a 3 T solenoid at 41 GeV. Figures 3.12 and 3.13 show the corrected orbit and beam optics, respectively, in that case. Due to the simultaneous scaling of the normalized solenoid and corrector strengths, the absolute values of the corrector strengths remain essentially the same as 275 GeV. The optical effect of the

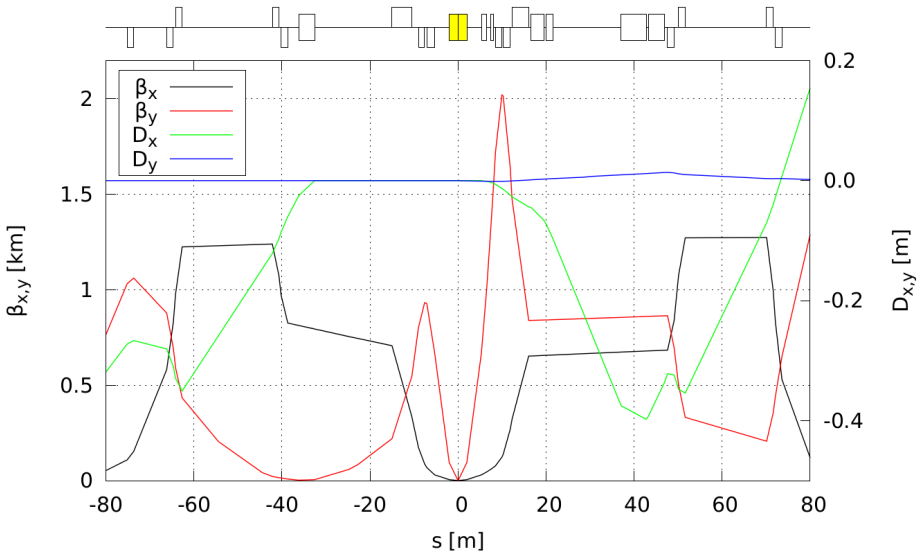

Figure 3.11: Ion optics with a 4 m long 3 T solenoid at 275 GeV showing the horizontal and vertical Twiss β-functions on the left-hand-side vertical axis and the horizontal and vertical dispersion function on the right-hand-side vertical axis.

solenoid is still negligible even at this low energy. The orbit displacement grows to a substantial size of about 9 mm. The beam may sample stronger multipoles in the quadrupole aperture causing a concern for the dynamic aperture. However, the forward quadrupoles have large apertures for detection purposes and are designed to accommodate an about 20 mm horizontal orbit shift. Since the aperture is round and the obit excursion by the solenoid is vertical, it should not create additional difficulties for the dynamic aperture.

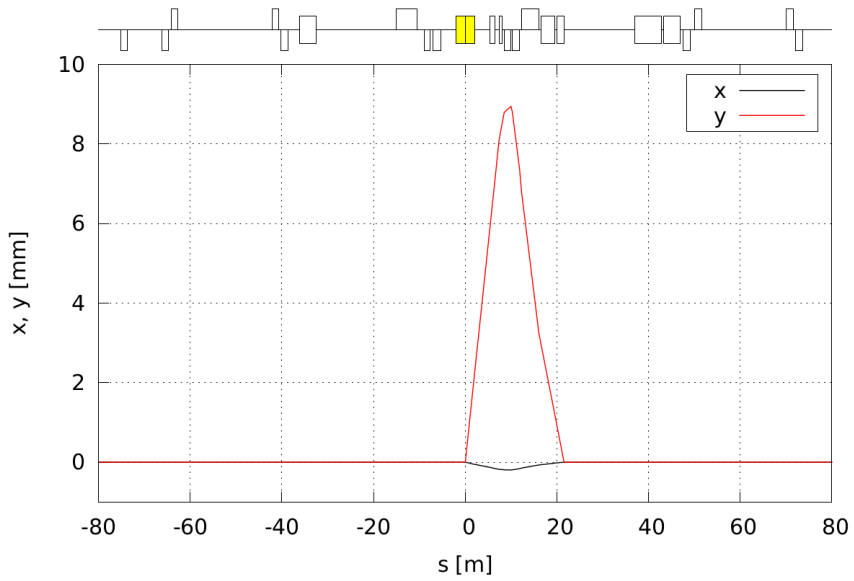

Figure 3.12: Corrected ion orbit at 41 GeV.

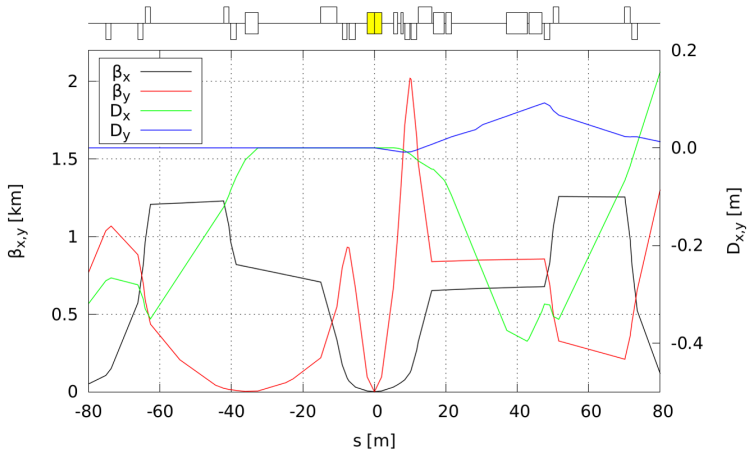

Figure 3.13: Ion optics with a 4 m long 3 T solenoid at 41 GeV.

Polarization Effect

The polarization direction of the electron beam is always aligned with the detector solenoid axis. Therefore, the solenoid does not change the polarization orientation. However, it causes an additional spin rotation φ_s shifting the spin tune ν_s by

$$\Delta\nu_s = \frac{\varphi_s}{2\pi} = \frac{(1+G)}{2\pi}\frac{B_{sol}L}{B\rho}, \tag{3.33}$$

where $G \approx 1.160 \times 10^{-3}$ is the electron's anomalous gyromagnetic ratio, $B_{sol}L$ is the solenoid field integral, and $B\rho$ is the electron magnetic rigidity. The spin tune shift $\Delta\nu_s$ reaches a maximum of about 0.115 with the strongest 3 T field of the 4 m long solenoid at the lowest electron energy of 5 GeV. The spin tune shift may affect spin matching and polarization lifetime and must be accounted for in the analysis of the electron polarization dynamics.

The hadron beam can have both transverse and longitudinal polarization directions at the IP. As discussed above, the hadron beam goes at a 25 mrad angle to the solenoid axis and experiences not only the longitudinal but transverse components of the solenoid field on its way to and from the IP. Both field components influence not only the beam orbit but the spin as well. While the spin effect of the longitudinal field is inversely proportional to the hadron beam momentum, the spin effect of the transverse field is almost independent of the beam momentum and can be significant over the entire energy range.

The solenoid perturbs the closed orbit causing an orbit shift inside the forward quadrupoles. The orbit distortion is compensated locally using dipole correctors. The fields experienced by the displaced beam inside the quadrupoles and in the dipole correctors contribute to the spin rotation in addition to the field of the solenoid itself. Thus, to determine the spin effect due to the pitched solenoid, one must consider the entire region of the perturbed beam with all of its elements.

The spin rotation by each of the elements including the pitched solenoid can be calculated analytically. Therefore, the net spin effect of all elements combined can also be in principle obtained analytically. However, it is more efficient to calculate the range of the spin rotation directions and angles numerically.

Correction of Crabbing Plane Rotation

The crab cavities are located close to the final focusing quadrupoles, and the betatron phase advance from the detector solenoid to the crab cavities on each side of the IP is small, less than $\pi/2$. Therefore, coupling induced by the solenoid cannot be compensated locally between the rear and forward sets of the crab cavities using only skew quadrupoles. One can use the rotated frame technique to compensate coupling in this case, which involves addition of a skew quadrupole component or a lumped skew quadrupole next to each of the straight quadrupoles in the coupled region and insertion of anti-solenoids at the two ends of the coupled region. The crab cavities themselves may also be rotated to produce coupled crab bumps that are locally decoupled at the interaction point. This would work with global coupling compensation, though it would also involve additional local decoupling and might complicate the tuning of collision optics.

Linear Decoupling

The general local decoupling problem is shown symbolically in Figure 3.14 [96–102]. An insertion segment AB contains n couplers (solenoids or skew quadrupoles) and a reference point C, typically the collision point. The insertion as a whole does is locally decoupled if the 4×4 matrix across it is block diagonal. If the block-diagonal matrix M_{jC} represents the linear motion from C to location j with all couplers off, and if motion across coupler i is represented by $N_{2i,2i-1}$, then it is very useful to introduce the 4×4 projection matrix

$$P_i \;=\; M_{C,2i}\, N_{2i,2i-1}\, M_{2i-1,C} \tag{3.34}$$

which represents the coupler. The transfer matrix across the insertion then becomes just

$$T_{AB} \;=\; M_{BC}\, P\, M_{CA} \tag{3.35}$$

where the insertion is decoupled if

$$P \;=\; P_n \cdots P_2 P_1 \tag{3.36}$$

is block-diagonal. Four independent coupler strengths k_i are needed to achieve this in general. This representation is powerful because P_i is usually close to the 4×4 identity matrix I, in a polynomial expansion

$$P_i \;=\; I \,+\, k_i K_i \,+\, k_i^2 \cdots \tag{3.37}$$

where K_i is block anti-diagonal. The insertion is decoupled to first order in coupling strengths if

$$\sum_{i=1}^{n} k_i K_i \;=\; 0 \tag{3.38}$$

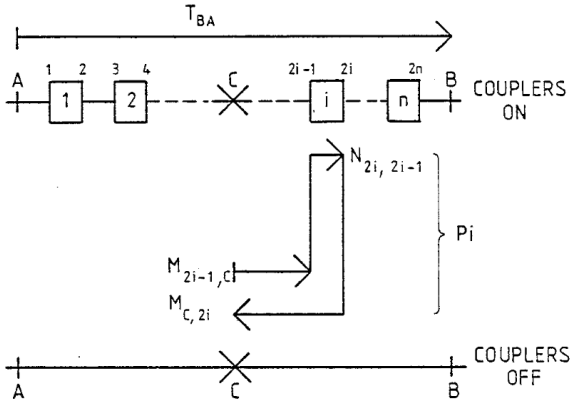

Figure 3.14: Symbolic representation of couplers and transfer matrices near a reference point C in an insert AB.

K-matrices for Solenoids and Skew Quadrupoles

An experimental solenoid centered at *C*, or an anti-solenoid only a drift away, has the simple *K*-matrix

$$K_{solenoid} \;=\; \left(\begin{array}{c|c} 0 & I_2 \\ \hline -I_2 & 0 \end{array}\right) \tag{3.39}$$

with a strength

$$k_{solenoid} \;=\; \theta \tag{3.40}$$

which is the characteristic angle given by Equation 3.17. Similarly, the *K*-matrix for a thin skew quadrupole is

$$K \;=\; \left(\begin{array}{c|c} 0 & Q \\ \hline -Q^{\dagger} & 0 \end{array}\right)$$

where $Q^{\dagger}$ is the adjoint of

$$Q = \frac{1}{\sqrt{\beta_x \beta_y}} M_x^{-1} \begin{pmatrix} 0 & 0 \\ 1 & 0 \end{pmatrix} M_y \tag{3.41}$$

$$= \begin{pmatrix} -S_x C_y \sqrt{\beta_x^*/\beta_y^*} & -S_x S_y \sqrt{\beta_x^* \beta_y^*} \\ C_x C_y / \sqrt{\beta_x^* \beta_y^*} & C_x S_y \sqrt{\beta_y^*/\beta_x^*} \end{pmatrix} \tag{3.42}$$

where

$$C = \cos(\phi), \quad S = \sin(\phi) \tag{3.43}$$

and ϕ is the horizontal or vertical phase advance from location C, which has Twiss parameters β_x^* and β_y^*. The dimensionless strength of the thin skew quadrupole is

$$q = \frac{\sqrt{\beta_x \beta_y}}{f} \tag{3.44}$$

where f is the focal length of the skew quadrupole. Putting all this together, the insertion is decoupled (to first order in coupler strengths) when

$$\theta \begin{pmatrix} 1 & 0 \\ 0 & 1 \end{pmatrix} + \sum_{i=1}^{n} q_i Q_i = 0 \tag{3.45}$$

In general this requires 4 skew quadrupoles if the only consideration is to decouple the insertion – to make ΔQ_{min} zero. The situation is even simpler if the optics are symmetric about the collision point, in which case 2 pairs of anti-symmetrically power skew quadrupoles do the trick. Unfortunately, EIC optics are *not* anti-symmetric, and there are other issues besides overall insertion decoupling.

Two Skew Quadrupoles per Side for Hadrons

If the hadron ring needs local decoupling, but beam-beam issues are not important, then a solution with two skew quadrupoles on each side of the IP is appropriate. The solution is especially easy if the lattice and the optics are symmetric about the IP. In that case the elements of the skew quad Q-matrix are odd or even functions about the IP, according to

$$Q = \begin{pmatrix} \text{odd} & \text{even} \\ \text{even} & \text{odd} \end{pmatrix} \tag{3.46}$$

and so the solenoid as a whole is decoupled if

$$\theta \begin{pmatrix} 1 & 0 \\ 0 & 1 \end{pmatrix} + 2 \sum_{i=1}^{2} q_i \begin{pmatrix} -S_x C_y \sqrt{\beta_x^*/\beta_y^*} & 0 \\ 0 & C_x S_y \sqrt{\beta_y^*/\beta_x^*} \end{pmatrix}_i = 0 \tag{3.47}$$

where $\pm q$ is the strength of each of a pair of symmetrically placed skew quadrupoles. It is easy to solve these linear equations in two variables, so long as the two vectors of diagonal elements $\left(-S_x C_y \sqrt{\beta_x^*/\beta_y^*},\ C_x S_y \sqrt{\beta_y^*/\beta_x^*}\right)_i$ are not nearly collinear. Even with four variables – when there is no helpful symmetry – the solution is quite straightforward if the skew quadrupoles are well-placed.

Three Skew Quadrupoles per Side for Electrons

It is likely that the electron storage ring needs not two but three local skew quadrupoles on each side of the IP, assuming that the beam-beam conditions in CESR also apply to the EIC. This (arguably) needs to checked in simulation, after a preliminary scheme has been devised. In the worst case a scheme with 4 skew quadrupoles per side might be necessary.

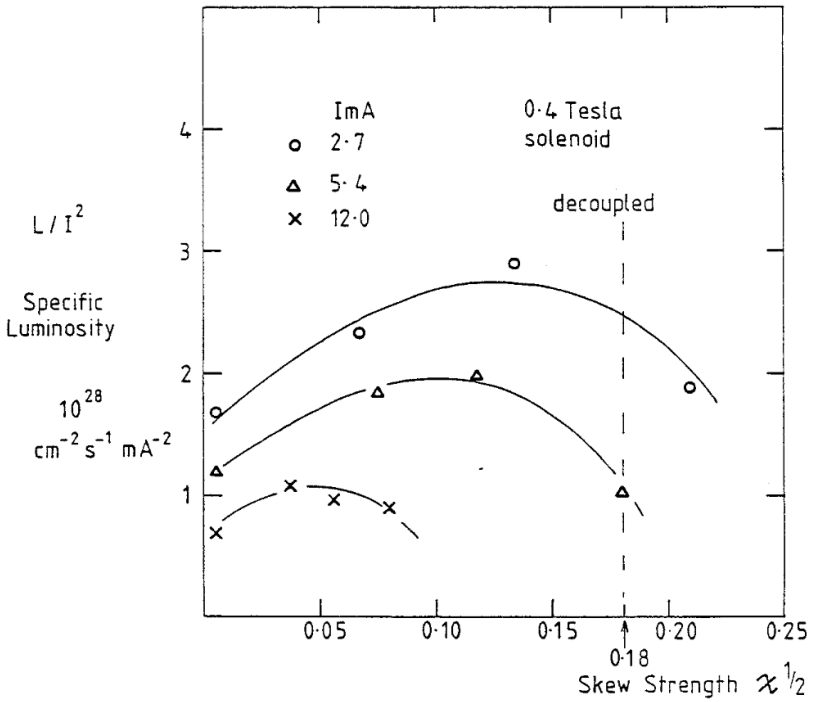

Figure 3.15: Beam studies data showing specific luminosity versus skew strength in the trial of a two-pair compensation scheme in CESR.

Figure 3.15 shows summary data from a beam studies session in CESR, during which a two-pair solution was powered with the anti-solenoids turned off in the pre-upgrade configuration [91]. The hope was that the specific luminosity L/I^2 at each value of beam current I would increase to a maximum when the (scaled) skew quad strength reached its design value of $\chi = 0.18$. Instead it was found that the compensation scheme itself contributed to decreased luminosity, in addition to the decrease with increasing I due to the beam-beam effect, via increasing vertical beam size. Analysis after the fact showed that the beam-beam effect requires a third pair, as described below. Details of the beam-beam analysis can be found in reference [91].

Coupling Compensation in ESR

Considerations for the vertical electron emittance and polarization lifetime require precise local control of detector solenoid coupling. Due to lack of the forward and rear optical symmetry in the electron IR, we have to use the general skew quad coupling compensa-

tion scheme. It includes four skew quadrupoles for compensation of the four off-diagonal transverse elements of the transfer matrix and two additional skew quadrupoles for suppression of the size and slope of the vertical dispersion, D_y and D'_y if some or all of the skew quadrupoles are located in dispersive regions. To control coupling at the IP, such a scheme must be implemented on each side of the interaction region.

Skew quadrupoles provide orthogonal control of the off-diagonal matrix elements when the horizontal and vertical betatron phase advance values $(\Delta\mu_x,\ \Delta\mu_y)$ between them are given by

$$(\Delta\mu_x,\ \Delta\mu_y):\ (\pi/2,\ 0), (\pi/2,\ \pi/2), (0,\ 0), \text{ and } (0,\ \pi/2)\ (\text{mod}\ \pi). \tag{3.48}$$

It is not always possible to design a lattice with skew quadrupoles located at these precise phase advance points. Therefore, we empirically identified locations in the existing lattice where the skew quadrupoles are as independent as possible. We added skew components to the existing straight quadrupoles in the matching sections between the interaction region and electron spin rotators as shown in Figure 3.16(top). We then found which of the skew quad components have the strongest impact on the coupling coefficients and vertical dispersion and narrowed down the number of skew quadrupoles to the conceptual minimum of six per IP side. In practice, the skew quadrupoles can be implemented as separate elements next to the straight quadrupoles. We also adjusted the strengths of ten existing straight quadrupoles to keep the optics fixed at the IP and the matching points indicated in Figure 3.16(top). This procedure included matching of the horizontal dispersion as well. The solenoid field strength was 3 T. The result of coupling compensation at 5 GeV where the solenoid induces the strongest coupling is shown in Figure 3.16(top) using the Ripken parameterization of coupled β functions. β_{12} and β_{21} being zero along with their slopes indicates compensation of coupling. Correction of the vertical dispersion is shown in Figure 3.16(bottom).

Figure 3.17(top) and (bottom) illustrates coupling compensation and vertical dispersion correction, respectively, at 18 GeV. Note the reduction of β_{12} and β_{21} and of D_y compared to Figure 3.16 due to the weaker effect of the 3 T solenoid at the higher energy. The maximum required field gradient of the skew quadrupoles is about 3.3 T/m. The absolute value of the gradient is essentially independent of energy, since the solenoid field does not scale with energy.

The coupling compensation scheme described above can also be used to control the aspect ratio of the electron beam spot size at the IP. A flat electron beam with a small vertical emittance is favorable from the polarization lifetime point of view. However, the height of the electron beam spot at the IP must match that of the hadron beam. Simply increasing β^*_y to reach the necessary vertical beam size may not be acceptable because of the associated growth of the beam-beam tune shift. Another approach to the beam aspect ratio control is to adjust the vertical beam size by controlled coupling of the horizontal emittance into the vertical plane at the IP. This is done by adjusting β^*_{21} at the IP while keeping the horizontal beam size fixed and the slopes of all β functions at zero until the desired vertical beam size

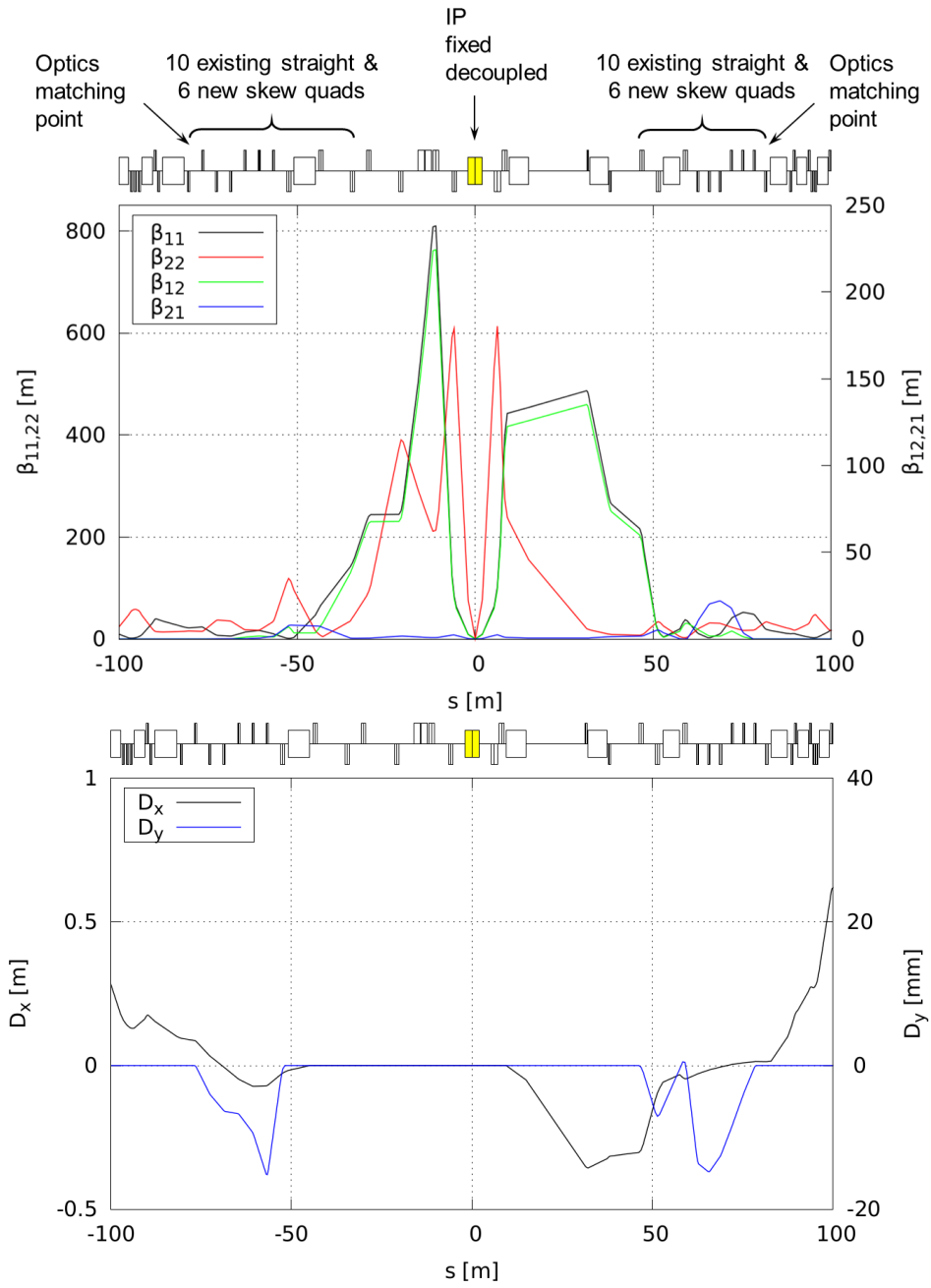

Figure 3.16: Ripken coupled β functions (top) and horizontal D_x and vertical D_y dispersions (bottom) in the electron interaction region after coupling compensation at 5 GeV.

σ_y^* is established

$$\sigma_y^* = \sqrt{\beta_{21}^* \varepsilon_x + \beta_{22}^* \varepsilon_y}, \tag{3.49}$$

where ε_x and ε_y are the two transverse (horizontal and vertical, respectively, in an uncoupled case) canonical geometric emittances. An example of adjusting the beam aspect

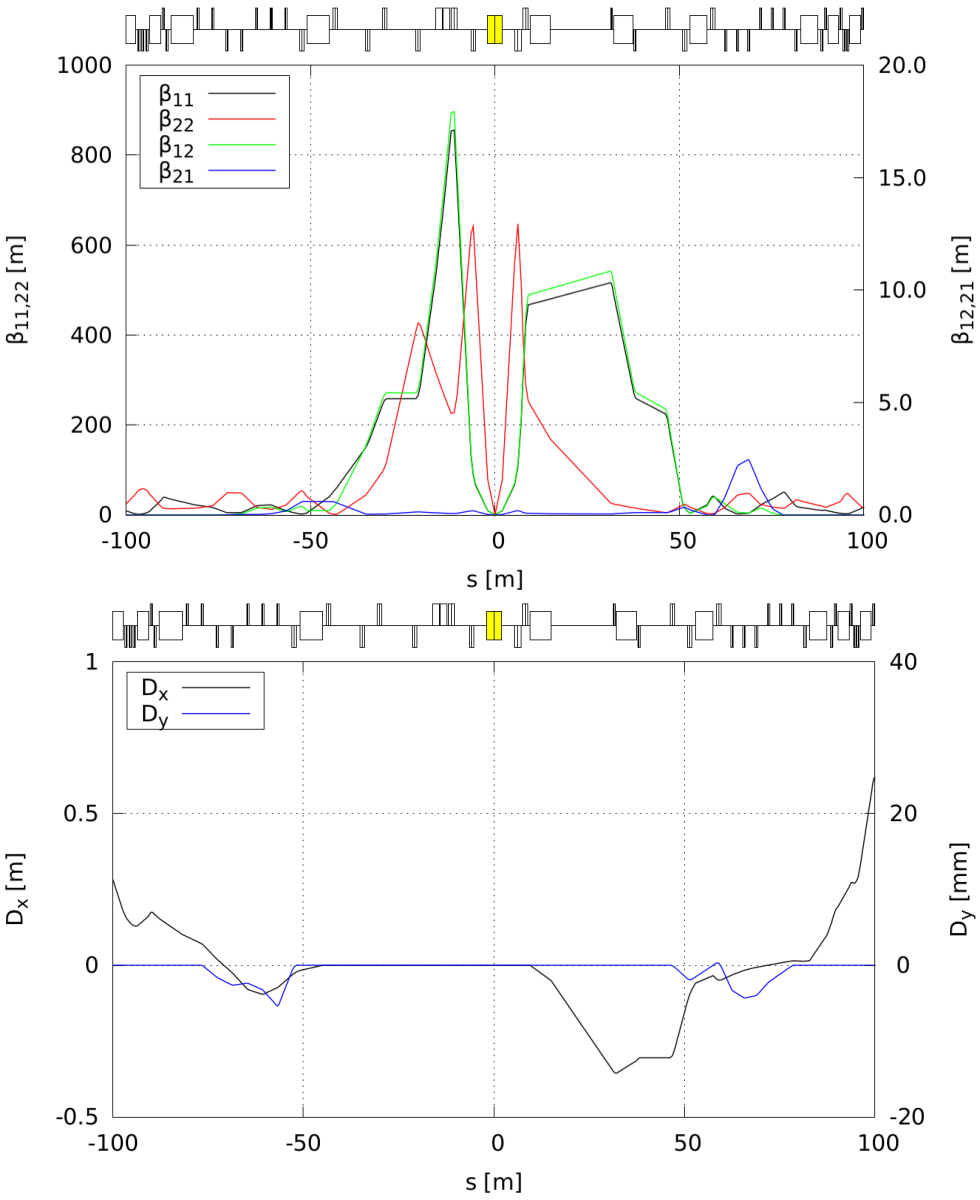

Figure 3.17: Ripken coupled β functions (top) and horizontal D_x and vertical D_y dispersions (bottom) in the electron interaction region after coupling compensation at 18 GeV.

ratio is presented in Figure 3.18. Assuming ε_x and ε_y of 24 nm and 30 pm, respectively, the electron beam aspect ratio σ_x^*/σ_y^* in the case of the uncoupled IP shown in Figure 3.17 is about (100 µm)/(1.2 µm)≈82. After introducing controlled coupling at the IP primarily through β_{21} in the case shown in Figure 3.18, the aspect ratio σ_x^*/σ_y^* is reduced to about (100 µm)/(10 µm)≈10.

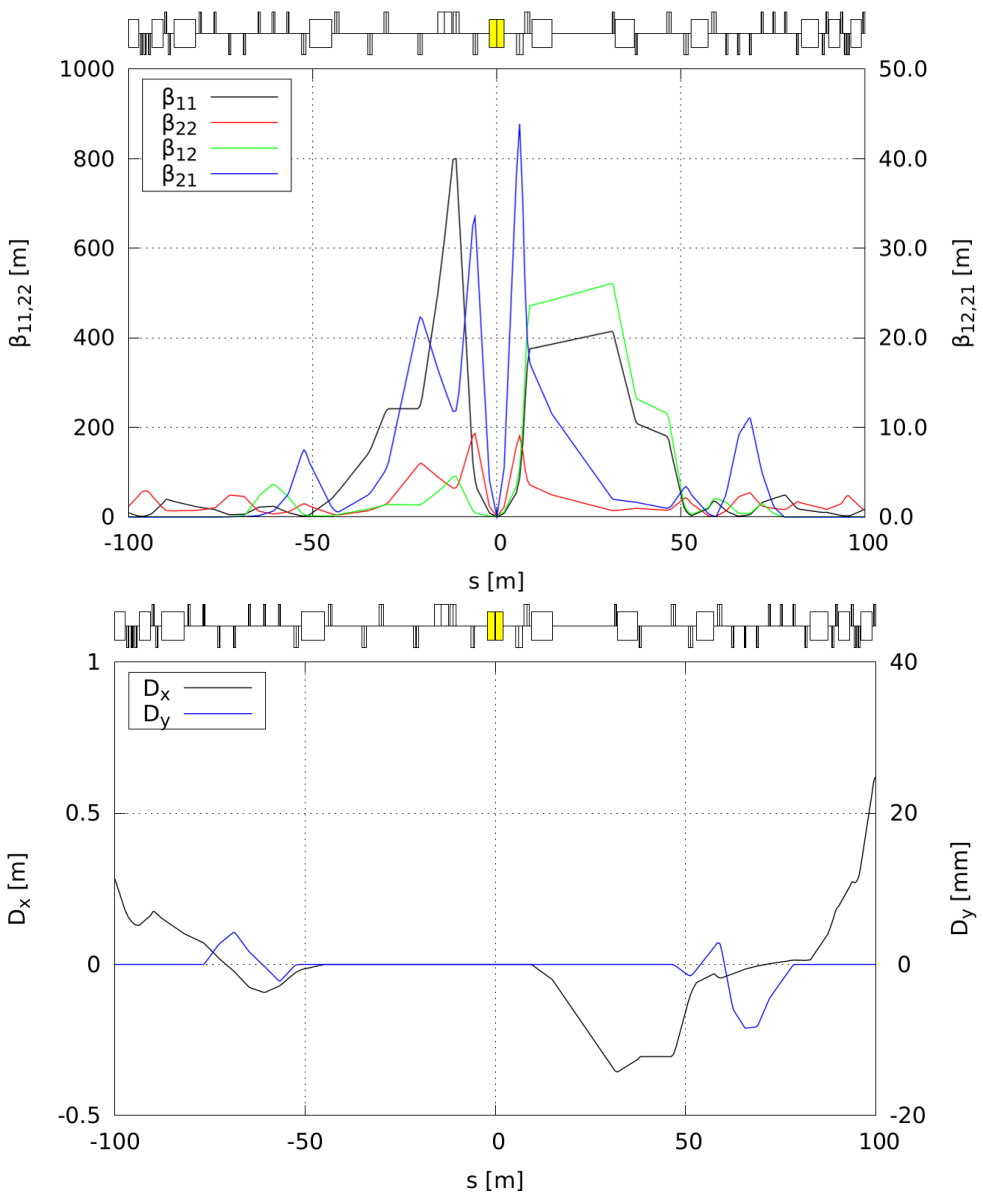

Figure 3.18: Ripken coupled β functions (top) and horizontal D_x and vertical D_y dispersions (bottom) in the electron interaction region at 18 GeV with coupling intentionally introduced at the IP in such a way that the beam aspect ratio σ_x^*/σ_y^* is reduced by about a factor of 8.

Coupling Compensation in HSR

The HSR is based on one of the existing RHIC collider rings, so there is an existing coupling correction scheme. Therefore, we rely on existing correction knobs. The main difference of the EIC parameters from RHIC's as far as coupling is concerned is that the EIC proton beam is flat with a horizontal to vertical emittance ratio of up to almost 20. This requires more careful coupling control than in the case of the round beams in RHIC. The global de-

coupling scheme is adequate for hadrons. There are no emittance growth or polarization lifetime concerns associated with the extent of local coupling around the ring. Possible exceptions from this claim are the facts that a large vertical dispersion excited by the distributed skew quadrupoles may shorten the vertical IBS time and affect the chromaticity correction scheme. Therefore, it must be kept in check.

We identified six existing families of 4 skew quadrupoles each. They are indicated by odd numbers from 1 through 11 in Figure 3.19. In RHIC, all skew quadrupoles are combined into three families. However, the HSR requires six independent families for the reasons discussed above. These families were used to correct the four off-diagonal transverse elements of the single-turn periodic orbital transfer matrix and the vertical dispersion D_y and its slope D'_y at the IP. The resulting Ripken coupled β functions and the horizontal D_x and vertical D_y dispersions at 275 GeV are shown around the ring in Figure 3.20(top) and (bottom), respectively. Figure 3.21 shows an expanded view of these quantities in the interaction region.

The maximum values of the coupling β functions β_{12} and β_{21} are less than 0.5 m compared the 2 km size of the uncoupled projections β_{11} and β_{22}. The maximum required gradient of the skew quadrupoles is about 1.3 T/m. The absolute values of the skew quad gradients are practically independent of the beam energy because of the constant solenoid field. The maximum and rms D_y are about 6.1 and 1.7 cm, respectively.

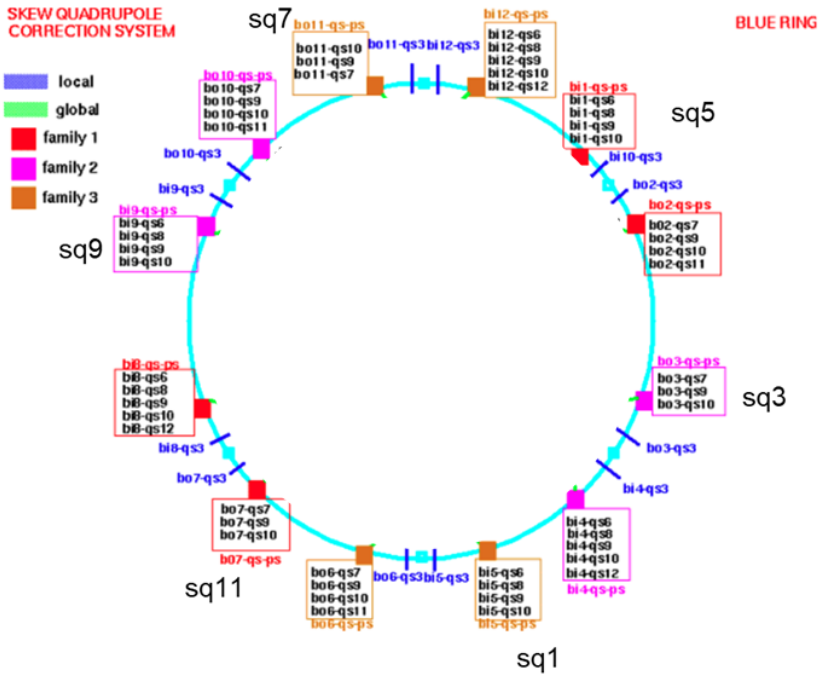

Figure 3.19: Location of the six skew quad families used for coupling compensation and vertical dispersion control in the HSR. The six families are indicated by labels from $sq1$ through $sq11$ using odd numbers only.

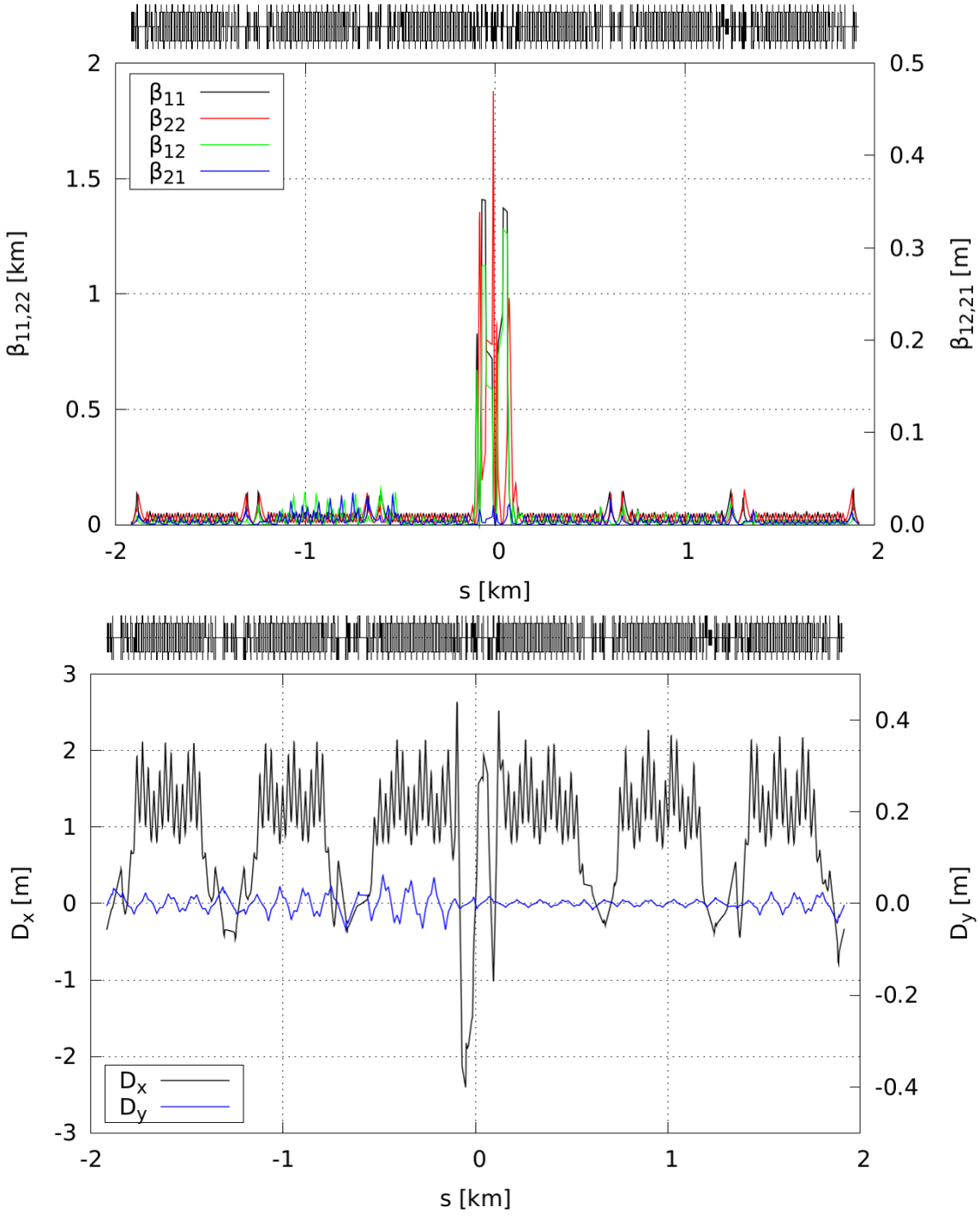

Figure 3.20: Ripken coupled β functions (top) and horizontal D_x and vertical D_y dispersions (bottom) around the HSR at 275 GeV after coupling compensation and vertical dispersion correction.

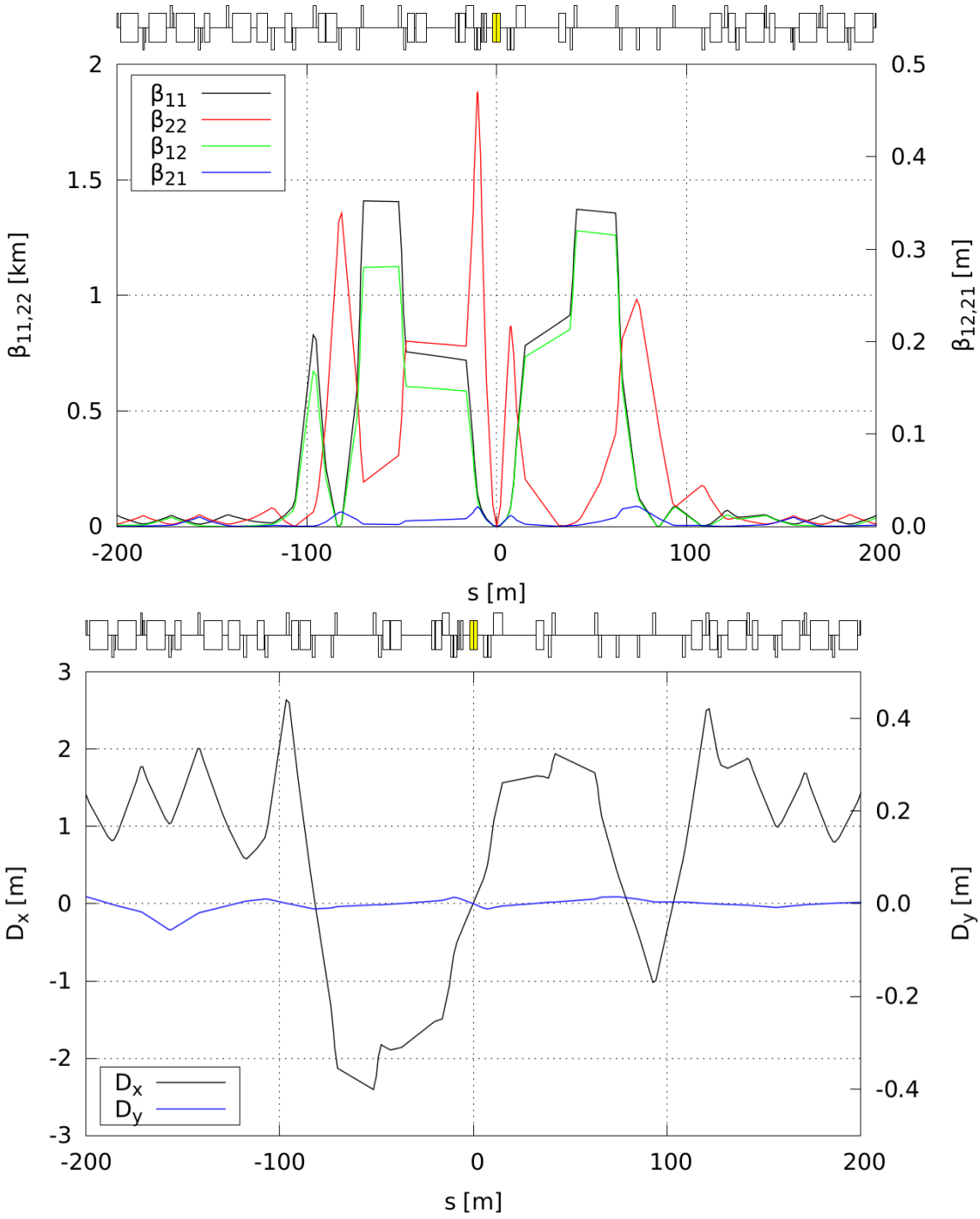

Figure 3.21: Ripken coupled β functions (top) and horizontal D_x and vertical D_y dispersions (bottom) in the hadron interaction region at 275 GeV after coupling compensation and vertical dispersion correction.

3.2.3 IR Vacuum Design

The interface requirements within the IR present several complex challenges, which require close attention to detail. The vacuum chamber in this region will become the primary interface between the particle beams and the different detector components.

One of the first challenges is to meet all of the geometrical requirements of the region. First and foremost the vacuum chamber must be designed to allow clear passage of the two high energy particle beams. Space constraints for the synchrotron radiation (SR) fan resulting from the strong focusing electron quadrupoles also need to be taken into account. Designing the central vacuum pipe with a large diameter would easily meet these requirements, and would also provide large conductance to the vacuum pumps that is required to achieve the lowest possible pressure in the detector region. However, to ensure large acceptance for all the collisions products, detectors must be placed as close as possible to the interaction point. Since these particles must pass through the walls of the beam pipe, every effort must be made to minimize their thickness.

The design is further complicated by the fact that the charged particle beams induce electromagnetic fields in the walls of the vacuum chambers. These induced fields create an image current inside the vacuum chamber walls, which travels with the particle bunches as they move through the accelerator. Changes in the material resistivity or abrupt steps result in wake fields, which can impede the image current and lead to energy loss and heating of the vacuum system.

Every effort must be made to reduce the dynamic pressure inside the IR vacuum chamber in order to minimize beam-gas interactions. The particles in the circulating beams can scatter on the residual gas molecules, which can result in high detector backgrounds. Any synchrotron radiation (direct or scattered) impinging on surfaces will result in a high dynamic pressure from photon induced desorption and surface heating. This further increases the beam-gas interaction problem and the resulting background of the detectors.

Geometry

In order to define an initial acceptable envelope for the IR vacuum chamber, a full scale layout of the central detector region was developed (see Figure 3.22). It soon became clear that, as a result of the shallow crossing angle between the beams, there was not adequate space for two independent beam pipes leading up to the inner detector region. In order to mitigate this problem, the decision was made to combine the two pipes into one common vacuum flange in order to save space. It also became clear that there is very little space remaining between the start of the detector region and the final focusing magnets in the forward hadron beam direction. Further work will be needed in this area to ensure all critical vacuum elements such as RF shielded bellows and UHV pumps will fit.

In addition to the crossing angle, one of the leading parameters driving the size of the central beam pipe is synchrotron radiation. This radiation is produced when relativistic electrons are accelerated radially, or perpendicular to their velocity. To minimize this problem

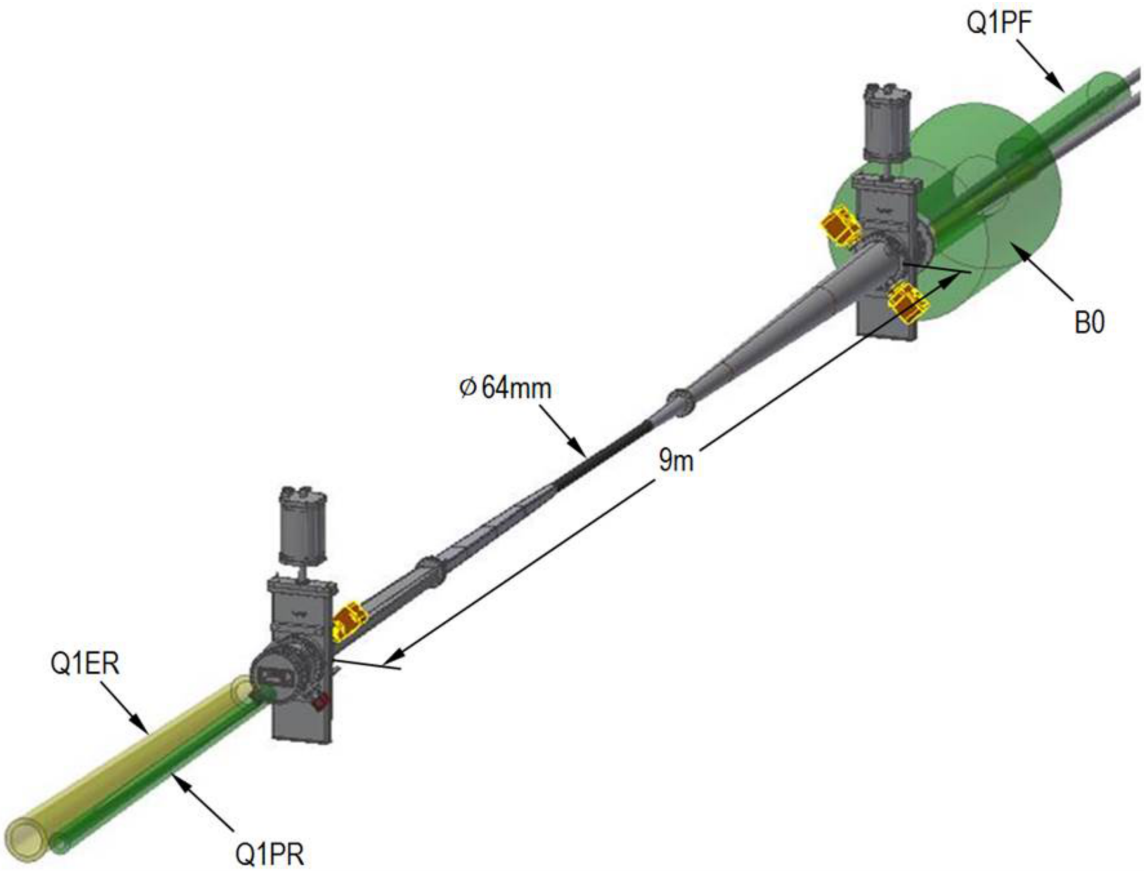

Figure 3.22: Interaction region layout with magnets. The incorporation of gate valves is still under consideration

the closest electron dipole magnet has been located as far as possible ($> 36\,\text{m}$) from the IR to leave space for collimating the radiation produced. While the dipole magnets are responsible for the majority of the synchrotron radiation, the strong final focusing electron quadrupoles located just upstream of the detector also need to be taken into account. In order to study the resulting radiation (see Figure 3.23) multiple simulation studies were performed using the SynRad software package developed at CERN [103]. A stay-clear envelope was established based on the final magnet and beam parameters which result in the highest electron beam divergence.

Considering the central portion of the beam pipe will be made from beryllium and taking into account its limited fabrication possibilities, an inside diameter of 62 mm was defined. This value provides some additional clearances for mechanical and positioning tolerances. In the outgoing electron beam direction, the beam pipe will continue to increase in size to ensure the synchrotron radiation can travel through the IR without impinging on the

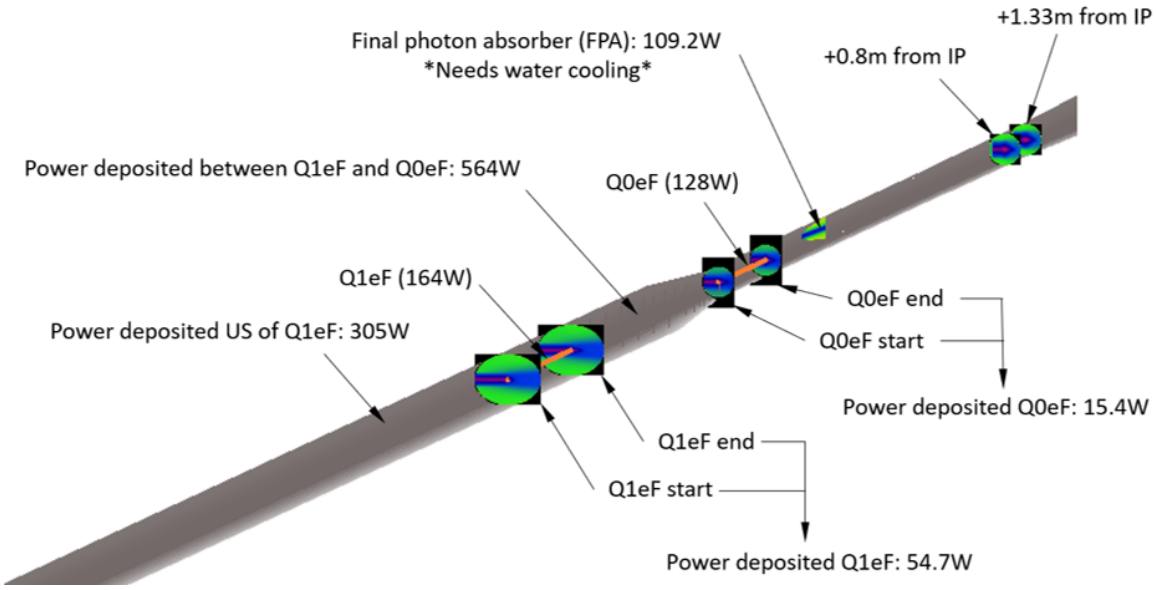

Figure 3.23: SynRad code simulation showing the resulting synchrotron radiation from the electron focusing quadrupoles Q0EF, Q1EF and DB1EF

chamber walls. In the forward hadron beam direction the beam pipe will have a conical cross section in order to provide an unobstructed path to the forward spectrometer located in the B0 magnet bore. To minimize the beam impedance for the electrons, a conducting screen will be installed which will maintain a uniform geometry for the induced image currents. Once outside the central detector region the forward traveling particles will pass through a vacuum-air interface made of thin aluminum or stainless steel before entering the B0 spectrometer. The design and position of the required chamber supports will need additional care. These supports must ensure that the chamber does not encroach into the stay clear area and must also guarantee the mechanical stability of the chamber during operations and bake out. Careful consideration to the natural frequency of the suspended system must be taken into account to avoid amplifying mechanical vibrations, which can lead to stress and fatigue of the chamber. Where possible, machine vibration frequencies will be kept above 50 Hz.

Material Considerations

To minimize the interaction of the collision products in the vacuum chamber walls, their thickness must be kept at a minimum. The 'transparency' of a material is usually quantified through the radiation length (χ_0) for elastic collisions and the interaction length (l_T) for inelastic hadron collisions.

The radiation length is defined as the mean distance over which a high-energy electron loses all but $1/e$ of its energy by bremsstrahlung radiation. This property is inversely proportional to the density and atomic number of the material. The interaction length is the mean distance traveled before experiencing an inelastic nuclear interaction.

In order to reduce the background produced by these material properties, the walls of the vacuum chamber should be made as thin as possible. A limit is clearly defined by the mechanical integrity of the vacuum chamber. If the chamber is too thin, the vessel will collapse under the outside atmospheric pressure or fail to meet the tight mechanical tolerances required to stay clear of sensitive instrumentation. To compare the nuclear and mechanical performances of various materials, $\chi_0 E^{-1/3}$ has been used to define the figure-of-merit, with E being the Young's modulus. The required chamber wall thickness is directly proportional to $E^{-1/3}$. The properties of several materials are listed in Table 3.11.

Table 3.11: Table of material properties considered for the IR vacuum pipe.

Material	χ_0 [cm]	l_T [cm]	E [GPa]	$\chi_0 E^{-1/3}$
Beryllium	35.3	41.8	290	2.34
Carbon fiber	27.0	40.0	200	1.58
Aluminum	8.9	28.7	70	0.37
Titanium	3.6	21.4	110	0.17

While beryllium would seem to be the best choice, it has several drawbacks including fabrication difficulties, safety concerns, and high cost. For these reasons, only the central portion of the IR chamber will be made from beryllium. Additional aluminum sections made from AA2219 will be electron beam welded to the center section to complete the approximately 9 m long vacuum section. This particular aluminum alloy can be used at operating temperatures up to 250° C and is weldable using conventional techniques. Three separate vacuum pipes are envisioned with flange joints located at positions compatible with the central detector. The shorter pipe sections will not only simplify the fabrication, transportation and handling of the fragile chambers and also facilitate NEG coating on the interior vacuum surfaces.

The magnetic properties of materials used in the interaction region must be carefully considered. Most of the vacuum chamber components will be made of beryllium, aluminum and copper which are non-magnetic. Any stainless steel used in this region will be 316LN. This austenitic stainless steel maintains its very low magnetic permeability after welding or cold working. In general the use of stainless steel in the IR will be avoided due to the presence of cobalt in the material and the possible formation of ^{60}Co due to neutron activation. Once formed, this radioactive isotope has a half-life of 5.3 years, severely limiting the serviceability of the area.

Impedance and Instabilities

From an electromagnetic standpoint, the ultimate beam pipe would be a perfectly smooth flawless conductor. This would allow the induced image currents to travel along the chamber walls without losses or forces acting back on the particle beam. In reality this is not possible and one has resulting electromagnetic interactions, called wake fields. Longitudinal and transverse fields are generated when a bunch passes a sudden change in geometry or wall resistivity. These transverse fields can deflect the beam and lead to instabilities while the longitudinal wake fields lead to energy loss of the particles and localized heating of vacuum components.

In order to reduce effects related to resistivity changes, materials such as stainless steel pipes with small diameters will be copper plated. The required copper thickness depends on the shape of the beam pipe, distance from the beam and the average bunch current. Critical elements will be simulated to determine the minimum thickness required. To minimize detrimental effects from sudden geometry changes a radial tapering requirement of 10:1 will be followed, unless absolutely not possible. This means a 1 mm change in the radial distance between the particle beam and the chamber wall will occur over at least 10 mm of longitudinal space. RF shielding will be used to bridge all vacuum flange joints to prevent trapped modes and to help maintain uniform wall geometry. Even a few watts of deposited power on an uncooled vacuum surface can result in an extremely high temperature rise. Bellows, which need to be installed to compensate for mechanical misalignment and provide room for thermal expansion during bake outs, will also be internally shielded to avoid trapped modes. Steps inside the bellows RF shielding will be kept to a minimum.

Vacuum Requirements

Every effort must be made to reduce the residual gas pressure in the interaction region to minimize beam-gas interactions. The first concern is related to scattering, both elastic (Coulomb) and inelastic (Bremsstrahlung). Particles in the beam which are scattered off of the remaining gas molecules can further interact with vacuum chamber walls. This in turn leads to a 'positive feedback' loop which can quickly turn catastrophic. The second concern is related to phenomena such as ion induced desorption and electron multipacting. In both of these cases charged particles, freed electrons or ionized residual gas molecules are accelerated by the electric fields resulting from the charged particle beams. These accelerated particles can bombard the vacuum chamber walls and lead to large localized pressure rises and additional scattering. This is another self-feeding process. All of these mechanisms decrease the beam lifetime and intensity, influence the detector background signal and have an overall impact on the luminosity of the machine.

In order to eliminate the potential of unwanted contamination and ensure the lowest possible base pressure, best UHV practices will be followed from start to finish. This entails special processing of fabricated parts, careful surface treatment and minimizing the surface area exposed to vacuum. All parts will be chemically cleaned and/or vacuum baked

prior to welding or assembly. After cleaning, no vacuum surfaces will be touched with bare hands and all openings to vacuum surfaces will be wrapped in clean vacuum grade aluminum foil.

Given the limited space for lumped pumping as well as the need for ultra-high vacuum throughout the entire interaction region, the vacuum chamber will be coated with a non-evaporative getter (NEG) layer. This coating will be magnetron sputtered directly onto the interior surfaces of the IR vacuum chambers. NEG layers are a composition of active metals (Ti, Zr and V) which chemically pump most of the gases found in a UHV system (N_2, CO and CO_2). It also has a high diffusivity for H_2 which is the predominant gas in a baked leak tight vacuum section. The film also creates a hydrogen barrier on the interior surfaces which limits the permeation of H_2 into the system. In addition to all of these benefits the film has a low secondary electron yield, which reduces the risk of electron cloud formation, and being in the order of microns, adds negligible mass between the experiment and the detectors.

Incorporating NEG coating into the design has two implications. First is the degradation of the pumping performance after successive regenerations. Anytime the vacuum section is vented for maintenance, the NEG layer becomes completely saturated and needs to be regenerated to regain its pumping characteristics. Regenerating the layer requires dissolving the surface oxides and nitrides into the bulk material which creates a new metallic surface facing the vacuum system. Since the film is thin, it has a limited storage capacity. Some of the pumping capacity can be regained by activating at higher temperatures but the upper bound is limited by the material choices for the vacuum chambers. To increase the potential number of activations, the detector vacuum section will be vented with an extremely pure noble gas which is not pumped by NEG film.

Given the limited access inside the central detector region, permanently mounted heaters are envisioned to facilitate baking. Thin polyamide heaters which are made from thin metal foils sandwiched between Kapton films will be used. These heaters can be made in almost any size or shape with varying watt densities to ensure adequate heating and activation of the NEG coatings. While adding some radiation length, these are a good compromise considering the alternatives and will only be used where removable heaters cannot be installed. Depending on the final design of the detector, additional insulation may be required to protect sensitive components located close to the beam pipe or they will need to be removed for the bake out.

Since NEG coatings only pump active gases, ion pumps will be installed at either side of the interaction region for residual noble gases. Ion pumps are Penning traps with crossed electrical and magnetic fields. The magnetic field increases the flight time of free electrons which ionize incoming gas molecules. These ions are then accelerated in the presence of the electric field and impact on a metallic cathode typically made of titanium or tantalum. This freshly sputtered material can physically or chemically react with gas present in the system.

3.2.4 Interaction Region Performance for Scientific Requirements

The physics program of an EIC and the resulting requirements for the detector and the IR have been discussed in Sections 2.2 and 3.2. In order to verify that the IR design fulfills all the requirements as summarized in Table 2.2, an EIC general purpose detector, the auxiliary detectors, the vacuum chamber, and the machine components up to the crab cavities, have been implemented in the EicRoot Geant simulation framework [104]. To make the simulations as realistic as possible the beam line element 3-dimensional locations and magnetic fields are directly taken from the MADX files used for optics calculations. Their apertures precisely reflect our present understanding of how these magnets can be built in reality. The vacuum system is modeled by importing the essential part of the engineering design into Geant.

In the following, results from these simulations will be presented.

Realization of the Scientific Requirements for the Central Detector

A shown in Figure 3.2, the beam element free region L^* along the beam lines is $\pm 4.5\,\mathrm{m}$ from the IP. In order to have the acceptance required for inclusive and semi-inclusive DIS as well as exclusive reactions it is critical to reconstruct events over a wide span in pseudo-rapidity ($-4 \leq \eta \leq 4$), as discussed in section 2.2. Therefore the design of the vacuum system in the detector volume (see Figure 3.22) needs to fulfill these specifications:

- Provide enough space to pass the synchrotron radiation fan through the detector.
- Do not extend beyond a 2° opening angle from the interaction point.

Figure 3.24 shows the integration of the various detector components around the beam

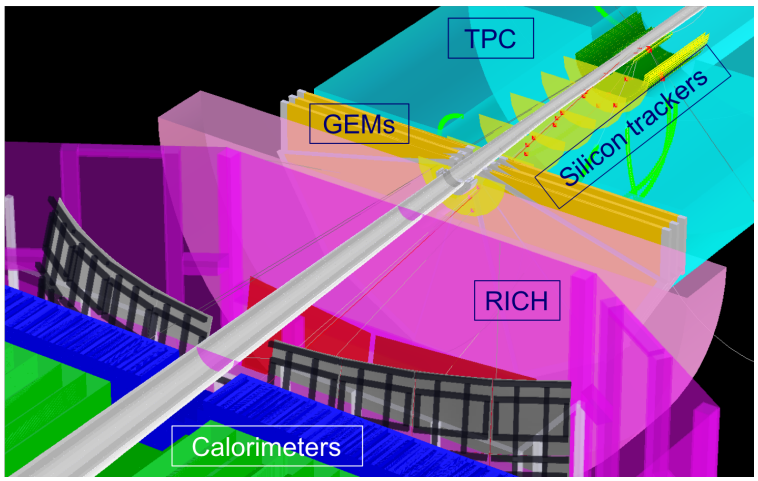

Figure 3.24: The integration of the beam pipe and various detector components in the outgoing hadron beam direction.

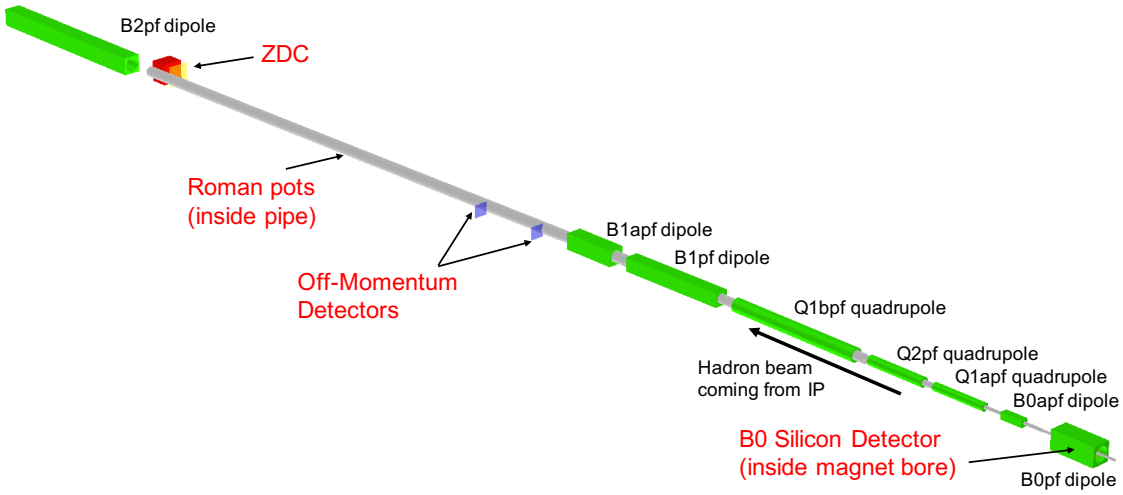

Figure 3.25: EicRoot/Geant4 Drawing of the far-forward IR region including the seven dipole and quadrupole magnets for the hadron beam and the four detector subsystems.

pipe elements in the outgoing hadron beam direction, overlaid by a deep inelastic electron-deuteron scattering event with the secondary particle tracks and hits in the TPC and the silicon trackers.

Realization of the Scientific Requirements for the Interaction Region

Exclusive Processes

As emphasized below the detection of forward-going scattered protons from exclusive reactions as well as of neutrons from the breakup of heavy ions in incoherent and non-diffractive reactions is particularly challenging. All of the exclusive channels rely on robust acceptance in the so-called "far-forward" region of the IR. Multiple detector subsystems are required to cover the full acceptance, as shown in Figure 3.25.

Electron-Proton Scattering: Extreme care has been taken to transport protons with $0.2\,\mathrm{GeV/c} < p_T < 1.3\,\mathrm{GeV/c}$ through the IR such that they can be detected as soon as they can be separated from the core of the beam. To achieve this p_T coverage over a wide range of center-of-mass energies a multi-prong approach is required. Protons with scattering angles up to 5 mrad are detected in the Roman Pots, while the range from 6 to 20 mrad is covered by the B0 large-acceptance spectrometer (see Sec. 8.4.4 for more details). In general the main detector starts seeing secondary particles above ~ 30 mrad ($\eta \sim 4$), and bending power of the 3 T solenoid is sufficient for momentum measurement above ~ 50 mrad ($\eta \sim 3.5$ or so).

The current Roman Pot configuration has two stations each with 2–5 silicon planes at 26.1 m and 28.1 m downstream of the IP, with a relatively modest single point XY-resolution. As shown later, even this very basic setup provides sufficient acceptance and a good momentum and scattering angle measurement.

There are several effects influencing the low p_T acceptance. We have been following the general rule of thumb that the distance between the inner edge of the Roman Pot silicon sensors and the beam orbit should be 10σ in X and Y. The physical size of the separation $\sigma_{x,y} = \sqrt{(\beta_{x,y}\epsilon_n)/\gamma}$ is driven by the normalized beam emittance ϵ_n and the β-functions $\beta_{x,y}$ at the location of the Roman Pots. The acceptance at large p_T is mainly constrained by the magnet apertures, vacuum system, and the overall size of the electron quadrupole magnet, which shares the bore of the B0pf containing the B0 spectrometer.

Figure 3.26 summarizes the p_T acceptance for three different proton beam energies, $E_p =$ 41 GeV, 100 GeV, and 275 GeV for the "high beam divergence optics" (see Table 3.12) for the EIC for the case of e+p DVCS events. In this case, the longitudinal momentum fraction of the scattered proton with respect to the beam, x_L, is $x_L > 0.8$, where the lower values come from events with $Q^2 > 50\text{GeV}^2$. The figures illustrate the need for a multi-prong detector approach to provide the full p_T acceptance over a wide range of hadron beam energies. For $E_p = 41\,\text{GeV}$ the limiting factor in acceptance at high p_T is the inner dimension of the vacuum chamber and the magnet apertures. At $E_p = 100\,\text{GeV}$ one in general has full acceptance in p_T but there exists some "grey" (transition) area separating the forward scattered proton acceptances in the B0 spectrometer and the Roman Pots. We are currently investigating how much of this "grey" area can be filled by optimizing the layout of the outgoing vacuum beam pipe, or potentially having more space between the hadron beam pipe and electron quadrupole inside the B0pf bore. For $E_p = 275\,\text{GeV}$ the acceptance is mainly limited at low p_T, however this region can be partly filled by taking data with the "high acceptance beam optics" (see Table 3.12) for the EIC, which reduces the beam envelope size at the Roman Pot location and consequently relieves the 10σ separation cut, as illustrated in the x-y acceptance plots in Figure 3.27.

Table 3.12: Selected beam parameters for high divergence and high acceptance beam optics configurations for 275 GeV protons with strong hadron cooling. The increased β^* and from high divergence to high acceptance subsequently decreases the beam envelope size at the Roman Pots, increasing the low-p_T proton acceptance. Angular divergence in the proton beam is also reduced in the high acceptance configuration, reducing its contribution to smearing of the reconstructed transverse momentum.

Parameter	High Divergence	High Acceptance
RMS norm. emit. (h, v) [µ]	4.6, 0.75	4.9, 0.62
β^* (h, v) [cm]	90.0, 4.0	395.0, 4.0
RMS $\Delta\theta$ (h, v) [µrad]	132, 253	65, 229

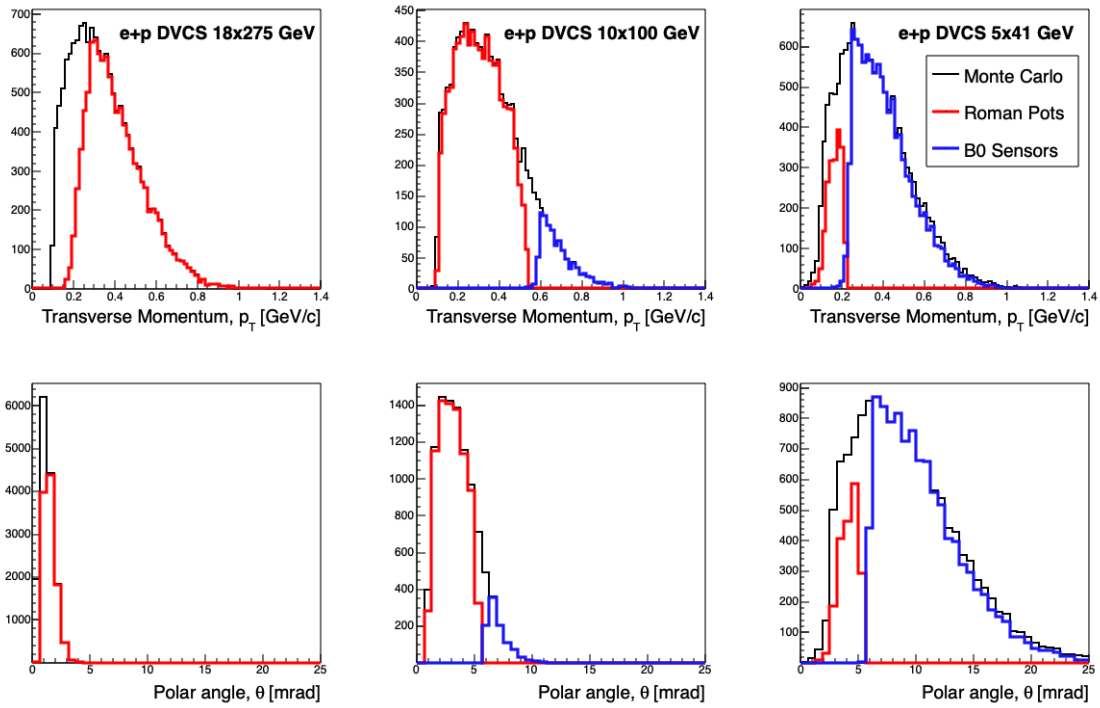

Figure 3.26: p_T (top row) and polar angle (θ; bottom row) acceptance for DVCS protons in the Roman Pots (red) and B0 detectors (blue) for three different energy combinations. In the medium (middle column) and low-energy (right column) configurations, both the Roman Pots and B0 are required to cover the full acceptance. At high energy (left column), the low-p_T acceptance is limited by the optics configuration which determines the size of the beam at the Roman Pots location.

The p_T resolution of these forward scattered particles is of equal importance as their acceptance. There are several effects that can influence the momentum resolution and need to be mitigated:

- The finite width of the vertex distribution at the IP adds uncertainty in the angle determination. This uncertainty can be eliminated by determining the vertex of the event through other tracks in the event being registered in the main detector and benefit from the excellent vertex definition from the µ-vertex detector.
- The finite pixel size of the sensors used for the proton reconstruction impose uncertainty of the hit location, and therefore potentially smear the reconstructed momentum of the particle. This can be mitigate by choosing pixels for the silicon sensors of a reasonably small pitch.
- The angular divergence $\sigma_\theta = \sqrt{\epsilon_n/(\beta^*\gamma)}$ of the beam, which directly leads to a smearing of the scattering angle.
- The hadron bunch "rotation" at the IP due to the crab cavities. Crabbing implies

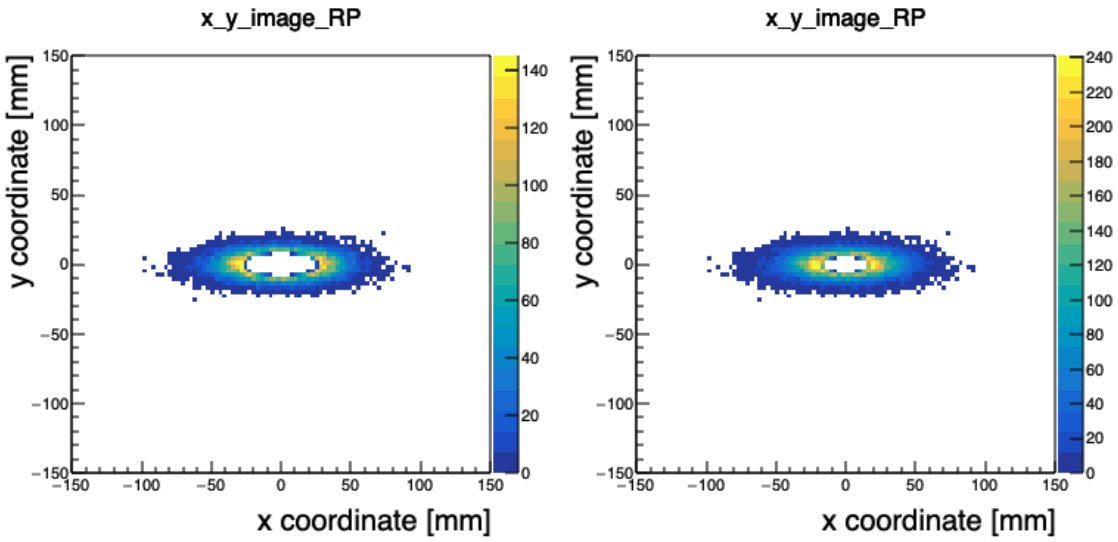

Figure 3.27: Acceptance image of protons from 18×275 GeV e+p DVCS events using the high divergence (left) and high acceptance (right) optics configurations. The transverse beam size, σ, at the Roman Pots decreases by a factor of 2 when going from the high divergence to high acceptance configuration, which increases the acceptance of low-p_T protons.

a transverse momentum kick $p_x(z)$ to the particle bunch, with the kicking strength proportional to the longitudinal position z of particles in the bunch. Therefore at the IP particles at the "head" of the bunch will have a slightly different orientation and/or transverse offset compared to the ones in the "tail" of the bunch, which leads to additional smearing of the apparent scattering angle. The z-vertex determination of the event provided by the main tracker as well as high-resolution timing of the Roman Pot silicon sensors (of an order of $\sim$ 35 ps or so) is able to fully mitigate this effect.

- The spread in the beam energy, which normally has a width (RMS) of $\sim 10^{-4}$.

The track reconstruction is based on a Kalman filter (either with or without the vertex constraint) for the protons registered in the B0 spectrometer and a matrix transport method (with the realistic beam envelope size at the IP) for the protons registered in the Roman Pots. Under relatively conservative assumptions one obtains a p_T resolution as low as $\sim 15 - -50$ MeV/c for reconstructed protons in the far-forward region with all smearing effects included.

The other important quantity to test for acceptance is the momentum fraction of the scattered proton compared to the beam, x_L. For DVCS, the beam energy choice and the Q^2 range can both affect the produced x_L range of scattered protons. Figure 3.28 shows plots of the x_L vs. p_T coverage for the highest (18×275 GeV) and lowest (5×41 GeV) e+p beam energy configurations for the "high acceptance" optics configuration (for the high energy option).

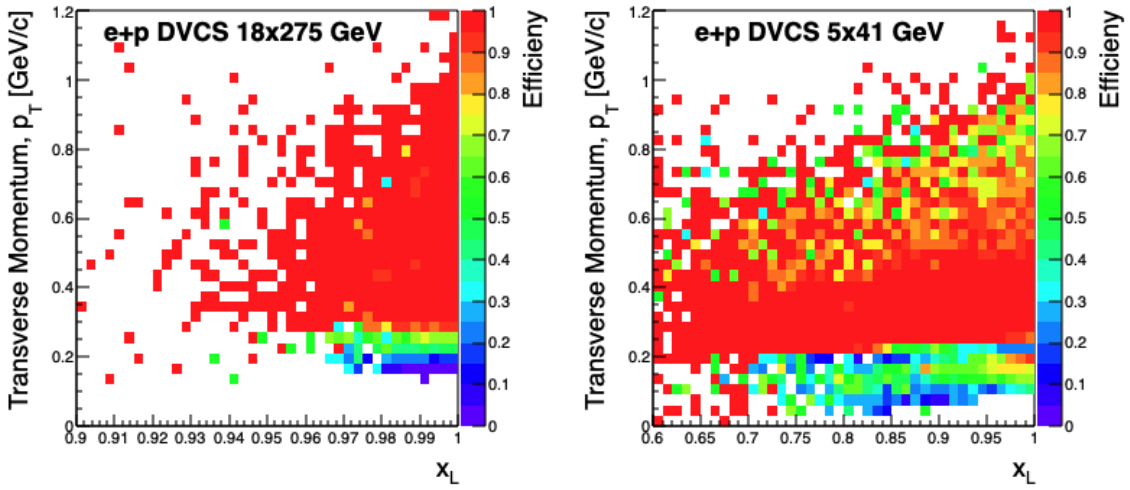

Figure 3.28: x_L vs. p_T acceptance coverage for the highest (18×275 GeV; left column) and lowest (5×41 GeV; right column) e+p beam energy configurations. The plots depict the ratio of the reconstructed events (without smearing) over the generated events, with the z-axis noting the efficiency in the (x_L, p_T) bins. The 18×275 GeV case uses the high acceptance optics configuration, which maximizes low-p_T acceptance. Note: the x_L range on the two plots is different.

The acceptance at low-p_T and high-x_L is limited by the beam size at the Roman Pots, which limits how close the detector can get to the beam safely (10σ distance). Different optics combinations can be developed to aid in improving the low-p_T acceptance at the various beam energies. In the low energy case, the 10σ region is larger in x than in y, allowing better acceptance for p_T with different x and y components.

Electron-(heavy)Nuclei Scattering: The only possible way to tag exclusive electron-nucleus events for heavy nuclei is to veto the nuclear break-up. To demonstrate the generic geometrical acceptance of neutrons, a particle gun was used to sample neutrons at various energies from 0.0 to 135 GeV, and at scattering angles up to 20 mrad, as shown in Figure 3.29.

Using BeAGLE, we are also able to study the tagging efficiency for neutrons in e+Pb nuclear break-up events. Figure 3.30 shows the break-up neutron and proton momentum vs. scattering angle in the laboratory frame for different beam energies.

One needs to transport neutrons within a cone of 0 mrad to 6 mrad, depending on the beam energy, through the IR to a Zero-Degree Calorimeter (ZDC). The ZDC is placed right in front of the B2APF magnet at $\sim$ 30 m from the IP. Detection of protons requires additional detectors for small scattering angles since the breakup protons have a different magnetic rigidity than the Pb beam, the so-called "off-momentum detectors". Figure 3.25 shows the layout of the beam elements towards the ZDC. The acceptance image shown in Figure 3.29 (right) illustrates that currently neutrons are not really well centered at the $60 \times 60\,\text{cm}^2$

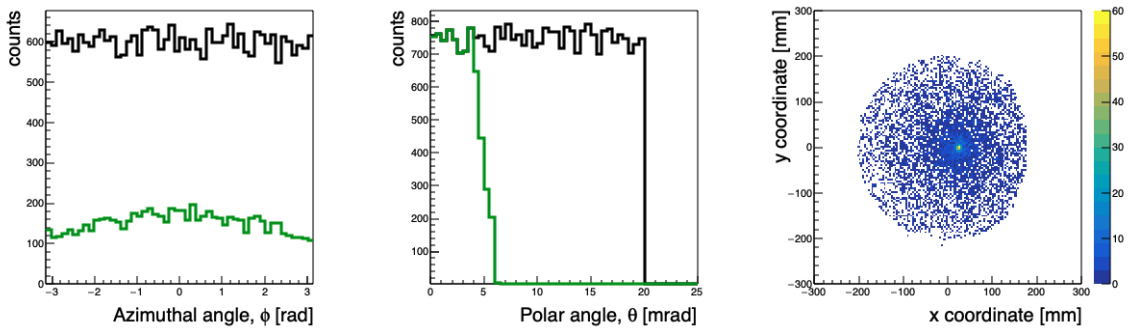

Figure 3.29: Plots of the neutron azimuthal angle, ϕ, acceptance (left), polar angle, θ, acceptance (middle), and an image of the hits on the ZDC (right) with the axes representing the assumed 60 cm $\times$ 60 cm size of the proposed detector in the far-forward region. These neutrons were generated with a particle gun to illustrate the neutron acceptance with the restriction of the aperture size, which only allows neutrons to be accepted up to about 4.5 mrad, with slightly better acceptance up to 5.5 mrad, asymmetric in ϕ.

ZDC front surface. This is improved by the new IR design. Preliminary estimates show that the new option provides sufficient containment of the hadronic shower for the whole ZDC angular acceptance from of 0 to 4 mrad. Figure 3.31 shows the resulting acceptance for neutrons from nuclear break-up. The required angular acceptance of $\pm$4 mrad has been achieved and even extended beyond that by careful consideration of machine beam line element apertures.

With the goal to tag and veto events where a nuclear breakup occurs, maximal acceptance for protons, neutrons, and photons is required. However, the photons produced in nuclear breakup are mainly from events with small values of $\hat{t}$, with many at energies $\sim 10 - -150$ MeV, making them very challenging to detect (see Figure 3.32 left). Figure 3.32 (right) shows the veto efficiency as currently achieved but the rejection of events with nuclear breakup through photons is still under investigation.

Electron-(light)Nuclei Scattering:

The physics program of an EIC requires proton and neutron collisions to allow for a full flavor separation of parton distribution functions. As neutron beams are not feasible, (un)polarized ^{3}He and deuteron beams are used for these purposes. To ensure the scattering really occurred off the neutron the spectator proton(s) need to be detected. Figure 3.33 shows the momentum, azimuthal, and polar scattering angle for the spectator protons (top) and active neutrons (bottom) from incoherent diffractive J/ψ electron-deuteron events for deuterons with $E_d = 110$ GeV/n. This study was carried out using the BeAGLE e+A Monte Carlo event generator, with the full Geant4 simulation of the far-forward IR region, detailed in [105]. The detection of the spectator protons in e+d scattering requires an additional detector system because the spectator proton has approximately half the rigidity of the deuteron beam. This means the protons will be bent outside of the beam pipe after the B1apf dipole magnet. Inclusion of so-called "off-momentum detectors" will al-

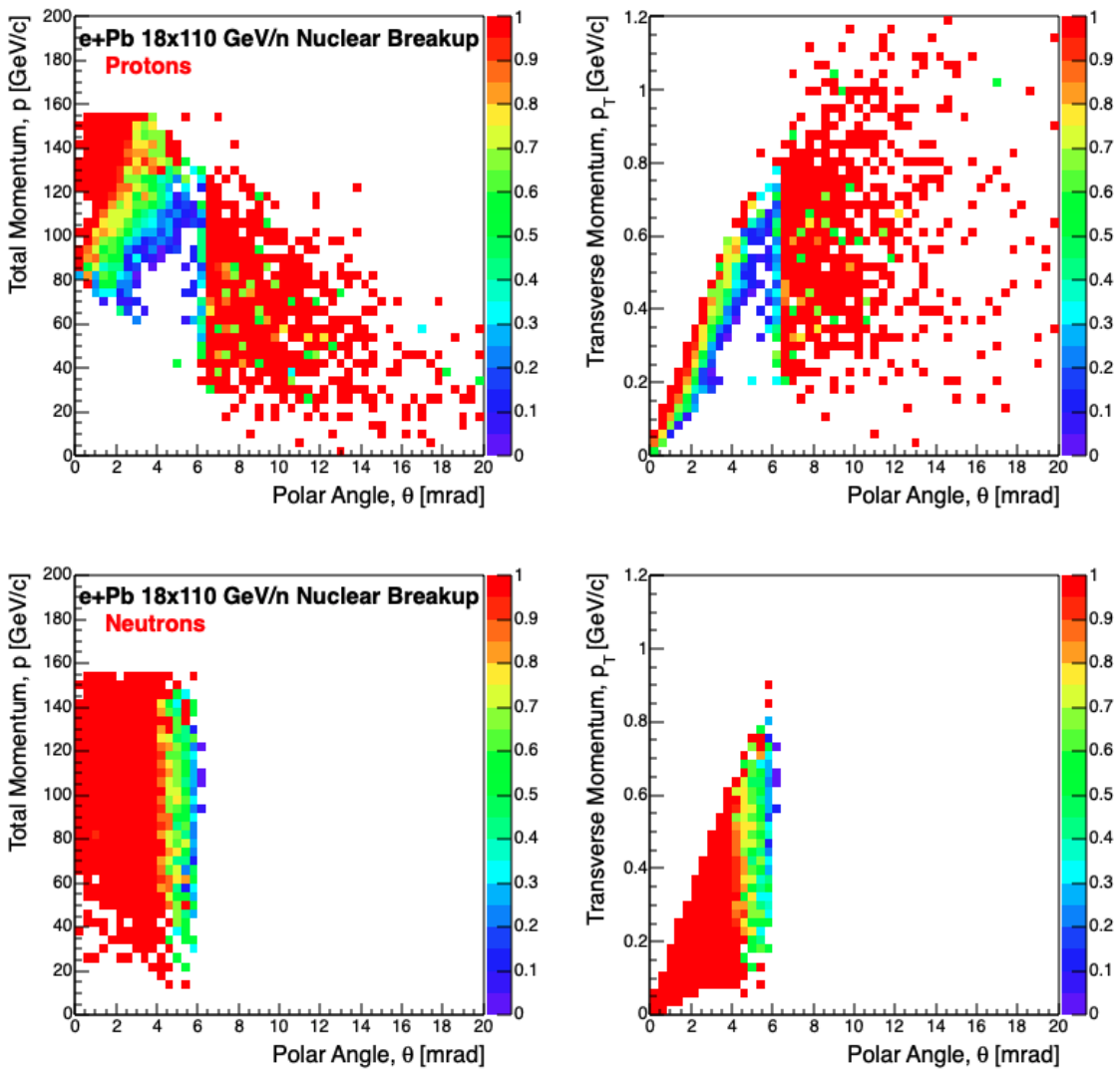

Figure 3.30: Plots of the ratio of accepted particles over those generated by e+Pb 18×110 GeV/n incoherent J/ψ BeAGLE events. The top row depicts the proton acceptances (p vs. θ, left; p_T vs. θ, right), while the bottom row is the same plots but for the neutrons. The proton acceptance is more complicated due to the nature of the protons experiencing more extreme bending in the lattice because of their smaller rigidity, necessitating multiple sub-detectors for full coverage of the kinematic space.

low for detection of these spectator protons. Figure 3.34 shows the same setup, but for the case where the neutron is the spectator. In the case where the proton is the active nucleon, the larger scattering angle places those protons into the acceptance of the B0 spectrometer, while the active neutrons have a reduced acceptance due to the cutoff of the acceptance because of the aperture. Additionally, the active protons have a larger range of p (longer tail in the p distribution) and therefore more protons are severely off-momentum from the

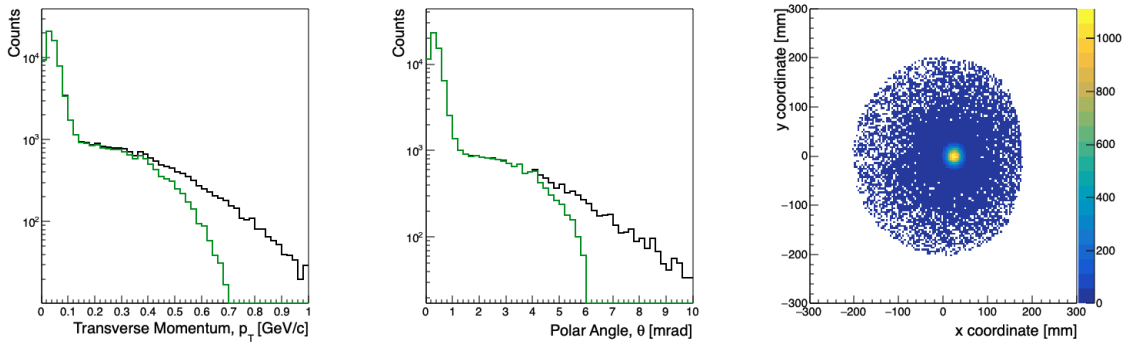

Figure 3.31: Plots of the neutron transverse momentum, p_T, acceptance (left), polar angle, θ, acceptance (middle), and an image of the hits on the ZDC (right) with the axes representing the assumed 60 cm $\times$ 60 cm size of the proposed detector in the far-forward region. These neutrons come from e+Pb 18$\times$110 GeV/n incoherent J/ψ events generated with BeAGLE.

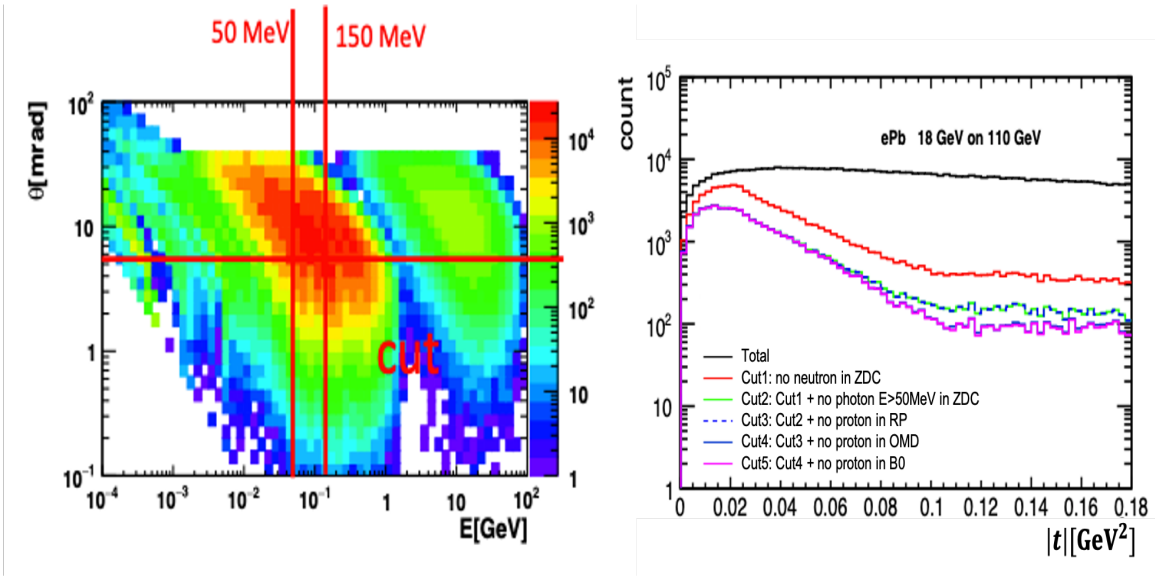

Figure 3.32: Plots of the photon energy, E, vs. scattering angle, θ (left), and the incoherent event veto efficiency as a function of $|t|$ (right). The right plot shows how the incoherent vetoing improves with better tagging efficiency for protons, neutrons, and photons.

beam and lost in the quadrupoles, as seen in the top-middle panel of Figure 3.34. For the scattered neutrons, the active neutron case has a broader range of scattering angles (see Figure 3.33) and the aperture size limits the overall acceptance of these neutrons. The proton spectator case shows an overall optimized acceptance for both final-state nucleons, enabling access to observables requiring tagging of the complete final state.

In the case of e+^{3}He collisions, the situation is complicated by the fact that there are two spectator nucleons to tag in the final state. The case of the active neutron gives access to

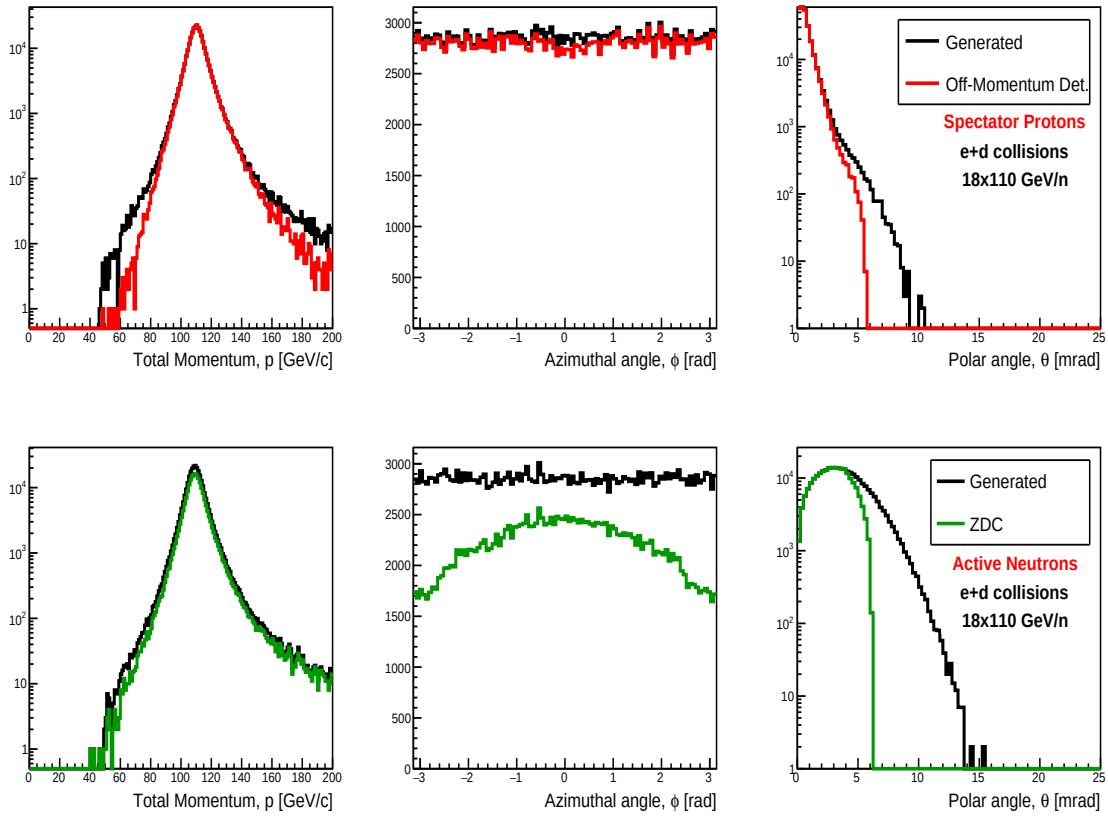

Figure 3.33: 3-momentum p, azimuthal angle (ϕ), and polar angle (θ) acceptance for protons (top row) and neutrons (bottom row) from nuclear breakup in $18\times110\,\mathrm{GeV/n}$ e+d incoherent J/ψ events for the proton spectator case.

the polarized neutron structure functions, and is therefore of prime interest. These active neutron events are tagged by reconstructing both of the final state spectator protons in the far-forward detector region. Figure 3.35 shows the acceptance for these two final state protons in two different kinematic regimes, namely DIS on the neutron with the two protons acting as spectators, and a case where one proton forms a short-range correlation pair with the active neutron, yielding very different p_T distributions for the two spectator protons. At the higher ^{3}He beam energy (110 GeV/n), the acceptance is above 85% for the SRC case, and above 95% for the DIS case.

Because of the complicated acceptances for scattered protons from various processes, it is instructive to analyze the proton acceptance as a function of proton momentum and scattering angle for a fixed beam energy (or fixed far-forward magnet settings). This essentially probes the dependence on the longitudinal momentum fraction (x_L) of far-forward proton acceptance. Figure 3.36 depicts the resulting momentum, polar angle, and azimuthal angular acceptance for scattered protons assuming 275 GeV proton beam settings, but with protons ranging in momentum from 0.0 to 275.0 GeV/c.

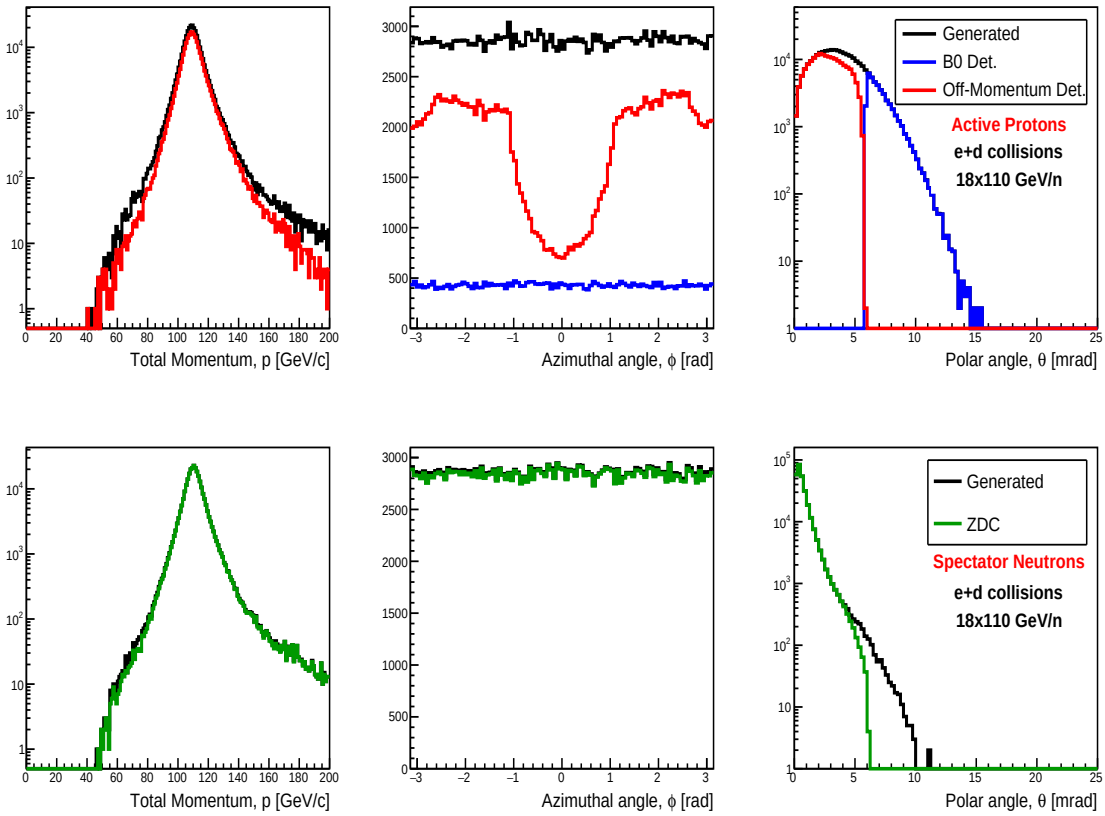

Figure 3.34: 3-momentum p, azimuthal angle (ϕ), and polar angle (θ) acceptance for protons (top row) and neutrons (bottom row) from nuclear breakup in $18\times110\,\mathrm{GeV/n}$ e+d incoherent J/ψ events for the neutron spectator case. In this case, the proton azimuthal (top-middle) and polar angle (top-right) plots show the contributions from the two individual far-forward detectors, while the momentum distribution (top-left) shows the combined acceptance.

Inclusive Processes:

Many physics topics beyond the ones discussed in the EIC White Paper [7] benefit from tagging the scattered electrons at Q^2 values significantly below $1\,\mathrm{GeV}^2$. Scattered electrons with $Q^2 < 0.5\,\mathrm{GeV}^2$ cannot be detected in the main detector. Therefore, similar to the HERA collider detectors, a special low-Q^2 tagger is needed. In this case, we consider two independent low-Q^2 taggers as shown in Figure 3.37. The taggers should include calorimeters for triggering and energy measurements, and they should be finely segmented to disentangle the multiple electron hits per bunch crossing from the high rate bremsstrahlung process. The taggers should also have position sensitive detectors, such as silicon planes, to measure the vertical and horizontal coordinates of electrons. The combined energy and position measurements allow reconstruction of the kinematic variable Q^2 and x_{BJ}. If the position detectors have multiple layers and are able to reconstruct the electron direction this will over-constrain the variable reconstruction and improve their measurement; this

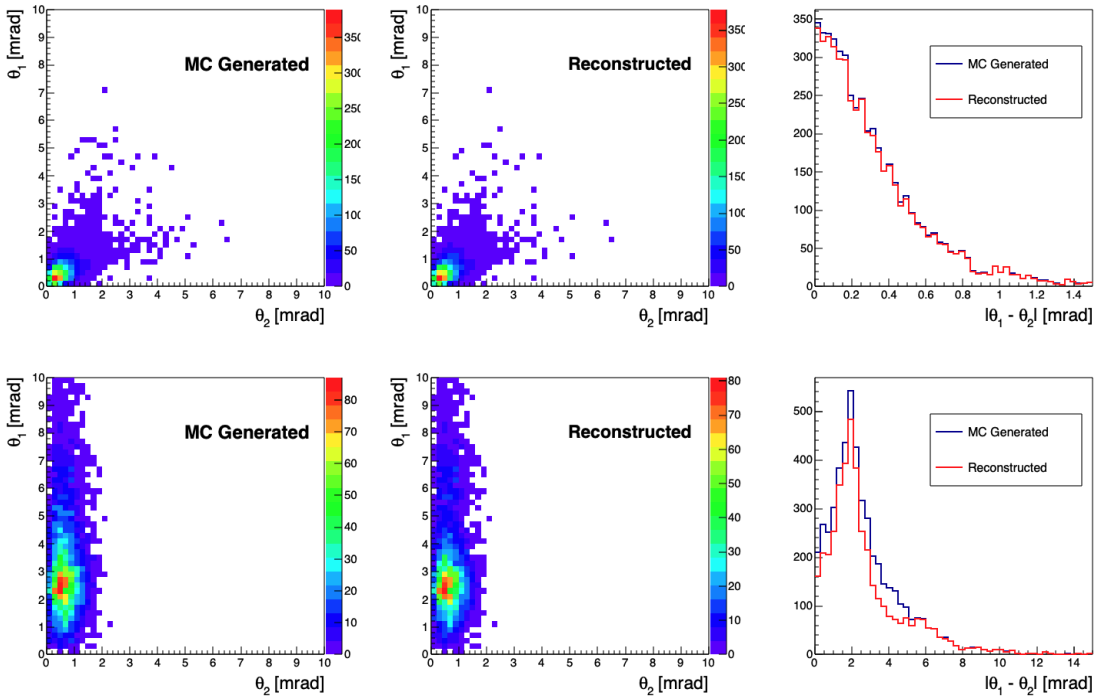

Figure 3.35: Scattering angle plots for spectator protons from e+^{3}He collisions using BeAGLE DIS events at 10×110 GeV (top row) and SRC events at 18×110 GeV (bottom row). The rows are organized as follows: MC generated θ of proton one vs. proton two (left), reconstructed θ of proton one vs. proton two (middle), absolute value of the difference of the two scattering angles (right) with the MC shown in black, and reconstructed shown in red.

may also provide some measure of background rejection.

Tagging of low-Q^2 processes provides an extension of the kinematic range of DIS processes measured with electrons in the central detector. It crosses the transition from DIS to hadronic reactions with quasi-real photons. An example of acceptance as a function of Q^2 and electron energy, E_e is shown for the two taggers in Figure 3.38. The acceptance for the full Q^2-range including measurements with the central detector and electron taggers as depicted in Figure 3.37 is shown in Figure 3.39.

Electrons with energies slightly below the beam are bent out of the beam by the first lattice dipole after the interaction point. The beam vacuum chamber must include exit windows for these electrons. The windows should be as thin as possible along the electron direction to minimize energy loss and multiple scattering before the detectors.

The preliminary conclusion of these physics simulation studies is that the current IR design fulfills most of the requirements summarized in Table 2.2. Several potential improvements to the design are identified already, which will extend the EIC physics reach even further.

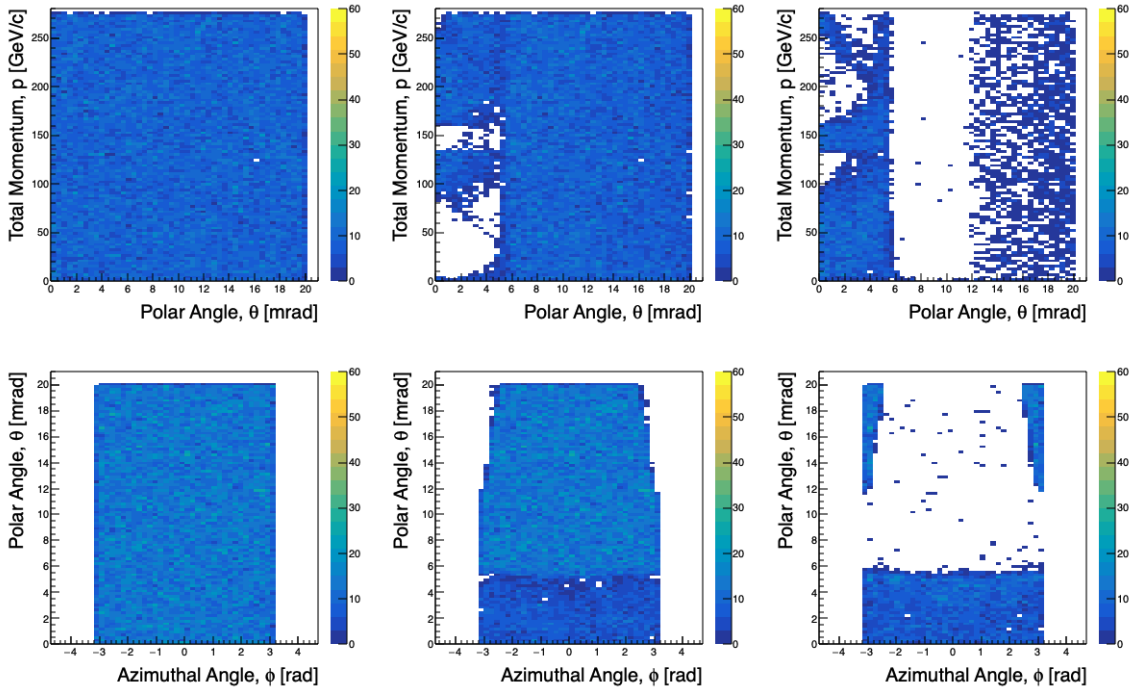

Figure 3.36: Distributions for generated protons (left), reconstructed protons (middle), and the difference between the two (right) for momentum vs. polar angle (top row) and polar angle vs. azimuthal angle (bottom row). These distributions show the combined for the three proton detector subsystems, as well as effects of asymmetric loss of protons in the lattice quadrupoles (for the off-momentum detectors), and asymmetric loss of protons due to the placement of the electron quadrupole within the B0pf magnet bore.

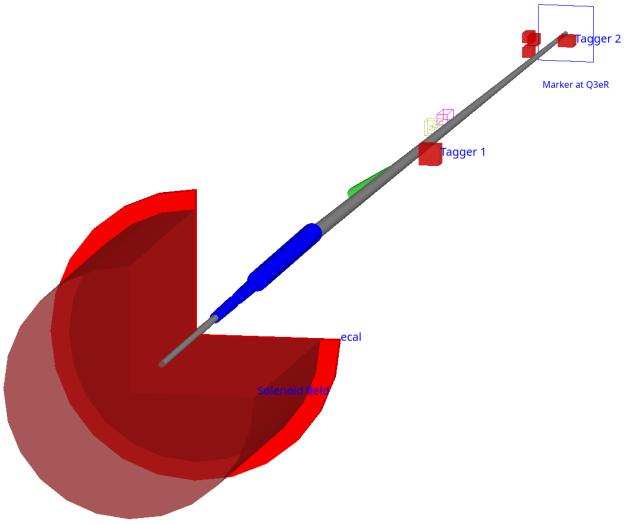

Figure 3.37: A view along the outgoing electron beam from the main detector towards the low-Q^2 tagger and luminosity monitor.

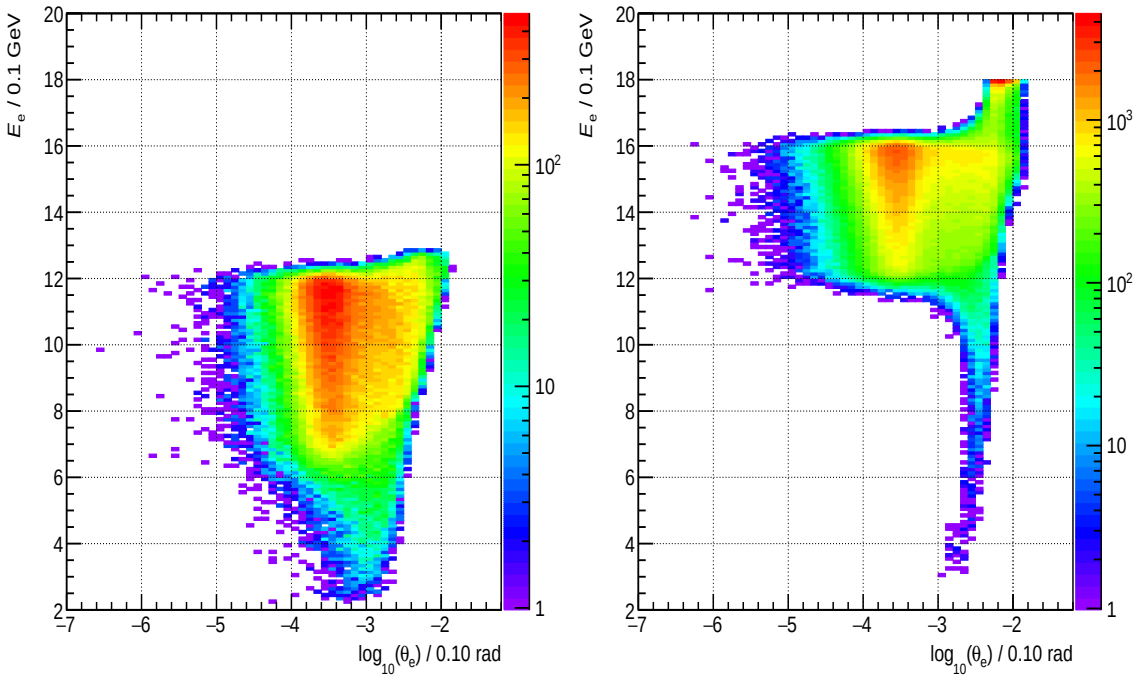

Figure 3.38: Scattered electron energy E_e and polar angle θ_e for events of quasi-real photoproduction with a hit in Tagger 1 (left) or 2 (right).

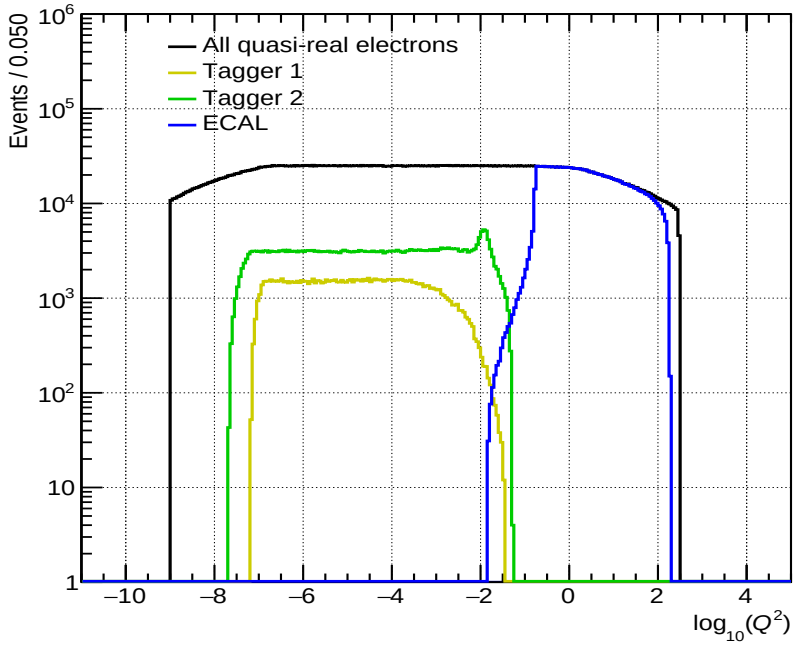

Figure 3.39: Coverage in Q^2 for tagger detectors and ECAL.

3.2.5 Crab Cavity Requirement and Specifications

EIC Crab Cavity Introduction

Robert Palmer introduced the concept of crab cavity as a countermeasure to the geometric reduction in luminosity caused by the crossing angle in colliders [18]. Crab cavity imparts a transverse momentum kick $p_x(z)$ to the particle bunch, with the kicking strength proportional to the longitudinal position z of the particle. At the right phase, the bunch arrives at the cavity with its center particle receives an accumulative zero deflection. The transverse momentum kick can be expressed as

$$p_x(z) = \frac{eE_0}{\omega}\sin(kz)\sin\left(\frac{kL}{2}\right)\sin\phi_{\text{crab}} \approx \frac{eE_0 z}{c}\sin\left(\frac{kL}{2}\right)\sin\phi_{\text{crab}} \tag{3.50}$$

where E_0 is the amplitude of the electric field acting on the bunch, ω and k are the angular frequency and the wave number of the crab cavity respectively, L is the bunch length, and ϕ_{crab} is the phase advance of the crab cavity. The longitudinal coordinate z is referencing to the center of the bunch, where $z = 0$.

For beam energy of E_b, transverse oscillation translates the longitudinally dependent kick p_x to a transverse offset x_{IP} at the interaction point (IP), which gives

$$x_{IP} = R_{12}\frac{p_x c}{E_b} = \sqrt{\beta_{\text{crab}}\beta^*}\frac{eE_0 z\sin\left(\frac{kL}{2}\right)\sin\phi_{\text{crab}}}{E_b} \tag{3.51}$$

where R_{12} is the element of transverse transfer matrix from the crab cavity to the IP, β_{crab} and β^* are the beta functions at the crab cavity and IP.

At desired cavity voltage, the transverse offset will cancel the crossing angle in the optics and restore the head-on collision. The requirement to the transverse offset can be exchanged with the crossing angle as

$$\theta_c = \frac{2x_{IP}(z)}{z} = \sqrt{\beta_{\text{crab}}\beta^*}\frac{2eE_0\sin\left(\frac{kL}{2}\right)\sin\phi_{\text{crab}}}{E_b} \tag{3.52}$$

The required crabbing voltage should be

$$V = \frac{cE_b\theta_c}{2e\omega\sqrt{\beta_{\text{crab}}\beta^*}\sin\phi_{\text{crab}}} \tag{3.53}$$

where we assume that the phase advance between the crab cavity location and IP is exactly $\frac{\pi}{2}$.

EIC Crab Cavity Requirement and Specifications

The EIC crossing angle is in the horizontal direction. Given the current proton bunch length for EIC is 6 cm at high energy and 7 cm at low energy, in order to increase the beam lifetime, a long wavelength of the crab cavity at low frequency is required to linearize the transverse kick within the proton bunch with respect to the longitudinal position, therefore reduces the synchro-betatron oscillation as well as the non-linearity in the bunch geometric shape. Consider the current SRF fabrication technology and the main frequency of the proton ring, the crab cavity frequency is chosen to be 197 MHz, which is the 2520th harmonic of the revolution frequency. A set of second harmonic crab cavities at 394 MHz is planned to be added to the main cavities for optimum performance. To minimize the design risk and single cavity fabrication cost, the electron beam will share the same design of the second harmonic crab cavities for the ions. Due to a much lower energy, the voltage required from the electron crab cavity system is about 60% of the voltage from the second harmonic ion crab cavity system. Thus, the crab cavity system development focused on the ion beam requirement, which would fulfill both beams, and recognize the more stringent higher order mode damping for the electron beam. The detailed crab cavity RF designs are elaborated in detail in Section 6.5.5.

In addition, the beta function, together with the emittance ϵ determines the beam size σ_{crab} along the ring as shown in the equation below, and therefore sets limits on the aperture diameter d_{crab} for the crab cavity.

$$\sigma_{\text{crab}} = \sqrt{\epsilon_{\text{RMS}}\beta_{\text{crab}} + D^2\delta_{\text{RMS}}^2} \tag{3.54}$$

where ϵ_{RMS} is the RMS emittance, D is the dispersion function, and δ_{RMS} is the energy spread. In the case of EIC, $D\delta_{\text{RMS}}$ is negligible. The crab cavity system minimum aperture is determined based on the beam size multiplied by a safety factor for each beam. Each requirement is listed in Table 3.13 respectively. The aperture of the crab cavity system is chosen to meet the larger required diameter of both directions in the same ring. The large emittance during low energy operations can be compensated by a smaller beta function at the crab cavity site to maintain the same bunch size for the aperture.

Table 3.13: Crab cavity system aperture diameter limitation at high energy case.

	proton		electron	
Parameter	horizontal	vertical	horizontal	vertical
ϵ_{RMS} [nm]	15.8	2.5	24	2.0
β_{crab} [m]	1300	1300	150	150
Safety factor	20	20	27	45
Minimum diameter [cm]	10.3	10.3	5.7	1.2

Table 3.14 shows the crab cavity related lattice parameters and the calculated voltage requirement for each scenario. The table also compares the EIC crab cavities with the existing crab cavities from KEKB and Hi-Lumi LHC [106–108]. The Hi-Lumi Large Hadron Collider (LHC) project introduced two novel designs of compact crab cavities for proton beam. The Hi-Lumi LHC shares a similar bunch length as the EIC, and same frequency as the 2nd harmonic crab cavities in the EIC proton ring. Therefore, the LHC crab cavity program can directly benefit the EIC in many aspects from design through out commissioning.

The location of the crab cavity is chosen with consideration of minimizing the voltage, i.e. maximizing the beta function. However, the dispersion functions and their derivatives at the crab cavity locations are non zero for both rings, which would generate linear and nonlinear instabilities with beam-beam interaction. Analysis of the detailed beam dynamics with crab crossing is discussed in Section 4.6.

The spacial allowance for crab cavity system installation is limited by the distance between the electron and the ion beam lines in horizontal direction, and the local structures in the vertical plane, e.g. cable trays, cryogenic transfer lines, and the tunnel floor, but the limitation is much more relaxed compared to the LHC requirement. The parallel beam lines can accommodate the crab cavity cryomodules with 70 cm radius. In the meantime, the IR is a popular region for various species of magnets, instrumentation devices, along with their

Table 3.14: Comparison of crab cavity parameters.

	KEKB		Hi-Lumi LHC	EIC		
Parameter	LER	HER	both	proton		electron
Full crossing angle [mrad]	22	22	0.59	25		25
Energy [GeV]	3.5	8	7000	275		18
RMS bunch length [cm]	0.7	0.6	7	6		0.9
Frequency [MHz]	509	509	400	197	394	394
Wave number	10.6679	10.6679	8.3834	4.13	8.26	8.26
Wave length [m]	0.5890	0.5890	0.7495	1.52	0.76	0.76
Scheme	global		local	local		
6σ of wavelength	0.07	0.06	0.56	0.24	0.47	0.07
β at IP [m]	1.2	1.2	0.15	0.9		0.59
β at crab cavity [m]	51	122	2616	1300		150
Horizontal beam size [µm]	110	110	7	119		135
Piwinski angle [rad]	0.70	0.60	2.95	6.30		0.79
Voltage [MV]	0.92	1.36	12.43	33.83	-4.75	2.21

auxiliaries. With the current matching lattice, the crab cavity systems are given 15 m of longitudinal installation space on both sides of the IP for hadron beam to provide the total deflecting voltage, and 4 m for electron beam. Figure 3.40 shows the crab cavity cryomodules installed in both rings on one side of the IP, and the RSC ring is also shown in the picture. The red tunnel illustrates the injection line tunnel for hadron beam. The location of the crab cavity cryomodule starts after 40 m on both sides to the interaction point (IP) for hadron beam, and resides in the similar region for electron beam. These limits are well considered at the beginning of the cavity, coupler, helium vessel, tuner and cryomodule development to avoid any significant change in the future.

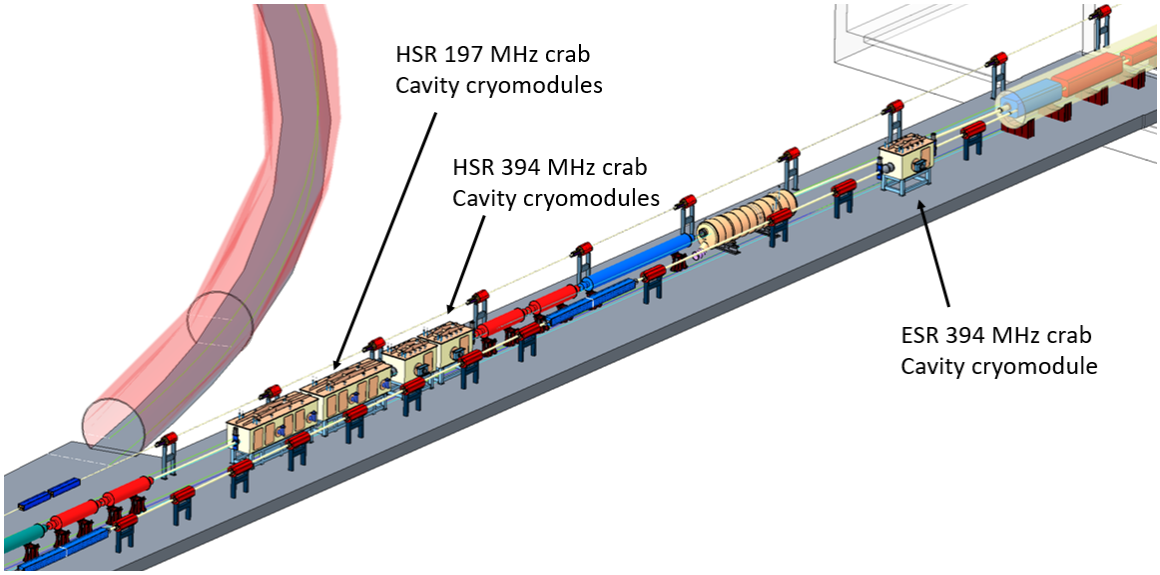

Figure 3.40: Schematic drawing of the local configuration of all beam lines near the crab cavity installation region.

3.2.6 Impedance Modeling

The main parameters used to evaluate the collective effects of the electron beam are given in Table 3.15. To estimate instability thresholds, the wake-potential for a 0.3 mm bunch length was used for beam dynamics simulations in the SPACE particle tracking code [109]. This simulated length is much shorter than the expected nominal bunch length of 19 mm for the unperturbed circulating beam.

Table 3.15: Parameters used for threshold calculation.

Parameter	Value
Energy E [GeV]	10
Revolution period T_0 [μs]	12.79
Momentum compaction α	1.45×10^{-3}
Energy loss U [keV]	9100
RF voltage V [MV]	41
Synchrotron tune ν_s	0.0815
Damping time τ_x, τ_s [ms]	70, 35
Energy spread σ_δ	5.5×10^{-4}
Bunch length σ_s [mm]	19

IR Chamber

The vacuum chamber geometry for the interaction region (IR) is very complex with abrupt changes in the cross section as the particle beams cross each other. A cross-sectional top view of the preliminary IR chamber is shown in Figure 3.41 (upstream) and Figure 3.42 (downstream). Figure 3.43 shows a sectional view of the upstream section of the IR chamber.

An impedance analysis of this geometry has been performed using the GdfidL code [110]. The results of the numerical simulations are shown in Figure 3.44 and Figure 3.45. Using the machine parameters presented in Table 3.15 and the simulated results, the heat load due to multiple passes of the bunch train through the structure can be estimated by

$$P_{\text{loss}} = \kappa_{\text{loss}} I_{\text{av}}^2 T_0 / M, \tag{3.55}$$

where M is the number of bunches, T_0 is the revolution period, and I_{av} is the average current. Using the simulated geometric loss factor $k_{\text{loss}} = 0.2\,\text{V/pC}$, the power loss is $P_{\text{loss}} = 22.6\,\text{kW}$ for $M = 660$ bunches and $I_{\text{av}} = 2.48\,\text{A}$. Most of this heating is a result of the large step transitions which needs to be optimized from the impedance point of view. Reducing the abruptness of the transitions and providing better RF bridging will significantly reduce the heat load on the chamber walls.

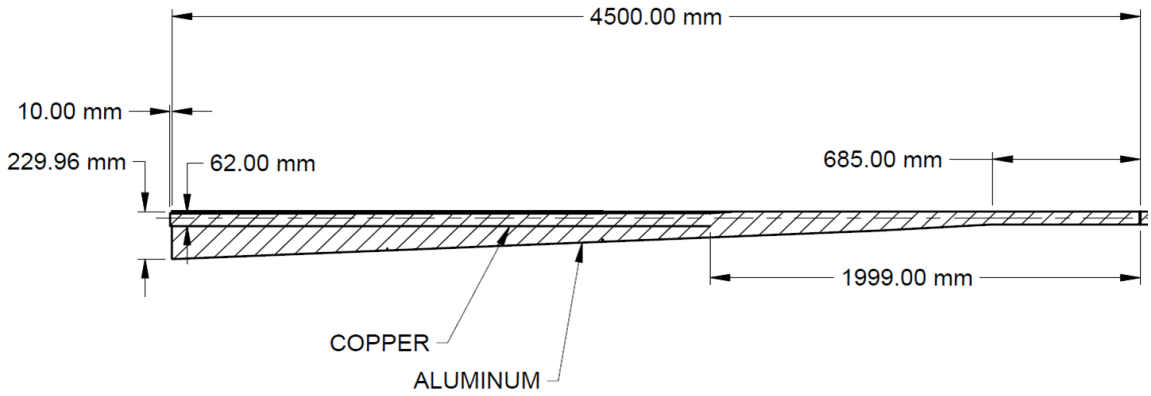

Figure 3.41: Cross-sectional top view of the upstream IR chamber.

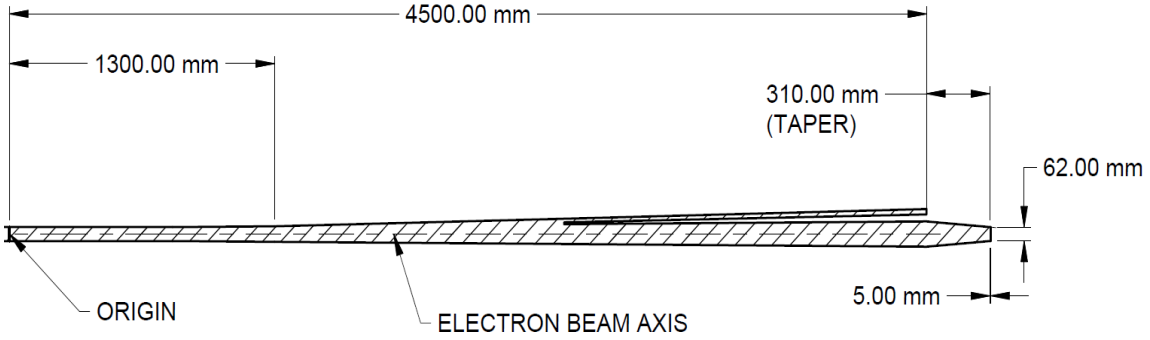

Figure 3.42: Cross-sectional top view of the downstream IR chamber.

The IR chamber design has been iterated on several times since the EIC pCDR. One of the major contributions to the local impedance are discontinues where the electron and hadron beam pipes merge. The electron pipe geometry needs to be designed so it does not block the propagation of forward moving particles resulting from collisions within a 25 mrad cone starting from the interaction point. This requirement complicates the transition between the two beam pipes. As a first attempt, the electron beam pipe with a diameter $2d = 62$ mm was grounded to the hadron pipe with a small taper angle (see Figure 3.44). Half of the taper was left open. This arrangement results in a cavity type structure between the area of the electron pipe grounding and the larger hadron beam pipe. The initial taper length was chosen to be 30 mm. The results are shown in Figure 3.24 and labeled "L=30 mm".

To reduce the cavity effect, the electron beam pipe was extended, and a horizontal slot was added on one side to provide clearance for the particle propagation to the forward detec-

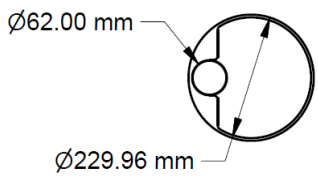

Figure 3.43: Section view of the upstream IR chamber entrance. The electron beam chamber with a 62 mm diameter.

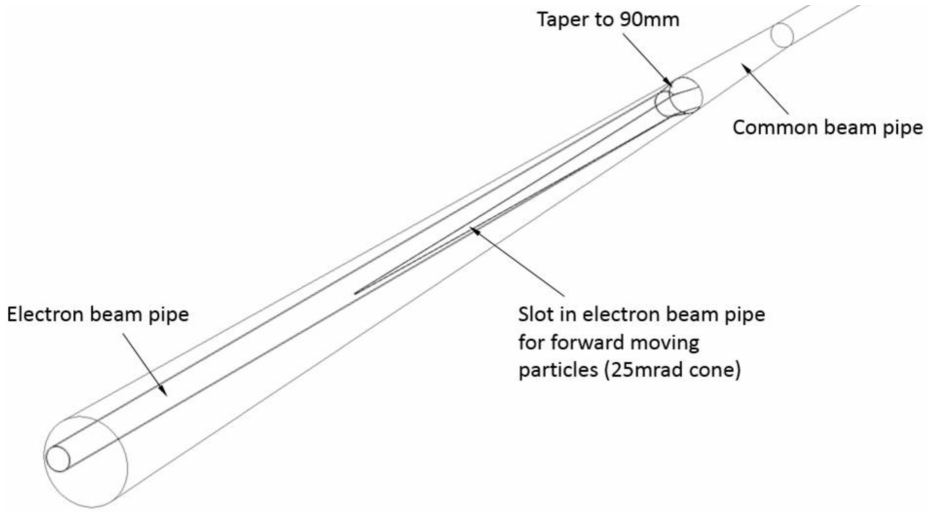

Figure 3.44: The EIC IR vacuum chamber design (version 2).

tor. The length of the taper was also increased to 90mm. These results are also shown in Figure 3.45 and are labeled "L=90 mm with slot". The longitudinal wakefield is presented in Figure 3.45a for a 0.3 mm bunch length (pseudo-Green's function). For L=90 mm, the short-range wakefield becomes inductive. Increasing the tapered transition helps to decrease the longitudinal impedance and the loss factor (Figure 3.45b and Figure 3.45d). The real part of the longitudinal impedance shows existence of the narrow-band impedance at low frequency, generated due to the horizontal slot. The imaginary part of the longitudinal impedance $ImZ_{||}$ divided by $n = \omega/\omega_0$, where $\omega_0 = 2\pi \times 78.186\,\text{kHz}$, increases slightly. The tapered transition predominantly contributes to the high-frequency impedance. The resonance modes at frequency below 2 GHz, have been eliminated by lengthening the tapered transition. However, the horizontal slot contributes to the low-frequency impedance and $(ImZ_{||}/n)_0$ and becomes slightly larger at $f \to 0$ (Figure 3.45c).

Further refinement to the main detector chamber is shown in Figure 3.46. The electron beam pipe was extended all the way to the center of the detector chamber. This approach

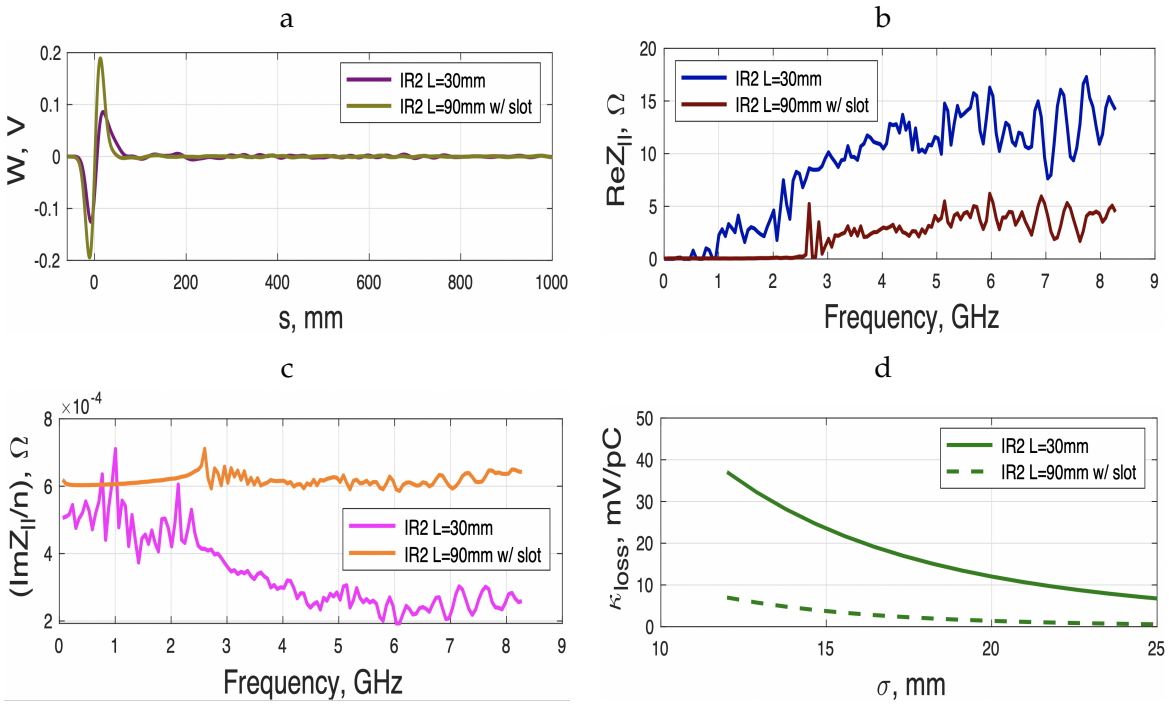

Figure 3.45: IR chamber summary results. (a) The longitudinal wakepotential simulated for a $\sigma_s = 0.3\,\text{mm}$ bunch length and 1 pC charge. (b) Real part of the longitudinal impedance up to $f = 350\,\text{GHz}$. (c) The imaginary part of the longitudinal impedance divided by $n = \omega/\omega_0$, where $\omega_0 = 2\pi \times 78.186\,\text{kHz}$. (d) The loss factor as a function of bunch length.

maintains the same diameter of the electron beam pipe and eliminates the need for a taper. An opening large enough for the forward moving collision particles is added to the side of the electron beam pipe. The summarized results are presented in Figure 3.47. The longitudinal wakefield is shown in Figure 3.47a and the real part of the longitudinal impedance is presented in Figure 3.47b. The low-frequency resonance modes around ~3 GHz have been eliminated (Figure 3.47b) since there is no cavity formed between the two beam pipes. The loss factor has also been reduced to $k_{loss} = 2.2\,\text{mV/pC}$ for a bunch length of $\sigma_s = 12\,\text{mm}$.

Using the machine parameters presented in Table 3.15 and the simulated results, the heat load due to multiple passes of the bunch train through the structure can be estimated by

$$P_{\text{loss}} = \kappa_{\text{loss}} I_{\text{av}}^2 T_0 / M, \tag{3.56}$$

where M is the number of bunches, T_0 is the revolution period, and I_{av} is the average current. Applying the expected average current $I_{av} = 2.48\,\text{A}$, number of bunches $M = 660$ and the expected revolution period T_0 =12.79 µs the total expected power loss $P_{loss} = 262\,\text{W}$. This value can be reduced even further by doubling the bunch length. For a bunch length $\sigma_s = 24\,\text{mm}$, the power loss factor drops by almost a factor of 10 to $k_{loss} = 0.2\,\text{mV/pC}$ resulting in a total power loss $P_{loss} = 30\,\text{W}$.

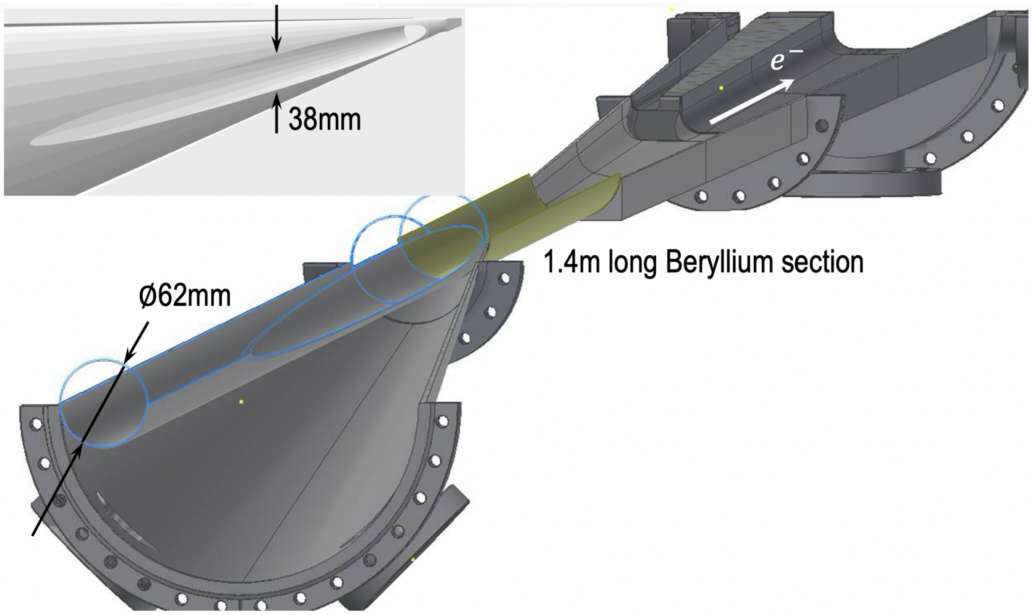

Figure 3.46: The EIC IR vacuum chamber design (version 3).

Table 3.16: List of the vacuum components contributing to the total impedance of the electron storage ring.

Object	Abbreviation	Qty	Project
Bellows	BLW	380	NSLS-II
LA BPM	LABPM	494	NSLS-II
Stripline	SL	18	NSLS-II
Gate Valve	GV	45	NSLS-II
Flange Absorber	FABS	200	NSLS-II
RF Cavity	CAV	23	NSLS-II
RF Tapered Transition	TPRDRF		NSLS-II
IR Chamber	IRCHM	1	EIC

Longitudinal Impedance Model

By passing through the vacuum chamber, the electron beam generates electromagnetic fields, which can affect the beam stability. This makes it important to determine the impedance/wakepotential for all of the vacuum components distributed around the ring. A list of preliminary vacuum components is presented in Table 3.16. The exact geometric dimensions and surface resistivity of many of the vacuum components have not been finalized yet. For a first pass analysis the wakepotential and impedances simulated for sev-

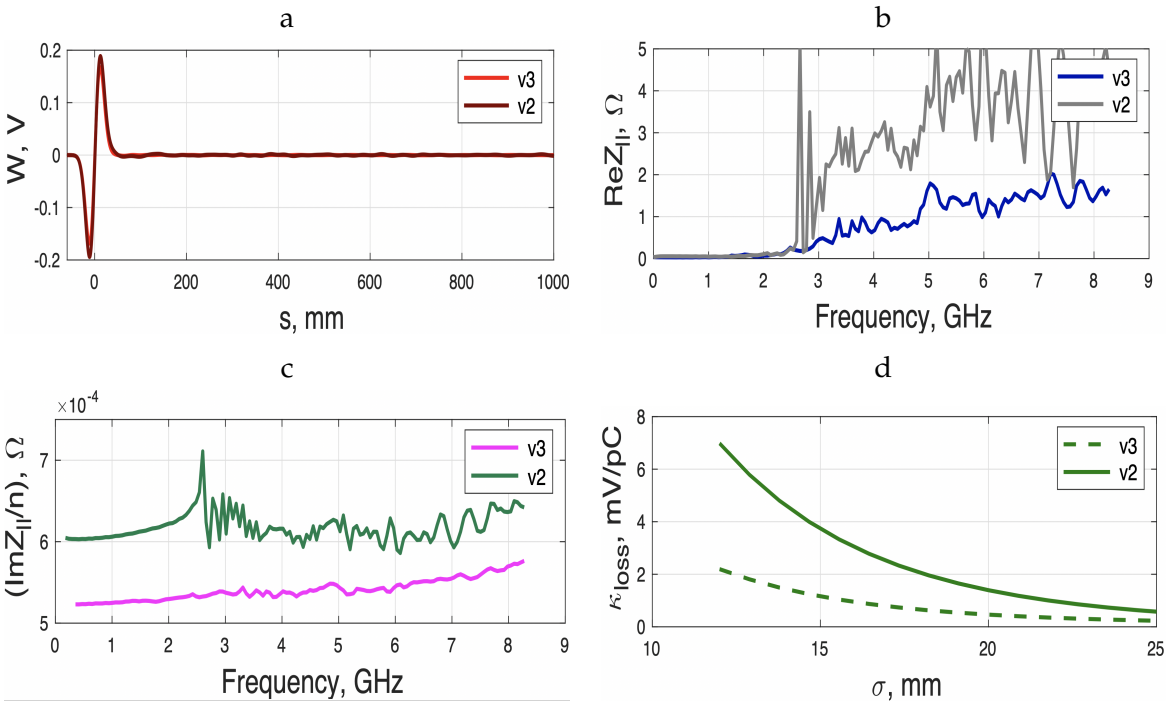

Figure 3.47: Summary results for IR chamber v3. (a) The longitudinal wakepotential simulated for a $\sigma_s = 0.3$ mm bunch length and 1 pC charge. (b) Real part of the longitudinal impedance up to f=350 GHz. (c) The imaginary part of the longitudinal impedance divided by $n = \omega/\omega_0$, where $\omega_0 = 2\pi \times 78.186$ kHz. (d) The loss factor as a function of bunch length.

eral of the NSLS-II vacuum components have been scaled using the EIC lattice parameters to study the instability thresholds. The geometric impedance due to the cross-sectional changes of the vacuum components has been calculated by the GdfidL code. Table 3.16 indicates the origin of the data which is being used for the applied wakepotential. As the storage ring geometry is finalized, updates to the simulations will be performed and used to generate the total impedance budget for particle tracking simulations and analytical evaluation. The contribution of the resistive wall to the total impedance is calculated separately by applying the analytical approach derived by Bane and Sands [111]:

$$W_{\parallel}(\tau) = \frac{r_e mc^2 N_e}{2b\sqrt{2\mu_r Z_0 \sigma_{\text{con}}}} i \left|\frac{\tau}{\sigma}\right|^{3/2} e^{-\tau^2/4\sigma^2} \times \left[I_{1/4}\left(\frac{\tau^2}{4\sigma^2}\right) - I_{-3/4}\left(\frac{\tau^2}{4\sigma^2}\right) - \text{sgn}(\tau) I_{-1/4}\left(\frac{\tau^2}{4\sigma^2}\right) + \text{sgn}(\tau) I_{3/4}\left(\frac{\tau^2}{4\sigma^2}\right)\right] \tag{3.57}$$

where b is the vacuum chamber radius, $Z_0 = 120\pi$ is the impedance of free space, σ is the electrical conductivity and μ_r is the relative permeability of the chamber surface. As a preliminary estimate for the resistive wall surface, six 257 m long arc sections and twelve

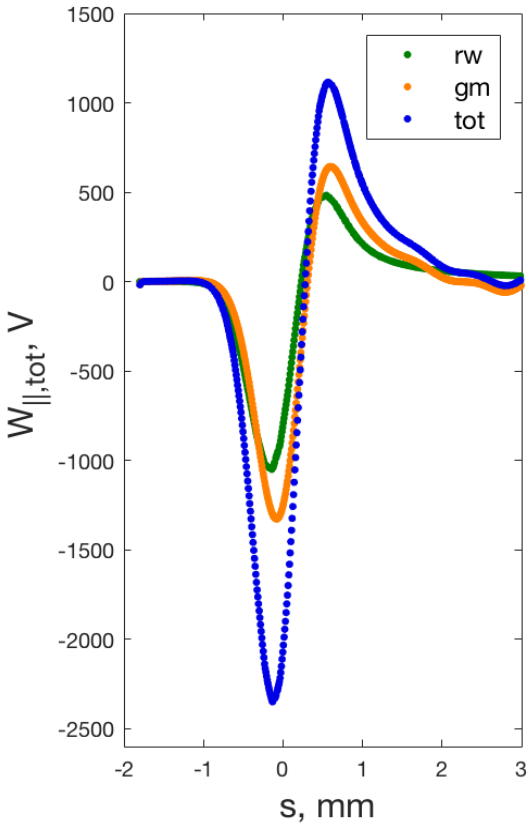

Figure 3.48: Longitudinal short-range wakepotential calculated for a bunch length of $\sigma_s = 0.3$ mm. The total longitudinal wakepotential of the EIC (blue trace) is a sum of the resistive wall contribution (green trace) calculated analytically (Equation 3.57) and the geometric wakepotentials (orange trace).

123 m long copper straight sections with a radius of 20 mm are assumed.

The total longitudinal wakepotential, which is a sum of the short-range geometric and resistive-wall longitudinal wakepotentials, is shown in Figure 3.48. The real part of the frequency spectrum of the total longitudinal impedance is presented in Figure 3.49 up to 350 GHz. The total longitudinal wakepotential $W_{\parallel,\mathrm{tot}}$ was used as an input file for the SPACE particle tracking code along with the parameters presented in Table 3.15. Numerical simulations were done using 30 million macro-particles and 800 grid points in order to accurately determine the first microwave instability threshold and to characterize the microwave dynamics. The energy spread of the unperturbed Gaussian bunch at low current is estimated at $\sigma_\delta = 5.5 \times 10^{-4}$. From this the first microwave instability threshold is observed at $I_{\mathrm{th}} = 4.5$ mA (see Figure 3.50), which is above the single bunch current of 3.8 mA. The bunch lengthening effect due to potential-well distortion (see Figure 3.50) is small enough up to 4 mA for the applied total longitudinal wakepotential.

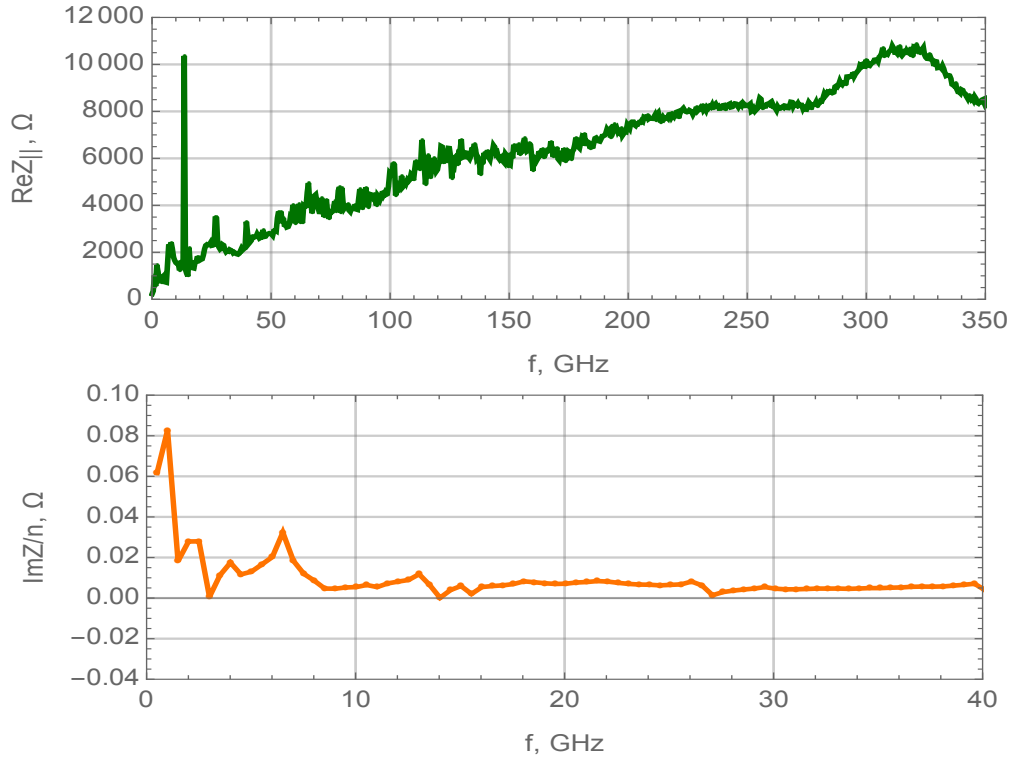

Figure 3.49: Top: Real part of the longitudinal impedance. Bottom: Imaginary part of the longitudinal impedance divided by $n = \omega/\omega_0$, where $\omega_0 = 2\pi \times 78.186\,\text{kHz}$.

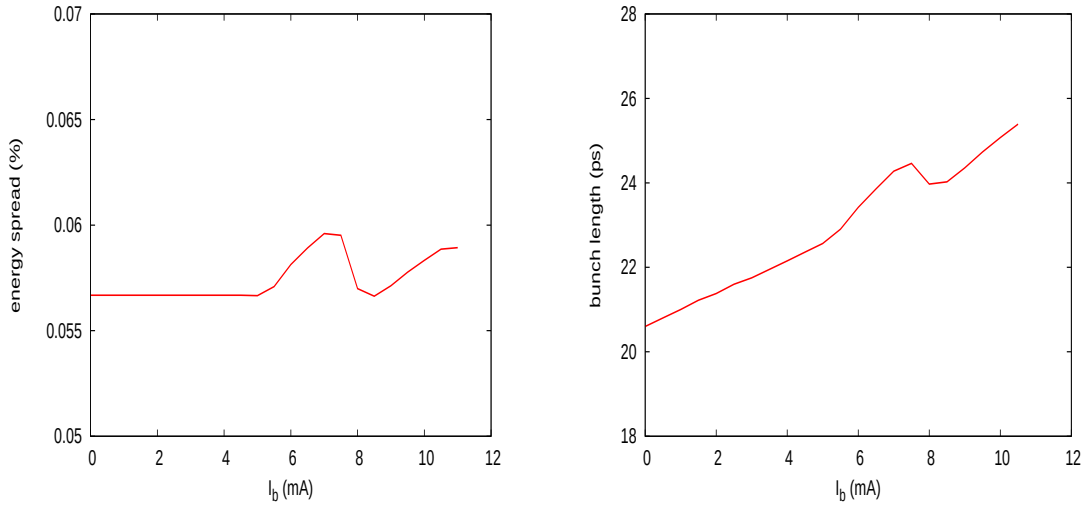

Figure 3.50: Left: Energy spread as a function of single bunch current. Right: Bunch lengthening dependence on the single-bunch current.

3.2.7 IR Synchrotron Radiation Analysis

The IR crossing angle scheme avoids the necessity of separator dipoles in or near the detector, which would generate a wide fan of hard synchrotron radiation photons. However, the nearby low-β quadrupoles generate a synchrotron radiation cone that can be equally harmful for different detector components, if not handled appropriately.

In contrast to the homogeneous fan produced by dipole magnets, the photon cone generated by quadrupoles consists of a huge number of weak photons in its center, and a comparatively small number of very high energy photons with increasing distance from the center. These high energy photons stem from electrons in the transverse tails of the beam distribution that experience strong magnetic fields at large amplitudes in these low-β quadrupoles. Additionally, since the beam-beam interaction tends to cause an overpopulation of the transverse electron beam tails, especially in the vertical plane, the number of hard photons produced in the quadrupoles by large-amplitude electrons can be significantly higher than expected for a pure Gaussian distribution. Therefore it is important to take all these factors into account when evaluating the synchrotron radiation background in the detector, and designing a masking scheme.

Nonlinear effects in the beam-beam interaction lead to the formation of non-Gaussian tails with an enhanced electron density. Figure 3.51 illustrates this for the case of the electrons +colliding with a short ($\sigma_{s,p} = 0$) proton bunch. The colliding electron beam requires about 50% larger aperture than without beam-beam interactions. The magnets and synchrotron radiation masks have to provide sufficient aperture for these tails to pass through in order to provide beam lifetimes of several hours.

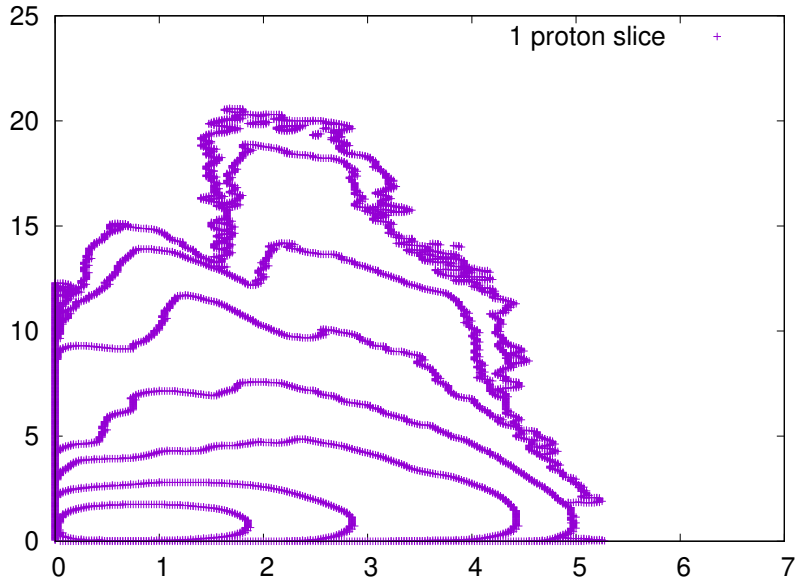

Figure 3.51: Transverse electron density distribution resulting from beam-beam interaction with a short ($\sigma_{s,p} = 0$) proton bunch. The contour lines are spaced by a factor $5.4 \approx 2e$.

However, this effect is significantly reduced due to the relatively long proton bunches, with $\sigma_{s,p} \approx \beta_{y,e}$, which results in a significant "smear" of the vertical beam-beam kick over a substantial vertical betatron phase during the interaction of any individual electron with the long proton bunches. This is illustrated in Figure 3.52 for different numbers of longitudinal slices of the proton bunch. In this simulation, the proton bunch is assumed to have a Gaussian longitudinal distribution, truncated at $3\sigma_{s,p}$, and is sliced into an odd number of slices with equal intensity. As Figure 3.52 shows, the far-reaching vertical tail observed when the proton bunch is represented by a single slice almost completely vanishes as soon as the number of slices is increased to three. Only minor differences occur when the number of slices is increased further, indicating rapid convergence.

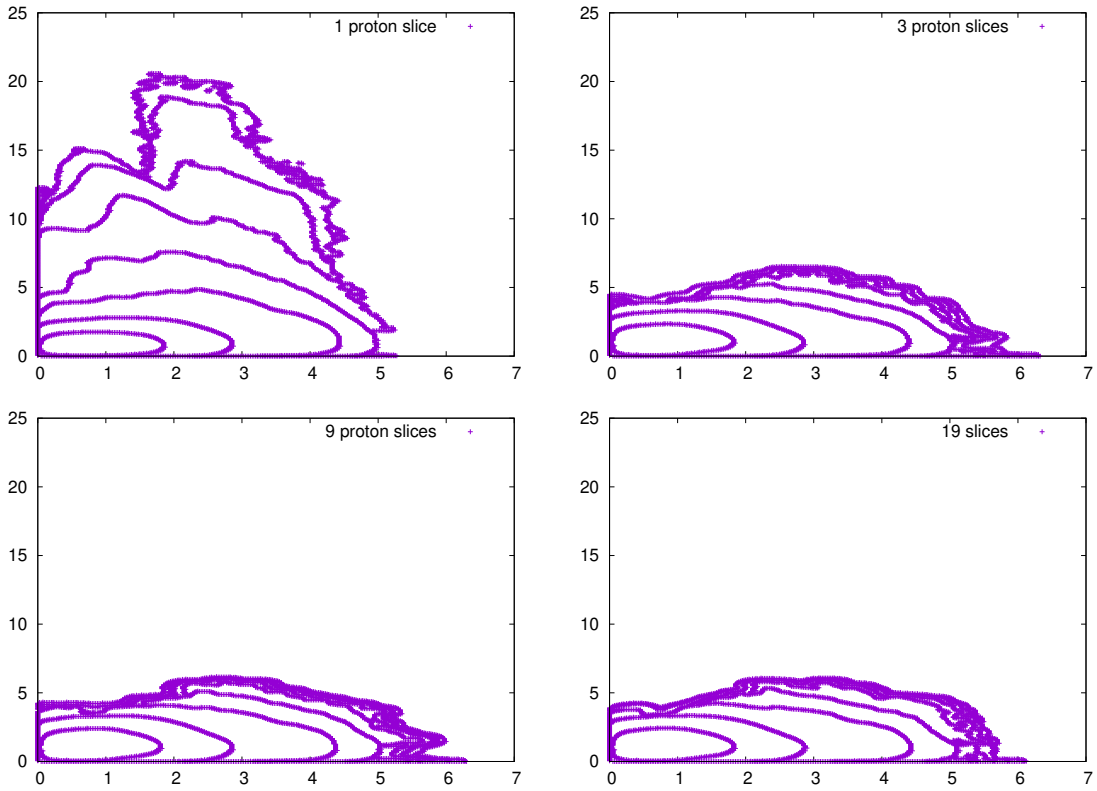

Figure 3.52: Transverse electron density distribution resulting from the beam-beam interaction with the proton bunch, for four different numbers of slices of the proton bunch — 1, 3, 9, and 19 slices. The contour lines are spaced by a factor $5.4 \approx 2e$.

The design of an EIC general purpose detector requires a machine element free region of ± 4.5 m around the IP. As a consequence, any synchrotron radiation mask that gets hit by direct radiation can only be installed outside the detector volume in the incoming electron beam direction. The aperture of those masks must be sufficiently large to ensure beam lifetimes on the order of several hours. Therefore, one expects a beam lifetime of more than 24 hours [112] with a 13σ horizontal and 23σ vertical aperture and beam-beam effects alone. Additional effects that potentially lead to generation of non-Gaussian tails, such as

lattice nonlinearities and beam-gas scattering events, need to be taken into account and are presently under study.

The first focusing element (quadrupole Q0EF) starts at a distance of 5.3 m from the IP. In order to reduce the peak magnetic fields encountered by electrons in the transverse tails, this magnet as well as the following quadrupole Q1EF are comparatively long; the length is limited by the requirement to interleave focusing elements in the hadron beam line [113]. Table 3.17 lists the design parameters of the last two quadrupoles upstream of the IP.

Table 3.17: Electron IR magnet parameters on the upstream side of the detector, for the highest design energy of 18 GeV.

Magnet	s_i [m]	l [m]	IR [cm]	B [T]	g [T/m]
Q1EF	5.00	1.2	2.2	0.309	-14.1
Q2EF	8.74	1.72	4.85	0.282	6.0

A dual stage masking scheme is what is required to limit the synchrotron radiation fan through the central detector. On the incoming side, its cross section will be identical to that of the masks before the central detector. Their size is determined by the 13σ beam size requirement at their specific location. Assuming radii of the upstream ellipse of 11 mm in the horizontal plane, and 10 mm vertically, at the downstream end of the central detector, the cone radii will have substantially increased, to 71 mm horizontally, and 19 mm vertically. This growth of the synchrotron radiation fan determines the minimum dimensions of the detector beam pipe that ensure strongly reduced background from primary photons generated by the electron beam.

In the next step, the impact of potentially backscattered photons on the detector is simulated using the code DESYNC [114].

The focusing upstream of the detector is designed to minimize the magnetic fields of the last two quadrupoles seen by electrons in the transverse tails of the beam. This is accomplished by designing quadrupoles Q1EF and Q2EF with a low gradient and an extended length. Even at the highest electron beam energy of 18 GeV this results in peak fields of only 0.3 T at the 15σ design aperture of these magnets. However, since the movable upstream mask at $s = 4.5$ m has an aperture radius of only 10σ, no electrons are present in the beam beyond this limit. Therefore, the maximum magnetic field sampled is only 2/3 of the peak field of those quadrupoles, namely $B_{\max} = 0.2$ T. The corresponding critical energy of the synchrotron radiation generated by the small number of electrons at the outer edges of the beam is therefore reduced to

$$\begin{aligned} E_c &= \frac{3}{2}\frac{\hbar c^2 e E^2 B}{E_0^3} \\ &= 43.2\,\text{keV}, \end{aligned} \tag{3.58}$$

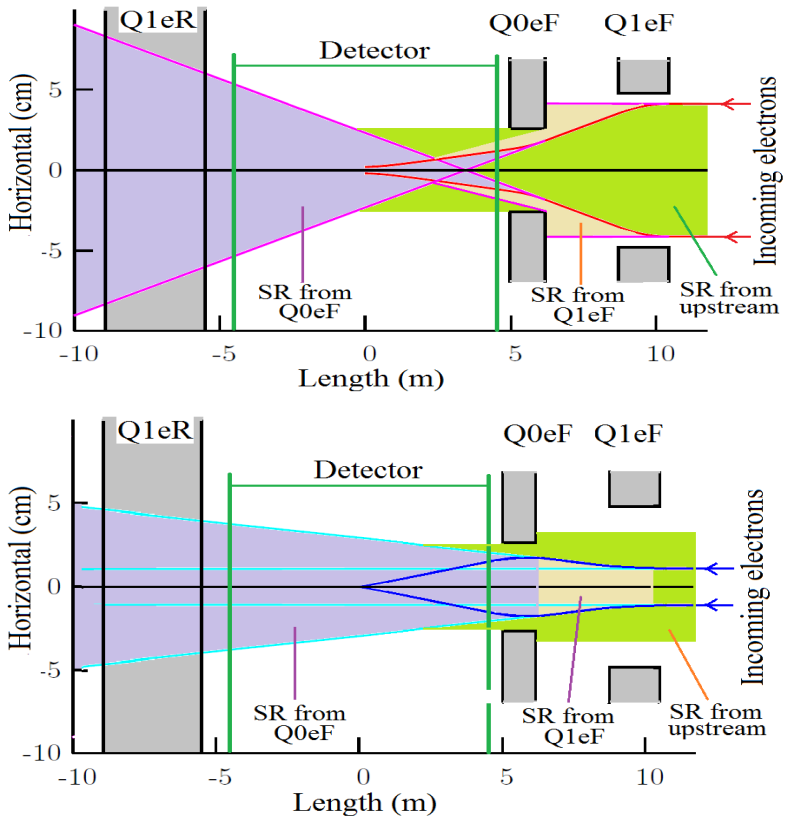

Figure 3.53: Synchrotron radiation fans from the low-β quadrupole doublet through the IR. Top: top view; Bottom: side view.

at 18 GeV, or $E_c = 13.3$ keV at $E = 10$ GeV. Here $E_0 = m_e c^2$ is the electron energy at rest.

Photon scattering in the IR geometry described above has been simulated with the code DESYNC [114]. Assuming a detector beam pipe that is tailored to accommodate the primary synchrotron radiation fan according to Figure 3.53, the radiation load outside the 1 mm thick beryllium detector pipe reaches a maximum of 2.2 rad/hour at 18 GeV in the 1 m long section right after the mask, and less than a µrad/hour everywhere else throughout the central detector. At a beam energy of 10 GeV the maximum rate reduces by 2–3 orders of magnitude.

While these radiation levels are likely acceptable more detailed simulations including the actual EIC detector are required. These simulations are beyond the capabilities of DESYNC and will therefore be carried out using a simulation code such as Geant4 [115].

The test particle Monte Carlo code SynRad, developed at CERN, has been used to determine the synchrotron radiation flux distribution in the interaction region due to the upstream dipole and last two quadrupoles. This code was used with an electron beam energy of 18 GeV and a beam current of 260 mA, ten percent of which is distributed in tails as described earlier. The SynRad output has been used as input in two separate studies: the detector backgrounds expected due to photon flux on the beampipe, and interaction

region vacuum studies as a function of beam dose.

For the detector occupancy studies, SynRad was used to generate photon trajectories and energies for photons likely to hit the beamline in the vicinity of the interaction region. To enhance the efficiency of this simulation, transparent planes were generated at a radius of 2.92 cm, 97 percent of the inside diameter of the Be central pipe. These test facets extended from 3.3 m upstream of the IR to -4 m downstream of the IR. Most photons that are incident on these test facets are traveling in a trajectory where they will intersect the wall and cause detector background.

The detector background studies were performed for several configuration: the March optics, the May optics with the final photon absorber at 390 cm, and the May optics with the final photon absorber at 350 cm. The photon data was input into full Geant based detector simulation to generate expected detector backgrounds for all scenarios.

In addition, an independent program (called SYNC_BKG) used to study SR backgrounds developed at SLAC has also been applied to the EIC IR design. This program and has been used to study SR backgrounds for the SLAC B-Factory, the KEK B-factory, the SuperKEKB current B-factory, the FCC-ee design [116, 117], the CEPC design, the ILC and the JLEIC design. The Programs (SynRad and SYNC_BKG) are in very good agreement. The total power numbers are in very close agreement and the total number of photons incident on a given surface also agree.

SYNC_BKG is derived from a program developed in the 1980s by Al Clark called QSRAD. The program was originally built to study a Gaussian beam going through final focus magnets for colliders. SYNC_BKG has included in it the ability to introduce a non-Gaussian beam tail that is described as a lower and wider Gaussian and the ability to accept bend magnets. SYNC_BKG performs a grid integration of the transverse beam profile using weighted macroparticles at each grid point and tally up the photon hit rate and energy spectrum on selected beam pipe apertures that are used to model the IR beam pipe. The SR background study of the IR has pointed out the importance of the non-Gaussian beam tail distribution. This non-Gaussian distribution has several sources. Initially, when the accelerator is in the commissioning phase, the beam tail distribution is dominated by beam-gas interactions from around the entire ring (primarily Bremsstrahlung and Coulomb scattering). In this stage, the beam-beam effects mentioned above are not yet prominent as the luminosity and bunch currents are still low. As the accelerator collects more running time and the number of A-hrs increases, the beam pipe outgassing from SR begins to decrease and this reduces the beam-gas interactions. Then the beam-beam effects become a noticeable generator of non-Gaussian beam tail particles as well as other bunch related interactions (i.e. Touschek scattering, Inter-Beam Scattering) and even the effects of luminosity in the form of radiative Bhabha scattering. All of these effects populate the non-Gaussian beam tail distribution and this quasi-stable distribution controls how close collimators settings can be before the beam lifetime becomes too short.

A very preliminary study of beam tail distributions indicate that the IR design as described should have acceptable background levels in the detector from SR at 18 GeV with electron non-Gaussian beam tails that have approximately a 1–2 hour beam lifetime. This lifetime

is defined by collimator settings that are placed at or near the Beam-Stay-Clear envelope. This includes back-scatter estimates from the IP face of the rear electron magnets as well as a preliminary calculation of the back-scatter rate from the beginning of the high-power SR surface located about 19 m downstream of the IP. A much more thorough study of the SR background for the detector is needed both at this energy of 18 GeV as well as at the beam energy of 10 GeV where the beam current is 10 times higher. This also includes a study of the SR background that will hit the very low Q^2 detectors foreseen to be near the beam in the downstream beam pipe. In addition, we have been and will continue to study the background experience of SuperKEKB as the accelerator is presently going through a startup and commissioning phase and is trying to take data at the same time. The background team of Belle II and SuperKEKB have done an enormous amount of work to classify and understand all of the background sources to date [118]. We will continue to draw on the experience gained by the SuperKEKB background team.

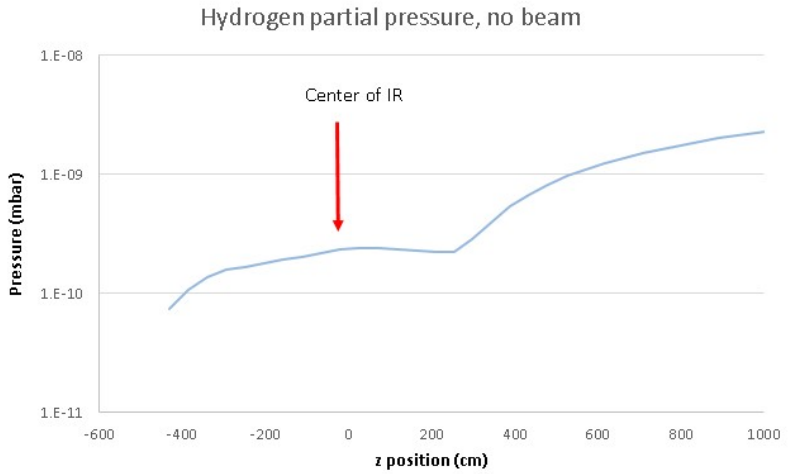

Figure 3.54: Molflow+ simulation of pressure distribution in the IR with no beam.

Molflow+ is a complementary code to SynRad, and can use the photon flux on each facet of a model in conjunction with experimental flux per dose rates measured from common vacuum materials to predict the pressure distribution in a system as a function of AmpHours. The pressure distribution for the interaction region vacuum system was first calculated in Molflow+ using the geometry shown in the next section, using an out-gassing rate of 1×10^{-12} mbar-L/scm^2, and the pump speed and geometry as shown in Figure 3.54. For this first iteration, water vapor outgassing was not considered, and the electron beam is traveling in the -z direction in these simulations. The calculated pressure distribution for the system without beam yields an interaction region pressure in the 10^{-10} mbar range.

To calculate the pressure that is expected with electron beam in the region, the output for the flux on each facet, as calculated by SynRad, can be imported into Molflow. Molflow then will use this photon flux and a library of Photon Stimulated Desorption (PSD) yield vs. beam dose. For hydrogen desorption from aluminum, the PSD rate starts at 0.01 hydrogen molecules desorbed per incident photon until a dose of 4×10^{-18} photons/cm^2, then

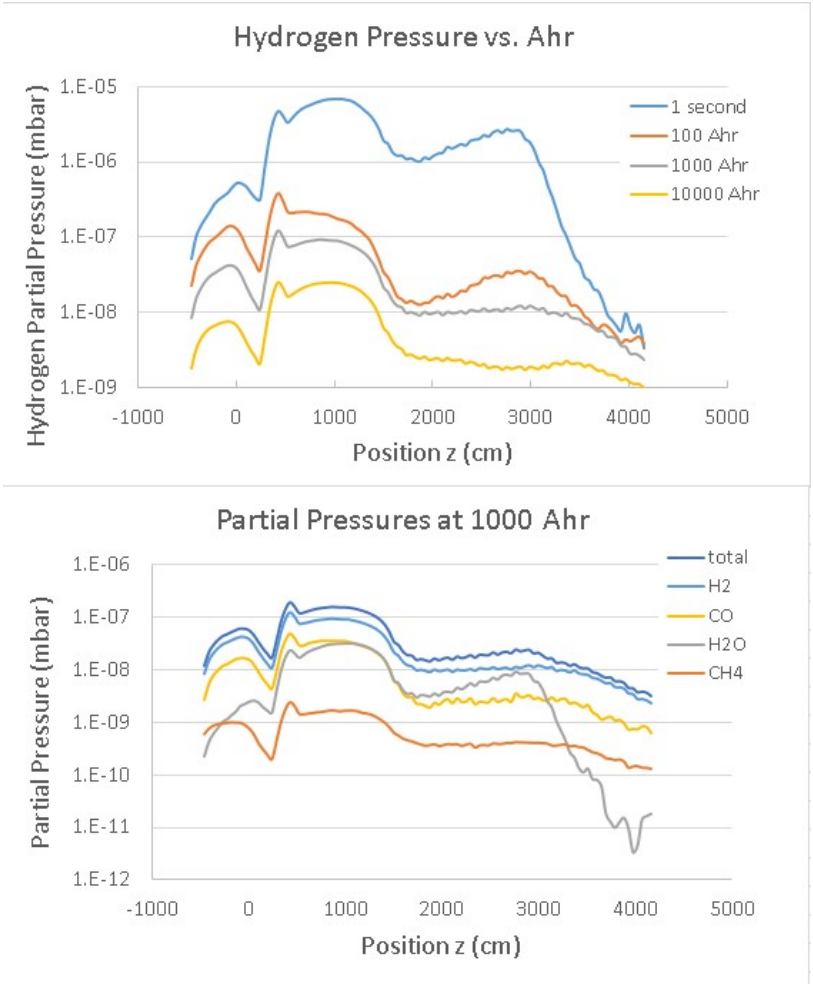

Figure 3.55: top: Pressure evolution vs. conditioning time in AmpHours for hydrogen. bottom: The expected gas composition for a conditioning time of 1000 Ahr.

falls in a power law distribution with time. Molflow will use the dose per facet to calculate PSD induced outgassing on each facet of the model, and determine pressure distributions. In addition to hydrogen, the partial pressures of H2O, CH4 and CO can be calculated for the system.

The results of these coupled SynRad and Molflow+ simulations are shown in Figure 3.55. In all cases, the May geometry has been used, and combination NEG-ion pumps are in the model at the ends of the interaction region as shown in CAD layouts. In addition, a series of smaller NEG-ion pumps distributed along the incoming electron beamline to provide pumping between the final electron dipole before the IR where there is a significant synchrotron radiation load. The hydrogen partial pressure vs. dose is shown in the top graph, and the gas composition at 1000 Ahr is shown in the bottom graph.

3.3 Hadron Storage Ring Design

The hadron beams, heavy ions as well as polarized protons and ^{3}He, will be accelerated and stored in the Hadron Storage Ring which is Yellow ring of present RHIC. The beam in HSR will travel in the counter-clockwise direction, as in present Yellow ring. Here the modifications to the existing RHIC superconducting rings necessary to accommodate requirements for the EIC are listed:

- Raising maximum proton operation energy from 255 to 275 GeV.
- Adding four additional Siberian Snakes to ensure He3 polarization
- Using 12–2 inner arc in order to match electron and hadron revolution frequencies at 41 GeV per nucleon hadron energy.
- New interaction region for electron-hadron collisions.
- Realizing new injection system at 4 o'clock area.
- Using 6–4 inner arc for transferring hadron beam from AtR to the 4 o'clock injection area
- Beam screen for the reused RHIC superconducting magnet beam pipes (see Section 6.4.4).
- Modifications of RF system including a number of new cavities (see Section 6.5.1).
- Upgrading beam instrumentation for high hadron current

3.3.1 Hadron Storage Ring Beam Energy Increase to 275 GeV

The proton beam energy of the present RHIC facility is limited to about 260 GeV by the quench limit of the DX separator dipoles in the interaction regions. However, those dipoles will no longer be needed in EIC, which will allow us to raise the proton beam energy to 275 GeV. The DX magnets are installed in separate cryostats, their removal does not affect the triplet and D0 magnets of both the Yellow and Blue superconducting rings which are placed in a single very large cryostat. The DX magnet superconducting cables and cryostat connections are connected only to the Blue ring.

The D0 magnet design current and magnetic field are $I_{\text{design}} \sim 5\,\text{kA}$ and 3.52 T, respectively. The present operating bending angle of the D0 dipole is $\theta_{\text{D0}} = 15.19\,\text{mrad}$, with an arc length $l_{\text{D0}} = -3.589\,\text{m}$. The present layout of the triplet with the D0 and DX is shown in Figure 3.56.

If the DX magnet is removed, the two D0 magnets need to be connected with a straight warm vacuum beam pipe between the two warm section vacuum valves, as shown in Figure 3.57 for the case of IR4 and IR10 where beam goes from outer to inner ring. The

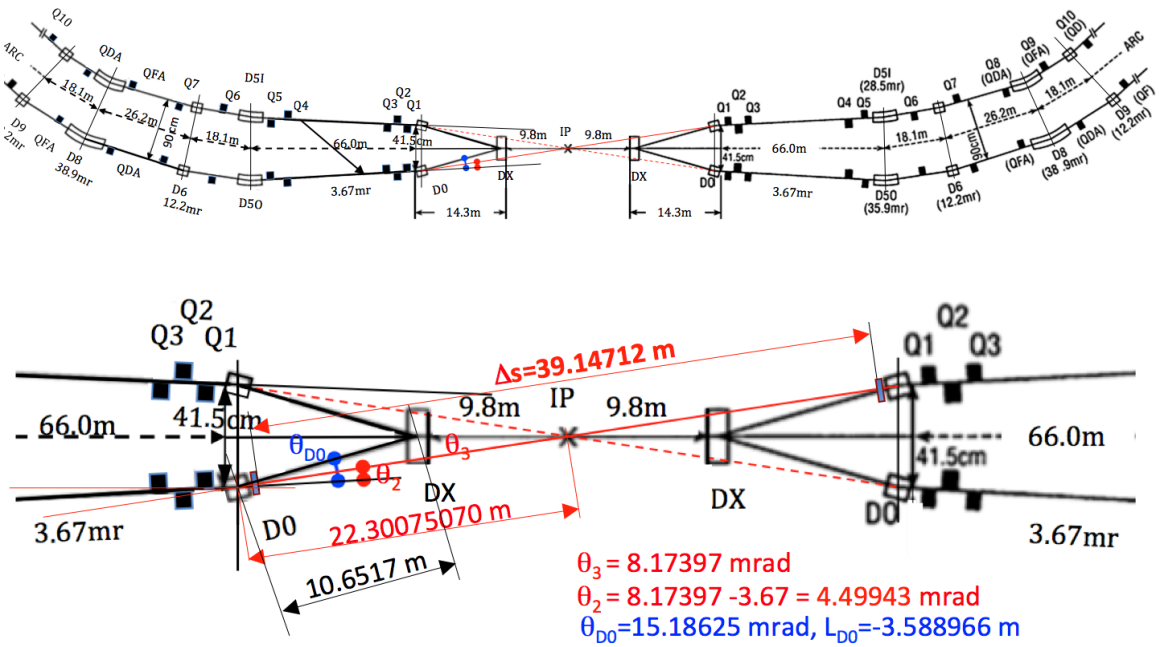

Figure 3.56: Present interaction region with the DX magnets.

required new D0 bending angle is $\theta_{\mathrm{D0-new}} = 4.5\,\mathrm{mrad}$. The D0 is a sector bending magnet with a sagitta of $S_{\mathrm{D0}} = 6.83\,\mathrm{mm}$. In the EIC layout the D0 bending angle is only 1/3 of the original one. Re-positioning one end of the magnet by $\Delta x = 1.8\,\mathrm{cm}$ away from the central IP line is required. This changes the path length per straight section by $\Delta s = 1.69\,\mathrm{mm}$, for a total of $\Delta s_{\mathrm{tot}} = 5 \cdot 1.69\,\mathrm{mm} = 8.45\,\mathrm{mm}$.

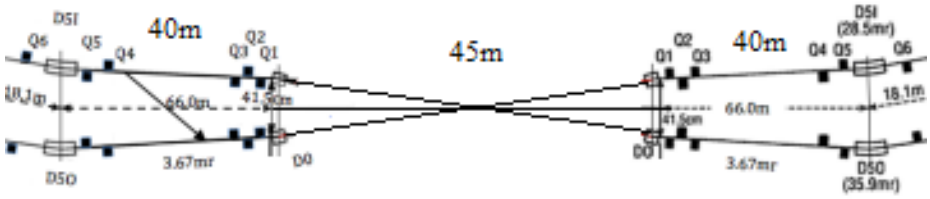

Figure 3.57: The schematic of IR4 and IR10 with DX magnets removed.

With DX magnets removed at IR12, the D0 magnets bend the beam in the opposite direction so it goes from outer ring to out ring as shown in Figure 3.58. The required new D0 bending angle is $\theta_{\mathrm{D0-new}} = 3.67\,\mathrm{mrad}$., which is 1/5 of the original one. Re-positioning one end of the magnet by $\Delta x = 3.38\,\mathrm{cm}$ away from the central IP line is required.

The aperture of D0 magnets are enough for both scenarios with proper re-positioning of the end based on the expected beam trajectories. The beam trajectories in D0 magnets for current RHIC, modified IR4/IR10 and IR12 for EIC HSR are shown in Figure 3.59. The

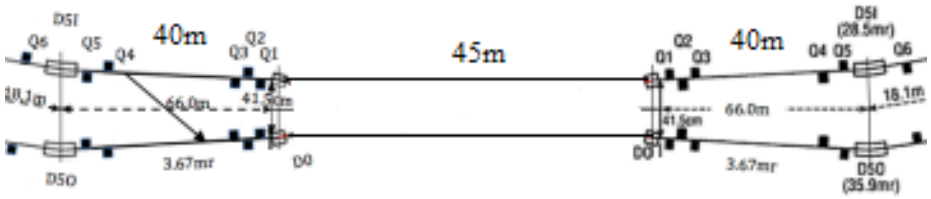

Figure 3.58: The schematic of IR12 with DX magnets removed.

large angle is for current RHIC setup, the medium angle is for IR4/IR10 in HSR where beam goes from inner to outer or outer to inner ring, and the small is for IR12 in HSR where beam goes from outer to outer ring. The difference of the trajectories in the middle point of the magnet is ∼8.5 mm which is relatively small compared to the beam pipe diameter of 85 mm.

The operating current of the D0 magnet must be reduced to $\sim 1/3$ of the present one. The power supply schematic for the D0 magnets in the Yellow ring is shown in Figure 3.60. The power supply PS1 is a shunt supply with a range of 2 kA. The current of the D0 magnet in the present RHIC configuration is the sum of the main dipole bus and the corresponding shunt power supply PS1, supplies the two D0 magnets on opposite sides of the IP.

The excitation current for the D0 magnet in the EIC configuration can be provided by the PS1 power supply alone. This requires a change of the superconducting cold bus cables, namely connections in the interconnects inside of the cryostat as shown in Figure 3.61. Some reconnections in the valve box are required for these new D0 operating condition.

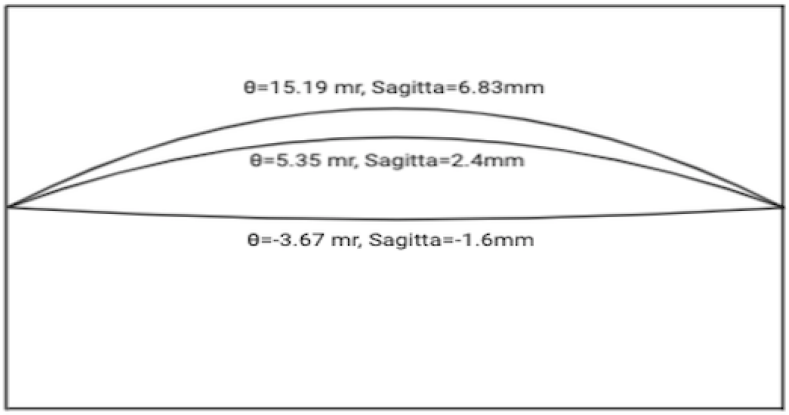

Figure 3.59: The beam trajectories in D0 magnets for current RHIC, modified IR4/IR10 and IR12 for EIC HSR.

At 275 GeV the main dipole and quadrupole power supply will operate very close to their limit (they are both rated at 5500 A). Further evaluation would show if these power supplies need upgrade.The detailed lattice of straight sections of the hadron ring will also

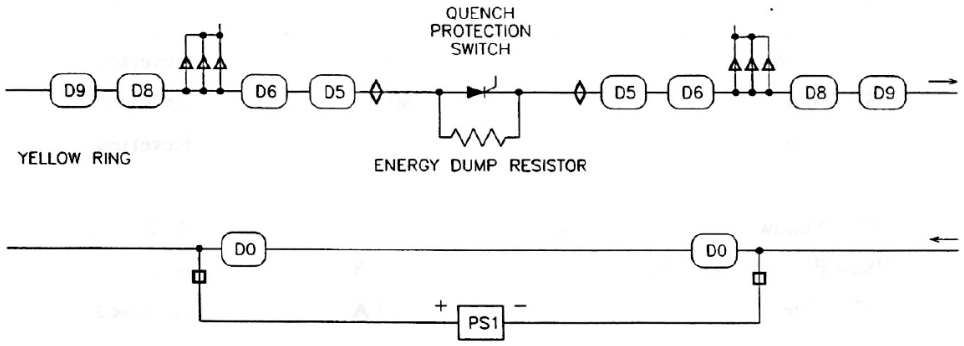

Figure 3.60: Yellow ring D0 power supply diagram.

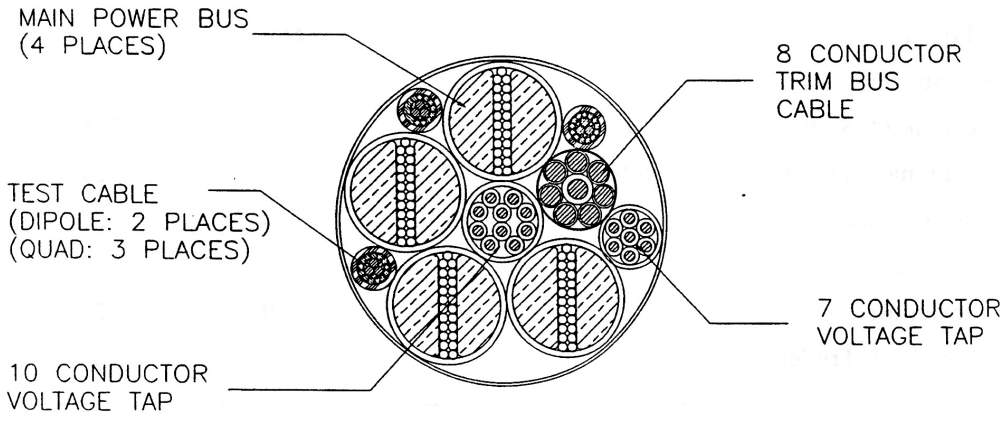

Figure 3.61: Cold crossing bus.

tell us if some of the straight section quadrupole feed-throughs would need upgrade for higher current.

3.3.2 Synchronization of Hadron-Electron Collisions

Electrons and hadrons in the ESR and HSR must circulate their respective storage rings with the same revolution period

$$\tau_{\text{hadron}} = \tau_{\text{electron}} \approx 12.8\,\mu s \tag{3.59}$$

during storage, to maximize luminosity and to avoid deleterious beam-beam effects. The electron beam is highly relativistic over the entire EIC energy range from 5 to 18 GeV, so the electron revolution period is practically constant, except for the modest circumference

shortening that occurs, by as much as about 8 mm, when super-bends are used to enhance synchrotron radiation at 5 GeV.

In contrast, the hadron relativistic speed β varies significantly over the proton energy range 100 GeV$< E <\sim$275 GeV, with

$$\beta \;=\; \sqrt{1-(m_p c^2/E)^2}$$

where $m_p = 0.9383$ GeV/c^2 is the rest mass of the proton. The design orbit circumference must be

$$C \;=\; \beta C_1 \;=\; C_0 + \Delta C \tag{3.60}$$

where C_1 is the ultra-relativistic circumference and $C_0 = 3833.824$ m is the on-axis reference circumference at a mid-range energy of about 133 GeV. The circumference is adjusted in one or both of two ways, depending on the energy:

- 100 GeV$< E <\sim$275 GeV: A radial shift is induced in all 6 arcs, 3 inner and 3 outer.
- E = 41 GeV: Protons (or ions with the same speed) pass on-axis through 4 inner and 2 outer arcs.

Table 3.18: Circumference offsets and average radial shifts for protons at different energies. The very large circumference reduction required in the low energy scenario is achieved by passing hadrons through 4 inner and 2 outer arcs.

$E_{\rm tot}$ [GeV]	γ	$1-\beta$ [10^{-3}]	C [m]	ΔC [mm]	$\langle \Delta R \rangle$ [mm]
41.0	43.70	0.26189	3832.9153	-908.7	–
100	106.58	0.04402	3833.7506	-73.4	-11.7
133	141.75	0.02488	3833.8240	0.0	0.0
275	293.09	0.00582	3833.8971	73.1	11.6

In high-energy operation with a radial shift of ΔR in 3 inner and 3 outer arcs, the total additional circumference is

$$\Delta C \;=\; \int_0^C \frac{\Delta R(s)}{\rho}\, ds \;=\; \int_0^{2\pi} \Delta R\; d\theta \tag{3.61}$$

where the local bending strength $1/\rho$ is zero except in dipoles. The average radial offset therefore spans a range of

$$-11.7\,[\text{mm}] \;<\; \langle \Delta R \rangle \;=\; \Delta C/2\pi \;<\; 11.7\,[\text{mm}] \tag{3.62}$$

Table 3.18 and 3.19 lists the design orbit circumferences C across the high-energy range

and at the on-axis low energy value of 41 GeV for protons, and 40.7 GeV/u for gold ions, respectively.

Table 3.19: Circumference offsets and average radial shifts for gold ions at different energies. The very large circumference reduction required in the low energy scenario is achieved by passing hadrons through 4 inner and 2 outer arcs.

E_{tot} [GeV/u]	γ	$1-\beta$ [10^{-3}]	C [m]	ΔC [mm]	$\langle \Delta R \rangle$ [mm]
40.7	43.70	0.26189	3832.9154	-908.7	–
110	118.09	0.03586	3833.7819	-42.1	-6.7

Beam Screen Aperture Constraints

The HSR vacuum beampipe is fitted with a copper beam screen liner coated with a thin film of amorphous carbon, in order to reduce the cryogenic heat load to an average of less than 0.5 W/m in the arc dipoles. The resistive wall effect dominates the electron cloud effect in limiting the maximum practical radial shift, if the Secondary Emission Yield is about 1.0 or less. Quadrupoles and sextupoles are of relatively minor interest for resistive wall heat load considerations, because the arc dipoles occupy most of the HSR circumference. Figure 3.62 shows how the resistive wall heat load increases as a function of the local radial shift in an arc dipole. The heat load is concentrated in the mid-plane where heat conduction to the helium coolant is less than optimum. A radial shift of 20 mm is estimated to enhance the mid-plane heat load by a factor of 13.4 over the average around the perimeter. The total heat load will be about 0.37 W/m in the best case scenario, with high RRR copper at a maximum temperature of 10 K or cooler.

Simulations confirm that sextupoles suffer the worst cryogenic head load from electron cloud. Electron cloud formation can be suppressed by applying amorphous carbon to the beam screen surface with an SEY of less than about 1.0. All the beam screens will be coated with low-SEY amorphous carbon.

Radial offsets as large as 14 mm in quadrupoles do not increase the cryogenic load through electron cloud heating, which is further ameliorated when the amorphous carbon surface has an SEY of less than $\sim$1.0.

The radially shifted closed orbit needs to be smooth and well-matched in the arcs, carefully avoiding peak displacements of more than about 20 mm.

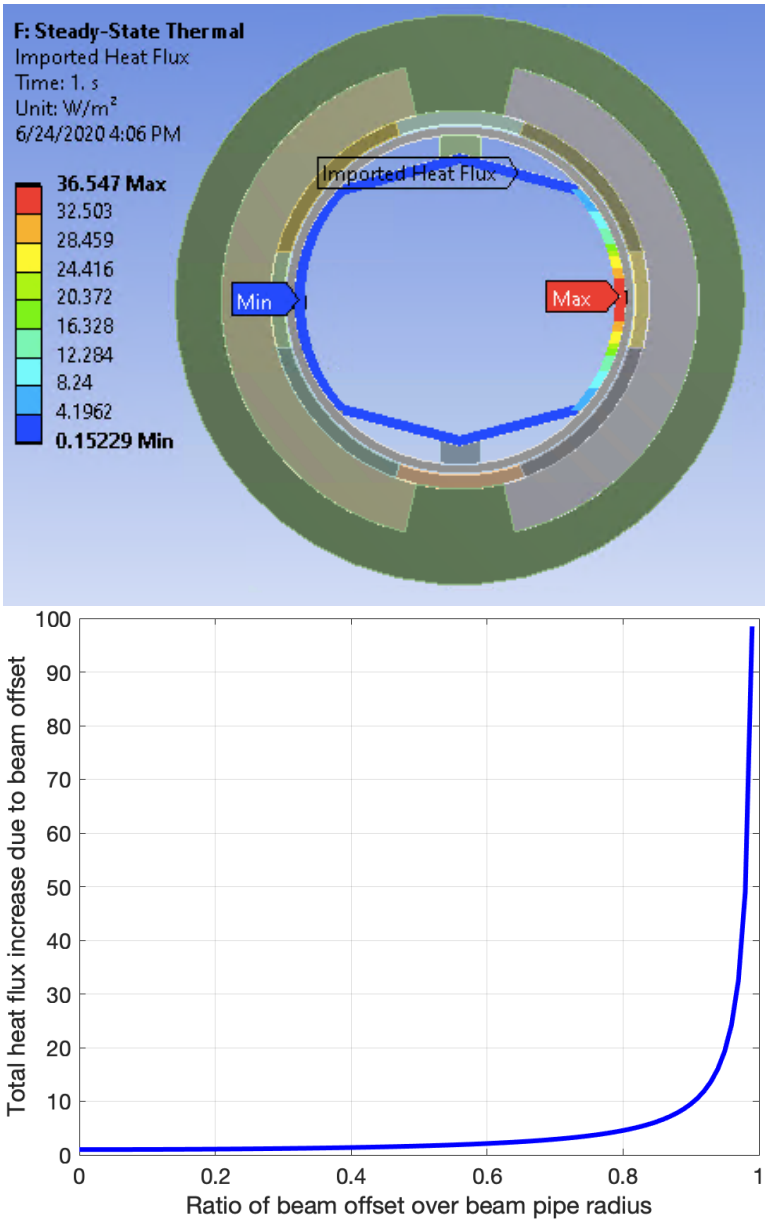

Figure 3.62: Top: resistive-wall heat flux distribution around the perimeter of polygonal beam screen for off-centered beam. Bottom: total heat flux on the beam screen as a function of the beam offset (arbitrary units). The flux increases quickly for offsets of more than about 20 mm.

The Off-field Parameter δ_B and the Geometric Compaction Factor α_B

In all 6 arcs the main dipole strength is adjusted by the *off-field parameter*

$$\delta_B \equiv \frac{\Delta B}{B} = \frac{\Delta(B\rho)}{(B\rho)} \tag{3.63}$$

that also measures the mismatch of beam and arc dipole rigidities. The goal off-axis closed orbit in the body of an arc has a radial offset of

$$x(s) \;=\; -D_{\text{matched}}(s) \cdot \delta_B \tag{3.64}$$

where D_{matched} is the dispersion function of a series of matched arc FODO cells, because this minimizes the maximum value of $|x|$ in an arc and makes the best use of the physical aperture. An ideal off-axis closed orbit is generated even when the arc dispersion itself is *not* perfect, by properly launching and capturing it at the beginning and end of each arc.

In the simple approximation that all dipoles (including those between the arcs and in the dispersion suppressors) have the same δ_B, then

$$\Delta C \;=\; -\delta_B \int_0^{2\pi} D\, d\theta \;=\; -\alpha_{B,\max}\, \delta_B \tag{3.65}$$

where the maximum geometric compaction factor is

$$\alpha_{B,\max} \;=\; \frac{C_0}{\gamma_T^2} \;=\; 7.18\ [\text{m}] \tag{3.66}$$

and $\gamma_T = 23.12$ is the transition gamma. In practice the geometric compaction factor

$$\alpha_B \;=\; -\frac{\Delta C}{\delta_B} \tag{3.67}$$

is somewhat smaller than the maximum, because the closed orbit offset x is zero or small in some dipoles between the arcs. It is maximized by the judicious selection of the 4 (or more) dipole correctors in each arc that launch and capture the off-axis closed orbits.

Figure 3.63 shows how 2 typical alternative sets of dipole correctors – "inner" and "outer" – span 10 or 12 FODO cells in each arc. The "outer" set extends into the partial dispersion suppressors at the interface to the neighboring straights. In the case shown ($\delta_B = -.010$) the extreme radial shift of the closed orbit is about $x_{\text{extreme}} = 18\,\text{mm}$.

Figure 3.64 shows how ΔC depends on the independent parameter δ_B. The outer set is more efficient at generating ΔC, due to the additional 2 FODO cells per arc. Similarly, Figure 3.65 shows the correlation of the circumference change ΔC and the extreme radial offset x_{extreme}.

Table 3.20 shows the geometric compaction factor for each set, and its theoretical maximum, along with the off-field parameter range

$$\frac{\Delta C_{\text{min}}}{\alpha_B} \;<\; \delta_B \;<\; \frac{\Delta C_{\text{max}}}{\alpha_B} \tag{3.68}$$

that is required to change the circumference by $\Delta C = \pm 73.2\,\text{mm}$.

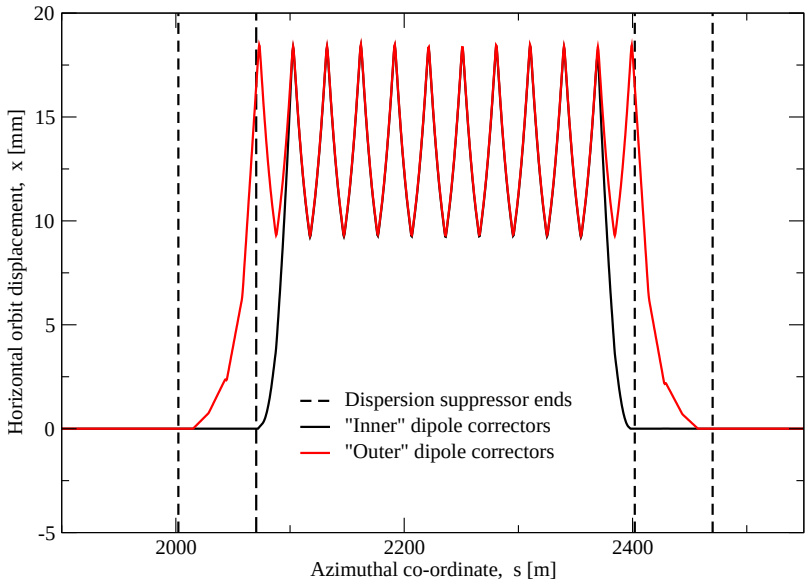

Figure 3.63: The ranges of the 'inner" and "outer" sets of dipole correctors that were studied, with $\delta_B = -0.010$ in a typical HSR arc. The "outer" range is slightly broader, and so is somewhat more efficient in changing the nominal particle circumference.

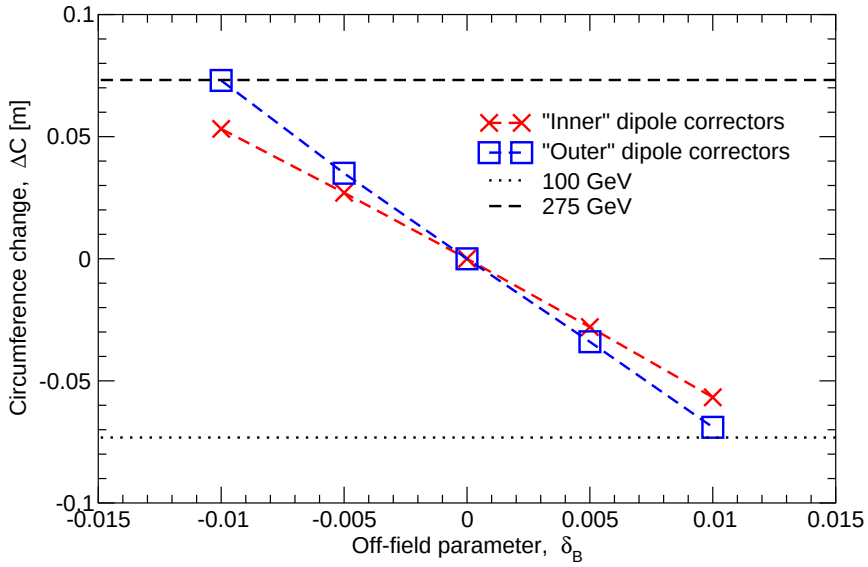

Figure 3.64: The dependence of the change in circumference ΔC on the independent off-field parameter δ_B for two different dipole corrector sets – "inner' and "outer".

Launching and Capturing Off-axis Closed Orbits

The design closed orbit is on-axis in the 6 straights and interaction regions between the arcs. Beam is centered in the experiments, crab cavities, radio frequency systems, et cetera, in spite of the presence of a small number of bending dipoles, and in locations where the

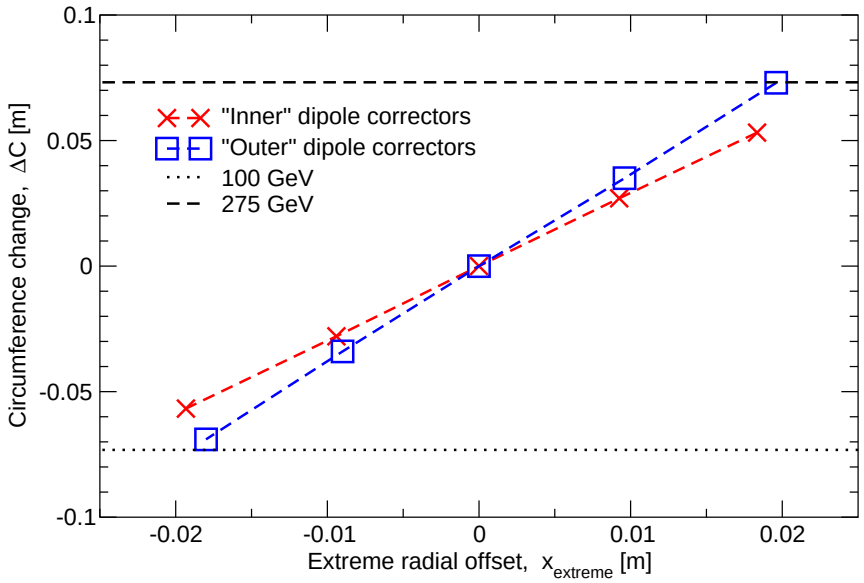

Figure 3.65: The dependence of the change in circumference ΔC on the extreme closed orbit offset for the "inner" and "outer" dipole corrector sets.

Table 3.20: Geometric compaction factor and the off-field parameter range required to make $\Delta C = \pm 73.2\,\text{mm}$, for the "inner" and "outer" dipole corrector sets, and in the ideal case.

Name of Dipole Corrector Set	Geometric Compaction Factor α_B [m]	Off-field Parameter Range $\delta_{B,\text{min}}$	$\delta_{B,\text{max}}$
Inner	5.50	-0.0133	0.0133
Outer	7.10	-0.0103	0.0103
Ideal	7.18	-0.0102	0.0102

dispersion is non-zero. The few dipoles in the interaction regions and utility straights have fields that are matched to the rigidity of the beam.

In contrast, the design closed orbit is off-axis with

$$\begin{pmatrix} x \\ x' \end{pmatrix}_{\text{arc}} = -\begin{pmatrix} D \\ D' \end{pmatrix}_{\text{matched}} \delta_B \tag{3.69}$$

in all 6 arcs. Two dipole correctors in each of the 12 arc-IR and arc-straight interfaces match the on-axis and off-axis orbits, with strengths that depend on the optical functions at their locations. The strengths would be zero if

$$\begin{pmatrix} D \\ D' \end{pmatrix}_{\text{dipole corrector}} = \begin{pmatrix} 0 \\ 0 \end{pmatrix} \tag{3.70}$$

at the correctors – if they were placed outside a full dispersion suppressor at the end of the arc. Their strengths are reduced significantly at locations outside a partial dispersion suppressor.

Table 3.21: The "inner" set of dipole correctors used for off-axis studies.

Sector	Dipole Corrector Name			
Numbers	1	2	3	4
12-1	YO1_TH10	YO1_TH12	YO12_TH12	YO12_TH10
2-3	BO3_TH10	BO3_TH12	BO2_TH12	BO2_TH10
4-5	BI5_TH11	BI5_TH13	BI4_TH13	BI4_TH11
6-7	YI7_TH11	YI7_TH13	YI6_TH13	YI6_TH11
8-9	BI9_TH11	BI9_TH13	BI8_TH13	BI8_TH11
10-11	BO11_TH10	BO11_TH12	BO10_TH12	BO10_TH10

Table 3.21 lists the "inner" set of dipole correctors used in the study of off-axis optical performance reported below [119–121]. Figure 3.66 shows that the currents required to power them are all within the range of ± 70 A, the quench-test acceptance minimum for all dipole correctors. However, most RHIC dipole corrector power supplies are rated at ± 50 A, generating the angular strengths listed in Table 3.22. Ten have been upgraded to 55 A, and two to ± 60 A [122]. Thus it is necessary to strengthen the power supplies used to launch and capture off-axis closed orbits, and/or to define a higher-performing set of dipole correctors.

The "outer" set performs somewhat better than the "inner" set (see Figure 3.65), but a few dipole correctors require more than 70 A. A more comprehensive search of potential corrector sets is necessary. *In extremis*, the current could be reduced by using 6 or 8 dipole correctors per arc. The correctors also need some headroom to continue with their original function – correcting the closed orbit.

Warm leads enter cryostats to power individual dipole correctors. Thermal runaway is absent up to 60 A, but needs further testing at 70 A [122].

Table 3.22: Maximum dipole corrector bend angles, at the nominal maximum RHIC power supply current of 50 A, and at the maximum current of 70 A applied during quench tests.

Maximum	Integrated	Maximum Bend Angle [mrad]			
Current	Field	with proton energy [GeV]:			
[A]	[Tm]	41	100	133	275
50	0.281	2.055	0.842	0.633	0.306
70	0.393	3.877	1.179	0.887	0.429

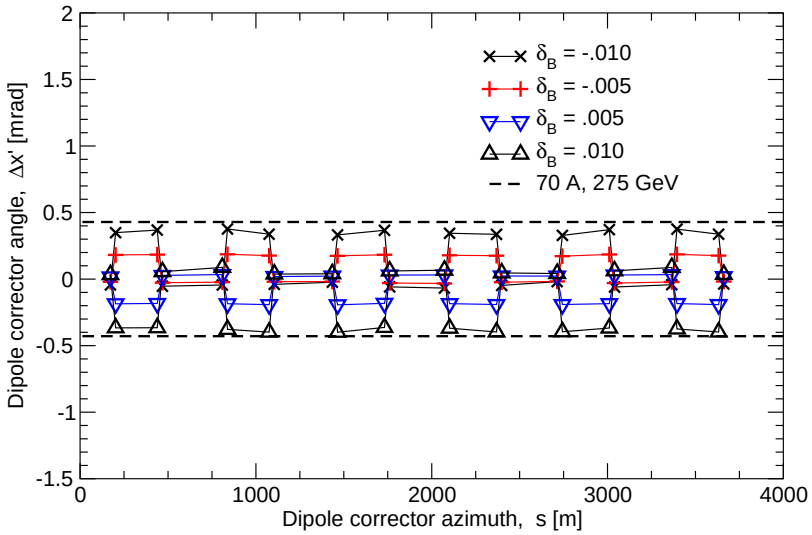

Figure 3.66: The angular strengths required of the "inner" set of dipole correctors.

Table 3.23: Primary parameters in off-axis studies of the collision lattice (HSR_200512 lattice).

Parameter	Horizontal	Vertical
Betatron tune Q_H, Q_V	28.228	29.210
Chromaticity C_H, C_V	1.0	1.0
IP2 β^* [m]	6.1	5.8
IP4 β^* [m]	6.2	5.8
IP6 β^* [m]	0.800	0.072
IP8 β^* [m]	6.0	5.9
IP10 β^* [m]	6.1	6.1
IP12 β^* [m]	6.1	6.1

Off-axis Optical Performance

In addition to setting δ_B to achieve the desired circumference, and setting the dipole correctors to deliver smooth off-axis closed orbits in the arcs, other magnets are tuned to return the optics to a goal state. Tunes and chromaticities are held at the primary values listed in Table 3.23 by adjusting the strengths of the main quadrupoles and main sextupoles in the arcs.

Twiss functions everywhere may then be optimized by small adjustments of individually tuned quadrupoles in the interaction regions and straights. Before that final tuning is performed, the root mean square value of $(\beta(\delta_B) - \beta(0))/\beta(0)$ is $(0.082, 0.064, 0.044, 0.064)$ for δ_B values of (-.010, -.005, .005, .010).

Figure 3.67 shows how the tunes vary with momentum over a $\Delta p/p$ range out to $\pm 8.3\,\sigma_p/p$, for 5 values of the off-field parameter ($\delta_B = -0.010, -0.005, 0.00.005, 0.010$). Although there is significant variation with δ_B, the off-axis cases are comparable in scale with the on-axis case $\delta_B = 0$.

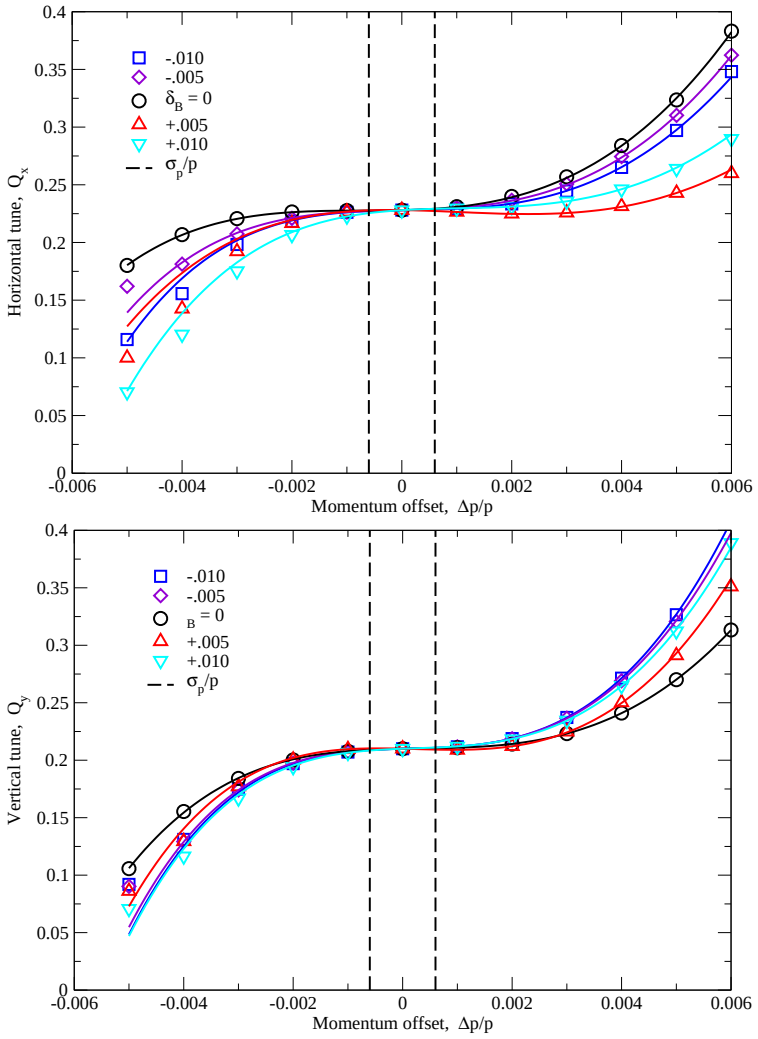

Figure 3.67: Horizontal and vertical detuning versus momentum offset for 5 δ_B values. Curves show quartic polynomial fits, with chromaticities of 1.0 . The vertical dashed lines show the nominal RMS momentum width of $\sigma_p/p = 6 \times 10^{-4}$.

Similarly, Figure 3.68 shows how detuning with respect to horizontal and vertical actions J_x and J_y varies with δ_B. The on-axis case with is typical of all off-axis cases. Straight line fits confirm the expectation that detuning is dominated by second-order chromaticity sextupole effects.

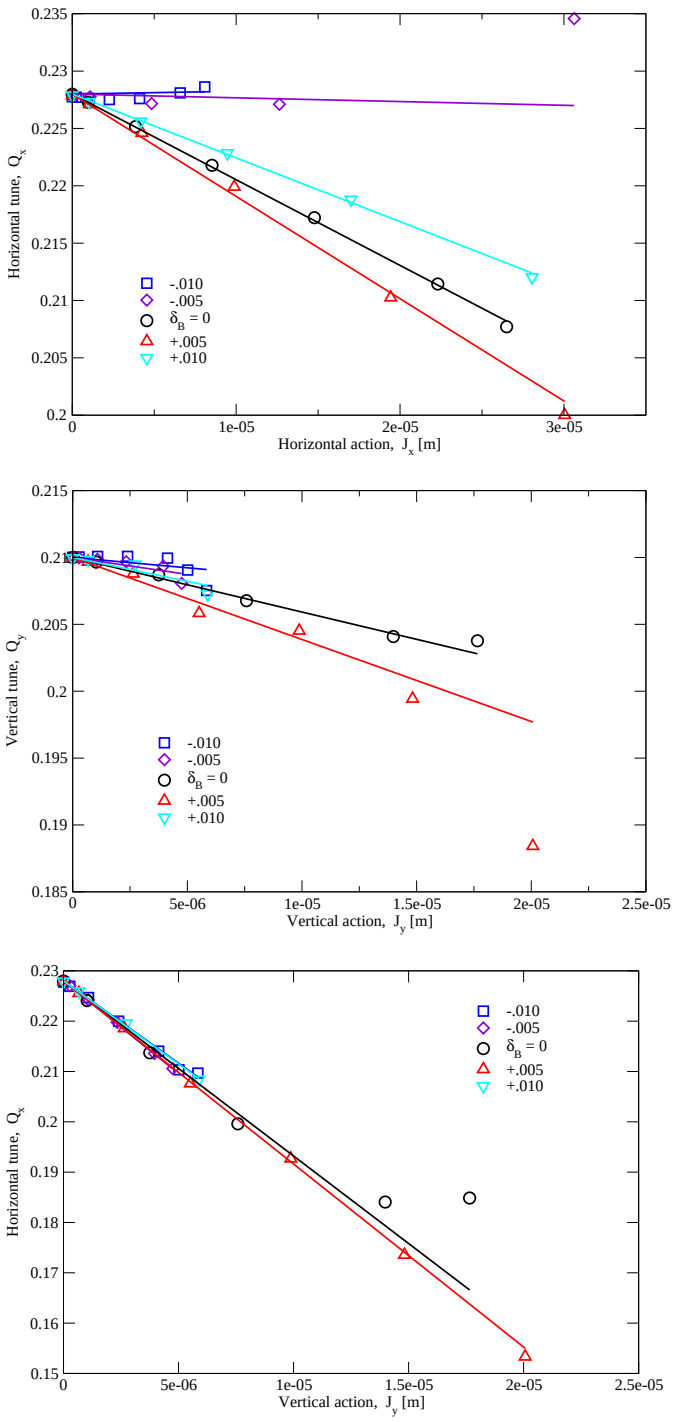

Figure 3.68: Detuning versus action for 5 δ_B values. The on-axis case with $\delta_B = 0$ is typical of all off-axis cases.

Dynamic Aperture

Dynamic aperture studies were performed by Zgoubi [123], tracking for 30,000 turns with 5 values of the off-field parameter δ_B, with sextupole multipoles at arc dipole ends but without including any physical apertures. Synchrotron oscillations were included at one of 5 off-momentum amplitudes

$$a_s \;=\; |(\Delta p/p)_{\text{extreme}}| \;=\; (0, 0.4, 0.8, 1.2, 1.6, 2.0) \times 10^{-3} \tag{3.71}$$

that scan the bucket of the dual-harmonic RF system, as characterized in Figure 3.69. The (mainly) longitudinal parameters listed in Table 3.24 show that the RF bucket is "full", insofar as the bucket height is 3.0 σ_p/p.

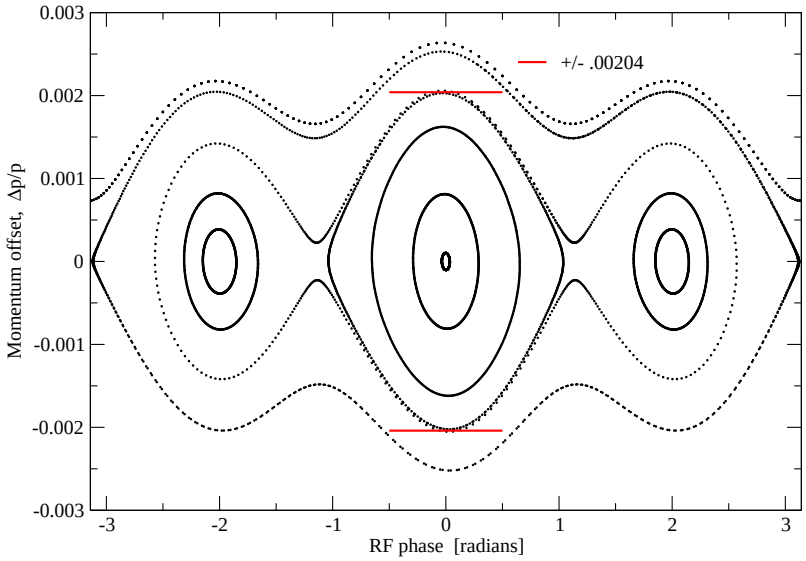

Figure 3.69: RF bucket.

The transverse lattice parameters listed in Table 3.23 show that this is collision lattice, with a dynamic aperture that is reduced by the stronger sextupoles that compensate for the largest natural chromaticities. This conservative perspective is partially offset by using the highest proton energy, shrinking the bean sizes since

$$\sigma \;=\; \sqrt{\frac{\epsilon_N \beta}{(\beta\gamma)}} \tag{3.72}$$

Maximum stable horizontal and vertical betatron amplitudes a_x and a_y are plotted against each other in Figure 3.70, in units of RMS transverse beam sizes σ_x and σ_y. The normalized initial emittance of $\epsilon_N = 2.0\,\mu\text{m}$ is conservative, since both horizontal and vertical emittances shrink with time due to Strong Hadron Cooling.

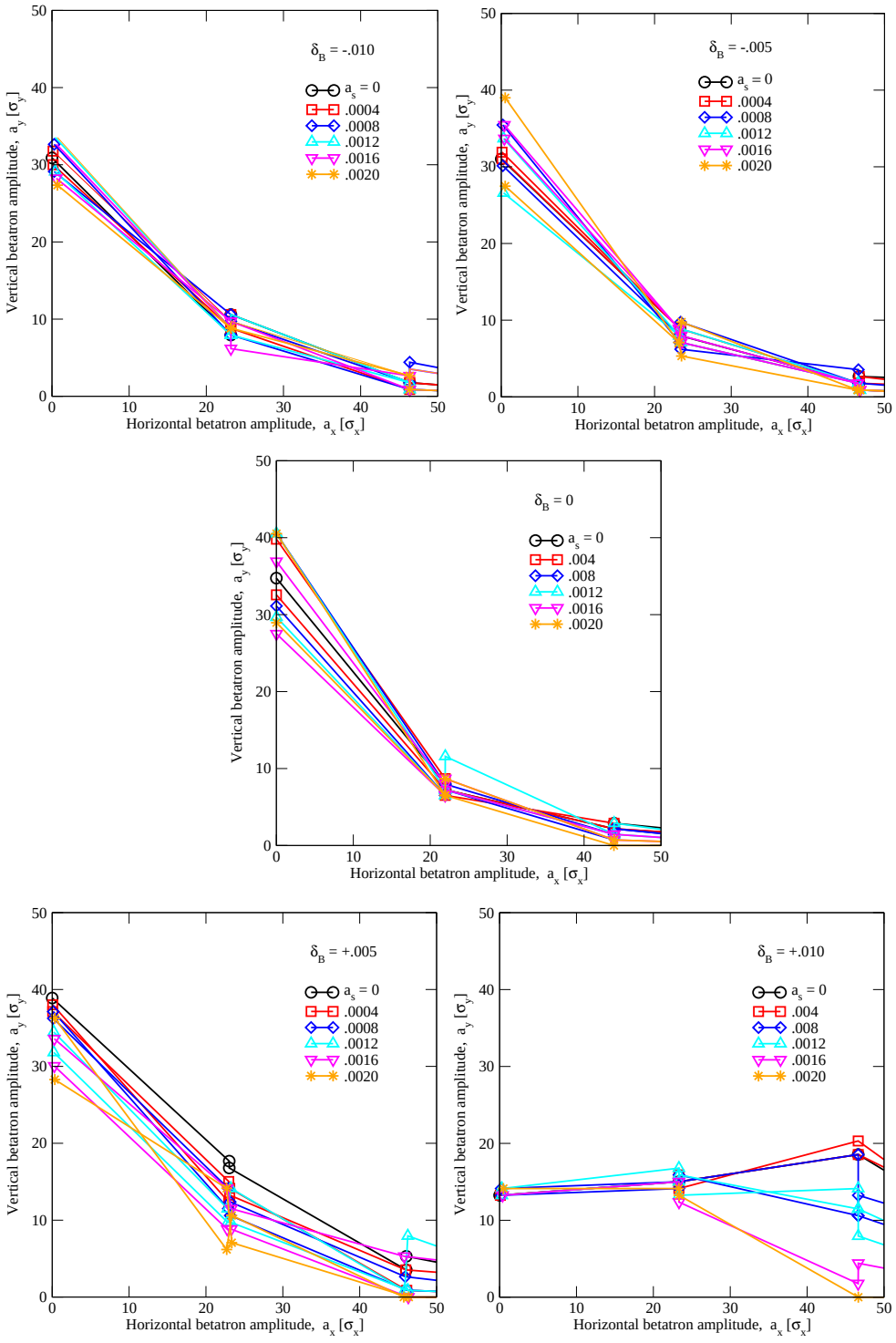

Figure 3.70: Dynamic aperture after 30,000 turns with $\delta_B = (-0.010, -0.005, 0, 0.005, 0.010)$.

Table 3.24: Longitudinal parameters used in the dynamic aperture study.

Parameter	Value
Proton energy, E [GeV]	275
Normalized emittance (both planes), ϵ_N [µm]	2.0
Synchrotron tune, Q_s	0.0133
RF voltage (h, f)	
at 2520, 197 MHz [MV]	6
at $3 \times 2520, 591$ MHz [MV]	20
RMS momentum spread, σ_p/p [10^{-3}]	0.68
RF bucket height, $(\Delta p/p)_{\max}$ [10^{-3}]	2.04
Scaled bucket height, $\Delta p_{\max}/\sigma_p$	3.0

The dynamic aperture does not vary significantly with δ_B, with stable betatron amplitudes of at least 11 σ through all of the RF bucket. The dynamic aperture varies with the synchrotron amplitude a_s, but without a simple dependency.

Beam Experiments and Operational Experience

In 2016 RHIC operations the pre-fire protection bump gave a maximum horizontal displacement of 20 or 21 mm to gold beam with an energy of 100 GeV/u and an emittance of 2.0 µm, at a location with $\beta_x = 40$ m and RMS beam size $\sigma = 0.9$ mm [124–126]. Larger displacements generated unacceptable beam losses. Gold ion losses include the generation of Au^{78+} through pair production and recombination, and the generation of $^{196}Au^{79+}$ through electromagnetic dissociation. Both Au^{78+} and $^{196}Au^{79+}$ are off-momentum with respect to $^{197}Au^{79+}$. Protons do not generate such halo and have a slightly smaller beam size – for example $\sigma_x = 0.6$ mm at the same rigidity. In this way gold ion studies are more critical and informative than proton studies.

In 2018 RHIC Accelerator Physics EXperiments (APEX) studies were performed by storing a large emittance gold beam at an injection energy of 10 GeV/u, with an RMS beam size of about $\sigma = 2.8$ mm [127]. A ramp from off-axis to on-axis operations was developed to maintain clean off-momentum optics, and to minimize the ratio of $|x|_{\max} / \langle \Delta R \rangle$ by careful control of the closed orbit. Performance with an average radial shift of $\langle \Delta R \rangle = -8.6$ mm was mostly satisfactory, but significant beam losses were seen with $\langle \Delta R \rangle = -11.0$ mm. An extreme displacement of -25.4 mm was observed, maintaining a 4.5 mm clearance with an assumed inner beampipe radius of 34.5 mm, including a 6σ envelope. Calculations extrapolating from these low-energy results at 10 GeV/u to high-energy gold beam operations at 100 GeV/u suggest that $\langle \Delta R \rangle$ could be reduced to about -15 mm, significantly outside the required range of $\langle \Delta R \rangle = \pm 11.7$ mm.

In 2020 a brief study took data at 26.5 GeV during an energy scan for Coherent electron Cooling. The RF frequency was held constant while the waveform manager was used to vary the value of the rigidity. Tune feedback was on, and closed orbit feedback was used as needed. Data showed spikes in Yellow ring losses, first on the outside when $x_{\max} \approx 12\,\text{mm}$, and later on the inside when $x_{\min} \approx -14\,\text{mm}$.

In 2021 dedicated high-energy studies are possible, with off-axis proton or gold ion lattices prepared following the HSR strategy:

1. Beam is on-axis in the 6 straights and off-axis in the 6 arcs
2. Non-zero δ_B is applied to all dipoles on the main dipole bus
3. One or more alternative sets of 24 dipole correctors are powered to launch and capture displaced closed orbits in the 6 arcs
4. Tunes and chromaticities are maintained at nominal values in a δ_B-ramp

Goals and implementation plans for these high-energy studies are in preparation at the time of writing.

A Mitigation Strategy to Reduce the Extreme Displacement

The extreme radial shift in the arcs depends on the maximum dispersion

$$|x|_{\max} \;=\; D_{\max}\;|\delta_B| \tag{3.73}$$

while the change in circumference depends on $\langle D \rangle$, the average off-axis dispersion. If

$$Y \;=\; D_{\max}/D_{\min} \tag{3.74}$$

is the ratio of maximum and minimum dispersions in the arcs, then the extreme and average displacements are approximately related through

$$|x|_{\max} \,/\, \langle \Delta R \rangle \;\approx\; Y^{1/2} \tag{3.75}$$

The extreme displacement could therefore be reduced at constant ΔC by reducing Y, which is a function of $\Delta\phi$, the phase advance per arc FODO cell. The results from Figure 3.71 recorded in Table 3.25 show that the extreme displacement could be reduced by almost 3 mm, by reducing the phase advance per cell to 40°.

However, Intra-Beam Scattering times decrease for smaller $\Delta\phi$ values, for both gold ions and protons. Reducing the phase advance per cell is therefore reserved as a potential mitigation strategy, to be adopted only if unexpected radial shift difficulties are encountered.

Table 3.25: The potential reduction of the extreme displacement $|x|_{\max}$ by lowering $\Delta\phi$, the phase advance per arc FODO cell, from 82° to 40°.

$\Delta\phi$ [deg]	Y	$\langle\Delta R\rangle$ [mm]	$\lvert x\rvert_{\max}$ [mm]
82	2.0	14.0	19.8
82	2.0	11.5	16.3
40	1.4	11.5	13.6

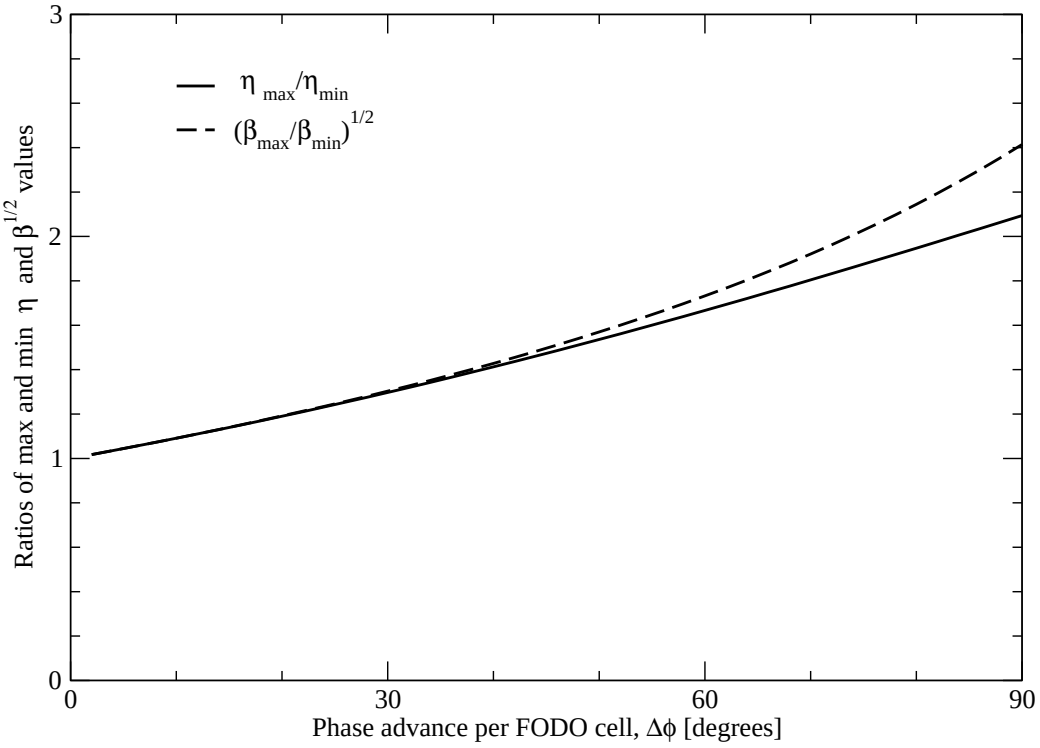

Figure 3.71: The dispersion ratio $D_{\max}/D_{\min}$ as a function of $\Delta\phi$, the phase advance per cell (in both planes) for FODO cells with thin quadrupoles. The ratio reduces significantly, from 2.0 to 1.4, when $\Delta\phi$ is reduced from the nominal RHIC value of 82° per cell to 40° per cell.

3.3.3 Hadron Storage Ring Optics

Ring Optics and Main Parameters

The hadron storage ring (HSR) is composed of six arcs with eleven FODO cells in each arc. The arcs are connected by five straight sections (SS) and an interaction region (IR) at the 6 o'clock area of the ring with the possibility of a second IR in the 8 o'clock SS. Figure 3.72 is a plot, generated by the computational model engine (CME) [128] BMAD accelerator toolkit [129], of the β functions and dispersion of the HSR. The interaction point is at the start of the lattice where s equals zero and s increases clockwise around the ring. The HSR is composed of the existing Relativistic Heavy Ion Collider (RHIC) [130] yellow ring with the exception of the IR. The path length circumference, without the radial shift, of the ring is 3833.824018 m at full energy. The transit time of the particle,t_p, and the velocity of the particle, v_p are used to calculate the circumference,$C = t_p \times v_p$. For 41 GeV, the blue inner arc between the 12 and 2 o'clock SS will be used for circulating beam which reduces the path length of the beam by approximately 90 cm. The SS are anti-symmetric in quadrupole polarity with respect to the SS midpoint.

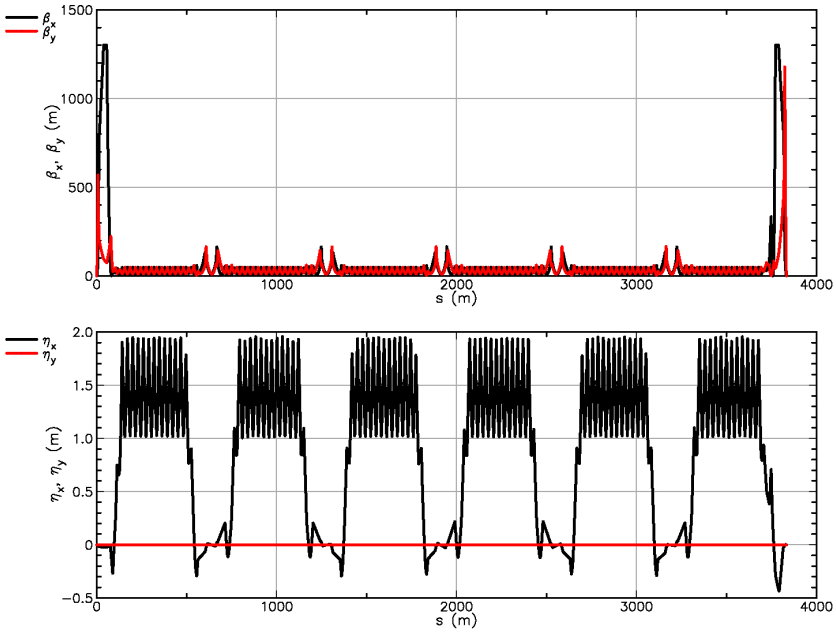

Figure 3.72: Hadron Storage Ring optics from s-coordinate increasing from IP 6 clockwise at top energy 275 GeV protons.

The HSR lattice version 20201208 horizontal and vertical tunes are separated by one unit, $(\nu_x, \nu_y) = (28.228, 27.210)$, with a horizontal and vertical $\beta^* = 10.0$ m at the midpoint of each SS. The absolute value of the horizontal dispersion, η_x, at the SS midpoint is less than 1 cm. Both protons and Au^{79+} ions have the same betatron tunes. The natural chromaticities $(\partial\nu_x/\partial\delta|_{\delta=0}, \partial\nu_y/\partial\delta|_{\delta=0})$ of the 275 GeV proton lattice are (ξ_x, ξ_y) = (-49.09,-72.17), hor-

izontally and vertically. The sextupoles are tuned to a strength that produces a chromaticity of 1 in both planes. Up to 8 sextupole families can be used to correct the first, second, and third order chromaticities [131]. The HSR uses the former RHIC arcs and redesigned straight sections. The RHIC DX magnets of the SS are removed because of power supply current constraints and magnet aperture limitations. Since the DX magnets are removed, the D0 magnets are readjusted to a bending angle of ± 5.34 mrad. In the 6 o'clock IR, the interaction point has a $(\beta_x^*, \beta_y^*) = (800, 72)$ mm, horizontally and vertically. The beam travels counter-clockwise in the magnetic lattice. The HSR acts as an accelerator, storage ring, and collider.

The momentum compaction is calculated by using the equation:

$$\alpha_c = \frac{\Delta C/C}{\Delta p/p} = \oint ds(\boldsymbol{g} \cdot \boldsymbol{\eta})/L$$

where $\boldsymbol{g}$ is the curvature vector and equal to (g_x, g_y), the geometric strengths in the horizontal and vertical plane. L is the length of the lattice. The geometric strength is defined as $g = 1/\rho$, where ρ is the radius of curvature. The momentum compaction for the HSR is 2.06×10^{-3}. The gamma transition, γ_t, is therefore $1/\sqrt{\alpha_c}$ which equals 22.02. When the differential of circulation time with respect to $\delta = \Delta P/P$ of the off-momentum particle is zero, transition occurs. Protons are injected above the γ_t at a γ of 25.38 while all other ion species are injected below. Transition crossing in the HSR is handled similar to RHIC. HSR uses a first order matched transition jump so that transition energy at γ_t, rapidly decreases across γ of the accelerating beam with little beam disturbance [132].

Arcs

HSR FODO cells in the arcs remain unchanged from RHIC (Figure 3.73). Each FODO cell is composed of two half quadrupoles, one full quadrupole, and two full dipoles. There are sextupoles and dipole correction magnets adjacent to each of the quadrupoles in the arc. The HSR lattice consist of 3 arcs of FODO cell length (inner) 29.5871 m and 3 arcs of FODO cell length (outer) 29.6571 m. Each main dipole has a bend angle of 38.924 mrad with a field of 3.782 T. The bending radius is 242.541 m with a geometric strength $0.004123\,\mathrm{m}^{-1}$. The dipole has a length of 9.441 m with a beam path through the dipole having a sagitta, $\rho - \sqrt{\rho^2 - (L_D/2)^2}$, of 45.932 mm. The beam separation between the center of the 12 to 2 o'clock inner arc to the outer arc is 90 cm. The phase advances and other parameters are listed in Table 3.26 for protons at 275 GeV. Figure 3.75 is a plot of a single outer FODO cell with a horizontal phase advance, ϕ_a, of 78° and a vertical phase advance, ϕ_b, of 81°. At low energy operation, an upper limit is placed on the quadrupole strength to keep γ_t energy below proton injection energy and phase shift below or at 90° [133]. The betatron tune adjustment is controlled by the arc focusing, QF, and defocusing, QD, quadrupoles and over a range of ± 1 unit.

The main quadrupole magnets remain constrained by the RHIC power supplies to a current limit of 5500 A which limits the arc quadrupole focusing strength at high energy.

Table 3.26: Arc FODO cell parameters. The focusing quadrupoles have a field gradient 72.00 T/m and with a rigidity of 917.294 Tm a normalized strength of 0.078443 m^{-2}. The defocusing quadrupoles have a field gradient of -73.53 T/m with a normalized strength of -0.080159 m^{-2}.

Parameter	Inner	Outer
Cell		
Length [m]	29.5871	29.6571
Bending angle [mrad]	77.8481	
Radius of curvature [m]	380.06194	380.9611
Dipole		
Magnetic length [m]	9.441	
Bending radius [m]	242.54058	
Distance between centerlines [m]	0.90	
Geometric strength [1/m]	0.004123	
Angle [mrad]	38.92409	
Quadrupole		
Magnetic length [m]	1.110	
Phase advance per cell, (H, V) [2π]	0.215, 0.223	0.216, 0.224
Horizontal β, (max, min) [m]	49.32, 10.84	49.44, 10.81
Vertical β, (max, min) [m]	48.43, 11.35	48.56, 11.32
Dispersion, (max, min) [m]	1.94, 1.02	1.94, 1.01
Natural chromaticity per cell, (H, V)	-0.046, -0.431	-0.052, -0.423

The polynomial fit of the current, I , from the main quadrupole bus to the normalized quadrupole strength is:

$$Q_{main}[k_1](I) = I \sum_{j=0}^{10} [cq_j \times I^j]$$

. The equation fits both focusing and defocusing quadrupoles. In the case of the defocusing quadrupole, the strength is multiplied by negative one. The coefficients of the polynomial are defined as:

$$cq_0 = 1.87065957965 \times 10^{-04}$$
$$cq_1 = 1.82972358172 \times 10^{-09}$$
$$cq_2 = -1.01303041692 \times 10^{-12}$$
$$cq_3 = 2.01085282381 \times 10^{-16}$$

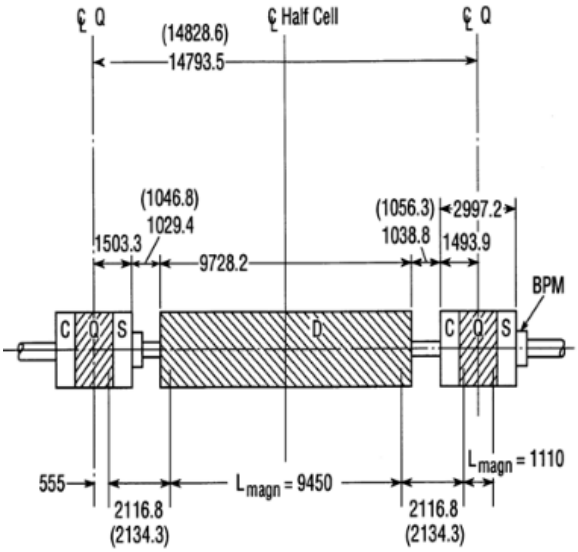

Figure 3.73: Layout of inner (outer) arc half cell.

$$
\begin{aligned}
cq_4 &= 1.57135850568 \times 10^{-21} \\
cq_5 &= -2.85204046011 \times 10^{-24} \\
cq_6 &= -2.51933991953 \times 10^{-28} \\
cq_7 &= 1.29158861243 \times 10^{-32} \\
cq_8 &= 4.86523477228 \times 10^{-36} \\
cq_9 &= 0.0 \\
cq_{10} &= 0.0.
\end{aligned}
$$

Each coefficient is multiplied by $(B\rho)_{\text{inj}}/(B\rho)_{\text{full}}$, where the $(B\rho)_{\text{inj}}$ is 79.3667 Tm and $(B\rho)_{\text{full}}$ is the beam rigidity at full energy, 917.2959 Tm for the 275 GeV proton configuration. The units of coefficients are $s/(Qm)$. Figure 3.74 depicts the quadrupole polynomial fit.

Each quadrupole in the arc has an associate sextupole. The simplest configuration of the sextupole families is to have in dispersive regions, a focusing sextupole by a focusing quadrupole and a defocusing sextupole by a defocusing quadrupole. These chromatic sextupoles are used to control the first order linear chromaticity of the HSR in the following way [134]:

$$\xi_x = -\frac{1}{4\pi}\sum_{i=0}^{N}[(b_1L)_i - 2(b_2L)_i\eta_{x_i}]\beta_{x_i}$$

$$\xi_y = \frac{1}{4\pi}\sum_{i=0}^{N}[(b_1L)_i - 2(b_2L)_i\eta_{x_i}]\beta_{y_i}$$

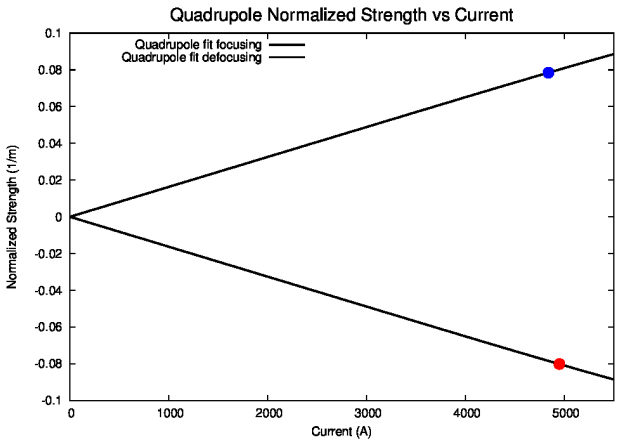

Figure 3.74: Polynomial fit of current versus normalized quadrupole strength. The blue and red points indicate the current and strength in the current HSR lattice

where the b_1 is the quadrupole field gradient, b_2 is the sextupole field gradient, and L is the length of the moment taken. N is the number of moments taken in the lattice.

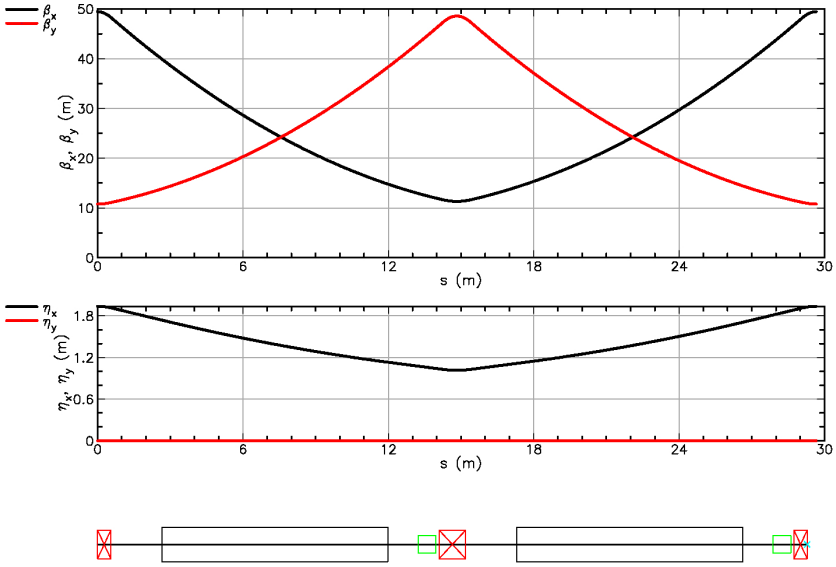

Figure 3.75: Arc FODO cell optics, with tune per cell (H, V) = (0.216, 0.224). Black box:dipole, red box: quadrupole, and green box: sextupole

Straight Section

The SS up to the midpoint has 12 quadrupoles with 5 dipoles. In the dispersion matching section from Q10 to Q4, the space between the Q10, Q9, Q7, Q6, and Q5 half cell insertions are equal in spacing and have the same spacing between the quadrupoles as the arc. The

dipoles in this region are used for dispersion control with two of dipoles in the region located at the 6 and 9 positions having a special length of 2.949 m. The Q5 and Q4 doublet with Q3, Q2, and Q1 triplets allow the flexibility of a adjustable waist at the midpoint of the SS. Additional focusing is given in the region from the trim quadrupoles TQ4, TQ5, and TQ6 which are adjacent to the Q4, Q5, and Q6 quadrupoles. The D5 magnetic length is dependent upon the inner or outer configuration, where D5I is 6.916 m and D5O is 8.698 m.

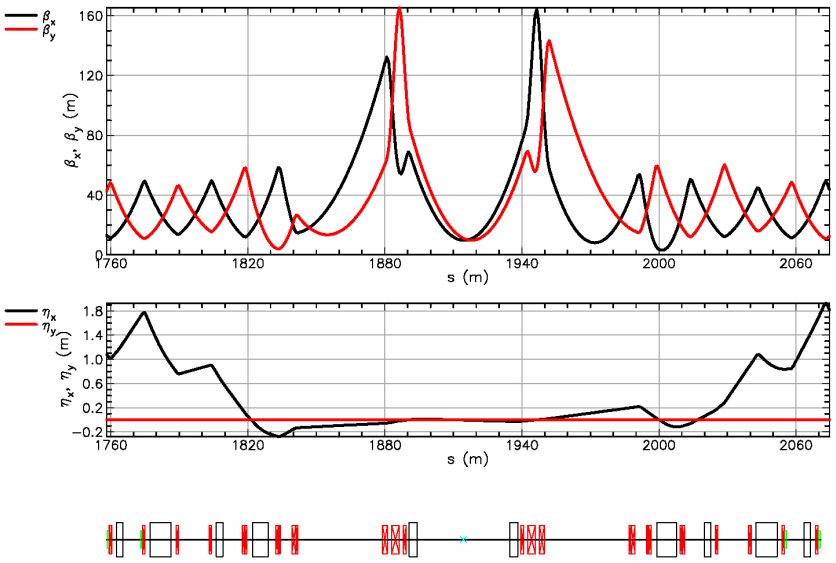

Figure 3.76: Top β functions, middle dispersion, and bottom lattice layout. Black box:dipole, red box: quadrupole, green box: sextupole, and green x: SS midpoint marker

For the insertion quadrupoles, the defocusing QD9 and QD8 have the same normalized strength. The Q7, Q6, Q5, and Q4 have equal but opposite strength to its optical dyad about the midpoint of the SS. The β_{max} values in the SS are 164 m horizontally and 165 m vertically. Figure 3.76 is a plot of the β functions, dispersion, and lattice layout for the 12 o'clock SS. The SS uses the same wiring scheme as the current RHIC where both the dipoles and quadrupoles are powered from the 4 o'clock region with return busses at the 10 o'clock region. Each insertion quadrupole type has a unique current transfer function. Shunt power supplies are used for the insertion quadrupoles with each of pair of the inner and outer QD89, Q7, and Q456 sharing a single power supply. For the 4 o'clock and 10 o'clock SS this is not the case. The trim quadrupoles TQ4, 5, and 6 each have there own auxiliary low current power supply. Table 3.27 is a list of the currents needed from the shunt power supplies in the SS if the wiring configuration remains unchanged from the RHIC. With the current shunt power supplies, the psqad is out of range with its lower and upper limits being between -280 A and +275 A. The trim quadrupoles limits are $\pm$100 A, except in 8 o'clock SS where the limits are $\pm$150. Depending on magnet type, the magnet currents are obtained from 8^{th}, 10^{th}, or 12^{th} order polynomial fits analogous to the equation used for the main quadrupole currents.

Table 3.27: Currents needed from shunt power supplies for SS quadrupoles for 275 GeV protons.

Power Supply	Current [A]	Relation
psqad	-469.695	QD89(I)-QD(I)
psqfa	-134.295	-QF9(I)+Q9(I)
psqfb	-241.160	-QF8(I)+Q9(I)
psiqt6	-22.351	Q6IT(I)
psiqt5	97.920	Q5IT(I)
psiqt4	63.743	Q4IT(I)
psoqt6	100.432	Q6OT(I)
psoqt5	-102.620	Q5OT(I)
psoqt4	-35.375	Q4OT(I)
psq7	549.538	Q7(I)-QF(I)
psq456	-33.610	Q456(I)-Q7(I)
psoq3	23.092	QD3(I)-Q456(I)
psoq2	-207.143	QD2(I)-QD3(I)
psqo1	16.765	QD1(I)-QD2(I)
psqi3	-118.862	QF3(I)-Q456(I)
psqi2	67.641	QF2(I)-QF3(I)
psqi1	84.831	QF1(I)-QF2(I)

Optics Matching

The transition from arc to SS occurs at the Q10 quadrupole magnets of the arc. At these magnets, a set of matching conditions for the beta-functions and dispersion are defined using the following formulas:

$$\begin{aligned} \beta_{\max} &= L\left(\frac{1+\sin(\mu/2)}{\sin(\mu)}\right) \\ \beta_{\min} &= L\left(\frac{1-\sin(\mu/2)}{\sin(\mu)}\right) \\ D_{\max} &= L\Omega\left(\frac{1+\sin(\mu/2)/2}{4\sin^2(\mu/2)}\right) \\ D_{\min} &= L\Omega\left(\frac{1-\sin(\mu/2)/2}{4\sin^2(\mu/2)}\right) \end{aligned} \tag{3.76}$$

where L is the cell length, μ is the phase advance per cell, and Ω is the bending angle of the FODO cell.

3.3.4 Hadron Storage Ring IR Optics

Here "interaction region" is meant in the broad sense as everything between the periodic arc cells on either side closest to the 6 o'clock point in the HSR. A corresponding beamline could be constructed near the 8 o'clock interaction point, but that will not be detailed here.

The interaction point is shifted from the RHIC interaction point by 81 cm toward the inside of the ring, and rotated by 17 mrad such that the excess bend is on the forward side (counter-clockwise from the interaction point, the side toward which the hadrons are moving). On the forward side, there is first a pair of dipoles that bend the beam away from a neutron detector. These are followed by a quadrupole doublet, vertically focusing nearest the interaction point, and where the vertically focusing part is split into two magnets for aperture optimization. This is followed by another dipole pair that continues to separate the beamline from the neutron detector. On the rear side, there is a quadrupole doublet, again with the vertically focusing portion nearest the interaction point and split into two magnets. Each side has just over 15 m allocated to the crab cavities. On the forward side, the crab cavities and any magnets upstream of it must be beyond the neutron calorimeter. On the rear side, the crab cavities must be sufficiently far from the IP to avoid a conflict with the electron crab cavity. Both sides have just over 12 m allocated to a spin rotator, and the forward side has the same length allocated to a spin manipulation snake.

Ideally, the interaction region should:

- Have a horizontal beta function at the crab cavities of 1300 m
- Have a horizontal phase advance to the crab cavities of 90°
- Have a small dispersion and its derivative at the crab cavities
- Have the snake on the hadron forward side with a geometric floor angle equal to that of the drift between DH6 and DH8 in RHIC
- The rotator on the forward side should be on the IP side of the snake
- Have the angle between the interaction point and each rotator be the same
- Re-use as much of the RHIC magnet system as possible

The beta functions and dispersion of the resulting interaction region are shown in Figure 3.77. The general design strategy is to allow the horizontal beta function to stay high from the interaction point up to the crab cavity, placing a weak quadrupole in front of the crab cavity to flatten the horizontal beta function through it. A quadrupole on the arc side of the crab cavity then brings the horizontal beta function down rapidly to enable the match into the arc. The vertical beta function in contrast is kept low through the crab cavity so as not to be heavily impacted by the horizontally focusing quadrupoles around the crab cavity and to have the vertical beta functions low through the section that matches into the arc. Values related to the design goals for the interaction region in the case of 275 GeV, $\beta_x^* = 80$ cm, and $\beta_y^* = 7.2$ cm are given in Table 3.28.

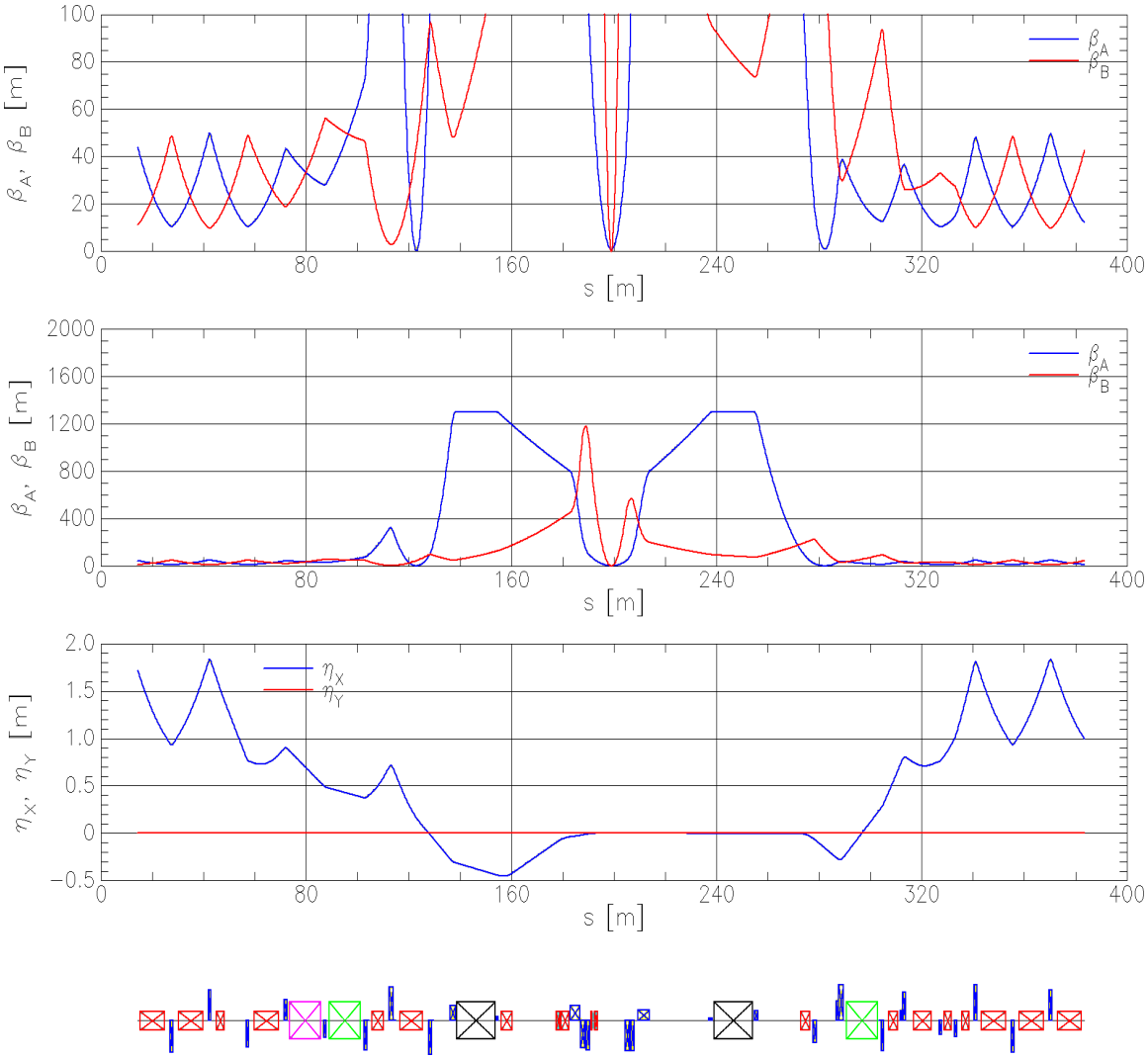

Figure 3.77: Beta functions and dispersion for the HSR interaction region, plus one full arc cell on each end, for the 275 GeV proton beam, $\beta_x^* = 80$ cm, $\beta_y^* = 7.2$ cm. The bottom indicates the positions of magnets and other objects. Red boxes are dipoles, blue boxes are quadrupoles with direction and height indicating their polarity and gradient, black boxes are crab cavities, green boxes are rotators, and the magenta box is the snake. The hadron beam is moving right to left.

The beamline is highly geometrically constrained. On the forward side, more of the dipole field must be on the IR end, whereas on the rear side the dipole field should be concentrated on the arc end. Since the forward side already requires an additional bend angle compared to RHIC, and the dipole near the interaction point bends in the wrong direction, there is very little space remaining on the forward side. Furthermore, to avoid creating sig-

Table 3.28: Values important to design goals evaluated for the interaction region design, for the case of 275 GeV, $\beta_x^* = 80$ cm, and $\beta_y^* = 7.2$ cm.

Parameter	Forward	Rear
Horizontal phase IP to crab cavity center	88.3°	86.8°
Beta function at crab cavity [m]	1300	1300
Dispersion at crab cavity center [cm]	−38	0
Dispersion derivative at crab cavity	+0.008	0
Dispersion amplitude ($\mathcal{H}_x$) [m]	0.084	0
Horizontal chromaticity	−16.4	−10.4
Vertical chromaticity	−14.4	−9.6
Rotator angle (relative to IP) [mrad]	61	17

nificant dispersion amplitude, the beta function must be reduced by time one gets to the first dipole after the crab cavity, which creates significant chromaticity just on the arc side of the crab cavities. Finally, these geometric constraints force the rotator on the forward side to be placed at a large geometric angle from the interaction point, whereas on the rear side the angle cannot be very large. This is expected to be manageable, see Section 3.2.1. It is, however, possible to place the snake at the desired geometric angle.

Most of the existing RHIC dipoles and quadrupoles in that region are used, but they are rearranged to satisfy the geometry. RHIC quadrupole assemblies (containing a quadrupole plus other magnets and diagnostics) 4 through 9 are used on both sides. In addition, on the forward side, one of the RHIC triplet quadrupoles is used. Two of the RHIC triplet quadrupoles will be used on the rear side. On the forward side, the DH5, DH8, and DH9 RHIC dipoles are used. On the rear side, the DH5, DH6, DH8, and DH9 RHIC dipoles are used, plus two DX RHIC dipoles.

The RHIC quadrupole maximum gradients are chosen to be 89 T/m for most quadrupoles, 57 T/m for the triplet quadrupoles, and 48 T/m for the trim quadrupoles, which exist in three of the quadrupole modules on each side. These are based on a conservative current limit (at which the magnets have been tested) of 6000 A for all the quadrupoles except for the trim quadrupoles, for which the limit is 150 A. Each quadrupole will require an individual supply, since there does not seem to be a good way to use main and shunt supplies (as is currently done in RHIC) with the matching configuration. A few of the quadrupoles are running at these limits for a 275 GeV proton beam, and in one case a trim quadrupole is at its limit as well. Other than the DX dipoles, all of the RHIC dipoles will operate at the same current as the main arc dipoles. The DX dipoles have a bend angle of at most 17 mrad.

A small number of new magnets will be required. The six quadrupoles and four dipoles adjacent to the interaction point are described in Section 6.2.2. On the forward side, two

4.4 m approximately 5 T dipoles are required, one near the crab cavity on the IP side, the other being the second dipole to the arc side of the crab cavity. These will need to accommodate the 100 mm inside diameter beampipe near the crab cavity. They are needed due to the excess bend on the forward side, and fields are chosen to be as high as reasonable due to the very limited space in that region. Iron quadrupoles with a maximum integrated strength of 8.3 T will be used adjacent to the crab cavities on the interaction point side since they are relatively weak and space is limited, at least on the forward side.

Table 3.29: Magnet fields and gradients for 275 GeV protons, forward side, $\beta_x^* = 80$ cm, $\beta_y^* = 7.2$ cm. The RHIC magnet being used is indicated where appropriate.

RHIC Magnet	Length [m]	Gradient [T/m]
—	1.460	+72.6
—	1.610	+67.2
—	3.800	−36.9
—	0.750	−9.2
QD3	2.100	−36.6
QD5	1.110	+82.9
QF4	1.812	−82.6
QF6	1.110	+71.9
QD7	0.930	+40.6
QF8	1.110	−52.3
QD9	1.110	+64.9

RHIC Magnet	Length [m]	Field [T]
—	1.200	+1.30
—	0.600	+3.45
—	3.000	+3.47
—	1.500	+2.70
—	4.400	−4.90
DH5	6.916	−3.78
—	4.400	−4.73
DH8	9.441	−3.78
DH8	2.949	−3.78

Tables 3.29 and 3.30 give the fields and gradients in the magnets for the 275 GeV match. For other β^* values, the matching conditions will change. The gradients in the quadrupole doublet will be left unchanged, allowing the beta functions at the crab to be reduced but maintaining the same crabbing strength because the product of β_x^* and the horizontal beta function at the cavity will remain the same (see Section 6.2.2).

The field in the first dipole on the forward side is fixed at 1.3 T for all energies (see Section 6.2.2).

Therefore the beam will follow a different orbit for each energy. The fields in the two dipoles downstream of the first are adjusted to restore the beam onto the axis; field values are shown in Table 3.31.

The most significant issues in Table 3.28 are the large chromaticity on the forward side and the low horizontal phase advances to the crab cavities. The chromaticity (particularly in the horizontal plane) on the forward side results from having little space between the crab cavities and the dipoles to bring the beta function down. Beam dynamics studies will

Table 3.30: Magnet fields and gradients for 275 GeV protons, rear side, $\beta_x^* = 80$ cm, $\beta_y^* = 7.2$ cm. The RHIC magnet being used is indicated where appropriate.

RHIC Magnet	Length [m]	Gradient [T/m]
—	1.800	+75.0
—	1.400	+75.0
—	4.500	−26.2
—	0.750	−11.1
QF3	2.100	−17.1
QD2	3.392	+23.7
QD4	1.812	−89.0
TQ4	0.750	−48.0
QF5	1.110	+75.1
QD6	1.110	−70.8
TQ6	0.750	−24.0
QF7	0.930	+34.3
QD8	1.110	+39.8
QF9	1.110	−89.0

RHIC Magnet	Length [m]	Gradient [T]
DX	3.700	+4.21
DX	3.700	−0.91
DH5	6.916	−3.78
DH6	2.949	−3.78
DH9	2.949	−3.78
DH8	9.441	−3.78

Table 3.31: Fields, in T, in the second and third dipoles on the forward side for the three proton design energies.

41 GeV	−2.46	0.59
100 GeV	−0.97	1.32
275 GeV	+3.45	3.47

determine if these are manageable. If the horizontal phase advance to the crab cavities is not acceptable, there are a few options. One can increase the phase advance by only a small amount by moving the cavities on the rear side further from the interaction point, and that would increase the chromaticity significantly. One could also add quadrupoles between the interaction point and the crab cavity on the rear side, reducing (significantly) the horizontal beta function in that region; to keep the vertical beta function under control, this would require significant increases in the integrated strengths of the quadrupoles adjacent to the interaction point, as well as creating a significant increase in chromaticity. Finally, one could switch to using new, higher-field dipoles (and possibly more compact quadrupoles) to allow the crab cavities to move further away from the interaction point.

3.3.5 HSR Polarization Preservation with 6 Snakes

Presently there are two helical Siberian Snakes installed in each RHIC ring. They are located on opposite sides of the ring, at 9 and 3 o'clock. With this configuration RHIC has achieved proton polarization levels of 65% at an energy of 100 GeV, and 55% at 250 GeV. For the EIC we expect a higher polarization level of 70%, for polarized protons. Also, getting highly polarized 3He beam calls for increasing the number of Snakes. The EIC polarization requirements will be achieved by installing four additional helical Siberian Snakes, so the total number will be six snakes in the (Yellow) hadron storage ring. Two Siberian Snakes will be transferred over from the Blue ring, while additional snakes will be constructed by reconfiguration of Blue spin rotators.

The latter is accomplished by combining helical magnets of the same helicity, from disassembled rotator modules, into a Snake module, as shown in Figure 3.78. These new, additional helical snakes will be installed in the EIC hadron ring in the drift space in the dispersion suppressor, correspondingly the equivalent location of the two existing snakes. An additional snake will be installed in the 41 GeV low energy arc between 2 and 12 o'clock.

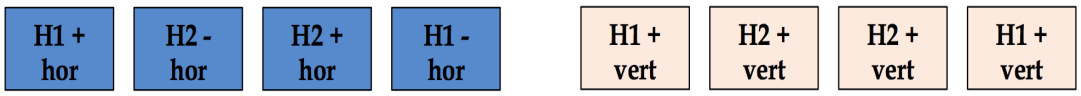

Figure 3.78: Rotator reconfiguration: The RHIC spin rotators (blue) consist of four helical magnets of different helicity with horizontal field at the magnet entrance. The sign demonstrates the magnet helicity: "+" is right-handed, "-" is left-handed (shown in the left side of the picture). The RHIC Siberian Snakes (pink) consist of four helical magnets of the same helicity with vertical field at the magnet entrance. Reconfiguration of a spin rotator into a snake can therefore be accomplished by a 90° rotation of the helical magnets.

3.3.6 HSR Collimation System

The HSR will be equipped with a two-stage betatron collimation system as well as a one-stage momentum collimator. The betatron collimation system consists of a primary collimator with jaws made of a light material such as carbon at a location with a beta-function that is preferably larger than the beta function in the arcs while still small enough to allow significantly larger beta functions at the locations of the secondaries. For flexibility each collimator will be two-sided as shown in Figure 3.108 in Section 3.5.10.

There will be one set for each plane, one horizontal and one vertical. The secondaries will have copper jaws. All collimators will be tapered for impedance minimization and will be cooled. Table 3.32 lists well suited collimator locations based on the May2020 HSR lattice for all six units (marked H for horizontal and V for vertical). The beta functions at

the location of the secondary collimators are significantly larger than those at the primary locations. Device length is preliminary and based on the design of the existing RHIC collimators. Exact length will depend on the specific mechanical design as well as the chosen length of the tapered section. It is assumed that phase advances in the straight sections around IR12 can be adjusted in a future operational lattice. The purple shaded area corresponds to the warm space that is available between the current RHIC magnets Q4 and Q3 on either side of an interaction region. The chosen collimator locations are all inside the available warm space.

Table 3.32: Twiss parameters at the potential HSR collimator locations around IR12. (The horizontal separator line indicates that the collimator units are in two different sectors.)

Collimator unit name	s [m]	L [m]	β_x [m]	μ_x $[2\pi]$	D_x [m]	β_y [m]	μ_y $[2\pi]$
COL-PrimH	1988.8	2	14.95	15.40	0.28	35.51	16.63
COL-PrimV	1986.8	2	14.70	15.39	0.27	35.52	16.62
COL-SecV1	1955.4	2	76.70	15.17	-0.27	204.93	16.56
COL-SecH1	1953.3	2	78.91	15.17	-0.28	208.85	16.56
COL-SecH2	1881.7	2	108.20	14.72	-0.11	210.07	16.11
COL-SecV2	1878.0	2	78.72	14.71	-0.07	204.85	16.10

Figure 3.79 shows the $\sqrt{\beta_{x,y}}$ functions around IR12 together with the approximate collimator locations of the primaries (1) and two sets of secondary collimators (2). The x-axis shows distance from the center of the straight section. Collimators will be on both sides of the center, four units in sector 12 and two units in sector 11.

Inside the available warm space there is no well suited location for a momentum collimator. The figure of merit for momentum collimation is the ratio of horizontal beam size to dispersion, specifically $6\sigma_x/|\eta_x|$ as plotted in Figure 3.80. The ratio is shown here as a function of s measured in distance from the center of IR12. The shaded areas are the same as in Figure 3.79. However, the purple shaded areas, i.e. the available warm spaces, are not applicable for momentum collimation. The location best suited for a momentum collimator corresponds to a minimum of the shown ratio.

The blue shaded areas, optimal for momentum collimators, are so-called dummy magnets. While still inside the current RHIC cryostat they do not contain a magnet but plain drift spaces. The smaller of these drift-spaces, the D9 half-cell area, covers about 7m and would be best suited to host a momentum collimator. To install a collimator in this space, a cold-

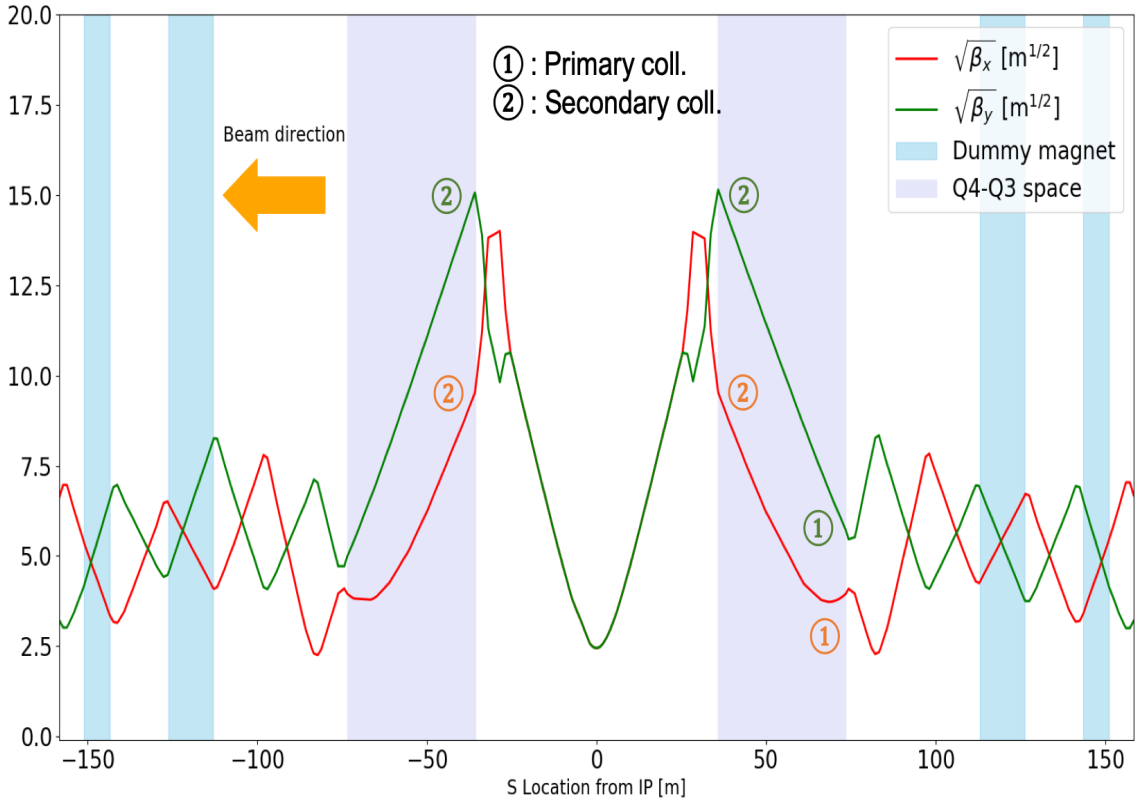

Figure 3.79: Location of the primary and secondary collimators around IR12 in the HSR.

warm transition is needed. In principle, all available D9 half-cell areas are similar and could be used for a momentum collimator, not just the ones around IR12.

3.3.7 HSR Beam Diagnostics Requirement and Specifications

The instrumentation in the EIC hadron storage ring is to a large extent an upgraded version of the existing system. These upgrades are necessary to cope with the increased number of bunches and peak current. Strong beam heating load on hadron BPMs is expected even with beam parameters without hadron cooling. 580 ion bunches with a bunch intensity up to 1.2×10^{11} protons per bunch and an RMS bunch length as short as 7 cm require replacement of the BPMs and their cryogenic BPM cables to avoid overheating and subsequent permanent damage. With strong hadron beam cooling, the number of bunches will be doubled (to 1160), while the RMS bunch length and intensity will be reduced to 6 cm and 0.7×10^{11} protons per bunch, respectively.

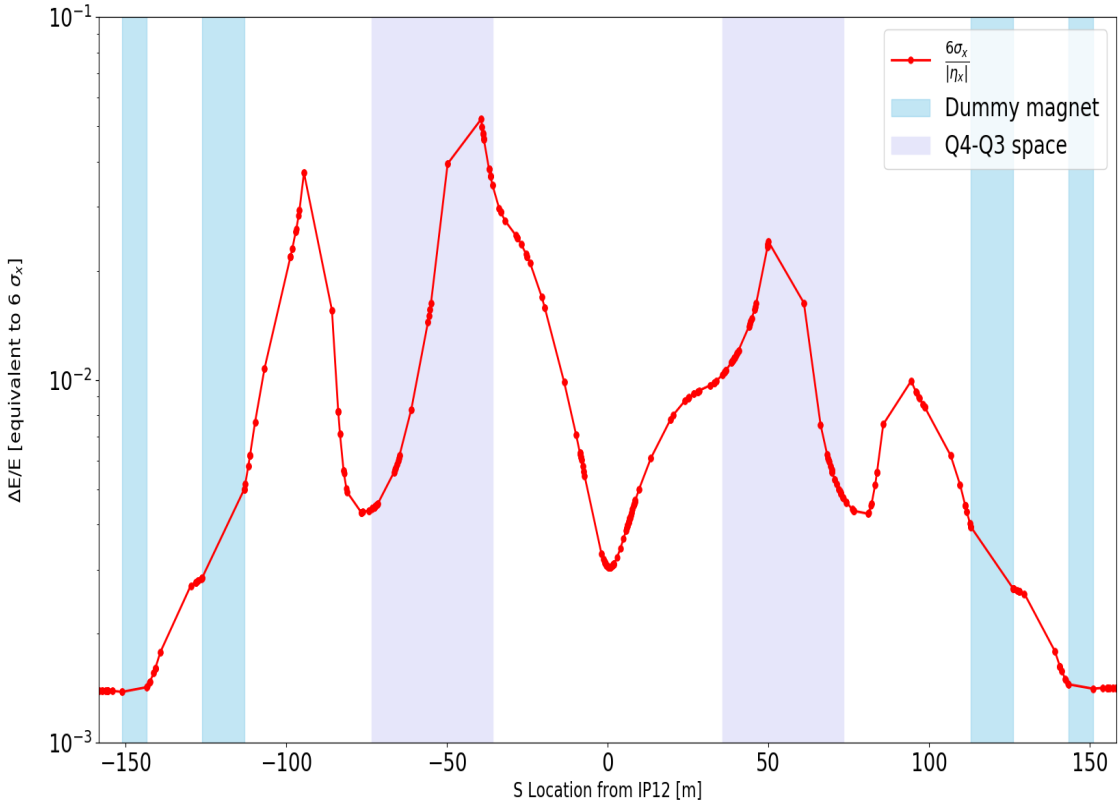

Figure 3.80: Figure of merit for momentum collimation, $6\sigma_x/|\eta_x|$, as a function of s around IR12 in HSR.

To commission the crab cavity system dedicated instrumentation is necessary. This system consists of a button BPM in a low-β insertion. With the vacuum pipe aperture being small compared to the ion bunch length, this configuration allows measurement of the transverse position within a bunch, and therefore the crabbing effect. With both crab cavities operating the crabbing effect reaches its maximum inside the EIC detector, which is not accessible for instrumentation. Instead, the crabbing effect of individual cavities can be monitored in an appropriate location outside the detector straight. Once amplitudes and phases of the two crab cavities are set, fine-tuning of these parameters is accomplished by zeroing the combined effect of the two cavities at the crab monitor location.

3.4 Hadron Injection System

3.4.1 Hadron Injector Complex Upgrades

The EIC uses the existing RHIC injector complex, which is capable of delivering the proton and ion beam intensities and emittances required by the EIC. Maximization of the physics potential of the EIC will, however, require modest upgrades to the injectors, which we discuss in this section. The upgrades focus principally on the polarization of the proton beam, since that requirement is the most demanding. Since the primary sources of polarization loss are emittance dependent intrinsic resonances, the improvement efforts focus on both direct suppression of these resonances and emittance reduction to ameliorate their effects. A modification of the injection septum is also described. This modification reduces the deflection angle required of the pulsed injection kicker magnets.

Proton Polarization

Polarization preservation in the AGS is accomplished with two helical dipole partial snakes [135]. The partial snakes alter the spin tune such that it never takes fractional values within a band around the integers called the 'spin tune gap'. The vertical betatron tune is set to a value near the integer inside the spin tune gap, thus avoiding the strong vertical intrinsic resonance condition $Q_s = Q_y \pm N$ where Q_y is the vertical betatron tune. The partial snakes also excite resonances that occur at energies where $Q_s = Q_x \pm N$ (where Q_x is the horizontal betatron tune). The resulting relative polarization loss from the 82 horizontal resonance crossings is about 20%. That polarization loss is currently mitigated with betatron tune jumps that increase the resonance crossing rate and reduce the relative polarization loss to 10% [136, 137]. The resulting polarization of the AGS proton beam at extraction is 70%.

Partial Snake Horizontal Resonance Suppression

Depolarizing resonances due to betatron coupling occur at the same spin tune as those excited by the partial snakes at $Q_s = Q_x \pm N$. It is thus possible to use skew quadrupoles to induce spin resonances to precisely cancel the driving terms of the snakes. The phasing of the coupling resonance drive terms vary strongly with $G\gamma$, so in order to provide suppression of all 82 horizontal resonances over the full energy range of acceleration in the AGS, additional skew quadrupoles need to be added to the AGS lattice.

Shown in Figure 3.81 are spin tracking results showing nearly full polarization transmission through several horizontal resonances. In the case shown, the AGS lattice contains 15 additional 0.35 m long skew quadrupoles, inserted in the short drifts between combined function main magnets. Optimization of the number and location of the correction skew quadrupoles for correction of all is the subject of ongoing efforts, but simulations currently show that $> 99\%$ of the loss due to horizontal resonances can be avoided with 15–20 skew quadrupoles with pole-tip fields less than 0.1 T.

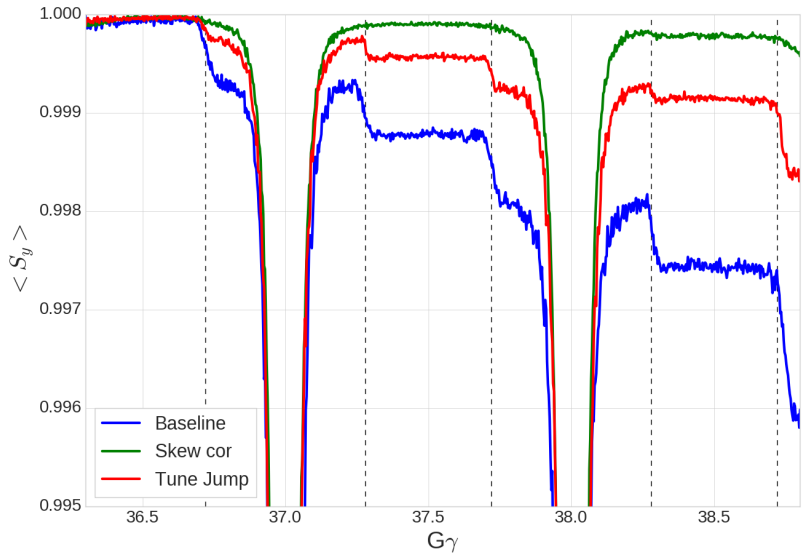

Figure 3.81: Projection of spin onto stable spin direction during acceleration in AGS, without correction for horizontal resonances (blue), faster resonance crossing via tune jump (red) and skew quadrupole corrected (green). Vertical lines indicate the timing of the horizontal resonances. Polarization loss is improved in the skew quad corrected case relative to the tune jumps. Simulation was done with 5000 particles with both transverse emittances set to 1.67 µm (normalized) and a longitudinal emittance of 0.8 eV-s.

The main operational challenge for the tune jump scheme is the tight timing requirement. The tune jumps need to occur in a window of ± 200 µs around the actual resonance crossing time. This requires energy measurement precision (in units of $G\gamma$) of 0.01. Maintaining the jumps within the timing tolerance requires frequent recalibration of the energy measurement and recalculation of the jump times to account for gradual changes in the field measurement. The skew quad corrections can be active for ± 500 µs, increasing the tolerance for the timing determination.

It should be noted that the three techniques for addressing horizontal resonances (tune jump, additional partial snakes, and resonance suppression) are not mutually exclusive and could be employed in combination if necessary.

Additional AGS Partial Snakes

The horizontal resonances could be avoided by setting Q_x inside the spin tune gap, but operational experience shows that this degrades the intensity and emittance without much gain in polarization [138]. One solution to this problem is to increase the width of the spin tune gap by adding more partial snakes to the AGS lattice.

Currently the AGS has two helical dipole partial snakes, separated by 1/3 of the AGS circumference. They are both helical dipoles: a superconducting 2.1 T and a normal conducting 1.5 T magnet, producing 10% and 6% spin rotation, respectively. If, instead of two

partial snakes, the AGS had four partial snakes placed equidistantly around the AGS ring, that would increase the width of the spin tune gap from $\Delta Q_s = 0.04$ to 0.1 as shown in Figure 3.82a. This provides a larger range of values in which to place both betatron tunes, which would allow avoidance of the horizontal resonances [139]. This would require the construction and installation of three additional superconducting helical dipoles magnets, identical in design to the existing superconducting 2.1 T partial snake, in the long straight

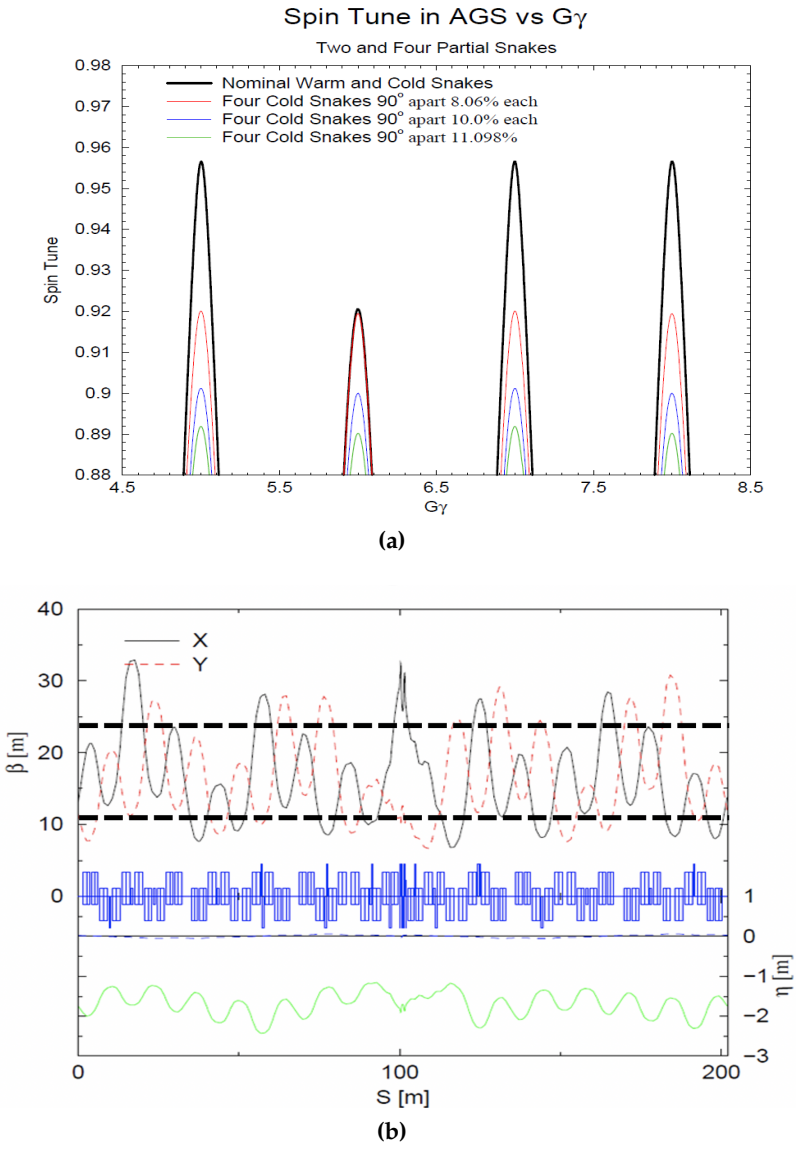

Figure 3.82: (a) Spin tune as a function of $G\gamma$ with different partial snake schemes. (b) Optical functions of the AGS in the presence of four partial snakes and compensation quadrupoles. Shown is the optics of one superperiod, which in this case is 1/4 the AGS circumference. The partial snake is located in the center of the superperiod. Black dashed lines indicate the range of the beta functions of the AGS with no snakes.

sections of the AGS. In both the existing and proposed cases the helical dipoles rotate the spin about the longitudinal direction. In the existing configuration, both snakes rotate the spin in the same direction. In the proposed four snake case, the sense of the rotation of one of the four snakes is reversed relative to the other three.

The difficulty in getting both tunes in the spin tune gap is that the partial snakes produce very large optical focusing, which is most pronounced near injection at low rigidity [140]. The symmetric layout of the four partial snakes allows for an optical solution shown in Figure 3.82b. With the additional of 24 quadrupoles to the AGS lattice, optical functions can be obtained which do not deviate substantially from those of the AGS lattice without snakes. This would further facilitate the placement of both betatron tunes in the spin tune gap.

Intensity, Emittance and Space Charge

The proton intensity required by EIC is within the demonstrated capability of the injector complex and 10% higher than that required for RHIC operation (3.0×10^{11} compared to 2.7×10^{11}). Space charge tune shifts for polarized protons at AGS injection for a per bunch intensity of 2.5×10^{11} are as high as -0.17 and -0.25 (horizontal and vertical, respectively). It was observed in RHIC Run 17 that reducing the peak current at AGS injection using defocusing RF voltage to lengthen the bunch longitudinally reduced the transverse emittance, consistent with space charge induced emittance growth [141]. A 20% reduction in the peak current produced a 15% reduction in the transverse emittances. Figure 3.83 shows the re-

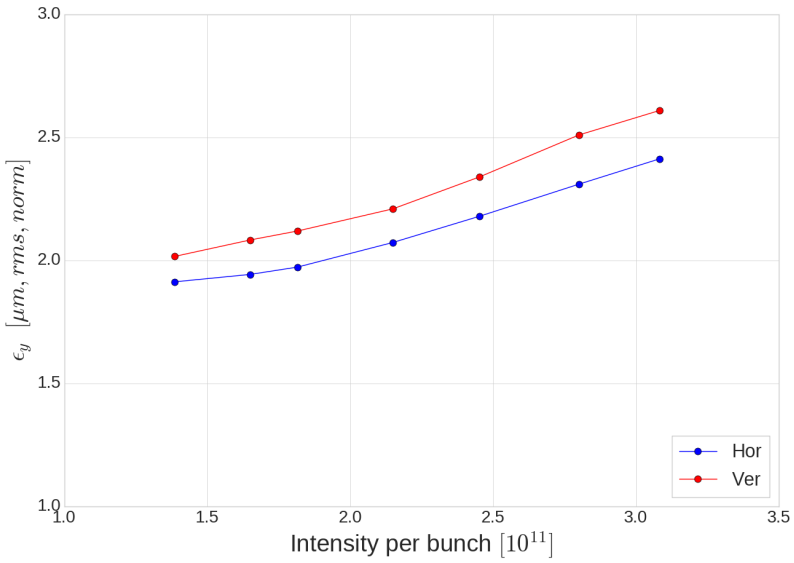

Figure 3.83: Normalized transverse emittances of polarized proton beam at AGS extraction energy ($\gamma = 25.5$) as a function of intensity.

maining dependence of the transverse emittances of the polarized beam at AGS extraction energy on the per bunch intensity in the presence of the defocusing RF.

The peak current at AGS injection can be lowered further by introducing a longitudinal bunch splitting scheme in the Booster. Longitudinally splitting the proton pulse in two reduces both the intensity and longitudinal emittance of each AGS bunch by a factor 2, resulting in a $\sqrt{2}$ reduction in the peak current.

Longitudinal merging of bunches in the Booster and AGS is common for RHIC heavy ion operations [142]. In order to make bunches suitable for EIC the split bunches need to be merged again at AGS flattop, once space charge effects are much smaller. The long synchrotron period at that energy (12 ms) requires a longer merge time. Simulations indicate that a merge can be performed that preserves the longitudinal emittance in 500 ms, which fits on the AGS extraction porch. This bunching scheme uses only existing equipment and can thus be tested in the injectors well in advance of EIC construction.

Reduced Injection Angle

The spacing between bunches at EIC injection is a factor of three smaller than the RHIC bunch spacing. This will require the injection kicker rise time to be reduced from the present 90 ns to 18 ns. In order to reduce the required voltage on the pulsed power supply for the injection kicker, it is desirable to reduce the required deflection angle. This section describes a modification of the injection line geometry that reduces the required deflection from 1.62 mrad to 1.42 mrad. The modification is discussed in detail in Reference [143].

The injection area geometry is shown in Figure 3.84. The present trajectory is shown in black. The end of the AGS to RHIC transfer line (AtR) is elevated 52 mm above the RHIC plane. The beam is first deflected 3 mrad downward to begin its descent toward RHIC. It then enters a Lambertson septum magnet, which provides the 38 mrad horizontal bend needed to match the horizontal trajectory of the RHIC circulating beam. The incoming beam trajectory intersects the RHIC circulating orbit at the vertical pulsed injection kicker magnet at a vertical angle of 1.62 mrad with respect to the RHIC mid-plane. This angle is then removed by the injection kicker to place the injected beam onto the circulating orbit.

The circulating beam channel of the present Lambertson septum contains a vacuum pipe whose primary purpose is to shield the circulating beam from leakage field from the septum injection channel. This pipe increases the effective width of the septum by 4 mm. Removing the pipe allows for lowering the septum by 4 mm without changing the aperture presented to the circulating beam. Injection with a lowered septum results in the trajectory shown in green in Figure 3.84. This trajectory intersects the RHIC plane at the same location, but with an angle of 1.42 mrad, a 13% reduction relative to the present RHIC injection system. Realizing that injection geometry also requires relocation of the initial downward pitching magnet upstream by 1 m.

Such a modification is straightforward and realizable with RHIC beams prior to EIC construction.

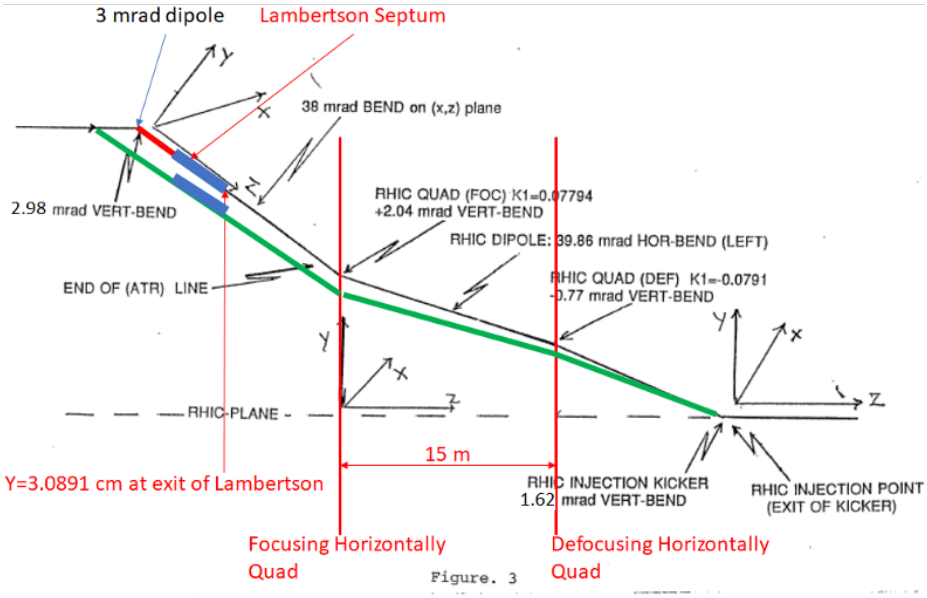

Figure 3.84: RHIC injected beam trajectory schematic, side view, not to scale

Summary

The hadron injectors are, with moderate upgrades, capable of meeting the highest performance requirements of the EIC for intensity, emittances and polarization. Table 3.33 summarizes the present and expected hadron injector performance for polarized protons as compared to EIC requirements in both the 'strong hadron cooling' and 'frequent on-energy injection' configurations. Parameters at AGS extraction assume a 10% intensity loss in EIC and full polarization transmission. Emittance requirements are based on the projected capabilities of the EIC cooling to cool the injector output emittances down to the EIC store emittance requirements.

Table 3.33: Summary table of polarized proton performance parameters at AGS extraction energy.

	AGS Extraction		EIC Required	
	Demonstrated	Improved	Strong H Cooling	On-energy Injection
Intensity [10^{11}]	3.0	3.0	3.0	3.0
$\epsilon_{x,y}$,norm. [µm]	2.5	2.0	2.5	2.0
Long. emittance [eV-s]	0.8	0.8	1.4	0.8
Polarization [%]	70	75–80	> 70	> 70

3.4.2 Polarized ^{3}He Ion Source

EBIS and ^{3}He Source Overview

The EIC will require an intense beam of polarized ^{3}He to achieve its physics goals. The polarized ^{3}He ion source will be an upgrade to the existing EBIS [144], which currently provides high charge state ions to RHIC and will remain the primary source of charged ions from D to U for the EIC. At one end of the EBIS an electron beam is produced, and then radially compressed by a 5 T solenoidal magnetic field before being dumped into an electron collector at the other end. The EBIS ion trap region is a series of cylindrical electrodes in the 5 T field. Ions are radially confined by the space charge of the electron beam and longitudinally confined by electrostatic barriers at the ends of the trap region. Ions are held in the trap until the desired charge state is reached, and then extracted by raising the potential of the trap and lowering the barrier. In the upgraded EBIS, there will be two 5 T solenoids. ^{3}He gas will be injected and ionized in the upstream solenoid, and ^{3}He ions will be trapped and breed to the $^3He^{++}$ state in the downstream solenoid. Parameters for the EBIS production of polarized $^3He^{++}$ are shown in Table 3.34. Modifications that need to be made for polarized ^{3}He production include the polarization of ^{3}He at 5 T fields, gas injection into the EBIS electrostatic trap, construction of a ^{3}He spin-rotator, and ^{3}He polarimeters. A conceptual illustration of primary components of the ^{3}He ion source inside the upstream end of the EBIS is shown in Figure 3.85.

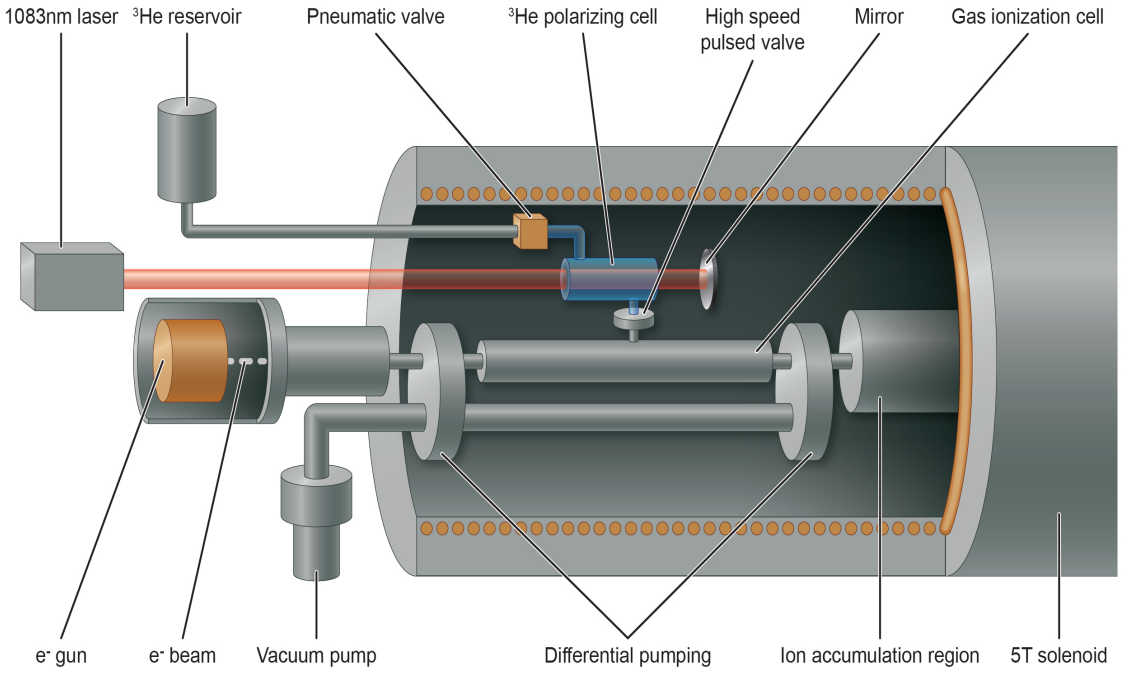

Figure 3.85: Conceptual illustration of the ^{3}He ion source components inside EBIS.

Table 3.34: EBIS parameters for $^3He^{++}$.

Parameter	Value
e-beam current [A]	10
e-beam energy [keV]	20
e-beam density [A/cm^2]	$\sim$575
^{3}He ion trap length [m]	1.5
Extracted beam pulse length [µs]	≤ 20
Trap capacity (charges)	1×10^{12}
$^3He^{++}$ yield	2.5–5$\times 10^{11}$
$^3He^{++}$ polarization	70%

^{3}He Polarization and Purification

The ^{3}He gas needs to be polarized before ionization such that a $^3He^{++}$ polarization of 70% is achieved in the EIC. ^{3}He gas at 1-5 Torr will be polarized in a cylindrical glass cell ($\sim$30 cm^3) inside the 5 T magnetic field of the EBIS solenoid using the technique of metastability exchange optical pumping (MEOP) [145]. An RF excitation of the ^{3}He gas will be created to populate the 2^3S metastable state, which will be optically pumped by a Keopsys 1083 nm fiber laser, and the nuclear polarization will be simultaneously polarized by hyperfine coupling. The ^{3}He polarization can be absolutely measured in the pumping cell by monitoring the transmission spectrum of a weak probe beam created by a 1083 nm Toptica diode laser. The ^{3}He pressure can also be inferred from the transmission spectrum since the polarizing cell must be isolated from pressure gauges during optical pumping. The maximum ^{3}He polarization is achieved in a time scale of about 10 minutes with some variation for ^{3}He pressure and purity. Continuous 5 Hz operation of the EBIS will require injection of $\sim 4 \times 10^{17}$ ^{3}He atoms per day, which corresponds to a 0.4 Torr pressure drop in the 30 cm^3 polarizing cell. Therefore, a 10 minute refill and polarize period will take place at most once a day to maintain a polarized ^{3}He reservoir for gas injection into EBIS. In between refills of the polarizing cell, the ^{3}He gas will be purified with a specialized 46 K cryopump to remove contaminants.

Gas Injection and Ionization

The ^{3}He gas will be ionized by the 20 keV, 10 A electron beam in a thin drift tube structure connected to the polarized ^{3}He reservoir by a high speed pulsed valve. A high vacuum is required outside the region of ^{3}He injection to produce a large $^3He^{++}/^3He^+$ ratio and for source recovery to generate other ion species after the 1 s switch time. The production of high charge states for heavy ions requires a high vacuum (10^{-9}-10^{-10} Torr) because ambi-

ent gas will neutralize the electron beam and undergo charge exchange interactions with the desired ions, both of which inhibit the production of high charge states. Therefore, the amount of gas injected into the EBIS needs to be minimized, the region for gas ionization needs to be isolated from the trap region for charge breeding, and the injected gas needs to be ionized and pumped out on a timescale compatible with the EBIS 5 Hz operation rep-rate to prevent build up of an ambient ^{3}He pressure after consecutive pulses.

In one configuration, the gas ionization cell is a 1 cm diameter 30 cm long drift tube with 0.5 cm constrictions at the ends and differential pumping. The small diameter will limit the amount of gas that needs to be injected into the EBIS to neutralize the electron beam, and the constrictions will limit gas flow from the gas ionization cell to the EBIS high vac-

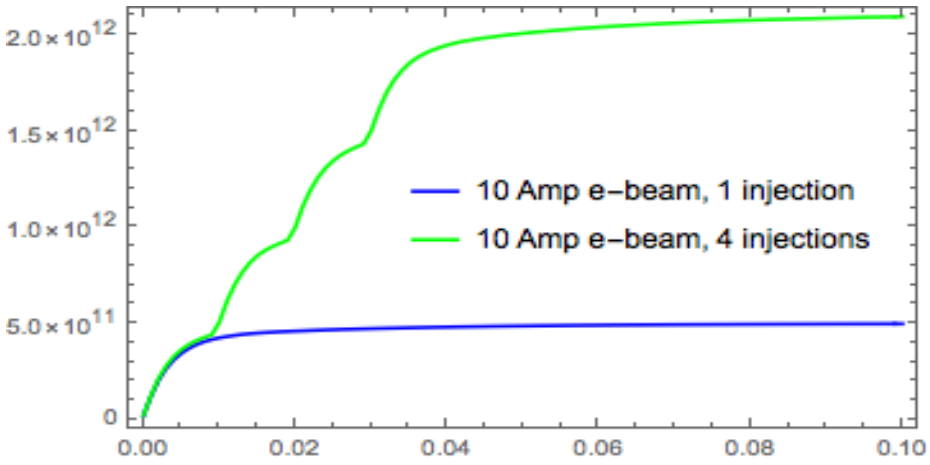

(a) Ionized ^{3}He.

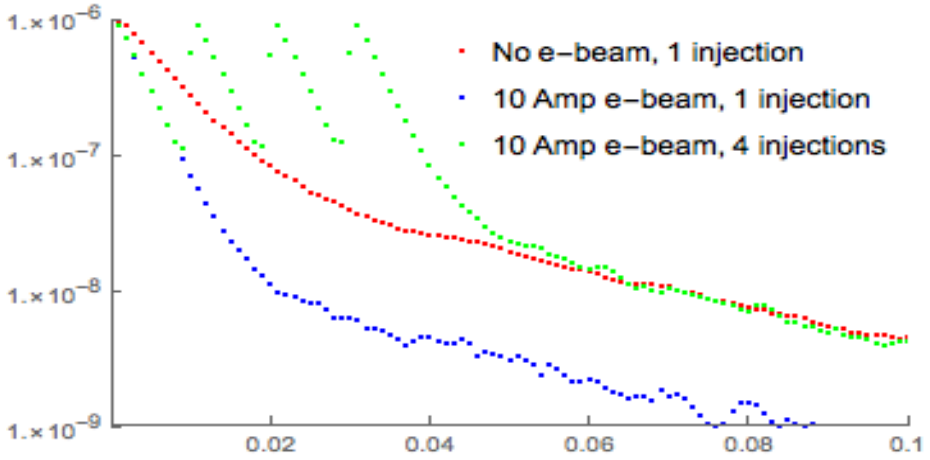

(b) Pressure (Torr).

Figure 3.86: The ionized ^{3}He atoms and ionization cell pressure versus time [s] after injecting 8.3×10^{11} of ^{3}He atoms per injection pulse. The number of ionized ^{3}He atoms trapped by the EBIS will be limited by the charge capacity of the electron beam.

uum regions. Polarized ^{3}He injection is implemented with a high speed pulsed valve that opens by the Lorentz force when a current is pulsed through a conductive plate in a high magnetic field. The conductive plate operates as a lever arm with a pad that seals a narrow orifice to the polarized ^{3}He reservoir. Such a valve has been in successful operation in the OPPIS source for several years. The pulsed valve opens on a time scale of ~500 µs and will have to inject ~10^{12} ^{3}He atoms to produce a uniform pressure of 10^{-6} Torr inside the gas ionization cell. The pressure is limited to 10^{-6} Torr for high vacuum EBIS performance. Simulations with MolFlow (a Monte Carlo simulator for high vacuum) show that the injected ^{3}He will diffuse into the ionizing region in 2 ms, and the 10 A electron beam will ionize ^{3}He to ^{3}He$^+$ with ~60% efficiency in <10 ms. If more ^{3}He gas needs to be injected to neutralize the electron beam while keeping the pressure below 10^{-6} Torr in the ionization cell, multiple gas injections can be used, see Figure 3.86a. In order to prevent build up of ^{3}He gas during consecutive pulses and enable fast switching of ion species, injected gas needs to be pumped out and the vacuum brought from 10^{-6} to 10^{-9} Torr in a time scale of 200 ms, see Figure 3.86b for estimated pump down times of the ionization region.

After ^{3}He is ionized to ^{3}He$^+$, the ^{3}He$^+$ ions quickly move downstream in less than 1 ms where conversion to ^{3}He^{++} will take place along the 1.5 m length of the ion trap in the downstream EBIS magnet. Separation of the gas ionization and ion trap regions reduces recombination effects and improves the ^{3}He^{++}/^{3}He$^+$ ratio. This separation is accomplished with potential barriers that limit the return of ^{3}He$^+$ and ^{3}He^{++} ions to the gas ionization cell. The conversion of 5×10^{11} ^{3}He$^+$ to ^{3}He^{++} in the 10 A electron beam takes place in 5 ms (see Figure 3.87), so the initial ionization of ^{3}He gas will be the limiting rate of production of ^{3}He^{++}. It will be necessary to limit the amount of injected ^{3}He gas so further ionization of ^{3}He after neutralization of the electron beam does not cause ^{3}He to be ejected from the ion trap downstream in the high vacuum region of EBIS. Time scales for the production of polarized ^{3}He^{++} in EBIS are shown in Table 3.35.

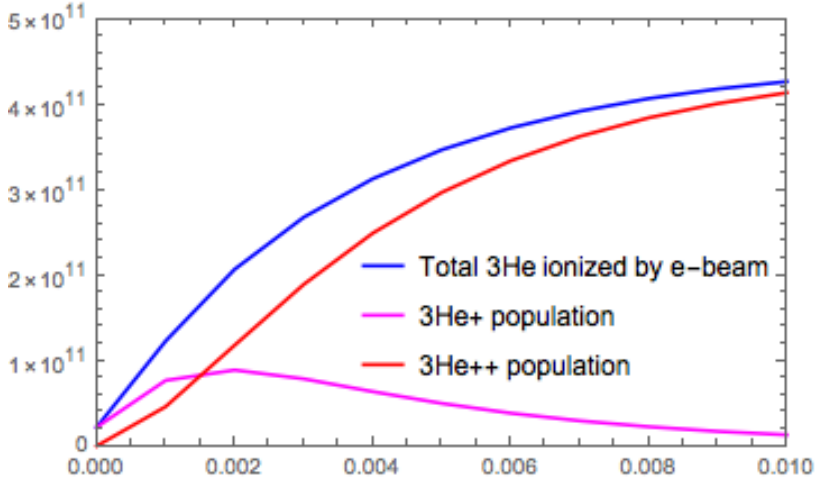

Figure 3.87: Ionization of ^{3}He gas and conversion of ^{3}He$^+$ to ^{3}He^{++} in a 10 A electron beam (time in seconds). Recombination effects are ignored.

Table 3.35: EBIS polarized $^3He^{++}$ production with 10 A electron beam.

Step Sequence	Time
^{3}He gas injection [ms]	0.5
Diffusion into ionization cell [ms]	2
Injected gas pressure falls 50% [ms]	3
Ionization of ^{3}He to $^3He^+$ per gas injection [ms]	∼10
Time constant for $^3He^+ \rightarrow {}^3He^{++}$ conversion [ms]	1
Pump down time (to 10^{-9} Torr) [ms]	100–150
5 Hz EBIS pulse repetition rate [ms]	200
Switching time between species [s]	1

Spin Rotator

The $^3He^{++}$ polarization state in the EIC will be set with a spin rotator in the HEBT (High Energy Beam Transport) line after the EBIS LINAC, which will align the $^3He^{++}$ polarization to the transverse vertical direction at 6 MeV beam energy.

One proposed layout for the spin direction alignment system is shown in Figure 3.88. The ^{3}He longitudinal polarization is first rotated to the transverse direction by the 21.5° bending magnet (1). Then the solenoid spin-rotator rotates the spin to the vertical direction. The spin-rotator will be a pulsed solenoid with a reversible field to enable spin flip of EBIS pulses on a pulse-by-pulse basis. The vertically polarized beam will be returned back to the straight HEBT line by the system of three dipole magnets (2,3,4) after the spin rotator solenoid. Beam quality will be preserved with a number of focusing quadrupoles, steering magnets, and beam diagnostics. A low-energy $^3He^{++}$ polarimeter can be installed in the straight beam line section after the dipole magnet (2).

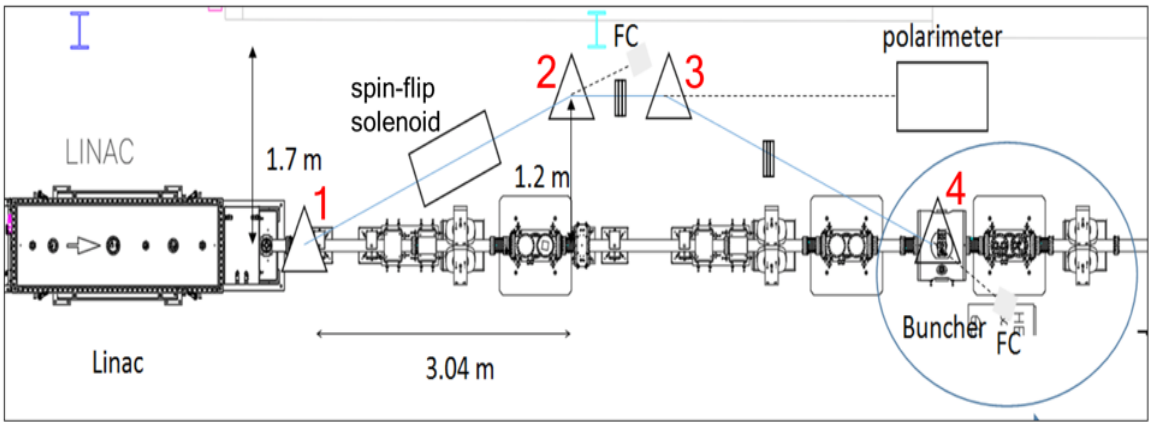

Figure 3.88: Concept of ^{3}He spin rotator.

Low-Energy Polarimetry

The $^3He^{++}$ polarization will be measured at 6 MeV after acceleration through the EBIS LINAC via scattering on an unpolarized ^{4}He gas target. A low-energy polarimeter design is shown in Figure 3.89. The analyzing power for elastic scattering of polarized ^{3}He on unpolarized ^{4}He is ideally $A_N = 1$ at a beam energy of ~5.3 MeV and $\theta_{CM} \approx 91^\circ$ [146,147]. For the 6 MeV polarized $^3He^{++}$ beam emitted from the EBIS LINAC, there is a local maximum at $A_N > 0.9$ and $\theta_{CM} \approx 96^\circ$ where the polarization can be determined by measuring the spin correlated asymmetry from scattered ^{3}He and ^{4}He. Silicon photodiode strip detectors will detect the scattered ^{3}He and ^{4}He over a range of center of mass scattering angles ($69^\circ < \theta_{CM} < 100^\circ$) and recoil particle energies (2.6-4.2 MeV for ^{3}He and 1.5-2.4 MeV for ^{4}He). Simultaneous detection of scattered ^{3}He and ^{4}He provides a coincidence signal to reduce background.

To produce an absolute polarization measurement, the polarimeter will be calibrated at 5.3 MeV either by decelerating the $^3He^{++}$ beam after the EBIS LINAC with a buncher or by detuning the EBIS LINAC to increase the energy spread. The ^{4}He gas target will be at 5 Torr with an effective target length of 1 cm. The statistical error for the ^{3}He polarization measurement is estimated at $(\delta P/P)_{stat} \approx 1.1\%/\text{min}$. Methods for high energy ^{3}He beam polarimetry farther down the accelerator chain are discussed in Section 6.7.

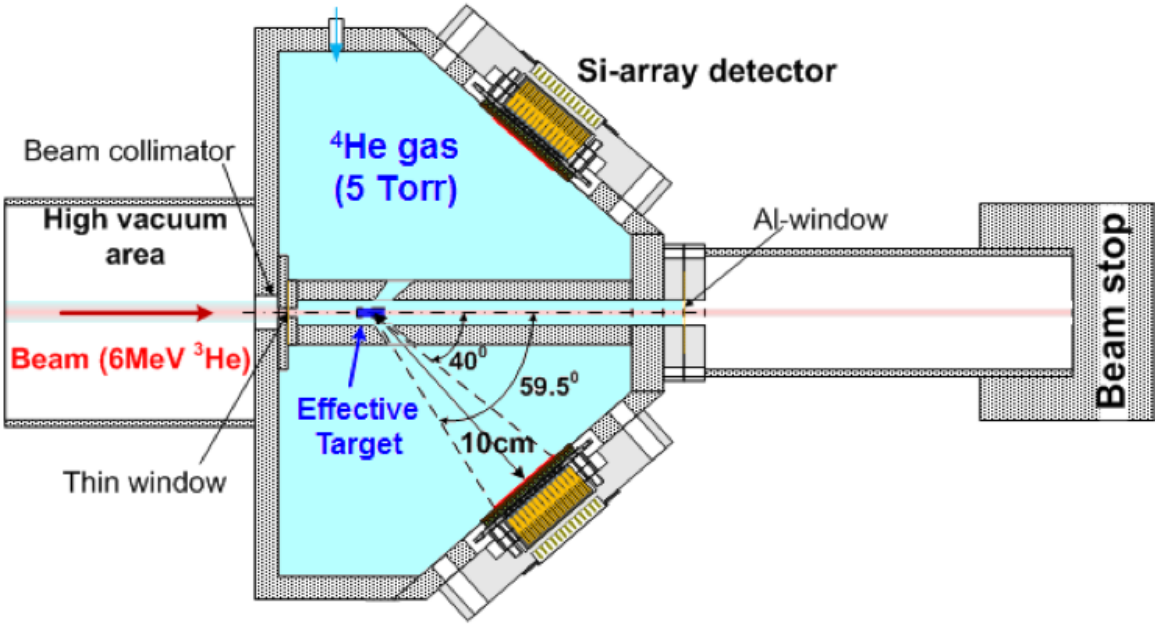

Figure 3.89: Concept for a low-energy ^{3}He polarimeter.

3.5 Electron Storage Ring Design

The electron storage ring with its 3834 m circumference will be installed in the existing RHIC accelerator tunnel. The elevation of the ring will be identical to that of the hadron ring as shown in Figure 3.90, thus avoiding vertical bends that would be detrimental to polarization. Similar to the hadron storage ring, the electron ring consists of inner and outer arcs as well in order to provide the required circumference.

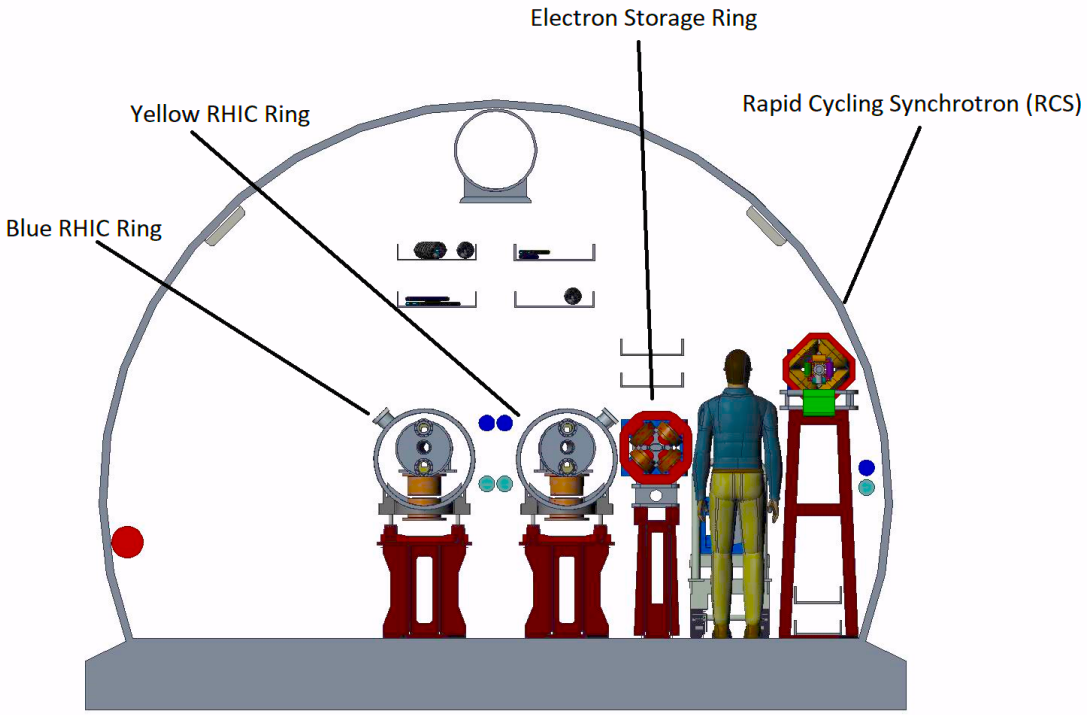

Figure 3.90: Tunnel cross section with the two RHIC hadron rings, the electron storage ring, and the Rapid-Cycling Synchrotron (RCS). There are 2 levels of cable trays per ring (shown above or below each ring). The water lines are represented by the solid circles (Red: water pipe for sprinkler system; Light-blue: cooling water supply; Dark-blue: cooling water return).

The six arcs consist of regular FODO cells with a cell length of 19 m. Each of these cells is comprised of two 0.6 m long quadrupoles, two 0.5 m long sextupoles, two 0.25 m long dipole correctors, and two bending magnet assemblies, as shown in Figure 3.91. To generate the required equilibrium emittances at different beam energies, appropriate betatron phase advances per FODO cell are chosen. At 5 and 10 GeV, the phase advance per FODO cell is 60°, while at 18 GeV it is set to 90°. The vertical emittance is adjusted by a vertical dispersion bump. Chromatic correction is accomplished by an interleaved scheme of sex-

tupole families, using 3 families per arc and per plane at for the 60° optics, and 2 families for the 90° optics. Additional sextupoles in the straight sections are available to fine-tune the driving term compensation and maximize the dynamic aperture.

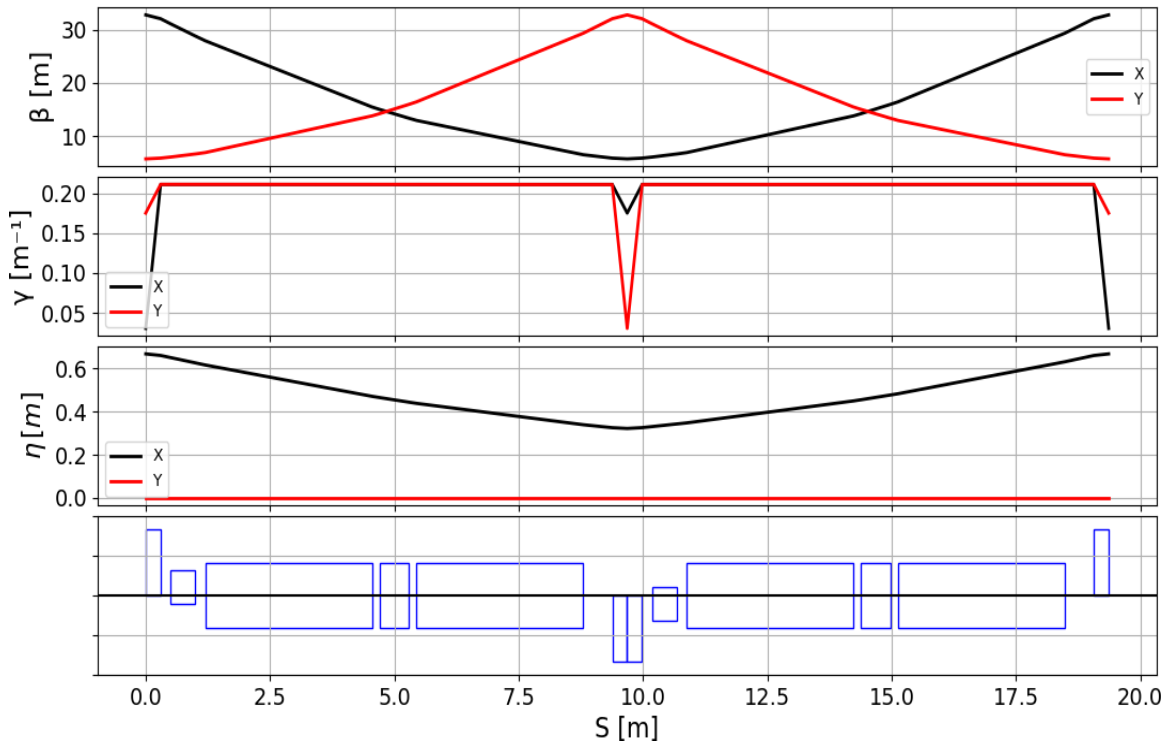

Figure 3.91: One FODO cell of the electron storage ring arc, tuned to 90° betatron phase advance.

The main bending dipoles consist of three segments each, with a short (0.597 m) dipole in the center in-between the two 3.352 m long magnets. This center dipole is powered independently in order to generate additional synchrotron radiation at low beam energies, thus increasing the synchrotron radiation damping decrement and therefore enabling large beam-beam tuneshift parameters over the entire energy range. At beam energies of 10 GeV and above, all dipoles have the same bending direction, thus maximizing the bending radius and therefore minimizing the synchrotron radiation losses. At 5 GeV, the center dipole provides a reverse bend with small bending radius in order to maximize radiation damping. Figure 3.92 illustrates the resulting orbits at different energies.

The EIC detector is assumed to be located in IR6. This straight section will be equipped with a low-β section around the collision point, using superconducting magnets. The electron and ion beam collide at the IP under a total crossing angle of 25 mrad. Spin rotation from the vertical orientation in the arcs to the longitudinal direction at the IP is accomplished by solenoid-based spin rotators. Two solenoids with subsequent horizontal bends are required on each side of the IP in order to provide longitudinal polarization at the IP

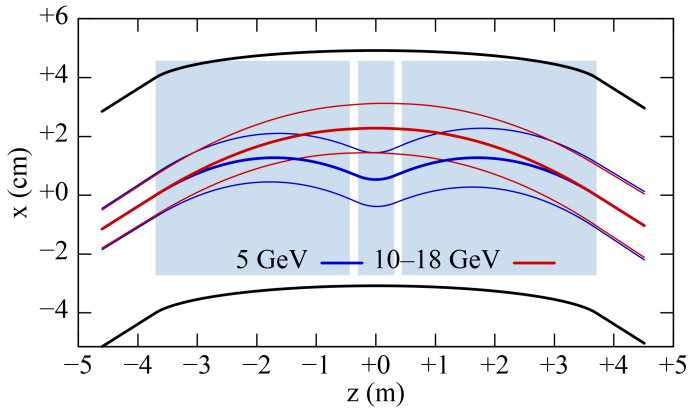

Figure 3.92: Superbend dipole assembly. The beam envelopes shown correspond to 10σ.

over the entire beam energy range from 5 to 18 GeV.

The ESR RF system (See Section 6.5.1) provides a total installed voltage of 68 MV and is located in IR10. Bunches from the Rapid-Cycling Synchrotron (RCS) will be injected into the storage ring in IR12. The bunch extraction and injection occur on the same turn using fast kickers. While the emittance and charge of the injected and extracted bunches are not identical, they are very close. This minimizes the discontinuity in the beam-beam force on the hadrons.

The vacuum system uses CuCrZr alloy beam pipes with a cross section of 80 mm $\times$ 36 mm. In the arcs the outer edge of the pipe is equipped with a water cooling channel to counteract the 10 MW of synchrotron radiation power impinging on the inside of the tube. This material has been chosen for its superior tensile strength and radiation shielding properties, as compared to both pure copper and aluminum.

3.5.1 ESR IR Straight Section

The colliding IR needs low β^* horizontally and very low β^* vertically. Furthermore, the IR contributes strongly to the chromatic properties of the ring and therefore has an adverse impact on the dynamic aperture. More lattice design is necessary to improve the IR design, and reduce the chromatic footprint and dynamic aperture of the storage ring. These IRs add to ring emittance as well.

The IR requires spin rotators to precess the spin longitudinally for the detectors. These spin rotators must be able to operate on a wide energy range from 5 GeV to 18 GeV. A dipole spin rotator would require too large an aperture due to orbit excursions at low energy. For this reason, we chose to use a spin rotator with two solenoid modules and two dipole modules as shown in Figure 3.93. The lengths of the solenoids were chosen such that the field will not exceed 7 Tesla.

Coupling compensation of these solenoids is accomplished by splitting each individual

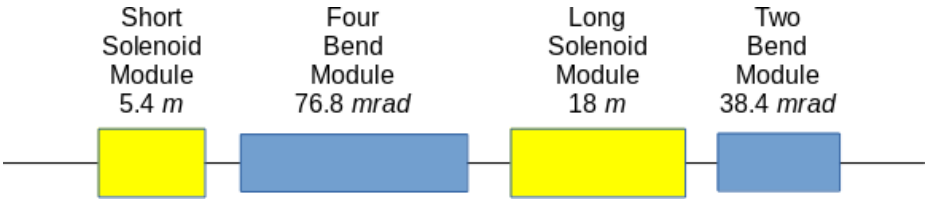

Figure 3.93: Schematic of the spin rotator modules used in the IR straight section. Yellow boxes indicate solenoid modules; blue boxes indicate bend modules. Lengths of solenoid modules are total lengths of solenoids, not total lengths of modules.

solenoid into two magnets of identical length. A set of six or seven quadrupoles in-between these two solenoids is tuned such that the they compensate each other in terms of betatron coupling and spin matching. A second interaction region and detector may be installed in IR8.

The IR straight is designed in three distinct modules denoted as:

1. Solenoid modules:
   These have two solenoids, each with half the length as indicated in Figure 3.93 , and six or seven quadrupoles, as shown in Figure 3.94. The spin-matched transfer functions for a fully decoupled solenoid insertion requires:

$$T = \begin{pmatrix} -\cos(\phi) & -\frac{2}{K_{\mathrm{sol}}}\sin(\phi) & 0 & 0 \\ \frac{K_{\mathrm{sol}}}{2}\sin(\phi) & -\cos(\phi) & 0 & 0 \\ 0 & 0 & \cos(\phi) & \frac{2}{K_{\mathrm{sol}}}\sin(\phi) \\ 0 & 0 & -\frac{K_{\mathrm{sol}}}{2}\sin(\phi) & \cos(\phi) \end{pmatrix} \tag{3.77}$$

   where $K_{\mathrm{sol}} = B_{\mathrm{sol}}/B\rho$, $\phi = (1+a)K_{\mathrm{sol}}L$, $a = 0.00115965$ and L is the solenoid length. Note, this only works for the case where we have regular quadrupoles between the solenoids.

2. Two and Four-bend modules:
   These provides the necessary spin precession along with the solenoid as part of the spin rotator.

3. The forward and rear magnets colliding modules:
   These modules are not symmetric and include a horizontal dogleg to shift the collision point 0.81 m into the ring relative to the current RHIC collision point. In addition, on the rear side, the beam is bent out of way for the luminosity monitor and e-tagger.

The full colliding IR is shown in Figure 3.95.

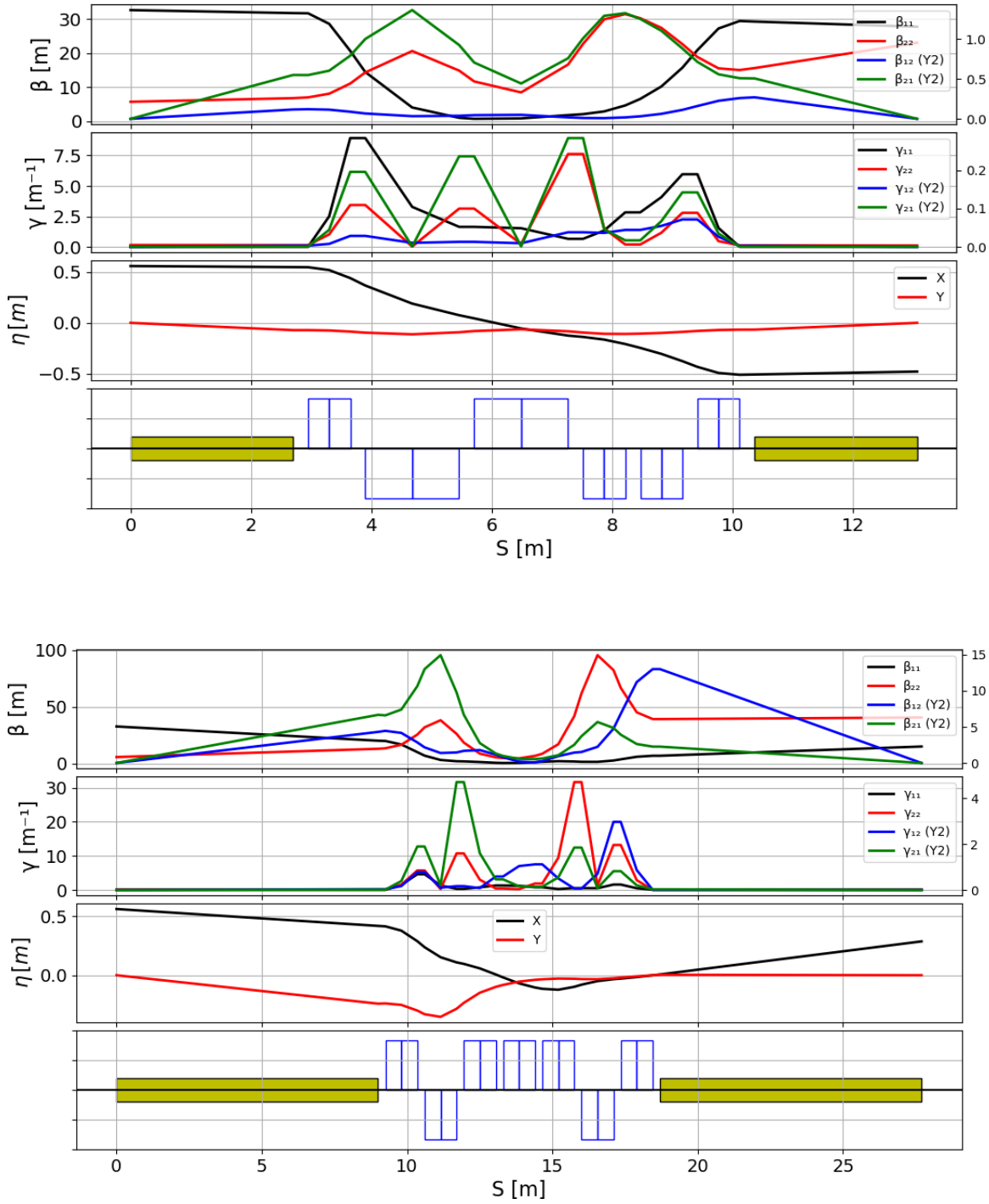

Figure 3.94: Short (top) and long (bottom) solenoid modules. For this design, the quadrupoles need to be super-conducting. Work on a design using normal quadrupoles is continuing. Yellow boxes indicate solenoids.

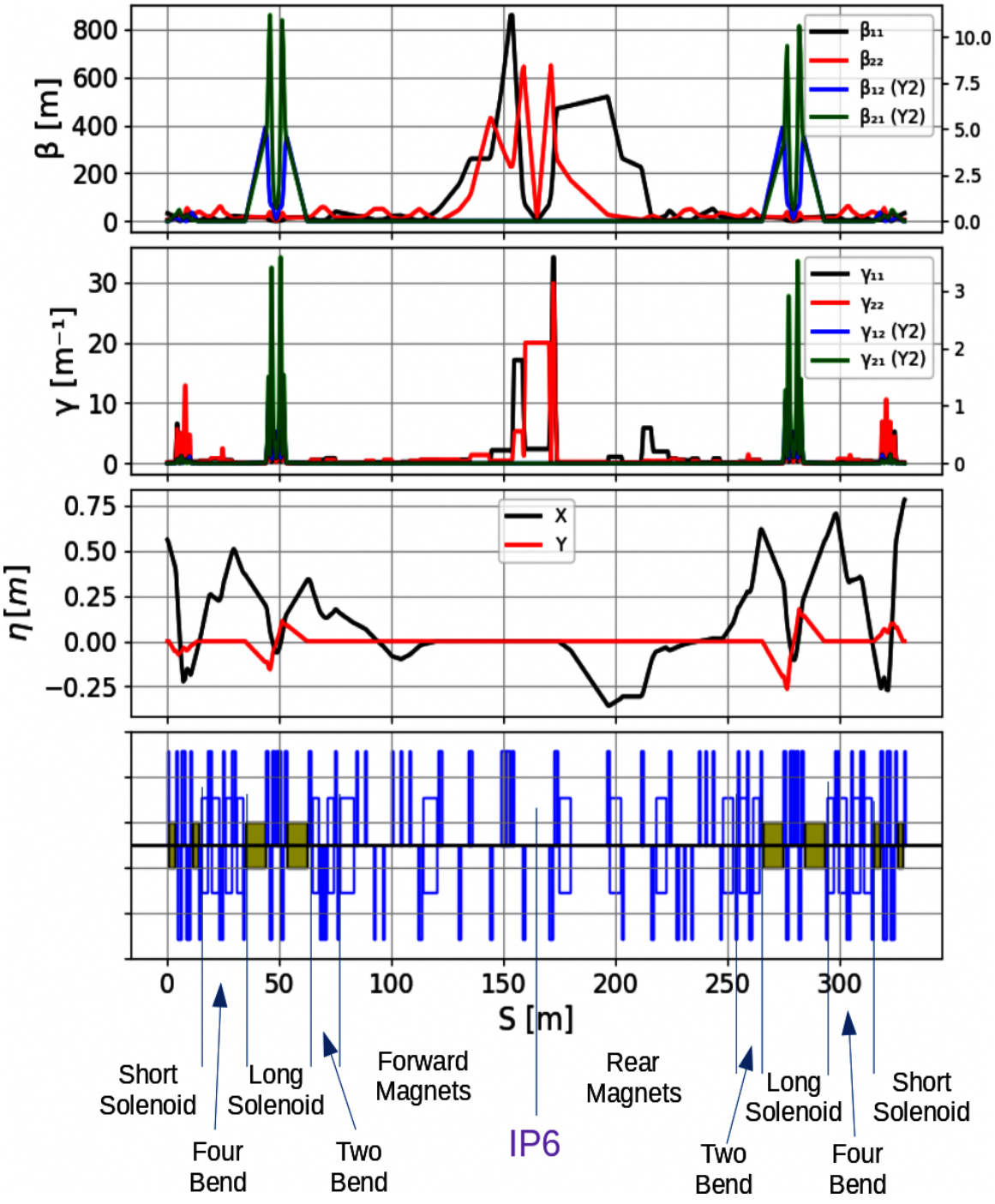

Figure 3.95: Full colliding IR, showing all modules. The most demanding case is shown with horizontal $\beta_{\max} \lessapprox 860\,\text{m}$ where $\beta_x^* = 42\,\text{cm}$ and $\beta_y^* = 5\,\text{cm}$.

3.5.2 ESR Spin Matching Conditions

In order to minimize the depolarization effects caused by synchrotron radiation induced diffusion the spin matching conditions on the rotator optics need to be satisfied. The spin matching conditions for solenoidal spin rotators can be obtained using general expressions for the function $F_5 = \gamma \partial \vec{n} / \partial \gamma$ [148]. Taking into account that the betatron coupling and vertical dispersion are fully compensated for each individual rotator insertion, one gets the following three conditions to nullify $\gamma \partial \vec{n} / \partial \gamma$ outside of the rotator area (in the bending arcs of the storage ring):

$$\sum_{\text{rot:}j=1,4} H_j(f_I) = 0 \tag{3.78}$$

$$\sum_{\text{rot:}j=1,4} H_j(f_I^*) = 0 \tag{3.79}$$

$$a\gamma \sum_{\text{rot:}j=1,4} H_j(D) + \sum_{\text{rot:}j=1,4} \phi_j k_{sj} - a\gamma \sum_{\text{bends:}i=1,4} \psi_i k_{si} = 0 \tag{3.80}$$

where

$$H_j(A) = \frac{\phi_j}{2} \left(\left(k_x A_1' + k_y A_3' \right)_{j,sol1} + \left(k_x A_1' + k_y A_3' \right)_{j,sol2} \right) \tag{3.81}$$

ϕ_j and ψ_i are correspondingly the solenoidal and bending angles of solenoid and bend modules of the IR straight. The summation (with the index j) is done over four solenoidal insertions, and indices $(j, sol1)$, $(j, sol2)$ denote correspondingly first and second solenoid of solenoidal insertion j. Indices x, s, y correspond to horizontal, longitudinal and vertical components. D is the dispersion function and f_I is a 4-D eigenmode of betatron motion corresponding to the horizontal motion in the arcs. Its components are: $f_{Ix} = \sqrt{\beta_{11}} e^{i\mu_I}$ and $f_{Ix} = \sqrt{\beta_{12}} e^{i\mu_I}$, where β_{11} and β_{12} throughout the IR straight are shown in Figure 3.95. The spin motion in this formulas is described by components of spin eigenvector $k = l - im$, where l and m are spin solutions on the design orbit orthogonal to the stable spin solution $\mathbf{n_0}$ and to each other. The first two spin matching conditions (Equations 3.78 and 3.79), related to the betatron degree of freedom, can be satisfied by a proper choice of the transport matrix of individual solenoid modules. The third spin matching condition (Equation 3.80), related with the longitudinal degree of freedom, is not satisfied in the present lattice. Satisfying this condition would require introducing dispersion in the rotator area. We plan to explore this possibility in future studies.

Figures 3.96, 3.97 and 3.98 show the optics, chromatic, and dispersion functions of the full ring, respectively,

Finally, IR8 is a second available colliding IR, if not in use, the solenoids are turned off and Figure 3.99 shows the optical functions.

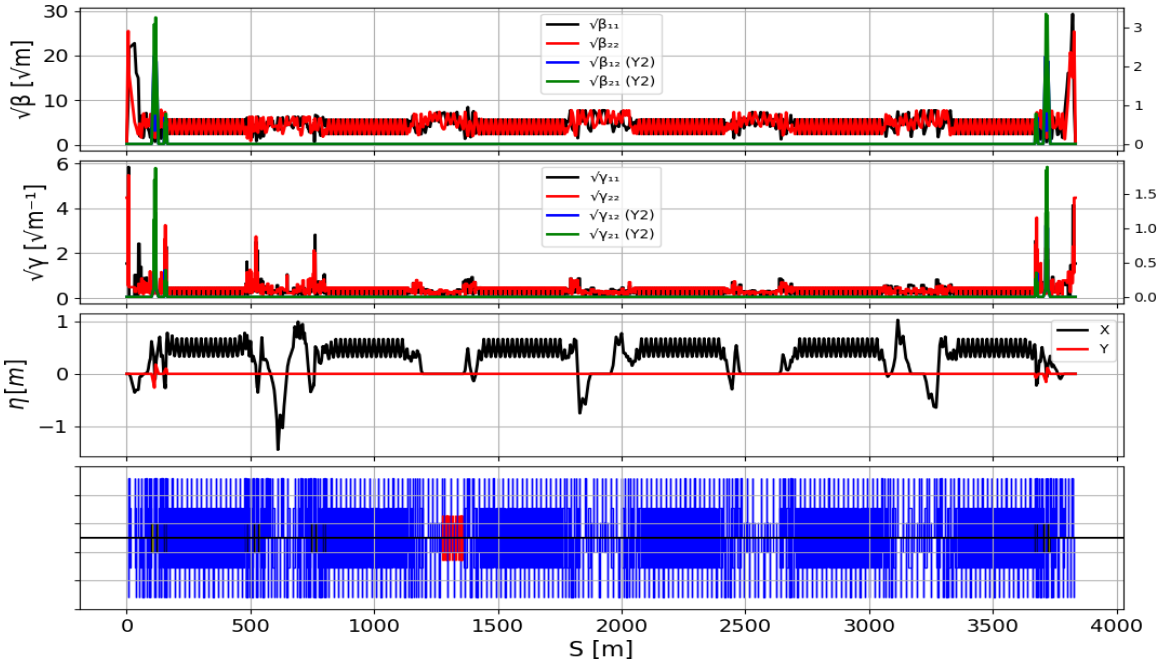

Figure 3.96: Twiss Optics functions for the full electron ring.

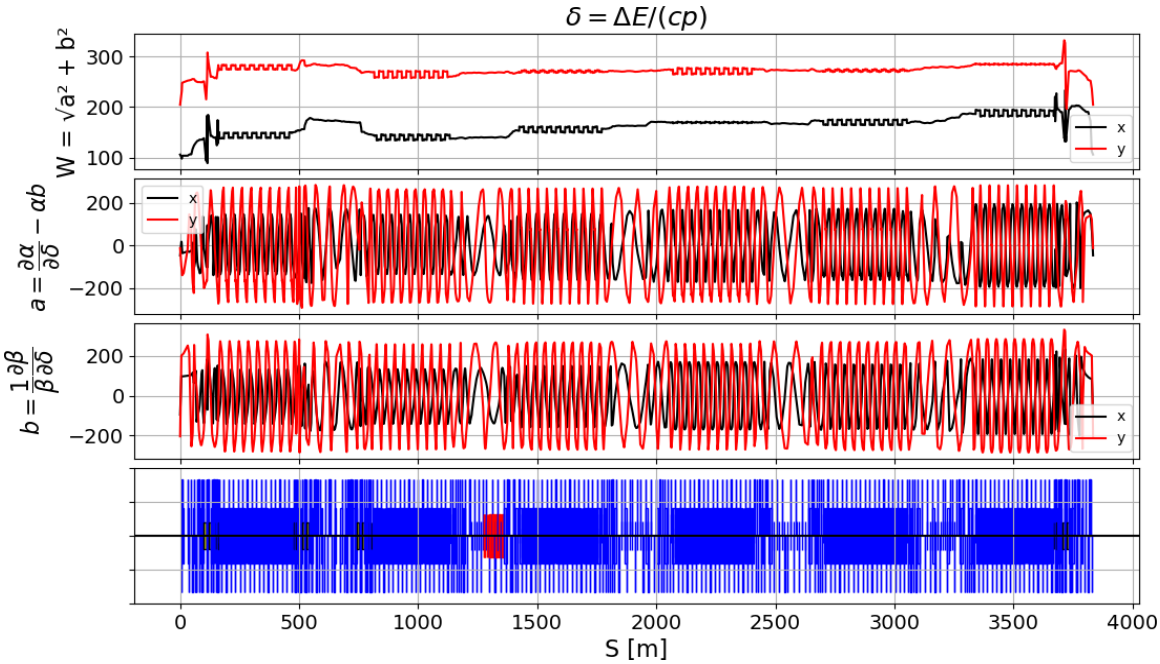

Figure 3.97: The chromatic functions of the full ring. This is with two families of sextupoles correcting only linear chromaticity.

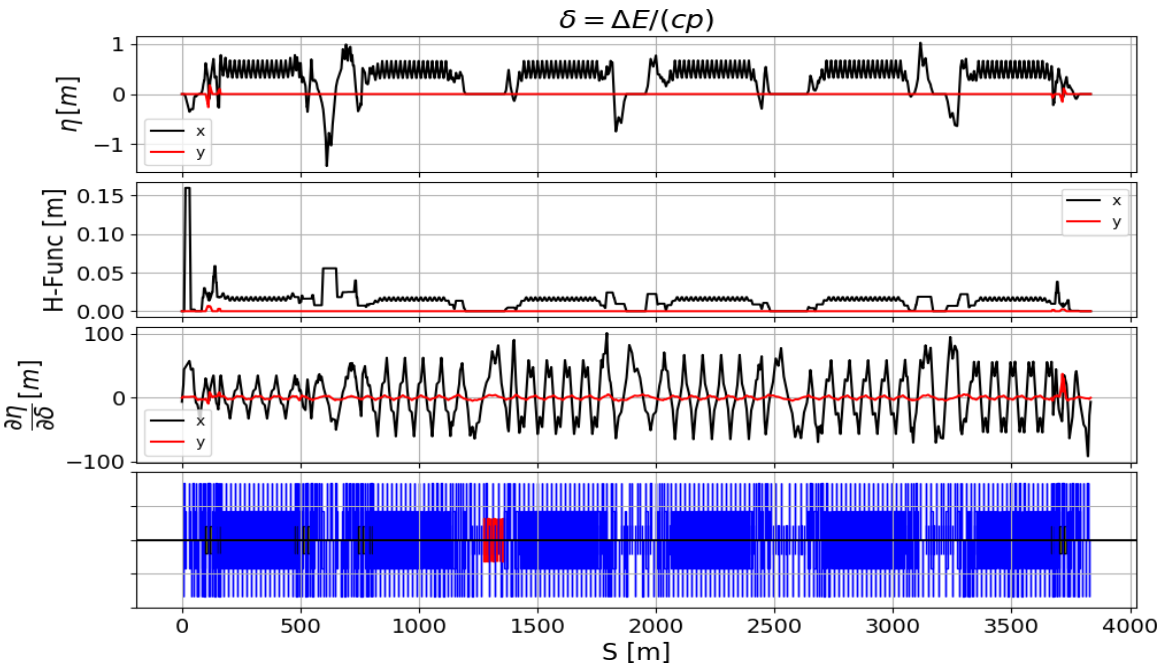

Figure 3.98: Dispersion functions of the full ring.

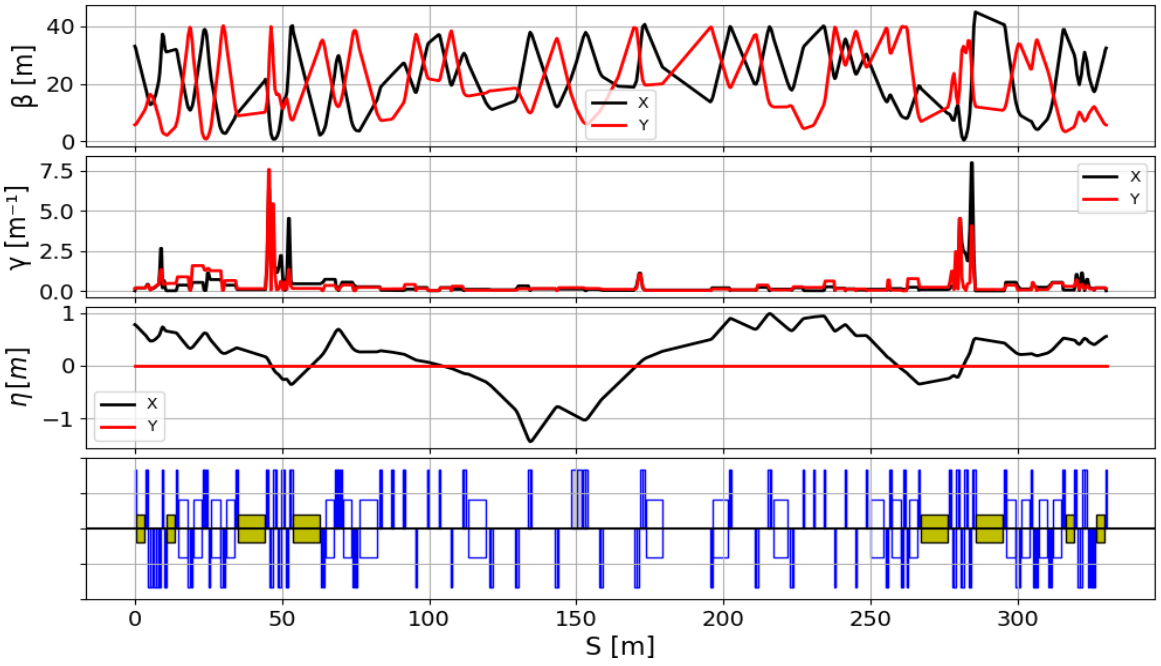

Figure 3.99: IR8 second colliding IR optimized for non-colliding mode. Solenoids are off.

3.5.3 ESR Utility Straight Sections

The utility straight sections where the beams do not collide are used in the ring for RF cavities, injection, extraction, amplitude dependent tune correction, etc. These sections include dispersion suppressors at the ends. Since the dispersion suppressors must work with both 60° and 90° arc FODO cells, enough quadrupoles through the dispersion suppressor are needed in the fitting. These straight sections should also have minimal impact on the dynamic aperture of the ring. This design follows a FODO-like structure with large enough space to include RF cavities, etc.

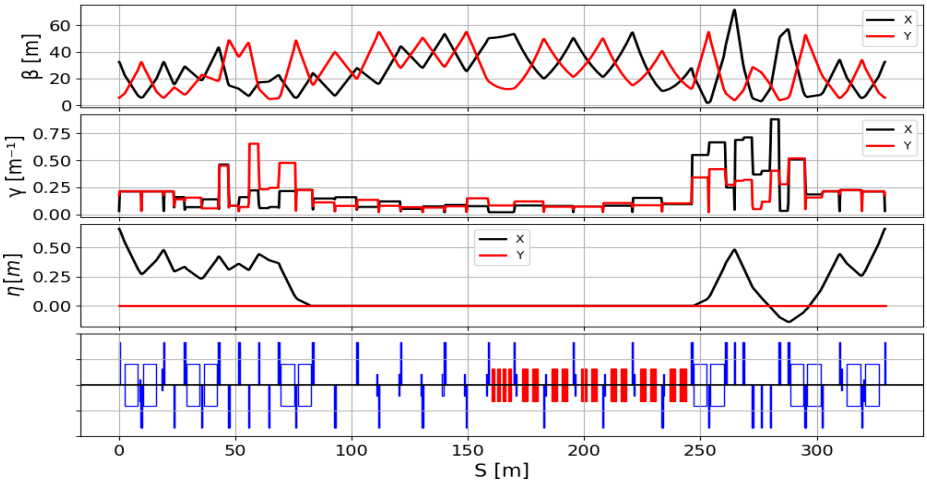

Figure 3.100: Optics of the IR10 straight section. Dispersion is fully corrected for the RF cavities. Both the normal and third harmonic cavities are shown.

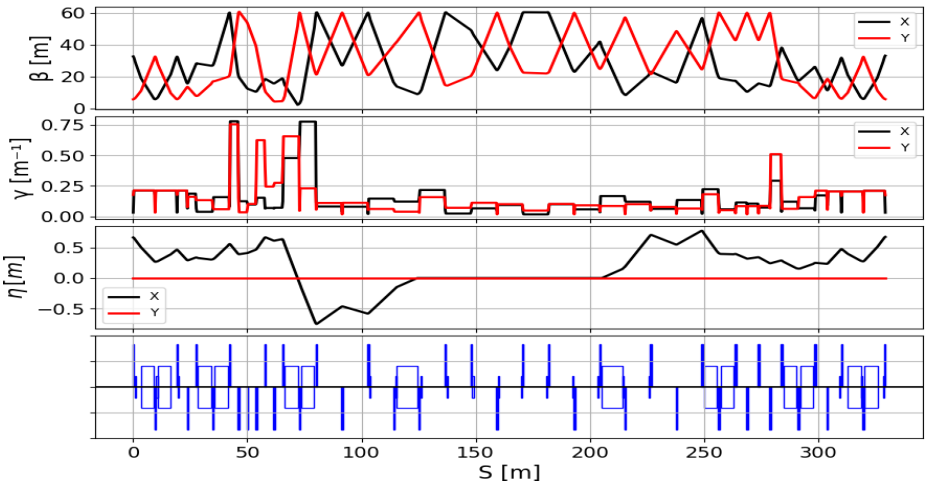

Figure 3.101: Optics of the IR12 straight section. This IR will be used for injection into the ring. Note, two dipoles were added to introduce a 32 mrad crossing angle to avoid the Hadron cryostat chamber.

The RF cavities will be installed in IR10 which must be dispersion free. IR10, IR2 and IR4 have sextupoles near each quadrupole in the dispersion-free areas for amplitude dependent tune correction. IR12 is planned for the injection line described in Section 3.8.5 as well as the polarimeters. The optics for these straight sections are shown in Figures 3.100 – 3.103.

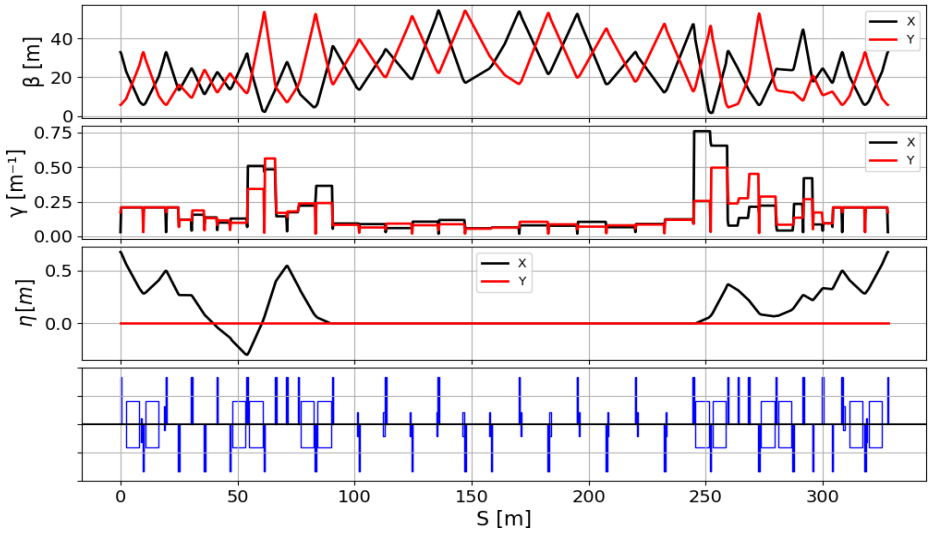

Figure 3.102: Optics of the IR2 straight section. The sextupoles for the amplitude dependent tune correction are included in the dispersion free areas.

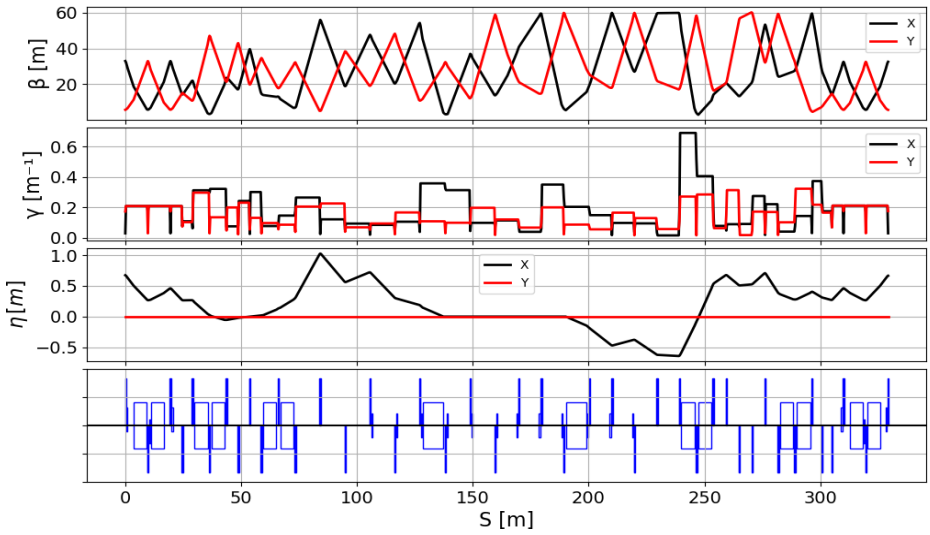

Figure 3.103: Optics of the IR4 straight section. Note, two dipoles were added to introduce a 32 mrad crossing angle to avoid the Hadron cryostat chamber.

3.5.4 ESR Arc Sections

The three goals for the design of the storage ring arcs is to (1) generate the small electron design emittance, (2) minimize radiation from the dipoles and (3) fit in the existing tunnel. The first two goals work against each other. To reduce the amount of radiation, a cell with a high packing is desired. To reduce the electron emittance, there are specialized cell designs to achieve this, but with reduced packing factor. Some cell designs – FODO cell, TAL (Triplet Achromat Lattice) and TBA (Triple Bend Achromat) [149, 150] – have been considered. Furthermore, the lower dispersion in the low emittance cells require larger sextupoles for correction. This could lead to smaller dynamic and momentum aperture. To reduce the cost of operation by minimizing the electron radiation, the FODO cell approach was chosen for its high packing factor. The electron emittance is acceptable in this design.

The main bending element is a super-bend consisting of three rectangular dipole magnets, see Figure 3.92. The super-bends allow us to increase the emittance at lower energies. Correctors, BPMs and sextupoles are kept next to the quadrupole. In order to increase the packing factor, the quadrupole is not centered between the super-bends, breaking the cell symmetry. To recover the overall machine symmetry, there are two kinds of arcs, denoted as F-Cells and its mirror-image G-Cells, as shown in Figure 3.104, the lengths of the elements are shown in Table 3.36.

Table 3.36: Dimensions for the F-Cell/G-Cell; the G-Cell is mirror-symmetric to the F-Cell. The BPMs will fit in the 20 cm space between the quadrupole and sextupole. The super-bend dipole consist of three dipoles separated with a 15 cm space, see Figure 3.92

Parameter	Value
Cell length [m]	19.365
Dipole Ends length [m]	3.352
Dipole Center length [m]	0.597
Dipole bend angle [mrad]	25.525
Dipole bending radius [m]	294.268
Quadrupole length [m]	0.6
Sextupole length [m]	0.5
Corrector length [m]	0.25

There are 16 FODO cells per arc with 6 arcs total. Figure 3.105 shows a schematic of the entire ring. IRs and straight sections, shown, will be matched to these arcs. The cell dimensions provide an emittance of about 22 nm in the ring at 10 GeV. At 18 GeV the emittance is about 32 nm with this cell. Using the super-bends or a small radial shift, the emittance can be manipulated. Currently, the super-bend is assumed to be off for 10 GeV and above. Figure 3.106 shows the electron ring doesn't deviate far from the existing RHIC rings. This solution fits in the tunnel.

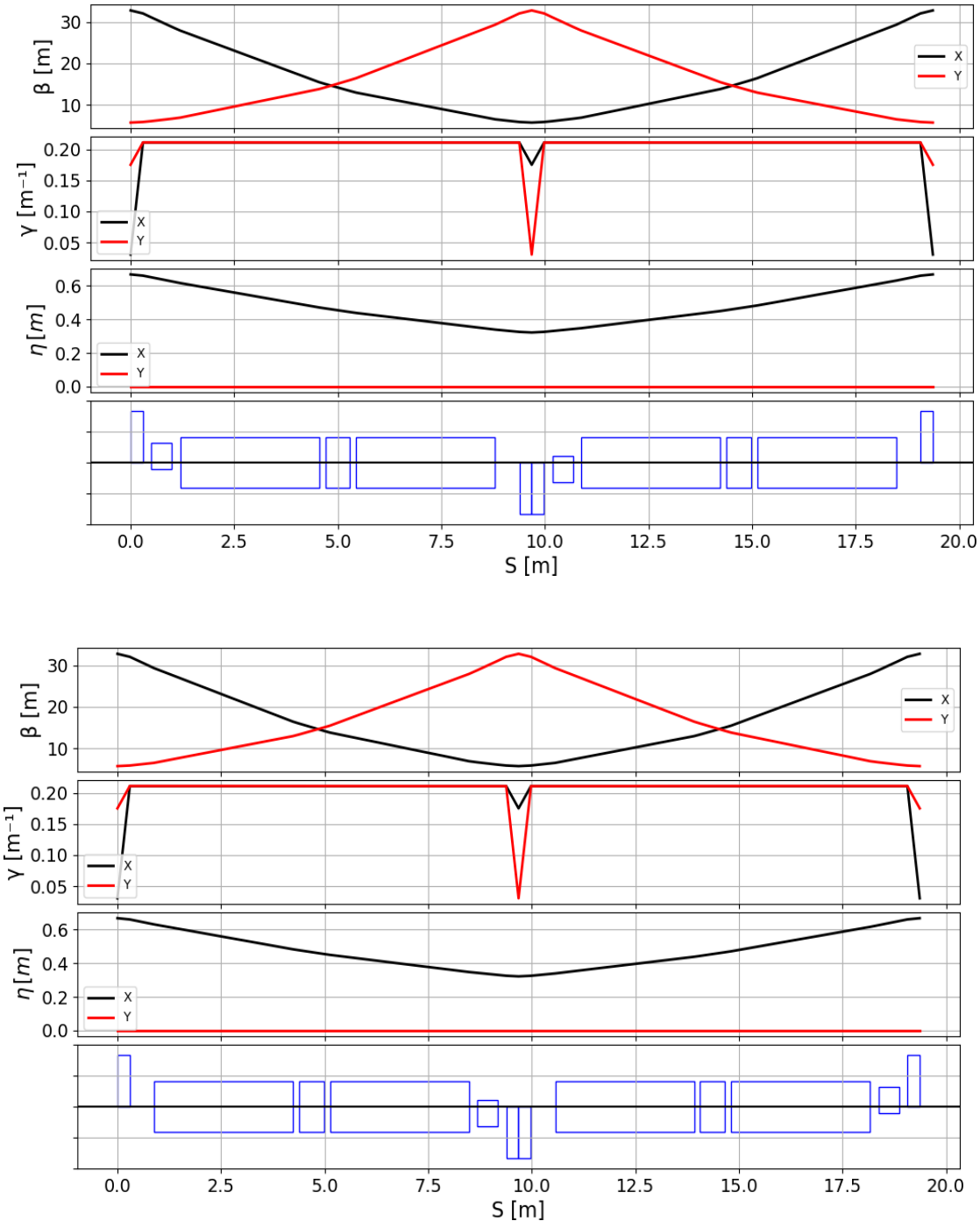

Figure 3.104: Arc FODO cells: F-Cell (top) and G-Cell (bottom). To increase the packing factor, the quadrupole is not centered between the dipoles. G-Cell is the mirror image of the F-Cell to retain overall ring symmetry.

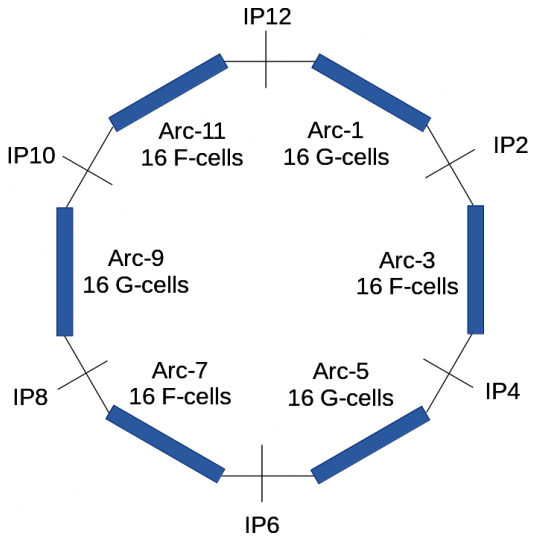

Figure 3.105: Schematic of the electron storage showing the arc FODO cell arrangement. The colliding IRs are at IP6 and IP8. The other IRs are straight sections.

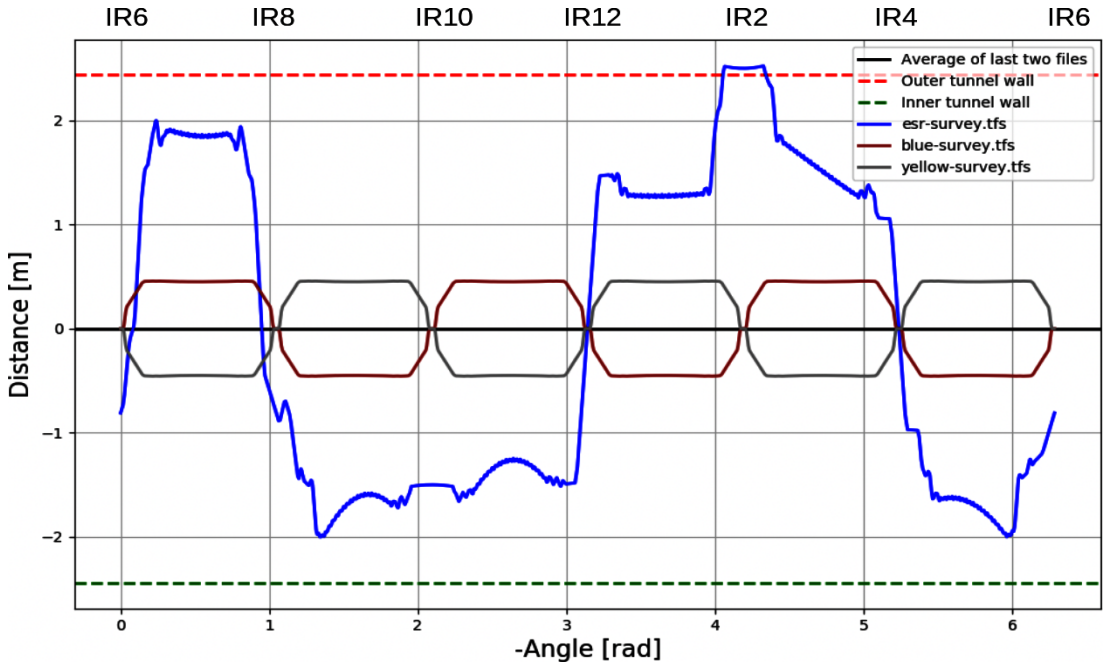

Figure 3.106: Fitting the electron storage ring (blue) into the tunnel. This shows the electron storage ring relative to the existing Blue ring (brown), Yellow ring (gray) and center line (black). The inner and outer tunnel walls are shown with dashed lines. This picture doesn't show the IR housing which extends beyond the tunnel walls, such as in IR2. The angle increases positively in the clockwise direction starting IP6.

3.5.5 ESR Orbit Correction Scheme

To establish beam during commissioning and to optimize the orbit during operation, a suite of orbit correction algorithms/schemes are indispensable for the electron storage ring. These algorithms will include the existing algorithms in RHIC and new developments. The orbit correction algorithms/schemes in RHIC [151], sliding bump, first turn SVD, MICADO and SVD, can all be adopted for the electron storage ring.

Minimizing spurious vertical dispersion is beneficial for electron beam polarization. To achieve minimal vertical dispersion, precision alignment of quadrupole magnets is required in the first place. With unavoidable misalignment of quadrupoles, the goal of orbit correction is to either center the beam in all the quadrupoles or all the BPMs. A compromise of these two should be obtained by dispersion-free steering [152, 153], which correct orbit and dispersion function simultaneously with proper weighting.

3.5.6 ESR Emittance Control Scheme

Synchrotron radiation gives the electron beam its equilibrium emittance, and we can adjust that emittance by varying the amount of radiation produced. Furthermore, increased radiation damping can permit operation at a higher beam-beam tune shift.

We control the amount of radiation produced in the storage ring by placing three dipoles, instead of a single dipole, between the arc quadrupoles. At high energies, where the radiation produced is if anything more than desired, all three dipoles will have the same field. At lower energies, the central dipole will have a high field, higher than even the field for the high energy beam. This can be used for radiation production for the lower energy beam. Figure 3.92 shows the dipole configuration and orbits at different energies. There are three costs to this scheme:

- higher dipole fields are required;
- the orbits are different for each energy, requiring wider dipoles and apertures;
- the additional drifts between dipoles reduces the dipole packing fraction, leading to more radiation production at higher energies.

The design requirements for the split arc dipoles are given in Table 3.37. The three dipoles will fit in place of a circular arc of a given length and angle. Not all dipoles in the ring will be split, only those which are identical to standard arc dipoles. The dipoles that are not split will have fields corresponding to the arc length and bending angle given in Table 3.37. Physical constraints will dictate a minimum drift length between dipoles; the length used here was chosen to be as small as possible while keeping the coupling between adjacent dipoles sufficiently low. The maximum dipole field is chosen to keep the dipoles sufficiently far from saturation that the field quality will be nearly identical for the field settings for any energy.

Table 3.37: Design requirements for the split dipoles.

Parameter	Value
Circular Arc Length for Dipoles [m]	7.4
Bend Angle [rad]	$2\pi/264$
Number of Super-bends in Ring	252
Drift between Dipoles [m]	0.15
Maximum Dipole Field [T]	0.7
Minimum Electron Total Energy [GeV]	5

The dipole design is capable of producing a transverse damping decrement (energy loss per turn divided by $2\beta^2 E$, where β is the relativistic β and E is the total beam energy) of 2.5×10^{-4} for the 5 GeV beam, though we do not intend to run with this level of radiation. The larger damping decrement was chosen based to be approximately the value used in KEK-B [19].

Taking the design requirements from Table 3.37, we split the arc dipole to minimize the maximum magnet width. Three rectangular dipoles are used. For our parameters, making the center dipole bend outward at the lowest energy and be as short as possible, while staying below the maximum dipole field at that lowest energy, gives the design with the smallest dipole width. The resulting parameters are given in Table 3.38.

The dipoles and their orbits are shown in Figure 3.92. Table 3.38 gives dipole field values, radiation loss, and the Sokolov-Ternov (de-)polarization time [154] at the design energies.

Table 3.38: Settings and resulting physical parameters at design energies.

Total Energy	5 GeV	10 GeV	18 GeV
Inner Bend Field [T]	-0.456	0.138	0.248
Inner Bend Angle [mrad]	-12.2	1.8	1.8
Outer Bend Field [T]	0.113	0.138	0.248
Outer Bend Angle [mrad]	18.0	11.0	11.0
Energy Loss per Turn [MeV]	1.3	3.7	38
Sokolov-Ternov Time [h]	12.4	9.8	0.5
Inner Dipole Length [m]		0.59	
Outer Dipole Length [m]		3.25	
Orbit Width [mm]		14	

3.5.7 ESR Aperture Requirement

The vacuum chamber of the EIC electron storage ring (ESR) must provide sufficient aperture to ensure a beam lifetime of several hours under realistic operational conditions. Besides providing a minimum aperture of 15σ around the design orbit, horizontal and vertical orbit errors Δx_{orbit} and Δy_{orbit} have to be accommodated. In addition, the horizontal design orbit varies as a function of beam energy due to the super-bends, as shown in Figure 3.92.

The requirements on the horizontal and vertical aperture radii can therefore be expressed as:

$$A_x \geq 15\sqrt{\sigma_{\beta_x}^2 + \sigma_\delta^2} + \Delta x_{\text{orbit}} + \Delta x_{\text{superbends}} \tag{3.82}$$

$$A_y \geq 15\sqrt{\sigma_{\beta_y}^2} + \Delta y_{\text{orbit}}. \tag{3.83}$$

When calculating the horizontal and vertical RMS beam sizes σ_{β_x} and σ_{β_y}, we take into account the uncoupled horizontal emittance ϵ_x and the fully coupled vertical emittance $\epsilon_y = \epsilon_x/2$ despite the fact that the design vertical emittance is significantly smaller. This ensures sufficient vertical aperture even under less-than-ideal conditions, as typically occurs during machine commissioning.

Table 3.39 lists the parameters and resulting aperture requirements for the two most extreme cases, 5 GeV and 18 GeV, of electron beam energy.

Table 3.39: Aperture requirements for 5 and 18 GeV electron beam energy.

Parameter	5 GeV	18 GeV
uncoupled ϵ_x [nm]	20	22
fully coupled ϵ_y [nm]	10	11
$\hat{\beta}_x$ [m]	30	30
$\hat{\beta}_y$ [m]	30	30
$\hat{D}_x$ [m]	1.0	0.5
$\Delta p/p$	1×10^{-3}	1×10^{-3}
Δx_{orbit} [mm]	10	10
Δy_{orbit} [mm]	5	5
$\Delta x_{\text{superbends}}$ [mm]	11	11
A_x [mm]	40	35
A_y [mm]	13	14

It is worthwhile mentioning that the maximum orbit excursion due to the superbends, $\Delta x_{\text{superbends}}$, occurs in the center of the dipole section, while both the RMS beam sizes and the orbit errors reach their maximum in the quadrupoles in-between those dipole sections. The minimum aperture radii listed are therefore slightly pessimistic by a few millimeters. A horizontal aperture radius of 40 mm is sufficient.

3.5.8 ESR Vacuum System Requirements

Introduction and Requirements

The EIC electron storage ring (ESR) is to store multi-bunch electron beam with current up to 2.5 A, energy up to 18 GeV and synchrotron radiation (SR) power up to 10 MW. The electron storage ring vacuum system provides sufficient and low impedance aperture for the circulating electron beam and maintains ultrahigh vacuum for adequate beam lifetime, low beam loss and low bremsstrahlung radiation. The storage ring vacuum system includes all vacuum chambers, vacuum pumps, vacuum valves as well as vacuum instrumentation and control. There are a few significant challenges in the storage ring vacuum systems:

- Provide sufficient aperture to the stored electron beams having energy from 5 GeV to 18 GeV, including the lower energy beam orbits with reverse bends;
- Handle the large heat load from SR with proper cooling and masking, while maintaining smooth surfaces to minimize the broadband impedance and heating;
- Shield the other accelerator components from the high energy X-ray radiation and damage;
- Reduce the background in the experimental detectors, with ultrahigh vacuum, proper masking and shielding.

Some details related to these requirements will be discussed briefly in this section. More details regarding the vacuum system design can be found in Sections 3.2.3 and 6.4.1.

Storage ring vacuum systems consists of a few distinct regions: the 6 arcs of $\approx$ 257 m length each, the 12 straight sections of $\approx$ 123 m length each bracketing the IRs, and 6 IRs of $\approx$ 136 m length, which contain EIC experiment(s), superconducting cavities, injection and extraction. Each arc section consists of 32 half-cells with a length of 9.683 m containing dipole, corrector, quadrupole and sextupole magnets. Each straight also has 6 dipole magnet sections. For ease of installation, maintenance and troubleshooting, each arc will be divided into 2 vacuum sections, while the straights and IRs will be divided into two to three vacuum sections, each isolatable with RF shielded gate valves. There will be $\approx$ 40 vacuum sections in the electron storage ring.

The average pressure in the arcs with beam is designed to be less than 1×10^{-8} Torr with the main residual gas being hydrogen. There are three major beam-residual gas

interactions which cause beam loss in the storage ring, namely electron-electron elastic scattering, electron-nucleus elastic scattering, and electron-nucleus inelastic scattering (bremsstrahlung). Both electron-electron and electron-nucleus elastic scattering decrease slowly with increasing electron energies, while bremsstrahlung is independent of electron energy at GeV range. All three cross sections are proportional to the atomic numbers of the residual gases, i.e. become much larger for higher Z molecules. Assuming a residual gas composition of 90% H_2 and 10% CO at a pressure of 10 nTorr, the estimated beam-gas lifetimes τ_{B-G} can be calculated by:

$$\tau_{B-G} = \frac{1}{Nc(\sigma_{e-e} + \sigma_{e-n} + \sigma_{brems})} \tag{3.84}$$

Here $c = 3 \times 10^8$ m/sec is the velocity of the electrons, N is the density of the gas (number of particle per cm^3) that can be expressed as $3.2 \times 10^7 P$, with P in nTorr. The calculated cross sections and lifetimes at 10 nTorr are given in Table 3.40 for a few electron energies. At this pressure level, τ_{B-G} will be over 20 hours, much longer than the Touschek lifetime [155] of a few hours caused by electron-electron scattering within the short bunches. The electron bunches in the storage ring will be replaced with new bunches from the injector at a rate of 1 Hz, such that the 290 bunches during 18 GeV operations will be refreshed every 2.4 minutes. Therefore, the beam-gas lifetime at the design pressure of 10 nTorr is more than adequate. Nevertheless, the ionized gas molecules can be trapped in the short bunch spacing and cause beam instability. Thus, ultrahigh vacuum of a few nTorr is still required to minimize the residual gas ionization in the arcs and straight sections. The required pressure at the IR and upstream of the detector must be less than 1 nTorr in order to minimize the background in the experiment detectors.

Table 3.40: Calculated beam-gas interaction cross sections and the beam-gas life times at 10 nTorr vacuum, assuming a residual gas composition of 90% H_2 and 10% CO.

E [GeV]	σ_{e-e} [cm^{-2}]	σ_{e-n} [cm^{-2}]	σ_{brems} [cm^{-2}]	σ_{B-G} [cm^{-2}]	τ_{B-G} [h]
5	1.6×10^{-26}	5.6×10^{-25}	9.0×10^{-25}	1.5×10^{-24}	20
10	8.2×10^{-27}	1.4×10^{-25}	9.0×10^{-25}	1.0×10^{-24}	28
18	4.5×10^{-27}	4.4×10^{-26}	9.0×10^{-25}	9.5×10^{-25}	31

Vacuum Chamber Materials

Aluminum was usually used as the vacuum chamber material for most electron storage rings, because it can be inexpensively extruded with multi-channel cross sections consisting of electron beam tube, ante-chamber for pumps, water cooling channels, and extrac-

tion slots for synchrotron radiation. Aluminum provides low magnetic permeability, ease of machining and welding, and good electrical and thermal conductivity. Discrete copper alloy absorbers are typically installed in these types of aluminum chambers to intercept photons wherever localized high heat load and high-power density are present.

However, for very high energy and high current electron storage rings such as B-factories, copper was selected as the chamber material, either oxygen-free copper (OFC) or special copper alloys. In addition to higher thermal conductivity and higher strength, copper, with higher Z than aluminum, provides better attenuation and shielding for high energy X-rays, thus protecting surrounding equipment from radiation damage. As shown in Figure 3.107, the attenuation length of Al is 20 times longer than that of Cu, and the radiation dosage outside a copper chamber of a few millimeter wall will be 2–3 orders of magnitude lower than that of an aluminum chamber. For the above reasons, copper alloy will be the choice material for EIC electron storage ring vacuum chambers.

A comparison of the energy, current, X-ray critical energy and SR power loads of a few high-power electron storage rings is given in Table 3.41. Copper alloy was selected for most of them when potential power density exceeded tens of W/mm^2. Due to high energies, high current and strong reverse bends, the EIC electron storage ring does have the highest linear power and power densities compared with KEKB, PEP-II, and HERA. It is therefore natural to select copper as storage ring chamber material.

Table 3.41: Comparison of power, power density, critical energy of X-ray and other parameters of a few high current and high energy electron storage rings. The power density at the chamber wall can be reduced by decreasing the angle of interception through tapering, and may not be the same as stated in this table.

Parameter	KEKB	S-KEKB		PEP-II		HERA	EIC	
	HER e^-	LER e^+	HER e^-	LER e^+	HER e^-	e^-	D2	D1/D3
E [GeV]	8	4	7	31	10	30	5	18
I [A]	1.1	3.6	2.6	3.2	2.1	0.06	1.28	0.27
C [m]	3016	3016	3016	2199	2199	6338	3834	3834
γ	15656	7828	13699	6067	19569	58708	9785	35225
P [MW]	3.8	1.1	5.3	1.3	11.1	7.1	3.0	10.5
$\hat{P}/l$ [kW/m]	5.8	2.2	8.0	1.2	11.6	1.8	19.9	6.9
$\langle \hat{P}/A$ [W/mm^2]$\rangle$	14	2	17	4	29	8	16.8	37
E_c [keV]	10.9	1.9	7.3	4.8	9.8	76	11.6	54
ρ [m]	104.5	74.7	104.5		165	610.4	23.8	240.2
material	Cu	Al	Cu	Al	Cu	Cu	Cu	Cu

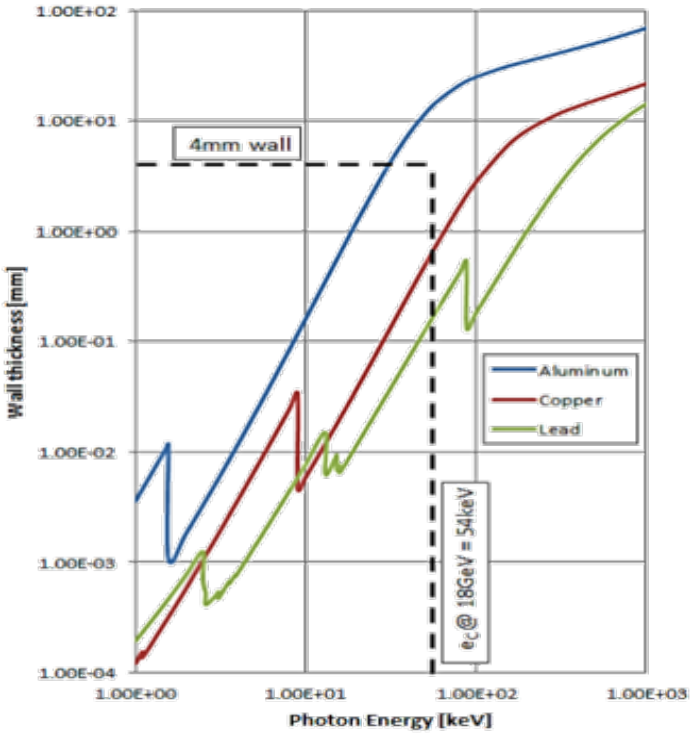

Figure 3.107: Comparison of the attenuation lengths of aluminum, copper and lead vs. photon energy. At 18 GeV with photon critical energy of 54 KeV, the radiation dosage outside the copper chambers will be 2–3 orders of magnitude lower than that of the aluminum chambers.

3.5.9 ESR Beam Diagnostics Requirement and Specifications

The EIC electron storage ring requires continuous bunch replacement at a rate of 2 bunches per second to provide a sufficiently high level of beam polarization. With bunch intensities up to 28 nC, individual bunch intensity accumulation using a bunch merging process in the RCS is necessary. These full intensity bunches will then be injected onto the closed orbit of the ESR. Beam instrumentation is required to monitor and tune the gradual increase in the number of electron bunches stored in the ESR during the accumulation process, during bunch replacement and when the store is aborted. A detector with adequate bandwidth and with turn-by-turn capability will be needed to monitor the evolution of the longitudinal bunch profile in the injection bucket.

Beam position monitors with turn-by-turn capability are required to measure betatron oscillations of the newly injected bunches so that these oscillations can be minimized by tuning. It is necessary to monitor the orbit of newly injected bunches while filling the ring, and then later during bunch replacement in the presence of stored beam in adjacent buckets. Due to the 25 mrad crossing angle at the interaction point crab crossing will be required. This crabbing can be monitored using a synchrotron light monitor (SLM) and a streak camera. Crab cavities will be installed on both sides of the interaction point, each

at a phase advance of 90 degrees from the IP. During physics operations the actual crabbing effect of these cavities reaches its maximum inside the EIC detector. There is no space available at or near the detector for installation of a SLM with streak camera to monitor the crabbing angle. However, while operating only a single crab cavity the bunches are crabbed essentially everywhere around the ring, with the amplitude of the crabbing angle governed by the well-known formula for closed-orbit distortions in a storage ring. With a SLM and streak camera installed at the appropriate location in the ESR, the crab tilt angle can be measured so that amplitudes and phases of the individual crab cavities can be optimized by tuning. In a second step, closure of the crab bump is then ensured by zeroing the residual crabbing angle using the same SLM and streak camera with both crab cavities operating.

Transverse beam sizes of the electron and ion beam have to be matched at the interaction point. The electron beam emittances in the horizontal and vertical plane therefore need to be measured and adjusted. This is accomplished by detecting the synchrotron radiation fan generated by a dipole in the ESR using an SLM and x-ray pin-hole profile monitor systems. Together with the known machine optics at the location of the dipole the emittances can then be determined.

Assuming an impedance of $Z/n = 0.1\,\Omega$ for the storage ring, feedback systems need to be capable of counteracting single-bunch rise times of 1 ms.

The following list summarizes the requirements for the individual instrumentation systems:

- Longitudinal profile monitor with sufficient dynamic range/resolution to monitor each bunch during the injection process.
- Dual-plane BPMs at each quadrupole with single bunch, turn-by-turn, and multi-turn averaging measurement capability.
- Capability to monitor orbit of each injected bunch during machine set-up, gradual storage fill, and 2 Hz bunch replacement.
- Synchrotron Light monitor with streak camera to monitor crab tilt angles.
- Synchrotron Light monitors with streak camera and x-ray pin-hole profile monitor capability to measure beam sizes and monitor (global) coupling.
- Tune measurement system with feedback capability.
- Transverse and longitudinal bunch-by-bunch feedback systems.
- Slow ($\sim$1 Hz) transverse orbit feedback system to ensure an RMS orbit stability of less than 10% of the RMS beam size everywhere in the ESR.
- DC beam current monitor to precisely measure average stored beam current and beam lifetime.
- Fast beam current monitor to monitor fill pattern and individual bunch intensity.

- Beam loss monitors at strategic locations, injection, extraction, collimators, etc...
- Bunch-by-bunch polarimeter.
- Bunch-by-bunch luminosity monitor.

3.5.10 ESR and RCS Machine Protection

The ESR and the RCS will have an emergency beam dump and a beam inhibit or machine protection system. For details see [156, 157]. Since the RCS will only have two bunches a deflector operating at a slower rate (several ms timescale) will suffice. However the ESR will have to be equipped with fast kickers to guarantee complete beam removal within one turn in case of a beam permit drop. This ESR emergency dump will require a short extraction beam line and is not the same dump that will receive the bunches that are being replaced on a Hz rate with fresh bunches from the RCS. The replacement dump will be located at the transfer location in IR12. No location is defined yet for the emergency dump and extraction beamline.

No collimators are needed for the RCS. However, the addition of betatron collimators could be considered for clean transfer into the ESR. The ESR will be equipped with a two-stage betatron collimation system as well as a one-stage momentum collimator. The betatron collimation system consists of a primary collimator and a secondary collimator with jaws made of a light material such as carbon, coated with a metal (Cu for instance). For flexibility and impedance minimization each collimator will be symmetric, two-sided and tapered as shown in the schematic drawing in Figure 3.108. Table 3.42 summarizes the main collimator parameters and their locations in the ESR.

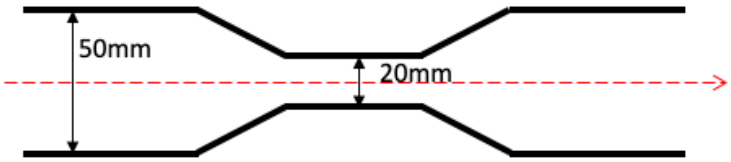

Figure 3.108: Symmetric two-sided collimator with a center jaw area and tapered transitions. Dimensions are typical.

Figures 3.109, 3.110 and 3.111 show the beta function (top) and dispersion (bottom) together with the ratio of $D_x/\sqrt{\beta_x}$ (bottom) at IR12, IR2 and IR4. The collimators are shown as two vertical black lines, drift spaces are green, dipole magnets red and quadrupoles blue. Figure 3.109 also includes the horizontal injection absorber.

The primaries and secondaries are set on both sides of a de-focusing quadrupole in the plane they are collimating in. This allows to benefit from the shorter focal length of particles having deposited energy in the primary collimator. Having the secondaries two

Table 3.42: Locations and twiss parameters of the ESR betatron collimators, injection absorber and momentum collimator. Twiss parameters are based on ESR lattice.

Collimator unit name	Location near	s [m]	L [m]	β_x [m]	β_y [m]	D_x [m]	Material
H1: PrimH	Q9, IR2	2505.5	0.27	54.0	15.8	0	C (coated)
H1: PrimH[a]	Q11, IR2	2482.9	0.27	60.0	15.9	0	C (coated)
H2: SecH	Q7, IR2	2527.5	0.81	52.4	20.6	0	C (coated)
V1: PrimV	Q10, IR12	1842.4	0.27	21.0	54.1	-0.31	C (coated)
V2: SecV	Q8, IR12	1864.6	0.81	23.7	34.3	0.31	C (coated)
V2: SecV[a]	Q6, IR12	1887.0	0.81	20.3	52.3	0.41	C (coated)
Inj. abs. (H)	Q9, IR12	1954.8	0.54	46.6	11.5	-0.69	C
Mom. col.	Q13, IR4	3116.1	0.45	55.8	4.1	1.08	Al (coated)

[a] An alternative unit or an additional location

quadrupoles further downstream allows for phase advances closer to 90 degrees but might conflict with other components such as a possible emergency dump or the RCS to ESR transfer. In Figure 3.110 the emergency beam dump location is assumed to be in IR2.

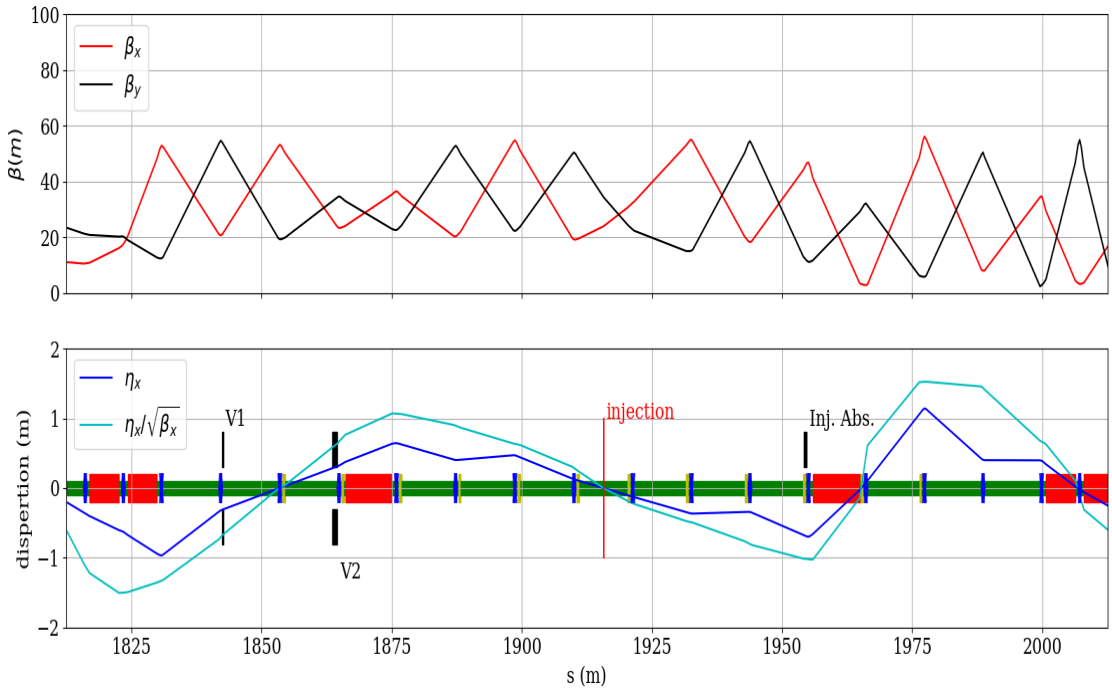

Figure 3.109: ESR betatron collimation location in the IR12 straight section. Primary V1, secondary V2.

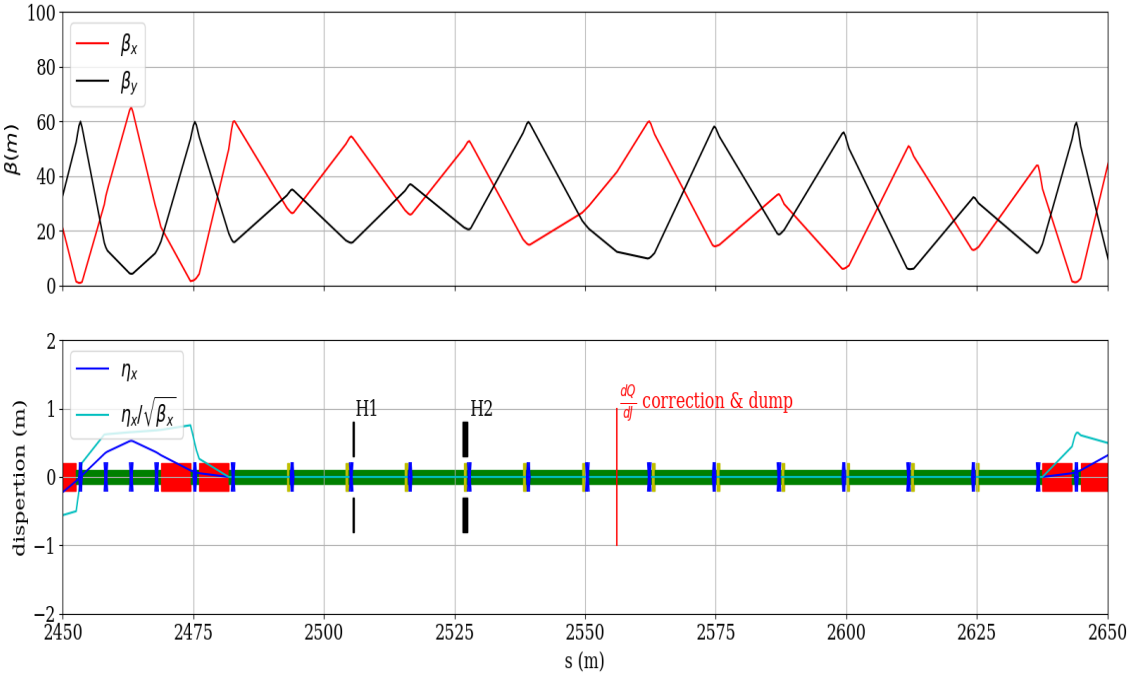

Figure 3.110: ESR betatron collimation location in the IR2 straight section. Primary H1, secondary H2.

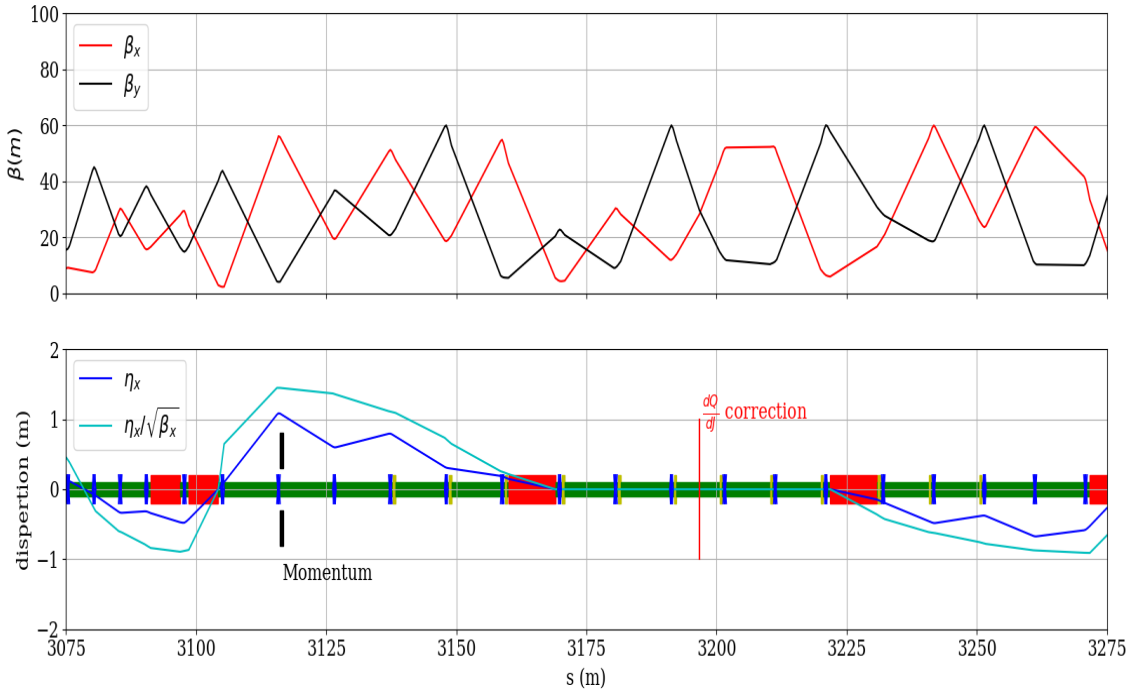

Figure 3.111: ESR momentum collimator location in the IR4 straight section.

3.6 Electron Rapid Cycling Synchrotron Design

A Rapid Cycling Synchrotron (RCS) will be used to accelerate, accumulate and inject up two 28 nC polarized electron bunches into the EIC electron storage ring (ESR) per second. In the peak current regimes, the RCS will take two trains of four 7 nC bunches for a total of 8 bunches injected from the LINAC. These will be injected at 400 MeV at a rate of two 7 nC bunches per LINAC cycle. Each LINAC cycle should take between 100–50 Hz thus requiring between 0.04 and 0.08 seconds to fill the RCS. These bunches will be injected into two trains of four adjacent 591 MHz buckets. Since a rise time of 1.69 ns is necessary to inject into neighboring buckets a special system of RF-crab like cavity kickers will be used to generate the necessary kick profile.

The two bunch trains will then be accelerated to 1 GeV and held there for 0.15 seconds while the eight bunches are merged into two 28 nC bunches. These will then be accelerated to their final energy of 5, or 10 GeV and extracted promptly. In the case of 18 GeV only two slightly lower charge bunches will be injected and merged per train. These yield two 11 nC merged bunches at 1 GeV which will be accelerated and extracted at 18 GeV.

The current design uses a spin resonance free lattice [158]. Such an accelerator will provide spin polarized electrons for energies up to 18 GeV. The accelerator will fit in the existing RHIC tunnel, employ standard technology, and accelerate an electron bunches using a ramp rate of 0.176 GeV/ms. In the past it was believed that such a device would cause profound polarization loss due the combined effects of many depolarizing resonances. However we have devised a lattice that by virtue of the symmetry of construction and high operating tunes, avoids all significant depolarization sources in the energy range of its operation. The main parameters of the RCS are summarized in Table 3.43. As there is significant natural vertical emittance damping in the RCS, the emittances given are what are delivered by the injectors and what is required to match the storage ring. Dipole kicks will be used on the last 100 turns of the acceleration ramp to blow-up the vertical emittance to match the storage ring on extraction.

3.6.1 RCS Spin Resonance-free Design

Several types of depolarizing spin resonances are encountered when polarized electrons are accelerated. The most important are the intrinsic spin resonances and the imperfection spin resonances. Both are due to coherent transverse spin kicks that occur primarily in the quadrupole fields of the lattice. Intrinsic spin resonances arise from vertical betatron oscillations, while imperfection spin resonances are due to vertical closed orbit distortions.

In a typical circular lattice where the field is dominated by the guide dipole field, the rate of spin precession per turn, or spin tune (ν_s), is determined by the energy and conveniently expressed as $a\gamma$, where $a = \frac{g-2}{2}$ is the anomalous magnetic moment coefficient for an electron (0.001159), and γ is the relativistic factor. For the case of a depolarizing intrinsic spin resonance this occurs whenever the spin tune $a\gamma = nP \pm Q_y$. Here n is an arbitrary integer, P is the periodicity of the lattice, and Q_y is the vertical betatron tune.

Table 3.43: Basic Parameters of the RCS injector.

Parameter	Value
Injection energy [MeV]	400
Top energy [GeV]	18
Momentum compaction α_c	0.000372
Max relative pol. loss	5%
Circumference [m]	3841.35
Ramping repetition rate [Hz]	1
Acceleration time [ms], [turns]	100, 8000
Total number of "spin effective" superperiods	96
Integer horizontal tune	57
Integer vertical tune	60
Max vertical orbit RMS [mm]	0.5
Number of arc Cells	192
Number of straights	6
Number of dipoles	384
Number of quadrupoles	552
Number of sextupoles	360
Round beam pipe inner diameter [mm]	32.9
Number of bunches	1
Charge per bunch [nC]	1–28
Radio frequency [MHz]	591
Total Cavity peak Voltage [MV]	60
Bunch length inj.(ramp),ext. [ps]	40 (16-91),30-23
Hor. and Ver. emittance normalized (inj.) [mm-mrad]	26, 26
Hor. and Ver. emittance normalized (ext. 18 GeV) [mm-mrad]	845–705, 60–71
Hor. and Ver. emittance normalized (ext. 10 GeV) [mm-mrad]	391, 20–102
Hor. and Ver. emittance normalized (ext. 5 GeV) [mm-mrad]	196, 18–113
RMS energy deviation $\mathrm{d}p/p$ inj.,ext [10^{-3}]	2.5,1.09-0.58
U_0 Energy radiated per electron (at 18 GeV) [MeV/turn]	39.8
Hor. damping time (at 18 GeV) [s]	0.0036

Thus the first two important intrinsic spin resonances that an accelerating electron will encounter occur at $a\gamma = Q_y$ and at $a\gamma = P - Q_y$ (for $P > Q_y$). If we now ensure that both Q_y and $P - Q_y$ are greater than the maximum $a\gamma$ value, (or Q_y is greater and $P - Q_y$ is less than the lowest $a\gamma$ value), then all the important intrinsic spin depolarizing resonances will be avoided.

We chose $P = 96$, constraining the integer part of the vertical betatron tune to be $41 < [Q_y] < 55$, since we accelerate to energies less than $a\gamma = 41$. Here $[Q_y]$ indicates the nearest integer of the vertical betatron tune. We chose $[Q_y] = 50$. As a result, the two first intrinsic resonances will occur near $a\gamma = 50$, and $a\gamma = 96 - 50 = 46$.

A side benefit is that in addition to the intrinsic resonances, the imperfection resonances are also minimized due to the design of this lattice. This is because the strongest imperfection resonances, like the intrinsic resonances for a pure ring, will be at $nP \pm [Q_y]$.

3.6.2 RCS Geometry and 3-D Footprint

The existing RHIC tunnel resembles a hexagon with rounded corners rather than a circle, and therefore has a natural periodicity of 6. However, the spin precession, which advances $a\gamma$, occurs in the dipoles, so one can maintain the periodicity of 96 from the point of view of $a\gamma$ precession. This can be accomplished by designing the straight sections such that each has a betatron phase advance equal to 2π. In this way the straight sections will not contribute to the integral that defines the strength of the spin resonance (see Figure 3.112). Thus we can maintain the 96 super-periodicity from the point of view of the spin precession.

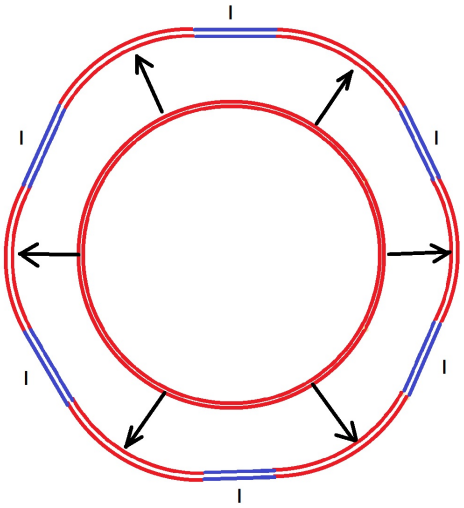

Figure 3.112: Projecting the pure ring lattice with 96 super-periodicity onto the RHIC six fold periodic ring.

The lattice incorporates the existing RHIC straight sections that do not contribute to the intrinsic spin resonance strength, thus preserving the 96 periodicity from a spin precession point of view.

The proposed layout for the RCS places it at a radius outside of the existing RHIC beam line but within the tunnel.

3.6.3 RCS Ring Lattice

Each of the six arcs are made up of 16 cells. These cells are composed of two types of FODO cells that differ only by the family of sextupole magnets used in between the Focusing and Defocusing quadrupoles. We classify these as FODO CELL A and FODO CELL B. The A and B FODO cells with sector bending magnets is outlined in the Table 3.44. Here D represents drift space, QF0/D0 focusing and defocusing quadrupoles respectively and SBEND the sector bend magnet. In the drift spaces 4 families of sextupoles are inserted (not shown).

Table 3.44: A and B arc FODO cell.

QD0/2	D	SBEND	D	QF0	D	SBEND	D	QD0/2

The straight sections are composed to two identical lattices placed in mirror image around each straight section center point as shown in Table 3.45. Here D is the drift space of approximately 7.4 m, QF(1–8) and QD(0–8) represent focusing and defocusing quadrupole families. For some of the sections RF cavities and sextupole magnets and dipoles are inserted (not shown). The breaking of the symmetry caused by these insertions are managed by tuning the quadrupoles to suppress their contribution to the intrinsic resonance strength over the 400 MeV to 18 GeV energy range (see Section 3.6.8). The dipole positioning is described in Section 3.6.8 so as to navigate around the detectors and accommodate the RF assemblies. The orientation around the straight section center point is shown in Table 3.46. In this table, sixteen Arc A and B cells ($16 \times$ (ACell, BCell) are shown, connecting to the forward straight section (TM), and the mirror TM lattice (-TM) and back to next arc-cells.

Table 3.45: Straight section line (named TM).

TM	(QD0/2	D	QF1	D	QD1	D	QF2	D	QD2	D	QF3	D	QD3	D	QF4	D	QD4
	D	QF5	D	QD5	D	QF6	D	QD6	D	QF7	D	QD7	D	QF8	D	QD8/2)	

Table 3.46: Arc to Straight Section beamline.

$16 \times$ (ACell,BCell)	TM	-TM	16x(ACell,BCell)

With the straight sections, the tunes now become $Q_x = 57.632$ and $Q_y = 60.732$. However since the vertical arc tunes are still 50 our spin resonance structure remains unchanged. The beta and dispersion functions are plotted in Figure 3.113. The straight sections across each IP is shown in Figures 3.114 and 3.115.

3.6.4 RCS Orbit Distortion Estimates and Correction Elements

The major contribution to depolarization for the RCS is imperfection spin resonances. To correct the residual imperfections below $G\gamma = 41$, correctors are located next to the

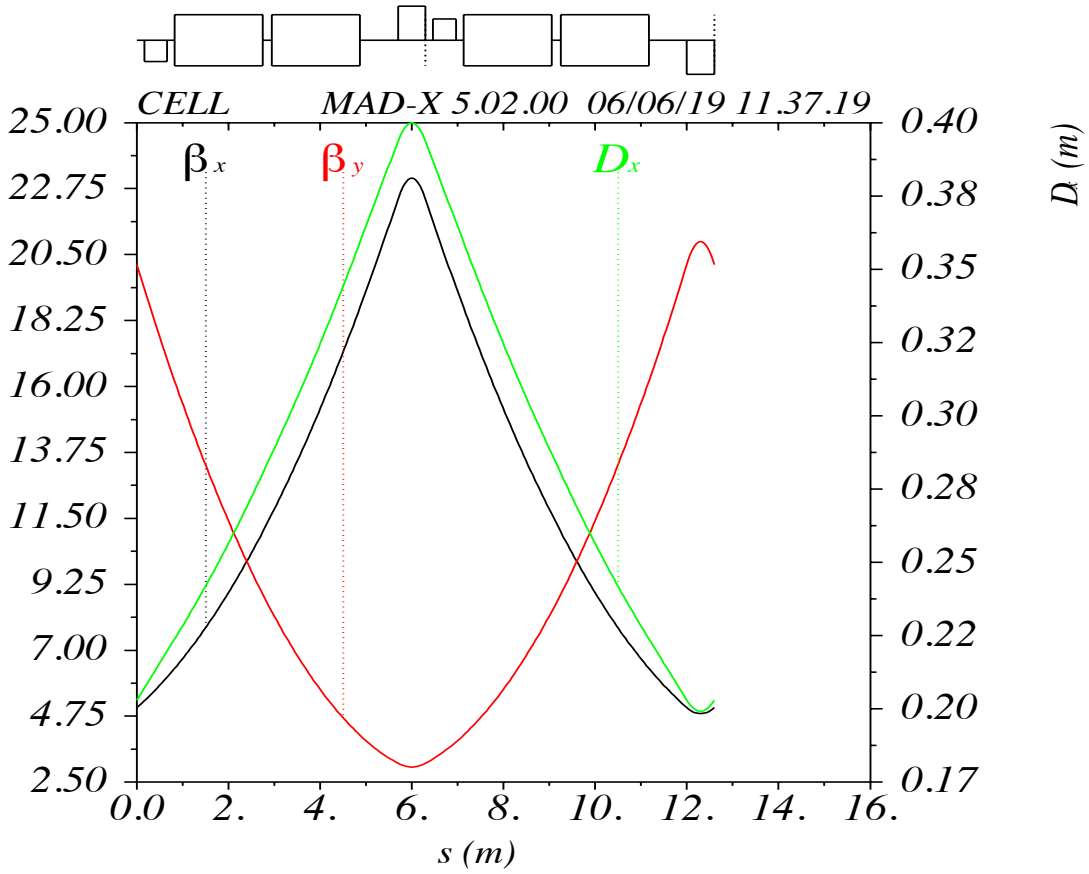

Figure 3.113: Twiss functions in RCS arc-cell.

quadrupoles. This is done since the primary drivers of vertical orbit distortions are due to quadrupole vertical misalignments. The effect of a quadrupole misalignment (Δy) is to deliver an effective angular kick $\Delta\theta$ at each quadrupole given by

$$\Delta\theta = K_1 L \Delta y. \tag{3.85}$$

Where $K_1[\mathrm{m}^2]$ is the quadrupole strength and L is the quadrupole length. Placing the corrector adjacent to the quadrupoles permits the immediate correction of kicks due to misalignments, so they do not propagate around the ring. The strength needed to correct for the misalignments is estimated by considering the tolerance when aligning the quadrupoles in the ring, which currently are 0.2 mm RMS. Using a 2.5σ cut off, our maximum quadrupole misalignment would be $\Delta y = 0.5\,\mathrm{mm}$. Considering the maximum quadrupole strength $K_1 = 0.42\,\mathrm{m}^{-2}$ and quadrupole L of 0.6 m we can estimate the maximum possible kick to be 0.126 mrad. This dictates the maximum corrector strength.

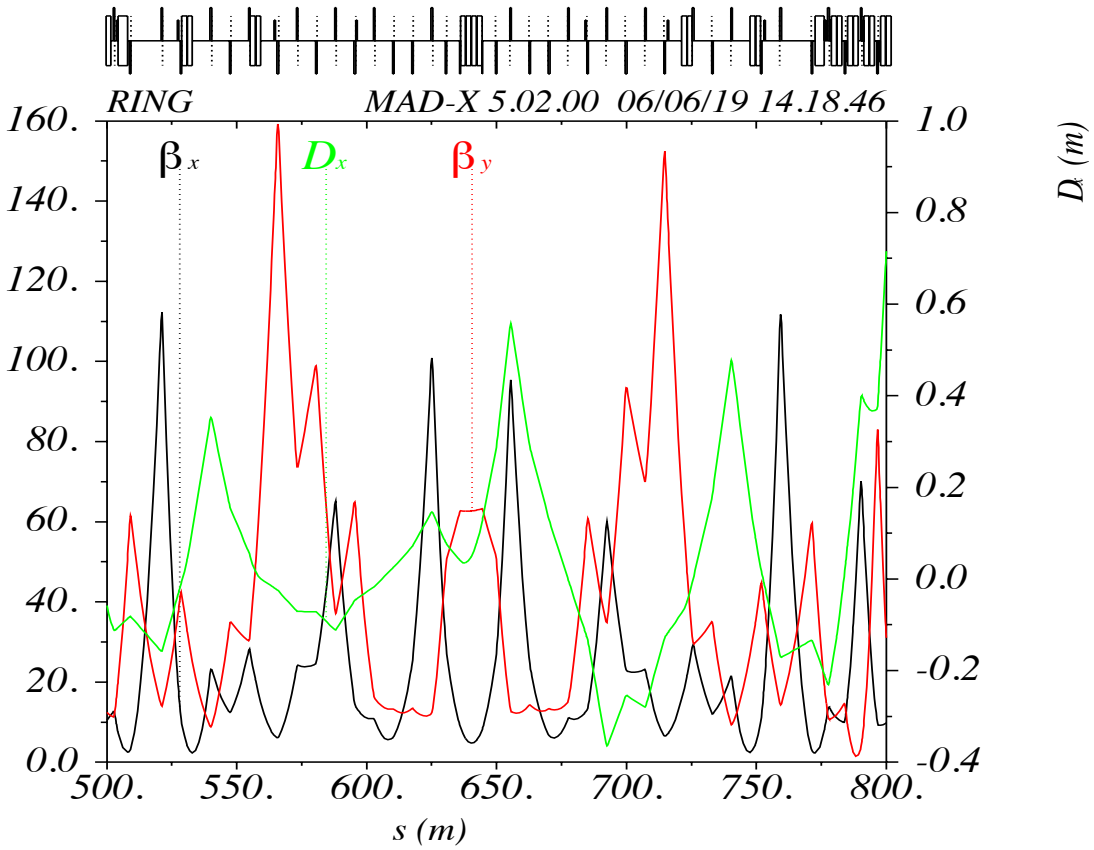

Figure 3.114: Twiss functions in RCS around IP06 and IP08.

A statistical estimate of the RMS closed orbit is given by,

$$\begin{aligned} y_{\mathrm{co,RMS}} &\approx \frac{\beta_{\mathrm{avg}}}{2\sqrt{2}|\sin \pi Q|}\sqrt{N_q}\Delta\theta_{\mathrm{RMS}} \\ &\approx \frac{\beta_{\mathrm{avg}} K_1 L \sqrt{N_q}}{2\sqrt{2}|\sin \pi Q|}\Delta y_{\mathrm{RMS}} \end{aligned} \tag{3.86}$$

With a tune of $Q_y = 60.732$, the number of quads, $N_q = 552$, $\beta_{\mathrm{avg}} = 24.75\,\mathrm{m}$, and $K_1\, L_{\mathrm{avg}} = 0.0225\,\mathrm{m}^{-1}$, we find the estimated RMS vertical orbit to be 1.244 mm. This estimate is somewhat smaller than our estimate of 5.5 mm given by the direct application of random misalignments to the RCS lattice for several random seeds.

Studies with calculated spin resonances and spin-orbit tracking indicate that imperfection resonances should not contribute more than 5% loss with vertical orbit errors less than 0.5 mm RMS with a 100 ms ramp rate (see Tables 5.1, 5.2 in Section 5.2). At the quadrupoles this represents uncorrected orbits of approximately 0.025 mm RMS relative to the quad center. This determines our minimum desired BPM resolution of 0.01 mm. In Section 5.2 there is a detailed discussion of our orbit tolerances and correction scheme.

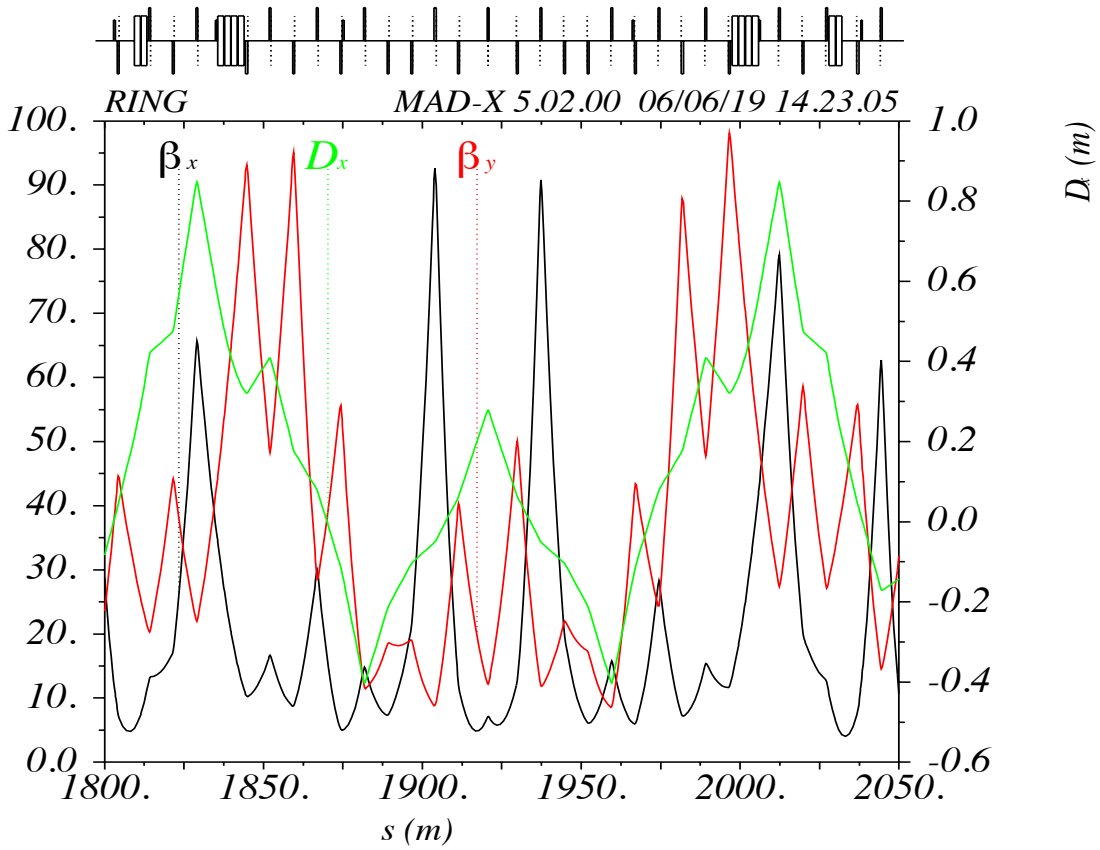

Figure 3.115: Twiss functions in RCS around IP10, IP12, IP02 and IP04.

3.6.5 RCS Bunch Merging Scheme

After the injection of eight 7 nC bunches into two four bunch trains, they will then be accelerated to 1 GeV and merged into two 28 nC with two steps of pairwise merging using 295.5 MHz and 147.8 MHz RF systems, respectively as shown in Figure 3.116). The bunches will begin with dp/p = 2.5×10^{-3} and a bunch length of 40 ps giving a longitudinal emittance $\sigma_t \sigma_E = 4 \times 10^{-5}$ eV-s, at 7 nC this should be above the longitudinal microwave instability threshold of Z/n = 0.138 Ω. During acceleration we will increase the voltage and slew the phase to keep the dp/p fixed at 2.5×10^{-3} while shrinking the bunch length to 16 ps and the synchrotron tune will increase from 0.059 to 0.14. With these bunch parameters our microwave threshold at 1 GeV would be 0.2 Ω.

Simulations show that through two successive merges from four to two to one will cause longitudinal emittance growth of approximately 42%. Thus our final merged longitudinal emittance will be 23×10^{-5} eV-s with a bunch length of 91 ps and dp/p remaining fixed at 2.5×10^{-3}. The microwave stability threshold for the merged bunches will be 0.196 Ω.

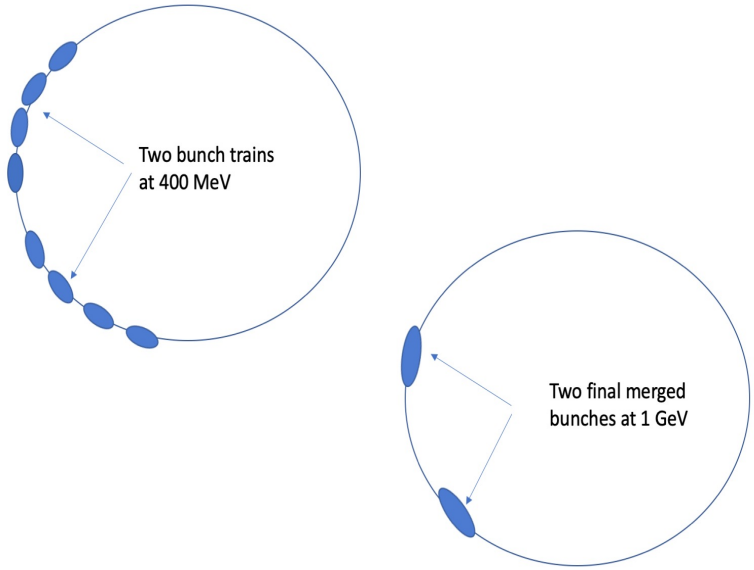

Figure 3.116: 8 bunches injected into two trains of four bunches in the RCS at 400 MeV. (left plot). Bunches merge at 1 GeV into two bunches.

3.6.6 RCS 3-D Emittance Control Scheme

The horizontal equilibrium emittance in the RCS at 18 GeV is $\epsilon_x/\pi = C_q\gamma^2\frac{I_5}{I_2}$. With $C_q = 3.83 \times 10^{-13}$, $I_2 = 0.02673695874$, $I_5 = 0.7371515445e-5$, that gives $\epsilon_x/\pi = 1.3 \times 10^{-7}$ m. This is larger than the horizontal equilibrium emittance of the ESR whose integrals are $I_2 = 0.02456$, $I_5 = 0.4573e-5$, that yields $\epsilon_x/\pi = 0.88 \times 10^{-7}$ m. Tracking simulations in Zgoubi accelerating from 0.4 to 18 GeV in 8000 turns (100 ms) yield a final horizontal emittance less than the equilibrium since there is not enough time at 18 GeV for the distribution to settle into the equilibrium values. Thus we obtain a horizontal emittance at the RCS extraction of $0.814 \times 10^{-7}m$.

For 5 GeV and 10 GeV the equilibrium horizontal emittance of the storage ring is much larger than the projected RCS emittances. Thus it will need to be blown up to match it on injection into the Storage Ring. We plan to replicate an approach similar to what has been accomplished in the SPS. During the last 200 to 500 turns kickers will be turned on briefly to deflect the beam to approximately 1/2 the sigma size of the beam. Nonlinear fields ensure filamentation of the phase space and increase the effective emittance. We have simulated this in Zgoubi and found with an energy deviation on the order of 10^{-5} we can blow up our horizontal emittance beyond 800 µm from 55 µm over 200 turns. Since the storage horizontal emittance is projected to be about 800 µm, this should be plenty to match the storage ring emittance. There is minimal coupling in the RCS, so the emittance blow up is confined to the horizontal plane. On the other hand the equilibrium vertical

emittance is projected to be almost zero in the ESR. For the 18 GeV case, accelerating over 8000 turns yields vertical emittance that damped down to nearly zero. In the case of the 5 and 10 GeV extraction, the vertical emittance of 26 mm-mrad normalized will be much larger than the nearly zero emittance of the ESR, since at these lower energies damping times are much longer.

3.6.7 RCS Chromatic Correction Scheme

Both the arc cells and straight sections will include six families of sextupoles. The 'A' arc cell includes two families of sextupoles in the drift section from the first defocusing quadrupole to the first SBEND dipole magnet. These sextupole magnets are labeled SX1 and SX2 and are located in the drift between the first focusing quadrupole and the bend and in the third drift between the first defocusing quadrupole and second bend. The 'B' arc cell also has only two sextupole magnets labeled SX3 and SX4 in the same relative locations as the 'A' arc cell. The forward and backward straight sections (TM and -TM) are also equipped with another three families of sextupoles (SX7, SX8, SX9). The SX7 are installed in the second drift space after the first focusing quadrupole (QF1), SX8 are located in the drift space after the third focusing quadrupole (QF3), and SX9 in the drift space after the defocusing quadrupole QD5. These sextupoles will keep the chromaticity below 10 units for the RCS ramp.

3.6.8 RCS Spin Transparent Detector Bypass

Experiments are located at interaction regions IP6 and IP8. At these locations the RCS beamline bypasses the detector achieving greater than 5 m displacement from the center of the IP based on the current sPHENIX and eSTAR detector design. This displacement is achieved by moving the last three and first three dipole from the arcs around IP6 and IP8 at the center of the IP and at two other symmetric locations in the straight section (see Figure 3.117). In this configuration the RCS beam trajectory misses the detector center by 3.86 m and avoids the other potential obstructions in the tunnel.

In the remaining IP2, IP4, IP10 and IP12 a geometry is adopted which yield approximately 153 m long straight through the IP center. This geometry is accomplished also by moving three dipoles from the arcs on either end. The long straight is necessary to accommodate the RF system modules located at IP10, but we maintain this geometry through the remaining IP's. This straight section geometry is shown in Figure 3.118. Accommodating both these bypasses while controlling the intrinsic spin resonances for the whole lattice has the negative consequence of raising our maximum β function from 50 to 160 m. It also reduces the threshold for emittance versus polarization loss. However, the polarization loss effect is mitigated by minimizing the sum of the intrinsic resonances up to $a\gamma < 40.8$. This keeps polarization effects well below any planned emittance magnitude as will be discussed in Section 5.2 on polarization performance.

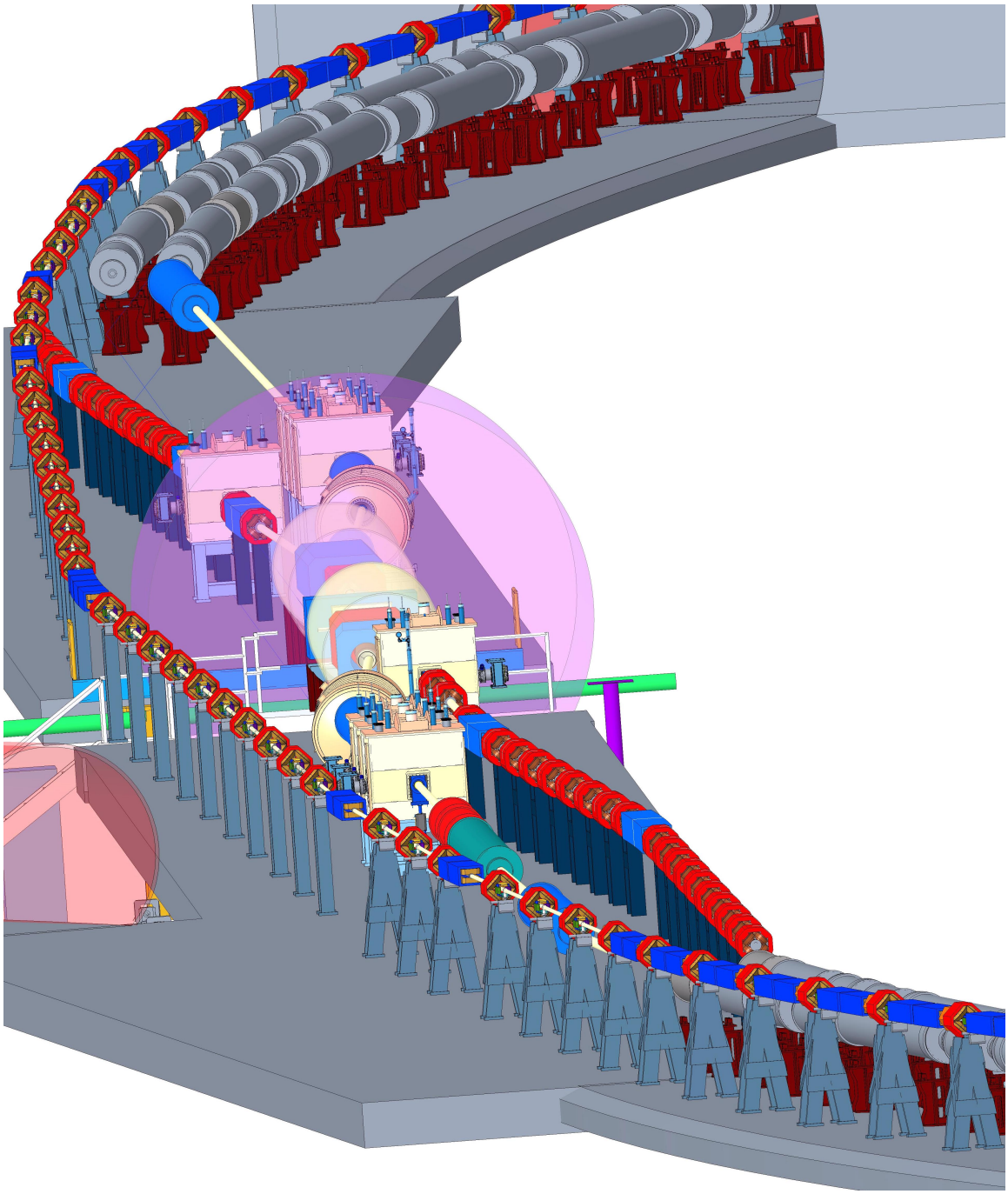

Figure 3.117: Beam line layout around the detectors at IP6 and IP8. Here the outer ring is the RCS and the blue magnets represent dipoles.

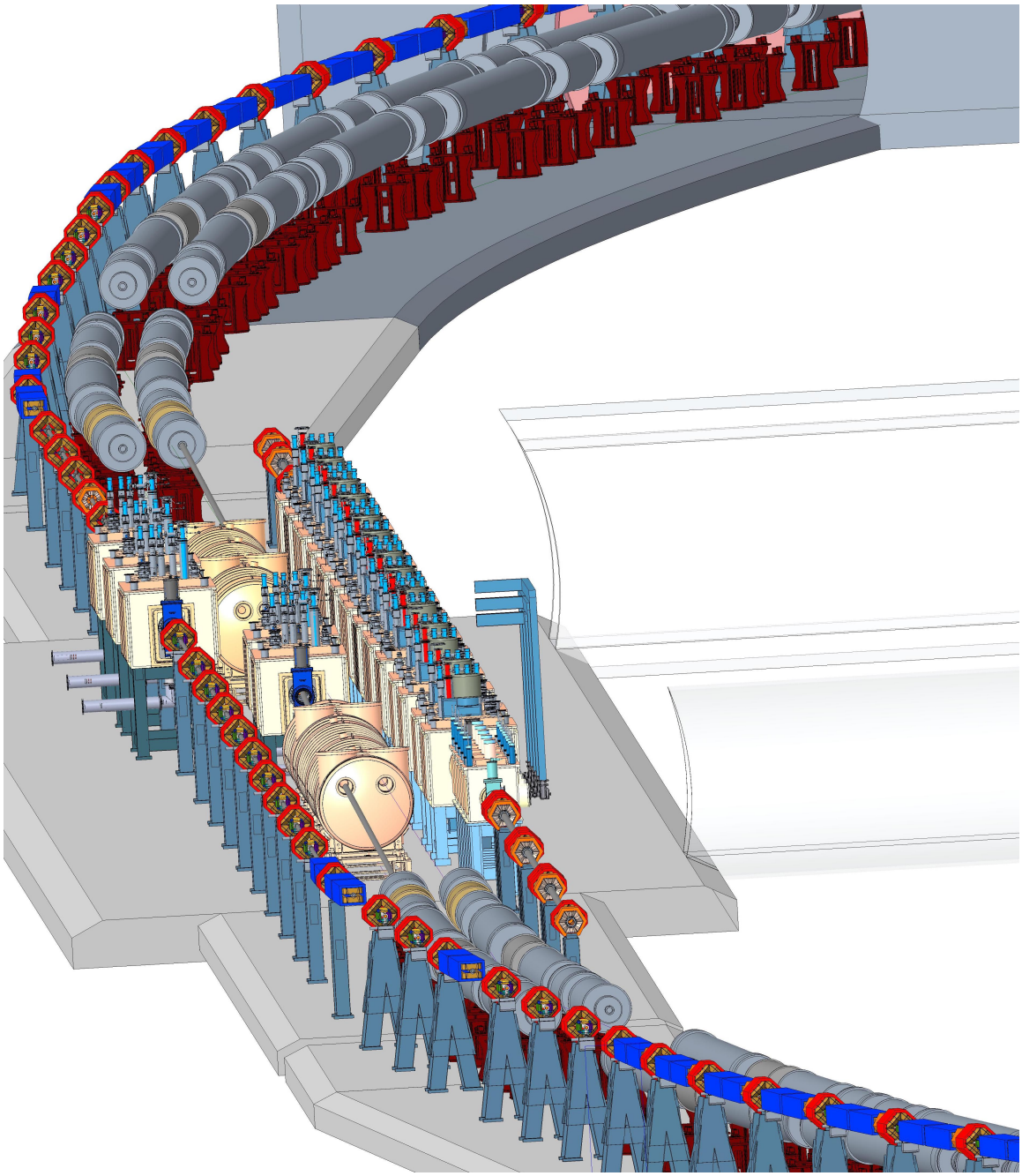

Figure 3.118: Beamline layout in the utility straight sections (IP2, IP4, IP10 and IP12). Here the outer ring is the RCS and the blue magnets represent dipoles. At IP10 the RF system modules will be accommodated.

3.6.9 RCS Magnetic Requirement and Specifications

Tables 3.47 and 3.48 contain a list of the specifications and numbers of magnets required for the RCS. Since the RCS will resided in the same tunnel as the Storage Ring, the ramping effects of the RCS magnets on the Storage Ring should be considered. The peak field in the RCS is comparable to the Storage ring, the potential effect of the magnet field flux has been calculated and shown to drop to the 10^{-5} relative field at 1 m distance from the RCS's magnet center.

Table 3.47: List of RCS magnets. S. is the standard arc connecting regions at 2, 4, 10 and 12 o'clock. IR denotes the larger bypass around 6 and 8 o'clock.

Name	Type of magnet	Length (m)	number	strength
QD	Arc Defocusing Quad	0.6	180	$0.42\,\mathrm{m}^{-2}$
QF	Arc Focusing Quad	0.6	174	$0.349\,\mathrm{m}^{-2}$
QD0	S. Defocusing Quad	0.6	8	$0.265\,\mathrm{m}^{-2}$
QD1	S. Defocusing Quad	0.6	8	$0.175\,\mathrm{m}^{-2}$
QF1	S. Focusing Quad	0.6	8	$0.340\,\mathrm{m}^{-2}$
QD2	S. Defocusing Quad	0.6	8	$0.154\,\mathrm{m}^{-2}$
QF2	S. Focusing Quad	0.6	8	$0.172\,\mathrm{m}^{-2}$
QD3	S. Defocusing Quad	0.6	8	$0.125\,\mathrm{m}^{-2}$
QF3	S. Focusing Quad	0.6	8	$0.189\,\mathrm{m}^{-2}$
QD4	S. Defocusing Quad	0.6	8	$0.175\,\mathrm{m}^{-2}$
QF4	S. Focusing Quad	0.6	8	$0.181\,\mathrm{m}^{-2}$
QD5	S. Defocusing Quad	0.6	8	$0.201\,\mathrm{m}^{-2}$
QF5	S. Focusing Quad	0.6	8	$0.275\,\mathrm{m}^{-2}$
QD6	S. Defocusing Quad	0.6	8	$0.089\,\mathrm{m}^{-2}$
QF6	S. Focusing Quad	0.6	8	$0.274\,\mathrm{m}^{-2}$
QF7	S. Focusing Quad	0.6	8	$0.271\,\mathrm{m}^{-2}$
QD7	S. Defocusing Quad	0.6	8	$0.123\,\mathrm{m}^{-2}$
QD8	S. Defocusing Quad	0.6	8	$0.225\,\mathrm{m}^{-2}$
QF8	S. Focusing Quad	0.6	4	$0.285\,\mathrm{m}^{-2}$
Dipole	Sbend	4.045	384	0.016 rad
SX1	Sextupole	0.5	90	$-3.373\,\mathrm{m}^{-3}$
SX2	Sextupole	0.5	90	$1.839\,\mathrm{m}^{-3}$
SX3	Sextupole	0.5	90	$-3.373\,\mathrm{m}^{-3}$
SX4	Sextupole	0.5	90	$1.839\,\mathrm{m}^{-3}$

Table 3.48: RCS quadrupole magnets in the detector bypass around IP6 and IP8 (IR).

Name	Type of magnet	Length (m)	number	strength
QDI0	IR Defocusing Quad	0.6	4	0.239 m^{-2}
QDI1	IR Defocusing Quad	0.6	4	0.200 m^{-2}
QFI1	IR Focusing Quad	0.6	4	0.283 m^{-2}
QDI2	IR Defocusing Quad	0.6	4	0.148 m^{-2}
QFI2	IR Focusing Quad	0.6	4	0.297 m^{-2}
QDI3	IR Defocusing Quad	0.6	4	0.163 m^{-2}
QFI3	IR Focusing Quad	0.6	4	0.205 m^{-2}
QDI4	IR Defocusing Quad	0.6	4	0.125 m^{-2}
QFI4	IR Focusing Quad	0.6	4	0.146 m^{-2}
QDI5	IR Defocusing Quad	0.6	4	0.179 m^{-2}
QFI5	IR Focusing Quad	0.6	4	0.217 m^{-2}
QDI6	IR Defocusing Quad	0.6	4	0.048 m^{-2}
QFI6	IR Focusing Quad	0.6	4	0.169 m^{-2}
QFI7	IR Focusing Quad	0.6	4	0.264 m^{-2}
QDI7	IR Defocusing Quad	0.6	4	0.091 m^{-2}
QDI8	IR Defocusing Quad	0.6	4	0.124 m^{-2}
QDI9	IR Defocusing Quad	0.6	2	0.07 m^{-2}

3.6.10 RCS Power Supply Requirement and Specifications

Tables 3.47 and 3.48 show the magnets required in the arcs and the straight sections. There are 384 standard arc dipole magnets connected to one supply.

In addition there are 174 arc focusing quads (QF) connected to one supply, 180 arc defocusing quads (QD) connected to another power supply. Four of the arc connecting regions contain 9 families of defocusing quadrupoles (labeled QD0 to QD8) giving a total of 8 magnets per family. In these four arcs connecting regions there are also 8 families of focusing quadrupoles (labeled QF1 to QF8) giving a total of 8 magnets for the QF1 to QF7 magnets and 4 magnets for QF8. In the larger bypass region crossing IP6 and IP8, there are 7 families of focusing quadrupoles (labeled QFI1 to QFI7) giving a total of 4 magnets per family and 10 families of defocusing quadrupoles (labeled QDI0 to QDI9) also with 4 magnets per family except for QDI9 with only has 2 magnets.

There are four families of sextupoles (SX1 to SX4) in the arcs with 90 magnets per family. Each quadrupole has its associated vertical and horizontal corrector. All the vertical corrector will be powered giving 552 vertical corrector power supplies. However since horizontal corrections are less stringent, only half of the horizontal correctors will be powered initially giving 276 horizontal power supplies. This gives a total of 828 independent

power supply for both planes. The power supply details are described in the RCS power supply section in Table 6.42.

3.6.11 RCS Vacuum Requirement and Specifications

The RCS vacuum system provides adequate aperture and friendly environment during the acceleration of the electron beam from the injection energy of 0.4 GeV to the extraction energy ranging from 5 GeV to 18 GeV. The RCS will accelerate a single bunch of electrons, with maximum current up to 0.01 A, over a magnet ramp-up time of $\approx$ 100 ms. The changing magnetic field during acceleration will induce eddy currents in the conductive vacuum chamber wall; their effect on the beam has been assessed (see Section 6.4.2 and 4.2.2). For the short acceleration cycle, the beam loss due to beam-gas interaction is insignificant; therefore, high vacuum of mid-10^{-8} Torr is sufficient. Thermal outgassing is the main source of gases in the RCS, while the photon stimulated desorption contributes only a few percent to the overall gas load.

In Section 6.4.2, the eddy current effects, the estimated gas load and the pressure distribution will be discussed. The vacuum chamber design and fabrication, and vacuum instrumentation and control are also be described.

3.6.12 RCS Diagnostics Requirement and Specifications

The RCS provides continuous bunch replacement to the storage ring at a rate of approximately 1 Hz in order to provide a sufficiently high level of beam polarization, with bunch intensities up to 28 nC. One of the important design factors driving the instrumentation is the control of the imperfection resonances that drive polarization losses, especially above 10 GeV. The primary factor controlling the strength of these resonances is the offset of the beam trajectory in the quadrupoles.

Thus we require careful beam position monitoring (BPM) and correction, targeting the control of the uncorrected orbits at approximately 25 µm RMS relative to the quad center. This is equivalent to less than 0.5 mm RMS in orbit. At this level of orbit distortion polarization losses shouldn't be more 5%. This drives our required BPM resolution to 10 µm at each quadrupole. This should be achievable using dual plane button BPMs similar to those used in the NSLS-II Booster shown in Figure 3.119.

These tolerances will also be assisted by using a beam based alignment approach where the strength of a quadrupole is varied to determine its center relative to the BPM's. This can be implemented for each quad independently by using an extra set of back-leg windings powered by a single power supply with a switch for each quadrupole to turn the power supply on and off. Beam position monitors with turn-by-turn capability are required to minimize betatron oscillations of the newly injected bunches, after monitoring the orbit of newly injected bunches during injection tuning.

The electron beam emittances in the horizontal and vertical plane are to be measured and

adjusted at extraction to match the storage ring emittance. This is accomplished by detecting the synchrotron radiation fan generated by a dipole in the storage ring. Together with the known machine optics at the location of the dipole the emittances can then be determined.

The following list summarizes the requirements for the individual instrumentation systems:

- Dual-plane BPMs at each quadrupole with single bunch, turn-by-turn capability to monitor the orbit of injected bunches during set-up and throughout the acceleration ramp.
- Synchrotron radiation monitor(s) to measure beam sizes and monitor (global) coupling.
- Tune monitors/feedback.

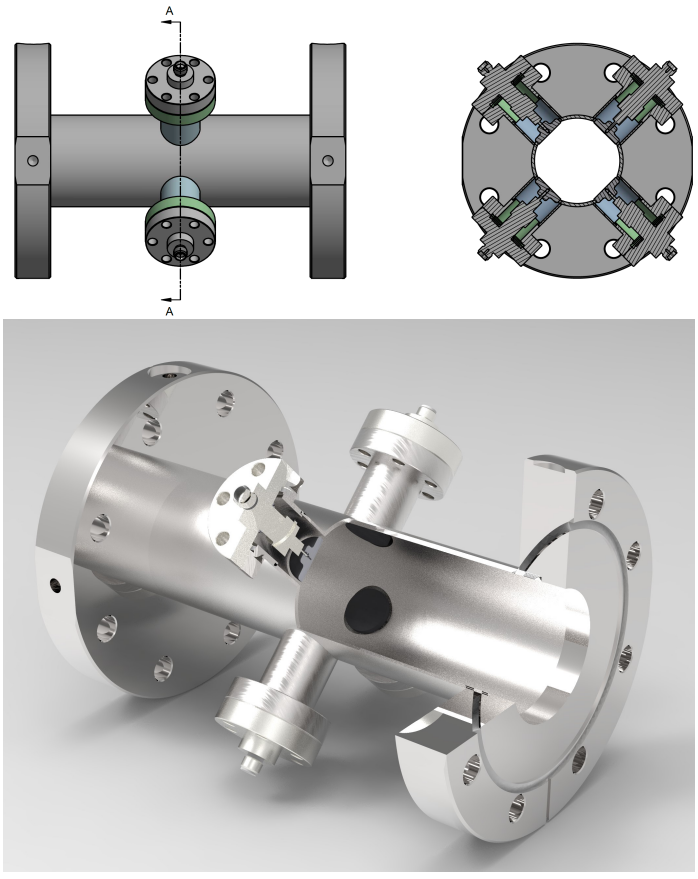

Figure 3.119: Mechanical drawing and 3D model of the NSLS-II Booster BPM pick-up with round chamber.

3.7 Electron Pre-injector Design

3.7.1 Electron Pre-Injector System Overview

The global layout of the 400 MeV pre-injector is shown in Figure 3.120. The injector must produce 85% polarized electron beam with 8 bunches in a repetition frequency of 1 Hz with up to 7 nC of charge. The polarized electron beam will be generated from a high voltage (HV) DC gun with a strained superlattice GaAs(SL-GaAs) photocathode. The bunch at the exit of the DC gun will be 1.5 ns to reduce space charge at the cathode. Buncher with ballistic compression will be used to compress the bunch length to 10 ps. The LINAC will use 2.856 GHz S-band normal conducting traveling wave plates (TWP) to boost the beam energy to 400 MeV. A longitudinal matching section will be placed between the LINAC and the spin rotator to assure beam stability in the RCS. The longitudinal matching section includes a zig-zag section for rotating the beam in longitudinal phase space and a de-chirp cavity to minimize the energy spread. The electron beam's average spin orientation is longitudinal from the cathode to 400 MeV. A dipole solenoid spin rotator will be placed after the LINAC. Two Mott polarimeters will be placed at cathode preparation system and gun beam diagnostic beamline. Table 3.49 shows the beam requirements at the exit of the pre-injector. The cathode operation lifetime must be on the order of weeks.

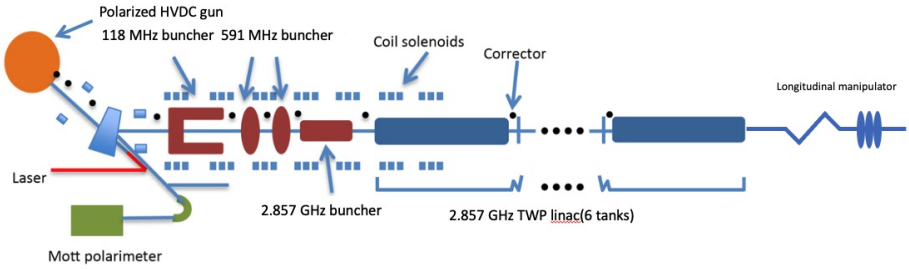

Figure 3.120: The layout of the 400 MeV beamline.

Table 3.49: EIC pre-injector beam requirements.

Parameter	Value
Charge [nC]	7
Frequency [Hz]	1
Energy [MeV]	400
Normalized emittance [mm-mrad]	< 40
Bunch length [ps]	40
dp/p	0.25
polarization [%]	85

3.7.2 Electron Gun Design

A polarized electron beam with bunch charge of 16 nC at 1 Hz from a strained GaAs photocathode in a DC gun was demonstrated in the 1990s at the Stanford Linear Collider (SLC). Table 3.50 lists the bunch parameters of the SLC gun compared to the required bunch parameters for the EIC gun.

Table 3.50: Comparison between the EIC electron gun and SLC electron gun.

Parameter	SLC	EIC
Polarization [%]	85	85
Voltage [kV]	90–120	100–350
Bunch charge [nC]	9–16	7
Repetition rate [Hz]	120	100 (8 bunches)
Bunch length [ns]	2	1–2

The photocathodes used to generate the polarized electrons are composed of super-lattice strain-compensated GaAs/GaAsP (SL-GaAs) crystals. This cathode material used to be commercially available. However, as of 2020 there are no commercial vendors for the SL-GaAs crystals. EIC project personnel are actively looking for U.S. industrial collaborators to develop the SL-GaAs crystals. These personnel are also researching the possibility of purchasing a molecular-beam epitaxy (MBE) system to grow SL-GaAs crystals onsite. The structure of SL-GaAs has been well-studied by the photocathode community. Figure 3.121 illustrates the detailed layered structure of the SL-GaAs photocathode and its quantum efficiency (QE) as the function of polarization. The SL-GaAs crystal will be activated in Extremely High Vacuum (XHV) using $NF_3(O_2)$ and Cs to lower the surface work function. As is shown in Figure 3.121, the typical QE is about 1% with 86% polarization at the threshold laser wavelength of 780 nm to 800 nm.

The gun design for EIC will be an inverted HV load lock DC gun, similar to a gun that has been successfully commissioned at TJNAF [159]. The advantages of using an inverted HV load lock type compared to the SLC gun are:

- The inverted HV gun is a compact design with less outgassing surface. Typically, 10^{-12} Torr scale vacuum is achievable.
- The elimination of field emission from feedthrough to ceramic, reducing the likelihood of a punch-induced vacuum break. 350 keV has been reached at TJNAF in routine operations.
- The load lock section is separated from the HV section. This will make it easier to activate and replace cathodes, and will significantly reduce the maintenance time for

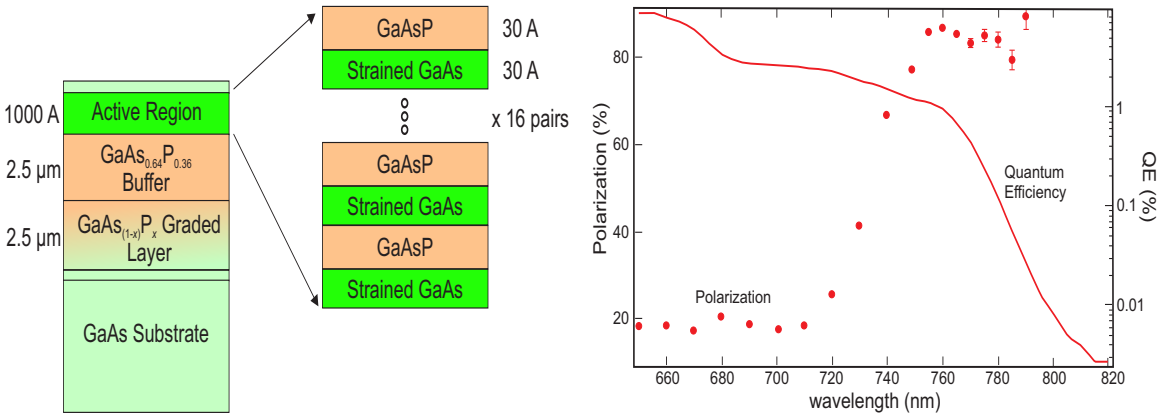

Figure 3.121: Superlattice GaAsP/GaAs structure and QE vs polarization.

this operation from a week to half an hour.

- Relevant high voltage parts are commercially available in the X-ray medical industry and thus are cost effective.

The gun provides 2×7 nC bunches within 2.4 μs every 10 ms for four cycles. A total of 8 bunches (4 pairs) will be provided at a rep rate of 1 Hz. The average current from the gun is 56 nA. The ion back-bombardment will not dominate the cathode quantum efficiency (QE) degradation. Compared to the SLC's 2.4 μA average current with cathode lifetime of 4 days, the gun for EIC will have an operational lifetime above a week. A cathode load lock system is essential to permit the exchange of the cathode in an hour.

Electron Gun Design Considerations

A pencil-shaped bunch will be used, and compressed in the pre-injector. The cathode gradient is 4 MV/m to eliminate field emission from the cathode and ensure long-lifetime operation. The bunch charge is 7 nC. These are not aggressive parameters; the SLC DC gun operated at 12 nC routinely and operated up to 16 nC [160], The peak current as the function of gap voltage can be estimated using the 2D Child law:

$$\begin{aligned} j_{2D} &= j_{1D}\left(1+\frac{d}{4r}\right) \\ j_{1D} &= 2.33\times10^{-6}\,V^{3/2}/d^2 \end{aligned} \tag{3.87}$$

where V is the voltage across the DC gap of width d, and r is the laser spot size. The gap distance is determined by the maximum gradient on the cathode electrode. The peak current as a function of voltage is shown in Figure 3.122.

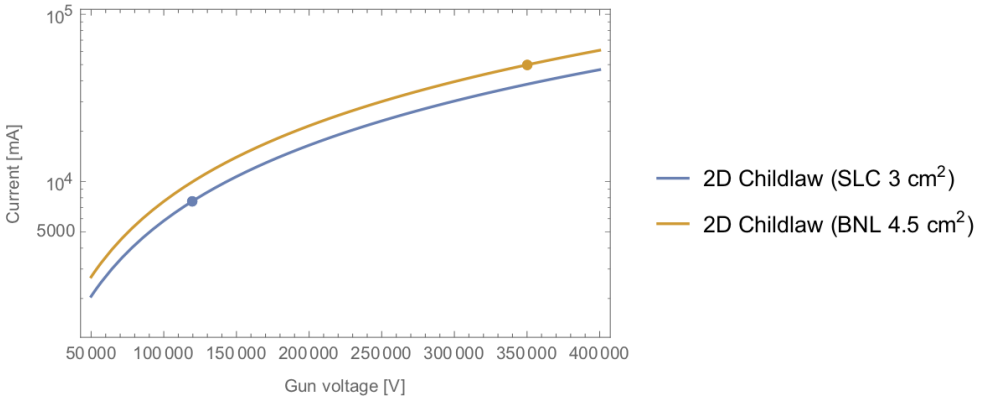

Figure 3.122: Peak current as a function of gun voltage according to the 2D Child Law (Equation 3.87.

To achieve 7 nC bunch charge with 3 A peak current, the bunch length is about 1.5 ns. The current density is less than 7 A/cm^2, the surface charge limit threshold observed in the SLC experiment. The electrode geometry is a ball with a Pierce shape. Figure 3.123 shows the gun electrodes with optimization parameters: the cathode size (L_c), Pierce angle(α_p) and anode aperture(L_a). The gap voltage can be up to 350 kV, limited by the peak gradient of the HV electrode. For operation in field emission free range, the voltage can be reduced down to 280 kV. The anode can be biased to reduce ion back-bombardment [161]. The gap between the cathode and anode is tunable to find the best focusing length during gun operations. These parameters were optimized by minimizing the normalized transverse emittance at 1 m from the gun, and by minimizing the beam envelop at anode aperture. This eliminates beam halo on the metal surface and reduces outgassing. Optimized parameters are shown in Table 3.51.

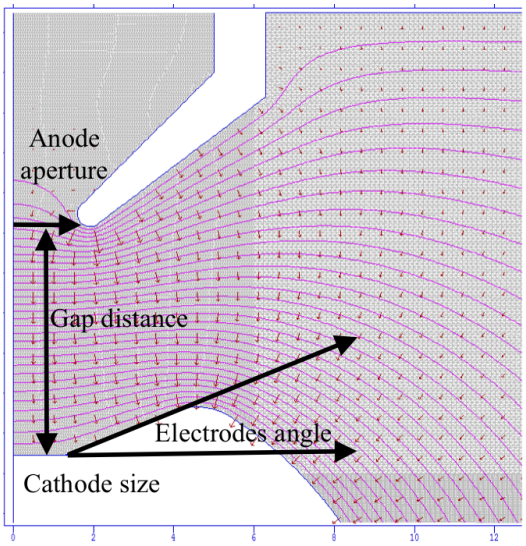

Figure 3.123: Electron gun DC gap geometry.

Table 3.51: Detail parameters of the EIC electron gun.

Parameter	Value
Electrodes diameter [cm]	20
Chamber diameter [cm]	50
Gap distance [cm]	5.7
Voltage [kV]	350
Cathode radius [cm]	1.5
Electrodes angle	28°
Cathode gradient [MV/m]	4
Maximum gradient [MV/m]	10
Anode diameter [cm]	2.2
Pumping speed [L/s]	35000
Space charge limit [A]	up to 45
Anode bias [V]	3000

Electron DC Gun Components Design

The high voltage (HV) feedthroughs are standard X-ray medical HV cable/plugs, such as those made by Dielectric Science. The R30-doped alumina is similar to that made by SCT-France. Both are thus commercially available. The doped alumina option should remove any trapped surface electrons [162].

The components are listed in Figure 3.125 b). The triple-point (alumina-metal-vacuum intersection) will exhibit breakdown if exposed to sufficiently high gradient. A triple-point shielding shed has been designed to generate uniform field distribution on the alumina, and minimize the triple-point gradient. The HV geometry, including electrode, cathode and triple-point shielding, were simulated using Poisson and CST. The maximum gradient on the HV sections is no larger than 10 MV/m. In HV tests, this HV feedthrough operated up to 450 kV with very small leakage current.

HV power consists of two standard Glassman LH-OS in parallel with a fiber optics link to run master/slave for 1 mA at up to -450 kV. Superfish was used to perform the gun's static electric optimization and simulation. The maximum gradient of 10 MV/m occurs at the cathode Pierce shape nose and the triple point shed. The triple point gradient is 3.8 MV/m which is in safe range.

The pumps in the gun are a combination of 2000 L/s sputtering ion pumps and Non Evaporation Getters (NEGs). The entire chamber, with internal stainless steel components, will be baked at 400° C for a week to eliminate diffused H atoms. The entire chamber will be coated by NEG material. 35000 L/s NEG pumps will installed to achieve a mid-10^{-12} Torr-

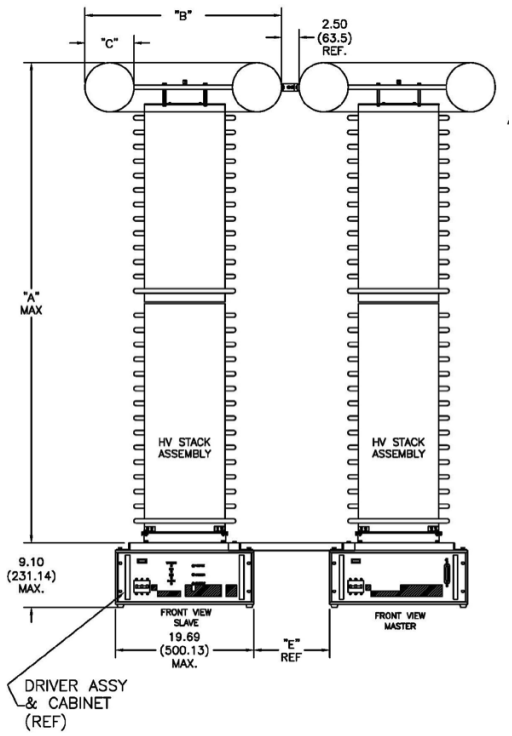

Figure 3.124: EIC electron gun -450 kV power supply configuration.

scale vacuum. The EIC prototype polarized gun has been fabricated and installed, with an achieved vacuum of 7×10^{-12} Torr. The prototype gun cathode electrode and triple point shed are shown in Figure 3.125.

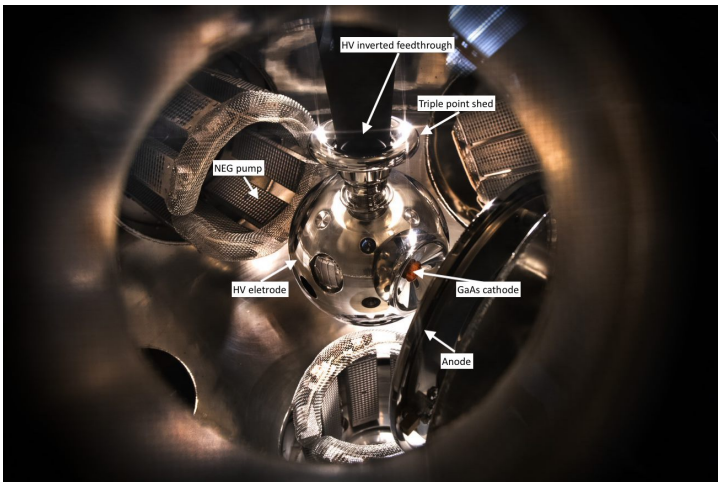

Figure 3.125: Interior photograph of fabricated prototype EIC electron gun.

Cathode Preparation System

A cathode preparation system suited for preparing a 30 mm diameter GaAs cathode under XHV conditions is required. A load-lock chamber, isolated from the preparation system, is included for loading of fresh samples.

Figure 3.126 shows the load-lock chamber, cathode preparation system, and storage chamber for the large cathode gun. The load-lock works as a storage for fresh samples to be activated and transported to the gun for beam operation. The load-lock is isolated from the preparation chamber using an all-metal valve. The cathode preparation chamber is an 18 inch diameter stainless steel sphere with 13 ports for various components. A rotatable vertical tray moves the sample inside the chamber from the heating station to the cooling/activation station.

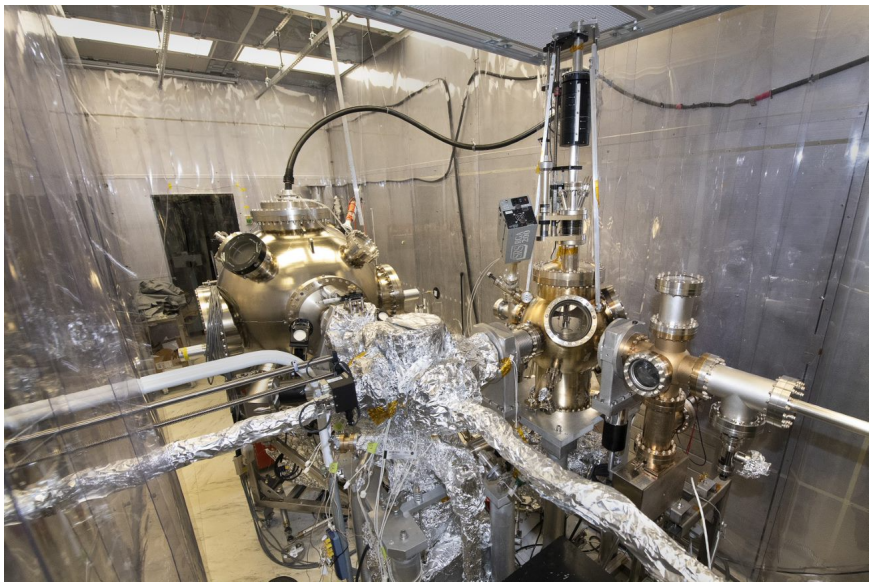

Figure 3.126: Cathode preparation system.

The surface of the samples must be atomically cleaned by heat treatment. The heat treatment must be controlled such that the temperature of the sample is maintained within $\pm 5^{\circ}$C of the desired value. After heat cleaning the sample, it is transferred to the activation station. When the cathode reaches room temperature, successive monolayer quantity deposition of Cs and $O_2(NF_3)$ achieves a negative electron affinity condition, and the cathode is activated.

Activated cathodes are transferred to the storage chamber and stored. The storage chamber vacuum is 10^{-12} Torr scale. Activated cathodes can survive in the chamber for months. When the gun is ready for beam operation, the sample is transferred to the gun. All movement in vacuum is done using magnetic manipulators to minimize friction and gas bursts. With this design, a prototype cathode preparation system has been commissioned: XHV has been achieved, and GaAs cathodes have been successfully activated. It has successfully activated a superlattice cathode with QE about 1% using a 780 nm laser.

3.7.3 Electron Gun Laser System Design

The laser system must meet a few key specifications of the pre-injector design:

1. 0.41 MHz repetition rate.
2. 1.5–2 ns Gaussian temporal profile.
3. 780 nm wavelength.
4. Two bunches as a pair with 2.43 µs spacing between bunches, four pairs of bunches (with 10 ms spacing between pairs) in every second.
5. Helicity flip and filter of laser pulses.
6. Transverse truncated Gaussian.
7. Laser pulse jitter $<$10 ps rms.
8. Pulse ON/OFF contrast $>$60 dB.

Laser pulses are transported to the photocathode via a free space transport through a steel pipe. A round aperture, imaged onto the photocathode and illuminated by the Gaussian laser beam, then generates the desired truncated Gaussian profile. The required laser pulse energies are estimated using approximations of a transport efficiency of 80% as well as a loss of 50% on the imaged aperture.

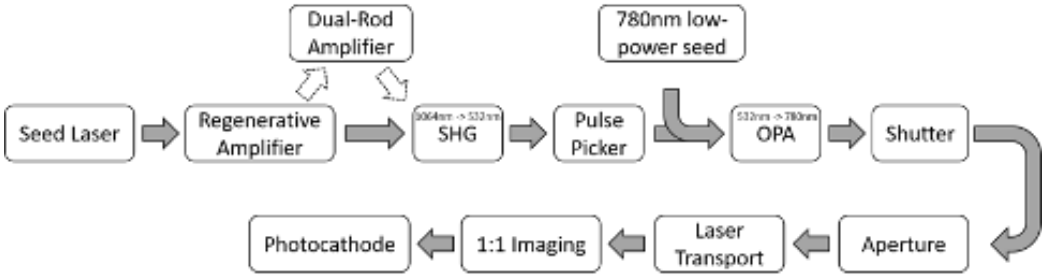

Figure 3.127: Electron injector laser system.

A schematic of the proposed system is shown in Figure 3.127. The master oscillator power amplifier (MOPA) system consists of a fiber seed laser generating longitudinal flat-top pulses with variable durations at a fixed rate of 20 MHz at 1064 nm. The power amplifier consists of a regenerative, dynamic repetition rate, solid-state, Nd:YAG rod amplifier, providing up to 60 dB of gain while also scaling the repetition rate of the seed via selective amplification. During high repetition rate operation, a dual-rod amplifier further increases the output power. This MOPA system is paired with a frequency doubling (SHG) stage and an optical parametric amplifier (OPA) to convert the 1064 nm (IR) output first to 532 nm (green) and then to 780 nm (red).

The regenerative amplifier running in saturation guarantees diffraction limited, Gaussian output with small intensity noise. The solid-state nature of the amplifier system avoids accumulation of non-linear distortions in the longitudinal flat-top profile during low repetition rate, high-energy operation. A Pockels Cell is used to pulse pick the green pulses before pumping the OPA to achieve the high pulse On/Off contrast of over 60 dB.

3.7.4 Electron Pre-injector LINAC Design

The RF LINAC for the pre-injector is designed to use existing technologies with some modifications for application to the EIC. The LINAC generates two trains of four 7 nC bunches for a total of 8 bunches. Each LINAC RF cycle accelerates two bunches. Electron bunches are generated by a DC gun with a voltage, or bunch energy, of 300–350 kV. Following the DC gun, there is a 118.2 MHz bunching cavity to boost the bunch energy up to 0.6 MeV and provide a chirp to the bunch. The peak voltage of the 118.2 MHz cavity is 500 kV. Afterwards, the bunch passes through two 600 kV 591 MHz cavities to align the longitudinal energy spread and bunch further. There is then a 2856 MHz bunching section for further compression and velocity matching, prior to reaching the 2856 MHz main LINAC. The bunching section and part of the first LINAC is inside a continuous solenoid field to maintain the bunch envelope. The main LINAC includes six structures of 2856 MHz traveling-wave disc-loaded constant gradient accelerating sections. Each 2856 MHz accelerating section is 4.2 m with an accelerating gradient of 16 MV/m, so the energy gain per section is 67 MeV. The bunch energy at the exit of the pre-injector is 400 MeV.

3.7.5 Electron Pre-injector Beam Transport

The pre-injector line follows the design of both the SLC injector and KEK-B [163–165]. The preinjector provides 2×7 nC bunches within 2 µs, which is typically the pulse length for an S-band LINAC. The LINAC must operate at 100 Hz to provide four pairs of bunches, with 10 ms spacing between pairs. A total of 8 bunches (4 pairs) will be provided at a repetition rate of 1 Hz.

The initial bunch radius is 0.8 cm at the cathode; this is sufficient area to generate high-charge bunches. The gun design gap voltage is 350 kV. Operate at 280 kV can provide beam with quality meets the requirement. The cathode-anode gap is tune-able. Ion back-bombardment is not an issue due to the low average current, so the laser spot will be centered on the cathode. A circularly-polarized laser beam will illuminate the cathode perpendicular to the cathode face since the electron bunch is deflected by 12° through a dipole bend. The dipole bend has its edge wedged by about 3° to provide the same focusing for both transverse directions.

There are two solenoids placed between the gun and dipole. One solenoid is also placed after the dipole to focus the bunch into the bunching section. Once the bunch is compressed to less than 5 ps, it traverses the LINAC, boosting the bunch energy to 400 MeV. To ensure injected bunch stability in the RCS, a zigzag-based longitudinal phase space ro-

tation section is placed after the LINAC to increase the bunch length to 40 ps, and reduce the energy spread to 0.25% with a 1182.3 MHz dechirp cavity. The electron's spin direction is longitudinal through the pre-injector. A dipole-solenoid-based spin rotator is placed in the transfer line between the LINAC and RCS.

The polarized electron bunch generated from the HVDC gun is described in Section 3.7.2. To reduce the bunch transverse size to fit in the 2.857 GHz LINAC acceptance, a solenoid field is placed from the 118 MHz cavity to the first half of the traveling-wave plate (TWP). The solenoid field is provided by a series of coils with 10–20 cm gaps for diagnostic components and power couplers. Once the bunch energy passes 10 MeV, space charge effects are tolerable and a solenoid field is no longer required.

Parmela 3.38 [166] was used to simulate the pre-injector with 3×10^5 particles. The initial bunch parameters from the cathode are listed in Table 3.52. A genetic optimization and multi-objective parabola optimization were used to optimize these parameters.

Table 3.52: Initial bunch parameters from the cathode.

Parameter	Nominal
Bunch charge [nC]	7
Bunch length (hard edge) [ns]	1
Bunch radius (hard edge) [mm]	8
Longitudinal distribution Gaussian σ [ns]	0.65
Transverse distribution Gaussian σ [mm]	5
RMS thermal emittance [mm-mrad/mm]	0.2
Gun voltage [kV]	280–350

The frequency of the RF cavities in preinjector is listed in Table 3.53. All the frequencies are the harmonics of 1.23 MHz which is 1/80 beam repetition frequency in the electron storage ring.

A standing wave (SW) 118 MHz normal conducting cavity pre-boosts the bunch to 0.6 MeV, and provides a chirp with a cavity gap voltage of 480 kV. Two normal conducting 5th harmonic cavities (591 MHz) then linearize the longitudinal energy spread of the bunch, and compress the bunch into the 2856 MHz cavities' longitudinal acceptance. The two 591 MHz cavities operate at 320 kV and 280 kV gap voltage. Before the 2856 MHz cavity, the RMS bunch length is 4 mm. The bunch length, energy spread, and emittance in the following discussion are all RMS sizes.

A taped 2856 MHz RF buncher cavity is used to boost the bunch energy to 2.8 MeV reducing the bunch length to 1.8 mm. The bunch is injected into the SLC type s-band TWP LINAC. There are 6 SLC TWP structures which raise the bunch energy to 400 MeV. In the first TWP, the bunch is off-crest to de-chirp the bunch. For the remaining TWP's, the bunch

Table 3.53: RF frequency in the pre-injector.

Cavity	Frequency [MHz]
Main LINAC	2856.23
Fundamental buncher	118.23
5th harmonic buncher	591.15
Taped buncher	2856
Dechirp cavity	1182.3
Bunch gap in one LINAC RF pulse	2436 [ns]

is on the crest to accelerate with maximum energy gain. Because two bunches are accelerated in 2 µs, one RF pulse of the LINAC will accommodate two bunches. The bunch-loading-induced bunch-to-bunch energy spread may be compensated by a small injection time delay of the first bunch, before the RF reach the saturation range [167]. Therefore simulations were only performed considering single-bunch dynamics. The voltage V_{acc} of each TWP is 50 MV. Drift space with quadrupole triplets are placed between each TWP structure to tune the bunch beta function. Transport then proceeds through a zigzag section and a 1182 MHz dechirp cavity. Details are discussed in Section 3.8.3.

Figure 3.128 shows the bunch trajectories for 7 nC bunch charge. Figure 3.129 show the bunch parameters such as RMS emittance, bunch size, bunch length, bunch energy and energy spread for 7 nC bunch charge. The emittance is optimized by initial bunch length and focusing optics before reaching the LINAC. The bunch energy spread in the preinjector is dominated by the TWP RF curvature. Table 3.54 summarizes the simulation results for 7 nC bunches at exit of the LINAC.

Table 3.54: Bunch parameters at the exit of the 400 MeV LINAC.

Parameter	Value
Bunch charge [nC]	7
Energy [MeV]	400
Bunch length [ps]	4.7
RMS normalized transverse emittance [mm-mrad]	26
RMS beam size [mm]	0.9
energy spread $\mathrm{d}p/p$	5.6×10^{-3}

Multiple air-core trim coils will be placed in the low energy (< 1 MeV) section, while window frame trim coils will be placed in the LINAC section. The dipole at the exit of the gun can bend beam into a diagnostic beam line which includes Mott Polarimetry for measuring the beam polarization and a Faraday cup. The details of Mott polarimeter are

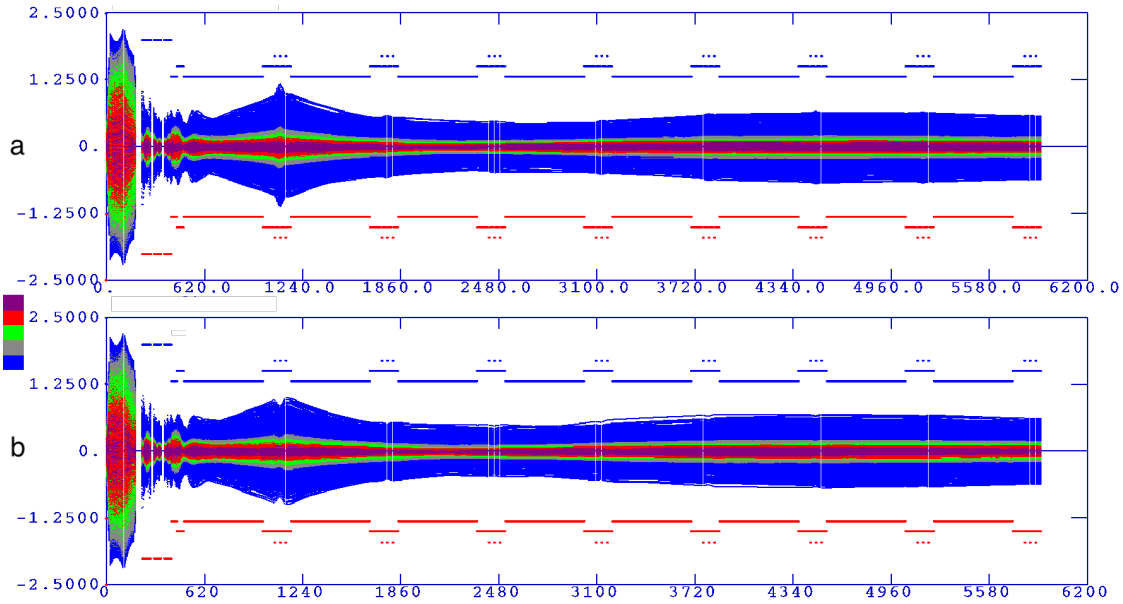

Figure 3.128: Trajectory of a 7 nC bunch. (a) $x - z$ trajectory. (b) $y - z$ trajectory.

discussed in Subsection 6.7.1.

The total length from cathode to end of pre-injector is 60 m. Considering the diagnostics and cathode preparation, the pre-injector hall will take up 65 m in length.

We also studied the requirements of laser longitudinal jitter. The small longitudinal emittance will be needed for future phase phase rotation. Figure 3.130 shows the laser jitter effects in both emittance and longitudinal phase space area. For 7 nC bunch charge, the laser jitter have to be less than $\pm 30^\circ$ to get transverse emittance less than 30 mm-mrad and longitudinal emittance in 1.2×10^{-5} eV-s.

To get the longitudinal microwave stability, the RCS injection bunch needs the longitudinal emittance $\sigma_t \sigma_E < 4 \times 10^{-5}$ eV-s and bunch length of 40 ps. At LINAC exit, we have longitudinal emittance $\sigma_t \sigma_E = 1.2 \times 10^{-5}$ eV-s. By rotation in longitudinal space, we can increase the bunch length to 40 ps. The dechirping cavity can control the energy spread to 0.25%.

The longitudinal match section is designed that a bunch stretching r_{56} will provide the required bunch stretching, utilizing the intrinsic energy spread in the bunches, followed by a dechirping cavity to reduce the total energy spread to certain value. The simulation was performed by Parmela. The longitudinal phase space is shown in Figure 3.131.

The zigzag includes four dipole magnets with bending angles of 22° and a 3 m drift in between the 1st and 2nd, as well as the 3rd and 4th dipoles. The zigzag stretches the bunch length to 40 ps. A dechirping cavity is needed to reduce the energy spread. Lower

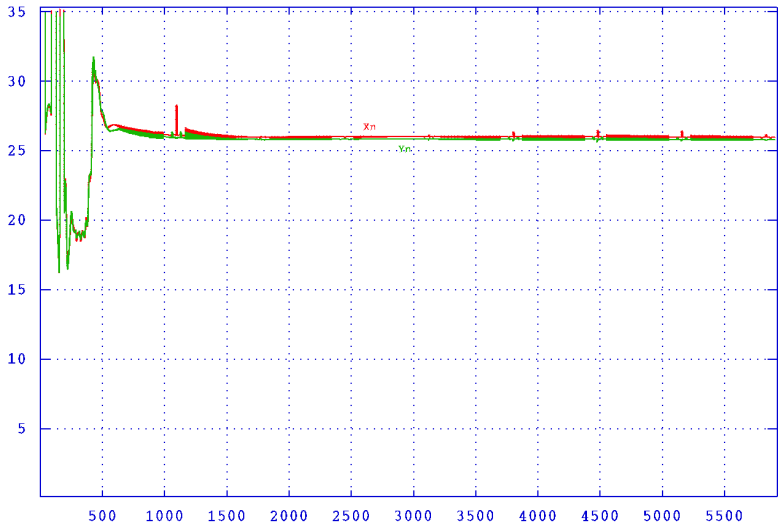

(a) RMS normalized transverse emittance (mm-mrad) vs. z (cm). Red: horizontal emittance. Green: vertical emittance.

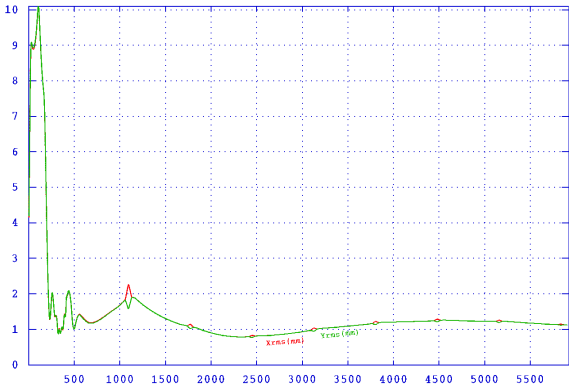

(b) RMS beamsize (mm) vs. z (cm). Red: horizontal beamsize. Green: vertical beamsize.

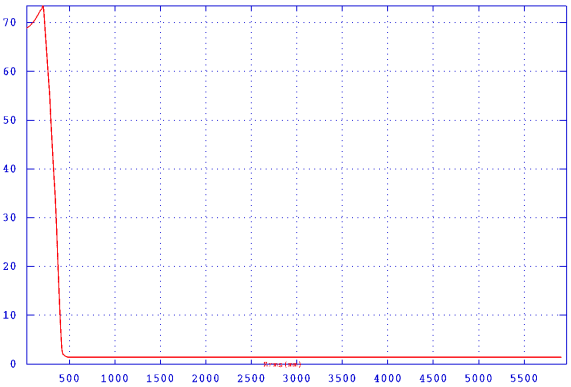

(c) RMS bunch length (mm) vs. z (cm).

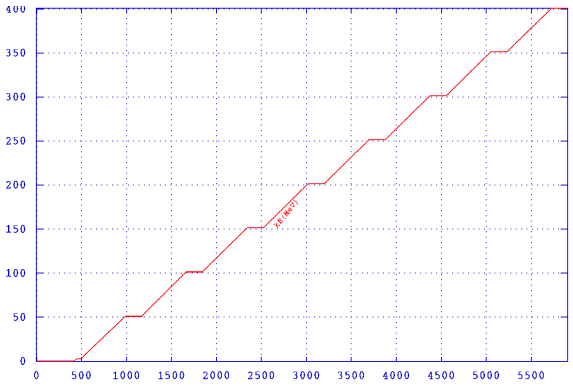

(d) Beam energy E (MeV) vs. z (cm).

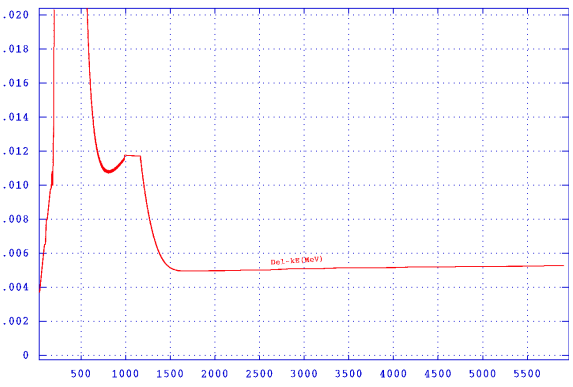

(e) Beam energy spread dE (MeV) vs. z (cm).

Figure 3.129: The bunch parameters along the beamline z (cm) with bunch charge of 7 nC.

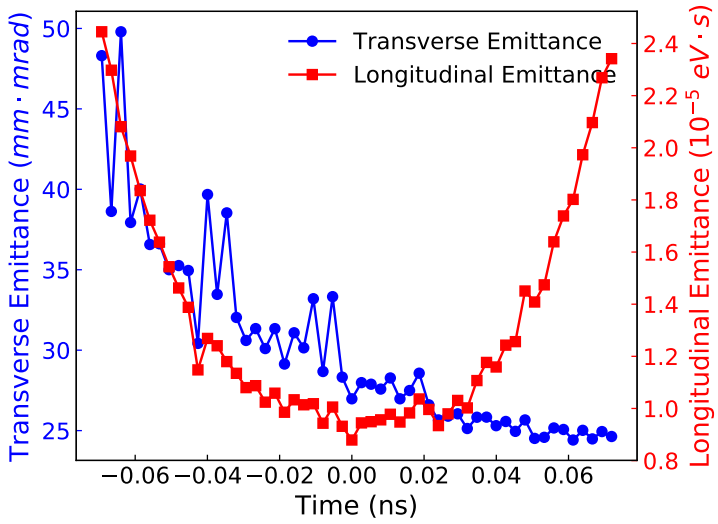

Figure 3.130: The transverse emittance and longitudinal emittance as functions of laser jitter.

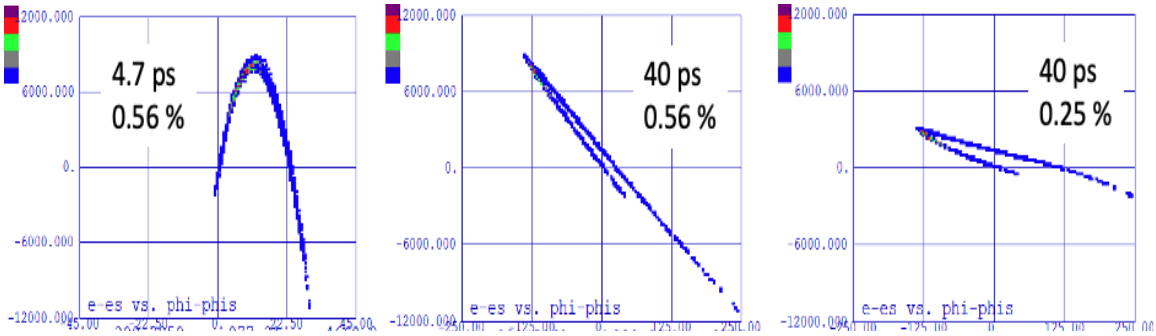

Figure 3.131: The longitudinal phase space at exit of LINAC (left plot), exit of zigzag (middle plot) and exit of dechirp cavity (right plot). The RMS bunch length and RMS energy spread are shown in each plot, respectively.

frequency is preferred to achieve minimum dp/p. However, higher frequency cavity can dechirp beam more efficiency and cost saving. By testing 591 MHz ,1182 MHz and 1773 MHz, we find 1182 MHz cavity can achieve the required energy spread. Therefore, we use 1182 MHz as the frequency of dechirping cavity. Figure 3.132 shows the dechirping cavity voltage as the function of the bunch length. The minimum rms energy spread could achieve 0.18%. By tuning the dechirping cavity, the rms energy spread can be controlled to 0.25% with the gap voltage is 9 MV. A five-cell 1182 MHz cavity can be used for this purpose. Table 3.55 summarizes the nominal beam parameters of the exit of preinjector.

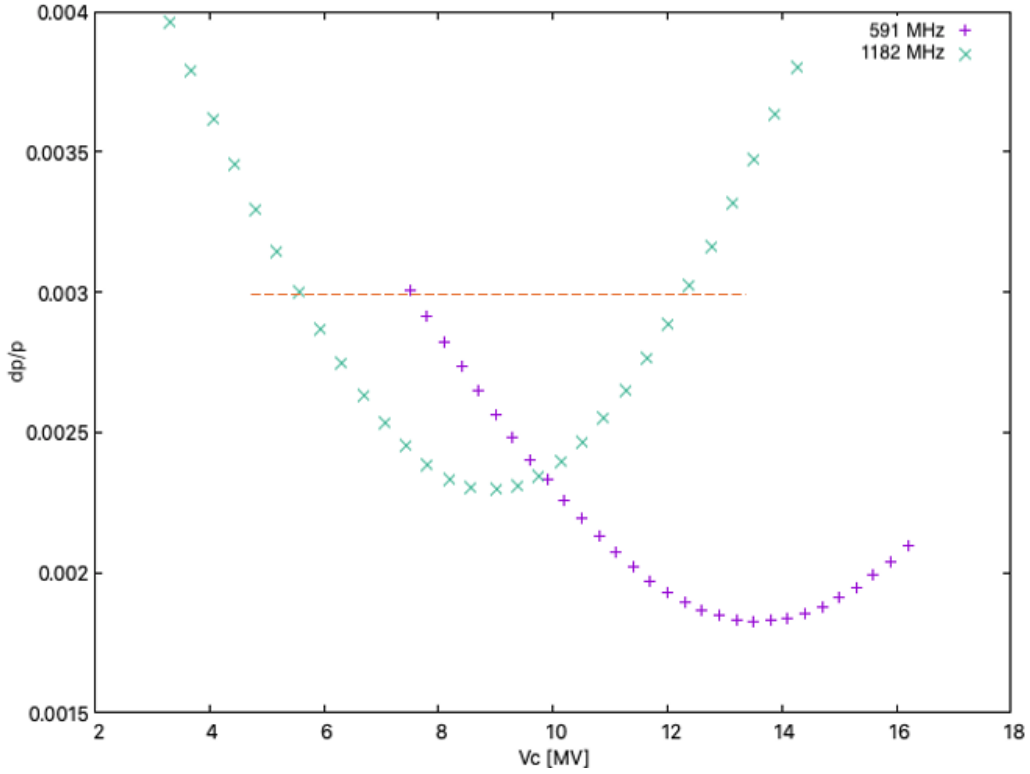

Figure 3.132: The energy spread as the function of dechirping cavity gap voltage. 591 MHz and 1182 MHz dechirping frequency are compared.

Table 3.55: Parameters for preinjector bunches and longitudinal phase space rotation

Parameter	Value
LINAC exit energy [MeV]	400
Number of chicane dipoles	4
Dipole bend angle at 400 MeV	22°
Total chicane length [m]	11
Chicane exit bunch length [ps]	40
Chicane exit RMS energy spread	2.5×10^{-3}
Dechirp RF frequency [MHz]	1182
Dechirp RF peak voltage [MV]	9
RMS transverse emittance [mm-mrad]	30

3.7.6 Electron Pre-injector Magnetic Requirement and Specifications

The pre-injector has multiple groups of magnets which are as follows:

1. **Gun dipole magnet:**
   The dipole magnet steers the polarized e-beam into the beam compression section. This also deflects the beam allowing the laser to illuminate the photocathode head on. It will also be used to deflect individual e-beam pulses into the diagnostic sector. Additional steering magnets will be used to steer the beam into a Faraday cup.

2. **Continuous solenoidal field:**
   The cavities reside inside a high solenoidal field in line with the beam line axis. The solenoidal field is generated by individual water cooled pancake coil assemblies as shown in Figure 3.133. The gaps in the coil structure will vary to accommodate the specific design of the RF buncher cavity's power coupler and the cavity waveguide.

3. **Gun box Solenoids and air core trim:**
   Three solenoids will be placed between the gun and the first bunching cavity to maintain the beam size for 5–10 nC bunch. In the diagnostic beamline, there are two solenoids to maintain the beam size up to either the Faraday cup or the Mott polarimeter. With a beam greater than 100 keV, all the corrections will be made by short air core trims.

4. **Helmholtz coils:**
   Between the gun and the 3 GHz tape cavity, the e-beam energy is lower than 1 MeV. The beam trajectory could be influenced by the earth's field and other stray magnetic fields. The beam path in this area is surrounded by a large external magnetic field canceling Helmholtz coil.

5. **Quadrupoles and trim coils:**
   A magnet girder is installed between each 2.856 GHz accelerator structure, which contains quadrupole triples and X-Y steering coils shown in Figure 3.133. Lower field X-Y trim magnets will be used between LINAC sections with beam energies up to 400 MeV. The steering coils will have higher field capability and will be used between sections of LINAC with e-beam energies more than 100 MeV. Figure 3.133 is also a view of the magnet and diagnostic girder that are located between each accelerator structure.

Table 3.56 presents the list of magnet requirements and preliminary specifications for the magnetic elements for the conceptual design of the pre-injector beam line.

Table 3.56: Magnet requirements and preliminary specifications for the EIC pre-injector.

Magnet type	Qty	Field [T]	Aperture [m]	L_{mag} [m]	I [A]	R [Ω]	V [V]	Power [W]
Guv air core trim (H)	2	0.001	0.104	0.154	0.7	0.79	0.55	0.4
Gun air core trim (V)	2	0.001	0.114	0.164	0.8	0.87	0.69	0.6
Gun dipole magnet	1	0.0016	0.206	0.306	0.8	0.69	0.55	0.4
Air core trim (H)	4	0.0005	0.104	0.208	0.5	0.66	0.33	0.16
Air core trim (V)	4	0.0005	0.106	0.212	0.5	0.69	0.34	0.17
Helmholtz coil (H)	1	0.00003	3	10	28.5	0.7	20	570
Helmholtz coil (V)	1	0.00003	3	10	14.6	1.4	20	292
Beamline solenoid	5	0.09	100	100	50	0.22	11.2	560
Buncher solenoid	18	0.3	0.4	NA	334	0.068	22.7	7586
Low field steerer (H)	4	0.0038	0.91	0.134	3	0.2	0.6	1.8
Low field steerer (V)	4	0.0038	0.91	0.134	3	0.2	0.6	1.8
LINAC steering magnet (H)	32	0.008	0.086	0.15	7.5	0.12	0.9	6.7
LINAC steering magnet (V)	32	0.008	0.086	0.15	7.5	0.12	0.9	6.7
Triplet quadrupole, outer	14	2 T/m	0.04	0.12	10	0.05	0.5	5
Triplet quadrupole, center	7	4 T/m	0.04	0.12	10	0.1	1	10
Transport line quadrupole	20	10.7 T/m	0.044	0.222	75	0.076	5.7	429
Vertical bending dipole	2	0.1	0.026	1	75	0.018	1.4	105

Figure 3.133: Continuous solenoidal field coils and quadrupoles from NSLS-II LINAC.

3.8 Injection, Extraction and Beam Transport

3.8.1 Overview of Injection, Extraction and Beam Transport

To achieve the final collision energies for the electrons and hadrons, both undergo an acceleration process in the various accelerators of the EIC complex. In this section we present the results from a study of the injection/extraction systems of each acceleration stage and the beam transfer lines that connect the acceleration stages. Although the hadron ring exists already and is currently operating to support the physics program of hadron-hadron collisions in RHIC, the conversion of the RHIC complex into the EIC still requires some changes in the hadron ring. One of the modifications is the injection of the hadrons into the Yellow ring which will accelerate and store the hadrons. The acceleration sequence of the hadron bunches is outlined below:

1. Protons are pre-accelerated by the 200 MeV LINAC, and heavy ions by the EBIS source.
2. The Booster and the AGS accelerate for injection into RHIC. The Booster extraction system (B Ext), the beam optics of the transfer line from the Booster to AGS (BtA), and the injection to AGS (A Inj) are described in [168].
3. The beam is extracted from the AGS (A Ext) as described in [169].
4. The Yellow ring receives the hadron bunches.
5. The hadrons in the Yellow ring circulate and collide with the electron bunches stored in the electron storage ring.

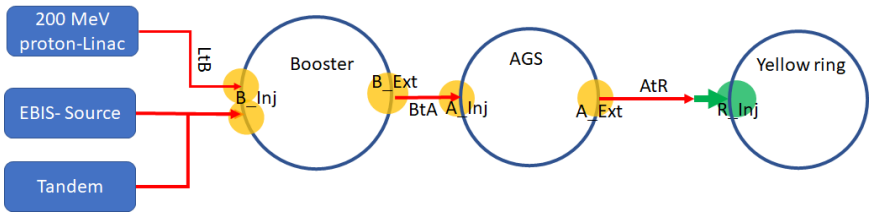

Figure 3.134: Acceleration stages for the existing RHIC hadron collider.

Figure 3.134 is a schematic diagram of the acceleration sequence of the hadrons including the injection/extraction systems and the transfer lines between the hadron accelerators. The details of the last part of the AtR hadron transfer line and the injection system into the Yellow ring are highlighted in yellow. The acceleration sequence of the electron bunch is outlined below:

1. Acceleration to 400 MeV in the LINAC.
2. Up to 8 bunches transferred from the 400 MeV LINAC over four 100–50 Hz cycles via the LtR transfer line.

3. Injection into the RCS.
4. Acceleration to 1 GeV in the RCS where they are merged into two bunches.
5. Further acceleration to 5, 10 and 18 GeV
6. Extraction of two bunches from the RCS.
7. Transfer of two bunches from the RCS via the RtS transfer line.
8. Injection into the storage ring.
9. Storage of the bunch in the storage ring for collisions with the hadron beam circulating in the Yellow hadron ring.
10. Electron beam bunch extraction for the storage ring.

In the following sections the results of the study of the injection and extraction systems and the transfer lines are provided. Figure 3.135 is a schematic diagram of the various acceleration stages of the electron bunches showing the systems described in this section highlighted in yellow.

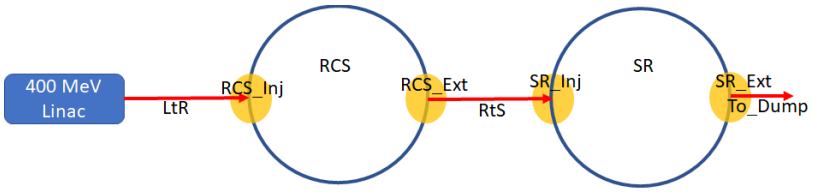

Figure 3.135: Schematic diagram of the electron acceleration stages showing the transfer lines that connect the acceleration stages and the beam injection/extraction systems

3.8.2 Hadron Injection from the AtR Line to the Hadron Storage Ring

This section describes the hadron beam injection from the AtR beam transfer line to the Hadron Storage Ring (HSR). During RHIC operations the AtR line [170] is being used to transfer the hadron ions from the AGS to the "Blue" and "Yellow" rings which circulate the hadrons clockwise and counterclockwise, respectively. Figure 3.136 is a schematic diagram of the AtR line with the AGS ring and the RHIC rings. The switching magnet of the AtR line (Figure 3.136) deflects the beam into either the X-line for injection into the "Blue" ring or the Y-line for injection into the "Yellow" ring. The EIC collider utilizes only the "Yellow" ring. For the EIC collider 290 bunches will be injected into the "Yellow" ring; therefore a kicker with ∼18 ns rise time is needed. To overcome the limitation of the long rise time of the present kickers the Y-line of the AtR line will be extended and connected to the Blue arc between IR6 and IR4. This arc will transport the hadron bunch to the IR4 straight section where it sill be injected into the Yellow ring at the center of the IR4 straight section, as shown in Figure 3.136.

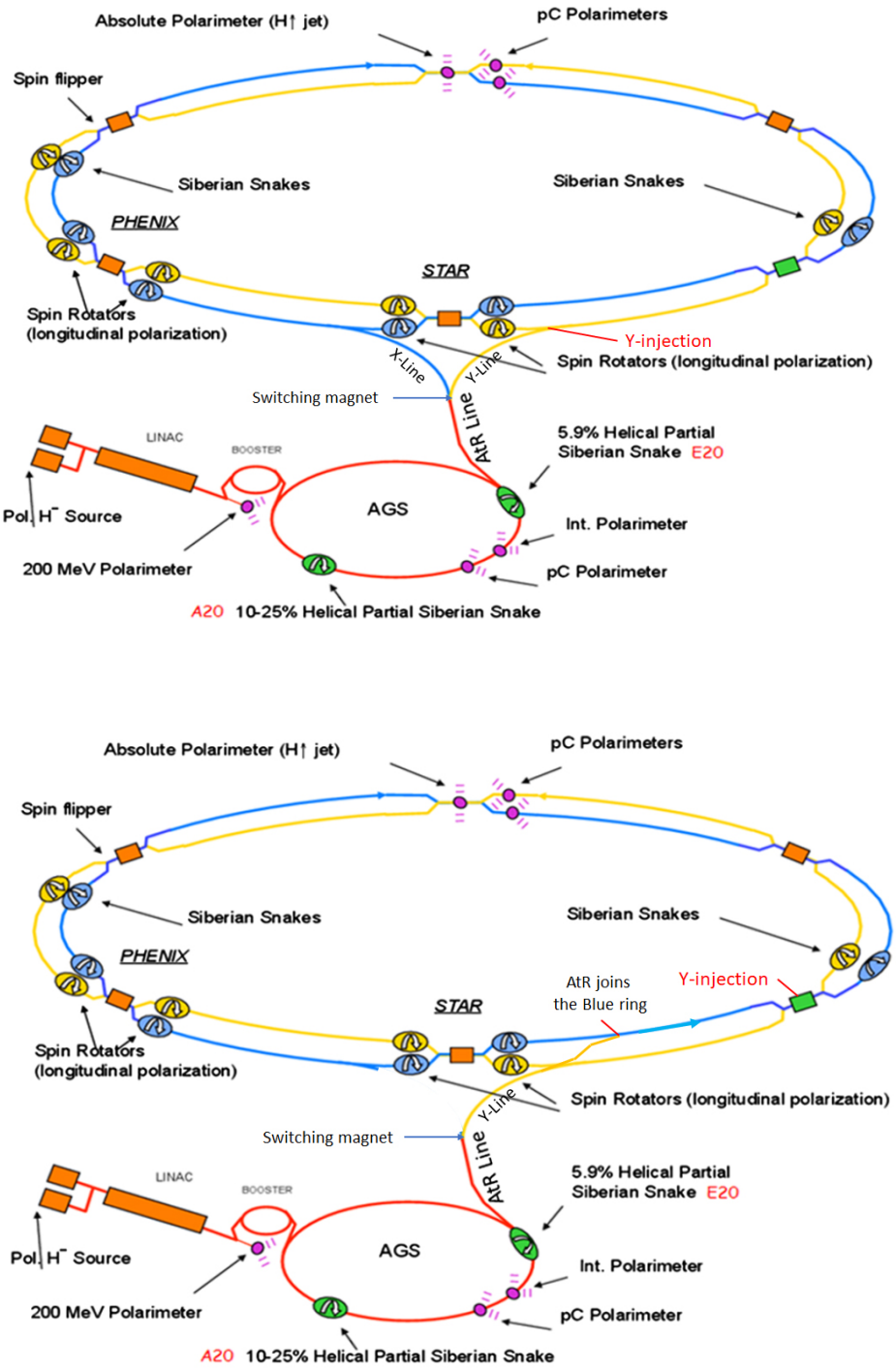

Figure 3.136: Schematic diagram of the RHIC collider. Top: The present AGS to RHIC (AtR) transfer line is located between the AGS and RHIC rings. The switching magnet of the AtR line deflects the beam into either the X-line for Blue ring injection or the Y-line for Yellow ring injection. Bottom: The Y-line will be extended to join the Blue ring which will transport and inject the beam at IP4 point of the Yellow ring.

The Y-Injection Region of RHIC

Currently the hadrons are injected into the "Yellow" ring from the Y-Line of the AtR beam transfer line using a ∼38 mrad Lambertson septum magnet as shown in Figure 3.137. Upstream of the Lambertson magnet a dipole magnet which bends the beam downwards by 3 mrad is followed by six RHIC quadrupoles that match the AtR optics to the Yellow ring lattice at the location of the 1.7 mrad vertically bending Y-Kicker.

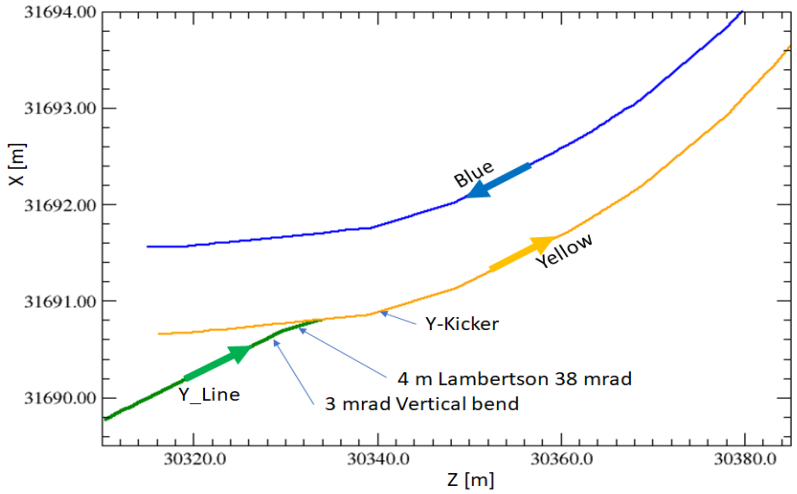

Figure 3.137: RHIC survey coordinates of the entrance and exit of the elements which comprise the Y-Line (green), part of the the "Yellow" ring and part of the "Blue" ring. The location of the 3 mrad vertical bend, the Lambertson septum magnet, and the 1.7 mrad vertically bending Y-kicker is shown.

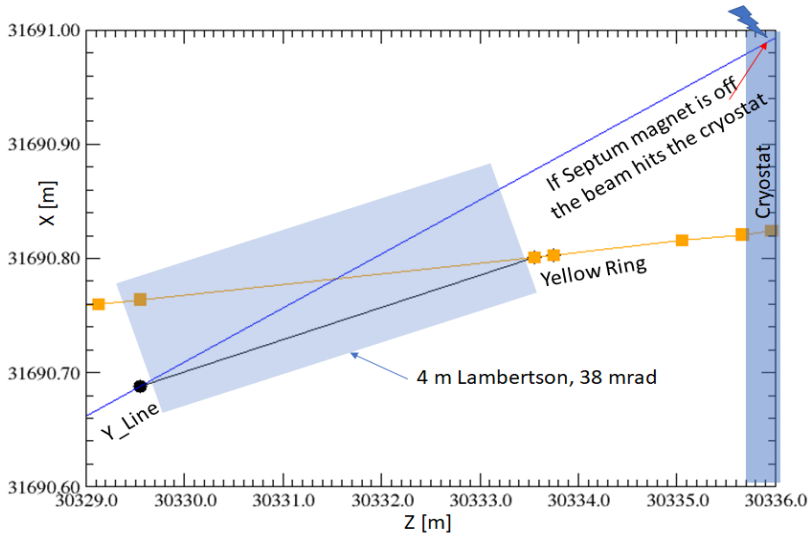

Figure 3.138: Closeup view showing the survey coordinates at the location of the Lambertson septum magnet.

A closeup view of Figure 3.137 is Figure 3.138 which shows the survey points at the location of the 4 m long and 38 mrad Lambertson septum magnet. If the Lambertson septum magnet is turned off the beam from the Y-line will hit the cryostat of the Y-arc. Figure 3.139 is an expanded view of Figure 3.138. It shows the survey coordinates of devices upstream of the Lambertson septum magnet. The picture on the left of the figure shows that the vacuum pipe of the Y-line is gouging the cryostat of the Yellow arc.

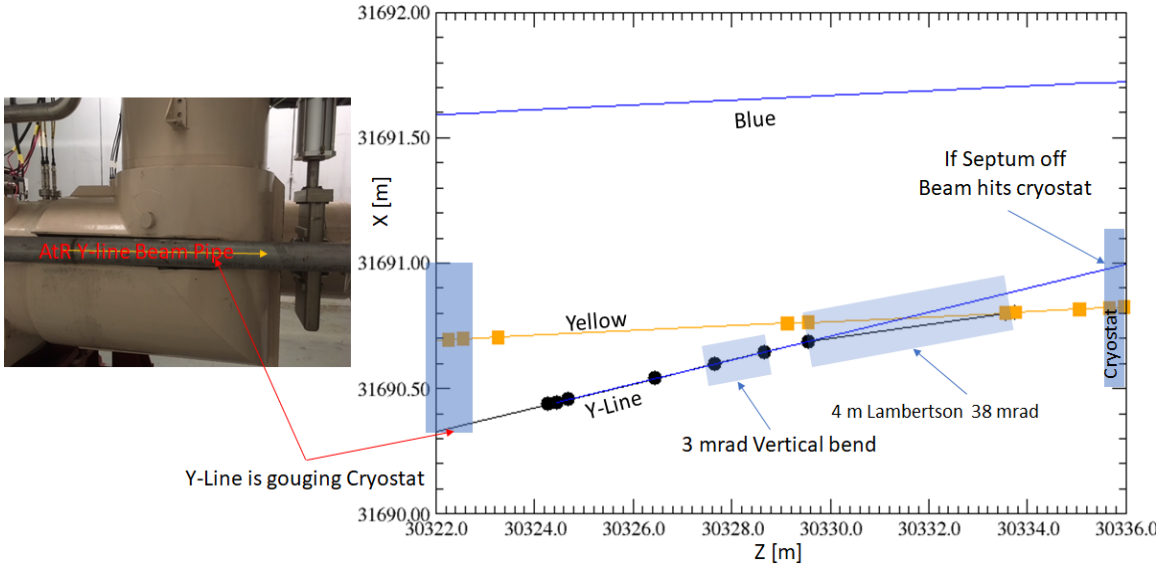

Figure 3.139: Survey coordinates of devices upstream of the Lambertson septum magnet. The picture on the left of the figure shows that the vacuum pipe of the Y-line is gouging the cryostat of the Yellow arc.

Modification of the Y-line Beam Injection System

Currently the maximum number of injected hadron bunches into either the "Blue" or "Yellow" rings is limited to 112 bunches. This limitation is due to the 90 ns rise time of the RHIC injection kickers. The EIC accelerator will be injecting 290 hadron bunches into the "Yellow" ring; therefore a system of kickers with ∼18 ns rise time is needed. The available space in the current location of the Y-Kickers is not large enough to accommodate kickers with such a fast rise time.

To overcome this limitation a new scheme of injecting into the "Yellow" ring uses part of the arc of the "Blue" ring, starting from the present Y-line injection region and ending at the mid-point of the IR4 straight section. Figure 3.140 visualizes the modification steps required which are also listed below.

This scheme of injecting into the Yellow ring is based on utilizing the space which will be available after removal of the the 3 mrad vertical dipole and the 38 mrad Lambertson magnet:

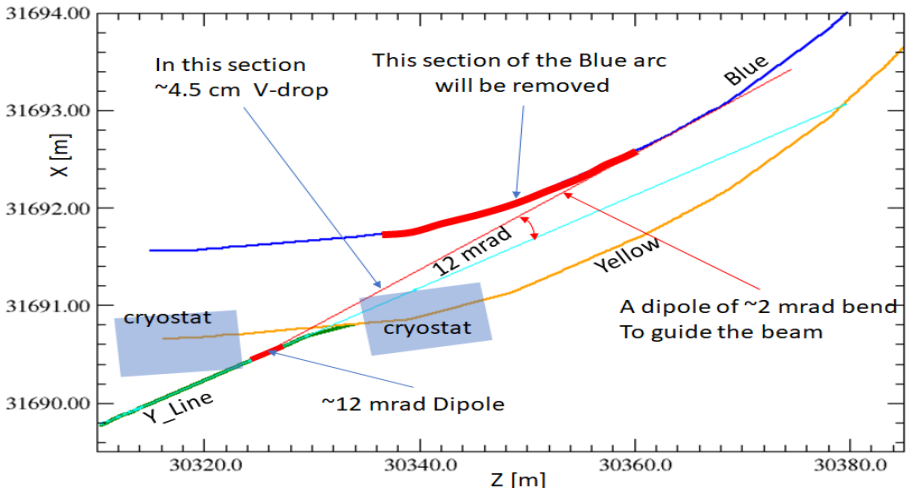

Figure 3.140: Schematic diagram of the Y-line injection region visualizing the steps required for the modification of the beam lines in this region as described in the text.

1. Remove the 3 mrad vertical dipole and the 38 mrad Lambertson septum magnet. This step will direct the beam of the AtR-line on to the cryostat of the Yellow arc, but the beam trajectory will never meet the Blue arc, as shown by the cyan line in Figure 3.140.

2. Just after the last horizontally bending dipole of the Y-AtR transfer line (see Figure 3.141) a vertically bending dipole will be placed to bend the beam ∼40 cm above the level of the Yellow line.

3. Part of the Blue line will be removed as it is indicated by the red arc in Figure 3.140.

4. Another vertical dipole will be placed near the Yellow line (see Figure 3.141) to level the beam horizontally and keep the line at ∼40 cm above the Yellow ring. A horizontally bending dipole is placed at the 40 cm elevated part of the beam line. This dipole will aim the beam towards the Blue arc as shown in Figure 3.141.

5. Two consecutive vertically bending dipoles will bring the beam to the same level as the Blue arc as shown in Figure 3.141.

6. Following the last vertical bending dipole a few quadrupoles and a 2 mrad dipole magnet guide the beam into the Blue ring.

Table 3.57 lists the number and some of the parameters of the magnetic elements which appear in Figure 3.141. Only one new quadrupole is needed, since other quadrupoles can be re-used from other areas of RHIC complex (X-line, Y-line and U-line).

Figure 3.142 shows the beam optics of the "Blue" ring. The part of the "Blue" ring which is of interest in this modification is the section defined from the Y-injection Lambertson magnet to the IR4 interaction point (IP4). Twiss parameters of this section of the Blue arc are plotted in Figure 3.143.

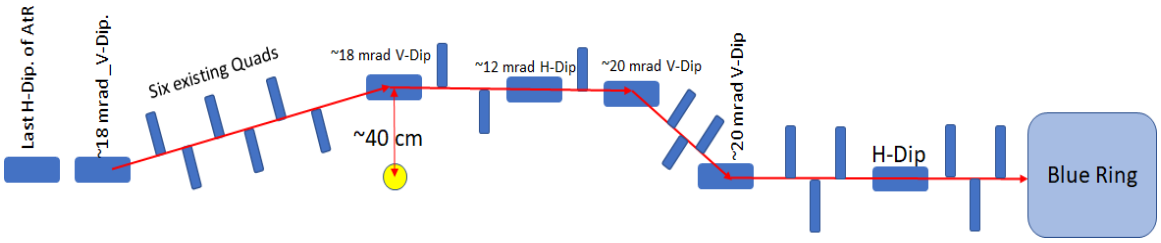

Figure 3.141: Schematic diagram of the extension of the Y-AtR beam-line. The yellow circle represents the cross section of the yellow arc

Table 3.57: The magnetic elements of the extension of the Y-line as they appear in Figure 3.141. Only the elements which have to be newly built appear in this table.

Magnetic Element	Qty	Length [m]	Half-gap/Radius [cm]	Bend-angle [mrad]	K1 [m^{-2}]
V- Dipole	2	1.25	4	18.0	
V- Dipole	2	1.50	4	20.0	
H-Dipole	1	0.75	4	12.0	
H-Dipole	1	0.5	4	2.0	
Quadrupole	1	0.5	3		0.2

The injection scheme is shown in Figure 3.144. Part of the elements upstream of the D5I magnet will be removed and replaced with warm magnets which will guide the beam towards the Yellow ring where the injection septum magnet is located. The right picture is a layout of two possible placements of the septum magnet, one with a 43 mrad dipole magnet and a 50 mrad septum magnet, and the other with a 20 mrad dipole magnet and a 26 mrad septum magnet.

Figure 3.145 shows the beam optics of the IR4 straight section. The layout of the beam elements is in Figure 3.145 with the highlighted region being the proposed injection region where the dipole and the injection septum will be placed.

The Beam Optics of the Connection Line Between the AtR and Blue Ring

The beam optics of the beam line which connects the AtR line to the Blue arc and is shown schematically in Figure 3.141.

The connection line starts from the entrance of YQ1 quadrupole element which is the first of the six quadrupoles of the RHIC injection line that are currently being used to match the beam parameters of the AtR beam to the yellow ring. The new beam line for the EIC project eliminates the 3 mrad pitching magnets and the Y-Lambertson magnet and makes

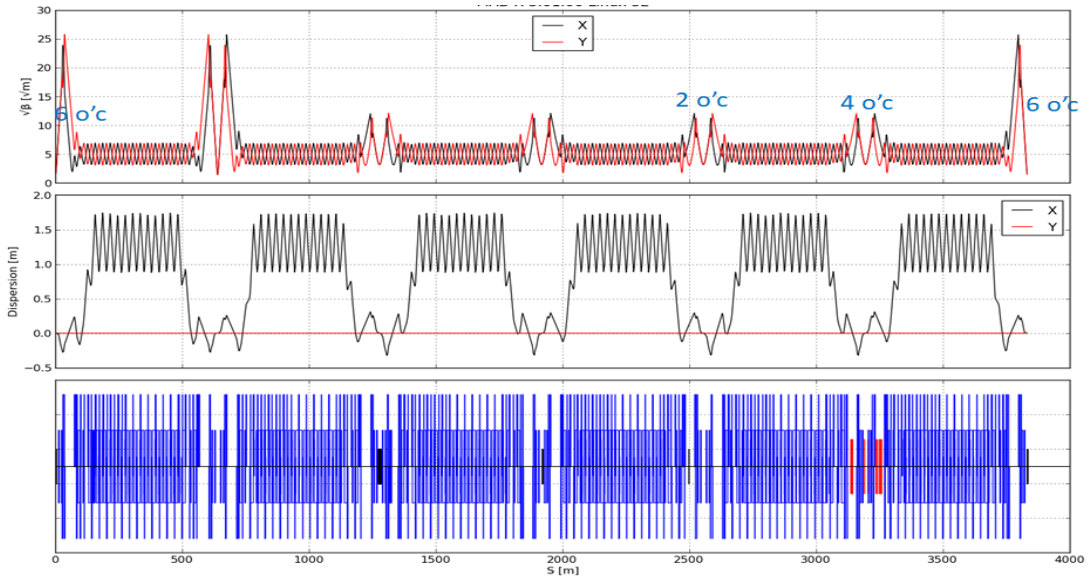

Figure 3.142: Beam optics of the Blue ring. From top to bottom plotted are the $\beta_{x,y}$-functions, the dispersion $\eta_{x,y}$, and the location of the elements along the Blue ring.

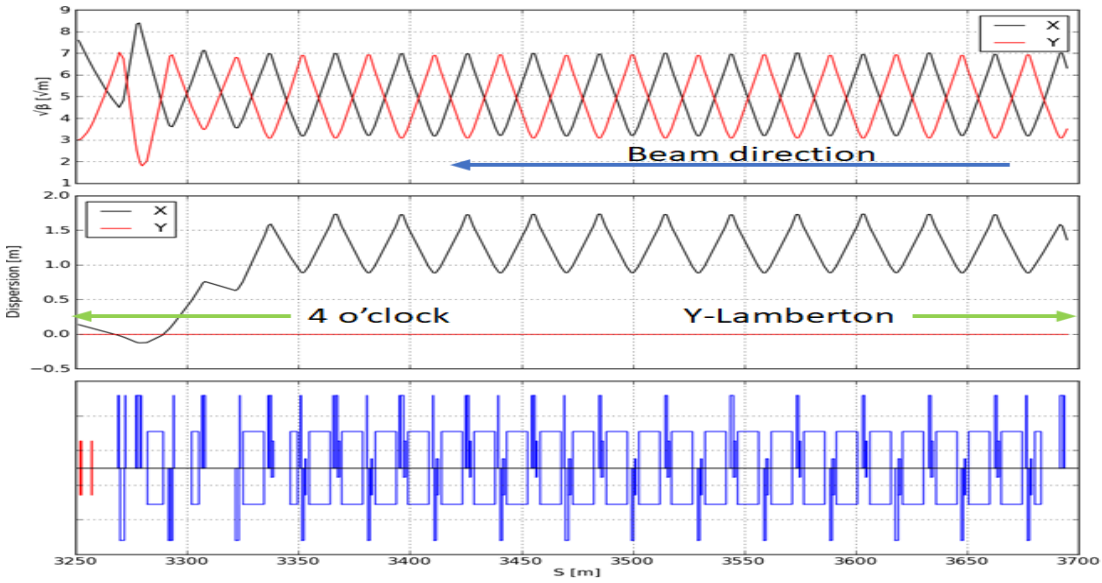

Figure 3.143: Beam optics of the Blue ring section from the Lambertson magnet to the IP in straight section IR4. From top to bottom plotted are the $\beta_{x,y}$-functions, dispersion $\eta_{x,y}$, and the location of the elements along the Blue ring.

use of additional dipole magnets and quadrupole magnets, to transport the AtR beam over the Yellow ring as shown in the schematic diagram of Figure 3.141 and connect it to the Blue arc.

Figure 3.146 shows the beam optics of this connection line as it is generated by the MAD

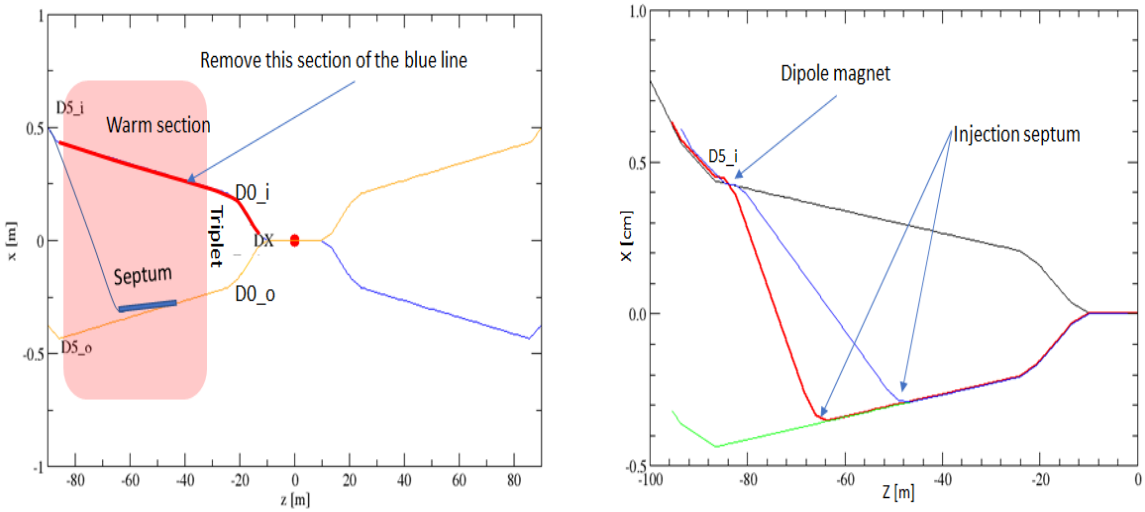

Figure 3.144: Left: Schematic diagram of the beam injection scheme in IR4. A dipole magnet following the D5I magnet will guide the beam into an injection septum magnet. Right: The layout of two possible arrangements of the dipole and septum magnet.

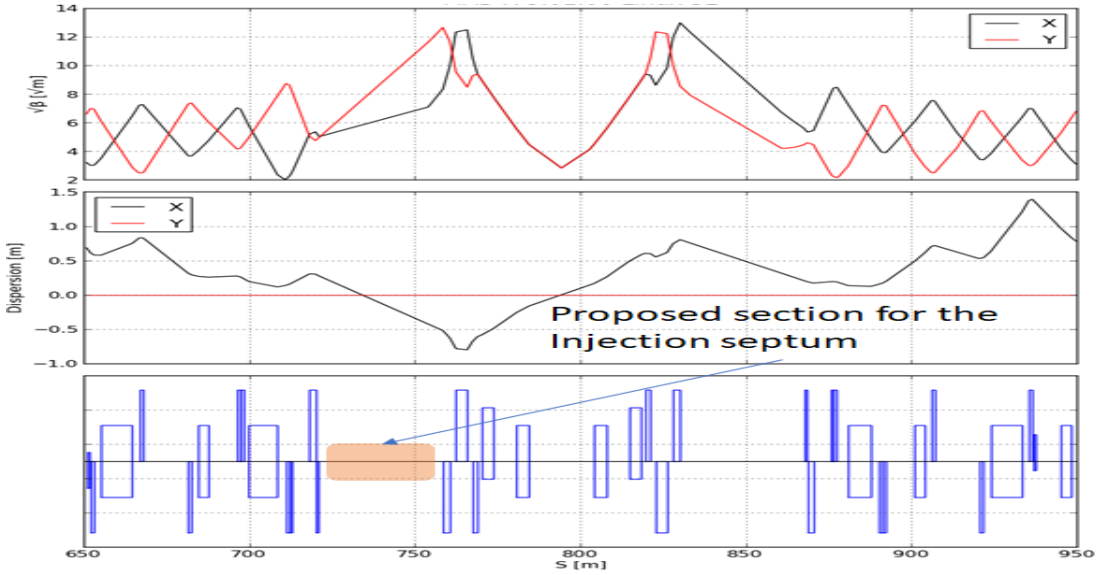

Figure 3.145: Twiss functions together with the placement of the elements in the IR4 straight section. The highlighted region indicates the proposed injection region where the dipole and and the injection septum magnet will be placed.

computer code. The main constrain of this beam line is to match the beam parameters of the AtR line to those ones of the blue arc at the entrance of the B5Q10 quadrupole of the Blue arc.

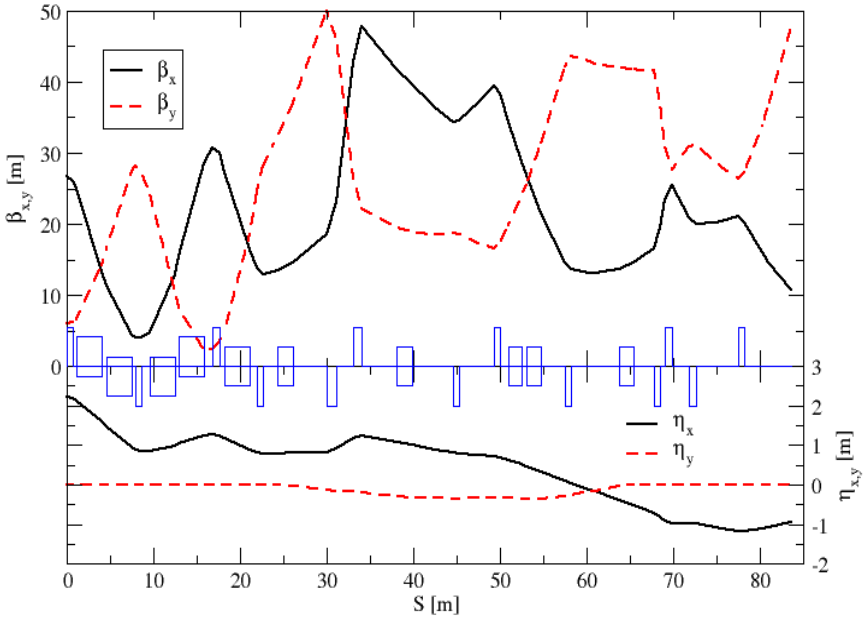

Figure 3.146: The beam optics of the beam line which connects the AtR line to the Blue arc at the location of the B5Q10 quadrupole.

Specifications of the Strip Line Kickers

The current scheme of hadron injection from the AtR line into HSR is to inject a single bunch per AGS cycle. After the hadron injection there will be a total of 290 circulating bunches in HSR, each bunch will be 15 ns long and the center to center distance between adjacent bunches circulating in HSR will be 40 ns as shown in Figure 3.147. The revolution time of a single bunch in HSR is 12.65 µs and there will be a 1 µs gap in the circulating bunches in HSR. Figure 3.147 is a schematic diagram of two consecutive bunches circulating in HSR just after injection from the AtR.

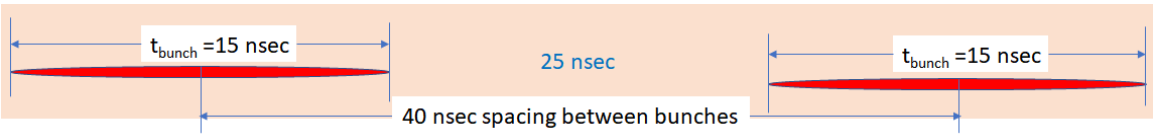

Figure 3.147: Schematic diagram of two consecutive beam bunches in HSR just after injection from AtR.

To calculate the required length L of each strip line kicker we should take into account the following quantities which are itemized below and also shown in Figure 3.148.

- The rise time of each strip line $\tau_{\text{rise-time}}$
- The length of the bunch t_{bunch}
- The speed of the bunch c_{bunch}
- The speed of the EM wave to transverse the strip line c_{EM}
- The time to fill strip line with the electromagnetic wave t_{fill}
- The time for the bunch to traverse the strip line t_{trav}

with the relationship:

$$\tau_{\text{rise-time}} + t_{\text{fill}} + t_{\text{trav}} + t_{\text{bunch}} = \tau_{\text{rise-time}} + \frac{L}{c_{\text{EM}}} + \frac{L}{c_{\text{bunch}}} + t_{\text{bunch}} = 40\,\text{nsec} \tag{3.88}$$

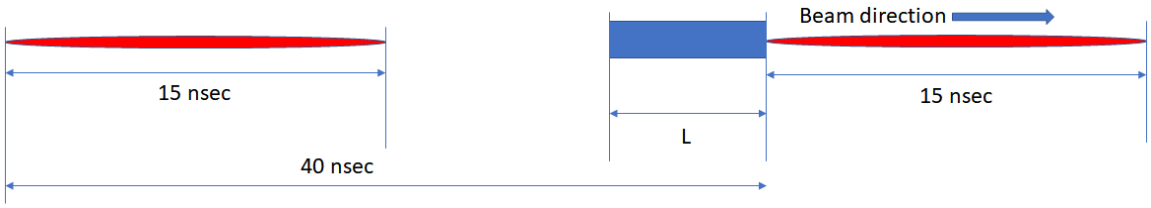

Figure 3.148: Schematic diagram of two consecutive beam bunches in HSR and the relation used to calculate the required length of strip line.

Table 3.58 lists the lengths L of the strip line kicker for different rise times. It is assumed that the speed of the electromagnetic wave traveling in the kicker is the same as that of the beam bunch, and each is equal to the speed of light in vacuum. The selected length of the strip line kicker is 90 cm. By accepting a maximum voltage drop of 40 kV across the electrodes, such a kicker can deflect an 82 Tm beam by 0.059 mrad. Therefore 17 of these kickers are required per 1 mrad of deflection angle.

Table 3.58: The required strip line kicker length L for different rise-times.

τ rise−time [10^{-9} sec]	t bunch [10^{-9} sec]	c EM [10^{8} m/sec]	c bunch [10^{8} m/sec]	L [m]
15.0	15.0	3.0	3.0	1.5
19.0	15.0	3.0	3.0	0.90
20.0	15.0	3.0	3.0	0.75

3.8.3 Electron Beam Transport from Pre-injector LINAC to RCS

The transfer line from the exit of the 400 MeV LINAC to the injection point of the RCS is shown in Figure 3.149. It schematically shows spin rotator, transfer line and injection.

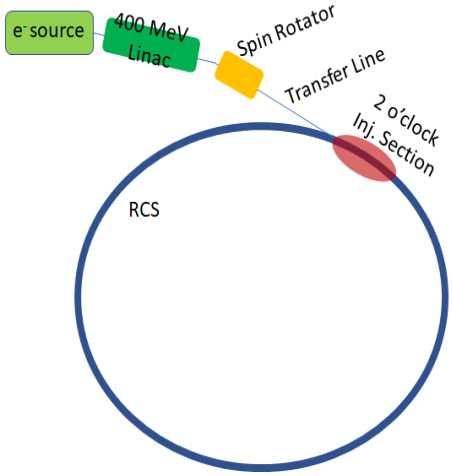

Figure 3.149: Schematic diagram of the 400 MeV electron beam transfer line. The first part of the transfer line is the spin rotator and the last part is the injection section. The "transfer line" matches the beam parameters at the exit of the spin rotator to those at the injection point of the RCS.

Spin Rotator

The spin rotator rotates the stable spin direction of the electrons exiting the 400 MeV LINAC from the longitudinal direction to the vertical direction. Figure 3.150 shows that the spin rotator consists of a 99.1° bending dipole magnet that rotates the stable spin direction about the vertical axis by 90° from the longitudinal direction (z-axis) to the transverse direction (x-axis), followed by a solenoid of strength 2.2 Tm that rotates the stable spin direction about the longitudinal axis from the horizontal direction (x-axis) to the vertical (y-axis). At the exit of the solenoid the stable spin direction is vertical. It remains vertical as long as only horizontally bending dipoles are involved in the transfer lines and the synchrotron rings.

The 99.1° bend angle of the dipole is given by

$$a\gamma\theta_{\text{bend}} = \theta_{\text{rot}}, \tag{3.89}$$

where $a = 0.00115965$ is the anomalous magnetic moment of the electron, γ is the relativistic factor of the 400 MeV electron, θ_{bend} is the 99.1° angle of bend of the electron beam and θ_{rot} is the 90° spin rotation angle. The strength of the solenoid to rotate the stable spin

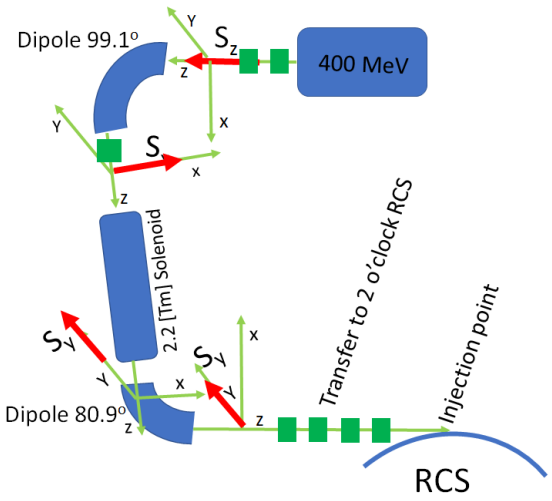

Figure 3.150: The spin rotator for the 400 MeV electron beam. The small green rectangles are quadrupoles on the transfer line. The arc at the bottom of the picture is part of the RCS ring.

direction by 90° is given by,

$$(1+a)\frac{B_{\rm sol}L_{\rm sol}}{B\rho} = \theta_{\rm rot}, \tag{3.90}$$

where $B\rho$ is the rigidity of the 400 MeV electron beam. These equations are derived as particular cases from the general BMT equation [171]. Using at least four quadrupoles upstream of the solenoid, we will generate a round beam at the entrance to the solenoid by ensuring that $\beta_x = \beta_y$ and α and η for both planes goes to zero. In this way the effects of coupling due to the solenoid can be ignored. Table 3.59 lists the energy, beam emittances and beam parameters at the exit of the 400 MeV LINAC. The horizontal and vertical dispersion functions and slopes at the exit point of the LINAC are zero.

Table 3.59: Beam parameters at the exit of the 400 MeV LINAC.

Parameter	Value
Energy [GeV]	0.4
γ	782.78
Rigidity [Tm]	1.33
$\epsilon_{x,y}$ [µm]Norm	55
$\epsilon_{x,y}$ [nm]	70.3
α_x	-0.2554
β_x [m]	13.866
α_x	-0.2518
β_x [m]	13.946

The 80.9° dipole following the solenoid does not affect the stable spin direction and can be replaced by any other dipole which bends the beam more or less than 80.9°, for the beam to be guided in the required direction.

The LtR Transfer Line

The main function of this transfer line is to rotate the stable spin direction from the longitudinal to the vertical direction and to match the Twiss parameters at the exit of the 400 MeV LINAC to those at the injection point of the RCS ring. These parameters are shown in Table 3.60. The dispersion and angular dispersion functions at the RCS injection point are non-zero.

Table 3.60: Twiss parameters at the exit of the 400 MeV LINAC and the RCS injection point.

Parameter	Exit 400 MeV LINAC	RCS Injection Point
α_x	-0.2554	0.81956
β_x [m]	13.866	11.137
α_y	-0.2518	-2.0339
β_y [m]	13.949	36.438
η_x [m]		0.6
η'_x		0.5

A schematic diagram of the 400 MeV electron beam transfer line which consists of three sections, namely the spin rotator, the main transfer line, and the injection section is shown in Figure 3.150.

The beam optics of the transfer line compensates for beam coupling due to the solenoid and maintains a reasonably small beam size. The following beam constrains are imposed at the entrance of the solenoid.

1. The beam should be achromatic $\eta_{x,y} = \eta'_{x,y} = 0$. This requires that the 99.1° dipole be split in two with quadrupoles placed in between.
2. The beam should be "round" with $\beta_x = \beta_y$ and $\alpha_x = \alpha_y = 0$. This requires additional quadrupoles in the line.

The Twiss parameters $\beta_{x,y}$ and $\eta_{x,y}$ of the transfer line are shown in Figure 3.151, which also shows four quadrupoles in between the two 99.1° dipole halves. Two additional quadrupoles have been placed at the exit of the 400 MeV LINAC. Figure 3.152 shows the layout of the complete beam transfer line from the exit of the 400 MeV LINAC to the RCS injection point. The RCS injection septum, the RCS quadrupole and the RCS injection kicker are included in the beam optics of the transfer line.

The parameters of the magnetic elements from the 400 MeV LINAC to the RCS injection point which appear in Figure 3.152 are shown in Table 3.61.

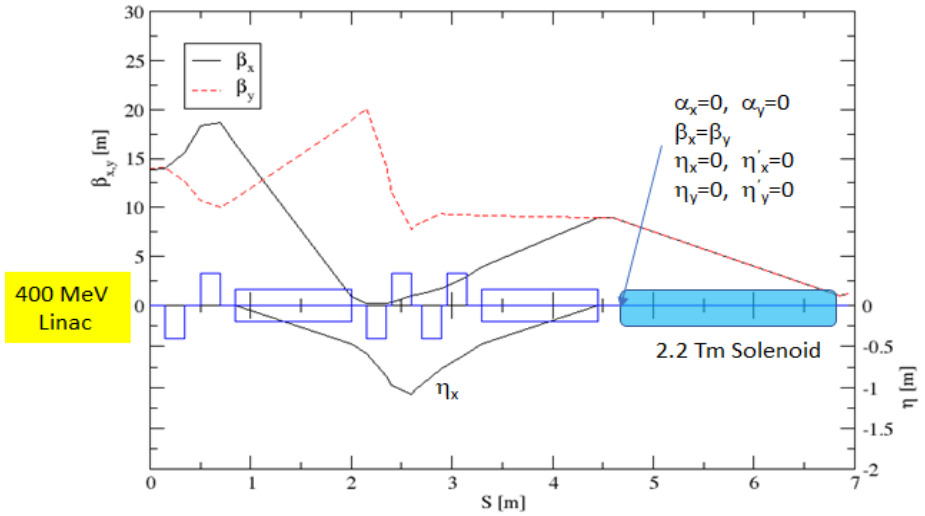

Figure 3.151: The Twiss parameters $\beta_{x,y}$ and $\eta_{x,y}$ of the transfer line from the exit of the 400 MeV LINAC to the exit of the solenoid.

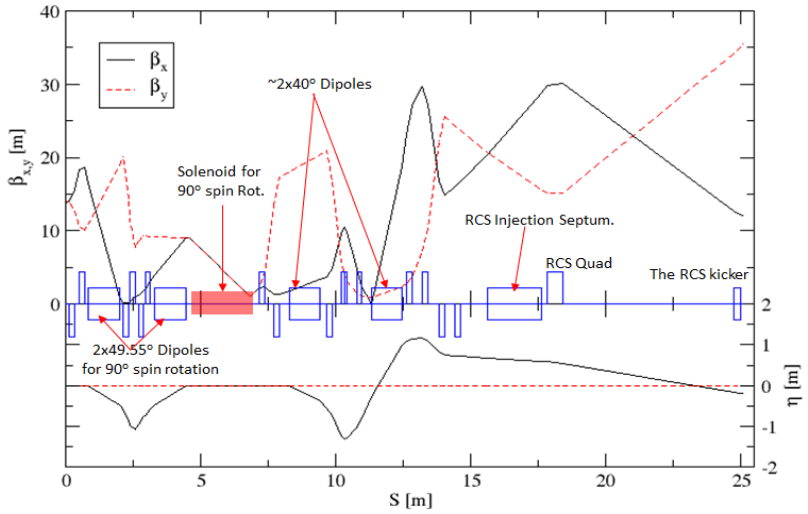

Figure 3.152: The layout of the elements for the 400 MeV beam transfer line and the Twiss parameters $\beta_{x,y}$ and $\eta_{x,y}$ of the transfer line from the exit of the 400 MeV LINAC to the RCS injection point.

Table 3.61: The magnetic elements of the 400 MeV LtR transfer line

Device	L [m]	Rad/Gap [cm]	Angle/K1 [Deg] [m^{-2}]	Gradient (quads) / BL [T/m] or [T-m]	$B_{pole-tip}$ [T]	Current [A-turns]	Induct/N^2 mH	Qty
Quad	0.2	2.0	8	10.6	0.21	1694.0	0.1	10
Quad	0.2	2.0	15	20.0	0.40	3175.0	0.1	4
Dipole	1.15	2.0	0.865	1.15	1.0	15918	NA	2
Dipole	1.15	2.0	0.710	0.944	0.82	13069	NA	2
Septum	1.0	2.0	0.02	0.027	0.027	423.4	1.9	1
Solenoid				2.2				1

Injection of 400 MeV e-bunches to RCS

The e-bunch pattern of the circulating beam in the RCS just after injection from the 400 MeV LINAC will consists of two sets of four-bunches as shown in Figure 3.153. The two sets of four bunches will be separated from each other by ∼2 µs and the revolution time of a bunch in the RCS ring is ∼12.79 µs. This section describes the beam optics of the beam injection region of the 400 MeV electron bunches into the RCS.

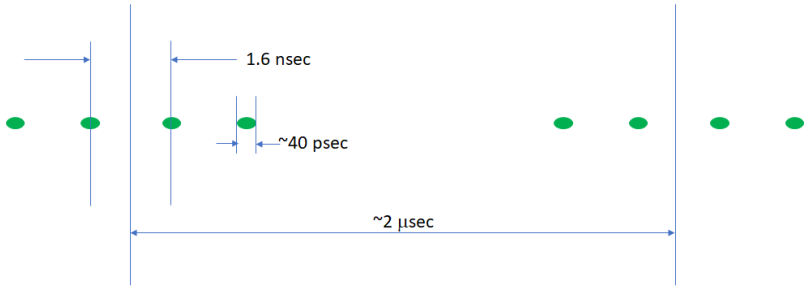

Figure 3.153: Schematic diagram of the two sets of four-bunches circulating in the RCS just after injection. The revolution time of each bunch in the RCS is 12.79 µs.

Beam optics of the 400 MeV beam injection region.

The 2 o'clock straight section is designated for the beam injection of the e-bunches from the 400 MeV LINAC into the RCS. The beam parameters $\beta_{x,y}$ and $\eta_{x,y}$ of 2 o'clock straight section are plotted in Figure 3.154. In this write up we assume that the beam injection region is located at the 2 o'clock straight section enclosed by the red line in Figure 3.154. The small spacing of the four bunches shown in Figure 3.153 requires a special kind of kicker-system which is described in a separation section below. Such a special kicker-system can only provide a rather small kick to the injected beam, this will be assisted by the use of a pulsed septum, the use of RCS corrector bumps to move the closed orbit closer to the septum and the use of a kicker with a rise and fall time of 10 µs and flattop of 2.5 µs. This fast kicker will be needed to offset the negative closed orbit kick caused by the special RF kicker to the circulating bunches (shown in Figure 3.155)

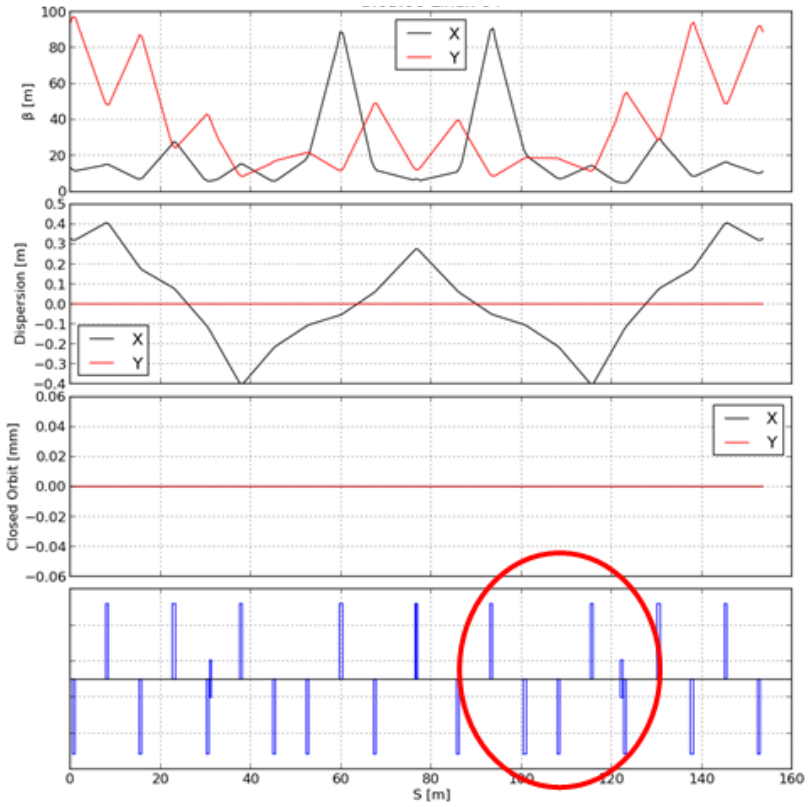

Figure 3.154: The beam optics of the RCS at the 4 o'clock region. Top plots the $\beta_{x,y}$ functions, middle the $\eta_{x,y}$ functions and the bottom plot beam trajectory of the beam at its reference orbit. The layout of the elements are at very bottom of the figure. The red ellipse on the figure indicates the location of the injection system.

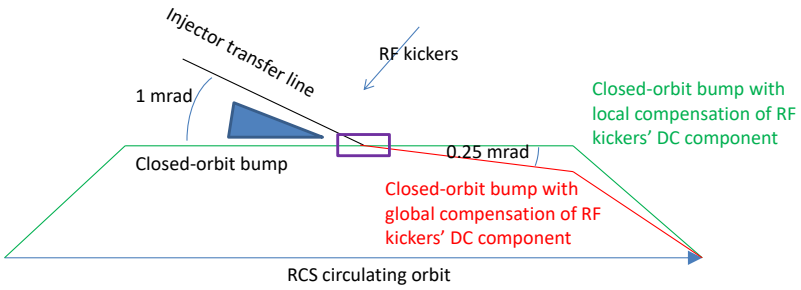

Figure 3.155: Green path: RF kickers + a pulsed magnet next to the RF kickers provide 1mrad total kick to injecting bunches and 0 kick to circulating bunches Red path: RF kickers provide 0.75 mrad kick to injecting bunches and -0.25mrad kick to circulating bunches. The amplitude of one or more of the closed orbit bump kickers will be adjusted to correct that -0.25 mrad kick.

The local beam bump will be generated by a set of three standard RCS correctors which and will be applied just before the injection of the bunch. Figure 3.156 shows the trajectory of the local beam bump generated by these correctors. The strength of these three magnets has been adjusted to generate a maximum beam displacement of ∼1.5 cm at the location of the focusing quadrupole (thin red rectangle) shown in Figure 3.156.

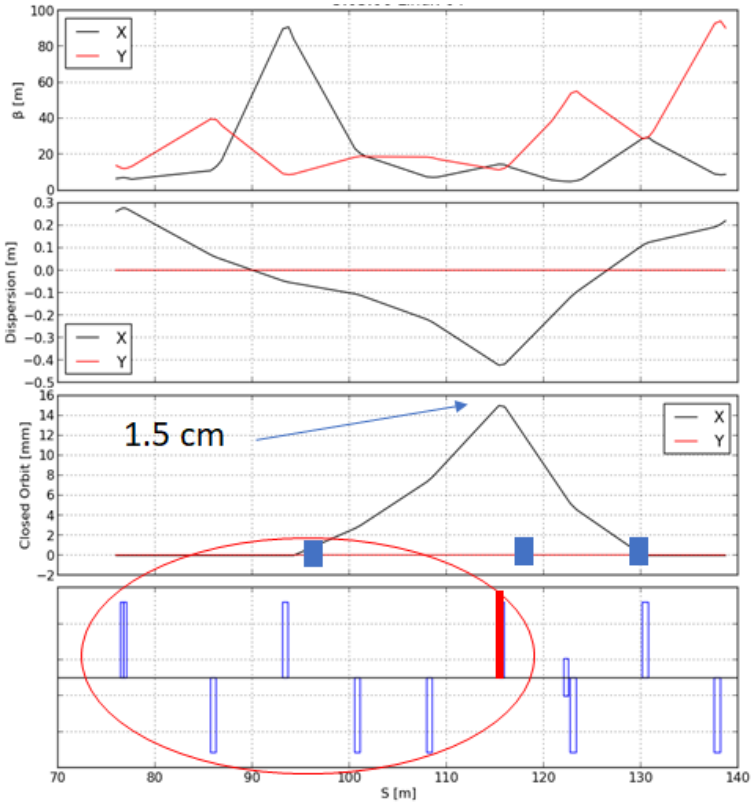

Figure 3.156: The closed beam bump generated by the three dipoles. The strength of the three magnets has been adjusted to generate a maximum beam displacement of ∼1.5 cm at the location of a focusing quadrupole.

The placement of a thick (∼1.5 cm) DC septum magnet placed upstream of the focusing quadrupoles as shown schematically in Figure 3.157 injects the 400 MeV bunch through the focusing quadrupole at a displacement of ∼3.2 cm. The injected trajectory crosses the reference orbit of RCS at an angle of ∼0.5 mrad at the location of the kicker which places the beam along the reference orbit. The focusing quadrupole should provide an aperture of ∼3.5 cm for the 400 MeV beam to be injected into RCS. Table 3.62 list some of the specifications of the magnets for the closed beam bump and the septum magnet. The specifications for the special kicker is included in the next section.

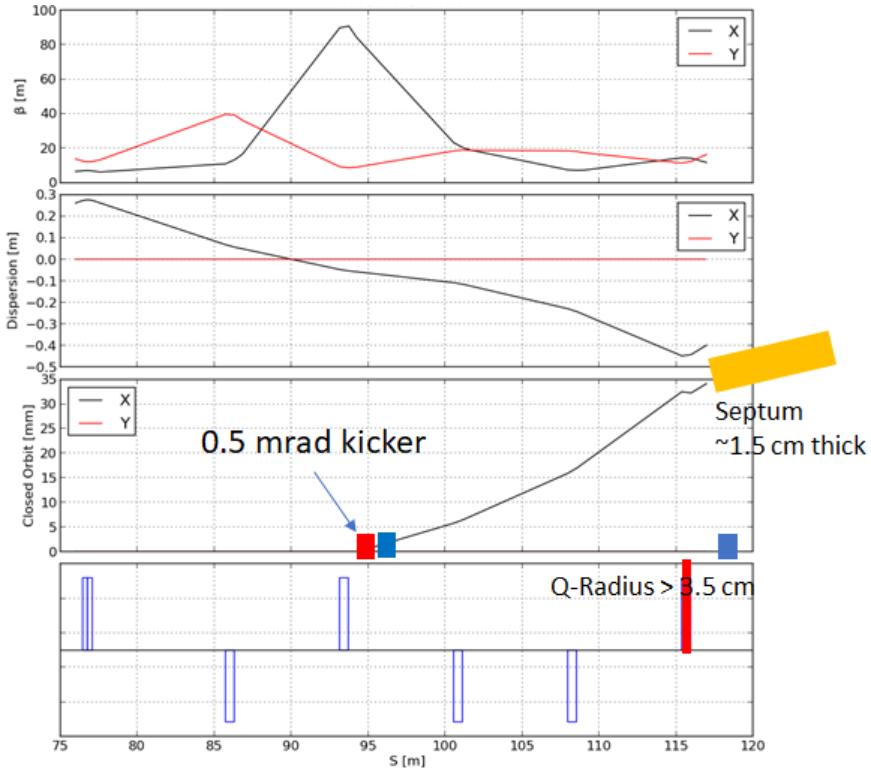

Figure 3.157: The closed beam bump generated by the three dipoles. The strength of the three magnets has been adjusted to generate a maximum beam displacement of ∼1.5 cm at the location of a focusing quadrupole.

Table 3.62: List of the DC magnets at the 4 o'clock region for the beam Injection from the AtR to the HSR for the low energy mode of the EIC operations.

Magnet Type	Mag. Qty	Material	Length [m]	Gap [cm]	Width [cm]	θ_{bend} [mrad]	B-field [kG]	T_{rise} [ms]
Bump Mag.	3	CMD-10	0.5	3.0	3.0	1.0	0.035	1
DC-Septum	1	Iron-1008	1.0	2.3	3.0	30	0.5	NA

3.8.4 RCS RF Injection Kicker Scheme

The ESR injection scheme calls for full bunch swap, requiring the RCS to provide up to 28 nC/bunch, with the possibility of further increase. Generating such a single bunch would be very challenging for the gun and the injector linac. Currently it is proposed that in one LINAC cycle, two 400 MeV bunches of ∼2 µs spacing (at the two equal voltage points of the rising and falling edge of the linac pulse) are injected into the RCS. In each RCS ramping cycle, 4 pairs of consecutive bunches (1.6 ns or 591 MHz spacing) are injected in 4 LINAC cycles to form 2 bunch trains. Each bunch train are then quasi-adiabatically merged into one bunch at 1 GeV to form the 28 nC bunch.

A kicker is needed to inject electron bunches from the linac into the RCS. To avoid kicking on any circulating bunches, a 1.6 ns rise/fall time is needed, which is not very practical for single pulse kickers. Instead, we proposed an RF harmonic kicker by combining a few harmonics with fundamental frequency of 148 MHz (1/4 of 591 MHz) to achieve a 1.6 ns rise/fall time in the micro pulse, requiring moderate peak power. To avoid kicking of the injected bunch at the 2nd turn and beyond, the macro pulse of the RF voltage envelop has a ∼2 µs flat top and a ∼10 µs fall time, repeating at the linac pulse rate (∼100 Hz). The rise time is also preferred to be ∼10 µs, so the rise of the multiple harmonics doesn't need to be synchronized. The macro pulse (RF envelop) is shown in Figure 3.158, and the micro pulse is shown in Figure 3.159.

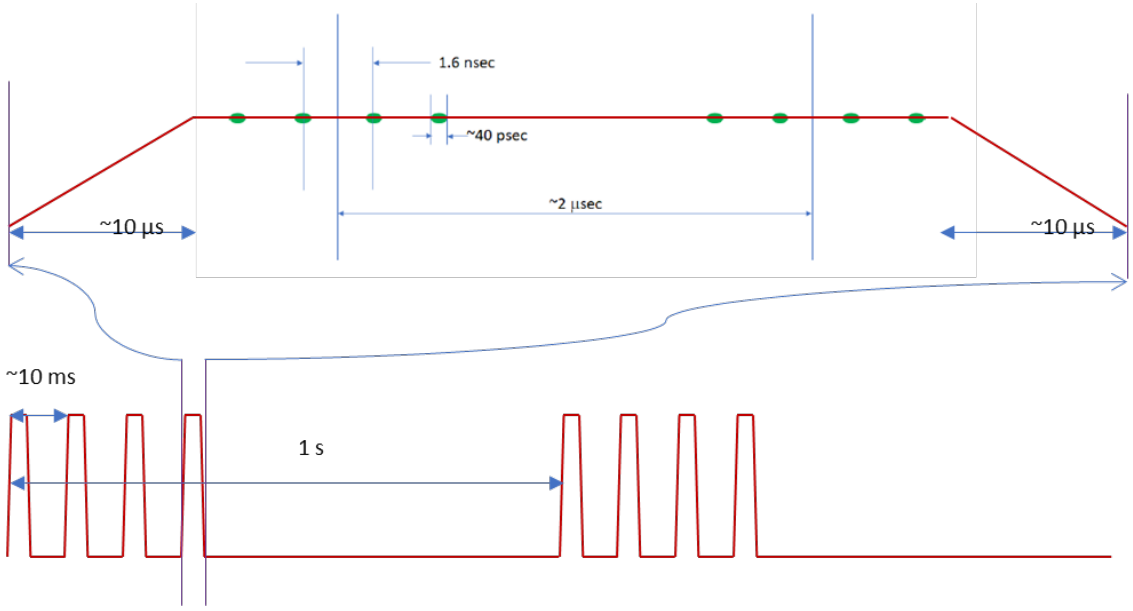

Figure 3.158: Envelope of RF kicker rise and fall for RCS injection.

Scientists at TJNAF have studied multimode harmonic kickers extensively for the JLEIC Circulating Cooler Ring (CCR). The JLEIC CCR injector design had beam injected/extracted every 10–11 circulations, and the kicker had ∼1 ns rise/fall time for the micro pulses repeating at 47.6–86.6 MHz continuously. A few odd harmonics of the funda-

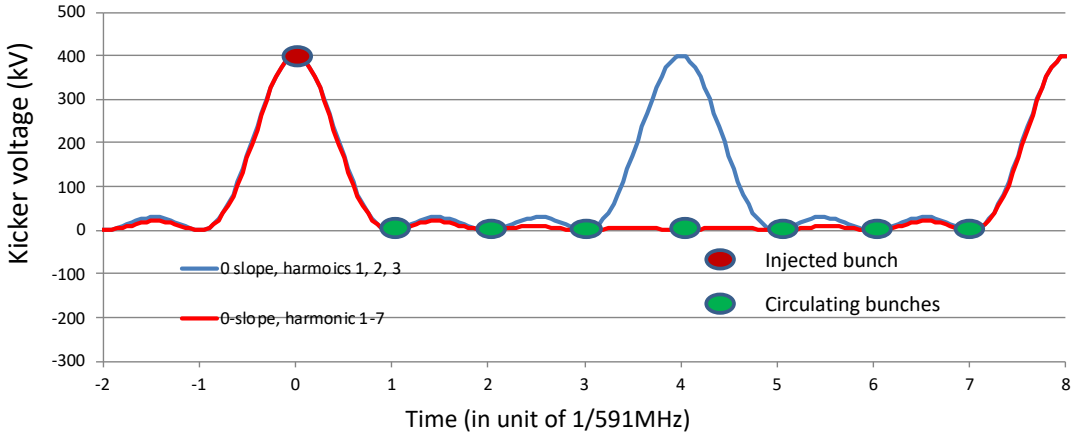

Figure 3.159: Micro pulse of the RF harmonic kicker for RCS injection.

mental mode can be excited in a quarter wave resonator (QWR) type of deflecting cavity with high shunt impedance to synthesize the desired kicking waveform, making it possible to design a system with a small number of cavities and high efficiency.

In the past, a few harmonic composition schemes have been studied and compared for JLEIC, and two schemes were picked out for detailed beam dynamics study, as well as cavity design and prototype. Before 2017, Y. Huang [172, 173] was focusing on the zero-slope scheme with first 10 harmonics of the fundamental frequency of 47.63 MHz, kicking one out of ten 476.3 MHz bunches in one pulse. That scheme has similar waveform shown in Figure 3.159, except that the scheme in Fig 3.159 kicks one out of four or eight 591 MHz bunches in one micro pulse. This waveform has minimal impact on the circulating bunches, but the even harmonics require more than one cavity to implement. Figure 3.160 shows the RF model of the 4 cavities needed to generate the 10 harmonics. A half scale (95.26 MHz) non-vacuum version of the 5-harmonics cavity was also prototyped, as shown in Figure 3.161.

Since 2017, G. Park [174,175] has been focusing on the "equal amplitude" scheme, using the first 5 odd harmonics of 86.6 MHz to generate the waveform to kick one out of 11 bunches of 952.6 MHz. This waveform can be generated with a single cavity, but has non-negligible time derivative (a.k.a. slope) when the circulating bunches arrive at the kicker. Beam dynamics study [176] showed that the JLEIC CCR can use the extraction kicker's symmetric slope to cancel the crabbing effect on the circulating bunches from the injection kicker's slope, with acceptable emittance growth. A high power prototype of this cavity is under construction, with mechanic model shown in Figure 3.162. This prototype is designed to handle $\sim$7 kW CW dissipated RF power, with motorized stub tuners. Beam test is planned after the completion of the cavity construction and bench test.

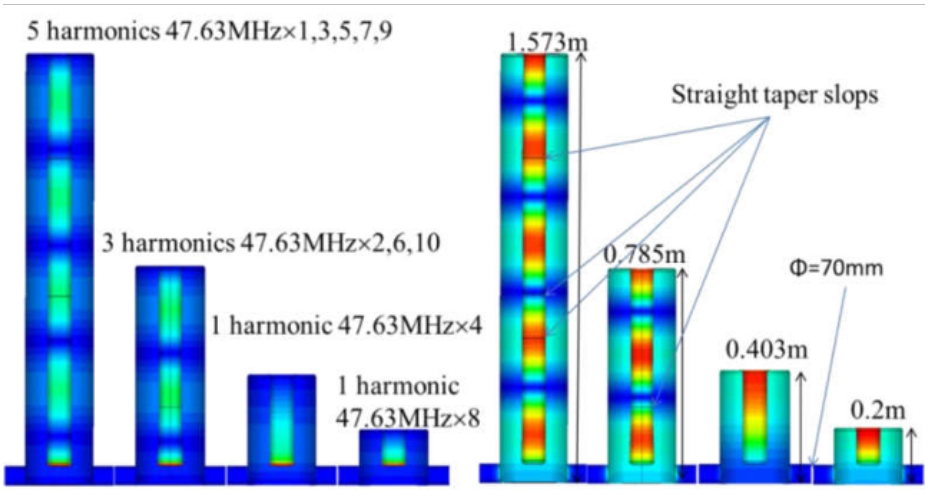

Figure 3.160: E field (left) and H field (right) of 4-cavities (Y. Huang's design).

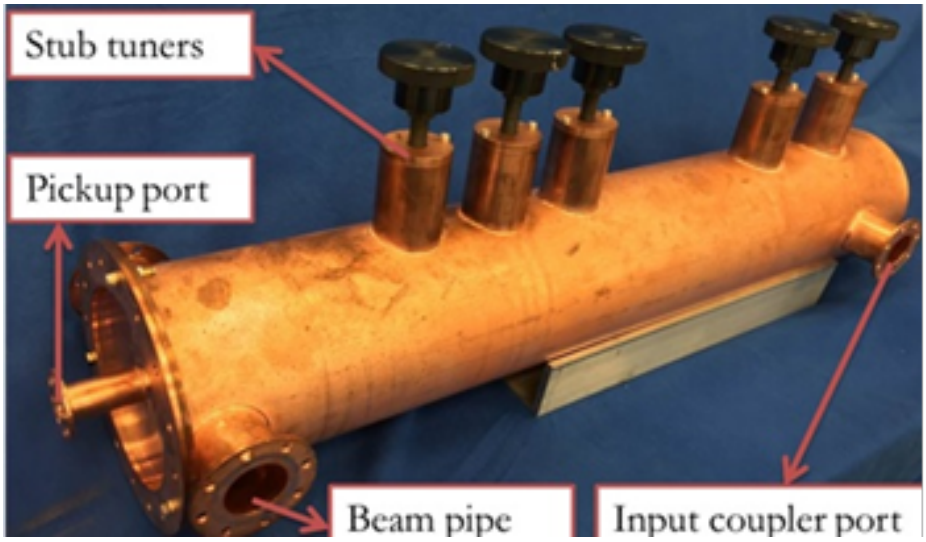

Figure 3.161: JLEIC CCR 1/2 scale 5-mode cavity prototype (95.26 MHz ×1, 3, 5, 7, 9, Y. Huang's design).

The RCS injection kicker currently adopts the zero-slope scheme as shown in Figure 3.159 The harmonic frequencies and amplitude required to generate this waveform are listed in the first column of Table 3.63. This scheme has a good waveform quality, requiring even harmonics and multiple cavities. Two cavities are needed initially for the scheme with a bunch train of 4, with the possibility to be upgraded later by adding another cavity to inject 8 consecutive bunches, whose frequencies are detailed in the second column. The "equal amplitude" scheme used in this design may require two cavities to cancel the effect of the slopes, making it less attractive.

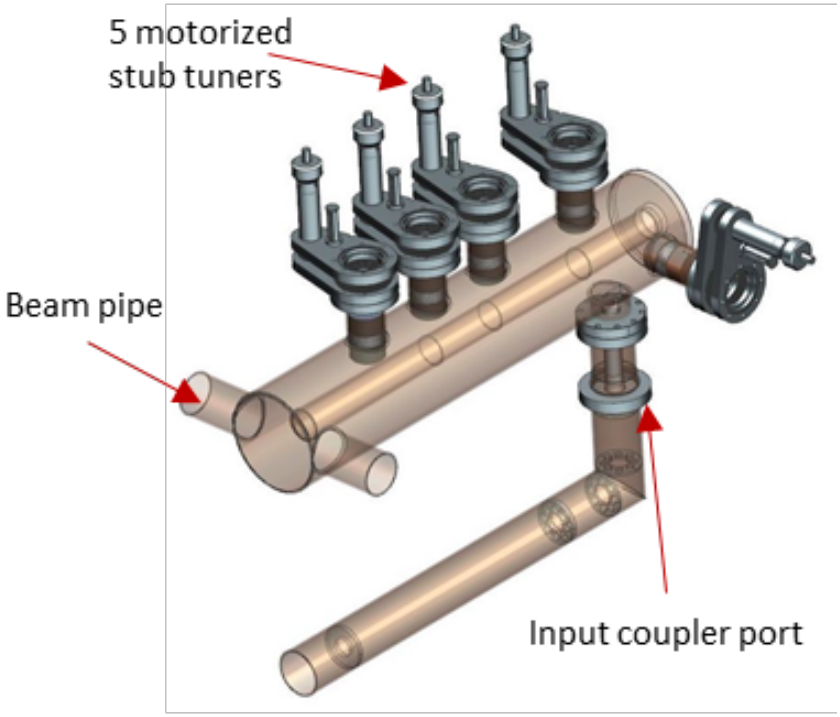

Figure 3.162: JLEIC CCR full power 5-mode cavity prototype (86.6 MHz ×1, 3, 5, 7, 9, G. Park's design).

The RF part of the injection kicker waveform will generate a displacement of 0.75 mrad for the injected bunches towards the injection septum and -0.25 mrad for the circulating bunches, resulting a 1 mrad separation in the injecting orbit. This will work in conjunction with a slow closed orbit bump and possibly a slow DC kicker near the kicker cavities, generating a combined kick of 3 mrad for the injecting bunches (2 mrad for the circulating bunches). The kick generated by an RF cavity kicker is approximately $\theta = V_{\perp}/\text{Energy}$, which gives 0.75 mrad for 0.3 MV.

The forward power needed to generate the desired kicker voltage in 10 µs rise time with three harmonics can be roughly estimated using the parameters scaled from Y. Huang's cavity 2 (3-mode) and cavity 3 (single mode), assuming 40 mm beamline aperture and realistic copper conductivity, as shown in Table 3.64. We expect that the actual 2-mode cavity design will have slightly better $R_{\perp}/Q$ and lower power requirement than Y. Huang's 3-mode cavity, while the single mode cavity parameters will be very close to Y. Huang's design. The coupling has been optimized to minimize the peak forward power, which is slightly over coupled for all the three modes. The cavity hosting harmonics 1 and 3 will share the power coupler for the two modes, so optimal coupling may not be achieved simultaneously. However our estimate shows that varying the coupling coefficient by factor of two from optimal only increases the peak RF power by less than 20%; with the low power needed for the third harmonic, this increase will be insignificant.

Table 3.63: Frequencies and voltages of RF kickers.

0-slope, harmonics 1–3		0-slope, harmonics 1–7	
Freq. [MHz]	Volt. [kV]	Freq. [MHz]	Volt. [kV]
DC	100	DC	50
147.8(C2)	150	73.9(C3)	87.5
295.5(C1)	100	147.8(C2)	75
443.3(C2)	50	221.6(C3)	62.5
		295.5(C1)	50
		369.4(C3)	37.5
		443.3(C2)	25
		517.1(C3)	12.5

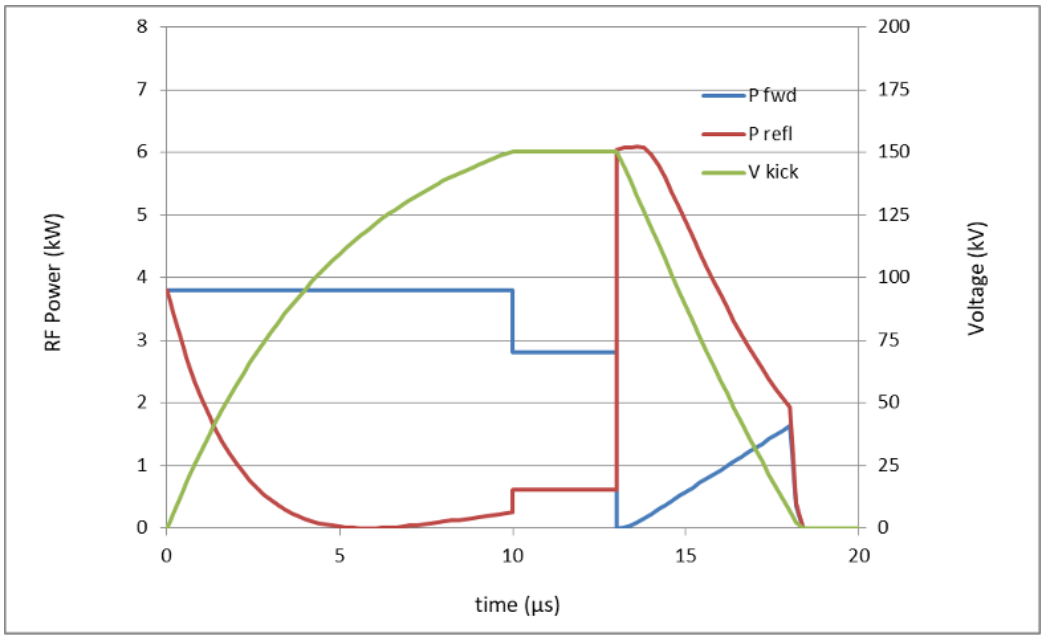

Figure 3.163: An example of the estimated RF kicker macro pulse envelop and power ramp.

An example of RF power ramp is shown in Figure 3.163. The calculation uses parameters from the first row of table 3.64. Forward RF power of 3.8 kW is used in the 10 μs rising stage of the kicker, ramping up the kicker voltage to 150 kV; then the forward power is reduced to 2.8 kW, so the 150 kV voltage can be maintained flat for 2 μs. At the fall edge of the macro pulse, a reversed phase forward RF is needed to help ramping down the RF voltage to zero in less than 10 μs, but that power need to ramp up slowly to keep the reflected power low. Without this reversed phase RF power, there will be ∼25 kV remnant kicking voltage after 10 μs. Pulse to pulse feedback can be used to ensure the correct waveform is generated.

Table 3.64: RF power estimate of the RCS harmonic RF kicker with parameters scaled from JLEIC CCR kickers developed by Y. Huang, assuming 40 mm aperture. Impedance uses linac definition $R_\perp = V_\perp^2/P_d$.

0-slope, harmonics 1–3									
f [MHz]	Scaled from f [MHz]	$R_\perp/Q$ [Ω]	G [Ω]	Q_0	Coup. β	T_{fill}	$V_\perp$ [kV]	$P_{fwd,peak}$ [kW]	$P_{fwd,flat}$ [kW]
147.78	95.3 (cav2)	1166	31	8770	2.74	5.1	150	3.8	2.8
295.6	190.5 (cav3)	975	55	11170	1.90	4.1	100	1.2	1.0
443.4	285.8 (cav2)	268	92	15180	1.77	3.9	50	0.8	0.7
Total								5.8	4.5

3.8.5 Electron Beam Transport from RCS to Storage Ring

The RtS transfer line, located in IR12 straight section of the RHIC tunnel, matches the beam parameters between the extraction point of the RCS and injection point of the electron storage ring.

The yellow line in Figure 3.164 indicates the hadron ring. The RCS shown in red, is placed above the storage ring (green line). The location of the RtS transfer line is also shown in Figure 3.164. Figure 3.165 shows the layout of the RtS transfer line.

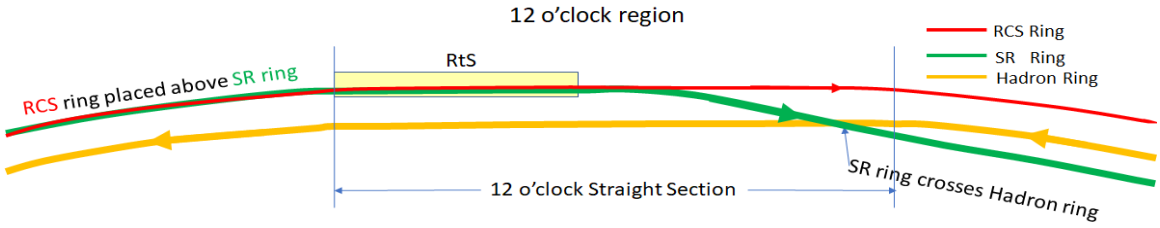

Figure 3.164: Plan view of the RtS transfer line, showing the arcs of the RCS, electron storage ring, and Hadron rings in the IR12 straight section.

Figure 3.166 shows the Twiss functions and the location of the magnetic elements of the RCS-to-Storage ring (RtS) beam transfer line including the beam optics of the RCS extraction system and the storage ring injection system described in the earlier subsections. The beam transfer line shown in Figure 3.166 starts from the RCS extraction point located just upstream of the RCS extraction kicker and ends at the storage ring injection point which is located at the exit of the storage ring injection septum, placed on the chicane described in the previous subsection. In the same Figure 3.166 the RCS extraction septum and the vertical dipoles which lower the level of the transferred beam by ≈0.5 m are shown. This section of the beam line preserves the stable spin direction using an achromatic beam transport. An alternative design scheme is under consideration for the section of the beam line which generates the achromatic vertical drop of the beam. In the alternate scheme which

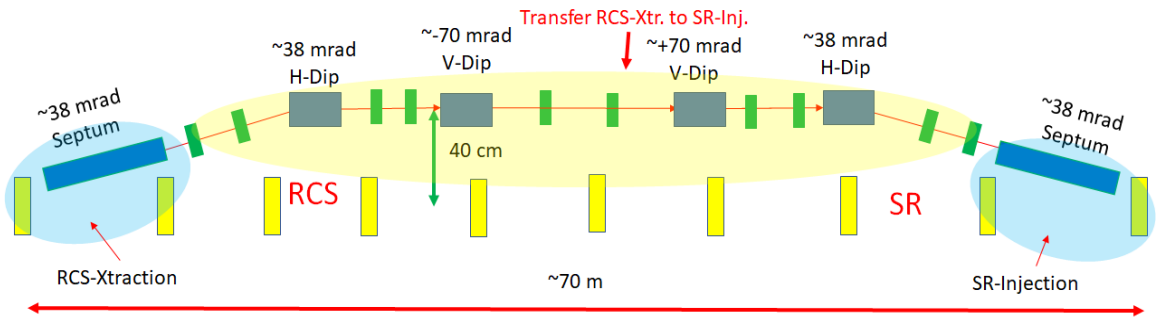

Figure 3.165: Schematic diagram of the layout of the RtS transfer line. The yellow rectangles represent the quadrupoles of the RCS which are placed above those of the electron storage ring. The blue highlighted areas are the extraction and injection regions. The drift space between the quadrupoles of each of the rings is about 7 m. The yellow highlighted area is the transfer line between the exit of the RCS extraction system and entrance of the electron storage ring injection system.

may reduce the strength of the quadrupoles we impose the achromatic condition in each of the two bends.

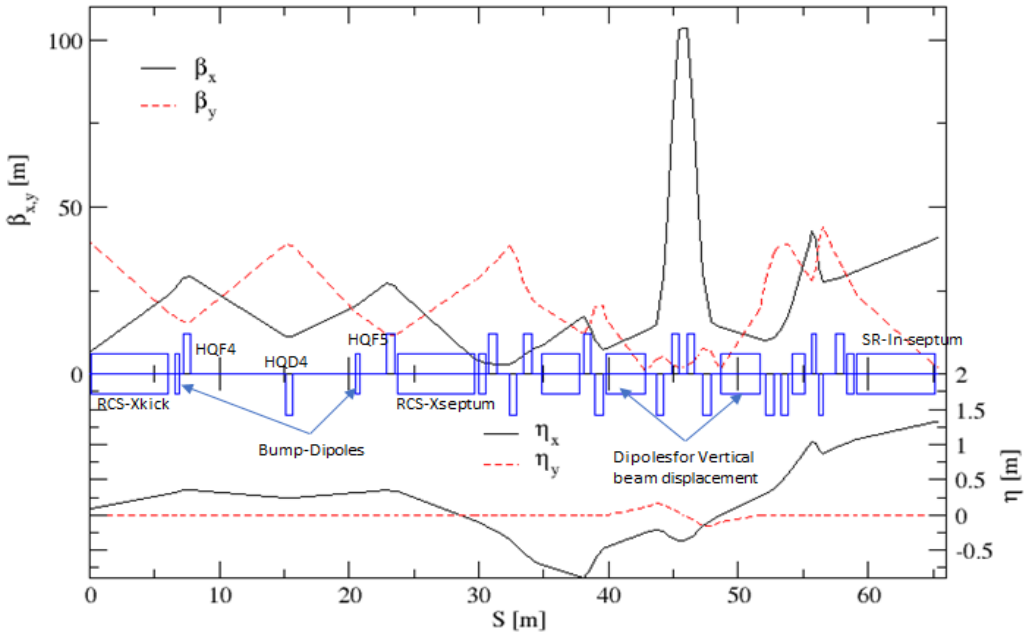

Figure 3.166: Twiss functions and location of the magnetic elements of the RtS extraction and injection system. The beam transfer line starts from the RCS extraction point located just upstream of the RCS extraction kicker and ends at the Storage ring injection point which is located at the exit of the Storage ring injection septum. The RCS extraction septum and the vertical dipoles that lower the level of the transferred beam by ≈0.5 m are also shown.

Electron Beam Extraction from RCS

To minimize the strength of the extraction kicker a local beam bump is generated within the straight section of the RCS ring. Figure 3.167 shows the closed orbit of the beam with the 20 mm beam bump generated by the three RCS corrector magnets. Figure 3.168 plots the Twiss functions and the location of the quadrupoles at the straight section of the RCS ring.

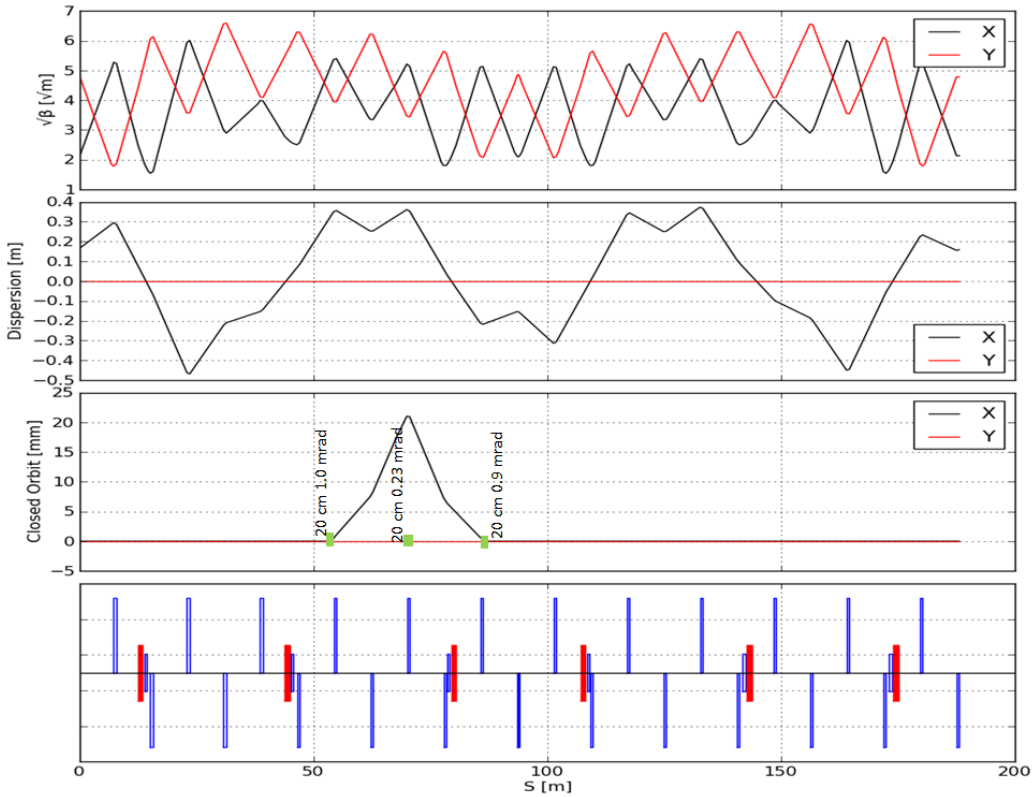

Figure 3.167: Local beam bump of 20 mm during extraction. From top to bottom the Twiss functions, the closed beam orbit with the location and strength of the three magnets (green rectangles) that generate this local beam bump, and the quadrupoles (thin vertical lines) at the straight section of the RCS.

The fast kicker is energized to extract the bunch right after the formation of the closed beam bump. Figure 3.169 shows the location of the fast kicker upstream the first corrector bump. A 1.2 mrad strong fast kicker displaces the 18 GeV electron beam from the closed orbit by 15 mm, at a location 15 cm downstream from the exit of the QHF4 quadrupole magnet as shown in Figure 3.169.

The 15 mm transverse separation allows the placement of a septum magnet to extract the kicked beam from the RCS. Figure 3.170 shows the sizes and the trajectories of the circulating and extracted beams. The copper conductor of the RCS extraction septum can be 4 mm

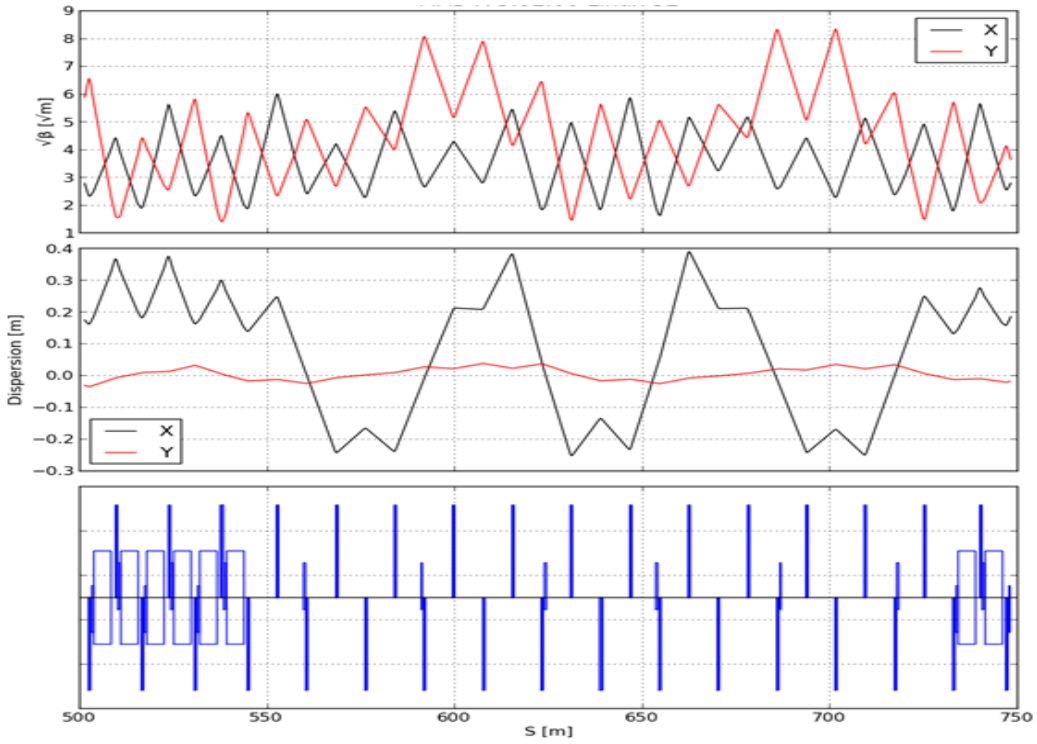

Figure 3.168: The RtS straight section. From top to bottom plotted are the Twiss functions and the location of the quadrupoles (thin vertical lines). The rectangles left and right are dipoles from the upstream and downstream arcs of the RCS straight section.

thick, allowing a current pulse to generate the required magnetic field in the septum magnet. The sizes of the circulating and extracted beams at the entrance of the RCS extraction septum are derived using the parameters of Table 3.65 as

$$\sigma_{x,y} = \sqrt{\beta_{x,y}\epsilon_{x,y} + (\eta_{x,y}\delta p/p)^2}. \tag{3.91}$$

Table 3.65: Beam parameters at the entrance of the RCS extraction septum magnet.

Parameter	Value
beam emittance $\epsilon_{x,y}$ [nm]	50
horizontal β-functions β_x [m]	36.0
vertical β-functions β_y [m]	25.0
RMS momentum spread $\delta p/p$	10^{-4}

Figure 3.171 shows a more detailed picture of the RCS extraction region. The displacement of the extracted trajectory at the entrance of the HQD5 quadrupole is 16 cm permitting the beam to pass undeflected through the quadrupole. A cross section of a possible design of

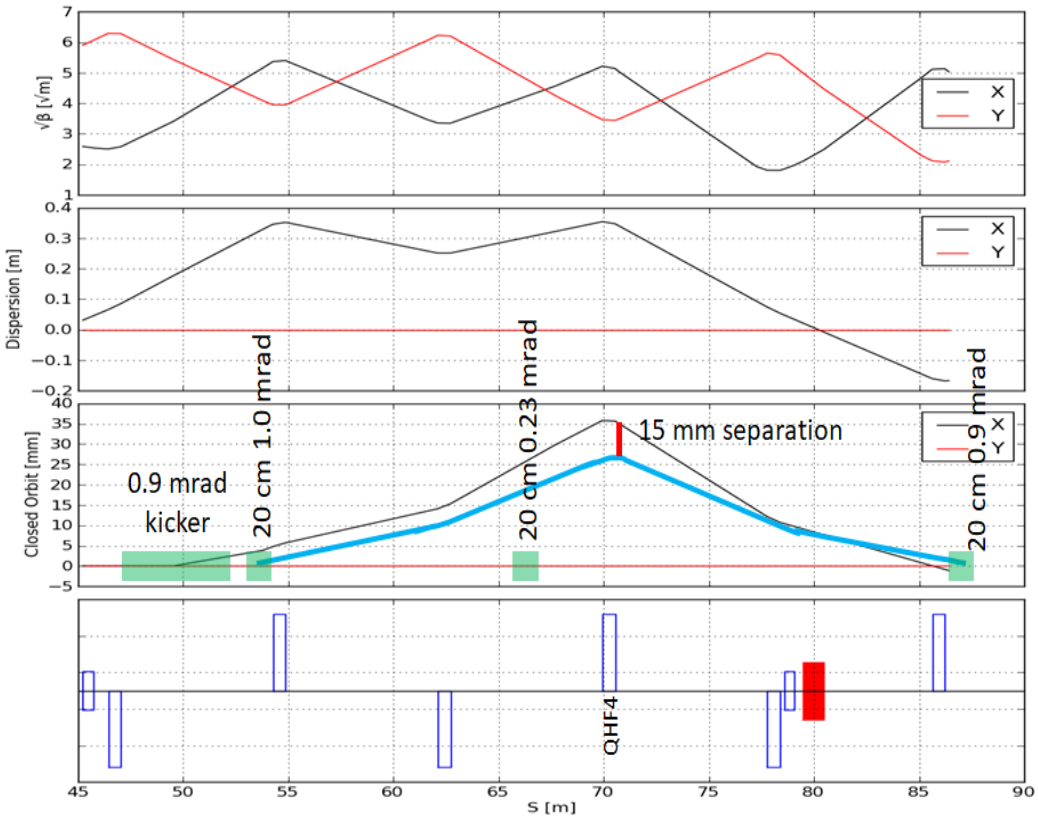

Figure 3.169: Generating the local bump during extraction. The beta ($\beta_{x,y}$), the dispersion ($\eta_{x,y}$) functions and the closed beam orbit at the magnets (green rectangles) that generate the 20 mm local bump. The long green rectangle is the location of the 1.2 mrad strong fast extraction kicker. The bottom graph is the location of the quadrupoles (thin vertical lines) at the RtS straight section.

such a quadrupole is shown in Figure 3.171. Tables 3.66 and 3.67 list the various parameters of the pulsed devices associated with RCS extraction.

Electron Beam Injection into ESR

The beam injection of the electron bunches into the ESR ring will take place in the 12 o'clock straight section. A schematic diagram of the RCS ring where the e-bunches will be extracted from, and the ESR ring where the e-bunches will be injected is shown in Figure 3.172 with the RCS ring placed at ∼50 cm above the ESR ring. The beam injection into the ESR should be as down stream as possible to provide the beam transfer line from the RCS to ESR enough length to satisfy the various constrains required for this beam transfer. Figure 3.173 plots the beam parameters of the ESR ring along the 12 o'clock straight section.

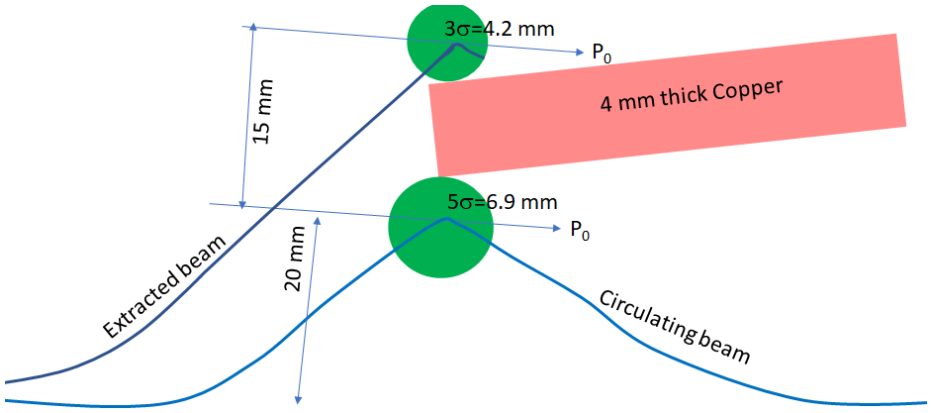

Figure 3.170: A schematic diagram of the extraction region showing the local bump of the circulating beam, the trajectory of the extracted beam and the sizes of the circulating and extracted beams. This diagram helps the calculation of the septum thickness which in this case is 4 mm.

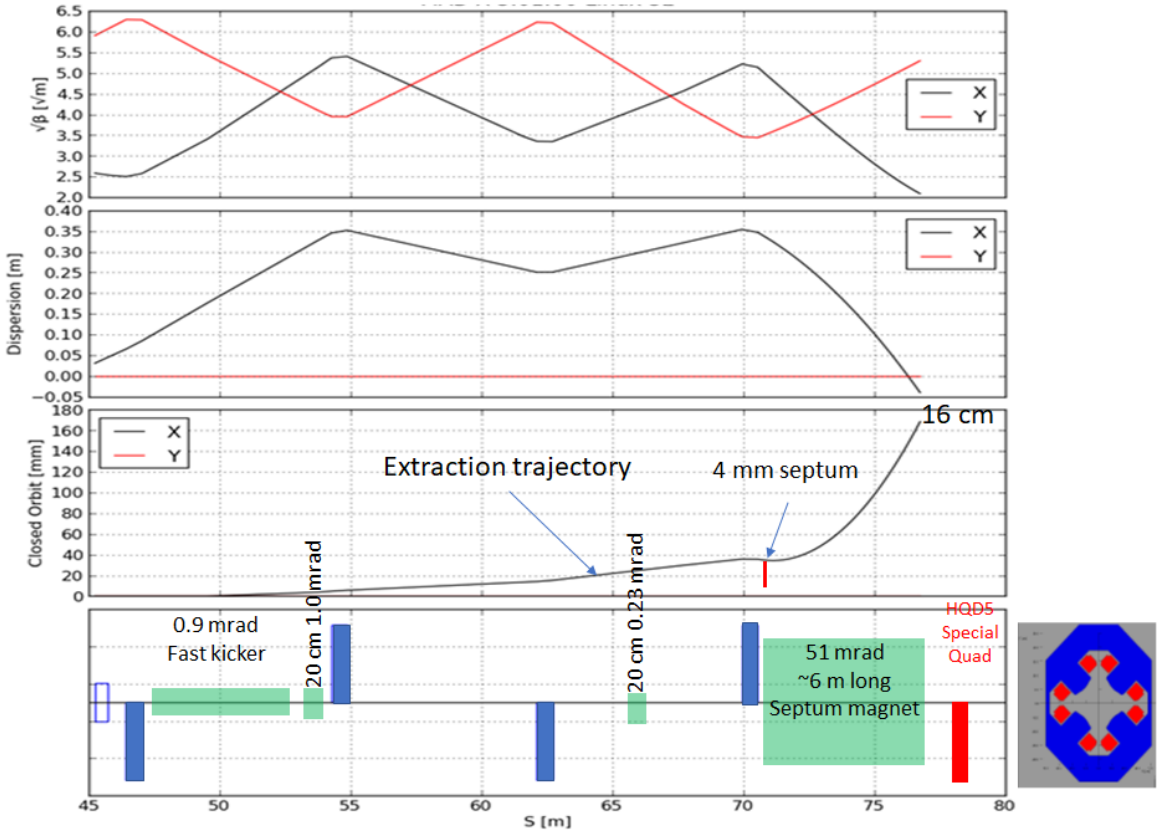

Figure 3.171: Twiss functions and the extracted beam trajectory are shown. The long green rectangle is the location of the 1.2 mrad strong fast extraction kicker. The bottom graph is the location of the quadrupoles (thin vertical lines) at the straight section of the RCS ring. The lower figure is a cross section of a possible quadrupole for the HQD5.

Table 3.66: Beam parameters and specifications of the beam extraction bump magnets at the RCS extraction region.

Parameter	Two RCS magnets	One RCS magnet
β_x [m] (max value)	36.0	36.0
β_y [m] (max value)	36.0	36.0
η_x [m]	0.3	0.3
η_y [m]	0.0	0.0
energy [GeV]	18.0	18.0
γ	35225.05	35225.05
$B\rho$ [Tm]	60.04	60.04
$\epsilon_{x,y}$ [nm]	50.0	50.0
$\delta p/p$	1.0×10^{-3}	1.0×10^{-3}
l [m]	0.25	1.0
beam height [cm] ($2 \times 5\sigma$)	1.35	1.35
magnet gap [cm] (less if elliptical)	4.5	4.5
beam width [cm] ($2 \times 5\sigma$)	1.38	1.38
magnet hor. aper. [cm]	4.5	4.5
kick angle [rad]	0.001	0.00025
BL [Tm] (DC or pulsed)	0.06	0.02

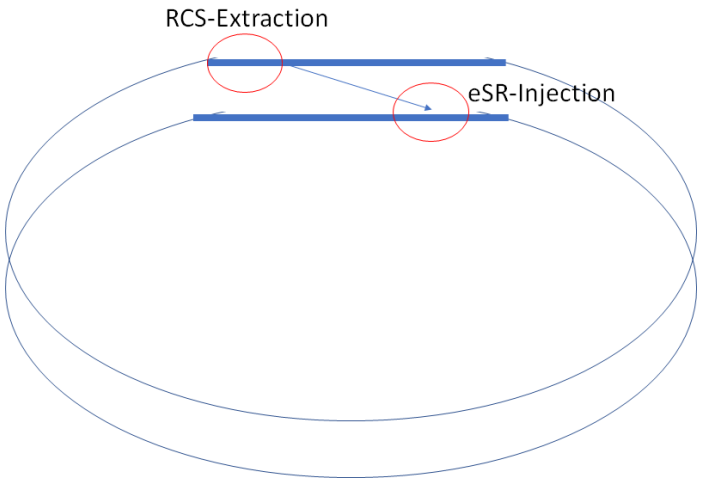

Figure 3.172: Schematic diagram of the RCS and ESR electron rings. The RSC ring will be located ∼50 cm above the ESR ring. The ESR injection region should be as far downstream as possible to provide enough length of the beam transfer line to satisfy the necessary constrains of the beam transfer line.

Table 3.67: Beam parameters and specifications of the RCS beam extraction fast kicker and septum magnet.

Parameter	RCS fast extraction kicker	RCS extraction septum
β_x [m] (max value)	36.0	36.0
β_y [m] (max value)	36.0	36.0
η_x [m]	0.3	0.3
η_y [m]	0.0	0.0
energy [GeV]	18.0	18.0
$\beta\gamma$	35225.05	35225.05
$B\rho$ [Tm]	60.04	60.04
$\epsilon_{x,y}$ [nm]	50.0	50.0
$\delta p/p$	1.0×10^{-3}	1.0×10^{-3}
length [m]	5.0	6.5
beam height [cm] ($2 \times 5\sigma$)	1.35	1.35
magnet gap [cm] (less if elliptical)	4.5	1.35
beam width [cm] ($2 \times 5\sigma$)	1.38	1.38
magnet hor. aper. [cm]	4.5	3.0
kick angle [rad]	0.0012	0.03
BL [Tm] (DC or Pulsed)	0.072	1.8
inductance [µH]	1.26	181
repetition rate [Hz]	1.0	1.0
revolution time [µs]	12.6	12.6
pulse wave	half-sine	half-sine
base width [µs]	5500.0	12.0

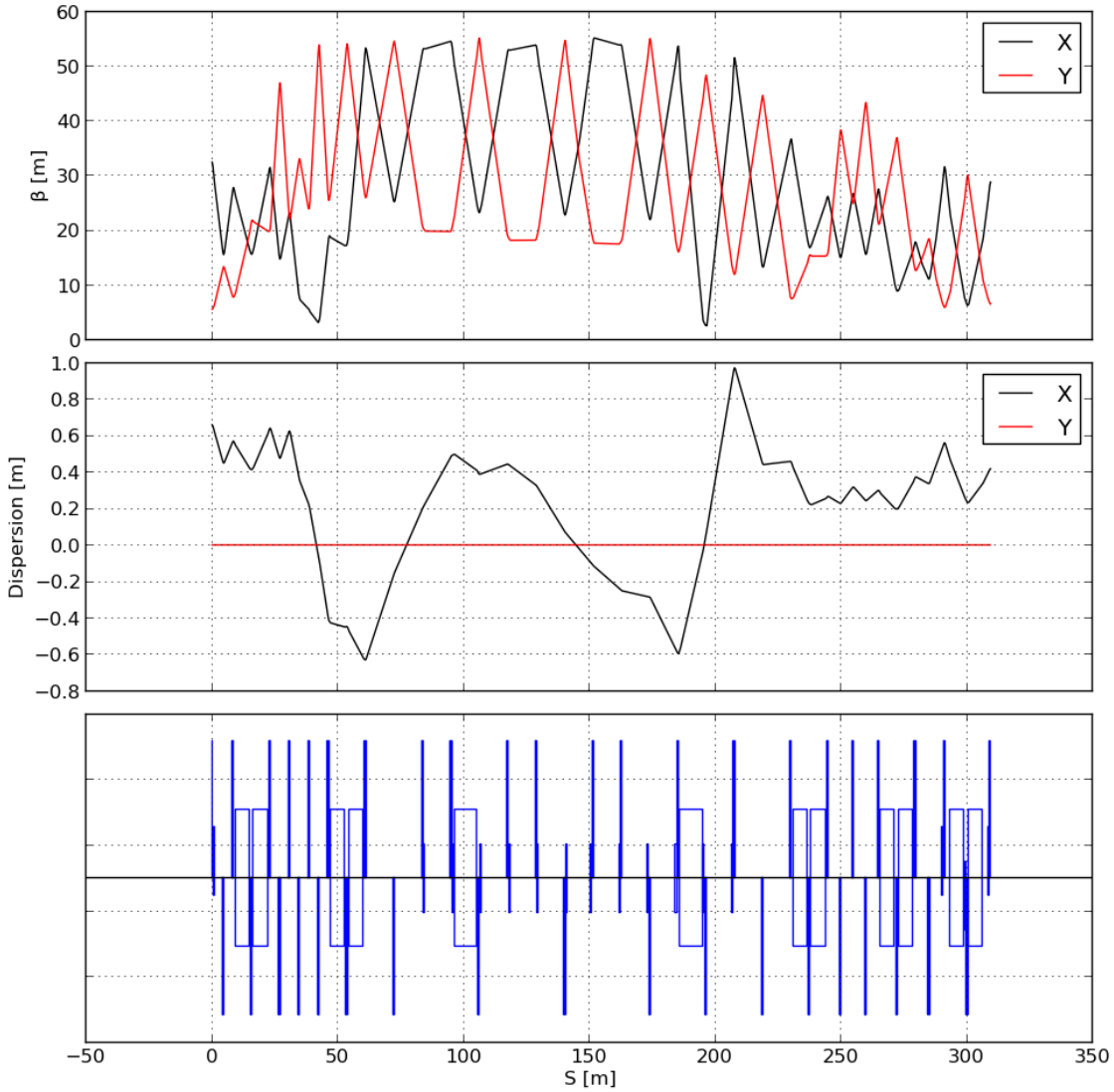

Figure 3.173: The beam parameters plotted along the 12 o'clock straight section of the ESR.

Electron Beam Optics of the ESR Injection Region

There will be two electron bunches circulating in the RCS to be extracted, transferred and injected into the ESR ring. Each e-bunch from the RCS will be injected into ESR in its own injection cycle. Just before beam injection into the ESR a local beam bump will be generated downstream of the 12 o'clock straight section. The maximum beam displacement of this local closed bump is ∼1.5 cm at the location of a focusing quadrupole shown by the red line in Figure 3.174.

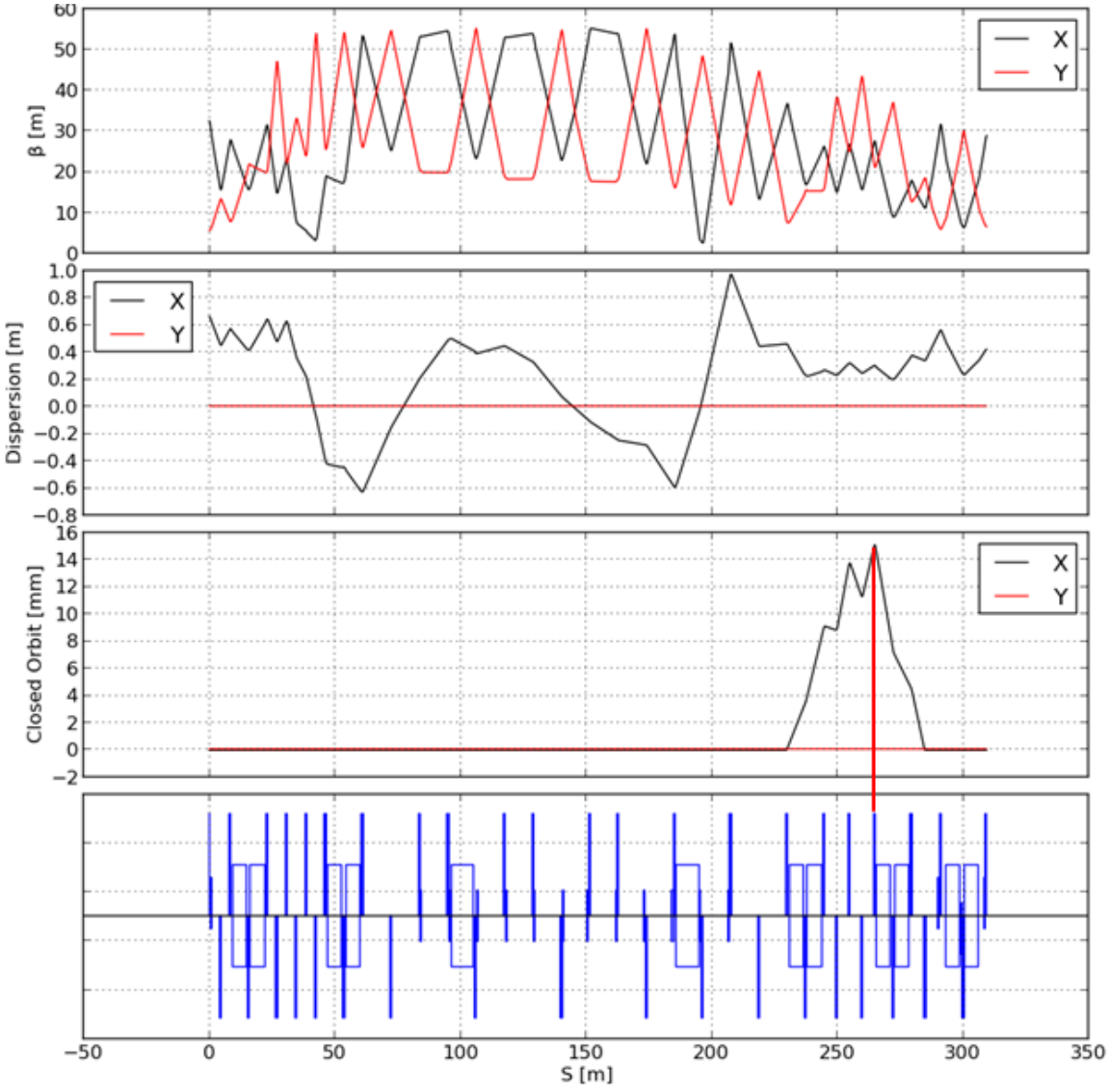

Figure 3.174: The local beam bump generated downstream of the 12 o'clock straight section. The maximum beam displacement of the bump is ∼1.5 cm at the location of a focusing quadrupole shown by the red line in the figure.

An expanded view of the 12 o'clock straight section which includes the local closed beam bump is shown in Figure 3.175. The location of the three magnets which generated this local closed bump are shown as little red boxes on the figure. Some of the specifications of these magnets are listed in Table 3.68. Some consideration is given as the type of septum magnet to be used. A DC type current septum can provide strong field but it requires a thick septum ∼1 cm which increases the strength of the kickers. An induction septum operates with ∼5 mm thick septum but it cannot generate very strong field due the eddy currents in the iron laminated material. Such septa magnets are currently under study.

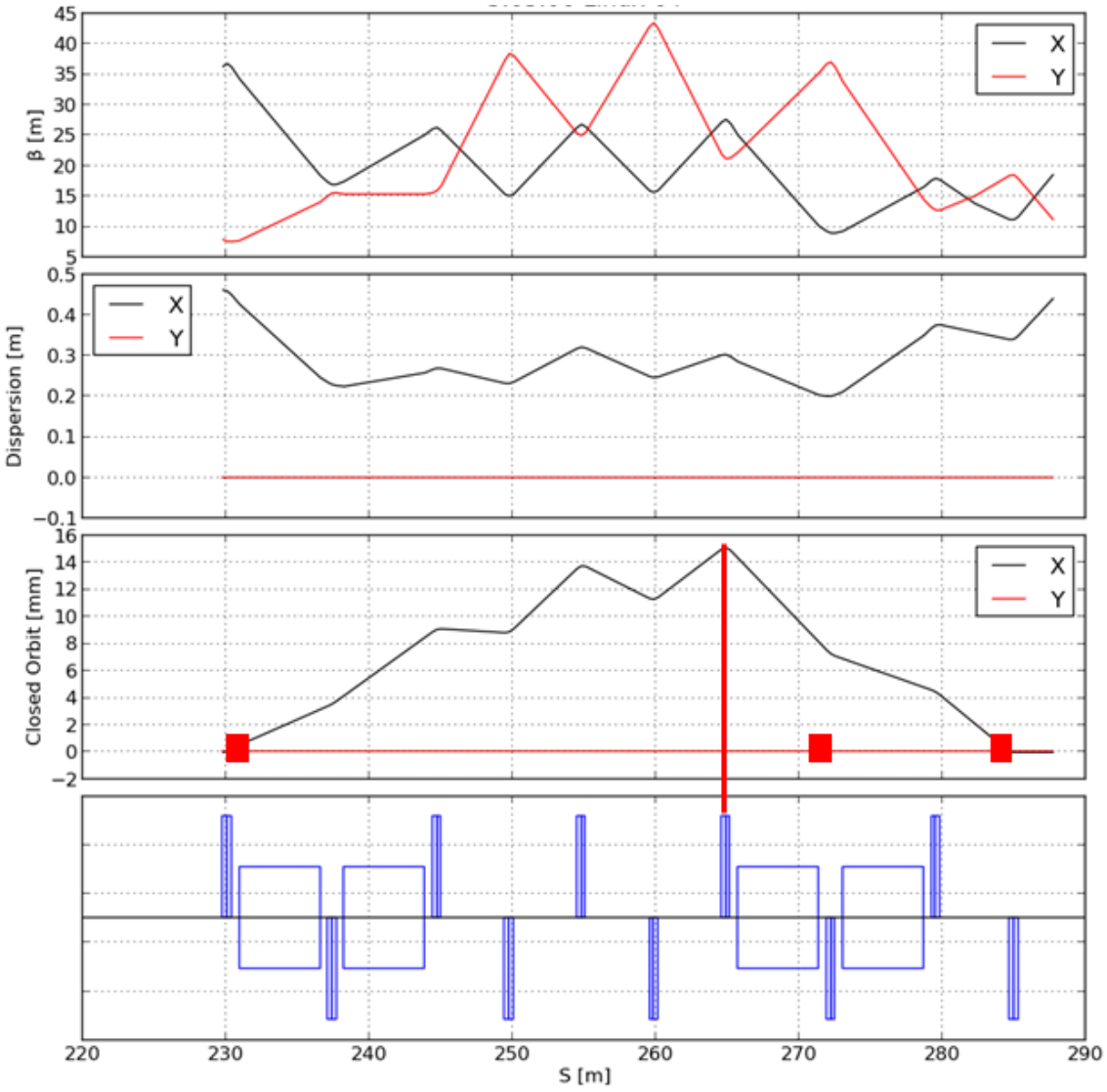

Figure 3.175: Expanded view of the 12 o'clock section which includes the closed beam bump. The location of the magnets which generate the beam bump is shown by red boxes in the figure.

To provide enough space for the placement of a septum between the reference orbit of the bumped beam and the reference trajectory of the injected beam the injected beam is displaced by an additional ∼2.0 cm from the circulating bumped beam at the location of the focusing quadrupole (red line in Figure 3.176) This ∼2.0 cm space allows a septum of ∼1.0 cm thick to be placed upstream of the focusing quadrupole which is lined-up with the red line in Figure 3.176. Thus the injected beam is displaced by ∼3.5 cm upstream of the focusing quadrupole where a ∼15 mrad injection septum is placed to guide the beam in the ESR. Two ∼1 mrad with fast 4 ns strip line kickers are bending the injecting beam into the reference orbit of the ESR. The location of the strip line kickers are shown schematically in Figure 3.176 and some details on the specifications of these kickers is discussed in the subsection below.

Table 3.68: List of some specifications of the beam extraction elements required for the beam extraction discussed in this subsection.

Magnet Type	# of Mag.	Material	Length [m]	Gap [cm]	Width [cm]	θ_{bend} [mrad]	B-field [kG]	T_{rise} [ms]
Bump Mag.	3	CMD-10	0.5	4.0	4.0	1.0	0.12	5
Septum	1	NSLS II type	1.25	2.0	3.0	15	0.7	0.5

Strip Line Kickers Consideration for Injection into the ESR

This subsection provides information on the specifications of the strip line injection kicker. The bunch spacing of the circulating beam in the ESR will be 10.15 ns for 5–10 GeV energy, and 40.6 ns for 18 GeV. The electron rms bunch length will be either 1cm (without 3rd harmonic RF) or 2 cm (with 3rd harmonic RF). This subsection assumes that the same type of strip line kickers will be used for both the low energy (5–10 GeV) and the high energy (18 GeV) operations. The information provided in Figure 3.177 aids in the calculation of the length of the strip line kickers for the low energy (5–10 GeV) operations. For the high energy operation of 18 GeV the same kickers can be used. Th following assumptions are used to calculate the required length of each strip line kicker.

- Length of e-bunch: τ_{length}=0.4 ns.
- Rise time of kicker: τ_{rise}=3.54 ns.
- Fall time of kicker: τ_{fall}=3.54 ns.

Using the above data and the information in Figure 3.177 the required length of the kicker is $L = 0.7$ m. A strip line kicker of 0.7 m length powered by a $\pm$40 kV can across 0.03 cm strip line electrodes can provide a 0.2 mrad kick for an 18 GeV electron bunch. Thus 5 such kickers are required to bend such a rigid beam.

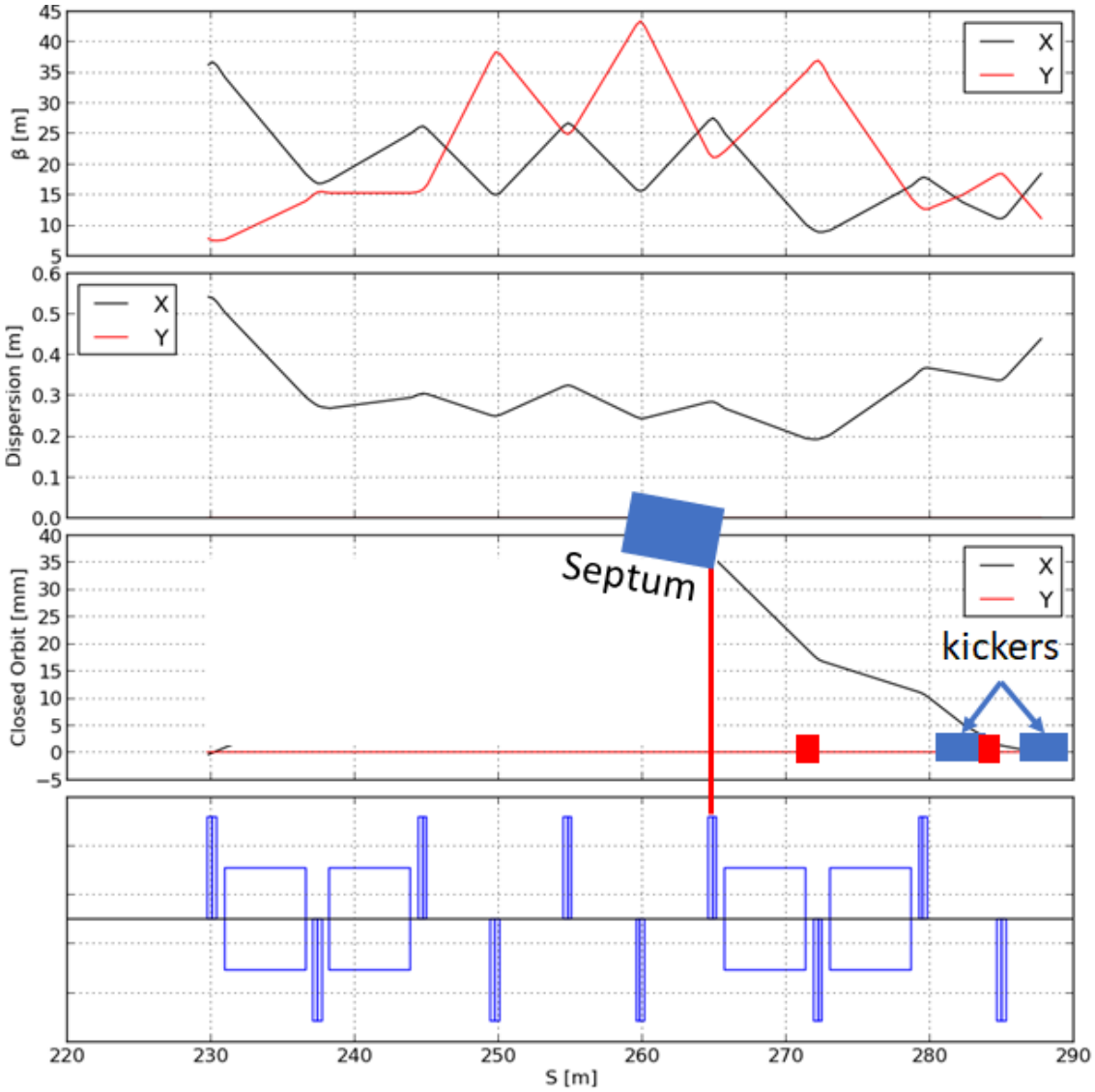

Figure 3.176: The injected beam is displaced by ∼3.5 cm upstream of the focusing quadrupole where a ∼15 mrad injection septum is placed to guide the beam in the ESR. Two ∼1 mrad fast (4 ns) strip line kickers are bending the injecting beam into the reference orbit of the ESR.

The DC Magnets in the RtS Line

Fourteen quadrupoles are required for the design of the RtS transfer line shown in Figure 3.166 , and four main dipoles not including the RCS extraction and the storage ring injection septa. Two rather strong dipoles (38 mrad) for guiding the beam horizontally,

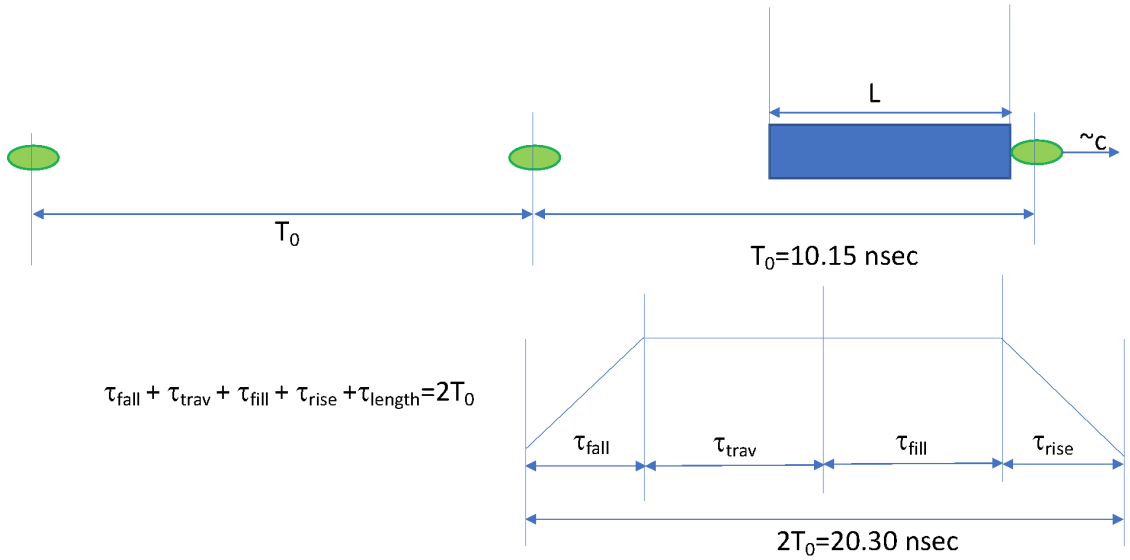

Figure 3.177: A schematic diagram to aid in the calculation of the length of the strip line given the rise time of the pulse and the length of the electron bunch.

and two dipoles (70 mrad) which will drop the level of the beam vertically by 0.5 m. Practical considerations in manufacturing the dipole magnets suggest that each of the four dipole magnets is segmented in two 19 mrad and four 19 mrad shorter magnets that are connected in series. Table 3.69 lists some of the parameters of the quadrupole and dipole magnets of the RtS. Most of the 14 quadrupoles have a lower K1 value than the K1 value listed in Table 3.69, which is the maximum K1 value of the line. A total of ten dipole corrector magnets (4 horizontal and 6 vertical) are included in Table 3.69.

Table 3.69: The magnetic elements of the RtS beam transfer line.

Mag. Type	L [m]	radius/$\frac{1}{2}$gap [cm]	Angle/$K1$ [deg] [m^{-2}]	Gradient/BL [T/m] [Tm]	$B_{\text{pole tip}}$ [T]	I_{max} [A-turn]	Qty
Quad	0.6	2.2	0.56	34.8	0.77	6706.0	14
Dipole	1.15	2.4	0.019	1.14	0.99	18946	2 in series
Dipole	1.15	2.4	0.019	1.14	0.99	18946	2 in series
Dipole	1.15	2.4	0.019	1.14	0.99	18946	8 in series
Corr.	0.5	2.2	0.06	0.12	0.82	2100	10

3.9 Strong Hadron Cooling

There are several cooling terms used in this Section that have specific definitions. These terms are listed below:

- strong hadron cooling : the cooling technique has stronger cooling rate compared to any other demonstrated cooling methods for comparable cooler parameters, e.g. electron current
- electron cooling: standard incoherent scattering cooling based on Coulomb scattering
- Coherent electron Cooling: the cooling method using coherent signals from electron beam
- micro-bunched cooling: A Coherent electron Cooling scheme using chicanes and space charge force as amplification
- e-cooler: The cooling facility to perform cooling
- Coherent electron Cooling PoP: Coherent electron Cooling proof of principle experiment, currently being carried out at RHIC

3.9.1 Introduction

To maintain a luminosity of $L = 10^{34}\,\mathrm{cm}^{-2}\mathrm{s}^{-1}$ in EIC during long collision runs, it is desirable to cool the hadron beams to balance emittance growth rates due to intrabeam scattering (IBS) thereby allowing to keep the same hadron beam for long collision runs ($\geq$ 24 hours). Strong hadron cooling could be replaced by frequent on-energy injections, but long un-interrupted luminosity runs are considered an advantage. The primary requirement for strong hadron cooling is to cool protons with an energy of 275 GeV. The parameters and the design described in this section are calculated for this case. Refining the cooling design for other cases (such as lower beam energies and ions instead of protons) requires additional study (partly due to issues associated with lower-energy beam quality) and is the subject of ongoing work.

For a luminosity of $L = 1.0 \times 10^{34}\,\mathrm{cm}^{-2}\mathrm{s}^{-1}$, we need 6.9×10^{10} protons per bunch. The proton beam RMS emittances are required to be $\varepsilon_x = 11.3$ nm and $\varepsilon_y = 1.0$ nm, respectively, and the proton RMS bunch length is only 6 cm. The proton beam energy is 275 GeV. These proton beam parameters imply intrabeam scattering emittance growth rates of up to $0.5\,\mathrm{hours}^{-1}$ in the longitudinal and the horizontal plane. These growth rates need to be compensated by a cooling mechanism with cooling rates which exceed the IBS growth rates. Table 3.70 summarizes the hadron beam parameters which are relevant for the calculation of IBS growth rates and are used to specify the required hadron cooling rates[2].

[2]The vertical emittance value $\simeq$0.5 nm. Pre-cooling with the RHIC electron cooler at low energy would reduce the cooling time at high energy needed to reach the desired value of the vertical emittance.

Table 3.70: Relevant beam parameters for Coherent Electron Cooling

Parameter	Value
Proton Beam Energy [GeV]	275
Proton Relativistic Factor γ	293.2
Number of protons per bunch [10^{10}]	6.88
Horizontal Proton RMS Emittance [nm]	11.3
Vertical Proton RMS Emittance [nm]	1.0
Proton relative Energy Spread [10^{-4}]	6.8
Proton bunch length [cm]	6
Horizontal intrabeam scattering growth time [hours]	2.
Longitudinal intrabeam scattering growth time [hours]	2.9
Electron Cooling Beam Energy [MeV]	149.8
Required Cooling Time [hours]	≤ 2
Hadron Beam Storage Time [hours]	> 8

In this section, we are presenting a possible layout for an electron cooler for micro-bunched electron cooling. The novel cooling mechanism is well-understood by a thorough theoretical analysis and by simulations, the results of which are presented below. This allows the definition of the parameters of the cooling facility to a high level of certainty. These parameters form the base of the facility layout described in the following sections.

Availability of strong hadron cooling is not yet certain. This uncertainty is associated with a design risk which has been mitigated by alternatives that would provide similar results. A lower-risk alternative which employs both of existing RHIC rings is described in [23]. While the hadron beam is stored at the store energy in one ring, the second hadron ring is used for frequent (every hour) acceleration cycles providing refills of the stored beam. A low energy cooler [22] operating at the injection energy of 24 GeV forms the beam emittances required by the Table 3.3 for maximum peak luminosity. On the other side this alternative creates frequent interruption of detector operation due to refills, and requires extremely good machine and experimental protection during high energy beam transfers. Another alternative under consideration implements incoherent electron cooling based on a storage ring with strongly enhanced radiation damping by using wigglers [177, 178] . Combined with the low energy cooler such design alternative could provide the required cooling at 275 GeV. But getting strong radiation damping in the cooler ring and the efficient cooling is problematic for the proton beam energies below 200 GeV.

Nevertheless, strong hadron cooling via coherent electron cooling with micro-bunched electron beam is our design choice. Given the good theoretical understanding, we are confident that with continuing beam-dynamics assessment and refined design work, the risk of the strong hadron cooling can be reduced to a manageable level, thus it can be consid-

ered a realistic option for the design of EIC. The strong hadron cooling would provide long stores with maximum average luminosity, and should be able to operate efficiently in the whole hadron energy range.

3.9.2 Coherent Electron Cooling with Micro-bunched Electron Beams

The principle of micro-bunched coherent electron cooling is explained in the following way: An electron beam with small energy spread and a smooth longitudinal density distribution co-propagates with the hadron beam in a section called "modulator" sharing the same central orbit. Both beams have an identical relativistic factor $\gamma \simeq 300$. A fluctuation of proton density along the bunch gives rise to a residual electrical field which is experienced by the electrons and which induces a correlated energy variation of the electrons along their longitudinal bunch coordinate.

After the modulator section, the electron beam is strongly focused transversely and passes through a dispersive chicane section where the energy modulation of the electrons is transformed into a density modulation referred to as "micro-bunching". This micro-bunching can be enhanced considerably by the Coulomb interaction of the electrons among themselves and by placing subsequent chicanes that are spaced by a quarter of the plasma oscillation wavelength of the electron beam.

Meanwhile, the hadrons pass through a dispersive section as well such that the higher energy particles move ahead and lower energy ones trail behind with respect to their original position in the bunch.

After the micro-bunching section, the electron beam and the proton beam are brought onto the same orbit again in a section we call "kicker". The pathlength of electrons and hadrons between modulator and kicker sections are adjusted to exactly the same value with a high precision of better than 1 µm.

In this configuration the residual electric field of the micro-bunched electrons will decelerate the higher energy hadrons and accelerate the lower energy ones, thereby reducing the proton energy spread. Repetition of this process over many turns leads to the desired longitudinal cooling with a timescale of an hour. Figure 3.178 illustrates this scheme.

Transverse cooling is achieved at the same time by introduction of dispersion of the hadron beam orbit in the modulator and the kicker sections.

Coherent electron cooling has first been proposed by Ya. Derbenev [179] and was then developed for electron ion colliders by Derbenev and Litvinenko [24] by proposing to amplify the signal picked up by the electron beam by a free electron laser and associated micro-bunching. D. Ratner [35] has proposed the variant of this method which is described above and which achieves the micro-bunching by sending the beam through a chicane or a series of chicanes with optimized linear longitudinal dispersion R_{56}. Micro-bunching was considered earlier by Litvinenko for seeding the FEL process [180]. More recently, the theory of coherent electron cooling with micro-bunched beams was further developed by G. Stupakov and P. Baxevanis [181–187]. The theory was extensively tested by particle

tracking simulations. These latter works constitute the basis of this design.

Here we provide a short description of the physics of coherent electron cooling with the electron micro-bunching amplification scheme. This includes theoretical estimates of cooling rates and associated quantities, and validation of those estimates by particle simulation. The section that follows summarizes the electron beam requirements, as well as requirement for the layout of the cooling channel. These considerations inform the layout of the cooler facility.

3.9.3 Introduction to the Physics of Coherent Cooling with Micro-bunched Electron Beams

In the following sections, we present the results of a theoretical analysis of the conceptual setup for the micro-bunched electron coherent cooling (MBEC) without amplification cascades. The schematic of the MBEC setup is shown in Figure 3.178.

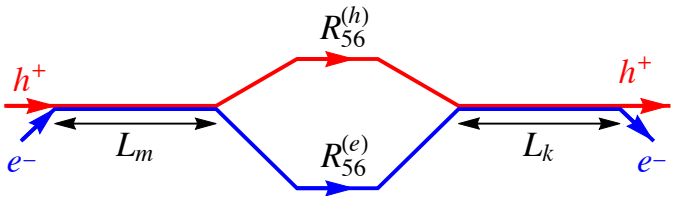

Figure 3.178: Schematic of the MBEC setup. The electron beam (shown in blue) first interacts with hadrons in the modulator of length L_m, then passes through the chicane with the dispersion strength $R_{56}^{(e)}$, and interacts again in the kicker of length L_k. The hadron beam (shown in red) passes through the chicane with the dispersion strength $R_{56}^{(h)}$.

The work reported in Sections 3.9.4–3.9.7 is based on several simplifying assumptions.

1. Use a one-dimensional model for the Coulomb interaction in the beam. In this model, each hadron is treated as an infinitely thin slice of charge Ze ($-e$ for electrons) with the transverse charge distribution over the surface of the slice defined by the Gaussian distribution function $(2\pi\Sigma_x\Sigma_y)^{-1}e^{-x^2/2\Sigma_x^2}e^{-y^2/2\Sigma_y^2}$, where Σ_x and Σ_y are the transverse RMS sizes of the beam in x and y directions, respectively. This model can be justified by the fact that the betatron phase advance over the length of the interaction is almost 360° and individual protons will sweep across the entire transverse beam size. We expect that the model of Gaussian slices is more accurate than the model used in reference [35], where the interaction between two charged particles was treated as that of a uniformly charged slice and a point charge on the axis of the beam.

2. Ignore the effect of the shot noise in both beams on the cooling. This effect becomes more pronounced if additional amplification stages are added to the system (see discussion in Section 3.9.9).

3. Ignore effects associated with plasma oscillations in the modulator and the kicker as, given the beam parameters in these sections, the lengths of these sections are significantly smaller than a quarter wavelength $\lambda_p/4$ of the plasma oscillations in the beam. However, we exploit plasma oscillations in the amplification sections where the beam size is strongly reduced and so is $\lambda_p/4$.

4. Assume equal sizes in the transverse directions and a perfect overlap of the electron and hadron beams in the modulator and the kicker.

5. Particles (slices) do not shift relative to each other longitudinally during the interaction in the modulator and the kicker. Such longitudinal shifts are assumed to be absorbed by statistical averaging over all particles involved in this process.

6. The only effect of the chicanes in the system is the longitudinal displacement of the particles proportional to the chicane strength as expressed by the parameter R_{56}. The micro-bunching in the chicane could be limited according to reference [188], which is not expected to affect the design considered here.

3.9.4 Qualitative Derivation of MBEC Cooling Rate

Interaction between two charged slices of transverse size $\approx a$ is efficient only if they are close to each other. If the distance between them is smaller than $\Delta z \lesssim a/\gamma$, where γ is the Lorentz factor, the electric field of a hadron of charge Ze can be estimated as Ze/a^2 (in our crude estimates we neglect numerical factors), and the interaction force between an electron and a hadron is $\approx Ze^2/a^2$. If $\Delta z \gtrsim a/\gamma$, the interaction force decays as $\approx Ze^2/\Delta z^2$. So, for estimates we assume

$$\Delta z \sim \frac{a}{\gamma}. \tag{3.92}$$

Particles at this distance provide the dominant contribution to the cooling. We use the notation η for the relative energy deviation $\Delta E/E_0$ where E_0 is the nominal energy of the beam. Using the interaction force Ze^2/a^2, a relative energy modulation η_e induced by a hadron in the modulator of length L_m can be estimated as

$$\eta_e \sim \frac{cZeL_m}{\gamma a^2 I_A} \tag{3.93}$$

where $I_A = m_e c^3/e = 17\,\mathrm{kA}$ is the Alfvén current. Here we assume that a hadron and an electron do not shift longitudinally with respect to each other during the interaction over the length L_m. The energy perturbation in Equation 3.93 is converted into a density perturbation when the electron beam passes through the chicane $R_{56}^{(e)}$. The optimum value of $R_{56}^{(e)}$ is found from the requirement that the electrons are longitudinally shifted by distance $\sim \Delta z$:

$$R_{56}^{(e)} \sim \frac{\Delta z}{\sigma_\eta^e} \sim \frac{a}{\sigma_\eta^e \gamma}, \tag{3.94}$$

where σ_η^e is the RMS relative energy spread in the electron beam. Electrons whose energy is perturbed by η_e due to the interaction with a hadron will have an additional shift $\delta z \approx R_{56}^{(e)}\eta_e$, and this will cause a density perturbation of the order of

$$\delta n_e \sim \frac{\delta z}{\Delta z} n_0 \sim \frac{\eta_e}{\sigma_\eta^e} n_0 \,. \tag{3.95}$$

Here δn_e and n_0 refer to the number of electrons in the beam per unit volume. This density perturbation creates an electric field in the kicker,

$$E \sim e\delta n_e \Delta z \sim e\frac{\eta_e}{\sigma_\eta^e}\frac{a}{\gamma} n_0 \,. \tag{3.96}$$

With the optimal choice of the value of the hadron chicane, $R_{56}^{(h)} \approx \Delta z/\sigma_\eta^h \approx a/\sigma_\eta^h\gamma$, where σ_η^h is the RMS relative energy spread in the hadron beam, the hadron energy change in the kicker, $\approx ZeEL_k$, works against the hadron beam energy spread. This gives the following estimate for the inverse cooling time expressed in the revolution periods,

$$N_c^{-1} \sim \frac{ZeEL_k}{\gamma m_h c^2 \sigma_\eta^h} \sim \frac{ZeL_k}{\gamma m_h c^2 \sigma_\eta^h} e\frac{\eta_e}{\sigma_\eta^e}\frac{a}{\gamma} n_0 \sim \frac{(Ze)^2 L_k L_m}{\gamma^3 m_h c^2 a^3 I_A \sigma_\eta^e \sigma_\eta^h} ecn_0 a^2 \,. \tag{3.97}$$

Replacing ecn_0a^2 in this formula by the electron beam current I_e and using the notation $r_h = (Ze)^2/m_hc^2$ for the classical hadron radius, we arrive at the following result:

$$N_c^{-1} \sim \frac{L_k L_m I_e r_h}{\gamma^3 a^3 I_A \sigma_\eta^e \sigma_\eta^h} \,. \tag{3.98}$$

As we will see below, this estimate agrees with the result of an accurate theoretical analysis.

3.9.5 Brief Survey of Theoretical Analysis of the Problem

The theoretical analysis of MBEC for a simple setup shown in Figure 3.178 was carried out in References [182, 189]. Here we present the main results of that analysis. We have used the assumptions outlined in Sections 3.9.3. As already mentioned, for the Coulomb interaction of beam particles a model of Gaussian slices was used. In addition, it was assumed that the beams have a round cross section, $\Sigma_x = \Sigma_y = \Sigma$ (this model has also been previously used in References [35, 190]). The longitudinal Coulomb force between two such slices located at distance z is given by the following formula:

$$F_z(z) = -\frac{Ze^2}{\Sigma^2}\Phi\left(\frac{z\gamma}{\Sigma}\right) \tag{3.99}$$

where the plot of function Φ is shown in Figure 3.179.

The function $\Phi(x)$ is odd, and for the negative argument $x < 0$ it is defined by $\Phi(-x) = -\Phi(x)$. The value of this function at the origin is $\Phi(0^+) = 0.5$; for the large values of the

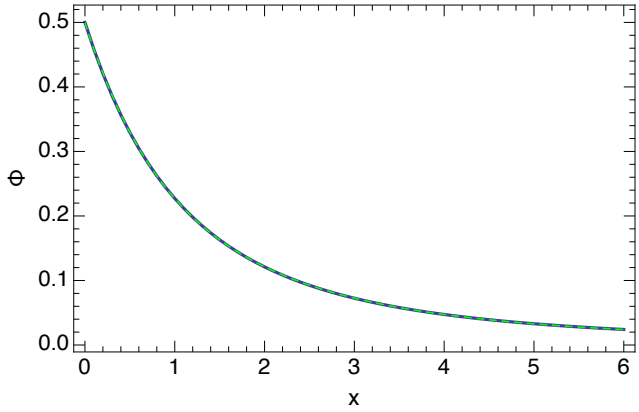

Figure 3.179: Function $\Phi(x)$ for positive values of the argument. The solid line shows the exact function $\Phi(x)$ and the dashed green line is the fit (Equation (3.100)).

argument, $x \gg 1$, we have $\Phi(x) \approx 1/x^2$. For a quick numerical evaluation of this function one can use the following interpolation formula,

$$\Phi(x) \approx b\frac{e^{-ax}+1}{2+dx+bx^2}, \tag{3.100}$$

with $a = 1.60081$, $b = 0.499606$, and $d = 0.14579$. Using this model for the particle interaction, the following formula for the cooling time N_{cool} expressed in the revolution periods in the hadron ring was derived:

$$N_{\text{cool}}^{-1} = \frac{4}{\pi}F(q)\frac{I_e r_h L_m L_k}{\Sigma^3\gamma^3 I_A \sigma_\eta^h \sigma_\eta^e}, \tag{3.101}$$

where the form-factor F depends on the strength of the chicanes $R_{56}^{(h)}$ and $R_{56}^{(e)}$. Analysis shows that for optimum cooling the ratios $q_e = R_{56}^{(e)}\sigma_\eta^e\gamma/\Sigma$ and $q_h = R_{56}^{(h)}\sigma_\eta^h\gamma/\Sigma$ should be made equal, $q_e = q_h = q$; in this case the form-factor F depends only on the parameter q. The plot of the function $F(q)$ is shown in Figure 3.180. We see that the maximum value of function F is reached at $q = 0.6$ and is equal to 0.079. Substituting this value into Equation 3.101 we find for the optimized cooling rate:

$$N_{\text{cool}}^{-1} = \frac{0.1}{\sigma_\eta^h\sigma_\eta^e}\frac{1}{\gamma^3}\frac{I_e}{I_A}\frac{r_h L_m L_k}{\Sigma^3}. \tag{3.102}$$

We see that this formula has the same scaling with all the parameters as Equation 3.98, but it also has a numerical factor 0.1. At the optimum cooling rate the chicane strengths are

$$R_{56}^{(e)} = 0.6\frac{\Sigma}{\sigma_\eta^e\gamma}, \qquad R_{56}^{(h)} = 0.6\frac{\Sigma}{\sigma_\eta^h\gamma}. \tag{3.103}$$

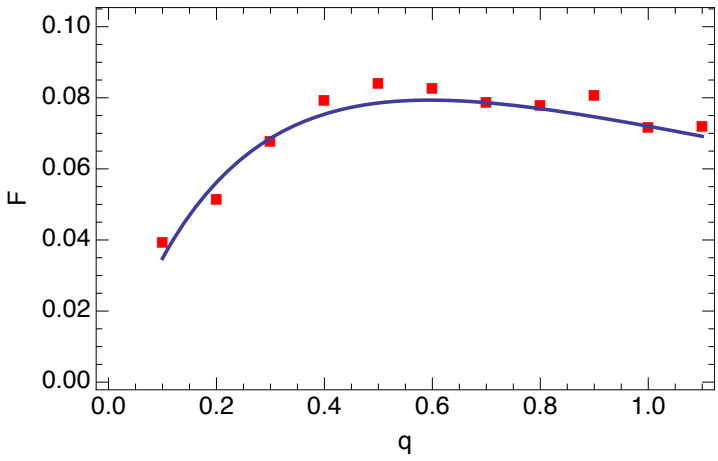

Figure 3.180: Plot of function $F(q)$ (solid line) and the result of numerical simulations (red squares) (see Equation 3.101).

Equation 3.102 gives the cooling rate when all hadrons interact with the same electron current I_e. In reality, we can assume that the electron beam will have a Gaussian longitudinal distribution with the RMS length σ_z^e. In this case, hadrons in the head and the tail of the bunch will interact with a smaller local electron current than the electrons at the center of the bunch, and Equation 3.102 should be averaged over the longitudinal coordinate. Assuming, in addition, that σ_z^e is equal to the RMS length of the hadron beam, the result of this averaging gives an additional factor $1/\sqrt{2}$,

$$N_{\rm cool}^{-1} = \frac{0.071}{\sigma_\eta^h \sigma_\eta^e} \frac{1}{\gamma^3} \frac{I_{e,p}}{I_A} \frac{r_h L_m L_k}{\Sigma^3}, \tag{3.104}$$

where $I_{e,p}$ is the peak electron current: $I_{e,p} = Q_e c/\sqrt{2\pi}\sigma_z^e$, with Q_e the charge of the electron beam.

3.9.6 Computer Simulations

We developed a computer code that simulates the cooling within the same model as was used for the analytical study (that is, the Coulomb interaction was treated for the Gaussian slices). In this computer simulation a part of the electron beam was represented as a collection of macroparticles and only one hadron was considered. First, the hadron was immersed into the electron beam (in the modulator) and the energy change of each electron in its surroundings was calculated. Then the electrons were transported through an electron chicane which resulted in their shift in the longitudinal direction equal to $R_{56}^{(e)}\eta_e$. The hadron was transported through a hadron chicane and was shifted longitudinally by $R_{56}^{(h)}\eta_h$ relative to its original position. Then the hadron was again immersed into the elec-

trons (in the kicker) and the kick from all the electrons to the hadron was calculated. The procedure was repeated many times with the initial hadron energy statistically distributed according to the Gaussian energy distribution with the RMS energy spread σ_η^h. From the result of this run the cooling rate was inferred and compared with the analytical formula in terms of the form factor shown in Figure 3.180. One can see that the numerical results agree well with the simulations.

3.9.7 Choice of Cooling Parameters for EIC

Because of the strong dependence of the cooling rate as expressed in Equation 3.104 on the transverse size of the bunches Σ in the modulator and the kicker sections, at a first glance, it seems that one should try to minimize Σ. The problem, however, is that a small Σ would require simultaneous focusing of both beams, which seems impossible because of the very different rigidity of the hadron and electron beams. Without focusing, the transverse size of the hadron beam is determined by its emittance and the value of the β-function, which cannot be much smaller than the length of the channels L_m and L_k. Assuming $\beta \approx L_m \approx L_k$ we obtain $\Sigma \approx \sqrt{\epsilon_h L_m}$, where ϵ_h is the hadron beam emittance, and $N_{\rm cool}^{-1} \propto \sqrt{L_m}$. This indicates that a stronger cooling is achieved in a longer channel and, correspondingly, a larger transverse size of the beams.

As an illustration, we will use the optimized cooling rate (Equation 3.104) to evaluate the performance of MBEC coherent cooling for a preliminary parameter set modeled after that of EIC. For the electron beam charge, we take $Q_e = 1\,$nC (which corresponds to $N_e = 6.24 \times 10^9$ electrons in the bunch), with the bunch length of $\sigma_z^e = 5\,$cm, while the peak current is $I_{e,p} = Q_e c/\sqrt{2\pi}\sigma_z^e = 2.4\,$A. With 1160 proton bunches in the ring, and hence the repetition rate of 98.5 MHz of the electron bunches, the average electron current through the cooling system is 98.5 mA. We also assume that $\Sigma = 0.67\,$mm, which (for a round 275 GeV proton beam with an emittance of $11.3\,\text{mm} - \text{mrad}$) corresponds to an average beta function of 40 m at the modulator and kicker. Substituting these parameters in Equation 3.104 gives for the cooling time in revolution periods $N_{\rm cool} = 2.1 \times 10^{10}$, which, with the revolution period in RHIC ring of 12.8 µs, corresponds to 75 hours. This is clearly too slow for EIC. To rectify this issue - and to include cooling of the transverse degrees of freedom - we first need to consider three additional topics: a) adding one or more amplification stages to the system b) considering the option of short electron bunches and c) treating flat beams in the modulator and kicker. These are, respectively, discussed in the next three sections.

3.9.8 Adding Amplification Stages

The cooling rate of MBEC in its simplest form shown in Figure 3.178 is too weak to be used in EIC. It however can be increased by several amplification stages, each of which consists of a one-quarter of plasma-oscillation drift, $\lambda_p/4$, where λ_p is the plasma wavelength in the electron beam, with additional chicanes at the end of the drifts. For the case of one and two amplification stages, such a system is shown in Figure 3.181. This amplification method was considered in the original paper [35], but it has been proposed, and studied in detail,

in Refs. [191, 192], for generation of UV and soft x-rays through beam microbunching. Experimentally this amplification was demonstrated in a proof-of-principle experiment at SLAC [193].

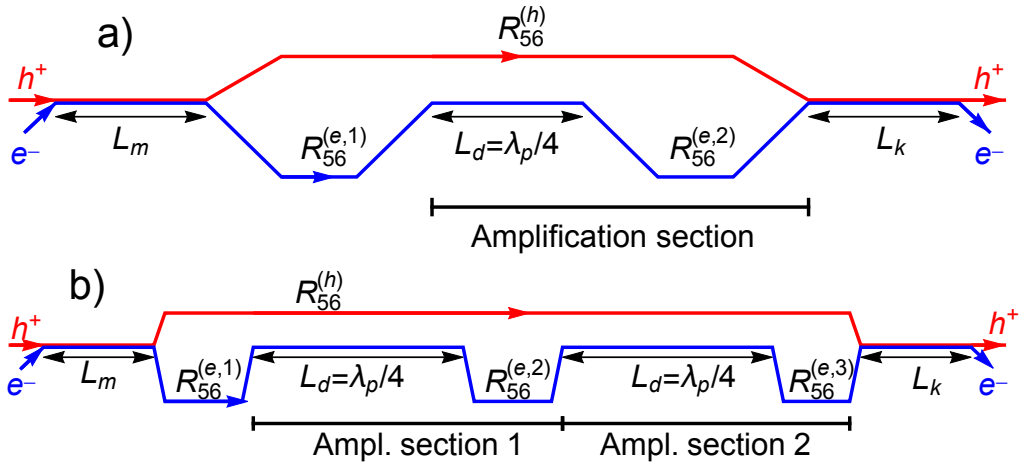

Figure 3.181: Schematic of the microbunched electron cooling system: a) with one amplification stage, b) with two amplification stages. Blue lines show the path of the electron beam, and the red lines indicate the trajectory of the hadron beam.

The mechanism of the amplification is the following. A perturbation of the electron beam density generated after the chicane $R_{56}^{(e,1)}$ (see Figure 3.181a) by a hadron, through a Fourier transformation, can be decomposed into sinusoidal density perturbations in the beam. Each such perturbation propagating though the drift executes a quarter-wavelength plasma oscillation, which converts the initial density perturbation into a sinusoidal energy modulation in the beam. When the beam passes through the chicane $R_{56}^{(e,2)}$, the energy modulation is converted back into a density perturbation with an amplitude that can be larger than the initial one [191, 192]. One can define the gain factor G as a ratio of the final amplitude to the initial one. For an optimal value of the chicane strength $R_{56}^{(e,2)}$, this gain factor is given by the following formula

$$G = \Gamma\left(\frac{k\Sigma_p}{\gamma}\right)\frac{1}{\sigma_\eta^e}\sqrt{\frac{I_e}{\gamma I_A}}, \tag{3.105}$$

where the numerical factor Γ depends on the wavenumber k of the sinusoidal oscillation. Here Σ_p is the RMS electron beam radius in the drift (this radius, in general, is different from the electron beam radius Σ in the modulator and the kicker). The plot of Γ is shown in Figure 3.182 by a black curve.

The red symbols in Figure 3.182 show the result of the numerical simulation of the gain factor which demonstrates a good agreement of theory and simulations.

Returning to the cooling mechanism, the dominant contribution to the coherent cooling comes from the spatial scale of the order of Σ/γ, and assuming for a moment $\Sigma_p \sim \Sigma$ we

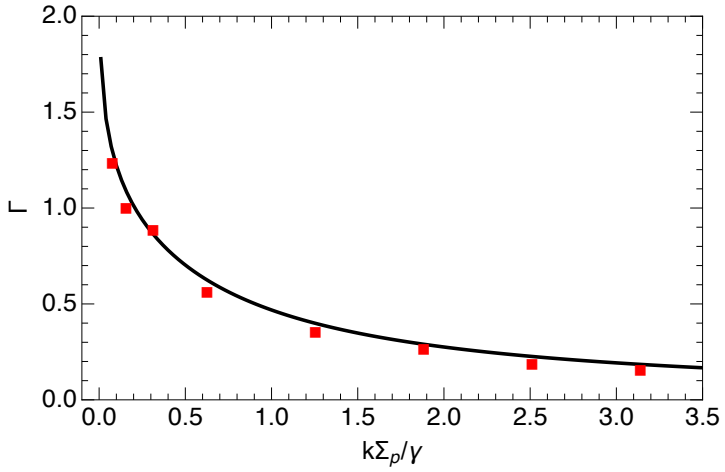

Figure 3.182: Plot of the factor Γ versus the normalized wavenumber $k\Sigma_p/\gamma$. Red symbols are computer simulations.

find that $k\Sigma_p/\gamma \approx 1$. This means that one can expect the gain in the cooling rate from one amplification stage to be equal to a fraction of the following factor,

$$A_{\rm amp} = \frac{1}{\sigma_\eta^e}\sqrt{\frac{I_e}{\gamma I_A}}, \tag{3.106}$$

which can be large for the electron beam with a small energy spread. Even for the relatively broad electron bunch considered so far (with a peak current of 2.4 A) the above factor is about 6.93. This naturally leads one to consider shortening the electron bunch in order to boost the amplification factor through the increased peak current, a scheme which is considered in the next Section.

3.9.9 An Option of Short Electron Bunches

The formula for the quarter of the plasma wavelength in a relativistic electron beam is[3]

$$\frac{1}{4}\lambda_p = \frac{\pi}{2}\Sigma_p\gamma^{3/2}\sqrt{\frac{I_A}{I_e}}\,. \tag{3.107}$$

Assuming $\gamma \approx 293.2$, $I_e = 2.4\,\mathrm{A}$ and $\Sigma_p = 0.154\,\mathrm{mm}$ (for an electron beam with a normalized emittance of $2.8\,\mathrm{mm-mrad}$, the latter corresponds to an average beta function of about 2.5 m at the location of the amplification stages), we find for the quarter of the

[3]The plasma wavelength actually depends on the wavenumber k of the modulation in the beam. This formula is valid for $k \gg \gamma/\Sigma_p$. Note also that this formula is specific for the Gaussian transverse distribution in the beam (a uniform radial distribution would have an extra factor $\frac{1}{2}$ when Σ_p is replaced by the beam radius a).

plasma wavelength

$$\frac{1}{4}\lambda_p = 102\,\text{m}. \tag{3.108}$$

This is a large length, especially - as we will show below - if one takes into account that there is a need for two amplification stages in the EIC cooling system. To shorten the total length of the amplification stages, one can use an electron bunch with a larger peak current. In the previous analysis it was assumed that the length of the electron bunch is equal to the length of the proton bunch (the nominal value is 5–6 cm). It seems that a better option is to use an electron bunch, say, approximately ten times shorter, with the same number of particles in the electron beam (that is $N_e = 6.24 \times 10^9$). In the subsequent analysis, we will assume the electron beam peak current of $I_{e,p} = 30$ A, which corresponds to the RMS electron bunch length $\sigma_z^e = 4$ mm.. For these new e-beam parameters, we have $\lambda_p/4 = 29$ m and $A_{\text{amp}} = 24.5$.

Because the electron beam now overlaps with less then 10% of the hadron beam this increases the cooling time more than ten times. However, with two amplification stages, the cooling rate can be shown to be proportional to $\sigma_z^e I_{e,p}^2 \propto Q_e^2/\sigma_z^e$ (see Ref. [185]), and the decrease due to the partial overlapping of the bunches is more than compensated by the increase in the peak current. An additional advantage of short bunches would be that the long bunch stretching and compressing arcs could be reduced in size considerably.

The detailed theoretical analysis of one and two amplification stages with supporting computer simulations was conducted in Reference [185]. This analysis also used the concept of round beams ($\Sigma_x = \Sigma_y = \Sigma$), first mentioned in Section 3.9.5. It was limited to the study of the longitudinal cooling time but included the effect of short electron bunches. Moreover, we should note that the large amplification factor for a multi-stage MBEC system also means that the noise in the electron beam is strongly amplified, leading to enhanced diffusion and heating of the hadron beam that counteract the cooling process. In addition, the initial statistical fluctuations in the electron beam can reach the level where nonlinear saturation effects become important and destructively interact with the cooling. Studies of these two important effects where also included in Ref. [185].

3.9.10 Flat Beams

The calculations of the cooling rate have been carried out so far for round electron and hadron beams (assuming a transverse rms beam size of $\Sigma_{x,y}^{e,p} \approx 0.67$ mm). However, EIC is planned to operate with flat proton beams with a horizontal emittance of $\varepsilon_x^p = 11.3$ nm, which provides the same horizontal beam size of $\Sigma_x^p = 0.67$ mm, but with a vertical emittance of $\varepsilon_y^p = 1.0$ nm, which corresponds to a vertical beam size of $\Sigma_y^p = 0.2$ mm in the modulator and kicker sections (these figures assume a hadron beta function of 40 m in both x and y and neglect dispersion). A formula for the interaction force between slices with unequal transverse dimensions has been derived in [186]— it modifies the function Φ defined in Equation 3.99, making it dependent of the ratio $r = \Sigma_y^p/\Sigma_x^p$. An illustrative plot of this function for $r = 0.33$ is shown in Figure 3.183. The force at small distances is enhanced by a factor of $1/r$ when compared with a round beam.

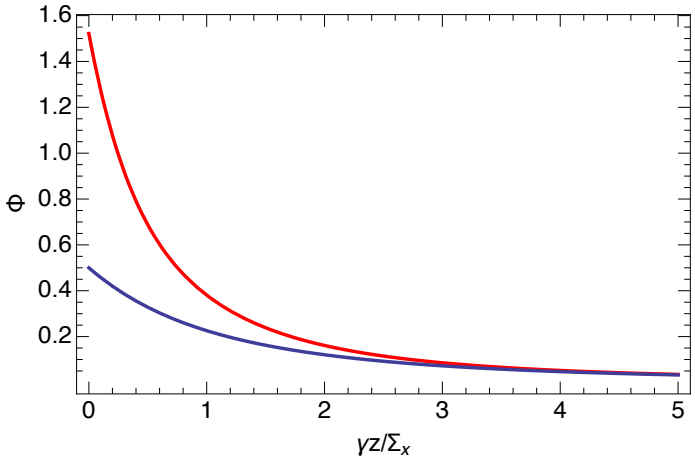

Figure 3.183: Interaction force for an elliptic beam profile with size ratio $\Sigma_y^{e,p}/\Sigma_x^{e,p} = 0.33$ (red line). The blue line shows the interaction force for the axisymmetric slices used previously in the derivation of the cooling rate (see Figure 3.179).

In Ref. [186] this improved model of the beam shape with the recalculated Coulomb interaction force between the slices has been incorporated into the analysis of the transverse cooling in MBEC. Some results of this analysis are described in the next Section. Lastly, it should be stressed that the updated interaction function discussed above still assumes perfect overlap between the two slices. However, it is straightforward to generalize this model to the case of two slices with Gaussian profiles that do not match perfectly (i.e. two slices with elliptical but unequal cross sections). This modification is important when considering realistic beams in the modulator and kicker, as a 100% size overlap (or size matching) may be difficult to achieve in practice.

3.9.11 Transverse Cooling and parameter optimization

In Reference [186] the 1D model of MBEC outlined above for the longitudinal cooling was generalized to include both the longitudinal and the transverse cooling of the hadron beam. In this model, the beam is still represented as a collection of Gaussian slices of an elliptical cross section (that is assuming that in general $\Sigma_x \neq \Sigma_y$) but the beam dynamics was extended, through a 4×4 transport matrix R, to include the transverse motion of the hadron beam when it propagates from the modulator to the kicker. As is well known [194], the energy dispersion D (and its derivative D') in these regions couples the cooling in the longitudinal and transverse directions and allows to direct a part of the longitudinal cooling into the transverse degree of freedom. Analytical expressions for the cooling time of the horizontal emittance, N_c^{ϵ}, and the cooling time for the energy spread, N_c^{η}, (both measured in units of the revolution periods of the ring) were derived in Ref. [186], and the resulting formalism can readily accommodate amplification stages and short electron beams. However, because these expressions are quite lengthy and most suitable for numerical work,

they are omitted here.

As we mentioned earlier, for the majority of interesting cases and configurations diffusion effects are quite considerable and cannot be ignored. For this reason, one typically needs to define a total (or net) cooling rate that combines the counteracting effects of cooling and diffusion and characterize the system by means of this effective rate and its corresponding timescale. In other words, any realistic system analysis has to incorporate diffusion as an integral part of the cooling rate and also keep track of possible nonlinear effects. In keeping with this requirement, we stress that the cooling times quoted in this Section are derived from the net cooling rates that fully include diffusion for the longitudinal and transverse degrees of freedom (still in the context of a 1D treatment of space charge forces). Moreover, the above-described rates are obtained after a proper averaging along the longitudinal position. Since the vertical dispersion in a ring is weaker than its horizontal counterpart, we have only considered transverse cooling in the horizontal plane.

Considering the EIC hadron beam parameters of Table 3.70, we used our analytical results to perform a full multi-variable optimization study for the MBEC cooler. The key results of this study, along with a collection of the parameters for the cooler electron beam, are summarized in Table 3.71. This cooling system contains two amplification sections (see Figure 3.181b) of equal length L_d. The various free parameters were optimized so that the peak value of the transverse cooling rate (along the hadron bunch) reaches a maximum. This is a simpler alternative for approximating the global maximum of the averaged transverse rate, which is significantly more computationally expensive to optimize. The optimal values for the hadron/electron chicane strengths are: $R_{56}^{(h)} = 0.19$ cm, $R_{56}^{(e,1)} = R_{56}^{(e,2)} = R_{56}^{(e,3)} = 0.71$ cm, while for the proton phase advance between the kicker and the modulator we have $\Delta\psi_\beta = 0.036 + 2\pi n$, where n is an integer. The length of each amplification section is $L_d = 43$ m. The horizontal dispersion at this optimum point is $D_{\rm opt} = 1.46$ m. However, for this dispersion value the longitudinal cooling is totally inadequate (in fact, there is *anticooling* for the energy spread). To rectify this issue it is necessary to reduce the dispersion somewhat, which balances the configuration by distributing the cooling between transverse and longitudinal directions. Indeed, as an illustration of this interplay between longitudinal and transverse cooling, Figure 3.184 shows the cooling times as functions of the horizontal dispersion $D_x = D$ in the modulator and the kicker, keeping all other parameters fixed to the previously-quoted values (in these calculations it was assumed that $D' = 0$). As one can see, ramping up the dispersion from small values leads to the decrease of the transverse cooling time and at the same time increase of the longitudinal one. Eventually, for $D \approx 1.17$ m the longitudinal and transverse cooling times are both approximately equal to 100 minutes. This figure is still adequate for purposes of IBS compensation. Finally, Figure 3.185 shows the cooling times as a function of L_d for the reduced dispersion of 1.17 m (this is the point in Figure 3.184 where the blue and red lines cross). As expected, because of the optimized nature of our configuration and the plasma oscillation effects, choosing a larger amplification stage length will not significantly improve the cooling.

Table 3.71: Summary of Coherent Electron Cooling parameters

Parameter	Value
Electron beam energy [MeV]	149.8
Electron rms normalized emittance [µm]	2.8
Electron beam average current [mA]	98.5
Average electron β_x at M/K [m]	40
Average electron β_y at M/K [m]	40
Electron rms beam size at M/K [mm]	0.61
Average proton β_x at M/K [m]	40
Average proton β_y at M/K [m]	40
Proton horizontal beam size [mm]	1
Proton vertical beam size [mm]	0.2
Required rms electron energy spread	10^{-4}
Electron beam bunch charge [nC]	1
Electron beam bunch length [cm]	0.4
First electron Chicane R_{56} [cm]	0.71
2nd electron Chicane R_{56} [cm]	0.71
3rd electron Chicane R_{56} [cm]	0.71
Electron rms beam size at the amplification sections [mm]	0.15
Average electron β function at the amplification sections [m]	2.5
Quarter plasma oscillation wavelength at the amplification sections $\lambda_p/4$ [m]	29
Drift space between chicanes L_d [m]	43
Length of the modulator section [m]	40
Length of the kicker section [m]	40
Overall length of the cooler lattice [m]	166
Proton beam R_{56} between modulator and kicker [cm]	0.195
Dispersion D_x of protons in modulator and kicker sections [m]	1.17
Horizontal phase advance of protons between M/K sections [rad]	$0.036 + 2n\pi$
Cooling time (longitudinal/transverse) [min]	≈ 100

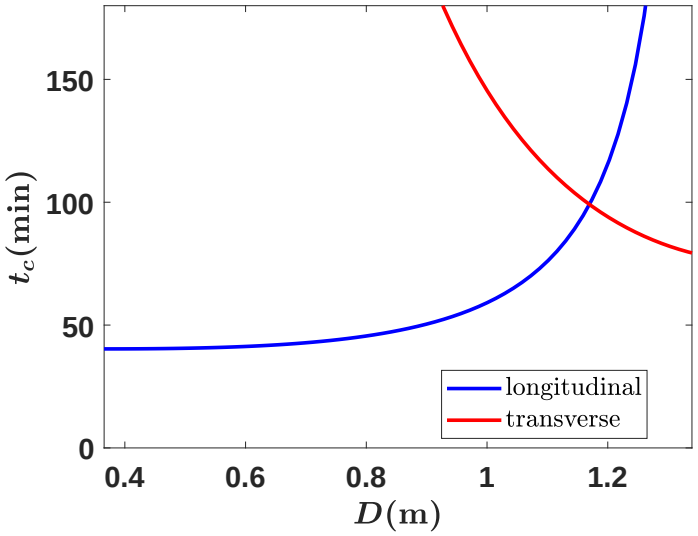

Figure 3.184: The longitudinal (blue) and the transverse (red) cooling time as a function of the dispersion D in the modulator and the kicker sections.

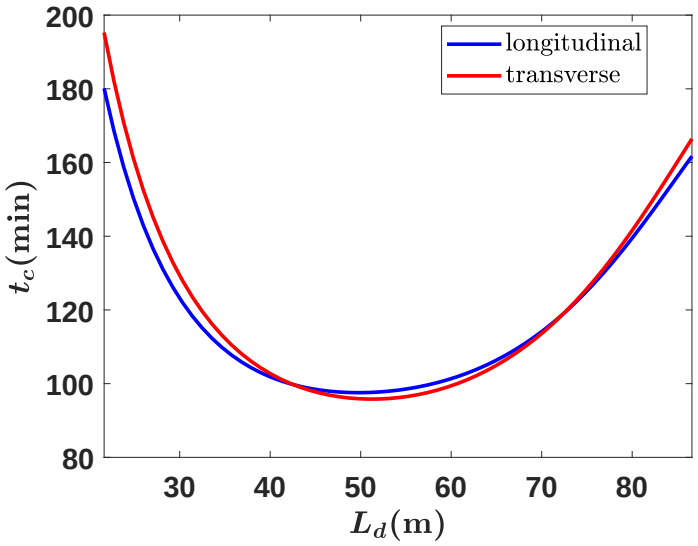

Figure 3.185: The longitudinal (blue) and the transverse (red) cooling times as a function of the amplification section length L_d, for a fixed dispersion $D = 1.17\,\mathrm{m}$.

3.9.12 Requirements for Micro-bunched Coherent Electron Cooling

In this section we summarize the requirements and parameters for the electron beam of the MBEC facility based on the considerations of the previous sections. First, we discuss the requirement on electron beam current, bunch structure and bunch length: The previous sections showed that the required electron bunch charge is 1 nC. With a bunch length of 4 mm, this gives the required peak current of $\simeq$30 A. Given the bunch frequency of 98.5 MHz, this results in an average electron beam current of $I_e = 98.5$ mA. Cooling rates have been calculated assuming that using short bunch lengths of electrons, thus $\sigma_{se} = \sigma_{sp} = \sim 4$ mm. These performance parameters can only be achieved with a state of the art DC gun. The requirement on beam current is somewhat beyond state of the art but is believed within reach by a modest extrapolation of available technology.

The total length of the straight section in the EIC tunnel is only 200 m. To fit the cooler lattice into the straight section we have to assume a modulator and kicker length of only 40 m. The total length of the cooler section is then about 180 m which provides room for matching the hadron optics.

It should be pointed out that a cooling scenario with short bunches, which will be considered in the next design iteration would offer substantial savings for higher harmonic RF structures as well as building space. Table 3.71 summarizes the results of the cooling calculations and the corresponding design parameters for a micro-bunched coherent electron cooling facility.

3.9.13 Overview of the EIC Coherent Electron Cooling facility

The electron cooler set up has the following constituents:

- An electron source for 98.5 mA CW beam current consisting of bunches of 1 nC,
- an injection channel with dogleg merge into the superconducting energy recovery LINAC,
- an energy recovery LINAC,
- an isochronous and achromatic bending section to launch the electrons on the hadron orbit,
- a betas bending to bend beam 180° in RHIC tunnel
- a 40 m-long modulator section,
- a micro-bunching chicane section with strong focusing of the electron beam and three chicanes spaced by 43 m of amplification section
- a hadron delay line which maintains the relative timing between electron beam and proton beam and which provides the required R_{56}. The hadron delay line requires

moving the last (first) dipole magnet closer to the middle of the straight section to achieve the corresponding delay. In addition quadrupole focusing needs to be included to realize the required of $R_{56} = 0.195\,cm$ for the hadron beam.

- a 40 m long kicker section,
- a 240 m beam line with two 180° bends to return the beam to the ERL
- a 800 kW beam dump.

Figure 3.186 shows a schematic view of the Hadron cooler facility.

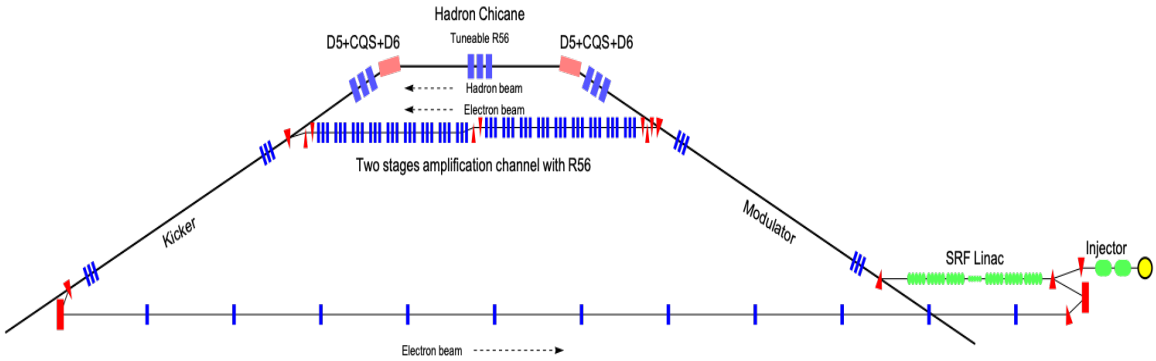

Figure 3.186: Overview of the EIC coherent electron cooling region. The electron beam is accelerated in the ERL and transported to the hadron beam orbit. The cooling section consists of the modulator section, the strongly focused micro-bunching section with three chicanes separated by two plasma amplification stages, and the kicker section. The last magnets of the hadron arc are moved close to center of the straight section. This creates a trapezoidal beam transport for the hadrons. The modulator (kicker) section has an angle of 2.4 (-2.4) degrees with respect to the direction of the straight section. After the modulator section, the electron beam passes through a bend of 2.4° which is integrated into the first bunching chicane and proceeds in parallel to the direction of the straight section. The hadron orbit continues straight-on until it reaches the displaced bending magnet after 20 m. This lengthens the hadron path length by 45 mm that then matches the path length of the electrons. Note that the electron path is lengthened by 45 mm due to the bunching chicanes. Focusing elements in the hadron beam transport in conjunction with the displaced bending magnets generated the desired hadron R_{56}. After the kicker section, the electron beam is transported back to the LINAC to extract its energy before the dump.

3.9.14 Electron Beam Transport

To enable cooling, the electron beam should have small transverse emittance which matches the hadron emittance, a small incoherent energy spread of less than 10^{-4}. The electron distribution function should be smooth in all three directions as any internal structure will be amplified by the plasma amplification mechanism which would not only pre-

vent cooling to happen but instead can induce strong emittance growth. Any energy modulation along the electron bunch is in direct competition with the energy spread induced as part of the cooling mechanism and must be avoided. Sources of energy modulation of the electrons along the bunch include:

- energy modulation due to residuals from bunch compression or RF curvature of the accelerating fields
- wake fields of the ERL accelerating structures or impedance of the vacuum chambers
- coherent synchrotron radiation due to curved central orbit in the beam transport

These effects need to be minimized by careful design of bunch compressors, introduction of higher harmonic RF components of the ERL, strong higher order mode (HOM) suppression in the design of the RF accelerating structures, careful choice of the bending radius in the beam transport to minimize coherent synchrotron radiation effects.

The coherent synchrotron radiation effects have been estimated for a bending radius of 5 m and a bending length compatible with the overall geometrical layout (1.2 m) and for various heights of the electron beam pipe (6–20 mm). The resulting correlated energy modulation of the electron beam along its longitudinal axis is in the order of 10^{-5}. which is not important.

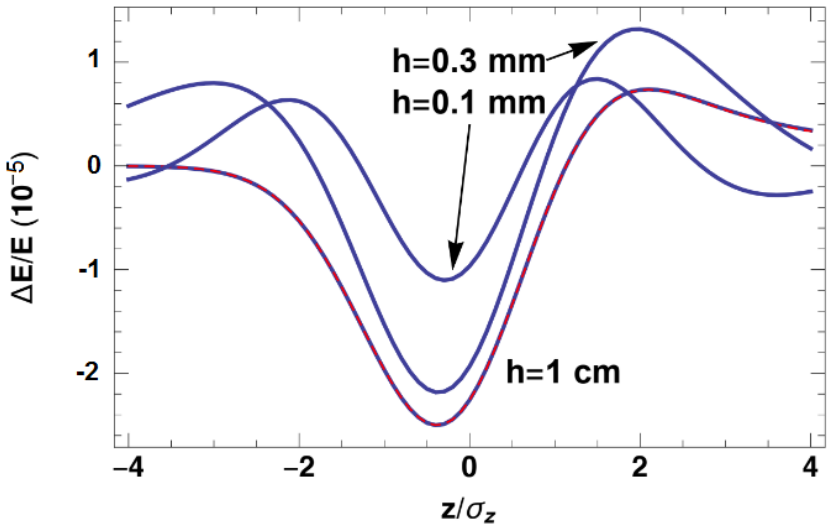

Figure 3.187: Energy modulation of the electron beam along longitudinal coordinate [189] (courtesy G. Stupakov) scaled to the present bending magnet length. The effect is ten time smaller than the tolerance for incoherent energy spread. The parameter h is half the distance of two parallel conducting plates which is taken as a model for the electron beam pipe.

To further mitigate the impact of residual energy spread, energy dependent pathlength variations in the beam transport (R_{56} tunable bending) need to be tunable.

The electron beam transport from the LINAC to the modulator requires a 4.8° bend onto the hadron orbit. The bending is split into two halves and two quadrupole triplets are inserted between the bend to create a 180° betatron phase advance which makes the bend achromatic. A chicane between the two triplets can be adjusted to cancel the total R_{56} of this arrangement. The same scheme is used to bend the electrons from the modulator orbit into the bunching orbit and vice versa from the bunching orbit into the kicker orbit. The chicane is in these cases adjusted to yield the R_{56} required for bunching. Figure 3.188 shows this arrangement. In the present context this scheme is useful as the triplet struc-

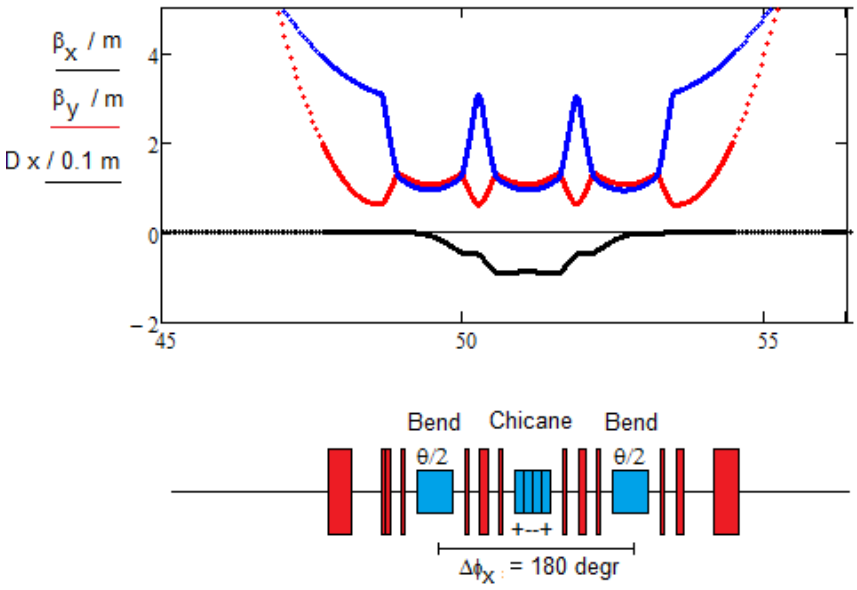

Figure 3.188: Shown is an R_{56}-free bend arrangement with a slit of the bend into two half with a 180° of betatron phase advance in between. In the center is a chicane, the R_{56} of which cancels the one of the two bending magnets. The horizontal axis is path length in [m].

ture is identical to the one used for strong focusing of the micro-bunching channel (see Section 3.9.16 which simplifies the beam optics design of the cooling channel.

3.9.15 Hadron Beam Transport

The hadron part of the cooling channel extends from the second last dipole RHIC D7 in the arc-sextant 4–2 to the corresponding dipole at the end of the straight section. The entire section is 325 m long. It includes the 40 m long modulator and kicker sections. The hadron beam passes through the matching section for the electrons and is exposed to the field of the electron magnets. Their effect is completely negligible and is not taken into account. The orbit geometry ensures that electrons and hadrons have the same path length between modulator and kicker sections.

After the modulator the electrons get bent into the bunching section which is parallel to the straight section. The chicanes lengthen their path length by 45 mm. The hadrons continue after the modulator section on their trajectory for another 30 m before the displaced last bending magnet of the arc bends it in the direction of the straight section as well. The structure has the desired R_{56}^{p}=0.195 mm and lengthens the path of the hadrons by 45 mm. All quadruples except for the 4 doublets are spaced by the nominal half cell in the RHIC arcs. Modular, with the possibility of using existing cryostats. The quads Q7, Q8, and Q9 have independently strengths to tune the beta function of modulator and kicker section to meet cooling all the energies. The straight section is filled with FODO half cell for dispersion and R_{56} tuning. With this design, we will need 4 warm to cold transitions in enter/exit of modulator and kicker section. The hadron beam optics is shown in Figure 3.189. The hadron beam optics has and average dispersion of $\simeq$1.17 m to enable transverse cooling.

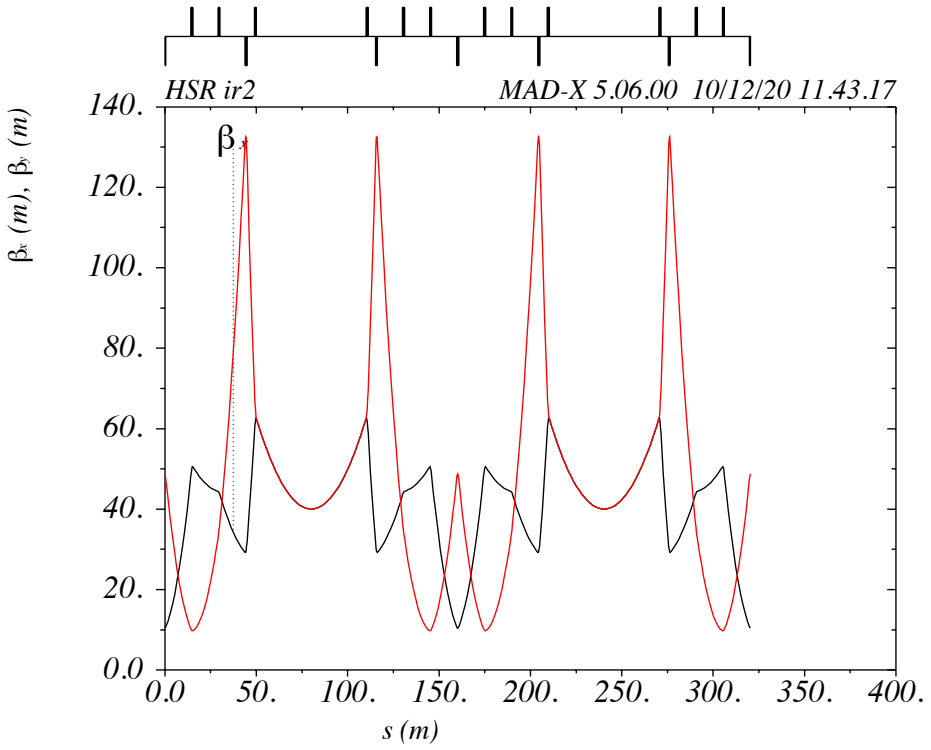

Figure 3.189: Optics of the hadron beam in IR2. The path length of the hadrons matches the path length of the electrons and the lattice has the required R_{56}

.

3.9.16 Cooling Channel Design Considerations

Electron and proton beam sizes should be matched in the modulator and kicker sections. The protons in the modulator cannot be focused because of the presence of the electron beam. For this reason, the proton beam optics in the 40 m long modulator and cooling sections need to be designed with a waist in both planes in the center and quadrupole at both ends. The horizontal β should have a average value of 50 m at the sections respectively. Given the horizontal proton beam emittance of $\varepsilon_{xp} = 11.3$ nm, the horizontal beam size varies between 0.67 mm in the center and 0.8 m at the entrance and exit of the two sections. The electron beam should have the same beta at the beginning of the modulator and cooling sections. To match the beam size, the electron emittance should match the proton emittance. This translates into the requirement of a normalized horizontal electron emittance of ε_{xe}^{N} =3.32 µm.

The vertical emittance of the electron beam is naturally the same as the horizontal. Both the electron and the hadron beam will pass through a dispersive section.

To separate protons which differ in energy by $1 \times \sigma_{ep} = 4.6 \times 10^{-4}$ by a suitable distance of about 2 µm, an R_{56} of $R_{56p} = \sigma_{xp}/(\gamma\sigma_{ep})$ =0.4 cm is required. (note change in nomenclature: $\sigma_{xp} = \Sigma$ and $\sigma_{ep} = \sigma_{\eta p}$ as introduced in the previous sections.)

To shorten the plasma wave length λ_p of the electron beam to reduce the cooling section to a practical length, the electron beam needs to pass first through a focusing section which reduces the β-function from 40 m to 1 m. This can be accomplished by adjusting the triplet behind the modulator section and a $\simeq$7 m long drift space. This small beta needs to be maintained through the entire microbunching section by a quadrupole triplet structure spaced by 1.4 m between the triplets.

The electron beam passes through a suite of three micro-bunching chicanes with an R_{56}^{e} of 0.71 m each. They are spaced by 43 m, optimized by cooling code described in Section 3.9.11 To avoid compromised electron beam micro-bunching in the drift between the last chicane and the cooling section, the electron transverse beam size needs to be re-magnified to its original size by an optical structure which is mirror symmetric to the focusing structure. The kicker section where the micro-bunched beam co-propagates again with the protons needs to follow closely after the third chicane to avoid deterioration of the micro-bunching by plasma oscillations. The kicker section has a length of 40 m. The calculated cooling rate is $\tau_{cool} = 100$ minutes. Figure 3.190 depicts the optical functions for the electron beam in the cooler section.

The distribution of betatron amplitudes and phases in the beam causes a distribution of electron pathlength cooling section between modulator and kicker sections. This causes a widening of the micro-bunched distribution and possibly a reduction in cooling rates. The pathlength distribution of the electrons was evaluated for the electron beam parameters and the beam optics described in this section. The result is $\delta L = 3.7 \times 10^{-7}$ m. This causes only a small reduction of cooling rates in the order of 10%.

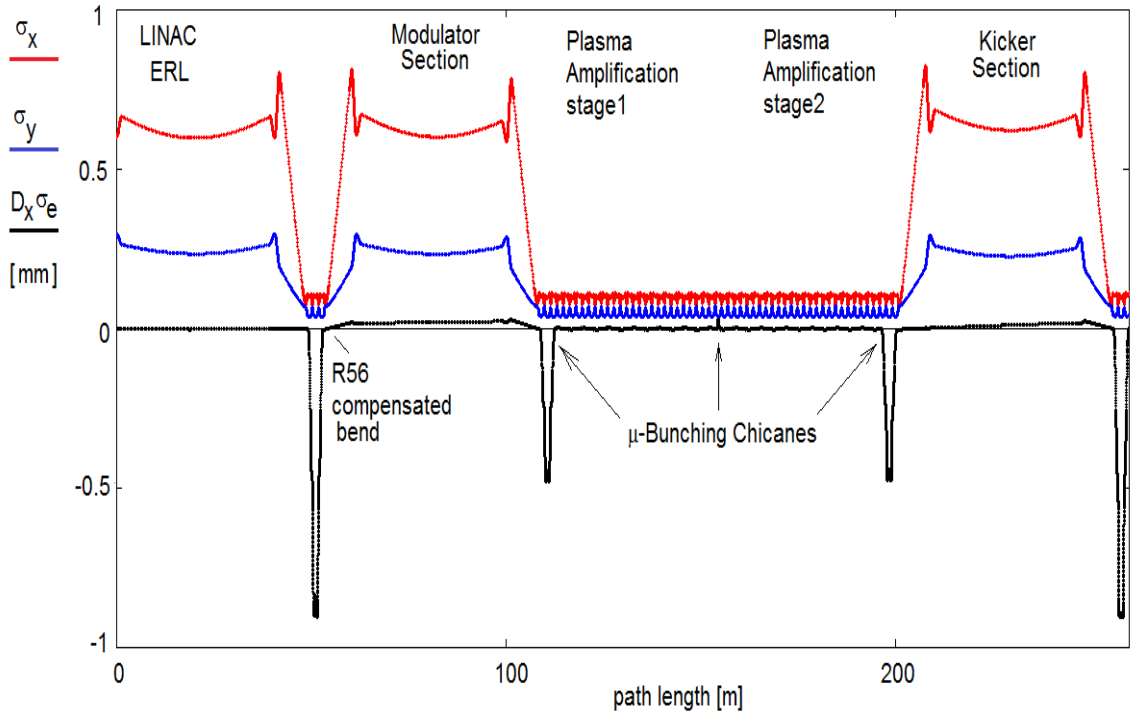

Figure 3.190: Horizontal and vertical electron beam envelopes and dispersion orbit in the cooling facility are plotted along the beam orbit in the ERL, the R_{56}-tunable bend into the hadron orbit, the modulator section, the bunching and plasma amplification section and the kicker section. The return of the beam to the ERL is not shown. In the modulator and kicker sections, the beta functions vary between 40 m and 60 m. In the section with the three micro-bunching chicanes, which are spaced by 47.8 m, the beta functions vary between 1.35 m and 0.64 m.

3.9.17 Coherent Electron Cooling Energy Recovery LINAC Design

(To request the content for this section, please contact the EIC Information Services Group Leader, Alyssa Petrone, apetrone@bnl.gov).

3.9.18 Conclusions on Hadron Cooling

The layout of MBEC for the EIC is at a pre-conceptual stage. Using the present physical model and developed cooling optimization code, MBEC is expected to provide the cooling required to maintain a luminosity of $L = 10^{34}\text{cm}^{-2}\text{s}^{-1}$. No insurmountable problems have been found thus far in the design, though there is much detailed calculation and design work to be done.

Chapter 4

Beam Dynamics

4.1 Beam Dynamics Assessment

The electron ion collider is comprised of state-of-the-art hadron and electron rings. Radiation damping for the electrons allows for a beam-beam parameter of 0.1 while the hadrons will experience a tune shift of 0.015. Feedback noise could lead to collective excitation in the beams and lead to unacceptable emittance growth in the hadrons, so passive stabilization is preferred. We have studied single and multi-bunch impedance driven instabilities in the electron injector, the electron storage ring and the hadron ring. We have studied the ion instability in the electron storage ring. Nominal intensities look achievable.

The dynamic aperture of the electron ring lattice is good. A 60° degree per cell lattice is used for energies of 10 GeV and below. For small betatron amplitude an electron with synchrotron amplitude $|p - p_0|/p_0 = 0.008$ survives. The on momentum dynamic aperture is 20σ in betatron amplitude, and drops to 10σ at $|p - p_0|/p_0 = 0.005$. For 18 GeV we plan on a 90° degree per cell lattice to keep the electron horizontal emittance at 20 nm. This lattice is still under development. For small betatron amplitude an electron with synchrotron amplitude $|p - p_0|/p_0 = 0.006$ survives. The on momentum dynamic aperture is 15σ in betatron amplitude, and drops to 8σ at $|p - p_0|/p_0 = 0.004$.

The beam-beam force has been studied using both weak-strong and strong-strong codes. We have a large crossing angle and have included the effect of finite crab cavity wavelengths. For strong-strong simulations the system is stable and identical to linear crabbing if we have crab cavities at both 197 and 394 MHz. The strong strong simulations are sensitive to collective modes and weak strong simulations are required to study weak chaos and other long term effects. With short bunches, radiation damping, and quantum excitation the electrons are well behaved. The protons require more attention. A dedicated simulation campaign is underway. The main issue seems to be the imperfect crabbing voltage profile, a linear crab voltage is ideal. Even with two harmonics there is some horizontal offset at the IP as a function of the longitudinal coordinate of the proton bunch. This drives synchrobetatron resonances leading to very slow emittance growth. The sophistication of

the simulations is such that the growth times are of the scale of the expected cooling times from strong hadron cooling.

Impedance driven instabilities in the electron storage ring were studied analytically and with simulations. The analytical studies were mainly done to determine which narrow band impedances might be problematic. The most dangerous longitudinal mode was taken from an early version of the RF cavities. We require the most dangerous transverse coupled bunch mode be driven by the resistive wall impedance. The electron beams at 18 GeV are very stable owing to small current and large rigidity. At 10 GeV a bunch charge of 48 nC is stable and 27 nC per bunch is design. At 5 GeV we just make the design intensity of 27 nC per bunch. This is relatively easy to understand in terms of the collisionless damping from the beam-beam force. To double this value a damper with a 20 turn damping time is required. The acceptable noise level in such a damper is of order $0.02\sigma_x$ per bunch measurement at the bunching frequency.

A computer code to estimate ion instability thresholds has been developed. As with the impedance driven case, the ion instability is primarily damped by the beam-beam force. We track both transverse dimensions with different emittances and use the soft Gaussian approximation for both the beam-beam force and the force on the ions. For 10 ns spacing the bunch charge at 10 GeV is 27 nC and there are 1160 bunches. In this case the threshold density of CO is 4×10^{12}molecules/m^3. At 300K this corresponds to a partial pressure of 1.6×10^{-8} Pa $= 1.2 \times 10^{-10}$ Torr.

Impedance driven instabilities in the hadron ring were studied analytically and with simulations. The measured longitudinal broadband (BB) Z/n of the Blue and Yellow RHIC rings are $1.55 \pm 0.15\,\Omega$ and $5.4 \pm 0.7\,\Omega$, respectively [32]. The transverse broadband impedance of the Blue and Yellow rings are 14 ± 5 MΩ/m and 3.2 ± 1 MΩ/m, respectively [31]. The EIC will be using the yellow ring and we took $|Z/n| = 5\,\Omega$ and $|Z_\perp| = 10$ MΩ/m. The narrow band (NB) longitudinal impedance of the RHIC RF system is known. For simulations during store the HOMs in the 197 MHz storage cavities dominate. The most dangerous narrow band transverse impedance is likely due to the new crab cavity system owing to the large beta function. The values we used in the calculations are shown in Table 4.1.

Table 4.1: Impedances assumed for calculations. The narrow band transverse impedance is an initial estimate for twelve 197 MHz crab cavities.

Impedance Type	$R_{\rm sh}$	Q	$f_{\rm res}$
BB longitudinal	640 kΩ	2	5 GHz
BB transverse	10 MΩ/m	2	5 GHz
NB longitudinal	316 kΩ	4400	308 MHz
NB transverse	2.64 MΩ/m	1985	360 MHz

For injection and ramping we assume some combination of collisionless damping and active damping will be sufficient. During store we rely on collisionless damping, especially from beam-beam. An important parameter is the beta function at the crab cavity. For 275 GeV, voltage limitations require $\beta_{crab} = 1300$ m. At 100 GeV we took $\beta_{crab} = 500$ m which is well within voltage limits. The beam is stable at 100 and 275 GeV at nominal intensities. For both these cases the expected growth rate in the absence of damping is comparable to the maximum damping that beam-beam can provide. At 41 GeV, even with $\beta_{crab} = 50$ m, a persistent instability with an e-folding time of 2 seconds remains. This is almost certainly due to the average space charge tune shift of $\Delta Q_{sc} = 0.013$. This value is significantly larger than the half width at base of the tune spread from beam-beam, about 0.004. Hence the coherent tune is shifted outside the incoherent band and any resistive impedance can drive growth. It is assumed that such a slow instability can be actively damped.

Electron clouds have been an issue in RHIC since early on. We coated the 12 cm diameter straight section vacuum chambers with non-evaporable getter to reduce the secondary emission yield (SEY). The 7 cm diameter arc chambers have not been of much trouble but with more bunches we expect both higher cryogenic loads and worse electron clouds. We are developing a beam screen to insert into the arc vacuum chambers. The interior surface of this beam screen will be copper to reduce Joule losses. Calculations show that we need an additional layer of amorphous carbon (aC) to get an acceptable SEY that mitigates electron cloud build-up. An aC coating system is under development to provide a thin film of aC to the interior surface of the beam screen.

4.1.1 Laslett Tune Shift

Next consider the Laslett tune shift in the electron storage ring. The horizontal tune shift is given by

$$\Delta Q_x = \frac{Z_0 I_{\rm avg} q R^2}{2\pi Q_x E_T} \left\{ f_{\rm flat} \frac{\epsilon_1}{h^2} + f_{\rm mag} \frac{\epsilon_2}{g^2} \right\}, \tag{4.1}$$

where $Z_0 = 377\,\Omega$, $I_{\rm avg}$ is the average current, q is the particle charge, R is the machine radius, Q_x is the horizontal tune, E_T is the total particle energy, h is the half vertical aperture of the vacuum chamber, g is the half aperture of the dipole magnets, $f_{\rm flat}$ is the fraction of the ring with a flat vacuum chamber and $f_{\rm mag}$ is the fraction of the ring filled with dipole magnets. For flat chambers the coefficients are $\epsilon_1 \approx \pi^2/48$ and $\epsilon_2 \approx \pi^2/24$. For the vertical tune shift substitute the vertical tune and multiply by -1. We assume the vacuum chamber is flat throughout so $f_{flat} = 1$. The dipole magnets only fill a fraction of the arc so $f_{\rm mag} = 0.40$. For 5 GeV , 10 GeV, and 18 GeV operation the beam current is 2.5 A, 2.5 A, and 0.23 A, respectively. The respective tune shifts are $\Delta Q_x = 0.29$, 0.15, and 0.0074. These tune shifts are due to smoothly distributed focusing and can be easily corrected with the quadrupole magnets. It will be necessary to adjust the quadrupoles as bunches are injected. The one second interval between injections is long compared to the few millisecond eddy current penetration time.

4.1.2 Impedance Budget of the ESR

Instabilities have been a concern for the EIC project from the beginning. One of the most challenging tasks is to accumulate the average bunch current of $I_{av} = 2.5\,\text{mA}$ within $M = 1160$ bunches in the electron storage ring. Beam-induced heating, single-bunch instabilities (Broad-band impedance), coupled-bunch instabilities (Narrow-band impedance) and ion instabilities are the main focus in the vacuum sub-system design. The beam-induced heating is estimated for each individual component and it includes the power loss calculations and the heat transfer analysis. Some of the components will require the water cooling or challenges in their design. R&D projects are expected for some of the key components including bellows, interaction region (IR) chamber, collimation system, and etc.. Currently we have rough design of the main vacuum components. As the first step we use the geometric impedances of the vacuum chamber components simulated for NSLS-II and SuperKEKB. The impedance budged will be updated next with more impedance data available for the optimized EIC vacuum components. It will allows us to keep track on the collective effects changes with more realistic components added to the ring.

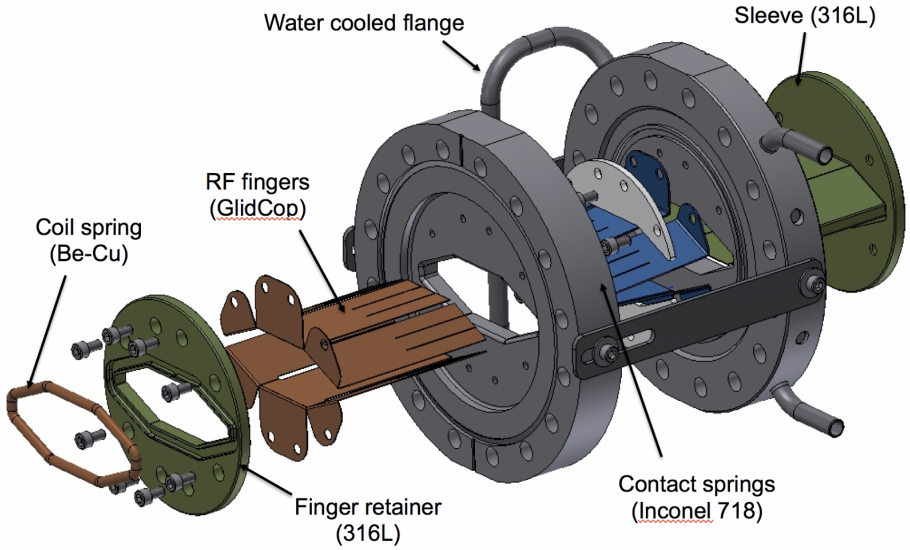

Figure 4.1: Design of NSLS-II bellows (blw) with removed bellows convolutions.

In Figure 4.1 and Figure 4.2, we present the design of the NSLS-II bellows and flange absorber, since their contribution to the total wakefield of the electron storage ring is significant with their estimated numbers of 380 bellows and 200 flange absorbers respectively. The design of the crab cavity used for the wakefield analysis is shown in Figure 4.3. The crab cavity contribution to the single-bunch effect is moderate. The most important thing, we need to address in this design, is the HOM mode generation (the narrow-band impedance) and their effect on the coupled-bunch instability. Since the collimation system for the EIC project is under development, the SuperKEKB design of the ramp geometry has been analyzed and included in to the total wakefield with the total number of ramps

to 16. The geometric impedance due to cross-section changes in the vacuum components has been calculated by the GdfidL code [110] as well as CST and ECHO. With more updates in the geometries and their optimization from an impedance point of view for the EIC project, the NSLS-II wakefield/impedance will be replaced individually and those new wakefields/impedances will be used to generate the total impedance budget for particle tracking simulations and for theoretical analysis. The resistive wall impedance and its contribution to the total impedance is calculated separately by applying the analytical approach derived by Bane and Sands [111] for L =3018 m of Cu with a 20 mm beam pipe radius.

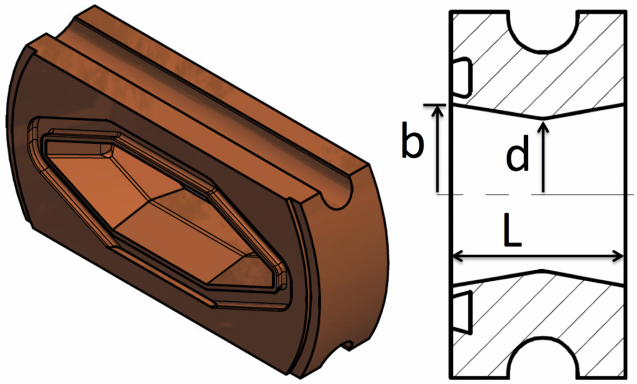

Figure 4.2: 3D rendered image of the NSLS-II flange absorber (abs).

The longitudinal wakefield times the number of components is presented in Figure 4.5 including: 380 bellows (blw), 494 beam position monitors (bpm), 45 gate valves (gv), 18 striplines (strl), 23 main cavities (cav), 200 flange absorbers (abs), 2 crab cavities (crabcav), 16 ramp collimators (ramp). The contributors to the geometric wakefield in order of size are the flange absorbers, bellows, ramp collimators, striplines, beam position monitors and etc. The total longitudinal wakefield (blue trace) as a sum of the short-range geometric (or-

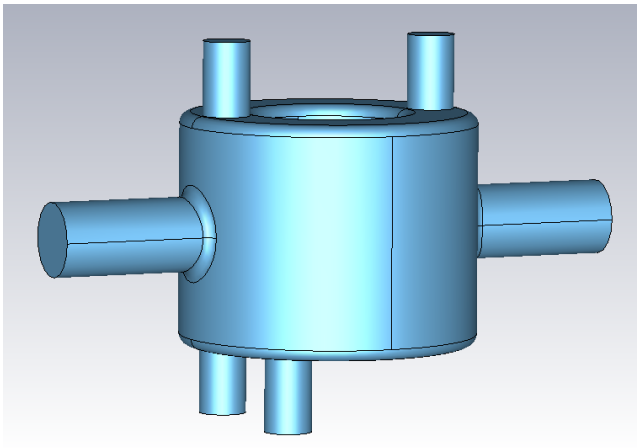

Figure 4.3: Preliminary design of the EIC crab cavity used for the wakefield analysis.

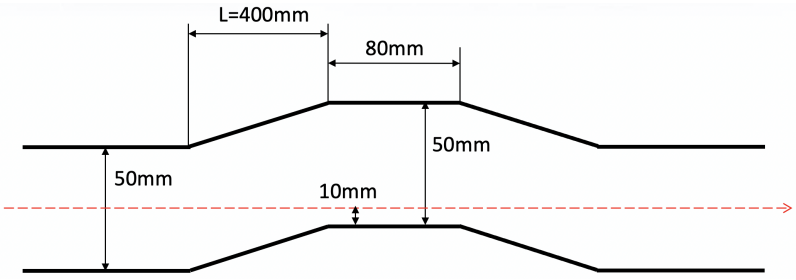

Figure 4.4: SuperKEKB-based collimator design with a taper length of 400 mm.

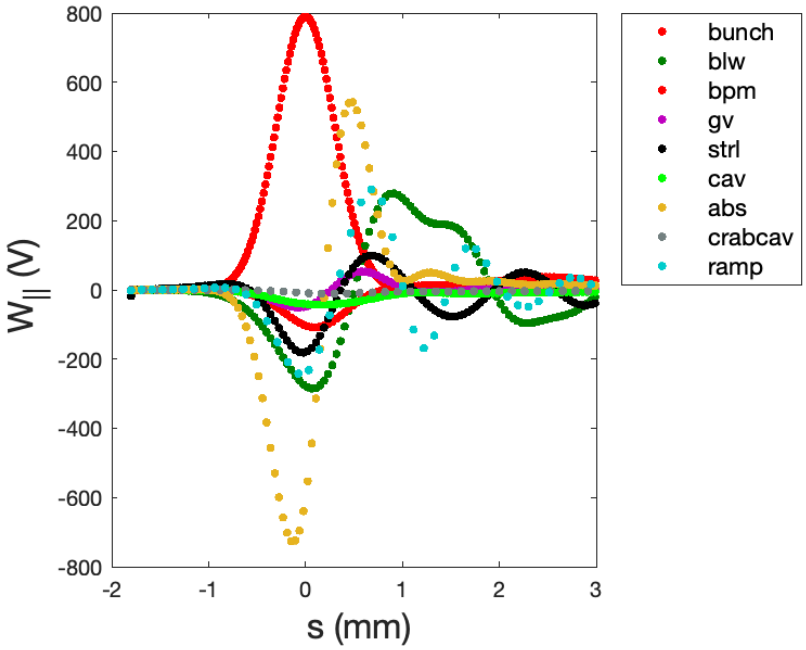

Figure 4.5: The longitudinal short-range wakefields numerically simulated for a 0.3 mm bunch length for each individual vacuum component.

ange trace) and resistive-wall (green trace) longitudinal wakefields is shown in Figure 4.6.

To study the vertical beam dynamics, the vertical dipole wakefield (W_{yD}) has been numerically calculated for a 2 mm bunch length. The wakefields times the number of components are presented in Figure 4.7. The main contributors to the short-range W_{yD} are the flange absorbers, bellows and beam position monitors. The total vertical dipole wakefield is presented in Figure 4.8 as a sum of the resistive wall contribution (rw) and the geometric wakefields (gm).

It should be noted here, due to operation at three different energies, 5 GeV, 10 GeV and 18 GeV, impedance needs to be calculated for each displaced trajectory for the vacuum components, those are predominantly located in the arcs of the storage ring.

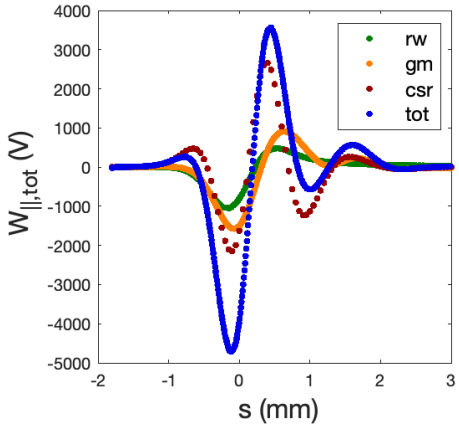

Figure 4.6: The total longitudinal wakefield for the EIC electron storage ring (blue) as a sum of the resistive wall contribution (green) calculated analytically, the geometric wakefields (orange) and the coherent synchrotron radiation (dark wine).

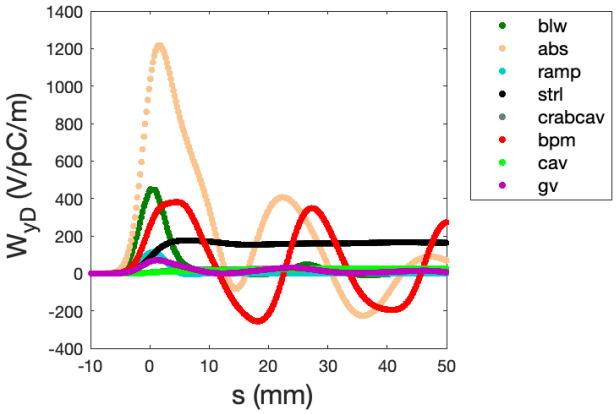

Figure 4.7: The vertical dipole short-range wakefield numerically simulated for a 2 mm bunch length.

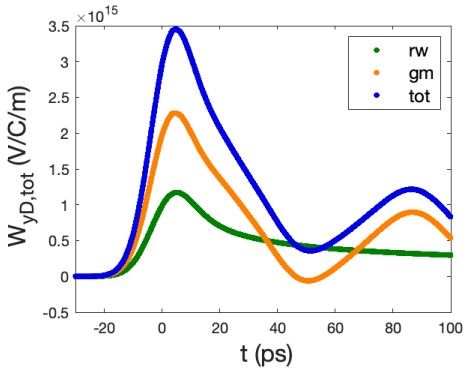

Figure 4.8: The total dipole short-range wakefield for the EIC electron storage ring (blue) as a sum of the resistive wall contribution (green) calculated analytically and the geometric wakefields (orange).

4.2 Collective Effects

4.2.1 Collective Effects in Electron Storage Ring

We have considered coherent instabilities, intrabeam scattering, and Touschek scattering. Intrabeam scattering times in the electron storage ring are of order minutes, much longer than the 100 ms radiation damping times. Touschek lifetimes are hours, much longer than the bunch replacement time based on polarization loss. Coherent instabilities in the electron ring have been studied using a modified version of TRANFT [29], which was used during the design of NSLS-II and evolved into the stochastic cooling simulation code. The code has evolved to simulate both single bunch and coupled bunch instabilities, by tracking typically 5 bunches and assuming a uniform fill. This allows one to use a few times 10^5 simulation particles per bunch when doing coupled bunch calculations. The code tracks all three dimensions. When beam-beam is used both transverse dimensions are subjected to the beam-beam force. The longitudinal and one transverse dimension are subjected to wakefields. There is no betatron coupling.

For coupled bunch calculations the frequencies of HOMs were adjusted slightly so they were driven resonantly by a mode allowed in the simulation. We track $M = 5$ adjacent bunches and assume a uniform fill of $N_{\rm fill}$ bunches. For longitudinal modes this means the resonant frequencies were of the form $f_{\rm res} = f_{\rm rev} N_{\rm fill}(k + p/M)$, where f_{rev} is revolution frequency and, k and p are integers with $0 < p < M$. For rigid Gaussian bunches with no synchrotron tune spread and an impedance spectrum that is not too narrow, the coherent tune shift is given by

$$\Delta\Omega = i\frac{\bar{I}|\eta|}{4\pi Q_s E_T/q}\sum_{m=-\infty}^{\infty}\omega_m Z_\parallel(\omega_m)\exp(-\sigma_t^2\omega_m^2), \tag{4.2}$$

where $\omega_m = \omega_0(mN_{fill} + s)$ with $s \neq 0$ the coupled bunch mode number, σ_t is the rms bunch duration, $\bar{I}$ is the average current, η is the frequency slip factor, $Z_\parallel(\omega)$ is the longitudinal impedance, Q_s is the synchrotron tune, E_T is the total particle energy and q is its charge. Here and throughout we use the circuit definitions for impedances. For $s = 0$ it is important to evaluate the impedance at the exact coherent frequency, including the impact of the coherent synchrotron frequency. See equation (4.4) and adjacent material.

For transverse modes the frequencies were of the form $f_{\rm rev}(kN_{\rm fill} + s - Q_x)$ with $0 \leq s < N_{\rm fill}$ the coupled bunch mode number. The rest of the ring was assumed to be filled with batches of bunches like the M tracked ones but with a betatron phase shift of $\Delta\psi_x = 2\pi(s - Q_x)M/N_{\rm fill}$ applied between successive batches. For rigid Gaussian bunches the frequency shifts are given by

$$\Delta\Omega = \frac{i\bar{I}c}{2CE_T/q}\beta_y\sum_{m=-\infty}^{\infty}Z_y(\omega_m - \omega_\beta)\exp(-\sigma_t^2(\omega_m - \omega_\beta)^2) \tag{4.3}$$

where $Z_y(\omega)$ is the vertical shunt impedance, ω_β is the unperturbed betatron frequency, β_y is the vertical beta function at the location of the impedance, and C is the machine

circumference. For several sources of impedance the beta functions at the various locations needs to be included. For transverse instabilities $s = 0$ is no problem. The code was tested and growth rates for bunches with small Landau damping agree with the formulas within a percent.

Before proceeding to the coupled bunch calculations we consider the single bunch thresholds. Simulations for 10 GeV bunches with radiation damping and no other sources of Landau damping are shown in Figure 4.9. The longitudinal single bunch threshold occurs first. The green curve labeled "IPAC18" corresponds to the threshold using the partial wakefield available then. It did not include CSR wakes or the wakes due to the sort of collimator shown in Figure 4.4. The IPAC18 results did not include transverse wakes. The purple curve in Figure 4.9 includes all these effects and uses four times as many macro particles per bunch.The increased number of particles gives cleaner results. The threshold current of 8 mA is 3 times nominal. At 5 GeV and 18 GeV single bunches are stable for nominal parameters.

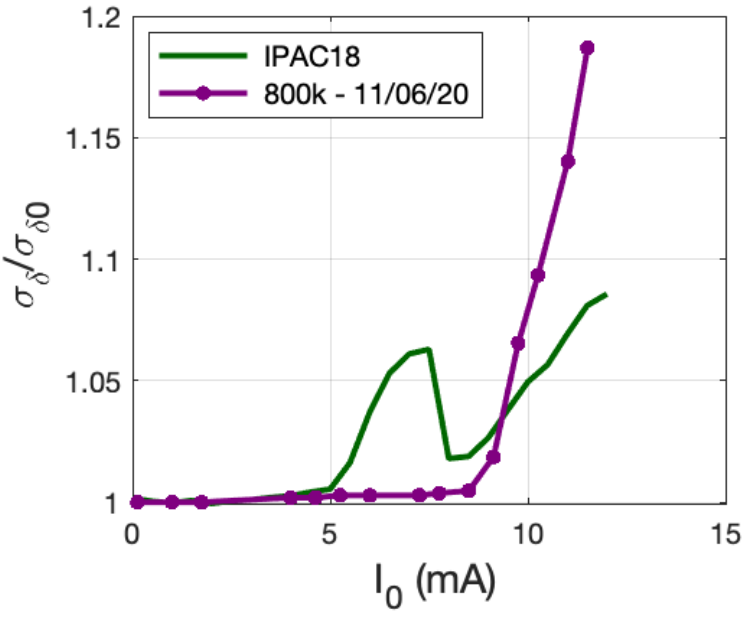

Figure 4.9: The normalized energy spread as a function of single-bunch current.

The electron storage ring vacuum chamber is made out of copper with a resistivity of $\rho_e = 1.7 \times 10^{-8}$ Ωm. The cross section is elliptical with half vertical aperture $b = 18$ mm and half horizontal aperture $a = 40$ mm. The low frequency approximations in [195] are used to obtain the vertical resistive wall impedance.

$$Z_y(\omega) = f(a,b)[i + \mathrm{sgn}(\omega)]\frac{C}{2\pi b^3}\left(\frac{2\rho_e Z_0}{|\omega|/c}\right)^{1/2},$$

where $f(a,b) = 0.8$ for our chamber aspect ratio, and $Z_0 = 377\,\Omega$. The operating point for the electron storage ring is likely below 0.5 but to be safe we assume it will be no larger than 0.6. Therefore, the real part of the sum in equation (4.3) is never larger than $12.2 \times 10^6\,\Omega/\mathrm{m}$.

For the narrow band longitudinal impedance we take a somewhat pessimistic estimate from an early version of the RF system. We take a resonator with shunt impedance $R_{\mathrm{sh}} = 23.6\ \mathrm{k}\Omega$, quality factor $Q = 70$, and resonant frequency 1.1 GHz. The resistive wall impedance described above is difficult to handle numerically. Fortunately, the transverse wake from the resistive wall varies as $t^{-1/2}$. The bunch spacing is large compared to the bunch length so, when considering kicks of a given bunch on all following bunches, we are free to substitute any slowly varying wake field for the resistive wall. We modeled the long range wake as due to a transverse wakefield of the form $W_\perp(t) = W_0 \exp(-\alpha t)$. This form of the wakefield allows us to use phasor type updates which are numerically efficient. Setting $W_0 = 60\ \mathrm{V/pC}$ and $\alpha = 2.45 \times 10^6\ \mathrm{s}^{-1}$ yields $\mathrm{Re}(Z_y) = \mathrm{Im}(Z_y) = 12.2\ \mathrm{M}\Omega/\mathrm{m}$ at $f = 5 f_{\mathrm{rev}}$. Since the resonant frequency and bandwidth of the impedance are much smaller than the inverse of the electron bunch length the model impedance behaves exactly like the resistive wall impedance except with a different coupled bunch mode number. Within a single bunch we use the actual resistive wall wake so the real part of the tune shift is accurate.

We have done simulations for 5, 10 and 18 GeV and results are summarized in Table 4.2. The beam-beam tune spread was sufficient to damp transverse coupled bunch modes and a longitudinal damper with $\mathrm{Im}(Q_s) = 1 \times 10^{-3}$ damped the coupled bunch longitudinal oscillations. Studies have shown that damping this level of oscillation will produce no ill effects [30] The beam beam parameter was set to 0.1 though smaller values worked above 5 GeV. At 10 and 18 GeV we are safe, 5 GeV has no head room.

Table 4.2: Stable electron beam parameters. A uniform fill was assumed for coupled bunch effects. For 5 and 10 GeV the narrow band impedance was $Z_y = 12.2 \times 10^6 \Omega/\mathrm{m}$ while it was $Z_y = 24.5 \times 10^6 \Omega/\mathrm{m}$ for 18 GeV.

Parameter	5 GeV	10 GeV	18 GeV
RF voltage ($h = 7560$)[MV]	12	24	68
N_{fill}	1260	1260	315
γ_T	31	31	39
V_{synch} [MV]	1.3	3.3	38
$\sigma(p)/p$ [10^{-4}]	6.8	5.5	10.
σ_s [mm]	9.6	7.5	8.7
$N_{e,max}$ [10^{10}]	16	30	12
$t_{rad,y}$[ms]	100	100	17

In Table 4.2 the transverse impedance driving the 18 GeV coupled bunch mode was $24.5 \times 10^6 \Omega/\mathrm{m}$, twice the value at 5 and 10 GeV. This is to take into account the possibility that other sources of impedance may dominate. In particular, the crab cavities create a longitudinally varying orbit offset at the IP. This offset as a function of longitudinal position within the bunch varies as

$$x(s) = \sin(k_{crab}s) q V_{crab} \sqrt{\beta_{x,crab}\beta_{x,IP}}/E_T$$

where $s = 0$ is the bunch center, k_{crab} is the RF wavenumber, $\beta_{x,crab}$, $\beta_{x,IP}$ are the horizontal beta functions at the crab cavity and IP. All energies need to satisfy the same $x(s)$. For $E_t/q = 18$ GV the limitations on crab voltage require $\beta_{x,crab} = 150$ m. For lower energies it is possible to obtain larger values of qV_{crab}/E_T. If adequate optics with lower values of $\beta_{x,crab}$ can be found, the tune shifts that need to be damped will be proportionally lower.

The concern over maintaining collisionless damping is not academic. The beam-beam tune spread is a very powerful damping mechanism. At 5 GeV, in the absence of damping, the instability e-folding time is 22 turns. Any damping system would need to produce a damping rate of this order to significantly improve operations during store. Consider a very simple model:

$$z_{n+1} = e^{i\psi}\left(z_n - \frac{z_n + \epsilon_n}{D}\right)$$

where $z_n = x_n - ip_n$ is the complex coordinate, ψ is the phase advance per turn, ϵ_n is noise and D is the damping time in turns. Taking the absolute value square and expectation values with $D >> 1$ gives $< |z|^2 >=< \epsilon^2 > /2D$. Consider damping one mode with M bunches. Let the error per individual measurement be $P\sigma$. Then $< \epsilon^2 >^{1/2} \approx P\sigma/\sqrt{M}$ and finally

$$< |z|^2 >^{1/2} = \frac{P\sigma}{\sqrt{2DM}}.$$

We have M=1260 bunches and D=22. The allowed rms orbit motion for white noise oscillations of the electron bunch is of order $10^{-4}\sigma$. Taken together this gives $P \approx 0.023$ Taking a vertical emittance of 2n m and a beta function of 20 m yields an absolute measurement error of 5 µm. Note that this 5 micron error is at a bunch by bunch rate, not averaged in any way. Remember, this corresponds to damping during collisions. When the ion beam is not present, as during beam scrubbing, more noise can be tolerated in the damping system.

Fast Ion Instability

The fast beam-ion instability is a multi-bunch transverse instability driven by the electromagnetic interaction between the electron beam and partially stripped ions [196–201]. A key feature of the instability is that gaps in the bunch train reduce the number of ions surviving to cause the instability [202]. We have written a simulation code to study this process. Since the beam-beam force is the primary source of collisionless damping it was necessary to use $\gtrsim 10^4$ electron macro-particles per bunch. The β-functions vary

around the machine which causes the principle axes of the electron ellipse to vary and with them the ion frequency distributions. As a start we took 40 slices around the ring with $(\beta_x, \beta_y) = (27.4\text{ m}, 9.4\text{ m})$ in the first slice and $(\beta_x, \beta_y) = (9.4\text{ m}, 27.4\text{ m})$ in the last slice with smooth variations in-between. Within each slice we typically create between 2 and 10 ion macro-particles during each electron bunch passage. To do this we calculate the rms horizontal and vertical size of the passing electron bunch and assume a Gaussian profile. An ion macro-particle is created at coordinates (x, y) according to the two dimensional Gaussian and another is generated at $(-x, -y)$ to account for the fact that the actual number of ions generated would be huge and the central limit theorem would lead to virtually no net offset. All ions present are kicked by the Gaussian electron bunch using the Bassetti-Erskine formula and the total momentum kick on the ion cloud is obtained. Each electron macro-particle in the passing bunch gets the same kick chosen so momentum is conserved. The ions drift until the next bunch arrives and are removed if they pass beyond a prescribed aperture. After all the electron bunches pass through a given ion cloud slice the simulation propagates to the next ion cloud slice and the process repeats. The beam-beam force is updated using a single Bassetti-Erskine kick once per turn. For now we assume a single species of ion and for given beam parameters find the maximum density that ion may have. We have focused on 5 and 10 GeV with carbon monoxide (CO). Table 4.3 summarizes our results. The maximum densities of CO for stable beams are given. In all cases we assumed a beam pipe radius of 2 cm and an ionization cross section of $2 \times 10^{-22}\text{m}^2$. Figure 4.10 shows every 100th bunch as it passes a fixed location in the lattice for the 10 GeV case with 1160 bunches.

Table 4.3: Beam ion instability thresholds.

Parameter	5 GeV	10 GeV	10 GeV
RF voltage ($h = 7560$) [MV]	12	24	24
$\sigma(p)/p$ [10^{-4}]	6.4	6.4	5.5
N_e [10^{10}]	34	34	17
N_{sym}	630	630	1260
N_{bunch}	567	599	1160
$N_{CO}[10^{12}/\text{m}^3]$	5.	10	4
ϵ_x, ϵ_y [nm]	20, 4.9	20, 4.9	20, 1.3

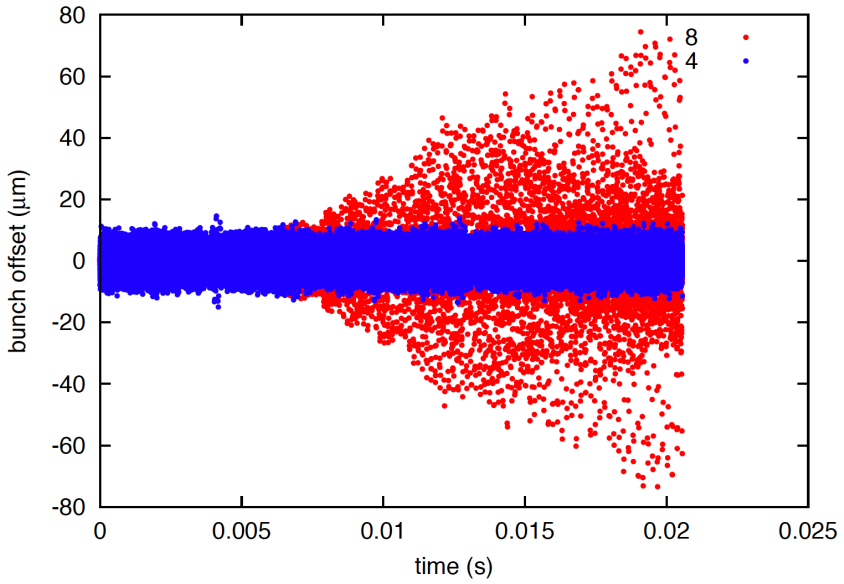

Figure 4.10: Vertical electron bunch offset at a fixed location in the ring for gas densities of 8×10^{12} CO/m^3 (equivalent to 0.249 nTorr, as shown in red) and 4×10^{12} CO/m^3 (equivalent to 0.124 nTorr, as shown in blue). This illustrates the 10 GeV case with 1160 bunches. 10% of the points are shown but this has no impact on the envelopes.

Working Point of the RF System in the Electron Storage Ring

One of the challenges we are facing in the electron storage ring is heavy beam loading. This is especially true in the 5 GeV and 10 GeV scenario where the DC current reaches 1.9 A and 2.5 A, respectively. The required detuning of the fundamental RF cavity is so large that the growth rate of the μ=-1 coupled bunch dipole mode exceeds the radiation damping rate and the beam becomes unstable. In order to reduce the detuning we take advantage of the fact that the fundamental cavity can provide higher voltage than needed when the machine is working under the heavy beam loading scenario. By using this Reversed Phasing method [37] we can detune the fundamental cavities in opposite ways so they all provide acceleration whereas part of the cavities provide focusing voltage and the rest of the cavities provide defocusing voltage. This allows us to maintain the same power per cavity and the bucket height while reducing the detuning of individual cavities. This keeps the impedance peaks near the RF line thereby reducing transient beam loading.

The search for the optimal condition was done in two steps. We first select a zone in the parameter space. Then for the uniformly filled beam, we used the formula (4.4) [203] to calculate the imaginary part of the coherent oscillation frequency of the dangerous modes and search for the point that gives us the best working margin. In the formula, $\Omega_{l,\mu}$ is the complex coherent frequency of the coupled bunch mode; ω_s is the incoherent synchrotron oscillation angular frequency; q_e is the elementary charge of electron; I_{av} is the average current of the beam; $(l, \mu)$are mode indices, l= 1,2,3,... and μ = 0,1,2,...,M-1; M is the

number of bunches; ω_0 is the revolution angular frequency; η is the phase slip factor; $Z_0^{\parallel}(\omega)$ is the total impedance of the resonators; $\sigma_\phi = \omega_0 \sigma_t$ is the rms bunch length in units of revolution phase.

After narrowing down the working point, we run time domain particle tracking simulations. The time domain simulation allows us to include the effect of the abort gap and it supplies other critical information such as the bunch phase slip and transient behavior of the reflected power. The working conditions of the fundamental RF system are listed in Table 4.4. For the 5 GeV case we used the combination of 12 focusing cavities and 6 defocusing cavities (12F6D). The $\mu = 0$ mode was stable and the individual cavity voltage high enough so radiative damping was sufficient to stabilize the $\mu = \pm 1$ mode. For the 10 GeV case we used 13 focusing cavities and 5 defocusing cavities (13F5D). For this case the $\mu = 0$ mode was stable as well and radiative damping was sufficient to stabilize the $\mu = \pm 1$ mode. For 18 GeV all the cavities are in phase. We slightly overtuned the cavity, adding 5 degrees of loading angle, to stabilize both the $\mu = 0$ and $\mu = \pm 1$ modes.

$$\Omega_{l,\mu}^2 - (l\omega_s)^2 - i\frac{1}{\pi} q_e I_{av} \frac{\eta \omega_0^{3-2l} l}{\beta^2 E_0 (l-1)! 2^l} \sigma_\phi^{2l-2} \times \sum_{p=-\infty}^{\infty} [(pM+\mu)\omega_0 + \Omega_{l,\mu}]^{2l-1} Z_0^{\parallel}((pM+\mu)\omega_0 + \Omega_{l,\mu}) e^{-(pM+\mu)^2\sigma_\phi^2} = 0 \tag{4.4}$$

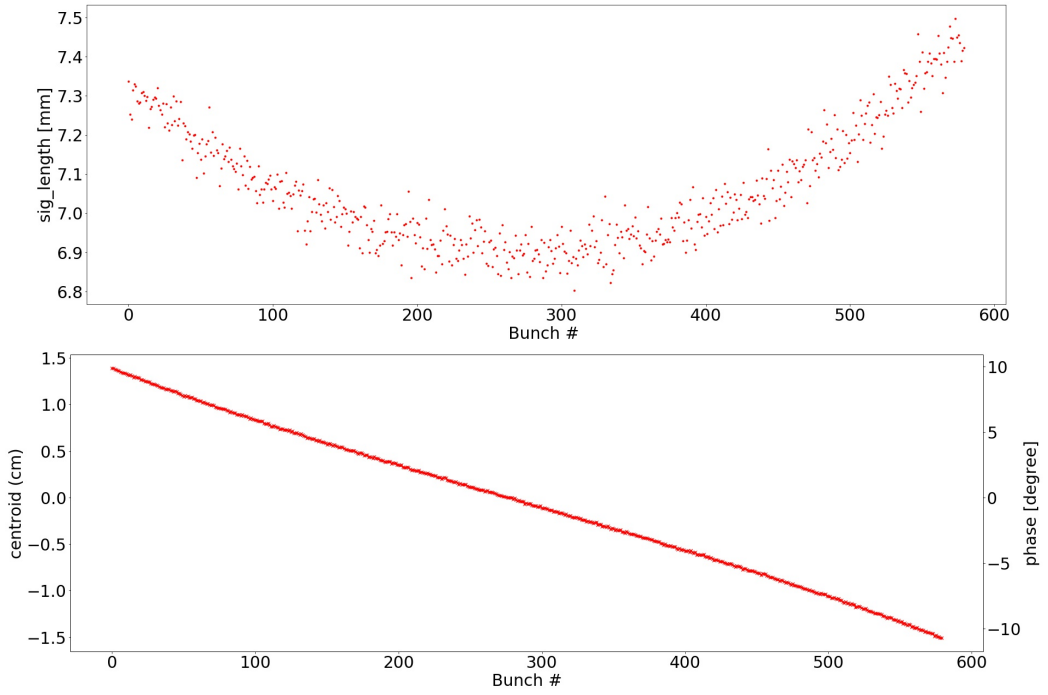

Figure 4.11: The bunch length distribution and phase slip along the train for 5 GeV scenario.

Table 4.4: RF parameters for the fundamental RF system in EIC ESR.

Parameters	5 GeV	10 GeV	18 GeV
RF harmonic number	7560	7560	7560
Frequency [MHz]	591	591	591
Number of focusing	12	13	18
Number of defocusing	6	5	0
Number of bunch	580	580	580
Cavity RoQ /cav, circuit [Ω]	37	37	37
Loading angle (focusing)	6°	5°	5°
Loading angle (deFocusing)	6°	-5°	
Beam power	2.50	9.72	10
Total synchronous voltage [MV]	1.316	2.888	37.037
Total quadrature voltage [MV]	14.596	29.191	50.236
Synchronous voltage (focusing) /cav [MV]	0.073	0.216	2.057
Quadrature voltage (focusing) /cav [MV]	2.433	3.649	2.791
Total voltage (focusing) /cav [MV]	2.434	3.655	3.467
Synchronous phase (focusing)	178.3°	176.6°	143.6°
QL (focusing)	576290	334364	292449
Detune frequency (focusing) [Hz]	-17176	-14934	-1547
Synchronous voltage (defocusing) /cav [MV]	0.073	0.216	
Quadrature voltage (defocusing) /cav [MV]	-2.433	-3.649	
Total voltage(defocusing) /cav [MV]	2.434	3.655	
Synchronous phase (defocusing)	1.7°	3.4°	
QL (defocusing)	576290	334363	
Detune frequency (defocusing) [Hz]	16960	14934	

The bunch length and phase slip of the bunches along the train are shown in Figures 4.11, 4.12 and 4.13. Due to the heavier beam loading, the 5 GeV case has the largest phase slip which gives a $\pm$1.5 cm shift of bunch centroids along the train. Assuming negligible hadron transient, this corresponds to a $\pm$0.75 cm shift of the collision point in the detector.

These detailed simulations were performed before reducing the number of RF cavities from 18 to 17. It is likely that such a small change will not destabilize things. Additionally, the simulations employed no RF feedback or low level RF control. When these are included the system stability will improve.

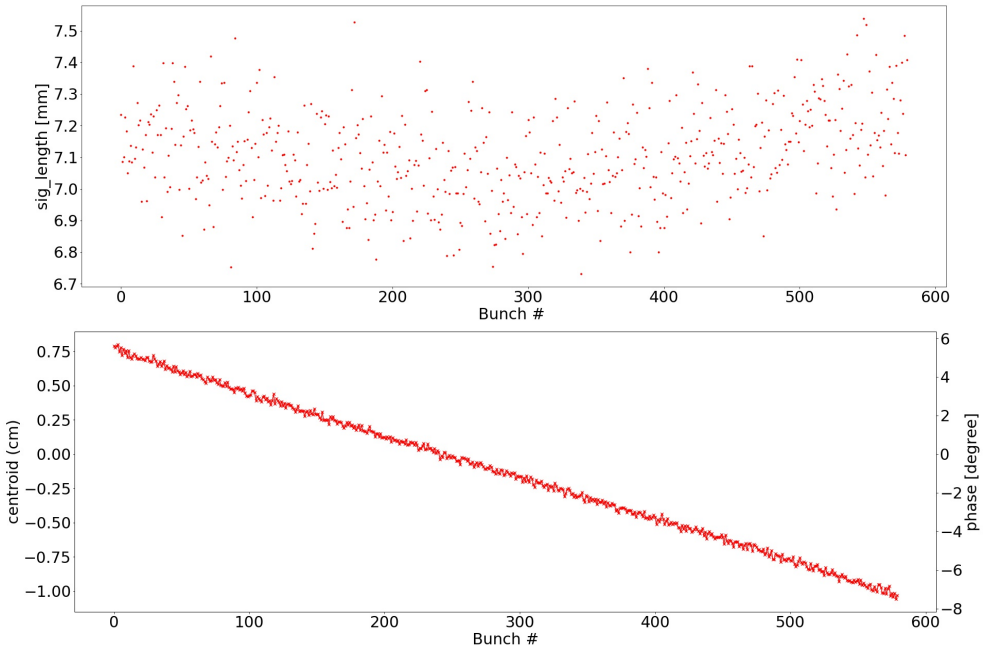

Figure 4.12: The bunch length distribution and phase slip along the train for 10 GeV scenario.

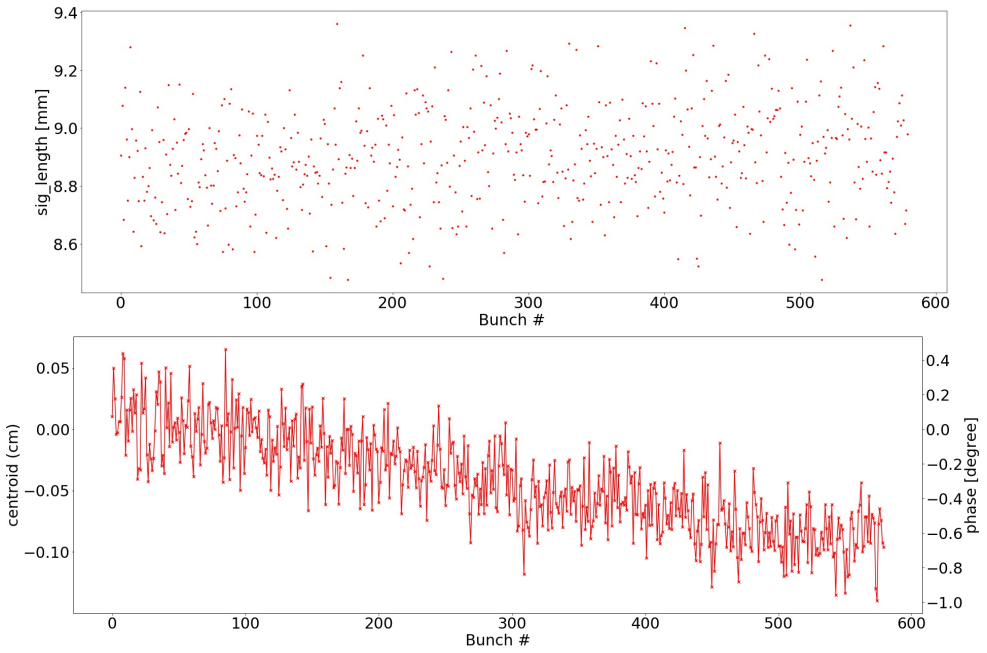

Figure 4.13: The bunch length distribution and phase slip along the train for 18 GeV scenario.

4.2.2 Collective Effects in RCS

A modified version of TRANFT [29] was used to simulate coherent instabilities while ramping a single bunch in the rapid cycling synchrotron (RCS) from 400 MeV to 18 GeV. Simulations incorporated both long and short range wake-fields although only broad band impedances had an impact on beam dynamics. Table 4.6 contains relevant injection and ramp parameters. This work has shown that given a fixed dp/p RMS of 2.5×10^{-3} given by the RCS dynamic aperture, a 28 nC bunch will be unstable against collective effects for bunch lengths less than 120 ps which is the limit at which effective acceleration becomes feasible. These results are also confirmed using the approximate formulas for the microwave instability thresholds less than $Z/n > 0.1\,\Omega$.

As a result we will instead of injecting two 28 nC bunch, inject two by four 7 nC bunches and merge them at 1 GeV to achieve two 28 nC bunches. The 7 nC injected bunches will have a length of 40 ps and dp/p =2.5×10^{-3} RMS. With these parameters we should be well above the microwave instability threshold at 400 MeV. Accelerating to 1 GeV while maintaining a bunch energy deviation of 0.25% and squeezing the bunch length to 16 ps should preserver the longitudinal emittance, keeping the bunches above the microwave instability threshold.

At 1 GeV the bunches will be merged to form two 28 nC bunches. Merge simulation including collective and radiative effects yield a growth of 42% with a final $\sigma_t\sigma_E$ emittance of 2.27×10^{-4} eV-s from the individual 4×10^{-5} eV-s. The bunch, instability and RF values are shown in Table 4.5.

Table 4.5: Bunch, RF and instability values from injection through merge at 1 GeV.

Parameters	Injection	Before merge 1 GeV	After merge 1 GeV
Bunch charge [10^{-9}]	7.0	7.0	28.0
dp/p [10^{-3}]	2.5	2.5	2.5
τ [ps]	40	16.0	90.9
Long. emit. [10^{-5} eV-s]	4.0	4.0	22.7
Peak RF voltage [MV]	3.3426	39.2	3.05
Qs	0.0594	0.1400	0.0345
Z/n threshold	0.138	0.207	0.149

Simulations were also done for a 10 nC range of broad band impedances to investigate the single bunch's longitudinal emittance while ramping from 400 MeV to 18 GeV. Both the longitudinal and transverse dimensions were tracked with the code, where the latter remained well behaved throughout. Along with broad band impedances; narrow band impedances, the short range resistive wall, radiation damping, quantum excitation, and space charge were included. Figure 4.14 shows the longitudinal emittance over the entire

ramp for various broad band impedances defined by $|\frac{Z}{n}|$ in $[\Omega]$. Figure 4.15 shows the $|\frac{Z}{n}| = 0.1[\Omega]$ case and the corresponding RF voltage in [MV].

Table 4.6: RCS parameters used for ramp instability simulations.

Parameter	Value
Injection Energy [MeV]	400
Electrons per Bunch	4.36906×10^{10}
RF Voltage at Injection (h=7200) [MV]	6
RMS beam radius at injection [mm]	1
$\sigma_E\sigma_t$ at Injection [eV-s]	4×10^{-5}
f_{res}[GHz]	20
Q	2
Electrical resistivity ρ [Ωm]	7×10^{-8}
Final energy at ramp-end [GeV]	18
Acceleration time [ms (turns)]	100 (8000)
Peak RF voltage (h=7200) [MV]	62

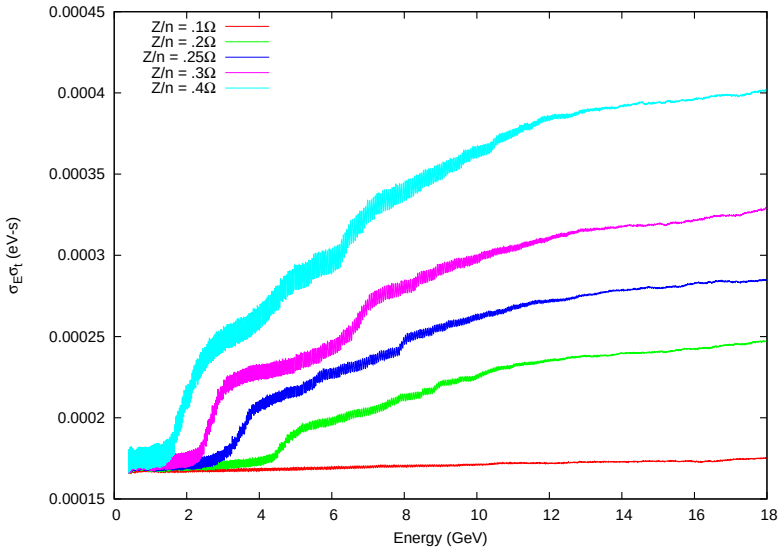

Figure 4.14: Longitudinal emittance growth on the ramp from 400 MeV to 18 GeV in 100 ms. Increasing the broad band impedance increases the emittance growth, but it is still under the required thresholds for the simulated impedances.

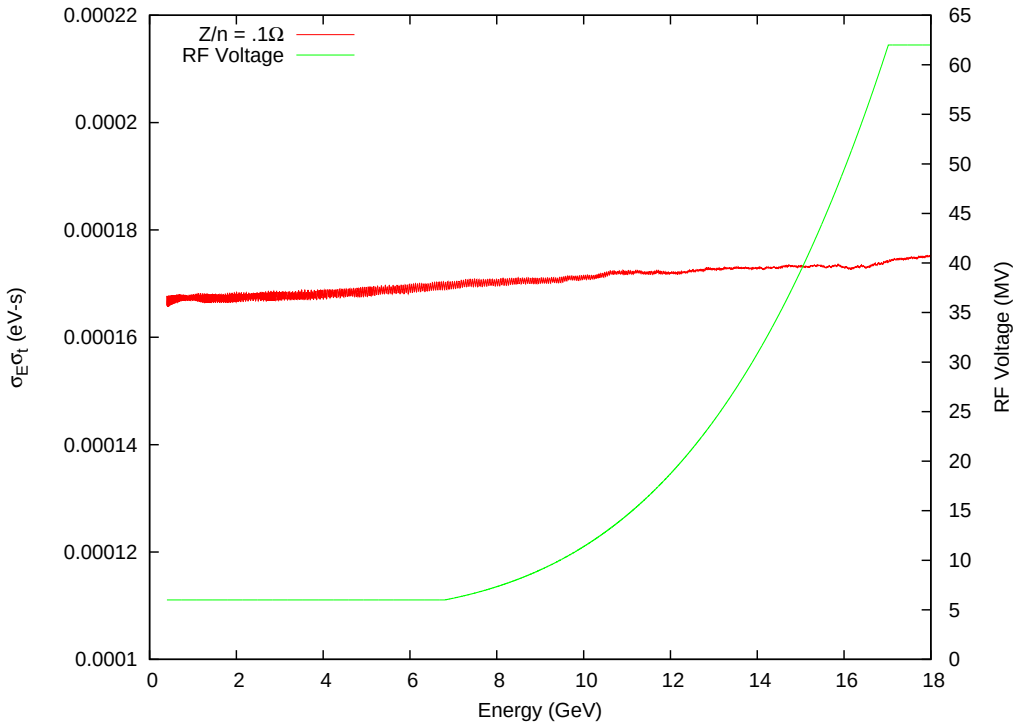

Figure 4.15: Longitudinal emittance growth for $Z/n = 0.1\Omega$ with the corresponding RF Voltage on the ramp. The peak RF voltage is 62 MV.

Effect of Eddy Currents in RCS

To increase the collective instability threshold a vacuum chamber with a copper surface has been selected. However the changing magnetic field during acceleration will induce eddy currents in the conductive vacuum chamber wall; their effect on the main dipole field was found to create a temporal delay in the Dipole fields of 0.65 ms. This is based on the resistivity of copper and assuming a beam pipe thickness of 1 mm and a internal diameter of 33 mm (we have 32.9 mm). Following [204] the frequency response of the net magnetic fields for a round beam pipe can be calculated as follows.

With an externally applied field given by,

$$\begin{aligned} \vec{A}_0 &= \hat{z} r \cos\theta B_0 \exp(-i\omega t) \\ \vec{B}_0 &= \nabla \times \vec{A}_0 \\ \vec{E}_0 &= -\frac{\partial \vec{A}_0}{\partial t}. \end{aligned} \tag{4.5}$$

In addition to the externally applied fields there are fields induced by a thin metallic shell

of radius r_0 and thickness d. The total net vector potential becomes,

$$A(r) = \begin{cases} B_{in} r, & r \leq r_0 \\ \beta_1 e^{\frac{(r-r_0)(1+i)}{\delta(\omega)}} + \beta_2 e^{-\frac{(r-r_0)(1+i)}{\delta(\omega)}}, & r_0 \leq r \leq r_0 + d \\ B_0 r + \frac{\gamma}{r} & r_0 + d \leq r. \end{cases} \tag{4.6}$$

Imposing continuity boundary conditions for the electric and magnetic fields and taking $d << r_0$ we obtain,

$$\begin{aligned} B_{in}(\omega) &= B_0(\omega) \frac{4z(\omega)x(\omega)}{z^2(\omega)(1+x(\omega))^2 - (1-x(\omega))^2} \\ \kappa(\omega) &= \frac{1+i}{\delta(\omega)} \\ x &= r_0 \kappa(\omega) \\ z(\omega) &= \exp(\kappa(\omega) d). \end{aligned} \tag{4.7}$$

Here $\delta(\omega)^2 = \frac{c^2}{2\pi\sigma\mu\omega}$ is the skin depth, μ and σ the magnetic constants and conductivity respectively. The plots of the frequency response are shown in Figure 4.16. The simple fit in the plot corresponds to an exponential smoothing function $H(t)\exp(-t/\tau)/\tau$ with $H(t)$ the Heaviside function and $\tau = 0.65$ ms. Such a smoothing will be easy to compensate using feedforward. Quadrupoles and sextupoles may have slightly different times but are certain to be easy to compensate.

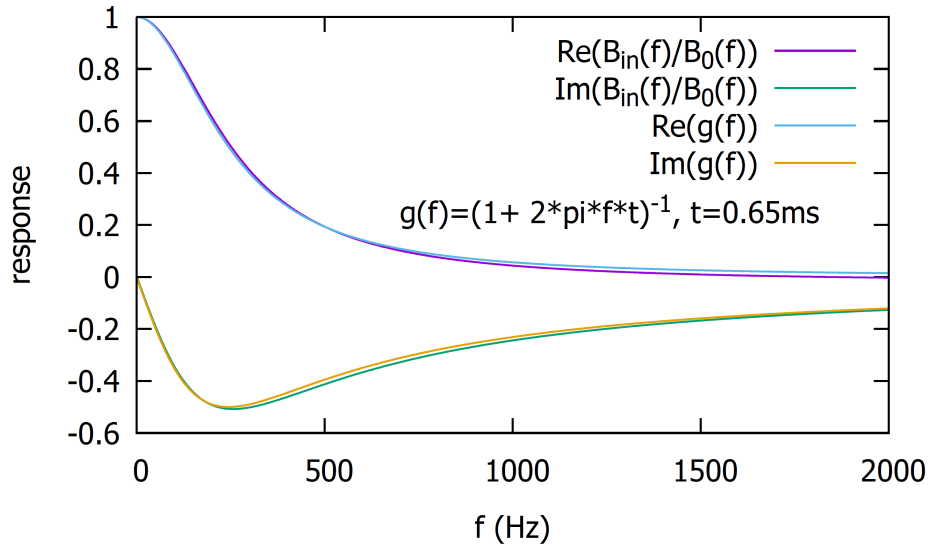

Figure 4.16: Frequency response of the net dipole field due to eddy currents. The time constant fit is 0.65 ms.

4.2.3 Collective Effects in Hadron Ring

Instabilities

Coherent instabilities in the hadron ring have been studied using the same modified version of TRANFT as was used for the electrons. We have only done simulations at top energy and assume that active damping can be applied if necessary during injection and ramping. Simulations were done for 41, 100 and 275 GeV protons and the results are summarized in Tables 4.8 and 4.7. The impedances in Table 4.7 along with the resistive wall impedance and space charge were included. The broad band impedances have been measured. The longitudinal impedance measurements were obtained by measuring the incoherent synchrotron frequency and seeing how it varied with intensity [32].

The transverse impedance measurements were obtained by measuring the coherent betatron tune and seeing how it varied with intensity [31]. The narrow band longitudinal impedance corresponds to the most dangerous mode from 6 of our 197 MHz storage cavities. The quoted transverse impedance corresponds to the most dangerous mode in a proposed crab cavity assuming 12 identical cavities.It is understood that only 6 crab cavities are on project but we look forward to a second experimental hall.

Table 4.7: Impedances assumed for calculations in Table 4.8. The narrow band transverse impedance is from the crab cavities and is discussed in the text.

Impedance Type	R_{sh}	Q	f_{res}
BB longitudinal	640 kΩ	2	5 GHz
BB transverse	10 MΩ/m	2	5 GHz
NB longitudinal	316 kΩ	4400	308 MHz
NB transverse	2.64 MΩ/m	1985	360 MHz

The beam parameters at 100 and 275 GeV in Table 4.8 are stable. At 41 GeV a persistent instability with an e-folding time of 2 seconds remains. It is assumed that such an instability can be actively damped. The values of $Im(\Delta Q)$ in the table correspond to the growth expected for no tune spread. The values of ΔQ_{bb} are the rigid bunch tune shift expected for the broad band impedance and ΔQ_{sc} is the average space charge tune shift within the bunch.The transverse space charge impedance Z_{sc} corresponds to the horizontal direction as does the average radius. This is because the crab cavities kick horizontally. The beta function at the crab cavity was adjusted within the voltage limits. It was assumed the focusing magnets can be adjusted to obtain collision optics with these beta functions. While there is some overhead it is likely no more than a factor of two in critical parameters. The beam-beam tune shift was 0.015 in all cases. The tune spread created can damp an imag-

Table 4.8: Proton beam parameters used for simulations. The rms beam radius is referenced to a 20 m beta function. The beam is stable at 100 and 275 GeV. At 41 GeV a coupled bunch instability with a growth time of 2 seconds is observed in simulations.

Parameter	41 GeV	100 GeV	275 GeV
number of bunches	1260	1260	1260
protons per bunch [10^{10}]	3	10	10
RF voltage ($h = 2520$) [MV]	2	5	6
RF voltage ($h = 7560$) [MV]	6.7	16.7	20
rms beam radius [mm]	0.83	0.65	0.38
$\sigma(p)/p$ [10^{-4}]	9.9	8.6	5.7
σ_s [cm]	5.5	5.5	5.5
Z_{sc} [MΩ/m]	44	12	4.6
β_{crab} [m]	50	500	1300
ΔQ_{bb}	0.0029	0.0040	0.0014
ΔQ_{sc}	0.013	0.0047	0.0007
$Im(\Delta Q)$	0.00013	0.0017	0.0016

inary tune shift of about 0.0016 if the real tune shift is small. The origin of the damping is fairly simple. For a maximum beam-beam tune shift of ΔQ_{BB} the tune distribution is roughly parabolic with a half width at base of $\Delta Q_{BB}/4$. A parabolic tune distribution of this width can damp an imaginary tune of:

$$Im(Q)_{max} = \frac{\Delta Q_{BB}}{3\pi}.$$

However, the damping in the parabolic distribution is influenced by the real tune shift too. This is the reason we have undamped instability at 41 GeV.

Additional damping using octupoles was tried with worrisome results. Adding octupoles appeared to reduce the instability but, a significant and strong transverse emittance growth occurred when space charge, octupoles, and the beam-beam force were all present at the same time. This emittance growth remained when all other sources of impedance were removed.

In this section and the one on electron instabilities the tune spread from the beam beam force played a critical role. For these simulations a weak strong model was used, where the beam causing the beneficial damping was assumed to be stationary. This is clearly an approximation and it is necessary to understand how good it is. Modeling of this effect

is ongoing. So far we find that the coupling is not a problem if the tune split between the rings is sufficient. Quantitative results are forthcoming.

Intrabeam Scattering

Intrabeam scattering (IBS) has been a concern at RHIC from the beginning. We have the BETACOOL code, and various other codes based on the Piwinski and Bjorken-Mtingwa formalisms. For some problems, like spin diffusion, one needs the action diffusion rates as opposed to just the total emittance growth rate. The Zenkevich formalism has been programmed so these effects can be estimated [205]. Figure 4.17 shows data and simulations [33] in RHIC. There are no free parameters.

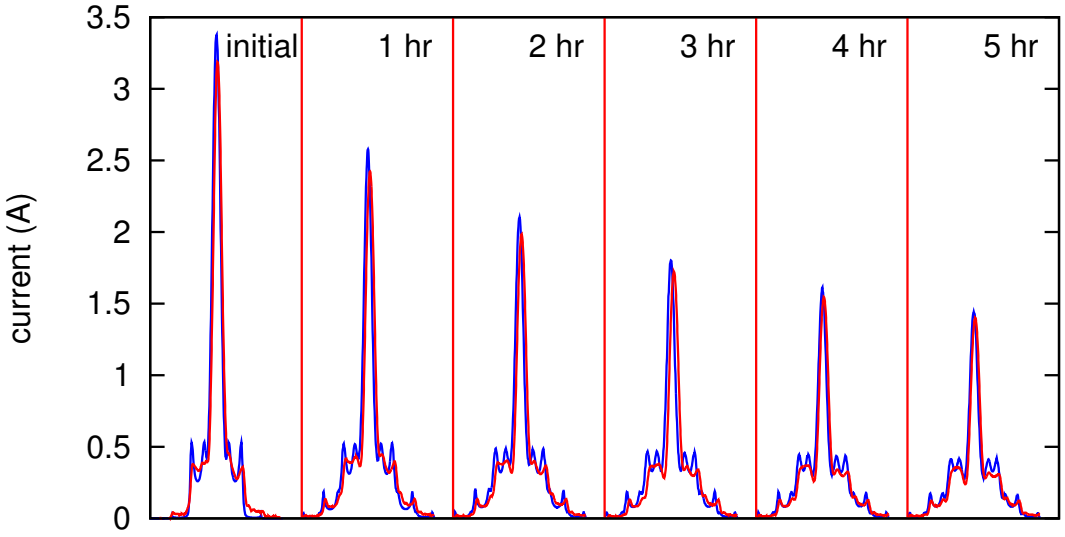

Figure 4.17: Comparison of data and simulations for gold beams under the influence of intrabeam scattering over 5 hours. The data are red and the simulation is blue. See details in Reference [33]. The 500 MHz bandwidth of the wall current monitor would wash out any sharp spikes in the data so agreement may well be better than shown.

4.3 Dynamic Aperture in Electron Storage Ring

4.3.1 Prerequisites on Linear Lattice

The required center-of-mass energy range of the Electron Ion Collider (EIC) from 29 to 140 GeV is realized by proton energies that range from 41 to 275 GeV, and by electron energies that range from 5 to 18 GeV. At the highest energy of the electron ring, namely 18 GeV, a 90° phase advance of regular FODO cells in the arcs is chosen to obtain the required design emittance. However, the stronger focusing makes the design much more challenging in comparison to the 60° lattice at 10 GeV. The main relevant parameters for the performance of single-particle dynamics are tabulated in Table 4.9. The increases in emittance, betatron tunes, and natural chromaticity relative to the corresponding values for the 60° lattice are at a level of several units, as expected. In particular, the increase of the RMS energy spread is substantial, reaching 0.1%. This leads to an absolutely minimum required momentum aperture of 0.6% to ensure an adequate quantum lifetime for the electron beam. The betatron tunes are selected by the optimization of the spin dynamics as well as the beam-beam interaction. They are very close to integers, making the chromatic compensation even more difficult.

Table 4.9: Main parameters of the electron storage rings.

Parameter	60° Lattice	90° Lattice
Beam energy, E_0 [GeV]	10	18
Circumference, C [m]	3834	3834
Emittance, ϵ_x [nm]	24.0	28.3
Energy spread, σ_δ [10^{-4}]	5.54	9.83
Betatron tunes, ν_x/ν_y	45.12/36.1	48.12/43.1
Chromaticity, ξ_{0x}/ξ_{0y}	$-83/-91$	$-85/-94$
IP betas, β_x^*/β_y^* [m]	0.42/0.05	0.42/0.05
Distance from IP to quad, L^* [m]	5.3	5.3

The sources of the chromaticity in the EIC lattice are the quadrupoles and the solenoids. The natural chromaticity must be minimized in the first place. In the optimum case the chromaticity contribution from one FODO cell is given by

$$\xi = -\frac{1}{\pi}\tan(\phi_c/2), \tag{4.8}$$

where ϕ_c is the total phase advance of the cell. Therefore the chromaticity is -0.32 for a 90° cell, and -0.18 for a 60° cell. In addition, the interaction region straight section generates about 1/3 of the total chromaticity of the storage ring.

The regular sectors (Sectors 2 to 5) consist of 16 regular FODO cells, 6 matching cells (3 on each end), and 14 cells without dipole magnets. According to Equation 4.8, the theoretical chromaticity is about -6.5 units. The actual chromaticity is 60% higher due to space limitations, the reverse bends, and the required length of the quadrupole and sextupole magnets.

The low-beta optics in the interaction region (IR) is shown in Figure 4.18. The starting point of the lattice is the interaction point with $\beta_y^* = 5\,\text{cm}$. Since the ratio of β_y^*/L^* is about the same to those in the B-factories, we expect a similar chromaticity generated in the IR. However, the difference in the β-peaks indicates that the IR symmetry is broken due to different physics requirements on each side of the detector. Moreover, the spin rotators and matching sections, which can be seen in the non-zero vertical dispersion, contribute more chromaticity and occupy the same space that would be necessary for any local chromatic compensation.

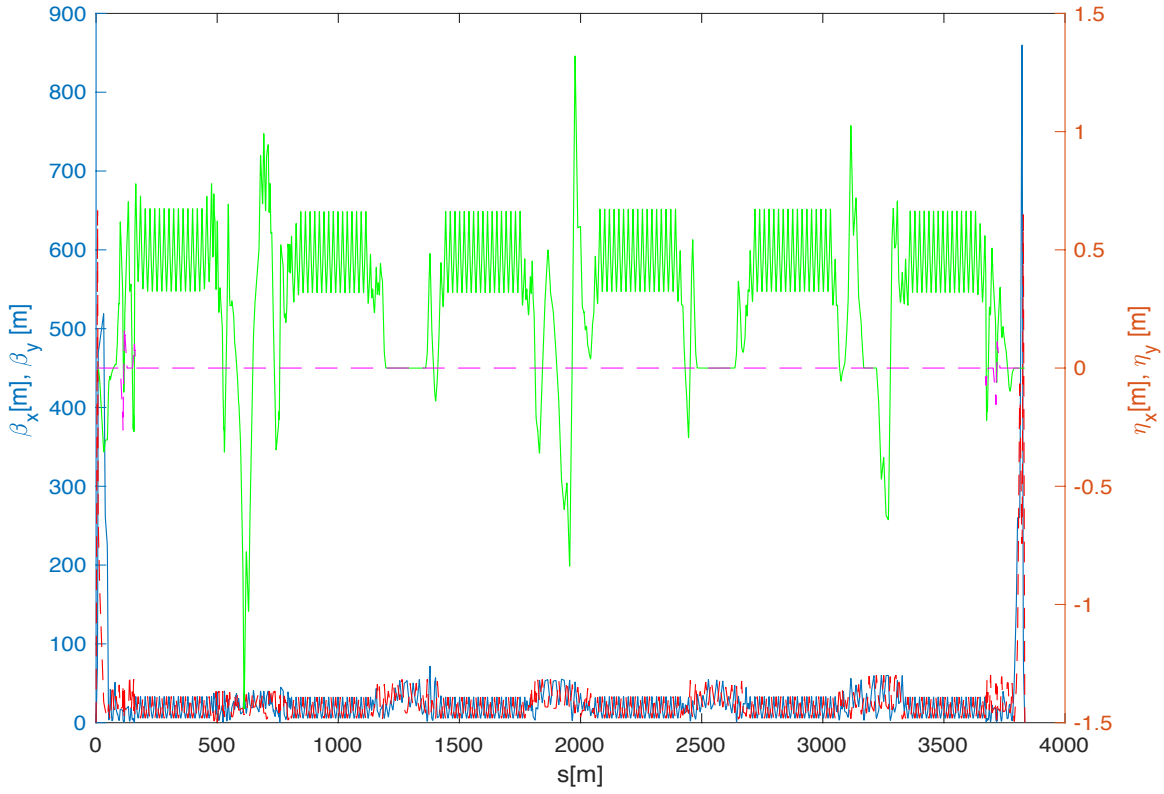

Figure 4.18: Lattice functions of the electron ring in the Electron Ion Collider.

The spin rotator solenoids contribute significantly to the total chromaticity, about 10 units from all four solenoids in the 10 GeV lattice. One way to minimize the effect is to reduce the β-functions in the solenoids.

The large β-functions in the IR generate a significant off-momentum β-beat which is characterized by the W-function. This β-beat is a major contributor to dynamic aperture reduc-

tions and therefore needs to be minimized. Minimizing the W-function in the IP section therefore helps dynamic aperture optimization. Particularly, the W-function at the IP, and the peak value in the IP straight, must be constrained when optimizing the linear lattice. This is accomplished using multiple sextupole families in conjunction with additional constraints on the linear lattice. Both the configuration of the sextupole families and the constraints on the linear lattice depend on the phase advance per FODO cell and are therefore different at the two beam energies studied here, 10 and 18 GeV.

In summary, the prerequisites on the linear lattice optimization are

1. The natural chromaticity must be minimized;
2. The W-function in the IP section must be minimized.

4.3.2 Requirements for Nonlinear Optimization

The goal of the nonlinear optimization is two-fold:

1. 10 times of the beam RMS size, or 10σ, of beam acceptance is needed for sufficient beam lifetime. The transverse beam size at the IP is on the order of 100 µm, therefore the required DA is a few millimeters at the IP. The requirement on the momentum acceptance is $10\sigma_p$.
2. Sufficient momentum aperture is needed to to provide a large enough Touschek lifetime.

Due to depolarization each electron bunch is frequently replaced; therefore long beam lifetime is required only to keep the charge variation small. For a current drop of 5% and 10% within 6 minutes, the corresponding lifetime is 4.55 and 2.22 hours, respectively. The lifetime is partly determined by the Touschek lifetime,

$$\frac{1}{\tau} \propto \frac{N}{\gamma^2 \sigma_x \sigma_y \sigma_z \delta_{\text{acc}}^3}, \tag{4.9}$$

where τ denotes the Touschek lifetime, N is the number of charges per bunch, γ is the relativistic γ-factor, $\sigma_x, \sigma_y, \sigma_z$ are the RMS beam sizes in the horizontal, vertical and longitudinal direction, and δ_{acc} is the momentum acceptance of the accelerator.

Using the parameters listed in Table 4.10, we obtain the Touschek lifetime to be 5.17 hours.

Here the vertical beam size is derived assuming 1% coupling. During collision the coupling needs to be significantly higher so the electron beam size matches the proton bunch. Therefore Touschek lifetime is not an issue for the EIC.

The Touschek lifetime is very sensitive to the momentum acceptance due to the third power. For the 10 GeV lattice $10\sigma_p$ of the momentum spread is about 0.56%, while for the 18 GeV it is about 1%.

Table 4.10: Beam parameters for Touschek calculation (10 GeV lattice)

Parameter	Value
N $[10^{11}]$	2.8
Q [nC]	45
I [A]	2.5
ϵ_x [nm]	17.9
ϵ_y [nm]	0.18
σ_z [mm]	5.0
σ_δ	5.5×10^{-4}
δ_{acc}	0.01
V_{RF} [MV]	41
h	7200

4.3.3 Dynamic Aperture of the 60° Lattice

An EIC sextant arc has 22 FODO cells (44 half-cells). There are 16 regular arc cells which form a periodic structure. The beam optics and dispersion of the arcs is matched to the adjacent straight sections by three dispersion matching cells, respectively, at each end. Sixteen pairs of sextupoles (consisting of a horizontally focusing and a vertically focusing one) are placed in the 16 FODO cells of each arc sector for chromaticity correction. Six additional pairs are placed in the dispersion matching cells at the two ends of the arc sector. The maximum sextupole strength was determined to be $K_2 = 8\,\text{m}^{-3}$, which is limited by the pole tip field and the large bore aperture.

To maintain sufficient dynamic aperture, it is important to design the chromaticity correction scheme such that there is no build-up of driving terms of nonlinear resonances over the arcs, but there is intrinsic compensation of such driving terms within a group of sextupoles which should be as small as possible. In a 60° lattice with two families of sextupoles (one horizontally focusing, one vertically focusing), intrinsic cancellation occurs over three FODO cells. However, the correction scheme must also generate an off-momentum β-beat which cancels the one generated by the IR quadrupoles. The IR off-momentum β-beat is the mechanism behind the second order chromaticity which contributes significantly to the tune spread with momentum, thereby limiting the dynamic aperture. The off-momentum β-beat of the chromatic sextupoles can be adjusted in amplitude and phase by detuning the sextupoles within the group of three FODO-cells. Subsequent groups of three cells will lead to an accumulation of off-momentum β-beat contribution as desirable to compensate the IR β-beat.

The detuned sextupoles, however, do not intrinsically compensate each other any more in their contribution to nonlinear resonance terms. Intrinsic cancellation, however, can be re-established by having each group of FODO cells followed by an identical group of three

cells. In this case, each sextupole has an identical partner at a betatron phase difference of 180° and there is no build-up of nonlinear driving terms (in leading order). This requires a lattice with the number of regular cells being a multiple of six per arc.

Unfortunately, the optimum EIC lattice which provides the desired beam emittance and still has a reasonable dipole fill factor has just 16 regular FODO-cells per arc and two times three matching cells as mentioned above. The EIC sextupole scheme is an attempt to mitigate this shortcoming.

Several sextupole layout schemes have been tested. For example, a non-interleaved scheme has been implemented and 70σ DA was obtained; however the required sextupole strength $K_2 = 20\,\mathrm{m}^{-3}$ is far beyond the attainable limit. We found a simple scheme of a six-fold sequence of the pattern

$$A - B - C \tag{4.10}$$

for the 60° lattice, with a few extra sextupoles extending to the dispersion suppressors. Within each family, two adjacent sextupoles form a pair with "-I" transformation in-between so their first-order geometric aberration is canceled. Meanwhile, the chromatic β-beating propagates at twice the betatron phase, and therefore every member in the family is in the same phase for compensation of the chromatic beating.

The sextupole families in each sector are powered independently, which provides more variability. A total number of 36 families is used for minimizing the global betatron tune variations with respect to the momentum deviation. We utilize the differential algebra and symplectic maps to accurately compute the high-order derivative of the tunes. The solution is found using a simplex downhill optimizer starting from the settings of two global families.

In this section the properties for a typical lattice solution of 10 GeV energy are presented. This is an on-going effort and some of the parameters are not yet ideal at this point. However, the lattice meets the main requirement, i.e., $20\,\sigma$ dynamic aperture has been achieved in both transverse planes, and the resulting momentum acceptance of 0.7% fulfills the minimum requirement as well.

The dependence of tunes on momentum deviation is depicted in Figure 4.19. Due to the optimization the tune variation is less than 0.05 within the required dynamic aperture; therefore strong resonance lines are avoided. However the working point, (45.12, 36.10), is very close to two major resonance lines, namely $Q_x - Q_y = 9$ and $Q_x - 2Q_y = -27$.

Figure 4.20 shows the dynamic aperture. The spin rotator solenoids are included in the lattice. The results are obtained from the ideal lattice, i.e., no errors have been added.

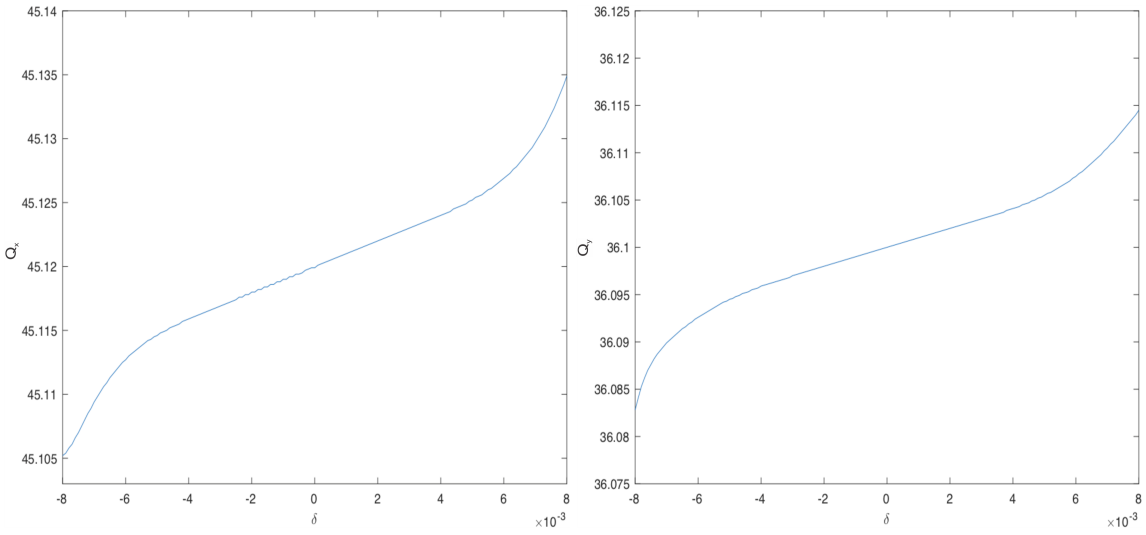

Figure 4.19: Tune dependence on the momentum deviation. Top: Q_x versus δ, bottom: Q_y versus δ.

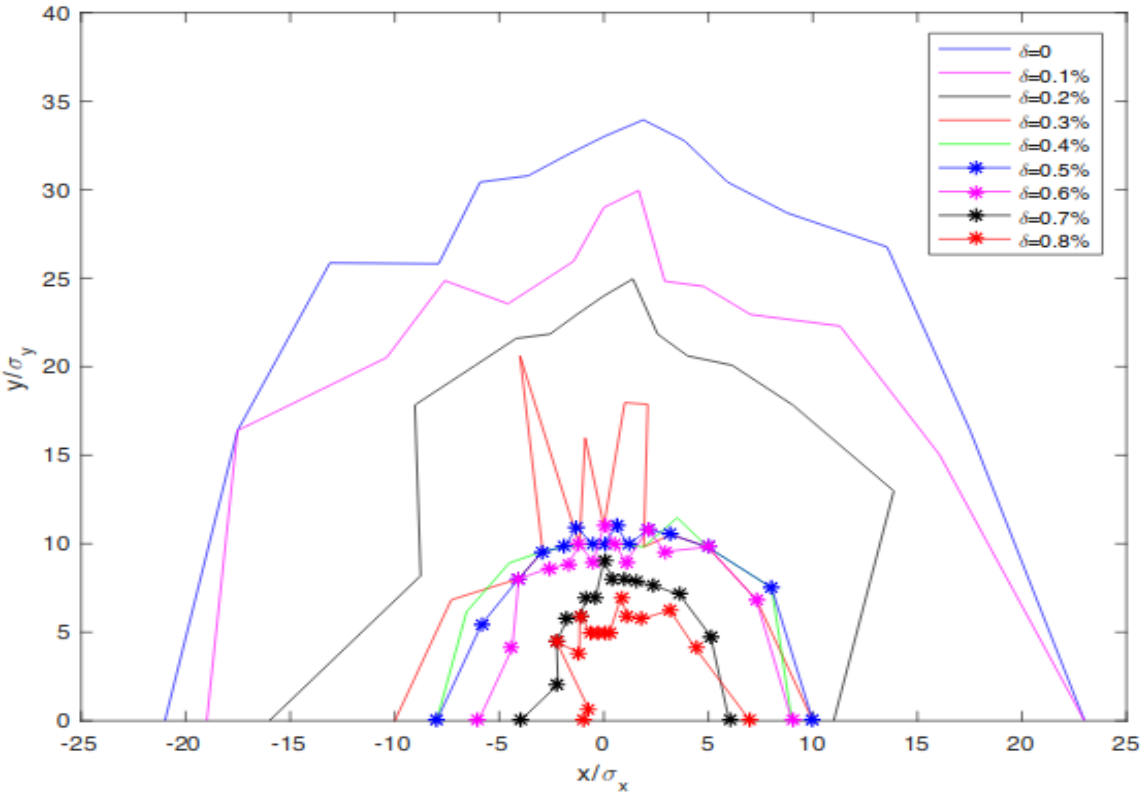

Figure 4.20: Dynamic aperture for different $\Delta p/p$ in (x, y) space.

4.3.4 Dynamic Aperture of the 90° Lattice

In the 18 GeV lattice with its phase advance of 90° per FODO cell, the sextupoles in each plane are placed at 90° from each other. Compensation of the off-momentum β-beat generated in the IR can therefore only be accomplished completely if this β-beat arrives at the first sextupole in the arc with the correct phase, such that the first sextupole is placed at 90° from the origin of the distortion. Proper setting of the sextupoles in the arc then allows for a gradual compensation of the off-momentum β-beat, characterized by the W-function, throughout the arc, as shown in Figure 4.21.

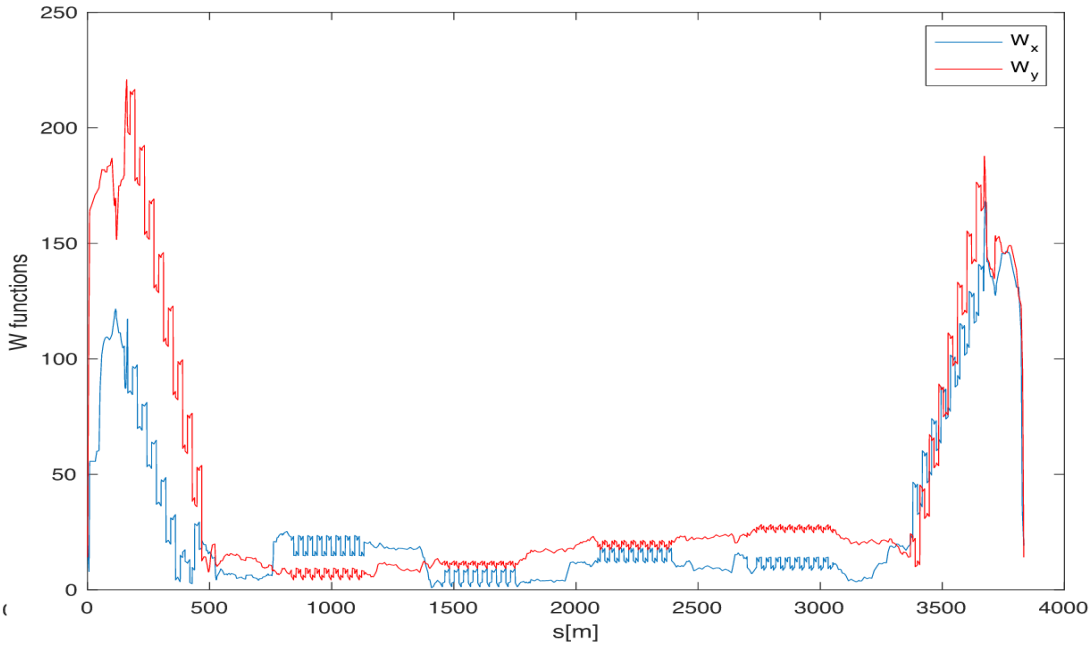

Figure 4.21: W-function in the 18 GeV, 90° lattice. The IR6 interaction point is located at $s = 0$.

The design of the chromatic correction scheme starts with two global families of sextupoles, setting chromaticity to one unit in both horizontal and vertical planes. It is well known that these sextupoles excite the third-order resonances and therefore reduce the dynamic aperture of the on-momentum particles. Their driving terms are computed [206] and shown on the top plot in Figure 4.22 as they are accumulated along the beamline. Clearly, there are significant residual values in the entire ring. After investigation, we find that some sextupoles near the ends of the regular arcs are not paired in "π" phase advances. Removing these singlets eliminates all residual terms as shown on the bottom plot of the figure. Moreover, all third-order driving terms are confined within the arcs with much smaller amplitudes, consistent with first-order perturbation theory. For a fair comparison, we have adjusted the remaining sextupoles to reset the chromaticity to one unit.

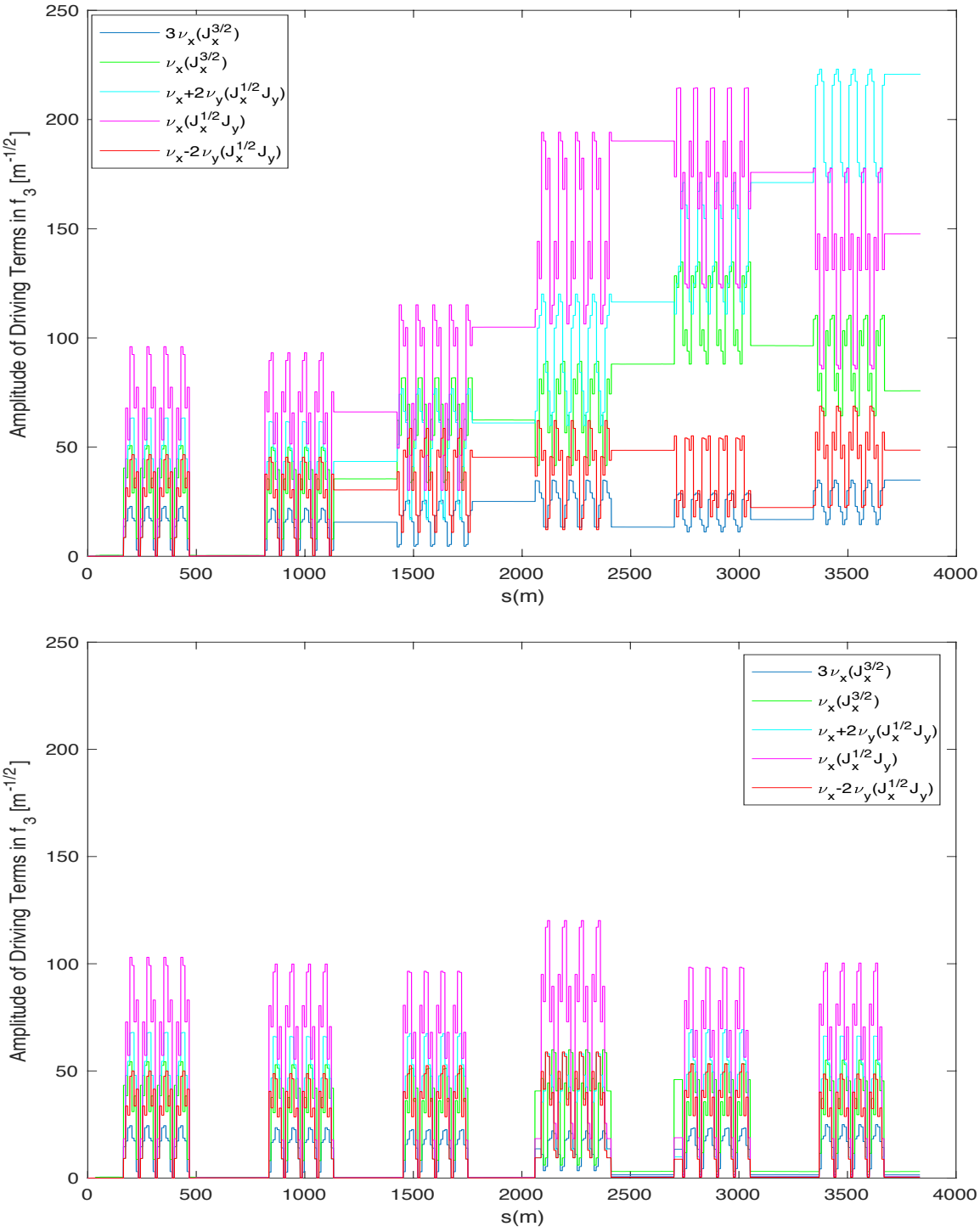

Figure 4.22: Third-order driving terms as they are accumulated in the electron storage ring of the EIC before (top) and after (bottom) pairing of sextupoles.

We evaluate the dynamic apertures of the collider by tracking particles with various momenta. The tracking is carried out over 1024 turns with synchrotron oscillation, but without radiation damping. The boundary of the stability defines the dynamic aperture. The results of the two different settings of the sextupoles are shown in Figure 4.23. Clearly, the elimination of the third-order driving terms significantly increases the dynamic aperture, but the momentum aperture remains low at 0.3%.

The reason for the small momentum aperture can be seen from the top plot in Figure 4.24 where we show the betatron tunes as functions of the momentum deviation $\delta = (p - p_0)/p_0$. Clearly, using two global families of sextupoles in the arcs is not adequate to compensate the large chromaticity generated in the low-β optics in the interaction region. Especially, we see a chromaticity wall in the vertical plane at the negative side, $\delta = -0.3\%$, forcing the tune towards the integer resonance.

As we have mentioned previously, there is no space for any local chromatic compensation in the interaction region. We therefore have to use the sextupoles in the arcs. As illustrated in Figure 4.25, we group them in each arc into four families. Each color in the plot labels a different family. Because of the 90° cells, all sextupoles in a family are in phase in terms of the β-beating. The interference among the families in different betatron phases generates higher order chromatic beatings and therefore changes the high order chromaticity. Moreover, every family has an even number of sextupoles so the third-order resonance driving terms vanish. As a result, the resonance correction in the previous section is retained in the chromatic compensation.

Since there are six arcs in the entire ring, we have a total of twenty-four families of sextupoles. They are used to set the first-order chromaticity to one unit and zero out the higher order chromaticity up to 6th order in each plane. The solution is found by running the downhill-simplex optimizer with application [207] of differential algebra to compute high-order derivatives of the betatron tunes as functions of momentum deviation. The result is shown in the bottom plot of Figure 4.24, where the stable region is enlarged to $\pm 0.9\%$.

The settings of the sextupoles are plotted in Figure 4.26. The strongest sextupole is in the de-focusing plane adjacent to the interaction region as expected. Some families in the focusing plane switch their signs. Required strengths are up to twice as high as in the two-family scheme.

With these settings, we track to determine the dynamic aperture. The result is shown in Figure 4.27. The momentum aperture is enlarged to $\pm 0.6\%$, reaching the minimal requirement for the stored beam.

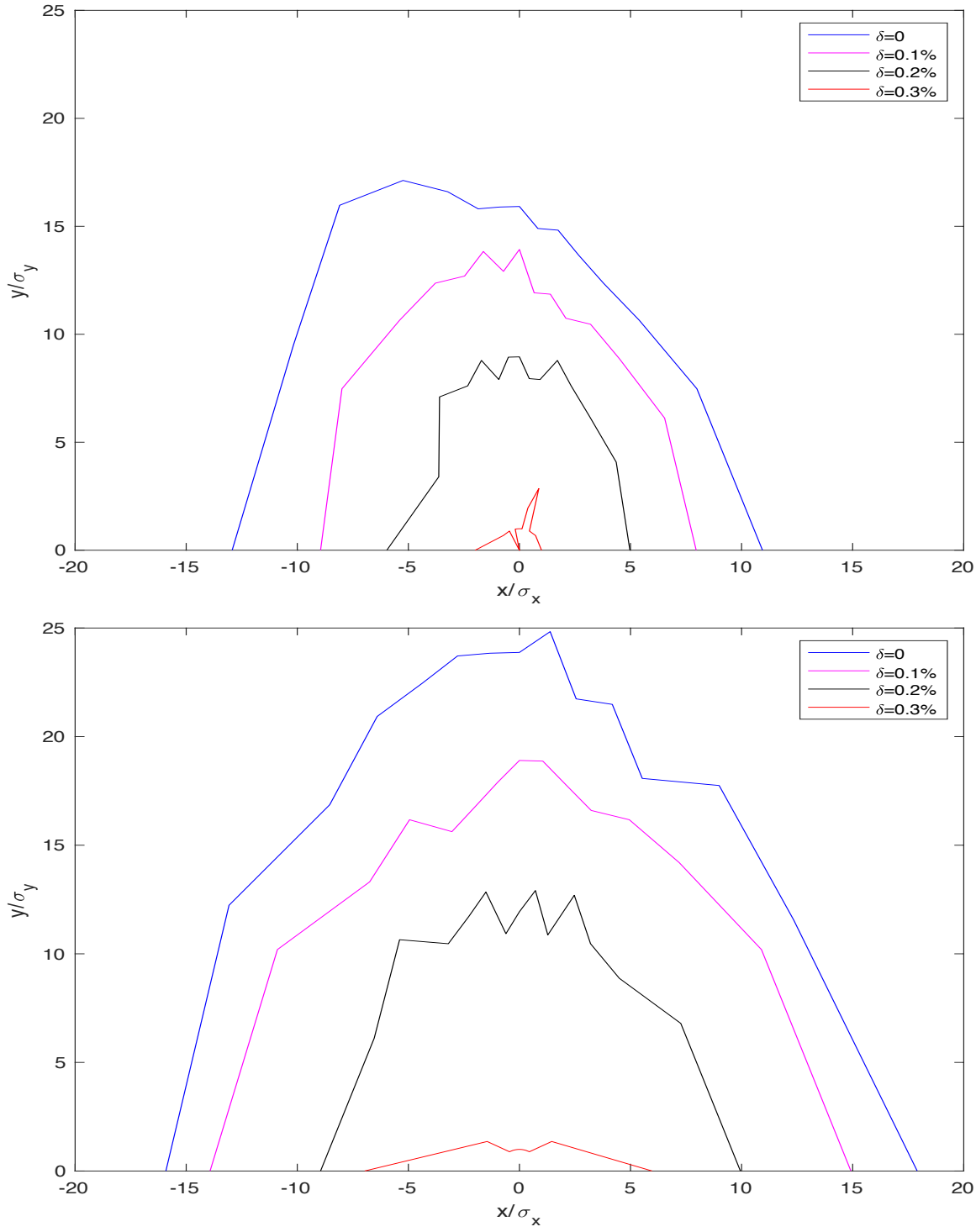

Figure 4.23: Dynamic apertures in the electron storage ring of the EIC before (top) and after (bottom) pairing of sextupoles.

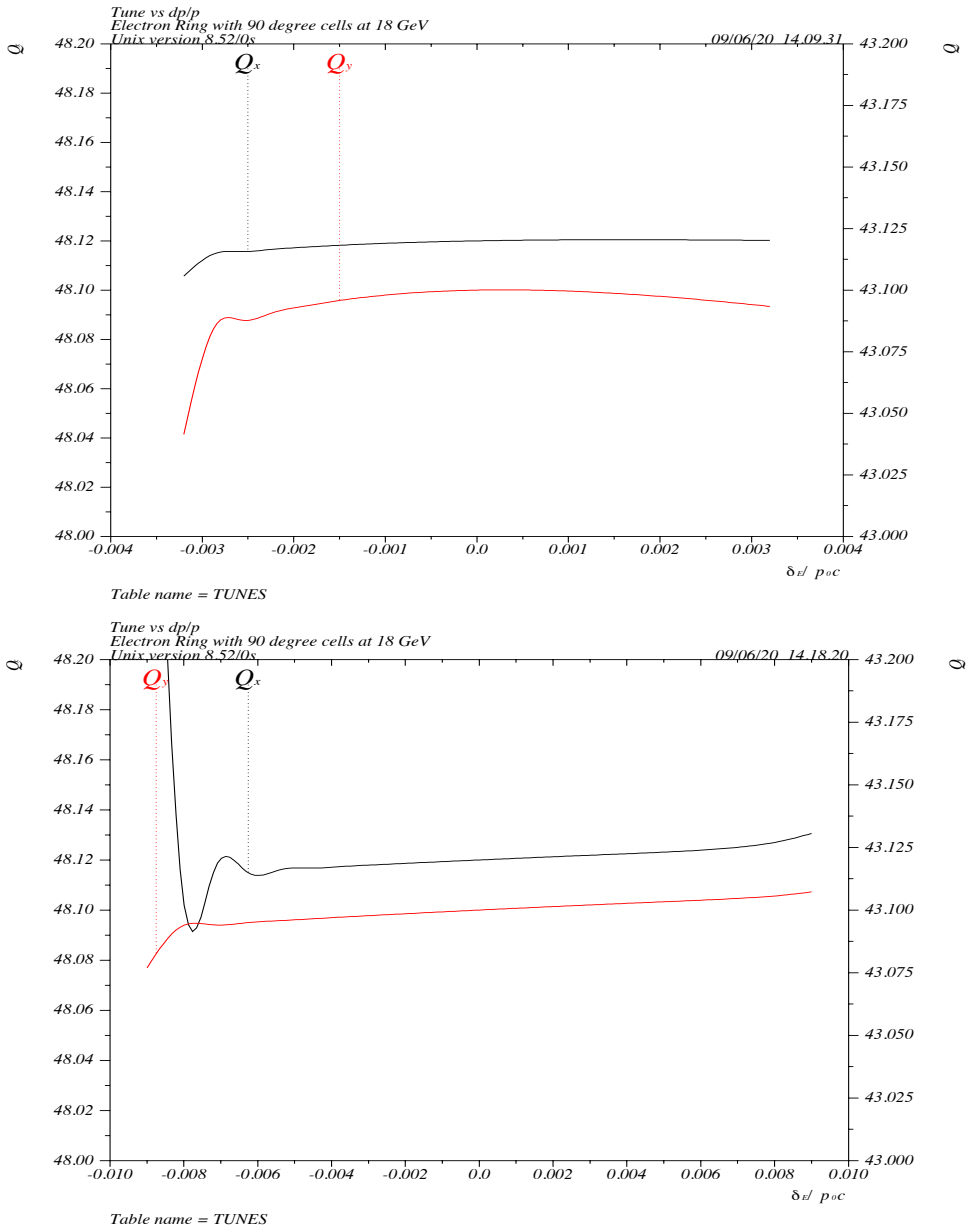

Figure 4.24: The betatron tunes as functions of momentum deviation with two families (top) and twenty-four families (bottom) of sextupoles.

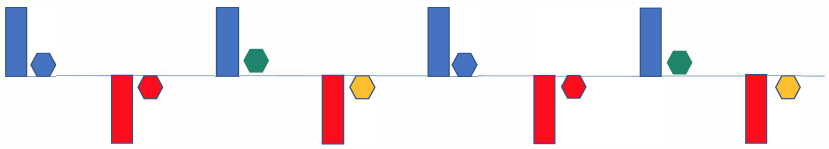

Figure 4.25: The sextupole layout in the scheme of global chromatic compensation; there are four sextupole families, grouped in alternating FODO cells.

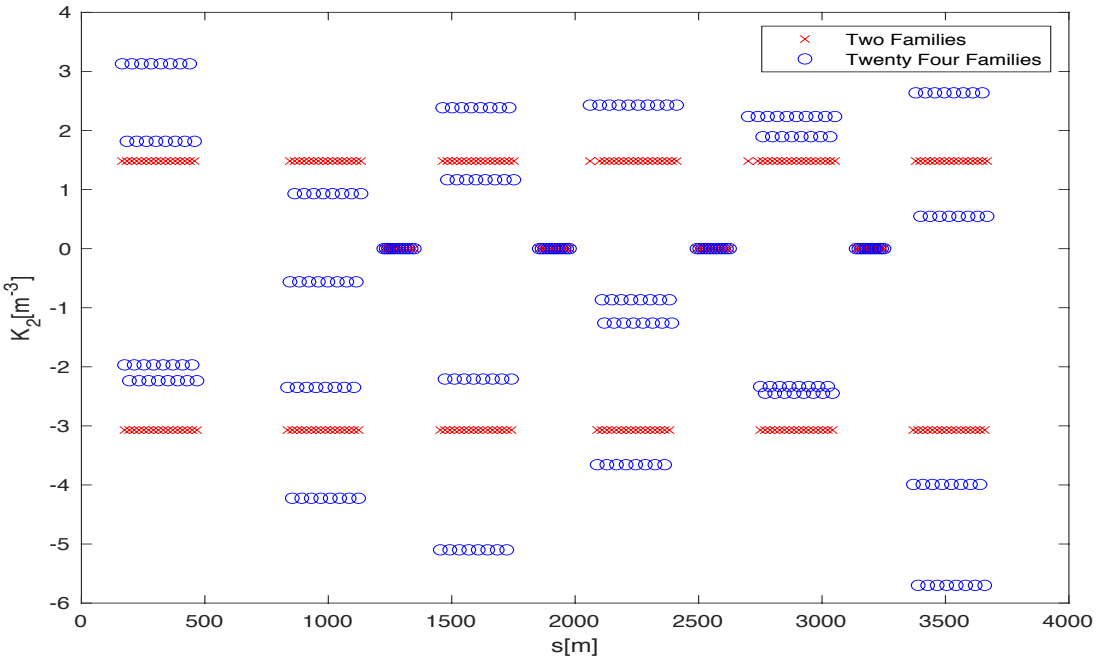

Figure 4.26: The sextupole settings in two schemes of chromatic compensation. The length of the sextupoles is 0.5 m.

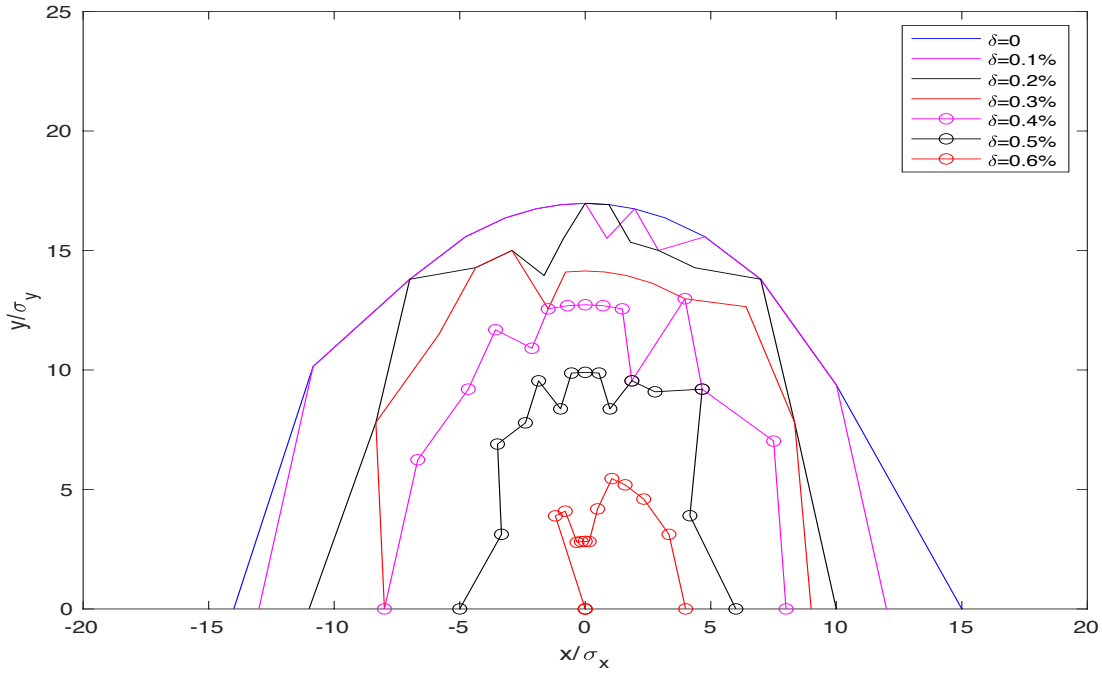

Figure 4.27: Dynamic apertures in the electron storage ring of the EIC with the global chromatic compensation using 24 families of sextupoles.

4.3.5 Dynamic Aperture with two Interaction Regions

With two interaction regions in IR6 and IR8 squeezed to low values of the β-function, the resulting off-momentum β-beat can be confined to the arc between the two interaction regions by setting the betatron phase advances between the respective sources of the β-beat to 90°. Thus, the off-momentum β-wave generated by one IR is compensated by the other. Figure 4.28 shows the resulting W-function in this arrangement. Tracking studies to determine the dynamic aperture with two IRs are in progress.

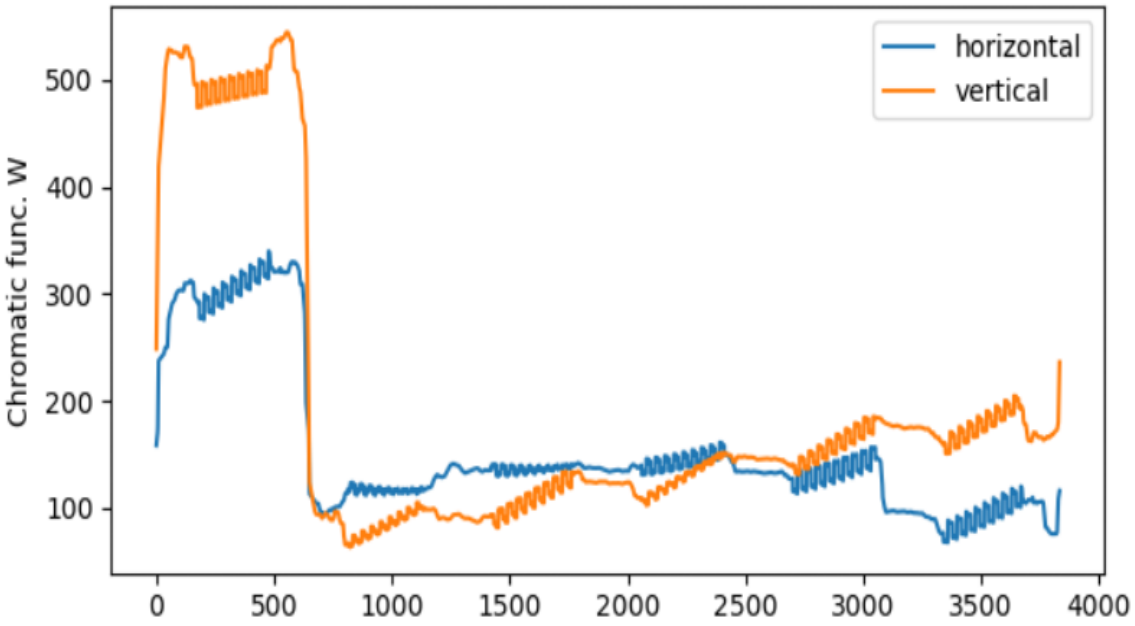

Figure 4.28: W-function in the 18 GeV, 90° lattice with two IRs. The IR6 interaction point is located at $s = 0$.

4.3.6 Dynamic Aperture with Errors

Dynamic aperture (DA) is reduced in presence of magnet errors. Here, we consider systematic and random non-linear field errors, magnet strength errors and misalignment. These errors cause a variety of optical distortions including focusing, coupling, chromaticity, orbit, and excitation of non-linear resonance effects which may significantly reduce the DA.

To produce a desired DA ($\sim 10\sigma$) two methods are used: 1) compensating the error effects by optical means, where possible, and 2) limiting the magnitude of the errors by imposing tolerances. The latter must be realistically achievable based on the present accelerator technology.

Dynamic aperture with errors is calculated using particle tracking in LEGO [208]. The calculations consist of tracking simulations for 10 different combinations of random errors (seeds), where each tracking is performed for 2000 turns, and the DA is sampled at 13 angles in x-y space. Synchrotron oscillations are included while the radiation is turned off. The DA is measured at the interaction point (IP) and expressed in units of RMS beam size assuming the beam emittance of 24 nm at 10 GeV and 30 nm at 18 GeV. The quoted DA value is the minimum DA value among the 10 seeds and the 13 angles.

In the simulations, the horizontal and vertical betatron tunes are always corrected to their nominal values, while the linear chromaticity is corrected to +1. Additional corrections are used, where needed, including correction of orbit, betatron coupling, β-function and vertical dispersion. The orbit and dispersion corrections utilize the horizontal and vertical dipole correctors and double-plane BPMs which are placed near most of the quadrupoles. Distortion of β-functions is minimized by adjustment of some of the quadrupole strengths; and the coupling correction is based on adjustment of vertical offsets of the sextupoles. SVD method is used to identify the most efficient correctors for optimal compensation.

The EIC lattice configuration is different at 10 GeV and 18 GeV beam energies which leads to different sensitivity to the errors. The relevant differences are the arc optics and beam emittance. At 10 GeV the arc FODO cell phase advance is 60° as compared to 90° at 18 GeV. The stronger arc focusing at 18 GeV helps to limit the natural growth of the beam emittance with energy, but leads to stronger quadrupoles and sextupoles which increase the effects of errors. The ∼30 nm emittance at 18 GeV is also larger than ∼24 nm emittance at 10 GeV which makes it even more difficult to obtain the desired 10σ dynamic aperture at 18 GeV due to the larger beam size.

The effects of errors are significantly amplified by large β-functions, most notably in the final focus quadrupoles (FFQ) near the IP, where β-functions are more than a factor of 10 larger than in most other magnets. For this reason, tighter tolerances are typically required for the high-β magnets to limit their impact on the DA.

The errors in the simulations are applied to all dipoles, quadrupoles, and sextupoles. Random errors are generated using Gaussian distribution; their tolerances are specified in units of one σ of the distribution. Alignment errors include random horizontal and vertical offset errors and a roll angle error. Random horizontal and vertical offsets are also applied to BPMs. Tolerance for magnet strength error is defined as the RMS of relative deviation from the nominal magnet strength.

Non-linear field errors can be systematic or random. They are defined using multipole coefficients. The total magnet field with multipole errors is:

$$B_y + iB_x = 10^{-4}\, B_N(r_0) \sum_{n=N}^{\infty} (b_n + ia_n) \left(\frac{x+iy}{r_0}\right)^{n-1} \tag{4.11}$$

where x and y are the horizontal and vertical coordinates relative to magnet center, r_0 is the reference radius at which the a_n and b_n multipole coefficients are determined, and $B_N(r_0)$ is the nominal magnet field at r_0. The index $N = 1$ is for dipoles, 2 for quadrupoles and

3 for sextupoles, while the index n is the order of a multipole. The nominal magnet field corresponds to $n = N$, where, for example, $b_N = 10^4$ and $a_N = 0$ for a "normal" magnet, and vice versa for a "skew" magnet. The b_n and a_n coefficients at $n > N$ determine the multipole errors. They can be systematic or random and are defined by systematic and random multipole coefficients. The systematic multipoles are the same for a given class of magnets, while the random multipoles change from magnet to magnet based on random distribution. Tolerances for the random multipoles are expressed in terms of their RMS values.

Dynamic Aperture with Errors at 18 GeV

The 18 GeV EIC lattice adopts 90° cells in the six arcs and uses a semi-local non-linear chromaticity correction scheme with 10 independent sextupole families. The 18 GeV emittance is about 30 nm. For DA evaluation, the multipole errors in dipoles and sextupoles are based on the realistic PEP-II High Energy Ring (HER) [20] measured multipoles scaled to both the EIC magnet reference radius and the coil diameter. Multipoles in most quadrupoles are assigned based on the preliminary estimate of field quality for the EIC regular quadrupole. The multipoles for dipoles, sextupoles and regular quadrupoles are listed in Table 4.11.

Table 4.11: Multipoles for regular quadrupoles at r_0 = 25 mm, dipoles at r_0 = 17 mm, and sextupoles at r_0 = 27 mm.

	Regular Quadrupoles			Dipoles		Sextupoles	
n	b_n	b_n	a_n	b_n	b_n & a_n	b_n	b_n & a_n
	Sys.	RMS	RMS	Sys.	RMS	Sys.	RMS
3	0.00	2.670	1.800	0.06	0.26		
4	0.00	0.480	0.024	0.00	0.20		
5	0.00	0.220	0.150	0.00	0.31	0.0	16.9
6	1.35	0.071	0.024	0.00	0.31		
7	0.00	0.013	0.012			0.0	4.2
8	0.00	0.006	0.029				
9	0.00	0.011	0.007			-19.6	0.0
10	-3.00	0.001	0.003				
11	0.00	0.004	0.003				
12	0.00	0.003	0.003				
13	0.00	0.001	0.002				
14	-0.69	0.001	0.001				
15						-2.4	0.0

The effect of multipoles in magnets, where β-functions are high, is significantly enhanced. Therefore, multipole tolerances for these magnets are evaluated separately based on the DA calculations. The high-β magnets are located in the vicinity of the IP and include four FF quadrupoles (FFQ) near the IP, six high-β quadrupoles (HQ3EF_5, HQ4EF_5, HQ5EF_5, HQ3ER_6, HQ4ER_6, HQ5ER_6) on the outer sides of the FFQ doublets, and two high-β dipoles — a large aperture superconducting dipole DB2ER_6 and a regular dipole DB3ER_6. The interaction region (IR) β-functions and the locations of these magnets are shown in Figure 4.29. Multipole tolerances for the high-β magnets and the FFQ, obtained in the DA simulations, are listed in Table 4.12 and Table 4.13, respectively. Since the order of these multipoles is $n \geq 3$, they do not affect the first order optics, therefore linear optics corrections are not required.

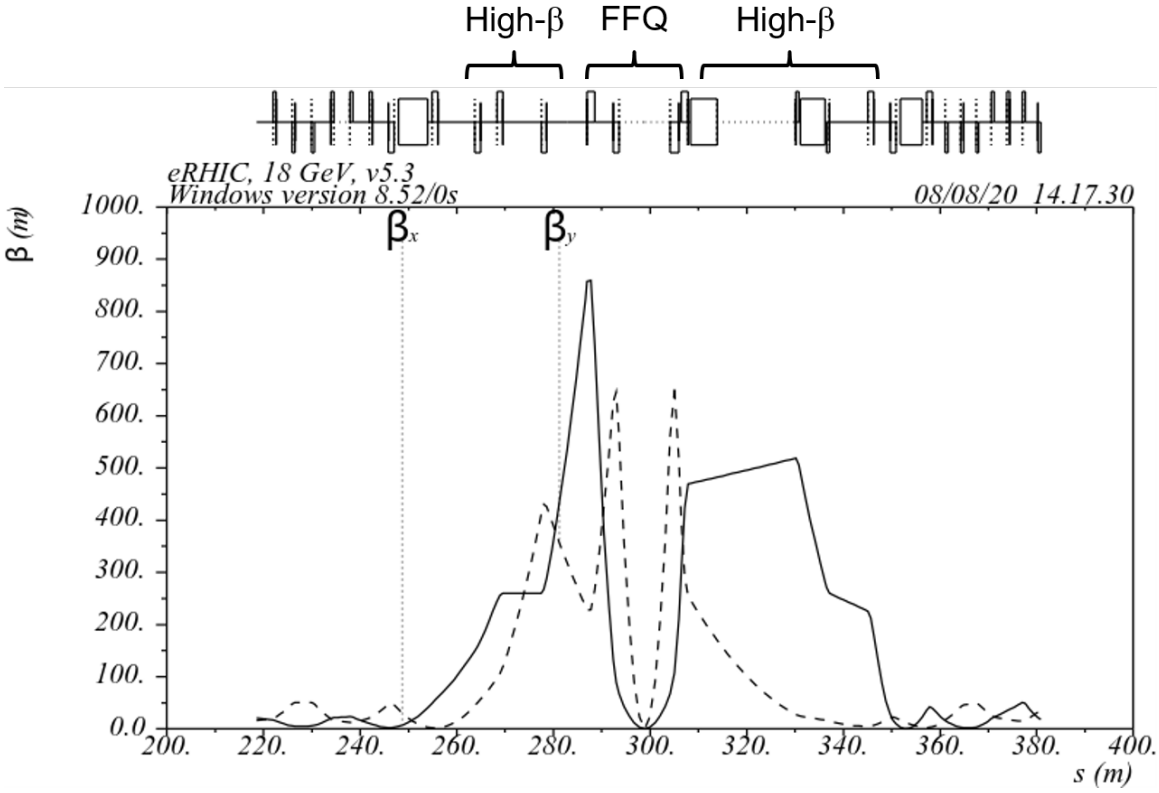

Figure 4.29: Interaction region of 18 GeV lattice and the locations of four FF quadrupoles, six high-β quadrupoles, and two high-β dipoles, where IP is near $s = 300$ m.

Dynamic aperture at 18 GeV with all the multipole errors is presented in Figure 4.30. The on-momentum DA in 10 seeds of random errors is 10.3σ, exceeding the desired target of 10σ. The off-momentum DA is shown at the momentum error of δ = 0.2%, 0.4% and 0.6%. The actual momentum range is slightly larger than 0.6% and is nearly the same as without

Table 4.12: Multipole tolerances for (left to right): Six high-β quads at r_0 = 25 mm, SC high-β dipole DB2ER_6 at r_0 = 67 mm, and high-β dipole DB3ER_6 at r_0 = 17 mm.

	Regular Quadrupoles		Dipoles		Sextupoles	
n	b_n	b_n & a_n	b_n	b_n & a_n	b_n	b_n & a_n
	Sys.	RMS	Sys.	RMS	Sys.	RMS
3	0.00	1.00	5.00	1.00	0.50	0.50
4	0.00	1.00	0.00	1.00	0.00	0.20
5	0.00	1.00	5.00	1.00	0.10	0.07
6	1.00	0.30	0.00	1.00	0.00	0.05
7	0.00	0.20	5.00	1.00	0.03	0.015
8	0.00	0.10				
9	0.00	0.04				
10	0.10	0.02				
11	0.00	0.02				
12	0.00	0.005				
13	0.00	0.008				
14	0.005	0.002				

multipole errors. Hence, the effect of multipoles on the momentum range at 18 GeV is minimal.

Dynamic Aperture with Errors at 10 GeV

The 10 GeV EIC lattice is based on 60° FODO cells in the six arcs which yields an emittance of ∼24 nm. The lattice utilizes a global non-linear chromaticity correction scheme with 36 independent sextupole families. For the DA evaluation, the multipole errors in Tables 4.11 to 4.13 are used, while the alignment and magnet strength errors are based on the errors in the PEP-II CDR study [20].

On-momentum and off-momentum dynamic apertures at 10 GeV with the multipole errors are presented in Figure 4.31. The on-momentum DA (δ = 0) in 10 seeds of random errors is 11.3σ, exceeding the desired target of 10σ. Figure 4.31 also shows the off-momentum DA for electrons with initial δ = 0.5%. The ∼0.5% is close to the lattice momentum range without errors, indicating that the effect of the multipoles on the momentum range is minimal.

Random misalignment and magnet strength errors are listed in Table 4.14. They are similar to the errors used in the PEP-II study [20]. Based on the DA evaluations, the corresponding

Table 4.13: Multipole tolerances for FFQ (left to right): HQ0EF_5 at r_0 = 27 mm, HQ1EF_5 at r_0 = 63 mm, HQ1EF_6 at r_0 = 73 mm, and HQ2EF_6 at r_0 = 89 mm.

	HQ0EF_5		HQ1EF_5		HQ1EF_6		HQ2EF_6	
n	b_n	b_n & a_n	b_n	b_n & a_n	b_n	b_n & a_n	b_n	b_n & a_n
	Sys.	RMS	Sys.	RMS	Sys.	RMS	Sys.	RMS
3	0.0	0.5	0.0	0.5	0.0	0.5	0.0	0.5
4	0.0	0.5	0.0	0.5	0.0	0.5	0.0	0.5
5	0.0	0.5	0.0	0.5	0.0	0.5	0.0	0.5
6	0.5	0.5	5.0	0.5	5.0	0.5	5.0	0.5
7	0.0	0.5	0.0	0.5	0.0	0.5	0.0	0.5
8	0.0	0.3	0.0	0.5	0.0	0.5	0.0	0.5
9	0.0	0.3	0.0	0.5	0.0	0.5	0.0	0.5
10	0.3	0.3	5.0	0.5	5.0	0.5	5.0	0.5
11	0.0	0.3	0.0	0.5	0.0	0.5	0.0	0.5
12	0.0	0.2	0.0	0.5	0.0	0.5	0.0	0.5
13	0.0	0.2	0.0	0.5	0.0	0.5	0.0	0.5
14	0.1	0.1	5.0	0.5	5.0	0.5	5.0	0.5

FFQ tolerances are made a factor of two tighter compared to regular quadrupoles due to the higher β-functions and stronger error effects in the FFQ. The horizontal and vertical offset errors are also assigned to all BPMs.

Alignment and strength errors cause distortions of the linear optics including tune, linear chromaticity, orbit, linear coupling, β-function, and dispersion. The tolerances in Table 4.14 apply only when correction systems are used to compensate the effects of these errors. The necessary correction schemes are implemented in LEGO and used in the simulations when the misalignment and strength errors are present. Beam orbits for 10 seeds of random errors after correction are illustrated in Figure 4.32. The RMS orbit in 10 seeds is in the range of 250 to 500 µm, and the RMS β beating is within a few percent after the corrections.

Dynamic aperture at 10 GeV with all the errors including multipoles, misalignment and magnet strength errors and the corrections for 10 error seeds is shown in Figure 4.33. The on-momentum DA is 10.7σ. The off-momentum DA is also presented in Figure 4.33 and is stable up to at least δ = 0.45%. The latter indicates that the alignment and strength errors cause a slight reduction of the momentum range by ∼10% as compared to the DA with multipole errors only (see Figure 4.31).

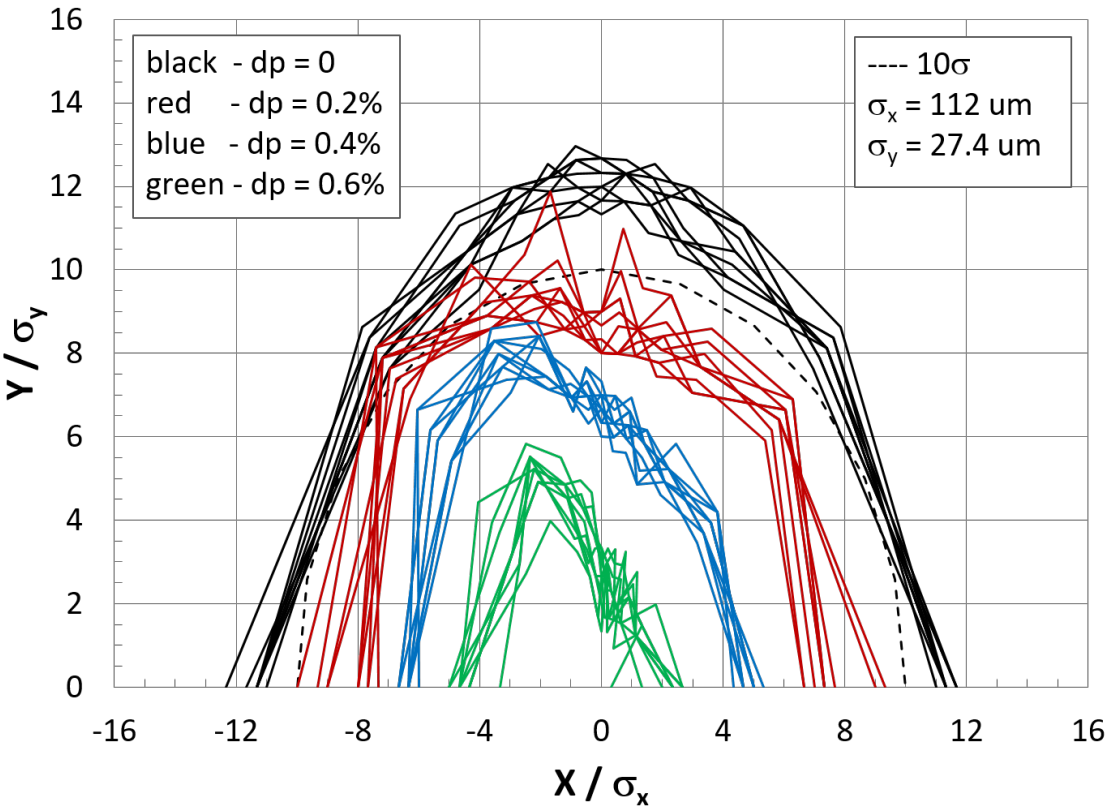

Figure 4.30: DA at 18 GeV for 10 seeds of multipole field errors at δ = 0, 0.2%, 0.4%, and 0.6%.

Table 4.14: Tolerances for random misalignment and magnet strength errors (1σ).

RMS Error	x [mm]	y [mm]	Roll [mrad]	Strength [%]
Dipole	0.2	0.2	0.5	0.1
Quadrupole	0.2	0.2	0.5	0.1
Sextupole	0.2	0.2	0.5	0.2
FFQ	0.1	0.1	0.5	0.05
BPM	0.1	0.1	0.0	

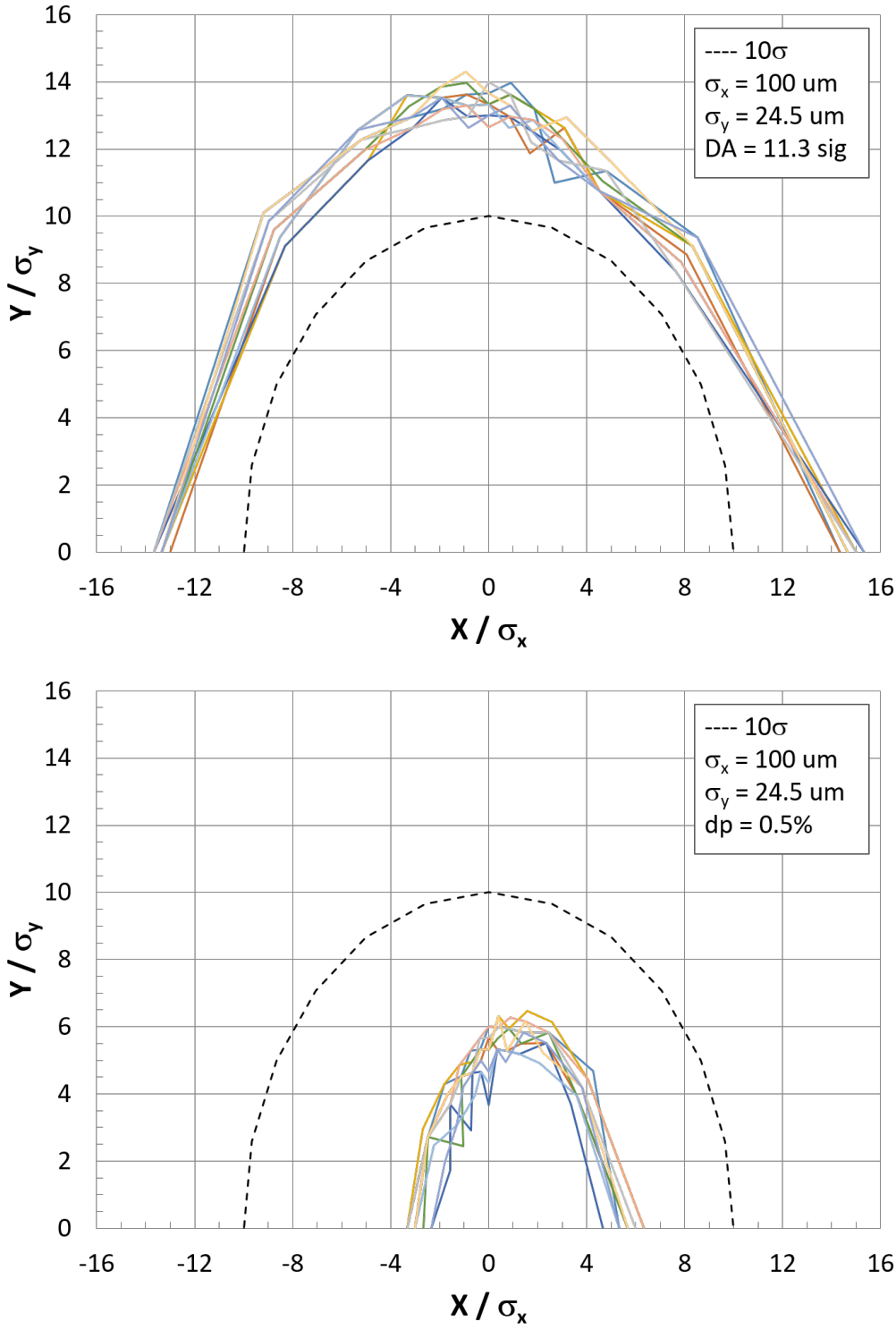

Figure 4.31: Dynamic aperture at 10 GeV for 10 seeds of multipole errors at $\delta = 0$ (top) and $\delta = 0.5\%$ (bottom).

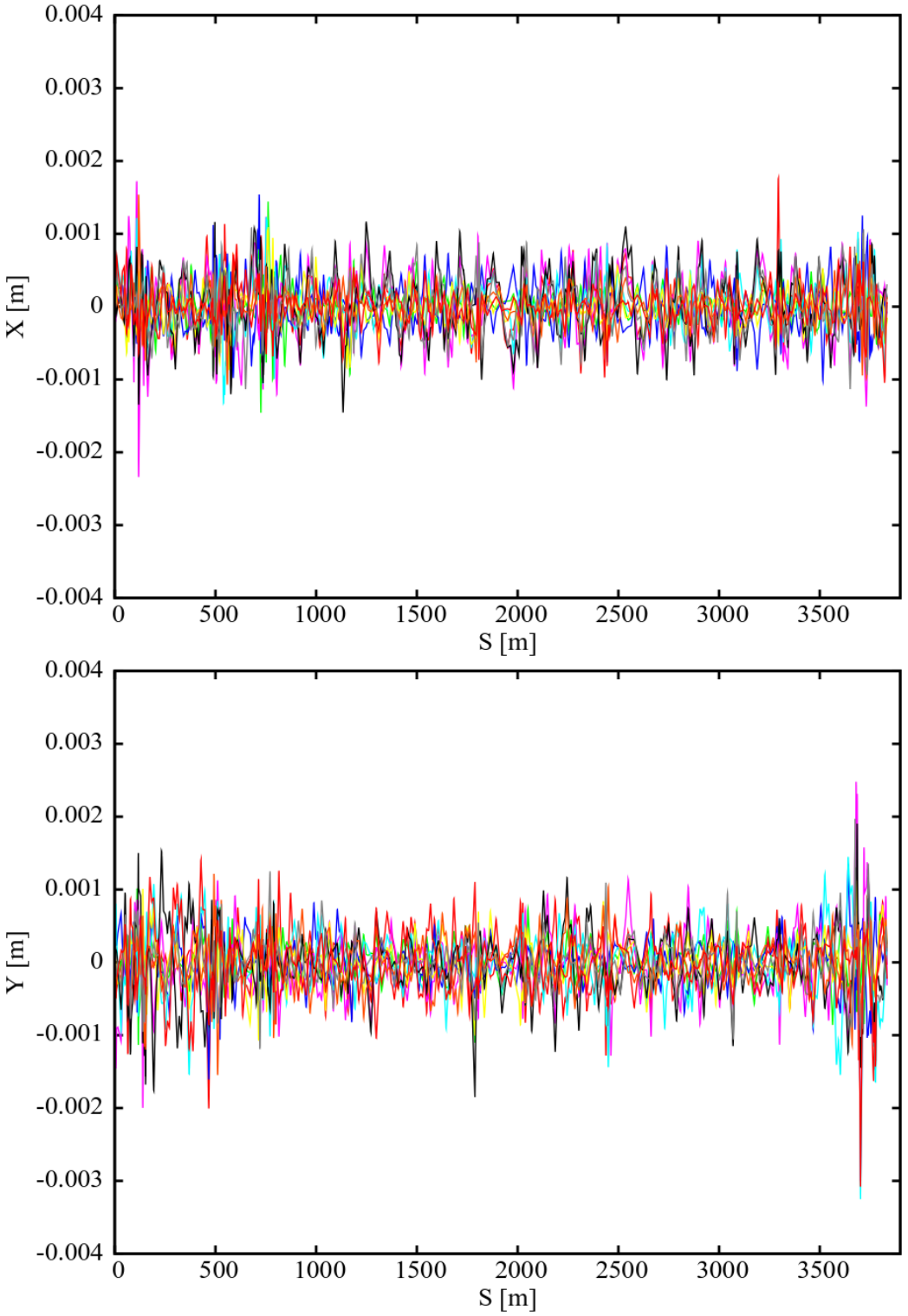

Figure 4.32: Horizontal (top) and vertical (bottom) orbit after correction for 10 seeds of random errors at 10 GeV, where the IP is at $s = 0$.

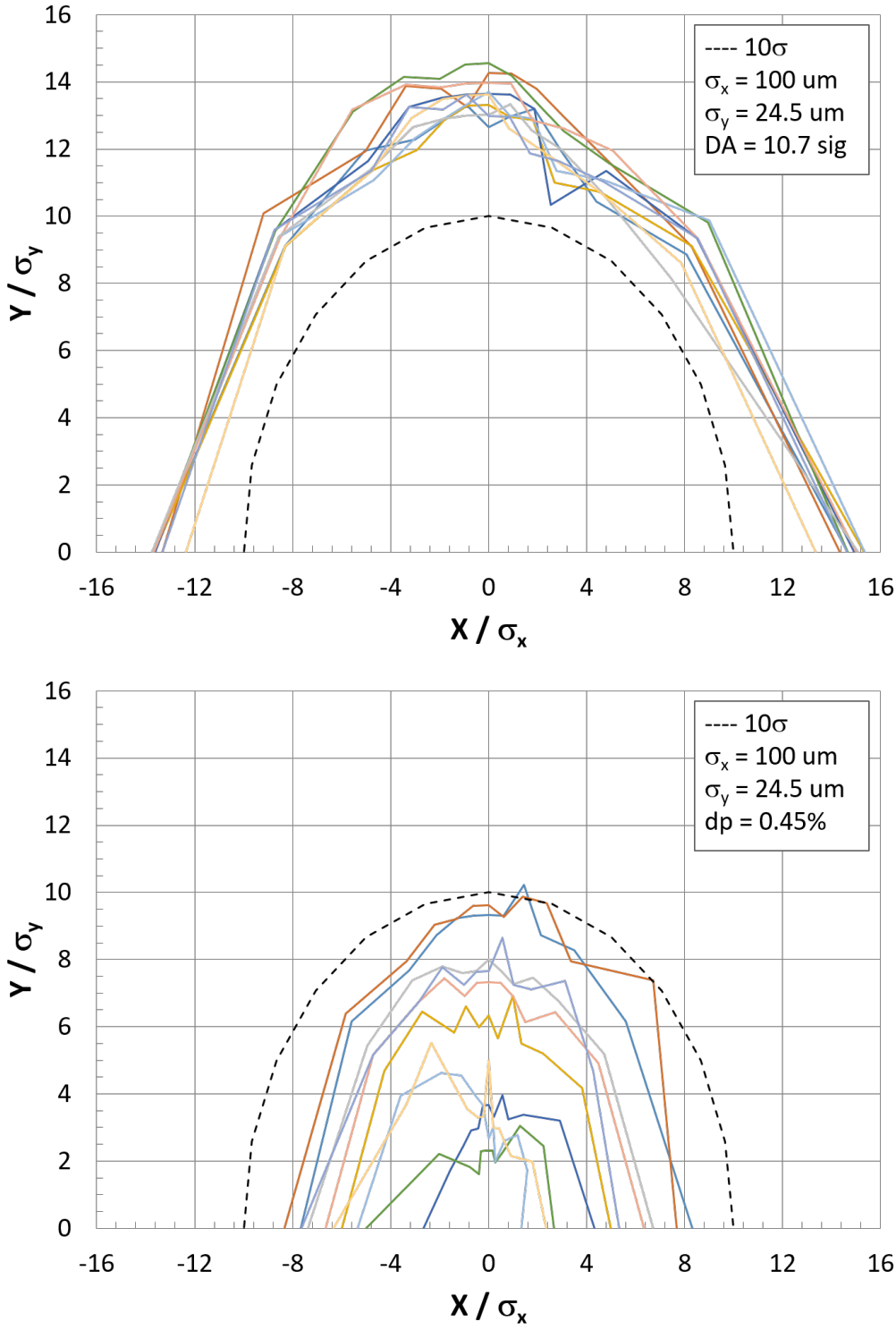

Figure 4.33: Dynamic aperture at 10 GeV at $\delta = 0$ (top) and $\delta = 0.45\%$ (bottom) for 10 seeds of alignment, multipole and strength errors after corrections.

4.4 Dynamic Aperture in the RCS

Tracking results have shown that the RCS lattice is capable of reaching an off-momentum dynamic aperture of dp/p=1.0% as shown in Fig. 4.34. This was achieved by controlling the betatron tunes, chromaticity and the sextupole settings. In Fig. 4.35 we can see the losses as a function of horizontal betatron tune. This shows the optimal tune has a fractional component of 0.88. Additionally, part of the mechanism for loss was due to tune-modulation effect which create a parametric resonance due to momentum oscillation caused by synchrotron oscillations. This was improved by lowering the linear chromaticity to close to zero. Further improvement was achieved by optimizing on the sextupole settings in the RCS. In order to keep our injected bunches below three sigma of the off-momentum aperture given by dp/p=1.0% we limit our RMS dp/p to be below 2.5×10^{-3}.

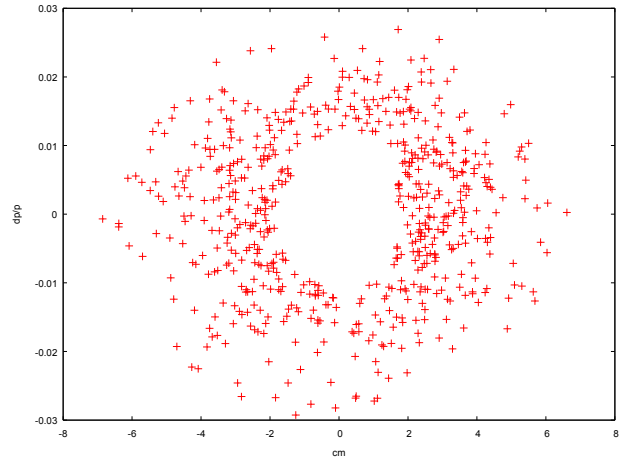

Figure 4.34: RCS lattice Phase space plot of dp/p and cm showing lost particles over 200 turns

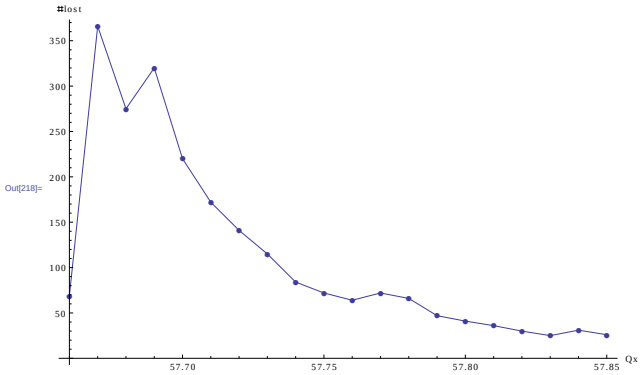

Figure 4.35: Particle losses through the 18 GeV RCS acceleration cycle as a function of horizontal tune. The initial bunch parameters were RMS dp/p = 4.3e-3, and bunch length of 71 ps RMS.

4.5 Dynamic Aperture in Hadron Storage Ring

Dynamic aperture studies are an essential tool in the design and operational tuning of proton and ion circular accelerators. They can contribute to the choice of design parameters, verify the long-term stability of a design, and be used to guide performance improvements for an existing machine. Based on operational experience in RHIC, the proton dynamic aperture including the beam-beam interaction and nonlinear magnetic field errors should be at least 5σ transversely with $3(dp/p_0)_{rms}$ in relative momentum deviation.

Here we will focus on the highest luminosity configuration, which has 275 GeV protons colliding with 10 GeV electrons. This configuration has the maximum beam-beam parameters for both the proton and electron beams. We explored a wide range of design parameters and performed beam-beam simulations to determine the luminosity and the proton beam emittance growth rate. We found that the performance tradeoffs could be characterized by the beam-flatness, defied as the ratio of the vertical to the horizontal beam sizes at the IP. While a flatter beam gives a higher luminosity, it also results in a larger proton emittance growth rate. We settled on a flatness of 0.09, resulting in $\beta_x^* = 80\,\text{cm}$ and $\beta_y^* = 7.2\,\text{cm}$.

4.5.1 Nonlinear Optics

The EIC hadron storage ring contains six arcs made up of FODO cells. Each arc quadrupole has an adjacent sextupole, denoted by "focusing" or "defocusing" based on which type of quadrupole they are adjacent to. The phase advance in each cell is approximately 90°, chosen to reduce the second order chromaticity and cancel geometric resonance driving terms. The sextupoles are powered together in interleaved "families," of which there are four per arc, two of focusing sextupoles and two of defocusing sextupoles. The arcs are connected by utility straights, and for these studies only one (IR6) contains an interaction region.

Based on the results of beam-beam simulations studies, the tune chosen for these dynamic aperture studies is $(28.228, 29.210)$. To correct chromaticity, the sextupoles are grouped into two families, one for all the focusing sextupoles and one for all the defocusing sextupoles. Chromaticity was corrected to be +1 in each plane. The resulting second order chromaticities are about $(40, -600)$, which from RHIC experience are acceptable. Figure 4.36 shows the off-momentum tunes as a function of relative momentum deviation $\delta = dp/p_0$. For the EIC design, $3(dp/p_0)_{rms} = 2 \times 10^{-3}$, which is the range shown in that figure. The third order chromaticity clearly dominates the tune variation with momentum deviation, and will be corrected in the future.

Figure 4.37 shows the off-momentum $\beta_{x,y}^*$ as a function of relative momentum deviation. The β^* variation with energy is clearly dominated by the second order β^* variation with δ.

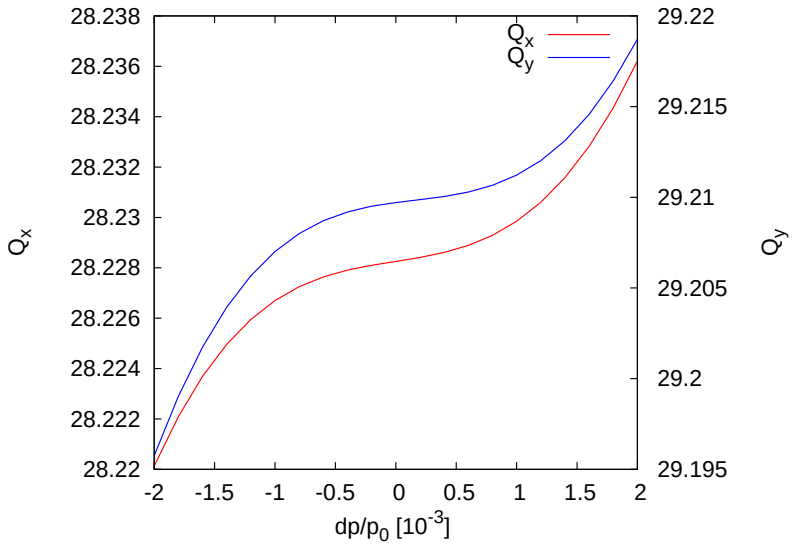

Figure 4.36: Off-momentum tunes Q_x, Q_y versus the relative momentum deviation δ, with 2 families of sextupoles.

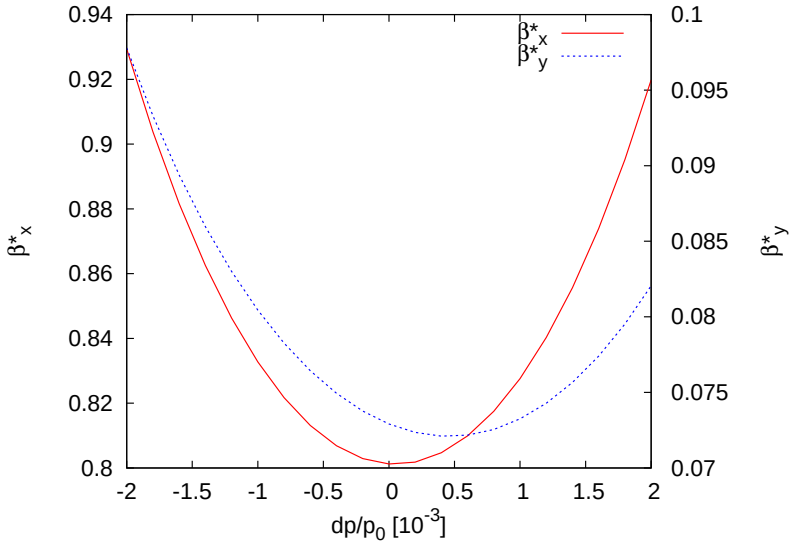

Figure 4.37: Off-momentum $\beta^*_{x,y}$ versus the relative momentum deviation δ, with 2 families of sextupoles.

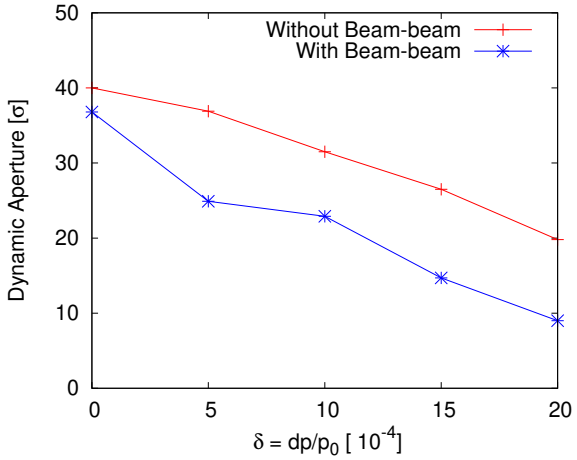

Figure 4.38: 10^6 turn dynamic aperture with and without the beam-beam interaction.

4.5.2 Dynamic Aperture with and without Beam-Beam Interaction

To evaluate the proton dynamic aperture, we use the symplectic particle tracking code SimTrack [209], which has been used for the dynamic aperture calculation for RHIC. It provides 6-D symplectic orbit tracking with 4th order symplectic integration for magnet elements and a 6-D symplectic synchro-beam map for the beam-beam interaction. RHIC studies indicated that 10^6 turns of tracking are sufficient for dynamic aperture studies. We used two sets of RF cavities, 6 MV of 197 MHz RF cavities and 20 MV of 591 MHz RF cavities. As described above, we correct chromaticity with two sextupole families since the second order chromaticity is acceptable.

When including the beam-beam interaction in dynamic aperture tracking, we treat the electron bunch as a rigid 6-D Gaussian charge distribution. The electron bunch is sliced longitudinally into 5 pieces. In the following we assume a head-on collision between the proton and electron bunches since we will install crab cavities in both rings to restore the head-on collision at the IP. In future studies we will include the crossing angle and crab cavities in the calculation.

Figure 4.38 shows the 10^6 turn dynamic apertures with and without the beam-beam interaction. Protons are launched at $x' = 0$ and $y' = 0$, and along radial lines in the $(x/\sigma_x, y/\sigma_y)$ that are equally spaced in the $x > 0$, $y > 0$ quadrant. Without the beam-beam interaction, the on-momentum dynamic aperture is $30\,\sigma$. The off-momentum dynamic aperture at $\delta = 2 \times 10^{-3}$ is about $15\,\sigma$. With the beam-beam interaction, the on-momentum dynamic aperture drops to $21\,\sigma$ and to $9\,\sigma$ at $\delta = 2 \times 10^{-3}$.

Figure 4.39 shows the dynamic aperture with the beam-beam interaction as a function of electron bunch intensity. In this study, the relative energy deviation of the test particle is set to 2×10^{-3}. The design electron bunch intensity is 1.72×10^{11}. The dynamic aperture continues to drop with increased electron bunch intensity.

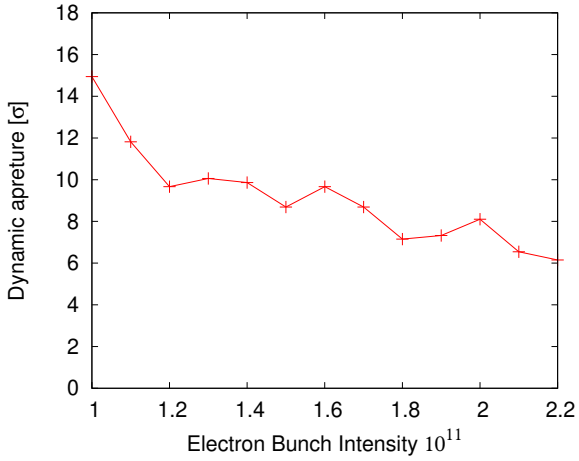

Figure 4.39: 10^6 turn dynamic aperture as a function of electron bunch intensity.

4.5.3 Dynamic Aperture with IR Nonlinear Magnet Field Errors

From operational experience in RHIC, nonlinear magnetic field errors in the interaction region magnets have a significant impact on the machine's dynamic aperture. Here we will perform some initial studies to estimate the tolerance for field errors in the interaction region magnets.

The measured magnet field errors are defined as

$$(B_y L)^M + i(B_x L)^M = B(R_r)L\left[10^{-4}\sum_{n=0}^{N_{max}}(b_n^M + ia_n^M)\frac{(x+iy)^n}{R_r^n}\right]. \tag{4.12}$$

Here L is the magnet length, R_r is the radius where the magnetic field is measured, $B(R_r)$ is the main field at R_r, b_n^M and a_n^M are the measured normal and skew magnetic components. For dipoles, $b_0^M = 10^4$. For upright quadrupoles, $b_1^M = 10^4$. Components other than these are field errors.

For a first study, we assign systematic field errors to all the interaction region dipole and quadrupole magnets. We only include sextupole errors in the dipoles and 12-pole errors in the quadrupoles and other multipoles that are located within 160 m from IP6. We assume R_r =25 mm in this study. Figure 4.40 shows the 10^6 turn dynamic aperture as a function of relative momentum deviation, including the beam-beam interaction, for systematic field errors of 1, 2, and 4 units. For small relative momentum deviations, the dynamic aperture is lower when the field errors are larger.

We also performed a study of random IR magnetic field errors. We randomly assigned sextupole and 12-pole errors to the IR dipoles and quadrupoles respectively, with a 2 unit RMS. The relative momentum deviation of the proton is set to 2.0×10^{-3}. Figure 4.41 shows the calculated 10^6 turn dynamic aperture, including the beam-beam interaction, for

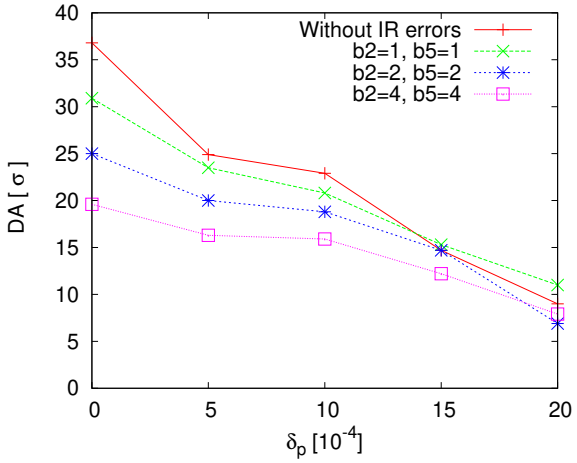

Figure 4.40: Calculated 10^6 turn dynamic aperture with beam-beam interaction and systematic IR nonlinearities.

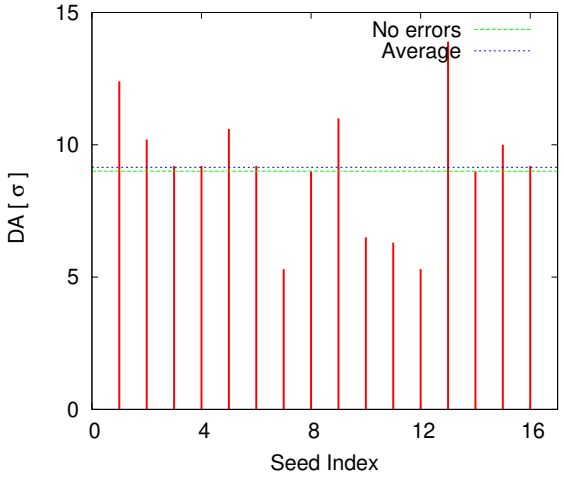

Figure 4.41: 10^6 turn dynamic aperture, including the beam-beam interaction, for 16 random IR magnet error seeds.

each seed. The average dynamic aperture with this random error is 9.1σ, with a RMS variation $\pm 3.3\sigma$. Among the 16 seeds, the lowest dynamic aperture was 5.3σ.

Based on the experience of RHIC and other hadron colliders, nonlinear correctors, either directly wound in the superconducting IR magnets or as stand-alone correctors outside of IR magnets, are needed for IR nonlinearity correction. The strengths of those correctors can be set based on magnet measurements or from online beam based measurements. The best way to include such correctors in the IR will be a subject of future studies.

4.6 Beam-Beam Effects

4.6.1 Introduction

Luminosity and the Beam-beam Interaction

The luminosity characterizes the number of physics events produced per unit cross section per second during the collision between two beams. For beams with a transverse Gaussian distribution, the luminosity is

$$L = \frac{N_p N_e f_c}{2\pi\sqrt{\sigma^{*2}_{p,x} + \sigma^{*2}_{e,x}}\sqrt{\sigma^{*2}_{p,y} + \sigma^{*2}_{e,y}}} H(\beta^* s, \sigma_l s, ...) \tag{4.13}$$

Here N_p and N_e are the proton and electron bunch intensities, f_c is the bunch collision frequency per second, and $\sigma^*_{e,p,x,y}$ the electron and proton bunches' RMS horizontal and vertical beam sizes at the interaction point (IP). H is a luminosity reduction factor arising from the hour-glass effect, crossing angle, and other effects.

During the collision, the motion of charged particles from one bunch will be affected by the electric and magnetic fields from the opposite bunch. The beam-beam parameter characterizes the strength of the beam-beam interaction force. For Gaussian beams, the beam-beam parameter is defined as

$$\xi_{e,p,z} = \frac{N_{p,e} r_{e,p}}{\gamma_{e,p}} \frac{\beta^*_{e,p,z}}{2\pi\sigma^*_{p,e,z}(\sigma^*_{p,e,x} + \sigma^*_{p,e,y})}, \tag{4.14}$$

where $z = x, y$ denotes the horizontal or vertical plane, $r_{e,p}$ the classical radius of the electron or proton, $\gamma_{e,p}$ the relativistic Lorentz factor of the respective beam, $\beta^*_{e,p,z}$ the electron and proton *beta*-function at the IP, and $\sigma^*_{e,p,z}$ the RMS beam sizes at the IP.

To increase the luminosity, we can increase the bunch intensities $N_{e,p}$, decrease the beam sizes $\sigma^*_{e,p,z}$ at the IP, or increase the bunch collision frequency. As Equation 4.14 shows, the first two methods will increase the beam-beam parameter. The beam-beam interaction leads to

- The dynamic β effect, where the β-function and size change due to focusing provided by the oncoming beam;
- The incoherent beam-beam tune shift, where particles at the core of the beam see additional focusing from the oncoming beam, while particles in the transverse tails see no additional focusing;
- Nonlinear beam-beam resonances, because the highly nonlinear nature of the beam-beam force results in strong nonlinear driving terms in the forces experienced by individual particles;

- Coherent beam-beam motion, because each beam is effected by the other and therefore must be seen as a single system of the two beams, the eigenmodes of which are potentially unstable.

Beam-beam effects can lead to particle loss, emittance blow-up, and coherent beam-beam instabilities, all of which can lead to luminosity reduction and poor luminosity lifetime.

For the EIC design, we set the maximum beam-beam parameter ξ to be 0.1 for the electron beam and 0.015 for the proton beam. The choice of the maximum beam-beam parameter for the electron ring is based on the successful operational experience of the electron-position collider KEKB, where it was achieved with a transverse radiation damping time of 4000 turns. The maximum beam-beam parameter for the proton ring is based on the successful operational experience during the RHIC polarized proton runs, where a beam-beam parameter of $\xi_p = 0.015$ was routinely achieved. However, such large beam-beam parameters together have never been demonstrated simultaneously in previous electron-proton colliders. The main goal of numerical beam-beam simulation studies for the EIC is to verify the feasibility of our design parameters to help guide changes in those parameters that might further improve the machine performance.

Crossing Collision with Crab Cavities

From Equation 4.13, the luminosity can also be increased by raising the frequency of bunch collisions. This is realized by increasing the number of bunches in each ring, which will decrease the longitudinal distance between adjacent bunches for a given ring circumference. To avoid parasitic collisions and to minimize the distance of the final focusing elements from the IP for both beams, the beams cross at a horizontal angle of 25 mrad at the IP.

To compensate the luminosity loss due to the non-zero crossing angle, crab cavities tilt the proton and electron bunches in the z-x plane by half of the full crossing angle to restore head-on collisions at the IP. Ideally, the crabbing force should be proportional to the longitudinal position of each individual particle in the bunch. For each ring, two sets of crab cavities are to be installed, ideally in a non-dispersive location, one on each side of the IP. The horizontal betatron phase advance between the IP and the crab cavities should be $\pi/2$ to close the z-x orbit bump. Figure 4.42 shows the local crabbing compensation scheme.

The crab cavities on each side of the IP will tilt the protons or electrons by 12.5 mrad in the z-x plane. The total voltage required in the RF cavities on each side of the IP is given by

$$\hat{V}_{\mathrm{RF}} = -\frac{cE_s}{4\pi f_{\mathrm{RF}}\sqrt{\beta_x^*\beta_{cc}}}\theta_c. \tag{4.15}$$

Here c is the speed of light, E_s is the particle energy in eV, f_{RF} is the crab cavity frequency, and θ_c is the full crossing angle. β_x^* and β_{cc} are the β-functions at the IP and the crab cavity, respectively. From Equation 4.15, raising the crab cavity frequency lowers the required crab cavity voltage, and larger horizontal β-functions at the IP and/or the crab cavity location reduce the required crab cavity voltage as well.

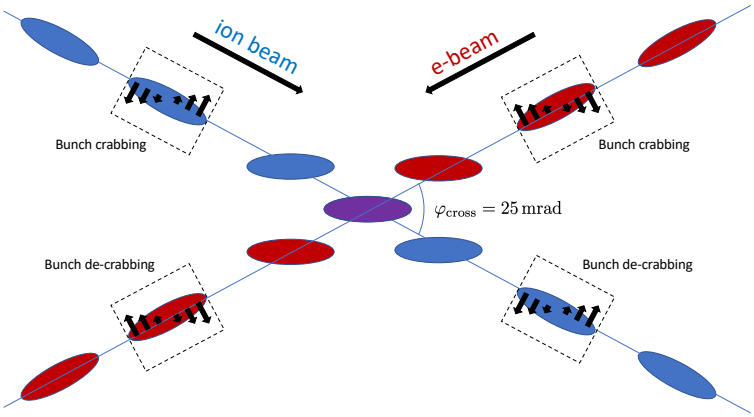

Figure 4.42: Schematic overhead view of collision between bunches separated by a crossing angle and optimized by crab cavities.

For crabbed crossing collision, when the bunch length is comparable with the wavelength of the crab cavity, the sinusoidal waveform of the crab cavity voltage generates a horizontal offset at the IP as function of longitudinal position of individual particles. As a result the entire bunch will not be crabbed perfectly onto the z axis along its entire length. A lower crab cavity frequency would provide a more uniform crabbing than a higher frequency, but a lower frequency crab cavity has a larger physical size and would require a higher crabbing voltage for a given crabbing angle.

At present, we are considering two crab cavity frequencies for the EIC: 197 MHz and 394 MHz. Based on beam-beam simulation studies, a 197 MHz crab cavity frequency is required for the proton ring to maintain an acceptable proton beam lifetime in collision. 394 MHz cavities can be added to further flatten the proton bunch at the IP and improve the proton beam lifetime. Due to the short electron bunch length, only 394 MHz crab cavities are required in the electron ring.

394 MHz is close to the 400 MHz frequency of the crab cavities used for the LHC High Luminosity Upgrade program. Brookhaven National Laboratory originally designed these crab cavities and actively participated in beam tests of the cavities in the PS accelerator at CERN. We benefit from the experience gained at CERN with the 400 MHz crab cavity design, manufacture, and commissioning. The 197 MHz crab cavity requires a larger physical size than 394 MHz crab cavity.

Simulation Methods and Tools

Both strong-strong and weak-strong beam-beam simulation methods have been used for EIC beam-beam interaction studies. The goal of these studies is to verify that the chosen machine parameter achieve the design luminosity with an acceptable luminosity lifetime, and to further adjust the machine parameters to improve performance. For the strong-strong simulation, we mostly use BeamBeam3D [26] and BBSS [25]. Weak-strong simulations were performed using SimTrack [209].

BeamBeam3D is a parallel three-dimensional particle-in-cell code to model beam-beams effects in high energy colliders. This code includes a self-consistent calculation of the electromagnetic forces from two colliding beams, a linear transfer map model for beam transport between collision points, a stochastic map to treat radiation damping and quantum excitation, and a single map to account for chromaticity effects. The beam-beam forces are calculated by solving the Poisson equation using a Green's function based algorithm.

BeamBeam3D also includes a soft-Gaussian model to speed up strong-strong simulations. It can also model a crab cavity. The code can handle multiple bunches in each beam and collisions at multiple interaction points. The parallel implementation is done using a particle-field decomposition method to achieve a good load balance. BeamBeam3D has been applied to studies of the beam-beam effect at RHIC, the Tevatron, the LHC, PEP-II, and KEK-B.

SimTrack is a compact C++ library for 6D symplectic element-by-element particle tracking in high energy accelerators. It was originally designed for head-on beam-beam compensation simulation studies in RHIC. The code uses 4th order symplectic integration to perform 6D orbit tracking through magnetic elements. Both 4D and 6D symplectic beam-beam interaction models are implemented. Collisions with a crossing angle and simulation of crab cavities were recently implemented in the code. Since SimTrack is a library-based code, it is straightforward to use and modify it to study various physics problems. SimTrack has been extensively used for linear and nonlinear optics calculations, single particle orbit tracking, particle loss map calculations, dynamic aperture computation, and beam-beam interactions and compensation in RHIC.

In a weak-strong beam-beam model, the strong bunch is assumed rigid and the weak beam is represented by macro-particles. Therefore, weak-strong beam-beam simulation is not self-consistent because the force of the weak beam on the strong beam is ignored. Normally, the rigid beam is assumed as a 6D elliptical Gaussian distribution and the beam-beam force of the strong beam on each particle in the weak beam is calculated using an analytical solution. In a strong-strong beam-beam model, both beams are represented by large numbers of macro-particles. The beam-beam forces are calculated by solving the Poisson equation using the particle-in-cell method. In contrast to a weak-strong simulation method, a strong-strong beam-beam model is self-consistent. However, it needs much more computing time and is inherently subject to numerical noise. Strong-strong simulations are mostly used to determine luminosity and beam sizes after equilibrium is reached. It is an indispensable tool to study coherent beam-beam motion and instability. For the study of long-term proton beam stability and dynamic aperture, in the absence of coherent beam-beam effects, we use weak-strong beam-beam simulations to reduce simulation time and the impact of numerical noise.

Beam-beam Related Design Parameters

In the EIC, there are several different configurations that have different combinations of electron and ion beam energies. In the following, we will only discuss collisions between

275 GeV protons and 10 GeV electrons, which is the configuration with the highest luminosity, reaching $1 \times 10^{34}\,\mathrm{cm}^{-2}\mathrm{sec}^{-1}$. This combination also requires the highest beam-beam parameter for both the proton and electron beams among all configurations. For other configurations, the required beam-beam parameters are smaller than for this combination. The beam-beam interaction at those other collision energies will be studied later.

There are several constraints on the choice of machine parameters:

- The proton and electron beam currents are limited to 1 A and 2.5 A, respectively;
- The proton and electron beam-beam tune shifts must not exceed 0.015 and 0.1, respectively;
- A maximum electron beam divergence of 220 µrad
- For the proton beam, $\beta_x^* \geq 90$ cm, $\beta_y^* \geq 5$ cm
- For the electron beam, $\beta_x^* \geq 35$ cm, $\beta_y^* \geq 4$ cm
- A minimum intrabeam scattering (IBS) growth time for the protons of 2 h.

We use the luminosity, its degradation rate, and the proton beam growth rates to evaluate performance for a given set of machine parameters. Due to radiation damping, the electron beam reaches a stable equilibrium distribution, with a transverse damping time of 4000 turns for our machine design. Growth rates in the electron beam are thus ignored, and the above parameters are evaluated well after the electron beam has reached equilibrium. Our studies showed that flatness, defined as the ratio of the vertical to the horizontal RMS beam sizes at the IP, is an important parameter characterizing the impact of the beam-beam interaction. A smaller value of the flatness at the IP will lead to a higher instantaneous luminosity, but will also lead to a more rapid growth in the vertical beam size. We found that to reach the design luminosity of $1 \times 10^{34}\,\mathrm{cm}^{-2}\mathrm{sec}^{-1}$, a flatness of 0.09 appeared to be near optimal. Table 4.15 lists the beam-beam interaction related design parameters for the simulation studies.

Our studies also showed that matching between the sizes of the two beams at the IP affects the vertical beam size growth rate. The electron beam size changes due to focusing from the beam-beam interaction during the collision, while the impact on the proton beam is significantly smaller. To match the beam sizes of proton and electron bunches at the IP, including the effects of the beam-beam interaction, we must adjust the horizontal $\beta*_x$ of the electrons as computed without the beam-beam interaction from its design value of 45 cm (shown in Tab. 4.15) to 55 cm, and the initial vertical emittance of the electrons from 1.3 nm to 1.1 nm. These corrected values are used in strong-strong beam-beam simulations along with radiation damping and quantum excitation effects. In weak-strong simulations, where the size and shape of the electron distribution is not affected by the beam-beam interaction, we use the beam parameters shown in Table 4.15.

Table 4.15: Machine and beam parameters used for the beam-beam interaction study.

Parameter	proton	electron
Ring circumference [m]	3833.8451	
Particle energy [GeV]	275	10
Lorentz energy factor γ	293.1	19569.5
Bunch population [10^{11}]	0.688	1.72
RMS emittance (H,V) [nm]	(11.3, 1.0)	(20.0, 1.3)
β^* at IP (H, V) [cm]	(80, 7.2)	(45, 5.6)
RMS bunch size σ^* at IP (H, V) [µm]	(95, 8.5)	
RMS bunch length σ_l at IP [cm]	6	2.0
Beam-beam parameters (H, V)	(0.012, 0.012)	(0.072, 0.1)
RMS energy spread [10^{-4}]	6.6	5.5
Transverse tunes (H,V)	(29.228, 30.210)	(51.08, 48.06)
Synchrotron tune	0.01	0.069
Longitudinal radiation damping time [turn]	-	2000
Transverse radiation damping time [turn]	-	4000
Luminosity [$10^{34}\text{cm}^{-2}\text{s}^{-1}$]	1.0	

4.6.2 Beam-Beam Simulation with Crabbed Collision

Dynamic β^* Effect with Linear Crabbing

As mentioned above, the beam size of the electron beam changes during the beam-beam collision; we refer to this as the dynamic β^* effect. Because the focusing from the beam-beam collision is different depending on where a particle passes through the opposite beam, there is a strong variation of the focusing strength with particle position, leading to a large increase in tune spread in the beam. In this section we present calculations of these two effects with crab crossing, but where the crabbing effect of the crab cavity is perfect linear (not taking into account the finite RF wavelength). In strong-strong simulations, we did not observe any difference in the results when we used this perfectly linear crabbing from the results for head-on collisions. We will show the tune footprint and frequency map analysis using crab cavities with a finite RF wavelength in the next section.

The dynamic β^* effect can be computed to first order by treating the beam-beam interaction as a thin-lens focusing element; this will change the one-turn linear map from what it was without the beam-beam element, and thereby change the ring tune and the β^* at the IP. Figure 4.43 shows the perturbed β^* and tune changes of the perturbed electron ring versus the lattice tunes when the beam-beam element is absent. When the design tunes are very

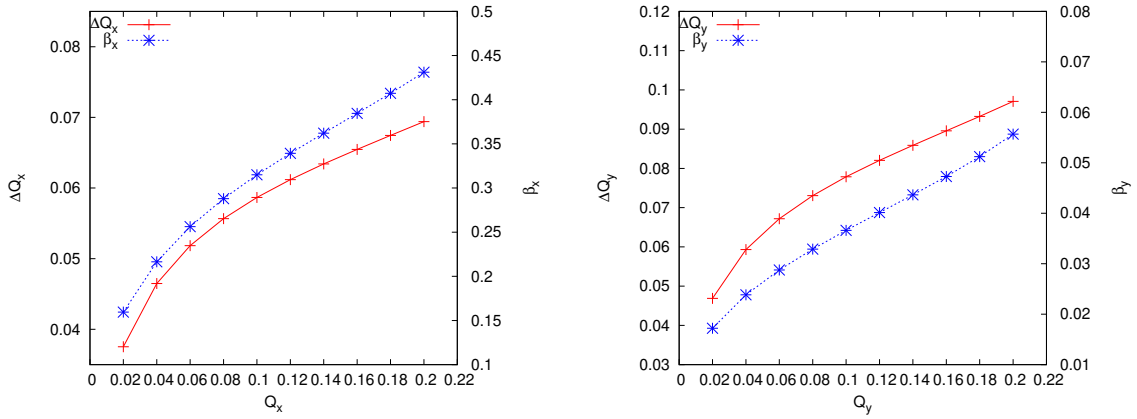

Figure 4.43: β^* and tune changes when the beam-beam effect is added to the lattice, plotted as a function of the tune values without the beam-beam interaction. The beam-beam interaction is treated as a thin focusing element.

close to an integer, the actual β^* in the presence of the beam-beam interaction will become smaller than the design values of the bare lattice. The unperturbed electron $\beta^*_{e,x,y}$ are 45 cm and 5.6 cm, respectively. For electron tunes of $(0.08, 0.06)$, the beam-beam interaction modifies $\beta^*_{e,x,y}$ to 29 cm and 2.9 cm, resp. The tune shifts caused by the beam-beam interaction are smaller than the beam-beam parameter computed with Equation 4.13 as well. For the electron tunes $(0.08, 0.06)$, the design beam-beam parameters $\xi_{e,x,y}$ are $(0.072, 0.10)$. With beam-beam interaction, the actual beam-beam tune shifts are much smaller, $(0.056, 0.067)$.

Tune Footprints with Linear Crabbing

Since the field gradient a particle sees when passing through the opposite beam depends on position, the beam-beam effect creates a large tune dependence on transverse amplitude. The particles at the bunch core experience a large tune shift, while the particles with a larger amplitude will have a smaller tune shift. If we plot the tunes of all the particles in a bunch in a 2D tune diagram, they will occupy an area which is called a tune footprint. The width of the tune footprint or tune distribution is the tune spread. The tune spread is dominated by the contribution from the beam-beam interaction.

Figure 4.44 shows the tune footprints of the proton and electron beams when the beam-beam interaction is included. The bare lattice tunes are $(0.228, 0.210)$ for the proton ring and $(0.08, 0.06)$ for the electron ring. In the plot, different colors indicate different orders of magnitude of tune diffusion during 2048 turns of particle tracking for test particles launched in the $(x/\sigma_x, y/\sigma_y)$ plane up to 6σ. The tune diffusion is defined as

$$\Delta Q = \sqrt{\Delta Q_x^2 + \Delta Q_y^2}, \tag{4.16}$$

where $\Delta Q_{x,y}$ are the differences between the tune averages in the first 1024 turns and the

last 1024 turns. Electrons with large transverse amplitude have tunes close to the integer and a large tune diffusion. Large tune diffusion is an indicator of chaotic particle motion. One can also observe resonance lines crossing the electron tune footprint in the plot. The resonance structure for the proton beam is discussed in Section 4.6.2.

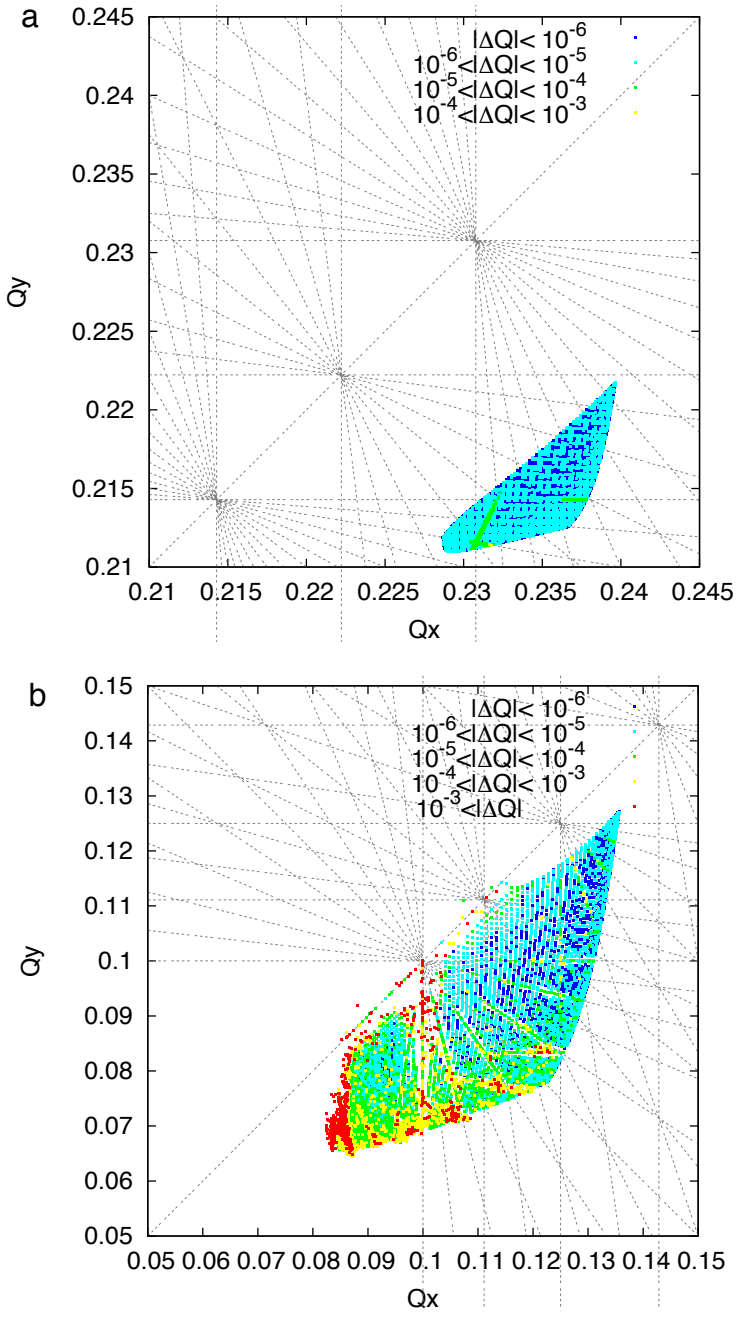

Figure 4.44: Tune footprints of (a) proton beam and (b) electron beam.

Luminosity and Beam Size Evolution

Figure 4.45 shows an example of particle distributions in the z-x plane at the IP from a strong-strong beam-beam simulation. For this calculation, we used 197 MHz crab cavities for the proton ring and 394 MHz crab cavities for the electron ring. The horizontal β-functions at the crab cavity locations are 1200 m for the protons and 150 m for the electrons. The required total crab cavity voltages on each side of IP are 26.9 MV for the protons and 1.7 MV for the electrons. As shown in the plot, the protons in the head and tail of the bunch are not crabbed completely onto the z-axis due to the sinusoidal waveform of the crab-cavity voltage.

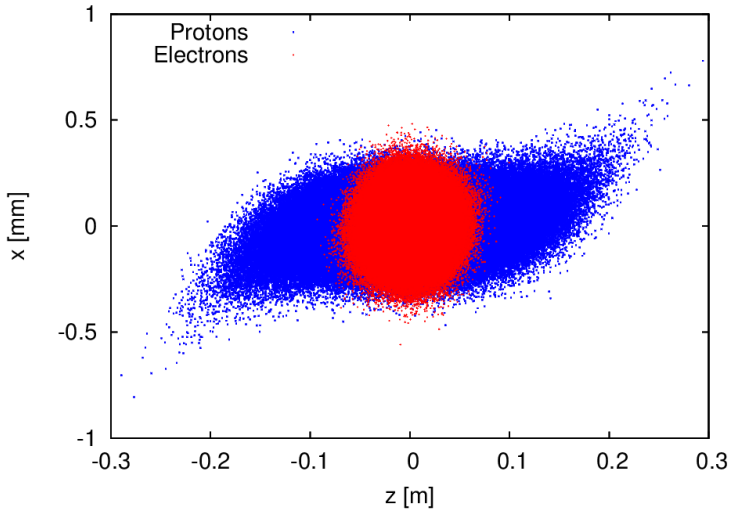

Figure 4.45: Proton (blue) and electron (red) particle distributions in the z-x plane at the IP.

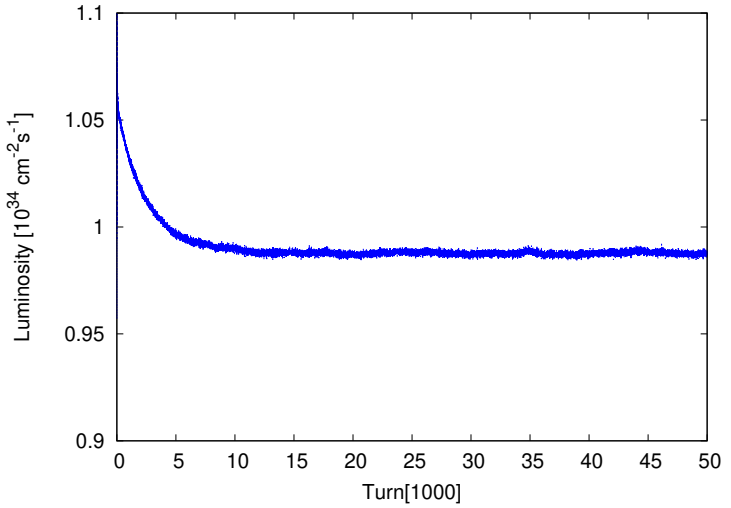

Figure 4.46: Luminosity evolution from a strong-strong beam-beam simulation.

We set the proton tunes to $(0.228, 0.210)$ and the electron tunes to $(0.08, 0.06)$. We deliberately let the electron vertical beam size be about 10% larger than that of the proton beam to obtain a lower vertical proton beam size growth rate. The luminosity after reaching equilibrium is about $0.99 \times 10^{34}\,\mathrm{cm}^{-2}\mathrm{sec}^{-1}$. Figures 4.46 to 4.48 show the evolution of the luminosity and the beam sizes over 50,000 turns.

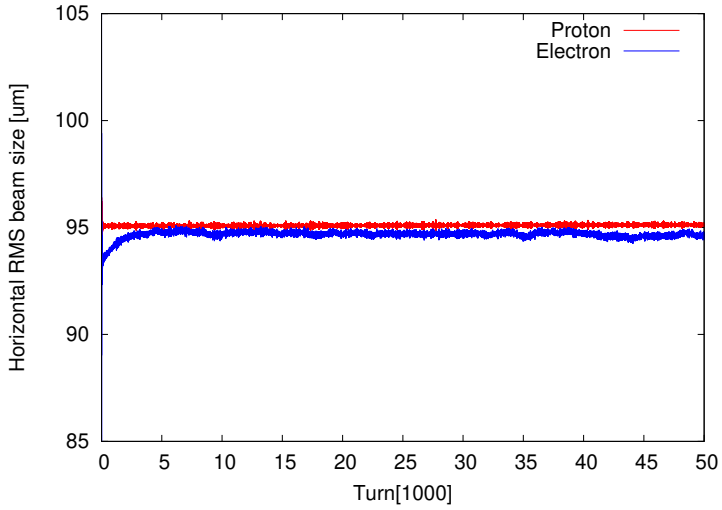

Figure 4.47: Evolution of horizontal beam sizes of both beams from a strong-strong beam-beam simulation.

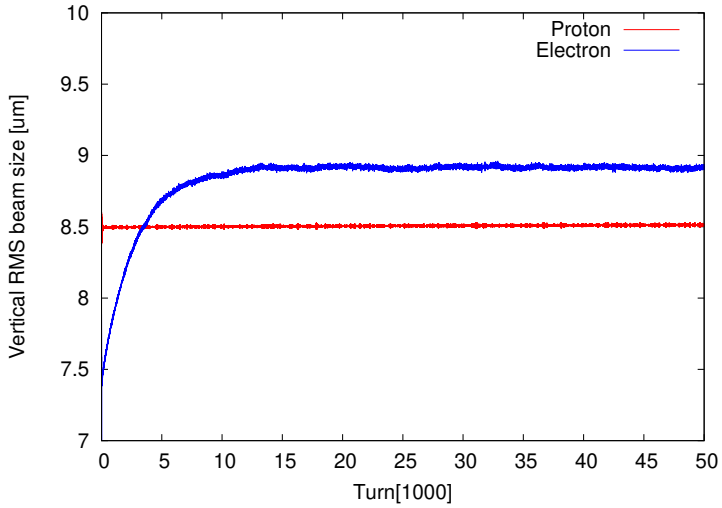

Figure 4.48: Evolution of vertical beam sizes of both beams from a strong-strong beam-beam simulation.

The exact value of the luminosity depends slightly on the machine and beam parameter settings. If we exactly match the vertical beam sizes of the proton and electron beams at the IP, the luminosity reaches $1.03 \times 10^{34}\,\mathrm{cm}^{-2}\mathrm{sec}^{-1}$. For electron tunes of $(0.07, 0.139)$, the resulting luminosity is $1.07 \times 10^{34}\,\mathrm{cm}^{-2}\mathrm{sec}^{-1}$. However, for both of these parameter changes,

the proton vertical emittance grows faster than it does for the slightly larger electron vertical beam size and electron tunes of $(0.08, 0.06)$. Second order harmonic crab cavities in the proton ring are under consideration, which will deliver a luminosity $1.03 \times 10^{34}\text{cm}^{-2}\text{s}^{-1}$ and reduce the proton emittance growth rate.

Proton Crab Cavity Frequency Choice

In Figure 4.49, we show the centerline of the proton bunch at the IP after passing through the crab cavities for three frequency combinations for the crab cavities: 197 MHz alone, 394 MHz alone, and a combination of 197 MHz and 394 MHz cavities. For the latter case, to achieve the 12.5 mrad crab angle, the voltage in the 197 MHz cavities is set to create a crab angle of 1.4×12.5 mrad, while the voltage in the 394 MHz crab cavities is set to create a crab angle of -0.4×12.5 mrad. The horizontal offset at $\pm 3\sigma_l$ longitudinally is reduced by a factor of 3.7 when using a 197 MHz crab cavity frequency relative to the offset for a frequency of 394 MHz. With both frequencies, the horizontal offset is reduced by another factor of 14 from the case where there are only 197 MHz cavities, leading to an offset at $\pm 3\sigma_l$ of only 14 µm, which is small compared to the design horizontal RMS beam size at the IP of 95 µm.

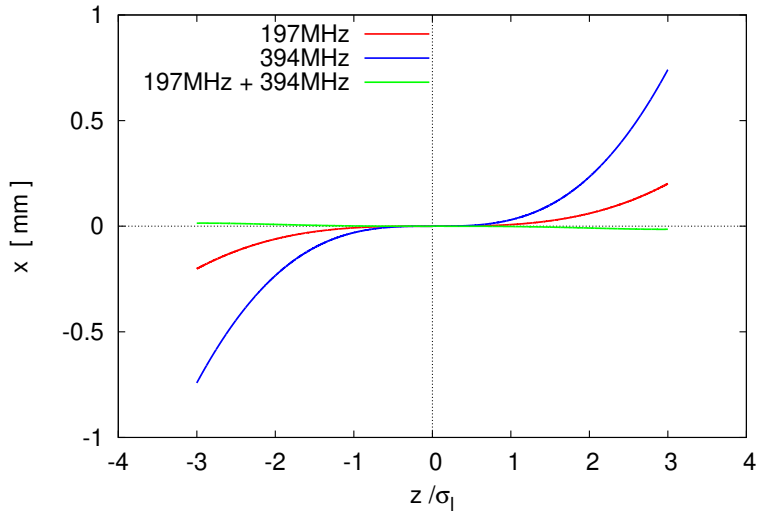

Figure 4.49: Proton bunch shapes in the z-x plane with different crab cavity frequency combinations.

Figure 4.50 shows the luminosity evolution from strong-strong simulations for the three different proton crab cavity frequency combinations described above. In this study, the electron beam is always crabbed with 394 MHz crab cavities. With 394 MHz proton crab cavities, the equilibrium luminosity is 88% of that with linear crabbing. With 197 MHz crab cavities, the luminosity is 97% of that with linear crabbing. With both 197 MHz and 394 MHz combined, the luminosity is the same as for the linear crabbing case.

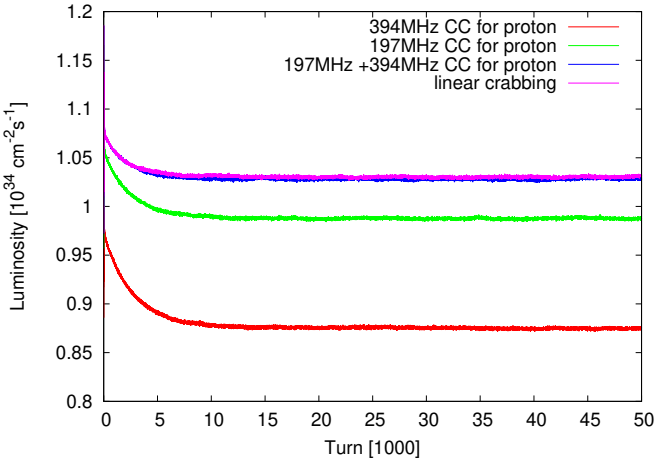

Figure 4.50: Luminosity evolution with different proton crab cavity frequency combinations.

Electron Crab Cavity Frequency Choice

In the present design, the RMS electron bunch length is 2.0 cm, which is 3 times shorter than the RMS proton bunch length of 6.0 cm. Figure 4.51 shows the luminosities with 197 MHz, 394 MHz, or no electron crab cavities. All cases use 197 MHz crab cavities for the protons. Crab cavities for the electron ring are clearly needed, as without them the luminosity would be reduced by a factor 3, but the 197 MHz cavities provide negligible improvement over the 394 MHz cavities. 394 MHz cavities are significantly smaller and less costly than 194 MHz cavities, and the higher frequency means a lower cavity voltage is needed. We will therefore use 394 MHz crab cavities in the electron ring.

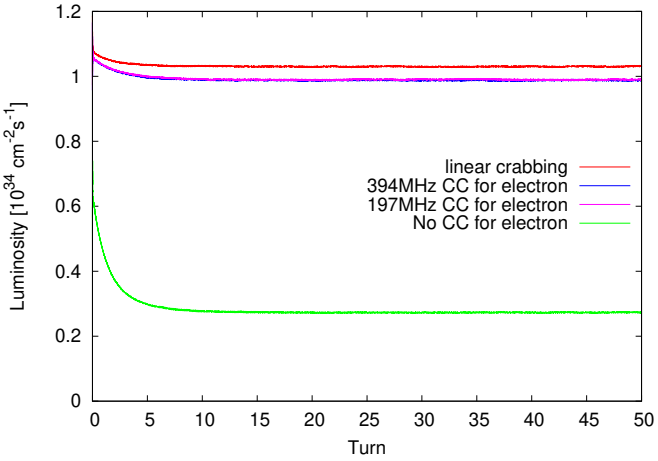

Figure 4.51: Luminosity evolution with and without electron crab cavities. Two different crab cavity frequencies are shown, and the lines for those two frequencies almost coincide.

Beam-beam Limit

The beam-beam limit is defined as the maximum beam-beam parameter that a collider can achieve and sustain over long periods of time. After the beam-beam limit is reached, the luminosity will no longer increase linearly with the bunch intensity since the beam emittance blows up due to the strong nonlinear beam-beam interaction.

Figure 4.52 shows the luminosity as function of the proton bunch intensity N_p. The proton bunch intensity is scanned from 0.41×10^{11} up to 1.25×10^{11}. As the plot shows, the luminosity will deviate from its scaling linearly with the proton bunch intensity when the proton intensity exceeds 0.9×10^{11}, which is about 30% larger than the design proton bunch intensity of 0.688×10^{11}.

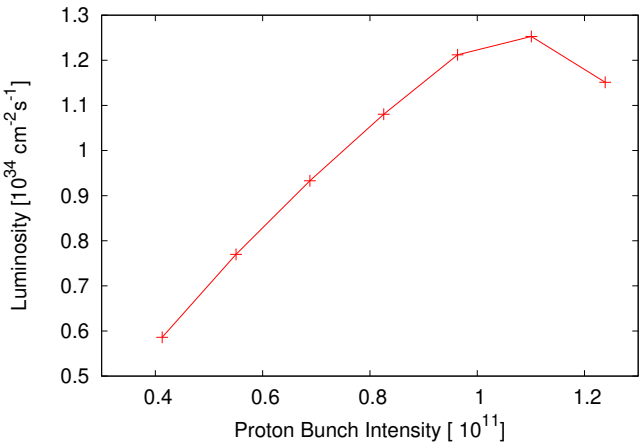

Figure 4.52: Luminosity as function of proton bunch intensity from strong-strong simulations.

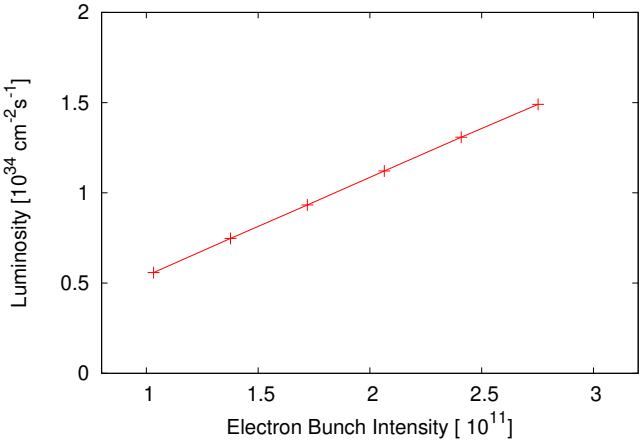

Figure 4.53: Luminosity as function of electron bunch intensity from strong-strong simulations.

Figure 4.53 shows the luminosity as function of the electron bunch intensity N_e. The electron bunch intensity is scanned from 1.0×10^{11} up to 2.7×10^{11}. As shown, the luminosity increases almost linearly with the electron bunch intensity in this range. The design electron bunch intensity is 1.72×10^{11}. However, with increased electron bunch intensity, we observed an elevated proton emittance growth rate. Since there is no radiation damping in the proton ring, any sizable proton emittance growth should be avoided.

Weak-Strong Electron Tune Scan

To determine a good tune choice for the electron ring in the presence of the beam-beam interaction, we performed weak-strong simulations for different values of the tune in the electron ring. Because of radiation damping and the dynamic-β effect, it is best to split the simulation into two passes. In the first pass, the proton bunch is rigid and the electron bunch is represented by macroparticles. In this pass, we obtain the luminosity and electron beam sizes after the electron beam reaches equilibrium. Then in a second pass, we assume that the electron bunch is rigid but with beam sizes derived from the first pass simulation; the protons are represented by macroparticles in this pass. The goal of this second pass is to assess the stability of the proton beam with the actual electron beam sizes. In these weak-strong simulations, the rigid bunch is always represented as an elliptically symmetric Gaussian distribution. 50,000 macroparticles are used for the weak bunch, and 50,000 turns of tracking are performed in each simulation.

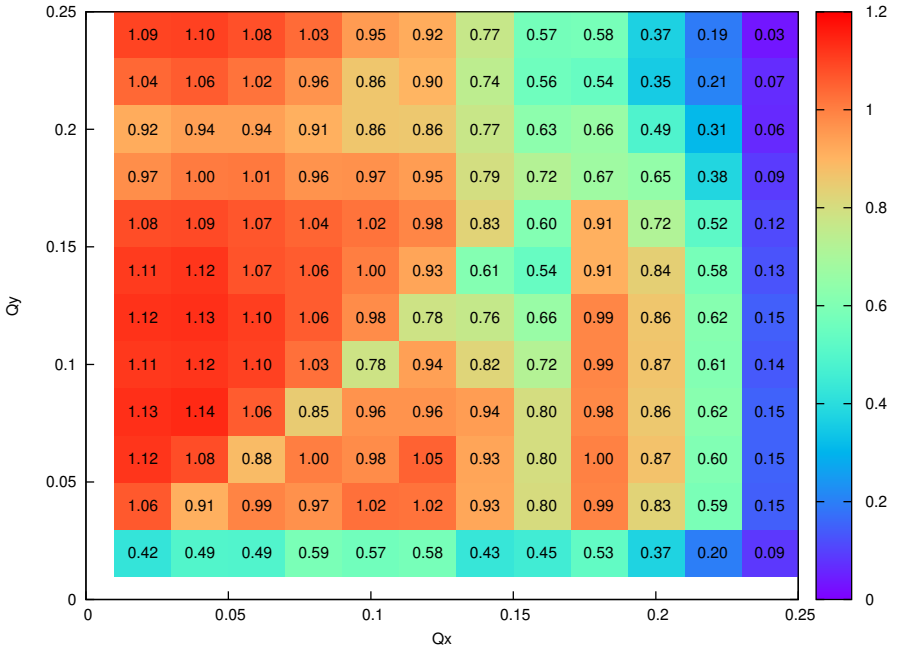

Figure 4.54: Luminosity, averaged over the last 1000 turns, as a function of electron tunes in the first pass weak-strong simulation. Values are in units of $10^{34}\,\mathrm{cm}^{-2}\mathrm{sec}^{-1}$.

Figure 4.54 shows the luminosity averaged over the last 1000 turns of tracking in the first

pass weak-strong simulation. Both the horizontal and vertical electron tunes are scanned between 0.02 and 0.25 with a step size of 0.02. Figure 4.55 shows the equilibrium vertical size of the electron bunch for that same grid of tunes. Figure 4.54 indicates that the luminosity is higher when the electron horizontal tune is close to an integer, which is a consequence of the dynamic-β effect.

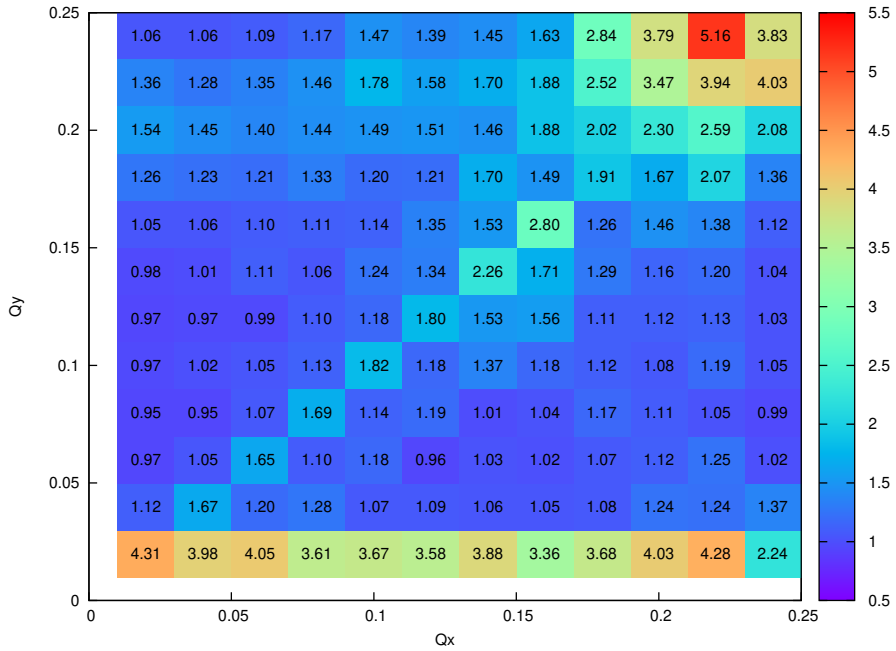

Figure 4.55: RMS vertical beam size of the electron bunch, divided by the design vertical size of 8.5 µm, after reaching equilibrium in the first pass weak-strong simulation.

In Figures 4.56 and 4.57 we show the results of the second pass weak-strong simulation, where the electron beam is the strong beam and the proton beam is the weak beam. The proton lattice tunes are set to $(0.228, 0.210)$. The figures show changes in the luminosity (Figure 4.56) and vertical proton beam size (Figure 4.57) between the first 1,000 turns and the last 1,000 turns of the simulation. The smaller the variation is, the more stable the beams are. The luminosity degradation is reduced when the electron horizontal tune is above 0.12. Increases in luminosity are the result of numerical noise. Vertical beam size growth is larger when the horizontal electron tune is closer to an integer. However, the instantaneous luminosity is higher for those tunes.

Strong-Strong Electron Tune Scan

Weak-strong simulations are not self-consistent since the distribution of one of the beams does not change; thus coherent modes involving motion of both beams would be missed in such simulations. We therefore repeat the electron tune scan using a strong-strong simulation. We scan the electron horizontal and vertical tunes from 0.02 through 0.20 in steps of 0.02. 197 MHz crab cavities are used in the proton ring, and 394 MHz crab cavities are

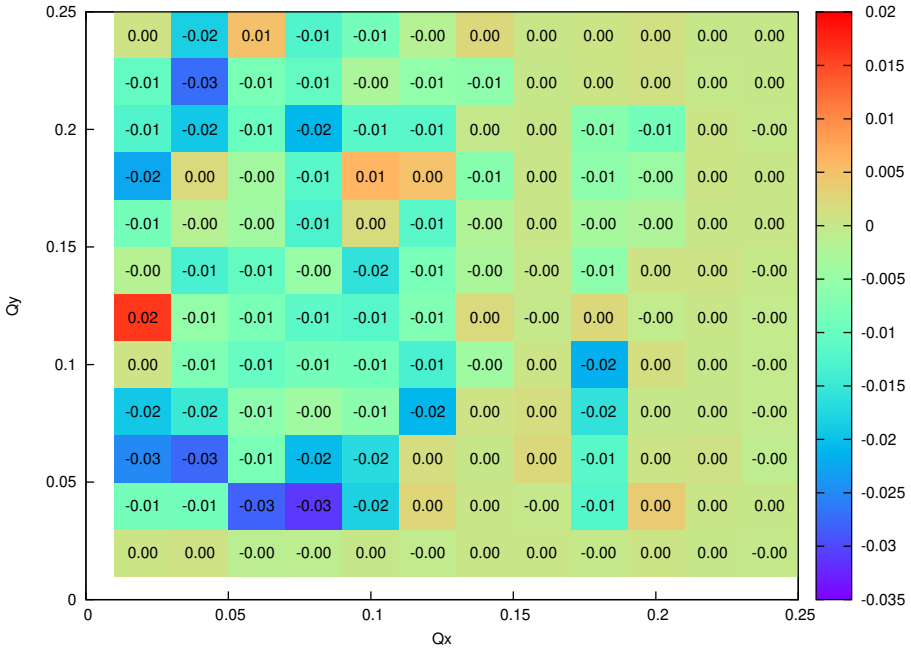

Figure 4.56: Relative luminosity variation in percent between the first and last 1000 turns for the second pass of the weak-strong electron tune scan.

used in the electron ring. 10^6 macroparticles are used for each bunch, and we track for 50,000 turns.

Figures 4.58 and 4.59 show the average luminosity in the last 1000 turns and the equilibrium vertical beam size, respectively, as function of electron tunes. We see that the luminosity is higher and the vertical beam size is smaller for smaller horizontal tunes and larger vertical tunes, showing a clear connection between these two quantities.

Figures 4.60 and 4.61 show the relative variation of the horizontal and vertical proton beam sizes from the beginning to the end of the simulation. We observe a larger proton beam size growth when the horizontal tune is around 0.06 and around 0.14. One possible reason is that the beam-beam interaction causes the tune footprint to overlap the 10th order resonance lines at 0.1 and 0.2.

We chose the fractional tunes $(0.08, 0.06)$ for the electron ring based on these tune scans and other considerations. Fractional tunes below 0.05 would be difficult to control in operation due to their proximity to the integer resonance. Tunes near the $\nu_x - \nu_y = m$ line, where m is an integer, can be in regions that are relatively free of low-order resonances. The region around $(0.08, 0.06)$ has among the best luminosities in both weak-strong and strong-strong simulations (Figures 4.54 and 4.58), and avoids resonance lines that show up in strong-strong simulations (Figures 4.60 and 4.61).

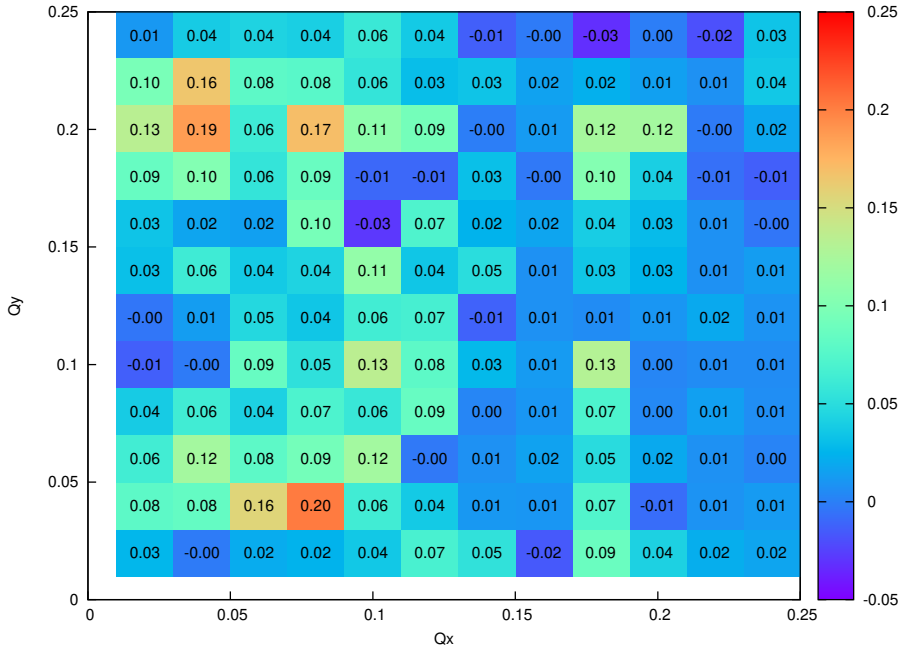

Figure 4.57: Relative proton vertical beam size variation in percent between the first and the last 1000 turns for the second pass of the weak-strong electron tune scan.

Proton Working Point Consideration

The proton working point for the routine RHIC polarized proton operation is between 2/3 and 7/10. For the EIC, since colliding beams have charges with opposing signs, the working point can be selected as (0.310, 0.305), which mirrors the tunes of the RHIC proton tunes below the half integer. However, there are many distinguishing features of the EIC, e.g. the large synchrotron tune of the ion beam, flat beams at the IP, and the crab crossing scheme. These features motivate the detailed tune scans shown in the previous section.

The crabbing tail of the proton beam may excite the synchro-betatron resonance. For working points around $(0.31, 0.305)$, the leading resonance for the horizontal motion is $3\nu_x + p\nu_z = 1$, where p is a positive integer. Theoretical studies and simulations suggest that the degradation improves if the tune moves to $(0.228, 0.224)$, between 2/9 and 1/4, where the leading resonance is $4\nu_x + p\nu_z = 1$.

In addition, the flatness of both beams (defined as σ_y/σ_x) at the IP is as low as 0.09 to achieve higher luminosity. The very flat beam makes the vertical direction more vulnerable to degradation due to synchro-betatron couplings as a result of the intrinsic nonlinear coupling effect of the beam-beam force as well as the hour-glass effect. The leading resonance for the vertical motion is $2\nu_x - 2\nu_y - p\nu_z = 0$. A typical working point close to the diagonal line, e.g. $(0.228, 0.224)$, excites low order, $p = 1$, synchro-betatron coupling resonances. Simulations have verified that moving the working point away from the diagonal line helps to improve the dynamics in the vertical plane. As a result, the working point $(0.228, 0.210)$ is proposed, where the resonance order increases to $p = 4$.

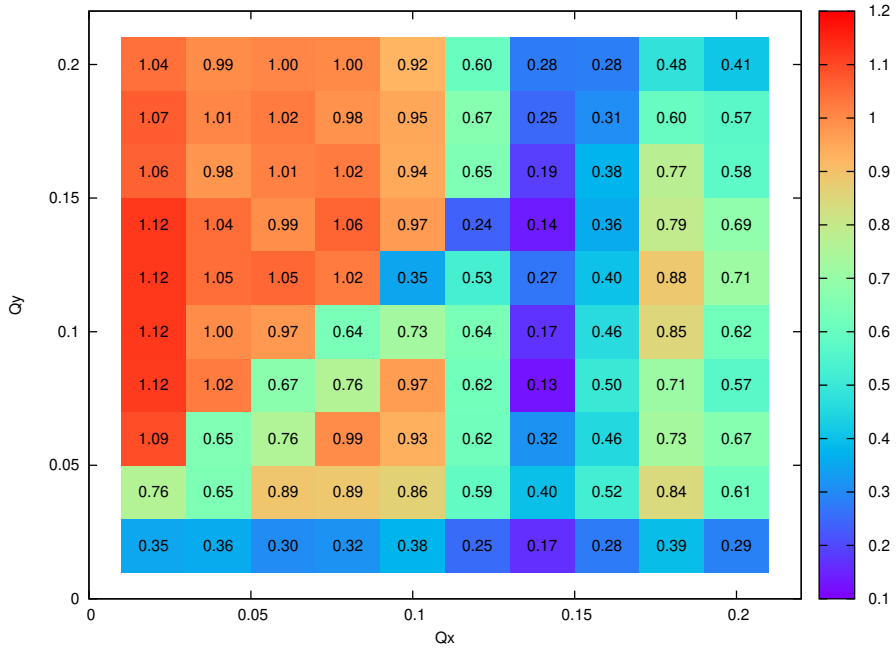

Figure 4.58: Luminosity averaged over the last 1000 turns of a strong-strong simulation as function of electron tunes. Values are in units of $10^{34}\,\mathrm{cm}^{-2}\mathrm{sec}^{-1}$.

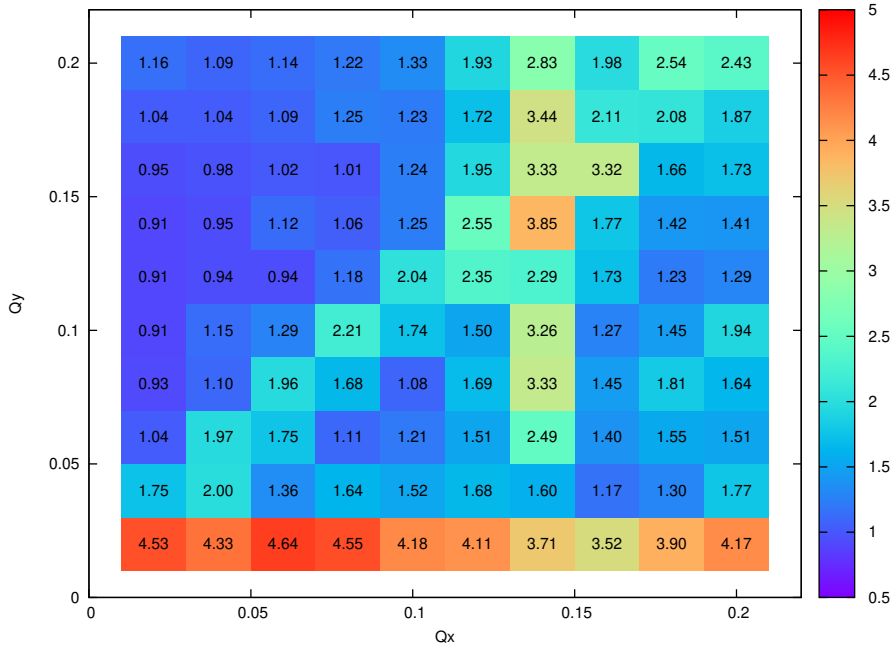

Figure 4.59: Equilibrium electron vertical beam size, divided by the design size of 8.5 µm, as function of electron tunes, from strong-strong simulations.

Figure 4.60: Relative proton horizontal beam size change in percent, computed as the fractional difference between the average size in the first 1000 turns and the last 1000 turns, as a function of electron tunes, from strong-strong simulations.

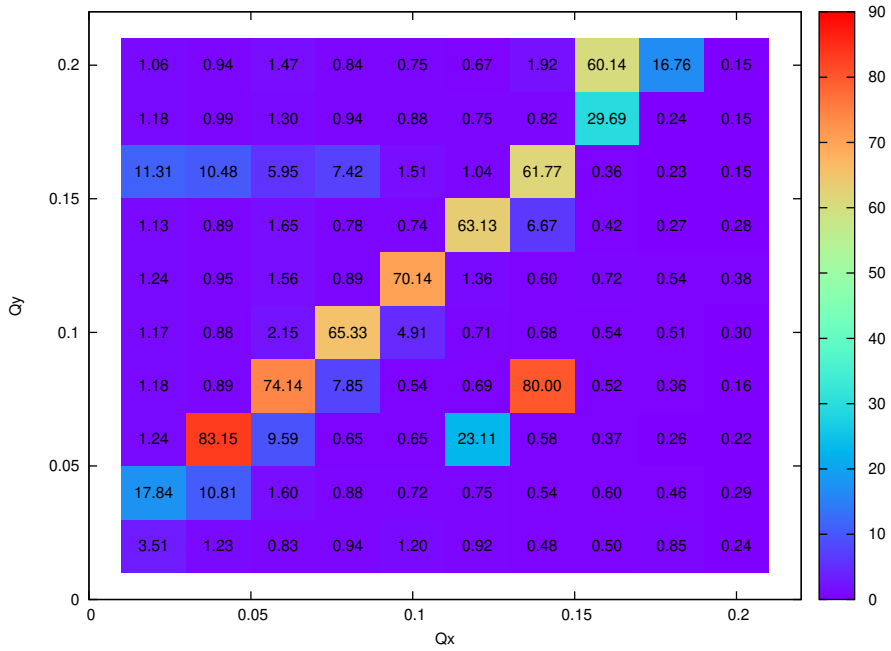

Figure 4.61: Relative proton vertical beam size change in percent, computed as the fractional difference between the average size in the first 1000 turns and the last 1000 turns, as a function of electron tunes, from strong-strong simulations.

Proton Stability with Crabbed Collision

For crabbed crossing collisions, when the bunch length is comparable with the wavelength of the crab cavity, the sinusoidal waveform of the crab-cavity voltage generates transverse offsets at the IP as function of the longitudinal position of individual particles within the bunch.

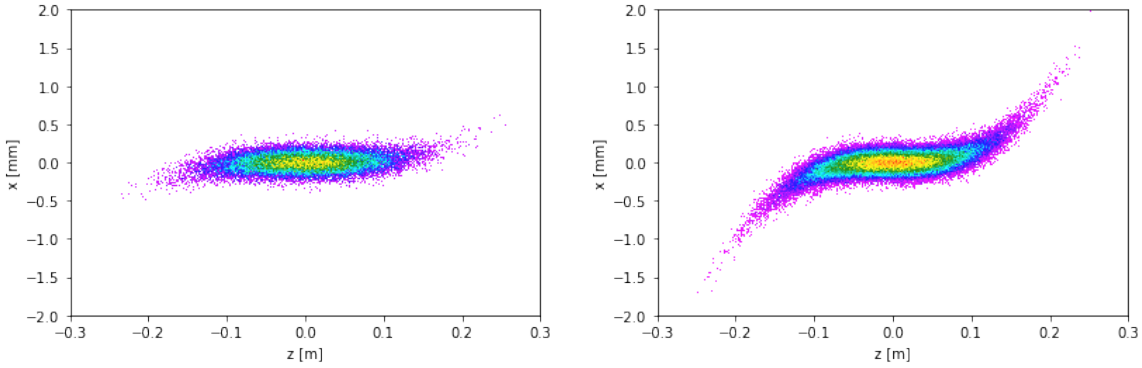

Figure 4.62: Proton beam $x - z$ distribution with 197 MHz (left) and 394 MHz (right) crab cavities.

A lower crab cavity frequency results in a more linear crabbing than a higher frequency. However, the low frequency crab cavity has a bigger physical size and requires a higher crabbing voltage. Figure 4.62 shows the comparison of the proton beam distribution (projection in x-z plane) with 197 MHz and 394 MHz crab cavity systems. The tails will excite synchro-betatron resonances via the nonlinear beam-beam interaction. To avoid excessive beam quality degradation, massive beam-beam simulations have been performed in order to understand the resonances and to optimize the design parameters.

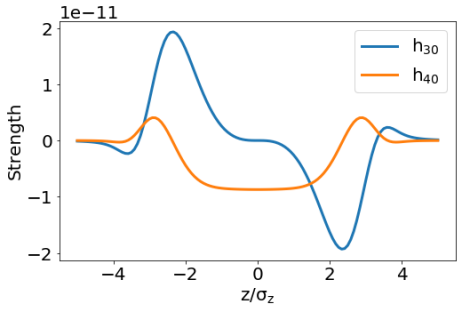

Figure 4.63: Spectrum of the horizontal centroid motion of the proton bunch with three different proton crab cavity frequencies.

- *Synchro-betatron Resonance*

  Many higher-order synchro-betatron resonances are excited in the crab-crossing collision scheme with a large crossing angle. This causes luminosity degradation and

should be avoided or mitigated in the design. If we choose the unperturbed working point around the diagonal resonance line $\nu_x - \nu_y = 0$, a family of synchro-betatron resonances $m\nu_x + p\nu_z = 0$ will be excited. The driving term strength h_{m0} can be calculated from the beam-beam Hamiltonian in the presence of the crab cavity, as shown by Figure 4.63. It shows that a larger m is preferable, which supports the tune change from below $1/3$ to below $1/4$.

- *Frequency Map Analysis*

  Frequency map analysis (FMA) is a powerful technique to visualize the impact of nonlinear resonances. This technique is applied after tracking test particles and recording their turn-by-turn positions for N turns. For each record, the data is split into two time windows, each of which has length $N/2$. The first time window starts from the beginning; while the second window starts from i^{th} turn, with $i \in [0, N/2]$. The frequency diffusion of horizontal motion is defined as:

$$dQ_x = \log_{10} \max_i \left| Q\left(x\left(0, \frac{N}{2}\right)\right) - Q\left(x\left(i, \frac{N}{2} + i\right)\right)\right| \tag{4.17}$$

  where Q is the frequency calculated by NAFF using the sequence in the argument. Similarly diffusion for vertical motion is also calculated.

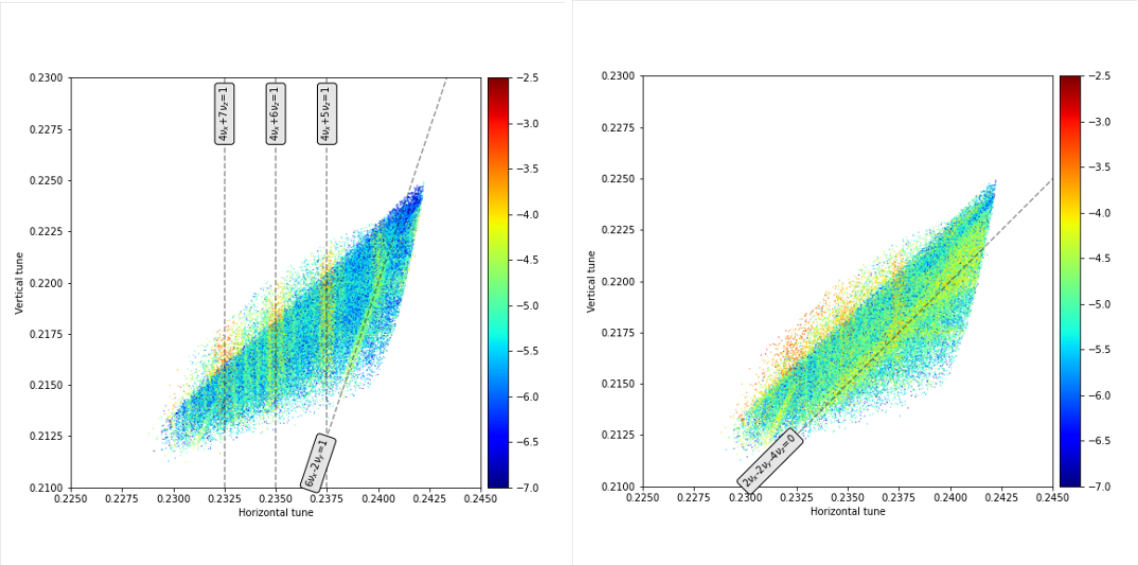

Figure 4.64: Frequency map analysis of proton beam with working point (0.228, 0.21). Left: horizontal diffusion; right: vertical diffusion

Figure 4.64 shows FMA plots of horizontal and vertical motion of working point $(0.228, 0.21)$. The data is calculated by the strong-strong simulation code BeamBeam3D using 1024 consecutive turns. This clearly shows that the horizontal motion has a dominating resonance at $4\nu_x + 5/6/7\nu_z = 1$, while the vertical motion has a resonance at $2\nu_x - 2\nu_y - 4\nu_z = 0$, a reduced strength compared with $2\nu_x - 2\nu_y - \nu_z = 0$ if the working point $(0.228, 0.224)$ is chosen.

Coherent Beam-beam Instability

The electromagnetic beam-beam interactions between the counter rotating electron beam and proton beam can cause coherent instabilities of the colliding beams. Those instabilities depend on the working points, i.e. tunes, of the collider. In this report, we carried out a systematic tune scan of the electron beam with the fixed tunes of the proton beam.

Figure 4.65 shows evolutions of the proton beam horizontal centroid (red) and the electron beam horizontal centroid (green) as a function of tune scan. It is seen that there is a major instability stopband in the electron horizontal tune space between 0.1 and 0.14. An initial spectral analysis of the centroid motion of both beams shows the presence of proton beam mode in the electron beam centroid motion and vice versa. This suggests strong coupling between the electron beam mode and proton beam mode during the beam-beam interactions. The instability associated with the 0.1 to 0.14 stopband could be due to the coupled sum resonance between the electron beam mode and the proton beam mode. Further study is on-going to have better understanding of the underlying mechanism of the coherent instability.

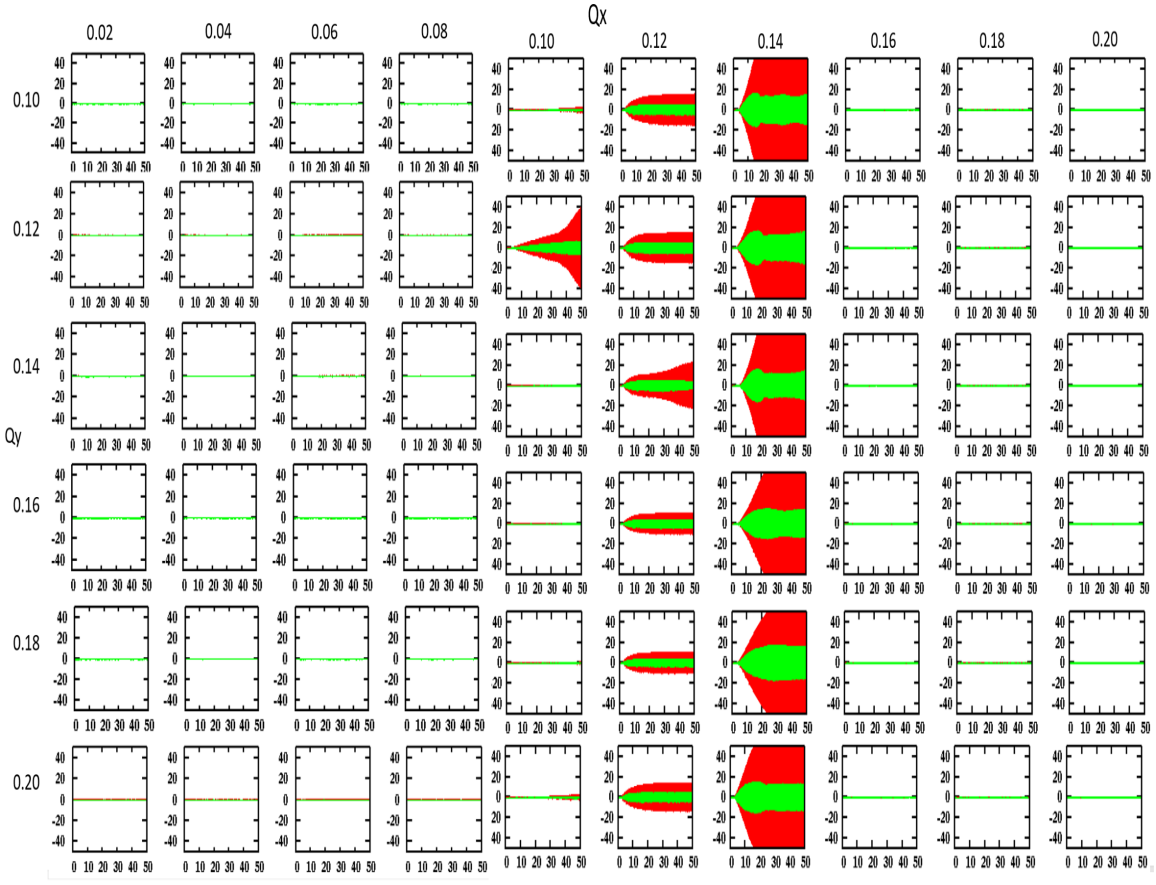

Figure 4.65: Evolutions of the proton beam horizontal centroid (red) and the electron beam horizontal centroid (green) as a function of tune scan.

4.6.3 Imperfections with Crabbed Collision

In the previous sub-sections, the beam-beam studies presented assume that the crab cavity has exact voltage with precise timing, and is located at the locations with ideal optics properties. The properties include the $\pm(2n+1)\,\pi/2$ betatron phase advance from IP and zero dispersion functions. In this section, the effect of imperfections of the crabbing scheme is presented. In the linear model used in this subsection, the 4D phase space refers to (x, x', z, δ).

Effect of Phase Advance Error

In the realistic lattice, the phase advance between the crab cavity and the interaction point is not $(2n+1)\,\pi/2$. We define $\delta\psi_i$ as the phase difference of the i^{th} cavity from the ideal phase. The phases of the two crab cavities will be $\psi_1 = -\pi/2 - \delta\psi_1$ and $\psi_2 = \pi/2 + \delta\psi_2$. The 'one-turn' map at interaction point including crab cavity is

$$M = \tilde{M}_{CC_1}\tilde{M}_{IP}\tilde{M}_{CC_2} \tag{4.18}$$

where $\tilde{M}_{IP}$ is the one turn map of IP of with head scheme without crab cavity. $\tilde{M}_{CC}$ is the matrix for linearized crab cavity kick, measured at IP:

$$\tilde{M}_{cc_{1/2}} = M_{CC_{1/2}\to IP}(-\psi_{1/2})M_{cc}M_{IP\to CC_{1/2}}(\psi_{1/2}) \tag{4.19}$$

By varying the voltage of the crab cavity, the beam may have ideal crab dispersions θ_c with vanishing derivative, same as the case without phase advance error. This requires the voltage of the crab cavity becomes:

$$\begin{pmatrix} V_1 \\ V_2 \end{pmatrix} = \begin{pmatrix} \frac{-\sin(\delta\psi_2)+\sin(\delta\psi_2-2\pi\nu_x)}{\sin(\delta\psi_1+\delta\psi_2-2\pi\nu_x)} \\ \frac{-\sin(\delta\psi_1)+\sin(\delta\psi_1-2\pi\nu_x)}{\sin(\delta\psi_1+\delta\psi_2-2\pi\nu_x)} \end{pmatrix} V_0 \tag{4.20}$$

where V_0 is the crab cavity's voltage when no phase advance error present. However, in the presence of the crab phase error, the crab dispersion will leak outside the pair of crab cavity and cause additional synchro-betatron coupling.

Alternatively, in a special case when $\delta\psi_1 = -\delta\psi_2$, the voltage of each crab cavity can be set to:

$$\begin{pmatrix} V_1 \\ V_2 \end{pmatrix} = \begin{pmatrix} \frac{1}{\cos(\delta\psi_1)} \\ \frac{1}{\cos(\delta\psi_2)} \end{pmatrix} V_0 \tag{4.21}$$

to vanish the crab dispersion out side the pair of crab cavities. The only side effect is that the derivative of crab dispersion at IP is non-zero, but $\theta_c \tan\delta\psi_1/\beta_x^*$. However, when the phase advance error is small, the small derivative is negligible as shown in below simulations.

Figure 4.66 shows the results from the strong-strong simulation with various phase error

on the proton (left figure) and electron (right figure) lattice. The simulations show that the proton lattice may tolerate 2 degrees phase error on each side of IP, if they are in opposite sign. The tolerance for the electron lattice is tighter. The finite crab dispersion out side the crab cavity pair affects the equilibrium beam size of the electron beam dramatically. This effect can be reduced by choosing a larger vertical tune of the electron beam. Alternatively, a third crab cavity is being considered to form a bump for the crab dispersion to eliminate the impact on the phase error.

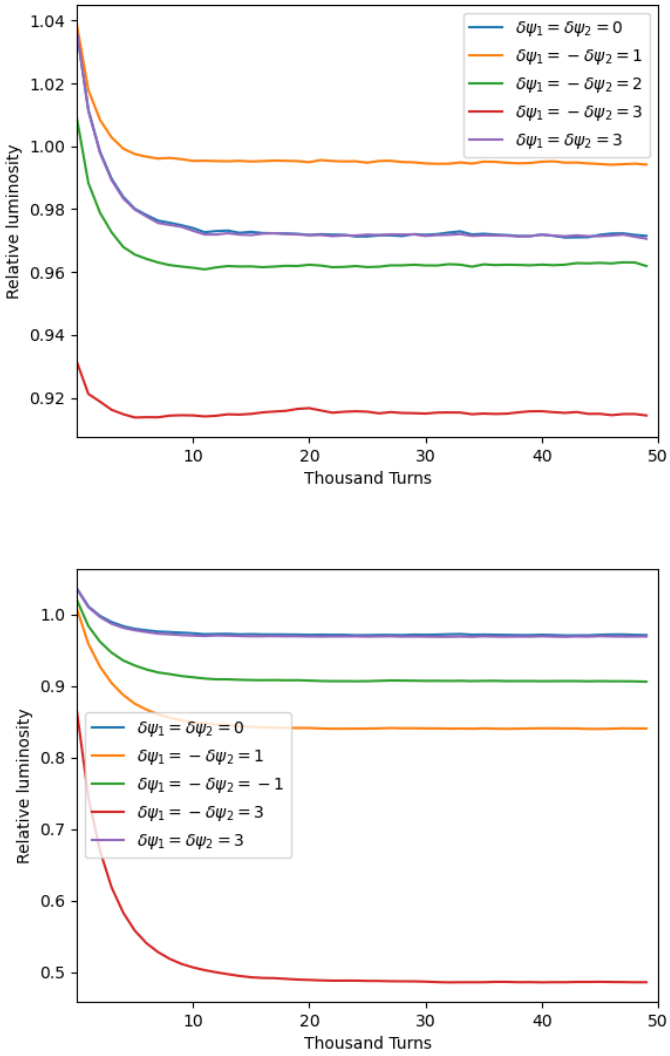

Figure 4.66: Luminosity comparison of, top figure: different phase error $\delta\psi_{1/2}$ at crab cavity in hadron lattice; bottom figure: different phase error $\delta\psi_{1/2}$ at crab cavity in electron lattice.

Horizontal Dispersion at Crab Cavity

In the interaction region design of the EIC, dispersion is helpful for the energy resolution of detecting the collision products. The location of the crab cavities is designed to have finite dispersion, especially on the forward side of the IP in the proton lattice and rear side in the electron lattice. When the dispersion and/or its derivative at the crab cavity do not vanish, the longitudinal position dependent energy kick will have a residual effect on both the longitudinal and the transverse plane. Following the matrix manipulation of the previous subsection, the linearized crab cavity matrix at the IR can be expressed using the unit-less dispersion functions, $\eta = d_x/\sqrt{\beta_c\beta_s}$ and $\eta' = (\alpha_c d_x + \beta_c d'_x)/\sqrt{\beta_c\beta_s}$, as

$$M = \begin{bmatrix} \eta^2\theta_c^2 + \eta\theta_c + 1 & \beta_{sx}\eta'\theta_c\,(\eta\theta_c + 2) & -\eta\theta_c^2 & \beta_{sx}\eta\eta'\theta_c \\ 0 & -\eta\theta_c + 1 & 0 & -\eta^2\theta_c \\ \eta^2\theta_c & \beta_{sx}\eta\eta'\theta_c & -\eta\theta_c + 1 & 0 \\ 0 & \eta\theta_c^2 & 0 & \eta^2\theta_c^2 + \eta\theta_c + 1 \end{bmatrix} \tag{4.22}$$

The linear effect of the dispersion includes the transverse tune shift and the coupling between the transverse and longitudinal motion. Since the factor $\sqrt{\beta_c\beta_s}$ is maximized to reduce the required voltage of the crab cavity, it is expected that the effect of the dispersion function at the crab cavity will be suppressed, and the derivative of the dispersion needs more attention. Nonlinear beam-beam tracking is performed to ensure the beam quality is preserved with the design dispersion at the crab cavity. As shown in Figure 4.67, the luminosity of the current design is not sensitive to the dispersion function at crab cavity up to values of 5 m. The current lattice has about 0.5 m dispersion at the crab cavities in both the proton and electron lattice. Simulations also show that the luminosity will not be negatively affected by the derivative of the dispersion if the value is less than 0.1. The current design has a safety margin of 10 below the threshold.

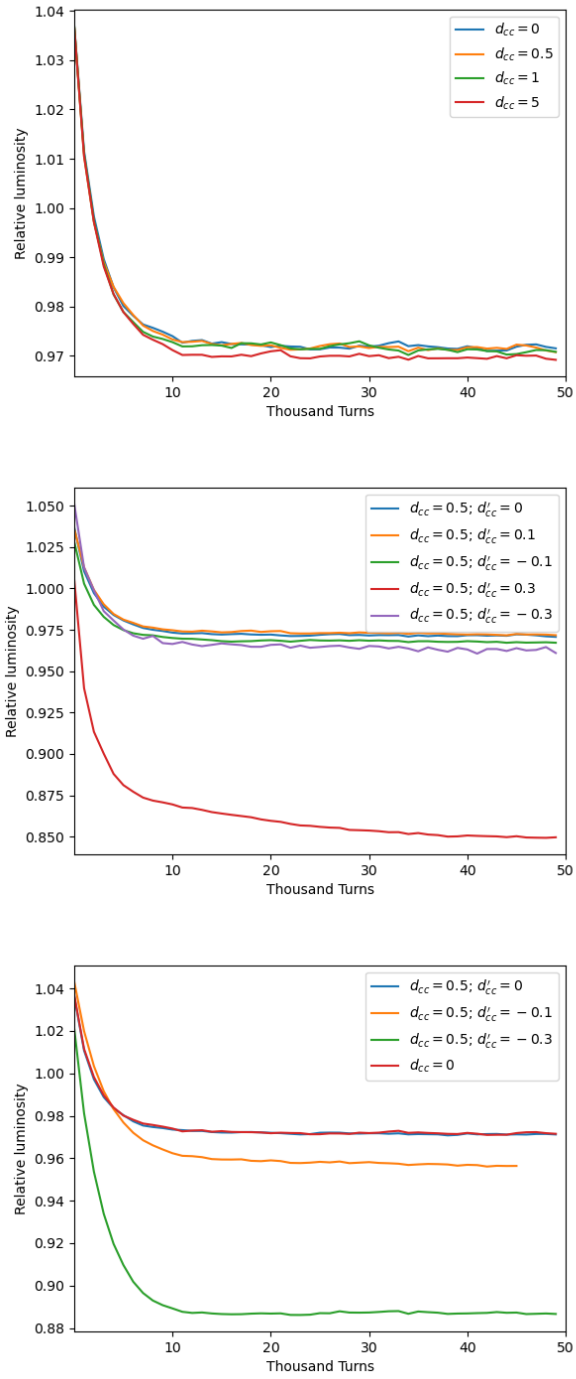

Figure 4.67: Luminosity comparison of, top figure: different dispersion function at crab cavity in hadron beam, with zero derivative of dispersion; middle figure: different derivative of dispersion function at crab cavity in hadron beam, with 0.5 m dispersion function; bottom figure: different derivative of dispersion function at crab cavity in electron beam, with 0.5 m dispersion function.

Compensation for the Detector Solenoid in Crab-crossing Scheme

The crab crossing scheme for the electron beam will be affected by the detector solenoid. The 4 m long detector solenoid is designed to provide up to 3 tesla longitudinal magnetic field aligned with the electron trajectory.

The rotation angle θ_s caused by the detector solenoid can be approximated using a hard-edge solenoid model,

$$\alpha_s = \frac{B_{\parallel} L_s}{2P_0}, \tag{4.23}$$

where $B_{\parallel}$ is the solenoid field, L_s is the length of the hard-edge model and P_0 is the momentum of the charged particle. The rotation combined with horizontal crab cavity will create an effective vertical crossing angle

$$\theta_{cv} = \theta_c \sin\left(\frac{\alpha_s}{2}\right) . \tag{4.24}$$

The effective vertical Piwinski angle Θ_{pv} is

$$\Theta_{pv} = \frac{\sigma_z}{\sigma_y}\theta_{cv} = \frac{\Theta_P}{r} \sin\left(\frac{\alpha_s}{2}\right) , \tag{4.25}$$

where Θ_P is the original Piwinski angle (horizontal) without detector solenoid and $r = \sigma_y/\sigma_x$ is the transverse beam size ratio at the IP.

As shown in Table 4.16, the effective vertical Piwinski angle clearly indicates that the rotation effect of the detector solenoid must be compensated for the electron beam due to the adoption of flat beam collision scheme ($r = 0.09$). Otherwise, a significant luminosity loss will occur. The compensation may be either a local scheme (in-between the pair of horizontal crab cavities) or a global version with vertical crabbing kicks to correct the vertical crossing angle θ_{cv}. The local compensation is the cleanest method, however may not be practical since the space between the IP and the crab cavity is fully occupied. One approach could adopt global coupling compensation; the effective vertical crossing angle

Table 4.16: Vertical Piwinski angle caused by detector solenoid.

	Proton	Electron
Energy [GeV]	275	10
RMS bunch length [cm]	6	2
RMS horizontal beam size [μm]	95	95
Transverse ratio, σ_y/σ_x	0.09	0.09
Piwinski angle, Θ_P	7.9	2.6
Vertical Piwinski angle, Θ_{pv}	0.29	2.6

could be compensated by vertical crabbing kicks with voltage

$$\hat{V}_{CC,y} = \pm \frac{cE_s}{4\pi f_{\mathrm{RF}} \sqrt{\beta_y^* \beta_{cc,y}}} \theta_{cv} \ . \tag{4.26}$$

Since the detector solenoid is aligned with the electron beam trajectory, the proton beam enters the same solenoid at a horizontal angle, equal to the crossing angle. As a consequence, the proton beam receives a vertical kick by the solenoid. This vertical kick could be corrected by nearby vertical correctors to achieve a vanishing closed orbit at the IP.

When both the rotation and the closed orbit are corrected in the IP, the interplay between the detector solenoid and the beam-beam effect can be estimated in the Lorentz boost frame where the beam-beam interaction is equivalent to a head-on collision. In this frame, the proton would experience a vertically deflecting force

$$F_y = 2qB_{\parallel} c \sin\left(\frac{\theta_c}{2}\right) \ . \tag{4.27}$$

The longitudinal collision position is $s = \left(z_e + z_p\right)/2$. With a 5σ cutoff, the maximum location for this interaction is at $s = 0.2\,\mathrm{m}$. Detector solenoid modeling is being implemented in strong-strong and weak strong simulation codes to simulate the long term effect on the beam dynamics.

Crab Cavity Voltage Miscalibration

The crab voltage may be have a calibration error, which differ from the ideal voltage. A higher voltage may have have benefit in the geometric luminosity when the proton bunch is long, compared with the crab cavity wavelength (Figure 4.68). However, an increased or decreased voltage from the calculated value leads to a linear correlation between the horizontal and longitudinal direction, therefore may enhances the synchro-betatron resonance as described earlier.

Figure 4.69 shows the simulation results with slightly modified crab cavity voltage. The impact of luminosity due to ion beam's finite bunch length can be partially compensated by the increased crab cavity voltage. However, the long-term luminosity degradation also slightly increases due to the over crabbing. (observed in the case of 2% voltage increment, which is the optimized value for the geometric luminosity). The voltage of the crab cavity of electron beam should be set to its design value, since there is no benefit on any modification.

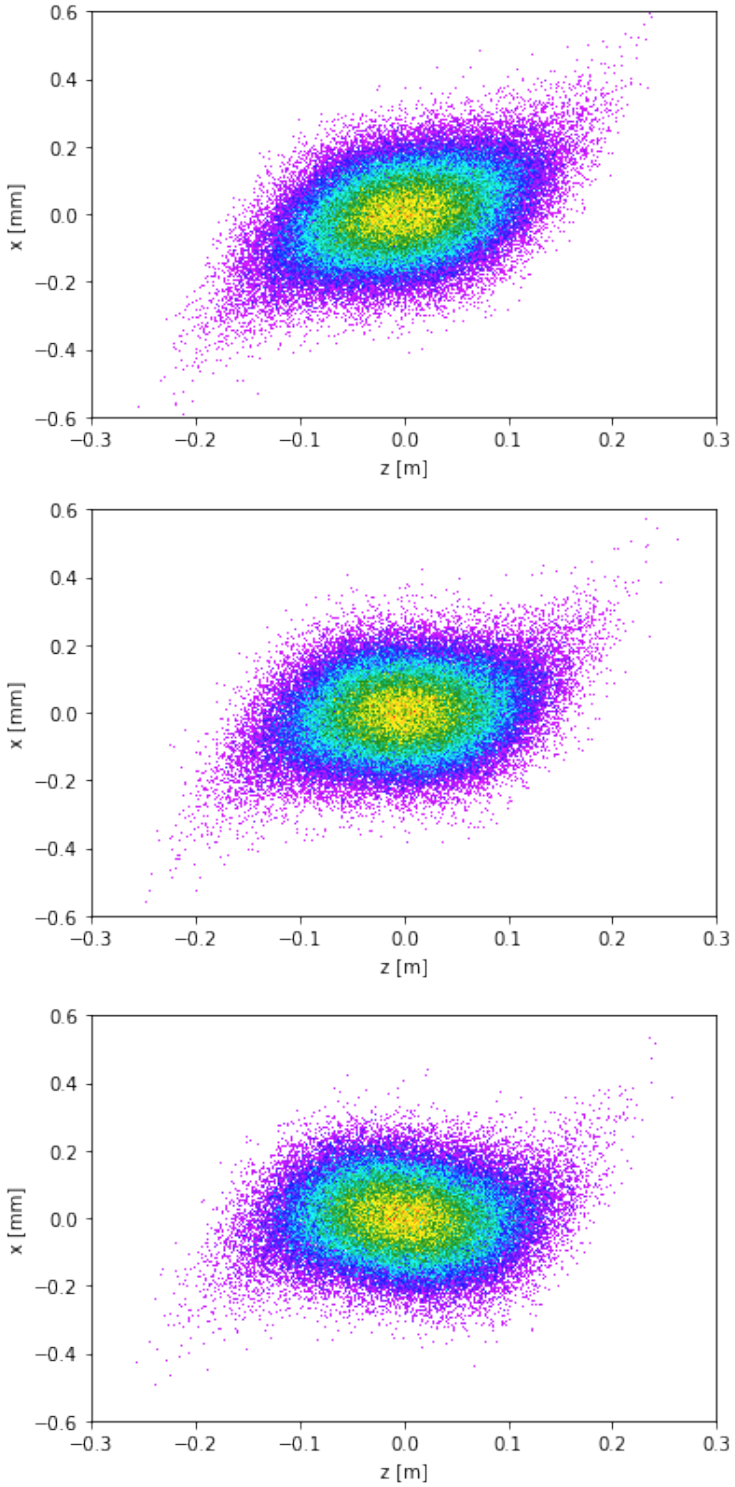

Figure 4.68: Horizontal-longitudinal distribution of protons at IP in the Lorentz frame under different crab cavity voltage, top: 3% less than design value; middle: design value; bottom: 3% larger than design value.

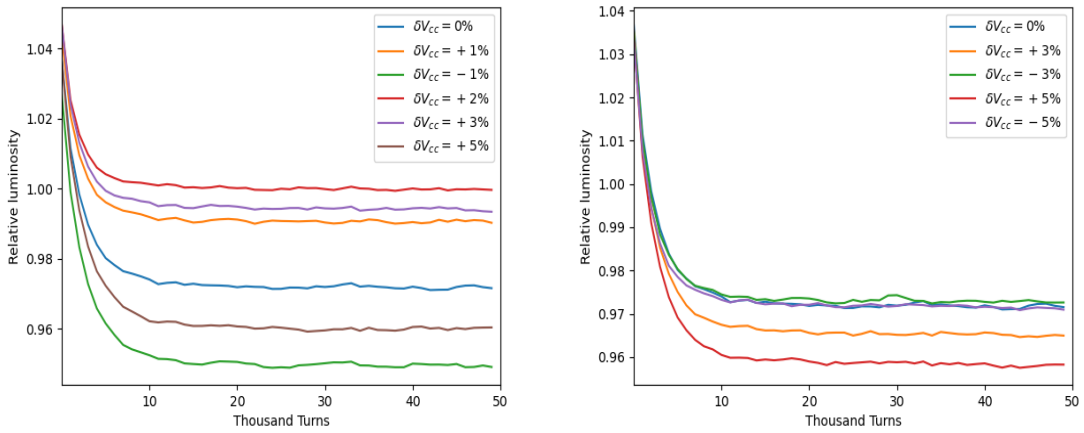

Figure 4.69: Luminosity comparison of different voltages at crab cavity in the proton ring (left plot) and in electron ring (right plot).

Crab Cavity Voltage and Phase Noise

Noise of the cavity voltage will produce a crossing angle error of the two opposing beams, while cavity phase noise creates a transverse offset at the interaction point. A theoretical approach can be found in Ref. [210].

A reliable approach for estimating the requirement of the cavity phase and voltage stability is to use the measured power spectrum density (PSD) of the low level RF controller for the crab cavity in the beam-beam simulation. Currently, the PSD information on the Low Level RF (LLRF) controller for the EIC crab cavity is not available. The exact requirements can be obtained from simulations using the PSD as input for the noise signal generation.

4.6.4 Additional Beam-beam Concerns

Beam-beam Effects with Two Experiments

One of the key requirement for the EIC is the capability to support two detectors. In the beam-beam interaction studies described earlier, we focus on one beam-beam interaction per turn. In the following, we assume there are two IPs at IR6 and IR8 and study the related beam-beam concerns.

- Filling Pattern and Beam-Beam Pattern

  To deliver collisions to two experiments at IP6 and IP8 simultaneously, with each bunch colliding only once per revolution in order to not exceed the beam-beam limit, we adopt a dedicated filling scheme. To achieve this, the following conditions have to be met:

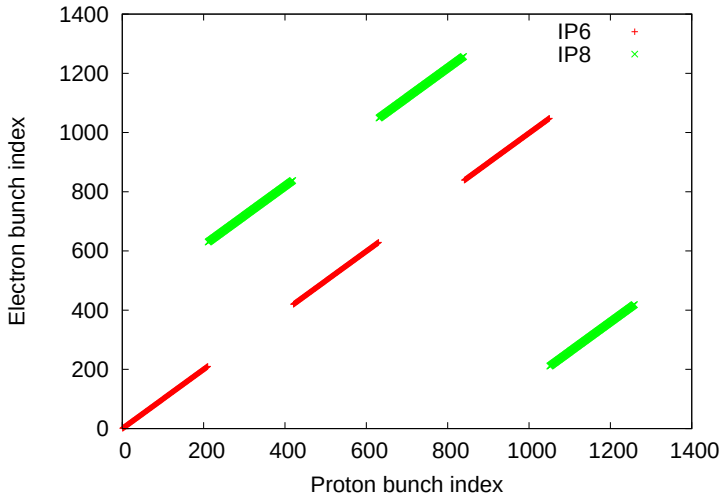

Figure 4.70: Bunch collision pattern with the bunch shift scheme.

- Fill proton bunches in every proton ring bucket;
- The electron ring filling pattern is (210*6 + 3 + 209*6 + 3)* 3. That is, fill the electron ring with 3 identical bunch trains. Each train includes two batches. The first batch has 210 electron bunches, the second batch has 209 electron bunches. The gap between adjacent electron bunches in each batch is 6 electron ring buckets. The gap between the first and the second batch is 3 electron ring buckets, while the gap between the second batch to the next train is 3 electron ring buckets.
- The detector at IP8 is to be moved counter-clockwise, or towards IP6, by 1.5 electron buckets, or 0.76 m.
- 197 MHz RF cavities for the proton ring with 1260 buckets, 591 MHz RF cavities for the electron ring with $1260 \times 6 = 7560$ buckets.

Here we temporarily ignore the abort gap.

With the above bunch shift scheme, there are totally 1260 proton bunches in the proton ring and 1257 electron bunches in the electron ring. Each electron or proton bunch only collides once per turn, at either IP6 or IP8. There are a total of 630 collisions at IP6 and 627 collisions at IP8 per turn. The integrated luminosity per experiment is therefore half of that with single experiment. Figure 4.70 shows the collision pattern. The horizontal and vertical axes are the bunch index of the proton and electron bunches. The red dots indicate collisions taking place at IP8, and the green dots show collisions occurring at IP6. In this plot, the abort gap has not been taken into account at this moment.

- Long-range Beam-beam Interaction

  In the present interaction region design, the common beam pipe is 9 m long with the interaction point at the center. With a single experiment, the bunch spacing of the proton and electron beams are equal. Each bunch will experience 6 long-range

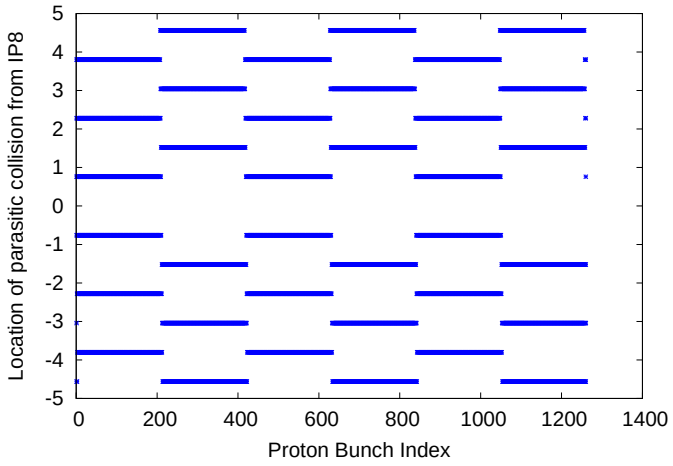

Figure 4.71: Locations of long-range beam-beam interactions with two experiments and bunch shift scheme.

beam-beam interactions, 3 on either side of the IP. The nearest long-range beam-beam interaction takes place 1.52 m from the IP.

With two experiments and the above bunch shift scheme, each bunch will undergo 12 long-range beam-beam interactions, with 6 long-range beam-beam interactions at each experiment.Figure 4.71 shows the locations of these long-range beam-beam interactions for protons at the interaction region IR8. The nearest long-range beam-beam interaction is 0.76 m away from the IP.

Table 4.17 shows the horizontal separation between the electron and the proton bunch at the nearest interaction points for the cases with one and two experiments. The horizontal crossing angle between the electron and proton rings at the interaction point is 25 mrad. The horizontal separation at the nearest long-range beam-beam interaction point corresponds to $146\,\sigma_p$ or $211\,\sigma_e$. Therefore, the long-range beam-beam effect is negligible for the present EIC design.

Table 4.17: The long-range beam-beam interaction with 1 and 2 experiments for the present EIC design.

Parameter	1 experiment	2 experiments
Number of long-range BB interactions	6	12
Nearest distance to IP [m]	1.52	0.76
Horizontal separation d [mm]	38	19
Local beam sizes σ_p, σ_e [mm]	0.20, 0.31	0.13, 0.18
Separation in beam sizes $\frac{d}{\sigma_p}$, $\frac{d}{\sigma_e}$	186, 123	145, 106

Transient Beam-Beam Effect During Electron Bunch Replacement

To maintain high electron bunch polarization in the electron storage ring, we will replace each electron bunch in about every five minutes. The full bunch charge is about 50 ns. When an electron bunch is kicked out, another electron bunch will be injected into the same electron bucket on orbit and on energy from the RCS. Transient beam-beam effect during electron bunch replacement needs to be studied, especially possible proton emittance growth during this process.

The proton beam emittance growth due to the optics mismatch caused by a newly injected electron bunch can be expressed as a function of the β-function of the bare lattice, β_0, and the β-function as modified by the beam-beam interaction with the electron bunch, β_1, as

$$\epsilon_1 = \frac{\epsilon_0}{2}\left(\frac{\beta_1}{\beta_0} + \frac{\beta_0}{\beta_1}\right), \tag{4.28}$$

where ϵ_0 is the unperturbed emittance, and ϵ_1 the resulting emittance after filamentation. The analytical calculated relative emittance growth is less than 10^{-3} for each bunch replacement.

The transient effects from the electron beam replacement injection was studied using a self-consistent strong-strong beam-beam simulation using the BeamBeam3D code. In these simulations, the accelerator lattice is approximated by a linear one-turn map. Macro-particles representing the proton and electron beams are tracked, and the beam-beam force between them is calculated numerically by solving Poisson equation with particle-in-cell method. A new electron bunch was injected on the axis after 20,000 turns where the old electron bunch in the electron ring already attained an equilibrium.

The upper two plots of Figure 4.72 show the proton bunch's emittance evolutions with one electron bunch replacement. The lower two plots shows the electron bunch's emittance evolutions. It is seen that the electron beam attained the equilibrium emittance after a few thousand turns. The proton beam emittances increased by less than 0.1% in horizontal dimension and about 0.2% in vertical plane after the electron beam injection. The trend of the proton beam evolution stays about the same.

As we can see, both electron bunches have similar emittance evolution with beam-beam interaction. For the proton bunch, although there is an increase of emittance less than 10^{-3}, the proton emittance growth rates keep the same before and after a new electron bunch is injected.

In the above simulation, we assumed an ideal injection scenario. In the real accelerator, there will be imperfections during the injection. Those imperfections include initial centroid positions, angles, and energy offset, and electron beam size and intensity fluctuations.

As an example, Figure 4.73 shows the proton beam emittance growth after electron beam replacement as a function of the electron beam offset amplitude. It is seen that the resulting proton beam emittance growth is small (less than 1%) even with 1 sigma vertical injection

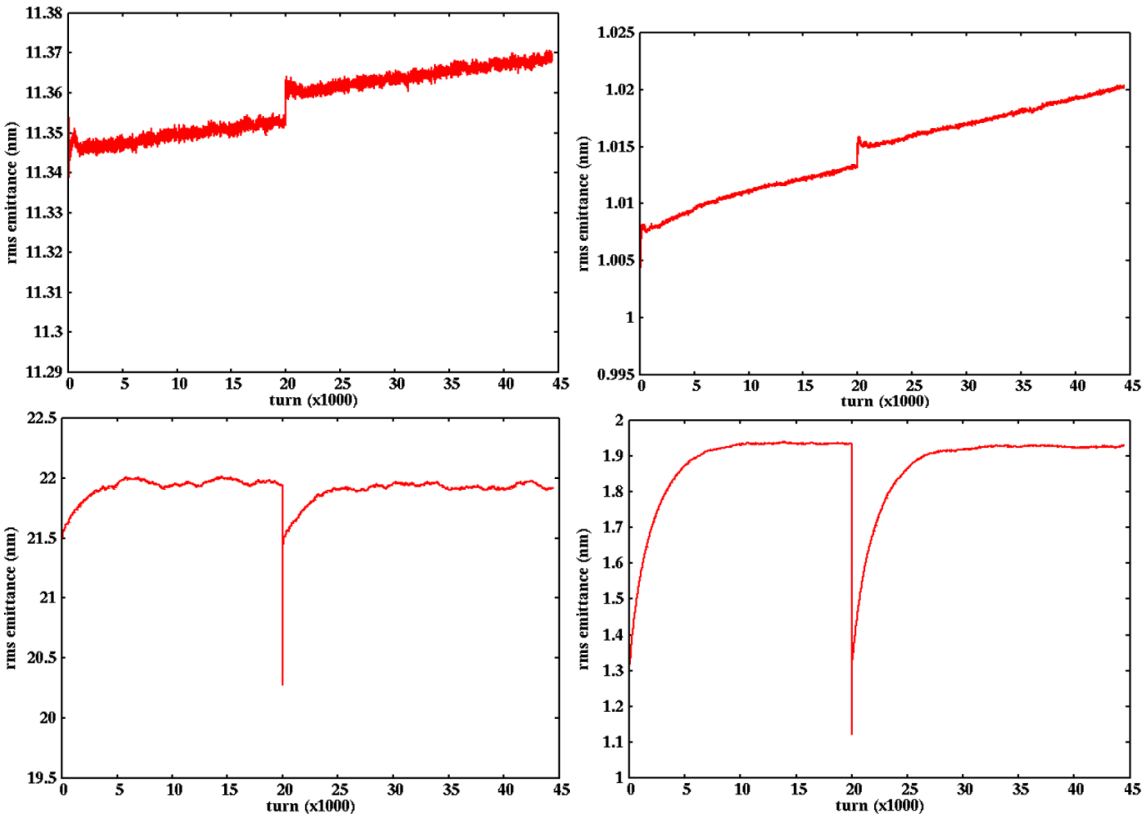

Figure 4.72: Simulated emittance evolution of the proton bunch during 100 electron bunch replacement. Injection error is not included.

offset. The proton beam horizontal emittance growth is not sensitive to those offset errors. The vertical emittance growth shows weak dependence on the offset error below 0.8 sigma. Here, one sigma corresponds to about 8 um of vertical rms beam size.

Figure 4.74 shows the proton beam emittance growth after electron beam replacement as a function of the initial electron beam vertical emittance mismatch. The proton beam emittance growth is small as long as the electron beam mismatch factor is above 0.6. The horizontal emittance growth is not sensitive to the electron beam vertical emittance mismatch during the electron beam replacement injection.

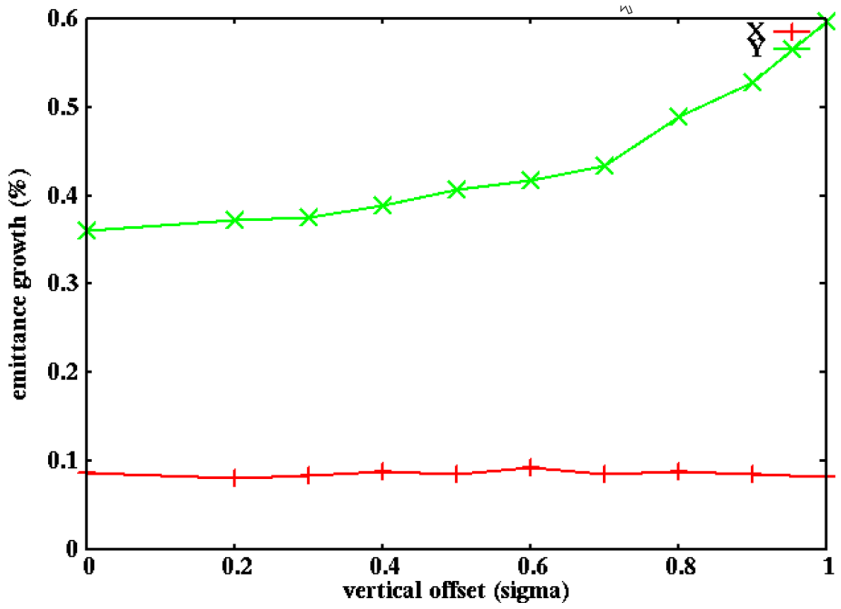

Figure 4.73: The proton beam emittance growth after electron beam replacement as a function of the electron beam offset amplitude.

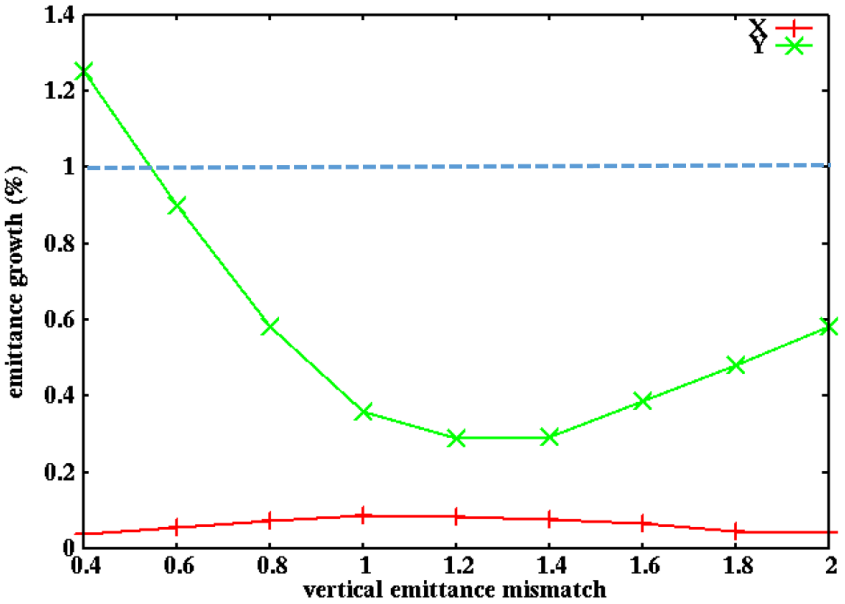

Figure 4.74: The proton beam emittance growth after electron beam replacement as a function of the initial electron beam vertical emittance mismatch.

Radiation Damping Decrement and Beam-beam Interaction

To reach a beam-beam parameter of $\xi = 0.1$ in the electron ring, a transverse radiation damping decrement of $\delta = 1/4000$, or a radiation damping time of 4000 turns, is required,

based on the experience at KEKB.

To achieve the same radiation damping time at the low electron beam energies, the electron ring lattice uses super-bends in the arcs. The purpose of these super-bends is to generate additional synchrotron radiation at low electron energies to increase the radiation damping rate. Since the relation between the damping decrement and the achievable beam-beam parameter is empirical, we carried out beam-beam simulations to study the beam performance with different radiation damping decrements.

As an example, Figure 4.75 shows the evolution of the horizontal beam size of the electron beam with different radiation damping times. In this simulation study, we did not observe any significant difference in the coherent beam-beam motion and luminosity over the damping time range under study. With a longer damping time, it takes a longer time to reach the electron equilibrium beam size. However, there is not much difference in equilibrium beam size and luminosity as long as the radiation damping time is shorter than 16,000 turns, or 4 times the design value. This study of the beam-beam interaction shows that we may relax the requirement on the damping decrement at low energy collisions so we may reduce the radiation power of the super-bends, and the required magnet current.

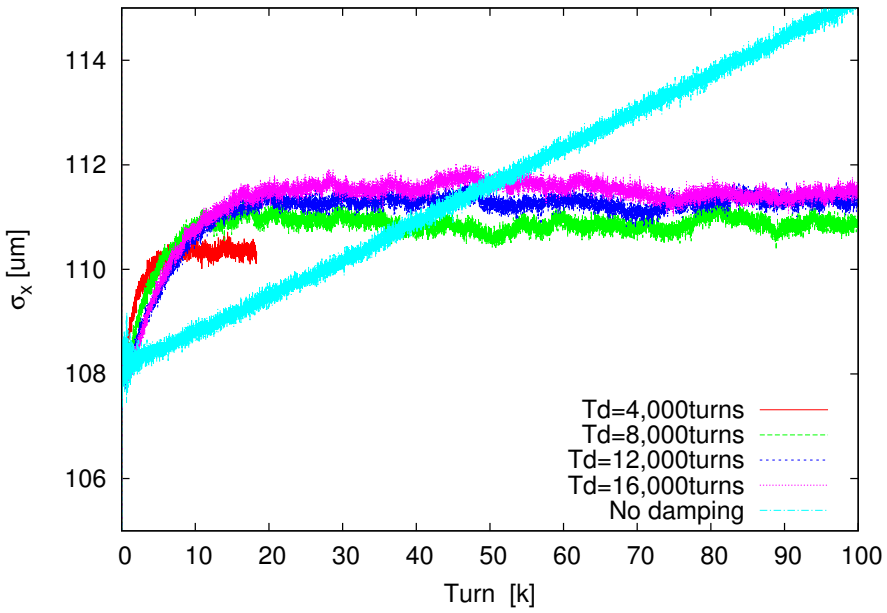

Figure 4.75: Evolution of electron horizontal beam size versus the radiation damping time.

Chapter 5

Beam Polarization

5.1 Overview of Beam Polarization in the EIC

Beam polarization is a key parameter of the EIC design. Preserving a high level of spin polarization in accelerators presents a challenge for accelerator design and operation. Loss of polarization can happen when depolarizing resonances are encountered on the energy ramp, and when depolarizing resonances are nearby during store for a beam with a certain betatron and spin tune spread. RHIC has a successful proton polarization program from which the EIC will fully benefit.

Polarized electrons are produced in the source with 85% longitudinal polarization (see Section 3.7.2). Two new rings are considered for the electron beam: a rapid cycling synchrotron (RCS) for electron beam acceleration and an electron storage ring (ESR). The longitudinal gun polarization is converted to vertical with a solenoid-based spin rotator at 400 MeV, just before the injection into the RCS (see Section 3.8.3). The polarization losses on the energy ramp in the RCS are mitigated by special lattice design and well-controlled vertical orbit. The polarization of the EIC electron beam at store is complicated by synchrotron radiation related effects, such as the Sokolov-Ternov self-polarization process and stochastic depolarization. The polarization performance in the electron storage ring is analyzed by simulations. A Mott polarimeter is used for polarization measurement at 400 MeV, while precise polarization measurements in the storage ring are performed with the Compton polarimeter.

EIC experiments call for polarized protons and polarized light ions (^{3}He and deuterons). Existing hardware in RHIC and its injectors for producing highly polarized protons and preserving their polarization during acceleration will be re-used in the EIC. The depolarizing resonance strength for ^{3}He ions is stronger than that for protons. Extending the number of Siberian snakes from presently used two snakes to six snakes will maintain polarization for ^{3}He beam on the energy ramp. Six Siberian snakes will also improve the proton polarization transmission efficiency on the energy ramp, compared to two Siberian snakes. The performance of proton and ^{3}He polarization in the hadron ring has been sim-

ulated and analyzed. The feasibility of providing highly polarized deuteron beams has been demonstrated as well.

Since the experimental detectors have strong solenoidal magnets the effect of a detector solenoid on the electron and proton beam polarization has been explored.

5.2 Electron Beam Polarization in the RCS

5.2.1 Spin Dynamics in the RCS

The longitudinally polarized electron beam produced by the gun travels through a spin rotator before entering the RCS, so the electron beam is vertically polarized. The RCS is designed to be free of intrinsic spin resonances in the entire energy range during the acceleration cycle. However, the beam transport through the tunnel straight sections, including horizontal orbit excursions for bypassing detectors or providing the space for RF components, have the potential to spoil the symmetry which keeps all the intrinsic resonances sufficiently low. By minimizing the contributions to the spin integral introduced by these insertions we can ensure that polarization is maintained to emittances well beyond foreseeable operational conditions.

In Figure 5.1 the intrinsic spin resonances are calculated for the RCS lattice. Assuming a 100 ms acceleration ramp rate (8000 turns) we can estimate the net polarization loss for a beam with a given RMS normalized emittance. Note that these include the effects of the horizontal orbit excursions in all the straight sections.

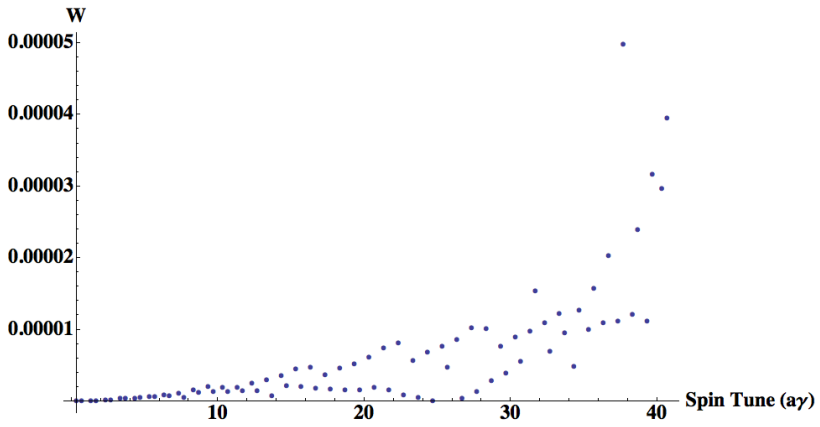

Figure 5.1: DEPOL [211] calculated intrinsic spin resonances for the RCS at 10 µm normalized emittance. $w = |\varepsilon_K|$.

For well isolated resonances the amount of depolarization caused by acceleration through any given spin resonance can be evaluated using the Froissart-Stora formula [212],

$$\frac{P_f}{P_i} = 2e^{-(\pi|\varepsilon_K|^2/2\alpha)} - 1, \tag{5.1}$$

where ε_K is the spin resonance strength at $a\gamma = K$, with $a = \frac{g-2}{2} = 1.16 \times 10^{-3}$ being the anomalous magnetic moment of the electron, and

$$\alpha = \frac{1}{\omega_{\text{rev}}} \frac{\mathrm{d}\nu_s}{\mathrm{d}t} \tag{5.2}$$

is the spin tune crossing rate divided by the angular revolution frequency ω_{rev}, and P_f/P_i is the ratio of initial vertical to final vertical polarization. For a flat orbit in a constant vertical field $\alpha \approx \mathrm{d}(a\gamma)/\mathrm{d}\theta$. The Froissart-Stora formula represents a solution to the T-BMT equation [171, 213] for the special case of crossing an isolated spin resonance.

Since the intrinsic spin resonance strength is proportional to the square root of the normalized emittance we can rescale an intrinsic spin resonance strength at one emittance to an arbitrary emittance ϵ using

$$|\varepsilon(\epsilon)|^2 = \frac{\epsilon}{\epsilon_c} \cdot |\varepsilon(\epsilon_c)|^2. \tag{5.3}$$

Here ϵ_c is the emittance of the calculated intrinsic spin resonance. With this the Froissart-Stora formula can be evaluated for an arbitrary emittance particle. Assuming the beam distribution follows a Gaussian, $\rho(\epsilon, \epsilon_0) = \frac{e^{-\epsilon/2\epsilon_0}}{2\epsilon_0}$, with ϵ_0 the RMS normalized emittance, we can integrate to obtain an estimate for the average polarization transmission after crossing a single resonance,

$$\langle \frac{P_f}{P_i} \rangle = \int_0^\infty \rho(\epsilon, \epsilon_0) \frac{P_f}{P_i}(\epsilon) \mathrm{d}\epsilon = \frac{1 - \frac{\pi|\varepsilon(\epsilon_0)|^2}{\alpha}}{1 + \frac{\pi|\varepsilon(\epsilon_0)|^2}{\alpha}}. \tag{5.4}$$

Using this formula one can take the product of all the spin resonances crossed from 400 MeV to 18 GeV ($a\gamma = 0.907$ to 40.82), to obtain with acceptable accuracy the relative polarization transmission through the accelerator ramp for a given RMS emittance,

$$F(\epsilon_0) \approx \Pi_K \langle \frac{P_f}{P_i}(\epsilon_0)_K \rangle \approx 1 - 2 \sum_K \frac{\pi|\varepsilon_K(\epsilon_0)|^2}{\alpha}, \tag{5.5}$$

where the index K denotes the spin resonances up to $a\gamma = 40.82$. For a normalized vertical RMS emittance as high as ϵ_0 =1000 µm, we calculate more than 98% transmission through the ramp for this lattice including the effects of the horizontal orbit excursion in all straight sections. Note that the EIC design parameters require considerably smaller vertical normalized RMS emittances namely 55 µm at the RCS injection and 115 µm at the RCS extraction energy.

More of an issue are the imperfection spin resonances which are driven by vertical closed orbit errors. Unlike intrinsic spin resonances, imperfection resonances are independent of the emittance. So the depolarization effect applies to all particles in the bunch equally.

We performed particle tracking using the 6D spin-orbit tracking code Zgoubi [214], including radiative effects, for 8 large amplitude particles at 419 µm vertical normalized emittance, and using a 50 to 200 ms ramp time with orbit errors generated by vertical kicks

equaling 1 mm RMS of orbit distortion. We also included up to 0.1% random Gaussian quadrupole gradient errors. The results in Figure 5.2 show that for the slowest ramp rate of 200 ms 94% polarization transmission was achieved. However when encountering repeated imperfection resonances one observes a phenomenon of polarization restoration, since the imperfections act coherently over the whole beam. We are doubtful that this represents the "true" physics since the simulation may be underestimating the level of phase mixing or spin diffusion. As a result we feel a more conservative measure would be to estimate polarization loss by calculating the imperfection resonance strengths up to $a\gamma = 40$ using DEPOL, then calculate the Froissart-Stora results for each of these imperfections encountered on the ramp, and, finally, take the product of all the Froissart-Stora results. We performed this type of calculation for various levels of quadrupole misalignments and various random seeds using the MADX program and DEPOL to calculate the imperfection resonance strength. We first consider the effects of misalignments without the use of orbit correction. Next we consider the effects of misalignments plus the use of SVD orbit correction. The result of the study without orbit correction yields the response of polarization transmission to RMS quadrupole misalignment and RMS orbit distortion shown in Table 5.1.

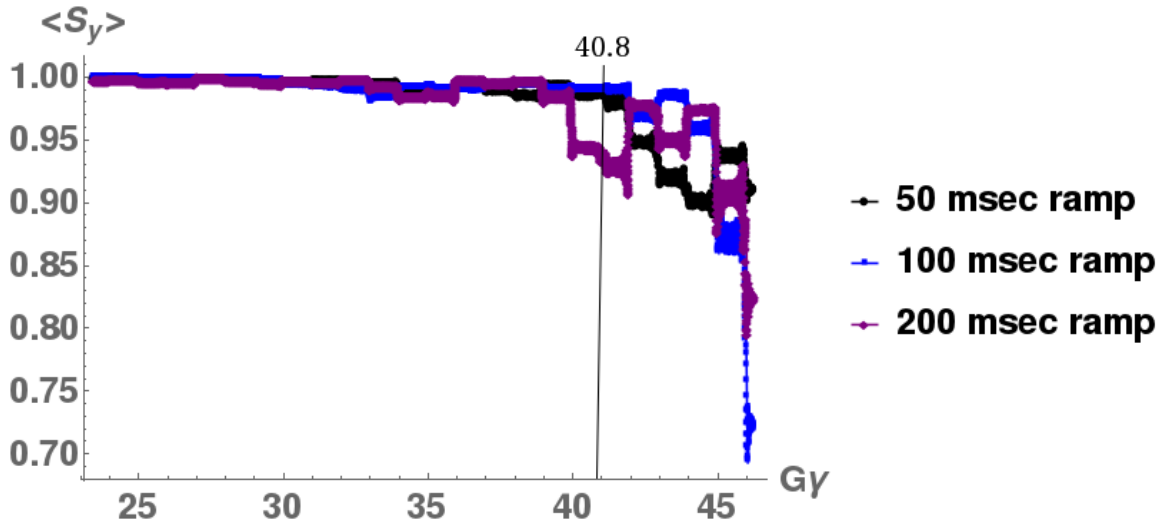

Figure 5.2: Zgoubi [214] tracking results for 8 particles at 419 µm normalized vertical emittance and between 470 and 2900 µm normalized horizontal emittance. The particles were also displaced longitudinally by 4 mm from the bucket center. The lattice included vertical closed orbit errors of 1 mm and 0.1% random Gaussian quadrupole gradient errors. Here ramp times of 50 to 200 ms are compared. The extraction energy is shown at $G\gamma = 41.8$ (black line).

We also looked more carefully near the quadrupole misalignment threshold for 95% transmission between 0.02 to 0.01 mm RMS (assuming no orbit correction scheme applied). The results are shown in Tables 5.2-5.4.

Table 5.1: Table of quadrupole misalignment, orbit RMS and polarization for two different random seeds assuming no orbit correction scheme applied.

Quadrupole misalignment RMS [mm]	Orbit distortion RMS [mm]	Polarization transmission [%]	100 ms Max $a\gamma$
0.2	3.29	95.17	25
0.1	1.7	96.1	32
0.05	0.88	95/96.2	36
0.025	0.4455	96.6	40
0.02	0.3565	97.8	40
0.2	3.7	95.6	26
0.1	1.9253	95.7	29
0.05	0.9716	95.2	34
0.025	0.4867	95.5	40
0.02	0.3895	97.15	40
0.01	0.1948	99.2	40

Table 5.2: Polarization transmission to 18 GeV for random Gaussian quadrupole misalignments of 0.02 mm RMS for 10 different random seeds assuming no orbit correction scheme applied.

Orbit distortion RMS [mm]	random seed	100 ms transmission [%]
0.712	12001	97.35
0.367	1200	97.593
0.716	12002	97.04
0.642	22002	96.0
0.412	32002	94.56
0.446	42002	97.5
0.4078	120015	96.88
0.655	120016	95.5
0.452	120013	95.8
0.952	120014	95.0

From all these results we see that even with uncorrected misalignment errors (estimated to be 0.2 mm RMS) we should be able to accelerate beam to as high as $a\gamma = 23$, or beam energies of more than 10 GeV, and still lose less than 5% polarization. Above that we find that we can get to above $a\gamma = 40$ (18 GeV) with uncorrected quadrupole misalignments equal to 0.025 mm RMS with a 100 ms ramp rate. This corresponds to a closed orbit dis-

Table 5.3: Polarization transmission to 18 GeV for random Gaussian quadrupole misalignments of 0.015 mm RMS for 10 different random seeds assuming no orbit correction scheme applied.

Orbit distortion RMS [mm]	random seed	100 ms transmission [%]
0.534	12001	98.5
0.275	1200	98.5
0.538	12002	98,3
0.482	22002	97.7
0.309	32002	96.9
0.4928	42002	98.62
0.306	120015	98.24
0.4928	120016	97.45
0.339	120013	97.67
0.715	120014	97.2

Table 5.4: Polarization transmission to 18 GeV for random Gaussian quadrupole misalignments of 0.01 mm RMS for 10 different random seeds assuming no orbit correction scheme applied.

Orbit distortion RMS [mm]	random seed	100 ms transmission [%]
0.356	12001	99.4
0.1836	1200	99.33
0.356	12002	99.25
0.312	22002	99.0
0.2064	32002	98.6
0.224	42002	99.3
0.204	120015	99.2
0.329	120016	98.8
0.226	120013	98.9
0.476	120014	98.7

tortion of ≈ 0.5 mm RMS though there is great variability in this number as one can see in random seed studies.

Beyond 0.2 mm RMS quadrupole misalignment achieving orbit closure is challenging without an orbit correction system. In Table 5.5 we show results using the orbit correction system with BPMs and correctors located at each quadrupole. In this case, up to 0.4 mm

Table 5.5: Polarization transmission to 18 GeV for random Gaussian quadrupole misalignments with SVD orbit correction for 4 different random seeds. $*$ indicates tests with bpm misalignments of 0.2 mm RMS.

RMS quad misalignment	random seed	100 ms transmission [%]
0.4	100000	97
0.4	12001	99
0.4	1200	99
0.4	120033	99.0
0.3	100000	99
0.3	12001	99
0.3	1200	99
0.3	120033	99
0.2*	100000	99
0.2	12001	99
0.2	1200	99
0.2*	120033	99

RMS quadrupole misalignment can be corrected to achieve above 95% polarization transmission efficiency. Above 0.4 mm RMS achieving orbit closure becomes very challenging using SVD in MADX. In addition to quadrupole misalignments, we also applied vertical misalignments to the BPMs. As shown in Table 5.5, with 0.2 mm RMS misalignment for both the quadrupoles and BPMs we were able to achieve above 98% polarization transmission efficiency. Basically, if one can thread the beam and achieve closure using the orbit correction system, using SVD to correct the orbit is good enough to reduce the spin resonances to achieve polarization transmission efficiency above 95%.

5.2.2 Dynamical Field Effects

While correcting down to 0.5 mm RMS orbit is easily achievable for a storage ring, this should be studied for a ramped machine. There is a possible concern that dynamic effects may cause fluctuations of the fields to an extent that would spoil the polarization transmission. We studied the RCS lattice with quadrupoles misaligned up to 0.2 mm RMS and applied SVD orbit corrections. Applying to this corrected lattice additional random field fluctuations to both the dipole and quadrupole fields of up to 0.5% showed little to no effect on the polarization transmission.

5.2.3 Orthogonal Imperfection Bumps

In the event that orbit smoothing does not achieve above 95% polarization transmission, orthogonal imperfection bumps can be constructed. These bumps target the real and imaginary part of the spin resonance. Before the commissioning of the partial snake in the AGS, imperfection bumps were used extensively to tune out imperfection driven polarization losses. More recently tests with orthogonal bumps using a spin response matrix method have been performed in RHIC [215].

By building a corrector to the imperfection spin response matrix ($\vec{M}_S$) using DEPOL calculated imperfection resonances, one can calculate the necessary corrector strengths to achieve isolated and orthogonal bumps at any point during the ramp. Here we use

$$\vec{C} \cdot \vec{M}_S = \vec{\varepsilon}, \tag{5.6}$$

where $\vec{C}$ is a vector containing all the correctors, and $\vec{\varepsilon}$ is a vector containing all the real and imaginary parts of the imperfection spin resonances which are targeted. In our case it is 80 elements long, containing the real and imaginary imperfection resonances in the range $1 < a\gamma < 40$. By inverting this non-square matrix to a pseudoinverse matrix one can use it to construct an arbitrary set of imperfection bumps across the whole energy range.

Using this approach we have constructed bumps representing arbitrary imperfection bumps in the imaginary and real plane for $a\gamma = 34$ to 40 with resonance strengths of ± 0.005. Everywhere else the imperfection strength is less than 10^{-5}. A value of 0.005 at 100 ms ramp rates represent a 10% spin kick. These bumps are plotted in Figure 5.3. The associated corrector magnet strengths are plotted in Figure 5.4.

With imperfection bumps constructed in this fashion, there is no need to alter the corrector strengths over the acceleration cycle.

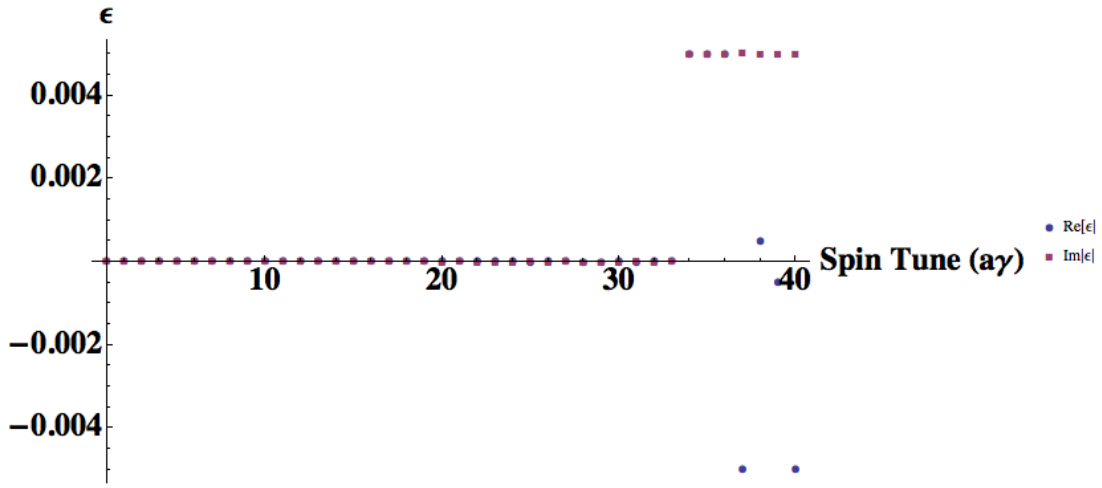

Figure 5.3: Set of orthogonal imperfection bumps at energies $a\gamma$ from 1 to 40.

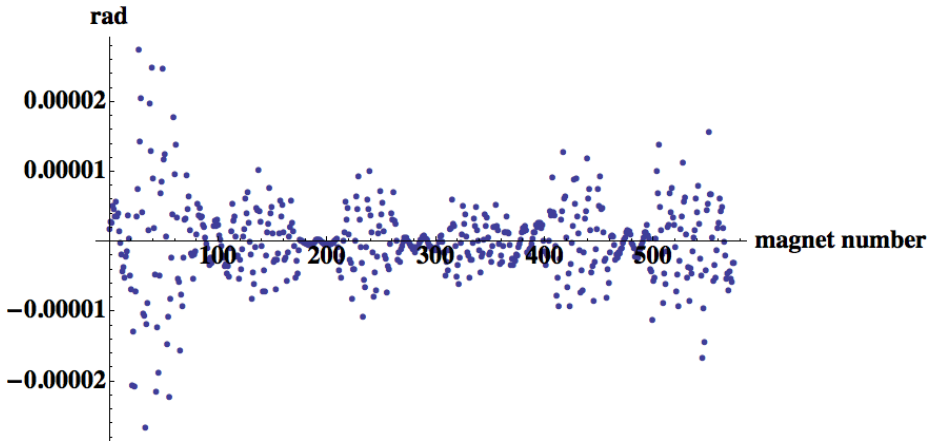

Figure 5.4: Magnet strengths used to construct the set of orthogonal imperfection bumps at energies $a\gamma$ from 1 to 40, shown in Figure 5.3.

5.2.4 Approach to Tuning Up the RCS

Tuning up of the RCS will occur in several steps. First the beam will be circulated and accelerated to top energy without beam losses. This will require achieving closed orbit distortions of 1.5 to 1 mm RMS. At this level of alignment we expect to reach up to $a\gamma \approx 34$ to 36 with 95% polarization transmission. This means that in reality polarization correction schemes are only required for the final 6 or 7 imperfection resonances of the ramp. Using the BPM/corrector pairs in the lattice with a standard SVD correction algorithm in MADX, we can readily achieve 0.1 mm RMS orbit and less. This also yields DEPOL calculated imperfections that give polarization values in excess of 95%. In the event that there remains residual polarization loss above 5%, static orthogonal harmonic bumps can be constructed targeting these final 7 resonances. Thus these bumps could be constructed to tune out any possible residual polarization loss after standard orbit correction.

In this case the approach would be to extract into the storage ring at energies just above each targeted imperfection resonance. The polarization could then be measured in the storage ring and the offending imperfection tuned out using these orthogonal bumps. We anticipate proceeding extracting at each successively higher imperfection resonance energy until the whole energy range is tuned.

5.2.5 Partial Snake Upgrade Option

We have performed preliminary spin tracking work considering a 12% partial solenoidal snake option. In this case the slower ramp rate of 200 ms should be used to both reduce the necessary ramp rate for the partial snake magnets and reduce the field strength necessary to achieve 12% snake since the slower one crosses a given the integer spin resonance the more spin rotation will be achieved. 12% should be sufficient to achieve a full spin flip at each imperfection spin resonance. This option would correct any polarization loss

due to imperfection resonances. The one concern was that the introduction of the solenoid element would disrupt the symmetry of the lattice enough to re-introduce intrinsic resonances. However our initial tracking work shows that the normalized emittance can still be maintained above 800 µm normalized without observable intrinsic resonance effects (see Figure 5.5). At this point in our studies the limit of 800 µm is given by the dynamic aperture and not by polarization; better decoupling should improve this. The technically

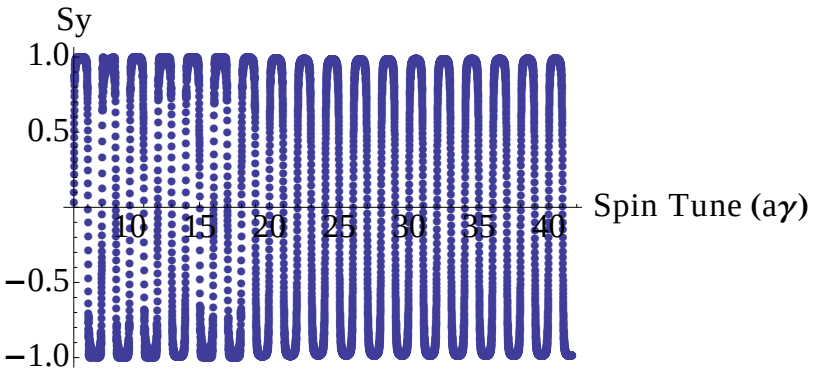

Figure 5.5: Zgoubi tracking results for 1 particle at 800 µm normalized emittance with a 12% partial snake

challenging part of this option is to construct a partial snake to ramp through the desired integrated field values in 200 ms. There are several options of varying cost under investigation:

- **Ramped Solenoid Partial Snake** One option is to use a 10 m long solenoidal partial snake to reach 2.2 T over 200 ms. This could be constructed using a superconducting magnet and a normal conducting magnet. The superconducting magnet would not be ramped and would provide about 1/2 the field. On the interior would be a normal conducting magnet, ramped at twice the rate from negative to positive field. This option appears feasible though costly.

- **Static Solenoid plus Helical Dipole Partial Snake** Another option would be to use both a solenoidal partial snake and a ramped helical dipole partial snake. The solenoid could be superconducting and provide a static field of $\approx$ .3 T over 4 m. This would provide a 30% snake at injection and a 12% snake at 1 GeV. The helical partial snake could be warm and ramped to its 12% peak value by 1 GeV. Above 1 GeV the helical snake would maintain the 12% snake even as the solenoid snake contribution fell off with γ in the acceleration to 18 GeV. This is because the strength of the helical snake has a much smaller dependence on energy than a solenoidal snake. This way we avoid the large orbit distortions caused by the helical dipoles at low energies plus compensating for the fall in snake strength with energy which solenoid snakes experience.

5.3 Electron Beam Polarization in the ESR

5.3.1 Spin Dynamics in the Electron Storage Rings

The collision of longitudinally polarized electrons and ions is a key requirement of an electron-ion collider, and a large effort has been undertaken to ensure good polarization of the electron beam during the store. The evolution of beam polarization in electron storage rings is defined by two processes related to synchrotron radiation: Sokolov-Ternov self-polarization, and depolarization caused by stochastic photon emission. The self-polarization process leads to a build-up of electron polarization in the direction opposite to the vertical guiding field, up to a maximum level of 92.4% in a perfectly planar storage ring without spin rotators. Stochastic photon emission leads to a randomization of the particle spin directions (*spin diffusion*).

Because experimenters call for the simultaneous storage of electron bunches with both spin helicities, the Sokolov-Ternov effect is not an option for EIC as it tends to polarize all bunches in the same direction, namely upwards for the clockwise rotating electrons. A full energy polarized electron injector is needed instead, so the electron bunches are injected into the storage ring with high transverse polarization ($\approx$ 85%) and the desired spin direction.

In the storage ring the polarization is then brought into the longitudinal direction at the IP by a couple of solenoidal spin rotators. However, *spin matching* [216] [217] is needed to minimize the spin diffusion introduced by the rotators (see Section 3.5.1).

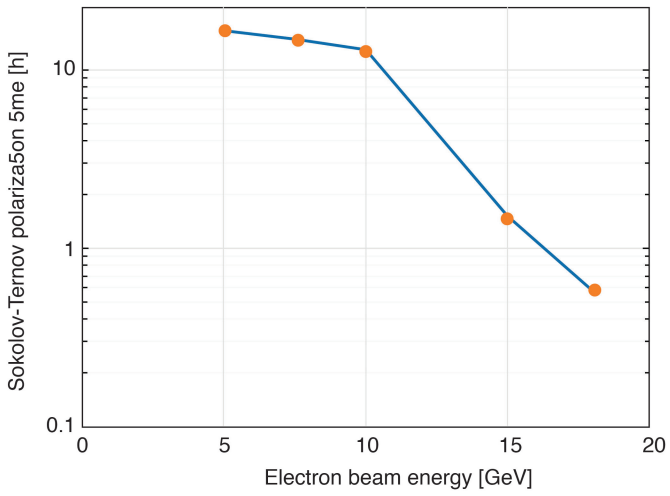

Figure 5.6: Sokolov-Ternov electron spin polarization time as a function of electron beam energy. The depolarization for spin parallel to the magnetic guide field due to the Sokolov-Ternov effect becomes important for beam energies well above 10 GeV. At 18 GeV, electron bunches with polarization in the direction of the guide field have to be replaced every six min.

The self-polarization rate has a strong dependence on beam energy (as γ^5) and average dipole bending radius (as $\langle 1/|\rho|^3 \rangle$). The self-polarization time for the EIC storage ring placed in the present RHIC tunnel is shown in Figure 5.6. It takes into account the split dipole structure that enhances the synchrotron radiation at energies below 10 GeV. The self-polarization time is quite long over the entire energy range, except when approaching 18 GeV where, for the ESR optics, it drops to about 35 minutes.

While the Sokolov-Ternov effect is a slow process, stochastic photon emission in the storage ring in the presence of misalignments and spin rotators may quickly destroy the polarization of the injected beam, thus requiring a continuous replacement of the depolarized bunches. The requirement on polarization in the EIC storage ring is assessed by considering that polarization varies with time as

$$P(t) = P_\infty \left[1 - \exp^{-t/\tau_p}\right] + P(0) \exp^{-t/\tau_p} \tag{5.7}$$

where P_∞, $1/\tau_p$ and $P(0)$ are the asymptotic polarization, the polarization rate, and the initial polarization, respectively. It holds that

$$P_\infty \simeq \frac{\tau_p}{\tau_{\text{BKS}}} P_{\text{BKS}} \qquad\qquad \frac{1}{\tau_p} \simeq \frac{1}{\tau_{\text{BKS}}} + \frac{1}{\tau_{\text{d}}} \tag{5.8}$$

where $1/\tau_{\text{d}}$ is the spin diffusion rate, while P_{BKS} and $1/\tau_{\text{BKS}}$ are respectively the asymptotic polarization and the polarization rate for the *ideal* machine in absence of spin diffusion (the Baier-Katkov-Strakhovenko generalization of Sokolov-Ternov quantities for a lattice where the magnetic field is not homogeneously vertical [218]). P_{BKS} and $1/\tau_{\text{BKS}}$ depend upon the fields on the design orbit. Their values for the EIC ESR optics at 18 GeV are about 83% and 35 minutes, respectively.

Figure 5.7 shows the polarization versus time under the assumption that the initial polarization is $\pm$85% and the asymptotic polarization is +40%. After 5 minutes the polarization of upwards polarized bunches is still 73.6% with a 5 minutes average of 79%, while for downwards polarized bunches the polarization decays to -53.4%, with an average of -68.5%.

Polarization after $\tilde{t}$ = 5 minutes and the 5 minutes average are shown in Figure 5.8 versus P_∞ for $P(0)$ = -85%. To get $< P >$=-70% over 5 minutes it must be P_∞=48%. This less demanding value with respect to the ATS optics of the pCDR is due to the larger τ_{BKS}.

Another source of spin diffusion, besides rotators, are magnet misalignments. Based on HERA-e and LEP experience, high polarization needs a well corrected orbit and possibly a special orbit correction scheme aiming to minimize $\delta\hat{n}_0(s)$, the polarization axis distortion w.r.t. the periodic solution to the Thomas-BMT equation on the ideal orbit [213] [171]. Correction at HERA-e, $\delta\hat{n}_0(s)$ correction was performed by empirically tuning the four most important orbit harmonics through closed orbit bumps (*harmonic bumps*) in the machine arcs. Diagnostics should permit the computation of those harmonics from the BPM

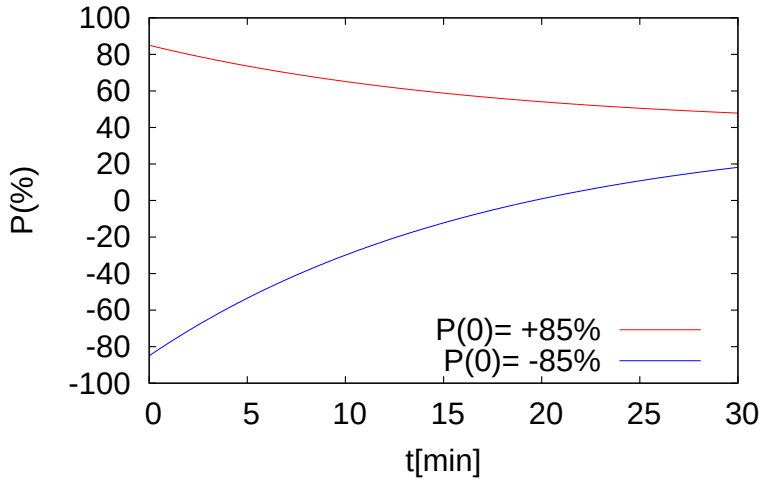

Figure 5.7: Electron beam polarization as a function of time for $P_\infty = 40\%$. Red: $P(0) = +85\%$; blue: $P(0) = -85\%$.

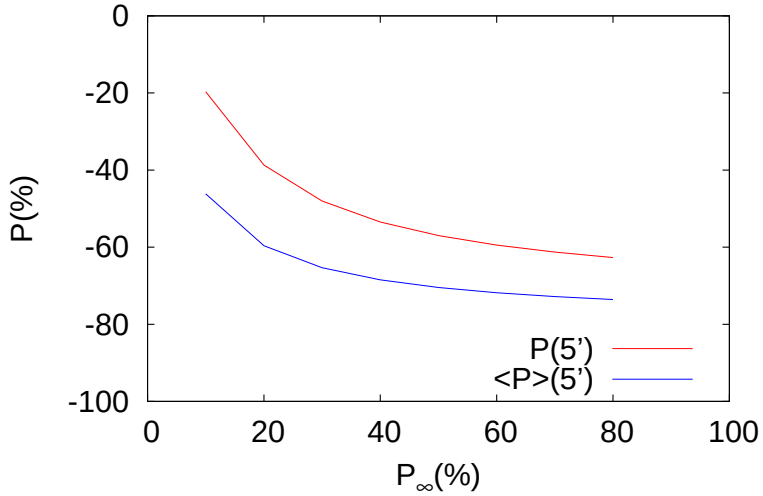

Figure 5.8: Electron beam polarization at $\tilde{t} = 5$ minutes (red) and polarization averaged over the first 5 minutes (blue) after injection versus asymptotic polarization P_∞, with initial polarization $P(0)$= -85% .

readings, as was done at LEP [28], thus speeding up the optimization process.

Additional tools that allowed the delivery of high $e^\pm$ beam polarization to the HERA experiments included fine adjustments of the betatron tunes, tracking beam energy fluctuations due to changes of the horizontal corrector settings, store-to-store tracking of harmonic bump settings, and the analysis of harmonic content of vertical corrector strength changes.

Polarization tuning to eliminate imperfection resonances will be easier in EIC than it was in HERA-e. A more efficient polarimeter design and the frequent injection of fully polarized bunches will speed up the tuning process by a factor 10 to 100.

The effect of beam-beam interactions on polarization must be evaluated. The large electron beam-beam tune shift effectively widens the intrinsic spin resonances. In HERA, the effect of beam-beam interactions on polarization was not critical. Usually it was observed that non-colliding electron bunches had a smaller polarization in collision mode because the tunes were optimized for colliding bunches, suggesting that a large horizontal beam-beam parameter pushes a large number of electrons away from the optimum tune. This will be mitigated in EIC, with only one collision per turn, not two.

The spin tracking study for the EIC electron beam is not yet complete. The following two sections present the results obtained so far for the ESR optics version 5.2.

5.3.2 Polarization Calculations for the ESR

The general expression for equilibrium polarization and polarization time in an actual storage ring has been worked out in a semi-classical approximation by Derbenev and Kondratenko [219]. Direct evaluation of their formula has been attempted in various codes with limited success.

Here we rely on the SITROS package [220]. The package includes a module, SITF, where orbit and spin motion are linearized, and a Monte-Carlo tracking module with second order orbit motion and non-linear spin dynamics in the presence of quantum excitation and radiation damping. Once the 6D equilibrium distribution is reached, the particle spins that are initially all aligned with the periodic solution of the Thomas-BMT equation are tracked over a number of turns chosen by the user. The depolarization rate and asymptotic polarization are evaluated from the fit of $P(t)$ in Equation 5.7. The fully 6D code SITF reads the same input file allowing preliminary checks before embarking on time consuming tracking.

SITROS results for HERA-e were in good agreement with observations, with the exception of the evaluation of beam-beam interaction effects which were somewhat pessimistic.

So far the ESR polarization studies have been limited to the 18 GeV case, which is the most challenging. For luminosity operation the fractional parts of machine betatron tunes are set to $Q_x = 0.12$, $Q_y = 0.10$, and the synchrotron tune to $Q_s = 0.046$.

Polarization Calculations for the Unperturbed ESR

Figure 5.9 shows polarization versus $a\gamma$ for the ideal machine, as computed by SITF in a linear approximation where $a = 0.0011596$ is the anomalous magnetic moment of the electron. In a planar machine without strong solenoids $\nu_s = a\gamma$ is the spin tune – the number of precessions per turn performed by a spin around $\hat{n}_0$,. The blue, magenta and cyan lines are the net polarization components,defined by the depolarization mechanisms due to horizontal, vertical and longitudinal motion, correspondingly. The dips correspond to the linear resonances $\nu_s \pm mQ_z =$ integer, with $z = x, y, s$.

Figure 5.10 shows the RMS value of $\delta\hat{n}_0$ evaluated outside the rotator region, where $\hat{n}_0$ is

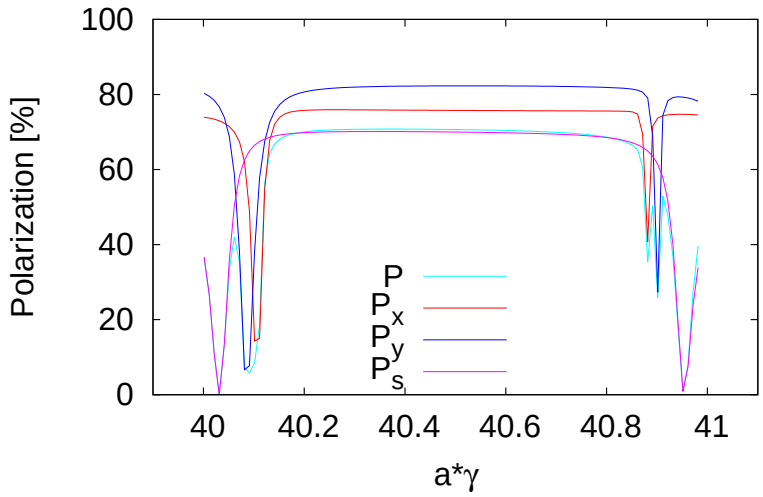

Figure 5.9: Asymptotic polarization as a function of spin tune $a\gamma$, in a linear approximation with tunes $Q_x = 0.12$, $Q_y = 0.10$ and $Q_s = 0.046$. The blue, magenta and cyan lines are the asymptotic polarization related to the horizontal, vertical and longitudinal motion components.

perfectly vertical in the absence of misalignments. Even though the energy scan is performed while keeping the strengths of the rotator magnets constant, $\delta\hat{n}_0$ is small over the whole range. The corresponding SITROS tracking results are shown in Figure 5.11.

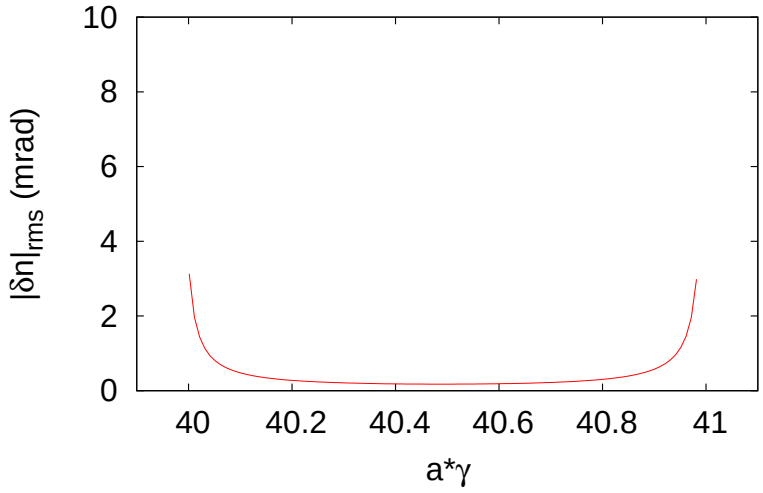

Figure 5.10: RMS value of $\delta\hat{n}_0$ as a function of spin tune $a\gamma$ with tunes $Q_x = 0.12$, $Q_y = 0.10$ and $Q_s = 0.046$.

Unlike observed in HERAe simulations, the difference between the maximum attainable polarization from linear and non-linear calculations is very large. Moreover polarization dips are observed also at high order synchrotron sideband resonances. For the (obsolete) ATS optics, SITROS tracking results have been cross-checked with PTC [221] by Z. Duan [222]. As shown in Figure 5.12, SITROS results are somewhat more pessimistic,

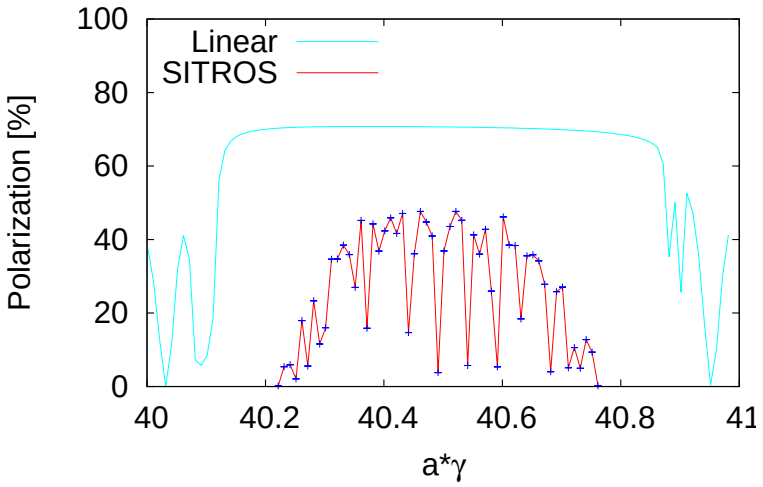

Figure 5.11: Asymptotic polarization P_∞ versus spin tune $a\gamma$ computed by SITROS for the unperturbed machine with tunes $Q_x = 0.12$, $Q_y = 0.10$ and $Q_s = 0.046$.

however the discrepancy with the linear computation is confirmed. It is worth noting that the discrepancy appears only for the case of an unperturbed optics.

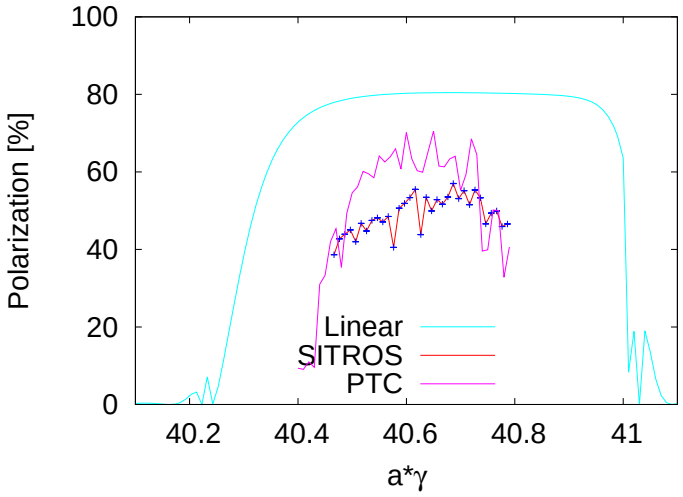

Figure 5.12: Asymptotic polarization (P_∞) computed by SITROS and PTC for the (obsolete) ATS optics with $Q_x = 0.12$, $Q_y = 0.10$ and $Q_s = 0.046$. (PTC calculations courtesy of Z. Duan.)

Spin Tune Modes

Often the design-orbit spin tune ν_0 is approximately proportional to the beam energy, so the energy must be chosen to avoid first-order spin-orbit resonances. Such resonances result from spin-orbit coupling and coherence between spin motion and the betatron and synchrotron motion excited by synchrotron radiation. Spin tracking simulations confirm that depolarization occurs at these resonances and also at their synchrotron sidebands. The latter result from a modulation of the spin precision rate due to synchrotron oscillations. There are techniques that make ν_0 independent of the beam energy, avoiding betatron and synchrotron tune resonances and improving the electron polarization.Spin tracking simulations will be performed to confirm these expectations.

The ESR design has two spin rotators, one upstream and one downstream of the collision point at IP6 to provide longitudinal polarization at the detector. The vector $\hat{n}_0$ is vertical in the arcs and has the same direction in the two halves of the ring. If the solenoid fields are reversed in one spin rotator as shown in Figure 5.13, the overall spin rotation axis of the pair of rotators changes from being vertical to being radial and makes the combined spin rotators equivalent to a Siberian snake that rotates $\hat{n}_0$ by 180° around the radial direction. Then by installing a Siberian snake at IP12 with a proper orientation of the rotation (snake) axis, the electron ring produces integer or half integer values for ν_0 at all beam energies, resulting in increased polarization lifetime. In addition, the net field integral to zero with spin rotator solenoid fields of opposite polarity, significantly facilitating spin matching for the longitudinal motion.

Figure 5.13: Reversing solenoid fields in one spin rotator turns the two-spin-rotator configuration into a Siberian snake.

The integer spin tune mode with $\nu_0 = k$ (for integer k) is obtained by having parallel snake axes at IP6 and IP12, with a design orbit bend angle of π between them. However, the reference ESR lattice design has an orbital bend angle 24.7 mrad less than π between IP6 and IP12 and 24.7 mrad more than π between IP12 and IP6. Therefore, the snake axis at IP12 should align with the local $\hat{n}_0$ lying at 147.87°with respect to the longitudinal due to the 24.7 mrad missing or extra bending angles between IP6 and IP12. Running with an integer spin tune is not practical for a realistic ring. The one-turn 3×3 spin matrix will be shifted slightly away from the unit matrix with a small additional appropriate magnetic field. Then $\hat{n}_0$ becomes unique. Simulations confirm that it is stable and lies very close to the vertical in the arcs as required, pointing upwards in one half and downwards in the other.

The spin tune mode with a half integer value for ν_0 are obtained through methods similar to those used to create the mode with $\nu_0 = k$. The differences are that the snake axis at

IP12 is either perpendicular to the snake axis at IP6 if the orbital bend angle is π between IP6 and IP12, or in the horizontal plane along the direction of 57.87° with respect to the longitudinal direction. In this case, $\hat{n}_0$ is unique.

Both integer and half-integer values of spin tune ν_0 are implemented in the ESR by reversing the solenoid fields in one spin rotator and placing a snake at IP12 with snake axis oriented appropriately with respect to the snake axis of the spin rotators at IP6. In both modes, $\hat{n}_0$ points upwards in one half of the ring and downwards in the other half. Figure 5.14 shows the evolution of spin components of with an initial spin $\vec{S}$ in the longitudinal direction at IP6.

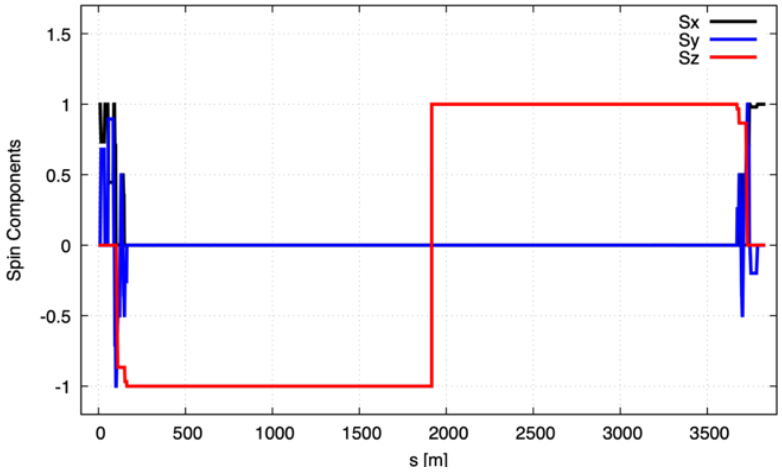

Figure 5.14: The evolution of spin components S_x, S_y, and S_z in the ESR with the initial spin aligning in the longitudinal direction at IP6 (x: longitudinal, y: radial, z: vertical).

The Effect of Misalignments on the Electron Spin Polarization

The MADX toolkit is used to simulate the effect of quadrupole misalignments with the RMS values listed in Table 5.6, before writing a lattice into a SITROS readable file. No BPM errors have yet been considered. The lattice includes 546 dual-plane BPMs and 546 horizontal and 546 vertical correctors next to each quadrupole.

Table 5.6: Assumed quadrupole RMS misalignments.

Parameter	Value
Horizontal offset, δx^Q [µm]	200
Vertical offset, δy^Q [µm]	200
Roll angle, $\delta \psi^Q$ [µrad]	200

Standard MADX tools fail to correct the orbit, due to the large coupling between the rotator solenoid pairs. Ignoring the 20 BPMs in that 150 m section of the ring leaves 38 quadrupoles uncorrected. A custom-built correction algorithm records the horizontal and vertical orbit response to the excitation of each of the 1092 correctors, and then corrects the MADX computed orbit in the horizontal and vertical plane simultaneously via SVD analysis. The resulting kicks are then fed back into MADX and if necessary the residual orbit is further corrected using the MICADO algorithm. This procedure works well when the tunes are not too close to each other or to the integer resonance. The orbit can be corrected down to a few microns and the agreement between MADX and SITF is reasonable.

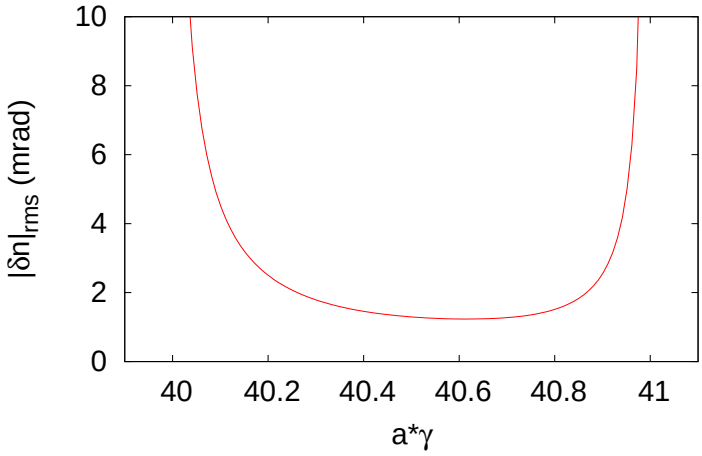

Figure 5.15: $\delta\hat{n}_0$ for a perturbed lattice with $Q_x = 0.12$, $Q_y = 0.10$, and $Q_s = 0.046$.

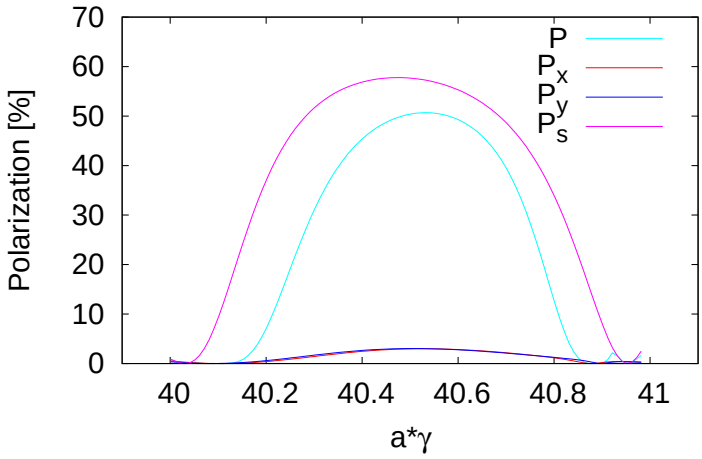

Figure 5.16: Asymptotic polarization, P_∞, computed by SITF for the perturbed machine after closed orbit correction with $Q_x = 0.12$, $Q_y = 0.10$, and $Q_s = 0.046$.

The residual RMS closed orbit achieved after correction computed by SITF in the presence of synchrotron radiation is $x_{\mathrm{RMS}} = 0.266\,\mathrm{mm}$ and $y_{\mathrm{RMS}} = 0.046\,\mathrm{mm}$. The beam emittances are $\epsilon_x = 23.6\,\mathrm{nm}$ and $\epsilon_y = 4.7\,\mathrm{nm}$, while the minimum tune distance $|C^-| = 0.017$, explaining

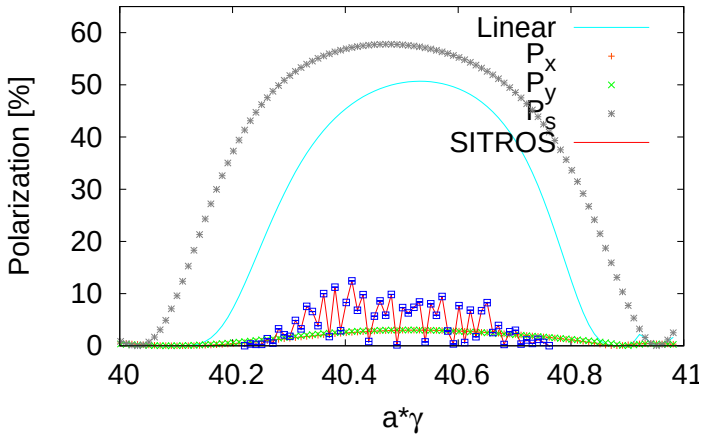

Figure 5.17: Asymptotic polarization, P_∞, computed by SITROS for the perturbed machine after closed orbit correction with $Q_x = 0.12$, $Q_y = 0.10$, and $Q_s = 0.046$. The dotted red, green and grey lines are the polarization values related to the 3 degrees of freedom separately from the linear calculation.

why ϵ_y is large despite the well corrected vertical orbit. The orbit is locally corrected, so $\delta\hat{n}_0$ is also small as shown in Figure 5.15, with the linear polarization shown in Figure 5.16. The approximate equality of P_x and P_yl is a typical hint of strong betatron coupling. The tracking calculation shown in Figure 5.17 confirms that polarization is larger than the small values of P_x and P_y.

The 4 most important harmonic components of $\delta\hat{n}_0$ are corrected by 12 harmonic bumps, which have the side effect of increasing the minimum tune distance $|C^-|$ from 0.0170 to 0.0196. The spurious vertical dispersion and the coupling functions $w^{\pm}(s)$ at the BPMs are further minimized by using 16 skew quadrupoles in an SVD analysis, reducing the mini-

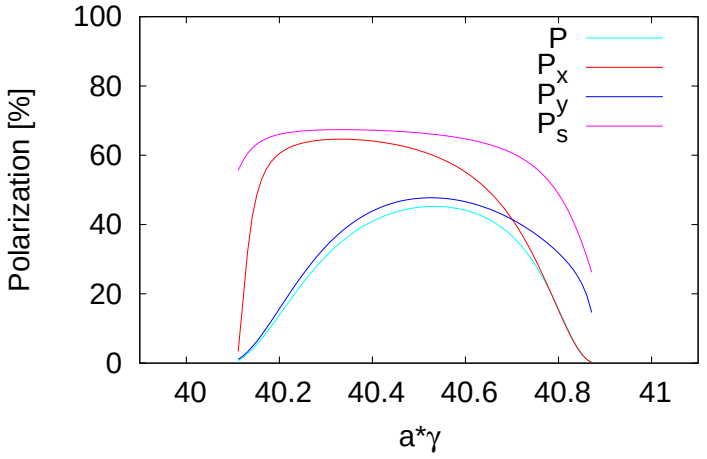

Figure 5.18: Asymptotic polarization (P_∞) computed by SITF for the perturbed machine with tunes $Q_x = 0.12$, $Q_y = 0.10$ and $Q_s = 0.046$. Spurious vertical dispersion, $\delta\hat{n}_0$, and betatron coupling have been corrected, in addition to the closed orbit.

mum tune distance to 0.0001 and the RMS vertical dispersion to 5 mm from 12 mm [223]. The resulting vertical emittance is 30 pm. The corresponding linear polarization is shown in Figure 5.18. The SITROS results in Figure 5.19 show a clear improvement over those in Figure 5.17.

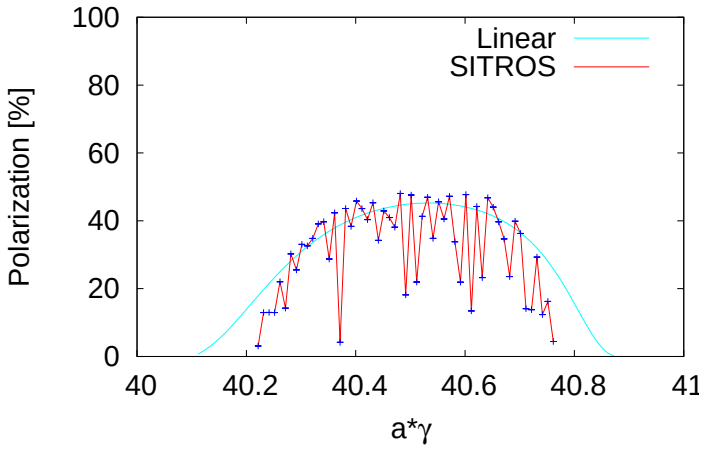

Figure 5.19: Asymptotic polarization (P_∞) computed by SITROS for the perturbed machine with $Q_x = 0.12$, $Q_y = 0.10$ and $Q_s = 0.046$. Spurious vertical dispersion, $\delta\hat{n}_0$, and spurious vertical dispersion and betatron coupling have been corrected in addition to the closed orbit.

Tuning the vertical beam size at the IP

HERA experience and beam-beam simulations show the need to match electron and proton beam sizes at the IP, in order to not to spoil luminosity and proton beam lifetime. The natural vertical emittance at 18 GeV is about 2 pm, while a well corrected realistic ESR can achieve a vertical emittance of some tens of pm at 18 GeV. Therefore σ_y^{*e} should be increased by about a factor of 10 to match the proton beam size. Some methods of increasing the vertical emittance, such as antisymmetric vertical orbit bumps around low-β locations or long vertical bumps through the sextupoles, have a large impact on polarization. The least disruptive method is to rely on local betatron coupling by using two pairs of skew quadrupoles around the IP. The skew quadrupole strengths needed to increase σ_y^{*e} from 2 µm to about 16 µm are quoted in Table 5.7, together with their positions with respect to the IP. The expected polarization is shown in Figure 5.20.

5.3.3 Summary

Simulation studies performed so far for the most challenging case of an 18 GeV electron energy, and in presence of realistic quadrupole misalignments and rolls, show that an asymptotic electron polarization of 40%–45% is achievable.

With P_∞=40% and $|P(0)|$=85% the 5 minute average polarization is about 79% for bunches injected with upwards polarization – parallel to the asymptotic polarization. The 5 minute

Table 5.7: Skew quadrupole positions, and integrated strengths necessary to increase the vertical beam size at the IP to $\sigma_y^{*e} \simeq 16\,\mu\text{m}$.

Skew quad	Location s [m]	Strength K [m^{-1}]
SKQA	-4.4	0.0045
SKQB	-1.0	-0.0198
SKQC	1.0	0.0198
SKQD	4.4	-0.0045

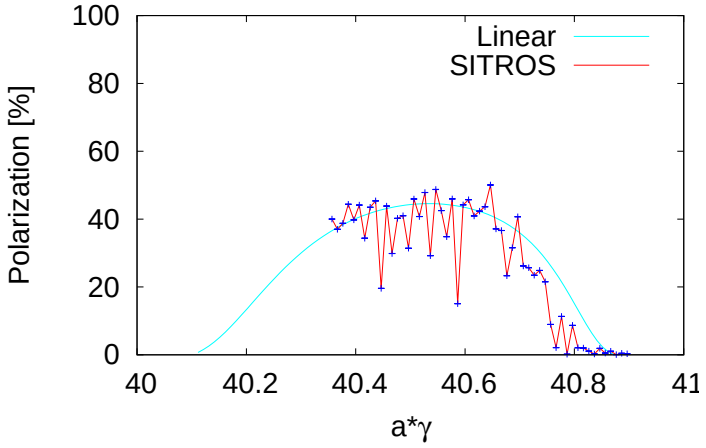

Figure 5.20: Asymptotic polarization, P_∞, computed by SITROS for a perturbed machine (with tunes $Q_x = 0.12$, $Q_y = 0.10$ and $Q_s = 0.046$) using two pairs of skew quadrupoles to increase the vertical beam size to $\sigma_y^{*e} \simeq 16\,\mu\text{m}$.

average drops to 68.5% for downwards initial polarization. Such bunches must be replaced every 4.5 minutes to keep the average polarization to about 70%. The same average is obtained over 15 minutes for bunches injected with upwards polarization.

Two pairs of skew quadrupoles around the IP (embedded in the experimental solenoid compensation scheme) transfer some horizontal emittance into the vertical plane to control the beam size for collisions.

Future study topics include the impact of BPMs errors and the acquisition of statistics, and the impact of beam-beam effects on polarization.

5.4 Proton Beam Polarization in the HSR

RHIC has provided polarized proton beams over an energy range from 31 GeV to 255 GeV during the past decade. To preserve polarization through numerous depolarizing resonances over the whole accelerator chain, harmonic orbit correction, partial and full Siberian Snakes, and a horizontal tune jump system have been used. In addition, close attention has been paid to betatron tune control, orbit control and magnet alignment. A polarization of 60% at 255 GeV has been delivered to experiments with an intensity of 1.8×10^{11} protons per bunch. For the EIC, the beam brightness has to be maintained to reach the desired luminosity. Since the EIC will use only the present RHIC Yellow ring, spin rotators and snakes from the Blue ring can be converted into additional Siberian Snakes in the HSR. With a proper arrangement of six snakes in the hadron ring and additional reduction of emittance growth in the AGS, the polarization is expected to reach 70% at 275 GeV beam energy.

5.4.1 Introduction

The AGS delivers polarized proton beams with 70% polarization at an intensity of 3×10^{11} protons per bunch. Strong hadron cooling will reduce the vertical emittance at store for the highest luminosities. During the acceleration ramp the emittances will be larger, initially as delivered by the AGS. This larger emittance has to be taken into account when calculating depolarizing resonance strengths.

The current proton acceleration chain is shown in Figure 5.21. High intensity, high polarization H^- is produced at the polarized proton source. The H^- beam polarization is measured at the end of the 200 MeV LINAC as 80–82%. The beam is then strip-injected into the AGS Booster. The Booster vertical tune is set high enough so that the intrinsic resonance in the Booster at $0 + \nu_y$ is avoided. Two imperfection resonances in Booster are corrected by harmonic orbit correction. In the AGS, two partial Siberian Snakes separated by $1/3$ of the ring circumference are used to overcome the imperfection and vertical intrinsic resonances [135]. The vertical tune ν_y on the energy ramp is mostly above 8.98, so that it is in the spin tune gap, away from the high order snake resonances. To avoid the horizontal intrinsic resonances driven by the partial snakes, a pair of pulsed quadrupoles is employed to jump the tune across the many weak horizontal intrinsic resonances on the ramp [136]. Two full Siberian Snakes are used in each of the two present RHIC rings to maintain polarization [224]. Feedback during acceleration – on the betatron tune, coupling, and orbit – is crucial for polarization preservation.

The polarization measured at AGS extraction energy is shown in Figure 5.22 as a function of beam intensity. The apparent polarization dependence on intensity is really a dependence on emittance, since emittance and intensity were simultaneously reduced by scraping in the Booster. As higher intensity is always associated with larger emittance, greater depolarizing resonance strengths and lower polarization is expected at higher intensities. The polarization at 3×10^{11} is about 65%.

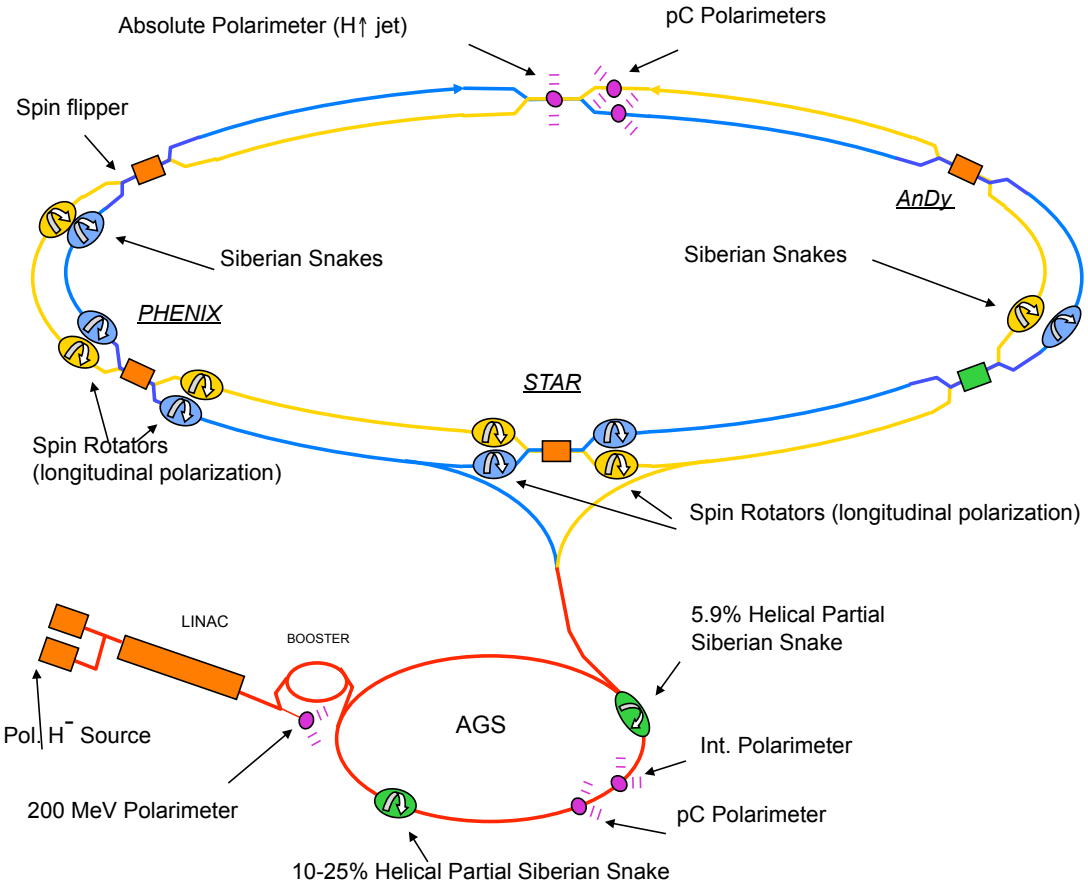

Figure 5.21: Layout of the current RHIC complex.

Emittances measured by the AGS Ionization Profile Monitor (IPM) are affected by space charge forces. To mitigate this effect, the RF is turned off during beam profile measurement at acceleration flattop. The emittance reported by the IPM with RF off is plotted in Figure 5.23. The projected emittance at zero intensity is non-zero because there is some emittance growth in the Booster and mismatch in the transfer line. The horizontal and vertical RMS normalized emittances are about 2.4 µm and 2.6 µm, respectively, at an AGS extraction intensity of 3×10^{11} protons per bunch,

The vertical emittance of ion beams will be cooled at the injection of HSR down to 0.75 µm. As the experience at RHIC shows, the polarization transmission efficiency up to 100 GeV is close to 100% but only about 92% for 250 GeV at 1.8×10^{11} bunch intensity due to stronger intrinsic resonances. The vertical emittance is about 2.4 µm. Figure 5.24 shows that the highest resonance strength, calculated by DEPOL [211], for a particle with 10 µm normalized action invariant is about 0.18 below 100 GeV, and about 0.45 above 100 GeV. The intrinsic resonance strength is proportional to the square root of vertical emittance, so the

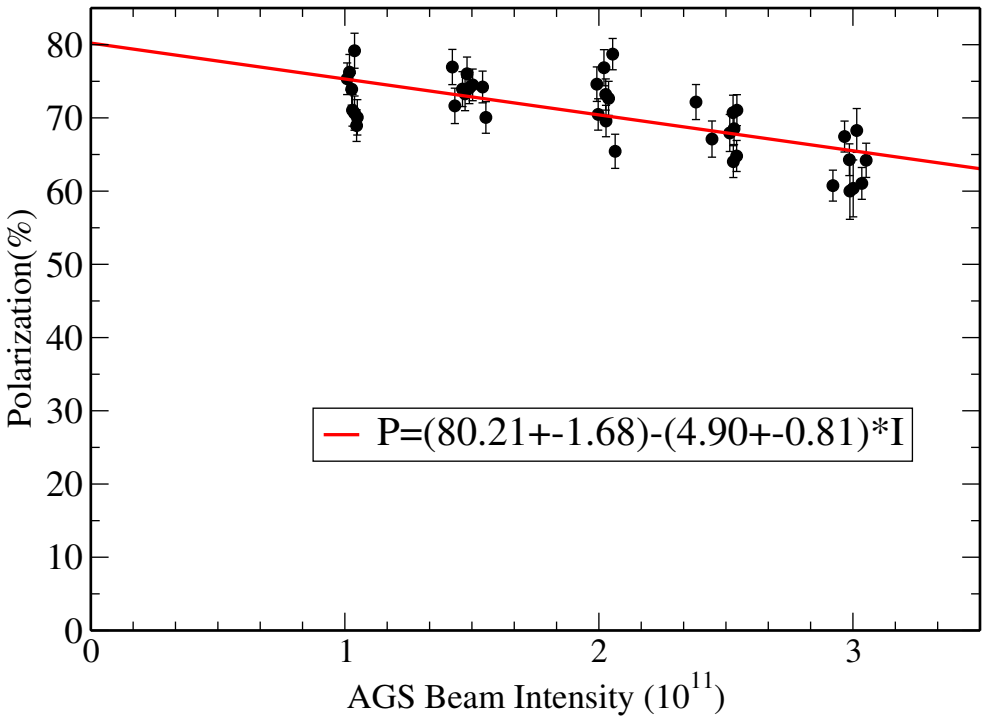

Figure 5.22: AGS polarization at extraction as function of bunch intensity. The polarized proton source can deliver an intensity of 9×10^{11} at the Booster input. Booster scraping (both horizontal and vertical) is used to reduce the beam emittance for AGS injection. The intensity in this figure is changed by varying the Booster scraping level.

resonance strength seen in RHIC is 0.09 below 100 GeV and 0.225 above 100 GeV. This implies that the two snakes can preserve polarization for an intrinsic resonance strength 0.09, but not for 0.225. The resonance strength threshold for 100% polarization transmission efficiency with two snakes is therefore in the range from 0.09 to 0.22.

As a rule of thumb, the resonance strength threshold increases in proportion to the number of snakes. The depolarizing resonances are stronger during ^{3}He operation (see below) so spin manipulating magnets will be moved from the RHIC Blue ring to the Yellow HSR, to build a configuration with a total of six Siberian Snakes from Yellow snakes, Blue snakes, and Blue rotators magnets. Since the real resonance threshold is unknown, simulations are needed to determine the level of polarization preservation.

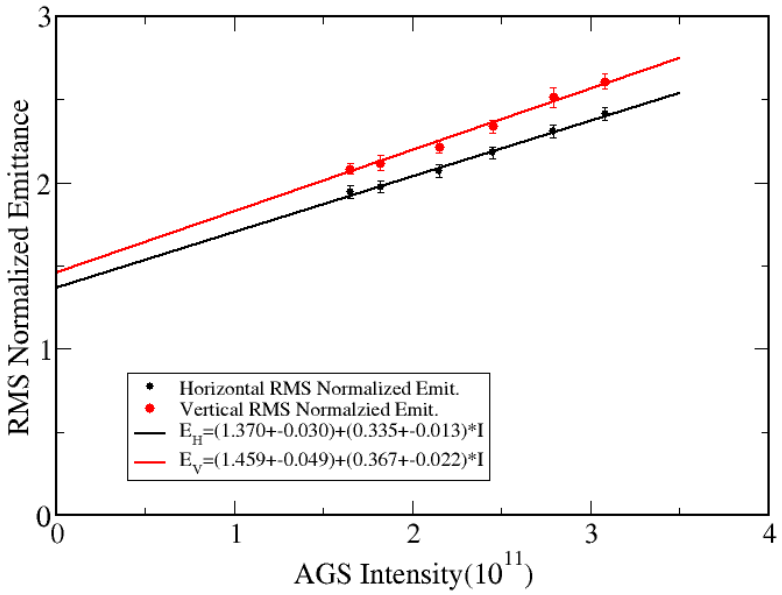

Figure 5.23: AGS emittance measured by the IPM versus intensity at AGS extraction.

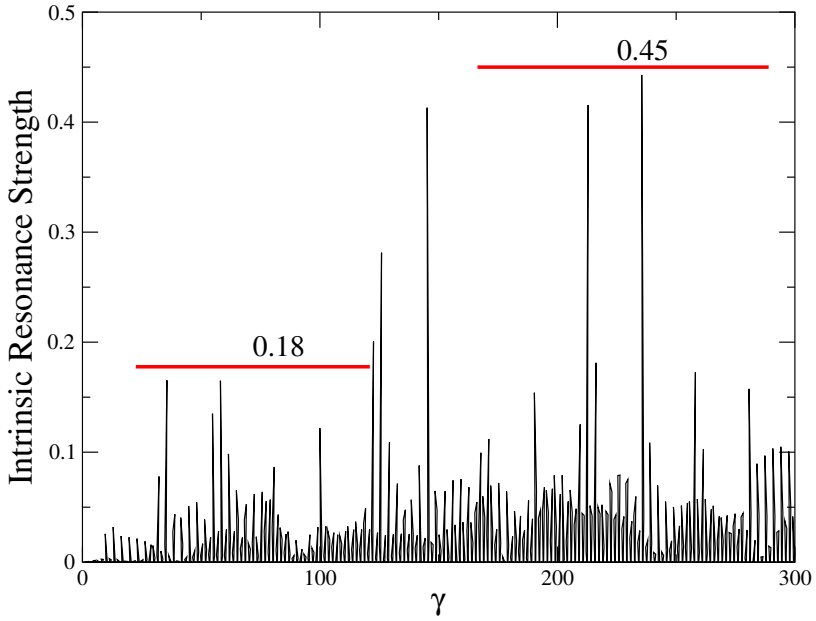

Figure 5.24: Intrinsic resonance strength of the present RHIC lattice for a particle on a 10 µm action ellipse as function of the Lorentz factor γ. Below 100 GeV, the resonance strength is less than 0.18. A stronger resonance strength of 0.45 has to be overcome, in order to accelerate a proton beam to 275 GeV.

5.4.2 Proton Spin Simulations During Acceleration

Spin tracking was performed with Zgoubi for one of the three strongest depolarizing resonances, $411 - \nu_y$, to estimate polarization transmission efficiency during acceleration [225]. The tracking was done for 8 particles on the ϵ =2.5 µm vertical action ellipse, with an acceleration rate 7 times faster than the actual, to speed up tracking. In the presence of a Siberian Snake the polarization loss is not sensitive to resonance crossing speed. Only vertical betatron motion was taken into account in the simulation.

For a configuration with multiple snakes, the snake arrangement has to satisfy the conditions for an energy independent spin tune, namely

$$\sum_{k=1,3,5} \theta_{k,k+1} = \pi \tag{5.9}$$

$$\sum_{k=2,4,6} \theta_{k,k+1} = \pi. \tag{5.10}$$

where $\theta_{k,k+1}$ are azimuthal distances defined in terms of design momentum rotation angle between the snakes. The snake axis angles are $\phi = \pm\pi/4$ from the longitudinal axis in the local Serret-Frenet frame, ensuring a spin tune of $\nu_{\text{spin}} = 3/2$ since

$$\nu_{\text{spin}} = \frac{1}{\pi} \left| \sum_{k=1}^{N_s=6} (-1)^k \phi_k \right|. \tag{5.11}$$

where $N_s = 6$ is the number of snakes. A symmetric arrangement with the 6 snakes equally spaced by $2\pi/6$ preserves polarization, although not all snake arrangements satisfying the above conditions do so.

The snake in the injection region near IP6 is constrained from being placed in the ideal location, so the snake near IP12 is moved to meet Equations 5.9 and 5.10. The snakes are located at the 6 bending angles $(\phi,\ \pi/3 - \phi,\ 2\pi/3 - \phi,\ \pi + \phi,\ 4\pi/3 - \phi,\ 5\pi/3 - \phi)$, where $\phi = 0.0435$ rad. If snakes 1 and 4 were not in their ideal locations, $-\phi$ and $\pi - \phi$, then all snakes would be separated by $\pi/3$. The simulation results shown in Figures 5.25 and 5.26 for ideal snake locations and for a pair of snakes with an offset in a RHIC lattice show little visible difference over the action range considered. Polarization is preserved for both the small and the large emittance cases, and the transmission efficiency through acceleration is close to 100%. Simulations with many particles in a 6-D distribution and with the true acceleration rate will follow.

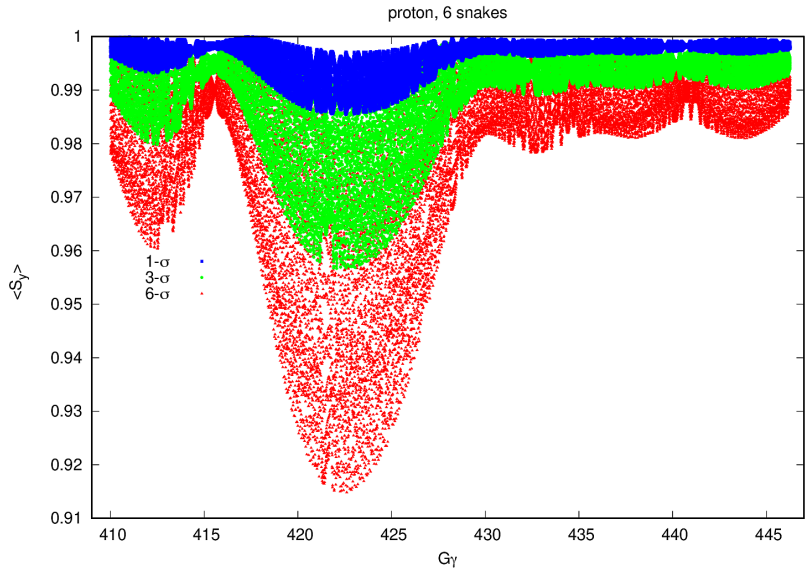

Figure 5.25: Simulation results for 6 snakes at ideal locations during acceleration through the strongest depolarizing resonance at $393 + \nu_y$. The vertical invariant is $\epsilon_y = 1,\ 3,\ 6\ \sigma$, with σ =0.75 µm the normalized action. Each trace shows the average vertical projection of the spin, computed by tracking 8 particles evenly distributed on the invariant ellipse. These results are used as a reference, for comparison with the case of one pair of snakes with an offset.

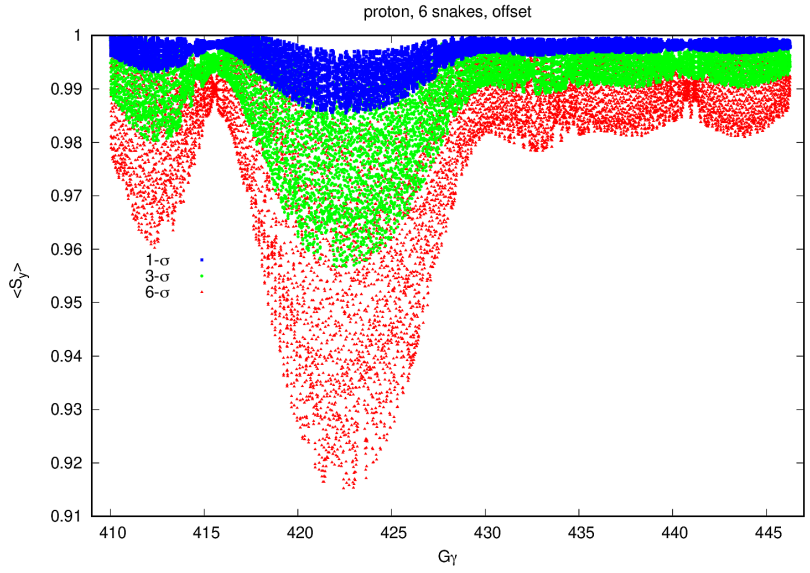

Figure 5.26: Simulation results for 6 snakes, with one pair of snakes with an offset of $\phi = 0.0435$ rad and snake axes at $\pm\pi/4$, for passage through the strongest depolarizing resonances at $393 + \nu_y$. The vertical invariant is $\epsilon_y = 1,\ 3,\ 6\ \sigma$, with σ =0.75 µm. Each trace shows the average vertical projection of the spin, computed by tracking 8 particles evenly distributed on the invariant ellipse. The effect of the horizontal invariant on spin is negligible. Polarization is preserved in all cases.

5.4.3 Space Charge Effects at Low Energies

The space charge tune shift at injection (25 GeV) is 0.1 and at the low collision energy (41 GeV) is 0.05, with a cooled ion beam. Although the depolarizing resonances are weaker at lower energies, the available betatron tune spread is larger. There are two configurations, depending on the proton collision energy:

1. In the range 100 GeV to 275 GeV, injection at 25 GeV is followed by acceleration in the HAR (if it is present) before storage in the HSR.
2. At 41 GeV, injection directly into the HSR at 25 GeV is followed by acceleration and storage. Beam passes through the inner arc from IP4 to IP2, instead of through the outer arc.

Operating the HSR at injection energy with only two snakes is most challenging. Space charge effect have been studied at both 25 GeV and 41 GeV. The polarization lifetime was simulated with lattice independent model [226]. The polarization loss rate is scanned as function of vertical betatron tune over a range of vertical emittances.

At 25 GeV the vertical emittance before cooling is 2.5 μm. The polarization decay rate with two snakes and a space charge tune shift of 0.1 is then flat at 0.0%/hr over a vertical tune range from 29.16 to 29.30, even for particles on the 10 μm action ellipse, due to the relative weak resonance strengths. Polarization lifetime is not a problem.

At 41 GeV, the vertical emittance after cooling is 0.75 μm. The polarization loss rate is also small over a wide range of vertical tune space from 29.16 to 29.30. The expected space charge tune shifts of 0.05 and 0.1 do not threaten the polarization lifetime.

5.4.4 Spin Rotator Settings

HSR will use existing RHIC spin rotators based on helical dipole magnets in order to transform the vertical beam polarization in the arcs into longitudinal polarization at IP6. The spin rotator includes 4 helical dipoles, each of them 2.4 m long with one period of helical twist. The rotator is characterized by two magnetic field values – B_1 and B_2 for outer and inner helices, respectively.

In the EIC interaction region, there is the bending angle +95 mrad between the upstream rotator and the IP and the bending angle +17 mrad between the IP and the downstream rotator. Thus, the rotators in EIC are placed much further away from the IP in terms of bending angles, and polarization vector may rotate more than one full turn between the rotator and the IP, depending on the beam energy.

The fields, B_1 and B_2, of the downstream spin rotator required for longitudinal polarization at the IP are shown in Figure 5.27, assuming maximum field of 3.6 T. The field plots show that at some energies the longitudinal polarization at the IP can not be achieved. Combining the data shown in Figure 5.27 with similar data from the upstream rotators,

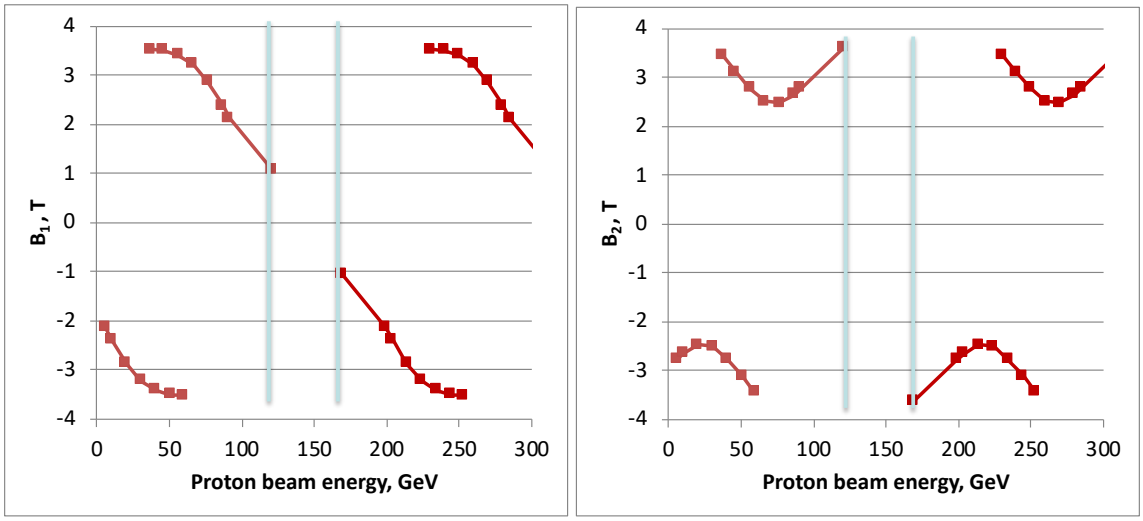

Figure 5.27: The magnetic fields of HSR spin rotators required for longitudinal polarization at IP6 versus the beam energy. Left: B_1 in the outer helices. Right: B_2 in the inner helices.

one can find that the IP longitudinal polarization can not be obtained in following energy ranges:
25.3–46.9 GeV, 120.9–127.4 GeV, 167.6–169.2 -GeV and 248.1–261.5 GeV.
Also it should be noted that unlike the RHIC spin rotator in the EIC the fields in helices will need to change their sign at different energies to cover as many energies as possible.

5.4.5 Alternative Spin Rotator Configuration

As discussed in the previous section, the HSR includes two Siberian snakes and two spin rotators on the two sides of IP6. The spin rotators change the spin direction from vertical in the arcs to longitudinal at IP6. There is an asymmetry of the orbital bending angles between the IP and the spin rotators on the two sides of the IP. It may cause a dependence of the invariant spin field $\vec{n}$ on the phase space coordinates thus reducing the polarization lifetime as discussed below. Modification of the spin rotator configuration for the EIC may also result in a gap in energies of the hadron collider ring where the spin rotators can no longer provide the longitudinal polarization at IP6. These problems can be solved by running the hadron collider ring in the spin transparent mode. In this mode, the axes of the two Siberian snakes are adjusted to nearly the same direction while their strengths are set to nearly π spin rotation angles. The spin tune is then close to zero. The polarization direction at IP6 can, in this case, be controlled without the spin rotators.

The required polarization orientation $\vec{n} = (n_x, n_y, n_z)$ can be set at IP6 by adjusting a small angle $\delta\alpha$ between the snake axes and small offsets $\delta\mu_1$ and $\delta\mu_2$ of the snakes' spin rotation angles from π:

$$\nu_x = \frac{\delta\mu_1 - \delta\mu_2}{2\pi} \sin\left(\frac{\gamma G \pi}{2}\right), \tag{5.12}$$

$$\nu_y = \frac{\delta\alpha}{\pi}\,, \tag{5.13}$$

$$\nu_z = -\frac{\delta\mu_1 + \delta\mu_2}{2\pi}\cos\left(\frac{\gamma G\pi}{2}\right)\,, \tag{5.14}$$

$$\nu = \sqrt{\nu_x^2 + \nu_y^2 + \nu_z^2} \tag{5.15}$$

where ν is the spin tune induced by the snakes serving as a 3D spin rotator. Equation (5.12) assumes that both snake axes are longitudinal.

The described rotator allows one to set any 3D polarization direction at the polarimeter by small variation of the snake currents. Exceptions are $\gamma G = k$ points where the snake rotators allows one to set any 2D polarization orientation in the (yz) plane for even k and in the (yx) plane for odd k.

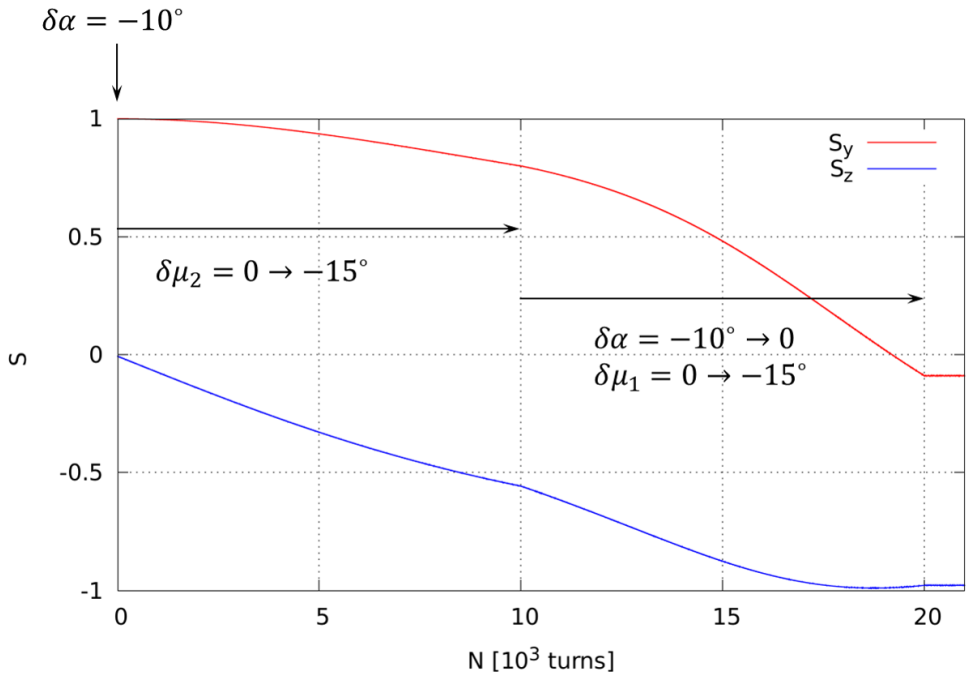

Figure 5.28: Illustration of adjustment of the polarization from vertical to longitudinal at the IP in the spin transparency mode without using the spin rotators.

Figure 5.28 illustrates the procedure for adjustment of the longitudinal polarization at the IP. The simulation is done using a spin tracking code Zgoubi. The calculation used the injection setup where $\gamma G = 45.5$ The beam is injected vertically polarized. An initially vertical stable polarization direction is set by running Snakes 1 and 2 with 180° spin rotation angles, making the Snake 2 axis longitudinal and tilting the Snake 1 axis by 10° from the beam direction in the horizontal plane. The Snake 2 angle is then ramped from 180° to 165° in 10 thousand turns while keeping its axis longitudinal. During the next 10 thousand turns, the Snake 1 angle is adjusted from 180° to 165° and its axis is at the same time

changed to longitudinal. All ramps are linear. Figure 5.28 shows that final polarization direction is nearly longitudinal. The difference is due to a change of the orbital effects of the snakes during the ramps and magnet misalignments.

The simulation in Fig. 5.28 was done considering element misalignments for the closed orbit shown in Fig. 5.29. The large orbital spikes due to the snakes are not shown in Fig. 5.29 for a better view of the orbit distortion around the ring. The simulation accounted for the orbit excursion due to the snakes. A statistical approach was used to find a level of misalignments giving an rms closed orbit distortion of 0.2 mm consistent with RHIC experience. The horizontal and vertical rms closed orbit excursions in Fig. 5.29 are 0.22 and 0.18 mm, respectively, in agreement with our expectations.

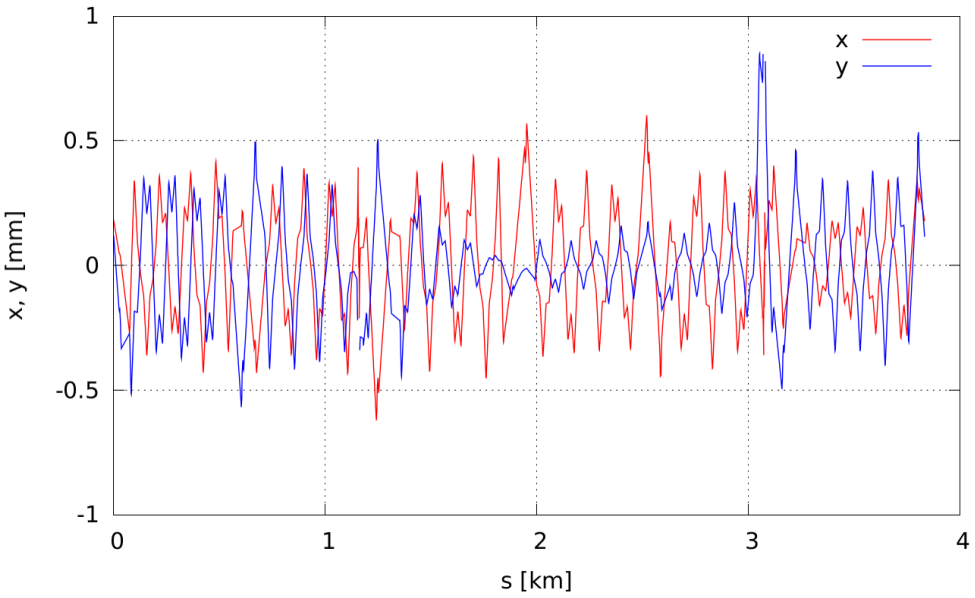

Figure 5.29: Closed orbit excursion used in the simulation shown in Fig. 5.28. The orbit distortion by the snakes is not shown for a better view of the orbit outside the snake sections but it is account for in the simulation.

The spin transparency mode is a novel technique that has not yet been used in operation. There is a plan to verify it experimentally in RHIC prior to construction of the EIC.

5.4.6 Effects of IBS and Cooling on Hadron Polarization Lifetime

Stochastic effects such as IBS, space charge, and cooling can potentially cause depolarization of the hadron beam. The mechanism is similar to that of the spin diffusion in electron rings. A stochastic scattering event instantaneously changes the particle phase space coordinates. The particle's spin orientation does not change but the stable spin field direction at the new coordinates may be different from that at the initial ones. Therefore, if the spin initially points along the spin field it is no longer aligned with the stable spin direction

after the scattering event. Only the spin component along the new spin field direction is preserved. As this process continues on, the beam gradually gets depolarized.

The polarization lifetime is determined by the diffusion rate of the particle's phase space coordinates and the sensitivity of the stable spin direction $\vec{n}$ to changes in the coordinates. Using the analogy of electron polarization lifetime τ_{pol} due to the synchrotron radiation, the polarization lifetime can be written as

$$\frac{1}{\tau_{\text{pol}}} \approx \frac{1}{2}\left\langle \left| \frac{\partial \vec{n}}{\partial \delta} \right| \frac{d(\delta^2)}{dt} \right\rangle_{\theta}, \tag{5.16}$$

where δ is the relative energy spread, $\partial\vec{n}/\partial\delta$ describes the change in the $\vec{n}$ direction with energy, and $d(\delta^2)/dt$ is the diffusion rate of the beam energy spread. Averaging inside the angular brackets is done over the accelerator azimuthal angle θ and, in general, over the beam phase space. In case of the hadron beam, the above equation describes the polarization lifetime due to the energy diffusion caused by the longitudinal IBS and electron cooling. One can write similar expressions for the polarization lifetime due to the transverse IBS and cooling rates and space charge.

The phase space diffusion rates are obtained using the appropriate analytic expressions with a specific linear optics design and design beam parameters. The sensitivity of $\vec{n}$ to changes in energy $\partial\vec{n}/\partial\delta$ and in other phase space coordinates can also be obtained to first order from the linear optics design. However, in complicated cases involving multiple Siberian snakes and spin rotators, it may be more efficient to obtain the derivatives of $\vec{n}$ with respect to the coordinates of interest by spin tracking.

The procedure for obtaining, e.g. $\partial\vec{n}/\partial\delta$, is the following. A set of particles with orthogonal spins is launched along the on-momentum closed orbit. The particles in the set have $\delta = \Delta p/p$ relative momentum offset. If a dispersion is present at the launch point the particles also have non-zero transverse coordinates, which can be described by the action J_δ and phase Φ_δ variables. J_δ and Φ_δ depend on δ and the dispersion value and slope. Therefore, they can in general be changing along the ring. The goal is to obtain

$$\frac{\partial \vec{n}}{\partial \delta} \approx \frac{\vec{n}(J_\delta, \Phi_\delta, \delta) - \vec{n}_0}{\delta} \tag{5.17}$$

at every element along the ring.

As the particles undergo transverse oscillations, their phase evolves and one can build up a multi-turn spin transfer matrix as

$$R(\vec{\Phi}_0, \vec{\Phi}_i) = \begin{pmatrix} s^i_{1x} & s^i_{2x} & s^i_{3x} \\ s^i_{1y} & s^i_{2y} & s^i_{3y} \\ s^i_{1z} & s^i_{2z} & s^i_{3z} \end{pmatrix}, \tag{5.18}$$

where i is the turn number and s^n_{jk} is the kth spin coordinate of the jth particle. The particles

are tracked for a sufficiently large number of turns N. The spin direction at the initial phase-space coordinate $\vec{\Phi}_0$ can be obtained as

$$\vec{n}(\vec{\Phi}_0) \approx \frac{\vec{n}_{ave}}{|\vec{n}_{ave}|}, \quad \vec{n}_{ave} = \frac{1}{N+1}\sum_{i=0}^{N} R^{-1}(\vec{\Phi}_0, \vec{\Phi}_i)\tilde{n}(\vec{\Phi}_i), \tag{5.19}$$

where $\tilde{n}(\vec{\Phi}_i)$ is the initial guess for the stable spin direction. It can be chosen as the periodic spin direction on the closed orbit, $\vec{n}_0$, which is straightforward to find using, e.g., a single-turn spin transfer matrix for the closed orbit. This procedure is called a stroboscopic averaging and has been extensively studied and validated in the past.

It is challenging to simulate the polarization lifetime directly. It requires accurate implementation of the depolarizing processes and is computationally demanding. Therefore, we validate our implementation of the above procedure by applying it to the EIC electron ring and comparing its results to the $\partial\vec{n}/\partial\delta$ and polarization lifetime calculations available from other verified codes such SLICK, SITROS, and more recently B-MAD. Figure 5.30 compares our Zgoubi simulation results for $\partial\vec{n}/\partial\delta$ to a SLICK calculation for the same lattice. The Zgoubi simulation used $N = 1000$ and $\delta = 10^{-5}$. Note the logarithmic vertical scale and the fact that the difference occurs at small values of $|\partial\vec{n}/\partial\delta|$.

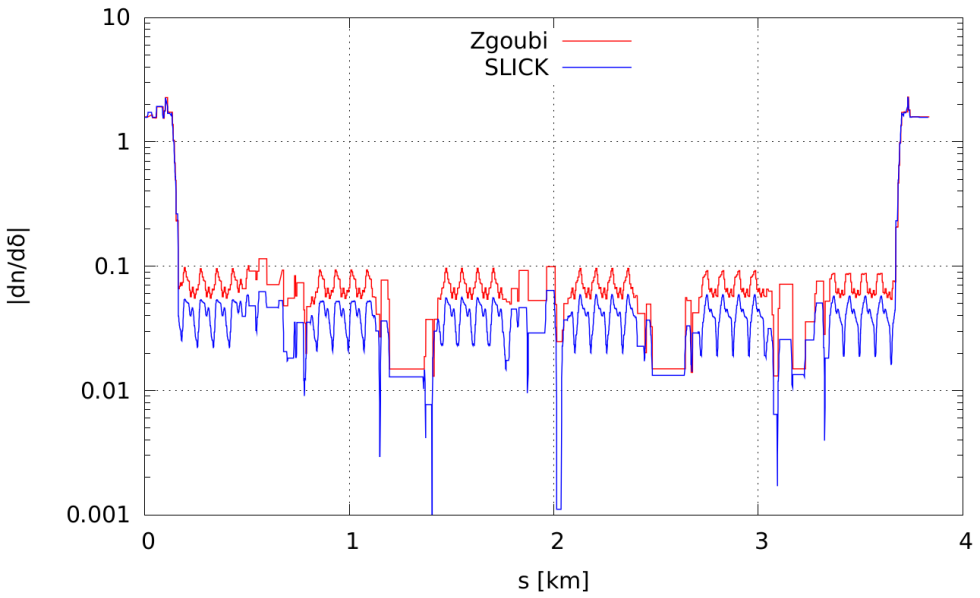

Figure 5.30: Comparison of the $|\partial\vec{n}/\partial\delta|$ calculations using Zgoubi and SLICK.

The difference between the two calculations in Fig. 5.30 may originate from two reasons. The orbital motion in Zgoubi is non-linear while SLICK considers linearized motion. The ring lattice contains strong solenoids that are used to rotate the electron spin. The solenoid models are treated differently in Zgoubi and SLICK. Zgoubi uses a solenoid field model with extending fringe fields while SLICK uses a hard-edge solenoid model. It appears that Zgoubi calculations depend on a particular choice of the solenoid parameters. The po-

larization lifetimes calculated using Zgoubi and SLICK are 203 and 200 min, respectively. Even with the above differences, these numbers are still in a good agreement and the approach described above can be used for estimating the impact of stochastic effects on the electron and hadron polarization lifetimes.

5.4.7 Effects of Crabbing on the Spread of Ion Polarization

The transverse kick a particle receives when passing through a crabbing cavity depends on the particle's timing. Therefore, particles with different longitudinal positions along a bunch experience different fields, which results in different spin rotations correlated with the distance along the bunch. Assuming that the crabbing kick is closed and there are no bending dipoles in the crabbing section, the net vertical spin rotation per pass is given by

$$\Psi_{crab} = \frac{1+G}{\gamma\beta}\int_C \hat{E}_x dz, \tag{5.20}$$

where G is the anomalous part of the gyromagnetic ratio and $\hat{E}_x$ is the electric field normalized to the magnetic rigidity.

When the betatron phase advance between the rear and forward crab cavities is $\Delta\mu_{crab} = 2\pi k$,

$$\Psi_{crab} = 0. \tag{5.21}$$

The phase advance of $\Delta\mu_{crab} = \pi(2k+1)$ results in an rms spread of the vertical spin rotation of

$$\Psi_{crab} = \frac{1+G}{\gamma\beta}\frac{\sigma_z}{\sqrt{\beta_{crab}\beta_{IP}}}\tan\phi_{crab}, \tag{5.22}$$

where σ_z is the rms bunch length, β_{crab} and β_{IP} are the horizontal β function values at the crab cavity and IP, and ϕ_{crab} is a half of the beam crossing angle. For typical EIC parameters, this spread has a numerical value of the order of 10^{-6} rad and can be neglected.

Analysis of the case when the crabbing kick is not close requires calculation of the spin response functions at the crab cavity locations to account for contribution of the ring to the spread of the spin rotation.

In the presence of bending dipoles in the crabbing section, all spin rotations occur about the vertical axis. Therefore, dipoles do not change the combined spin effect of the crab cavities as long as one can ignore the longitudinal dynamics. However, dipoles may change the longitudinal positions of the different momentum particles in the bunch. This may result in an incomplete cancellation of the crabbing kick and transverse to longitudinal coupling that requires specific analysis of both beam and spin dynamics.

Another potential polarization effect of the crab cavities is a spin spread at the IP. The

combined spin effect of the crabbing electric and magnetic fields is given by

$$\Psi_{crab} = \gamma G \Delta x', \tag{5.23}$$

where $\Delta x'$ is the net change of a particle's horizontal angle to the observation point. When a bunch initially exists the first set of the crab cavities, it has a correlated spread of the horizontal angles given by

$$\Delta x' = \frac{\sigma_z}{\sqrt{\beta_{crab}\beta_{IP}}} \tan\phi_{crab}, \tag{5.24}$$

Thus, there is a spin spread just after the cavities. However, considering only this correlated component of the betatron motion, the rms spin spread at the IP is

$$\Psi_{crab} = \gamma G R_{22} \Delta x' = \gamma G \frac{\sigma_z}{\beta_{IP}} \cos\Delta\mu \tan\phi_{crab} \approx \gamma G \frac{\sigma_z}{\beta_{IP}} \left(\frac{\pi}{2} - \Delta\mu\right) \tan\phi_{crab}, \tag{5.25}$$

Assuming typical EIC parameters and a betatron phase offset of 1°, this effect is of the order of 10^{-2} rad.

5.4.8 Summary

The AGS currently delivers 65% polarization with 3×10^{11} protons per bunch, while RHIC delivers 60% polarization in collisions at 250 GeV with 1.8×10^{11} protons per bunch [227].

The additional gains necessary to increase the EIC polarization will come in three ways. First, a skew quadrupole compensation scheme in the AGS will reduce polarization losses there. Second, hadron cooling at injection will reduce the depolarizing resonance strengths. Third, six snakes will preserve polarization through acceleration.

Simulation results show that the space charge effect does not pose a major threat to the polarization lifetime at lower energies – injection at 25 GeV injection and collisions at 41 GeV.

HSR spin rotators near IP6 are moved from their RHIC Yellow ring locations, providing longitudinal polarization at the experimental detector.

Simulation tools for polarization lifetime due to IBS and cooling section have been developed, and detailed simulations are underway.

5.5 Light Ion Beam Polarization in the HSR

5.5.1 ^{3}He Polarization

The EIC is able to use polarized beams of ^{3}He and deuterium ions. The gyromagnetic factor of ^{3}He is $G = -4.18$, about twice as large as for the proton, so only a fraction of the available Siberian Snake magnetic field strength is needed. However, the depolarizing resonances crossed during acceleration are stronger and denser, also due to the larger $|G|$ value. In addition, the overlap of imperfection resonances due to closed orbit distortions and intrinsic resonances excites even order snake resonances, which otherwise do not occur in a dual-snake configuration. Other sources for even-order snake resonances include errors in the snake settings. The overlap of an intrinsic resonance with an imperfection resonance also splits the existing odd-order resonances.

Polarized ^{3}He in the Booster and the AGS

Polarized ^{3}He is injected into the Booster from EBIS at $|G\gamma| = 4.193$. There are two partial snakes in the AGS, separated by 1/3 of the ring, so the stable spin direction is closest to vertical in every three units of $|G\gamma|$. Values of 4.5, 7.5 and 10.5 are therefore natural for extraction from the Booster. Optical distortions at AGS injection with the partial snakes on are stronger for smaller $G\gamma$ or $B\rho$ values, so extraction at $|G\gamma| = 10.5$ is preferred. with $B\rho = 10.78$ Tm.

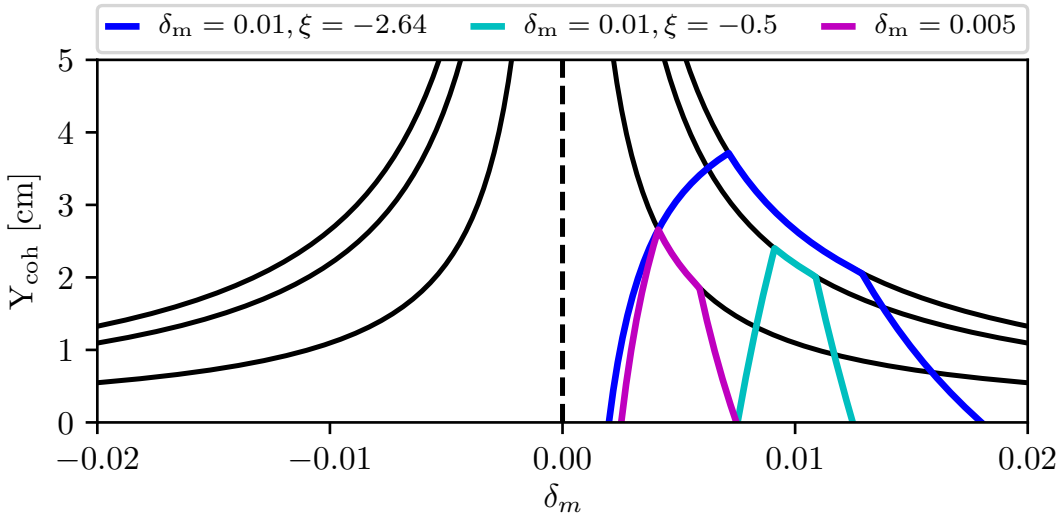

Figure 5.31: The coherent amplitude of the driven AC dipole oscillations at different δ_m and chromaticity values. The tune separation δ_m is preferred to be large and chromaticity is preferred to be near zero, in order to maintain the same coherent amplitude across the energy spread of the whole beam.

Polarized ^{3}He crosses two intrinsic resonances in the Booster, $|G\gamma| = 12 - \nu_y$ and $|G\gamma| = 6 + \nu_y$, as well as 6 imperfection resonances, $|G\gamma|$= 5, 6, 7, 8, 9, and 10. To overcome the intrinsic resonances, Simulations show that there is sufficient corrector strength to correct or enhance the imperfection resonances up to $|G\gamma| = 10$.

An AC dipole in the Booster mitigates the intrinsic resonance crossings by inducing 100% spin-flips [228–230]. It is 0.5 m long with a maximum strength of $B_m l = 0.0025$ Tm and a frequency of $f_m = 250$ kHz [231, 232]. With a nominal resonance proximity parameter of $\delta_m = 0.01$, the corresponding AC dipole driving tunes for the $|G\gamma| = 12 - \nu_y$ and $|G\gamma| = 6 + \nu_y$ resonances are $\nu_m = 0.199$ and $\nu_m = 0.177$, respectively. Because of the low injection energy and the large frequency sweep, ν_m for helions crossing $|G\gamma| = 12 - \nu_y$ can change by as much as 0.003. Due to this large variability and the natural vertical chromaticity, these parameters must be precisely controlled, as shown in Figure 5.31 [233].

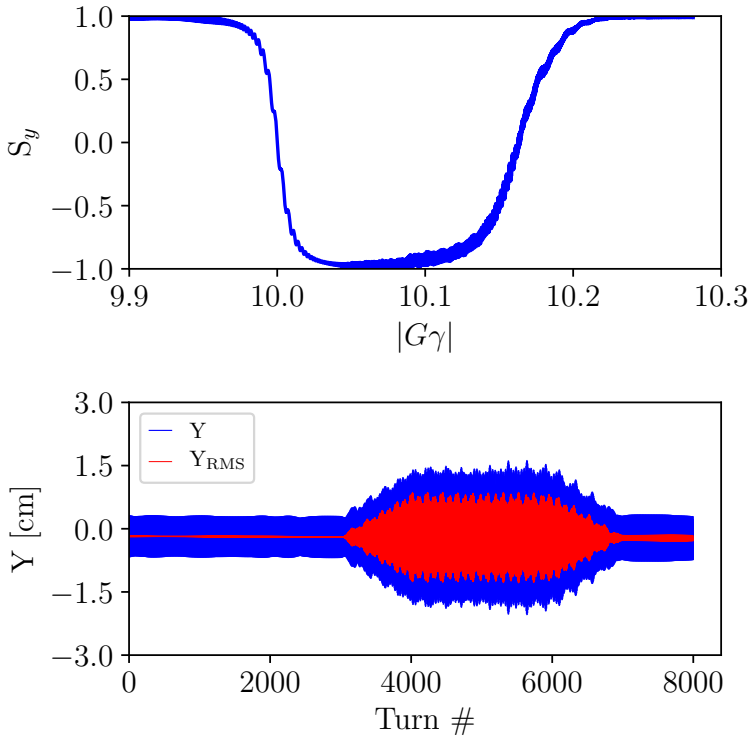

Figure 5.32: Booster acceleration simulation with 1,000 polarized ^{3}He particles crossing the $|G\gamma| = 10$ and $|G\gamma| = 6 + \nu_y$ resonances, with 100% transmission efficiency. The $|G\gamma|$=10 imperfection resonance is enhanced by dipole correctors to induce a full spin flip, and the intrinsic resonance at $|G\gamma| = 6 + \nu_y$ is enhanced by an AC dipole strength of $B_m l = 0.00141$ Tm to induce a full spin flip.

Simulations show that all 6 Booster imperfection resonances can be crossed while staying under the 25 A limit of the dipole corrector power supplies [234]. If necessary, stronger dipole corrector power supplies and magnets will be installed. Figure 5.32 shows that

polarization is preserved through one imperfection resonance by orbit correctors and one intrinsic resonance by AC dipole.

The Booster to AGS transport line supports a maximum rigidity of $B\rho = 9.5$ Tm, limited mainly by the pulsed kicker power supplies, although Booster fast extraction bumps can be configured to provide some relief. Similarly, only two of the six Booster main magnet power supply stations are capable of exceeding a current corresponding to $B\rho = 9.5$ Tm, meaning the ramp rate will be slowed to a third of normal. The slower ramp rate does not compromise polarization preservation, because all the imperfection resonances are compensated and the AC dipole overcomes the two intrinsic resonances.

The vertical tunes in the AGS at injection are kept below the half integer, with $\nu_y < 4.1$, to avoid the $|G\gamma| = 0 + \nu_y$ resonance. AGS partial snakes can generate a total of ~40% relative strength, making it possible to push both betatron tunes into the spin tune gap so both vertical and horizontal intrinsic resonances and imperfection resonances are avoided. Polarization preservation through the AGS acceleration ramp is shown in Figure 5.33.

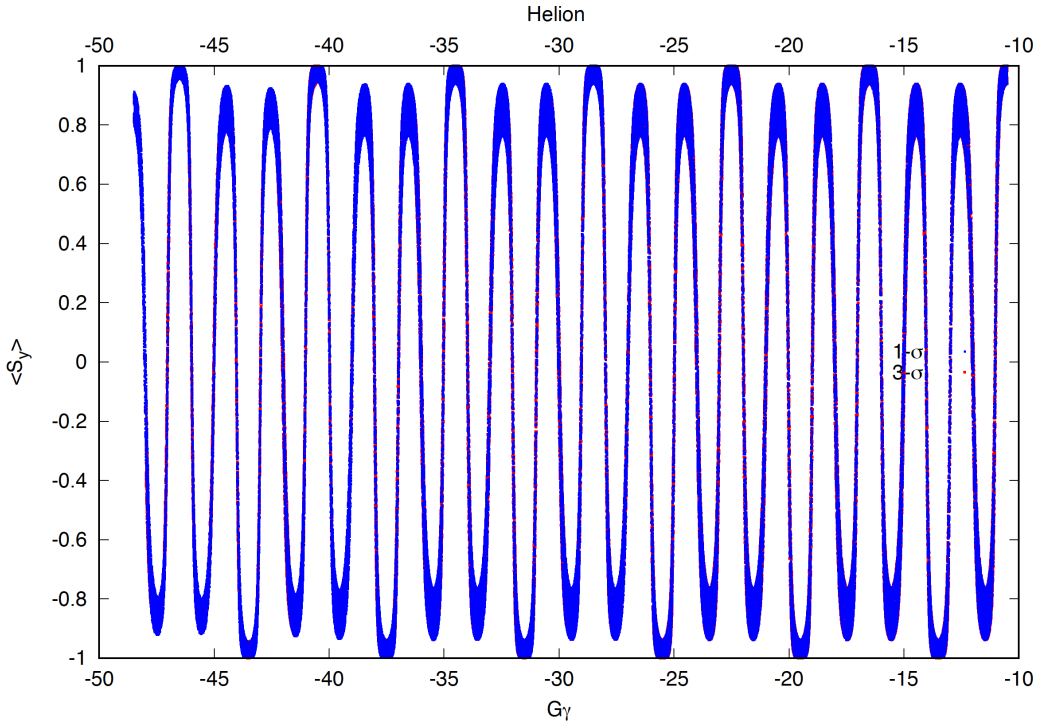

Figure 5.33: Tracking results of 8 polarized ^{3}He particles on each of the two emittance ellipses (σ=2.5 µm and 3σ=7.5 µm) through the $|G\gamma|$ range of 10.5 and 48.5. The two partial snakes were set as 25% and 14%, while ν_x and ν_y were set at 8.95 and 8.98, respectively. Both betatron tunes are inside the spin tune gap. Note that due to negative G value, the acceleration goes from right to left when energy increases.

Polarized ^{3}He in HAR and HSR

RHIC polarized proton transmission efficiency with two snakes is about 92% with a vertical emittance of 2.5 µm, equivalent to a depolarizing resonance strength of 0.225. Figure 5.34 shows the ^{3}He intrinsic resonance spectrum in RHIC, calculated using DEPOL [211]. In contrast a cooled ^{3}He vertical emittance of 0.75 µm leads to an intrinsic resonance strength is 0.3, larger than the strongest strength in RHIC. More snakes are therefore necessary to preserve ^{3}He polarization. The number of snake pairs should be an odd number, so the EIC accelerator has 6 snakes.

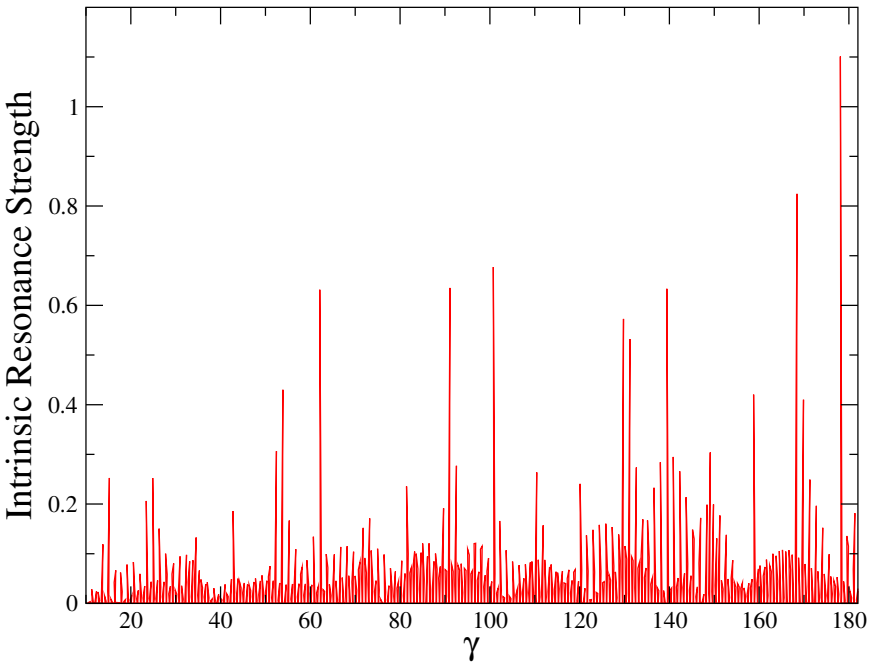

Figure 5.34: The intrinsic depolarizing resonance strengths in hadron ring of EIC for ^{3}He as a function of the Lorentz factor γ for a particle on a 10 µm action ellipse.

Figure 5.35 shows 2-snake spin tracking results from Zgoubi [225], accelerating ^{3}He ions from $G\gamma = -690$ to -790 and crossing the strongest intrinsic resonance at $|G\gamma| = 717 + \nu_y$. Eight particles with the same betatron amplitude were tracked with a perfect closed orbit and zero momentum offset. The results show that the 2-snake configuration maintains polarization for a 0.75 µm emittance, but not for 3×0.75 µm and 6×0.75 µm emittances. In contrast, Figure 5.36 shows that the 6-snake configuration maintains polarization through the strongest resonances between $\gamma = 168$ and 178.

These preliminary simulations show that the 6-snake configuration preserves ^{3}He polarization on the ramp up to a top energy of 183 GeV. More detailed spin tracking will be performed to determine the tolerance to orbit errors and momentum spread.

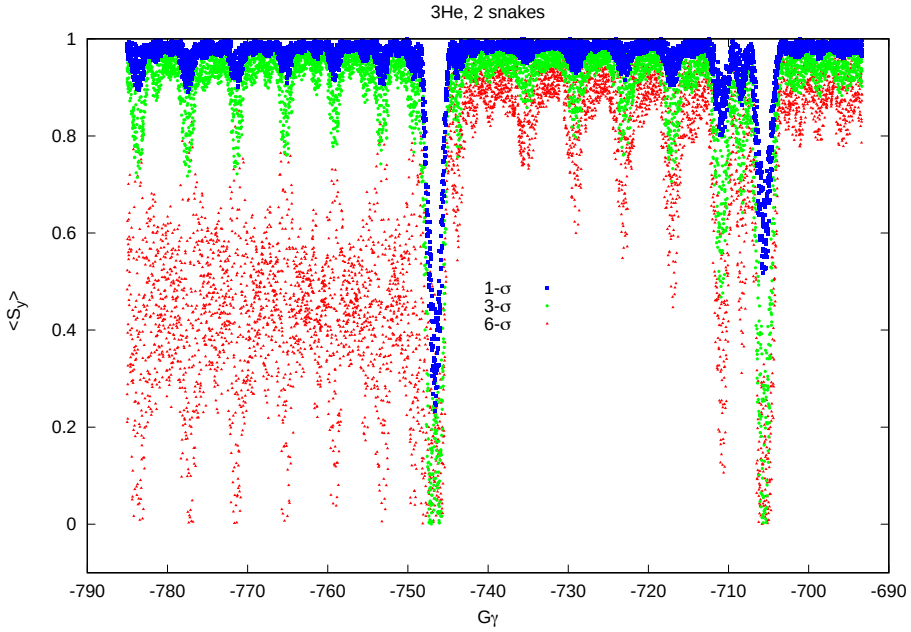

Figure 5.35: Zgoubi acceleration simulation results with a 2-snake configuration and with various beam emittances ($\epsilon_y = 1,\ 3,\ 6\sigma$, with σ =0.75 µm), crossing intrinsic resonance at $|G\gamma| = 717 + \nu_y$ ($\gamma \approx 178$) and $|G\gamma| = 735 - \nu_y$ ($\gamma \approx 168$). Acceleration goes from right to left, because G is negative.

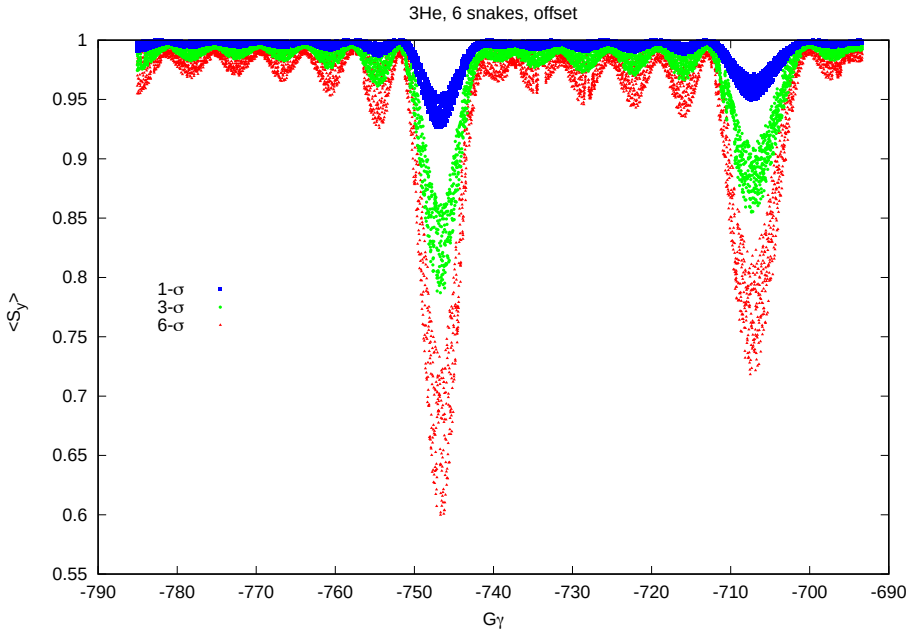

Figure 5.36: Zgoubi simulation results with a 6-snake configuration with one pair offset, and with various beam emittances ($\epsilon_y = 1,\ 3,\ 6\sigma$, with σ =0.75 µm), for intrinsic resonances at $|G\gamma| = 717 + \nu_y$ and $|G\gamma| = 735 - \nu_y$. Acceleration goes from right to left.

^{3}He Polarization Lifetime

The 2-snake HSR configuration works for polarization preservation during proton stores, but it needs development for ^{3}He with stronger resonances. Store energies are usually far from strong intrinsic resonances, but there are nearby weak intrinsic and imperfect resonances. These overlapping resonances are one source of polarization loss [235]. A recently developed lattice independent spin tracking method delivers simulation results that are in reasonably good agreement with RHIC proton operation when the beam-beam effect is not strong, without introducing strong imperfection resonances [226].

Two simulation efforts on ^{3}He polarization preservation in a 2-snake configuration are continuing in parallel. One effort, which includes beam-beam force interactions over a shorter time frame of less than a minute, is still under development. The other, without beam-beam, tracks for a longer time frame on the order of one hour. Figure 5.37 shows preliminary simulation results from the second method for an imperfection resonance strength of 0.07 near top energy corresponding to $|G\gamma| = 820$. The most promising tune ranges are below 29.25. The polarization decay rate is around 5%/hr with the vertical emittance as 0.75 µm. The imperfection resonance strengths near top energy vary between 0.02 and 0.08 for an rms closed orbit error of 0.5 mm. Choosing a region with a strength around 0.025, the polarization decay rate is a fraction of 5%/hr. However, the beam-beam interaction generates a large betatron tune footprint, shortening the polarization lifetime.

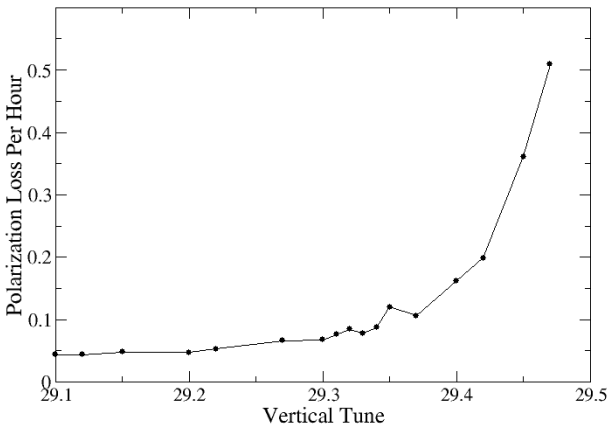

Figure 5.37: Polarization decay rate versus vertical tunes with emittance as 0.75μm for ^{3}He with imperfection of 0.07 strength, with beam-beam turned on and a 2-snake configuration. A value of 0.1 on the vertical axis indicates a loss rate of 10%/hr.

Polarization loss rates observed in 2015 RHIC operations in three different scenarios showed significant beam-beam effects. The loss rate with pp collisions was much worse than for p-Al and p-Au collisions, with the same proton bunch intensity but with weaker beam-beam tune shift parameters. Beam-beam parameters in HSR are stronger, so more snakes probably are necessary for good polarized ^{3}He lifetime. More studies of a polarization lifetime model with beam-beam are planned.

5.5.2 Deuteron Polarization During Acceleration and Storage

The gyromagnetic factor of the deuteron is quite small, $G = -0.14$, so the present Siberian Snakes are too weak even to be used as efficient partial snakes. On the other hand the number of spin resonances encountered by the deuteron beam during acceleration is significantly smaller, and the strength of those resonances is smaller than for protons or for ^{3}He ions. The feasibility of accelerating polarized deuteron beam was previously studied [236, 237]. Further recent studies explored the acceleration of a polarized deuteron beam, using realistic ramp rate and beam emittance parameters that were used for unpolarized deuteron beam in RHIC [238].

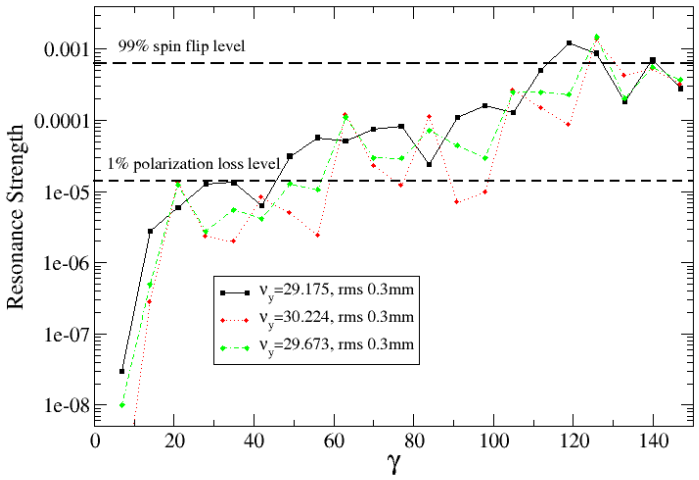

Figure 5.38: Imperfection resonance strengths for three ion ring lattices, including strength levels corresponding to 99% spin flip and 1% polarization loss.

Resonance strengths for various lattices are calculated with closed orbit RMS values of 0.3 mm, and transverse emittances of 2 µm, as shown in Figures 5.38 and 5.39. A partial snake with a 15 Tm solenoid – the same strength as the experimental detector solenoid at IP6 – takes care of all imperfection resonances. A 5.6 Tm solenoid is part of the second detector design that is under consideration for IP8. The more complicated two detector scenario has also been analyzed. Although the total partial snake strengths are modulated as a function of energy, they are sufficient to overcome the imperfection resonances.

With detector solenoids as partial snakes, the spin is in the longitudinal direction at deuteron energies corresponding to an integer spin tune. In the case of one detector this happens at every integer spin tune, but with two detectors the spin tune must be a multiple of 3. The induced resonance strength must be larger than the spin tune spread due to momentum spread, in order for all particles to maintain a longitudinal spin. The solenoidal field alone cannot do this, but the induced resonance strength is made strong enough by introducing orbit harmonics of a few mm at energies corresponding to an integer spin tune.

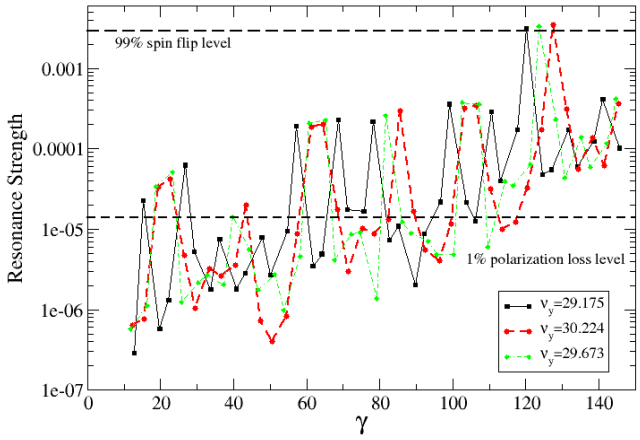

Figure 5.39: Intrinsic resonance strength for three ion ring lattices, including strength levels corresponding to 99% spin flip and 1% polarization loss.

A 50-turn tune jump system with an amplitude of 0.03, similar to the AGS system, maintains polarization over the whole energy range. This amplitude takes into account the large spin tune spread at higher $|G\gamma|$ values. Figure 5.40 shows the polarization remaining after crossing each intrinsic resonance with a nominal ramp rate, a vertical emittance of 2 µm, and with a modest tune jump amplitude that is sufficient except for the $|G\gamma| = \nu_y - 12$ resonance, which is overcome without firing the tune jump quads. The resonance strength is reduced by about 40% when the deuteron beam emittance is cooled to 0.75 µm, providing additional margin to the tune jump system.

In summary, polarized deuteron beams are feasible in the EIC. Longitudinal polarization is achieved at discrete energies when the spin tune is an integer. A modest tune jump system is included. Simulation studies to explore details of the deuteron polarization preservation and control are planned.

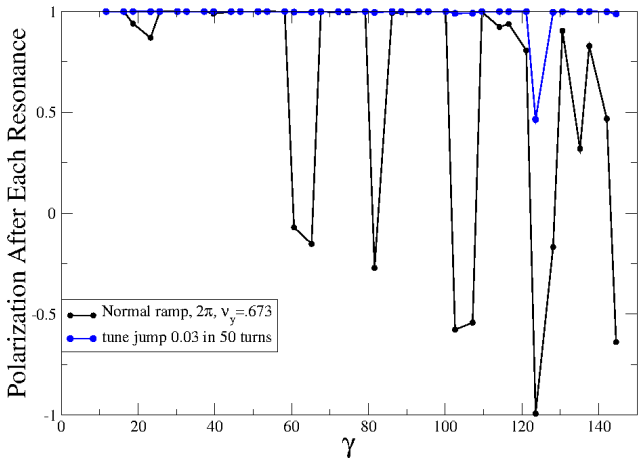

Figure 5.40: Deuteron polarization after crossing each intrinsic resonance during acceleration at a nominal ramp rate and with a modest tune jump.

5.6 Detector Solenoid Compensation Effects

Although the detector solenoids only weakly perturb the optics, they require compensation to maintain bunch polarization levels over the bunch replacement time interval. Detector solenoids are under discussion for the HSR have integrated strengths in the range from 5.6 Tm to 15 Tm. This preliminary discussion of optics and stored polarization performance assume the value of 5.6 Tm. The strongest effects on the electron beam are discussed in Section 5.6.1, while the weaker effects on proton polarization are analyzed in Section 5.6.2.

5.6.1 Electron Polarization

The nominal electron storage ring lattice is optically matched for spin transparency of the interaction region in the absence of a detector solenoid. It is error-free – in particular the vertical closed orbit is perfectly flat. Table 5.8 lists parameters of the IP6 detector solenoid and its effects, including polarization results for the *perturbed* lattice without any coupling compensation. The solenoid introduces weak coupling to the betatron motion, with a closest tune value of 0.024. The chromaticities are essentially unaffected. Polarization results assessed by dedicated computer tools [214, 239] are recorded in Table 5.8 and in Figures 5.41, 5.42 and 5.43.

Table 5.8: Model detector solenoid parameters, operating in the vicinity of the tune diagonal with fractional tunes of $(\nu_x, \nu_y) = (0.08, 0.06)$ at an electron energy of 18 GeV.

Parameter	Value
Length, L [m]	4
Diameter, d [m]	2.7
Field B_0 [T]	1.4
Integrated field $\int B\,dl$ [Tm]	5.6
Coupling Strength	0.024
Tune shifts $(\Delta\nu_1, \Delta\nu_2)$ $[10^{-3}]$	+5.4, -5.7
Lifetimes without solenoid (τ_d, τ_{eq}) [min]	58, 20
Lifetimes with solenoid (τ_d, τ_{eq}) [min]	20, 12

The solenoid is aligned with the electron ring axis and so has no effect on the on-momentum closed orbit, nor on the on-momentum periodic spin precession direction $\vec{n}_0$ so long as it is aligned *ab initio*, as is shown for the present case of a "perfect" lattice in Figure 5.41.

The evolution of electron polarization for up to 10^3 synchrotron radiation damping times under the effect of spin diffusion is computed in 512 energy bins with $a\gamma \sim 0.2$ intervals. There is one particle in each bin, initially with a longitudinal spin at IP6. The particles cover

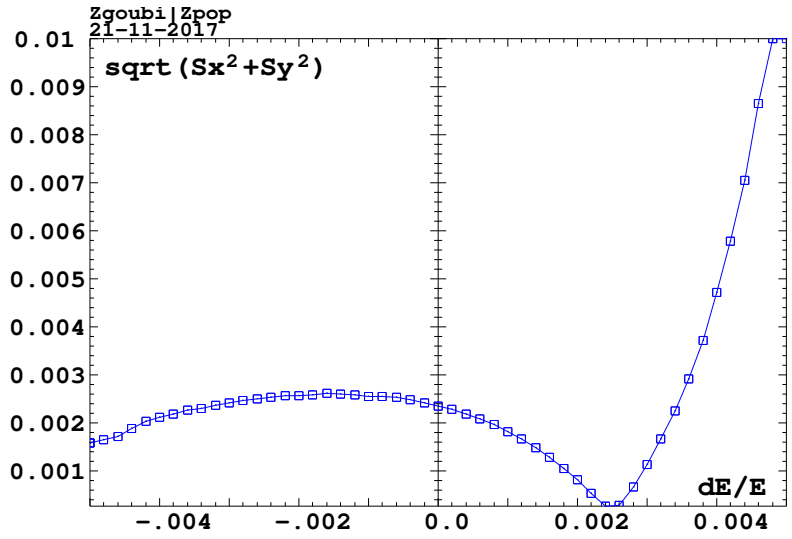

Figure 5.41: Momentum dependence of the stable spin precession orientation $(S_x^2 + S_y^2)^{1/2}$ at IP6, in the absence of the detector solenoid. The origin of the horizontal axis is at the reference energy, E = 18 GeV, so the stable spin direction $\vec{n}_0$ has a slightly off-momentum longitudinal alignment.

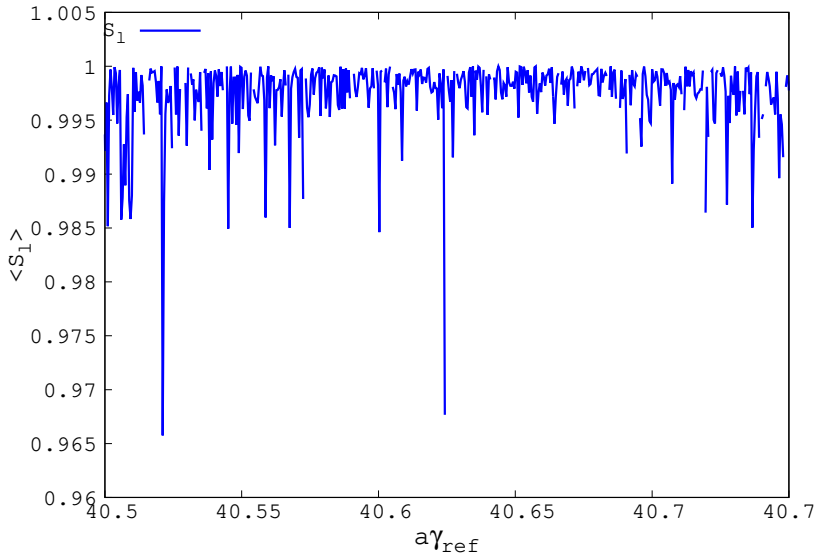

Figure 5.42: Typical results for the longitudinal spin component $< S_l >$ of 18 GeV electrons at IP6 without a solenoid after 10^3 damping times, or 5×10^5 turns. The initial spin is longitudinal, $< S_l >_{t=0} = 1$.

normalized horizontal and vertical emittances of 600 µm (the equilibrium value at 18 GeV) and 100 µm (with betatron coupling of about 15%). Figure 5.42 displays typical tracking results. Figure 5.43 shows the evolution of the average polarization of the 512 electron ensemble as a function of time in store, both with and without the detector solenoid turned

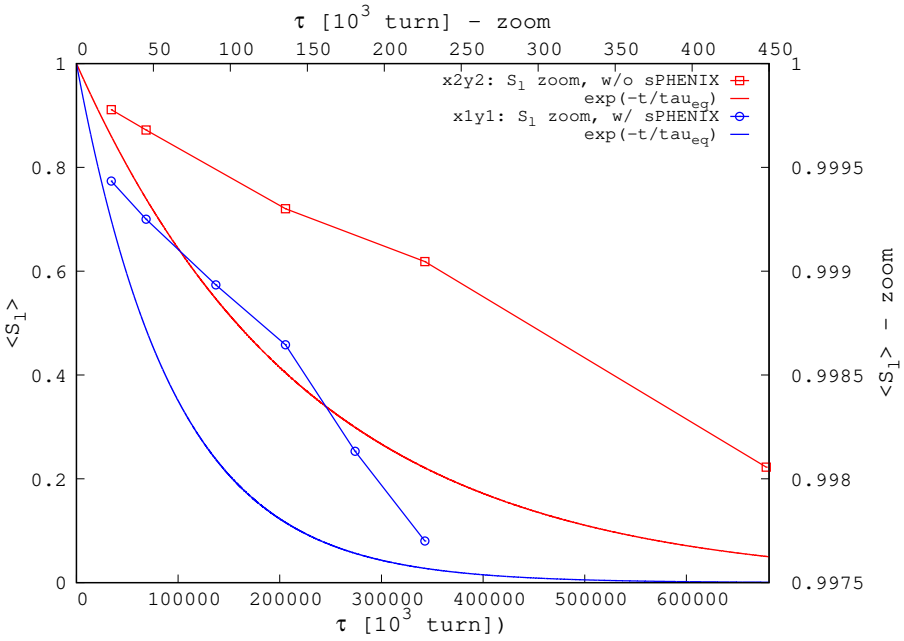

Figure 5.43: Longitudinal spin component versus turn number for 18 GeV electrons, without and with the solenoid. The synchrotron radiation damping time is 500 turns. The diffusion time constant ($\tau_d = 58$ and 20 minutes respectively) is obtained by fitting the data to a smooth exponentially decaying curve.

on.

The diffusion time constant τ_d is obtained from tracking in the absence of self-polarization, while the equilibrium time τ_{eq} is calculated through

$$\tau_{eq}^{-1} = \tau_d^{-1} + \tau_{ST}^{-1} \tag{5.26}$$

with a Sokolov-Ternov time constant of

$$\tau_{ST} = 99 \frac{\rho^2 R}{E^5\,[\mathrm{GeV}^5]} \approx 31 \ \text{minute} \tag{5.27}$$

at 18 GeV with an average radius of $R = 610$ m and a magnet curvature radius of $\rho = 242$ m. The resulting time constants are given in Table 5.8, both with and without the solenoid.

In summary, the effect of the detector solenoid on electron beam optics is weak enough that optics compensation can be achieved with minor adjustments of the unperturbed optics settings. Further detailed studies will be performed to confirm these generalities and to analyze the performance of an appropriate and thorough coupling compensation scheme in an electron lattice optimized for polarization, and accounting for realistic bunch param-

eters.

5.6.2 Proton Polarization

The main effect of the solenoid on EIC protons is to tilt the stable spin precession axis a little away from the vertical direction. At 275 GeV this is equivalent to a partial snake with a strength of 0.6% for the solenoid parameters in Table 5.8. This causes a spin rotation angle of 1.1° and changes the vertical spin component by 2×10^{-4}. For comparison, Figure 5.44 shows the spin tilt computed for RHIC operations for a realistic lattice with separation bumps, including a snake field map. The detector solenoid – in this case a magnet with a field integral of 5.6 Tm – has an insignificant effect on the vertical spin component. The RHIC proton depolarization rate is -0.3%/hour during 255 GeV proton stores.

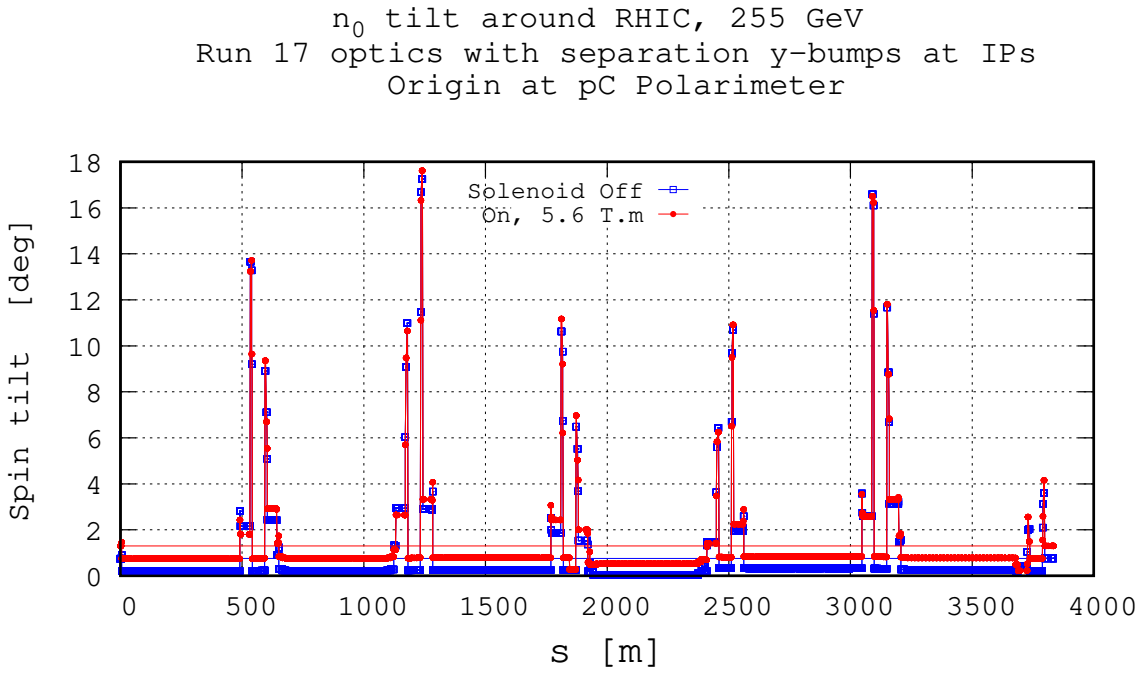

Figure 5.44: Vertical tilt of the stable spin precession axis $\vec{n}_0$ around RHIC for protons with an energy of 255 GeV. The lattice origin is at the pC polarimeter, 70 m downstream of IP12. RHIC snake angles are nominal, with spin rotation $\mu = \pi$ and rotation axes at $\phi = \pm\pi/4$. The red curve is with a 5.6 Tm field integral solenoid placed at IP6, while the blue curve has no solenoid.

Chapter 6

Accelerator Components Design

6.1 Introduction to Accelerator Components Design

The following sections contain descriptions of the accelerator components and subsystems including the required infrastructure to support the EIC. The layout of the accelerator subsystems constitutes a possible design of the future collider which could be built as described in these sections. The design optimization of all systems is expected to continue during the future final design process to arrive at the "Detailed Design" which is needed to start building the EIC. It is expected that for many systems we will find more elegant, less costly, less energy consuming, and more easily implementable solutions during that process.

There are a number of considerations which necessitate the efforts described in the following sections:

- The detailed layout of the hardware systems is the basis for a robust cost and risk estimate. The most important cost drivers have been identified and corresponding costs have been quantified. This motivated design iterations and value engineering at the earliest stage of the EIC.
- A thorough design effort helps to reveal any design concepts which lead to large technical difficulties that ought to be avoided
- A critical aspect of the EIC is the tight space in the RHIC tunnel which will host four accelerator rings of the EIC. The detailed layout of superconducting RF cryostats, room temperature RF cavities, injection elements, beam line crossings and corresponding magnet systems as well as the additional systems for strong hadron cooling demonstrated how all these components, including their power, cryogenic, and water cooling supply systems, fit, given tight constraints on tunnel space.
- The detailed definition and design of subsystems such as power supplies and other support hardware identifies any need for additional buildings and infrastructure that is an important factor in the cost of the EIC

While some of the described systems might still evolve and will be improved, many of the systems are already at a level where finalizing the design could be done in a fairly small amount of time. This gives us the flexibility and ability to complete the design on a relatively short time scale.

6.2 Magnets Design

6.2.1 Magnets Overview

Normal Conducting Magnets for the ESR and RCS

All EIC electron storage ring (ESR) magnets will be water-cooled, iron-dominated electromagnets. The yoke material is assumed to be good quality magnet steel (AISI 1006 or better). The BH-curve used in the simulations is shown in Figure 6.1. The magnets are powered in DC mode, so eddy currents are not a concern. The magnets can be fabricated from solid iron or from laminations.

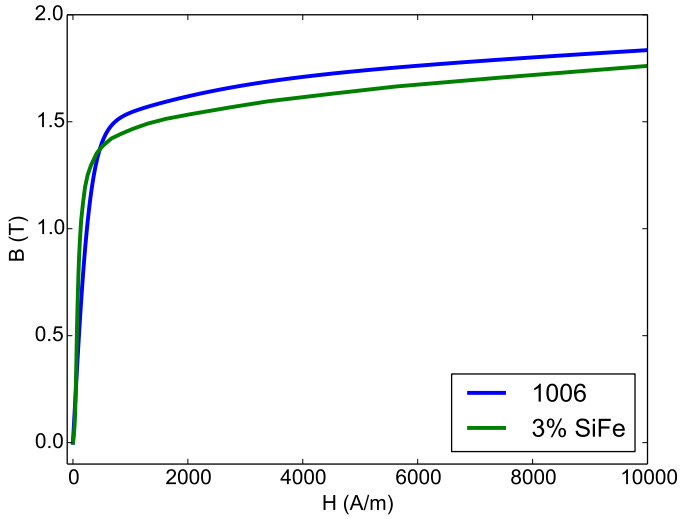

Figure 6.1: BH curves used for the EIC magnet designs.

Likewise, the magnets for the EIC rapid cycling synchrotron (RCS) will be iron-dominated water cooled magnets. Since the RCS will be ramped, 3% SiFe electrical steel (non-oriented) is suggested as the yoke material. The ramp rate for all magnets in the RCS is assumed to be 200 ms (from zero to peak field); the repetition rate is one pulse per second. To suppress eddy currents in the yoke the magnets will be made of laminations with a thickness of 250 µm.

To estimate the core losses the higher order harmonics of the triangular wave form have to be considered, which will contribute to the losses according to their amplitude. The

fundamental frequency is 2.5 Hz; the next higher order frequencies are 7.5 Hz, 12.5 Hz, and 17.5 Hz. The amplitudes of the higher order frequencies decrease rapidly (1/9 for 7.5 Hz, 1/25 for 12.5 Hz, 1/49 for 17.5 Hz, ...). As core-loss data is difficult to obtain for low frequencies we use data for 50 Hz, which is a worst case estimate. The data is shown in Figure 6.2.

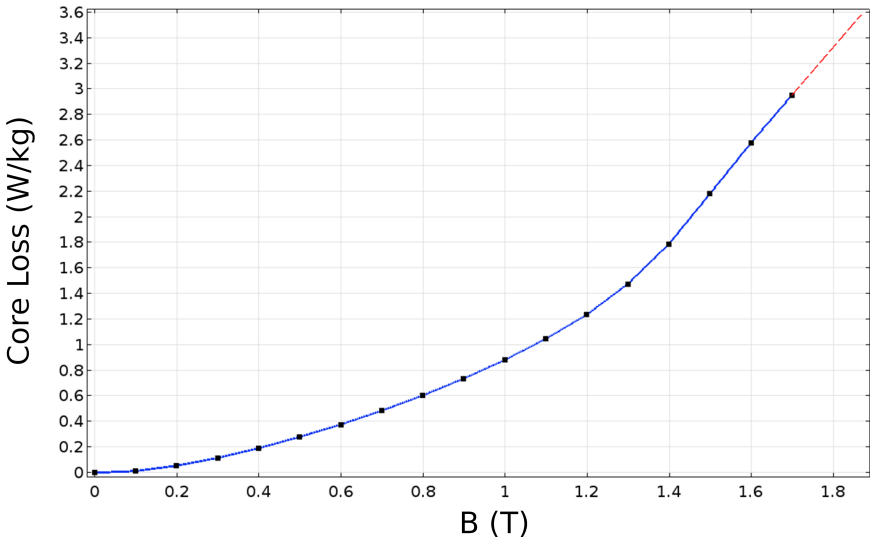

Figure 6.2: Loss curve of electrical steel at 50 Hz.

Where applicable the field quality is given in field harmonics. The normal (B_n) and skew (A_n) harmonics are defined as:

$$B = \sum_{n=1}^{\infty} [B_n + iA_n] \left(\frac{z}{R_{ref}} \right)^{n-1} \tag{6.1}$$

The field harmonics are usually normalized to 10000 units of the main multipole component and valid for a given reference radius R_{ref}.

Interaction Region Magnets

The EIC interaction region includes superconducting magnets for the low-β quadrupoles and spectrometer dipoles near the detector, and both normal-conducting and superconducting magnets for the matching section into the arcs of the electron and hadron storage rings, respectively.

Figure 6.3 shows an overview of the IR region. The central detector is shown in light green; the 10 σ beam envelope of the hadron beam is shown in magenta. The electron beam (15 σ envelope) is shown in light red. Magnet apertures are shown in light red (dipoles) or light blue (quadrupole magnets). The forward neutron cone is shown in yellow.

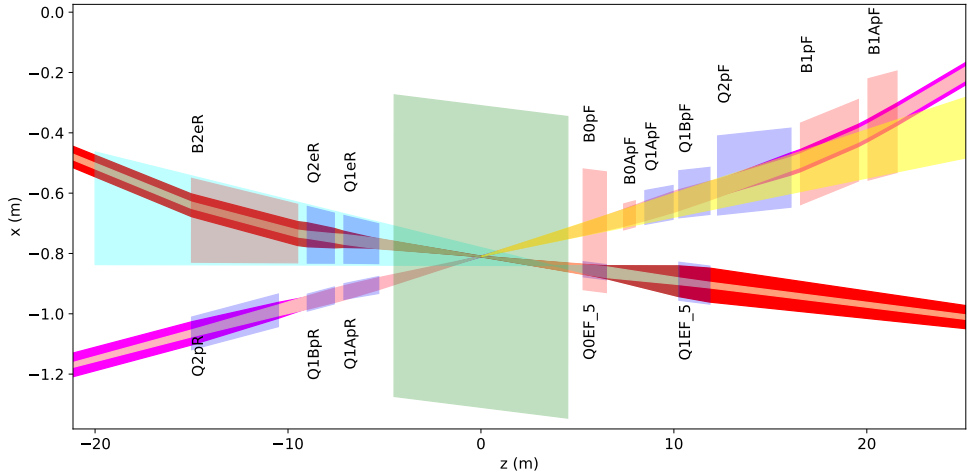

Figure 6.3: Overview of the IR Magnets.

As shown in the figure, 15 new superconducting magnets are necessary, which are all unique. All magnets are based on conventional NbTi technology; most magnets operate at a temperature of 4.2 K, apart from three magnets (Q1APF, Q1BPF and Q2PF) which due to the high magnetic field need to be cooled to 1.8 K.

Nine of the new superconducting magnets are presently foreseen to be made with BNL's direct wind method, which is advantageous because no tooling is required [240]. The technology has demonstrated that it can deliver very good field quality for a variety of magnets; an example of the coil winding process is shown in Fig. 6.4 (a). Four magnets (B0aPF, Q1APF, Q1BPF, Q2PF and B1PF) are planned to be made as conventional collared coils with a Rutherford cable, similar to the very successful RHIC magnets (see Fig. 6.4 (b)).

Most direct wind magnets are so-called serpentine coils, which have demonstrated superior performance in a variety of situations [241]. Several of the IR magnets are two-in-one magnets, with separate coils for the hadron and electron beam. A particular challenge for these magnets is the small crossing angle, which leads to a small separation of the magnet apertures. It is crucial for this design to minimize crosstalk, which requires soft-iron between the two magnets. The iron prevents flux from leaking from one magnet into the other; for this concept to work the iron must not saturate. It is helpful in this context to taper some of these magnets, thus increasing the amount of iron between the apertures. This is possible due to the fact that the minimum required aperture increases with distance from the IP (beam size and/or synchrotron radiation).

Tapered magnets have been made before, but without any special provisions this implies a change in multipole field along the length of the magnet [242]. A change in gradient is undesirable, so a novel winding concept has been developed to address this [243].

The winding pattern which allows the coil radius to change while keeping the gradient constant is based on a coil concept known as double-helix or canted cosine theta magnets.

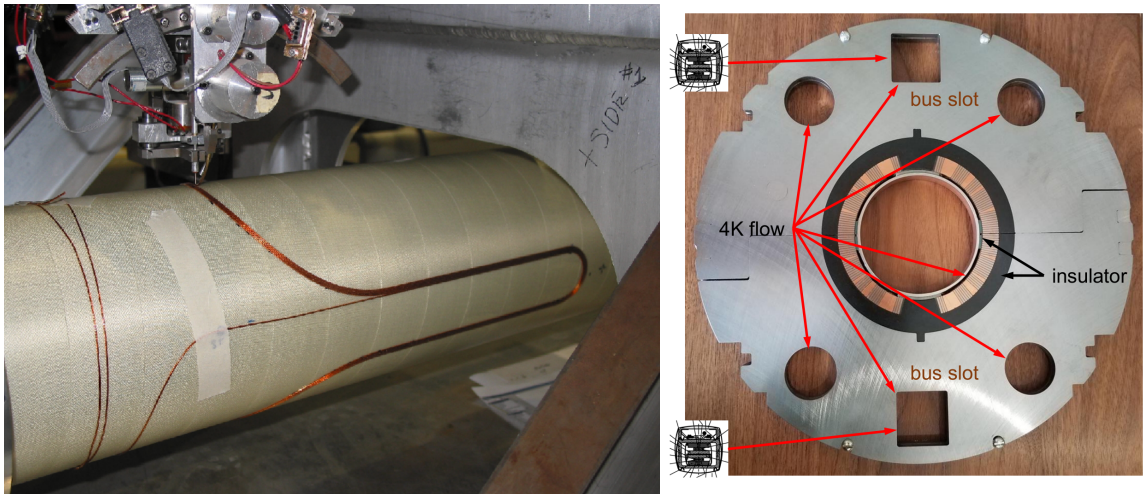

(a) Direct Wind Magnet **(b)** RHIC Dipole

Figure 6.4: Example of direct wind magnet (a) and cross-section of the RHIC dipole magnet.

The coil concept has been known since the 1960s [244] and has been extended several times; arbitrary multipole magnets [245] and combinations thereof [246] can be generated. Double-helix coils have been also considered for the next generation of high field magnets for hadron colliders [247,248]. A unique feature of double-helix magnets is their flexibility, which allows one to smoothly vary field components as necessary. The conductor path in three dimensions is described by the following equations:

$$x(\theta) = R \cdot \cos\theta \tag{6.2}$$

$$y(\theta) = R \cdot \sin\theta \tag{6.3}$$

$$z(\theta) = \frac{h\theta}{2\pi} + \frac{R}{\tan(\alpha)} \sum_n \varepsilon_n \sin(n\theta) \quad . \tag{6.4}$$

In the equations θ is the azimuthal angle, R the coil radius, h the winding pitch, α the tilt angle of a single turn with respect to the central axis and n the multipole order. ε_n is an additional parameter for combined function magnets, which allows the individual multipole components to be adjusted. For one multipole magnet at least two layers are required; the second layer is wound in the opposite direction with a negative tilt angle.

For a tapered coil design the radius R is changed linearly along the length of the magnet. To compensate for the change in multipole component ε_n is changed for each turn (e.g. for a quadrupole $n = 2$): by increasing ε_n the longitudinal vector of the current density at a particular longitudinal position is increased as well.

Tapered coils are foreseen for Q1ER, Q2ER, B2ER and Q1APR. The concept is well understood; a test magnet is presently being made to prove the concept. Figure 6.5 shows a picture of test windings produced by BNL's direct wind machine.

Similar to the normal conducting magnets the field quality for some magnets is given in

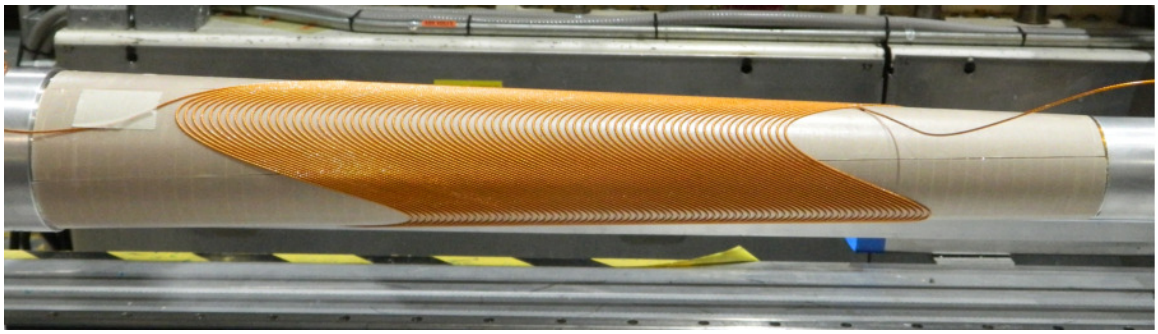

Figure 6.5: Tapered double-helix coil demonstrator, completed first layer.

field harmonics. The normal (B_n) and skew (A_n) harmonics are defined as:

$$B = \sum_{n=1}^{\infty} [B_n + iA_n] \left(\frac{z}{R_{ref}} \right)^{n-1} \tag{6.5}$$

The field harmonics are usually normalized to 10000 units of the main multipole component and valid for a given reference radius R_{ref}.

6.2.2 IR Magnets Design

The B0PF Forward Spectrometer Magnet

The B0PF forward spectrometer magnet is a 1.2 m long magnet with its center located 5.9 m from the IP. Due to the close proximity to the IP the separation between the beams is still rather small. The B0PF magnet has the dual-purpose of providing a bending field of up to 1.3 T to the hadron beam and a weak quadrupole field to the electron beam. The concept of the B0pF magnet is described in more detail in section 3.2.1.

The B0APF Corrector Dipole Magnet

The B0APF magnet is a corrector dipole magnet located directly after the B0PF spectrometer dipole. The purpose of the B0APF magnet together with B1PF is to correct the effects of keeping B0PF at a constant field of 1.3 T. Due to the fixed field of the B0PF magnet the lower energy particles experience a stronger deflection compared to the high energy particles. The corrector dipole magnet ensures with B1PF that particles of all desired energies have the same orbit after the B1PF magnet.

The cross-section of the magnet is shown in Figure 6.6. The B0APF magnet is a 60 cm long dipole magnet with a peak magnetic field of 3.3 T. The required good field region is 23 mm, but the aperture of the magnet is significantly larger to allow transport of the forward scattered particles with up to 1.3 GeV/c transverse momentum. As an example, we assume

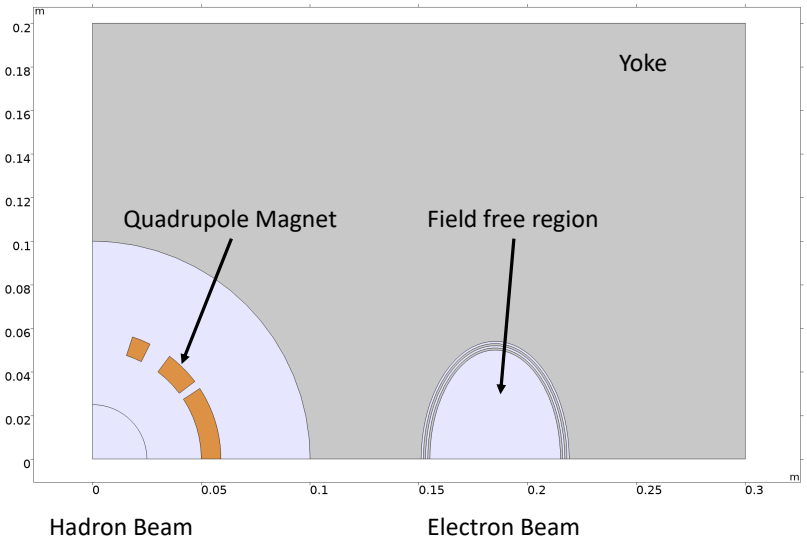

(a) Geometry

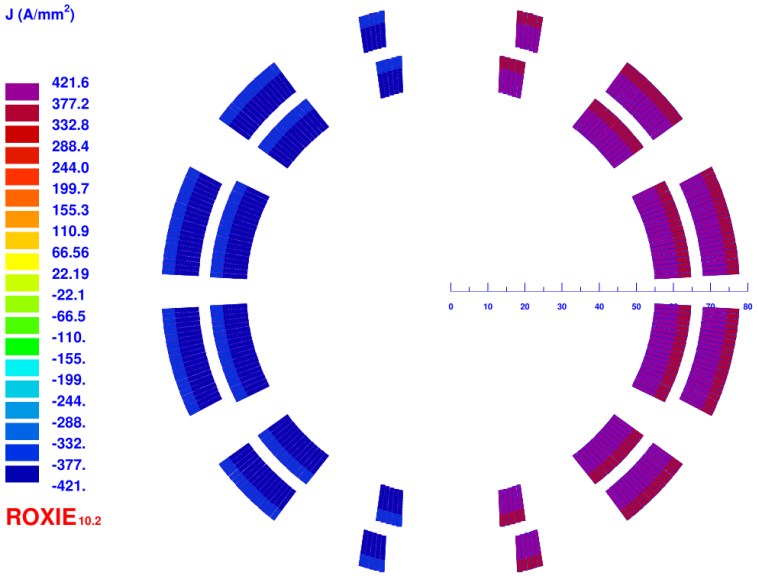

(b) Current density in A/mm^2

Figure 6.6: Geometry and current density of B0APF corrector dipole at the front end.

a coil geometry based on a Rutherford cable similar to the RHIC cable (9.73×1.2679). Two layers are necessary to allow for a reasonable current density of 421 A/mm^2.

The B0APF magnet is housed in an iron yoke, which returns the flux and provides a field free region for the nearby electron beam. The distance between the electron beam and the

center of B0APF is 190 mm on the front face and 205.5 mm on the rear face. The geometry of the field free region and the residual stray field are shown in Figure 6.7. As shown in the figure, the residual stray field is of the level of the earth's magnetic field.

Figure 6.8 shows the good field region (integral value) and the longitudinal field profile along the length of the magnet. As shown in the figures, a good field quality can be accomplished in the required aperture.

Figures 6.9 (a) and (b) show the peak field on the wire and the resulting load-line. As shown in the figures, the desired performance can be accomplished with a margin of 30%. The main parameters of the magnet are summarized in Table 6.1.

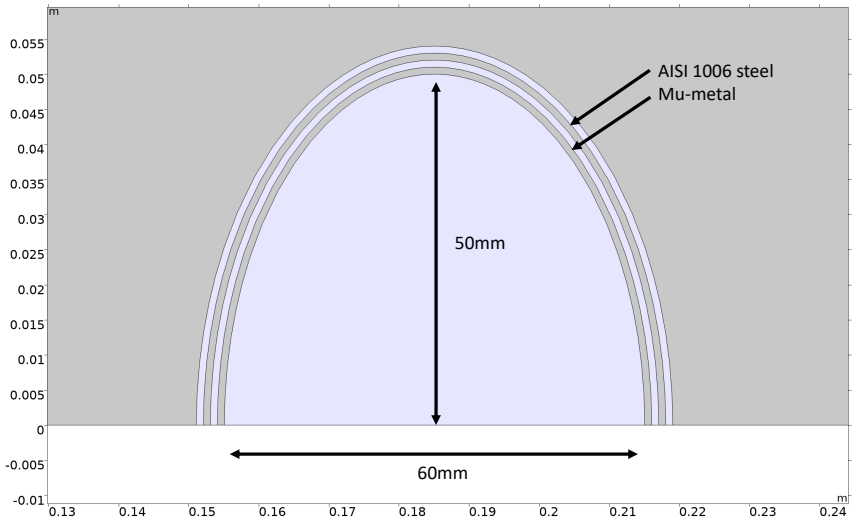

(a) Geometry

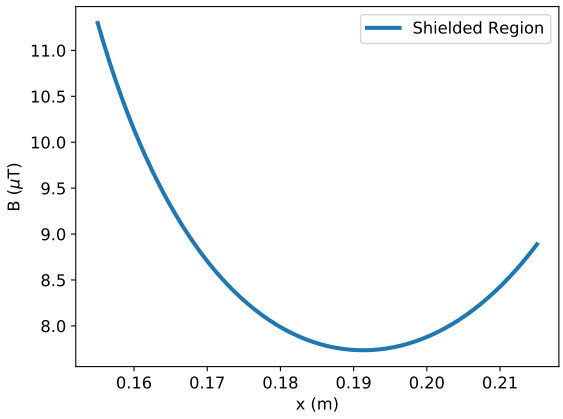

(b) Field Shielded Region

Figure 6.7: Geometry and residual field in the shielded region.

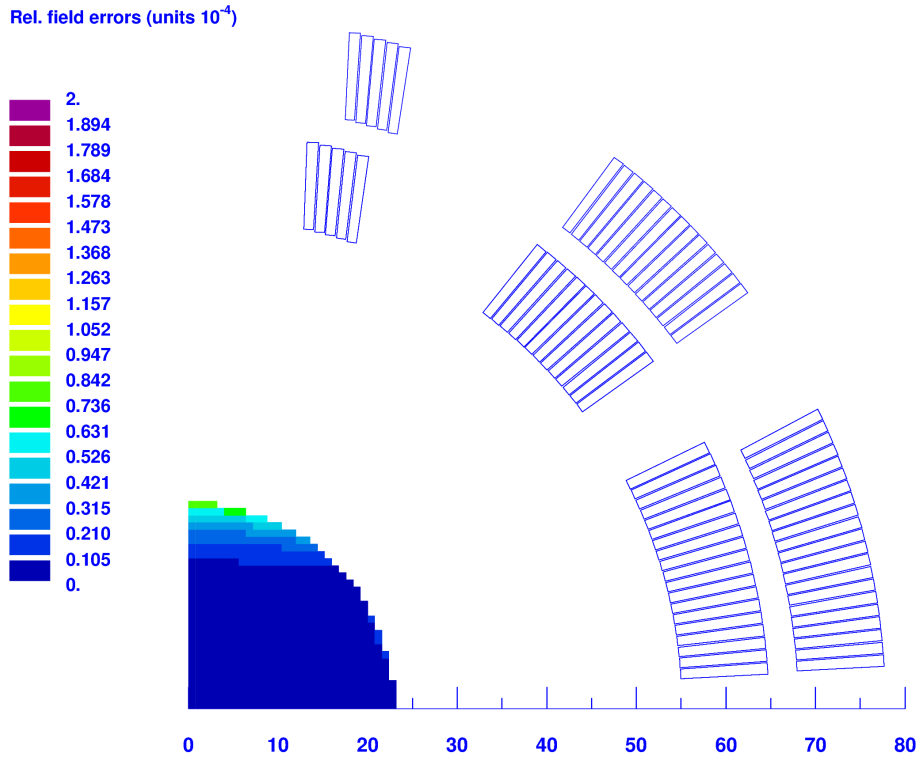

(a) Good field region

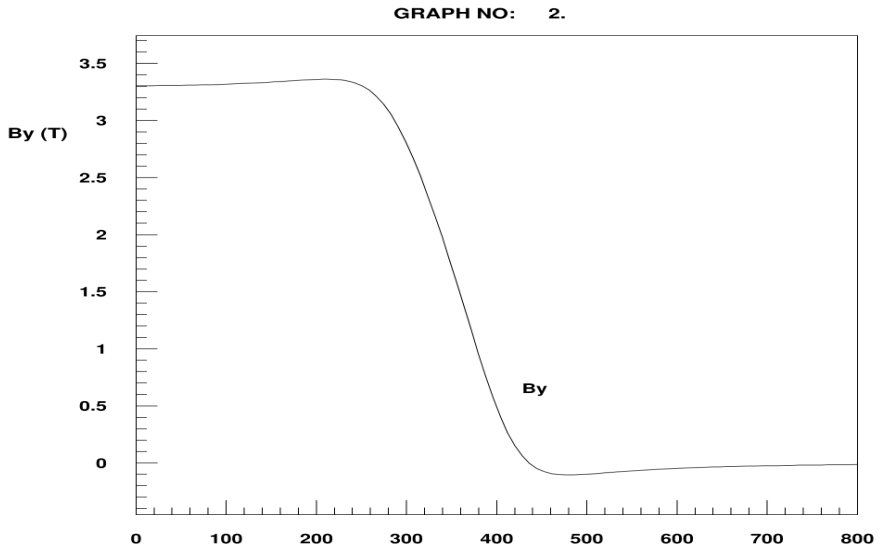

(b) Vertical magnetic field (Tesla) along the length of the magnet (mm)

Figure 6.8: Good field region (integrated along the length of the magnet) and longitudinal field profile of the B0APF magnet.

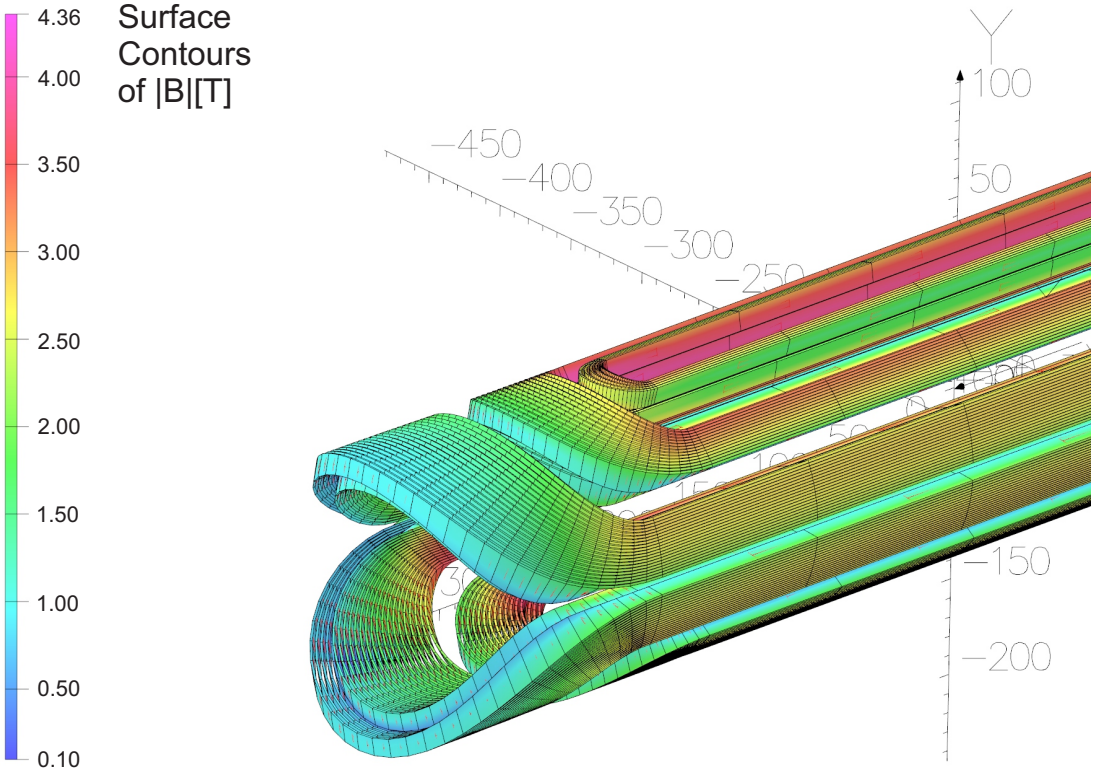

(a) Peak Field on the wire

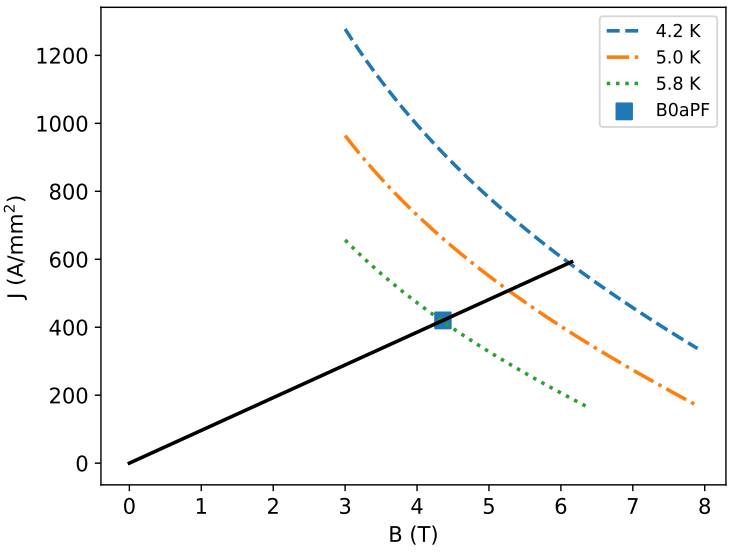

(b) Load-line

Figure 6.9: Peak field on the wire and load-line of the B0APF corrector dipole.

Table 6.1: Parameters of the B0APF magnet.

Parameter	Value
Magnetic length [m]	0.6
Maximum dipole field [T]	3.3
Aperture [m]	0.09
Required field quality	1×10^{-4}
Physical length [m]	0.6
Physical width [m]	0.16
Physical height [m]	0.16
Superconductor type	NbTi
Conductor (RHIC cable) [mm^2]	9.73×1.2679
Current density [A/mm^2]	421
Cu:Sc ratio	2
Temperature [K]	4.2
Peak field wire [T]	4.36
Magnetic energy [J]	264000
Ampere turns [A·t]	343200
Number of turns	78
Current [A]	4400
Inductance [H]	0.027273
Margin loadline [%]	30

The First Hadron Quadrupole Magnet Q1ApF

The first hadron quadrupole magnet, Q1ApF, has challenging magnetic design requirements. The Q1ApF aperture is dominated by the size of the neutron cone (4 mrad) as well as forward scattered particles with up to 1.3 GeV/c transverse momentum. This is shown schematically in Figure 6.10, which shows the magnet aperture in relation to the beam and neutron cone. In addition, the required gradient of 72.6 T/m, in combination with the large aperture requirement, leads to a large peak field on the wire; this necessitates 1.8 K operation as shown below.

The geometry of the Q1ApF magnet is shown in Figure 6.11. The Q1ApF magnet is placed in an iron yoke to return the flux; the outer dimensions of the yoke are $0.7 \times 0.5\,\mathrm{m}^2$ (width $\times$ height). The total estimated weight of the magnet is 3.4 t. The spacing between the apertures is 230.5 mm on the front side and 258.9 mm on the rear side. The shown figure is for the front end, which represents the worst case.

The expected gradient and gradient quality are shown in Figure 6.12. As shown in the figure, a good gradient quality can be accomplished in an aperture of ± 40 mm, which is

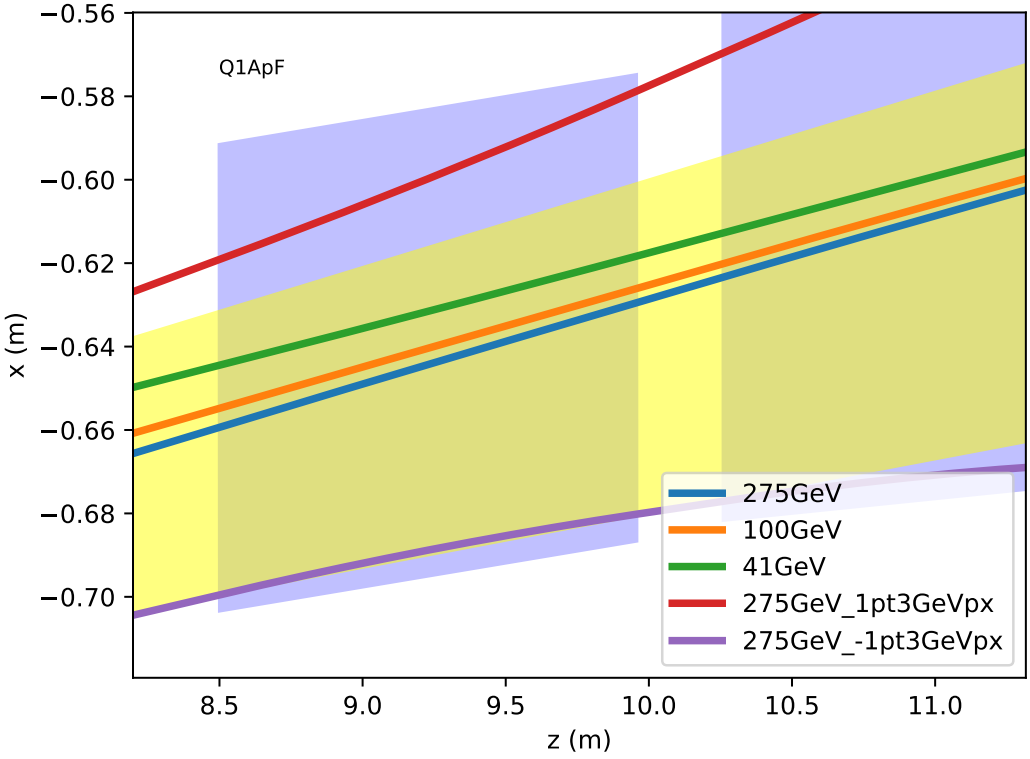

Figure 6.10: The magnet aperture of Q1ApF (blue) in relation to the particle orbits (41–275 GeV) and the neutron cone (yellow). Orbits of particles with 1.3 GeV/c transverse momentum are also shown. x and z are the floor coordinates of the interaction region.

larger than the required good field region ($\pm$25 mm for 10σ beam envelope).

The residual stray field in the field free region can be seen in Figure 6.12 (b). As shown in the figure, the residual field is of the order of the earth magnetic field. Better shielding can be accomplished by adding mu-metal to the inside of the electron aperture if required.

The expected peak field on the wire and yoke magnetization are shown in Figure 6.13 (a) and (b). As shown in the figure, the peak field on the wire is 6.85 T. In combination with the current density in the Rutherford cable of 512 A/mm^2 the coil can reliably operate at 1.8 K with sufficient margin. The load-line is shown in Figure 6.14.

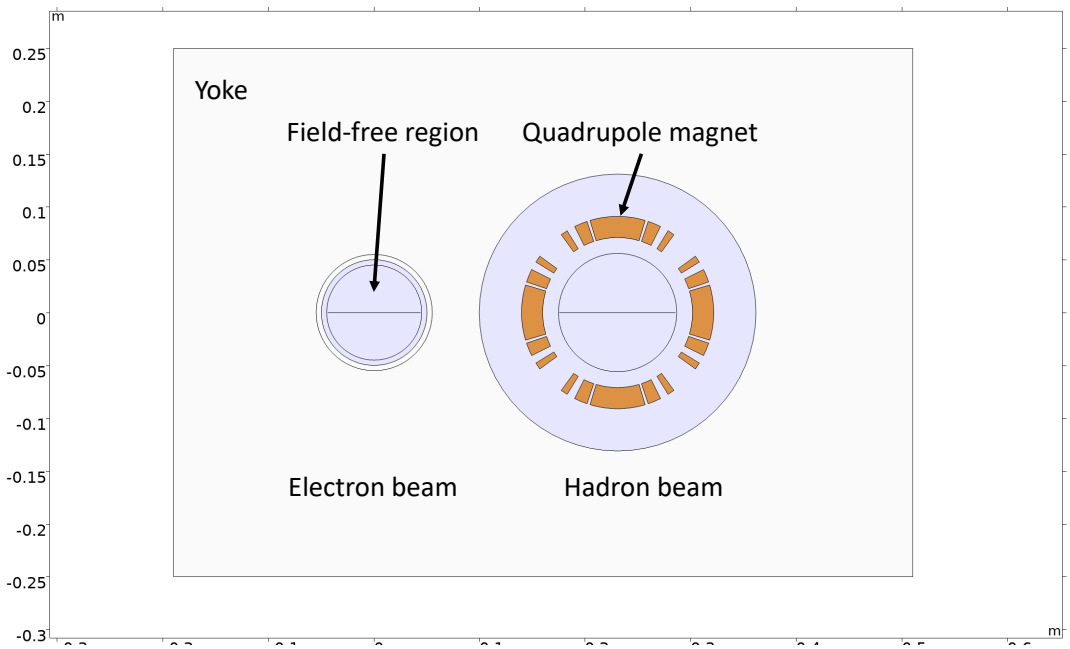

(a) Geometry front end

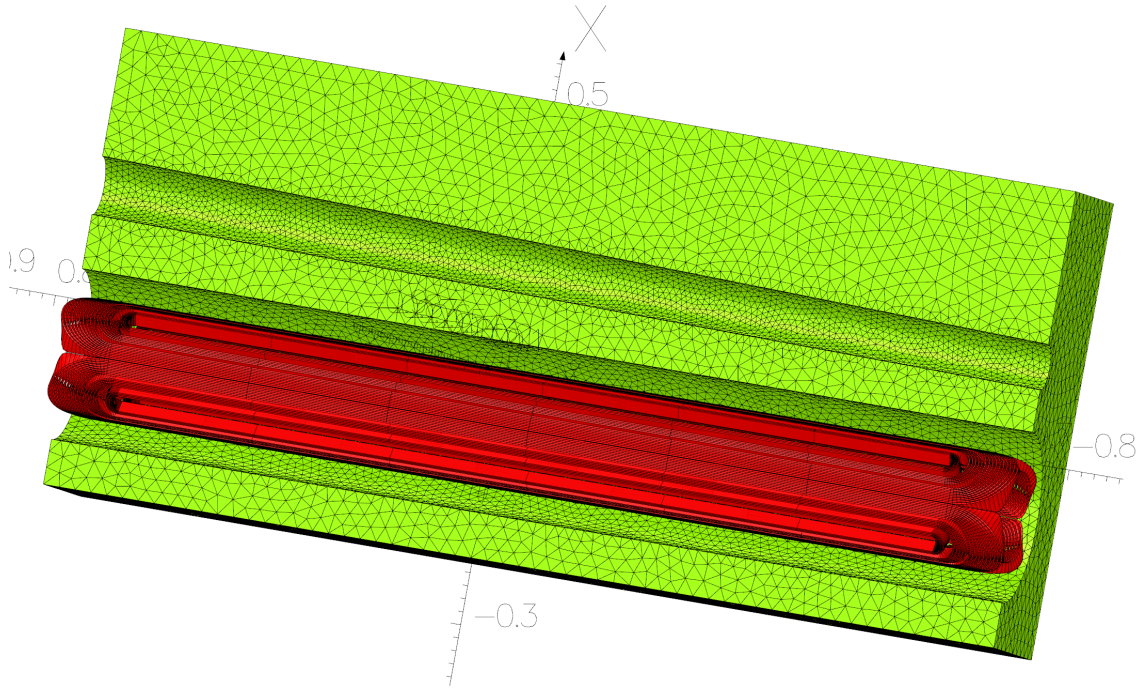

(b) 3D Geometry

Figure 6.11: Geometry of the Q1ApF magnet.

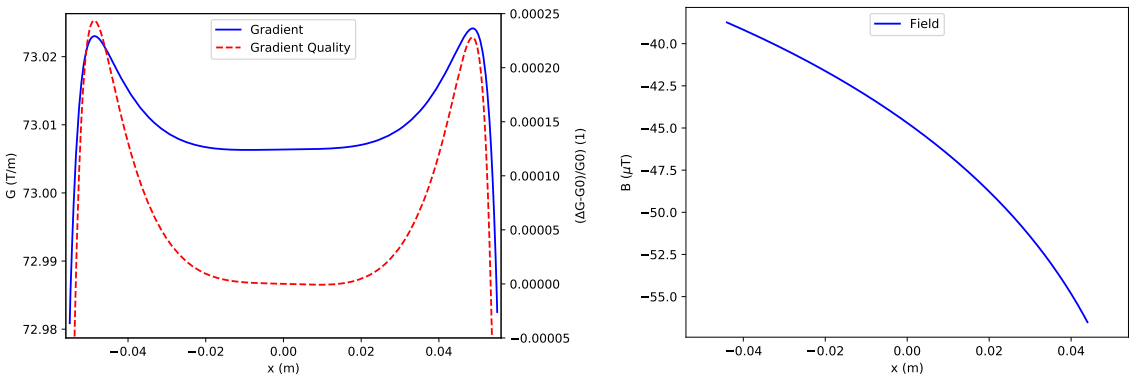

(a) Gradient and gradient quality

(b) Residual magnetic field

Figure 6.12: Gradient and gradient quality (a) of the Q1ApF magnet. Figure (b) shows the field in the field free region for the electron beam.

Table 6.2: Parameters of the Q1ApF magnet.

Parameter	Value
Magnetic length [m]	1.46
Maximum gradient [T/m]	72.6
Aperture diameter [m]	0.1120
Required field quality	1×10^{-4}
Physical length [m]	1.48
Physical width [m]	0.182
Physical height [m]	0.182
Superconductor type	NbTi
Conductor	Cable $20 \times 2\,\mathrm{mm}^2$
Current density [A/mm] ^{2}	512
Cu:Sc ratio	1.3
Temperature [K]	1.8
Peak field wire [T]	6.85
Magnetic energy [J]	360000
Ampere turns [kA·t]	360
Number of turns	18
Current [kA]	20
Inductance [mH]	1.8
Margin loadline [%]	32

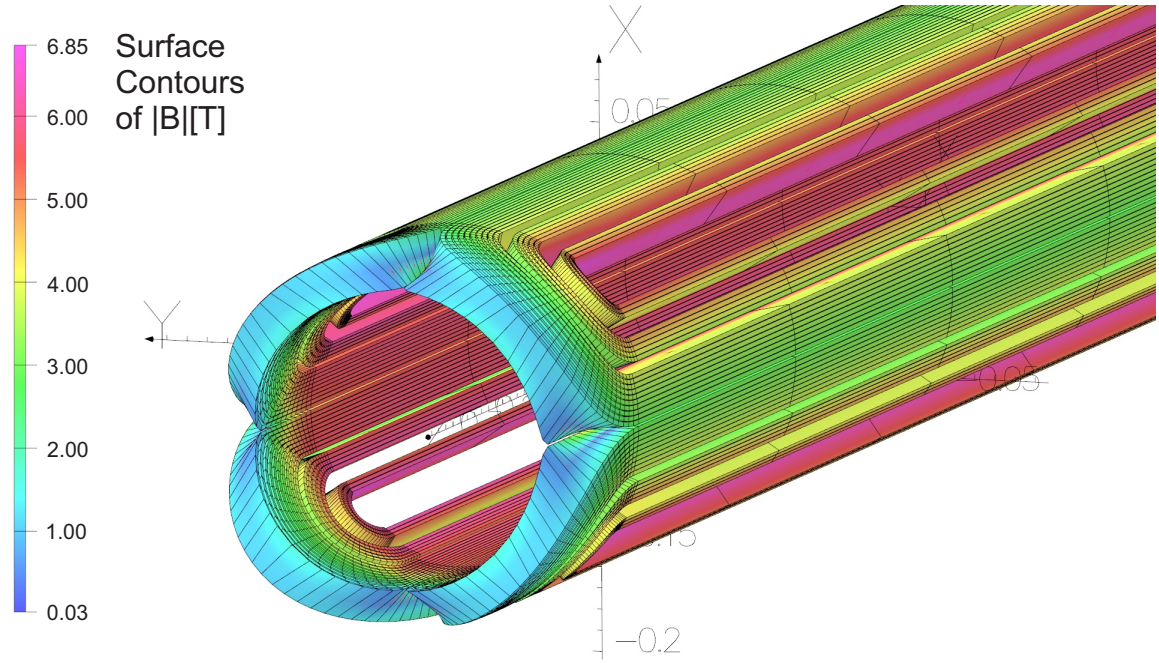

(a) Peak field on the wire

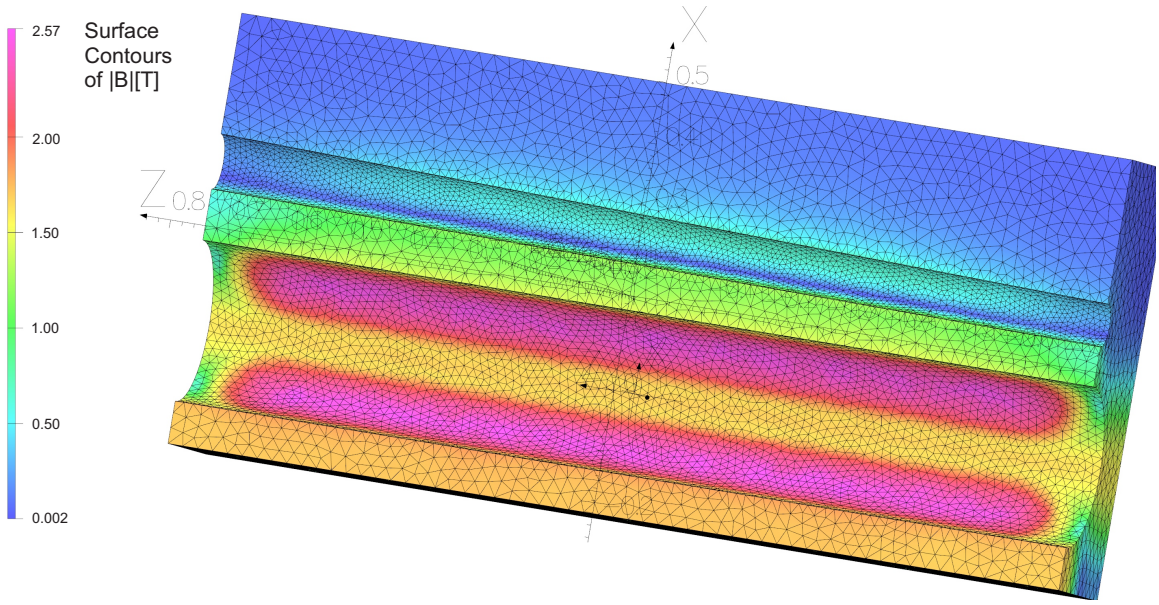

(b) Yoke magnetization in Tesla

Figure 6.13: Peak field on the wire (a) and yoke magnetization (b) of the Q1ApF magnet.

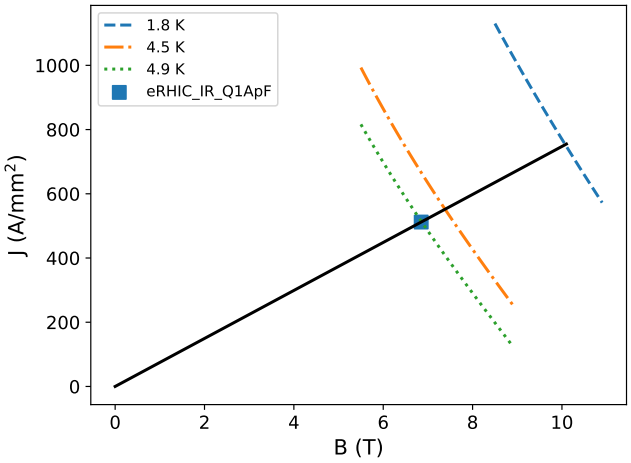

Figure 6.14: Load-line of the Q1ApF magnet.

The Q1BpF-Q1EF Magnet

The Q1BpF-Q1EF magnet is a two-in-one magnet with center about 11 m after the IP; it is designated to provide a high gradient to the hadron beam (Q1BpF) and a low gradient to the electron beam (Q1EF). Due to the small distance between the electron and hadron beam the required fields are provided by two separate superconducting magnets in a common iron yoke.

Both magnets have a magnetic length of 1.61 m and are enclosed in an iron yoke which is 0.9 m wide and 0.7 m tall. The iron yoke acts as a return yoke and should be made of low-carbon steel; the weight of the yoke is 6.8 tons.

Figure 6.15 shows the front end cross-section of the magnet. Due to the crossing angle the distance between the two apertures varies from 288 mm to 312.5 mm. The figure shows the face of the magnet closer to the IP, which is the more challenging one due to the smaller distance.

The iron between the two quadrupole magnets prevents flux from leaking from one magnet into the other. For this concept to work the iron must not saturate, in particular in the region between the two magnets. Figure 6.16 shows a 3D view of the magnet; as shown in the figure, the axes of the magnets are at an angle with respect to one another. The magnetic field equivalent to the magnetization is shown in Figure 6.17. As shown in the figures, the iron is not saturated, neither at the front nor the back as shown in the 3D simulation.

The provided gradients are shown in Figure 6.18. The limiting factor of this design is largely the gradient of the hadron quadrupole magnet, which is presently 65 T/m. The electron quadrupole field is about 8 T/m.

The load-lines of the magnets are shown in Figure 6.19. The hadron quadrupole magnet in the present design has a margin $> 35\%$; the margin of the electron quadrupole is $> 280\%$. The parameters of the magnets are summarized in Table 6.3.

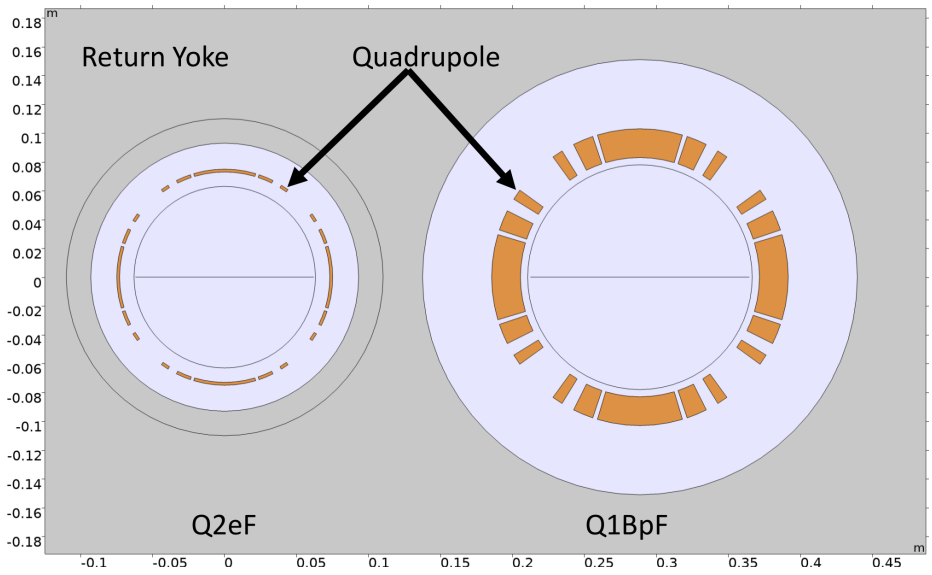

Figure 6.15: The Q1BpF-Q1EF magnet cross-section at its front end (nearer to IP). Q1BPF and Q1EF are the hadron and electron quadrupole magnets, respectively. The distance between the apertures is 288 mm on one end of the magnet and 312.5 mm on the other.

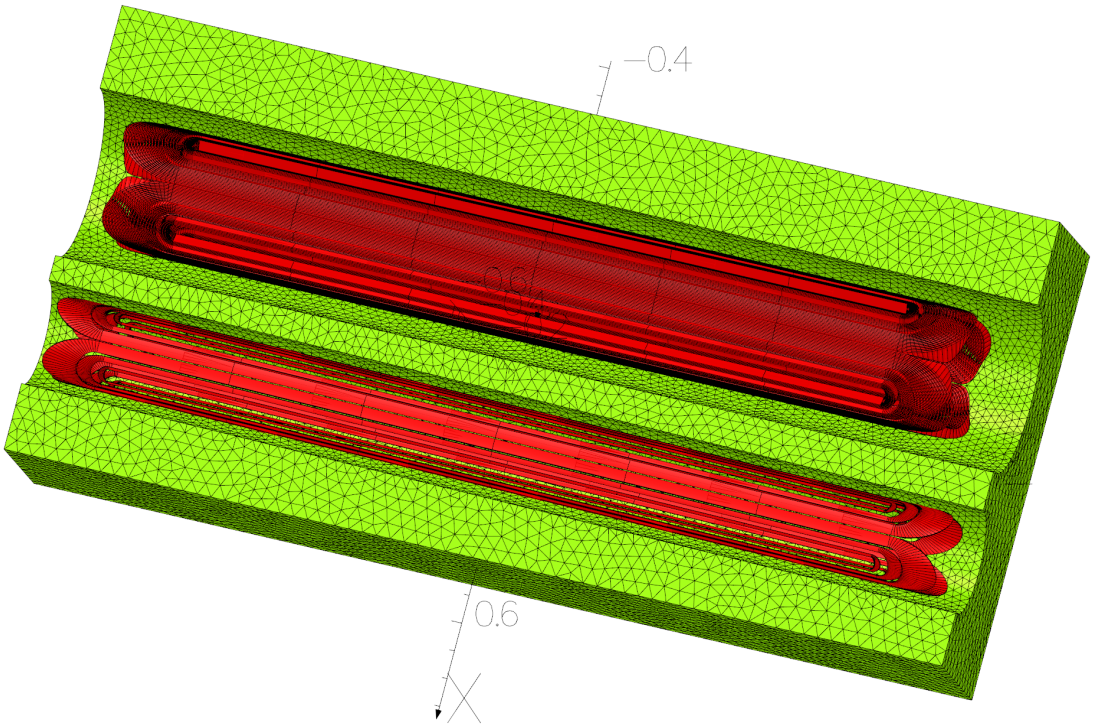

Figure 6.16: 3D geometry of the Q1BpF-Q1EF magnet.

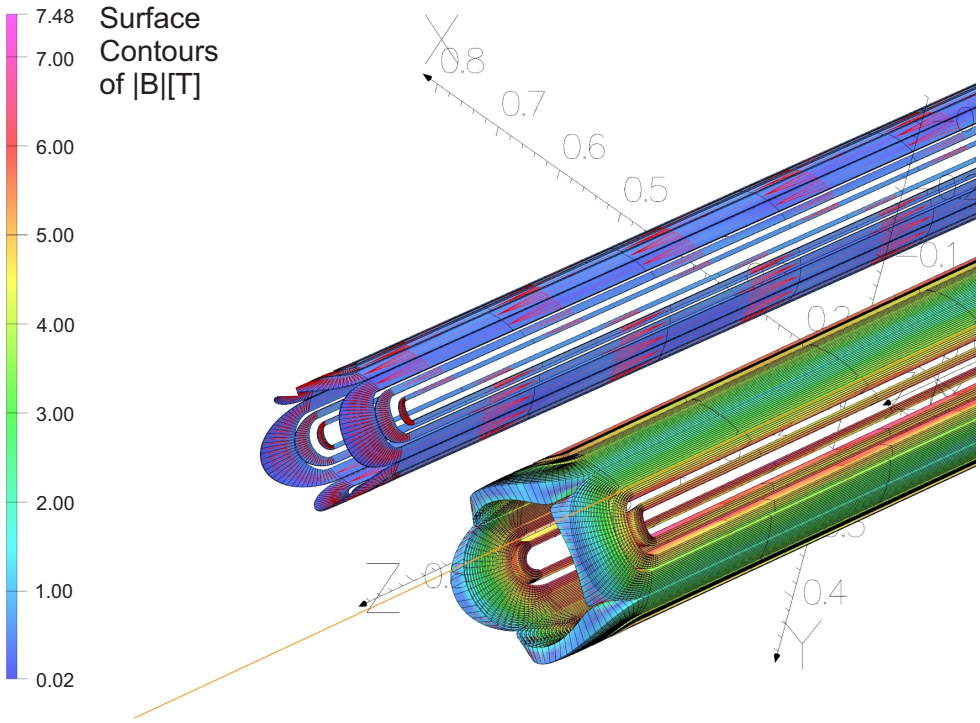

(a) Peak field conductor

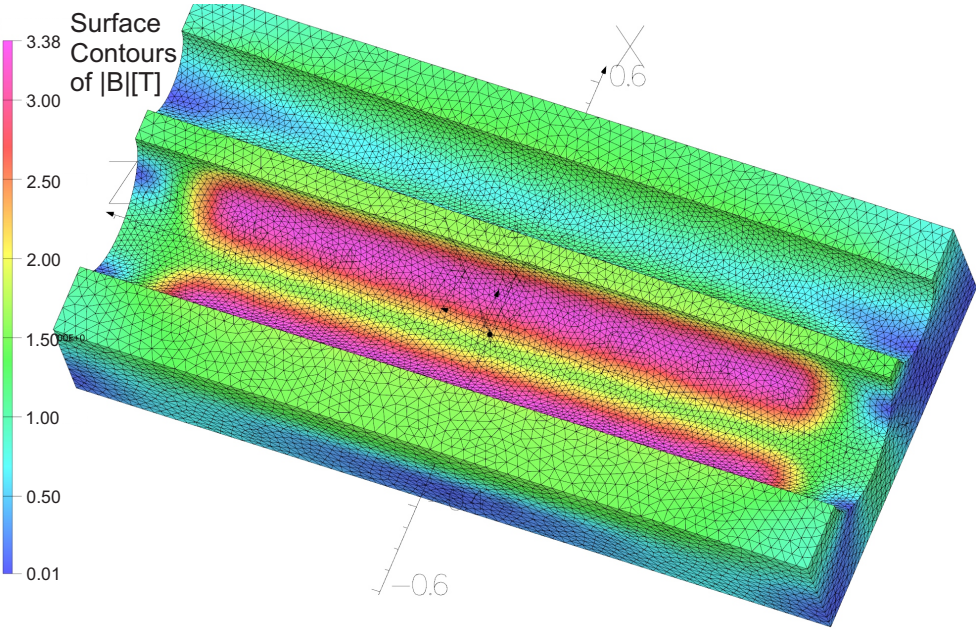

(b) Yoke Magnetization

Figure 6.17: Peak magnetic fields on the conductor of the Q1BpF-Q1EF magnet and yoke magnetization (3D).

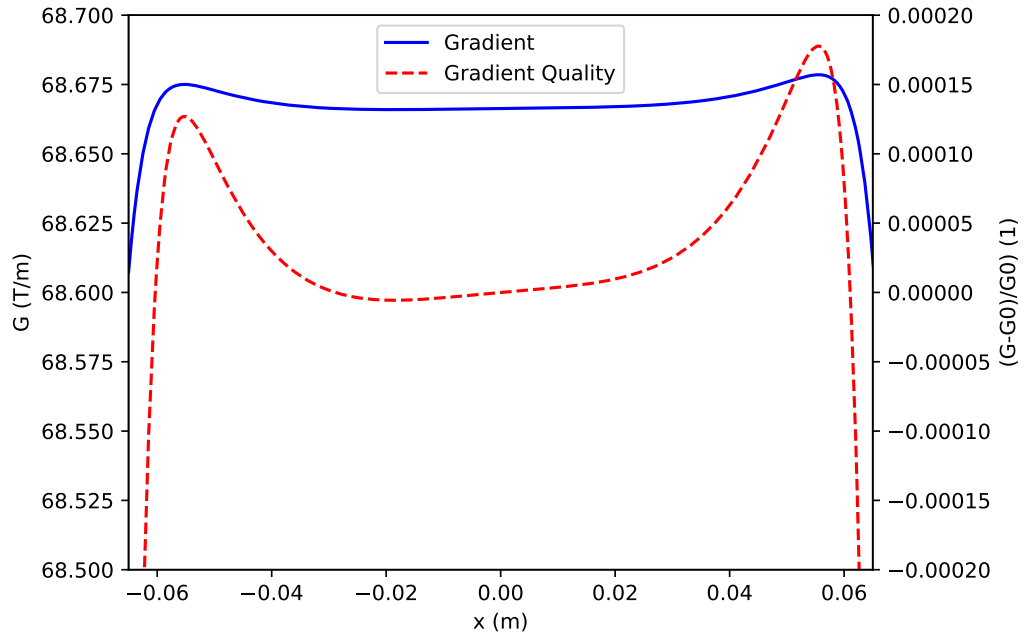

(a)

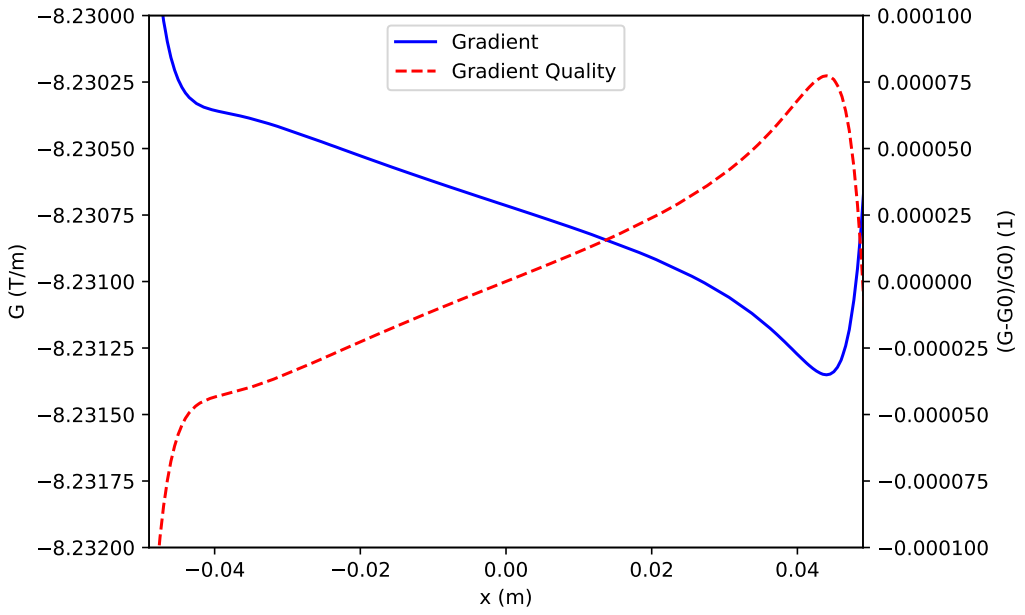

(b)

Figure 6.18: Gradient and gradient quality of the hadron (a) and electron (b) quadrupole magnets Q1BpF and Q1EF.

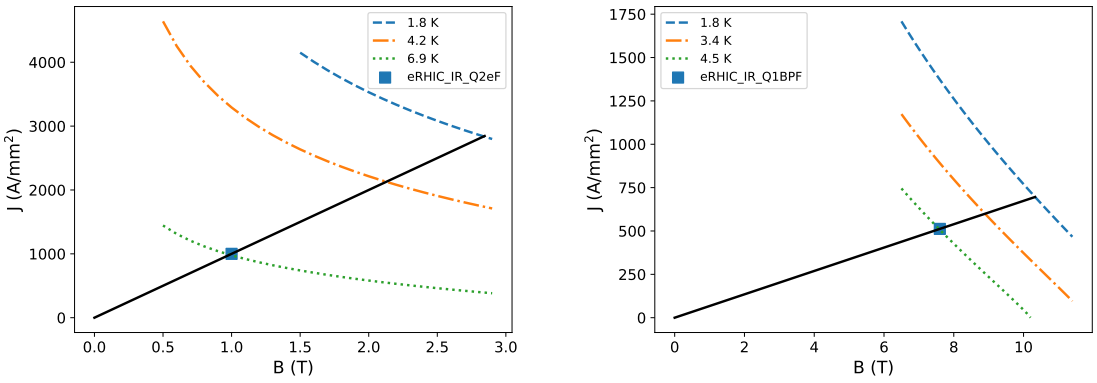

(a) Q1EF **(b)** Q1PR

Figure 6.19: Load lines of the electron (a) and hadron (b) quadrupole magnets Q1BpF and Q1EF.

Table 6.3: Specification Q1BpF-Q1eF, hadron and electron quadrupole.

Parameter	Hadron Quadrupole	Electron Quadrupole
Magnetic length [m]	1.61	1.61
Maximum gradient [T/m]	66.2	8.0
Aperture diameter front [m]	0.156	0.128
Required field quality [%]	0.1	0.1
Physical length [m]	1.61	1.62
Physical width [m]	0.206	0.15
Physical height [m]	0.206	0.15
Superconductor Type	NbTi	NbTi
Conductor Cable [mm^2]	20×2	1×1
Current density [A/mm^2]	512	1000
Cu:Sc ratio	1.3	1.3
Temperature [K]	1.8	1.8
Peak field wire [T]	7.6	1.0
Magnetic energy [J]	550000	2897.6
Ampere turns [kA-turn]	460	32
Number of turns	23	32
Current [A]	20000	1000.0
Inductance [mH]	2.75	5.8
Margin loadline [%]	36	284

The Q2PF Magnet

The Q2PF magnet is a large aperture 3.8 m long quadrupole magnet in the forward hadron direction. The aperture requirements are driven by the need to pass the neutron cone and forward scattered particles with up to 1.3 GeV/c transverse momentum. The maximum gradient of the quadrupole magnet is about 41 T/m, which in combination with the aperture (131 mm) leads to a significant peak field on the wire.

The flux of the Q2PF quadrupole magnet is returned in an iron yoke, which also contains a field-free region for the nearby electron beam. The size of the iron yoke is $1.2 \times 0.8\,\mathrm{m}^2$ (width$\times$ height); the total estimated weight is 23.3 tons. The circular cut-out region for the electrons is angled with respect to the axis of the quadrupole magnet and has a diameter of 121 mm; the distance between the center of the electron beam and the center of Q2PF is 366.8 mm on the front face and 423 mm on the rear face of the magnet. Figure 6.20 (a) shows an overview of the geometry (front face).

The simulated gradient and gradient quality are shown in Figure 6.21 (a). The hadron beam travels offset through the Q2PF magnet, so on the entrance face the good field region needs to extend to almost 80 mm (see Figure 6.20 (b)). As shown in the figure, the field quality requirement can be met. The field quality will improve towards the rear side of the magnet at the location of the beam, as the hadron beam will shift more towards the center of the magnet. The residual field in the field-free region for the electron beam is shown in Figure 6.21 (b), which is of the order of the earth's magnetic field level.

The load-line of the Q2PF magnet is shown in Figure 6.23. As shown in the figure, at 1.8 K the magnet can operate with a margin of 22.7%.

The integrated field harmonics for the Q2PF magnet are shown in table 6.5. The table shows the integrated harmonics normalized to 10000 units of the main quadrupole component. The reference radius is 83 mm.

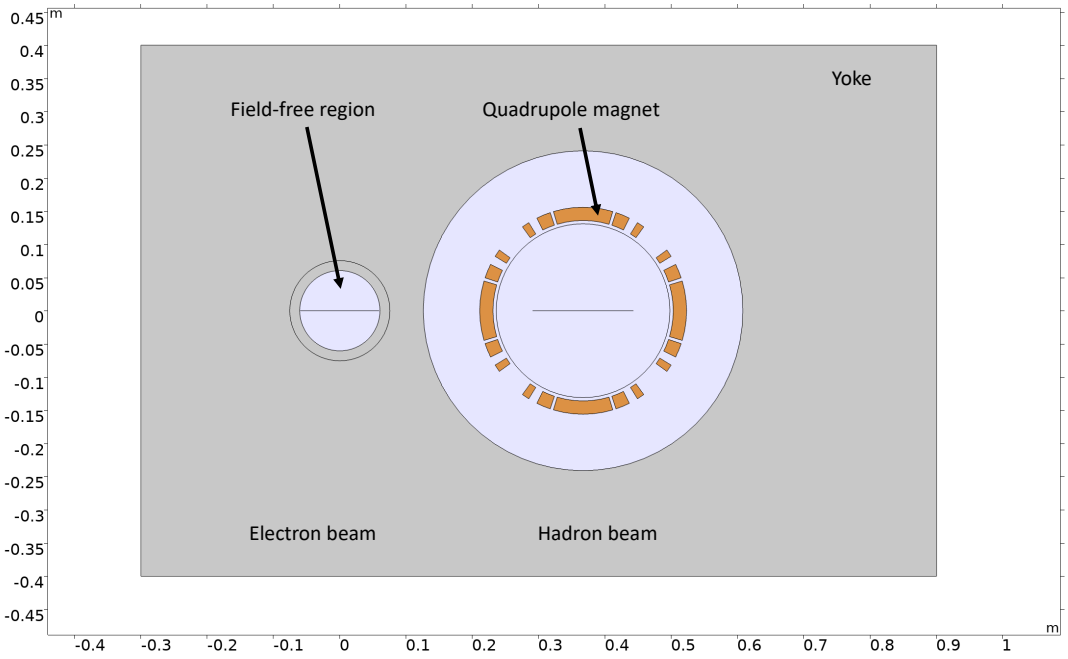

(a) Geometry of front end

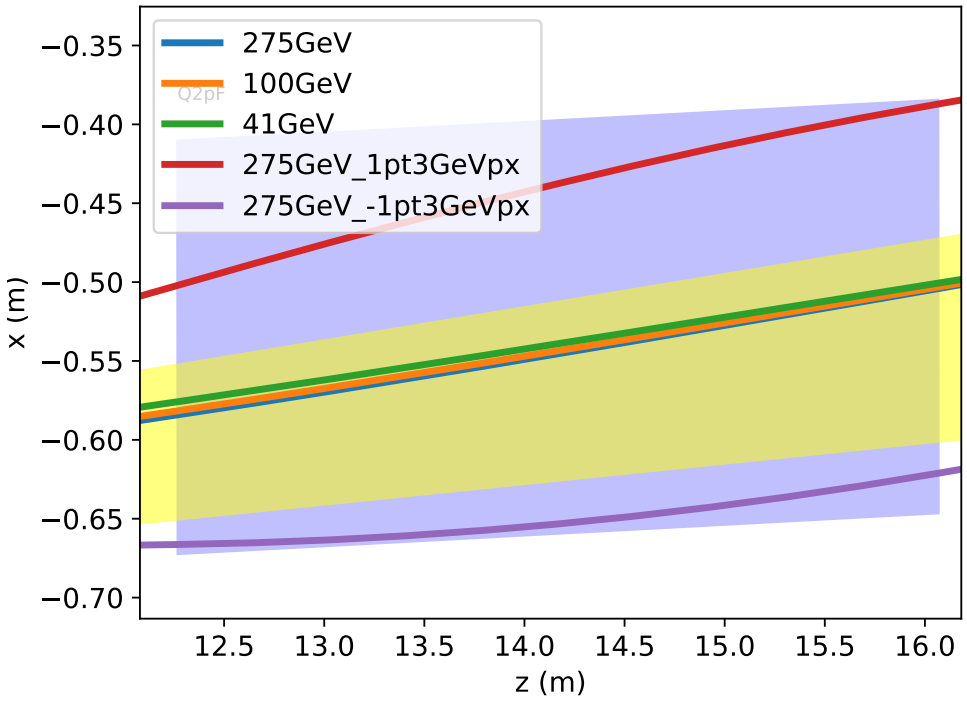

(b) Aperture requirements

Figure 6.20: Geometry (a) and aperture requirements (b) of the Q2PF magnet. Figure (b) shows the magnet aperture (blue), the neutron cone (yellow), and the paths of particles of different energy through the magnet.

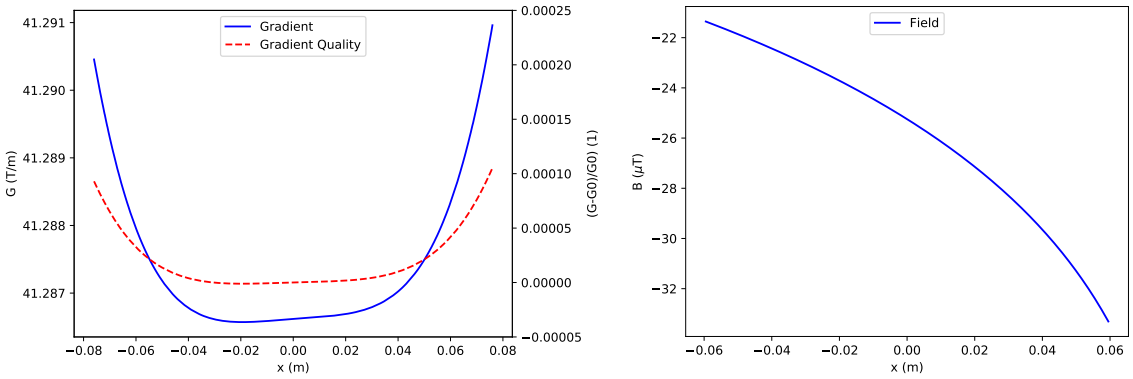

(a) Gradient/gradient quality **(b)** Field-free region

Figure 6.21: Gradient and gradient quality (a) and residual field in the field free region (b).

Table 6.4: Parameters Q2PF Magnet

Parameter	Value
Magnetic length [m]	3.8
Maximum gradient [T/m]	40.7
Aperture diameter (front) [m]	0.262
Aperture diameter (rear) [m]	0.262
Required field quality	1×10^{-4}
Physical length [m]	3.8
Physical width [m]	0.156
Physical height [m]	0.156
Superconductor type	NbTi
Conductor	Cable $20 \times 2\,\mathrm{mm}^2$
Current density [A/mm^2]	512
Cu:Sc ratio	1.3
Temperature [K]	1.8
Peak field wire [T]	6.85
Magnetic energy [MJ]	3.0
Ampere turns [kA·t]	420
Number of turns	28
Current [A]	15000
Inductance [mH]	26.67
Margin loadline [%]	32

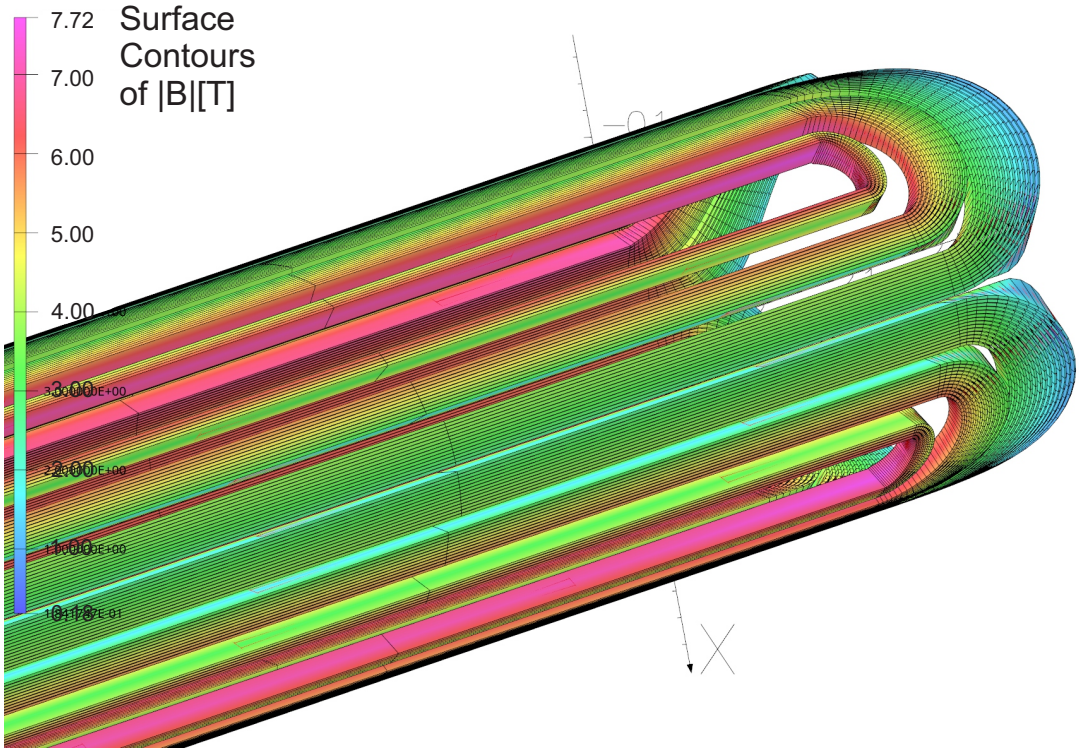

(a) Peak field wire

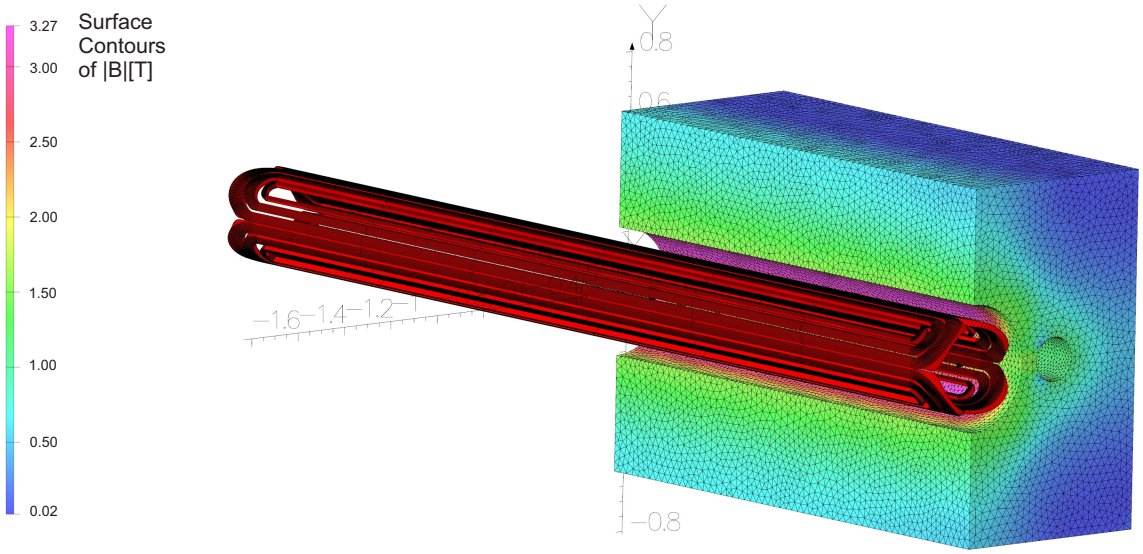

(b) Yoke Magnetization

Figure 6.22: Peak field on the wire (a) and yoke magnetization (b) of the Q2PF magnet.

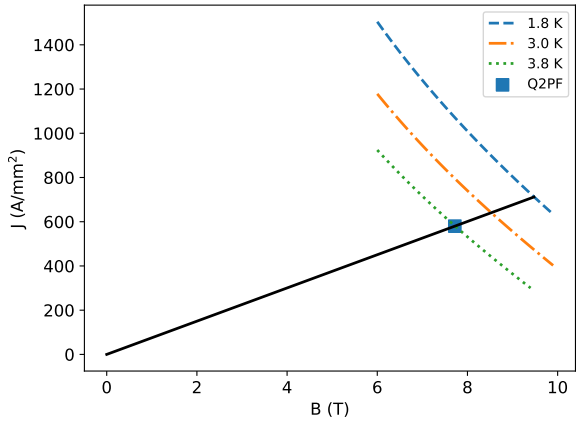

Figure 6.23: Load-line of the Q2PF magnet.

Table 6.5: Normal component (B_n) of n^{th} harmonics for the Q2PF magnet (Skew component $A_n = 0$ for all harmonics number $n = 1, 2, 3, ...$).

n	B_n
1	0
2	10000
3	0
4	-0.00256
5	0
6	0.03406
7	0
8	-9×10^{-5}
9	0
10	0.11018
11	0
12	-1×10^{-5}
13	0
14	0.25932
15	0
16	0
17	0
18	0.11135
19	0
20	0

The B1PF Magnet

The B1PF magnet is a 3 m long dipole magnet to separate hadrons from neutrons with its center at about 16.5 m distance from the IP. The B1PF magnet provides a 3.4 T dipole field to the proton beam; in addition to the $10\,\sigma$ beam envelope of the hadron beam the magnet aperture has to accommodate outgoing tracks from the collision and the neutron cone, which leads to aperture requirements of 270 mm. This is shown in Figure 6.24.

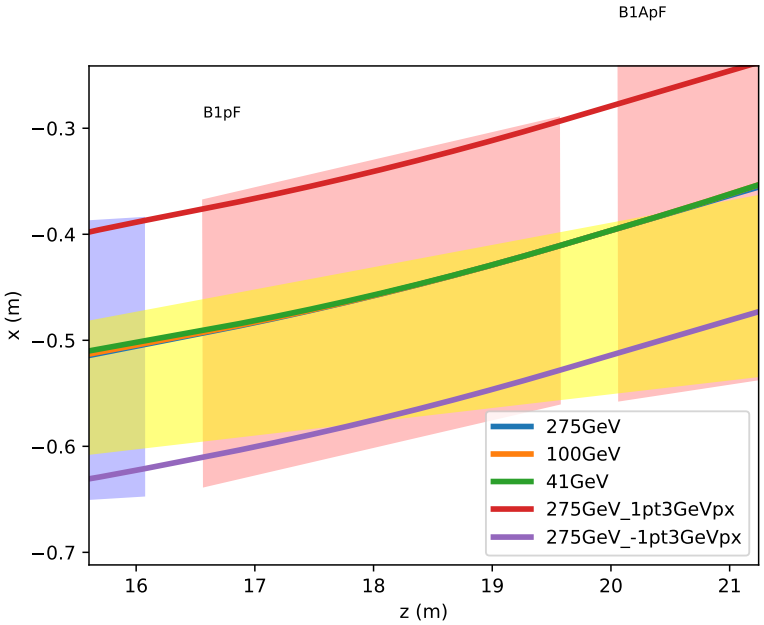

Figure 6.24: The B1PF magnet aperture (blue) in relation to particle orbits with different energies and particle orbits with 1.3 GeV/c transverse momentum. The neutron cone is shown in yellow.

The center of the electron beam is offset 439 mm (exit face 542 mm) from the center of the hadron beam. The electron beam needs to be shielded from the stray field of the dipole magnet. The required aperture for the electron beam is 100 mm horizontally and 160 mm vertically.

The required dipole field can be generated by a low-temperature superconducting NbTi dipole magnet; one possibility is a conventional collared magnet, which is shown in Figure 6.25. The coil can be wound from a 20 mm wide Rutherford cable. For mechanical support a stainless steel collar would be added. A large outer iron yoke ensures that the magnetic flux is returned.

Figure 6.25 shows the shielded region. In order to sufficiently reduce the stray field in the shielded region a multi-layer structure is employed: a 1 mm thick layer of good quality soft-iron (AISI 1006 or better) is followed by a 2 mm thick mu-metal shield. All layers are separated by a 1 mm air gap and elliptical in shape.

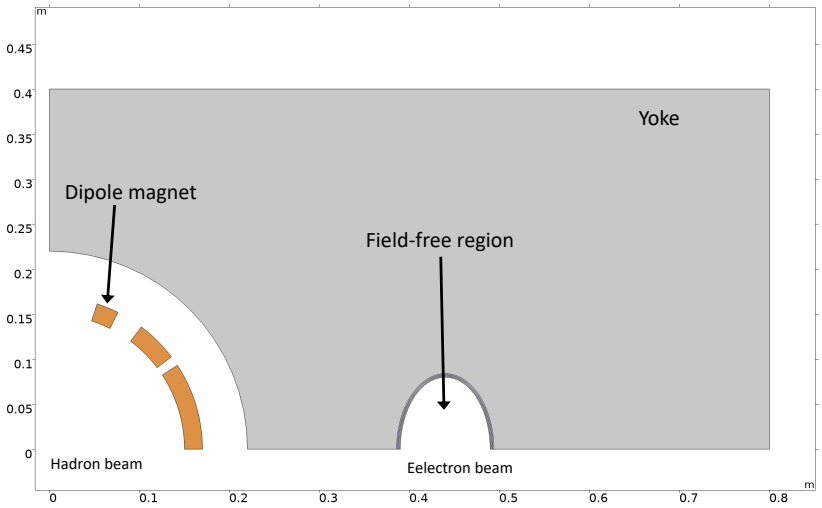

(a) Geometry

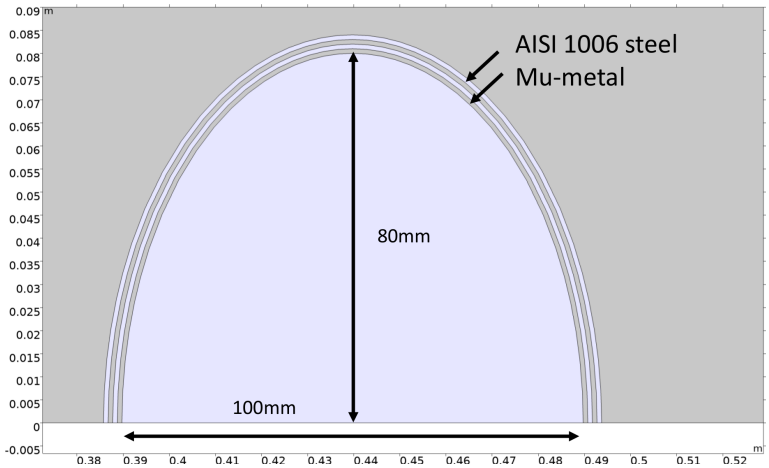

(b) Shielded Region

Figure 6.25: Geometry of the B1PF magnet at the front end (a); Figure (b) shows the shielded region in more detail. Both figures show the front face of the magnet; all dimensions in meters.

Figure 6.26 shows the vertical magnetic field on the center plane (a) and the good field region (b). The figures show that a field quality of 10^{-4} can easily be accomplished in an aperture of 150 mm, which is larger than the required good field region (120 mm). The residual field in the shielded region is on the level of a few Gauss.

The magnetic field in the shielded region is shown in Figure 6.27. As shown in the figure, the stray magnetic field is of the order of 80 µT. Due to the larger beam separation this can be expected to improve for the rear side of the magnet. Better shielding can be accomplished by thicker or more shielding layers.

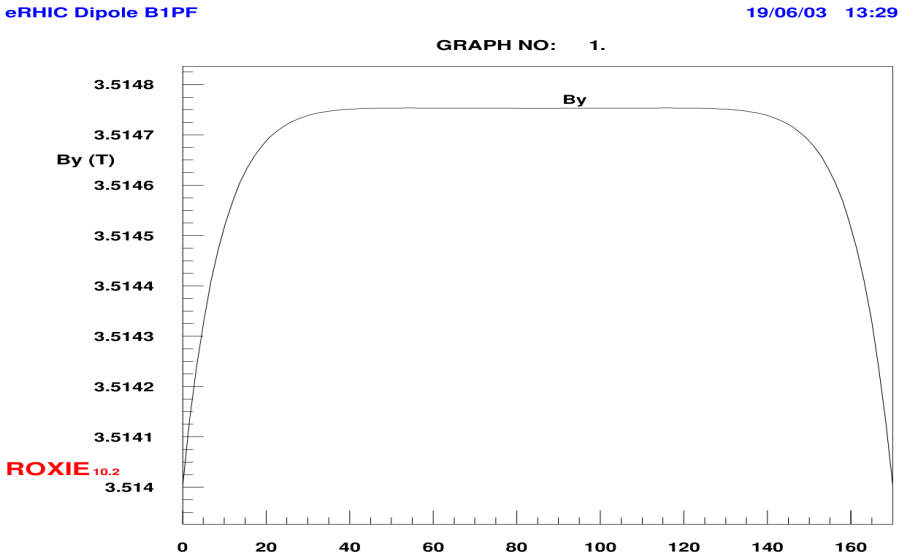

(a) Geometry

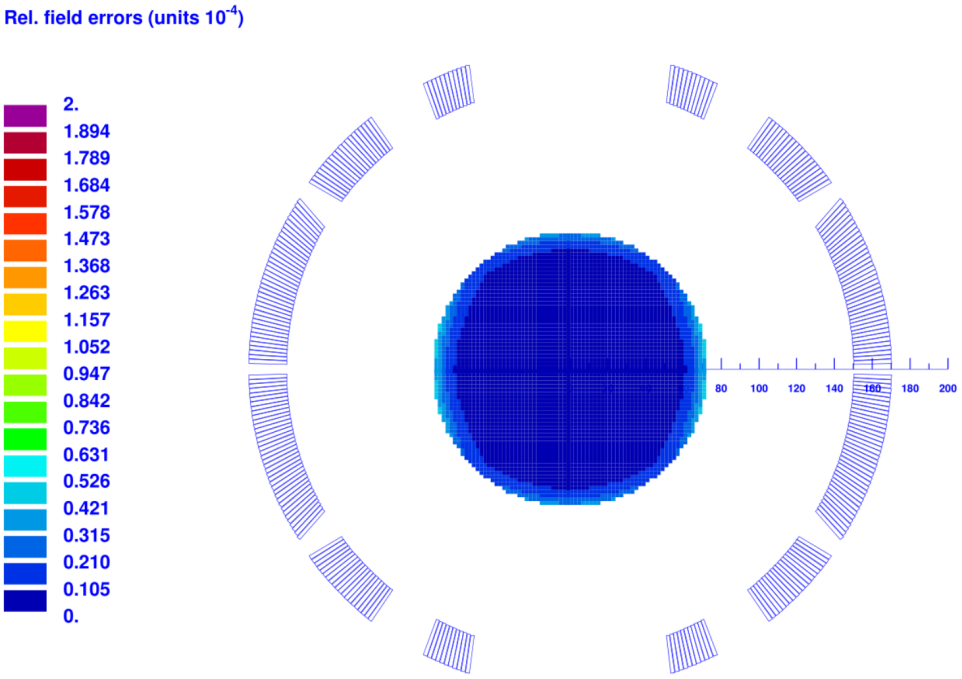

(b) Shielded region

Figure 6.26: Vertical magnetic field on the center plane for the hadron beam (a). Figure (b) shows the good field region.

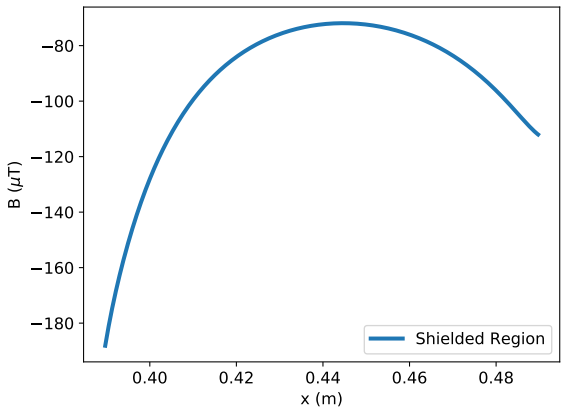

Figure 6.27: Field in the shielded electron region.

The peak magnetic field and saturation of the yoke is shown in Figure 6.28. As shown in the figure, the peak field on the wire is 4.37 T at peak excitation; using a NbTi superconductor with a copper to superconductor ratio of 1.3 the margin on the loadline is 58%. Figure 6.29 shows the loadline.

The iron return yoke is 1.8 m wide and 0.8 m tall. The estimated total weight of the magnet is 29 tons. The parameters of the B1PF magnet are summarized in Table 6.6.

Table 6.6: Parameters of the B1PF magnet.

Parameter	Value
Magnetic length [m]	3
Maximum dipole field [T]	3.4
Aperture [m]	0.262
Required field quality [%]	0.01
Coil width [m]	0.34
Coil height [m]	0.34
Superconductor Type	NbTi
Current density [A/mm^2]	241
Cu:Sc ratio	1.3
Temperature [K]	4.2
Peak field wire [T]	4.37
Magnetic energy [MJ]	1.36
Ampere turns [MA·t]	1.16
Margin loadline [%]	58

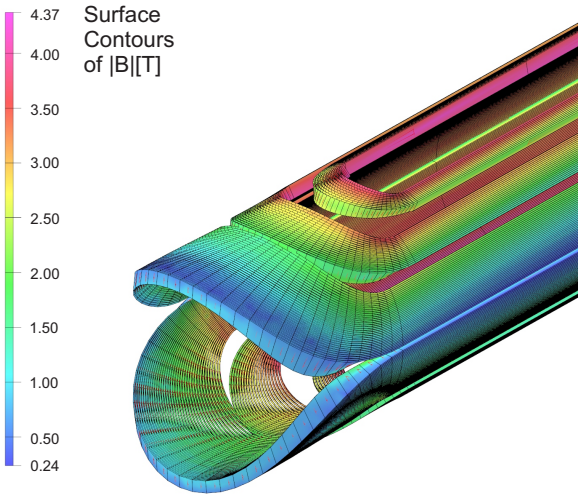

(a) Peak field wire in tesla

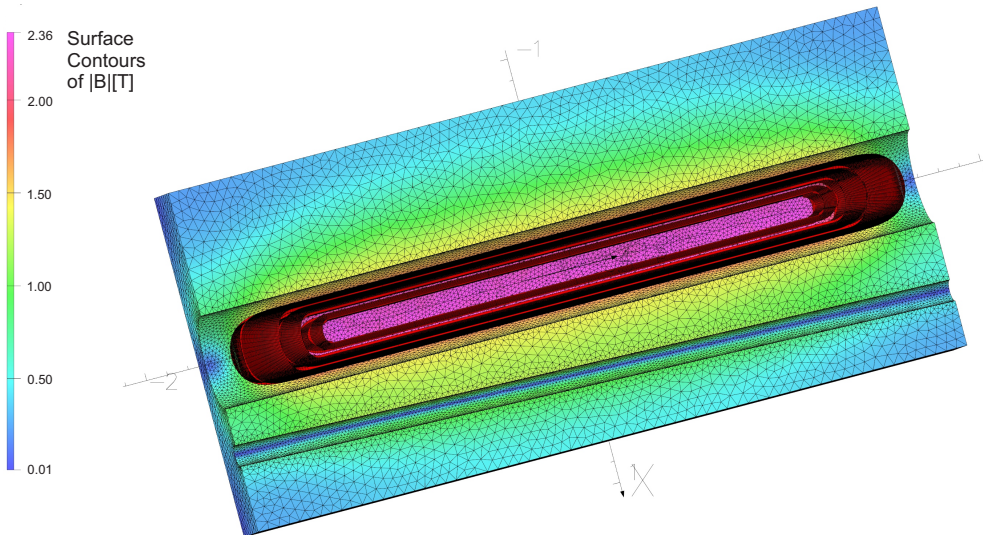

(b) Iron magnetization in tesla

Figure 6.28: Yoke magnetization (a) and peak field on the wire (b) of the B1PF magnet.

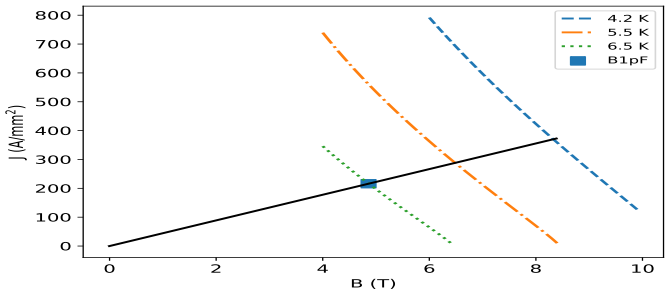

Figure 6.29: Load-line of the B1PF dipole magnet.

The B1APF Dipole Magnet

The B1APF magnet follows the B1PF magnet to further separate hadrons from the neutron cone. It is located 21 m from the IP in the hadron forward beam line. The aperture of the B1aPF magnet needs to be significantly larger in comparison to the B1PF magnet (168 vs 135 mm radius) due to the larger distance from the IP, the divergence of the neutron beam, forward scattered particles with up to 1.3 GeV/c transverse momentum and to allow particle tracks at 40% of initial momentum. To reduce the complexity and mechanical challenges the peak dipole field is reduced to 2.7 T.

Figure 6.30 shows an overview of the geometry (front face). Part of the B1aPF magnet is an iron yoke (dimensions $1.6 \times 1.04\,\mathrm{m}^2$) which entails a field-free region for the electron beam. The field free region is elliptical in cross-section (half-axis 50 mm and 80 mm) and in 581.7–619.2 mm distance from the center of the hadron beam. The estimated weight of the magnet is 11 tons. The main parameters of the magnet are summarized in Table 6.7.

Table 6.7: Parameters of the B1APF dipole magnet.

Parameter	Value
Magnetic length [m]	1.5
Maximum dipole field [T]	2.7
Aperture front [m]	0.3360
Aperture rear [m]	0.3360
Design field quality	1×10^{-4}
Physical length [m]	1.6
Physical width [m]	0.41
Physical height [m]	0.41
Superconductor type	NbTi
Conductor	Cable $20\times2\,\mathrm{mm}^2$
Current density [A/mm^2]	148
Cu:Sc ratio	1.3
Temperature [K]	4.2
Peak field wire [T]	3.5
Magnetic energy [MJ]	0.717
Ampere turns [MA·t]	1.16
Number of turns	154
Current [A]	7670
Inductance [H]	0.024376
Margin loadline [%]	60

The aperture of the magnet is primarily defined by the neutron cone and forward scattered particles; a good field region is only required in a fraction of the aperture as shown in Figure 6.30 (b). The figure shows the $10\,\sigma$ beam-size of the hadron beam in the aperture of the magnet. As shown in the figure, a good field quality is only required up to about a radius of 60 mm.

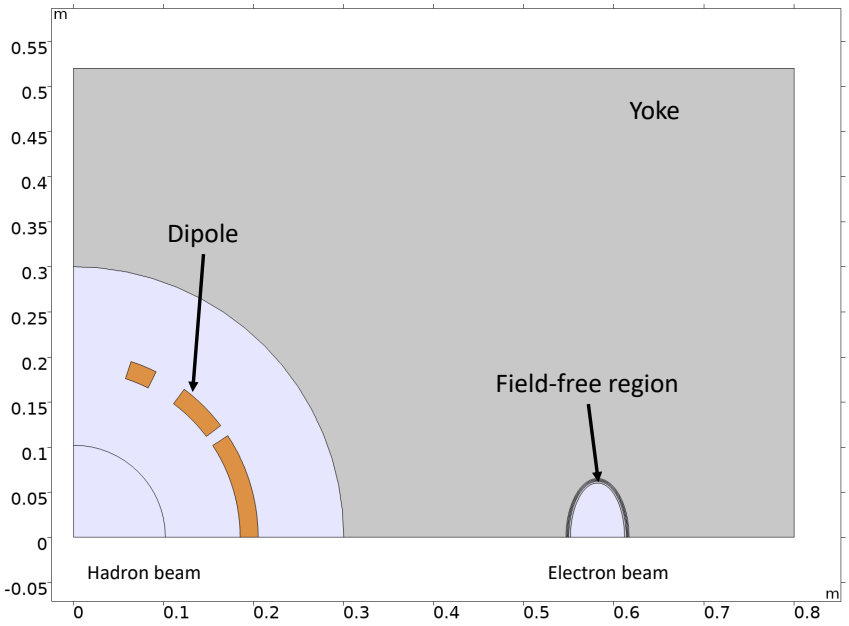

(a) Cross-section of B1APF

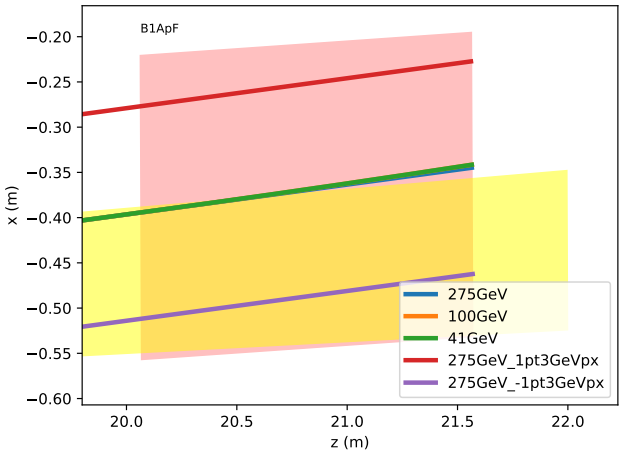

(b) Aperture requirements

Figure 6.30: Geometry of the B1APF magnet (a) and aperture requirements (b). Figure (b) shows particle orbits for different energies and particle orbits with a transverse momentum of 1.3 GeV/c transverse momentum. The neutron cone is shown in yellow.

The field and field quality of the B1APF magnet are shown in Figure 6.31 (a). As shown in the figure, the required dipole field can be generated with sufficient field quality. The residual field in the field-free region can be expected to be minimal, as shown in Figure 6.31 (b). This is due to the fact that the iron yoke between the two apertures does not saturate, as shown in Figure 6.32.

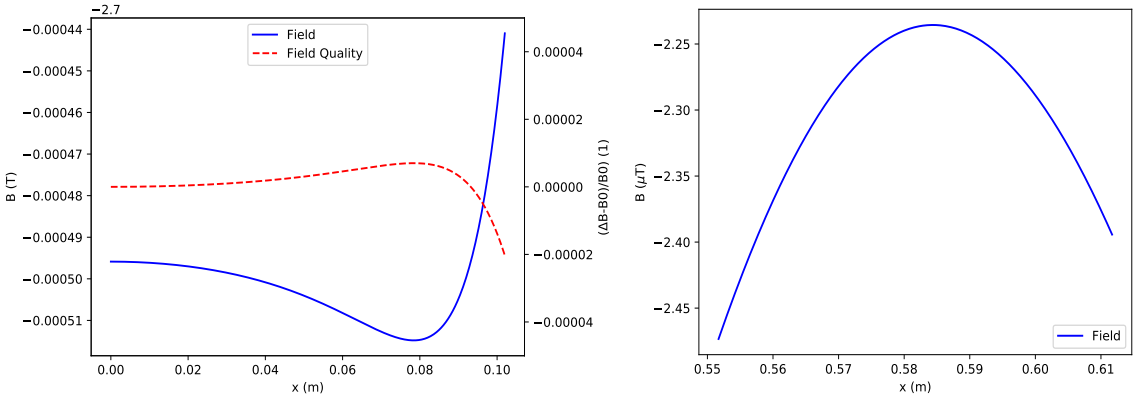

(a) B1APF **(b)** Field-free region

Figure 6.31: Field and field quality of the B1APF magnet (a) and residual magnetic field in the field free region (b).

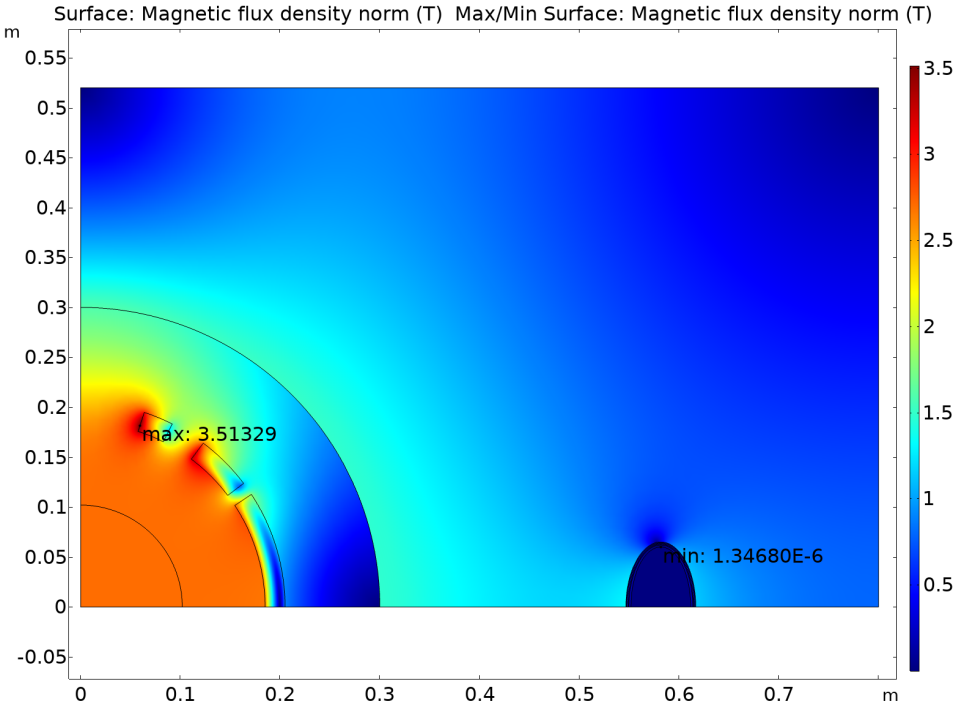

Figure 6.32: Magnetic field equivalent to the magnetization in the B1APF magnet.

The 3D geometry of the magnet is shown in Figure 6.33 (a). Due to the relatively small aspect ration of the magnet (aperture vs. useful length of the magnet) the current density needs to be increased by about 20% in comparison to the 2D simulations to meet the integrated field requirement. The vertical magnetic field along the length of the magnet is shown in Figure 6.33 (b).

The peak field on the wire is about 4 T as shown in Figure 6.34 (a). With a current density of 242 A/mm^2 the margin on the load-line is 92% as shown in Figure 6.34 (b).

The field harmonics at a radius of 60 mm, normalized to 10000 units of the main component, are shown in Table 6.8.

Table 6.8: Normal component (B_n) of n^{th} harmonics for the B1APF magnet (normalized to 10000 units of the main component). $R_{\text{ref}} = 60\,\text{mm}$. (Skew component $A_n = 0$ for all harmonics number $n = 1, 2, 3, ...$).

n	B_n
1	10000
2	0
3	0.64042
4	0
5	-0.10213
6	0
7	-0.23545
8	0
9	-0.06336
10	0
11	-0.01134
12	0
13	-0.0017
14	0
15	6×10^{-5}
16	0
17	0
18	0
19	0
20	0

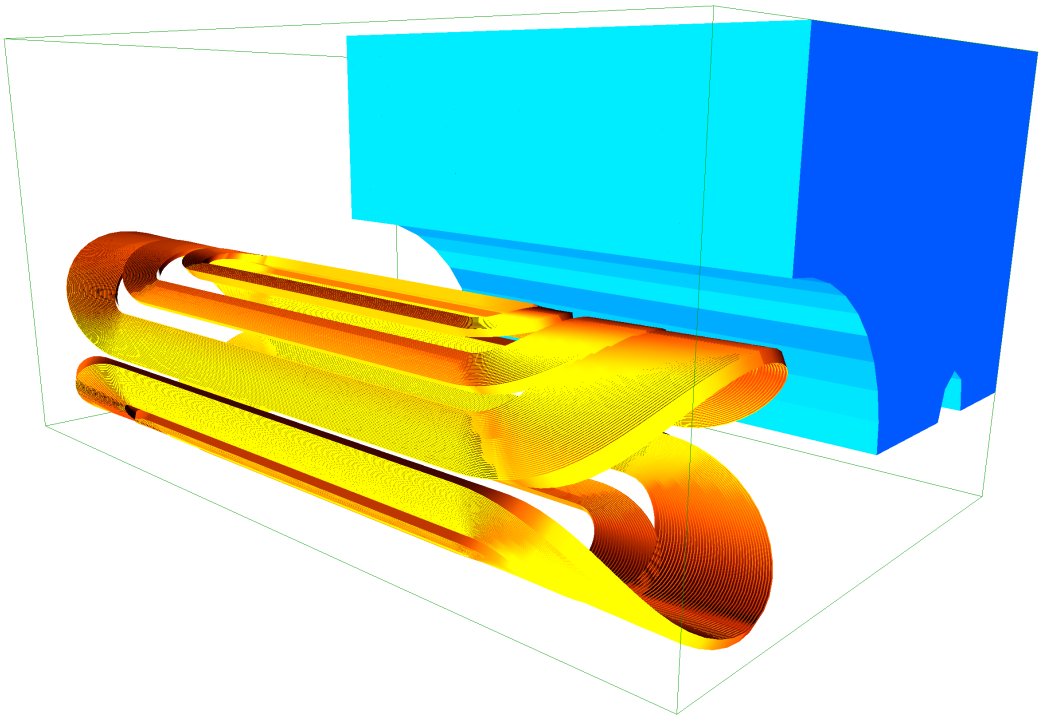

(a) 3D geometry of the B1APF magnet

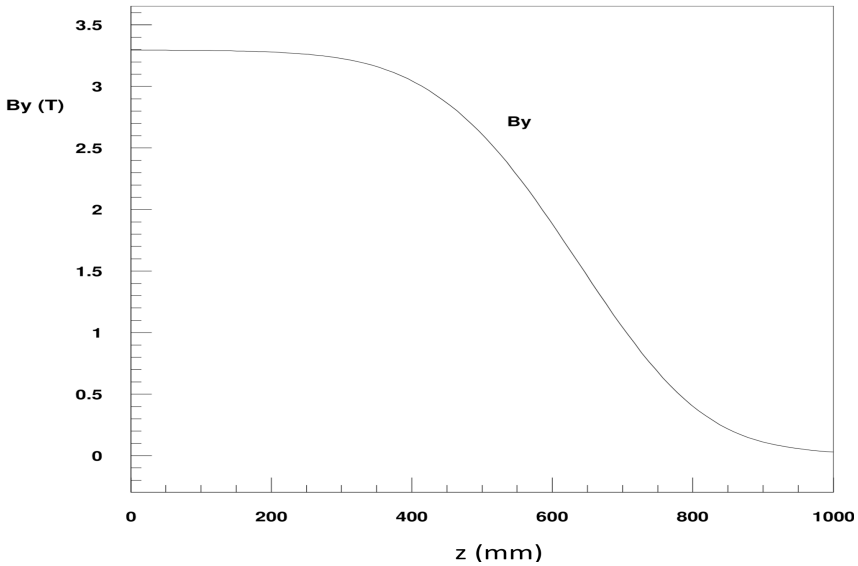

(b) Vertical magnetic field (Tesla) along the length of the magnet (mm)

Figure 6.33: The B1APF magnet. 3D geometry and longitudinal field profile.

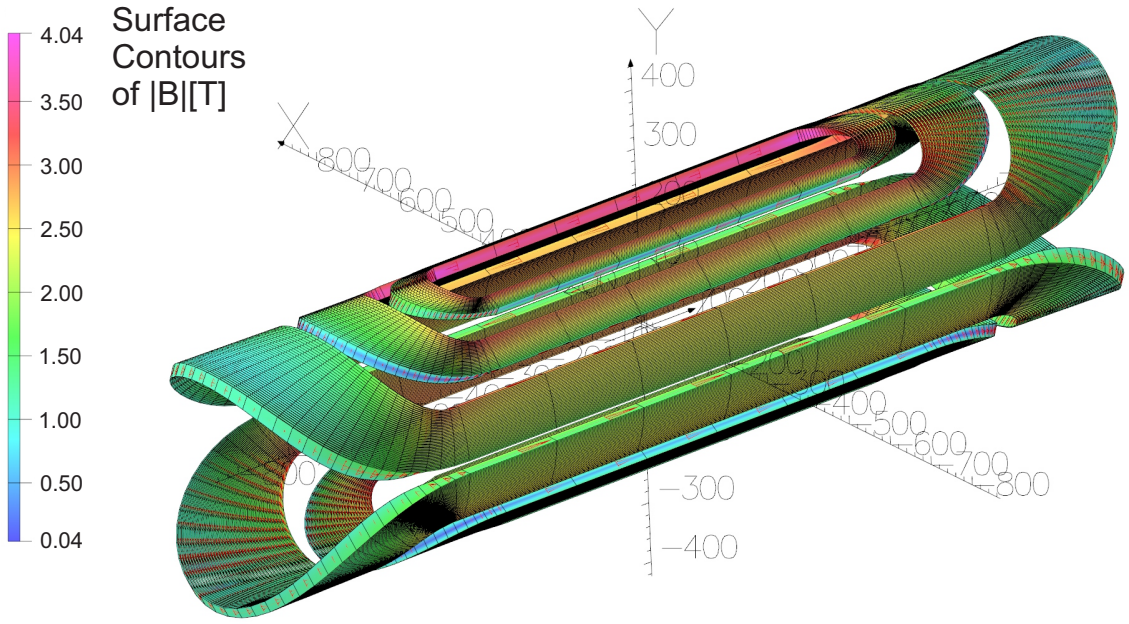

(a) Peak field wire

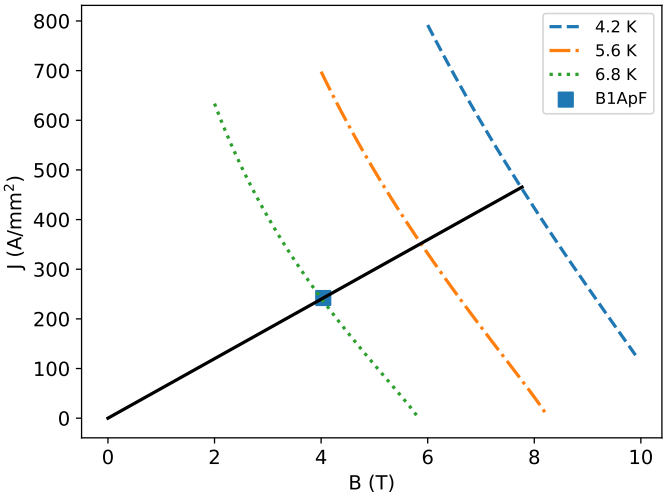

(b) Load-line

Figure 6.34: Peak field on the wire (a) and load-line (b) of the B1APF magnet.

The Q1APR/Q1ER Magnet

The Q1APR-Q1ER magnet is a two-in-one magnet on the rear side of the IP about 5.3 m from the IP. The purpose of the magnet is to provide a low gradient of up to 14 T/m to the electron beam and a high gradient (78 T/m) to the hadron beam. The magnet is challenging because the beams are not very separated especially on the magnet end close to the IP. The aperture of the electron quadrupole is determined by the synchrotron radiation fan, which is relatively large. The distance between the two magnet apertures varies from 132.5 mm to 177 mm due to the crossing angle. The aperture requirements are shown in Figure 6.35.

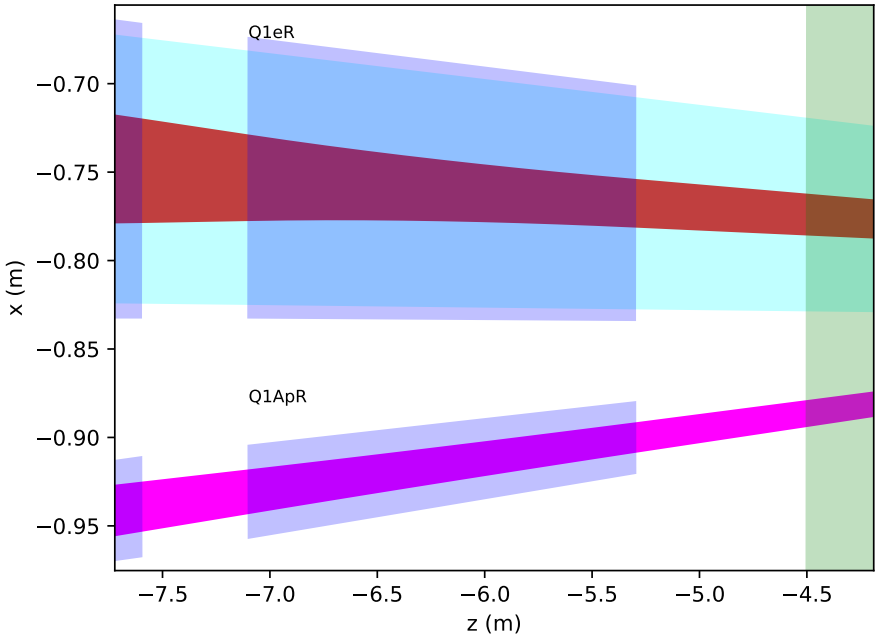

Figure 6.35: Aperture requirements of the Q1APR/Q1ER magnet. The magnet apertures are shown in blue; the 10σ and 15σ beam envelopes of the hadron and electron beams are shown in magenta and red, respectively. The synchrotron radiation fan is shown in cyan.

Both magnets are housed in a common iron yoke, which returns the magnetic flux and is designed to suppress cross-talk between the two magnets. This requires that the iron between the two magnets does not saturate. To facilitate this both magnets need to be tapered and are implemented as a double-helix coil (see Section 6.2.1 on page 477). Both 3D magnet geometries are shown in Figure 6.37.

The yoke magnetization for the more challenging front end of the magnet (closer to the IP) is shown in Figure 6.38. As shown in the figure, the peak magnetic field between the two magnet apertures is about 0.9 T. The yoke is therefore not saturated and provides adequate cross-talk suppression.

The gradient of both magnets was optimized to be constant along the length of the magnet,

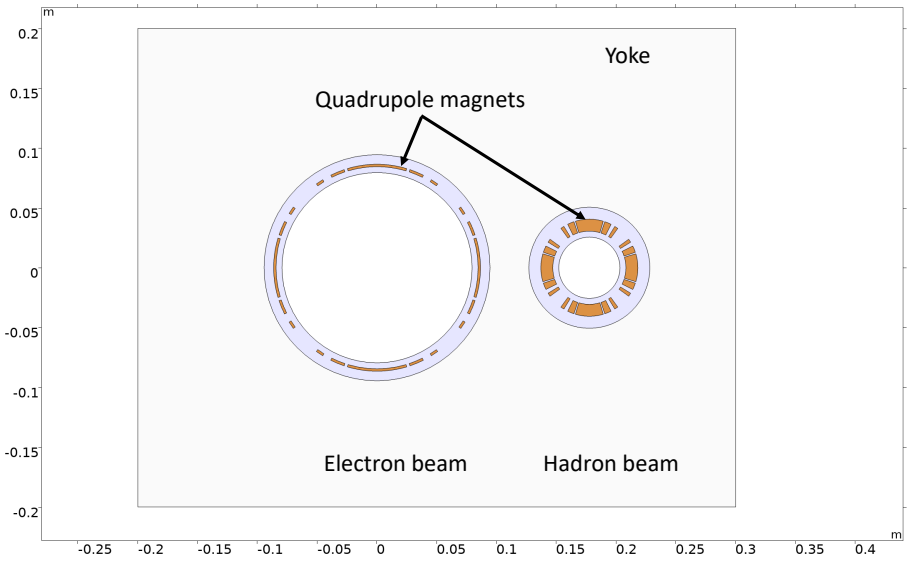

Figure 6.36: Geometry of the Q1APR/Q1ER magnet (front face).

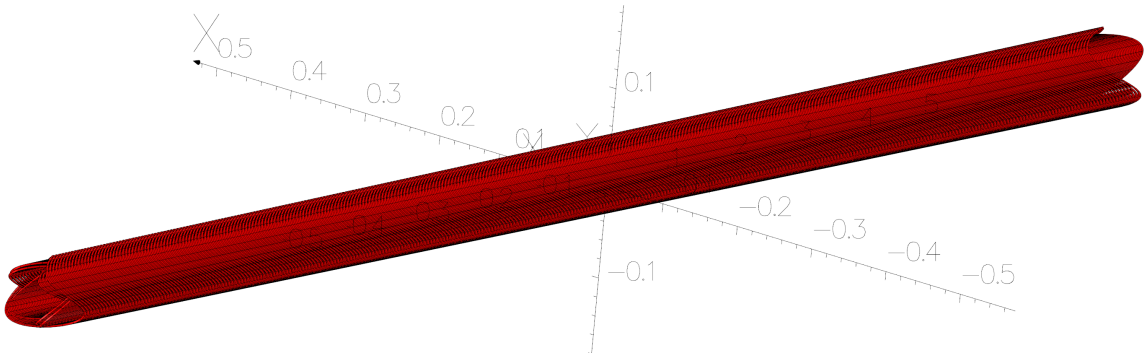

(a) Q1APR

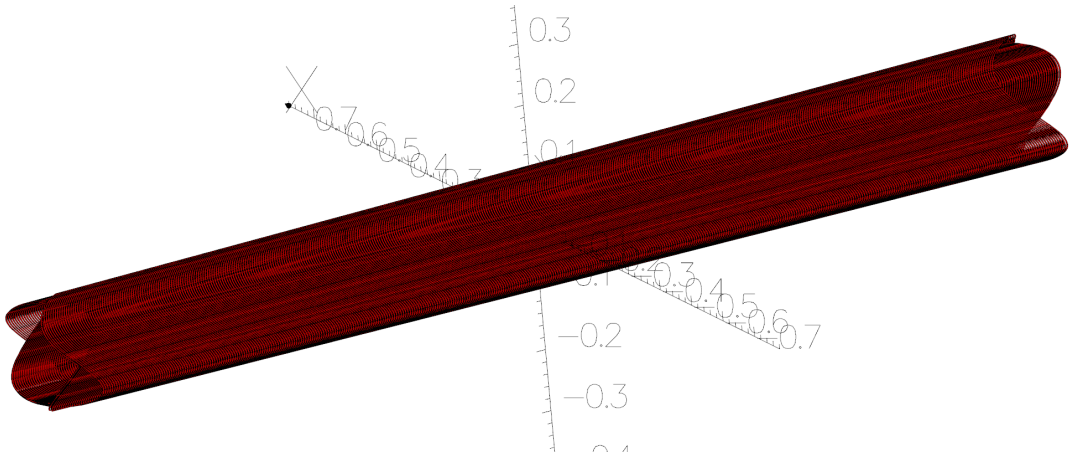

(b) Q1ER

Figure 6.37: Tapered double-helix Q1APR (a) and Q1eF (b) quadrupole magnets.

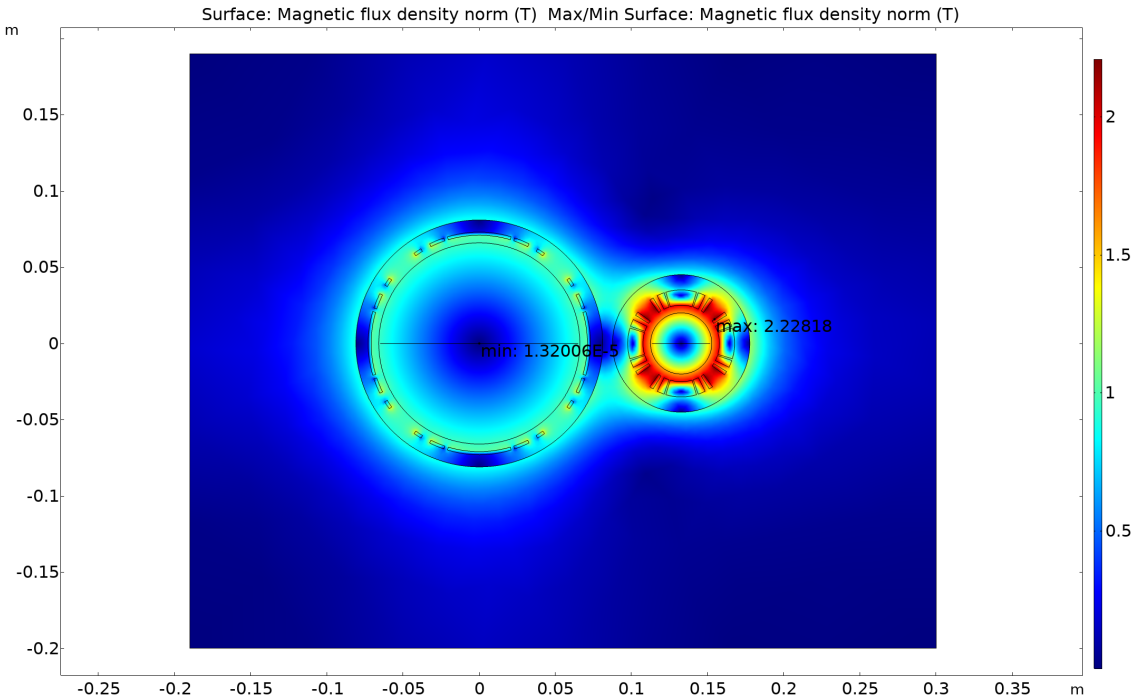

Figure 6.38: Magnetic field equivalent to the magnetization of the Q1APR/Q1eF magnet (front end).

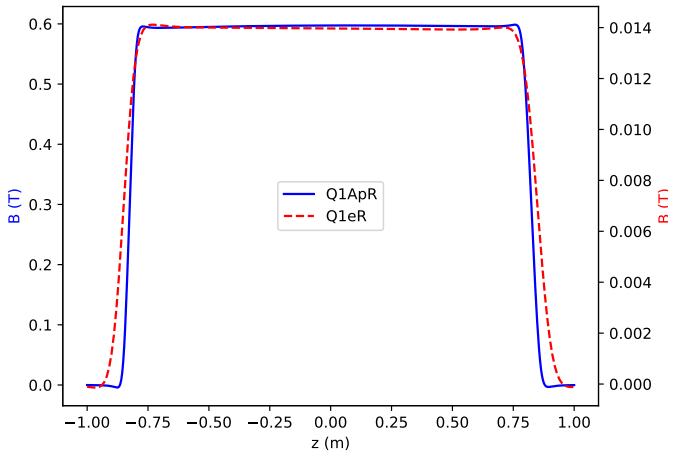

Figure 6.39: Vertical magnetic field on the center plane at a radius of 10 mm for the Q1APR and Q1eF magnet (right scale).

which is shown in Figure 6.39. The figure shows the vertical magnetic field on the center plane at a radius of 10 mm for both magnets. Further optimization is planned to improve the field shape.

The resulting gradient and gradient qualities are shown in Figure 6.40. As shown in the

figure, the good field region for the hadron quadrupole magnet is almost ± 20 mm, which is larger than required. For the electron quadrupole magnet the good field region is larger than ± 40 mm, which is sufficiently larger than the required good field region as the aperture of this magnet is determined by the synchrotron radiation fan size.

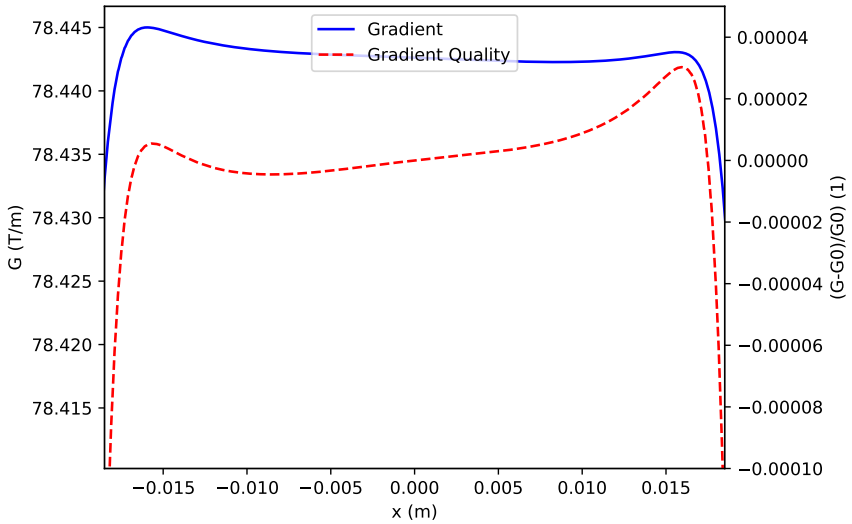

(a) Q1APR

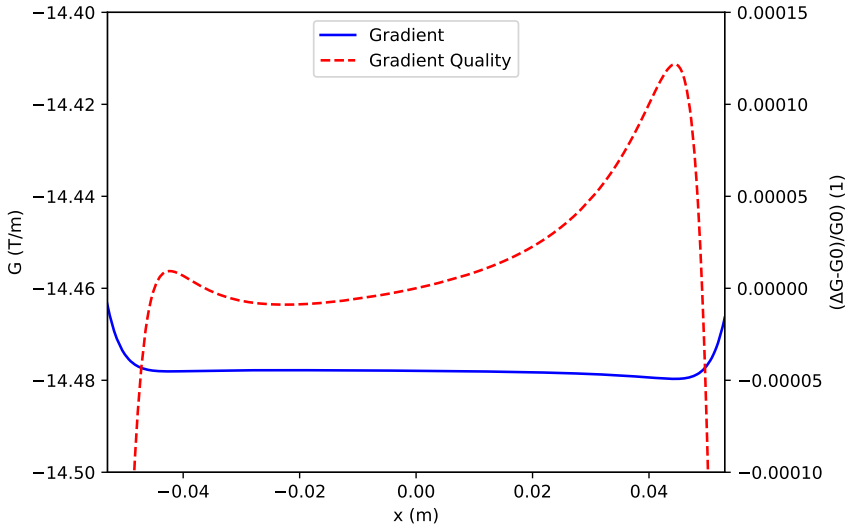

(b) Q1ER

Figure 6.40: Gradient and gradient quality for the Q1APR and Q1ER magnet.

The peak field on the wire is shown in Figure 6.41. As shown in the figures, the peak field on the wire are 2.2 T for Q1APR and 1.8 T for Q1eF. The load-lines are shown in Figure 6.42.

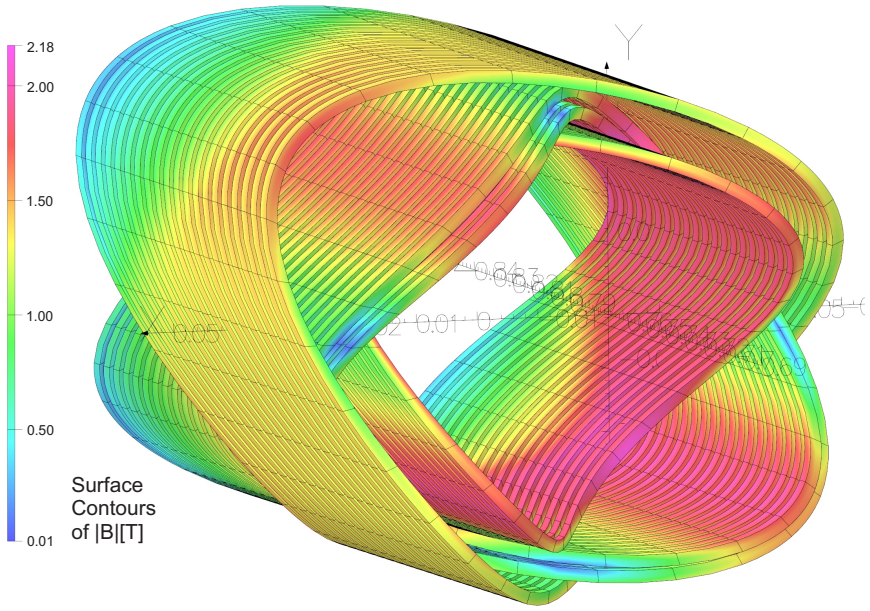

(a) Q1APR

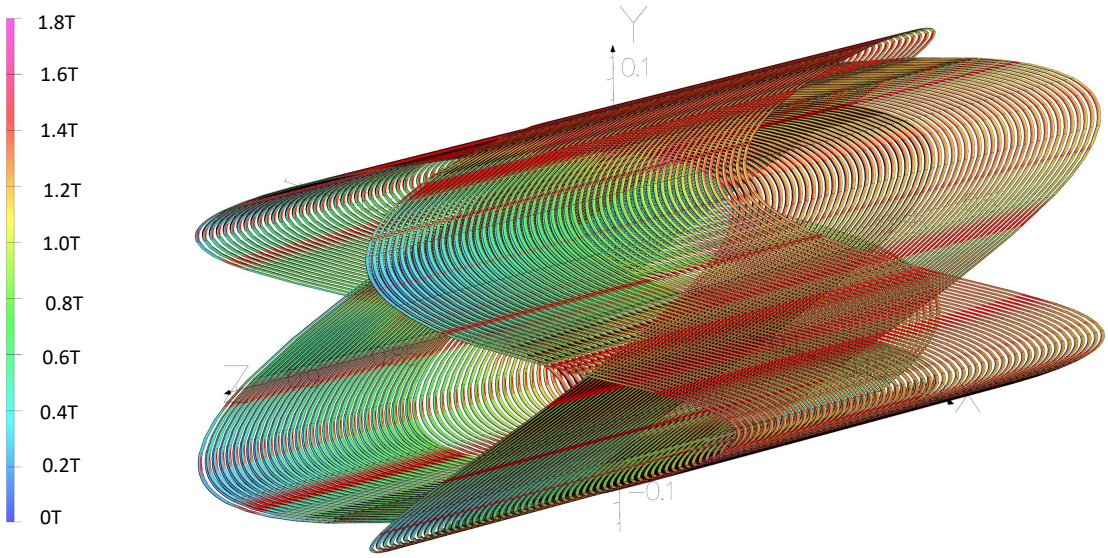

(b) Q1ER

Figure 6.41: Peak field on the wire for the Q1APR and Q1eF magnet (large end of each coil, other turns not shown).

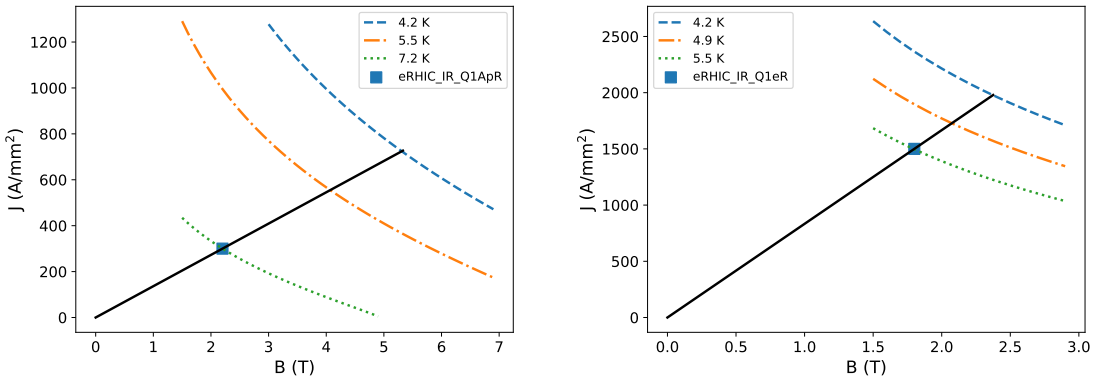

(a) Q1APR **(b)** Q1ER

Figure 6.42: Load-lines for the Q1APR and Q1ER magnet.

Table 6.9: Parameters of the Q1APR/Q1eR magnet.

Parameter	Q1APR	Q1eR
Magnetic length [m]	1.8	1.8
Maximum gradient [T/m]	78.38	14
Aperture diameter (front) [m]	0.0400	0.13
Aperture diameter (rear) [m]	0.0510	0.16
Required field quality	1×10^{-4}	1×10^{-4}
Physical length [m]	1.6	1.8
Physical width [m]	0.081	173
Physical height [m]	0.081	173
Superconductor type	NbTi	NbTi
Conductor diameter [mm]	1	0.25
Current density [A/mm^2]	300	1500
Cu:Sc ratio	2	1.3
Temperature [K]	4.2	4.2
Peak field wire [T]	2.2	1.8
Magnetic energy [J]	11500	11986
Current [A]	235.62	73.63
Inductance [H]	0.42	4.42
Margin loadline [%]	142	32

The Q1BPR/Q2ER Magnet

Similar to the Q1APR-Q1ER, the Q1BPR-Q2ER magnet is also a two-in-one magnet about 7 m from the IP (rear side). The gradients are identical to that of the Q1APR-Q1ER magnets (14 T/m to the electron beam and 78 T/m to the hadron beam). The main differences between the two magnets are the different length (1.8 vs. 1.4 m) and the different spacing between the two apertures (190 mm to 225 mm). The main parameters of the Q1BPR/Q2ER magnet are summarized in Table 6.10.

Geometry of the Q1BPR/Q2ER magnet (front face) is shown in Figure 6.43. The magnet apertures are defined by the beam envelopes and the synchrotron radiation fan for the electron magnet as shown in Figure 6.44.

Both magnets are housed in an iron yoke, which returns the magnetic flux and is designed to suppress cross-talk between the two magnets. This requires that the iron between the two magnets does not saturate. To facilitate this the electron quadrupole is realized as a tapered double-helix coil (see Section 6.2.1 on page 477). The spacing between the apertures is enough for a non-tapered hadron quadrupole, which is a direct-wind serpentine coil. Both 3D magnet geometries are shown in Figure 6.45.

Table 6.10: Parameters of the Q1BPR/Q2ER magnet.

Parameter	Value
Magnetic length [m]	1.4
Maximum gradient [T/m]	78.38
Aperture diameter (front) [m]	0.0560
Aperture diameter (rear) [m]	0.0560
Required field quality	1×10^{-4}
Physical length [m]	1.4
Physical width [m]	0.081
Physical height [m]	0.081
Superconductor type	NbTi
Conductor diameter [mm]	0.5
Current density [A/mm^2]	1347.2
Cu:Sc ratio	1.3
Temperature [K]	4.2
Peak field wire [T]	3.3
Magnetic energy [J]	23000
Current [A]	264.52
Inductance [H]	0.66
Margin loadline [%]	21

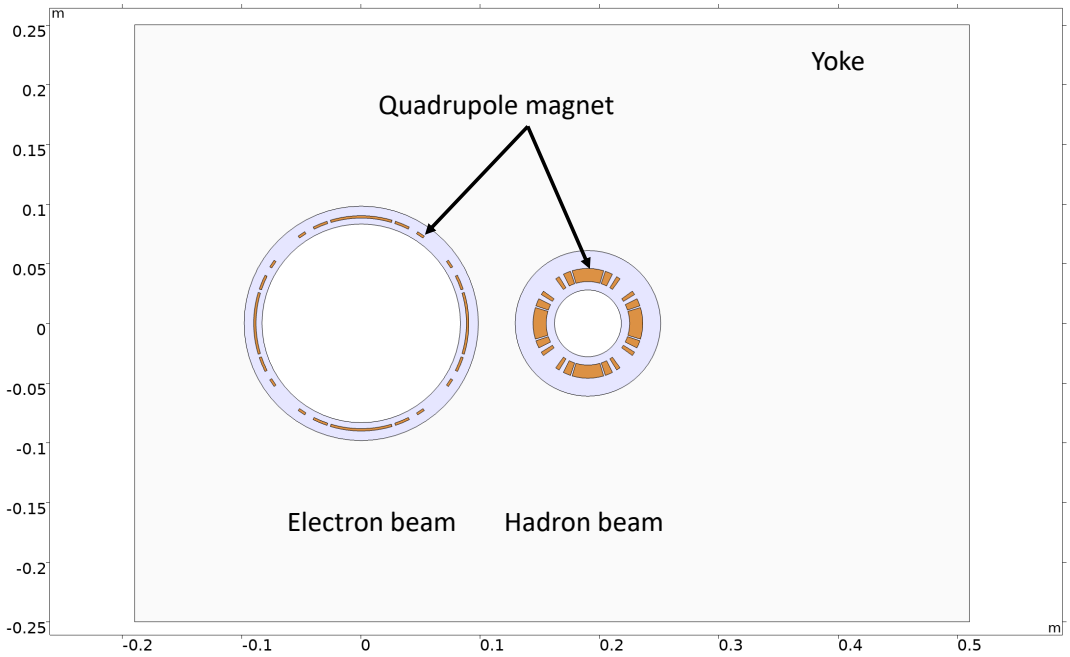

Figure 6.43: Geometry of the Q1BPR/Q2ER magnet (front face).

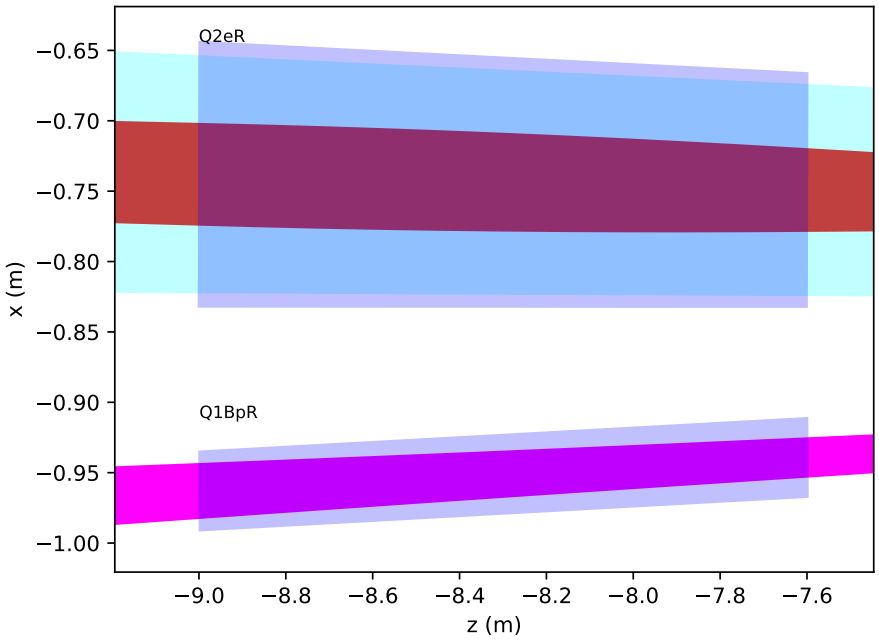

Figure 6.44: Aperture requirements of the Q1BPR/Q2ER magnet. The magnet apertures are shown in blue; the $10\,\sigma$ and $15\,\sigma$ beam envelopes of the hadron and electron beams are shown in magenta and red, respectively. The synchrotron radiation fan is shown in cyan.

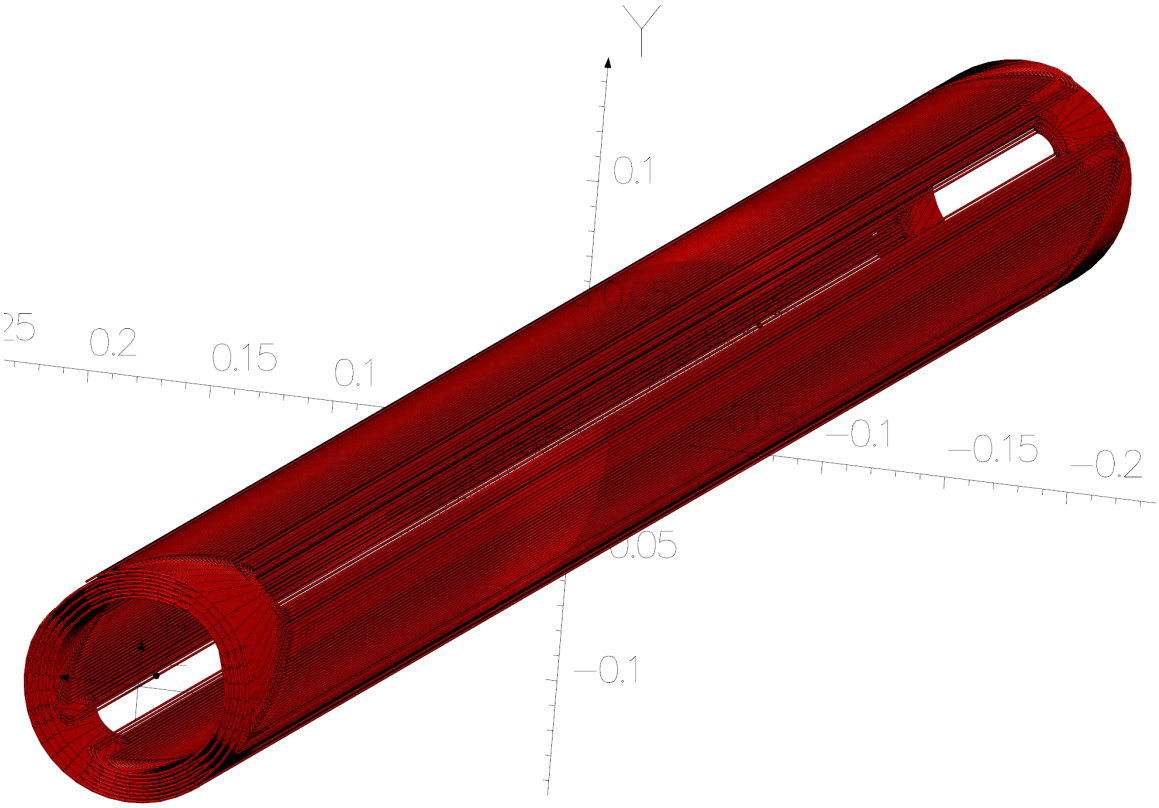

(a) Q1BPR

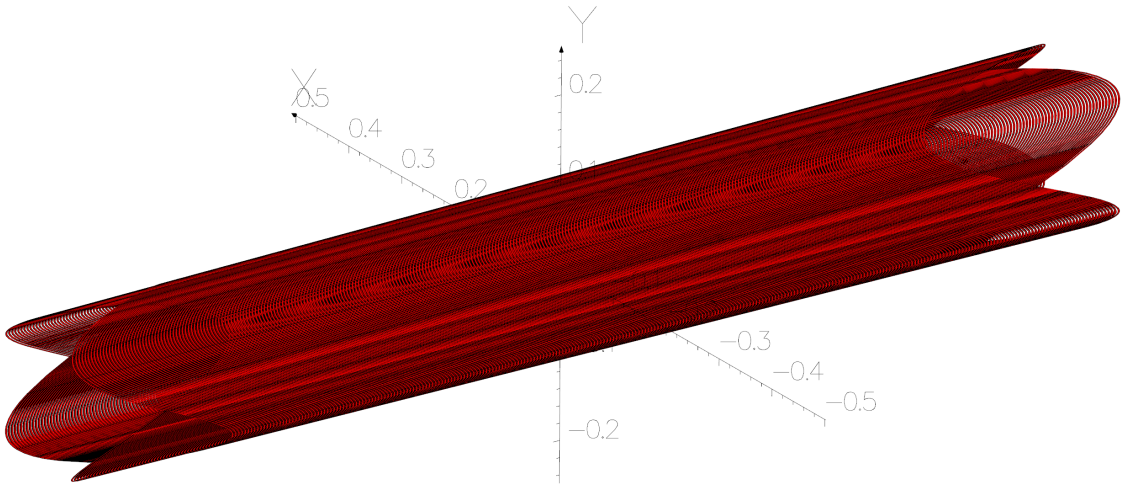

(b) Q2ER

Figure 6.45: Serpentine quadrupole Q1BPR (a) and tapered double-helix quadrupole Q2EF (b).

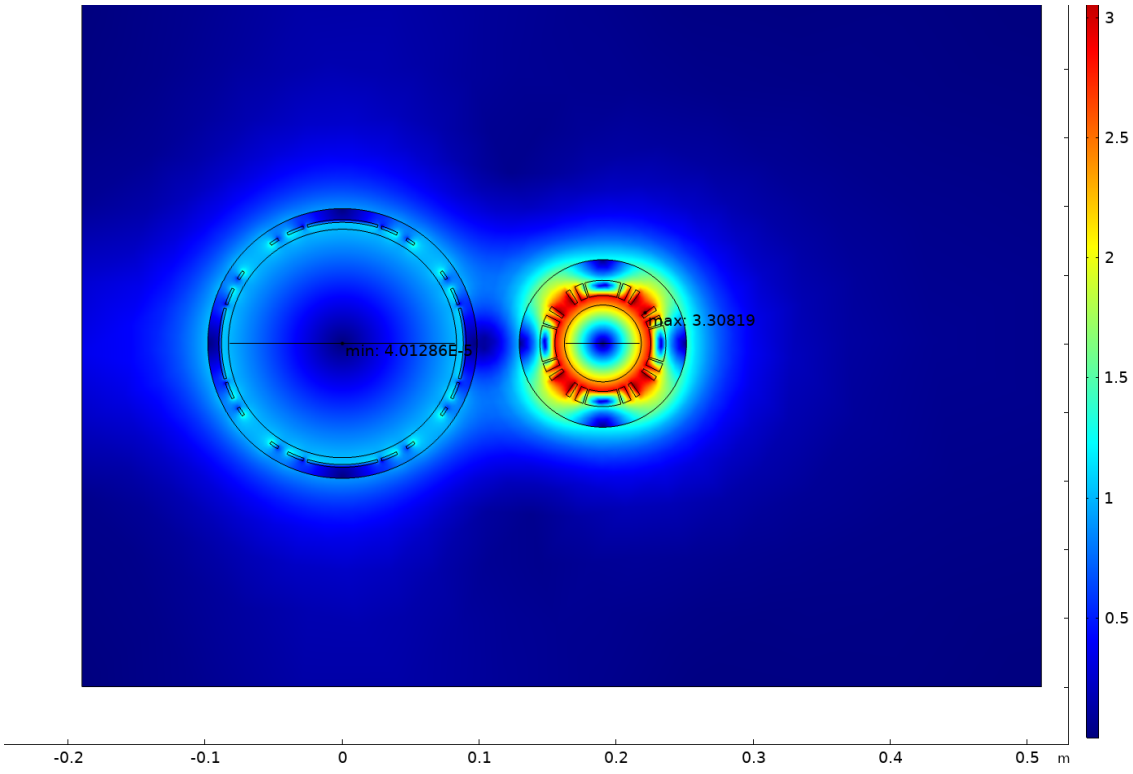

Figure 6.46: Magnetic field equivalent to the magnetization of the Q1BPR/Q2EF magnet (front end).

The yoke magnetization for the more critical front end of the magnet (closer to the IP) is shown in Figure 6.46. As shown in the figure, the peak magnetic field between the two magnet apertures is about 0.8 T. The yoke is therefore not saturated and provides adequate cross-talk suppression.

The resulting gradient and gradient qualities are shown in Figure 6.47. As shown in the figure, the good field region for the hadron quadrupole magnet is $\pm$20 mm, which is larger than required. For the electron quadrupole magnet the good field region is larger than $\pm$60 mm, which is significantly larger than the required good field region as the aperture of this magnet is determined by the synchrotron radiation fan size.

The peak field on the magnet wire is shown in Figure 6.48. As shown in the figures, the peak field on the wire are 3.3 T for Q1BPR and 1.8 T for Q2ER. The load-lines are shown in Figure 6.49.

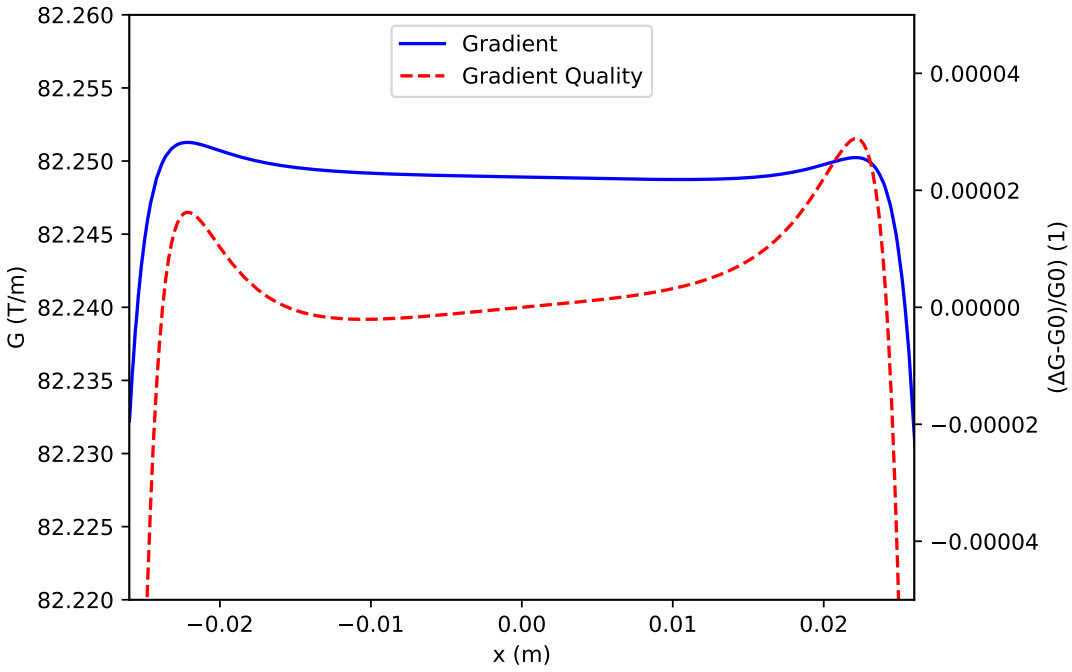

(a) Q1BPR

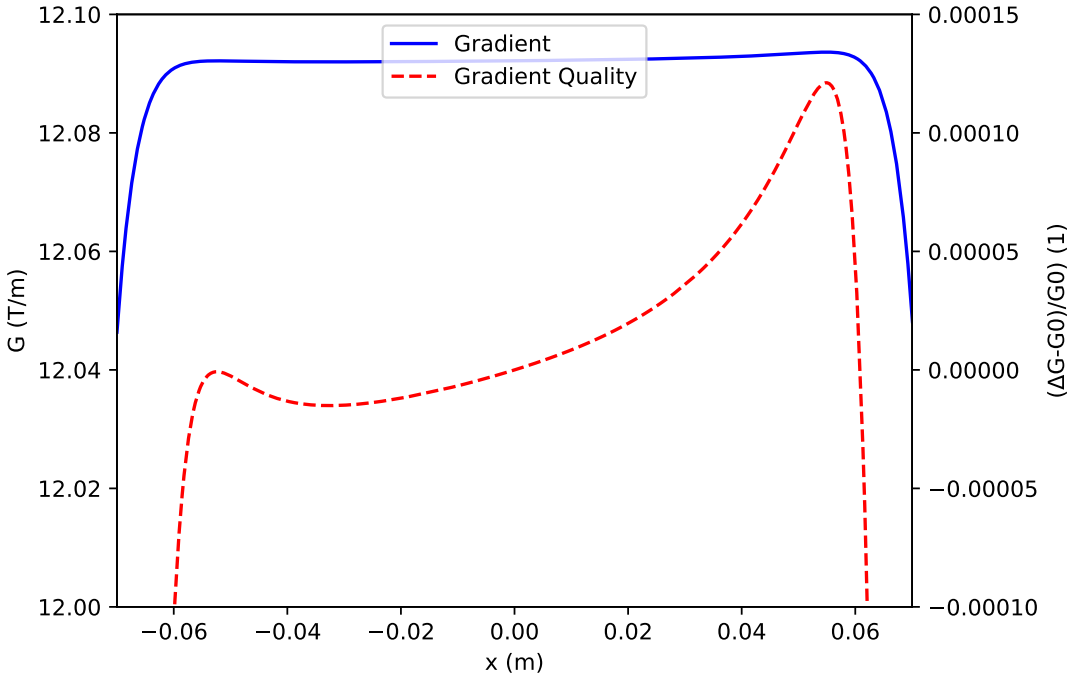

(b) Q2ER

Figure 6.47: Gradient and gradient quality for the Q1BPR and Q2ER magnet (front end).

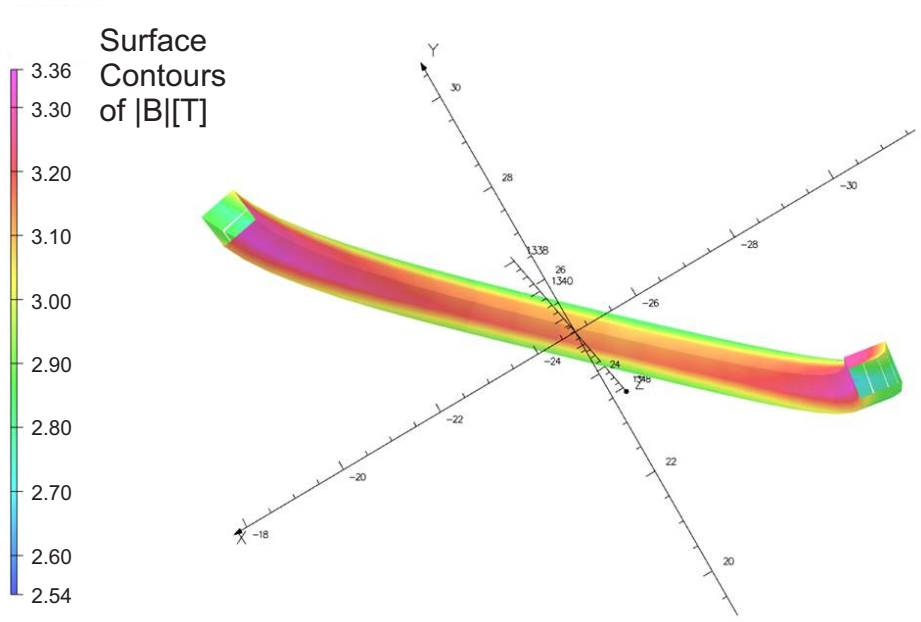

(a) Q1BPR

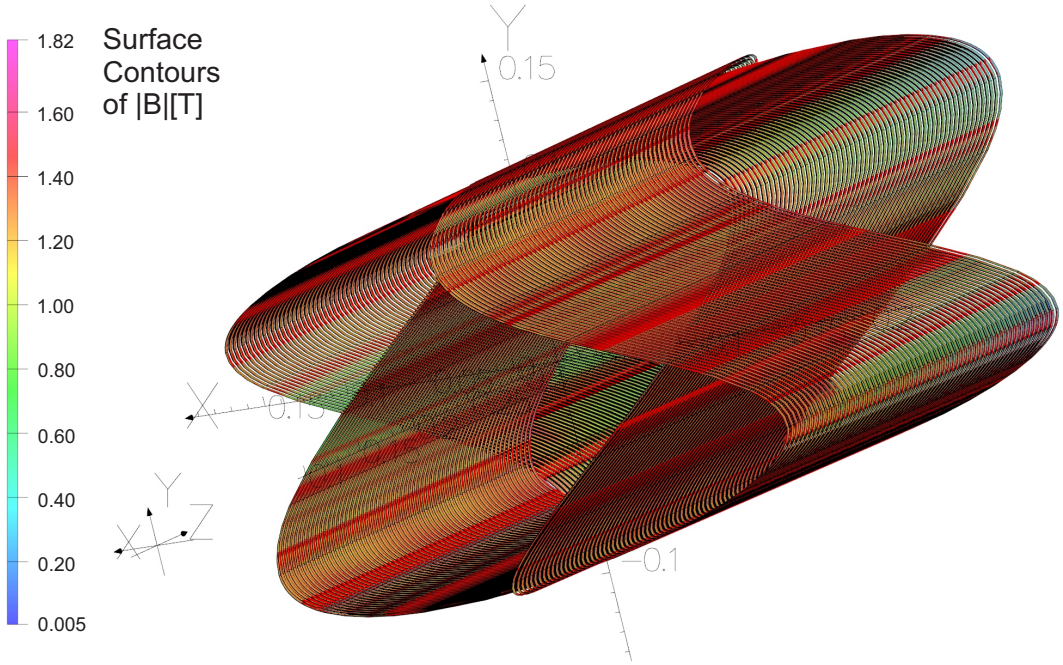

(b) Q2ER

Figure 6.48: Peak field on the wire for the Q1BPR (turn with the highest field) and Q2ER magnet (large end of coil, other turns not shown).

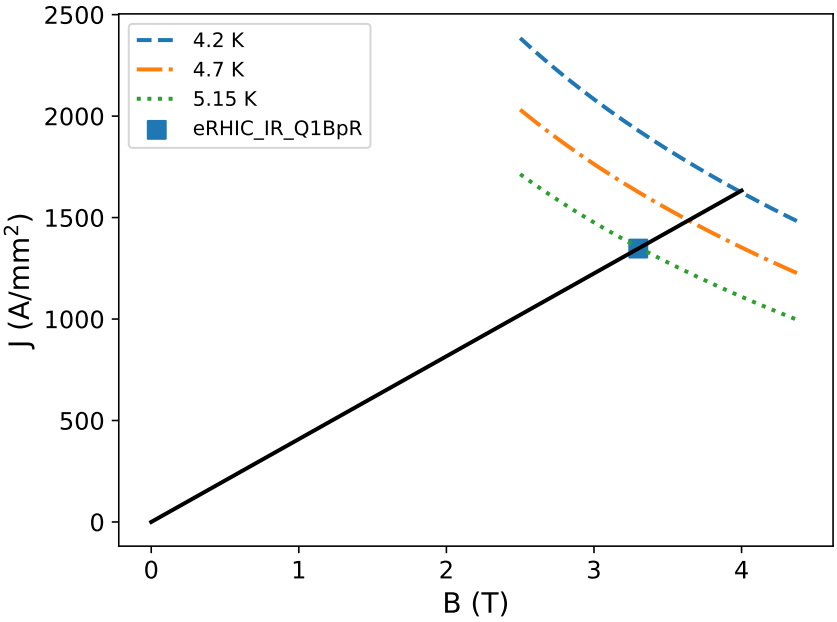

(a) Q1BPR

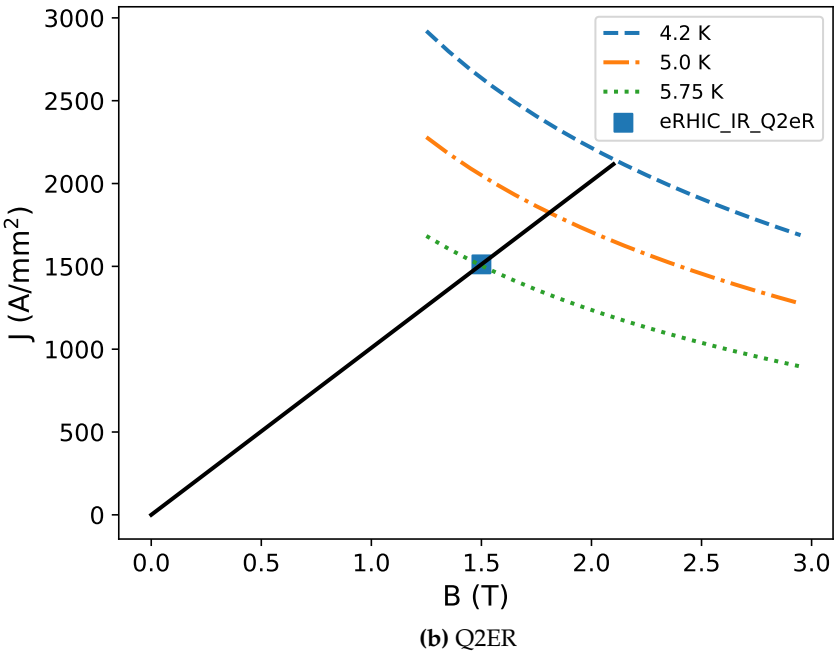

(b) Q2ER

Figure 6.49: Load-lines for the Q1BPR and Q2ER magnet.

The Q2PR/B2ER Magnet

The Q2PR/B2ER is a two-in-one magnet whose center is at 12.5 m from the IP on the rear side. Unlike the other two-in-one magnets this magnet houses a hadron quadrupole and a low-field dipole magnet for the electron beam. This magnet is also significantly longer ($\sim$ 5 m) than most of the other magnets in the IR. The low bending field of B2ER aids the suppression of synchrotron radiation and helps to reduce cross-talk by limiting the magnetic flux in the return yoke.

Figure 6.50 (a) shows the geometry of the magnet (front end). The distance between the apertures due to the crossing angle varies from 262.5 mm to 375.1 mm. The aperture of B2ER is determined by the synchrotron radiation fan and varies from 97 mm to 139 mm (radius). To limit cross-talk this magnet is assumed to be a tapered double-helix magnet. The Q2PR quadrupole magnet has a relatively smaller aperture (54 mm radius) and can be realized as a direct-wind serpentine magnet with constant aperture. The 3D magnet geometries are shown in Figure 6.51. As shown in the figure, both magnets are housed in an iron yoke which is 0.9×0.5 m^2 in cross-section; the yoke is 5.5 m long and weighs 14 tons. The yoke is assumed to be made of good quality soft-iron.

The required good field region of B2ER is relatively large because the electron beam traverses this magnet significantly off-center as shown in Figure 6.50 (b) in particular on the rear end. The field quality requirements (1×10^{-4}) can be met as shown in Figure 6.52, which shows the dipole field and field quality on the front (a) and rear (b) end of the magnet. As shown in the figure, the field quality requirements are met in an aperture of 120 and 160 mm respectively, which is sufficient.

The field quality of the hadron quadrupole is shown in Figure 6.53; the figure shows the field quality of the front face geometry of the magnet close to the IP. As shown, the magnet meets the 1×10^{-4} field quality requirement in an aperture of 80 mm, which exceeds the requirements.

The peak field on the wire for both magnets is shown in Figure 6.54. As shown in the figure, the peak field is 2.64 T for Q2PR and 0.55 T for B2ER. Both peak fields are relatively low, which allows to use a NbTi-conductor with a high current density to keep the coils compact in radial direction, which reduces cross-talk.

The load-lines for both magnets are shown in Figure 6.55; as shown in the figure, Q2PR has a margin of about 50% when operating at 4.2 K assuming a NbTi conductor with a Cu:Sc ratio of 1.3. The margin of B2ER is not a concern ($> 100\%$). The main parameters of both magnets are summarized in table 6.11.

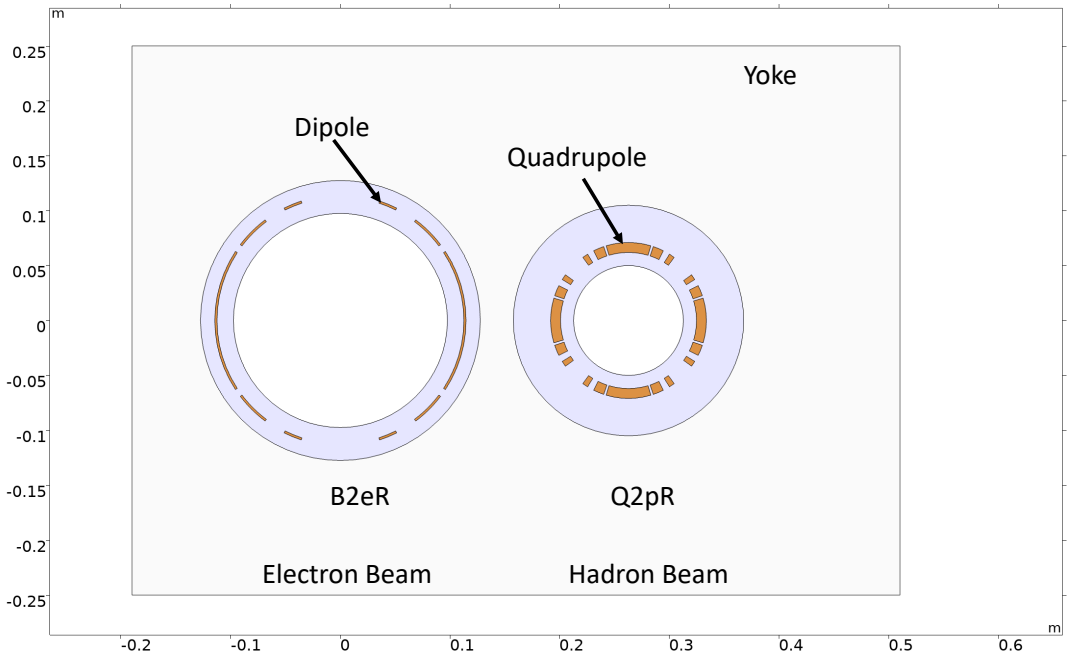

(a) Q2PR/B2ER

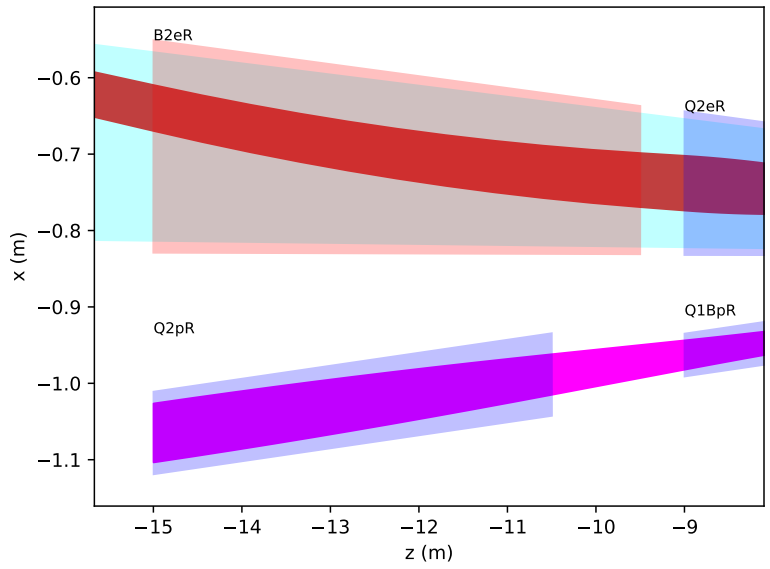

(b) B2ER

Figure 6.50: Geometry of the Q2PR/B2ER magnet front end (a) and aperture requirements of the Q2PR/B2ER magnet (b). B2ER is shown in red, Q2PR in blue. The 10σ hadron and 15σ electron beam envelopes are shown in magenta and red. The synchrotron radiation fan is shown in cyan.

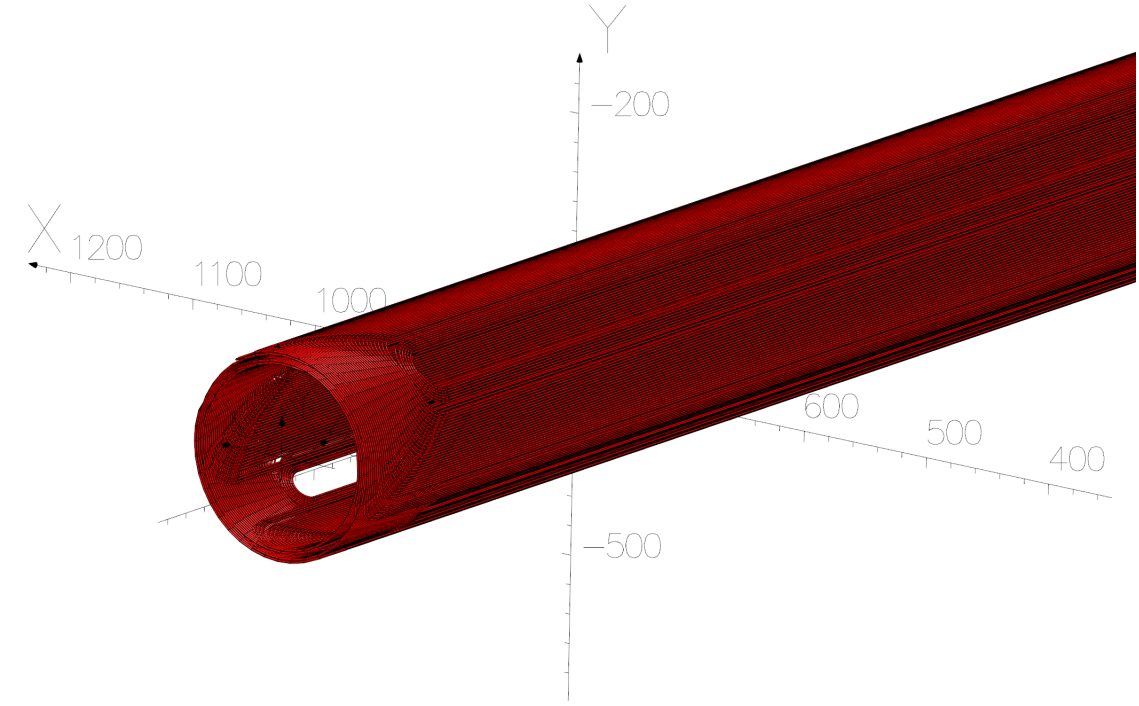

(a) Q2PR

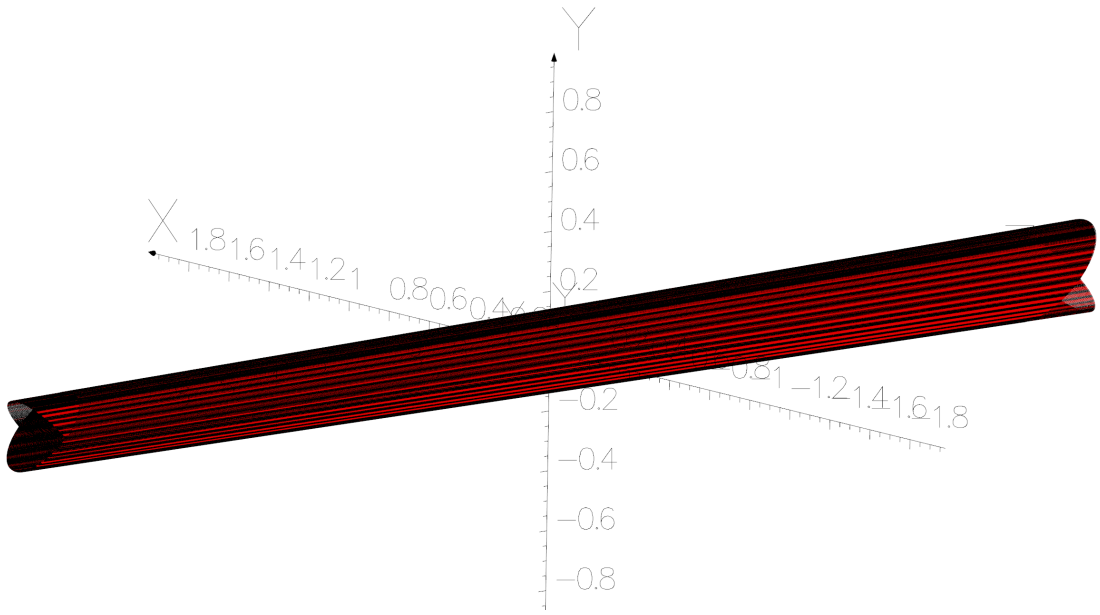

(b) B2ER

Figure 6.51: Direct wind serpentine Q2PR magnet (a) and tapered double-helix dipole magnet B2ER (b).

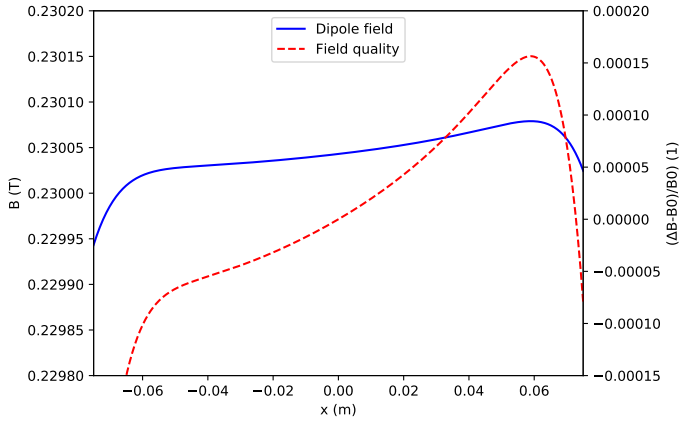

(a) Front

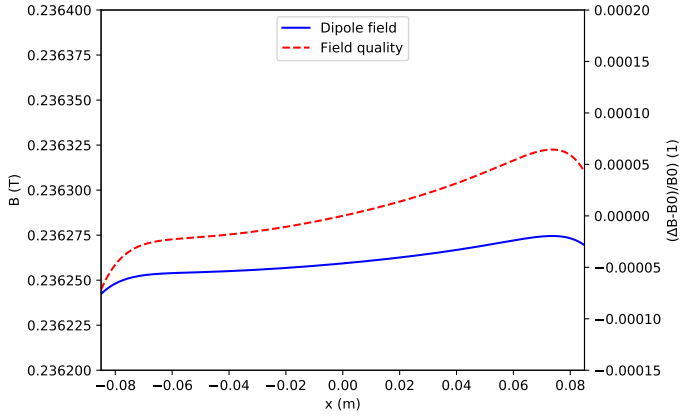

(b) Rear

Figure 6.52: Field quality of the B2ER magnet at the front (a) (close to the IP) and rear end (b).

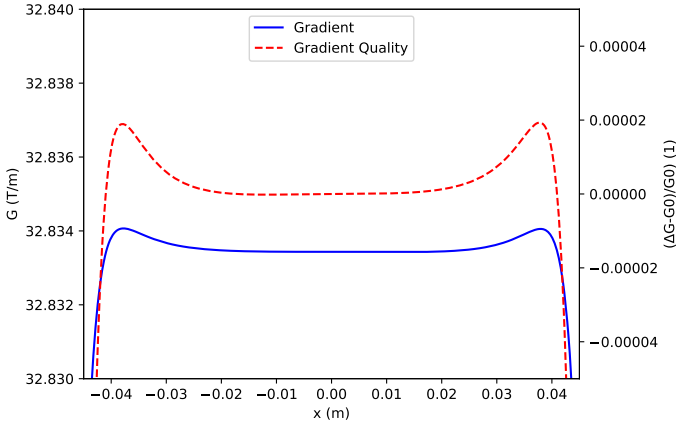

Figure 6.53: Gradient and gradient quality of the Q2PR quadrupole magnet.

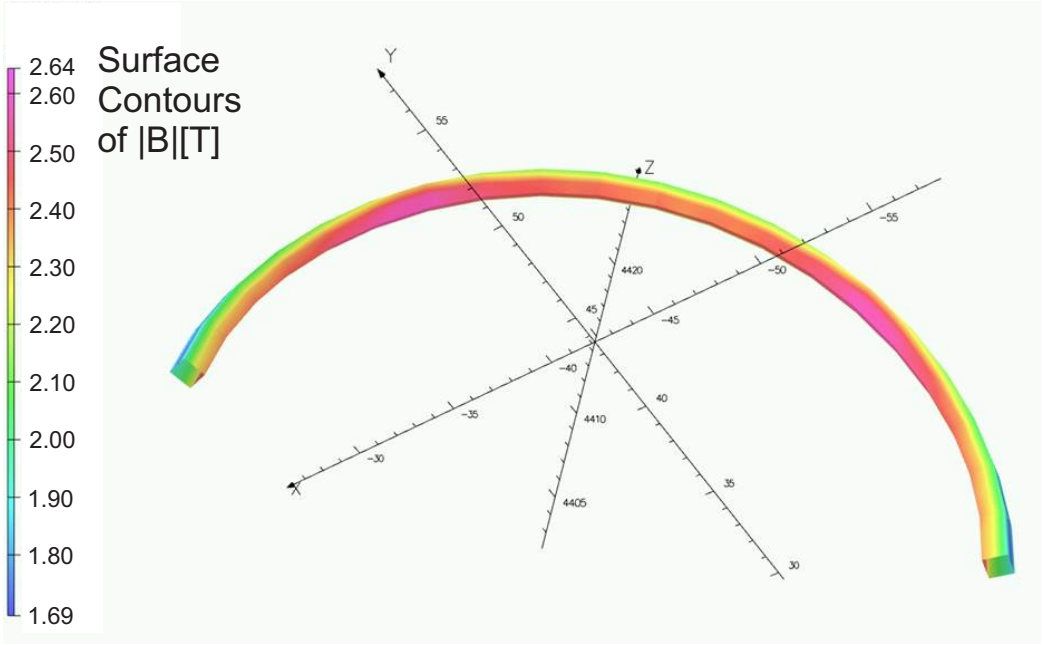

(a) Q2PR

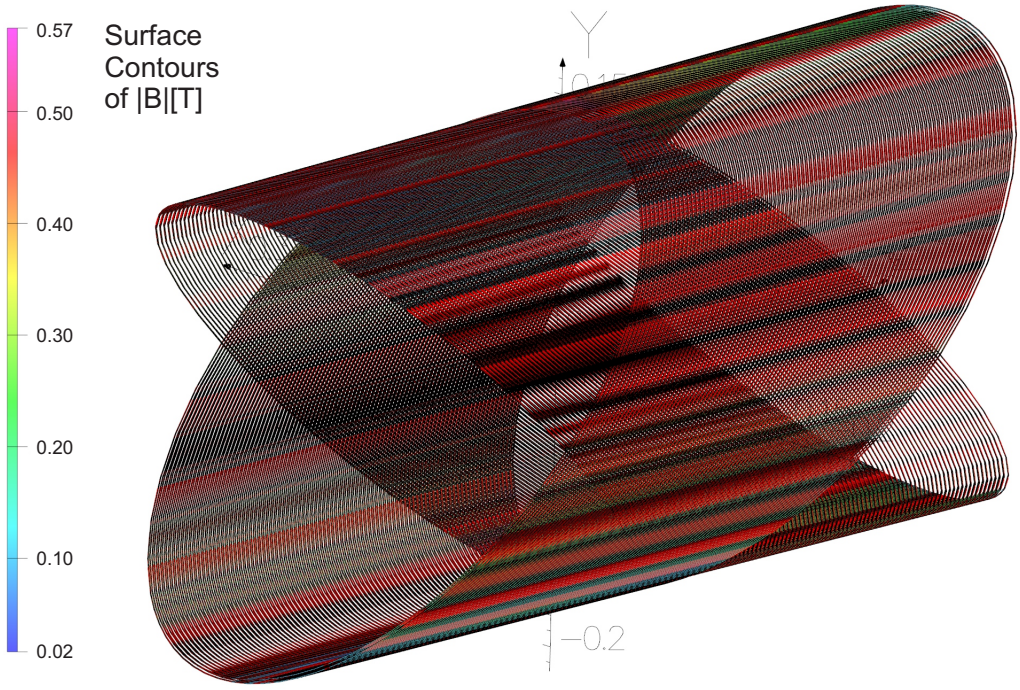

(b) B2ER

Figure 6.54: Peak field on the wire of the Q2PR (a) and B2ER magnet (b). For B2ER only the last 40 turns of the larger aperture end are shown.

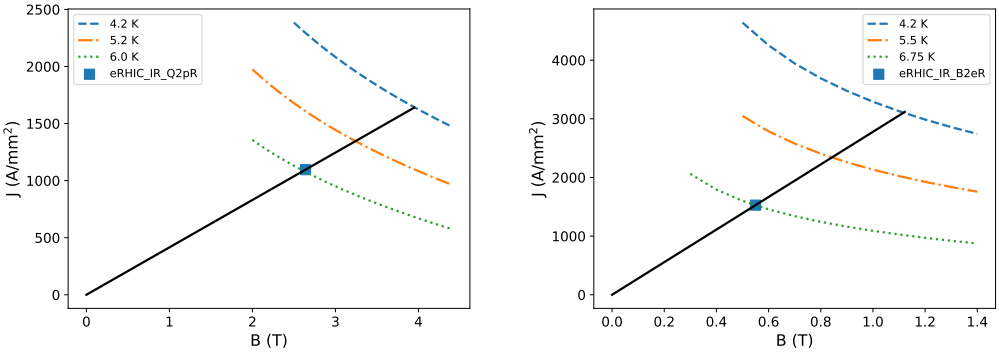

(a) Q2PR **(b)** B2ER

Figure 6.55: Load-lines of the Q2PR (a) and B2ER magnet (b).

Table 6.11: Parameters for the Q2PR/B2ER magnet.

Parameter	Q2PR	B2ER
Magnetic length [m]	4.5	5.5
Maximum gradient [T/m]	34	–
Maximum dipole field [T]	–	0.2
Aperture diameter (front) [m]	0.108	0.194
Aperture diameter (rear) [m]	0.108	0.278
Required field quality	1×10^{-4}	1×10^{-4}
Physical length [m]	4.5	5.5
Physical width [m]	0.142	0.312
Physical height [m]	0.142	0.312
Superconductor type	NbTi	NbTi
Conductor diameter [mm]	1mm, 6-on-1	0.5
Current density [A/mm^2]	1096	1528
Cu:Sc ratio	1.3	1.3
Temperature [K]	4.2	4.2
Peak field wire [T]	2.64	0.5517
Magnetic energy [J]	94805	11986
Current [A]	215.2	75
Inductance [H]	4.09	4.26
Margin loadline [%]	50	104

Spin Rotator Solenoids (SRS)

Several solenoid magnets are required to rotate the spin for the electron beam in the ESR. The lattice requires four 2.7 m long solenoids and four $\approx$ 9 m long solenoids which can provide a maximum field of 6.79 T and 6.4 T, respectively. To suit both requirements, a design decision was made to provide a single 2.7 m (short, magnetic length) solenoid unit. For the 9 m (long) solenoid application, three of these single (short) magnets are combined in series to provide the necessary integrated field. The maximum field for this application increases from 6.4 T to 7.11 T to accommodate a slightly shorter combined magnetic length of 8.1 m. The key performance requirement of these solenoids is integrated field along the beam path, within the good field radius. The integrated field for the 2.7 m solenoid is 18.3 T-m; for the 9 m solenoid, it is 57.6 T-m. Each 2.7 m solenoid coil is housed in an individual cryostat with associated electrical and cryogenic connections. The physical length in the beamline of the short magnet is 3 m. The physical length in the beamline of the long magnet is 9 m.

The spin rotator solenoid (SRS) conceptual design includes coil magnetic design, coil mechanical design, analysis of coil forces, cold mass mechanical design and analysis, cryostat design and analysis, shielding design study, and quench study. The conceptual design of the modular 3 m long magnet was evaluated in terms of inner and outer radius, coil length, and positions within the cryostat. The coil design uses a full-length inner support mandrel for convenience of winding and for locating coils within the cryostat. Coil leads are brought out separately.

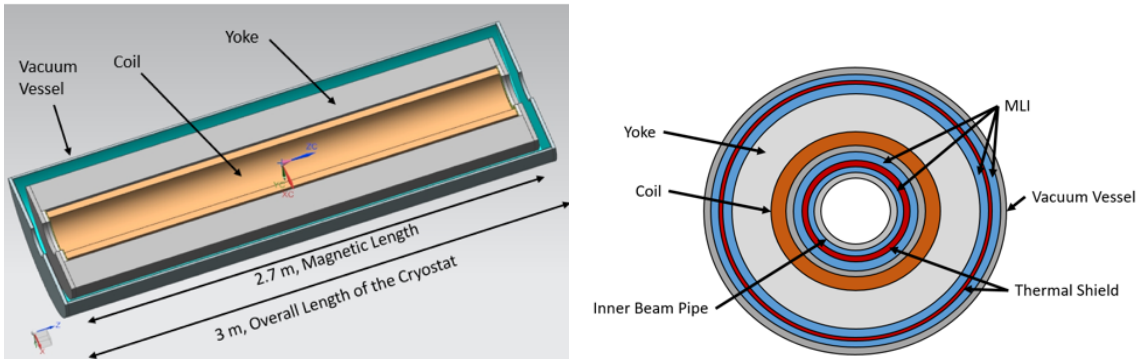

Figure 6.56: Geometry of the spin rotator solenoid. (a) Longitudinal cross section. (b) Transverse cross section.

SRS Magnet Design Overview

The geometry of the solenoid section is shown in Figure 6.56. The solenoid cross section consists of a single magnet coil. These are warm bore magnets with an ID capable of inserting a flanged vacuum chamber. Early in the design process, a review of the IR lattice showed strong dipoles in close proximity to the SRS magnets. The synchrotron radiation generated by these dipoles warrants a separate vacuum chamber and thereby a warm bore in the magnet. The cross section of the solenoid consists of a stainless-steel inner bore pipe,

inner and outer multi-layer insulation (MLI) and thermal shield, coil, and yoke. The coil is wound on a stainless-steel mandrel with an epoxy-glass insulator.

The solenoids are required to have a good field radius of 20 mm. The inside warm bore radius of the vacuum vessel is 68 mm, allowing clearance for the vacuum chamber to be inserted. The inside radius of the cold coil is 135 mm, allowing for inner thermal shield and insulation as well as the winding mandrel.

A single cryostat design is employed to package the common solenoid coil. A single solenoid is located on either end of the short spin rotators. Three solenoids in series are located on either end of the long spin rotators. Figure 6.57 provides an indication of the short and long spin rotator configurations including both the cold solenoids (silver cryostats) and warm quadrupoles (shown in red). The main parameters of the spin rotator solenoids are summarized in Table 6.12.

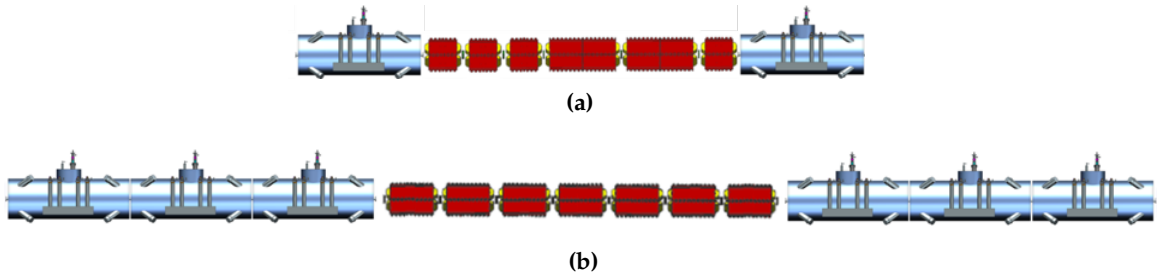

Figure 6.57: ESR spin rotators. SRS cryomodules shown in silver. (a) Short spin rotator; (b) Long spin rotator.

3 m SRS Magnet

The concept SRS, based on a single strand conductor winding, is used to evaluate the efficacy of the magnet design and safe operation, including quench [249]. Magnetic field analysis is carried out for both conductor-only and with iron in ANSYS Maxwell. The results from Maxwell were compared with an Opera analysis of the coil design as a check to make sure baseline results are consistent and can serve as the appropriate foundation for further structural analyses with ANSYS Maxwell.

The results for field profile along the beam line axis and peak field in the coil are shown in Figures 6.58 and 6.59.

9 m SRS Magnet

The 9 m (long) solenoid design is configured having three single 3 m long magnets combined in series to provide the necessary integrated field of 57.6 T-m as given in Table 6.12. The maximum field in the conductor increases to 7.11 T to accommodate a slightly shorter, combined magnetic length of 8.1 m. The field profile along the axis is shown in Figure 6.60 and peak field in the coil is shown in Figure 6.61.

Lorentz Forces and Stored Energy

The stored energy (in Joules) is calculated using the conductor file in Opera. The design

Table 6.12: Specifications of the IR electron spin rotator solenoid.

Parameter	Value
Magnetic length [m]	2.7 (short), 8.1 (long)
Integrated Field [T-m]	18.3 (short), 57.6 (long)
Solenoid central field max [T]	6.79 (short), 7.11 (long)
Peak field on conductor [T]	6.794 (short), 7.116 (long)
Good field radius [mm]	20
Vacuum Vessel OD [mm]	1001
Warm bore ID [mm]	136
Overall length in beamline [m]	2.99 (short), 9.05 (long)**
Overall width [mm]	1230
Overall height [mm]	1760
Fringe field [mT]	50***
Weight cold mass [kg (lb)]	∼11,800 (∼26,000)
(coil, yoke, mandrel, collar, He vessel)	

** — for 3 cryostats in series with 4 cm separation

*** — measured at 0.5 m from the beam centerline

requirements of integral Bdl is achieved by the total NI (ampere-turns) of the magnet and is the basis for calculating the stored energy ESTORED ENERGY at a defined operating current IOP (in Amperes). Inductance (L in Henry) is calculated as $L = 2\,E_{\text{storedenergy}}/\,I^2$.

The stored energy and associated amp-turns for operating current are shown in Table 6.13 for both the 3 m and 9 m SRS magnet designs. Similarly, field homogeneity within the good field radius of 20 mm for both 3 m and 9 m SRS magnet designs are shown in Figure 6.62.

Table 6.13: SRS stored energy and operating current.

Parameter	3 m (Short) Solenoid	9 m (Long) Solenoid
Stored Energy [MJ]	3.37	11.1
Operating Current [Amp-turns]	14,589.342	15,279.686

Lorentz forces are determined for the worst-case situation, within the 9 m solenoid configuration. The end mandrels carry an axial force (Lorentz force from coil) directed toward the middle magnet of 42.03 kN. The end yoke carries an axial force of 11.7 kN directed away from the middle, and the mild steel vacuum chamber carries a force directed toward the middle of 11.8 kN (approximately equal to yoke and of opposite sign). The total force is 42.2 kN directed toward the middle.

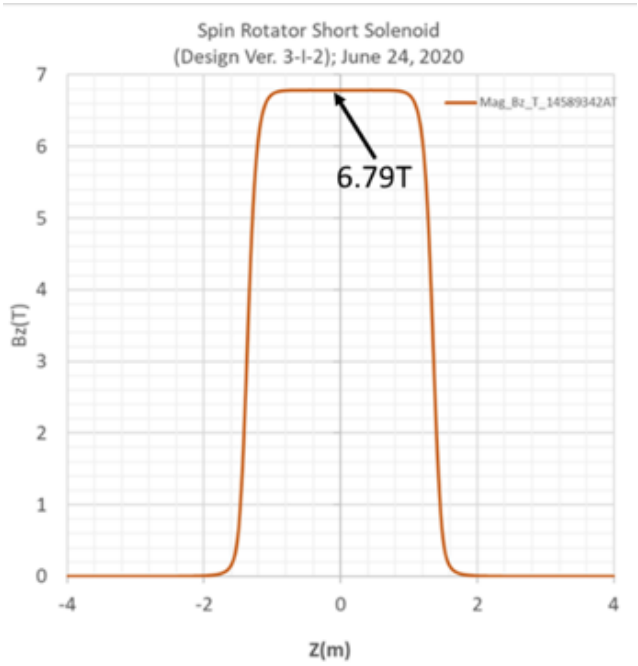

Figure 6.58: Longitudinal magnetic field on axis of the SRS over the full-length short solenoid coil.

Coil Design and Cold Mass Assembly

The conductor is engineered to qualify stability, performance, and safety (quench performance). A design decision and requirement is the use of NbTi conductor. A single strand, commercially available, rectangular conductor is the selected conductor for the SRS magnet design. The details of the conductor are shown in Table 6.14.

Using a NbTi superconductor with a copper-to-superconductor ratio of 4.75, the margin along the load-line is 30%, which exceeds the 20% margin requirement. For this application, the margin must be for the maximum field application in the long solenoid whose load line is shown in Figure 6.63.

The coil is designed to achieve the required specifications in Table 6.12. The coil structure is envisaged to be epoxy potted with a single coil structure with restraining over bind to limit the coil stress. Parameters of the coil are shown in Table 6.15.

Each solenoid coil is wound using the single strand, rectangular conductor. This strand is spiral wrapped with 0.1 mm (total) of glass cloth insulation with 1/2 lap and epoxy potted using CTD101, Stycast 2850 FT, or uncoated, 0.001" Kapton for two layers of insulation between wires.

Each coil block contains 32640 turns (1020 turns per layer, 32 layers) with a turn spacing of 0.1 mm in the coil block. This space is filled with 3M Stycast 2850 epoxy after each layer is wound. This can be achieved using B-staged fiberglass epoxy. After all 32 layers are wound, the coil block is wrapped with epoxy fiberglass and/or with over binds in order

Table 6.14: SRS choice of commercial superconductor

Parameter	Value
Conductor Material	Cu stabilized NbTi;
Conductor Shape	Rectangular; multi-filament strand
Manufacturer	Luvata
Conductor dimensions [mm]	2.41×1.175
Cu:SC ratio	4.75
Filament diameter [µm]	56
Total number of filaments	198
I_c [A], at 4.2 K, 5 T	1363
I_c [A], at 4.2 K, 7 T	< 860
Residual resistivity ratio	100
Twist pitch length [mm]	50

Table 6.15: SRS coil design. Dimensions are cold dimensions. 25 mm radial space reserved for axial restraint and insulation; 20 mm thick SS plates and 5 mm thick insulation disc.

Parameter	Value
Coil winding length [mm]	2700
Coil inner radius [mm]	135
Coil radial thickness [mm]	45
Over-band insulation for the coils [mm]	5
Insulation for SS support shell [mm]	5
Number of turns (per 2.7 m coil)	32,640
Coil operating current density [A/mm^2]	175.82
Operating temperature [K]	4.5
Current sharing temperature (T_{cs}) [K]	5
Temperature margin [K]	0.5
Peak current [A]	498.3
Inductance [H]	29.8

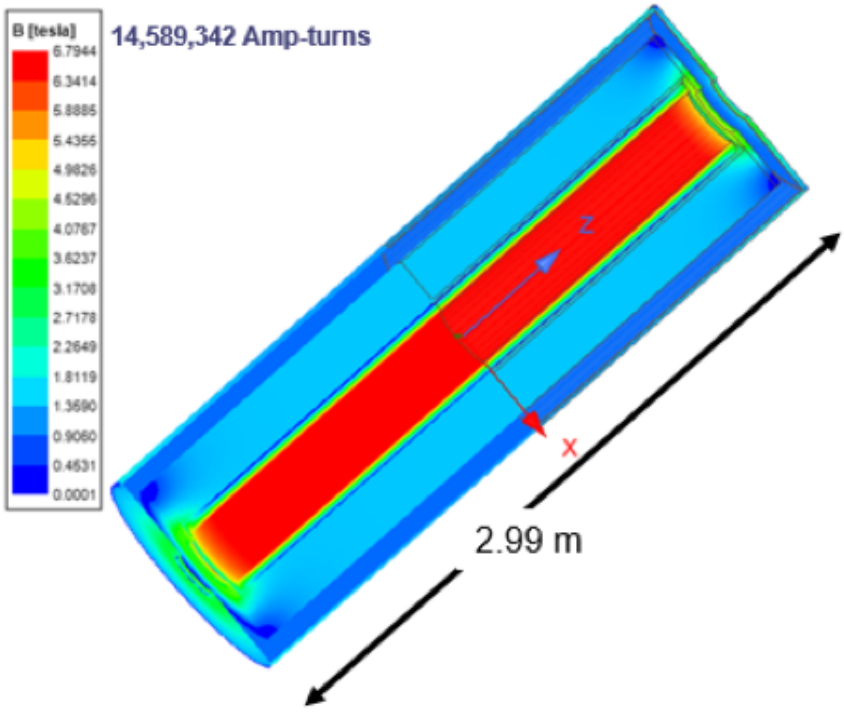

Figure 6.59: EIC short spin rotator solenoid, peak magnetic field (in Tesla) — peak field on the conductor occurs at the edge of the yoke.

to limit the coil hoop stress.

Construction elements of the cold mass are the mandrel, insulation, collar, yoke, and helium vessel [250]. The winding mandrel provides the support structure for the coil and is assumed to be 316L stainless steel. The mandrel supports the weight of the coil during winding and during coil potting. Between the coil and winding mandrel/collar, 5 mm is reserved around the entire coil for the ground insulation. The insulation is required to electrically isolate the coil from the structural components. The collar is designed to withstand the coil forces. The design of the magnet is based on a cold yoke with additional material covering the ends of the coils as a magnetic shield. The yoke drives the radial dimensions of the helium vessel and vacuum vessel. The cold iron also influences the design of the supports inside the helium vessel and the tension supports between the helium vessel and vacuum vessel. The helium vessel is designed as an ASME pressure vessel to 75 PSIG. The inside and outside cylinders have been set at 6.35 mm, which is more than adequate to meet the code requirements for pressure and buckling. The end plates of the coil have been sized based on ASME requirements. Preliminary design is based on Division 1 rules and a flat plate head and is 32 mm thick. No allowance for the inner cylinder of the helium vessel is included. A division 2 design which could include this effect should allow for a thinner head.

The estimated cold mass weight is given in Table 6.16 and is based on the cold yoke design. This is based on simple geometry and assumes the coil is solid copper.

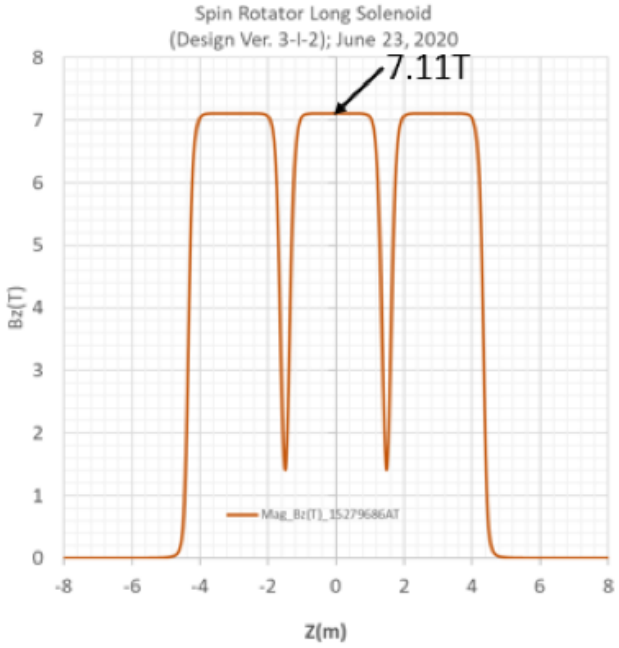

Figure 6.60: Longitudinal magnetic field on axis of the SRS over the full-length long solenoid coil.

Table 6.16: Estimate of SRS cold mass weight.

	Density [g/cc]	Length [m]	Inner radius [m]	Thickness [m]	Volume [m^3]	Weight [lbs]
Yoke	7.85	2.805	0.195	0.20	1.041	18018
Coil	8.94	2.705	0.135	0.045	0.173	2990
Mandrel	8.00	2.755	0.111	0.019	0.069	1191
Collar	8.00	2.755	0.185	0.010	0.035	611
He Vessel (ID)	8.00	2.869	0.102	0.006	0.022	385
He Vessel (OD)	8.00	2.869	0.415	0.006	0.022	385
He Vessel (ends)	8.00	–	–	0.0318	0.032	561
Misc	–	–	–	–	–	1800
Total						25941

A magnetostatic analysis of the SRS magnet 9 m string arrangement was done using ANSYS Maxwell [251]. Consider the three magnets which make up a 9 m SRS with the nomenclature as follows: Magnet 1 is the leading or first magnet in the string, Magnet 2 is the central magnet in the string, and Magnet 3 is the trailing or last magnet in the string. The analysis was done both as a 3D total model and as a 2D axisymmetric model with symmetry. The assumption is there is no interaction with adjacent structures or magnets. The

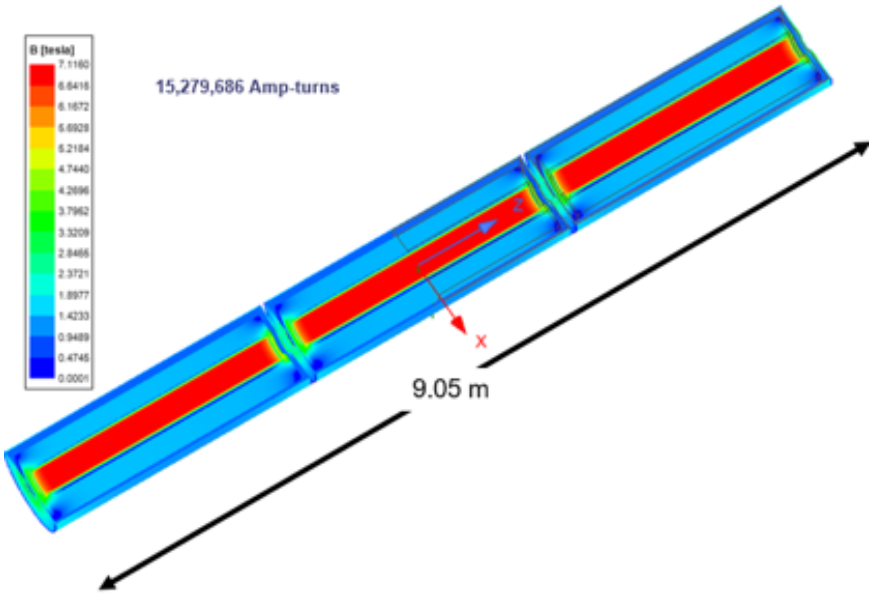

Figure 6.61: EIC long spin rotator solenoid, peak magnetic field (in Tesla) — peak field on the conductor occurs at the edge of the yoke.

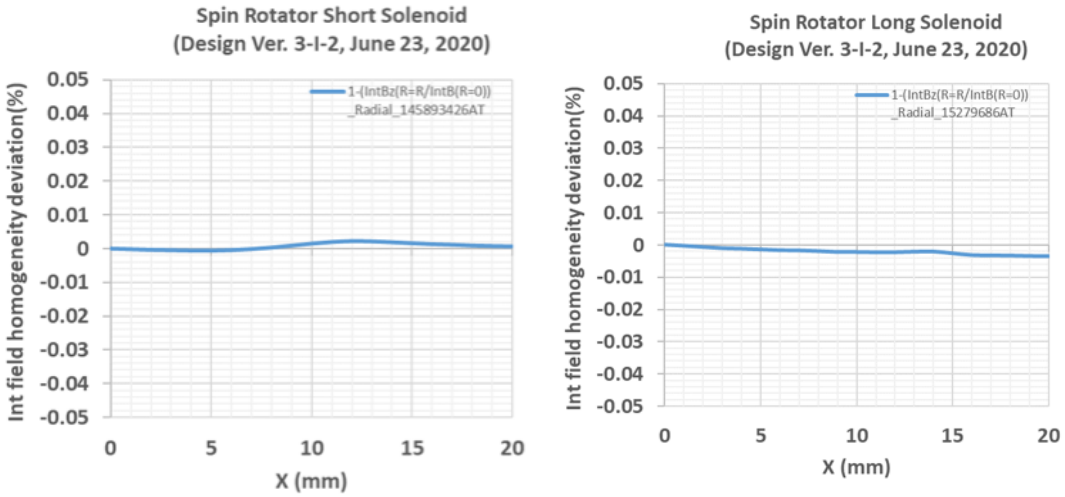

Figure 6.62: Integrated field homogeneity, radially within the good field radius. (a) Short spin rotator solenoid, better than 0.0025%. (b) Long spin rotator solenoid, better than 0.004%.

resulting body forces from both magnetic models was used as imported loads for ANSYS structural analysis.

The 3D and 2D models used the materials shown in the Figure 6.65. The air and copper (coil) materials are the Maxwell library models, and the other materials use TJNAF $B - H$ curves.

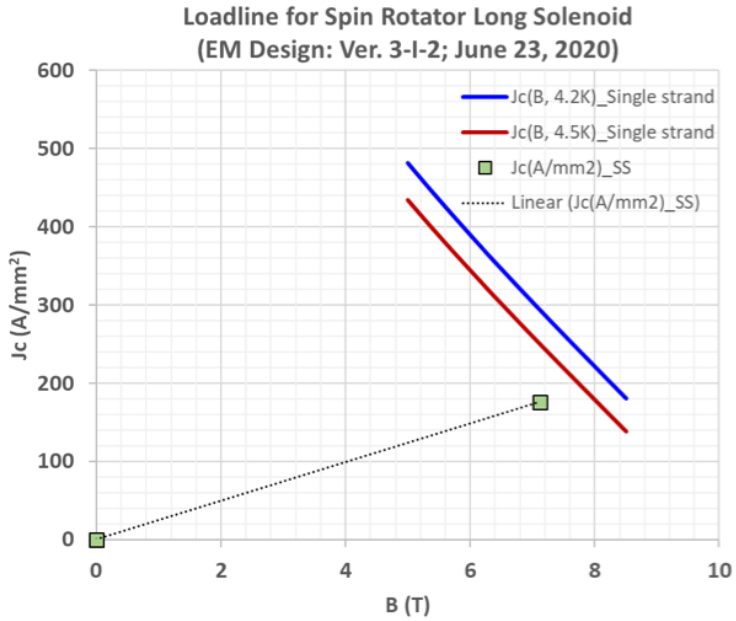

Figure 6.63: Load lines of coil for the long solenoid

Assumptions/Conditions:

- The input current value for the analysis is 15,279,686 A total NI.
- The yoke does not contact the compression sleeve or mandrel ends (suppressed in the model).
- Thermal contraction/expansion is ignored- the coil, ground insulation, mandrel and compression sleeve are initially just touching (no pre-stress in the sleeve). The environment is a static 4.2 K (for the correct material data).
- The ground insulation is glued to the coil.
- All other component contact is frictionless. This includes the compression sleeve — it is not attached to the mandrel ends, and is only restrained in the axial direction by the mandrel flanges.

Structural Analysis Results:

- The coil moves radially outward and is compressed axially as expected. The coils in Magnet 1 and Magnet 3 compress axially by 1.34 mm, while the coil in Magnet 2 compresses by 1.26 mm. The center of the Magnet 1 and Magnet 3 coils shift toward Magnet 2 by 0.55 mm. The Magnet 1 and Magnet 3 coils radial deformation are less than 0.1 mm. Yoke and vacuum chamber deformation due to virtual forces is less than 0.02 mm.
- Peak Von-Mises stress in the coil is 62 MPa, see Figure 6.66. Peak coil hoop stress is 52 MPa. Coil radial stress is 3.1 MPa. The peak coil axial compressive stress is

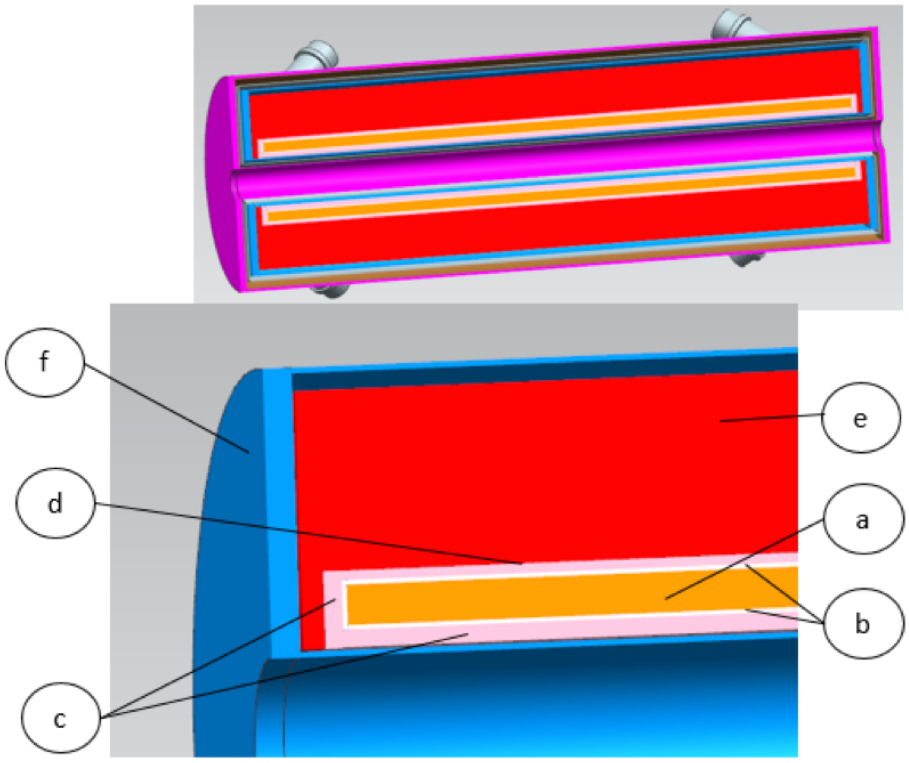

Figure 6.64: Cross sectional view of the cylindrical cryostat (above). Cold mass components are show as; a) coil pack, b) ground insulation, c) winding mandrel with ends, d) coil collar, e) cold yoke, and f) helium vessel.

29 MPa. The maximum stress in the coil sleeve is 82 MPa (yield for 316L at 4.2 K is greater than 500 MPa). Preloading the sleeve in compression should be incorporated into the final design

- As the coil expands radially and is compressed axially, it exerts no force on the mandrel (other than gravity, not included in this model). This might present an opportunity to decrease the thickness in the final design.
- The mechanical coil stresses are well below 100 MPa, which is safe for the materials defined in [252].
- Preloading the coil both radially and axially will better control stresses and displacements in the coil structure as it goes through cool down and powering.

The spin rotator solenoid magnet with cryostat, shown in Figure 6.67, has a warm bore, as previously described. As these solenoids are surrounded by warm beamline elements, the ID, OD, and ends require thermal shielding, sandwiched between layers of MLI. The materials for the outer vacuum vessel and yoke, along with the yoke thickness, have been selected to provide shielding to meet the fringe field requirement. The length parameters of the cryostat are shown in Table 6.17 and the component radial dimensions and materials are shown in Table 6.18.

Table 6.17: Length dimensions of the SRS cryostat conceptual design.

Parameter	Short Solenoid Modules	Long Solenoid Modules
Magnetic Length [m]	2.7	8.1
Section Physical Length [m]	2.992	9.055
# Solenoids per section	1	3
Individual coil length (cold) [m]	2.700	2.700
Space between cryostats [m]	N/A	0.04
Cryostat Length [m]	2.992	2.992
Individual coil length (warm) [m]	2.708	2.708

Table 6.18: SRS magnet component radial dimensions and materials.

Component	Material	Thickness [mm]
Inner aperture pipe (warm)	316L SS	3.0
Insulation/Vacuum	MLI	17.0
Inner thermal shield	1100 Al	3.0
Insulation/Vacuum	MLI	11.0
He vessel inner cylinder	316L SS	6.4
He space		3.0
Coil mandrel	316L SS	19.1
Coil to mandrel insulation	G10	5.0
Coil (w/turn to turn insulation)		45.0
Coil to collar insulation	G10	5.0
Coil collar	316L SS	20.0
Yoke	AISI 1006	200.0
He space		20.0
He vessel outer cylinder	316L SS	6.4
Insulation/Vacuum	MLI	20.0
Outer thermal shield	1100 Al	3.0
Insulation/Vacuum	MLI	30.0
Vacuum vessel outer cylinder	SA-36	12.7

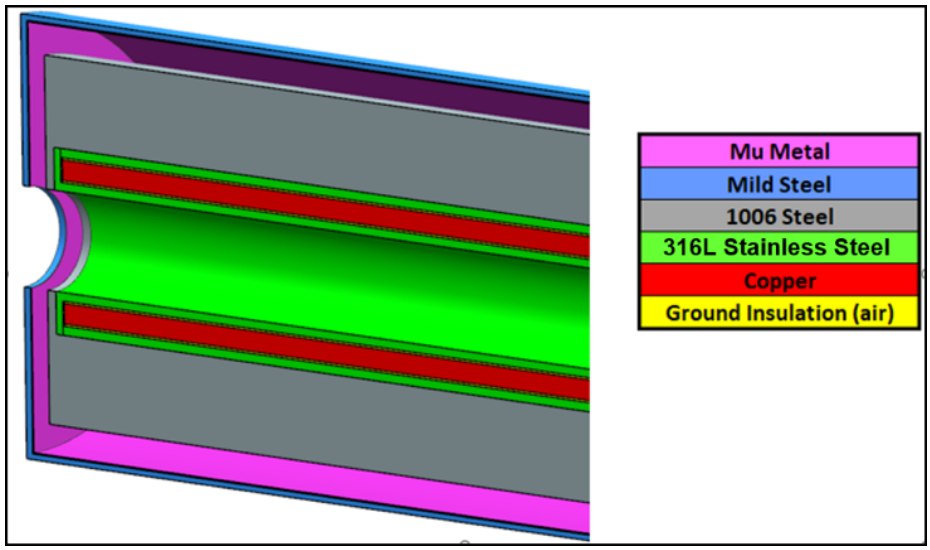

Figure 6.65: SRS FEA material assignments.

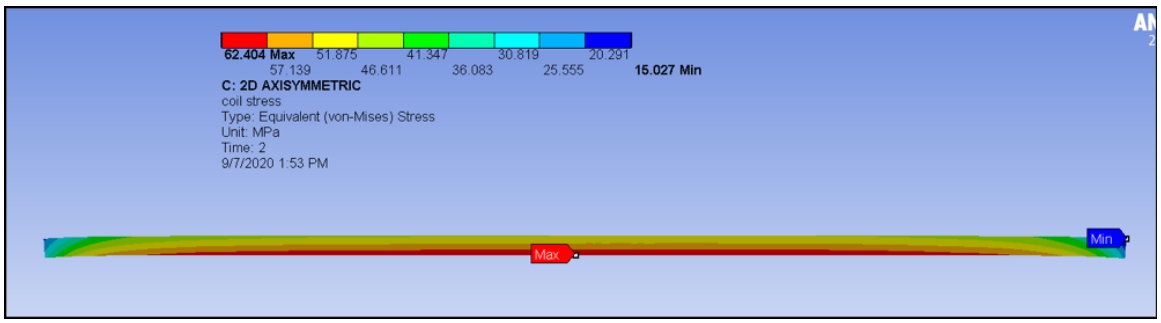

Figure 6.66: SRS Von-Mises coil stresses at peak field.

Bayonet connections for supply and return shield and cold mass LHe are provided. Vapor cooled 1000 A rated current leads bring power to the solenoid coil. A 4 K control valve and pressure relief stack are also included. The cold mass is suspended within the cryostat via eight cold mass tension supports to minimize heat leak to the magnet. A cryostat support system with six degree of freedom alignment capability is not shown in the figure.

Dipoles just upstream of the solenoids produce synchrotron radiation which will impinge on the warm vacuum chamber running through the solenoids. Active vacuum pumping and water cooling are needed along the vacuum chamber to meet the electron storage ring vacuum requirements. This sets the warm bore ID on the vacuum vessel at 136 mm. A single vacuum chamber will span the entire length of each solenoid configuration and will be longer than the installed cryostat lengths to allow for vacuum pumping and water cooling connects.

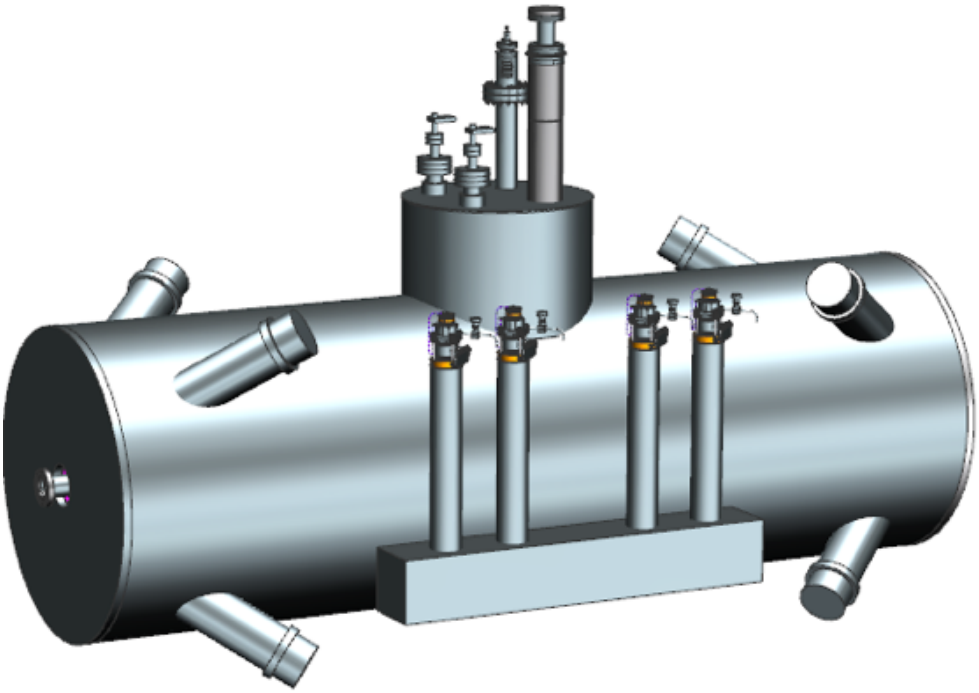

Figure 6.67: SRS conceptual cryostat illustration.

The insulating space, filled with multi-layer insulation (MLI), is provided between the 4.5 K cold mass, thermal shield, and vacuum vessel. This is kept at a minimum on the inner bore and ends to minimize the coil inner diameter and maximize the magnetic length. The provided space on the end takes advantage of the change in lengths of the cold mass and thermal shield from room temperature to cold. More space is provided on the OD to provide room for the support etc.

The leads, control valve, and primary cryogenic relief are all shown as part of the central tower in Figure 6.68. Further assessment of these features will be required for the detailed design. Two commercial 1000 A leads are used for the conceptual design. A TJNAF-style JT valve is shown, though a commercial valve should also be possible. A 2" NPS sch10 pipe is shown for the primary relief with a 60 PSIG burst disk. A failure of the vacuum space has been looked at with an assumed 4 kW/m^2 heat flux. The cold mass is estimated at 11 m^2, yielding a 44 kW heat flux and a 2.3 kg/sec boil of rate at 4.5 K. The pressure drop is estimated at 1–5 psi for exit temperatures of 5–10 K respectively, so a smaller relief pipe may be possible.

The tension supports have been analyzed to provide an initial structural and heat load estimate. Upset conditions, such as quench of a magnet, quench of and adjacent magnet, or transient conditions are still to be examined. The final design will also have a way to accommodate shipping loads, though this could be handled with temporary supports.

A 2D estimate neglecting the X components puts the load per support at 7000 lbs. To be conservative and include a preload, 8000 lbs has be used to set the support design loads

and should more than cover the neglected forces in the X direction.

A simple Process and Instrumentation Diagram (P&ID) is provided in Figure 6.68. This assumes separate primary and thermal shield circuits. Four TJNAF-style 1.5″ bayonets are assumed for helium ingress and egress. A floating shield is also under consideration and the final choice will be made in concert with the cryogenic refrigeration and distribution design. Safety reliefs are provided for each circuit and the vacuum vessel. Details for the lead flow return and control are still to be set.

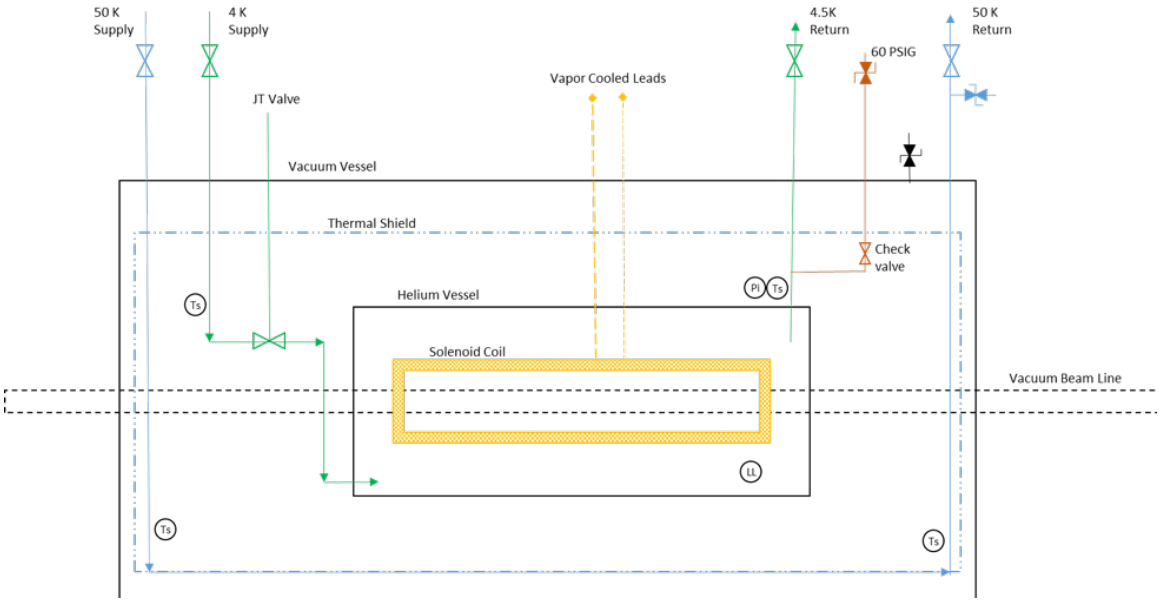

Figure 6.68: SRS simple process and instrumentation diagram.

The estimated heat loads are given in Table 6.19. The thermal radiation heat loads include an allowance for radiation, convection, and conduction through the MLI. Conservative values of 0.2 and 4.6 W/m^2 have been used for the 4 K and 50 K loads respectively. The lead flow is for the lead pair and based on recommended values from a commercial vendor. 120% of the design 500 A current is used. Bayonet heat loads are based on the TJNAF 1.5″ designs. The control valve heat load is based on published commercial valve numbers. The relief stack is based on a 2″ NPS SCH 10 pipe. The values for instrumentation and other sources are estimated.

No specific shielding requirement existed at the outset of the conceptual design activity. It was a design decision to apply the shielding requirement of 50 mT at a 0.5 m radial distance from the beam centerline. As the design evolved, this radial distance is equal to the OD of the cryostat vacuum vessel. The pilot studies [249] looked at various options, including single layer and multi-layer shielding with cold or warm or combination of cold and warm components. These were assessed for impacts on magnet performance, subsystem level integration, and compactness of the whole magnet system. To provide efficient flux return path and also to reduce the fringe fields, a 200 mm thick AISI 1006 grade steel yoke is integrated in the cold mass. Additional end plates are added to the cold mass

Table 6.19: SRS magnet heat load estimates.

Heat source	50 K load [W]	4 K load [W]	Lead flow [g/s]
Thermal radiation through MLI (all heatshield surfaces)	66	2.6	
Suspension system intercepts, all eight	25	2.6	
Lead liquifaction load (120% current rating)			1.9
4 K bayonets (2)	1.6	0.12	
50 K bayonets (2)	0.8		
Control valve	0.3	0.1	
Relief Stack	3.9	0.3	
Instrumentation (estimate)		0.2	
All other sources (estimate)	2.0	0.2	
TOTAL	99.6	6.1	1.9

to shield the ends of the solenoids. A 3 mm thick Mu metal shield is placed between the thermal shield and vacuum vessel of the magnet cryostat with all three elements adding to the magnetic shielding. The Mu metal shield is not saturated in the max field condition. The layout and dimensions were chosen such that the magnetic properties of shield components do not adversely impact the SRS magnet performance over the entire operating range. The overall shielding effectiveness results are a maximum of 18.1 mT at $y = 0.5$ m ($<$50 mT requirement). Further optimization is warranted on the detailed design towards cost, overall size, and manufacturability. Figure 6.69 shows the stray fields in the vicinity of the 9 m magnets (worst case).

Normal-Conducting IR Magnets

The interaction region requires ten additional normal conducting dipoles as well as 92 quadrupoles and sextupole magnets. All are normal conducting, DC water-cooled magnets and are identical to the magnets designed for the rest of the electron storage ring (see Section 6.2.3).

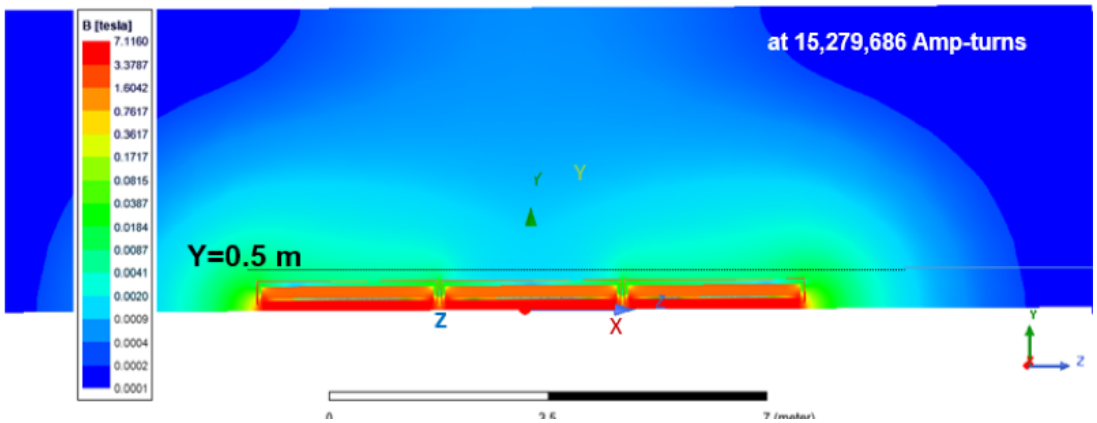

(a)

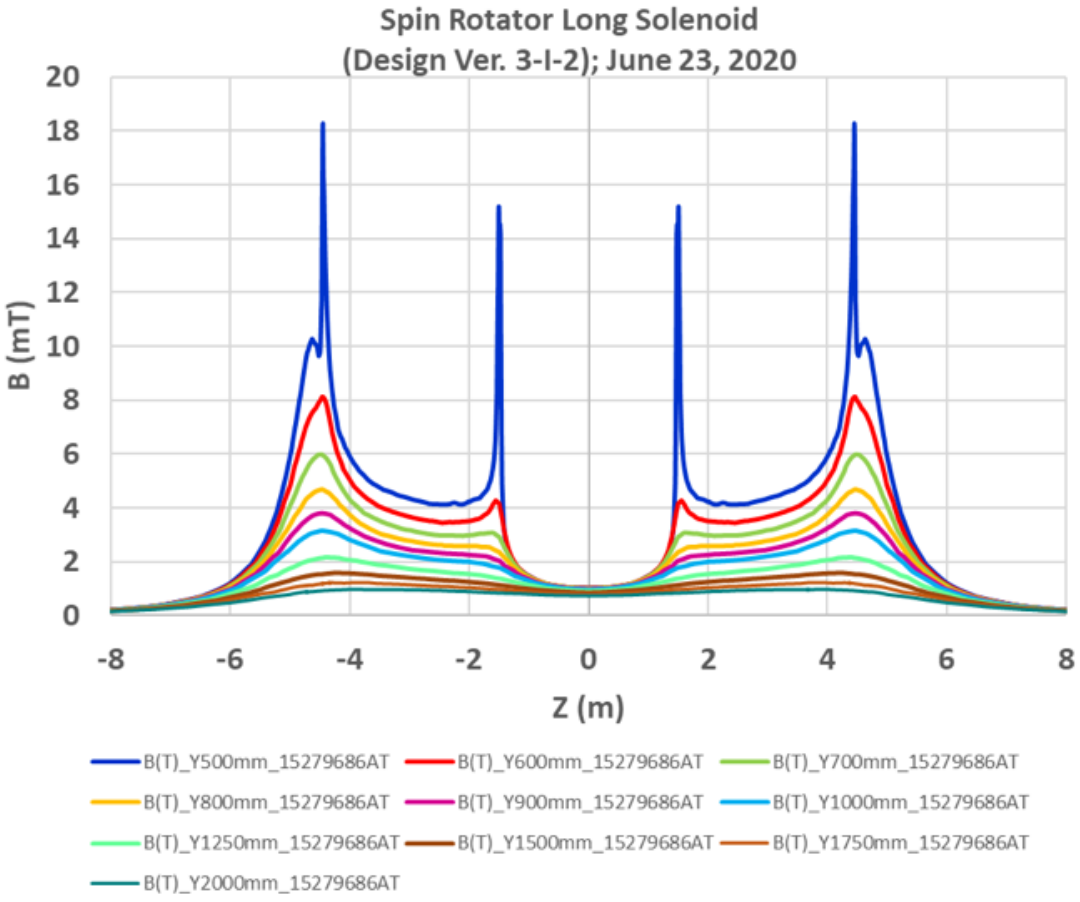

(b)

Figure 6.69: Field strength in the 9 m SRS magnets. (a) graphical representation, (b) chart of field vs longitudinal dimension for radial distances from the beam centerline.

6.2.3 Electron Storage Ring Magnets

The Dipole Triplet

The EIC electron storage ring employs a triplet of dipole magnets, called superbends, to provide the necessary bending. The triplets generate excess bending to create additional radiation damping to allow a larger beam-beam tune shift. Two of these magnets, labeled D1 and D3, are long low-field magnets. The D2 magnet, which is a short, high-field magnet, is located in-between D1 and D3. The drift sections between the magnets are 0.15 m long each; the length was chosen to ensure that crosstalk between the magnets is not a concern; this was verified by simulations. The general arrangement is shown in Figure 6.70.

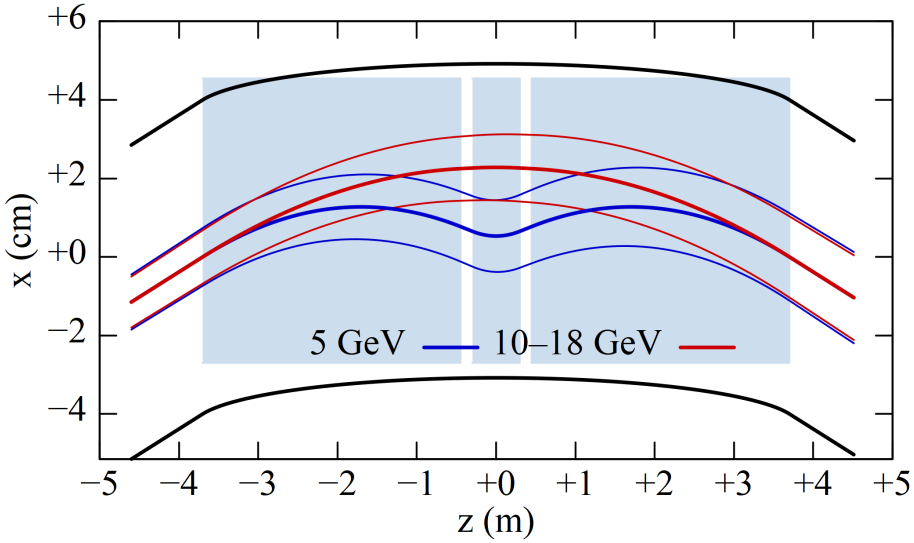

Figure 6.70: Dipole triplet superbends.

We present a design for a total superbend length of 7.4 m; the length of the individual magnets can be adjusted to suit different requirements. Uncritical is an increase in length, as the field quality of the magnets is expected to improve. The total power dissipation and electrical parameters are not expected to vary significantly, provided the total amount of bending remains constant.

As show in the figure, for low energies the D2 magnet bends in the opposite direction with respect to the D1/D3 magnets. The field of the D2 magnet is varied between -0.7 and $+0.248$ T. The D1/D3 magnets are unipolar and varied between 0.1533 and 0.248 T. The magnet parameters are shown in Table 6.20. For the entire EIC electron storage ring 252 triplets are required.

The cross-sections of the D1/D3 and D2 magnet are shown in Figure 6.71. As shown in the figure, for both designs a C-core geometry is chosen to allow easy access and synchrotron radiation to escape naturally.

The D1/D3 transverse magnet size is smaller due to the lower magnetic field (0.25T vs

Table 6.20: Specifications of the arc dipole magnets.

Parameter	D1/D3	D2
Count	504	252
Magnetic length [m]	3.253	0.594
Dipole field, min [T]	0.1533	-0.7
Dipole field, max [T]	0.248	0.248
Inscribed radius (good field) [m]	0.016	0.016
Required field quality	1×10^{-4}	1×10^{-4}
Physical length [m]	3.354	0.709
Physical width [m]	0.305	0.425
Physical height [m]	0.23	0.4
Weight iron [kg/m]	322	1010
Gap height [mm]	52	52

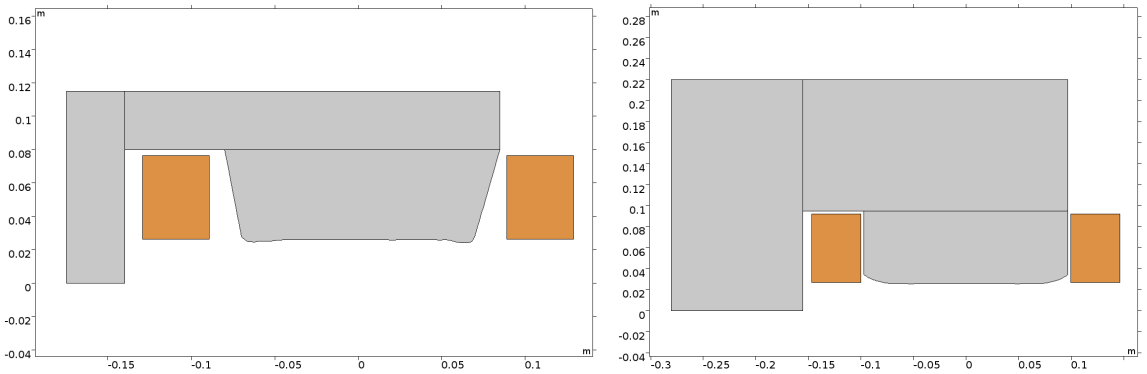

(a) D1/D3 **(b)** D2

Figure 6.71: The EIC ESR dipole arc magnets. Figure (a) shows the cross-section of the D1/D3 magnet and figure (b) of the D2 magnet. The coils are shown in orange.

0.7T); less iron is necessary to return the magnetic flux and no special precautions are necessary to avoid saturation in the pole. Both magnets assume a gap size of 52 mm to accommodate the beam pipe. The pole width for each of the magnets is driven by three factors: the field quality requirement (1×10^{-4} in a horizontal region of ± 16 mm), end effects (especially for D2) and saturation effects in the corners for the D2 magnet.

To avoid saturation effects the Rogowski profile or roll-off [253] is employed, which defines a pole end avoiding saturation effects. The Rogowski roll-off is not required for the D1/D3 magnet due to the relatively low field.

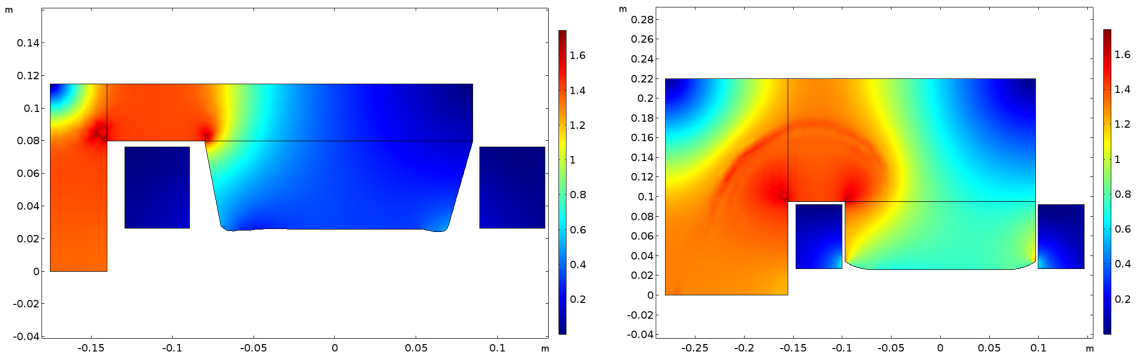

(a) D1/D3 **(b)** D2

Figure 6.72: Yoke magnetization of the EIC arc dipole magnets. Figure (a) shows the magnetization of the D1/D3 magnet and figure (b) of the D2 magnet.

The yoke magnetization is shown in Figure 6.72 for both magnets. The yoke is designed such that the magnetization in the back yoke does not exceed 1.4 T, which would limit the performance. As shown in the Figures, no saturation is predicted in the corners of the poles. Shims are added to the pole shape to improve the field quality.

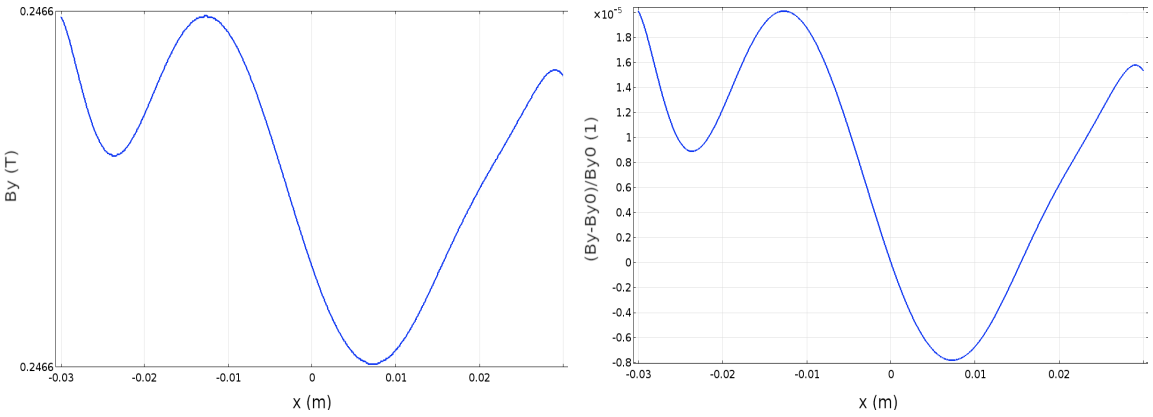

(a) B_y (T) **(b)** Field quality B_y/B_0 (1)

Figure 6.73: Vertical magnetic field (a) and field quality on the center plane of the D1/D3 magnet.

The vertical magnetic field and field quality are shown in Figure 6.73 and 6.74 for the D1/D3 magnet and the D2 magnet, respectively. As shown in the figures, a field quality of better than 1×10^{-4} can be accomplished in a 2D simulation.

The electrical specification of the arc dipole magnets is summarized in Table 6.21. For the D1/D3 magnet a relatively low average current density at peak field of 2.6 A/mm^2 is sufficient to provide the peak magnetic field. The power dissipation per meter length of the magnet is calculated assuming a filling factor of 80% of the designated space for the

Table 6.21: Coil specification of the arc dipole magnets.

Parameter	D1/D3	D2
Cross-section conductor [mm^2]	40×50	47×65
Cross-section conductor total [mm^2]	2000	3055
Current density (peak, av) [A/mm^2]	2.6	4.6
Ampere turns per coil [A]	5200	14053
Packing fraction	0.8	0.8
Power Loss per length magnet [W/m]	1162.5	5940
Conductor length end (single) [m]	0.11	0.25
Power loss ends [W]	127.875	1485
Conductor height × width [mm^2]	50×40	65×47
Conductor length [m]	11.4376	2.7796
Resistance DC [Ω]	0.0001972	4.79×10^{-5}
Current [A]	5200	14053
Voltage [V]	1.02544	0.6735
Magnetic energy [J/m]	252	2390
Inductance [μH]	50	10.8

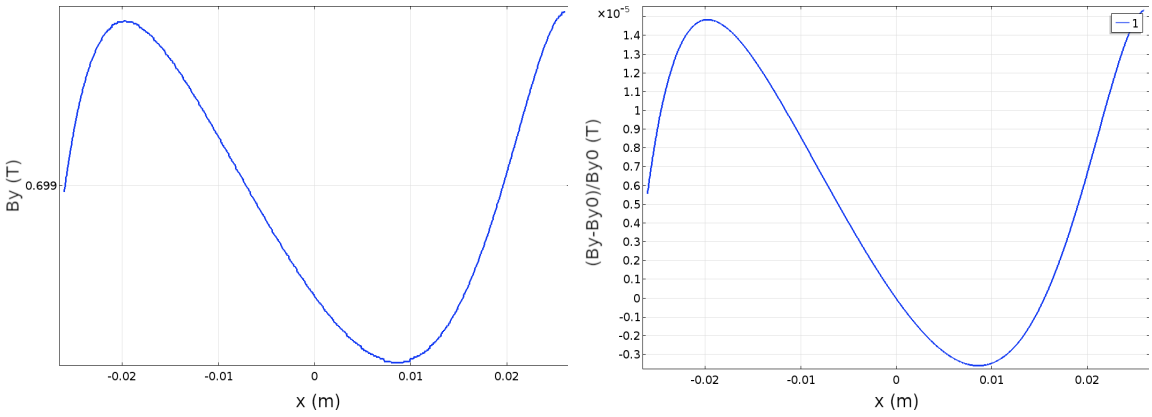

(a) B_y (T) **(b)** Field quality B_y/B_0 (1)

Figure 6.74: Vertical magnetic field (a) and field quality on the center plane of the D2 magnet.

coil.

As an example we assume a rectangular conductor from Luvata with a 50.8 × 38.1 mm^2 cross-section and a circular hole (25.4 mm) for cooling (Luvata 8464). With a water flow velocity of 0.5 m/s (0.25 l/s) the Reynolds number would be 13000; the pressure drop per

magnet is of the order of 0.015 bar. The water temperature will increase by 2.5 K per magnet. For the D2 magnet a higher flow velocity is required to limit the temperature rise; assuming the Luvata conductor 8464, a velocity of 1 m/s will result in a temperature rise of 9 K per magnet at full excitation. Higher flow rates in both magnets can be utilized to lower the temperature increase per magnet.

Table 6.22: Power dissipation arc dipole magnets.

Energy [GeV]	Field D1/D3 [T]	Field D2 [T]	Power Dissipation D1/D3 [MW]	Power Dissipation D2 [MW]	Total [MW]
5	0.15	-0.70	0.32	1.04	1.69
7.5	0.16	-0.45	0.37	0.42	1.16
10	0.17	-0.16	0.40	0.06	0.86
15	0.21	0.21	0.59	0.09	1.26
18	0.25	0.25	0.84	0.13	1.82

The operating fields and power dissipation of the individual superbend magnets for all operating modes are shown in Table 6.22. As shown in the Table, the D2 magnet is operating at its peak field for the lowest energy; at the lowest energy the D2 magnet dominates the power losses. With an increasing energy more bending is provided by the D1/D3 magnets, which become dominating for the highest energies. The power dissipation of the superbends for all magnets in the ring is expected to be 0.86–1.82 MW depending on the energy.

Mechanical Analysis The D2 magnet is subject to a significant vertical force of 40 kN/m at peak field between the poles. A linear mechanical analysis was carried out to verify that the mechanical deflection does not have a detrimental effect on the field quality.

The resulting von-Mises stress is shown in Figure 6.75; as shown in the Figure, the stresses are low and not a concern. The resulting deflection of the yoke is shown in Figure 6.76. The peak deflection, as shown, is of the order of 10 µm. This deflection causes a change in the field quality of the 3×10^{-6} level.

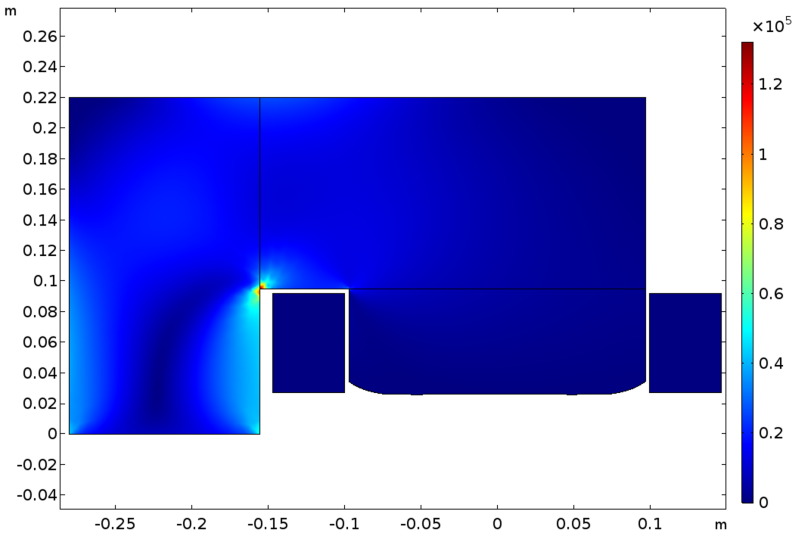

Figure 6.75: Von-Mises stress in the D2 magnet at full field

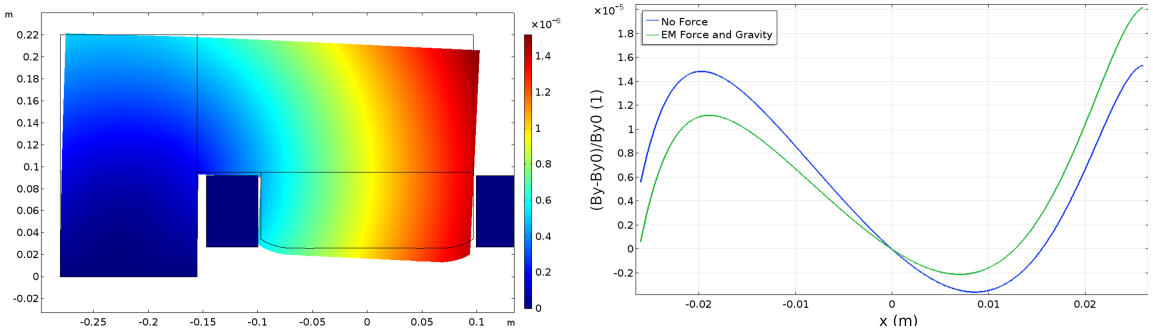

(a) Mechanical displacement (m)

(b) Field quality B_y/B_0 (1)

Figure 6.76: Displacement (a) and its effect on the field quality (b) of the D2 magnet at full field

Field Quality

The expected field quality was determined in a 3D non-linear finite element simulation using Opera[1]. To improve the field quality the Rogowsi-profile is used for the ends of the magnet. The geometry of the D1/D3 magnet is shown in Figure 6.77. The 3D magnetization of the yoke at peak excitation is in good agreement with the 2D simulation. No saturation in the ends is observed.

The higher order harmonics for a reference radius of 17 mm, and the integrated vertical magnetic field on the center plane are shown in Figure 6.78. Both the harmonics and the

[1]Cobham Technical Services, Network House, Langford Locks, Kidlington, OX5 1LH, Kidlington OX5 1GA, United Kingdom.

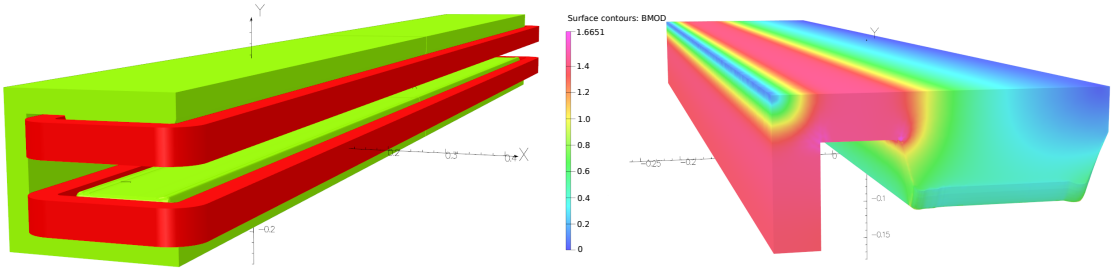

(a) 3D Geometry D1/D3 dipole magnet **(b)** Magnetization D1/D3 magnet

Figure 6.77: 3D Geometry and magnetization of the D1/D3 magnet at full field.

integrated dipole field are evaluated for $\pm 1.6\,\mathrm{m}$ in longitudinal direction.

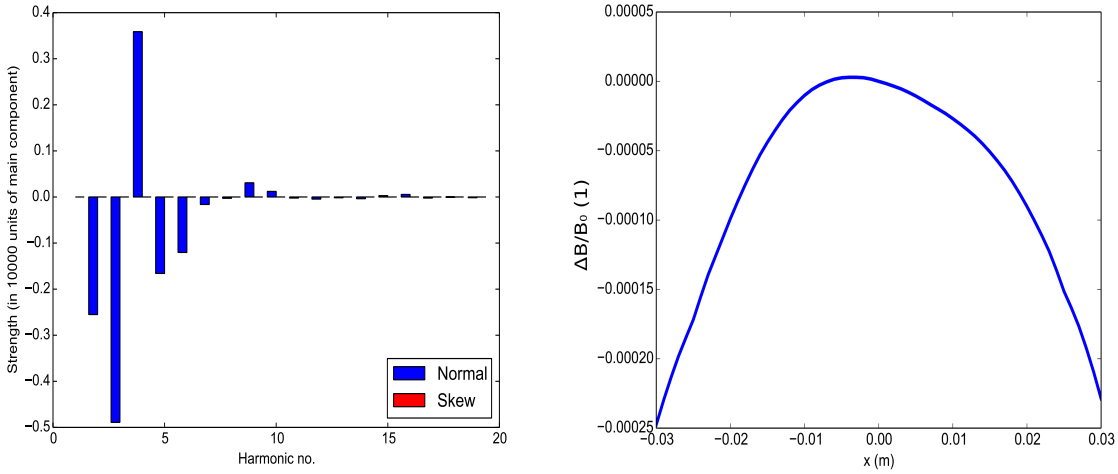

(a) Higher order harmonics of the D1/D3 magnet **(b)** Integrated dipole field D1/D3 magnet

Figure 6.78: Higher order harmonics and integrated vertical magnetic field on the center plane for the D1/D3 magnet.

As shown in the Figure, the harmonics as well as the integrated dipole field meet the field quality requirements. The higher order multipole components are small; outside the radius of 17 mm the field quality deteriorates slowly. The field quality is within the specification up to $\pm 20\,\mathrm{mm}$ of the aperture; for $\pm 25\,\mathrm{mm}$ the field quality drops to 2×10^{-4}.

The 3D geometry of the D2 magnet is shown in Figure 6.79. The magnet ends utilize the Rogowski-profile; in addition, the pole is notched. The depth of the notch in combination with the transverse position allows control of the sextupole and quadrupole component of the ends, respectively. The notch shown in the Figure is 1 mm deep and shifted by 2 mm from the center towards the backyoke of the magnet.

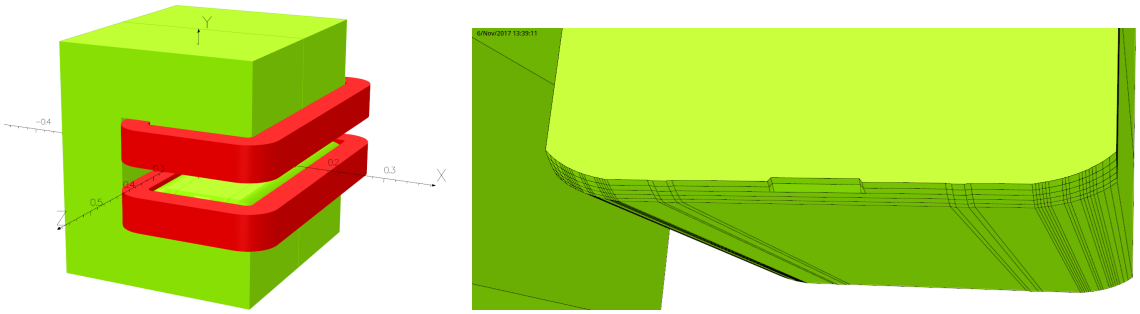

(a) 3D Geometry D2 dipole magnet **(b)** Pole end geometry of the D2 magnet

Figure 6.79: 3D Geometry and end pole design of the D2 magnet.

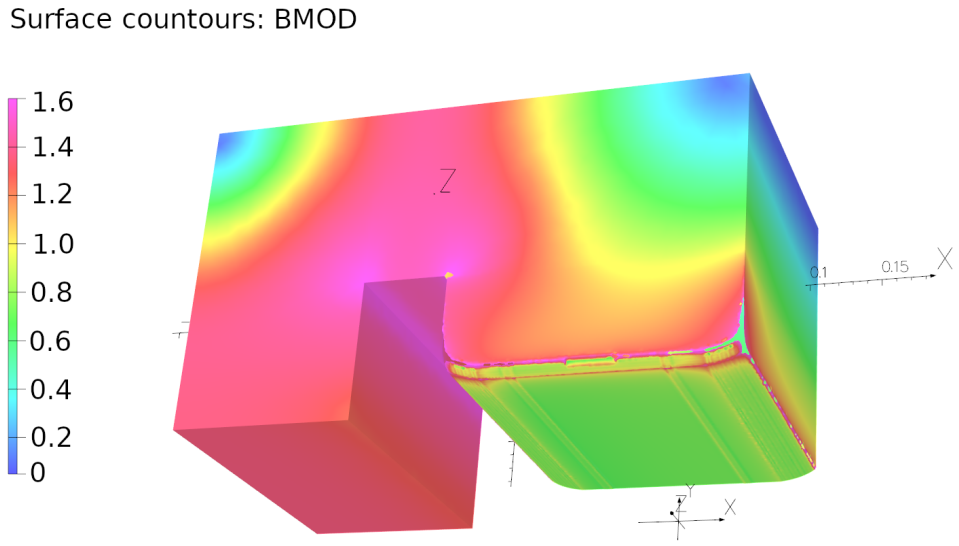

Figure 6.80: Yoke magnetization of the D2 magnet at full field.

Due to the Rogowski end-profile the saturation in the magnet ends does not exceed 1.5–1.6 T as shown in Figure 6.80. Figure 6.81 shows the higher order harmonics at a radius of 17 mm and the integrated vertical magnetic field on the center plane for the D2 magnet.

As shown in the Figure, the highest order multipole has a weak quadrupole component (1 unit); other higher order units are not significant and decay quickly. The good field region extends to about ± 20 mm and deteriorates slowly beyond this.

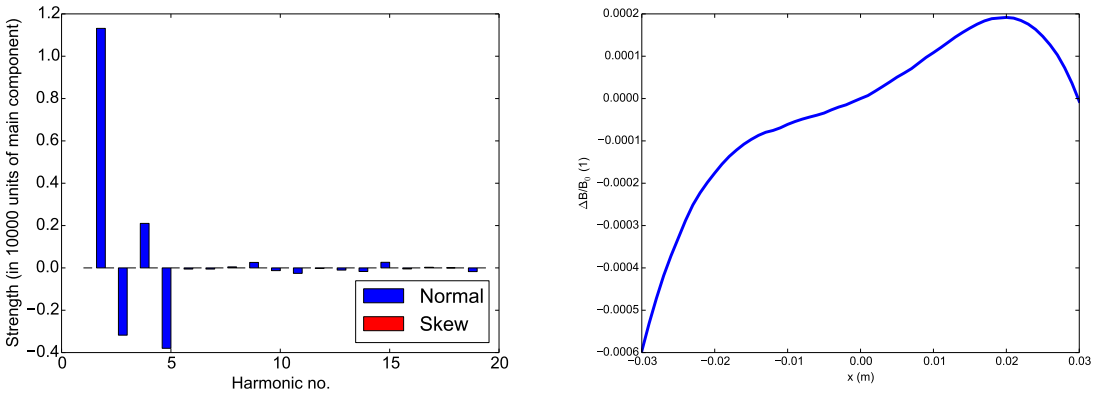

(a) Higher order harmonics of the D2 magnet

(b) Integrated dipole field errors in D2 magnet

Figure 6.81: Higher order harmonics (± 0.65 m longitudinally) and integrated vertical magnetic field error on the center plane for the D2 magnet.

Arc Quadrupoles

The focusing and defocusing quadrupole magnets for the EIC electron storage ring have very similar requirements; the required specification is shown in Table 6.23. Due to the similarity of the gradient we propose a single quadrupole geometry which is suitable for both cases. A quadrupole design is required which delivers about 18.4 T/m over a length of 0.6 m. A relatively large inscribed radius of 37 mm is necessary to clear the beam-pipe. 380 quadrupoles in total are required for the arcs and a further 84 quadrupoles are necessary for the straight sections.

Table 6.23: Specification arc quadrupole magnets.

Parameter	QF	QD
Count	253	241
Magnetic length [m]	0.6	0.6
Gradient [T/m]	18.1	-18.4
Radius good field [m]	0.015	0.015
Required field quality	1×10^{-4}	1×10^{-4}
Physical width [m]	0.42	0.42
Physical height [m]	0.42	0.42
Weight iron [kg/m]	784	784
Pole inscribed radius [mm]	37	37

Figure 6.82 shows a cross-section of the quadrupole magnet design. The pole is modestly tapered which helps to decrease the magnetization; the pole itself is generally hyperbolic with chamfers at the corners in order to achieve the required field quality. The excitation coil is given as much space as possible which limits the power dissipation. The figure also shows the geometry of a possible beam-pipe, which clears the pole comfortably.

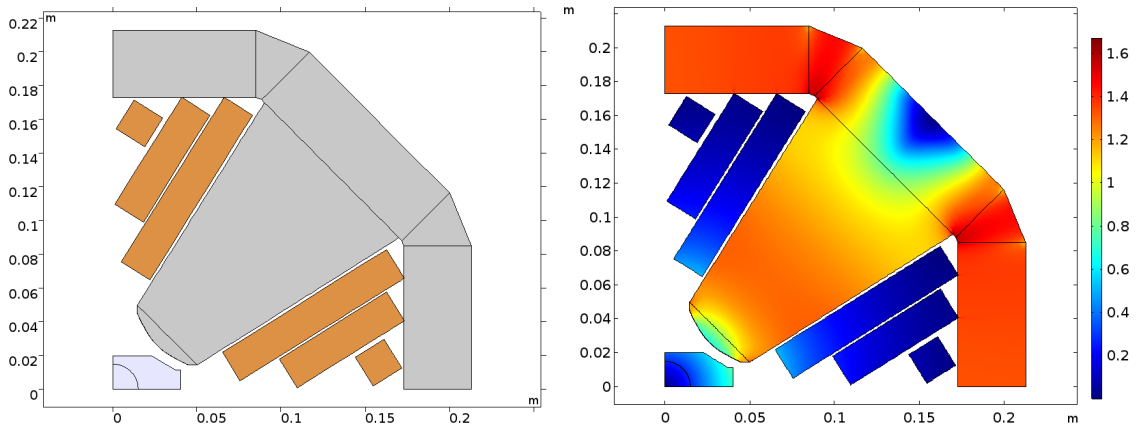

(a) Geometry of the arc quadrupole magnet **(b)** Magnetization

Figure 6.82: Geometry (a) and magnetization (b) of the arc quadrupole magnet.

The yoke is designed to have a magnetization around 1.4 T at peak excitation. The maximum pole tip field is about 0.8 T. Figure 6.83 shows the gradient and expected gradient quality (2D). As shown in the Figure, the design can provide the required gradient as well as gradient quality.

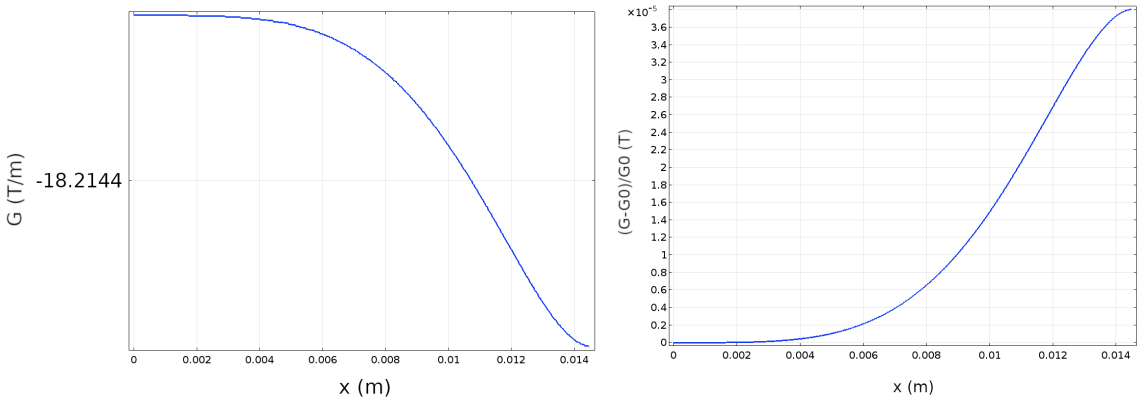

(a) Gradient (T/m) **(b)** Gradient quality $\Delta G/G_0$

Figure 6.83: Gradient (a) and gradient quality (b) of the arc quadrupole magnet.

The higher order harmonics for an inscribed radius of 15 mm are shown in Figure 6.84; the highest order multipole is the dodecapole with 0.15 units. The current density at peak excitation is 2.4 A/mm^2 as shown in Table 6.24.

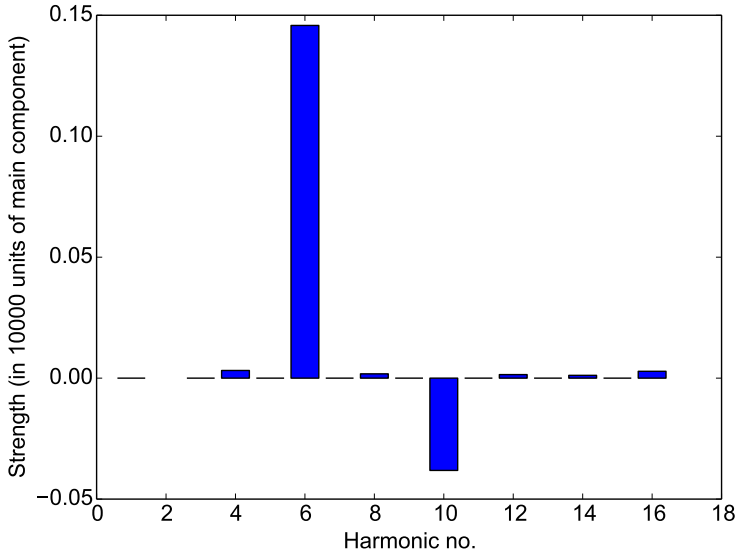

Figure 6.84: Higher order harmonics of the arc quadrupole magnet.

Table 6.24: Electrical specs for arc quadrupole magnets.

Parameter	QF/QD
Cross-section conductor [mm^2]	20×100, 20×60, 20×20
Cross-section conductor total [mm^2]	3600
Current density (average) [A/mm^2]	2.4
Ampere turns per coil [A]	10000
Packing fraction	0.8
Power Loss per length magnet [W/m]	4104
Length coil end single [m]	0.125
Power loss magnet ends [W]	513
Conductor h $\times$ w [mm^2]	20×10
No turns per coil	10
Coil current [A]	480
Conductor length [m]	57.6
Magnet resistance DC [Ω]	0.005
Inductance [H/m]	0.0176
Magnetic energy [J/m]	2030

Arc Sextupoles

Two different types of sextupole magnets are required for the EIC electron storage ring, which differ in their strengths. Sextupole magnets located near the QF quadrupole magnets require a strength of $122\,\mathrm{T/m^{-2}}$, whereas sextupole magnets near the QD magnets need to provide a sextupole strength of $-216\,\mathrm{T/m^{-2}}$. Both sextupole types have a magnetic length of 0.5 m. The required good field radius is 15 mm. To clear the beampipe the minimum inscribed pole radius is 40 mm. Figure 6.85 shows the geometry of the EIC arc magnet sextupole magnet, which can satisfy the field strength requirements of both types. The main parameters are summarized in Table 6.25.

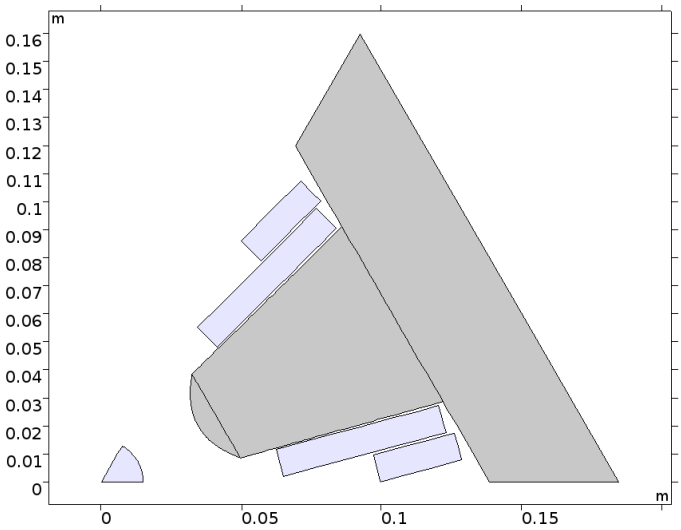

Figure 6.85: Geometry of the arc sextupole magnet. $1/6^{\mathrm{th}}$ of the geometry is shown.

Table 6.25: Arc sextupole magnets.

Parameter	SX	SY
Count	156	152
Magnetic length [m]	0.5	0.5
Strength $[\mathrm{T/m^2}]$	122	-216
Radius good field [m]	0.015	0.015
Required field quality	1×10^{-4}	1×10^{-4}
Physical width [m]	0.36	0.36
Physical height [m]	0.36	0.36
Weight iron [kg/m]	504	504
Pole inscribed radius [mm]	40	40

The peak magnetization for both maximum excitations are shown in Figure 6.86. For the more challenging design of the QD sextupole magnet the magnetization in the pole is about 0.8 T, which reduces to about 0.5 T for the QF design.

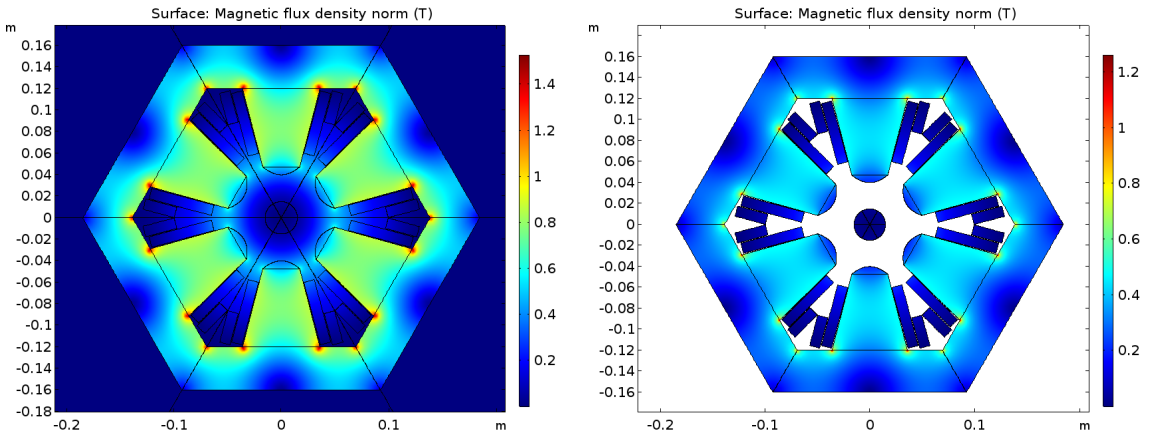

(a) SY **(b)** SX

Figure 6.86: Magnetization of the arc sextupole magnets

The pole shape of the sextupole design follows the well-known hyperbolic curve. Due to the large aperture of the magnet the field quality requirements of 1×10^{-4} can be met; Figure 6.87 shows the expected higher order harmonics at the reference radius of 15 mm. As shown in the Figure, the highest order multipole with a significant contribution is the 18-pole with 0.25 units.

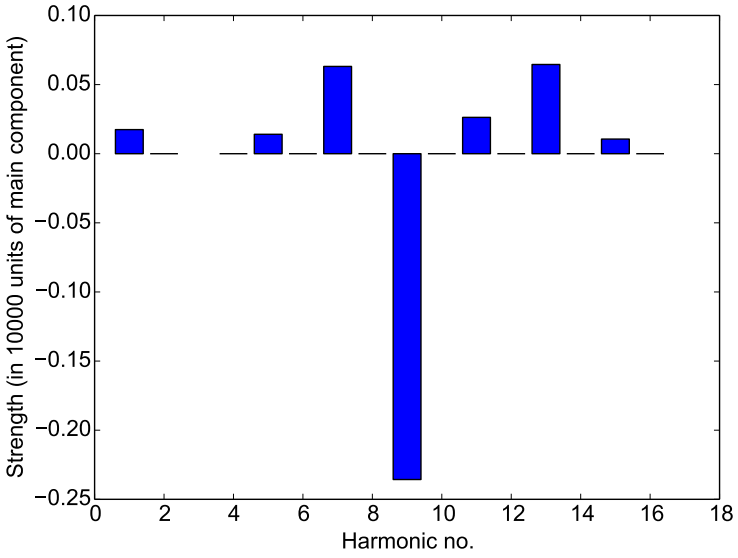

Figure 6.87: Higher order harmonics of the arc sextupole magnet.

The lower field sextupole magnet can be excited with a $15 \times 10\,\mathrm{mm}^2$ conductor. Each pole winding requires six turns. The average current density for the QF sextupole is $2.35\,\mathrm{A/mm}^2$, whereas the higher field strength of the QD sextupole requires $4.14\,\mathrm{A/mm}^2$. The electrical specifications of the arc sextupole are summarized in Table 6.26.

Table 6.26: Electrical Specs Arc Sextupole Magnets.

Parameter	SX	SY
Cross-section conductor [mm^2]	60×100, 30×100	60×100, 30×100
Cross-section conductor total [mm^2]	9000	9000
Current density (average) [$\mathrm{A/mm}^2$]	2.346	4.14
Ampere turns per coil [$\mathrm{A/mm}^2$]	702+1404	1243+2486
Power Loss per length magnet [W]	1281	3989.4
Power loss magnet ends [W]	128.1	128.1
Conductor h $\times$ w [mm^2]	15×10	15×10
Magnet current [A]	351.9	621
No turns	6	6
Wire length [m]	43.2	43.2
Magnet DC resistance [Ω]	0.0050	0.0050
Magnet voltage [V]	1.7474	3.0836
Inductance [H]	0.0093	0.0093
Magnetic energy [J]	578	1800

Special Arc Sextupoles

A limited number of high strength sextupole magnets will be required to increase the dynamic aperture. The required strength of these sextupoles is $360\,\mathrm{T/m}^2$, as shown in Table 6.27.

The 2D geometry of the high strength sextupole is shown in Figure 6.88. In order to accomplish the higher performance the magnet pole is kept slimmer to minimize crosstalk between the poles. The inscribed pole radius is kept at 40 mm. The pole face is optimized to provide an acceptable field quality; as shown in the figure, the pole face is almost straight.

The magnetization in the pole is about 1.4 T at peak excitation with a pole tip field of about 0.6 T. The peak power dissipation is about 7 kW per sextupole at peak excitation. The average current density is $5.75\,\mathrm{A/mm}^2$. Further details are given in Table 6.28. Figure 6.89 shows the yoke and pole magnetization at peak excitation, while Figure 6.90 shows the higher order harmonics at a radius of 15 mm. The Figure shows that in the 2D simulation none of the higher order harmonics have a significant strength.

Table 6.27: High strength sextupole.

Parameter	SX	SY
Magnetic length [m]	0.5	0.5
Strength [T/m^2]	360	360
Required field quality	1×10^{-4}	1×10^{-4}
Physical width [m]	0.36	0.36
Physical height [m]	0.36	0.36
Weight iron [kg/m]	504	504
Pole inscribed radius [mm]	40	40

Table 6.28: Electrical specs high strength sextupole.

Parameter	SX	SY
Current density (average) [mm^2]	5.75	5.75
Ampere turns per coil [A·t]	1725+5175	1725+5175
Power Loss per length magnet [W/m]	10261	10261
Power loss magnet ends [W]	1026.1	1026.1
Conductor h $\times$ w [mm^2]	15×10	15×10
Magnet current [A]	862.5	862.5
No turns	6	6
Wire length [m]	43.2	43.2
Magnet DC resistance [Ω]	0.0050	0.0050
Magnet voltage [V]	4.2828	4.2828
Inductance [H]	0.0036	0.0036
Magnetic energy [J]	1350	1350

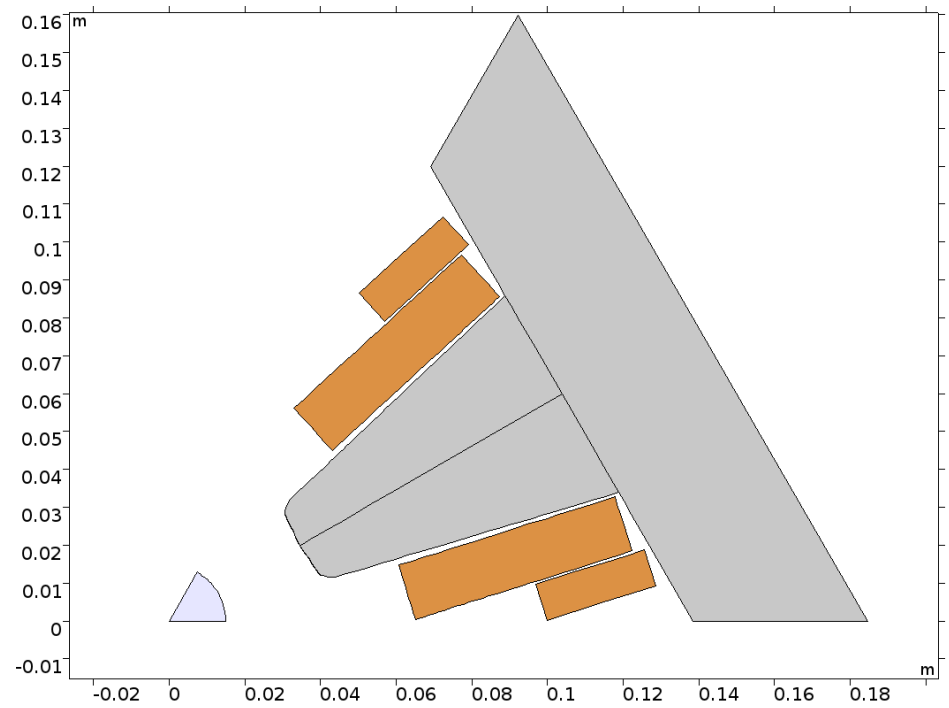

(a)

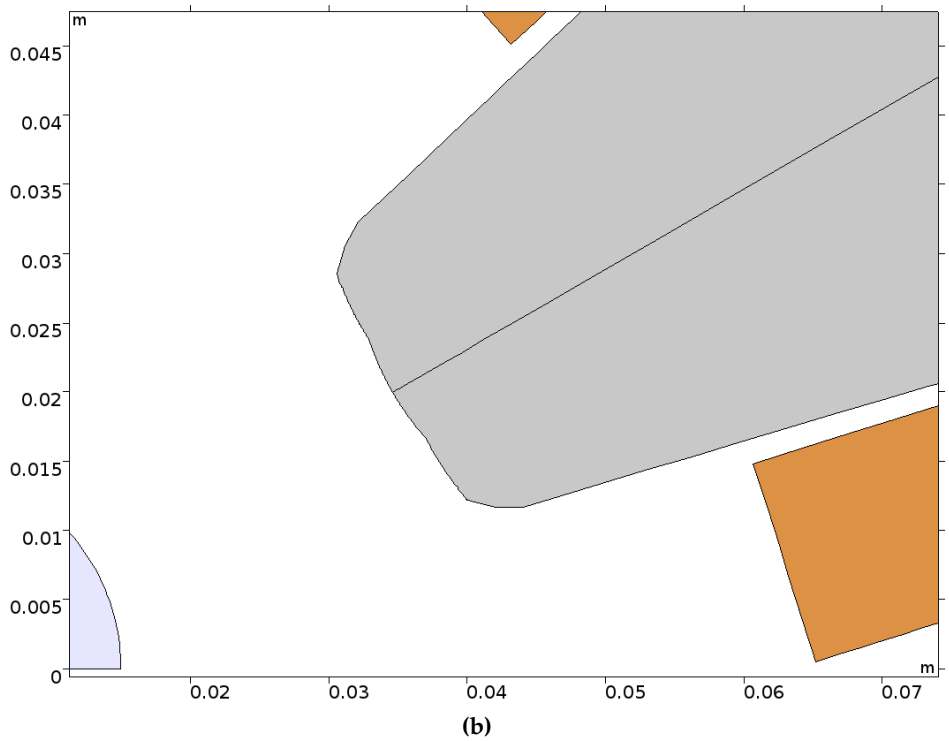

(b)

Figure 6.88: High strength sextupole magnet – Geometry.

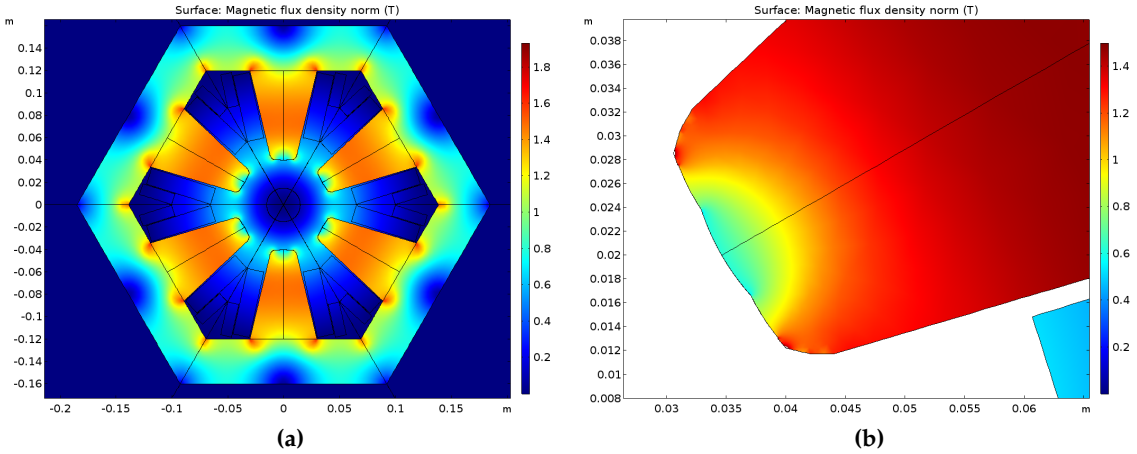

Figure 6.89: High strength sextupole magnet – Magnetization

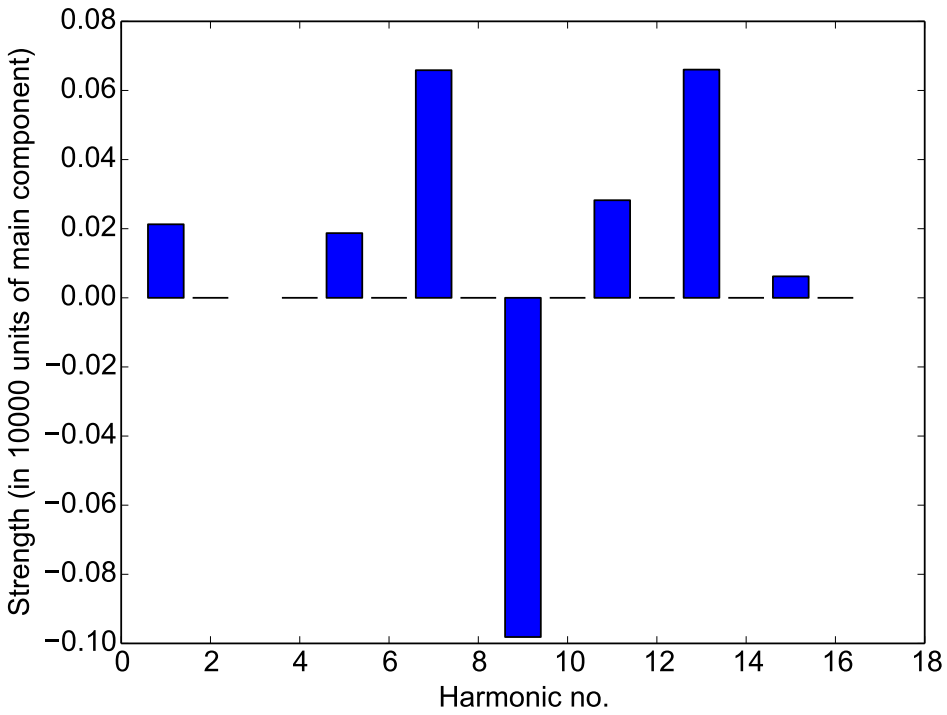

Figure 6.90: Higher order harmonics of the high strength arc sextupole magnet.

Correctors

Horizontal and vertical correctors are required for the EIC electron storage ring. The correctors should provide a minimum integrated dipole field of 6 mTm. The correctors, because of geometrical constraints, need to have a clear bore of 150 mm and are required to fit into a longitudinal space of 0.47 m. The requirements are summarized in Table 6.29.

Table 6.29: Specification for storage ring correctors.

Parameter	Value
Count	220
Integrated corrector strength [Tm]	0.006
Corrector Inscribed radius (good field) [m]	0.017
Corrector Required field quality	1×10^{-2}
Corrector physical length [m]	0.25
Corrector physical width [m]	0.3
Corrector physical height [m]	0.3
Weight iron [kg]	36
Weight coil [kg]	48
Gap height [mm]	150

As shown in Figure 6.91, the corrector design is a simple window-frame geometry with back-leg windings, which can generate the horizontal and vertical dipole field. The corrector design is 0.25 m long and will therefore fit comfortably in the available space.

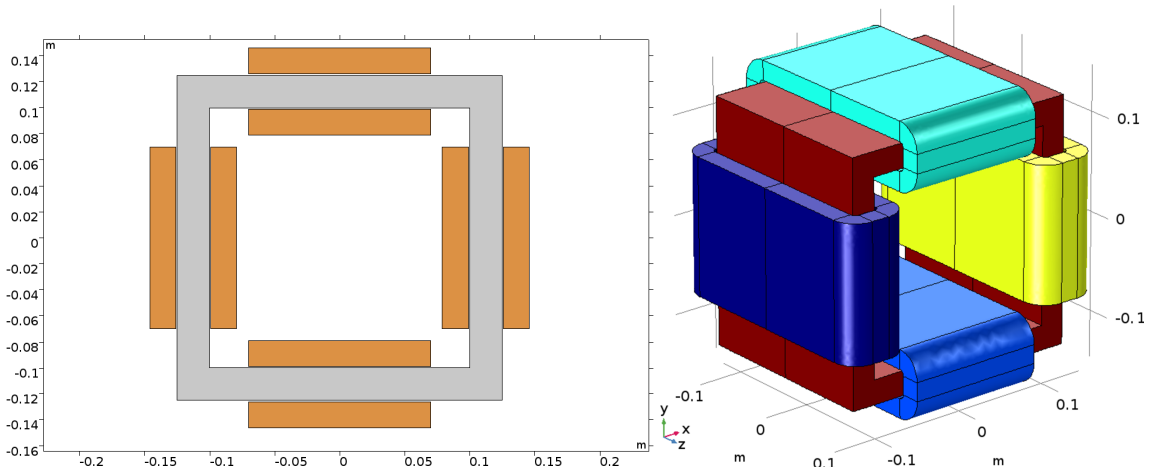

(a) 2D **(b)** 3D

Figure 6.91: Storage ring corrector.

With a current density of 1 A/mm^2 in the coils the design can provide a dipole and skew dipole field of integrated 10 mTm. Figure 6.92 shows the dipole component along the length of the magnet and the higher order harmonics (normalized to 10000 units of the main component). The skew harmonics are identical to the normal harmonics and not shown.

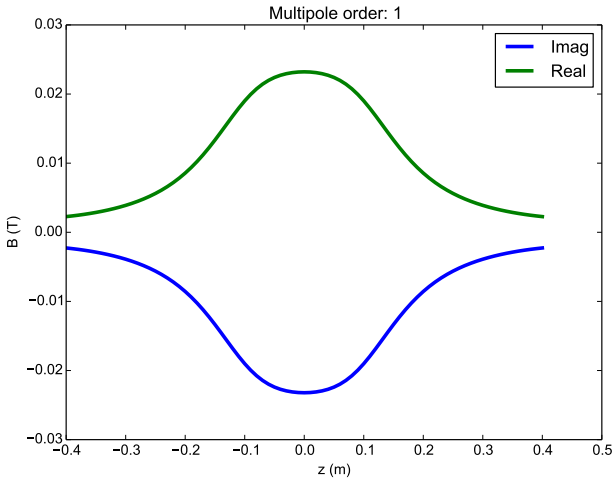

(a) Dipole Component

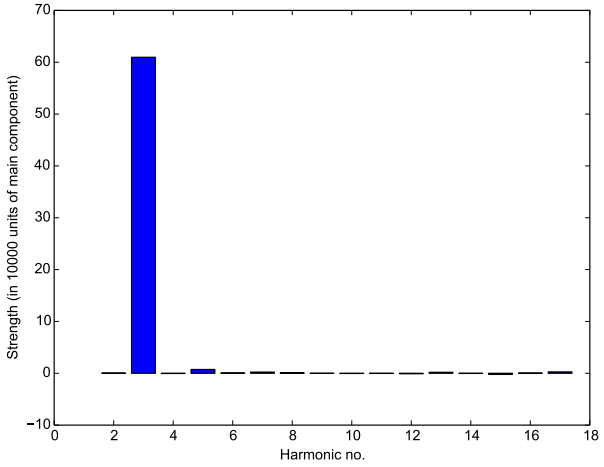

(b) Higher Order Harmonics

Figure 6.92: Normal field harmonics of the storage ring corrector.

The electrical parameters of the storage ring correctors are summarized in Table 6.30. The corrector coils can be wound from large diameter round copper wire; for a wire with a diameter of 2 mm a single corrector can be powered by a 4 A/50 V power supply. The power loss at full field is about 180 W; for all correctors in the ring the power loss is 40 kW excluding leads and busbars.

Table 6.30: Electrical specification for the storage ring correctors.

Parameter	Value
Cross-section [mm^2]	20×140
Cross-section [mm^2]	2800
Current density [A/mm^2] (peak, av)	1.28
Ampere turns per [A] coil	3600
Packing fraction	0.8
Power Loss per length magnet [W]	178
Conductor diameter [m]	0.002
Wire length [m]	1909.9
Resistance DC [Ω]	10.48
Current [A]	3.927
Voltage [V]	41.16
Magnetic energy [J]	12.44
Inductance [H]	1.613

Power Dissipation

The power dissipation for all ring magnets is shown in Figure 6.93. The overview excludes the higher strength sextupole magnets (which are few in number) and corrector magnets. Losses in busbars and current leads are also not included.

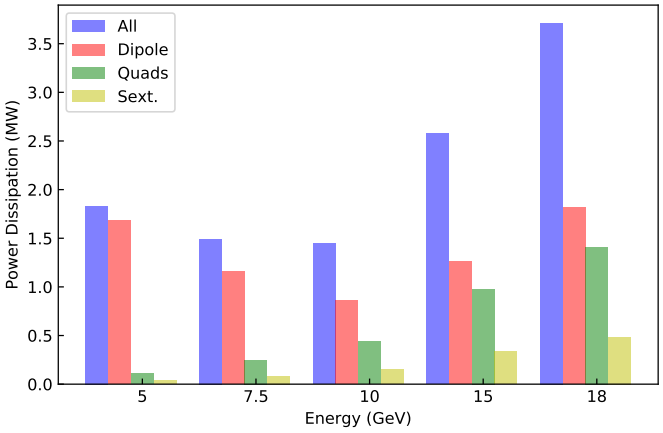

Figure 6.93: Power dissipation of the arc storage ring magnets

As shown in the Figure, depending on the energy between 1.4 and 3.3 MW are dissipated in the EIC electron storage ring magnets. Most of the energy is dissipated in the dipole magnets. Due to the structure of the superbends the energy dissipation does not necessar-

ily increase with energy; for low energies most of the power is dissipated in the D2 magnet due to the reverse bend. With increasing electron energy the field and power dissipation of the D2 magnet drops, while more energy is dissipated in the D1 and D3 magnets.

The lowest power dissipation is predicted for 10 GeV operation; the highest is predicted for 18 GeV operation followed by 15 GeV, while the 5 GeV operation is the third highest in power dissipation.

6.2.4 RCS Magnets Design

RCS Dipole Magnets Design

The main requirements for the RCS dipole magnets are summarized in Table 6.31; as shown in the Table, in total 384 magnets are required with a length of 4.24 m. The dipole field at peak energy is 0.234 T; the relatively low dipole field helps to keep the power dissipation in the excitation coil and the core losses low.

Table 6.31: Specification of the RCS dipole magnets.

Parameter	Value
Count	384
Magnetic length [m]	4.24
Dipole field, min [T]	0.012
Dipole field, max [T]	0.234
Inscribed radius (good field) [mm]	15
Required field quality	1×10^{-3}
Physical width [m]	0.34
Physical height [m]	0.26
Weight iron [kg/m]	401
Gap height [mm]	40

The field quality should be better than 1×10^{-3} in an aperture of 30 mm; the physical gap of the dipole magnets is 40 mm to allow for sufficient space for a beam pipe.

Figure 6.94 shows the geometry of the dipole magnet. As shown in the Figure, a simple H-frame geometry is chosen for this magnet. The magnets are expected to be 34 cm wide and 26 cm tall. The excitation coils are simple racetrack coils with two turns each. The peak magnetization is kept relatively low at 0.7 T to minimize the core loss in this region. Assuming a pessimistic 50 Hz pulse the average core losses are expected to be 2.41 W/m for a single cycle. In reality the core losses should be much less, as the power dissipation is roughly proportional to the frequency.

The magnetic field as a function of time and the field quality at peak field on the center

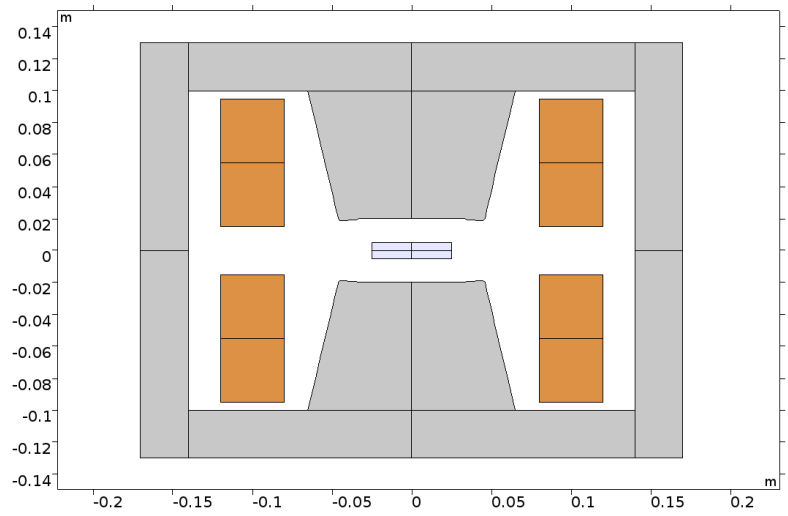

(a) Geometry

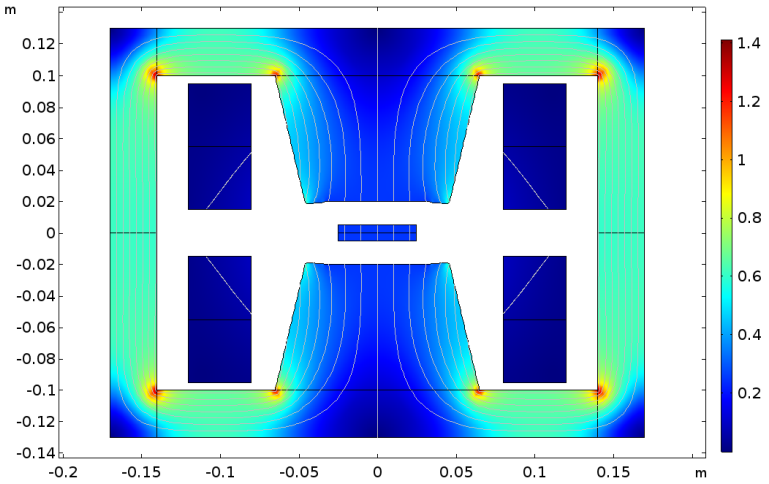

(b) Magnetization

Figure 6.94: The RCS dipole magnet; (a) shows the geometry and (b) the magnetization at peak excitation.

plane are shown in Figure 6.95. It was verified that the field quality does not change significantly during the ramp.

Eddy currents in the excitation coil do not play a significant role at this frequency, as shown in Figure 6.96. The figure shows the current density in the horizontal direction for different times during the ramp; as shown, the current density varies, but this does neither affect the field quality nor the power dissipation.

Figure 6.96 also shows the simulated power dissipation of the excitation coils in comparison to calculated I^2R losses without eddy currents. The comparison shows that the power dissipation with eddy currents is almost identical to the pure I^2R losses.

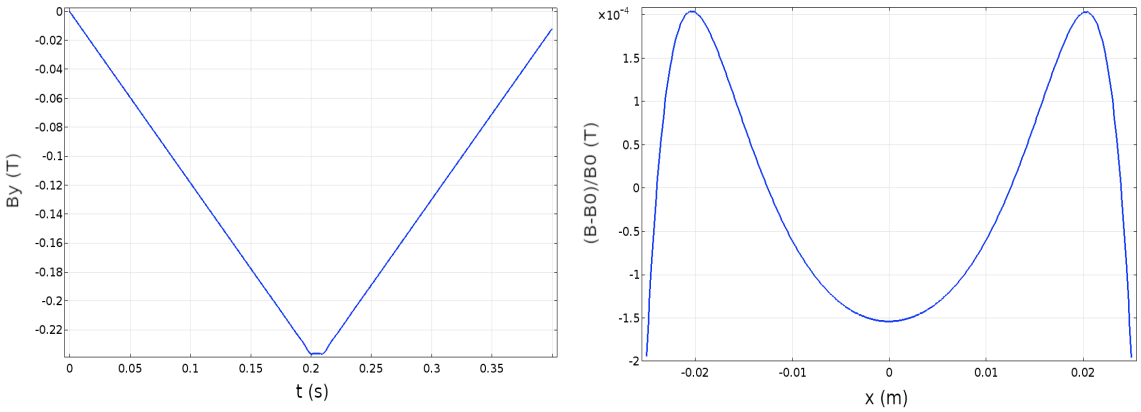

(a) Dipole field **(b)** Field quality

Figure 6.95: Dipole field as a function of time (a) and field quality (b).

Figure 6.97 shows the coil current and voltage (per meter length of magnet) evaluated by finite element analysis for a 200 ms rise time. As shown in the Figure, the voltage drop is mostly inductive. Voltage and coil current can be tuned by changing the number of turns to suit power supply needs if necessary. The electrical specifications of the dipole magnets are summarized in Table 6.32.

Table 6.32: Coil specification of the RCS dipole magnet.

Parameter	Value
Cross-section conductor [mm^2]	40 × 40, 4 turns
Current density (peak, av) [A/mm^2]	1.3
Ampere turns per coil [A]	4000
Power loss per length magnet [W/m]	50
Magnetic energy [J/m]	150
Inductance [µH/m]	0.75
Voltage [V/m]	0.375

The effect of eddy currents in the yoke was studied in a 3D time transient FEA simulation. The simulation consists of 5 mm thick laminations with a 0.5 mm air gap in between; boundary conditions ensure that the magnet is infinitely long. To reduce the simulation time linear material properties are assumed ($\mu_r = 1000$). The simulation represents a worst case scenario.

The results of the study are shown in Figure 6.98. As shown in the figure, at the planned ramp rate the current density in the yoke is expected to be less than 0.025 A/mm^2 in localized regions. The effect on the field quality is likewise small; as in reality the laminations will be thinner by an order of magnitude, the eddy currents in the yoke can be ignored.

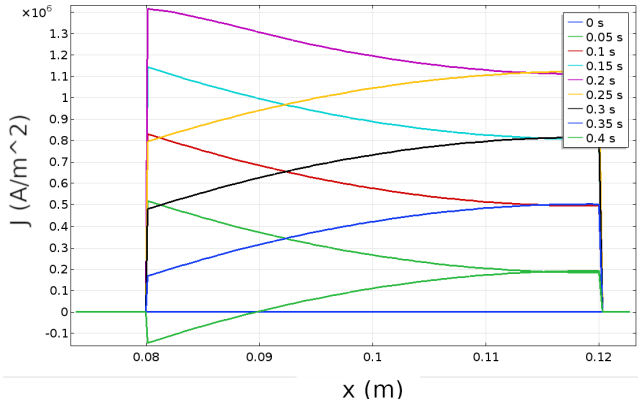

(a) Current density in A/mm^2

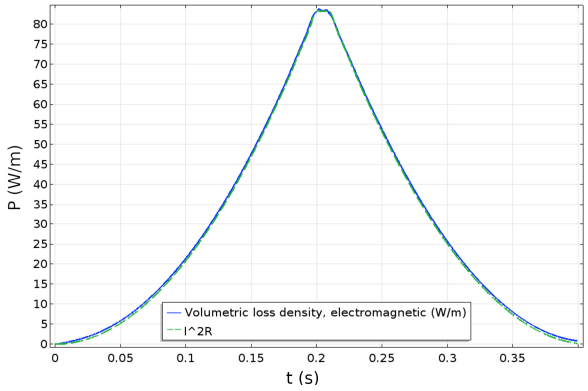

(b) Power dissipation per length

Figure 6.96: Current density across the conductor (a) power dissipation (b).

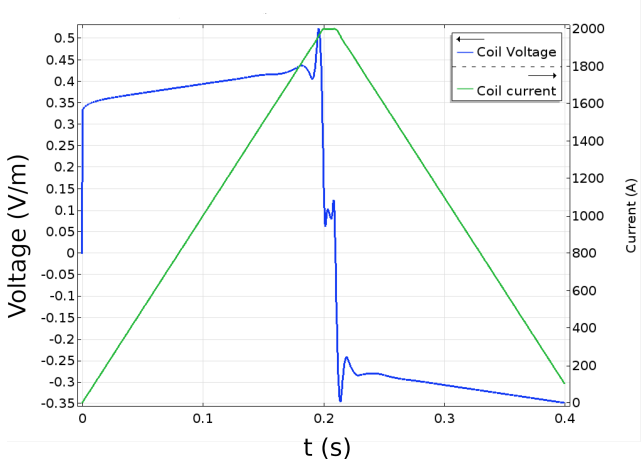

Figure 6.97: Coil current and voltage (per meter length) of the RCS dipole magnet.

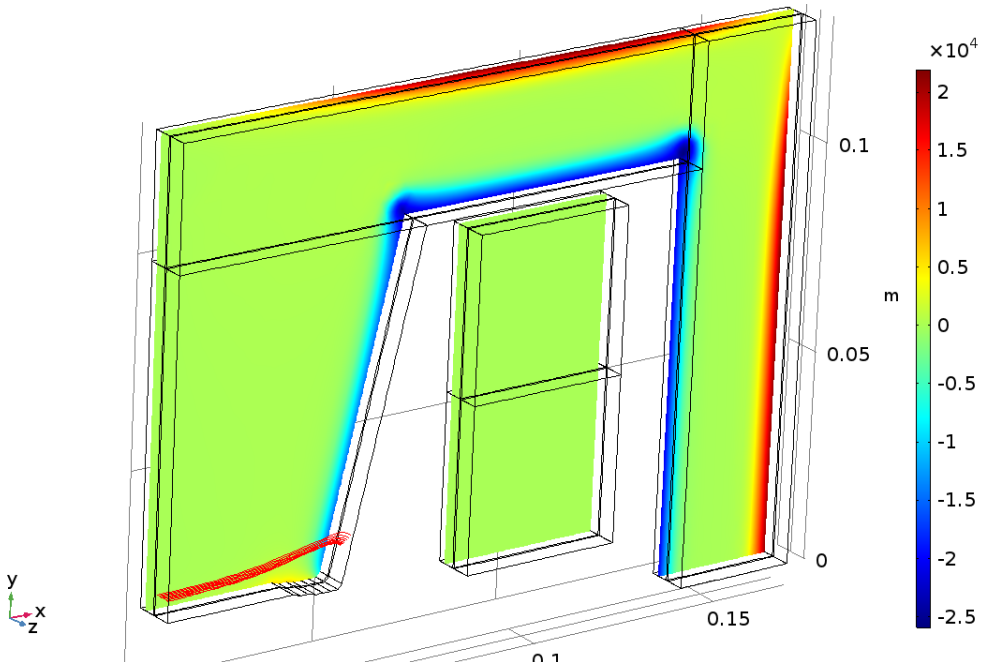

(a) Current density in A/m^2

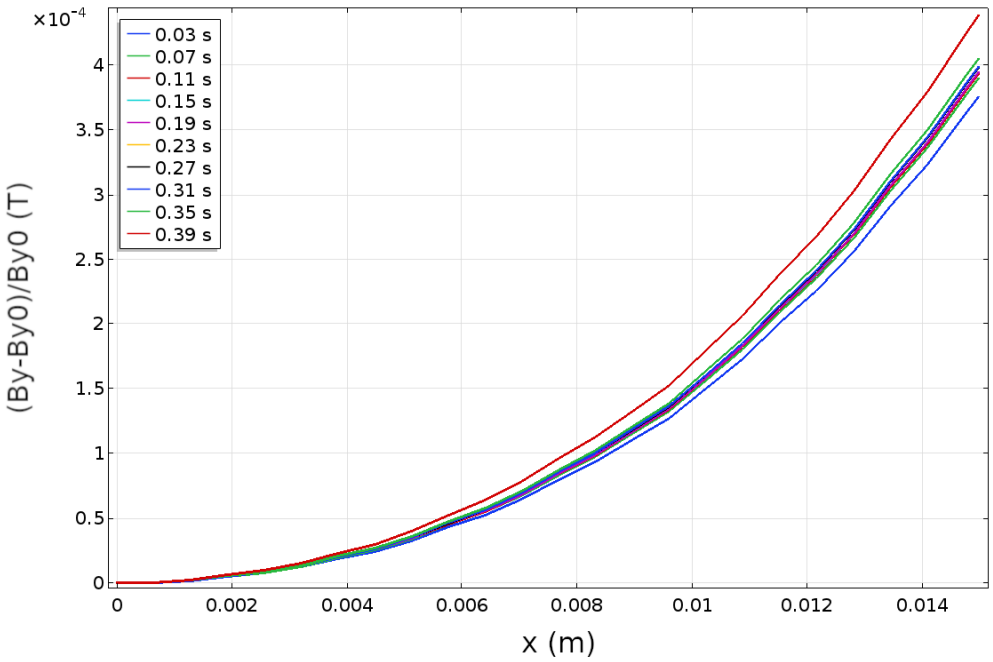

(b) Field quality at different times

Figure 6.98: Eddy current simulation.

RCS Quadrupole Magnets Design

The main parameters for the RCS quadrupole magnets design are shown in Table 6.33; in total 534 quadrupoles are necessary for the entire RCS ring (half focusing and half defocusing quadrupoles). Each quadrupole is 0.6 m long; the required peak gradient is 22.2 T/m. The required field quality is 1×10^{-3} in an aperture of 30 mm. The preliminary geometry is shown in Figure 6.99. The back-yoke geometry of this design is not optimized and can be re-designed to satisfy space requirements.

Table 6.33: Specification of the RCS quadrupole magnets.

Parameter	Value
QF count	267
QD count	267
QF/QD magnetic length [m]	0.6
QF/QD gradient [T/m]	22.2
QF/QD radius good field [m]	0.015
QF/QD Required field quality	1×10^{-3}
QF/QD physical width [m]	0.6
QF/QD physical height [m]	0.6
Weight iron [kg/m]	350
Pole inscribed radius [mm]	18

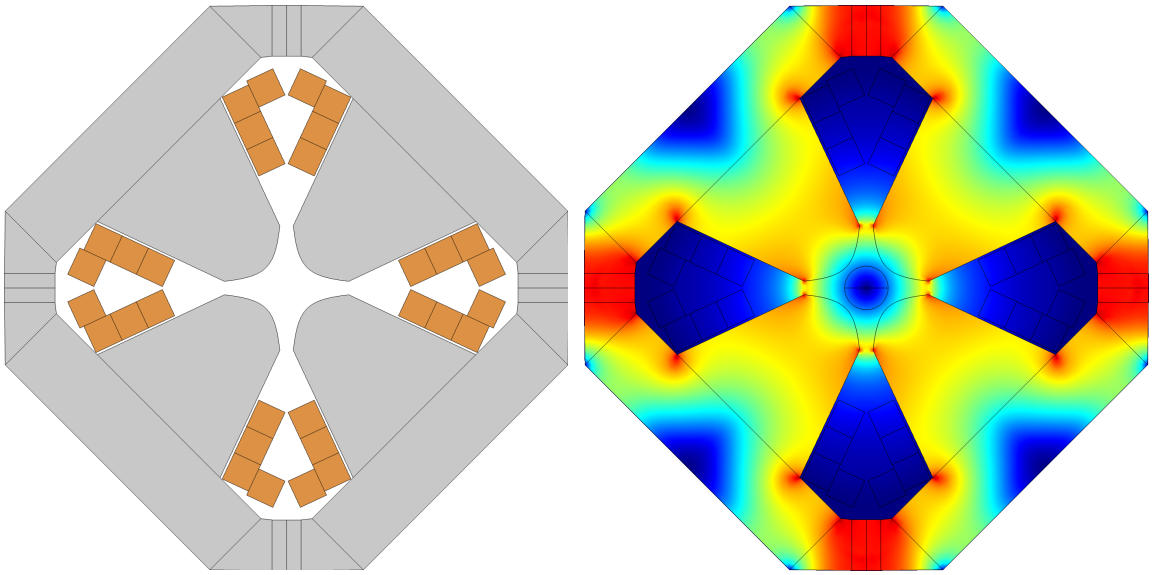

(a) Geometry **(b)** Magnetization

Figure 6.99: Geometry (a) and magnetization (b) at peak excitation.

Figure 6.99 (b) shows the magnetization at peak excitation. The pole has the usual hyperbolic shape; the corners of the pole are adjusted to obtain a better field quality. The pole is modestly tapered which lowers the magnetization in this area. The peak gradient and gradient quality (2D simulation) are shown in Figure 6.100. The Figure shows that the peak gradient can be accomplished with good field quality while maintaining a magnetization of $< 1.3\,\mathrm{T}$ in the pole.

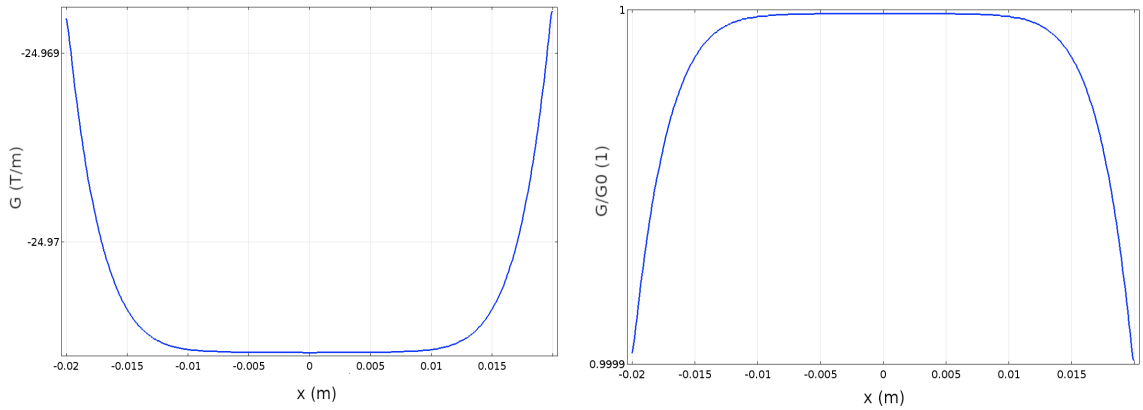

(a) Gradient **(b)** Gradient quality

Figure 6.100: Gradient (a) and gradient quality (b) on the center plane at peak excitation

Initial discussions show that coils with four turns for each pole lead to acceptable currents and voltages. Figure 6.101 shows the expected current and voltage (for a 1 m long magnet) for a 200 ms linear ramp. As shown in the Figure, most of the voltage is inductive; the peak voltage per magnet is about 5 V per coil. For a single pulse and the entire yoke we expect a core loss of $< 9\mathrm{W/m}$ for a 50 Hz pulse, which is small in comparison to the ohmic losses in the excitation coil. The electrical parameters of the quadrupole magnet design are summarized in Table 6.34.

Table 6.34: Coil specification of the RCS quadrupole magnet.

Parameter	Value
Cross-section [mm^2]	4 turns 20×20
Current density peak (average) [$\mathrm{A/mm}^2$]	2.5
Ampere turns per coil [A]	4256
Peak current [A]	1064
Power Loss per length magnet [W/m]	220
Inductance [H]	0.000768
DC Resistance [Ω]	0.0008276
Mag energy [J/m]	725

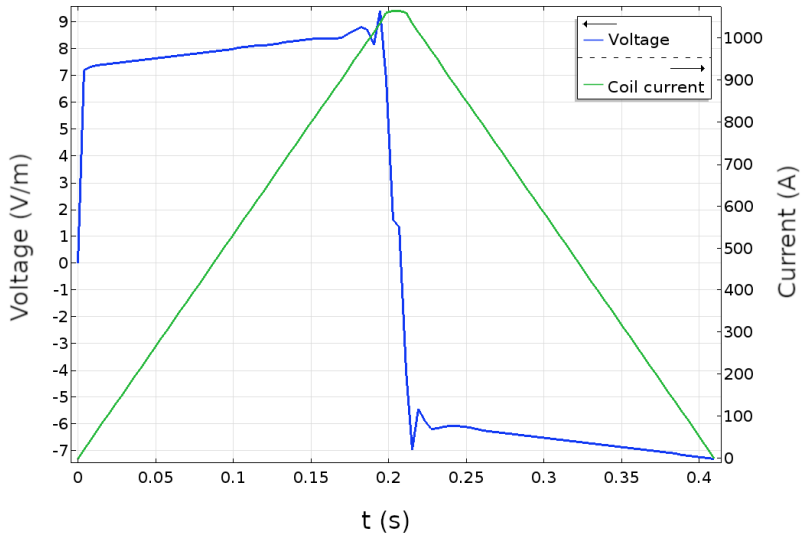

(a) Current/voltage

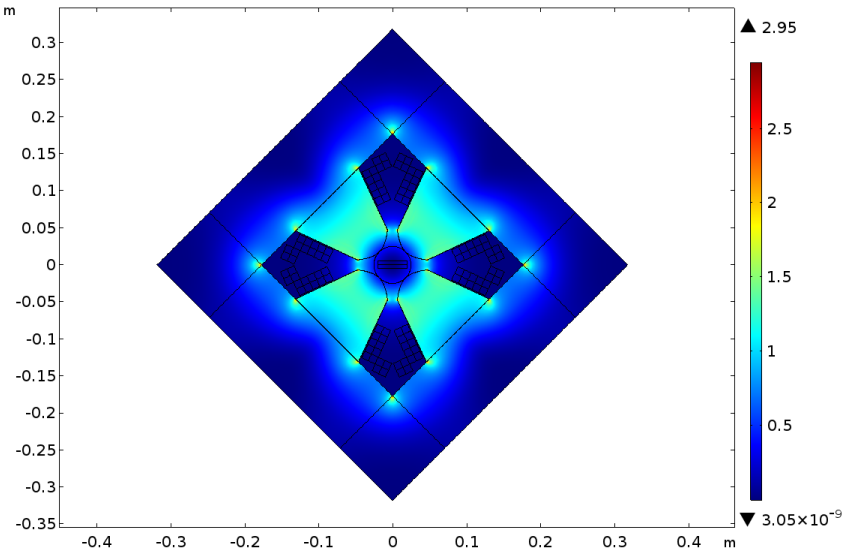

(b) Core loss (W/kg)

Figure 6.101: Current and voltage (V/m) (a) and core loss (b) of the RCS quadrupole magnet

RCS Sextupole Magnets Design

The requirements for the sextupole magnets for the RCS are shown in Table 6.35. In total 420 sextupole magnets are needed, each 0.5 m long. The required sextupole strength is 280 T/m ($\mathrm{d}B_y/\mathrm{d}x^2$); the requested field quality is 1×10^{-3} in an aperture of 30 mm.

A preliminary design is shown in Figure 6.102. The pole shape is hyperbolic; the pole corners are adjusted to achieve the required field quality. The poles are slightly tapered

Table 6.35: Specification of the RCS sextupole magnets.

Parameter	Value
Count	420
Magnetic length [m]	0.5
Strength [T/m^2]	280
Radius good field [m]	0.015
Required field quality	1×10^{-3}
Physical length [m]	0
Physical width [m]	0.36
Physical height [m]	0.36
Weight iron [kg/m]	450
Pole inscribed radius [mm]	25

which helps to reduce the magnetization. The poles are relatively slim in order to minimize flux leakage. The peak magnetization is calculated to be less than 1 T which is conservative for 3% SiFe.

Preliminary calculations showed that 10 turns per coil will lead to reasonable currents and voltages for the power supply. Figure 6.103 shows the calculated coil current and voltage (per meter length of magnet) for the envisaged linear ramp of 200 ms. As shown in the Figure, most of the voltage drop is inductive, even though there is also a significant resistive part. The peak excitation current is 700 A. The field quality is evaluated in a 2D static simulation at peak excitation. As shown in the Figure, the higher order harmonics are well behaved. About 1.2 units of 18-pole is expected, which meets the field quality requirement.

The electrical specification of the RCS sextupole magnets is summarized in Table 6.36.

Table 6.36: Coil specification of the RCS sextupole magnets.

Parameter	Value
Cross-section [mm^2]	20×20, 2 turns per pole
Current density (average) [A/mm^2]	1.42
Ampere turns per coil [A]	1425
Power Loss per length magnet [W/m]	73
Inductance [H]	0.000163
DC Resistance [Ω]	0.0005172
Mag energy [J/m]	80

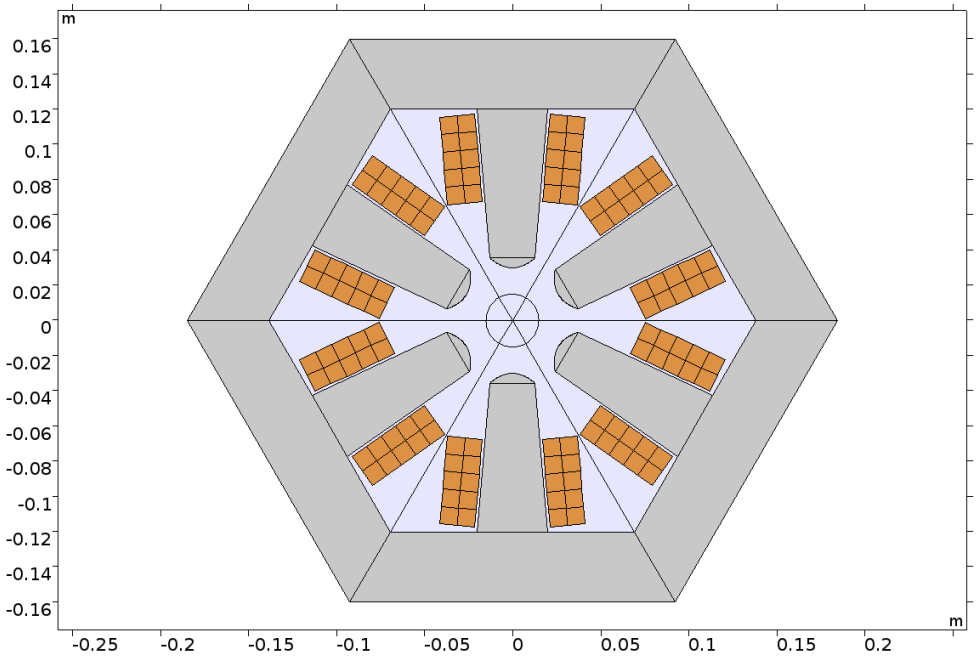

(a) Geometry

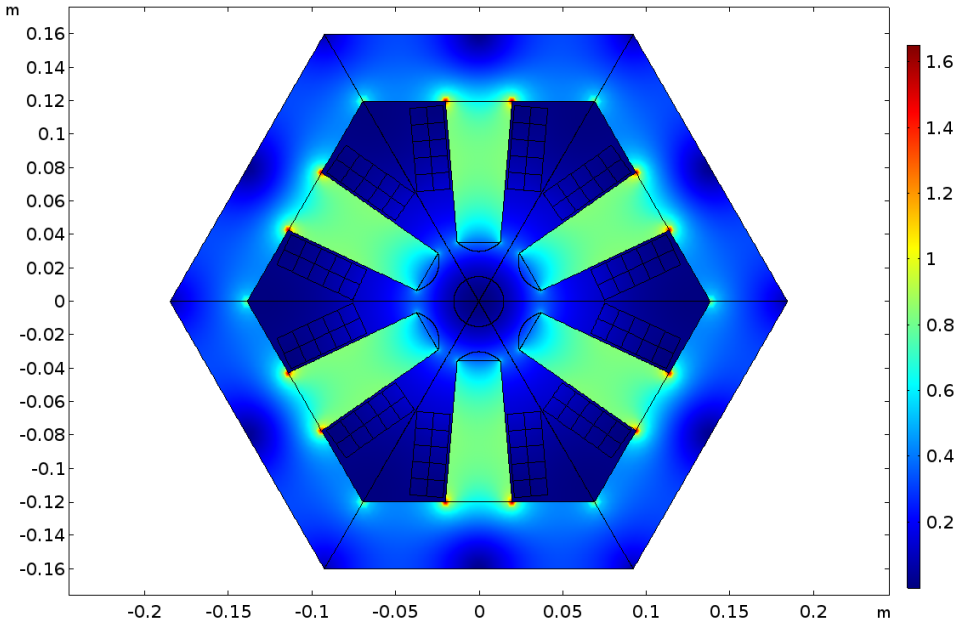

(b) Magnetization

Figure 6.102: The RCS sextupole magnet. (a) Geometry. (b) Magnetization.

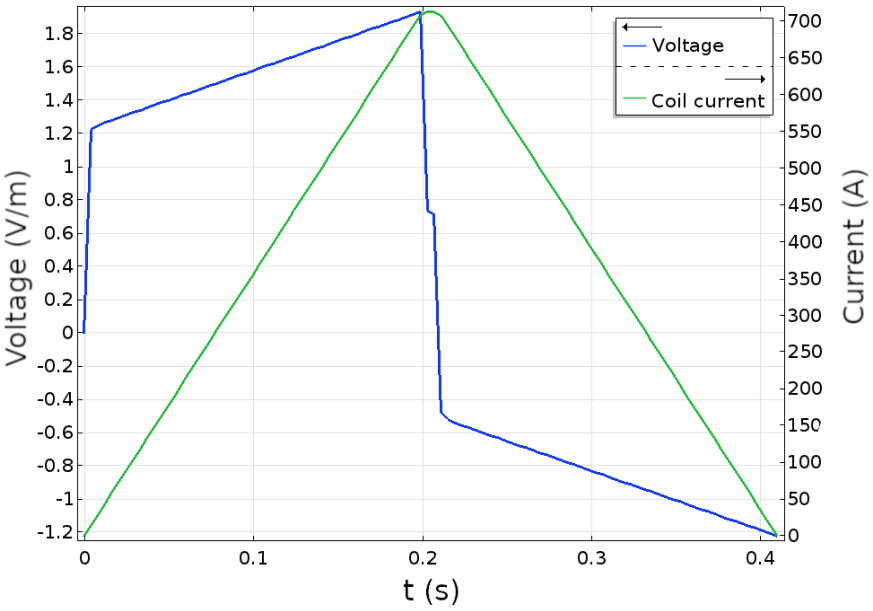

(a) Current and voltage (per meter length)

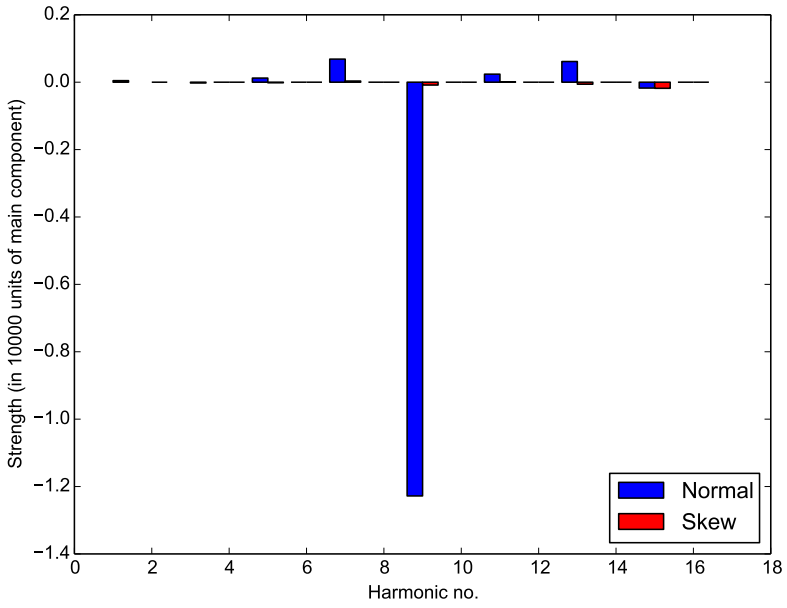

(b) Harmonics

Figure 6.103: Current and voltage (per meter length) (a) and higher order harmonics (b) of the RCS sextupole magnet. The harmonics are evaluated for a radius of 15 mm and normalized to 10000 units of the main component.

RCS Correctors Design

The requirements for the horizontal and vertical steering correctors for the RCS are summarized in Table 6.37. The correctors need to provide a maximum integrated dipole field of 6.5 mTm; the design chosen for the correctors is a simple window frame magnet as shown in Figure 6.104.

Table 6.37: Specification RCS corrector magnets.

Parameter	Value
Integrated corrector strength [10^{-3} Tm]	6.5
Corrector Inscribed radius (good field) [m]	0.015
Corrector Required field quality	0.01
Corrector physical length [m]	0.175
Corrector physical width [m]	0.2
Corrector physical height [m]	0.2
Weight iron [kg]	8.3
Weight coil [kg]	18.4
Gap height [mm]	90

The corrector shown in Figure 6.104 fits in a longitudinal space of about 0.175 m. The peak current density in the excitation coils is 4 A/mm^2; the corrector can therefore be air-cooled.

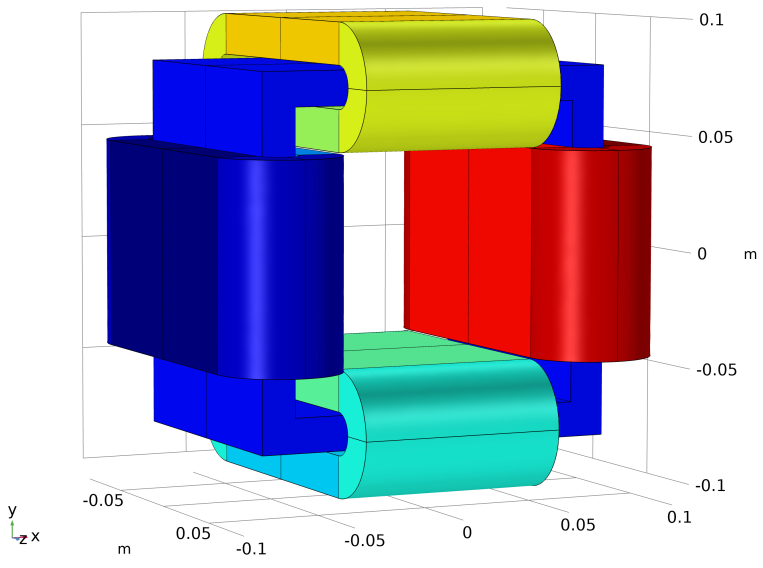

Figure 6.104: Geometry of the RCS corrector magnet

Table 6.38: Normal (B_n) and skew (A_n) harmonics of the Q2PF magnet.

n	B_n	A_n
1	10000	10000
2	-0.01	-0.01
3	147.4	147.4
4	0.01	0.01
5	3.63	3.63
6	0.0	0.0
7	-0.07	-0.07
8	0.0	0.0
9	0.0	0.0
10	0.0	0.0

Table 6.38 shows the integrated normal and skew multipoles of the corrector at a radius of 15 mm, normalized to 10000 units of the dipole component. As shown in the Figure, the highest expected multipole component is the sextupole component with 150 units, which is equivalent to a field quality of about 1.5%.

The electrical specifications of the RCS corrector are shown in Table 6.39. The expected inductance of each corrector is 0.02 H; the voltage drop is mostly resistive assuming a 3 mm round conductor and the design ramp rate of 200 ms. The peak current is about 35 A. The corrector can be air-cooled; the power dissipation per corrector is 63 W at full excitation (DC).

Power Dissipation RCS Magnets

The power dissipation of all RCS magnets is shown in Figure 6.105. The calculation excludes the core losses, which are expected to be a fraction of the total losses. Also not included are the losses in the busbars and current leads.

Faster Ramp Rates

If required the outlined magnet solutions can be ramped at a faster rate than 200 ms. Simulations confirm that a linear ramp of 100 ms is well possible. The largest change is the required voltage to drive the magnets; even at these frequencies the losses are not eddy current dominated, so the overall power dissipation decreases due to the shorter pulse length.

Table 6.39: Electrical specification RCS corrector magnet.

Parameter	Value
Cross-section [mm^2]	18×90
Cross-section [mm^2]	1620
Current density (peak, av) [A/mm^2]	4.0
Ampere turns per coil [A]	6480
Packing fraction	0.8
Power Loss 200ms pulse [W]	63
Conductor diameter [m]	0.003
Wire length [m]	318
Resistance DC hor./vert. [Ω]	0.77
Current [A]	35.34
Voltage DC, peak [V]	13.7
Magnetic energy (both correctors) [J]	26
Inductance hor./vert. [H]	0.02
Rise time ramp [s]	0.2
dI/dt [A/s]	176
Voltage AC hor./vert. [V]	3.68

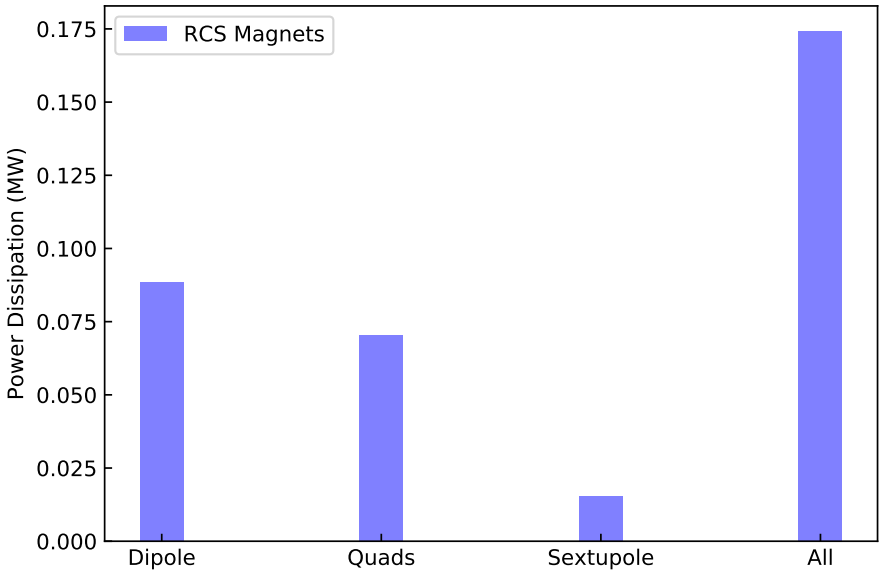

Figure 6.105: Power dissipation of the RCS magnets.

6.3 Power Supply Systems

6.3.1 RCS Magnet Power Supplies

Introduction to RCS Magnet Power Supplies

There are four different type magnet designs used for the Rapid Cycling Synchrotron (RCS). Table 6.40 lists the parameters of these magnets. Tables 6.41 lists all the power supplies needed and their parameters. Table 6.44 lists the magnets and power supplies in the Arcs and the magnets and power supplies in the straight sections as specified by physics.

There are, a total of 870 power supplies needed for the EIC RCS: 2 dipole supplies in series, 2 arc quadrupole supplies (1 focusing 1 defocusing), 4 arc sextupole supplies, 34 quadrupoles supplies, 552 vertical correction power supplies and 276 horizontal correction power supplies. All these supplies will be four quadrant switch mode converters and will produce pulsed current with rise and fall times of 100 ms, a flattop of 10 ms, for 18 GeV and 270 ms for 5 GeV. There will be two front porches in the current of every power supply. The first front porch will at 400 MeV and its flat top time will be 320 ms. The second front porch will be at 1.8 GeV and its flat top time will be 90 ms. The repetition rate will be 1 Hz. The repeatability of each power supply shall be no worse than 0.1%.

The transport line power supplies from the RCS to the storage ring are not included in this section. Magnet Eddie current losses and core loses are not included since they are relatively insignificant. The power supply and magnet parameters as well as the required cable lengths and estimated power losses are given in tables 6.41 to 6.43. The average power dissipated in the cables, the magnets and the power supplies and the approximate space requirements for each power supply are also given in tables 6.42. Note the circumference of RHIC is 3.96 km (2.46 miles). The average bending radius in the arcs is 380 m and the length of a straight section 280 m. The RHIC tunnel has a sixfold periodicity with six arcs and six straight sections.

Table 6.40: List of magnets and their parameters.

Magnet type	Resistance per magnet [mΩ]	Inductance per magnet [mH]	Peak current [A]	RMS current [A]	Power per magnet [W]
Dipole	0.37	0.32	2000	558	113.81
Quadrupole	0.83	0.77	1064	296	72.51
Sextupole	0.517	0.163	712.5	199	20.48
Corrector	1530	35.28	10	2.8	12

Table 6.41: List of power supplies and their parameters. T=1 s, the dipole supply, consists of 2 dipole supplies in series. (100 ms rise time, copper cable, 18 GeV, T=1 s).

Power Supply	Mag /PS	PS Qty	Input Volt. [V]	Resist. /Mag [mΩ]	Induc. /Mag [mH]	Tot. mag. res./ps [Ω]	Tot. mag. ind./PS [H]	Cable type kcmill/leg	Cable Res. /1000 ft [Ω]	Cable Res./PS [Ω]	PS I_{peak} [A]	PS V_{peak} [V]
Dipole	384	1	460	0.40	0.32	0.1536	0.1221	2, 444	0.0252	0.340	2000	3429.44
QD	180	1	460	0.83	0.77	0.1494	0.1386	1, 535	0.0209	0.526	1064	2192.87
QF	174	1	460	0.83	0.77	0.1444	0.1340	1, 535	0.0209	0.526	1064	2138.41
QD0 to QD8	8	9	460	0.83	0.77	0.0066	0.0062	1, 535	0.0209	0.331	1064	424.62
QDI0 to QDI8	4	9	460	0.83	0.77	0.0033	0.0031	1, 535	0.0209	0.150	1064	195.70
QF1 to QF7	8	7	460	0.83	0.77	0.0066	0.0062	1, 535	0.0209	0.331	1064	424.62
QFI1 to QFI7	4	7	460	0.83	0.77	0.0033	0.0031	1, 535	0.0209	0.150	1064	195.70
QF8	4	1	460	0.83	0.77	0.0033	0.0031	1, 535	0.0209	0.331	1064	388.31
QDI9	2	1	460	0.83	0.77	0.0017	0.0015	1, 535	0.0209	0.150	1064	177.55
SX[a]	90	4	460	0.52	0.16	0.0465	0.0147	1, 535	0.0209	0.526	712.5	512.14
CH[b] and CV[c]	1	828	120	1530	35.28	1.53	0.0353	1, 10AWG/leg		2.5	10	43.83

[a] SX1, SX2, SX3, SX4
[b] CH1 to CH276
[c] CV1 to CV552

Table 6.42: List of power supplies and their parameters continuation.

Power Supply	Mag /PS	PS Qty	PS I_{RMS} [A]	Input P_{ave}/PS [kW]	Tot Input Avg Pwr [kW]	Power /Mag [W]	Tot Mag Power [kW]	Input cur./PS [A]	Cable pwr./PS [kW]	Cable pwr in all PS [kW]	Loss /PS [kW]	Tot PS Loss [kW]
Dipole	384	1	558	192.11	192.11	124.55	47.83	241.41	105.86	105.86	38.42	38.42
QD	180	1	296	73.92	73.92	72.72	13.09	92.89	46.05	46.05	14.78	14.78
QF	174	1	296	73.38	73.38	72.72	12.65	92.21	46.05	46.05	14.68	14.68
QD0 to QD8	8	9	296	36.96	332.64	72.72	5.24	46.44	28.99	260.88	7.39	66.53
QDI0 to QDI8	4	9	296	16.77	150.94	72.72	2.62	21.07	13.13	118.13	3.35	30.19
QF1 to QF7	8	7	296	36.96	258.72	72.72	4.07	46.44	28.99	202.90	7.39	51.74
QFI1 to QFI7	4	7	296	16.77	117.40	72.72	2.04	21.07	13.13	91.88	3.35	23.48
QF8	4	1	296	36.60	36.60	72.72	0.29	45.99	28.99	7.32	7.32	
QDI9	2	1	296	16.59	16.59	72.72	0.15	20.85	13.13	13.13	3.32	3.32
SX[a]	90	4	199	28.32	113.28	20.47	7.37	35.59	20.81	83.25	5.66	22.66
CH[b] and CV[c]	1	828	2.8	0.04	32.70	12	9.93	0.33	0.02	16.23	0.01	6.54
Total PS	869											
Total dipoles	384				Tot input		Tot mag			Tot cable		Tot PS
Total quadrupoles	546				Pwr [kW]		Pwr [kW]			Pwr [kW]		Loss kW
Total sextupoles	360				1398.27		105.27			1013.35		279.65
Total corr. mag.	558											

[a] SX1, SX2, SX3, SX4
[b] CH1 to CH276
[c] CV1 to CV552

Table 6.43: List of power supplies and cables to be purchased, T=1 s. (100 ms rise time, copper cable, 18 GeV 2 Dipole supplies).

Power Supply	Mag /PS	PS Qty	PS Curr [A]	PS V(+/-) [V]	Cap Bank [F]	Cap Bank [V]	Cable Length [km]	Cable Type copper	Tot Cable [Ω]/PS	Parallel cables /leg	Cap Bank Energy [J]	Total Cables in & out
Dipole 1[a]	192	1	2000	1800	0.3	2500	8.22	2,444/leg	0.170	2	937500	4
Dipole 2[a]	192	1	2000	1800	0.3	2500	8.22	2,444/leg	0.170	2	937500	4
QD	180	1	1100	2300	0.25	2500	7.66	535 kcmill	0.526	1	781250	2
QF	174	1	1100	2300	0.25	2500	7.66	535 kcmill	0.526	1	781250	2
QD0 to QD8	8	9	1100	500	0.1	700	43.42	535 kcmill	0.331	1	24500	18
QDI0 to QDI8	4	9	1100	300	0.1	500	19.66	535 kcmill	0.150	1	12500	18
QF1 to QF7	8	7	1100	500	0.1	700	33.77	535 kcmill	0.331	1	24500	14
QFI1 to QFI7	4	7	1100	300	0.1	500	15.29	535 kcmill	0.150	1	12500	14
QF8	4	1	1100	500	0.1	700	4.82	535 kcmill	0.331	1	24500	2
QDI9	2	1	1100	300	0.1	500	2.18	535 kcmill	0.150	1	12500	2
SX[b]	90	4	720	600	0.2	700	30.66	535 kcmill	0.526	1	49000	8
CH[c] and CV[d]	1	828	10	50	0.1	140	n/a		2.5	1	980	1656

Total PS	869
Total dipoles	192
Total quadrupole	546
Total sextupoles	360
Total corr. mag.	558

444 kcmill cable [km]	530 kcmill cable [km]		#10 AWG (2) copper [km]	#10 AWG tot cables	Tot cables
16.45	165.152		207	1656	88

[a] Dipole 1 and Dipole 2 are in series
[b] SX1, SX2, SX3, SX4
[c] CH1 to CH276
[d] CV1 to CV552

Table 6.44: List of magnets and power supplies for RCS.Break down between arcs and the two large detector bypass straight sections and the four smaller bypass straight sections.

	No. of Power Supplies	No. of Magnets	PS name
Dipole Magnets in Arcs and Straights			
Dipoles	1	384	Standard Dipole
Arc Quadrupoles and Sextupoles			
30 QD quads per arc $\times$6 arcs	1	180	QD
29 QF quads per arc $\times$6 arcs	1	174	QF
15 SX1 sext. per arc $\times$6 arcs	1	90	SX1
15 SX2 sext. per arc $\times$6 arcs	1	90	SX2
15 SX3 sext. per arc $\times$6 arcs	1	90	SX3
15 SX4 sext. per arc $\times$6 arcs	1	90	SX4
Straight Section Quads, Small/Large Bypass			
2 QD0 per sec. $\times$ 4 small /2 large	2	8/4	QD0, QDI0
2 QD1 per sec. $\times$ 4 small /2 large	2	8/4	QD1, QDI1
2 QF1 per sec. $\times$ 4 small /2 large	2	8/4	QF1, QFI1
2 QD2 per sec. $\times$ 4 small /2 large	2	8/4	QD2, QDI2
2 QF2 per sec. $\times$ 4 small /2 large	2	8/4	QF2, QFI2
2 QD3 per sec. $\times$ 4 small /2 large	2	8/4	QD3, QDI3
2 QF3 per sec. $\times$ 4 small /2 large	2	8/4	QF3, QFI3
2 QD4 per sec. $\times$ 4 small /2 large	2	8/4	QD4, QDI4
2 QF4 per sec. $\times$ 4 small /2 large	2	8/4	QF4, QFI4
2 QD5 per sec. $\times$ 4 small /2 large	2	8/4	QD5, QDI5
2 QF5 per sec. $\times$ 4 small /2 large	2	8/4	QF5, QFI5
2 QD6 per sec. $\times$ 4 small /2 large	2	8/4	QD6, QDI6
2 QF6 per sec. $\times$ 4 small /2 large	2	8/4	QF6, QFI6
2 QD7 per sec. $\times$ 4 small /2 large	2	8/4	QD7, QDI7
2 QF7 per sec. $\times$ 4 small /2 large	2	8/4	QF7, QFI7
2 QD8 per sec. $\times$ 4 small /2 large	2	8/4	QD8, QDI8
1 QF8 per sec. $\times$ 4 small /2 large	2	4/2	QF8, QFI8
Correctors			
1 corrector per quad	828	276,552	HCorr, VCorr
Total number of power supplies	869		
Dipole	384		
Quadrupole	552		
Sextupole	360		
Correctors	828		

RCS Main Dipole Power Supplies

There are two types of dipole power supplies required for the RCS connected in series and in series with all 382 dipole magnets. Power supply 1 will be current regulated and power supply 2 will be voltage regulated. The peak current will be 2000 A. The period to repeat this waveform will be one sec. Figure 6.106 displays the Dipole Power supplies and magnet, connections as well as the building, where the power supplies will be housed. These power supplies will be water cooled. The power supplies will be switch mode four quadrant power supplies to regulate at 0 current. The current repeatability of these supplies will be 0.1% or better of maximum current.

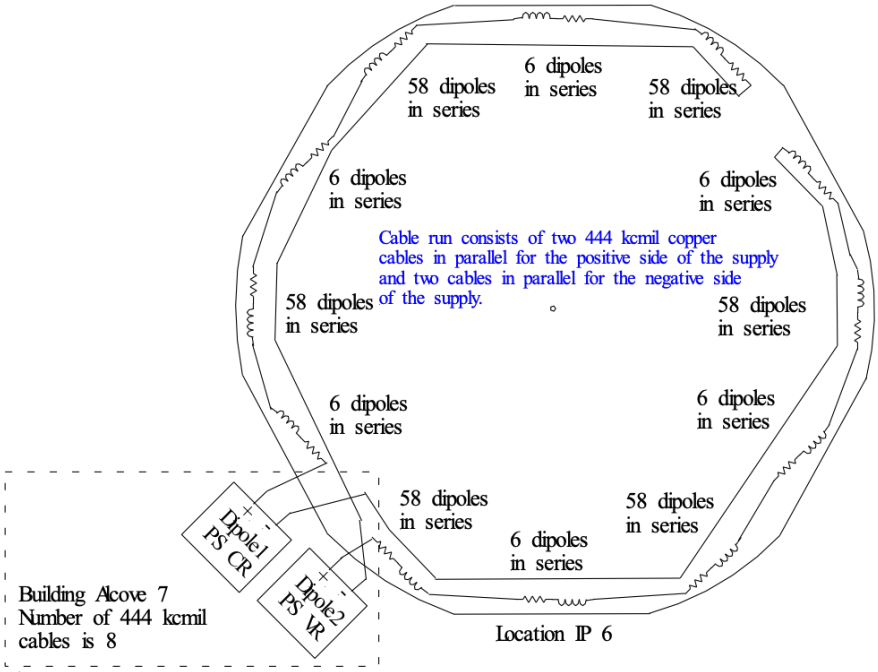

Figure 6.106: Dipole Power supplies and magnet, connection diagram.

The planned cable run to connect the power supplies to the magnets and the connection between magnets, consists of two parallel connected 444 kcmil copper cables for both the supply and return connections. Parallel cable runs are used to minimize the cable resistance and corresponding voltage drops. Each dipole power supply will have a capacitor bank of 0.3 F where energy is drawn, when we are pulsing the magnets. Each capacitor bank will be charged to 2300 V. Also, for every power supply there will be a front-end power regulator which will maintain the input average power constant and stop charging the capacitor banks, when the voltage gets to 2300 V. Figure 6.107, displays the Magnet current, power supply voltages, and capacitor bank voltages for the dipole power supplies at 5 GeV. The field will stay at an injection energy (400 MeV) for 320 ms and then ramp to 1.8 GeV. It will stay there for 90 ms. Then it will go to 5 GeV and it will stay there for 270 ms.

The ramp rate will be the same and it will be 20,000 A/sec. The period to repeat this waveform will be one sec. The average input power for both dipole supplies including losses will be 60 kW.

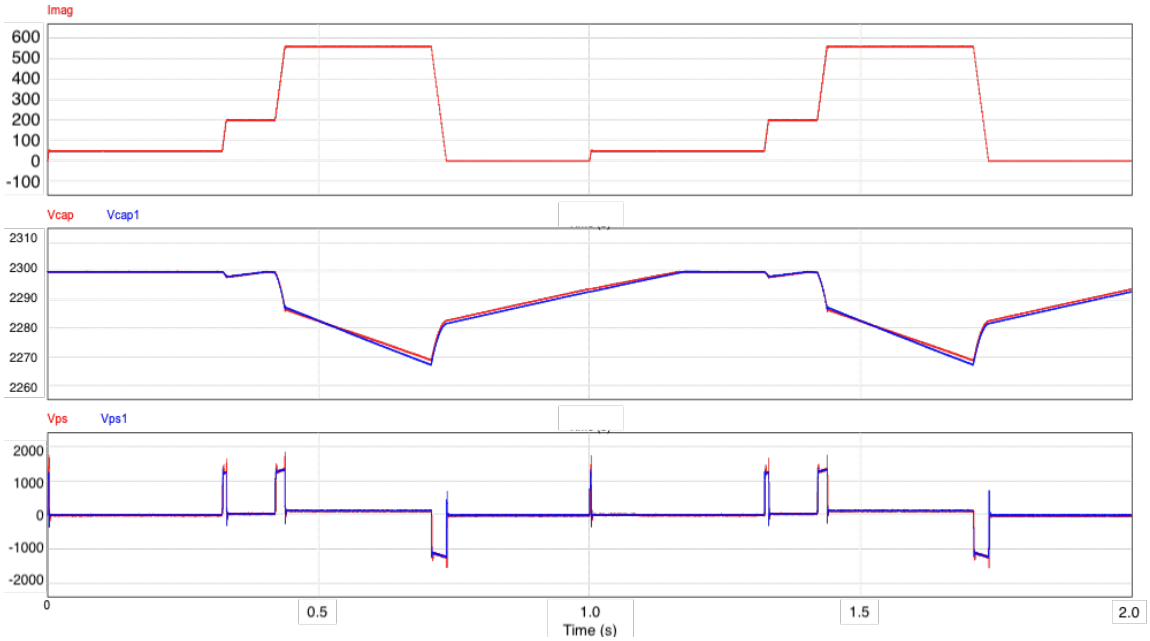

Figure 6.107: Simulation of dipole supplies at 5 GeV: Magnet current (top), power supply voltages (middle), and capacitor bank voltages (bottom) vs. time (s). The period is 1 s.

Figure 6.108, displays the Magnet current, power supply voltages, and capacitor bank voltages for the dipole power supplies at 18 GeV. The field will stay at an injection energy (400 MeV) for 320 ms and then ramp to 1.8 GeV. It will stay there for 90 ms. Then it will go to 18 GeV and it will stay there for 10 ms. The ramp rate everywhere in the cycle will be the same and it will be 20,000 A/sec. The period to repeat this waveform will be one sec. The average input power for both dipole supplies including losses will be 192 kW.

RCS Arc Quadrupole Power Supplies

There are two identical arc quadrupole power supplies. One supply drives 174 focusing quadrupole magnets connected in series and the other drives 180 defocusing quadrupole magnets connected in series. The power supplies will generate current pulses with a peak current of 1100 A. The period to repeat this waveform will be one sec. There are 29 focusing and 30 defocusing quadrupole magnets in each of the 6 arcs. These power supplies will be water cooled. The power supplies will be switch mode four quadrant power supplies to have the ability to regulate at 0 current. The current repeatability of these supplies will be 0.1% or better of maximum current. The period to repeat this waveform will be one sec.

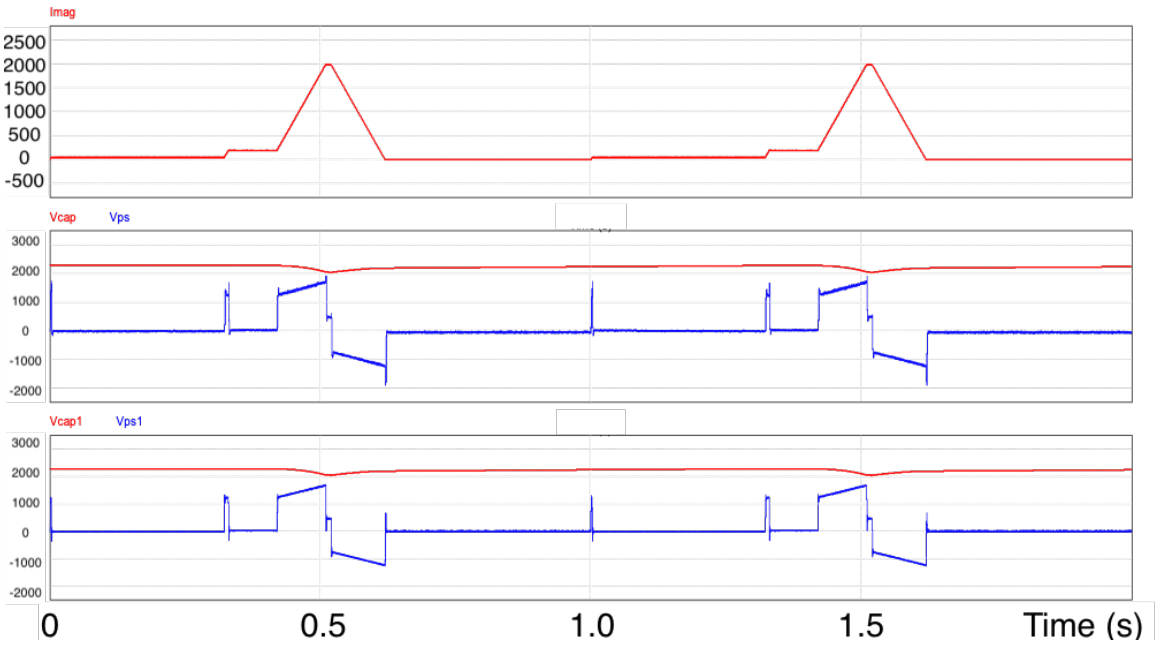

Figure 6.108: Simulation of Dipole supplies at 18 GeV: Magnet current (top), power supply voltages (middle), and capacitor bank voltages (bottom) vs. time (s). The period is 1 s.

Each type magnet string will be connected, with one 535 kcmil copper cable for both the supply and return connections. Figure 6.109 shows the connections of the arc quadrupole power supplies and magnets, as well as the building location. These power supplies will have a front-end regulator with capacitive storage to minimize power line fluctuations. The peak magnet power will come from the energy stored, in a 0.3 F capacitor bank charged to 2600 volts.

Figure 6.110, displays the Magnet current, power supply voltages, and capacitor bank voltages for the Arc Quad defocusing power supply at 5 GeV. The field will stay at an injection energy (400 MeV) for 320 ms and then ramp to 1.8 GeV. It will stay there for 90 ms. Then it will go to 5 GeV and it will stay there for 270 ms. The ramp rate will be the same and it will be 10,000 A/sec. The period to repeat this waveform will be one sec. The average input power for both dipole supplies including losses will be 20 kW.

Figure 6.111, displays the Magnet current, power supply voltages, and capacitor bank voltages for the Arc Quad defocusing power supply at 18 GeV. The field will stay at an injection energy (400 MeV) for 320 ms and then ramp to 1.8 GeV. It will stay there for 90 ms. Then it will go to 18 GeV and it will stay there for 10 ms. The ramp rate will be the same and it will be 10,000 A/sec. The period to repeat this waveform will be one sec. The average input power for the arc quad supply QD including losses will be 74 kW.

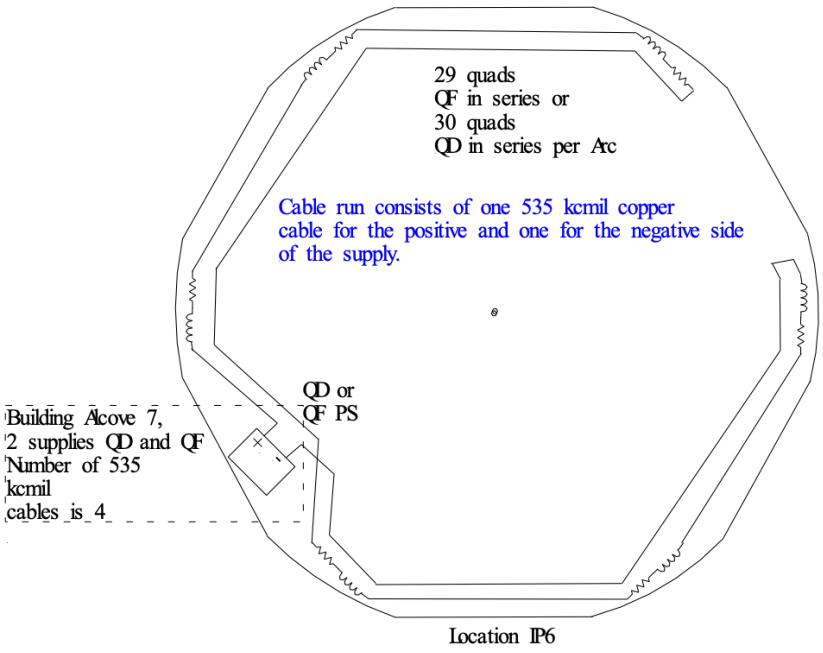

Figure 6.109: Arc Quad focusing or defocusing, Power supply, magnet, block diagram.

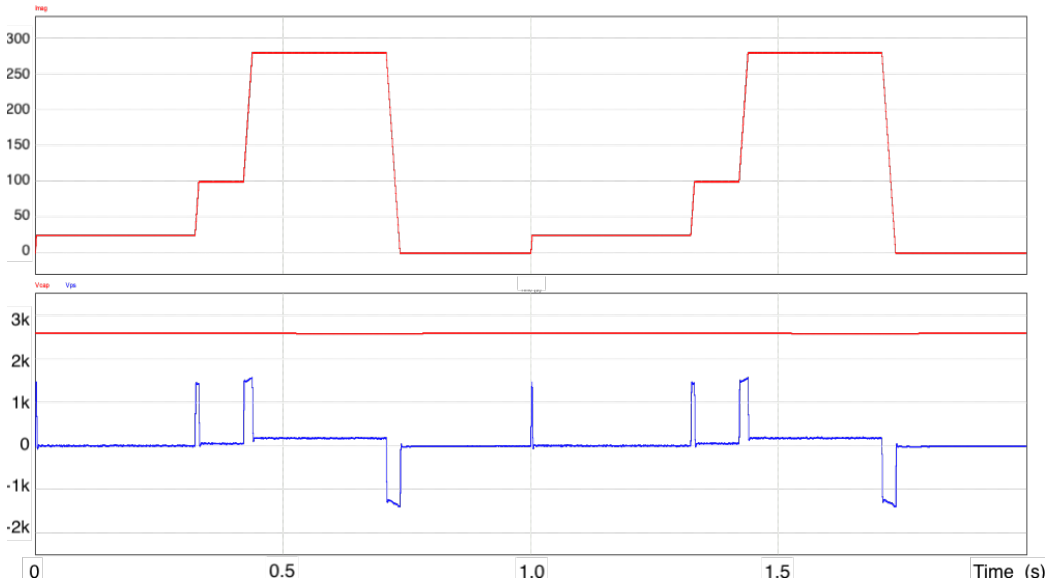

Figure 6.110: Simulation of Arc Quad defocusing power supply at 5 GeV: Magnet current, power supply voltage, and capacitor bank voltage, Period 1 s.

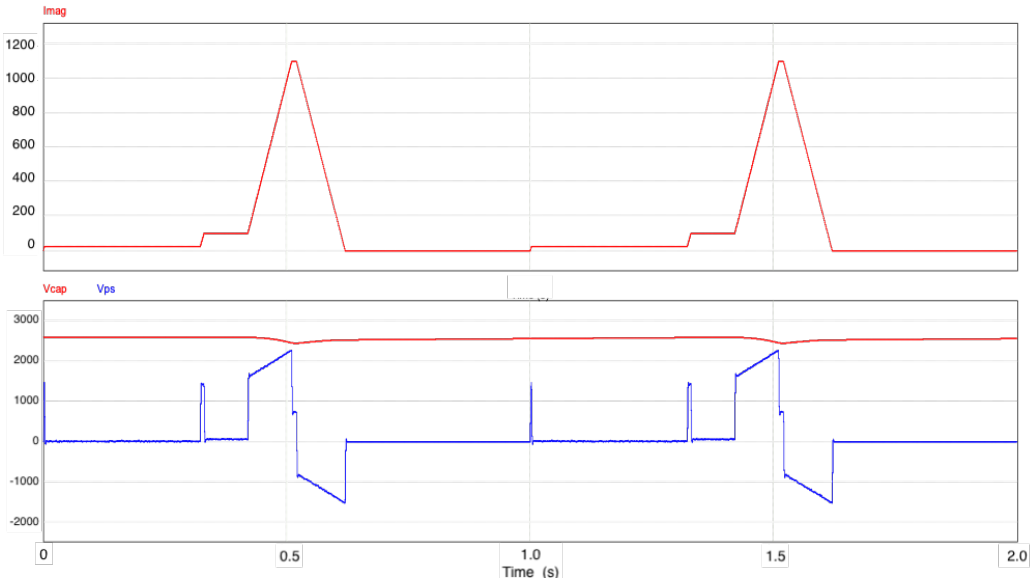

Figure 6.111: Simulation of Arc Quad defocusing power supply at 18 GeV : Magnet current, power supply voltage, and capacitor bank voltage, Period 1 s.

RCS Straight Section Quadrupole Power Supplies

There are 34 straight section quadrupole power supplies, 15 focusing and 19 defocusing. The power supplies will generate current pulses with a peak current of 1100 A. The period to repeat this waveform will be one sec. Tables 6.41 and 6.44 show the details of these power supplies and the magnets associated with each power supply. The power supplies will be switch mode four quadrant power supplies to have the ability to regulate at 0 current. The current repeatability of these supplies will be 0.1% or better of maximum current. These power supplies will be air cooled supplies. Each type magnet string will be connected, with one 535 kcmil copper cable for both the supply and return connections. Figure 6.112 shows the connections of the straight quadrupole power supplies and magnets, as well as the building locations.

The topology of the arc quadrupole QDI9 is the same except there are 2 magnets connected in series for this power supply. The power supply, magnet parameters and cable resistance are shown in Table 6.42. These power supplies will have a front-end regulator with capacitive storage to minimize power line fluctuations. The peak magnet power will come from the energy stored in a 0.15 F capacitor bank charged to either 700 volts or 500 volts depending on the power supplies.

Figure 6.113, displays the Magnet current, power supply voltages, and capacitor bank voltages for the straight Quads QD0 to QD8 or QF1 to QF7 power supplies at 5 GeV. The field will stay at an injection energy (400 MeV) for 320 ms and then ramp to 1.8 GeV. It will stay there for 90 ms. Then it will go to 5 GeV and it will stay there for 270 ms. The ramp rate will be the same and it will be 10,000 A/sec. The period to repeat this waveform will

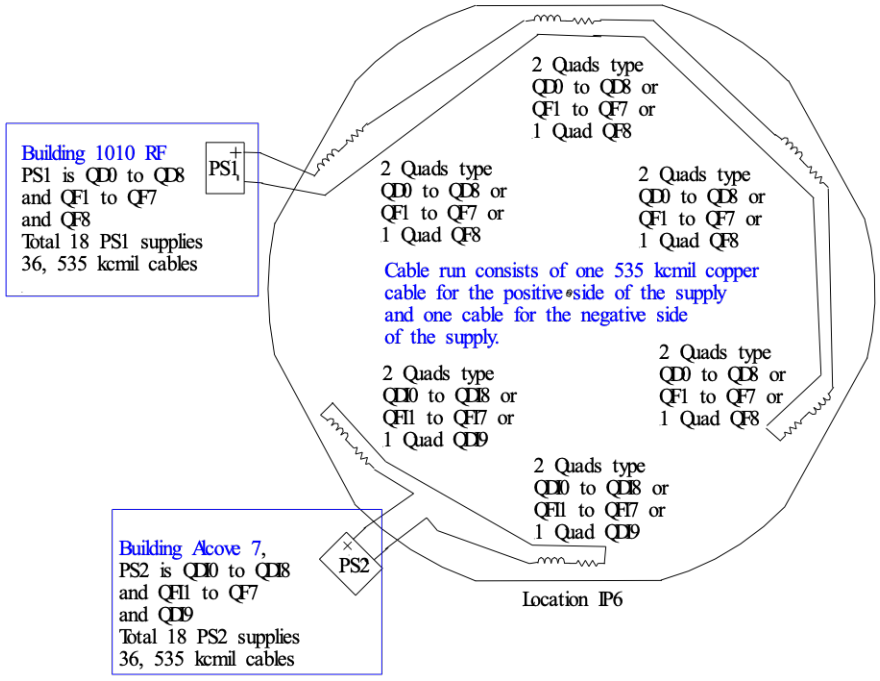

Figure 6.112: Straight Section Quads power supplies, magnets, building location, block diagram.

be one sec. The average input power for the straight Quads QD0 supply including losses will be 10 kW.

Figure 6.114, displays the Magnet current, power supply voltages, and capacitor bank voltages for the straight Quads QD0 to QD8 or QF1 to QF7 power supplies at 18 GeV. The field will stay at an injection energy (400 MeV) for 320 ms and then ramp to 1.8 GeV. It will stay there for 90 ms. Then it will go to 18 GeV and it will stay there for 10 ms. The ramp rate will be the same and it will be 10,000 A/sec. The period to repeat this waveform will be one sec. The average input power the straight Quads QD0 supply including losses will be 37 kW.

Figure 6.115, displays the Magnet current, power supply voltages, and capacitor bank voltages for the straight Quads QDI0 to QDI8 or QFI1 to QFI7 power supplies at 5 GeV. The field will stay at an injection energy (400 MeV) for 320 ms and then ramp to 1.8 GeV. It will stay there for 90 ms. Then it will go to 5 GeV and it will stay there for 270 ms. The ramp rate will be the same and it will be 10,000 A/sec. The period to repeat this waveform will be one sec. The average input power for the straight Quads QDI0 supply including losses will be 5.1 kW.

Figure 6.116, displays the Magnet current, power supply voltages, and capacitor bank voltages for the straight Quads QDI0 to QDI8 or QFI1 to QFI7 power supplies at 18 GeV. The field will stay at an injection energy (400 MeV) for 320 ms and then ramp to 1.8 GeV.

It will stay there for 90 ms. Then it will go to 18 GeV and it will stay there for 10 ms. The ramp rate will be the same and it will be 10,000 A/sec. The period to repeat this waveform will be one sec. The average input power for the straight Quads QDI0 supply including losses will be 33 kW.

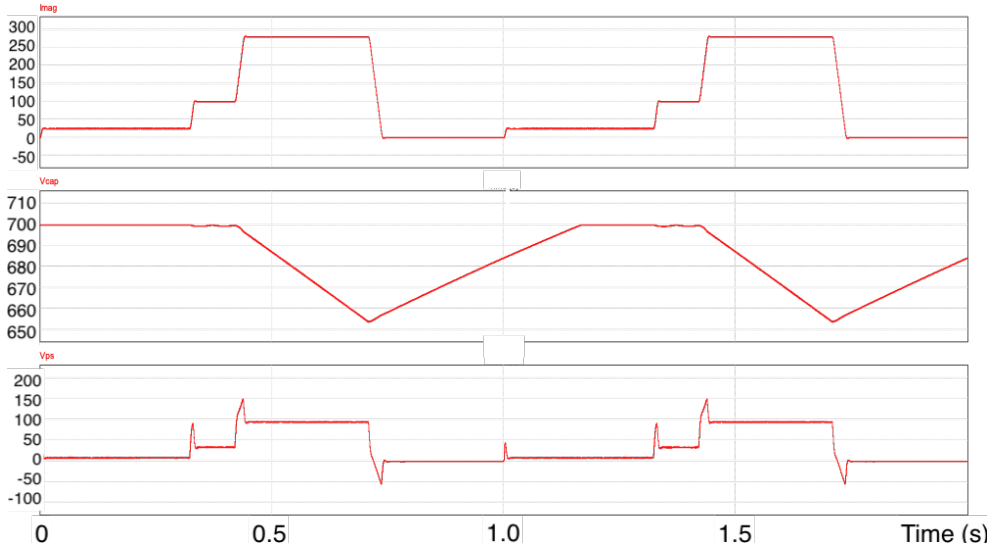

Figure 6.113: Simulation of straight Quad QD0 to QD8 or QF1 to QF7 power supplies at 5 GeV: Magnet current, capacitor bank voltage and power supply voltage, Period 1 s. PS's in Alcove 5.

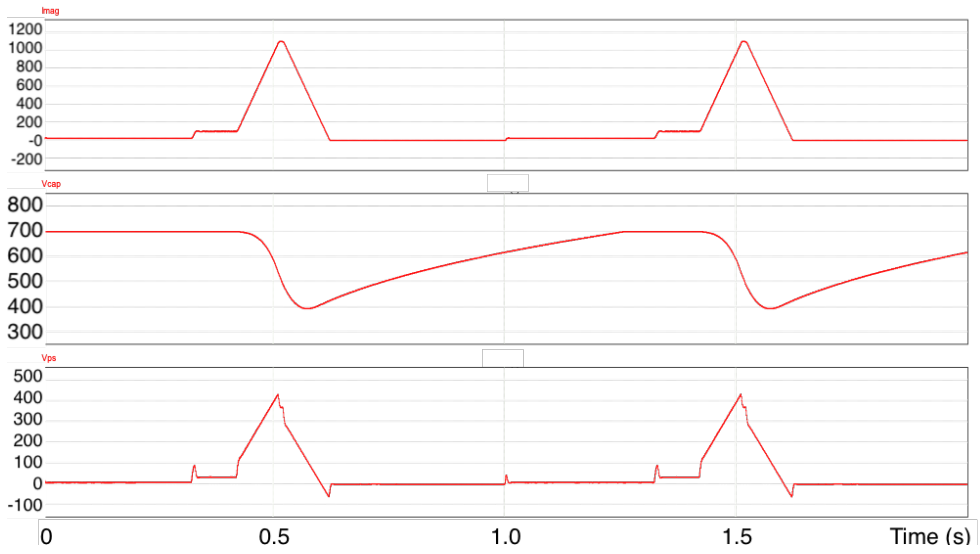

Figure 6.114: Simulation of straight Quad QD0 to QD8 or QF1 to QF7 power supplies at 18 GeV: Magnet current, power supply voltage, and capacitor bank voltage, Period 1 s. PS's in Alcove 5.

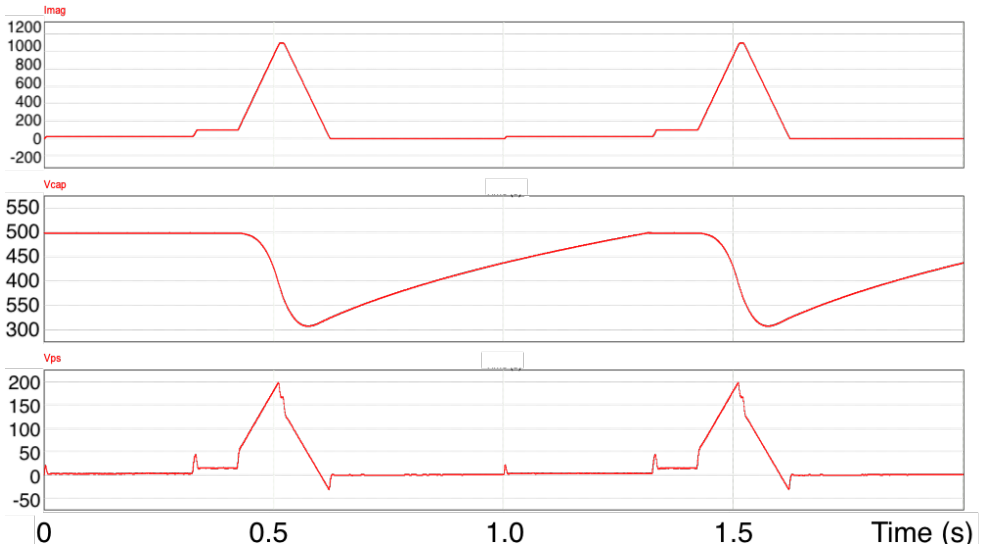

Figure 6.115: Simulation of straight Quad QDI0 to QDI8 or QFI1 to QFI7 power supplies at 5 GeV. Magnet current, power supply voltage, capacitor bank voltage. Period 1 s. PS's in Alcove 7.

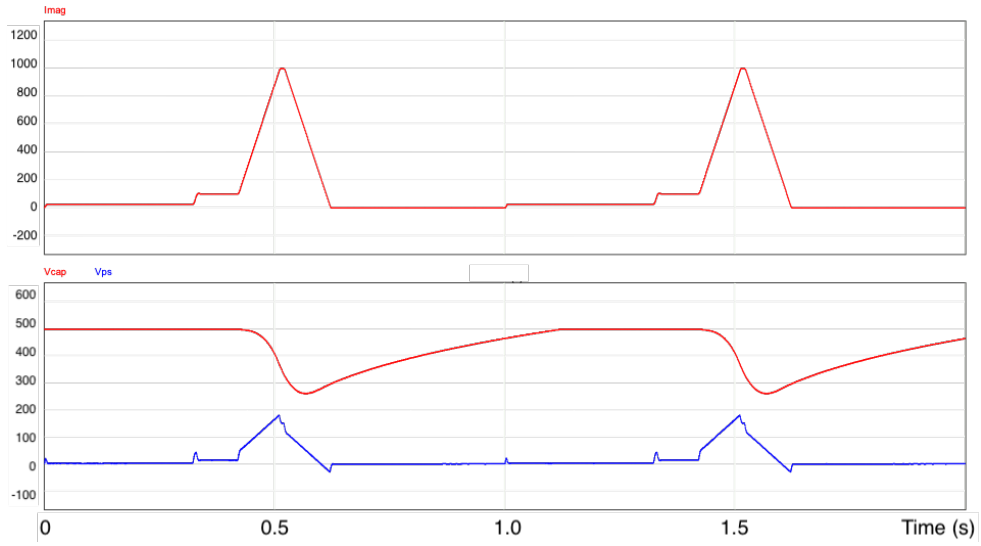

Figure 6.116: Simulation of straight Quad QDI0 to QDI8 or QFI1 to QFI7 power supplies at 18 GeV. Magnet current, power supply and capacitor bank voltages. Period 1 s. PS's in Alcove 7.

RCS Arc Sextupole Power Supplies

There are four identical arc sextupole power supplies. One supply drives 90 sextupole magnets connected in series, with 15 sextupole magnets per arc. These power supplies will be air cooled. The power supplies will be switch mode four quadrant power supplies to have the ability to regulate at 0 current. The current repeatability of these supplies will

be 0.1% or better of maximum current. The power supplies will generate current pulses with a peak current of 720 A. The period to repeat this waveform will be one sec. Each type magnet string will be connected, with one 535 kcmil copper cable for both the supply and return connections. Figure 6.117, shows the connections of the arc sextupole power supplies and magnets, as well as the building location.

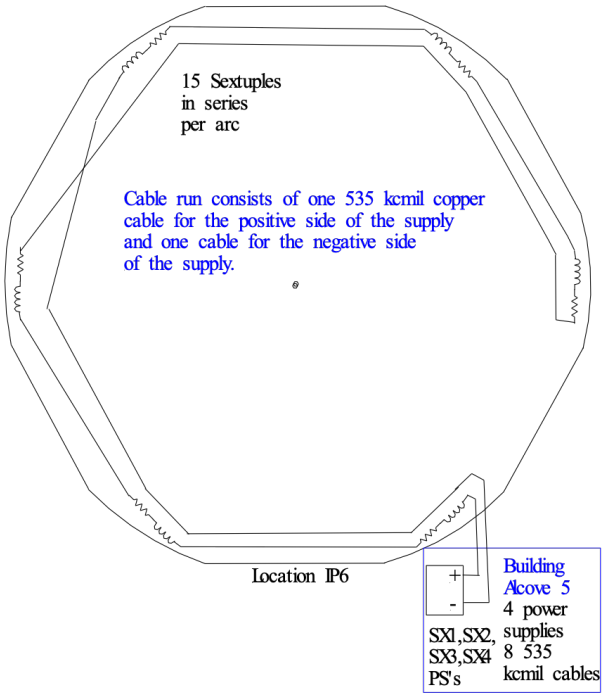

Figure 6.117: Arc sextupole power supply, magnet, block diagram.

These power supplies will have a front-end regulator with capacitive storage to minimize power line fluctuations. The peak magnet power will come from the energy stored in a 0.2 F capacitor bank charged to 700 volts.

Figure 6.118, displays the Magnet current, power supply voltages, and capacitor bank voltages for the Arc sextupole power supplies at 5 GeV. The field will stay at an injection energy (400 MeV) for 320 ms and then ramp to 1.8 GeV. It will stay there for 90 ms. Then it will go to 5 GeV and it will stay there for 270 ms. The ramp rate will be the same and it will be 7,000 A/sec. The period to repeat this waveform will be one sec. The average input power for both dipole supplies including losses will be 7.5 kW.

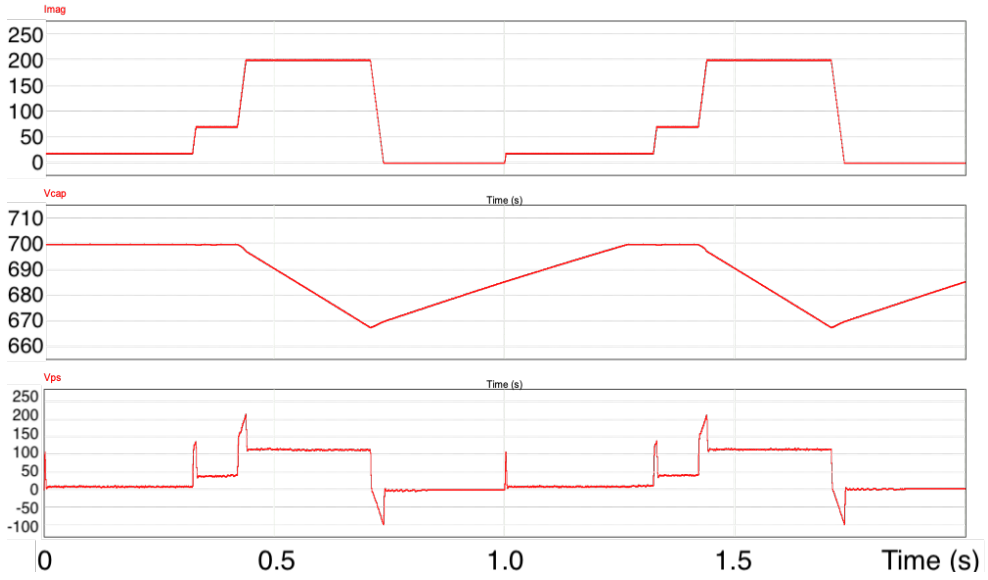

Figure 6.118: Simulation of Arc sextupole power supplies at 5 GeV. Magnet current, capacitor bank voltage and power supply voltage. Period 1 s.

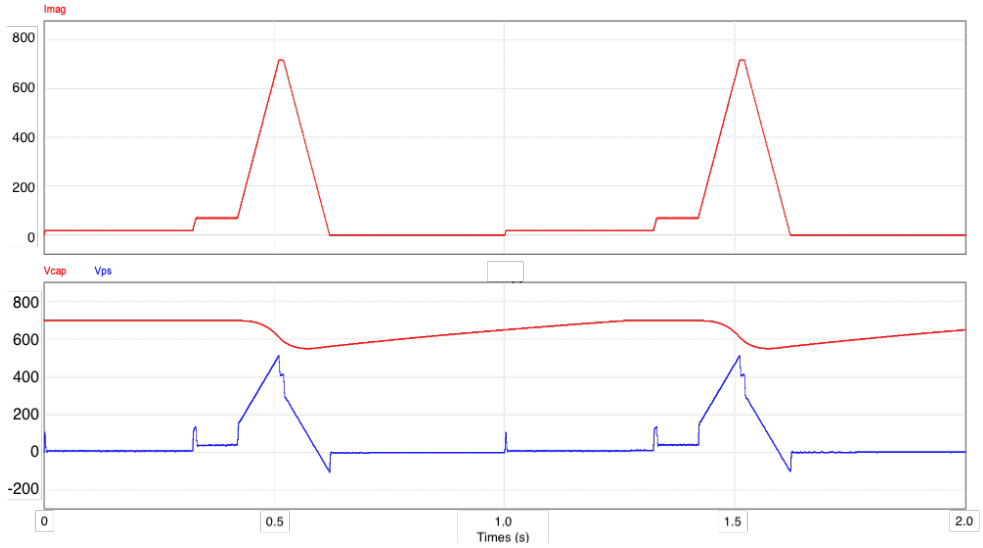

Figure 6.119: Simulation of Arc sextupole power supplies at 18 GeV. Magnet current, power supply voltage, capacitor bank voltage. Period 1 s.

Figure 6.119, displays the Magnet current, power supply voltages, and capacitor bank voltages for the Arc sextupole power supplies at 18 GeV. The field will stay at an injection energy (400 MeV) for 320 ms and then ramp to 1.8 GeV. It will stay there for 90 ms. Then it will go to 18 GeV and it will stay there for 10 ms. The ramp rate will be the same and it will be 7,000 A/sec. The period to repeat this waveform will be one sec. The average input power for the Arc sextupole power supply including losses will be 28 kW.

RCS Dipole Corrector Power Supplies

There are 828 correction power supplies. One corrector magnet and power supply per each of the 552 quadrupoles for vertical correction and 276 power supplies for horizontal correction. The power supplies will generate a peak current of +/-10 A. The power supply peak voltage will be rated at +/- 50 V. These power supplies will be housed in six new buildings around the RHIC tunnel, Alcove1, Alcove3, Alcove5, Alcove7, Alcove9, Alcove11. Figure 6.120 displays the location of all power supply buildings and their location. There will be 140 correction power supplies installed per new Alcove building, except Alcove 9, it will house 137 correction supplies. The maximum cable length between each power supply and its magnet will be 2400 feet round trip. A 10 AWG copper cable will be used per power supply. The maximum cable resistance will be 2.5 Ω.

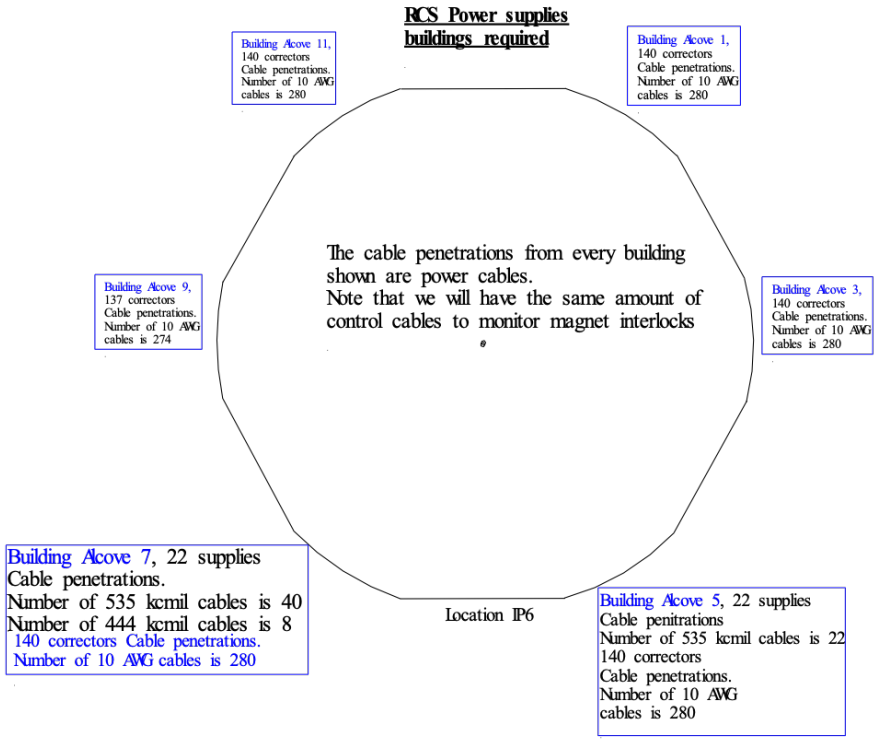

Figure 6.120: RCS Power supplies and building they are housed.

There is a front-end power regulator, which will maintain the input average power constant per 20 dc to dc converters, with a repetition rate of 1 sec. The peak magnet power comes from the energy stored in a 0.1 F capacitor bank charged to 140 volts. These power supplies will be air cooled supplies.

Figure 6.121, displays magnet current, magnet voltage, capacitor bank voltage for 20 supplies, and power supply input power for 20 supplies, at 5 GeV, period 1 sec. The field will stay at an injection energy (400 MeV) for 320 ms and then ramp to 1.8 GeV. It will stay there

for 90 ms. Then it will go to 5 GeV for maximum correction and it will stay there for 270 ms. The ramp rate will be the same and it will be 100 A/sec. The period to repeat this waveform will be one sec. The average input power for 20 dipole supplies including losses will be 375 W.

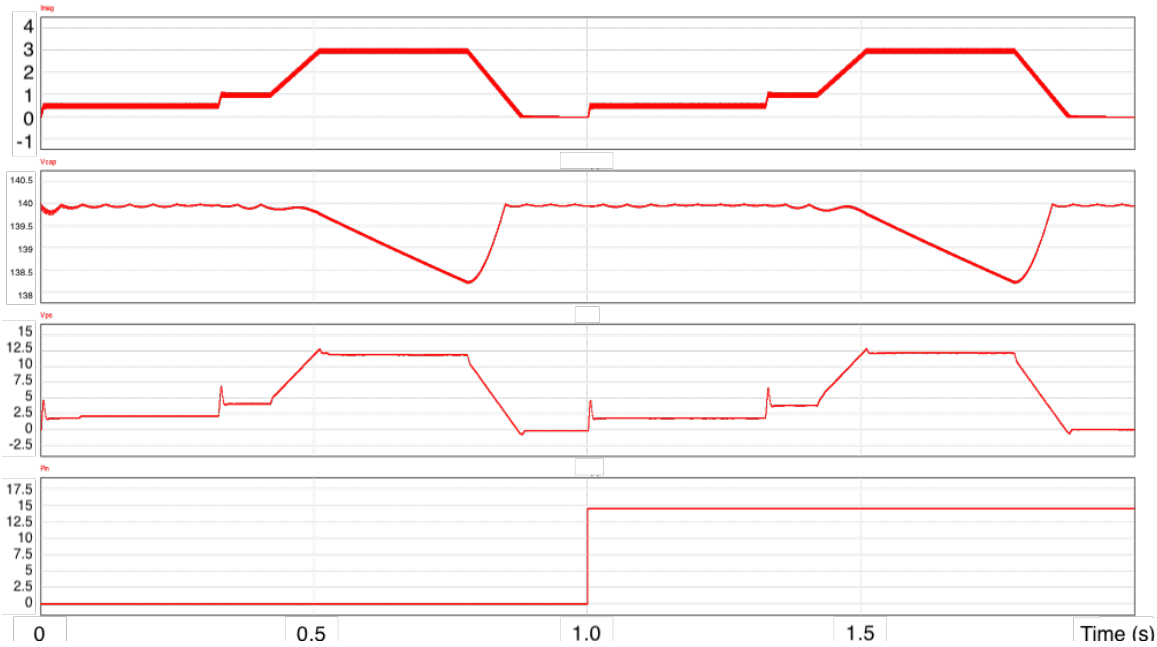

Figure 6.121: 5 GeV, Correction power supply magnet current, magnet voltage, capacitor bank voltage for 20 supplies, and power supply input power for 20 supplies, period 1 s.

Figure 6.122, displays magnet current, magnet voltage, capacitor bank voltage for 20 supplies, and power supply input power for 20 supplies, at 18 GeV, period 1 sec. The field will stay at an injection energy (400 MeV) for 320 ms and then ramp to 1.8 GeV. It will stay there for 90 ms. Then it will go to 18 GeV and it will stay there for 270 ms. The ramp rate will be the same and it will be 100 A/sec. The period to repeat this waveform will be one sec. The average input power for 20 dipole supplies including losses will be 850 W. Note also that the bandwidth of all corrector supplies should be 500 Hz. There may be a ± 1 A at 100 Hz riding on the current reference. This reference should be able to be transferred on the magnet current without any delays or distortions.

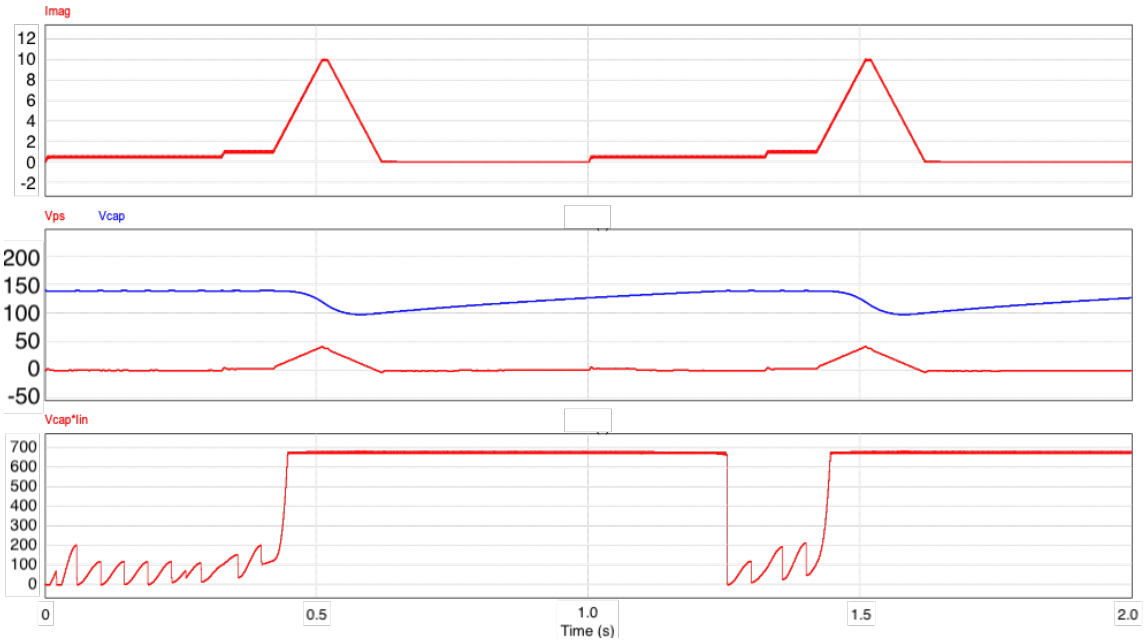

Figure 6.122: 18 GeV, Correction power supply magnet current, magnet voltage, capacitor bank voltage for 20 supplies, and power supply input power for 20 supplies, period 1 s.

Conclusion

There are 869 power supplies associated with the EIC RCS. The list of power supplies and their parameters are displayed in Tables 6.41. Table 6.43 displays the power supply ratings, the capacitor banks ratings, the type and length of all magnet cables we need in kilometers. All power supplies and cables are specified for repetition rates of 1 s. All power supplies will be switch mode four quadrant to be able to regulate at 0 current. The repeatability of all power supplies is 0.1% or better of maximum current. The current tracking during ramping up should be specified. Table 6.44 should be upgraded by the physicist. Table 6.45 displays a list of all RCS power supplies and their voltage, current and capacitor bank ratings.

Table 6.46 displays all RCS power supplies (except correctors), their building location and the approximate area needed in every building in square feet. Table 6.47 displays all RCS corrector power supplies, their building location and the approximate area needed in every building in square feet.

Table 6.45: 100 ms rise time, copper cable, 18 GeV 2 Dipole supplies.

PS name	Mag. /PS	PS No.	PS AMPS	PS VOLTS(+/-)	Cap Bank [F]	Cap Bank [V]
Dipole1	192.00	1.00	2000	1800	0.3	2300
Dipole2	192.00	1.00	2000	1800	0.3	2300
QD	180.00	1.00	1100	2300	0.25	2600
QF	174.00	1.00	1100	2300	0.25	2600
QD0 to QD8	8.00	9.00	1100	500	0.15	700
QDI0 to QDI8	4.00	9.00	1100	300	0.15	500
QF1 to QF7	8.00	7.00	1100	500	0.15	700
QFI1 to QFI7	4.00	7.00	1100	300	0.15	500
QF8	4.00	1.00	1100	500	0.15	700
QDI9	2.00	1.00	1100	300	0.15	500
SX1,SX2,SX3,SX4	90.00	4.00	720	600	0.2	700
CH1 to CH276, CV1 to CV552	1.00	828.00	10	50	0.1	140
Total power supplies	**869.00**					
Total Dipole mag.	**192.00**					
Total Quad mag.	**546.00**					
Total Sextupole mag.	**360.00**	Circumference of RHIC 2.4606 miles or 3.96 km				
Total Correction mag.	**558**	1 mile is 5280 feet				

Table 6.46: List of all RCS power supplies (except correctors), their building location dimensions, and the approximate area needed in every building in square feet. For 100 ms rise time, copper cable, 18 GeV and T=1 s.

Power Supply	PS Qty	Bld. Alcove	Cooling Type	Water ΔT [C]	GPM	Cap Bank [F]	Cap Bank V [V]	Cap Bank E [J]	PS Width [ft]	PS Depth [ft]	PS Height [ft]	Bld. Height [ft]
Dipole 1[a]	1	7	water	5.555	11.42	0.3	2500	937500	35	8	8	14
Dipole 2[a]	1	7	water	5.555	11.42	0.3	2500	937500	35	8	8	14
QD	1	7	water	5.555	7.81	0.25	2500	781250	30	8	8	14
QF	1	7	water	5.555	7.75	0.25	2500	781250	30	8	8	14
QD0 to QD8	9	5	air			0.15	700	36750	6	5	6	14
QDI0 to QDI8	9	7	air			0.15	500	18750	5	5	6	14
QF1 to QF7	7	5	air			0.15	700	36750	6	5	6	14
QFI1 to QFI7	7	7	air			0.15	500	18750	5	5	6	14
QF8	1	5	air			0.15	700	36750	6	5	6	14
QDI9	1	7	air			0.15	500	18750	5	5	6	14
SX[b]	4	5	air			0.2	700	49000	6	5	6	14
CH[c] and CV[d]	828	1-11[e]	air			0.1	140	980				

[a] Dipole 1 and Dipole 2 are in series
[b] SX1, SX2, SX3, SX4
[c] CH1 to CH276
[d] CV1 to CV552
[e] 1, 3, 5, 7, 9, 11

Table 6.47: RCS magnets and parameters.

Building Alcove	sq ft per for cor.	Rack width (in)	Per ps depth (in)	Rack height (ft)	Building height (ft)
1	252	36	36	8	14
3	252	36	36	8	14
5	252	36	36	8	14
7	252	36	36	8	14
9	252	36	36	8	14
11	252	36	36	6	14

6.3.2 Electron Storage Ring Power Supplies

The electron storage ring will be located in the existing RHIC tunnel. The magnet power supplies will be located in six new equipment houses, centrally located external to each sextant.

The elements of the storage ring power supply system will be described and grouped by function and location: arc dipoles, arc and straight section quadrupoles, arc and straight section sextupoles, and fast and slow orbit correctors. Finally, the power supply requirements for the storage ring will be summarized with power and space requirements.

ESR Arc Dipole Magnet Power Supplies

The arc dipoles are configured as 252 triplets with all the outer dipoles, D1 and D3, powered in a circuit from a single power supply. All inner dipoles, D2, are powered by a second single power supply. The maximum current and power requirements are shown in Table 6.48.

Table 6.48: Maximum current and power requirements for the dipole power supplies.

Parameter	D1 + D3	D2
Max operating current [A]	5,200	7027
Max magnet power in string [kW]	1,687	1,040
Max total power with bus [kW]	2,193	1,352
Max total voltage with bus [V]	422	192

Over a beam energy range from 5 GeV to 18 GeV, D1 + D3 will have their maximum strength at 18 GeV, but D2 will be at its maximum strength at 5 GeV. In addition, the current in D2 will change polarity below 10 GeV.

The power supply technology to be used to satisfy the magnet requirements is interleaved H-Bridge. It is a mature technology that is suited for this voltage, current, and power range.

A simplified schematic of the output stage is show in Figure 6.123. Three H-Bridges are placed in parallel, isolated by inductors. This triples the effective ripple frequency. This output design has the advantage of being capable of being put in parallel with other identical output modules to increase the current rating of the power supply.

This technology is already being used at BNL for the e-lens warm solenoids (1,100 A to 1,200 A), the e-lens octal power supply (400 A $\times$ 8), the EBIS pulsed quadrupoles (925 A), and the NSLS-II main dipole power supply (400 A). The same local manufacturer (APS, in Hicksville) that produced these has built a photovoltaic simulator for another customer, which is 4,000 A. This 4,000 A unit is comprised of two output compartments rated 2,000 A in parallel.

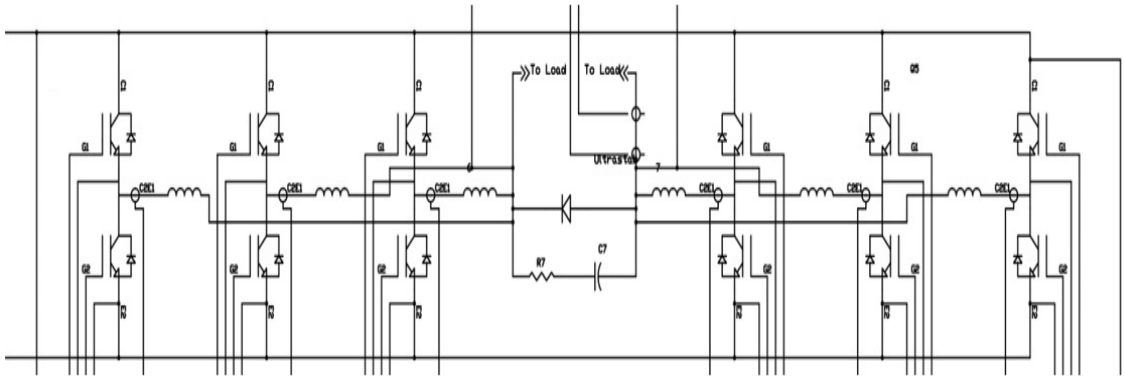

Figure 6.123: Output stage for an interleaved H-bridge power supply.

For the EIC, the power supply will be built from multiple 2 A cabinets connected in parallel. For the D1 + D3 current of 5.2 kA, three modules will be required, while four modules will be needed for the 7 kA current of D2. Each set of output modules will be controlled by electronics in a single 19″ rack.

The units will be $15'\,(\mathrm{W}) \times 4.5'\,(\mathrm{D}) \times 7'\,(\mathrm{H})$ for D1 + D3, and $20'\,(\mathrm{W}) \times 4.5'\,(\mathrm{D}) \times 7'\,(\mathrm{H})$ for D2. Each of these will be installed in one of the new sextant buildings. This particular building will be larger than the other five to accommodate these large units. In addition, the unit will require water cooling, as will the bus going from the equipment house to the tunnel.

These are the only two storage ring power supplies that will use water cooled bus. The RHIC tunnel is 3.8 km in circumference. When considering adding the distance to the equipment building, the routing around experimental areas and other obstacles, the one-way path of the bus is estimated to be 5 km. For the two arc dipole power supplies, this results in 20 km of bus carrying high currents. The circuit will consume several megawatts of power, which is most economically removed from the tunnel using cooling water.

ESR Arc and Straight Section Quadrupole Magnet Power Supplies

Altogether, there are 196 focusing arc quadrupoles (QF) and 184 defocusing arc quadrupoles (QD) in the storage ring. In each of the six arcs, there is one circuit of all QF and another of all QD quadrupoles.

There are 57 focusing straight section quadrupoles (QF) and 57 defocusing straight section quadrupoles (QD) distributed around the storage ring. Each of these is independently powered to provide the required flexibility.

Each quadrupole will consume about 3 kW, but will require different impedances to best match a power supply. The arc quadrupoles, which are designed to be in strings of up to 33 units connected in series, will run at 960 A, and have a voltage at the power supply (including cable drop) of 128 V. The straight section quadrupoles will have a ten-fold increase

in the number of turns compared to the arc quadrupoles, bringing their operating current down to 96 A. Because they are individually powered, that will, with cable drop, present a voltage on the power supply of 39 V.

The power supplies for the arc quadrupoles, with an output current of about 1 kA and a power rating of about 180 kW, are most suited to an interleaved H-Bridge design. At this power level, unlike the larger arc dipole supplies, everything fits in a single cabinet with dimensions $3.5'$ (W) $\times$ $3.5'$ (D) $\times$ $7'$ (H).

However, for the lower power units, the approach would be to buy commercial power supplies and add zero flux current sensors and an Ethernet controller.

Each of the sextant equipment buildings will house two of the arc quadrupole power supplies, one for focusing and the other for defocusing magnets. The output cables for each will be a pair of 535 kcmil cables.

In addition, there will be up to ten individual straight section power supplies in these buildings, connected to the magnet loads with AWG #2 cable.

ESR Arc and Straight Section Sextupole Magnet Power Supplies

There are 120 arc sextupoles SF, located near a QF quadrupole, and 116 arc sextupoles SD near a QD. In each arc, there is one circuit of all SF sextupoles and another of all SD sextupoles. The powering requirements for these two strings are different.

There are 36 straight section SF sextupoles and 36 straight section SD sextupoles distributed around the storage ring. Each of these is independently powered.

The powering method for the sextupoles is similar to that used for the quadrupoles. The corresponding straight section sextupole will have more turns by a factor of ten as compared to an arc sextupole. That will result in the circuit current and voltage requirements of Table 6.49.

Table 6.49: Current and voltage requirements for sextupole circuit.

Circuit	Current [A]	Voltage [V]
Arc sextupoles SF	352	57
Straight section sextupoles SF	35	29
Arc sextupoles SD	621	100
Straight section sextupoles SD	62	50

The power supplies for the arc sextupoles are still high enough in power to be best implemented as interleaved H-Bridge. But the power is low enough that some cost savings might be incurred by housing both power supplies for each sextant in a single cabinet with a common bulk power supply.

The individually powered sextupoles will use commercial power supplies with an Ethernet controller and external DCCTs.

Each of the sextant equipment buildings will house two of the arc sextupole power supplies, one for the SF sextupoles, which will use a single 535 kcmil per leg, and the other for the SD magnets, which will use a pair of 535 kcmil cables.

In addition, there will be 12 individual straight section power supplies. They will be connected to the magnet loads with AWG #8 cable for SF sextupoles and AWG #4 for SD sextupoles.

ESR Fast and Slow Dipole Corrector Magnet Power Supplies

There are 220 horizontal and 220 vertical slow dipole correctors, all of which are rated to run at a maximum of 7.85 Amps. The power supplies for these do not need to have a bandwidth any more than 100 Hz. However, they do need to have the ability to be triggered such that all correctors around the ring change simultaneously.

Additionally, there are 220 fast orbit correctors, which are rated to run at a maximum of 2 A. The power supplies for these need to have a bandwidth of at least 1 kHz.

There are several commercially available corrector power supplies with digital regulators and the capability to be triggered.

It is likely that at the required quantities, manufacturers would offer similar circuits and controls with a unit of multiple outputs. That would result in cost savings.

Ratings and Requirements

Based on the circuit power, the power supply ratings are determined. It is prudent to have 20% design margin, in both voltage and current, over the circuit requirements. This is important to the long-term reliability of the power supply.

The power supply ratings and requirements are summarized in Table 6.50. The sum of the circuit power shown is the requirement to outfit the equipment buildings. Because the power required by the D2 power supplies decreases with increasing energy, the maximum total power required during operation for the storage ring magnet power supplies is 6,895 kW instead of the 8,077 kW shown.

All the power supplies required for the storage ring are located at the sextant equipment buildings. These will house equipment from other accelerator functions as well.

The space requirements are summarized in Table 6.51. Quantities shown are per equipment building, except for the D1 / D3 power supply and the D2 power supply. There is only one each of those in the entire accelerator.

Table 6.50: Power supply ratings and power requirements.

PS Function	# of Ckts	Current [A]	Voltage [V]	Total Ckt Power [kW]
D1 / D3	1	6,200	520	2,193
D2	1	8,400	192	2,997
Arc Quadrupoles	12	1,100	160	1,476
Straight Section Quadrupoles	114	115	48	422
Arc Sextupoles SF	6	425	70	180
Arc Sextupoles SD	6	745	125	552
Straight Section SF	36	45	35	36
Straight Section SD	36	75	62	112
Slow Dipole Correctors	440	10	33	92
Fast Dipole Correctors	220	5	20	17
Total Circuit Power				8,077

Table 6.51: Space requirements.

PS Function	#19″ Racks	Qty	Size
D1 / D3	1	1	$15'$ W $\times$ $4.5'$ D $\times$ $7'$ H
D2	1	1	$20'$ W $\times$ $4.5'$ D $\times$ $7'$ H
Arc Quadrupoles	0	2	$3.5'$ W $\times$ $3.5'$ D $\times$ $7'$H
Straight Section Quadrupoles	4	0	N/A
Arc Sextupoles SF	0	1	$3'$ W $\times$ $3.5'$ D $\times$ $7'$ H
Arc Sextupoles SD	0	1	$3'$ W $\times$ $3.5'$ D $\times$ $7'$ H
Straight Section SF	1	0	N/A
Straight Section SD	1	0	N/A
Slow Dipole Correctors	3	0	N/A
Fast Dipole Correctors	2	0	N/A

6.3.3 Transfer Line Power Supplies

The EIC requires three new transfer lines to transport the electron and hadron beams between the various accelerators and storage rings:

1. The LtR (LINAC-to-RCS) transports electrons from the 400 MeV LINAC to the RCS.
2. The RtS (RCS-to-Storage Ring) transfers electrons from the RCS to the electron storage ring.

3. The extended Y-line transports hadrons from the existing Y-line to the RHIC "Blue" arc in Sector 5, which will serve as a transfer line to the hadron injection area in IR4.

The power supplies for these three EIC beam transfer lines are described bellow.

400 MeV LINAC to the RCS (LtR)

- **Quadrupole Power Supplies**

  The LtR line employs ten low field and four high field quadrupoles. Each of these fourteen magnets are individually powered.

  The power levels and precision required make them suitable for commercial power supplies with an external Ethernet controller and an external ZFCT for current feedback.

- **Dipole Power Supplies**

  There are two bends in the spin rotator portion of the transfer line. The first dipole bends by 99.1° and the second by 82°. Both are implemented as a pair of shorter dipoles. The two halves for each bend are powered in series.

  The power levels and precision required make them suitable for commercial power supplies with an external Ethernet controller and an external ZFCT for current feedback.

- **Dipole Corrector Power Supplies**

  There are ten horizontal and four vertical corrector magnets used in the transfer line. Each of these fourteen magnets are individually powered. These will be powered by commercial off-the-shelf (COTS) units.

The power supplies in the LtR-line are listed in Table 6.52.

Table 6.52: Power supply specifications for the LtR beam line.

	Qty	Current [A]	Voltage [V]	Power [kW]	Power Supply Type
Low field quadrupole	10	50	50	2.5	Ext. regulated COTS
High field quadrupole	4	160	55	8.0	Ext. regulated COTS
Low field dipole	1	160	55	8.0	Ext. regulated COTS
High field dipole	1	160	55	8.0	Ext. regulated COTS
H dipole corrector	10	5	20	0.1	COTS
V dipole corrector	4	5	20	0.1	COTS
Total	30				

RCS to the Storage Ring

- **Quadrupole Power Supplies**

  There are fourteen quadrupoles in the transfer line. Each of these fourteen magnets are individually powered.

  The power levels and precision required make them suitable for commercial power supplies with an external Ethernet controller and an external ZFCT for current feedback.

- **Dipole Power Supplies**

  There are twelve dipoles in this transfer line. They are configured as two circuits of two dipoles each, and one circuit containing eight dipoles.

  The power levels and precision required make them suitable for a multiple output custom switch mode power supply. This would be constructed as one bulk power supply and three DC-DC converters.

- **Dipole Corrector Power Supplies**

  There are ten horizontal and ten vertical corrector magnets in the transfer line. Each of these fourteen magnets are individually powered. These will be powered by commercial off-the-shelf (COTS) units.

The power supply requirements for the RtS-line are shown in Table 6.53.

Table 6.53: RCS-to-Storage Ring power supply parameters.

	Qty	Current [A]	Voltage [V]	Power [kW]	Power Supply Type
Quadrupoles	14	135	40	5.4	Ext. regulated COTS
Dipole, small string	2	455	24	10.9	Custom Switch mode [a]
Dipole, large string	1	455	60	27.3	Custom Switch mode [a]
H dipole corrector	10	10	45	0.5	COTS
V dipole corrector	10	10	45	0.5	COTS
Total	37				

[a] multiple outputs

Hadron Extended Injection Line

The power supplies for extended Y-line from AGS to RHIC Blue-line at Sector 5 are described bellow.

- **Quadrupole Power Supplies**

  There are eleven quadrupoles in the transfer line. Each of these eleven magnets are individually powered.

  The power levels and precision required make them suitable for commercial power supplies with an external Ethernet controller and an external ZFCT for current feedback.

- **Dipole Power Supplies**

  There are two vertical bends and two horizontal bends in this transfer line. Each of them are individually powered.

  The power levels and precision required for three of these make them suitable for a multiple output custom switch mode power supply. This would be constructed as one bulk power supply and three DC-DC converters. These are very similar to the three power supplies needed for the RCS-to-SR (RtS) dipoles, and would be the model of this power supply.

  The second horizontal bend requires less power, and would be implemented as a commercial power supply with an external Ethernet controller and an external ZFCT for current feedback.

- **Dipole Corrector Power Supplies**

  There are ten horizontal and four vertical corrector magnets in the transfer line. Each of these fourteen magnets are individually powered. These will be powered by commercial off-the-shelf (COTS) units.

The power supply parameters for the extended Y-Line are listed in Table 6.54.

Table 6.54: Power supply specifications for the extended Y-arc.

	Qty	Current [A]	Voltage [V]	Power [kW]	Power Supply Type
Quadrupoles	11	190	40	7.6	Ext. regulated COTS
Dipole, V Bend 1	4	550	60	33.0	Custom switch mode [a]
Dipole, V Bend 2	1	550	60	33.0	Custom switch mode [a]
Dipole, H Bend 1	1	550	30	16.5	Custom switch mode [a]
Dipole, H Bend 2	1	160	25	4.0	Ext. regulated COTS
H corrector	10	5	35	0.1	COTS
V corrector	4	5	35	0.1	COTS
Total	32				

[a] multiple outputs

6.4 Vacuum Systems

6.4.1 Electron Storage Ring Vacuum System

Arc Chamber Layout, Design Approach and Analysis

The electron storage ring is divided into a total of 264 super-bend sections, 192 in the arc half-cells and 72 in the straight sections. A schematic layout of one arc half-cell is shown in Figure 6.124. It consists of a dipole chamber which passes through the three dipole magnets that make up the super-bend, followed by a multipole chamber which passes through a quadrupole and a sextupole magnet. These two chambers are separated by an RF-shielded bellows which provides room for thermal expansion of the chambers as well as mechanical misalignments. A corrector magnet will be positioned over the RF bellows due to space limitations. The multipole chamber also provides a mounting provision for beam position monitors as well as lumped pumping.

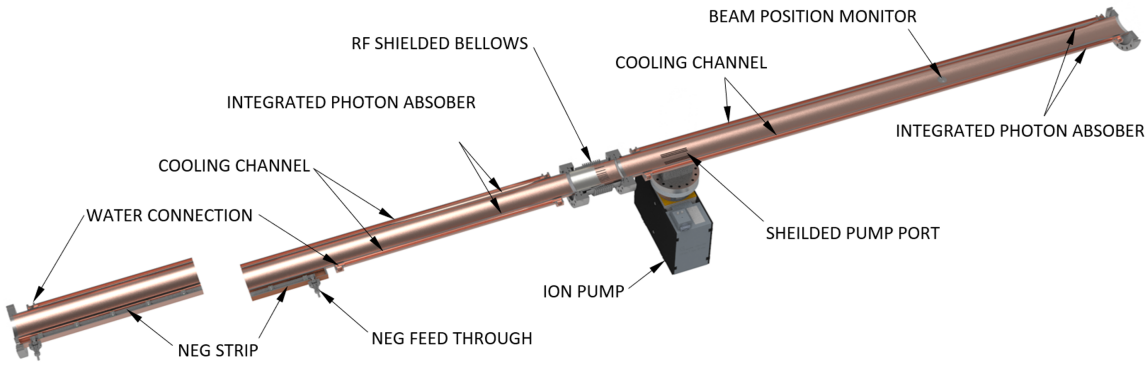

Figure 6.124: Half-cell layout consisting of a dipole chamber, RF-shielded bellows and multipole chamber with pump port and BPM.

The super-bend is made up of 3 separate dipole magnets D1, D2 and D3. The field strengths of these dipoles for the different operating modes are given in Table 6.55. The negative value shown in the 5 GeV case represents reverse bend. The bending radii, the synchrotron radiation power from each magnet, and the total power for the whole ring are also given. The synchrotron radiation power from the electron beam through each dipole magnet can be calculated as [254]:

$$P[\mathrm{kW}] = \frac{14.08 \cdot L[\mathrm{m}] \cdot I[\mathrm{A}] \cdot E^4[\mathrm{GeV}^4]}{\rho^2[\mathrm{m}^2]}, \tag{6.6}$$

where L is the length of the dipole magnet, I is the beam current, E is the beam energy and ρ is the bending radius of the magnet. The bending radius and field strength B are related

by

$$\rho = \frac{E[\text{GeV}]}{0.2998 \cdot B[\text{T}]}. \tag{6.7}$$

Table 6.55: Energies, currents, dipole fields, bending radii, and synchrotron radiation power from each magnet, as well as the entire ring, for the various operating modes.

E [GeV]	I [A]	B (D1&D3) [T]	ρ (D1&D3) [m]	P (D1&D3) [kW]	B (D2) [T]	ρ (D2) [m]	P (D2) [kW]	P_{ring} [kW]
5	2.50	0.128	130.7	4.26	-0.710	-23.5	23.45	8438
10	2.50	0.118	282.1	14.6	0.118	282.1	2.60	8409
18	0.25	0.213	282.1	15.4	0.213	282.1	2.73	8825

The proposed cross sections for the dipole and multipole chambers are shown in Figure 6.125. The dipole chamber has an inner cross section size of 80 mm wide by 36 mm high. An ante-chamber is planned on the inboard side to provide space for a NEG strip pump assembly. A water cooling channel will be required on the outboard side of the chamber to remove heat generated by synchrotron radiation incident on the interior walls. In addition, a small section of water cooling will be required on the inboard side at the downstream end of the dipole chamber to absorb synchrotron radiation produced by the reverse bend in the 5 GeV operating mode. The proposed cross section will have a 4 mm wall thickness which will allow the dipole chamber to fit comfortably inside the 52 mm dipole magnet gaps. The multipole vacuum chamber will have same internal cross section but will not have an ante-chamber allowing it to fit inside the quadrupole and sextupole magnet coils. Cooling channels will be provided on both sides of the multipole chamber to deliver better thermal stability for the beam position monitor which will be mounted directly to the chamber.

The vacuum chamber geometry is designed to provide adequate apertures for the various operating energies which require different bending radii. In addition the geometry must be able to accommodate the reverse bend through the dipole magnets in the low energy configuration. The orbits of the 5 GeV and the 18 GeV beams differ by 26.5 mm at the entrance of the D2 dipole. The stay clear envelope is defined by $15\,\sigma$ of the rms beam size plus an additional 10 mm in both planes for orbit errors. The horizontal width of the vacuum chamber in the proposed design is limited to 80 mm due to the constraints of the quadrupole and sextupole inner radii. The vertical size is limited by the gap in the dipole magnet.

In order to ensure compliance with the required beam stay clear aperture, a 3D layout of a standard arc cell was developed using the lattice information for the 5 and 18 GeV cases. This model was further expanded to include the magnet geometry in order to determine

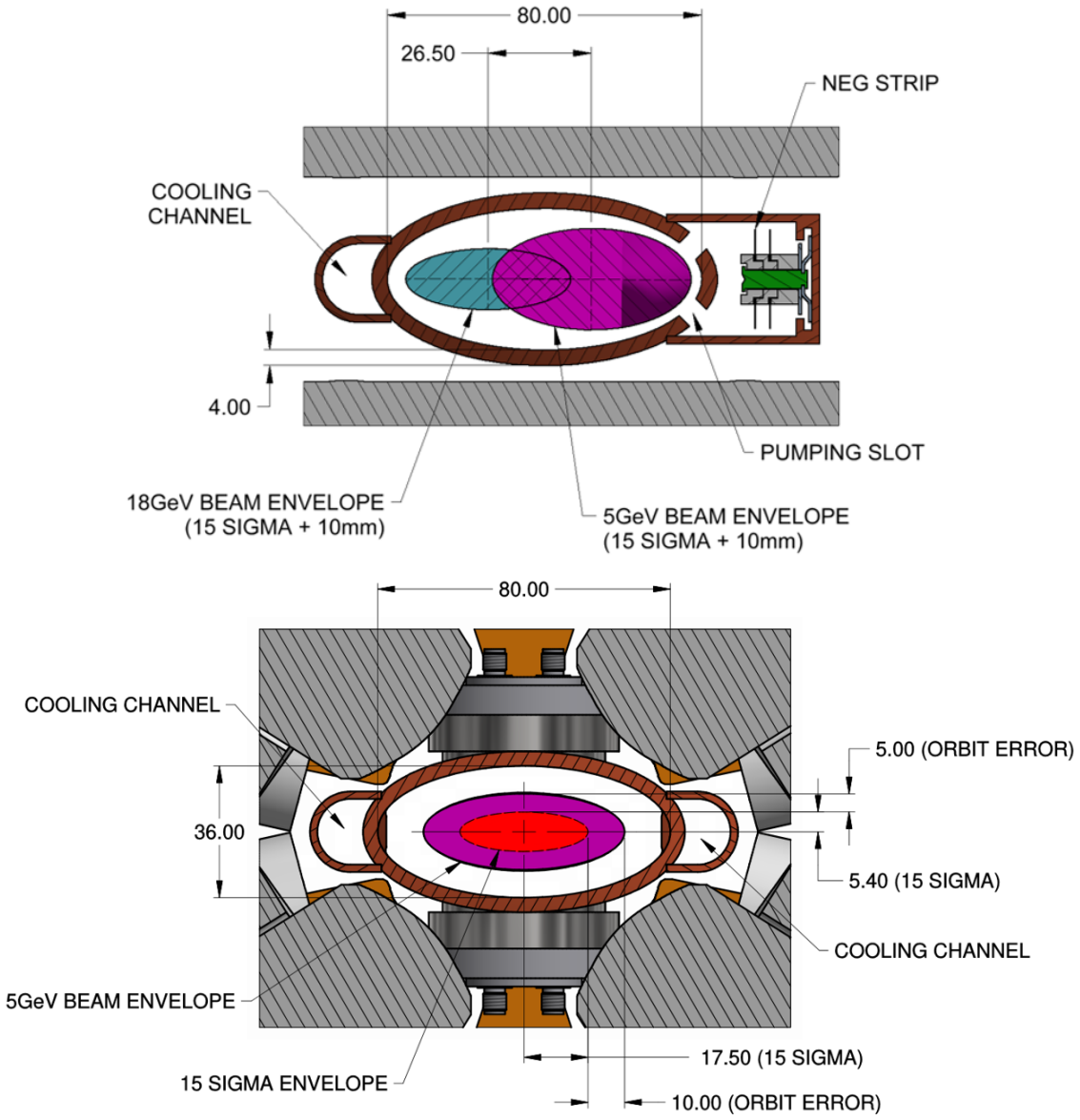

Figure 6.125: Top: Cross section of the dipole vacuum chamber with ante-chamber on the inboard side and cooling channel on the outboard side; Bottom: cross section of the multipole chamber with cooling channels on both sides.

chamber lengths, location of flange joints as well as discrete pumping ports. A simplified "kink" geometry was chosen instead of bending the chamber into a precision arc which is very difficult given the length. The dipole chamber will be bent to a specific angle in the center of the D2 magnet. Vacuum chamber stands will be located near this central pivot point as well as the beginning and end of the dipole chambers to ensure proper positioning during installation and operation. The angle of the bend was optimized to ensure all of the stay clear requirements were achieved.

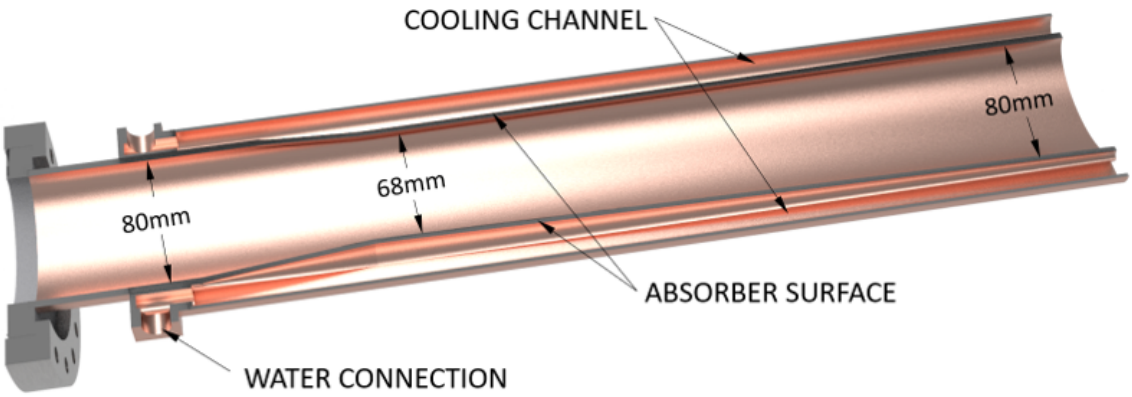

Figure 6.126: Integrated photon absorber located at the downstream end of the dipole chamber.

Another important requirement of the vacuum system is to safely intercept and absorb any synchrotron radiation while shielding un-cooled components such as flange joints, RF-shielded bellows and BPMs. In order to meet this requirement an integrated photon absorber at the downstream end of the chambers is being proposed as shown in Figure 6.126. The intention is to mechanically form the required shape into the beam pipe before welding the cooling channel covers and flanges onto the chamber. The absorbing surface will provide a long taper with a shallow intercept angle to reduce the power density to manageable levels. This long taper will also help minimize the broadband impedance associated with discrete photon absorbers.

The resulting chamber geometries were studied utilizing SynRad+ [103] and ANSYS [255] simulation codes. After developing an acceptable layout which shadows the non-water cooled components, the 3D geometry was created for the simulations. The simulation results from the 5 GeV operational mode are shown in Figure 6.127. The magnetic dipole regions are defined in Table 6.55 and were used to determine the photon flux impinging on the vacuum chamber walls. The total power absorbed in the simulation was cross-checked and found to be within 0.5% of the value listed in Table 6.55. It should be noted that more than 50% of the synchrotron radiation travels through the first dipole and subsequent multipole chamber and is deposited on the following dipole chamber. With the given operating parameters, only scattered photons hit the inboard wall of the dipole chamber along most of the length. The only exception is the 5 GeV case where approximately 3.6kW of power is deposited at the downstream end due to the reverse bend. For this reason, the antechamber will not run the entire length of the chamber to provide space for active water cooling.

A summary of the power deposited in the chambers, photon absorbers and the resulting maximum power densities can be found in Table 6.56. These results consider using OFS copper as the vacuum chamber material with a thermal conductivity of $383\,\mathrm{W/(m \cdot K)}$ and modest cooling water flow rate of 11.4 l/min [3 gpm]. The maximum temperatures

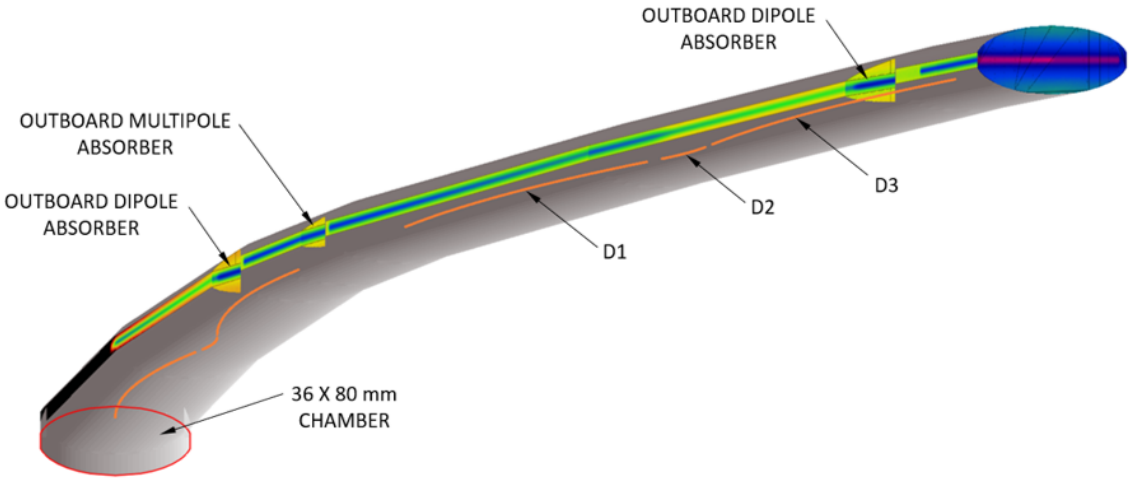

Figure 6.127: SynRad+ simulation showing the 5 GeV dipole regions (D1, D2 and D3) and absorber surfaces.

are well within the acceptable range for all cases studied. The results from the worst case scenarios with the highest incident power densities are shown in Figure 6.128

Table 6.56: SynRad+ results for the multiple and dipole chambers at the various operating modes.

E [GeV]	P_{chamber} [kW]	P_{absorber} [kW]	PD_{MAX} [W/mm^2]
Multipole Chamber			
5	5.6	2.0	4.5
10	2.8	1.7	4.0
18	3.3	2.0	4.5
Dipole Chamber			
5	14.6	5.0	8.9
10	22.1	3.0	6.8
18	25.8	3.2	7.4

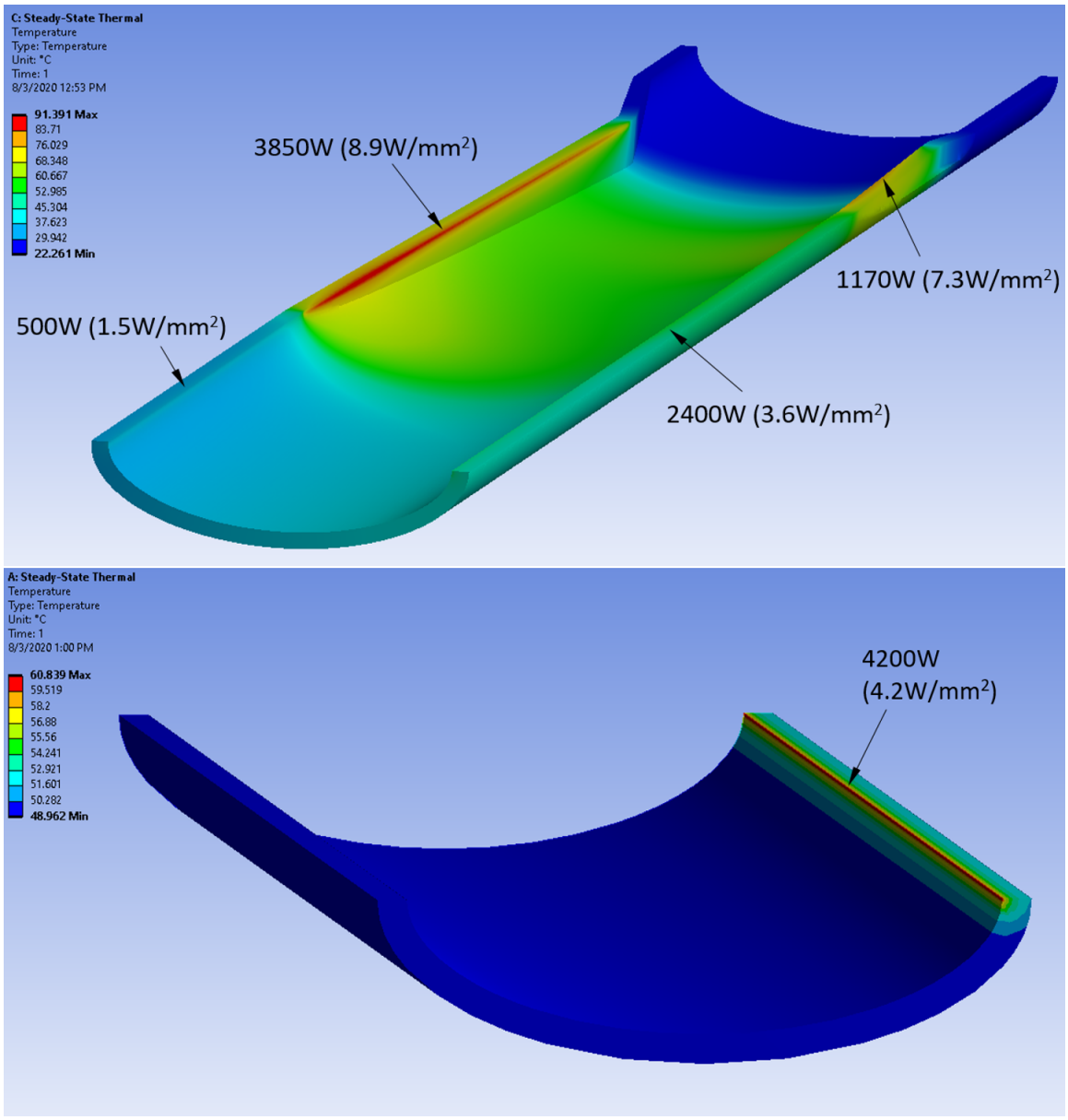

Figure 6.128: Top: ANSYS thermal results for dipole absorber heat loading for 5 GeV mode.; Bottom: ANSYS thermal results for for dipole chamber wall heat lading for 18 GeV case.

Chamber Fabrication Considerations

Unlike aluminum, copper profiles cannot be easily extruded with multiple cavities and are typically produced with only a single hollow channel. While there have been recent developments in producing copper profiles with multiple hollow cavities, the current con-

ceptual design relies on joining 3 individual profiles. The proposed chamber cross sections are shown in Figure 6.125. In order to complete the vacuum chamber, cover plates will need to be welded to the main profile to close the NEG pumping chamber and water cooling channels. The copper billets will be hot-extruded into circular tubes of the required size. Special dies will be needed to form the elliptical cross sections from the circular tubes. The tubes are cold-drawn through the forming dies to achieve the required profile. Straightness of less than a few millimeters can be achieved over a length of 8 m using conventional fabrication techniques. Polished dies may be necessary to achieve an inner surface roughness better than 1 µm.

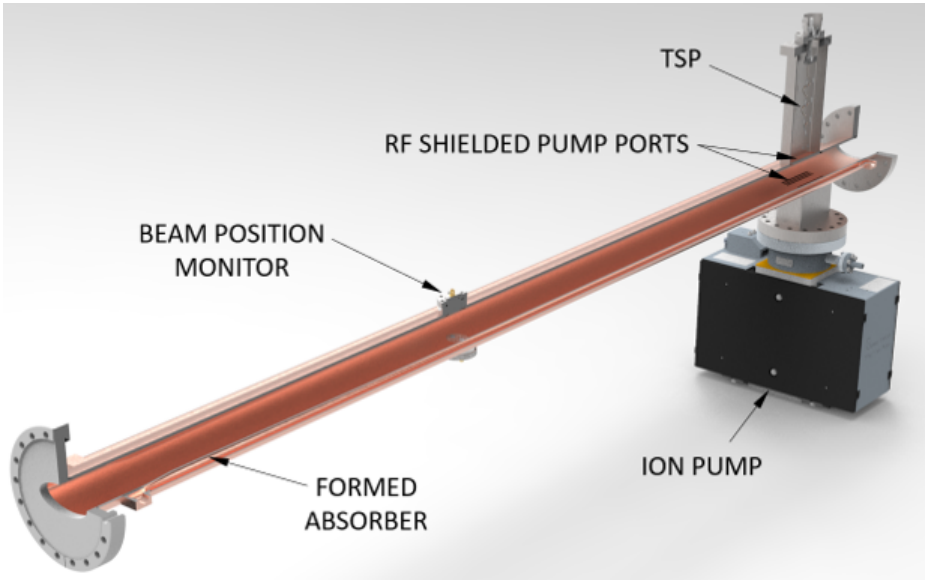

Figure 6.129: Multipole chamber with formed absorber, RF-shielded pump ports and beam position monitor.

The profiles will need to go through several additional steps before they are completed. After being cut to length, the integrated absorbers will be formed into the downstream end of the profiles as shown in Figure 6.129. Welding preparations will need to be machined on the ends for the flanges and along the sides for the cover plates. The dipole chambers will require additional machining on the inboard wall to provide pumping slots between the ante-chamber and the beam channel. These narrow openings will be added off the midplane to reduce beam impedance. Dipole chambers will also require bending to achieve the proposed geometry previously discussed. The multipole chambers are also complicated, even though they are straight and shorter than the dipole chambers. These profiles will require machining for the RF shielded pump ports located at the upstream end of the chamber. In addition, the wall thickness will need to be built up to accommodate the installation of beam position monitors. To meet this requirement, a stainless steel ring welded directly to the OFS profile is proposed. The depth between the BPM mounting surface and the interior of the beam channel will be tightly controlled to minimize the step seen by the beam. TIG welding will be used to join the flanges to the main profile

while electron beam welding is envisioned to join the cooling channels and antechamber cover plates in order to minimize distortion. Early development of the extrusions with potential vendors and in-house development of the TIG welding process are a must for the successful fabrication of the storage ring vacuum chambers.

The twelve straight regions will each house six super-bend dipole sections. The design of these dipole chambers, which contain the same super-bend magnet set, D1, D2 and D3, will be identical to the arc half-cell chambers. Additional absorbers and masks may be implemented to protect special diagnostic components in the straights from the intense synchrotron radiation fans. The design of the downstream chambers, absorbers and masks will be carried out together with the details of the diagnostic components.

Outgassing, Desorption, Pumping and Achievable Pressure

The base pressure in the storage ring will be determined by the thermal outgassing from the vacuum chamber internal surfaces and the available pumping. The copper chambers will be thoroughly cleaned and vacuum baked prior to installation. Best UHV practice will be employed during assembly and commissioning to minimize the outgassing rate. A thermal outgassing rate of 1×10^{-11} Torr l/(sec $\cdot$ cm^2), comprised mostly of hydrogen and water, can be reached in a few days after pump down. This would be equivalent to approximately 4×10^{-8} Torr l/(sec $\cdot$ m) for the arc half-cell chambers. A lower outgassing rate could be achieved with in-situ bake-outs, but, given the added expense and complication, this practice will only be implemented for the critical regions such as the IR and areas around SRF. Ultrahigh vacuum pumping of a few hundred liters/sec/m, in the form of NEG strips, sputter ion pumps (IP) and titanium sublimation pumps (TSP), will be implemented throughout the storage ring. This pumping arrangement should achieve an average base pressure of low 10^{-10} Torr after sufficient pumping time.

The storage ring pressure during beam operation will be dominated by photon stimulated desorption (PSD). There are copious photons emitted by the electron beam when passing through the dipole fields. These photons strike the walls of the vacuum chamber generating photoelectrons and desorb surface gas molecules. The PSD yield η, the number of gas molecules desorbed per incident photon, depends loosely on the energy and the incident angle of the photon, but strongly on the surface conditions of the chamber wall. The initial PSD rate can be as high as a few percent for copper. The desorption rate will decrease rapidly with the accumulated photon dosage, which is proportional to the integrated beam current over time. This value is usually expressed in photons per meter of chamber length or in Ampere-hours (Ah). Plots of PSD yield and $\mathrm{d}P/\mathrm{d}I$ vs. photon dosage in log-log scales are shown in Figure 6.130 [256].

During initial beam commissioning, there will be severe limitations on the achievable beam current and beam lifetime caused by the large pressure increases due to high PSD yield. Based on data from other operating facilities with similar machine parameters, the PSD yield is expected to drop below 1×10^{-5} after a beam dosage of 100 Ah and below 1×10^{-6} after 1,000 Ah. These dosages correspond to approximately 10 days and 100 days,

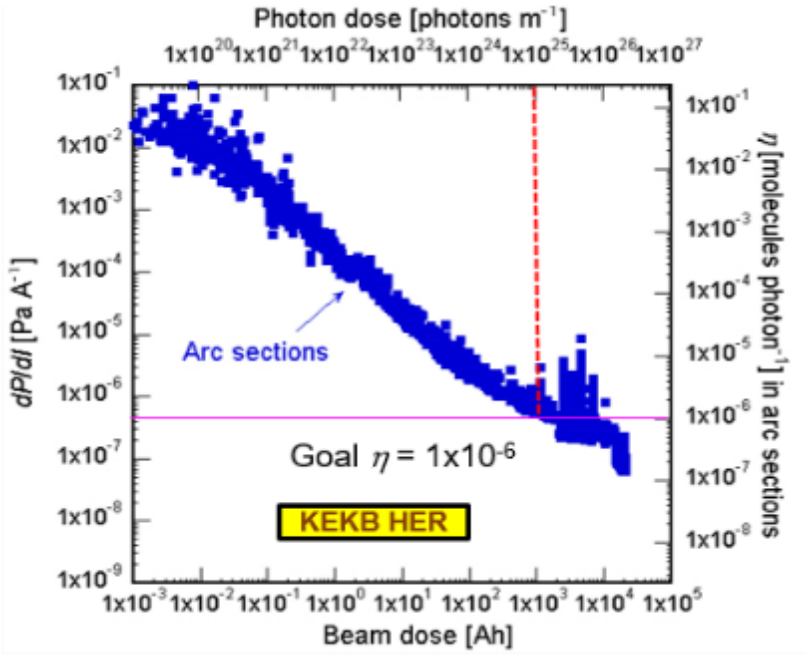

Figure 6.130: Photon stimulated desorption (PSD) yield η and pressure increase vs. accumulated photon dosage for copper chambers.

respectively, of continuous stored beam current of 500 mA or about 20% of the design current at 10 GeV. The achievable pressure inside the arc beam channel can be estimated using the above PSD yield and the total photon flux Γ, given by [254]

$$\Gamma = 8.08 \times 10^{17} \cdot I\,[\mathrm{mA}] \cdot E\,[\mathrm{GeV}]. \tag{6.8}$$

With a current of 2.50 A at 10 GeV, the total photon flux will be $\Gamma = 2.2 \times 10^{22}$ photons/sec for the entire ring. Assuming all of the photons are generated in the dipole magnets which occupy 1900 m, the linear photon flux would be 1.15×10^{19} photons/(m · s). With a PSD yield of 1×10^{-6} there would be 1.15×10^{13} molecules/(m · s) being desorbed which is approximately equivalent to 3×10^{-7} Torr l/(m · s). The dipole chambers will have NEG strips which provide linear pumping, while the multipole chambers will have lumped pumping as previously discussed. With over 100 l/(s · m) of pumping speed available in the storage ring arcs, a pressure in the low 10^{-9} Torr can be achieved which satisfies the pressure requirement for the storage ring.

The ante-chamber portion of the dipole chamber must be separated from the beam channel to reduce the impedance impact on the beam. In order to connect these two volumes the inboard wall of the beam channel will be machined with many long narrow and tilted openings off the mid-plane. A 10% opening will provide over 300 l/(s · m) conductance for H_2, exceeding the required 100 l/(s · m) pumping speed mentioned above. The dimensions and shape of these channels will be evaluated by accelerator physics to minimize

their contribution to the transverse impedance. The NEG strips are made of Zr-V-Fe alloy which is pressed onto a constantan substrate that provides rigidity to the assembly. The NEG material can be activated by heating it to 400° C via resistive heating by passing current through the constantan substrate. The pumping speed of the NEG strips will be over 1000 $l/(s \cdot m)$ initially, and decrease slowly as gas is pumped from the ring. Due to the high initial gas load expected, re-activation of the NEG is expected to achieve the required average operating pressure.

In the multipole chambers, the width is constrained by the poles of the focusing magnets. This constraint means there is no space for an ante-chamber. Pumping ports with screens will be machined into the top and bottom walls of the chamber to provide RF shielding between the beam and the pumping elements. The size of the ports will be constrained by the upstream corrector magnets. A combination of NEG cartridges or TSPs along with sputter ion pumps will be mounted to these ports. The achievable pumping speed will depend on the openings of the pump screens. The final configuration will need to be developed in conjunction with accelerator physics to minimize the impact on the stored electron beam.

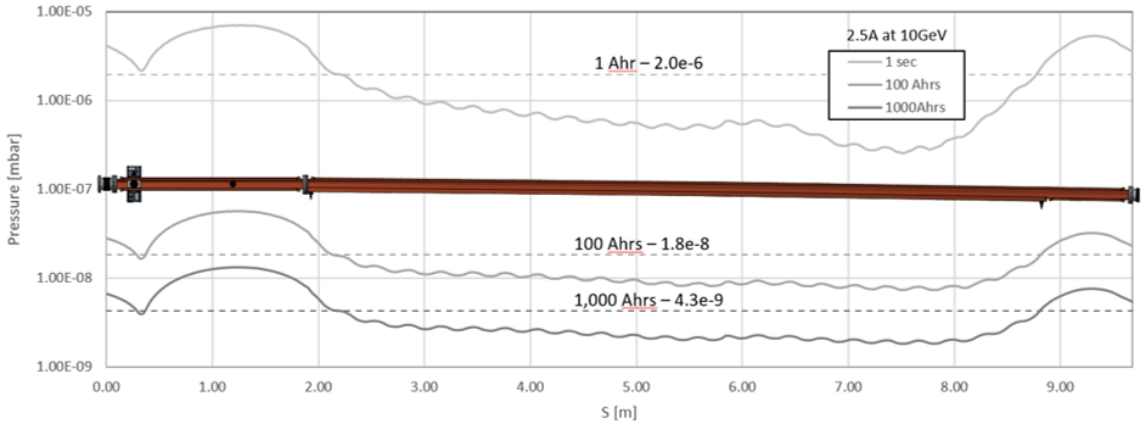

Figure 6.131: Pressure simulation using SynRad+ and MolFlow+ codes for arc halfcell region for 10 GeV beam at 2.5 A. SynRad+ traces the beam emitted photons to calculate the flux and power distribution on the chamber surfaces, and MolFlow+ calculates the pressure distribution based on desorption and available pumping.

A detailed pressure simulation was performed for an arc half-cell region using MolFlow+ [257] which is a Monte-Carlo simulation code for complex ultrahigh vacuum systems. Photon distribution profiles from SynRad+ where imported to provide an accurate model of the expected outgassing resulting from PSD. The simulation results for the 10 GeV beam with 2.5 A current are shown after various operating periods in Figure 6.131. The 10 GeV operating mode with a reverse bend has the highest photon flux. The pressure is highest in the multipole chamber due to limited pumping and the high photon flux.

Commercial ion pump controllers residing in the service buildings will power and monitor the ion pump currents and voltages. Additional vacuum gauge readings in the arcs will provide an accurate pressure profile around the ring. TSPs will be installed with the

ability to remotely sublimate. NEG pumps will need to be activated locally when access is permitted. TSPs have the advantage of only generating a small burst of gases during their short sublimation period. NEG activation takes longer, during which time a large amount of hydrogen is produced and will need to be removed by portable turbomolecular pump stations (TMP). Therefore, TSPs are more suitable at special areas such as the IR and around SRF cavities so they can be sublimed as needed to restore UHV in a few minutes. The NEG strips and cartridges are best activated during maintenance periods with portable power supplies and TMPs to remove the desorbed gases. Both TSP and NEG can only pump active gases, such as H_2, CO, or N_2. Inert gases, such as CH_4 and Ar must be removed by sputter ion pumps. NEGs do have higher capacity than TSP films so the interval between activations is considerably longer for NEGs.

RF-Shielded Bellows, Flange Joints, and Pump Ports

To reduce the broadband impedance and to minimize the localized HOM heating, the inner cross-section of the electron beam chamber wall should be maintained as smooth as possible. The changes in the cross sections of the beam chamber should vary gradually, with an inclination 10:1 or greater for all tapered transitions. For vacuum components with cavity-like or discontinuous structure, such as bellows and flange joints, RF contact fingers or springs will be installed to reduce the impedance and provide a smooth path for the beam image current. The height of any steps at RF fingers and flange joints should be less than 1 mm. Slots or screens will be implemented at the pump ports to reduce impedance while still providing adequate pumping conductance. Commercially available RF-shielded gate valves will be used along the storage ring beam channel. Two types of RF-shielded bellows have been used in electron storage rings, one with inside fingers like those used at APS [258] and the ones with outside fingers which were used at PEP-II [259] and NSLS-II. The NSLS-II design [260] uses wider fingers to increase the contact force on the sleeve and narrower gaps between the fingers to reduce the leakage of RF power. The performance of the NSLS-II bellows has been shown to be satisfactory with electron bunch length down to 3 mm, and will be adopted for the EIC. A proposed design for the EIC bellows is shown in Figure 6.132.

The storage ring chambers will not be baked in-situ, therefore a shorter bellows with less compression and lateral movement will be sufficient for the storage ring arcs. Bellows with comb type RF contacts have been developed at SuperKEKB [261]. These bellows are longer and more expensive than the finger types. A detailed analysis will be carried out by the accelerator physics group to ensure that the selected bellows designs will meet the impedance requirement and will be able to manage the resistive wall heating expected during high current operations.

There are over one thousand flange joints in the storage ring that will contribute to the total impedance. The types of RF contacts at the flange joints and their impact on the overall impedance budget must be studied in detail. The PEP-II design used Be-Cu type solid spring contacts [259] to bridge the gaps between adjacent Conflat flanges, as shown in Figure 6.133. The remaining step was greater than 1 millimeter.

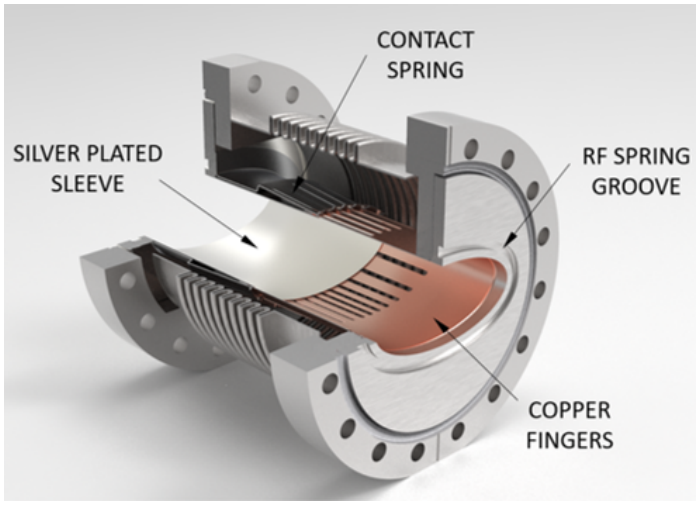

Figure 6.132: Cross section of RF-shield bellows located between the dipole and multipole chamber in the storage ring arc. This design concept is based on the NSLS-II bellows design.

There were many failures and damage to these contacts as a result of misalignment after assembly. The NSLS-II design used a soft Be-Cu coil spring to bridge the flange gaps with good results. The resulting flange joint created steps of less than 1 mm. One drawback with this approach is the challenging installation in tight spaces. Springs in two locations fell out of the retaining groove and went unnoticed until beam commissioning was started. There were also 15 locations were the spring was not set correctly in the groove so it did not bridge the gap between the flanges. This problem was not discovered until higher currents were stored in the machine and excessive heating was observed. Considering over 800 of these springs were installed in the NSLS-II ring, these problems represent a very small percentage. The KEKB design used Helicoflex Delta seals for the primary UHV seal instead of a more conventional copper gasket. These seals also doubled as the RF contact between the adjoining flanges. This arrangement resulted in beam channel steps of 0.5 mm. The soft aluminum coating on the outside of the seal was easily scratched resulting in vacuum leaks. This sealing arrangement also requires tight control of the surface finish which adds cost and requires special handling to avoid damage to the polished surfaces. MO-type flanges and seals were recently developed for SuperKEKB [261], with the copper seals following the shape of the beam channels. With precision design and machining, the step at the gasket is reduced to less than 0.5 mm. However, the extra machining and alignment of the flanges and the seals adds significantly to the cost of the flanges. Weighing the pros and cons of the various options, the proposed design is to use the soft coil spring implemented at NSLS-II.

All pump ports along the beam channels will be shielded with screens or slots. Examples of pump port screens used at KEKB are shown in Figure 6.134. The design of the storage ring pump ports will be evaluated by accelerator physics for their impedance impact while maximizing the pumping conductance.

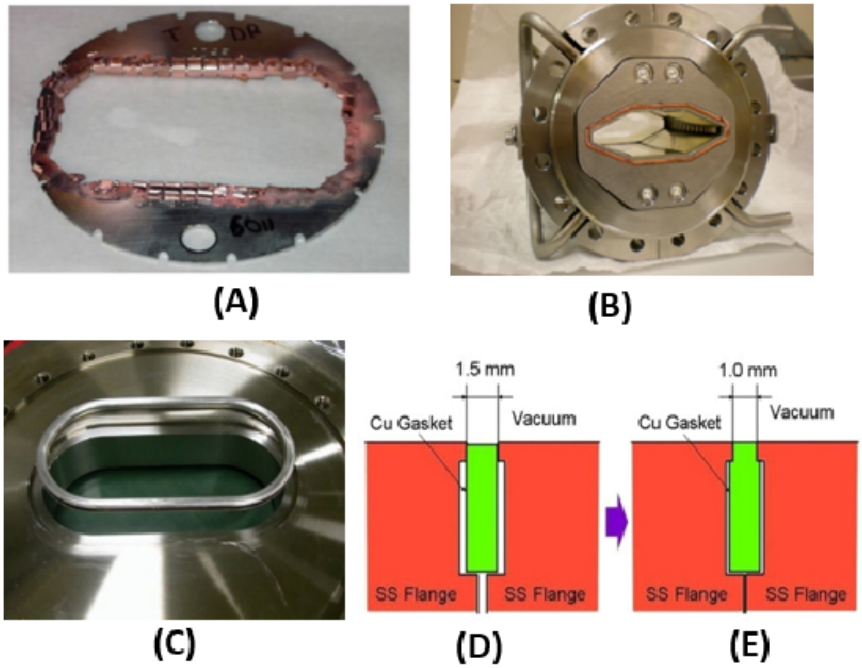

Figure 6.133: RF contacts at flange joints: (A) solid Be-Cu contacts used at PEP-II;(B) soft Be-Cu coil springs used at NSLS-II nested in a groove;(C) Helicoflex seals also served as RF contact in KEKB, which was susceptible to scratches and leaks; MO-type flanges and seals used in SuperKEKB, (D) before assembly and (E) after assembly with less than 0.5 mm steps.

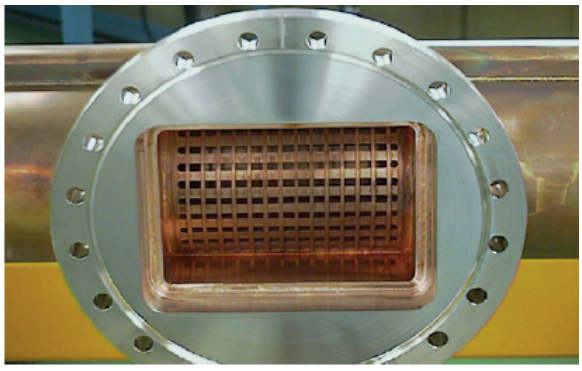

Figure 6.134: RF shielded pump port screen used at KEKB.

Vacuum Measurement and Control

The pressure distribution in the storage ring will be monitored by ion pump currents and vacuum gauge readings. Portable residual gas analyzers (RGA) will also be used for monitoring and diagnosis. Each vacuum sector will have a convection-enhanced Pirani gauge and two ionization gauges. Additional vacuum gauges will be installed to protect special devices, such as SRF cavities. Due to the high level of radiation in the accelerator tunnel,

gauge and pump controllers will be placed in service buildings. The Pirani gauge can monitor pressure from ambient to 10^{-4} Torr while the inverted-magnetron type cold cathode ion gauges (CCG) have a usable range from 10^{-4} to 10^{-11} Torr. CCGs can be operated through long cables, eliminating the need for locating electronics in the storage ring tunnel. The accuracy of CCG readings is normally better than $\pm 30\%$. Erroneous readings from CCGs due to copious photoelectrons have been observed at many synchrotron radiation facilities. To mitigate this problem the gauge tubes will be mounted on elbows preventing line-of-sight between the beam channel and the CCG. In addition, shielded baffles may be necessary to prevent photoelectron interference with the gauges. A similar approach was implemented at NSLS-II. Quadrupole-type RGAs will be installed at selected locations to measure the partial pressures of residual gas species and for trouble shooting. Additional RGAs will be mounted on several of the portable turbopump stations to aid in troubleshooting during maintenance periods. RGAs, with an electron multiplier, can measure partial pressure with sensitivity down to 10^{-13} Torr.

The vacuum control system will interface directly with vacuum devices as part of the storage ring equipment control and protection systems. Critical controllers will be backed by uninterruptible power supplies. Vacuum devices include gauge controllers, ion pump controllers, chamber temperature readouts, cooling water flow sensors, and gate valve solenoids. Multi-gauge controllers will communicate with the control system through RS232 or Ethernet links to provide remote monitoring and control. The signals from the gauge controllers will be hardwired to vacuum PLCs for interlocking gate valves and other vacuum components. For gate valve control, the PLCs will use a voting scheme which takes the inputs from the gauge and pump controllers to initiate closure or prevent opening if vacuum levels are above a predefined set point. Using a voting scheme minimizes the risk of a false trigger which could result from the malfunction of a single device. The water flow and temperature monitoring system will read and compare the live values with the pre-set values, and trigger an output to the EPS systems when necessary.

Vacuum Facility and Utility

To ensure proper chamber processing and to ensure the required vacuum levels are achieved, dedicated vacuum facilities will be needed for cleaning, welding, assembling, and evaluating all of the vacuum components which will be installed in the storage ring and the injectors. A dedicated chemical cleaning facility is required to remove surface contaminants and oxide layers from the long chamber extrusions and other vacuum components. The facility should consist of three long stainless steel tanks and a gantry crane capable of handling components up to 8 m in length and 300 kg in weight. These tanks will be used for ultrasonic cleaning with hot water, commercial bio-degradable cleaning agents, and de-ionized water rinse. Components with gross contamination will be flushed with high pressure hot water before ultrasonic cleaning.

The fabrication of storage ring vacuum chambers depends on the successful welding of the long copper profiles made of OFS copper. A welding development program should be started during the prototype stage with adequate TIG welding equipment to develop

the procedures and processes necessary to ensure reliable and consistent weld joints. Mechanical inspection will be needed to measure the dimensions and the shape of the welded chambers with sub-millimeter accuracy. The weld quality, cooling channel integrity and vacuum tightness will be checked at the inspection stations, using ultrasonic gauges, water pressurization, rough vacuum pumping, and leak detectors. The welding and the testing should be carried out in a class 10,000 clean room environment to prevent contamination during these processes. Once welded, the chambers cannot be thoroughly re-cleaned due to the risk of trapping cleaning solution which will cause accelerated corrosion in a radiation environment.

A Class 1,000 clean room with 150 m^2 floor space is needed for the installation of NEG strips, ion pumps, BPM buttons and other components into the welded chambers. Adjacent to this clean room, a vacuum evaluation area with multiple stations for leak checking and bakeout will be set up for the final vacuum qualification of the cell vacuum chambers. The chambers will be pumped down with TMPs, leak checked using leak detectors with minimum helium sensitivity of 5×10^{-11} Torr l/s, and baked with portable ovens or heaters to 150° C. Vacuum gauges and RGA will be used throughout to ensure the chambers remain leak tight and free of contamination. All of the pumps, gauges, and BPM buttons are to be tested and measured to ensure their proper operation during and after the final bakeout cycle. After bakeout, the chambers will be back-filled with dry nitrogen for the subsequent assembly into magnets and installation into the storage ring tunnel. Several portable laminar flow hoods will be needed to cover the chamber flange joints during the assembly of chambers into magnet girders, and during the installation and connection of the chambers in the storage ring tunnel.

All of the vacuum device controllers will be located in service buildings and will be operated remotely, except for the activation of NEG strips and NEG cartridges. Due to the large amount of gas desorbed during NEG activation, several portable TMPs need to be used to remove the desorbed gas. Portable NEG pump power supplies will be used along with these TMPs. AC power of approximately 50 kW will be needed in each arc to simultaneously activate all the NEG strips in the 120 m long vacuum sections. A compressed dry air supply of 100 psi will be needed to operate the gate valve solenoids in the storage ring tunnel. De-ionized cooling water will be used to remove the heat from the vacuum chambers and maintain the average chamber temperature to within a few degrees. This requirement is especially important at the BPM button locations where changes to the chamber geometry will impact the BPM readings. Based on FEA of the current design, a flow rate of 11.4 l/min [3 gpm] will be adequate. Additional cooling water will be required in the straight sections and for the IR vacuum systems. Each water circuit will have a separate flow meter on the return line to ensure adequate water flow and cooling for the vacuum chambers. As a precautionary measure, RTD or one wire type temperature sensors will be installed on chamber surfaces where high levels of power are being absorbed as well as beam channel flange joints to confirm a proper RF seal. These locations will be monitored as part of the equipment protection system and some locations will be used to interlock the beam in case of unexpected operating conditions.

6.4.2 RCS Vacuum System

Vacuum Requirement and Arc Cell Layout

The RCS vacuum system will provide an adequate aperture during the acceleration of the electron beam from the injection energy of 0.4 GeV to the extraction energy ranging from 5 GeV to 18 GeV. Each approximately 400 m long arc will be broken into four vacuum sections separated RF shielded gate valves. The long straights are approximately 235m long and will be divided into shorter vacuum sections to accommodate injection, extraction, RF and diagnostics equipment. A layout of an arc half-cell consisting of one dipole chamber and one multipole chamber separated by a RF shielded bellows is shown in Figure 6.135. All of the chambers will have a circular cross section with an outer diameter of 34.9 mm with a 1 mm wall. Using a round beam pipe minimizes the multipoles which are generated by the induced eddy currents during ramping. In order to reduce longitudinal impedance and resistive wall effects, the vacuum chambers will be made of C12200 copper. Chambers made of stainless steel would need to be copper coated, increasing the cost significantly. The induced eddy current effects and their impact on the beam have been evaluated and found to be acceptable.

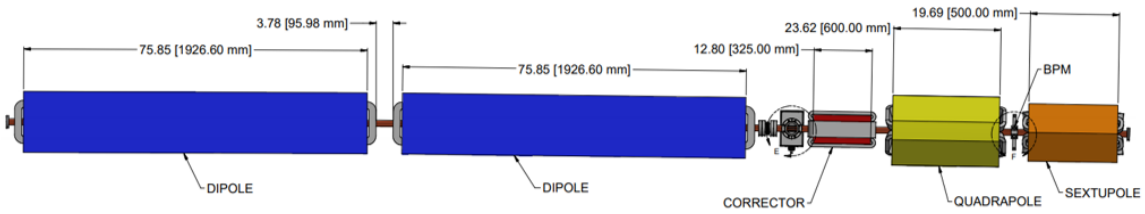

Figure 6.135: RCS half-cell vacuum chamber layout, with one dipole chamber and one multipole chamber separated by a RF shielded bellows.

For the short acceleration cycle, the beam loss due to beam-gas interaction is insignificant; therefore, an average vacuum pressure of mid-10^{-8} mbar is sufficient. Thermal outgassing will be the main source of gases in the RCS, while the photon stimulated desorption contributes only a few percent to the overall gas load. In the following sections, the eddy current effects, the estimated gas load and the pressure distribution will be discussed. The vacuum chamber design and fabrication as well as the vacuum instrumentation and control will be outlined.

Vacuum Chamber Eddy Current and Heating

To minimize eddy currents, a material with a high electrical resistivity would normally be chosen for the vacuum chamber inside magnets with changing magnetic fields. Due the high bunch charge of up to 28 nC which will be circulated in the RCS, a beam pipe with high resistivity such as stainless steel would have to copper coated. Applying this type of coating to the long beam pipes which are required would add significant cost given the

size of the RCS ring. As an alternative, thin wall copper tubing has been selected for the vacuum chamber material. A wall thickness of 1 mm was chosen as a compromise between the resulting phase lag of the magnetic fields penetrating the chamber wall and the need to ensure mechanical stability.

The power deposited on the chamber wall by eddy currents can be expressed as [254, 262]

$$P_{\text{eddy}} \approx \frac{\pi \dot{B}^2 t L b^3}{\rho_r} \tag{6.9}$$

where L is the length of the chamber in the magnetic field (4.24 m), t and b are the thickness and ID of the vacuum chamber respectively. At 10 Hz, $\dot{B} \approx 2.24\,\text{T/sec}$ for the 18 GeV ramp and the electrical resistivity of copper $\rho_r \approx 1.68 \times 10^{-8}\,\Omega\text{cm}$. The average power dissipation per dipole chamber is ≈ 3.6 watt, assuming a duty cycle of 0.2 s, or less than $8 \times 10^{-4}\,\text{watt/cm}^2$ of the dipole chamber surface. No noticeable increase in dipole chamber temperature is expected therefore no additional increase in thermal outgassing is anticipated.

Outgassing, Desorption and Achievable Pressure

Even in a thoroughly cleaned vacuum system, water vapor will always dominate the outgassing rate in an unbaked system. It has been shown experimentally that the outgassing rate for metal alloys is inversely proportional to the pumping time (t) and the empirical relationship shown below provides a good approximation

$$q_{\text{H}_2\text{O}}[\frac{mbar \cdot l}{s \cdot cm^2}] \approx \frac{3 \times 10^{-9}}{t[hr]} \tag{6.10}$$

The other source of gas load is from photon stimulated desorption (PSD). The circulating electron beam will emit energetic X-ray photons when passing through the dipole magnetic field. These photons hit the chamber wall and liberate or desorb gas molecules from the surface of the vacuum chamber. The total photon flux Γ for the whole ring can be expressed as [254]:

$$\Gamma = 8.08 \times 10^{17} IE. \tag{6.11}$$

Here I is the electron current in mA, and E the electron energy in GeV. The total photon flux during the 100 ms acceleration cycle can be conservatively estimated using the above equation, and is 3.55×10^{18} photons assuming 56 nC (2×28 nC) circulating for 0.1 s at an energy of 10 GeV. The number of desorbed molecules is proportional to the PSD yield of the surface, which depends on the conditioning of the surface by the photons. Since the photons will strike a narrow zone of the chamber wall at mid-plane on the outboard side of the ring, a PSD yield of $< 1 \times 10^{-4}$ molecule/photon will be reached for this surface after a short beam commissioning period. Assuming this desorption rate, the total amount of gas desorbed will be equivalent to $1.44 \times 10^{-5}\,\text{mbar} \cdot \text{l/s}$ for the whole ring, or an average outgassing rate of $5.77 \times 10^{-13}\,\text{mbar} \cdot \text{l}/(\text{s} \cdot \text{cm}^2)$ in the arcs which is similar to the

outgassing rate of a well baked UHV system.

The heat load from synchrotron radiation can be calculated by [254]

$$P[\text{kW}] = 88.46E^4 I/\rho \tag{6.12}$$

Here $\rho = 247\,\text{m}$ is the bending radius of the dipole magnet and I = 0.44 mA for the high bunch charge case mentioned above. The total power radiated P will be about 15.8 kW per cycle at 1 Hz for the whole ring. This is equivalent to ≈ 7 watts/m average heat load in the arcs. While this is almost one order of magnitude higher than eddy current heating, it can still be passively managed while not significantly increasing the thermal outgassing of the system.

A pressure simulation was performed using the geometry shown in Figure 6.135 assuming an outgassing rate of 3×10^{-11} mbar $\cdot\, l/(s \cdot cm^2)$ which is expected after approximately 100 hours of pumping. The pump slot design was chosen to balance RF shielding requirements with pumping conductance limitations. Lumped pumping locations are limited due to the density of magnet in the ring further complicating the vacuum system. A 45 l/s ion pump was chosen and the results are shown in Figure 6.136. The outgassing rate will gradually decrease with continuous pumping, and low 10^{-8} to high 10^{-9} mbar pressure will be reached shortly after initial operation.

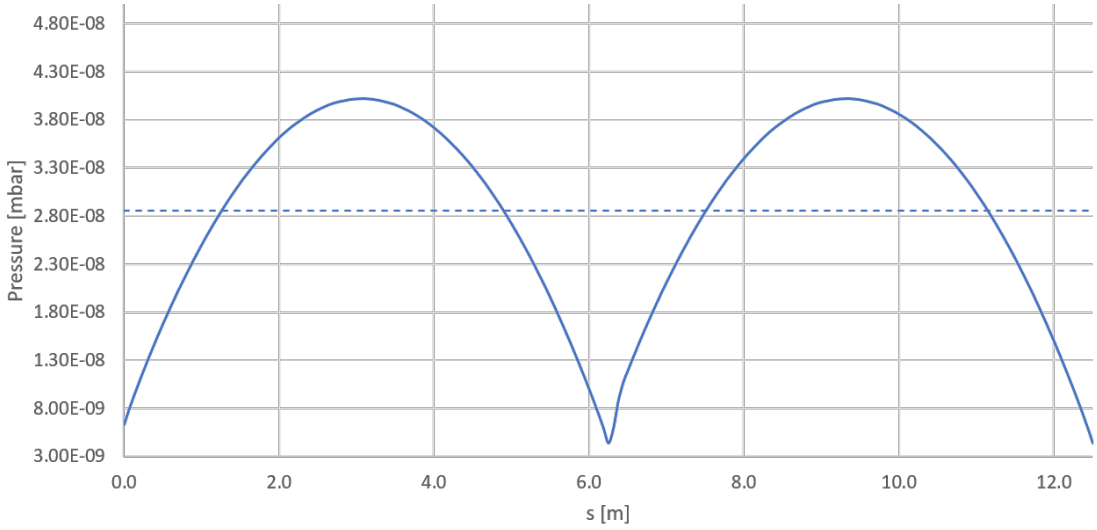

Figure 6.136: Calculated pressure distribution in a standard RCS cell with one 45 l/s ion pump spaced every 6.3 m

Chamber Design and Fabrication

The layout of the vacuum system for an arc half-cell of the RCS is shown in Figure 6.135. Both the multipole and dipole chambers will be fabricated from round copper tubing with

an outside diameter of 34.9 mm diameter and a wall thickness of 1.0 mm. Conflat flanges will be welded directly to this copper tubing using TIG welding. The length of the dipole chamber will be $\approx$ 4.3 m long and will be curved to match the beam orbit through the dipole magnet. The multipole chamber will be $\approx$ 2.0 m long and pass through the corrector, quadrupole and sextupole magnets. There will be a discrete pumping port at the beginning of the multipole chamber with RF shielding for installing an ion pump as well as gauging and rough valves where needed. The two chambers will be separated by an RF shielded bellows to accommodate any thermal expansion and misalignment. The multipole chamber will also provide provisions for installing BPMs which will be mounted in a dedicated block as shown in Figure 6.137.

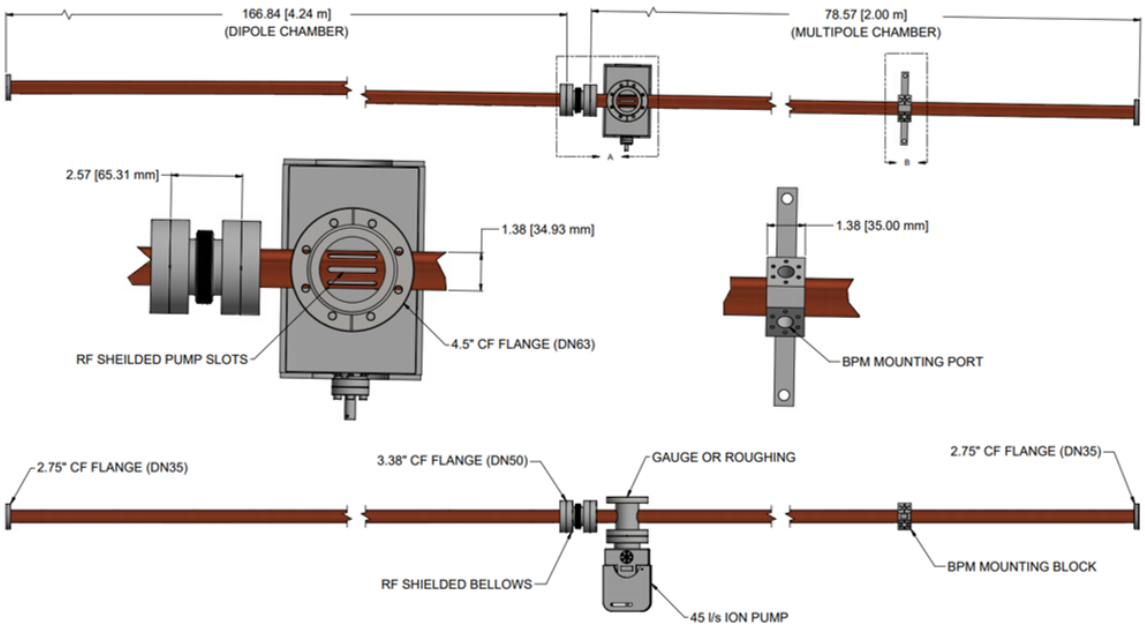

Figure 6.137: Vacuum chamber layout for one arc half-cell of the RCS.

To reduce the broadband impedance and to minimize the localized HOM heating, the inner cross-section of the electron beam chamber wall should be maintained as smooth as possible. The changes in the cross sections of the beam chamber should vary gradually, with an inclination 10:1 or greater for all tapered transitions. For vacuum components with cavity-like or discontinuous structure, such as bellows and flange joints, RF contact fingers or springs will be installed to reduce the impedance and provide a smooth path for the beam image current. The height of any steps at RF fingers and flange joints should be less than 1 mm. Commercially available RF-shielded gate valves will be used along the RCS beam channel. The RF shielded bellows in the RCS will be based on the NSLS-II design [243] which implements an 'outside' finger approach. These fingers are held in tight contact with the fixed sleeve by contact springs. A proposed design for the RCS bellows is shown in Figure 6.138

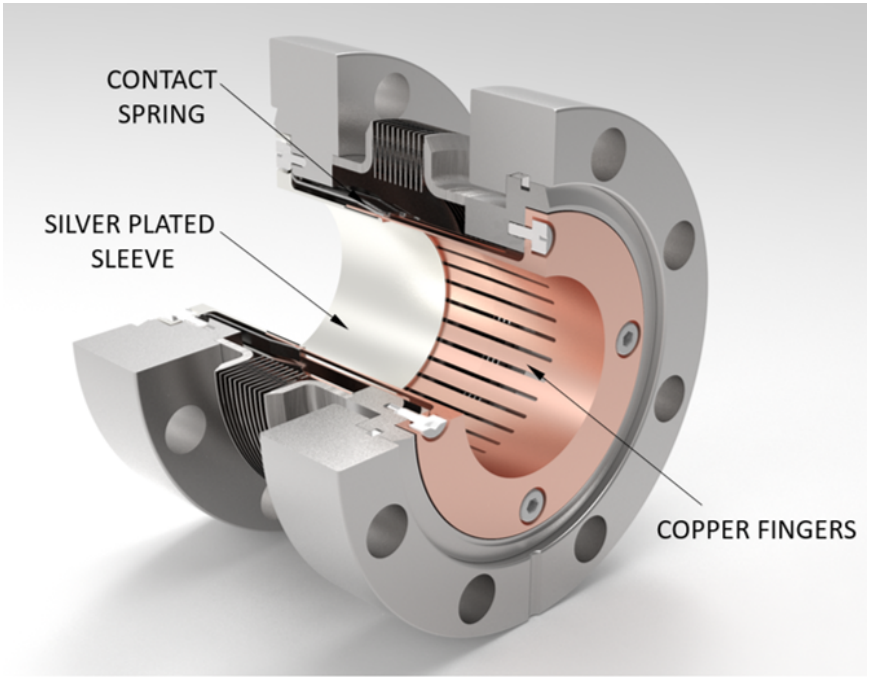

Figure 6.138: RF shielded bellows for the RCS ring.

Vacuum Monitoring and Control

One 45l/s noble diode type ion pump will be mounted at the pump cross in each half-cell chamber. Noble diode pumps have one titanium cathode (which is standard) and one tantalum cathode. These types of pumps are more stable when they are exposed to noble gases such as argon. Since o-ring seals will be used for the roughing valves, there is the expectation of small amounts of argon entering the vacuum system. The pump current will be used to monitor the RCS vacuum, providing detailed information of the pressure distribution throughout the ring. In addition, one convection-enhanced Pirani gauge and two cold cathode vacuum gauges (CCG) will be installed in each vacuum section to monitor the vacuum during initial pump down and during operation. Selected ion pump currents and CCG readings will feed to a PLC to interlock the gate valves and other critical systems such as RF, injection and extraction equipment, thus isolating any sections during catastrophic failure. Portable residual gas analyzers mounted on turbopump stations will be used for trouble shooting.

The vacuum control system will interface directly with vacuum devices as part of RCS equipment control and protection systems (EPS). They will be backed by uninterruptible power supplies. The low-level vacuum controls, consisting of dedicated PLCs with digital and analog I/O modules, take inputs from the vacuum devices and send out commands through dry contact relays. The PLCs will provide the logic for the operation and control of the vacuum devices. For gate valve control, the PLCs will use a voting scheme, with inputs from gauges and pumps, to initiate valve interlock and closure, therefore minimizing false triggering due to the malfunctioning of a single device.

6.4.3 Electron Pre-injector Vacuum System

The pre-injector vacuum system is composed of an extreme-vacuum compatible polarized electron source. The source is composed of a cathode load lock chamber system, a cathode preparation and low energy polarimetry system, an extreme-vacuum cathode storage chamber, and a large chamber that contains the high voltage DC-gun. The beam exits the gun at 350 keV. Down beam from the gun chamber is a diagnostic and highly differentially pumped beam line. A dipole chamber houses the port by which a high power pulsed laser illuminates the surface of the photocathode and provides switching capability to send the beam either to a full voltage polarimeter and end station with beam diagnostic capabilities, a Faraday cup beam dump, and machine protection sensors, or to send the beam to the copper cavity buncher sector of the 400 MeV LINAC. The buncher cavity sector is composed of a 114 MHz pre-buncher cavity, a pair of 570 MHz buncher cavities, and a 3 GHz tapered cavity that accelerates the electron beam up to an energy of 4 MeV prior to its injection into the first LINAC structure. The LINAC section is composed of a minimum of six UHV SLAC-style 2856 MHz cavity structures. Each structure has a nominal minimal acceleration gradient of 16.6 MeV per meter.

Polarized Source Vacuum System

The vacuum system of the polarized electron source for the EIC pre-injector will be state-of-the-art due to its extreme vacuum requirements. The polarized source chamber, cathode storage chamber and beam line forward of the electron gun will be designed to maintain a vacuum pressure within the gun chamber of less than or equal to 10^{-12} Torr. This is accomplished by selecting and conditioning appropriate gun and chamber materials to minimize the outgassing rates of all vacuum surfaces and the incorporation of an optimized combination of capture pump technologies into the gun chamber and beam line systems to minimize individual residual gas pressures. An optimized vacuum bake-out and pump activation sequence will be used to obtain a minimum base pressure. This technique has been successfully demonstrated by BNL as part of the EIC R&D program for large stainless steel chambers that can now routinely achieve vacuum in the less than or equal to 10^{-12} Torr range making them suitable for polarized source development.

Figure 6.139 shows a conceptual layout of the components of the polarized DC gun system. From the left, large aperture molybdenum gun cathodes, made with GaAs substrates, are introduced into the gun vacuum system through the load lock of the cathode preparation system. The vacuum system of the load lock will consist of a UHV turbo pump, an ion capture pump, and a bake-out system to bring vacuum levels down to the 10^{-10} Torr range, before an ultra-high vacuum magnetic manipulator is used to transfer cathodes from the load lock to the preparation chamber. The vacuum system of the cathode preparation chamber consists of a vacuum fired 316L stainless steel chamber, a UHV turbo pump and ion capture pump systems that control the vacuum environment throughout the stages of cathode preparation. Upon cathode creation, the chamber pressure is reduced to the low 10^{-11} Torr range before an all-metal valve is opened to the cathode storage chamber. A magnetic ma-

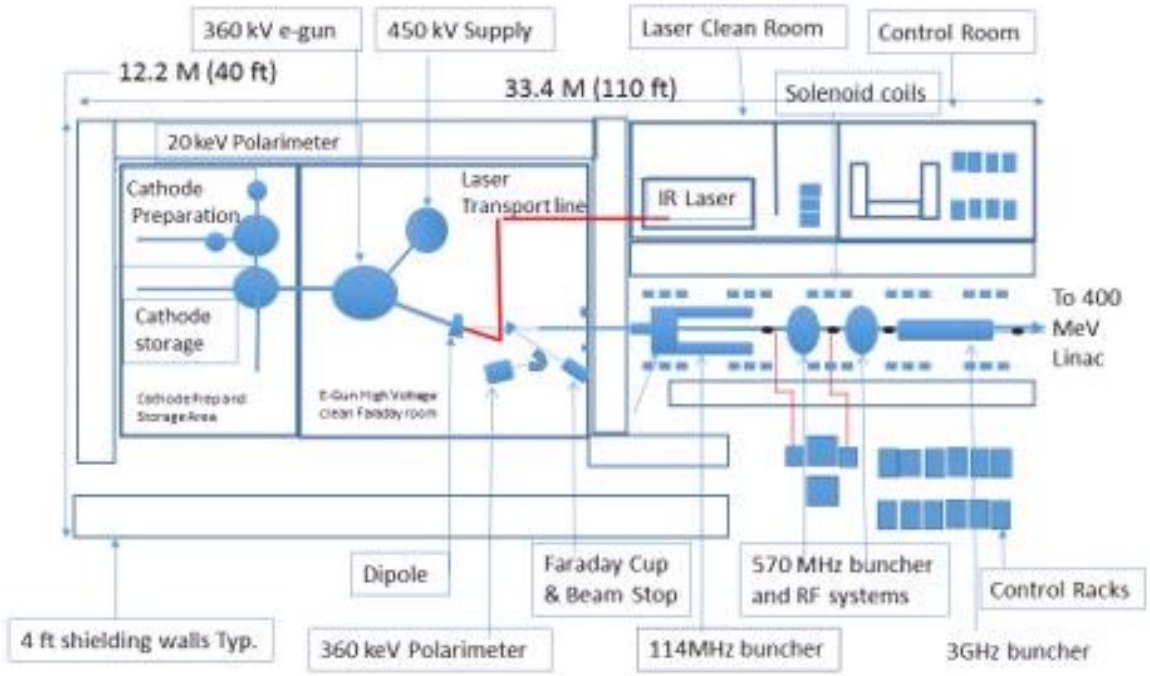

Figure 6.139: Polarized electron-gun and 3 MeV source conceptual layout.

nipulator, optimized to operate in the extreme vacuum environment with-out significant pressure excursions, transfers the cathode into the titanium storage chamber where after the all-metal valve is closed the chamber is brought to less than 10^{-12} Torr. A series of inline TSP and NEG pump arrays will be installed at optimal locations to provide vacuum stationing and the beam tube will be NEG coated at certain locations to optimize inline pressure differential in the chamber. At this pressure cathode degradation over time is negligible. Multiple cathodes are stored in this chamber to assure an adequate supply for reliable EIC operation. A long magnetic manipulator designed to operate in the extreme vacuum environment without significant pressure excursions is used to transfer fresh cathodes from the storage chamber into the DC gun chamber and spent cathodes back into the storage chamber. The gun chamber will be designed with adequate pumping capability to minimize pressure excursions from potential gas sources to maintain pressures at the cathode surface of less than 10^{-12} Torr even during full beam operation. The gun chamber material will be determined during upcoming studies of outgassing rate measurements of vacuum fired stainless and titanium chambers as part of the EIC R&D program.

The polarized e-gun, gun chamber and beam line components will be designed, manufactured and conditioned to minimize atomic hydrogen content of all in-vacuum surfaces, and electron beam optics will be designed to minimize the rate of electron beam halo interaction with the beam line chamber walls.

Figure 6.140 shows the polarized electron gun system; note the inserted photo of a NEG pump module assembly. NEG modules of this type will represent over 11,000 l/s of NEG pumping per module. Titanium sublimation pumps (TSP) provide additional top off capacity enhancing the XHV reach of the NEG pump arrays and have been designed to establish ultimate base pressure below the 10^{-12} Torr range. The TSP modules are located externally to eliminate the possibility of sputtered titanium reaching the high voltage surfaces of the DC gun.

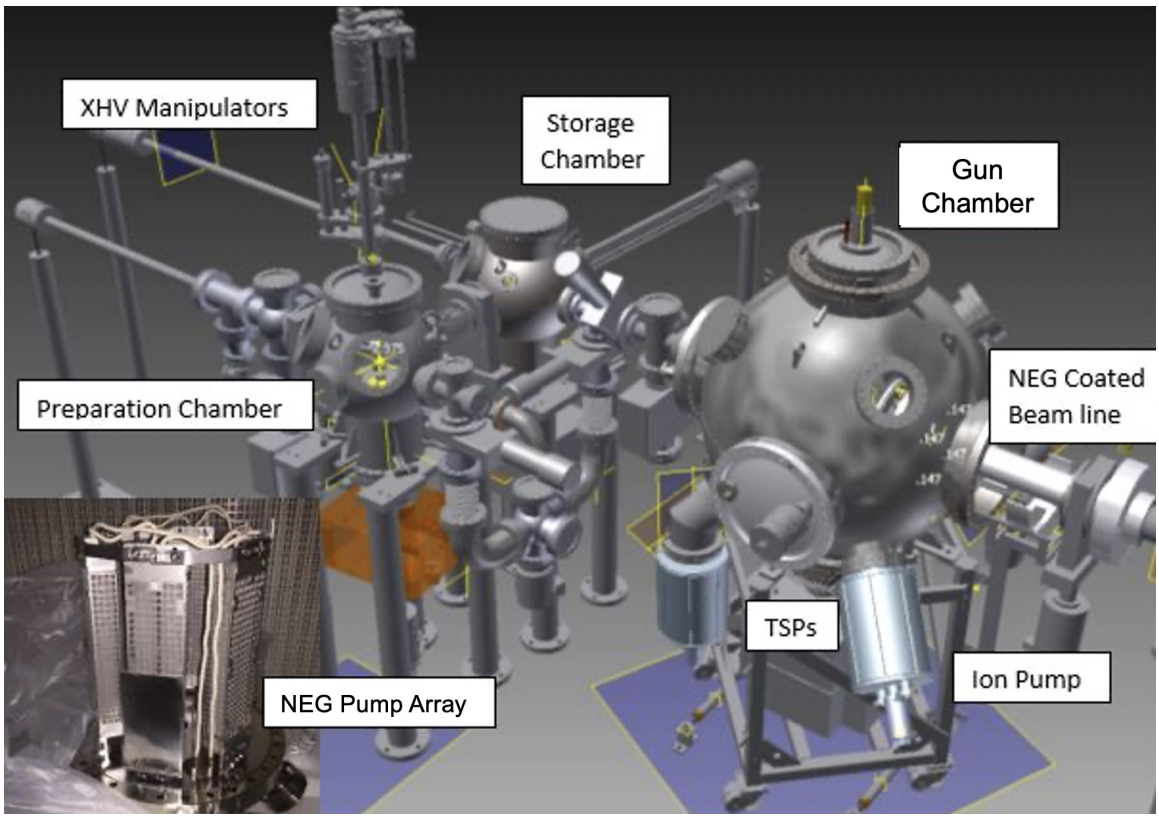

Figure 6.140: Polarized e-gun system with a sectioned view of the gun vessel.

Extreme Vacuum Isolation

A very important aspect of the pre-injector source vacuum system design is differential pumping between the extreme vacuum source and the ultrahigh vacuum cavity and LINAC sectors. It is anticipated that the quantum efficiency of the cathode and the electron beam polarization will be monitored frequently. The electron beam will be deflected into a diagnostic beam line where both beam current and polarization measurements are performed. However, these measurements are destructive and will produce significant de-

gassing of the bombarded surfaces. To mitigate the risk of cathode poisoning due to this pressure rise, a differential pumping system will be implemented between the gun chamber and the diagnostic sector that provide distributed inline pumping of all residual gas species.

A series of inline TSP and NEG pump arrays will be installed and portions of the beam tube will be NEG coated at optimal locations to optimize inline pressure differential. Vacuum models indicate that under steady state conditions more than five decades of pressure differential can be maintained between the gun and the Faraday cup. We plan to validate this model with the prototype gun and beam line that is being built and will test this as part of the EIC R&D program.

Additional vacuum requirements and specifications for elements of the polarized source and extreme vacuum isolation systems are presented in Table 6.57.

Vacuum Systems Components of the 400 MeV LINAC

The LINAC at the BNL NSLS-II as shown in Figure 6.141, was selected as the reference design for the pre-injector 400 MeV LINAC. Though bunch charge, length, and repetition rate are significantly different, detailed beam dynamics modeling indicate that other than

Figure 6.141: NSLS-II pre-injector LINAC.

changes to the beam compression and buncher cavities the design of many of the NSLS-II LINAC system components can be used as-is for the EIC pre-injector, Figure 6.142. The following description of the pre-injector 400 MeV LINAC vacuum system is based on what currently exists at the 200 MeV LINAC at NSLS-II. All copper buncher cavities will each have an ion pump appropriately sized to accommodate the rate of surface outgassing from the cavity construction, window and flange joint leak rates and the rate of electron beam scattered ion desorption from the inside surface of the cavity and beam tube apertures to reliably achieve a vacuum range in the mid-to-low 10^{-11} Torr.

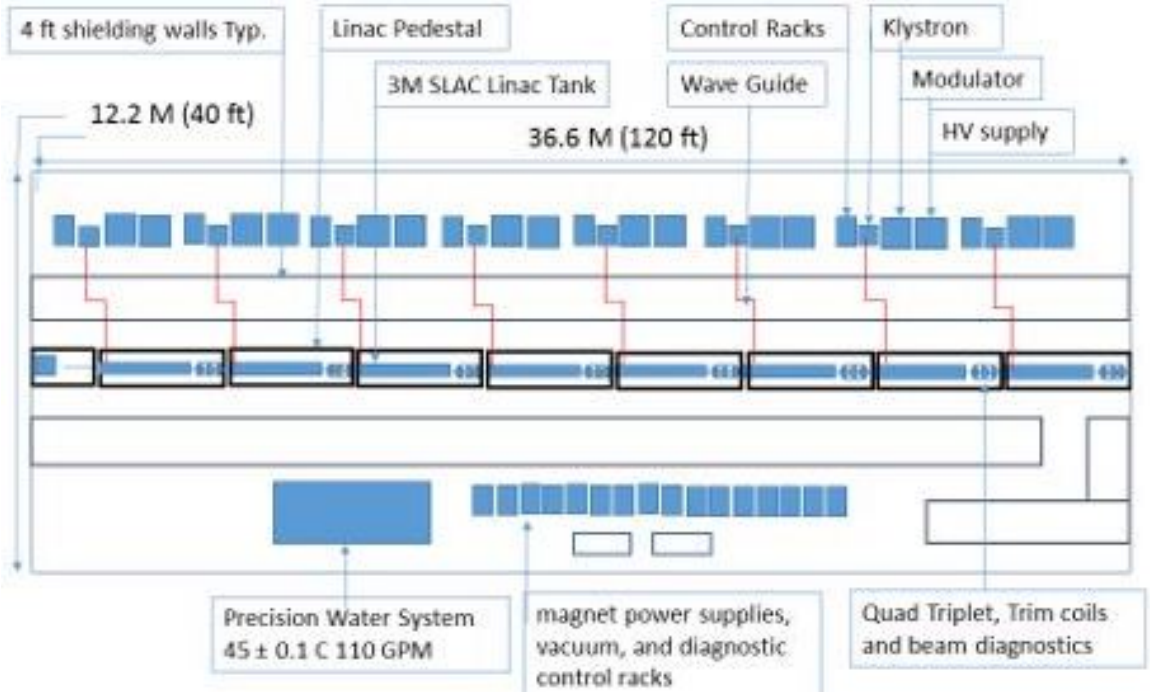

Figure 6.142: Preliminary 400 MeV Pre-Injector Layout

The EIC 400 MeV pre-injector as depicted in the conceptual layout as shown in Figure 6.142 is based on SLAC style 2856 MHz 3 meter long all-copper LINAC structures and stainless flanged high vacuum all-copper water cooler waveguides.

Appropriately sized ion pumps will be installed at either end of each LINAC structure to maintain the vacuum level on the beam line axis in the low to medium 10^{-10} Torr vacuum range. Water cooled RF windows will be installed to isolate beam line from waveguide vacuum. Ion pumps will be located at either end of each accelerator structure and each length of high vacuum RF waveguide.

Wave guide pumping will be accomplished by appropriately sized ion pumps to maintain waveguide pressure in the 10^{-9} Torr vacuum range. For the LINAC , conventional sputter ion pumps with titanium sublimation will be used to achieve UHV conditions but special precautions will be taken to prevent titanium from being sputtered onto surfaces that transmit RF power. There will be one isolation valve between each of the six 3 meter long accelerator structures. Should a vacuum excursion be detected in the transfer line down beam from the LINAC , all the vacuum valves will be programmed to close simultaneously to prevent gas excursions from propagating through to the bunching sector or the extreme vacuum source or significantly contaminating the pristine copper surfaces of the LINAC structure aperture. This action rapidly increases the conductance along the approximate 40 m of LINAC, thus effectively protecting the extreme vacuum polarized source without the need for a fast valve. Due to the high bunch charge, each valve in their open condition will have a tubular RF finger assembly that will span the gap creating a contiguous RF surface across the opening of each gate valve.

The triplet girder as shown in Figure 6.143 supports the isolation valve, a set of triplet magnets, and beam diagnostics.

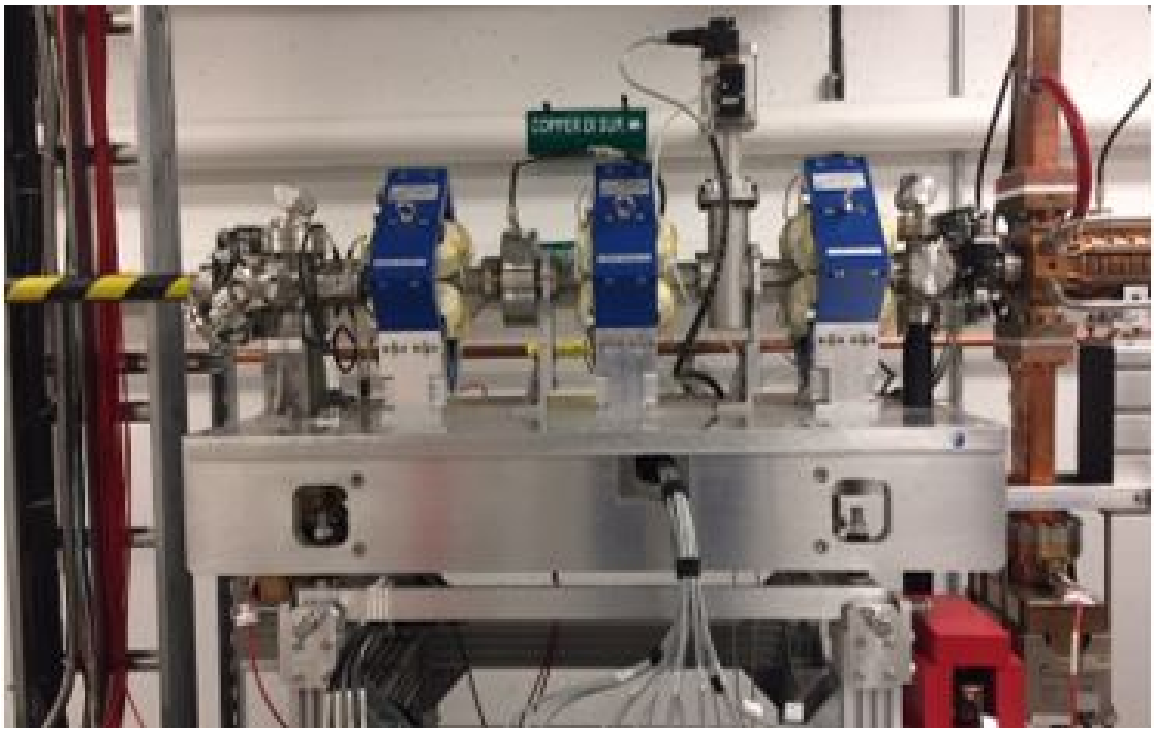

Figure 6.143: Triplet girder supporting the isolation valve, a set of triplet magnets, and beam diagnostics.

The vacuum chamber between each LINAC structure will be designed to accommodate a right angle all-metal pump-out port valve, a four button beam position monitor, an integrating current monitor, and a wire scanner and/or YAG crystal beam profile monitor. The system features independent structural supports for the vacuum system components and supporting structures for ion pumps located at either end of the LINAC structures.

Pre-Injector Transport Line Vacuum System

Past the end of the 400 MeV LINAC a transport line is used to bring the polarized electron beam to the RCS injection kicker in the 2 o'clock straight of the collider tunnel. All-metal isolation valves will be located at the end of LINAC structure #6 just prior to the start of the spin rotator sector and between the spin rotator sector and the RCS injection kicker. Ion pumps will be located approximately every 5 to 10 meters to maintain a vacuum pressure in the 10^{-10} Torr vacuum range.

It is anticipated that a portion of the transport line vacuum system and beam line will be inclined. Vertical bend dipole magnets located at either end of the transport line straight will form a dog leg beam path from the point where the transport line enters the EIC tunnel until its axis nears the elevation of the RCS ring. The vacuum chambers of the vertical bend dipoles will be "Y"-shaped allowing the beam to proceed along the LINAC axis into the diagnostic end station and beam dump to study pre-injector LINAC performance or up the inclined transport line when the vertical bend dipole in powered. It is anticipated that a water cooled synchrotron radiation absorber cooling line may be needed to cool the forward surface of the spin rotator dipole vacuum chambers. Appropriately sized ion pumps with NEG or TSP capture will be installed on the dipole chamber down beam from each spin rotator dipole magnet.

Stands will be used to support and align the inclined segments of the beam line vacuum chamber. All formed metal bellows along the transport line will be equipped with internal RF fingers. Prefabricated pedestals will be grouted to the EIC tunnel floor. The pedestals will support magnet base plates that will in turn support beam line focusing quadrupole magnets, vertical and horizontal steering magnets, four button beam position monitors, integrating current monitors and a wire scanner beam profile monitor, cold cathode gauges and a right angle all-metal valve pump-out port that will be positioned between each of the all-metal isolation valves.

As a potential cost savings, consideration is being given to locate the 400 MeV LINAC in the spectrometer spur tunnel just south of the 2 o'clock straight. This would significantly reduce the required foot print of the pre-injector support building by utilizing the present RHIC ring berm as shielding for the LINAC and reducing the length and complexity of the otherwise very long high vacuum LINAC-to-RCS (LtR) transport line.

Additional vacuum requirements and specifications for elements of the pre-injectors 400 MeV LINAC and transport line are presented in Table 6.57.

Table 6.57: Vacuum Requirements and Specifications for Pre-Injector Vacuum Elements.

System	Requirements	Element Specification
Cathode Load Lock	10^{-10}	$>$ 100 l/s turbo pump
	250° C bake out	100 l/s Ion pump
Cathode Prep chamber	10^{-12}	300 l/s UHV Turbo pump
	Vacuum Fired stainless steel	300 l/s Ion pump
	400° C bake out	8000 l/s NEG pump system
Cathode Storage Chamber	$< 10^{-12}$	300 l/s UHV Turbo pump
	400° C bake out	8000 l/s NEG pump system
		TSP capable
Polarized Gun Chamber	$< 10^{-12}$	300 l/s UHV Turbo pump
	TBD based on EIC R&D	1200 l/s ion pump
	400° C bake out	35000 l/s NEG pump system
		$>$ 8,000 l/s TSP pumping system
Valves on DC gun system	All-metal gate and right-angle	VAT series 48 XHV rated valve
		63 mm manual
		100 mm air operated
		100 mm manual
Vacuum beamline segments	100 mm nominal	NEG coated
	grade 2 titanium	$> 0.2 l/s \cdot cm^2$, H_2
	250° C bake out and activation temp.	
Dipole chamber	>100 mm nominal	NEG coated
	grade 2 titanium	>0.2 l/s cm^2, H_2
	250° C bake-out and activation temp.	>100 l/s ion pump
		>700 l/s TSP pump
Inline beam line TSP	>100 mm nominal	>8000 l/s TSP pumping
	grade 2 titanium	
	250° C bake out and activation temp.	
Faraday Cup beam stop	10^{-12}	300 l/s UHV Turbo pump
	Vacuum Fired stainless steel	300 l/s Ion pump
	250° C bake out	8000 l/s NEG pump system
		$>$ 3000 l/s TSP pump system
Beam line to buncher system	$< 10^{-11}$	
	$>$ 100 mm nominal	NEG coated
	Vacuum fired stainless steel	$>$ 0.2 l/s cm^2, H_2
	250° C bake-out and activation temp.	$>$ 100 l/s ion pump
		$>$ 700 l/s TSP pump
Buncher Cavities	$< 10^{-10}$	
	OFHC Copper	100 l/s ion pump/cavity
	200° C bake out max.	$>$ 700 l/s TSP pump
Beam line Segments	10^{-10}	
	1.5″ OD $\times$ 0.063″ wall	75 l/s ion pump
	2.73″ CF flange	
	200° C bake out max.	
LINAC structure s	10^{-10} in #1, $< 10^{-9}$ in #6	Water Temp. 45° C $\pm$ 0.1° C Stabilization
	OFHC Copper	75 l/s ion pump/structure
	200° C bake out max.	
LINAC Isolation Valves	2.75″ CF All-Metal Valve bonnet	VAT series 48 valve air operated
RF wave guide	10^{-9}	
	copper 2856 MHz	Two 20 l/s ion pumps per wave guide segment
	150° C max. bake	Water Temp. 1° C Stabilization

6.4.4 Hadron Rings Vacuum Chamber Update

Overview

The EIC HSR will make use of the existing RHIC storage rings including the superconducting magnet arcs. This design choice will spare the project from building new, expensive superconducting magnets. At the same time, the RHIC superconducting magnets were not designed for the EIC beams and their vacuum chamber must be updated to reduce the resistive-wall (RW) impedance and suppress electron clouds. Without an update, the cryogenic system will have significantly increased heat loads which will result in superconducting magnets quenching. An expansion of the cryogenic system can resolve the problem at the expenses of increasing both capital and operational costs. To avoid high RW heating and electron cloud without compromising the EIC luminosity goal, a stainless-steel beam screen with co-laminated copper and a thin amorphous carbon (aC) film will be installed in the beam pipe of the RHIC superconducting magnets. The interior surface of this beam screen – the surface seen by the beam – will be copper since it has much lower electrical resistivity than stainless steel especially at cryogenic temperatures. The addition of a thin aC film on top of the copper will mitigate the emission of secondary electrons that feed the electron cloud. Previous work inspected the possibilities of in-situ coating the RHIC superconducting magnet arcs [89, 263], an alternative to the beam screen which is not longer pursued.

The EIC screen design is based on the CERN LHC screen which has a thin copper surface on a stainless-steel liner screen [264]. There are major differences between the two designs. The LHC screen design includes an integrated 4.5 K supply ($\sim$20 K return) cooling system mounted to the screen itself. This is because the LHC beam screen has a higher heat load from the addition of synchrotron light heating from higher beam energy operation. The 4.5 K cooling reduces the heat load on the 1.8 K magnet cold bore and therefore the heat load on the 1.8 K cryogenic distribution system. The second difference is that the LHC beam screen was installed before the magnets were installed in the ring. This allowed space to install the screen and to do the plumbing necessary for the separate beam screen cooling cryogenics. Installing this in the RHIC cryogenic system would be highly invasive to the existing cryogenic distribution system. Therefore, the screens are designed to have contact cooling with the RHIC magnet cold bore pipe at 4.5 K. Finally, the LHC beam screens were not installed with aC coating. CERN is in the process of upgrading some of there vacuum chambers with aC coating to mitigate electron clouds [265]. The RW impedance and the electron cloud formation will be discussed in detail in the next sections along with the additional design requirements.

Resistive-wall Impedance

High resistive-wall impedance in accelerators can result in unacceptable levels of resistive heating or in resistive-wall induced beam instabilities [266]. Some of the beam parameters that enable the EIC's high luminosity challenge operation with the RHIC's super-

conducting magnets unless modifications are implemented. The large number of short, high-intensity bunches leads to large resistive-wall (RW) heating being deposited in their stainless-steel beam pipes. In a similar way, the vacuum chamber portion in the cold mass interconnects is also subject to the same issues and needs to be updated.

For on-axis passage of a beam consisting of M Gaussian bunches with rms bunch length σ_t and bunch charge Q, the resistive-wall heating per unit of length (P'_{RW}) expected in the circular beam pipe with radius b and electrical resistivity ρ of a circular accelerator with revolution period T_0 is:

$$P'_{\mathrm{RW}} = \Gamma \left(\frac{3}{4}\right) \frac{Q^2 M}{4\pi^2 b T_0} \left(\frac{\mu\rho}{2}\right)^{\frac{1}{2}} \left(\frac{1}{\sigma_t}\right)^{\frac{3}{2}} \tag{6.13}$$

where μ is the magnetic permeability of the beam screen. The full-scope, high-luminosity 275 GeV proton beam with 290 bunches and 19.8×10^{10} protons per bunch leads to the largest RW heating of the beam pipe. For the current stainless-steel beam pipe (ρ = 5.07×10^{-7} Ω-m), the expected resistive-wall heating is about 4 W/m, well above the dynamic heat load budget available (about 0.5 W/m); with an all-copper beam screen operating at 10 K or below (ρ = 1.75×10^{-10} Ω m for RRR100 Cu, no anomalous skin effect accounted), the resistive-wall heating becomes 0.08 W/m. Any variation from the strictly round shape will show larger RW heating. Furthermore, the expected RW heat is much larger due to the large radial shift (in the following, beam offset) projected to guarantee synchronicity between the non-relativistic hadrons and the ultra-relativistic electrons. While the required radial shift for the 275 GeV proton beams is, in average, about 14.5 mm, it could be as large as 18 mm in some locations. The offset beam will introduce a non-uniform angular distribution of the induced currents, given by [267]:

$$\frac{dF(\theta)}{d\theta} = \left(\frac{b^2 - x^2}{b^2 + x^2 - 2bx\cos\theta}\right)^2 \tag{6.14}$$

where x is the beam offset. Integrated over the inner angle θ, the RW heat increase due to this beam offset is [268]:

$$F = \frac{b^2 + x^2}{b^2 - x^2} \tag{6.15}$$

These beam offset dependencies are illustrated in Figure 6.144. Assuming a maximum beam offset of 20 mm to account for orbit errors, the RW heating at the point closest to the beam is a factor 14 larger than when the beam is on-axis, with the integrated RW heating increasing by a factor 2.

A beam screen, inserted in the cold bore of the RHIC superconducting magnets, will show a larger electrical resistivity by the effect of magnetoresistance. For polycrystalline copper, the dependence of the electrical resistivity on the magnetic field strength follows Kohler's law [269]. With RRR100 Cu and 3.5 T, the electrical resistivity increases by a factor 2 and

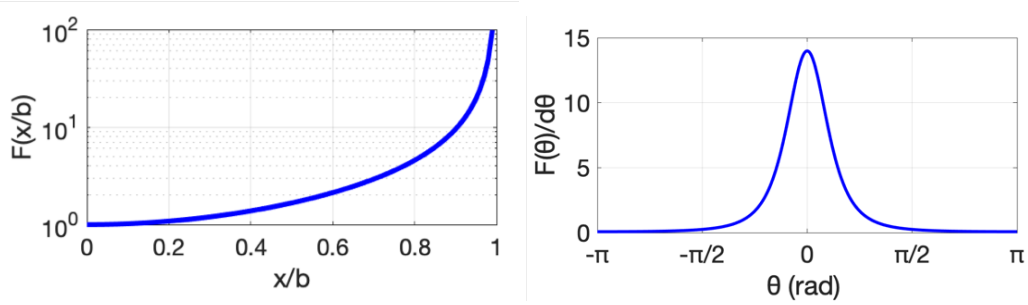

Figure 6.144: [Left] Relative variation of resistive-wall heating due to beam offset. [Right] Angular dependency of resistive-wall heating for 20 mm offset in 35 mm pipe radius.

the RW heat by a factor $\sqrt{2}$. The aC thin film will also contribute to the RF impedance of the surface. The RW impedance for a bi-layer metal is given by [270]:

$$Z_{\parallel,RW}(\omega) = \frac{Z_0}{2\pi c_0}\left\{\frac{\delta_2\mu_2\omega[sgn(\omega)]-i}{2a_2\mu_0}\times\frac{\alpha tanh(x_1)+tanh(x_2)}{\alpha+tanh(x_1)\,tanh(x_2)}\right\} \tag{6.16}$$

where Z_0 is the characteristic impedance of free space ($Z_0 = 120\pi\,\Omega$), μ_i is the permittivity of layer i, a_i is the radius of the layer i, δ_i is the skin depth of layer i, $x_i = \lambda_{i+1}(a_{i+1}-a_i)$, $\lambda_i \approx [1-i\,sgn(\omega)]/\delta_i$ and $\alpha \approx (\delta_2\mu_2)/(\delta_3\mu_3)$. In our case, layer 2 is a 150 nm aC film, with $\rho = 1.5\times10^{-5}$ Ω m and layer 3 is a 0.075 mm-thick RRR100 Cu sheet at 10 K or below. For the shortest EIC proton bunch, σ_z = 0.06 m, the RW heating increase due to the presence of the aC film is a factor 1.5.

Thus, the minimum RW heat with a RRR100 Cu round beam screen at 10 K or below is 0.08 W/m, but can reach 0.37 W/m for a racetrack beam screen when all the previous contributions take into effect. The RW heating is within the available dynamic heat load with some good margin (above 30%) but is greatly dependent on temperature. The electrical resistivity of copper can be written as the sum of two terms. The first term dominates at cryogenic temperature and is the resistivity caused by collisions of the electrons with impurity atoms and mechanical imperfections in the lattice, which is temperature independent and often referred as residual resistivity ρ_{0K}. The second term dominates at room temperature and is given by the interaction of the electrons with the phonons of the lattice. The residual resistivity ratio RRR of a specimen is defined as the ratio of its resistivity at room temperature to its residual resistivity: $RRR = \rho_{293K}/\rho_{0K}$. For typical metals like copper, the temperature-dependent term can be computed using the Bloch-Grüneisen function [271, 272]:

$$\rho_i(T) = C\left(\frac{T}{\theta}\right)^5\int_0^{\theta/T} z^5 e^{-z}\left(1-e^{-z}\right)^{-2}dz \tag{6.17}$$

where C is a constant and θ is the Debye temperature. The integral can be numerically solved with the expansion $x/(1-x)^2 = x+2x^2+3x^3+...$ and integrated term by

term [273]. Adding up all the possible contributions and using the approach described above, the variation of RW heating per unit of length with respect to temperature is as shown in Figure 6.145. To keep the dynamic heat load below 0.5 W/m, the beam screen must operate at a temperature not higher than 50 K.

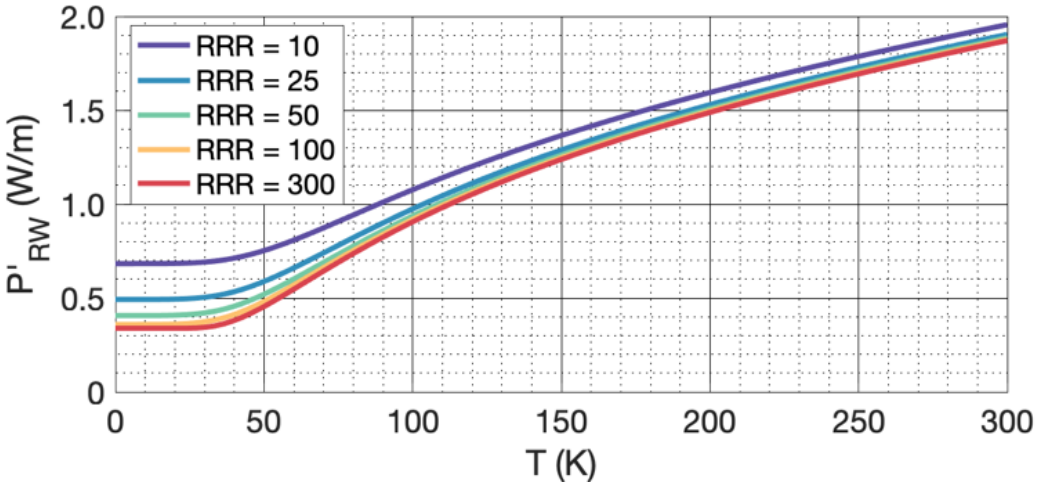

Figure 6.145: Variation of resistive-wall heating per unit of length with temperature.

Electron Cloud Buildup

Electron cloud formation has been observed in many accelerators, including RHIC [274–276]. Formation of electron clouds can be suppressed by a low secondary electron emission (SEE) surface within the accelerator vacuum chamber, typically reducing the peak SEE or secondary electron yield (SEY) to 1.3 or below. In the non-cryogenic (warm) sections of most accelerators, including RHIC, the electron cloud problem was solved by using non-evaporable getter (NEG) coating [277]. The short spacing between the high-intensity bunches of the EIC favors the electron cloud buildup, an undesired instability which can lead to sudden, abrupt vacuum pressure rises and general vacuum degradation; beam instabilities; emittance growth; interferences with diagnostic instrumentation; excessive heat deposition on the chamber walls; etc.

PyECLOUD is a 2D macroparticle code developed by CERN for electron cloud studies and extensively used to study electron cloud in the CERN's LHC, SPS, and PS [278–280]. We employ PyECLOUD simulations to predict electron cloud buildup in the EIC hadron rings due to the passage of the EIC beams. Special attention is paid to specific components such dipole, quadrupole and sextupole magnets. As electron cloud builds up, the electrons impacting on the vacuum chamber walls will deposit some energy in form of heat. Our studies monitor the heat load due to electron cloud as an indication to the formation of the electron cloud. Three different surfaces are considered for a round vacuum chamber: the existing RHIC stainless steel SS316LN beam pipe, with well scrubbed surfaces (SEY $\sim$ 1.48 – 1.55, based on measurements performed for the Fermilab's Main Injector [281] and

CERN's SPS beam pipes [282], of the same material as the RHIC beam pipe); the effect of inserting a beam screen, with a fresh copper surface (SEY $\sim$ 1.1 – 1.7); and the beam screen with a thin aC film (SEY $\sim$ 1.06).

Confidence on the electron cloud predictions relies on how well the SEE curve model and the parameter values used to conduct the simulations represent the behavior of the surface. The model used in our simulations incorporates the contributions of the true secondary electrons and the elastically reflected electrons, expressed as follows [278]:

$$\delta_{\text{true}}(E) = \delta_{\max} \frac{s\,E}{E_{\max}} \left\{ \left(\frac{E}{E_{\max}} \right)^{s} + s - 1 \right\}^{-1} \tag{6.18}$$

$$\delta_{\text{elas}}(E) = R_0 \left(\frac{\sqrt{E} - \sqrt{E + E_0}}{\sqrt{E} + \sqrt{E + E_0}} \right)^{2} \tag{6.19}$$

where $\delta_{\max}$ and $E_{\max}$ are the SEY and its corresponding energy; R_0 is the weight of the reflected electron component; E_0 and s are the shape parameters of the reflected SEE curve and the true SEE curve, respectively; μ_{true} and σ_{true} are the two fitting parameters to the log-normal energy distribution in the model. $\delta_{\max}$ and $E_{\max}$ are re-scaled as a function of the angle of incidence. Table 6.58 and Table 6.59 list the secondary emission parameter values and the beam and machine parameters used in the simulations. The Twiss parameters and the required magnetic field from dipole, quadrupole, and sextupole magnets for operation with 275 GeV proton beams are listed in Table 6.60 and Table 6.61.

Table 6.58: Secondary electron emission parameter settings.

Parameter	Scrubbed SS316LN [281]	Copper [278]	aC [283]
R_0	0.5	0.7	0.7–0.9
E_0 [eV]	225	150	150
$E_{\max}$ [eV]	250	332	275.1
s	1.35	1.35	1.773
$\delta_{\max}$	1.48	1.1–1.7	1.06
σ_{true} [eV]	1.0828	1.0828	1.0828
μ_{true} [eV]	1.6636	1.6636	1.6636

Figure 6.146 shows the heat load contributed by electron cloud formed with the passage of the 275 GeV proton beams for the initial and maximum luminosity scenarios. All the SEE curve parameter values are fixed (see Table 6.58, "Copper") except the SEY, which ranges from 1.1 to 1.7. The electron cloud starts for SEY values above 1.1 – 1.2 except at the quadrupoles with the initial luminosity beam. On the other hand, Figure 6.147 shows the heat load expected for the maximum luminosity scenario, including the effect of running with a 14 mm beam offset, in dipole, quadrupole and sextupole magnets and also in warm straight sections. All the SEE curve parameter values are fixed (now using Table 6.58, "Amorphous Carbon"), except the SEY. The beam offset was found to have a significant

Table 6.59: Machine and beam parameters for the initial and the maximum luminosity scenarios used for electron cloud simulations [284].

Parameter	Initial luminosity	Max. luminosity
Particle energy [GeV]	275	275
No. of bunches per beam	290	1160
No. of bunches in gap	25	100
Bunch population [10^{10}]	10.2	6.9
RMS emittance (H,V) [nm]	(17.9,8.5)	(9.2,1.6)
Norm. rms emittance (H,V) [µm]	(5.25,2.5)	(2.7, 0.47)
Average β^* in arc [m]	25	25
RMS bunch size σ^* (H, V) [mm]	(0.67, 0.46)	(0.48, 0.2)
RMS bunch length σ_l [cm]	9.9	5 (6*)
RMS energy spread [10^{-4}]	4.6	4.6 (6.8*)
Bunch space [ns]	40.5	10.14
Radius of beam pipe [m]	0.035	0.035

* for amorphous carbon simulation

Table 6.60: Twiss parameters for the EIC lattice (hCR-200429).

Parameter	Dipole	Quadrupole	Sextupole
β_x [m]	29.76	35.60	34.54
β_y [m]	31.38	44.57	32.14
D_x [m]	0.93	0.77	1.16

,

Table 6.61: Strengths k_n of typical magnets in the HSR lattice hCR-200429 normalized to a rigidity $B\rho$ of 917.3 T·m at the maximum proton energy of 275 GeV, where $k_n = b_n \cdot B\rho$. Gradients b_n defined according to $B_y + iB_x = \sum_{n=0}^{\infty} \frac{1}{n!} (b_n + ib'_n)(x + iy)^n$. The sextupole strength varies with the natural chromaticity, which in turn depends on β^* at the experiment (and the number of experiments).

Magnet	Strength k_n [$1/m^n$]	Gradient b_n [T/m^{n-1}]	Field at 25 mm [T]	Bore ID [m]	Comments
Arc dipole	0.00412	3.78	3.78	69	Constant
Arc quad-kf/kd	0.078	72	1.8	69	Almost const.
Triplet quad	0.052	47.4	1.185	113	Almost const.
Sextupole-sd	0.717	658	0.206	69	Variable
Sextupole-sf	0.305	280	0.088	69	Variable

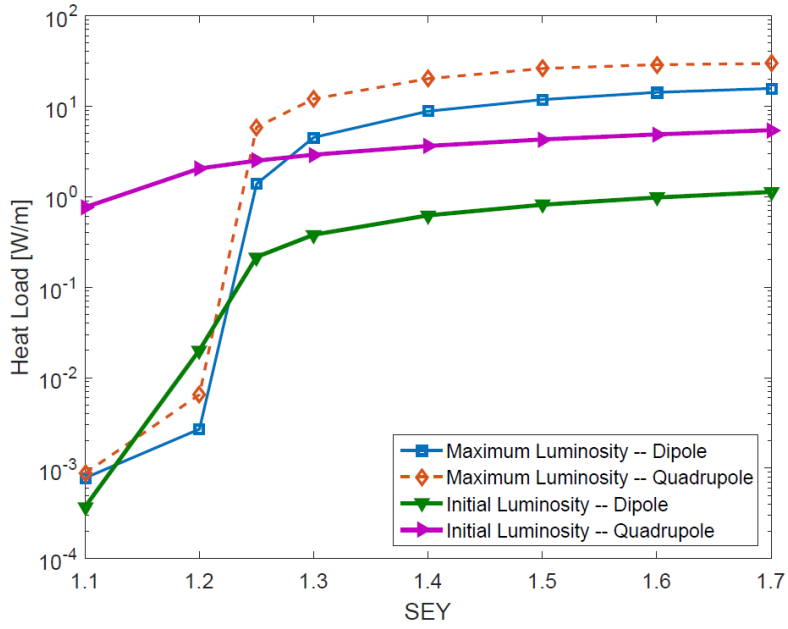

Figure 6.146: Heat load as a function of SEY for the EIC proton beams for initial and maximum luminosity scenarios.

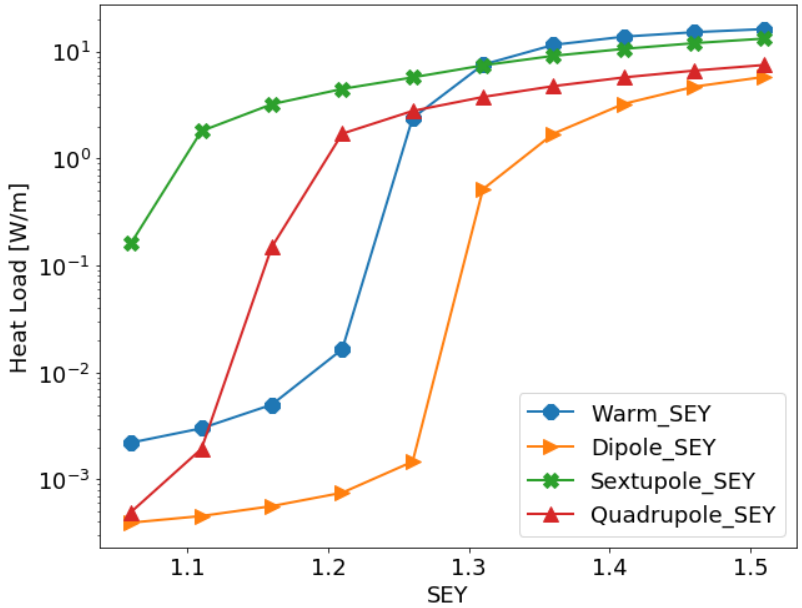

Figure 6.147: Heat load as function of SEY for maximum luminosity scenario including a beam offset of 14 mm.

effect on the heat load from electron cloud. The results highlight the necessity of equipping the beam screen with a thin aC film, with a SEY ≤ 1.06, to avoid the formation of electron clouds and their undesired effects. In the warm straight sections, presently coated with

NEG, the SEY needs to be below 1.3. The SEY of NEG films can be "tuned" by selecting the baking temperature necessary for its activation [285].

Beam Screen Conceptual Design

To reach nominal EIC luminosity under reliable operation, the beam screen must ensure:

- Low impedance to limit dynamic heat load to the cryogenic system and to avoid impedance-driven instabilities.
- Adequate vacuum level and stability, which also involves the control of e-clouds.
- Compliance with beam optics requirements, mainly aperture.
- Mechanical resistance to eddy-current forces resulting from magnet quench.
- Installation and removal.

The beam screen will be made of non-magnetic 316LN stainless steel roll-bonded with oxygen-free high-conductivity (OFHC) copper. The OFHC copper has a conductivity that is several orders of magnitude larger than 316LN stainless steel at 4 K, leading to smaller RW impedance and dynamic heat load expected from beam-induced currents. A copper thickness of 0.075 mm has been found to be sufficient for the expected beam-induced currents. The stainless steel is necessary to reduce the forces generated by quench-induced eddy-currents on the copper liner [286]. The $B(t) \times dB(t)/dt$ for the RHIC arc dipoles can be as high as -30 T^2/s after quench. For an all-copper screen with 1 mm-thick walls and RRR100 copper, the pressure exerted by the quench-induced eddy-currents on the screen walls would be a few thousands of psi. Because the EIC beam screen features a thin copper layer with high resistivity stainless steel underneath, the expected eddy currents are much smaller and the quench-induced forces are thus weaker.

Screen fabrication is a multistep effort that requires 1 mm-thick stainless steel base with a high-quality 0.075 mm-thick commercially pure copper layer. The layers are to be roll bonded together in lengths necessary to allow full length screens for the 10 m long superconducting arc dipole magnets and 5 m long sextupole, quadrupole, and corrector assemblies. After roll bonding, the screen material needs to be sent to a stamping vendor for the pumping slots needed along the length of the screen assembly. These slots will be on the top and bottom surfaces to allow the gas to travel to the colder inner beam tube surface. Next the screens need to be formed into the screen profile by vendors who specialize in this type of product which is common for fabricating heat exchangers and other custom pipe shape processes. All of these steps must be performed by vendors who use clean oil-free equipment to maintain ultra-high vacuum (UHV) compatibility. The next steps are to be performed by the UHV facility at BNL. After inspection, the screens are cleaned in an vacuum group ultrasonic cleaner. The screens are then vacuum baked in the aC deposition system and then the aC deposition process is performed as described below.

An aC film will be deposited on the copper surface to help with the electron cloud. The aC proved its capability to mitigate the formation of electron clouds in COLDEX and SPS [287, 288]. In the lab, aC even shows an SEY slightly lower than 1 [289]. During in-situ coating of stainless steel pipes in SPS, the SEY of the aC film was in average 0.98 with a standard deviation of 0.02, and for ex-situ coated parts, the maximal SEY was in average 0.99 with a standard deviation of 0.03 [290]. Beam conditioning was found to reduce the SEY of aC coatings at CERN and FNAL [291] and could be used in case the installed coated surfaces show a SEY above the electron cloud threshold. The thickness of the aC film can have significant impact on the RW impedance and the coating time. Recent studies found that the minimal aC film thickness to attain a certain SEY value was few tens of nm [292].

The EIC beam screen will have an aC film with nominal thickness of 100 nm. On the other hand, a titanium sublayer is typically added to improve adhesion and reduce the presence of hydrogen during the aC coating as hydrogen has been associated to an enlarged SEY value [293]. We will test the application of the aC thin film without the titanium sublayer to reduce coating times.

The minimum vertical aperture is set to 29.5 mm by the Q4-Q5 in the dispersion suppression section. The beam screen will adopt an almost round shape to be well adjusted against the beam pipe for good thermal contact with the beam pipe, except on top and bottom, where shape features will provide the flexibility necessary for insertion and for the vacuum pumping surface at 4.5 K. The beam screen needs to be sufficiently flexible to be inserted through the almost 10-meter-long RHIC arc dipoles, specially challenging due to the large sagitta of the RHIC arc dipole magnet beam pipe, of about 45 mm. The screen design features a locking system that prevents the screen from moving with cooldown and warmup and during quench.

Thermo-mechanical Considerations

Two-dimensional steady-state thermal simulations were conducted in ANSYS 2020 to evaluate the temperature distribution in the cross-section of the RHIC arc dipole magnet cold mass. Two particular locations are of special relevance. The temperature at the NbTi coils in the RHIC arc dipoles shall remain below the quench temperature with sufficient margin to avoid quench. The quench temperature is 5.3 K at the operational current that provides the 3.783 T necessary to keep the 275 GeV proton beams in their design orbit. On the other hand, the operating temperature range of the beam screen is important to assess the vacuum conditions and adequately engineer the vacuum system to meet the beam lifetime and emittance growth specifications. The finite-element model of the magnet cross-section is shown in Figure 6.148. Temperature-dependent thermal conductivity is considered for all the materials in the cryogenic temperature range. Thermal contact conductance between the beam tube and the beam screen, adjusting wedge and beam screen, and between the wedge and the beam tube is set to a conservative value of $5\,W/m^2K$. A temperature boundary of 4.55 K is applied to the outer cooling channels and the electrical bus slot. There is some concern that the interior cooling channels around the beam pipe might be partially or fully obstructed, so stagnant liquid helium properties are applied to the inte-

rior cooling channels.

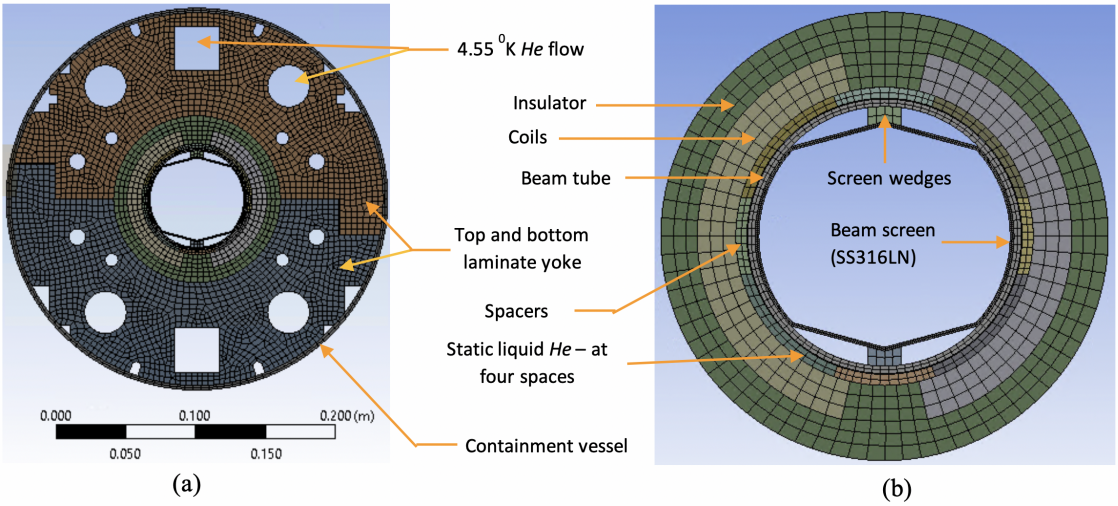

Figure 6.148: Finite-element model of (a) the RHIC arc dipole magnet cold mass cross-section and (b) close view around the beam tube.

The maximum peak temperature for a centered beam is found in the beam screen, near the wedge, because not only the straight sections are closer to the beam and thus the beam-induced currents are stronger and the RW heating larger, but also the thermal path to the cooling channels is longer. Take for example the case of a centered beam generating 0.5 W/m of RW heating, for which the peak temperature is 6.1 K in the screen and 4.93 K in the coil, as shown in Figure 6.149. The peak temperature in the coil appears in the horizontal plane. This can be explained by the higher heat flow in the horizontal direction due to better conducting path: the thermal conductivity of the G10 spacers installed in the horizontal plane, between the beam pipe and the coils, is three to four times that of liquid helium and seven times that of the ULTEM 6200 spacers installed in the vertical plane. If the beam now circulates with an offset of 20 mm in the x-axis, the RW heat doubles to 1.0 W/m and the temperatures increase as expected. The peak temperature in the screen is almost 8 K, found in the closest point to the beam, and the peak temperature in the coil is about 5.4 K, as shown in Figure 6.150. Now, our conservative estimates for the RW heating, discussed in the previous section, found that for a beam screen with RRR100 Cu at less than 50 K the RW heat would be lower than 0.5 W/m after including magneto-resistance, beam offset, aC film, and screen geometry effects. For that case, simulations find that the peak temperature at the screen is 6.2 K, as shown in Figure 6.151. The coil reaches a maximum temperature of 4.94 K with the highest magnetic field region being at 4.75 K, only few tenths of degree below the quench temperature.

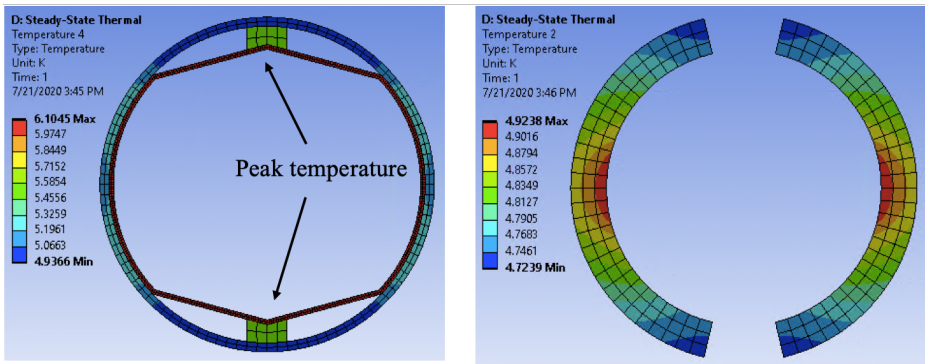

Figure 6.149: Temperature profile for 0.5 W/m heat load and centered beam at (a) beam screen, beam tube and spacer area, (b) coil.

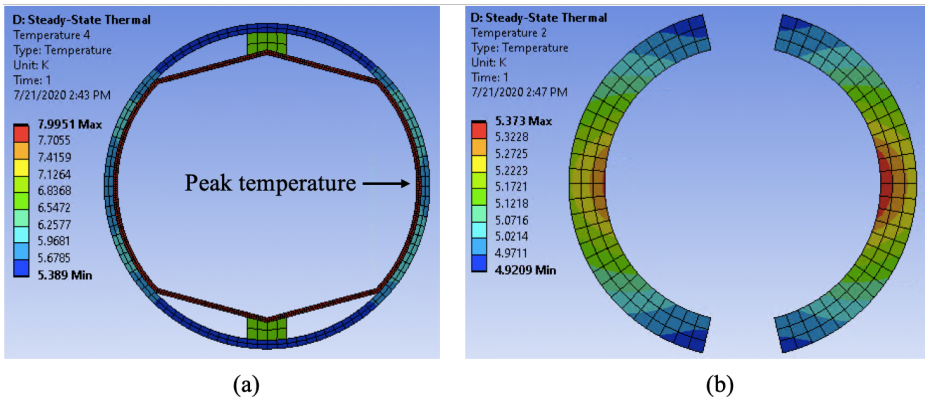

Figure 6.150: Temperature profile for 1.0 W/m heat load and 20 mm off-center beam at (a) beam screen, beam tube and spacer area, (b) coil.

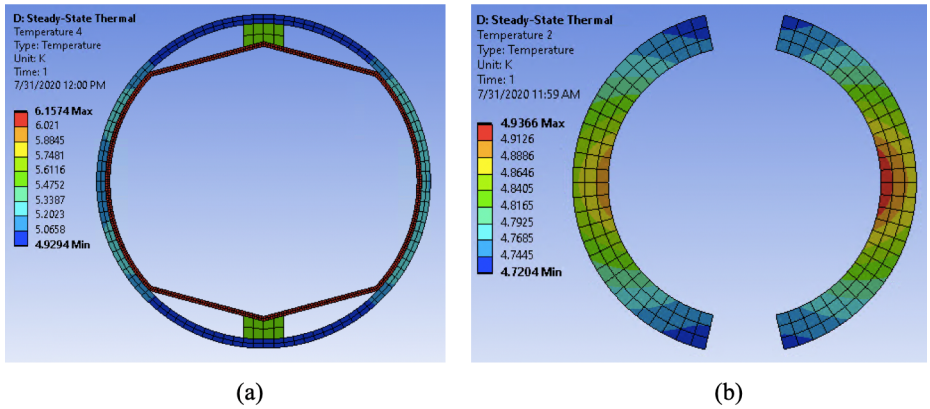

Figure 6.151: Temperature profile for 0.5 W/m heat load and 20 mm off-center beam at (a) beam screen, beam tube and spacer area, (b) coil.

Vacuum Level and Stability

The HSR is divided into 8 arc sections formed by the RHIC Yellow ring plus one RHIC Blue arc for hadron injection and another RHIC Blue arc for path length matching. The beamline layout is illustrated in Figure 6.152. The 60° bends in the EIC run continuously for 480 m through superconducting magnets, except in the vicinity of the EIC's IR06 where the arc will start anywhere from dipoles D8 to D10 on both sides. Each arc section consists of a continuous cryostat (without vacuum barriers), housing 64 superconducting magnets interconnected to form a continuous cold beam tube. The beamlines in the straight sections are primarily warm sections with the exception of 2 superconducting sections each with 3 quadrupole magnets (triplet) and a single dipole magnet (D0) in IR04, IR08, IR10 and IR12. A HSR triplet magnet strings contains the 4 interconnected magnets with a total length of about 20 m. HSR arcs and triplets are separated by variously configured room-temperature beamlines. Each warm section is isolatable from the adjacent cold bore sections with the RF-shielded all-metal gate valves mounted on the warm-to-cold transitions. The total length of cold bore and insulating vacuum is about 4 km, divided into 8 arc sections and 10 triplet sections.

Protons and ion beams of different species, with up to 1160 bunches and an energy from 25 to 275 GeV/nucleon will circulate through these vacuum chambers. The intensity and emittance of the particle beams degrade when the stored particles are lost from their contrived orbits as a result of charge exchange processes, through nuclear and Coulomb scattering with residual gas molecules or due to vacuum instabilities arising from RW heating and primary and secondary beam-induced desorption. To preserve the beam lifetime and contain emittance growth, a low vacuum level and stable beam vacuum wall surface in the EIC hadron beamlines is very important.

About 10% of the life of the hadron beam is spent at warm sections in the combined beamlines; the remainder is spent in cryogenic sections with interconnected superconducting magnets operating at about 4.55 K (the so-called cold-bore). An average pressure of 5×10^{-10} Torr (2×10^{7} molecules/cm^3) or less is required in the warm sections, with residual gases in the ratio 90% H_2, 5% CO and 5% CH_4. The maximum allowable pressure for beam components not baked in-situ such as kickers, septum and rf cavities is 2×10^{-9} Torr, in the same gas species proportions as above. The goal for the average total pressure of the cold-bore is 10^{-11} Torr maximum (2×10^{7} molecules/cm^3 after correcting for thermal transpiration), comprising exclusively H_2 and He to match the previous cold-bore operating vacuum conditions at RHIC. At this vacuum level, the emittance growth of a gold beam with $\gamma = 100$, due to elastic scattering, will be about 1×10^{-4} mm-mrad/h in the warm sections and about 2×10^{-4} mm-mrad/h in the cold-bore sections. With these vacuum conditions achieved, the beam lifetime due to central nuclear collisions of the gold beam with residual gas is about 600 hours in the warm sections and about 240 (80 [294]) hours in the cold sections.

The attainment of these vacuum conditions in the cold-bore sections of the EIC hadron storage ring with the much higher energy and intensity of the EIC hadron beams, depends upon the implementation of the stainless-steel beam screen with roll bonded high-purity

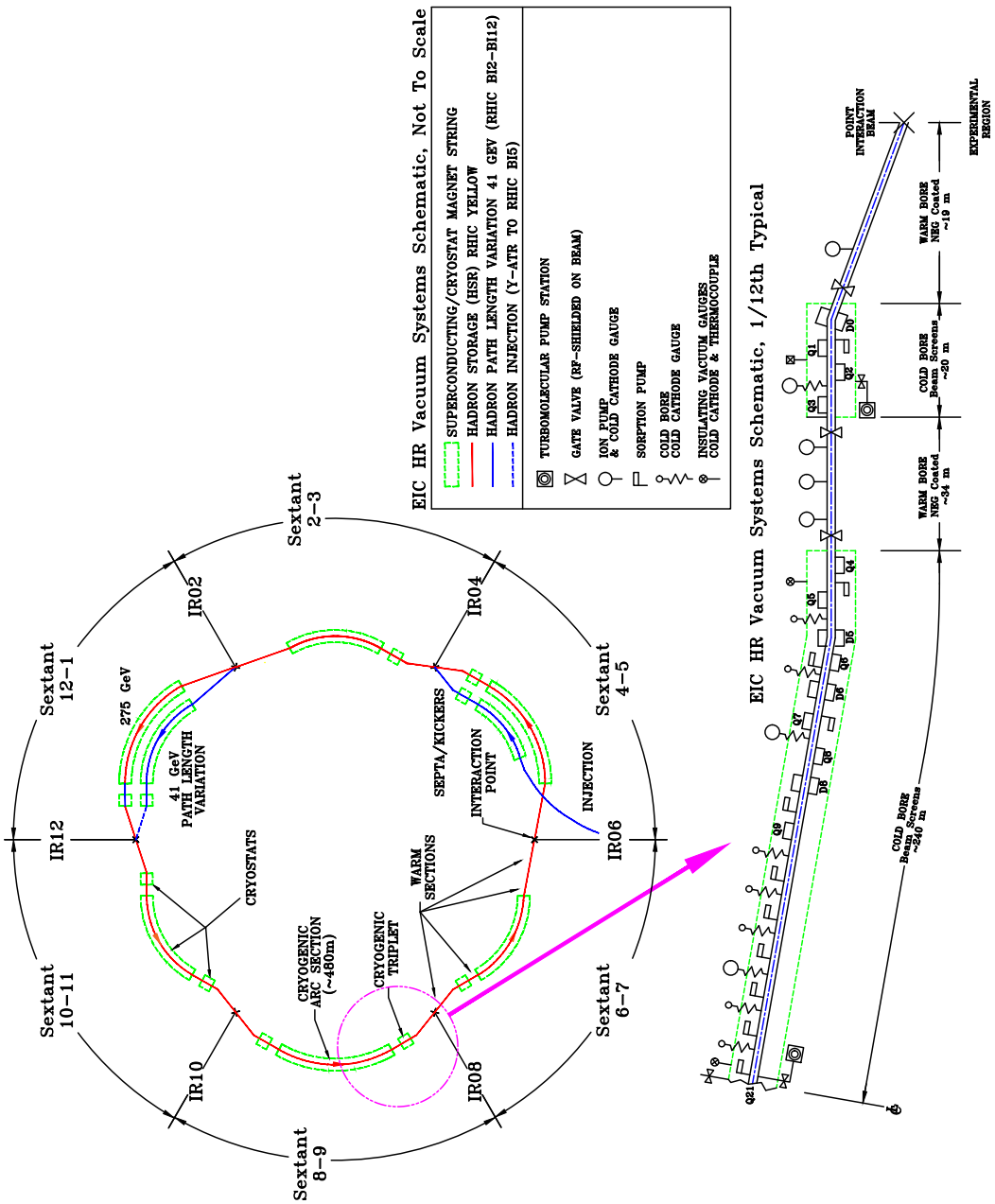

Figure 6.152: Layout of the EIC hadron ring vacuum system.

OFHC copper and a thin film of aC. (Note that the IR06 area will be populated with new magnets, some warm and others cold, which may require special copper lining and aC coating. On the contrary, the Blue arc for hadron injection will handle low intensity beams and will not require beam screens for the cold magnet beam pipes or the magnet interconnect bellows.) The aC film, with its low SEY, suppresses the electron cloud formation and, due to its much greater monolayer capacity and higher temperature adsorption isotherm compared to bare stainless steel and copper, also improves the cryogenic vacuum performance. The aC film will increase the monolayer coverage by a factor 100 (i.e., about 10^{17} H_2/cm^2) and presents higher desorption temperatures for H^2 and CO, respectively, 30 and 60 K. Perforations in the screen will allow desorbed gas in the beam volume to migrate to the 4.55 K beam tube. If vacuum analysis and testing indicates that greater adsorption capacity is needed, a woven carbon fiber cryosorber running the length of the beam screen will be added to the space between the screen and beam tube. Such material can adsorb about 10^{18} H^2/cm^2 at temperatures in the range of 25 – 30 K [295].

Early in the RHIC program, as beam intensity was increased, electron cloud formation and pressure instabilities in the beamlines motivated the implementation of several modifications. Specific to the cold bore was the addition of ion pumps to reduce the beamline vacuum level prior to cooldown. With the vacuum level at cooldown below 1×10^{-4} Torr, less than a monolayer of H_2 is formed on the beam tube surface. The same arrangement and operating practice will be sufficient for the cooldown of the EIC's superconducting strings. The addition of an aC coated beam screen is expected to reduce the monolayer coverage by two orders of magnitude. With this low monolayer coverage, the saturation vapor pressure for the 25 K adsorption isotherm of the aC coated surface is expected to be less than 1×10^{-11} Torr. With these modifications and provided the beam screen temperature can be maintained below 25 K, the expected average cold-bore gas density is about 2 $\times10^6$ H_2/cm^3, a full order of magnitude lower than current RHIC conditions. Conditions near the warm to cold transitions and perhaps at magnet interconnects, pending further design and thermal analysis, may require additional considerations and desorption control measures near the adjacent magnet interfaces.

aC Coating System and Strategy

There have been many studies of aC deposition on copper [296]. At CERN, aC deposition on stainless steel is accomplished by graphite sputtering i.e. via physical vapor deposition (PVD). This method is also adequate to our purposes. An existing DC sputtering coating system used for NEG coating of the RHIC beampipes will be configured to provide a test bed to develop the aC coating parameters and test the coating on prototype screens until a production facility can be built for the EIC. Figure 6.153 shows a sketch of the coating system. The existing coating system consists of a 10 inch-diameter solenoid magnet in a vertical pit. There are four separate solenoid coils each with a 5 inch length, providing a total length of 20 feet. The solenoid is designed to provide a magnetic field up to 350 G. Each 5-foot coil can be powered separately for coating short samples of pipe or powered together to coat pipes up to 20 feet long.

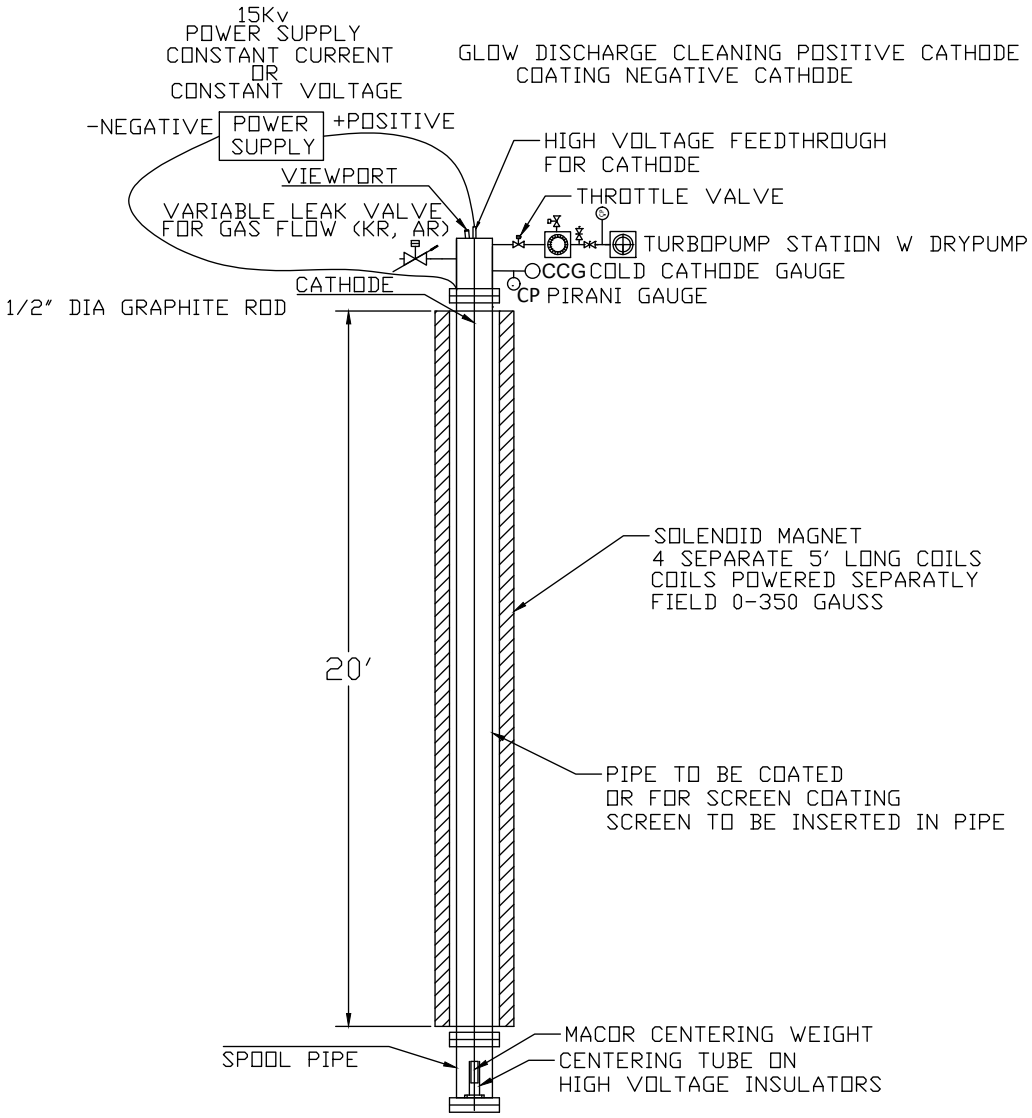

Figure 6.153: Sketch of the amorphous carbon (aC) coating system.

The pumping system used for the coating system is a turbomolecular pumped backed with a dry mechanical pump. The pump has a throttle valve to control pumping during coating operations and is also fitted with a set of vacuum gauges on each side of the throttle valve. Each gauge set consists of a cold-cathode gauge and a Pirani gauge which provides vacuum readout from atmospheric pressure down to 10^{-11} Torr. The system is also fitted with a variable leak valve used to introduce gas into the system and control pressure during glow discharge cleaning and coating operations. The top of the coating system is outfitted with a high-voltage feedthrough used to attach the cathode to and be centered within the pipe. There is also a viewport on the top of the system which allows viewing of the plasma along the length of the cathode during coating or glow discharge cleaning. The viewport is important and allows observing the plasma to ensure it is uniform along the length of the cathode. The DC power supply used for powering the cathode is constant current power supply capable of delivering 2 kW. The estimated coating parameters for the 63 mm diameter beam screens using a half-an-inch diameter high purity graphite rod for the cathode will be to power the cathode at approximately 200 W/m at about 1000 V with a partial pressure of argon of approximately 3×10^{-2} mbar within the chamber. This will provide an estimated deposition rate to coat the screens with 100 nm in approximately 9 hours [297]. Figure 6.154 shows the first two carbon-coated copper coupons produced in the BNL's aC coating system.

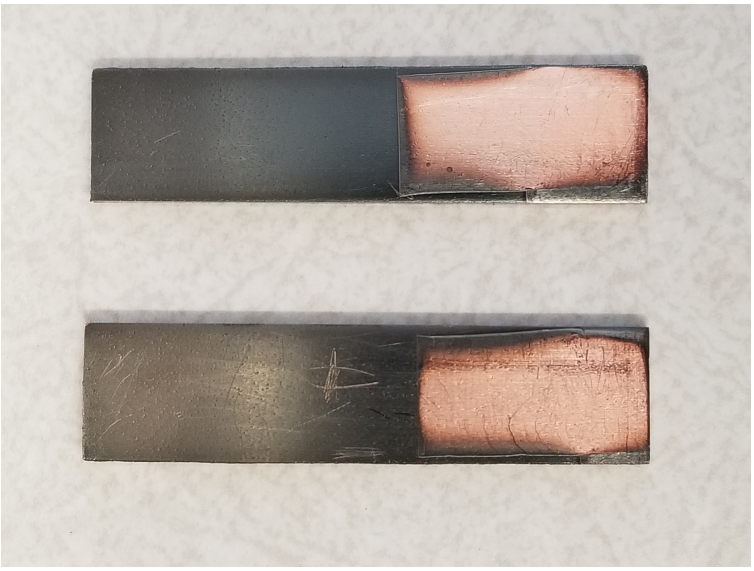

Figure 6.154: First carbon-coated copper coupons produced in the BNL's aC coating system.

The EIC production facility will consist of a large below floor pit to house two separate 24-inch-diameter 30-foot-long vertical solenoid magnets. A strongback will be built to hold 4 separate pipes in each solenoid into which the beam screens can be inserted into for coating. The expected output of the facility is 4 coated screens every 2 days. The coated screens will be stored in an 8-inch-diameter aluminum pipe under a storage atmosphere of dry air to prevent degradation of the low-SEY properties of the aC [298, 299]. Four beam screens

will be stored in 8-inch-diameter pipes until they are ready for installation. The storage pipes will be fitted with vacuum flanges and roughing valves to allow for the screens to be removed from the storage pipe and the remaining screens pumped back down under a storage vacuum. It is expected that the deposition system will be in operation during the installation so the storage system will not be overloaded.

Installation

The fabrication and installation of the copper and low SEY carbon lined stainless steel screens into the hadron ring superconducting arc magnets will be labor intensive. A goal is to minimize the risk of damaging the RHIC magnets and the RHIC bus work. The enterprise will include installing the screen, replacing and/or reworking all of the bellows assemblies so they have copper and low SEY interior surfaces. As noted previously the screen design is based on the CERN LHC screen design. Because the EIC screen is passively or contact cooled, it can be installed without removing the superconducting magnets. This does require the screens to be flexible to allow them to be pulled through multiple magnets before they reach their assigned magnet. Because all of the bellows must be removed to allow rework this provides 21 inches of beam line access at each magnet connection interconnect for pulling through the screens and then locking them into place when they reach the designated magnet.

The screen installation will be done as a continuous process on each superconducting magnet 60° arc. A detailed project schedule has been developed to better understand the order and procedure needed to install the screens and the upgraded bellows assemblies. Because the present bellows are not compatible like the superconducting magnet beam tube they must be removed and reworked or replaced. Therefore, that is the start of the process.

1. Because there will be large scale metal cutting the first step is building a temporary wall in the tunnel and covering equipment to prevent dust migration.

2. The RHIC cryostat at each magnet interconnect location where the beamline bellows are located must be cut open for access. This cutting includes the outer vacuum cryostat, the inner heat shield location, and the final MLI covering the magnet end volume 4.5 K interconnect.

3. After all of the interconnects are cut open, significant cleanup of the tunnel must be completed to prevent the beamline from being contaminated. At this time all of the BPM coax lines in the cryostat will be removed as part of the clean-up.

4. All of the bellows are removed. Some will be sent for rework to install the copper screen and some will be saved as spares. The feedthroughs for the stripline BPM will be removed and replaced with blank flanges.

5. Clean areas will be set up at both ends of the arcs, the arc end beamline warm beam line sections will be removed at a length needed to install the 10 m long screens. The cryogenic arc end vacuum valves will be removed providing space

6. Clean pull through cables will be installed through each magnet length. The screen assemblies will be removed from vacuum storage and pulled in order to the center of the arc from both directions. The early pulls will be 200 m through 40 magnet lengths.

7. Once a magnet screen section reaches it assigned magnet it will be aligned and locked into place.

8. As the bellows access is not longer needed when the screens are installed the bellows will be installed. This will include both the reworked copper/aC lined bellows and the new bellows with BPM buttons (also copper/aC lined). The bellows themselves will have integrated copper/aC lined integrated RF sleeves. The bellows gasket will be a custom conflat gasket which will provide continuous copper surface electrical contact with the magnet screen and the bellows copper surface. The gasket will also prevent longitudinal shifting of the beamline screen from cool down and warm up cycles.

9. Near end of each four hour installation shift, the beam section with screens installed will be blanked off at both ends, pumped down, leak checked, and left under storage vacuum.

10. This process will continue with screens being installed from both ends of the arc until the entire arc is complete. Then the interconnects with blank flanges will have their bellows installed, the entire arc will be continuous, pumped down, leak checked again, inspected and ready for final installation steps. At this time the arc end beamline RF shielded valves will be reinstalled.

11. The final installation starts with installing the new BPM coax lines to the cryostat feed through and electrical testing.

12. Then the first layer of 4 K cryogenic super insulation can be installed. The opening in the heat shield is closed up and the final layer of cryogenic super insulation is installed. The last step is welding closed the cryostat and doing the vacuum leak check.

13. The beamline will be kept under active ion pumping until the first EIC cryogenic cooldown.

The goal of this installation procedure is to minimize the upset of the superconduction magnet system in the arc. None of the superconduction magnets needs to be disconnected and moved into the RHIC aisle or outside with this method. The cryogenic lines stay closed up and clean. The superconducting magnet bus does not have to be opened and the magnets do not need to be moved and resurveyed. While the end pull will be time consuming for the first magnets, it saves significant labor and risk to the magnets.

6.5 RF Systems Design

6.5.1 EIC RF Systems Overview

This section provides a high level overview of the RF system conceptual design for the EIC: summaries of key RF parameters, narratives describing requirements and challenges, and the rationale for design choices. For detailed information on the RF designs for each subsystem, the reader is directed to the RF sub-system detail sections noted in Table 6.62.

A number of cryomodule concept are illustrated in various sections. Some of these concepts illustrate box type cryomodules utilizing top plate suspended spaceframe and coldmasses. Others illustrate cylindrical type cryomodules utilizing a space frame suspended coldmass which rolls in from the end. It is anticipated that as the preliminary design effort advances that one type of cryomodule will be favored and selected.

Table 6.62: EIC RF System Summary.

RF System	RF Sub-System	Freq. [MHz]	RF Type	Location	Overview Page	Detailed Section
ESR RF	ESR Fundamental (H1)	591	SRF	IR-10	654	6.5.2, Pg. 685
RCS RF	RCS Fundamental (H1)	591	SRF	IR-10	667	6.5.3, Pg. 692
	RCS Bunch Merge 1	295	NCRF	IR-4		
	RCS Bunch Merge 2	148	NCRF	IR-4		
HSR RF	HSR Capture / Accel	24.6	NCRF	IR-4	671	6.5.4, Pg. 695
	HSR Bunch Split 1	49.2	NCRF	IR-4		
	HSR Bunch Split 2	98.5	NCRF	IR-4		
	HSR Store 1	197	NCRF	IR-4		
	HSR Store 2	591	SRF	IR-10		
IR Crab RF	Crab Cavity 1	197	SRF	IR-6	679	6.5.5, Pg. 706
	Crab Cavity 2	394	SRF	IR-6		
Low Level RF	All				679	
High Level RF	All				684	

The RF systems represent a large cost contributor to the EIC. Due to the high installed RF power requirement, the Electron Storage Ring RF system is the dominant cost driver within all EIC RF systems. The ESR and IR Crab RF systems are the two most challenging systems for EIC and have received to most conceptual design effort. The EIC ring RF systems are located in long straight sections (Interaction Regions or "IRs"). With available space in the IRs at a premium, effort was put toward minimizing the total number of cavities and associated support equipment. Reuse of RF cavity designs across multiple systems has also been employed where feasible. This helps to reduce the scale of analy-

sis and design efforts, reduce overall system complexity, minimize fabrication costs, and enhance operational reliability and uptime.

Electron Storage Ring RF Systems Overview

One limitation on the luminosity of the EIC is the synchrotron radiation generated in the high energy, high current Electron Storage Ring (ESR). As a practical limit, the power lost to synchrotron radiation is limited by choice to a maximum of 10 MW, and this power must be replaced by the ESR Fundamental (H1) RF system. In addition, the ESR RF system must provide adequate bucket height to store electron bunches without loss, strongly damp HOM impedances to ensure adequate stability thresholds and minimize HOM power generation, control periodic transient beam loading and longitudinal coupled bunch instabilities, and maintain synchrotron tunes to acceptable values to avoid chaotic behavior and synchro-betatron resonances. Beam dynamics analyses (Section 4.1) indicate that a third harmonic RF system is not required for bunch stability and such a system is not currently included in the conceptual design.

In highest luminosity operation, the electron beam radiates roughly 9 MW, and the ESR RF systems are designed for the maximum of 10 MW. With 17 cavities installed, each cavity requires nearly 800 kW of amplifier power when factoring in HOM power, power margin for control and transmission losses. The conceptual design employs two couplers per cavity, each capable of delivering up to 400 kW CW. Given the range of operating parameters from 5 GeV to 18 GeV, using a conventional operating mode where all cavities are phased identically with respect to the beam, the ESR cavity fundamental power couplers would require a Q_{ext} which varies by roughly a factor of 10 from 18 GeV and 5 GeV. An active R&D effort is continuing (described in the ESR RF detailed design section) with the goal of developing a robust 500 kW CW, variable Q_{ext} power coupler.

The need to deliver high power at 5 GeV and 10 GeV with relatively low total voltage implies challenges related to transient beam loading, large detuning and associated fundamental mode driven coupled bunch instabilities. Motivated by the successful test of an "RF Reverse Phasing" mode at KEK [37], we have investigated employing the same technique at the EIC. The technique is alternatively sometimes referred to as "RF Focus-Defocus". The technique utilizes two families of cavities, each phased to deliver the same real power to the beam while providing the opposite sign for the longitudinal focusing. Put another way, one family of cavities is operated at the above transition synchronous phase, and the other at the below transition synchronous phase. This allows for the individual cavities to be operated as close to maximum voltage as possible while maintaining a vector sum voltage appropriate for the desired bucket height and synchrotron frequency. The resultant high stored energy minimizes transient beam loading and the optimal detuning frequency, in turn reducing longitudinal coupled bunch growth rates to controllable levels. Key operational parameters for the Electron Storage Ring Fundamental RF system are shown in Table 6.63, for the traditional all focusing scheme. An example parameter set for the RF Reverse-Phasing scheme is found in Table 4.4.

Table 6.63: Maximum luminosity operation parameters of electron storage ring RF systems.

Parameter	18 GeV	10 GeV	5 GeV
Revolution frequency [kHz]	78.25	78.25	78.25
Harmonic number	7560	7560	7560
Frequency [MHz]	591	591	591
Total voltage [MV]	61.5	21.6	9.6
Number of active cavities	17	17	17
Number of cells per cavity	1	1	1
Cavity voltage [MV]	3.62	1.27	0.57
Cavity (R/Q) [Ω_{ckt}]	37	37	37
Cavity Q0 [10^{10}]	2.0	2.0	2.0
Operating temperature [K]	2.0	2.0	2.0
E_{acc} [MV/m]	14.3	5.0	2.2
E_{peek} [MV/m]	39.2	13.8	6.2
B_{peek} [mT]	74.2	26.1	11.7
Cavity dynamic loss [W]	8.8	1.1	0.2
Number of bunches	290	1160	1160
Bunch intensity [10^{10}]	6.25	17.23	17.23
Charge per bunch [nC]	10.0	27.6	27.6
Average beam current [A]	0.23	2.50	2.50
dE per turn [MeV]	36.95	3.52	0.95
Synchrotron radiation power [MW]	8.38	8.80	2.38
HOM power per Cavity [kW]	1.0	33.5	30.0
Total Power Delivered per cavity [kW]	494	551	170
Synchronous voltage [MV]	2.18	0.22	0.07
Synchronous phase [deg]	143.0	170.0	173.1
RMS bunch length [mm]	8.7	7.7	9.6
Qty of fundamental power couplers	2	2	2
Total power margin [%]	20	20	20
RF power per coupler [kW]	296	331	102
Transmission losses [%]	10	10	10
RF power per cavity [kW]	651	728	224
Q_{ext} [10^4]	71.5	7.91	5.12
Half bandwidth [kHz]	0.83	7.48	11.5
Detuning [kHz]	-1.1	-42.4	-95.7
γ_{T}	38.0	27.3	27.3
dE/E (bucket half height) [10^{-3}]	10.0	10.0	10.0
Q_{sync} (zero amplitude)	0.048	0.059	0.056

Electron Storage Ring Fundamental 591 MHz RF System

Design Considerations: The RF systems for the EIC has been carefully analyzed and optimized for both performance and cost from the earliest stages of design. After evaluating possible options including optimal geometry and frequency, the cavities chosen for the Electron Storage Ring Fundamental RF system are 591 MHz, 1-cell elliptical SRF cavities, arranged as single cavity cryomodule units with broadband SiC Beamline Higher Order Mode Absorbers (Beamline Absorbers or BLAs) located in the adjacent warm beamline space (see Figure 6.155). Factors in the design choice include:

- **Operational Cost:** At 10 GeV and above, up to 10 MW of RF power are required at up to 62 MV (37 MV synchronous voltage) to replace beam energy lost to synchrotron radiation. For an SRF system, minimal RF power is dissipated by the cavity although it is of course an extremely important consideration for the cryogenic power load and system cost. A normal conducting RF system would require substantial additional power both to produce the required cavity voltage, and for cooling the cavities. A rough estimate of RF power required to drive normal conducting cavities (i.e. cavity ohmic loss) yields about 10.5 MW, based on a 2-cell structure with a Q_0 of 3.0E4, a circuit (R/Q) of 100Ω per cell, and a voltage of 1 MV per cell, doubling overall CW RF power requirements compared with an SRF system, and adding the additional 11 MW of cooling load to the water system.
- **High Order Mode (HOM) Impedances and Power Generation:** Given the high beam current and short bunch lengths, HOM damping and power generation are significant challenges. Large aperture 1-cell structures minimize HOM impedance by propagating all HOMs to the external BLAs and avoid potential issues with trapped modes. Total HOM power allowable per cavity is limited by the absorbed surface power density and dissipation capability of the BLAs.
- **Low (R/Q) to Reduce Beam Loading Effects:** Low (R/Q) is a desirable feature for a high current electron storage ring RF cavity to control transient beam loading and reduce required detuning. Employing an SRF design allows for minimum fundamental mode (R/Q) without the RF power penalty for achieving high voltage which would occur in a normal conducting (NCRF) structure. The minimum practical R/Q is in determined by tolerable peak surface fields. A low fundamental (R/Q) geometry with large iris and beampipe radius is also exactly what is desired to minimizing HOM impedance and corresponding power generation.
- **Number of Cavities and Ring Real Estate:** The high CW accelerating gradient compared to a NCRF system allows installation of the full system in much less space than a NCRF system. The very aggressive NCRF system compared above would require 34 2-cell cavities to provide the same installed voltage. The space savings is extremely important given the number of accelerator sub-system components to be installed in limited IR space. The reduction in the total number of cavities also reduces total impedance, beam loading, detuning, etc. as well as installation and operational costs.

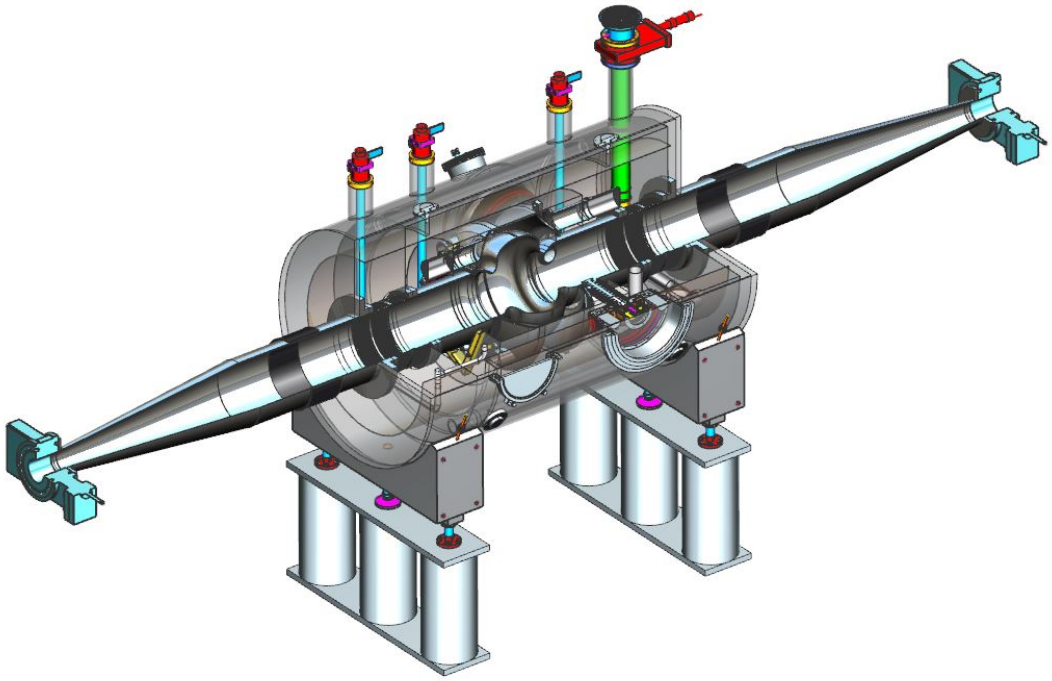

Figure 6.155: Cutaway view of the ESR 591 MHz cryomodule concept. Shown is the cryomodule, with a nominal valve to valve length of 4.8 m, including the adjacent warm spaces with two SiC beam pipe absorbers per cryomodule, beampipe tapers and gate valves. Shown also are the cryogenic feeds and the RF input coupler.

Design Optimization and Resulting Parameters: To satisfy the EIC operating requirements, and to reduce cost for cavities and cryomodules, the EIC Electron Storage Ring 591 MHz fundamental RF system includes design features which are at current state of the art:

- **1-Cell RF Cavity:** The cavity per se is not state of the art. A 1-cell, elliptical, 591 MHz SRF cavity has been designed providing a high performance, compact and cost effective RF structure. The cavity shape has been optimized to minimize fundamental mode (R/Q) and HOM impedances, with large beam tubes to efficiently propagate generated HOM power to the BLAs. The overall design optimization leads to the cavity design parameters referenced in Table 6.64.
- **High Power HOM Absorbers (BLAs):** Strong damping of HOMs is important to achieve robust beam stability and to limit requirements for active damping systems. The choice made in the design of the EIC electron storage ring RF is to employ SiC BLAs — HOM absorbers consisting of cylindrical SiC absorber sections located in the warm beamline space adjacent to each cryomodule on each side of the cavity. Such a design greatly reduces the complexity of the cavity and cryomodule compared to

Table 6.64: Design Parameters of the 591 MHz Cavity.

Parameter	Value
RF frequency [MHz]	591
Number of cells per cavity	1
Number of cavities per cryomodule	1
Operating temperature [K]	2.0
Maximum accelerating voltage per cavity [MV]	4.0
Maximum accelerating gradient per cavity [MV/m]	15.8
Cavity peak surface E field [MV/m]	33.6
Cavity peak surface B field [mT]	76.8
Cavity Dynamic Power Loss [W]	9.5
Maximum CW Power per Input Coupler [kW]	500
Input Couplers per Cryomodule	2
HOM Absorber Type	Warm Beampipe SiC
HOM Absorbers per Cryomodule	2
HOM Power per Cryomodule [kW]	48.6

alternatives employing waveguide HOM couplers near or on the cavity. The HOM absorber design benefits from the work of many labs and follows the ANL design for the APS upgrade [300]. Total power dissipated in the absorbers reaches a maximum of about 49 kW, deposited relatively uniformly across them (See Section 6.5.2). Because these absorbers are significantly larger and dissipate higher power than the ANL APS-U design, an R&D effort is currently underway. A complete BLA assembly has been successfully fabricated and is awaiting high power RF testing. The SiC cylinders have also been characterized for vacuum outgassing and shown very good results. An overall assessment of beam dynamics including the resulting worst case longitudinal and transverse HOMs is found in Section 4.1. Figures 6.156, 6.157, 6.158, 6.159 illustrate the completed BLA prototype assembly and the details of the design and analysis. Figure 6.155 shows the locations of the BLAs in the warm beamline section.

- **500kW CW, Variable Q_{ext} Fundamental Power Couplers (FPC):** The maximum RF power required to replace beam energy lost to synchrotron radiation and power lost to HOMs can reach 10.6 MW. With 20% power margin the total forward power at the couplers would be 12.7 MW. The present conceptual design utilizes 17 cavities for an operational power per cavity of 750 kW, and we have chosen to employ two couplers per cavity for a maximum of 375 kW per coupler.

  Based on prior experience with development and commissioning of 500 kW CW, 704 MHz couplers at BNL [301], we selected this coupler as the basis for an EIC de-

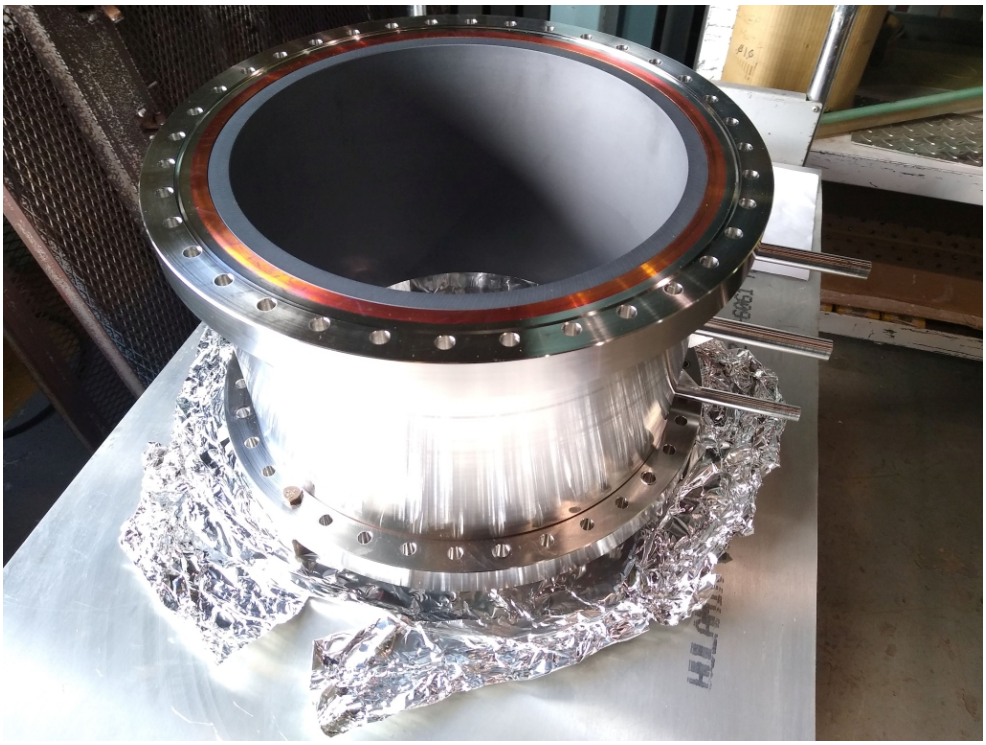

Figure 6.156: Fully assembled prototype SiC Beamline HOM Absorber (BLA).

sign and elected to set the design maximum RF power per cavity to 1 MW CW, or 500 kW per power coupler. The 500 kW FPC was retested as part of an off project R&D prior to the CD-0 decision, with the goal of validating for the ESR application. Utilizing an available 704 MHz, 1 MW CW klystron, it was successfully tested to 500 kW standing wave, but did eventually suffer a window failure. Detailed post-mortem analysis indicated that the failure was not due to a design or fabrication flaw but instead to insufficient high power protection interlocks which led to excessive and unprotected arcing. The window failure also brought to light a safety concern because it was designed with BeO ceramic window. Mechanical analysis of the design also exposed potential concerns about maximum stresses which would occur during transpiration of cryomodules from TJNAF to BNL. Taken together, these concerns have led the team to initiate a new R&D effort to design a more robust and nontoxic ceramic window from Al_2O_3.

The design must also address the requirement to provide variable coupling over a factor of about 10. CW, high power, variable Q_{ext} couplers have been developed for other applications, for example the LHC Variable Power Coupler [302]. Experience from those design efforts will benefit high power variable coupler design efforts for the EIC. For EIC, the variable coupling will be implemented by utilizing an adjustable waveguide tuning section with the fixed coupler design, as opposed to developing a movable antenna structure. Figure 6.160 illustrates the proposed

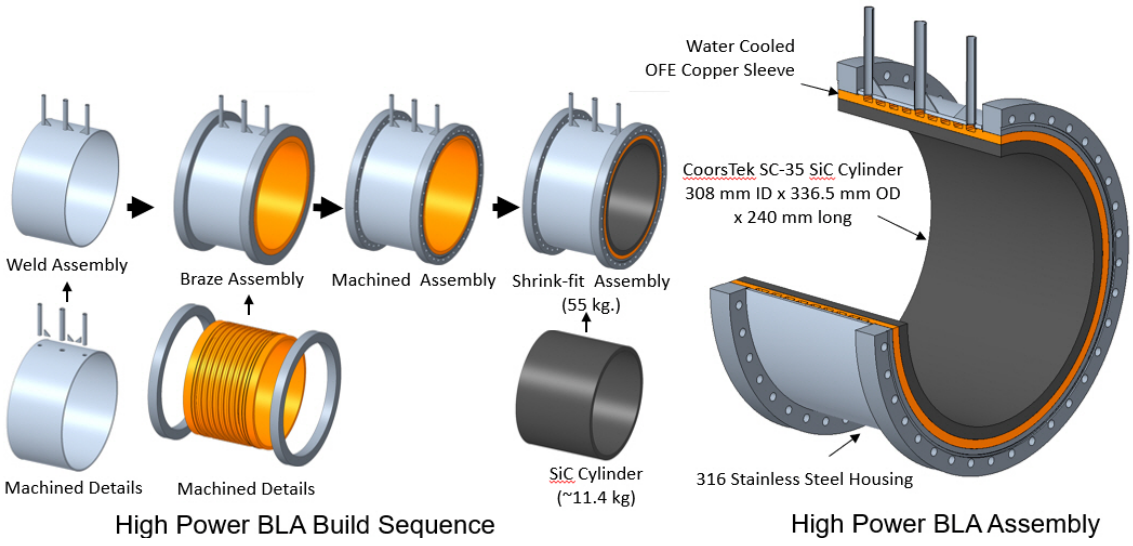

Figure 6.157: SiC BLA components and buildup sequence.

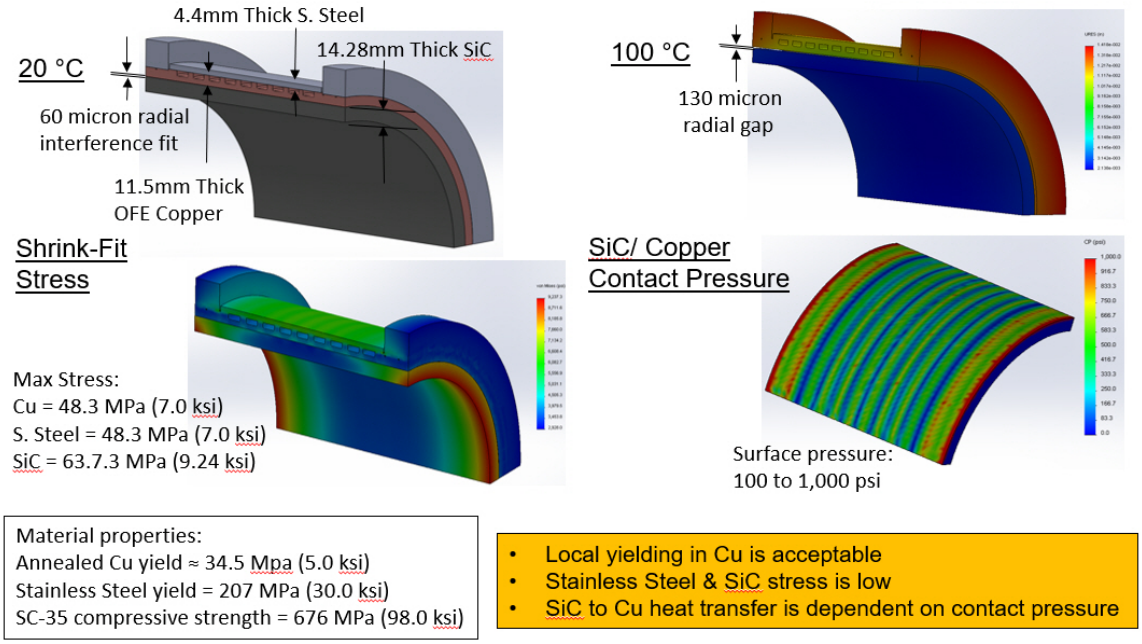

Figure 6.158: Sic BLA shrink fit stress analysis and copper contact pressure.

waveguide tuning section used to adjust the FPC Q_{ext}, and Figure 6.161, the FPC high power RF test stand. This waveguide tuner was successfully tested (without the couplers) to 500 kW CW standing wave at all required operating positions for the two waveguide plungers.

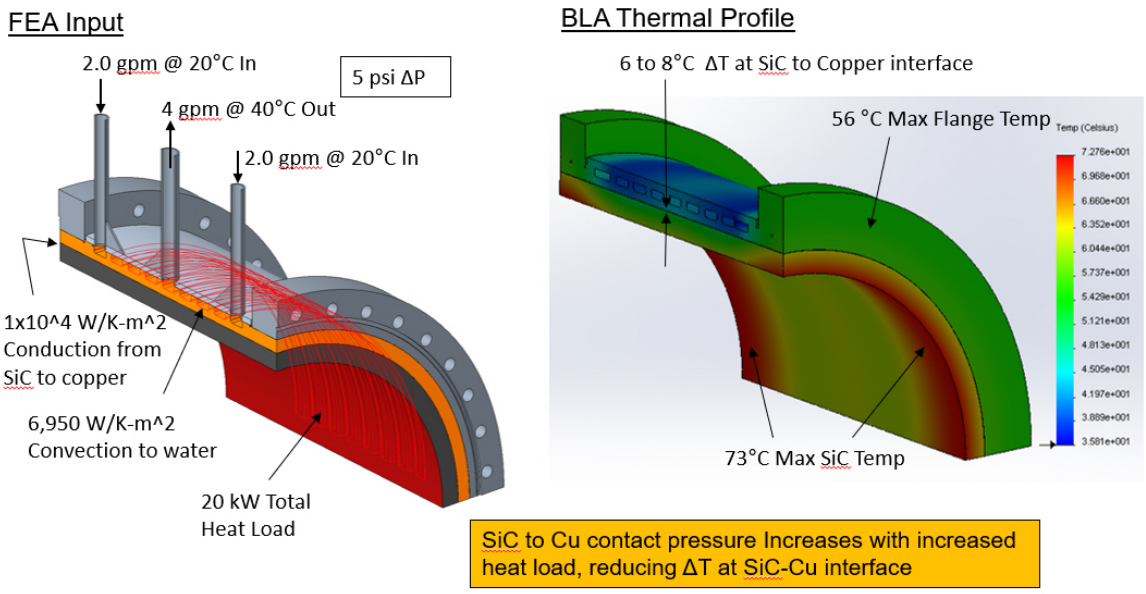

Figure 6.159: SiC BLA thermal profile for 20 kW uniform heat flux.

- **RF Power Sources:** For the current parameter set, the RF power source for the electron storage ring RF will have to deliver a maximum of about 9.8 MW to the beam to replace energy lost to both synchrotron radiation and HOM power. Maintaining a 20% reserve at the couplers for RF control and assuming a 10% transmission loss, the total installed RF power will be about 13 MW. The conceptual design is based on solid state 591 MHz , 400 kW CW power amplifiers, each comprising four 100 kW cabinets with a high power combiner network. Two such units are are required for each cavity, one for each power coupler. Such a large RF power installation will require significant AC line power, water cooling and space in a new support building to be located adjacent to the RHIC IR10 region (See Infrastructure Section 7.1).

  CW IOT and klystron transmitters were also considered, but it is clear that the RF power market has shifted strongly in favor of solid state solutions even at these power levels. Costs have declined dramatically in recent years and the trend continues, though more slowly. Modularity of solid state amplifier designs provides for enhanced configuration flexibility, greater reliability and uptime, with less loss of total power in the event of component failure compared to large tube based amplifiers. Power densities and cost are very competitive with tube based solutions as well, and safety concerns are greatly reduced given the 50V DC rails typical in solid state vs ∼35 kV for IOTs and up to 100–120 kV for high power klystrons. Experience at BNL with a 1 MW CW 704 MW klystron has shown that the increased complexity, x-ray shielding requirements and very large space required for 100 kV, megawatt class power supplies made them a less appealing choice. Across the the full power range, IOTs would offer improved efficiency over klystrons, reducing operational costs. The greater modularity of the IOT solution would also limit potential for downtime and

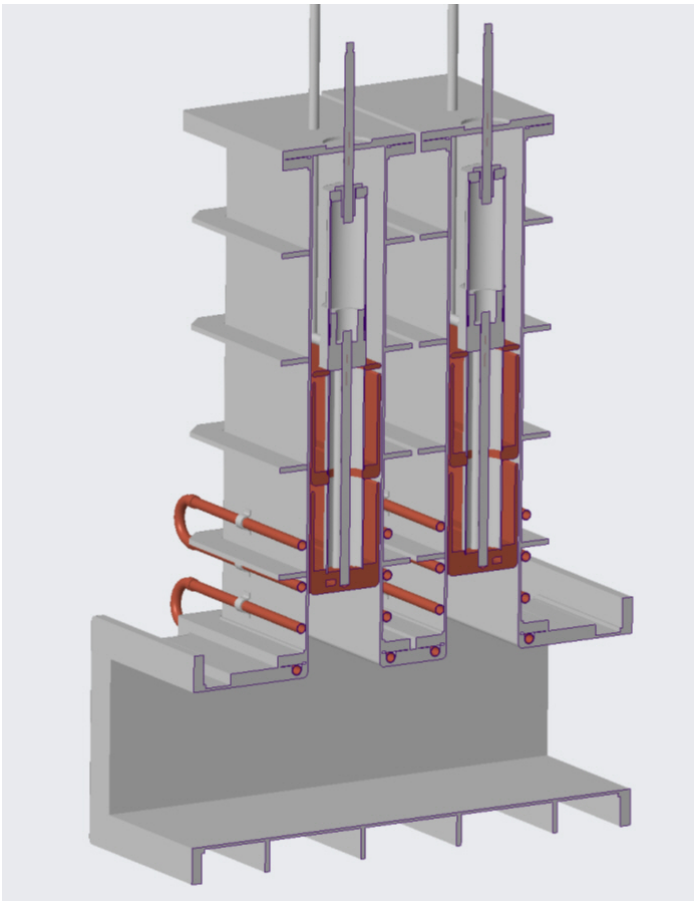

Figure 6.160: Cutaway section of the 3D model of the 500 kW FPC WR1500 waveguide tuning section. Seen is the main waveguide section, with two vertical sections housing adjustable depth plungers. The Qext of the FPC is adjusted by changing the position of these plungers.

luminosity reduction in the event of a single RF power unit failure, compared to the klystron solution. Nonetheless, both technologies continue to be supplanted by solid state and for a project with a 30+ year construction and operating time horizon, solid state is most suitable.

Evaluation of the high power amplifiers for the EIC electron storage ring will be an area of continued study, offering the potential for significant value engineering and resulting cost savings, improved operational agility and reliability, and simplified maintenance.

Section 6.5.1 contains references to large high power solid state RF installations worldwide.

See Section 6.5.2 for the details of cavity design.

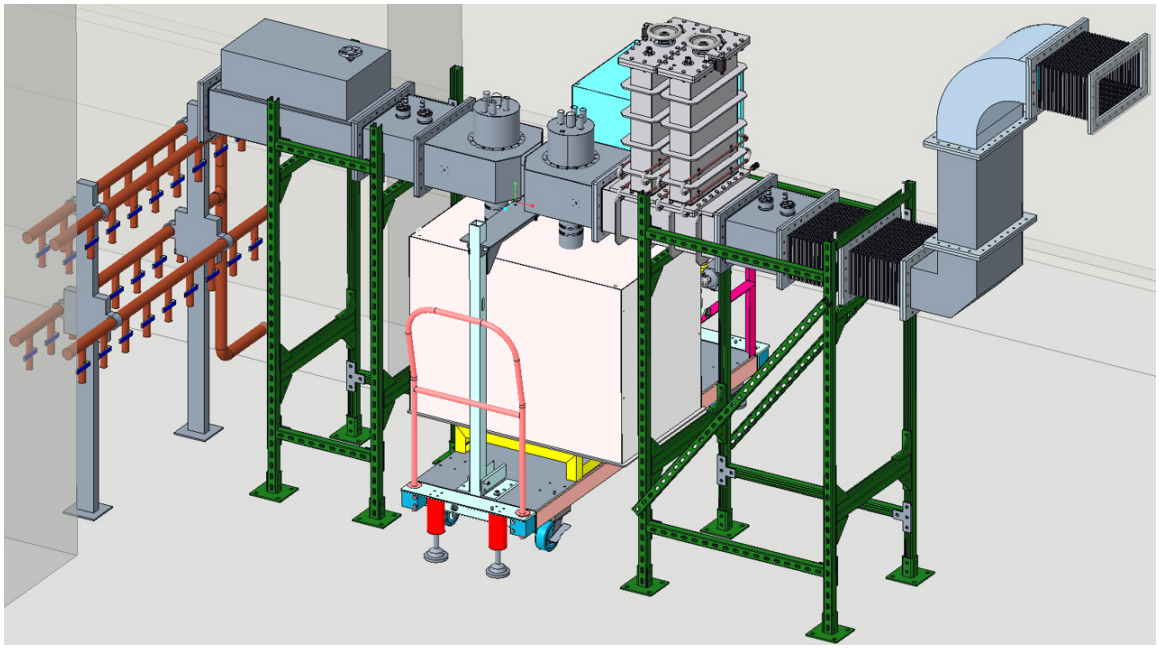

Figure 6.161: 3D model of the FPC high power RF test stand. The open waveguide port at right is the connection to the waveguide from the 1 MW CW klystron. The waveguide tuner section described shown in Figure 6.160 extends vertically above the assembly. The large beige box is simply a rendering of a bakeout enclosure, surrounding the FPC test box. The waveguide doorknob transitions are seen above this box. At the left end of the waveguide is a high power phase shifter and terminating shorting plate, used to provide full reflection at all phase for test.

Electron Storage Ring Cryomodule Concepts

Although detailed cryomodule design is not part of the conceptual design effort, cryomodule conceptual design models have been developed to assess general design challenges and validate space for cryomodule locations in the IRs. The modeling effort provided the opportunity to begin evaluation of different ideas and concepts. Concepts have included both box type cryomodules well known to BNL and SNS style cryomodules well known to JLAB. The cryomodule structures and build up sequences allow for clean room assembly of the complete hermetic string, including high power FPCs and windows, prior to any other assembly work. Cryomodule penetrations for major components are considered (mechanical tuner interface, FPCs, cryogenic valves, helium supplies, returns, and vent headers). Major internal cryomodule components (heat exchanger, 2-phase header/ballast, valves, major piping elements, tuner frame, helium vessel, thermal transitions) are also considered, with sizes estimated from existing cryomodules.

The pre-conceptual design efforts were extremely valuable, and generated overall cryomodule concepts which enhance confidence that such cryomodules can be fabricated and

assembled in a way that preserves cavity RF performance first and foremost, and also helps minimize cost by simplifying assembly, required tooling and resources. Integrating these models with models of IR10 installation location allowed for the development of conceptual component layouts for the real machine, providing confidence that all RF components can be readily installed, operated and maintained in the available space in RHIC IR10.

Figure 6.162 shows relevant cryomodule dimensional data. Figure 6.163 shows the buildup of the conceptual cryomodule components.

Figures 6.164 and 6.165 show 3D model layouts of the IR10 region, with the electron storage ring RF system, representative beamline optical elements, the RCS and HSR SRF cryomodules and associated high power RF transmission lines. Note that the IR model utilizes the box type cryomodule as a reference for space allocation.

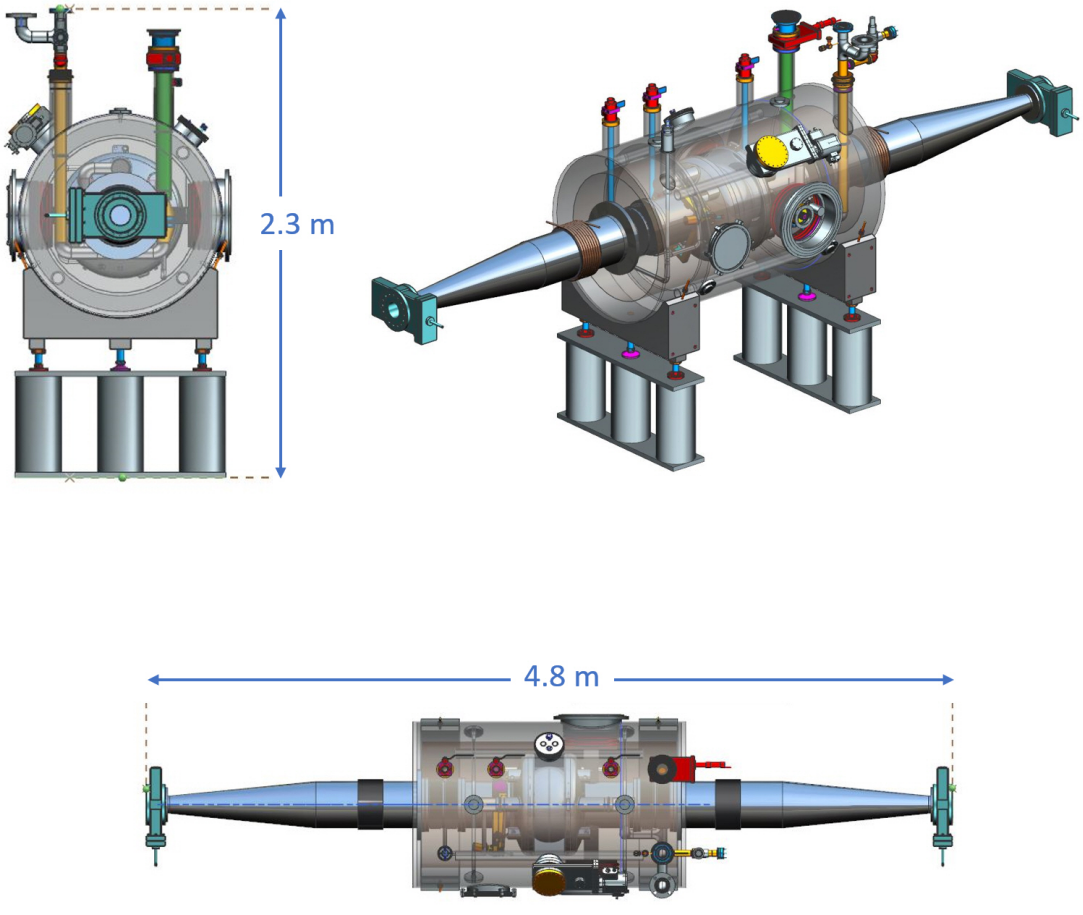

Figure 6.162: CAD model of the ESR 591 MHz cryomodule concept, showing major dimensions.

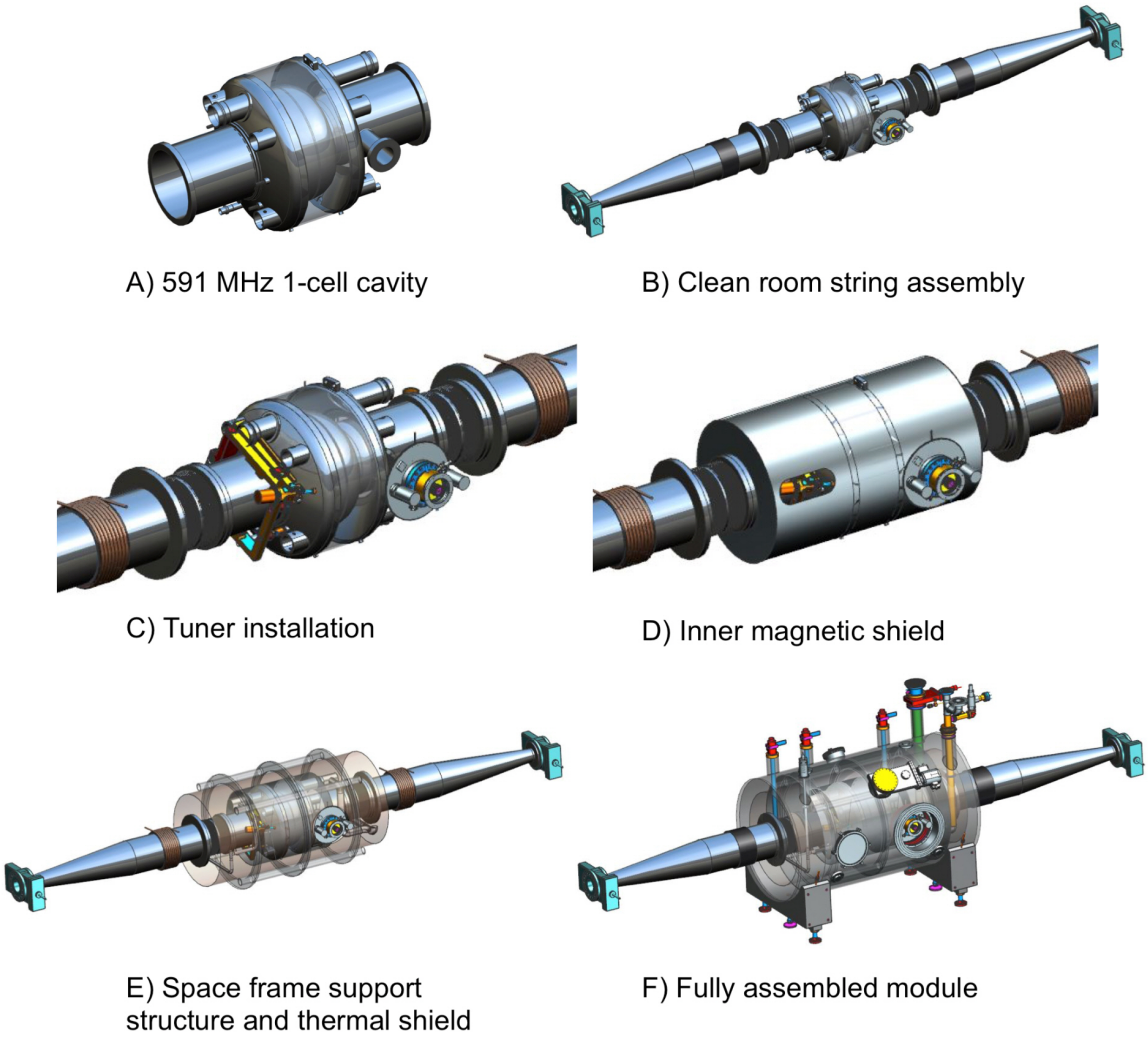

Figure 6.163: CAD model of the ESR 591 MHz cryomodule concept, illustrating the overall buildup sequence.

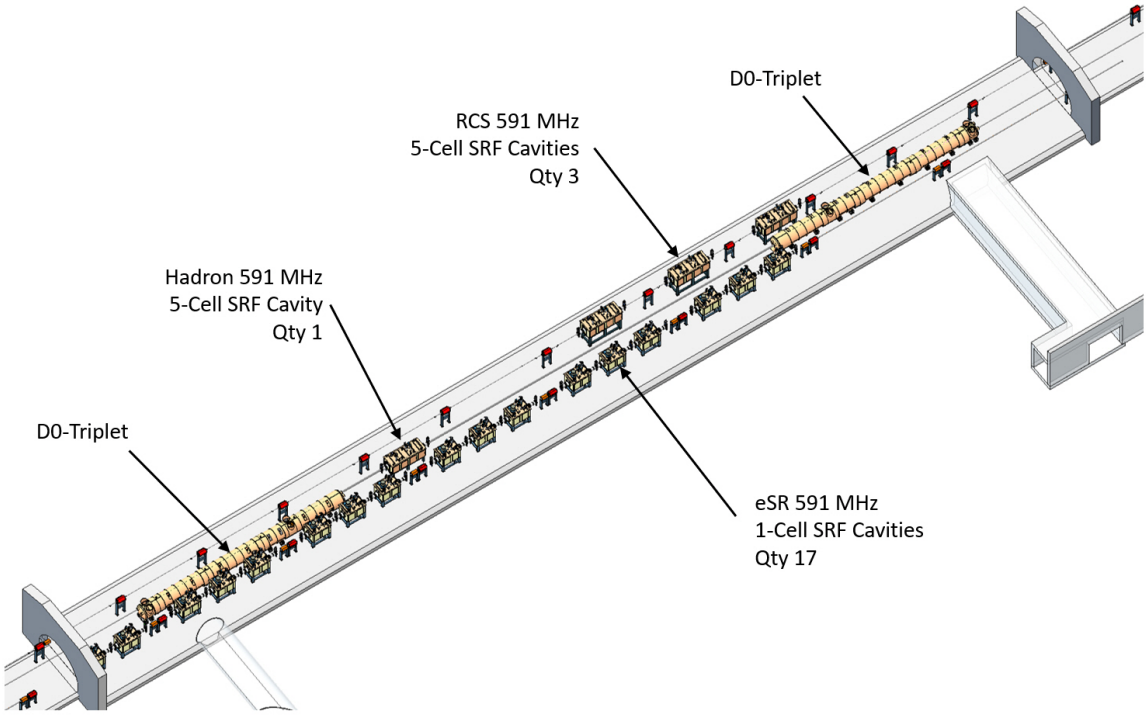

Figure 6.164: CAD model of the RHIC IR10 interaction region, with electron Storage Ring 591 MHz and 1773 MHz, RCS 591 MHz and Hadron Ring 591 MHz Cryomodules.

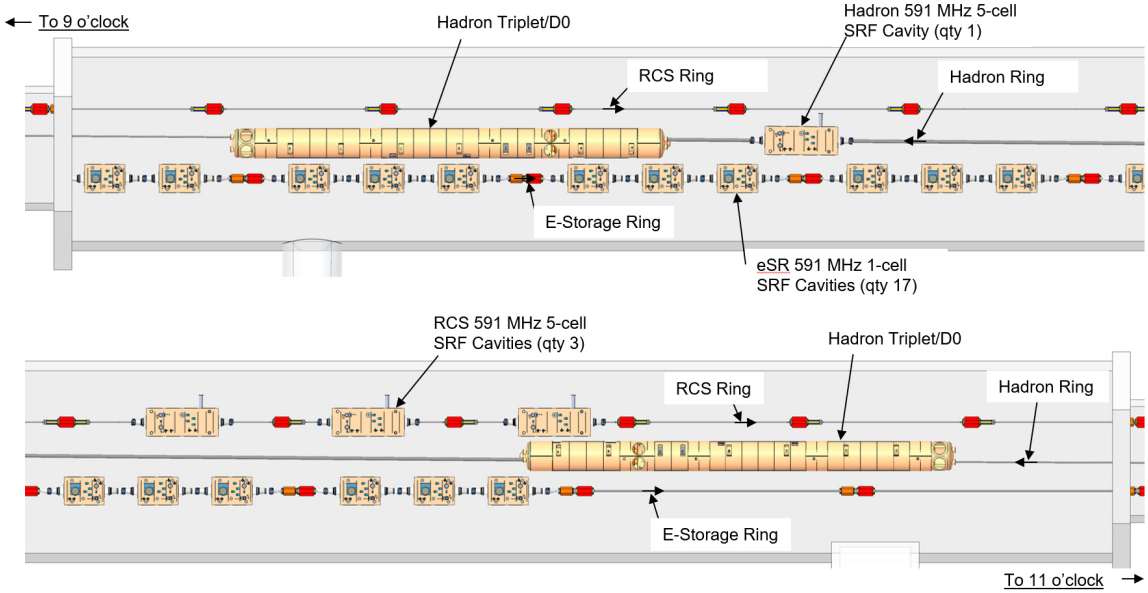

Figure 6.165: Piece-wise zoom of the CAD model of the RHIC IR10 interaction region.

Electron Rapid Cycling Synchrotron RF System Overview

A Rapid Cycling Synchrotron (RCS) is proposed to inject on-energy polarized electron bunches into the Electron Storage Ring. The RCS physics design is described in Section 3.6. The RCS will capture eight, 400 MeV, 7 nC electron bunches from the pre-Injection LINAC, merge them into two bunches and then accelerate them up to a maximum energy of 18 GeV over an acceleration ramp time of 100 ms. The repetition rate of the RCS is nominally 1 Hz. The RCS RF utilizes a fundamental 591 MHz SRF system for linac beam capture and for accelerating the merged bunches. Two sets of NCRF cavities are used to perform the bunch merging. Table 6.65 shows the RCS parameters relevant to the 591 MHz RF system design.

RCS Fundamental 591 MHz RF System

Detailed Cavity Design: The details of the RCS 591 MHz SRF cavity design can be found in Section 6.5.3.

The NCRF bunch merger cavities are a relatively recent addition and no cavity design work has been done yet. They are discussed in general terms later in this section.

591 MHz SRF Cavity Design Factors: The fundamental RF system for the RCS comprises 3, 5-cell SRF single cavity cryomodules, producing up to 60 MV total at 591 MHz. The 5-cell cavity design is based on scaling of 5-cell designs developed at BNL for other projects, in particular a 650 MHz 5-cell cavity designed for high current, heavily HOM damped operation.

The use of a common design across multiple RF systems provides a number of significant advantages:

- Reduced design effort and overall project scope
- Reduced procurement cost resulting from increased production quantities
- Reduced complexity for installation, commissioning, operation and maintenance
- Reduced requirement for unique spares, improved overall reliability and up-time

With two, 28 nC bunch accelerated per cycle, the average beam current and resulting HOM power generation are quite low. Nonetheless, strong HOM damping is potentially important due to the high bunch charge, to limit the effect of long range wakefields surviving turn to turn.

Accelerating RF power is non-trivial at the highest energy where energy loss per turn reaches $\sim$40 MeV. The 28 nC bunches are nominally only used for 10 GeV and 5 GeV operation. However, they could conceivably be used at 18 GeV for accelerator development

or high bunch charge operation in the ESR at 18 GeV. As a worst case, 2 bunch acceleration at 28 nC require about 180 kW at 18 GeV, or about 60 kW per system. We will employ standard Toshiba 75 kW couplers and expect to use modular solid state amplifiers of the same design as the ESR, but configured for 75 kW to 80 kW. This commonality again helps to realize the same benefits as mentioned above.

Optimal coupling for 60 kW per cavity yields a Q_{ext} of about 1.3×10^7 for a half bandwidth of about 22 Hz. Given the dynamic nature of these cavities, it's conceivable that a lower operating Q would be beneficial, at the cost of higher operating power. Given the roughly 20% RF duty cycle expected, pulsed operation could be considered to reduce the average operating power even with a lower operating Q.

Although the electron Lorentz gamma factor is already 783 at 400 MeV RCS injection energy, there is a finite change in electron velocity from 400 MeV to 18 GeV, leading to an approximately 500 Hz change in the 591 MHz RF frequency across the energy ramp. Dynamic Lorentz detuning effects are also expected. It is anticipated that relatively fast dynamic voltage adjustments will be required, for example to optimize the accelerating bucket during the energy ramp. The change in cavity resonant frequency will need to be implemented via a fast tuning mechanism which is assumed to be provided by piezo tuning stacks integrated into the tuner mechanism. This will require detailed study as the design progresses.

It should be noted that Cu RF structures were investigated for this application. However, the large installed peak voltage requirement results in a very large installed RF power requirement (approximately 2.5 MW across 20, 4-cell Cu structures), leading to a substantial escalation in cost and required building and IR beamline space. While a Cu RF system eliminates all of the tuning requirements discussed (due to the large operating bandwidth), the added cost and system size outweigh the simplification in tuning.

591 MHz Cryomodule Concept: Figure 6.166 illustrates the overall 3D model concept developed for the cavity.

NCRF Bunch Merging Cavities: Section 3.6.5 briefly describes the RCS the bunch merging RF scheme which will utilize NCRF cavities at 295.5 MHz and 147.7 MHz. No detailed design has begun. For the purpose of estimating the required number of cavities and RF power, it was assumed that these would be scaled version of the 197 MHz cavities in the HSR. Simulations of the merge indicated required total voltages of 1.3 MV at 295.5 MHz and 0.7 MV at 147.7 MHz. The 197 MHz cavity R/Q is about 170Ω (ckt) with Q_0 =50000. The 295 MHz Q_0 was scaled to 41000 and the 147 MHz Q_0 kept at 50000. Basic operating parameters are shown in Table 6.66.

Table 6.65: Operating Parameters for the RCS Fundamental 591 MHz RF.

Parameter	Value
Injection Energy [MeV]	400
Top Energy [GeV]	18
U_0 (at 18 GeV) [MeV/turn]	39.8
α_c momentum compaction	0.000372
Gamma$_T$	51.848
Circumference [m]	3841.35
Repetition Rate [Hz]	1
Acceleration Time [ms (Turns)]	100 (8000)
Number of Bunches (Injected)	8
Charge per Bunch (Injected) [nC]	7
Number of Bunches (Ramp)	2
Charge per Bunch (Ramp) [nC]	28
RMS Injected Bunch Length [mm (ps)]	20.4 (68)
RMS Injected Bunch Energy Spread	6.25×10^{-3}
RF Frequency [MHz]	591 (h=7560)
Number of Cells per Cavity	5
Number of Cavities per Cryomodule	1
Operating Temperature	2K
Total Installed Voltage [MV]	60
Accelerating Voltage per Cavity [MV]	20
Accelerating Gradient per Cavity [MV/m]	15.8
Cavity Peak Surface E Field [MV/m]	35.8
Cavity Peak surface B Field [mT]	69.7
Cavity Dynamic Power Loss [W]	32
Rated CW Power per Input Coupler [kW]	75
Nominal CW Power per Input Coupler [kW]	60
Input Couplers per Cavity	1
Coupler Qext	1.3E7
Cavity Loaded Half Bandwidth [Hz]	22
HOM Absorber Type	Warm Beampipe SiC
HOM Absorbers per Cryomodule	2
HOM Power per Cryomodule [W]	Negligible

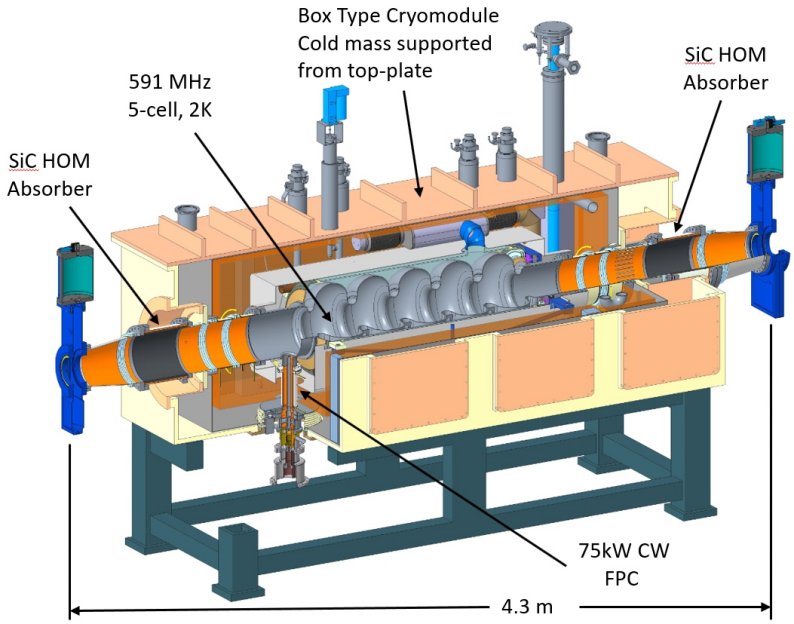

Figure 6.166: 3/4 cutaway view of the RCS cryomodule concept.

Table 6.66: Operating Parameters for the NCRF Bunch Merging Cavities.

Parameter	Bunch Merge 1	Bunch Merge 2
RF frequency [MHz]	295.5	147.8
Harmonic number	3780	1890
Installed voltage [MV]	1.3	0.7
Number of cavities	2	1
Cavity R/Q	170	170
Cavity Q_0	41000	50000
Maximum cavity voltage [MV]	0.65	0.7
Cavity power dissipation [kW]	30.3	28.8
Coupling Beta	1	1
Coupling Q_{ext}	41000	50000
Cavity loaded half bandwidth [kHz]	7.2	3.0

Hadron Ring RF Systems Overview

Because the EIC hadron bunch parameters (see Tables 3.3 through 3.4 in Section 3.1.1) differ from historical RHIC operational parameters, the Hadron Ring RF System will require modification of the existing RHIC 28 MHz RF system [303] used for capture and acceleration. This is driven by a change in operating frequency from 28 MHz to 24.6 MHz, and a significant increase in average beam current in the EIC Hadron Storage Ring, compared with historical RHIC operations.

The typical RHIC collision store bunch pattern is currently 111 bunches in an h=120 bunch pattern. Bunches at store are compressed longitudinally to approximately a 1 ns (30 cm) RMS bunch length, using a non-adiabatic "rebucket" gymnastic [304]. For the EIC, 290 bunches will be injected, captured and accelerated using the upgraded h=315, 24.6 MHz RF system. Several store scenarios are planned, involving 290, 580 or 1160 bunches. The 580 and 1160 bunch patterns will be produced via adiabatic bunch splitting, and the bunches will then be adiabatically compressed to their store length. Thus, several new RF systems are also required for bunch splitting and final bunch length compression.

EIC hadron RF cavity parameters are shown in Table 6.67. The warm Cu cavities will be located in the RHIC 4 o'clock Interaction Region (IR4), where RHIC acceleration and storage RF systems are currently located. It is not anticipated that any new support building or infrastructure will be required, as the existing RF building has sufficient space and utilities to support the EIC RF systems. The SRF 591 MHz hadron cavities will be located in the RHIC 10 o'clock interaction region (IR10).

Table 6.67: EIC Hadron Ring RF System Parameters.

Parameter	Capture & Acceleration	Bunch Split 1	Bunch Split 2	Store 1	Store 2
Harmonic number	315	630	1260	2520	7560
RF nrequency [MHz]	24.6	49.3	98.5	197.1	591.1
Installed voltage [MV]	0.6	0.6	0.6	6.0	20.0
Number of cavities	2	2	2	6	1
Voltage per cavity [MV]	0.3	0.3	0.3	1.0	20.0
Cavity type	NCRF	NCRF	NCRF	NCRF	SRF
Cavity geometry [a]	QWR	QWR	QWR	Reentrant	Elliptical
Cavity R/Q [Ω_{ckt}]	61	65	65	162	251
Cavity Q_0	16E3	19E3	14E3	44E3	2.3E10

[a] QWR = Quarter Wave Resonator

Hadron Capture and Acceleration RF Systems

Overview: The two existing RHIC Yellow Ring $h = 360$, 28 MHz RF cavities will need to be modified, driven by a change in operating frequency ($h = 315$, 24.6 MHz), and an increase in the number of bunches injected into RHIC, from 110 to 290 for the EIC. The change of harmonic number results from the decision to reuse existing RHIC $h = 2520$, 197 MHz storage cavities, as described in Section 6.5.1.

Maximum injected per bunch proton intensity is increased to 2.8×10^{11} per bunch maximum for the EIC vs about 2.2E11 for typical RHIC operations. The average beam current seen by the HSR 24.6 MHz RF system thus increases by about a factor of 3.3 to 1 A, and so an evaluation must be made to determine any new requirements for the power amplifiers, HOM damping, fundamental mode damping, required detuning, etc. Because ions cross the transition energy in the EIC during acceleration, the analysis for power requirements must include the transition phase jump, which along with the rebucket gymnastic [304], typically dominates the amplifier power requirement in the current RHIC operating regime. While these analyses have not yet been completed, preliminary analysis (Section 6.5.4) indicates that the new requirements will not present any insurmountable technical challenges. A wealth of experience and data on cavity performance exist from nearly two decades of system operation. Two of the 28 MHz RHIC cavities, modified for 24.6 MHz operation, will be reused for the EIC, with such modifications as needed. The remaining two RHIC Blue Ring $h = 360$ cavities can also be modified and maintained as spares.

Hadron Bunch Splitting RF Systems

Detailed Cavity Design: The details of the bunch splitter cavity RF designs can be found in Section 6.5.4.

Overview: Possible store bunch patterns in RHIC include 290, 580 or 1160 bunches in an h=315, 630 or 1260 patterns respectively. In order to generate the latter two patterns, new bunch splitting cavities at 49.3 MHz (h=630) and 98.5 MHz (h=1260) are required. 1:2 or 1:2:4 adiabatic bunch splits will be performed to produce the desired bunch patterns. The RF gymnastic [305] and parameters associated with such splitting are not excessively demanding. Voltages required strictly for the split gymnastics are quite low, on the order of $\sim$100 kV (see Figure 6.167).

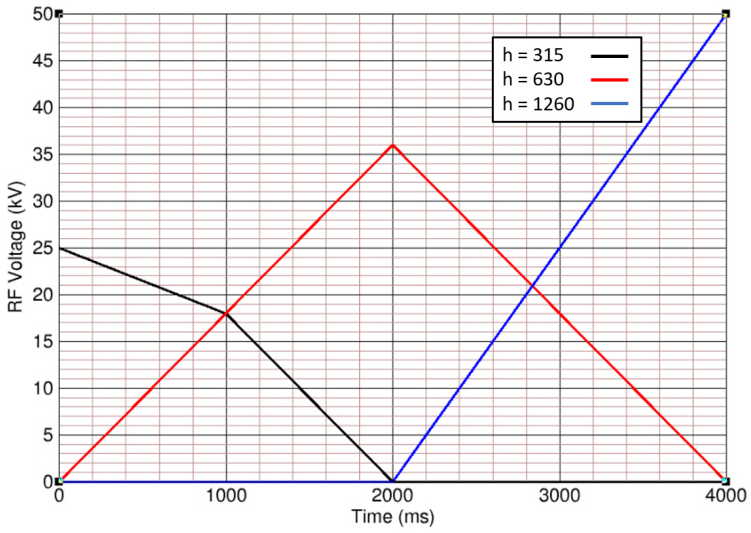

Figure 6.167: RF voltages for h=315, h=630 and h=1260 to perform 1:2:4 bunch splitting.

Such 1:2 bunch splittings are in principle straight forward in terms preserving total longitudinal emittance. As the average beam current will be high, a combination of precision LLRF control and possibly direct RF feedback will likely be employed to maintain cavity voltages and phases within the required precision. Complex RF gymnastics for bunch manipulation, including for high current beams, have been part of routine operation in RHIC, the AGS and the AGS Booster for many years [306–308] and thus these gymnastics are not expected to present any insurmountable challenges. In addition, as with all EIC RF systems, simulations are being developed to ensure accurate understanding of all dynamics involved including realistic effects such as beam loading, RF noise, etc.

Figure 6.168 illustrates the evolution of the conserved longitudinal phase space for the 1:2:4 bunch splitting simulation (single particle dynamics only).

Hadron Store RF Systems: Store 1 and Store 2

Store 1 — 197 MHz Storage RF System: Once the final bunch pattern is produced, the bunches must then be adiabatically compressed to the required store bunch length to minimize the hourglass effect and maximize central luminosity in the detector (see Tables 3.3 and 3.4 in Section 3.1.1). The storage RF systems represent major cost drivers for the Hadron RF system, and scenarios were evaluated to minimize the number of different frequencies required and the number of cavities. RHIC currently operates with a total of ten, NCRF, 1 MV, h=2520, 197 MHz storage cavities, with five cavities each in the Blue and Yellow rings, as well as several spares in warehouse storage. To reduce overall cost and resource requirements, and avoid the need to develop a new system at $h = 2880$, it was decided to reuse the existing 197 MHz cavities as the required intermediate frequency Store 1 RF system. Operating at 1 MV each, six cavities will be required for the EIC HSR. As

these cavities are $h = 2520$, via the bunch splitting requirement they define the capture harmonic to be $h = 315$, or $1/8$ of $h = 2520$, resulting in the requirement to modify the two existing $h = 360$, 28 MHz Capture and Acceleration cavities. The harmonic numbers for the bunch splitter cavities follow from the pairwise splittings.

Store 2 — 591 MHz Storage RF System: To achieve the specified store bunch lengths, a second higher frequency RF system is required. Compatibility with the 197 MHz system and the possibility to re-use a common cryomodule design across multiple systems made the 591 MHz 5-cell cavity (See Sections 6.5.1 and 6.5.3) an attractive choice. This system provides high installed voltage and strong, high power HOM damping — both requirements for the HSR. Single particle simulations show that 20 MV is sufficient voltage to produce the specified bunch lengths given the longitudinal emittance expected. Note that the primary limitation to adiabatic bunch length compression is that it rapidly becomes inefficient, due to the $V^{-1/4}$ scaling of bunch length vs voltage. On the one hand, this implies that minimum achievable bunch length is strongly limited by installed total RF system voltage. On the other hand, it similarly implies that very modest relaxation of store bunch length requirements can substantially reduce required installed voltage. Thus a 10% increase in store bunch length relaxes the voltage requirement by almost 35%.

Table 6.68: EIC hadron ring RF store parameters for highest luminosity operation (see Table 3.3.)

Energy [GeV]	275	275	100	41
Gamma	293.1	293.1	106.6	43.7
Bunch fill pattern harmonic	315	1260	1260	1260
Number of bunches	290	1160	1160	1160
Full emittance (95%) [eV-s]	0.70	0.70	0.40	0.20
RMS emittance [eV-s]	0.037	0.037	0.021	0.011
RMS store bunch length [cm]	6.0	6.0	7.0	7.5
RM store bunch length [ns]	0.20	0.20	0.23	0.25
RMS bunch dE/E [10^{-4}]	6.2	6.2	8.8	11.0
Required voltage (197 MHz) [MV]	6.0	6.0	6.0	6.0
Required voltage (591 MHz) [MV]	20.0	20.0	10.0	2.0
Particles per bunch [10^{11}]	1.91	0.69	0.69	0.26
Bunch charge [nC]	30.6	11.0	11.0	4.2
Average beam current [A]	0.69	1.0	1.0	0.38
Peak bunch current [A]	40	14	12	5

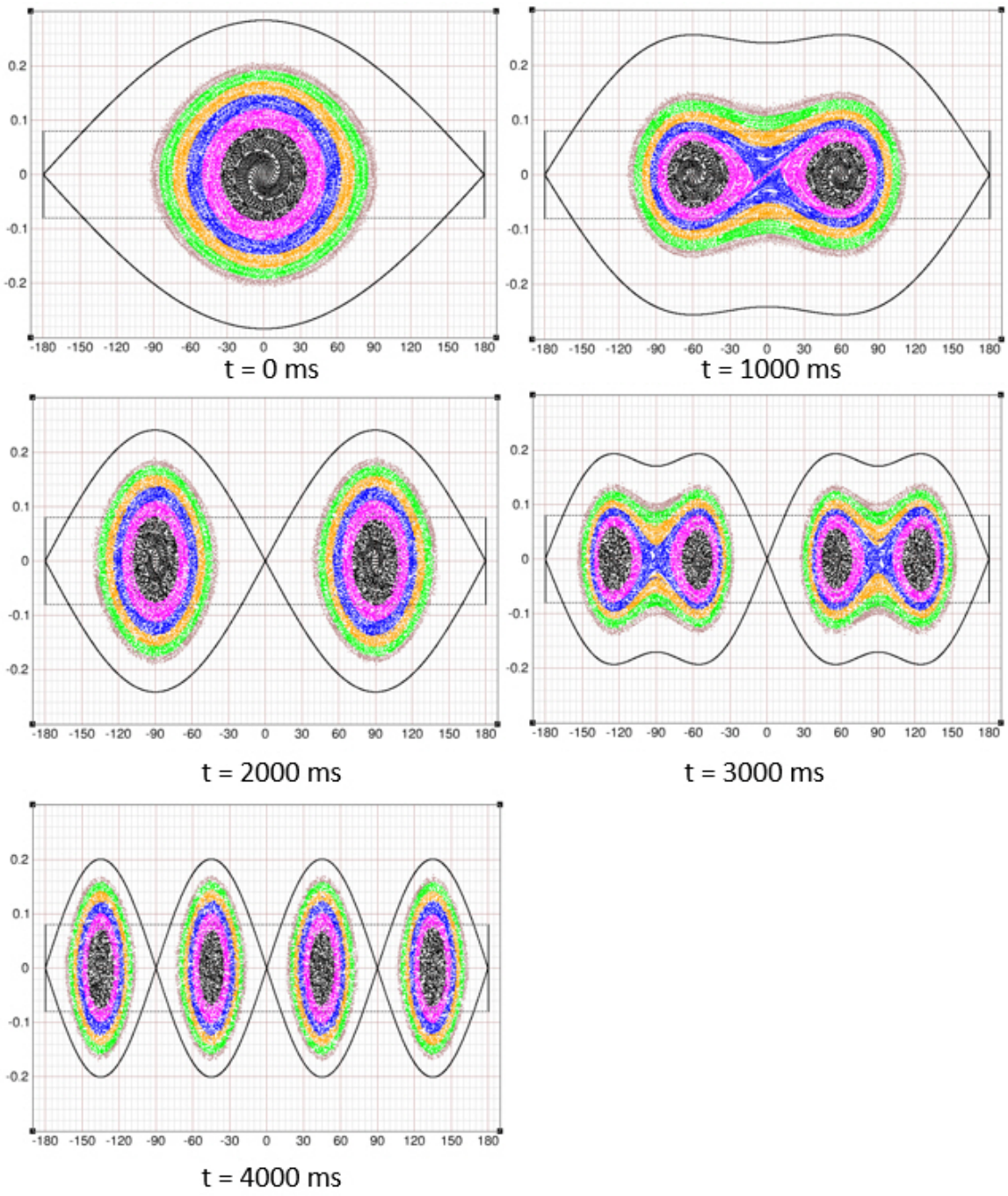

Figure 6.168: Longitudinal phase space evolution produced by the 1:2:4 Split Simulation. Progression is left to right, top to bottom. X-Axis is RF degrees of lowest frequency (h=315). Particle amplitudes are color coded, to emphasize preservation of phase space area, i.e. no mixing.

RHIC IR4 Layout for EIC Hadron Warm RF Systems

The EIC warm Cu cavities will be located in the RHIC 4 o'clock interaction region (IR4), where the RHIC RF systems are currently located. Evaluation of any need for a new support building or infrastructure is continuing, but it appears likely that the existing RF building has sufficient space and utilities to support the EIC warm RF systems. The SRF 591 MHz hadron bunch compression cavities will be located in the RHIC 10 o'clock interaction region (IR10), where main EIC SRF systems (with the exception of the IR crab cavities and SHC ERL) are located.

IR4 is also the new location for the hadron injection septum and kicker. As with the IR10 space, IR4 space is very constrained, and so conceptual 3D models were developed for each of the EIC Cu RF systems for integration into an overall IR concept model. These pre-conceptual modeling efforts were very valuable, providing the ability to iterate layouts and give confidence that all IR4 EIC RF and beamline components can be readily installed, operated and maintained. Figures 6.169, 6.170 and 6.171 illustrate the conceptual layout of the RHIC IR4 region.

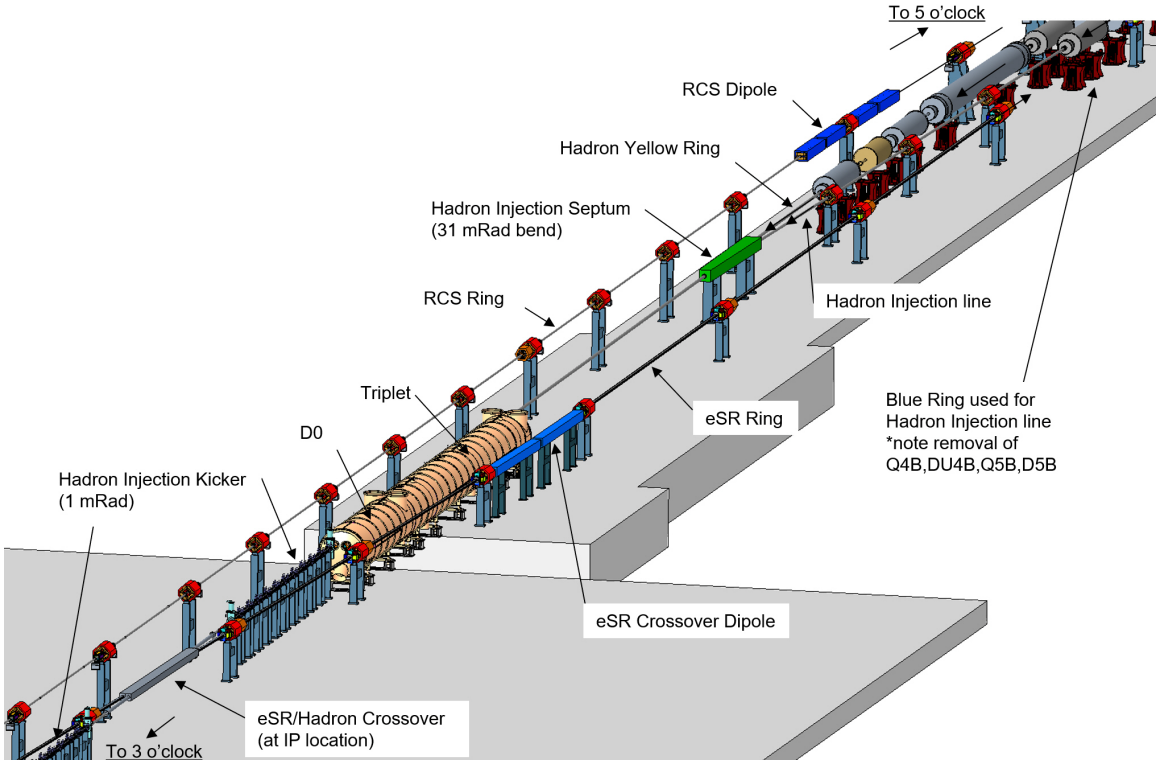

Figure 6.169: Perspective view of the 5 o'clock side of the IR4 interaction region, illustrating the hadron injection line from the RHIC Blue Ring (with required magnets removed), through the septum and into the existing D0/Triplet cryostat.

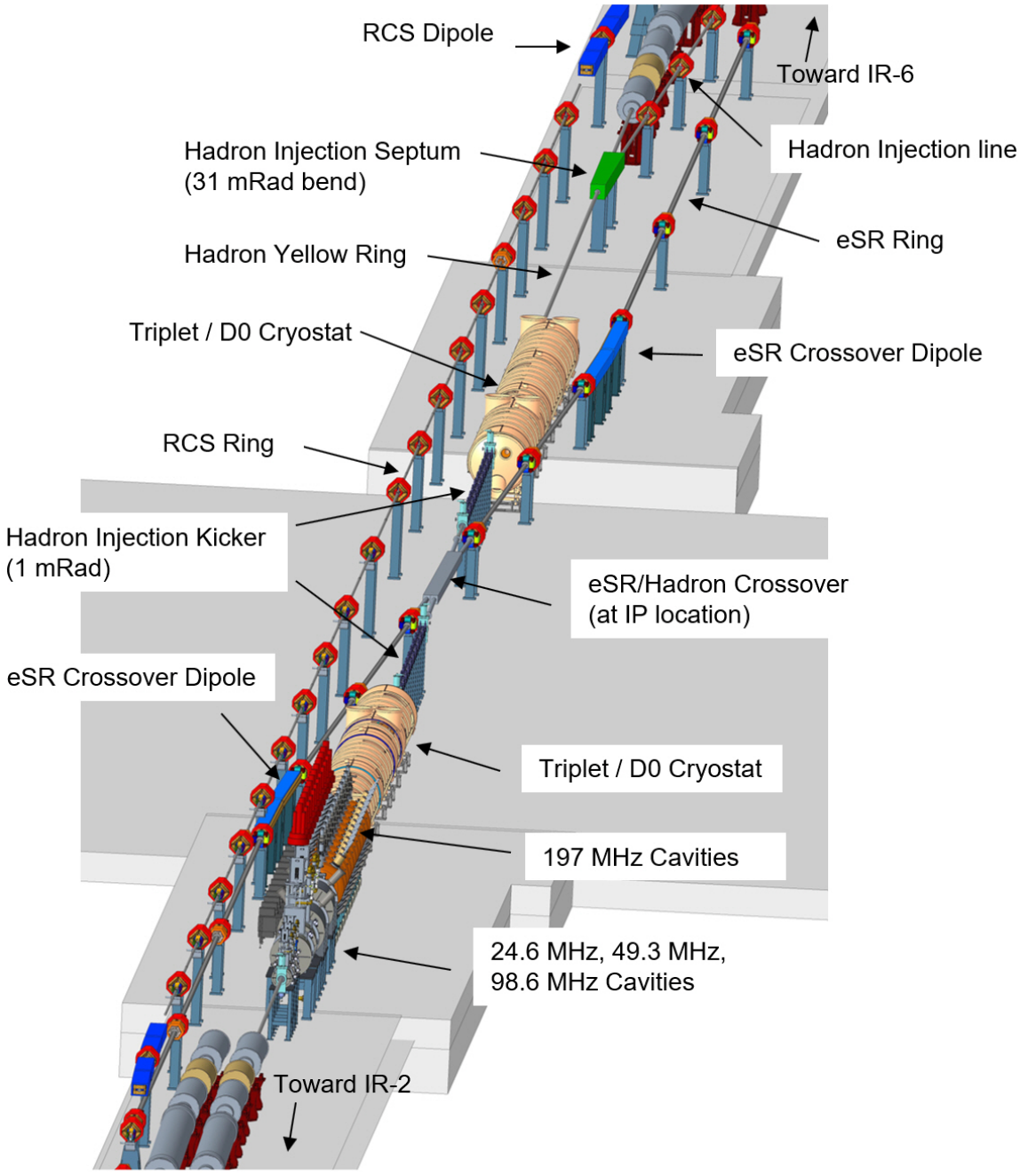

Figure 6.170: Perspective view from the 3 o'clock side of the IR4 interaction region, where the Cu hadron RF cavities are located, across to the 5 o'clock side of the IR, where the hadron injection line enters.

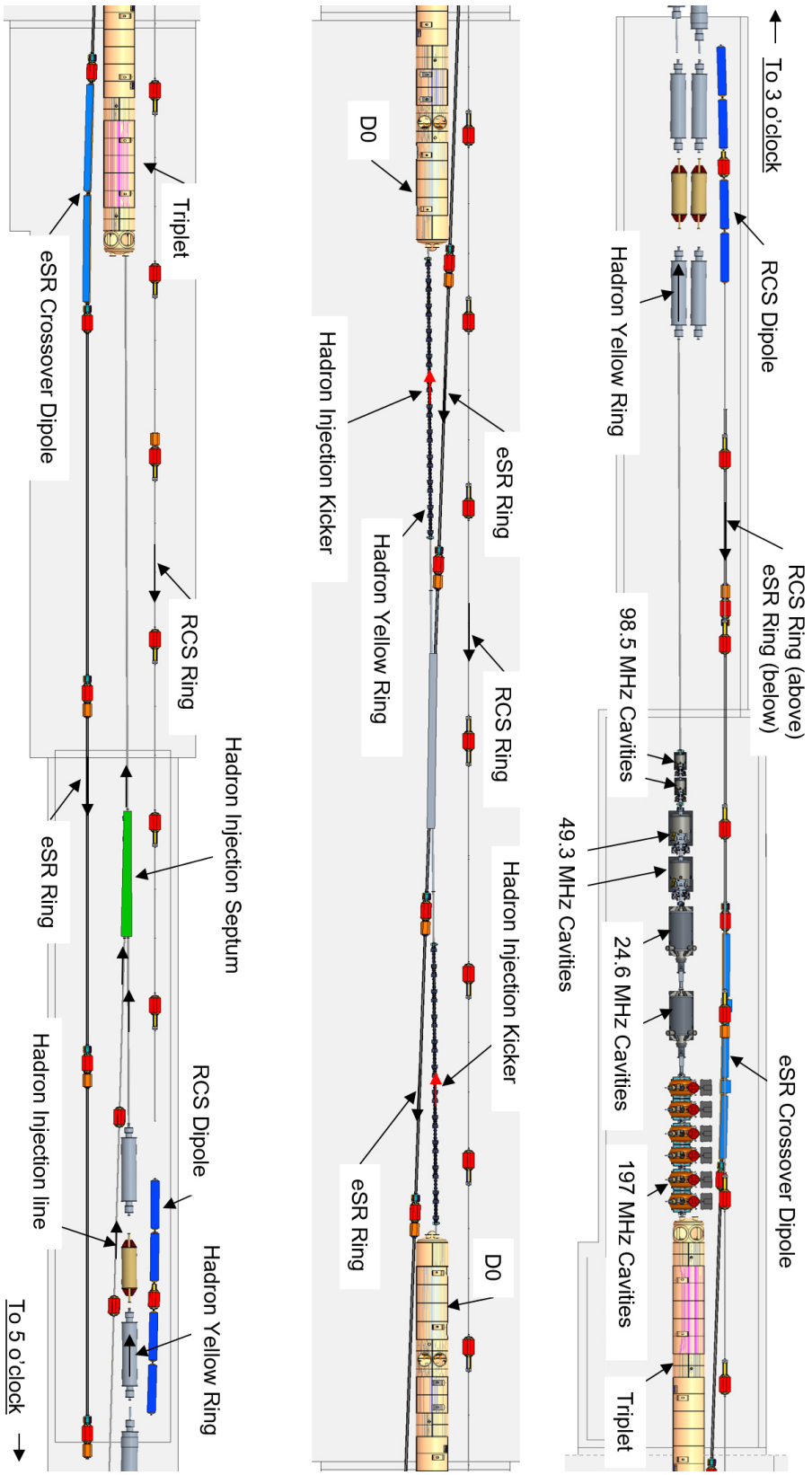

Figure 6.171: Top view of CAD model of the RHIC IR4 interaction region, with all hadron RF system Cu cavities, representative beamline optical elements, the required electron storage ring beamline crossover, and the hadron injection septum and kicker.

Crab Cavity RF Systems Overview

The IR crab cavity system (See Section 6.5.5) is a special RF system to compensate the loss of luminosity due to a 25 mrad crossing angle at the interaction point (IP) . There will be six crab cavities, with four 197 MHz crab cavities and two 394 MHz crab cavities, installed on each side of the IP in the proton/ion ring, and one 394 MHz crab cavity on each side of the IP in the electron ring. Both rings share identical 394 MHz crab cavity design to minimize the cost and risk in designing a new RF system.

The crab cavities developed for the high luminosity LHC (HL-LHC) provide the crabbing kick at 400 MHz and are compact resonator structures as the ones adopted for the EIC, named double quarter wave (DQW) and RF-dipole (RFD). The development of the LHC crab cavities is well advanced, and first beam tests of the cavities were successfully completed at the Super Proton Synchrotron (SPS) during 2018. Experiences and results from the SPS beam experiments can benefit the EIC crab cavity system in various ways, such as the coupler and cryomodule design, precise LLRF control, cavity operation, etc. The EIC designs differ from LHC designs mainly on the HOM damper, since in the EIC the impedance budget is tighter, especially longitudinally. In Section 6.5.5, both DQW and RFD crab cavities for EIC are presented in depth for 197 MHz, and the design of 394 MHz is also introduced.

Strong Hadron Cooling ERL RF

(To request the content for this section, please contact the EIC Information Services Group Leader, Alyssa Petrone, apetrone@bnl.gov).

EIC Low Level RF System Overview

Introduction: For the conceptual Design, efforts to analyze in detail the requirements for Low Level RF (LLRF) control throughout the complex are at a very early stage. However, some general comments can be made regarding existing LLRF systems at C-AD and plans moving forward.

LLRF Control Requirements and Simulations: In addition to the RF beam physics simulations described in Section 4.1, an effort to study LLRF control requirements has also been undertaken . These studies include both the ESR and HSR systems, with the ESR study being the most advanced at this time. The studies utilize and further develop proven tools to understand transient beam loading, optimal detuning, coupled bunch thresholds and growth rates, required feedback architectures and RF power requirements. They will include real world non-ideal effects such as linearity, loop delay, noise, dynamic range, etc.

Transient beam loading has been one focus of these studies, comparing the standard all focusing RF operating mode to the RF “Reverse Phasing” [37] mode already described. In

the ESR, the circulating beam will have a roughly 1 µs beam abort gap which will induce strong transient beam loading. Figure 6.172 illustrates the significant reduction in transient beam loading that results from employing the RF Reverse-Phasing mode. At the time the simulations were performed, up to 18 cavities were planned for the ESR. The simulation thus compares two modes: 1) 18 cavities phased identically (all focusing), and 2) 13 cavities phased for focusing and 5 for defocusing. The peak to peak transient is shown on the Y-Axis as the shift in phase (at 591 MHz) along the bunch train around one turn of the ring. The RF Focus-Defocus reduces the transient from roughly 13 deg pk-pk to 2.5 deg pk-pk.

Optimal detuning, required power, peak power, fundamental mode driven coupled bunch instabilities without and with feedback have also received attention in these studies.

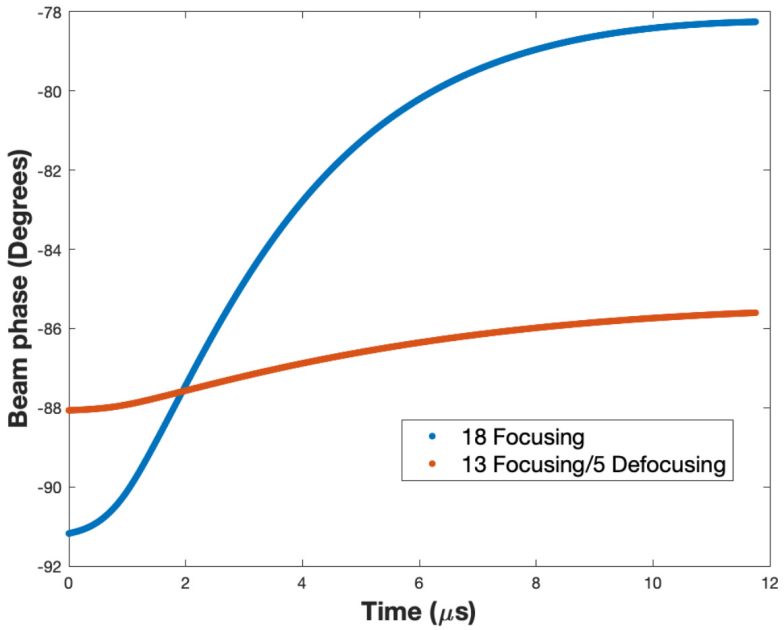

Figure 6.172: Comparison of the transient beam loading induced phase shift along the bunch train for one turn. Y-Axis is phase in degrees of 591 MHz.

The LLRF Platform for the BNL Collider-Accelerator Complex: The current complex of accelerators operated by the Collider-Accelerator Department is quite large, diverse and exceptionally flexible in terms of operational modes. The RF systems integral to each of these accelerators therefore present a diverse array of LLRF control challenges:

- High dynamic range cavity amplitude and phase control.
- Precision cavity amplitude and phase control in CW and pulsed operating modes
- Operation at both fixed and variable frequency, with up to a decade in frequency sweep range.

- Operating frequencies from ∼100 kHz to2.1 GHz.
- Machine to machine timing, synchronization and locking, at both fixed and varying frequency.
- Complex RF bunch manipulation gymnastics: Frequency Hop Rebucketing, bunch merging and splitting, non-integer harmonic squeezing, controlled shape oscillations, etc.
- Cavity Control, Beam Control (Beam Phase and Radial loops for example), Longitudinal and Transverse Damping.
- RF system protection and interlock.

To address the range of control challenges and applications, beginning in 2010 the RF Group developed and deployed a universal, digital LLRF control platform, referred to as the "LLRF Upgrade Platform" [309–312]. The platform has since been rolled out to control every RF system in the accelerator complex. The platform has been operationally proven [313–315] to provide the primary features it was designed for:

- **Precision and Low Noise:** The hardware utilizes very low noise clocking and high speed 16 bit D/A and A/D conversion to provide excellent sampling quality for digital RF synthesis and sampling.
- **Flexibility and Modularity:** The architecture is designed to provide enormous flexibility to accommodate the range and diversity of systems under control. This is due in large part to utilizing a very modular, FPGA based component base from which complete LLRF systems are built up.
- **Scalability and Ease of Integration:** The platform utilizes two key elements that enable systems to readily scale and allow easy integration of sub-systems within and across locations and machines: 1) A common, fixed frequency low noise master clock, and 2) A deterministic, high speed serial timing and communication link.

Low Level RF Systems for the EIC: The existing LLRF Platform could readily be utilized to provide the required LLRF functionality for all EIC RF systems. However, by the time EIC construction commences, the platform hardware will be roughly 15 years old, with many components no longer supported or available from their manufacturers, leading to obsolescence and maintenance issues. In addition, performance specifications for some systems will exceed those of existing systems at RHIC. The Crab Cavity systems for example may require rms amplitude stability better than 1E-4, and achieving such performance would require a new generation of LLRF system hardware.

From an architectural standpoint, we don't anticipate any major changes in direction. EIC RF systems may require specific changes to existing code, new code development, etc. Hardware component performance has undoubtedly improved over the existing components, and this will be used to advantage for further performance enhancement. Certainly

the lessons learned from both the 10 years plus of existing platform development and operation, as well as from high performance LLRF systems across the world, will play an integral role in the overall design of the new system.

It is planned that as part of an EIC project, we would deploy a revised and updated platform ("EIC Common Platform") with the hardware based on newer FPGA/SOC components with ready availability and extended support life from the manufacturers. Much of the existing software and firmware can be reused, with some effort to port them to the latest generation of FPGA/SOC and associated development tools.

Timing and Synchronization for the EIC: In this document, timing and synchronization refer to the kinds of precise timing and synchronization required by systems which generate and manipulate the beams. Such precision timing for existing Collider-Accelerator systems is generally provided by the LLRF systems, with some overlap and shared responsibility with the Controls Hardware Group. It is anticipated that this will remain the case for the EIC with the timing system development closely coordinated around the EIC Common Platform. Examples of precision LLRF timing at RHIC include:

- **Laser Timing and Triggering:** Photocathode electron guns for the Low Energy RHIC electron Cooling (LEReC) project and Coherent Electron Cooling Proof of Principle (CeC PoP) project require timing signals precisely synchronized with and provided by the RF systems.
- **RHIC Beam Synchronous Timing:** RHIC instrumentation, protection systems and experiments rely on a so-called beam synchronous timing system providing flexible, RF synchronous triggers locked to a revolution fiducial marker and bunch pattern. The separate beam synchronous timing system is in the purview of the Controls Group. The precision RF reference clock and fiducial clock are provided to the beam synchronous timing system from the RHIC LLRF system.
- **Machine to Machine Synchronization:** The accelerator complex for RHIC involves synchronous, bucket to bucket transfers between a number of machines which form the injector chain. These transfers involve both fixed frequency transfers between machines with fixed magnetic fields at transfer time, as well as "on the fly" transfers between machines where magnetic fields (and thus RF frequencies in hadron synchrotrons) are changing rapidly. In addition, so-called "cogging" of bunch patterns in injecting and receiving machines is performed to achieve the desired fill patterns. The LLRF systems are responsible for this synchronization.
- **Kicker Timing**: Closely related to the machine to machine synchronization and cogging is the synchronization, cogging and generation of the triggers required by extraction and injection kickers. These triggers are generated by the LLRF systems.

In general, any precision, very low noise clocking or timing is provided by utilizing RF reference signals synthesized from LLRF Controllers. How this is accomplished is described

in the references cited, but some description here is in order. The ability of the LLRF to generate precision, low noise, synchronized RF clocks (and RF drives for cavities) is, by design, intrinsic to the LLRF Platform architecture, and relies on three key components:

- **100 MHz Master Reference Clock:** The RHIC (and EIC) LLRF systems differ in a significant way from most LLRF architectures at other facilities. A single, fixed frequency, RF asynchronous, low noise, 100 MHz master clock is the source for every sampling clock used by the LLRF. This master clock is distributed throughout the C-AD accelerator complex, to any location where LLRF systems are located.
- **Update Link:** The Update Link is a multi-gigabit serial link used to interconnect all LLRF systems across the C-AD accelerator complex. The key feature of this link is that it is synchronous in the 100 MHz master clock domain, and that the timing and data on the link are received at every LLRF controller with an absolute, deterministic delay.
- **LLRF Controllers:** LLRF Controllers are a stand-alone (i.e. not VME, uTCA or other hardware platform), 3U, 19" rackmount chassis which are generally configured in one of two major sub-types: 1) Cavity Controller, and 2) System Controller. Every controller receives the RF master clock, and can both receive and transmit on the Update Link. In addition of course, controllers have ethernet connectivity to provide back end integration into the distributed Controls network.

  The architecture provides very powerful and flexible capabilities, allowing for easy expansion of functionality, scaling and integration of systems across multiple accelerators and wide geographic areas.

Noise/Jitter Performance and Long Term Stabilization: Low noise (jitter) performance starts with the noise characteristics of the 100 MHz Master Reference. For most of the RHIC operating era, the noise requirements for this clock were dominated by the need for very low, close in phase noise. That characteristic was driven by the need to avoid driving longitudinal emittance growth during the 8–10 hour long RHIC hadron stores, where synchrotron frequencies were typically very low, in the tens to hundreds of Hz. In more recent years, as new electron cooling experiments began commissioning, systems like lasers which were sensitive to broadband jitter required a change of focus from close in noise to broadband noise performance.

Distribution of the Master Reference tends to degrade the broadband noise performance, but not the close in noise. The LLRF Controller modular hardware, and in particular the DAC and ADC modules, utilize local VCOs and PLLs to lock to and scale up the 100 MHz Master Reference to desired sampling frequencies. These local PLLs can easily be configured to adjust lock bandwidth such they preserve the close in noise characteristic of the Master Reference, but exhibit the broadband noise floor of the local VCO/VCXO. As such, they effectively serve as clean up clocks, thus providing a low overall noise/jitter performance.

For applications to date, noise performance has been sufficient to meet requirements. Using closed loop cavity amplitude and phase noise performance as the metric, RF systems achieve short term stability approaching dA/A = 1E-4 rms and $d\phi/\phi$ = 0.01 deg rms. Low noise, high stability performance for LLRF is an ongoing focus of LLRF efforts at BNL and in fact across the accelerator LLRF community. Worldwide this has been driven for example by LLRF requirements for large electron LINAC light sources such as the European X-FEL [316] and the LCLS-II [317], and many other accelerators and storage rings. A careful analysis of RF noise requirements for the EIC has not yet been carried out. However, it is expected that most EIC RF amplitude and phase stability requirements will remain near the 1E-4 and 0.01 deg RMS level respectively, and there should be no technological impediment to achieving such levels. Existing LLRF systems worldwide have reported performance exceeding even this level [318, 319]. The effort to surpass this level of performance for the Crab Cavities will present a significant engineering challenge.

Stabilization against long term phase drift is also a technological issue rather than a fundamental issue. LINACs typically employ temperature stabilized phase reference lines as the primary phase reference to which cavities are locked. LCLS-II saves cost by employing a so-called phase averaging reference line [317], utilizing the average of forward and reflected signals from reference line directional couplers to provide first order cancellation of temperature drifts in the line. The critical cavity signal to be drift stabilized (cavity field probe) is typically run on a common path with the phase reference sampled pickoff signal from the cavity, through a relatively temperature stable environment over as short a distance as practical, to the LLRF. LLRF electronic racks are also temperature stabilized if necessary.

Once all practical measures are implemented to achieve the lowest drift possible, in general beam based feedbacks are employed to provide the final correction of any drifts. No effort has yet been directed toward analyzing such requirements. But again, the challenges encountered in such systems are technological rather than fundamental, and beam bases feedbacks are in common use at accelerators worldwide.

EIC High Power RF System Overview

Introduction: System power requirements for the EIC RF are dominated by the ESR 591 MHz Fundamental RF system described in section 6.5.1 with roughly 13 MW of installed power planned for the operational parameters described in in Table 6.63. Considerable effort has been dedicated to identifying the optimal solution for such a large RF power installation. The technology choices available include: Klystron, IOT (inductive Output Tube) and SSPA (Solid State Power Amplifier). Klystrons and IOTs represent traditional, well tested and proven solutions with decades of experience behind them. Solid state RF power has become competitive and more widely used over the last decade and has been maturing rapidly in terms of increased power density and lower cost. This has been spurred as is typical by the communication industry which has been pivoting to solid state.

The outlook going forward for availability and cost of high power klystrons and IOTs is quite limited, making solid state a strong preference in new systems. In addition to market forces, a preference for solid state RF power is also being driven by the rapid decrease in cost per watt and increase in power density. Because solid state inherently involves the modular addition of many smaller power stages, reliability and uptime are actually improved vs single high power vacuum tubes because failure of a single solid state power module only reduces available output power fractionally whereas failure of a high power tubes removes the full RF power. Solid state power modules can be replaced fairly quickly and easily during maintenance periods. Solid state RF power installations also eliminate serious safety concerns with high power tubes like klystrons and IOTs. such tubers require high voltage and high current power supplies ranging from 30 kV up to 100 kV or more. Solid state amplifier transistor rails typically utilize 50 VDC.

Interest in this project from commercial vendors has been strong and a number of proposals have been received. Detailed performance specifications have not yet been developed, so vendors were only asked to submit proposals based on amplifier power and frequency.

Existing Solid State RF Power Installations: The EIC SRF power installation will be the largest accelerator RF solid state power installation in the world. Nonetheless, it is based on individual amplifiers of roughly 400 kW CW rating. A number of high power CW solid state amplifier installations exist at accelerators worldwide, with notable examples at light sources, and the largest to date at the CERN SPS. Light source installations up to 180 kW at 352 MHz exist at facilities including SOLEIL and ESRF. 100 kW–200 kW class 500 MHz solid state power installations exist or are under consideration at DIAMOND, ALBA, SESAME SPRING8 and elsewhere [320], and the NSLS-II has recently installed a system rated to 320 kW CW at 500 MHz. The highest power installation is currently at the CERN SPS which has installed two 200 MHz, 2 MW amplifiers rated at 50% duty cycle. These amplifiers combine 16×144 kW commercial units delivered by Thales [321] .

6.5.2 Electron Storage Ring RF System Design

ESR 591 MHz Fundamental Storage Cavity

In the electron Storage Ring (ESR), a total RF voltage per turn up to 62 MV is needed to compensate for beam energy loss due to synchrotron radiation. This voltage is provided by 17, 1-cell superconducting RF (SRF) cavities. Factors contributing to the selection of the cavity design are discussed in the ESR RF Systems Overview in Section 6.5.1.

Nominal and Maximum Available Operating Parameters Table 6.69 summarizes the nominal and maximum operating parameters of the cavity. Here, "nominal" refers to parameters corresponding to the operating gradient expected for the EIC, which occur for the specified 62 MV total voltage per turn at 18 GeV. "Maximum" refers to parameters corresponding to the maximum design accelerating voltage, defined as 4.0 MV CW.

Table 6.69: Nominal and maximum operating parameters for the EIC ESR, 1-Cell, 591 MHz Fundamental Cavity.

Parameter	Nominal	Maximum
Voltage per Cavity [MV]	3.65	4.0
Accelerating Gradient [MV/m]	14.6	15.8
Peak Electric Field [MV/m]	30.6	33.6
Peak Magnetic Field [mT]	70.0	76.8
Dynamic Loss at 2K [W]	8.67	9.51

Target Design Requirements At the start of the conceptual design effort, targets for operational cavity parameters were established as follows:

- **Frequency:** 591.177 MHz (h = 7560).
- **Maximum Accelerating Gradient:** 16.0 MV/m CW
- **Peak Surface Magnetic Field:** 80 mT [$B_p/E_{acc} \leq 5.0$ mT/(MV/m)]
- **Peak Surface Electric Field:** 40 MV/m [$E_p/E_{acc} \leq 2.5$]
- **Longitudinal Impedance:** Total for all cavities.
  - **Target Limit:** 26 kΩ-GHz
  - **Goal:** 2.6 kΩ-GHz
- **Transverse Impedance:** Total for all cavities.
  - **Target Limit:** 12 MΩ/m
  - **Goal:** 1.2 MΩ/m

These requirements are generally within the state of the art for SRF cavities. 1.3 GHz cavities operate routinely at higher gradients up to 31 MV/m in pulsed mode at EU-XFEL or 16 MV/m CW at LCLS-II. 31 MV/m pulsed gradient corresponds to peak surface fields of up to 130 mT and 62 MV/m. The operational goal of 16 MV/m CW for LCLS-II comes from cryogenic power considerations due to the overall system size, and is not due to fundamental field limitations. Impedance targets are determined from beam dynamics simulations and we further set the impedance goals at 10% of target to avoid beam instabilities. The HOM impedance requirements should be achievable with state of the art SiC HOM absorber technology, which can handle the expected high HOM power generated by the high beam current.

Cavity Design The cavity design is focused on HOM propagation to the room temperature beam line absorbers (BLA). BLAs with a Silicon Carbide (SiC) dielectric are chosen for their high power handling and relative simplicity in cooling. The BLA design will follow the ANL design for the APS Upgrade [322], with a SiC dielectric such as Coorstek SC-35. The fabrication of these dielectrics becomes more challenging with increasing cylinder diameter. Therefore a maximum inner diameter (ID) of 274 mm for the beam pipe and SiC was chosen. An R&D effort has successfully proven out fabrication of both the large SiC cylinders and the overall BLA assemblies. Each cryomodule will have its own dedicated absorbers as illustrated in Figure 6.173.

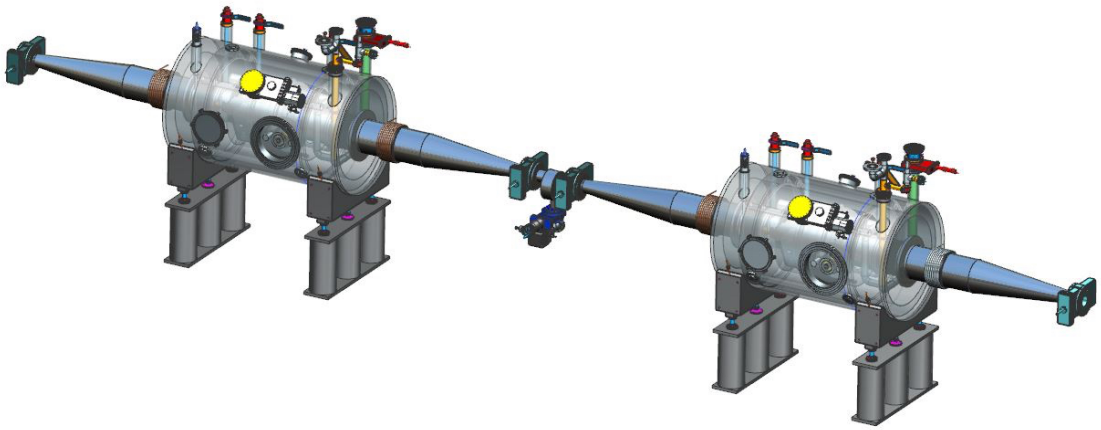

Figure 6.173: Conceptual layout of the electron Storage Ring SRF installation with one-cell cavity, cryomodule and beam line absorbers.

The basic requirement for the cell length $L_{cell} = \beta\lambda/2$ sets the length of the half-cells to 126.780 mm. Simulations with CST Microwave Studio were done to optimize the cell shape for low peak surface fields with a large aperture in the iris. Because the R/Q of the cavity should be low by design (to minimize beam loading and detuning), the iris can be large and the transitions on both sides designed to optimize HOM propagation. The resulting RF parameters for the fundamental mode in Table 6.70.

To allow for sufficient attenuation of the fundamental mode the beam pipe attached to the cavity must have a length of at least 339 mm. At this point the surface currents are low enough, ∼0.25 mT, to avoid heating of any gaskets. Following this is a cold-to-warm transition which was assumed to be approximately 500 mm long. This length was chosen to provide a long enough path to reduce thermal loads from the room temperature installation into the 2 K cryogenic system.

The beam line absorbers were optimized to effectively reduce the Q of the first dipole passband modes, which are close to the TE11 cutoff frequency. The details of the iris are optimized to ensure good coupling to these modes. The BLA length is 250 mm and thickness is

Table 6.70: RF parameters of the accelerating mode for the one-cell cavity.

Parameter	Value
Frequency (MHz)	591.177
R/Q (Ω) (Circuit Definition)	36.6
Maximum Voltage (MV)	4.0
Operating Gradient Eacc (MV/m)	15.8
E_p / E_{acc}	2.13
B_p / E_{acc} (mT/(MV/m))	4.87
U / E_{acc}^2 (J/(MV/m)^2)	0.237
G (Ω)	293
Q_0 (2.0 K) (Including 10 nΩ Rres)	2.3×10^{10}
P @ 15.8 MV/m = 4 MV (W) (2.0K)	9.51

14.0 mm. The BLAs are placed symmetrically on each side of the cavity, directly following the cold-to-warm transition. Although the BLAs are very effective in damping the cavity modes they are also directly heated by the beam contributing to the total extracted power. This will be studied further in the future development.

Gate valves between cryomodules allow for installation and maintenance of individual modules without the need to vent the whole SRF section, thus preventing sources of contamination from getting into the cavities and degrading performance. The largest available RF shielded gate valve available as a catalog item has an ID of 200 mm, however these are heavy and expensive. 100 mm ID gate valves are shown on the ESR 1-cell cavity concept. Since the beampipe has an ID of 274 mm, a taper section is needed. The taper section is planned with a 5:1 ratio between the length to ID change. An additional BLA in between modules in the section with reduced ID is planned to prevent HOMs traveling between cryomodules.

HOM Power Calculation The HOM power density at a given frequency is calculated as the product of the bunch power spectrum and the real part of the shunt impedance. This power density integrated over frequency then results in the total HOM power. For these calculations, the impedance (Figure 6.175) above 8 GHz was assumed constant at the average value from 6-8 GHz.

The beam parameters used for the HOM calculation are listed in Table 6.71, representing the worst case HOM power generation over the fill patterns analyzed. The beam current spectrum is shown in Figure 6.174.

Wakefield simulations revealed that there are no large impedance spikes at higher frequencies as can be seen in Figure 6.175. The longitudinal single bunch loss factor including

Table 6.71: Worst case electron beam parameters and the resulting HOM power for the 591 MHz electron Storage Ring cavity.

Parameter	Value
Number of Bunches	1160
Bunch Harmonic Number	1260
Bunch Frequency [MHz]	98.5
Energy [GeV]	10
Particles per Bunch [1E10]	17.2
Bunch Charge [nC]	27.6
Bunch Length [mm]	8
HOM Power [kW/cavity]	48.6
HOM Power per Absorber [kW]	24.3

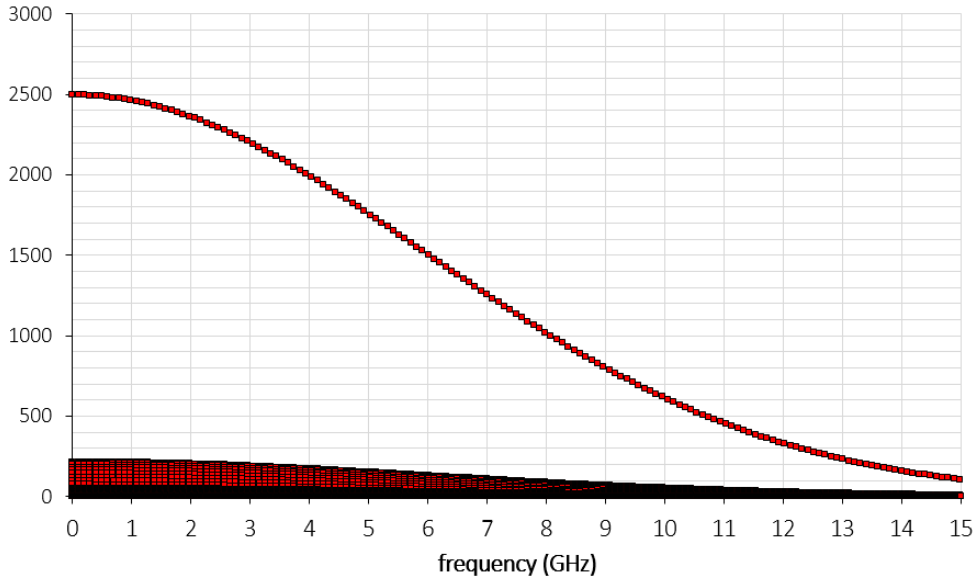

Figure 6.174: Beam spectrum for electron beam with parameters shown in Table 6.71.

the fundamental mode integrates to 0.418 V/pC, or 0.350 V/pC without the fundamental mode. Figure 6.177 shows the transverse impedance.

The total amount depends strongly on the bunch charge with a Q_b^2 dependence. Therefore the higher energy beam, with its reduced bunch charge to avoid synchrotron radiation, creates less HOM power. This is partially compensated by the shorter bunch length at high energy because the bunch spectrum extends to higher frequencies. The worst case HOM power is calculated to be 48.6 kW/cavity (Figure 6.177), absorbed in the BLAs at each

end of the cryomodule. Wakefield calculations show to first order that the BLAs absorb the power evenly, so each BLA needs to absorb 24.3 kW. It can be reasonably expected that the absorber for the EIC will have a higher power capability due to the increased size compared to the ANL design. This results in a bigger volume for the power to be absorbed in and larger surface area for heat transfer to cooling water channels. The worst case power density on the cooling surface, corresponding to 24.3 kW absorber power, is about 0.1 W/mm^2, significantly smaller than for the ANL absorber with 0.2 W/mm^2.

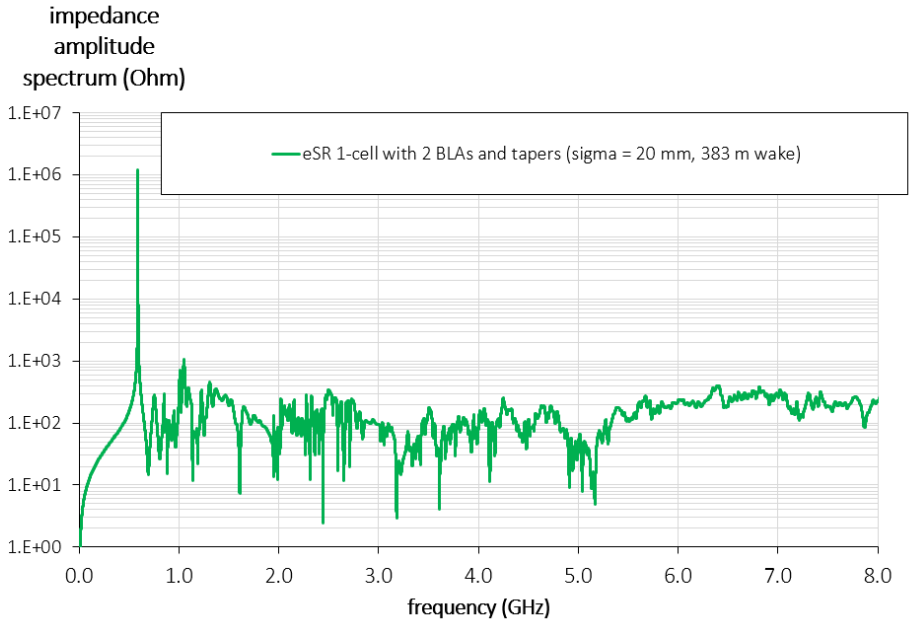

Figure 6.175: Results of the wakefield simulations with CST show strong damping of the cavity trapped modes and no high impedance peaks at higher frequencies. The loss factor integrates to 0.418 V/pC including the fundamental mode.

The maximum impedance is relevant to longitudinal and transverse instability thresholds. In the longitudinal case, the maximum value for $R_{sh}f$ is $1.1 \times 10^{12}\,\Omega$Hz, (Figure 6.175), well below the specified threshold. The maximum transverse shunt impedance (in circuit definition) is $1.5 \times 10^{4}\,\Omega$/m, (Figure 6.176), well below the limit of $1.5 \times 10^{6}\,\Omega$/m.

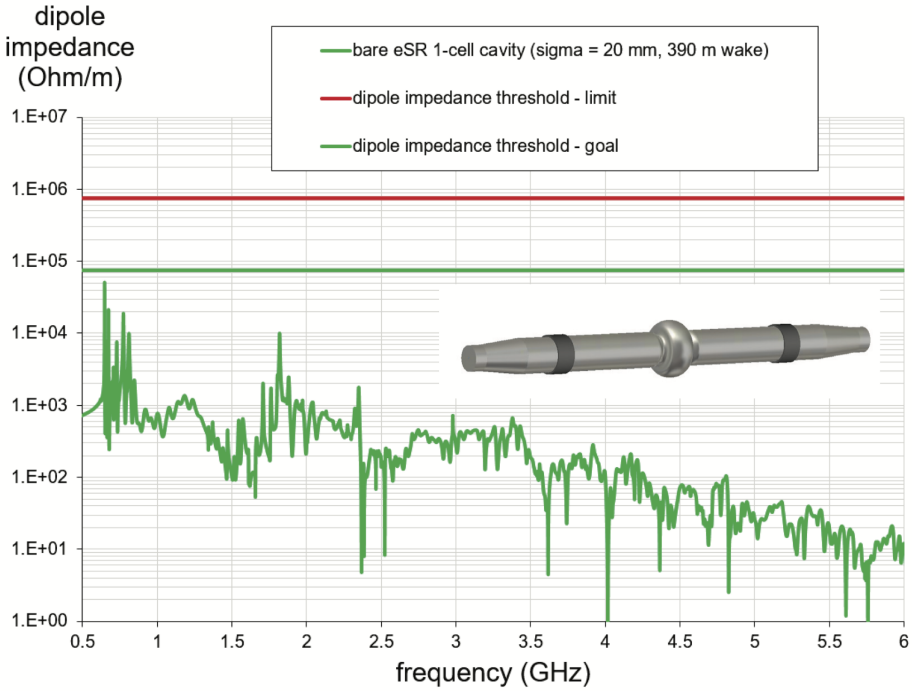

Figure 6.176: Results of the transverse wakefield simulations with CST show no high impedance transverse modes remaining.

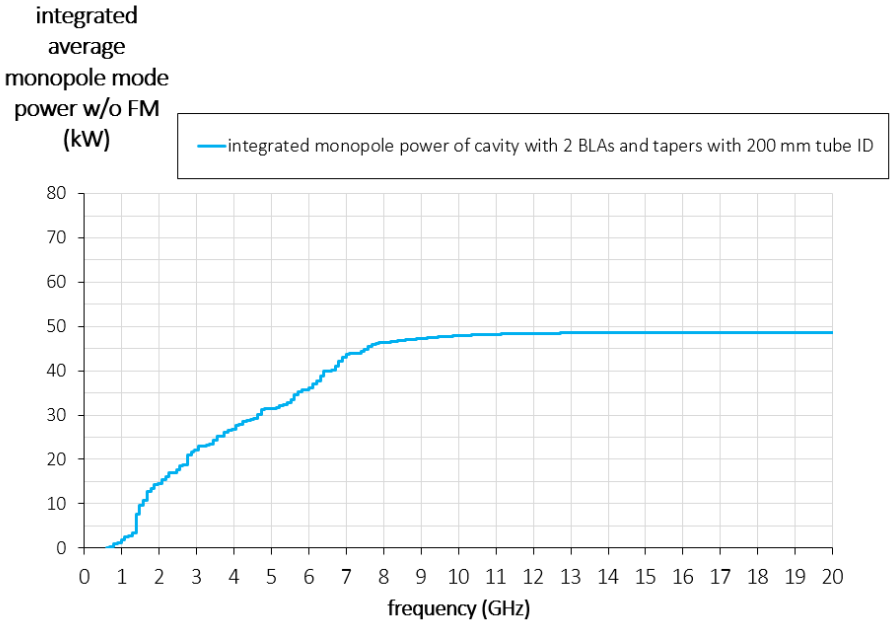

Figure 6.177: Integrated longitudinal HOM power with 8mm bunch.

6.5.3 RCS RF System Design

The Rapid Cycling Synchrotron (RCS) (Section 3.6) provides on-energy injection (up to 18 GeV) of high charge, polarized electron bunches for the EIC electron storage ring. Although the RCS ring circumference of 3841.35 m is slightly larger than the ESR circumference of 3833.77 m, we can still use the same frequency as ESR, i.e. 591 MHz, but with a different harmonic number (7575 vs 7560). The RCS RF system comprises three, 5-cell 591 MHz SRF cavities in 3 cryomodules (one cavity per cryomodule), providing up to 60 MV per turn. The cavities nominally operate in pulsed mode with 20% duty factor, at a repetition rate of 1 Hz, but the cryomodule design will support CW operation at maximum gradient. This same cryomodule design is used in two other EIC RF systems, the Hadron Ring (Section 3.3) and a possible Strong Hadron Cooling ERL (Section 3.9).

The design of the 5-cell, 591 MHz cavity is derived as a scaled version of a 650 MHz 5-cell cavity, designed for high current applications. Figure 6.178 shows the 5-cell 591 MHz SRF cavity, with beam pipe absorbers on each side. The cavity parameters are listed in Table 6.72. The cavity employs enlarged beampipes to propagate all the HOMs out of the cavity, but still attenuate the fundamental mode to avoid losses at the cavity flanges and warm to cold transition beampipes. The maximum required voltage for the RCS is 50 MV, or 16.7 MV per cavity, corresponding to a maximum operating gradient of 13.1 MV/m.

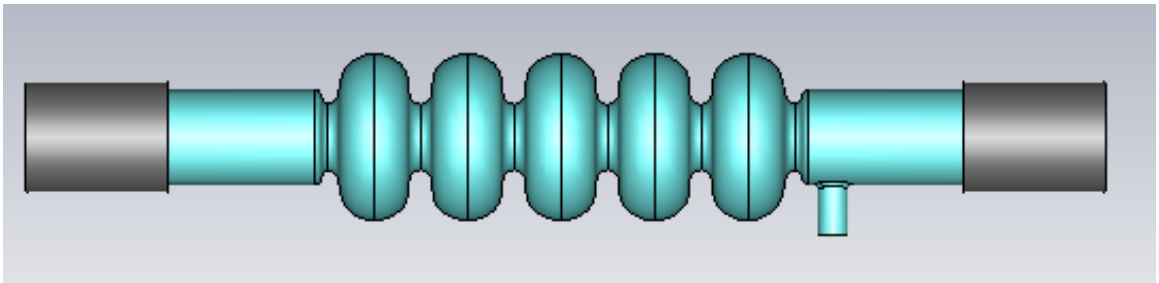

Figure 6.178: 5-cell 591 MHz SRF cavity with SiC beampipe absorber.

Figure 6.166 shows a conceptual design of the 5-cell 591 MHz SRF cavity cryomodule. Two SiC beampipe absorbers are used for damping HOMs, one on each side of the cryomodule in the warm beamline sections. An SNS type coaxial-window will be used for the fundamental power coupler, delivering up to 60 kW to the cavity in normal operation. The design of FPC and RF window is shown in Figure 6.179. This window and FPC have been tested up to 70 kW CW. The external Q for RCS is nominally set at about 3.0E6, corresponding to a 100 Hz half bandwidth. This provides reasonable bandwidth to accommodate microphonics as well as dynamic changes in cavity voltage, whether arising from pulsed operation or a voltage program along the energy ramp. It is likely that an economical choice for the power amplifier will be to utilize the same modular solid state units which comprise the very high power amplifiers for the electron Storage Ring fundamental cavities.

Table 6.72: 5-cell 591 MHz cavity maximum operating parameters.

Parameter	Result
Frequency [MHz]	591
R/Q [Ω (Accel)]	502
Geometry Factor	273
Epeak/Eacc	2.27
Bpeak/Eacc [mT/(MV/m)]	4.42
Coupling Factor	2.8%
Operating Voltage [MV]	16.7
Operating Eacc [MV/m]	13.1
Peak Magnet Field [mT]	58.1
Peak Electric Field [MV/m]	37.8
Cavity Dynamic Loss [W]	22
Operating Temperature [K]	2.0

During acceleration from 400 MeV to 18 GeV over a 100 ms ramp, the electron bunch revolution frequency changes by 0.063 Hz, and thus the RCS cavity frequency will need to increase by 482 Hz. As this is much higher than the design cavity bandwidth, an active piezo tuner will be used to track the frequency change.

The repetition rate of the RCS is 1Hz, with two 28 nC bunches accelerated per cycle. The HOM power generated is small, about 20 W including both longitudinal and transverse HOMs. A very large electron bunch transverse offset of 1 cm is assumed for transverse HOM power calculation. The cryomodule assembly will utilize the same SiC HOM absorber here as for the Hadron Ring Store 2 and the proposed Strong Hadron Cooling ERL fundamental H1 systems. In the RCS, HOM power is of no concern. Nonetheless, the damping provided is crucial to ensure stability of the high charge electron bunch against long range wakefields.

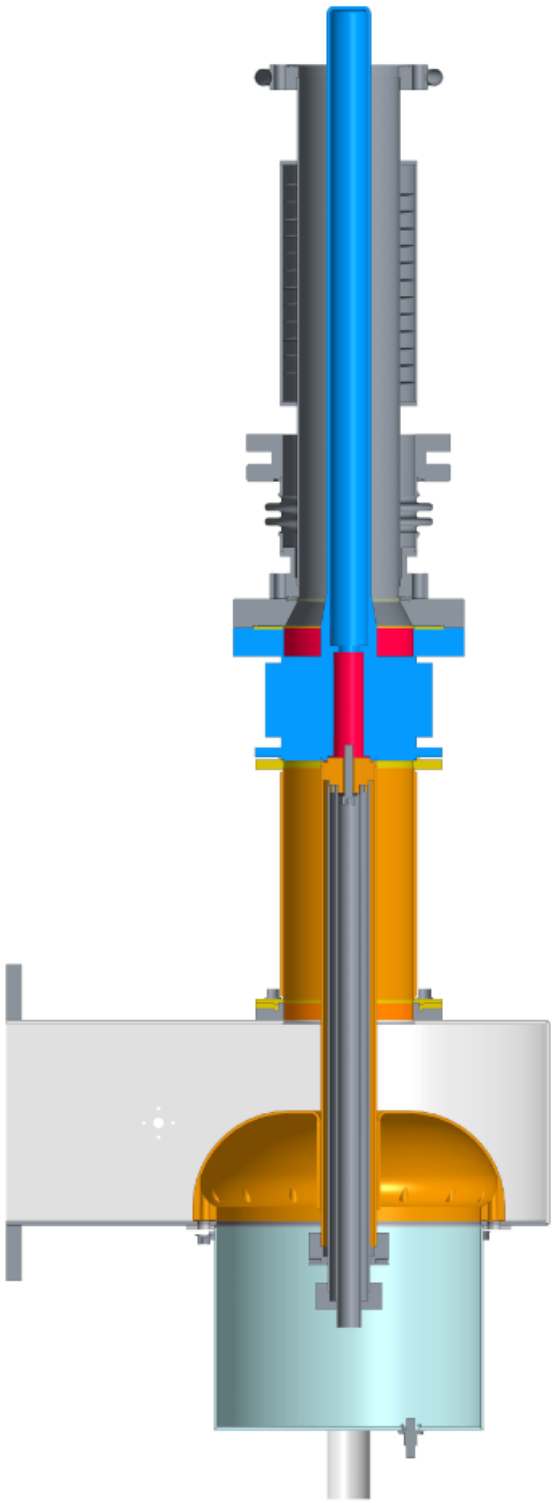

Figure 6.179: FPC for 5-cell 591 MHz SRF cryomodule.

6.5.4 Hadron Ring RF System Design

The EIC includes five different RF systems used for capture, acceleration, bunch splitting and bunch compression. The Hadron Ring RF Systems Overview (Section 6.5.1) describes the considerations driving the selection of each RF sub-system. As stated in the overview, the EIC Hadron RF systems rely in large measure on reuse — reusing the existing RHIC 28 MHz and 197 MHz RF systems, and a common, new EIC 591 MHz single cavity cryomodule design that will also be used in the RCS. New, Cu 49.2 MHz and 98.5 MHz bunch splitter cavities will also be required.

This section will describe the possible modifications required for reuse of the RHIC 28 MHz and 197 MHz RF systems, and the new 49.2 MHz and 98.5 MHz bunch splitter cavities. The 591 MHz SRF cryomodule is described in Section 6.5.3.

Hadron Capture and Acceleration RF System

The 28 MHz, Cu, quarter-wave cavities at RHIC have served as the primary capture and acceleration system since RHIC was commissioned in 1999. The cavities are proven to be robust and reliable, providing up to 300 kV each, and operating in groups of two in each of the two RHIC rings, Blue and Yellow. The 28 MHz cavity frequency corresponds to harmonic number h=360, and thus the primary modification required for the EIC is to reduce the operating frequency to 24.6 MHz, corresponding to the new EIC capture harmonic number h=315. The cavities will also need to accommodate higher beam current for the EIC where the 1 A average current is approximately three times the historical RHIC operating beam current. These considerations are discussed in the following.

Frequency Retuning

The current 28 MHz cavity design employs a quarter wave resonator geometry foreshortened by introducing significant capacitance at the high voltage gap end of the cavity. The capacitance results from a re-entrant type gap end geometry where the center conductor (beam tube) sits within a bell type structure that includes the ground end of the high voltage gap (see Figure 6.180). This section resides entirely within the cavity high vacuum volume and does not rely on ceramics or other dielectric materials. This section is detachable from the main body of the cavity and thus a straight forward redesign of this section will provide the added capacitance required to retune to 24.6 MHz. Analysis of a proposed structure shows no increase in peak electric fields in this region.

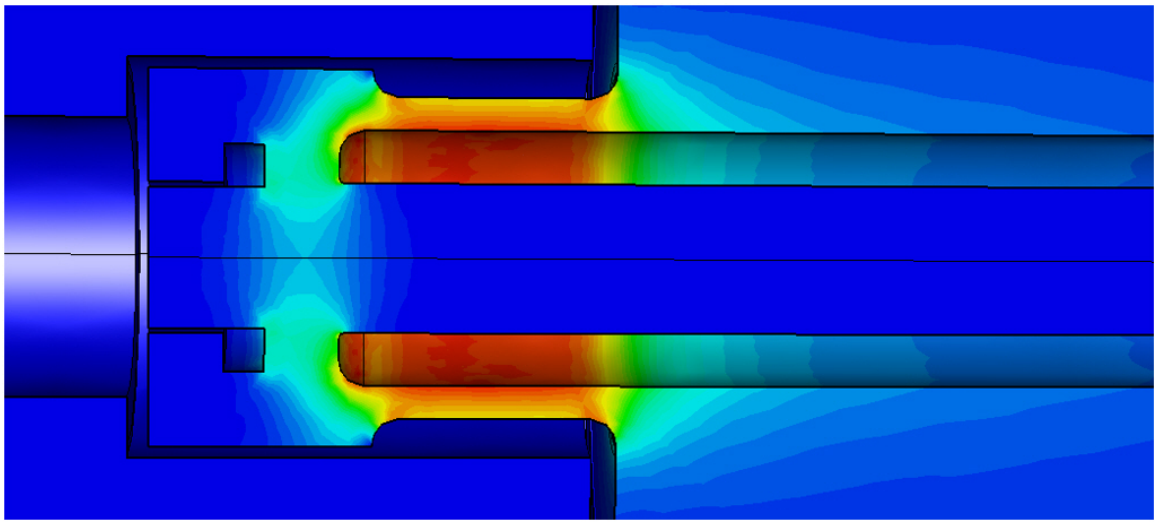

Figure 6.180: Simulation model of the high voltage gap end of the cavity structure, modified to reduce frequency to 24.6 MHz.

Power Amplifier and Coupling

At RHIC, the cavity typically operates at 240 kV, a maximum synchronous phase of about 3.5° with 111 proton bunches of 2.2×10^{11} protons each. The maximum required forward power is about 47 kW with a required detuning of about 2.5 kHz for reactive beam loading compensation. Assuming the same ramp rate for the EIC and an increase in beam current by a factor of three the required forward power increases to about 62 kW and required detuning increases to about 7.5 kHz. The existing close coupled tetrode power amplifiers are rated for 150 kW plate dissipation and so provide ample reserve. This reserve is in fact utilized to provide higher peak powers during RF gymnastics, e.g. transition phase jump and the rebucket gymnastic. Given the new beam loading regime it is likely that the FPC coupling will be re-optimized in order to reduce required forward power.

HOM Damping

The cavity currently has two HOM couplers with associated high pass filters and under RHIC operating parameters these require only 30 W termination loads. Since the cavity maximum voltage does not change for the EIC the fundamental RF stresses on the HOM structures do not change. However, the EIC hadron bunch lengths are significantly shorter than for RHIC operation and thus higher HOM power is to be expected, which we presume can be accommodated by larger termination loads. The existing damper structures are mounted to cavity port flanges with a reasonable amount of available space to accommodate reactive element design changes should they be required.

Hadron Bunch Compression 2 RF Systems

As discussed in Section 6.5.1, two storage RF systems are required for the EIC to satisfy bunch compression requirements across the wide range of store energies and specified store bunch lengths. This section will describe the 197 MHz storage RF system considerations for the EIC. The 197 MHz cavities are CERN SPS cavities modified to reduce their frequency slightly from 200 MHz to the RHIC 197 MHz operating frequency [323]. Because the operating frequency of this system is unchanged from RHIC, the 197 MHz cavities are reused almost "as-is" with possible required modest modifications described in the following. This reuse provides significant economy in overall EIC RF system capital cost and eliminates the design and prototype effort which would be required for a new system.

As mentioned previously, the 591 MHz storage RF system, which utilizes a new cryomodule to be deployed across three EIC RF systems, is discussed in Section 6.5.3.

Power Amplifier and Coupling

As mentioned, the typical RHIC stored proton beam consists of 111 proton bunches with about 2.2×10^{11} protons per bunch. For 800 kV the forward power is about 45 kW with a required detuning of 7 kHz. For 1 MV EIC operation the forward power increases to about 70 kW and detuning increases to about 32 kHz due to the increase in beam current. The existing close coupled tetrode power amplifier is rated for 90 kW of plate dissipation. As with the 24.6 MHz system, it is likely that the FPC coupling will be re-optimized for the new loading regime. An upgrade of the driver amplifier used in the fast feedback loop may also be required. As resources allow, we plan to test the existing cavities to 1.1 MV to confirm the optimal working point and to determine any required optimizations. It is anticipated that all current cavity and coupler sub-assemblies will handle the increased fundamental RF operating stresses without issue.

HOM Damping

Two orthogonal, high-Q HOM notch couplers and filters (see Figure 6.181) are currently installed on the cavities requiring 800W termination loads. Fundamental RF stresses at the 1 MV EIC operating voltage should not present an issue. Fundamental power dissipated on the notch filter RF surfaces will be about 600W and will be removed by the existing water cooling of the structure. When tuned properly only 200 mW of fundamental RF power will be extracted to the termination load. High order mode power is transmitted to the termination load except for any HOM power aligned with the higher frequency notches of the filter structure (see Figure 6.182). An analysis of the HOM spectrum against these notches remains to be completed, but as the filters are connected via a flange mount any required changes can be accommodated if needed.

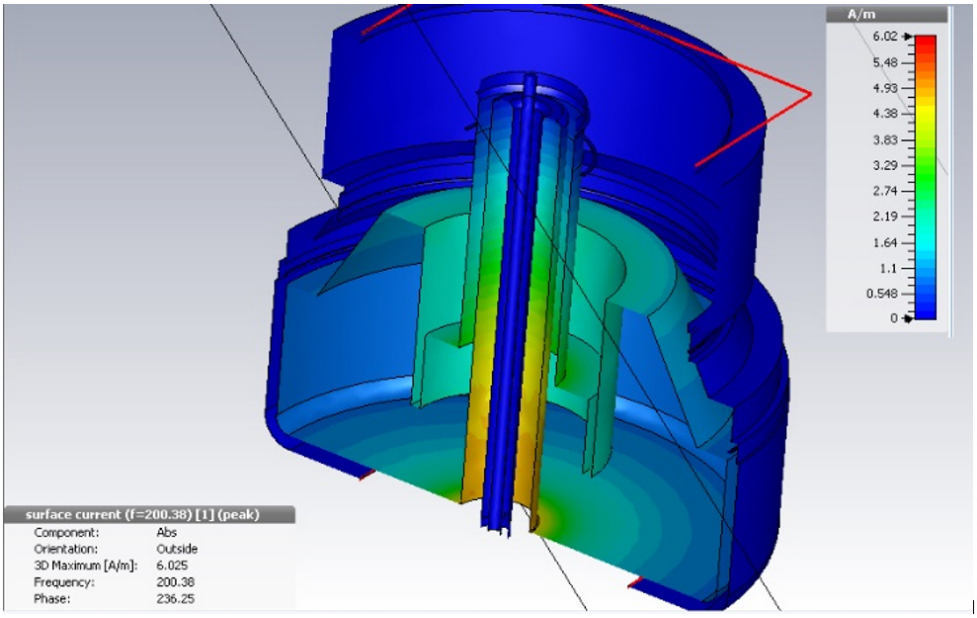

Figure 6.181: Simulation of the fundamental mode surface currents on the 197 MHz notch filter structure of the HOM coupler.

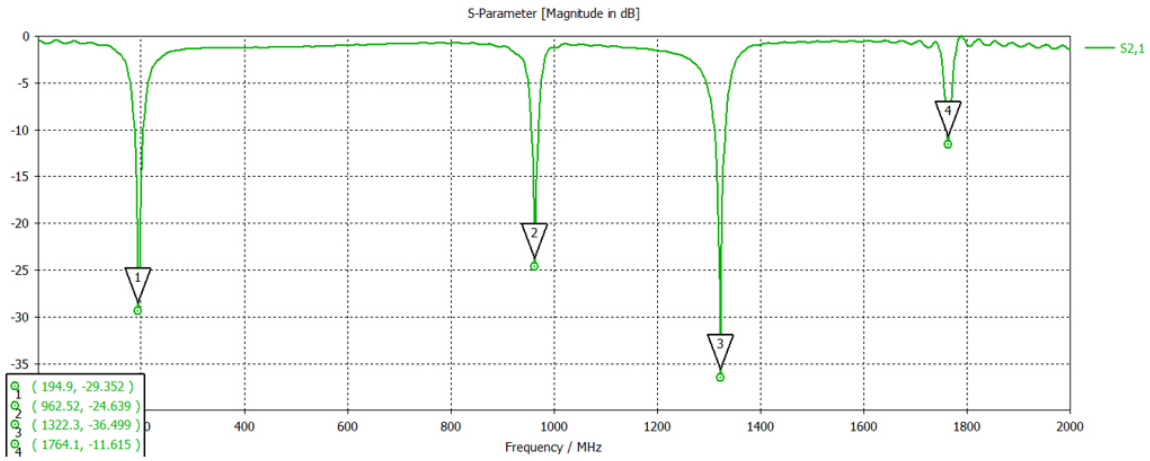

Figure 6.182: S21 plot of the 197 MHz notch filter structure of the HOM coupler.

Hadron Bunch Splitter Cavities

In order to achieve design luminosity in the EIC the stored 290 bunches need to be split two times into 580 and finally 1160 bunches. 49.2 MHz and 98 MHz cavities are selected to perform this RF gymnastic together with the 24.6 MHz system that provides initial RF buckets.

Requirements: Performance requirements and RF cavity geometric boundaries are shown in Table 6.73.

Table 6.73: Requirements and and geometric limitations for the 49.2 MHz and 98.5 MHz RF cavities.

Parameter	49.2 MHz Cavity (h = 630)	98.5 MHz Cavity (h = 1260)
Frequency [MHz]	49.2	98.5
Voltage [kV]	300	350
Tuning Range [kHz]	10.7	18.3
OD [mm]	< 800	< 800
Length [mm]	< 2000	< 2000
Peak HOM power [kW]	< 20	< 20

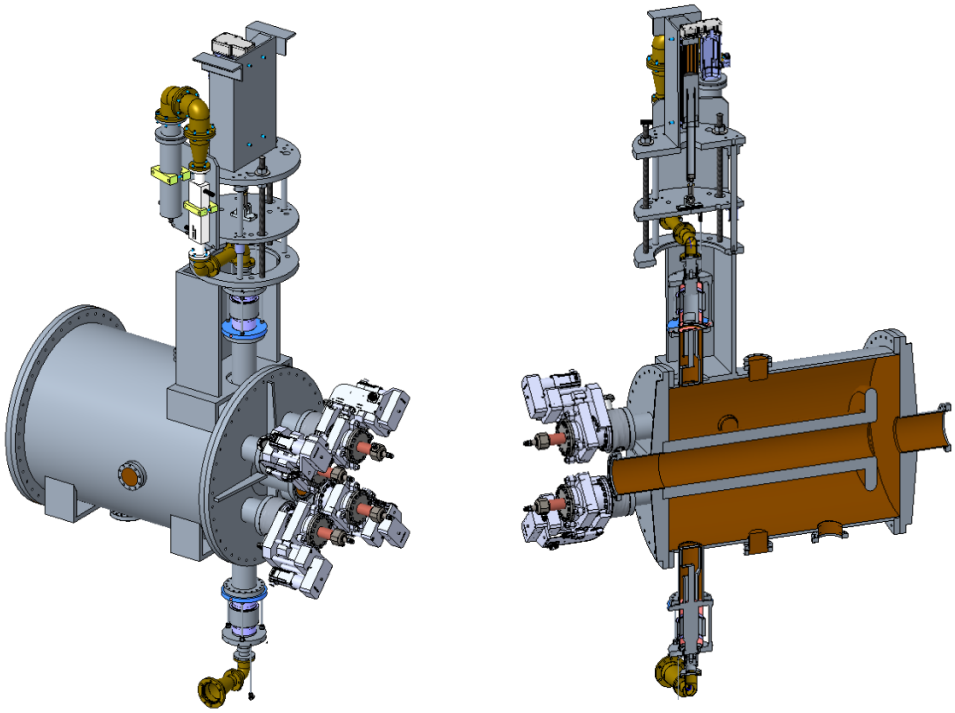

Figure 6.183: The conceptual design view of 49.2 MHz splitter cavity. The 98.5 MHz cavity will be a direct scale from the 49.2 MHz cavity.

Cavity Design: The relatively low frequencies of the cavities calls for a quarter wave resonator (QWR) geometry in order to keep the diameter of the cavities within the requirements. Although the QWR cavity has lower R/Q ($\simeq 100\,\Omega$) compared to cavities morphed from a pillbox shape ($> 200\,\Omega$), the extra power requirement can be tolerated because of the relatively low voltage of the cavity. In order to keep the cavity length below budget, we adopted the capacitor disk design from the MAX IV, 100 MHz cavity [324]. At the tip of the center conductor there is a disk that provides the extra capacitance needed to compensate the reduced inductance due to the decreased length of the cavity. Figure 6.183 shows a conceptual design view of the 49.2 MHz cavity. The design parameters of 49.2 MHz and 98.5 MHz cavities are shown in Table 6.74.

Table 6.74: Design parameters of the 49.2 MHz and 98.5 MHz cavities.

Parameter	49.2 MHz Cavity	98.5 MHz Cavity
Diameter [mm]	800	400
Length [mm]	1600	800
Gap [mm]	117	58.5
Beampipe radius [mm]	85	42.5
Thickness of nose cone [mm]	55.8	27.9
Radius of capacitor disk [mm]	253.2	126.6
Thickness of capacitor disk [mm]	50	25
Radius of corner blending [mm]	10	5
Frequency [MHz]	49.2	98.5
R/Q [Acc. Def.]	130.7	130.7
E_{acc} [MV/m]	2.6 @ 300 kV	6.0 @ 350 kV
E_{max} [MV/m]	4.5 @ 300 kV	10.4 @ 350 kV
Q_0	1.9×10^4	1.36×10^4
R_{sh} [Ω]	2.48×10^6	1.77×10^6
RF power loss [kW]	36 @ 300 kV	70 @ 350 kV

FPC Design: The position of the fundamental power coupler was chosen to cause the least perturbation to the frequency of the cavity since it will need to move during operation. The FPC design was adopted from the fundamental damper for current BNL 56 MHz SRF cavity [325]. The copper loop is cooled by water running through the center conductor and the FPC will be able to handle the 40 kW without issues based on previous experience. As for the window and feedthrough the existing design for the 56 MHz SRF cavities will be used with very little modification.

HOM Power Considerations: For the HOM power estimation mainly the monopole and dipole components were considered. To get the total impedance spectrum, the following formula was used to calculate the impedance of each mode:

$$Z_n \leq Q_{L,n} \times \left((\frac{R}{Q})_{T,n} (\frac{\omega}{c} r)^2 + (\frac{R}{Q})_{L,n} + 2(\frac{\omega_n}{c} r) \sqrt{(\frac{R}{Q})_{T,n} (\frac{R}{Q})_{L,n}} \right) \tag{6.20}$$

Where $Q_{L,n}$ is the loaded Q, $(\frac{R}{Q})_{T,n} = (\frac{R}{Q})_{x,n} + (\frac{R}{Q})_{y,n}$ is the transverse R/Q, $(\frac{R}{Q})_{L,n}$ is the longitudinal R/Q, ω_n is the resonance frequency of nth mode, respectively and r is the assumed offset of the beam.

The HOM power estimation is the worst-case scenario, namely all HOM peaks aligned resonantly with the closest peak in beam spectrum within $\pm 0.5\%$ range. For all scenarios considered, the HOM powers are well under the 20 kW threshold.

The HOM power is calculated by multiplying the square of the beam current spectrum with the real part of the impedance spectrum of the cavity. The worst-case scenario is considered by scanning the position of the peaks in the impedance spectrum ($\pm 0.5\%$) to find the maximum possible overlap between two spectra. Five different scenarios were considered that are shown in Table 6.75. The case that gives the most HOM power is case number 2.

Table 6.75: Different beam pattern scenarios.

Case	1	2	3	4	5
Bunch numbers	290	1160	1160	1160	1160
Bunch Length (sigma z) [cm]	5	5	7	7	7.5
Bunch Charge [C]	29	11	11	7.5	1.8
Average Current [A]	0.66	1	1	0.68	0.16
Gamma	293	293	107	107	43.7

The cavity impedance spectrum (with HOM couplers), beam spectrum and HOM power spectrum are shown in Figure 6.184. The total HOM power is less than 7 kW. There are two relatively dangerous modes, at 396 MHz and 789 MHz. Between those two modes the 396 MHz one is more dangerous since it is closer to a harmonic of the bunch spectrum, 450 kHz away for the 396 MHz mode vs 2.5 MHz away for the 789 MHz mode.

The same considerations are taken for the 98.5 MHz splitter cavity. The cavity impedance spectrum, beam spectrum and HOM power spectrum are shown in Figure 6.185.

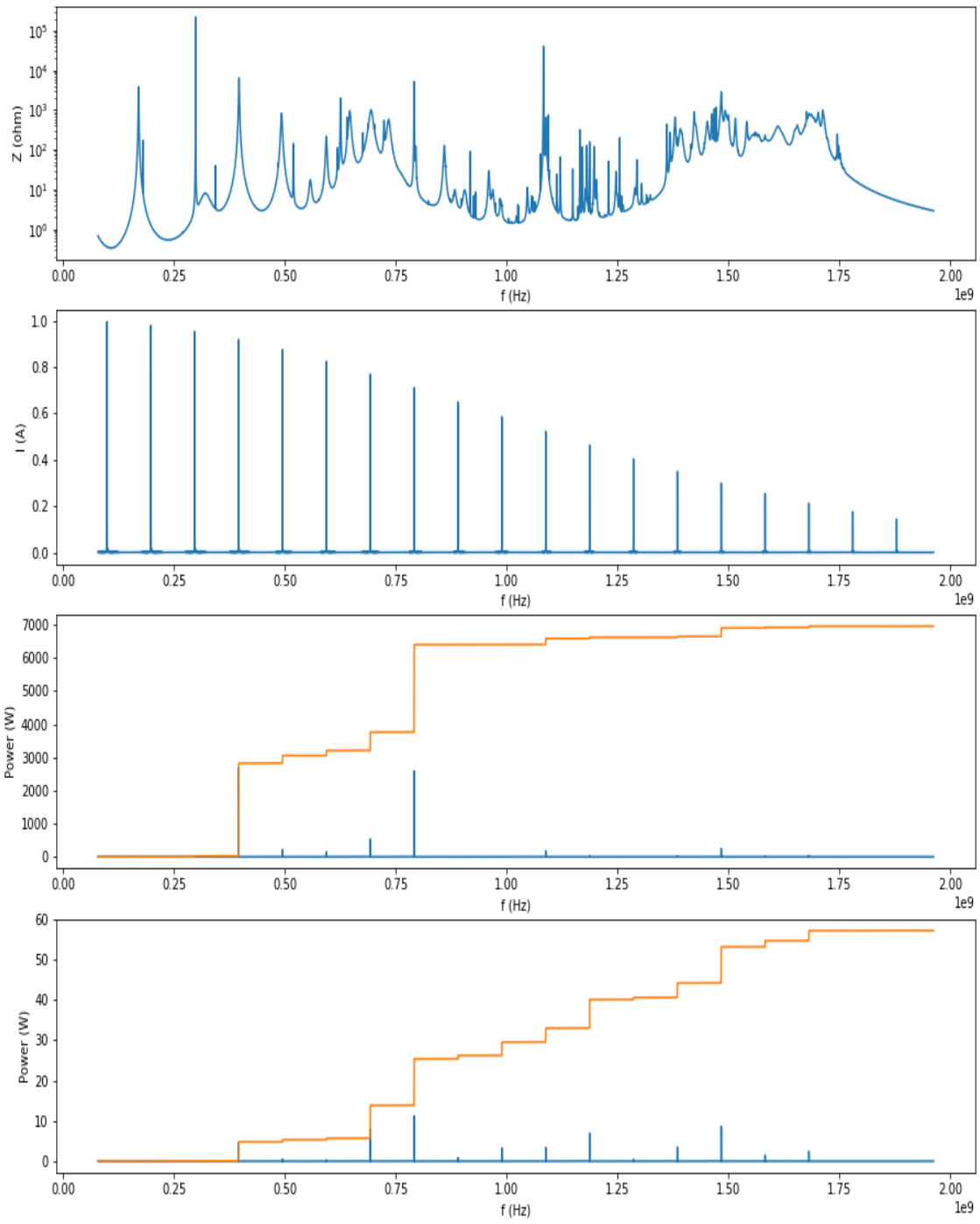

Figure 6.184: Cavity impedance, beam current spectrum and integrated HOM power of 49.2 MHz splitter cavity. Top: 49.2 MHz cavity impedance spectrum, Mid top: Beam current spectrum, Mid Bottom: HOM power spectrum and integrated HOM power, Bottom: HOM power due to the offset of bunch by 5 mm.

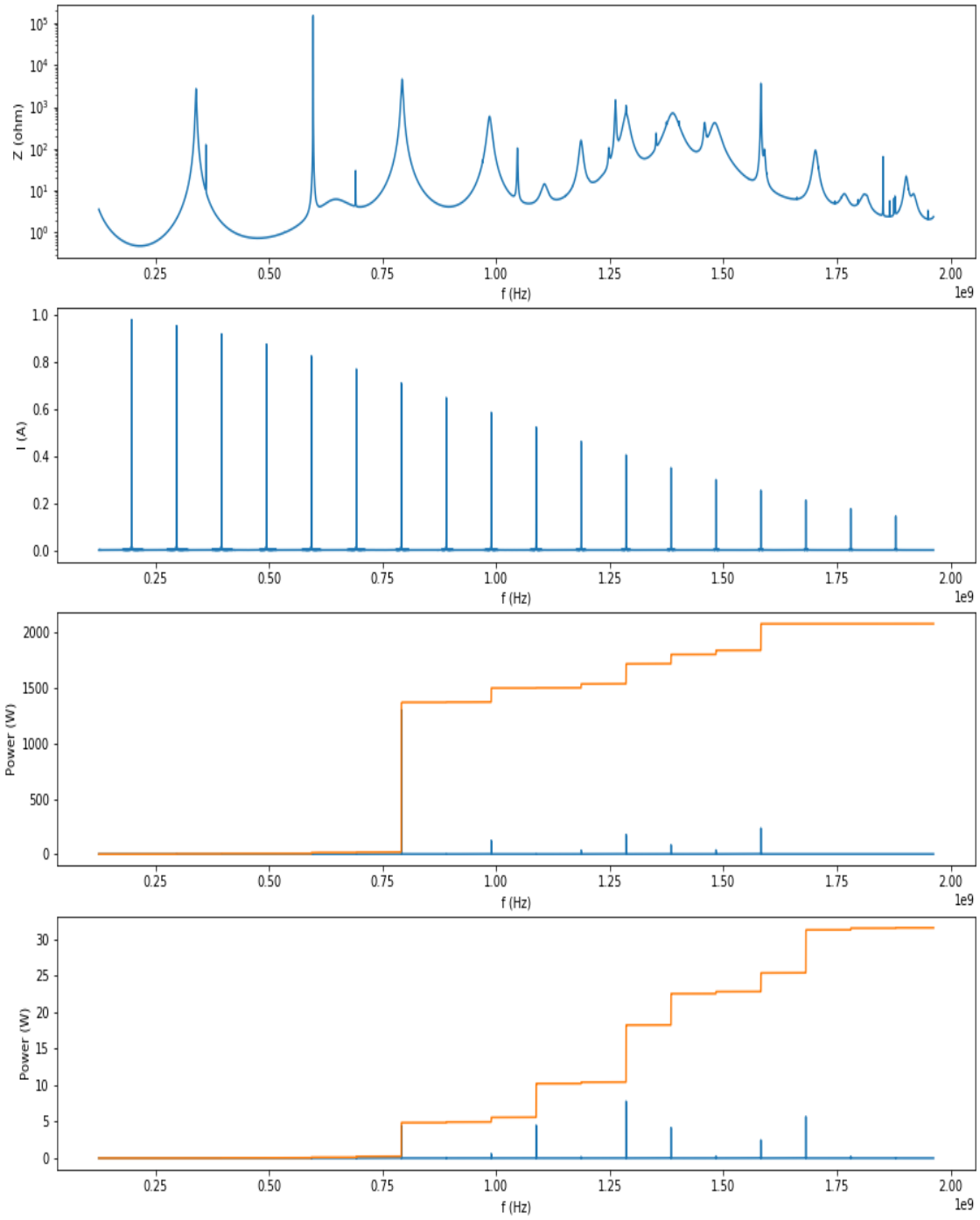

Figure 6.185: Cavity impedance, beam current spectrum and integrated HOM power of 98.5 MHz splitter cavity. Top: 98.5 MHz cavity impedance spectrum, Mid top: Beam current spectrum, Mid Bottom: HOM power spectrum and integrated HOM power, Bottom: HOM power due to the offset of bunch by 5 mm.

Tuner Design: The frequency of the fundamental mode must be tuned away from the repetition frequency of the bunch to compensate the active beam loading. Define the detuning as $\delta = \frac{\omega - \omega_c}{\omega_c}$ and $\tan\psi = -2Q_L\delta$. Then we have:

$$\tan\psi = \frac{I_{\mathrm{RF}} R_{\mathrm{sh}}}{V_c(1+\beta)} = \frac{2 \times 1.26 \times 10^6}{3 \times 10^5 \times 2} = 4 \tag{6.21}$$

Where $I_{\mathrm{RF}} = 2\,\mathrm{A}$ is the beam current at RF frequency, $R_{\mathrm{sh}} = 1.26 \times 10^6\,\Omega$ is the circuit definition shunt impedance of the fundamental mode of the 49.2 MHz cavity and β is the coupling factor, which is 1 since there is no real beam loading. Therefore the detuning of the 49.2 MHz cavity in terms of frequency is:

$$\Delta f \approx 10.4\,\mathrm{kHz}. \tag{6.22}$$

The fundamental tuners for the cavity conceptual design have an estimated tuning range of more than 70 kHz, which is more than enough to cover the detuning requirement from beam loading.

The 98.5 MHz cavity fundamental mode also needs to be detuned to compensate for beam loading. In this case, the calculation is exactly the same as the 49.2 MHz case. For the 98.5 MHz cavity the shunt impedance is

$$R_{\mathrm{sh}_{98}} = \frac{R_{\mathrm{sh}_{49}}}{\sqrt{2}}, V_c = 350\,\mathrm{kV}. \tag{6.23}$$

Hence the detuning tangent of 98.5 MHz cavity is

$$\tan\psi_{98} \approx 2.5 \tag{6.24}$$

and in terms of frequency the detuning is

$$\Delta f_{98} \approx 18.2\,\mathrm{kHz}. \tag{6.25}$$

Again, the tuner for the 98.5 MHz cavity can tune the fundamental mode by about 140 kHz which is more than enough to cover the range of detuning required by beam loading compensation.

Hadron Bunch Store 2 RF System

To achieve the shortest hadron bunch lengths required, RCS type 5-cell 591 MHz SRF cryomodules (Section 6.5.3) will be used to provide up to 20 MV total voltage. One single-cavity cryomodules will be needed,operating at up to 20 MV, or a 15.8 MV/m gradient in CW mode.

The highest HOM power generation occurs for the case: 290 bunches, 0.74 A and 6 cm rms bunch length. The HOM spectrum and HOM power for the highest HOM power case is

shown in Figure 6.186 and Figure 6.187. The HOM power can be up to 1.75 kW per cavity. Note that the HOM power calculation assumes the most pessimistic scenario, calculating the highest HOM power by scanning each HOM frequency in the range of ±0.1% of resonant frequency to locate the maximum local beam current spectral component. This HOM power can be easily dissipated in the SiC absorbers.

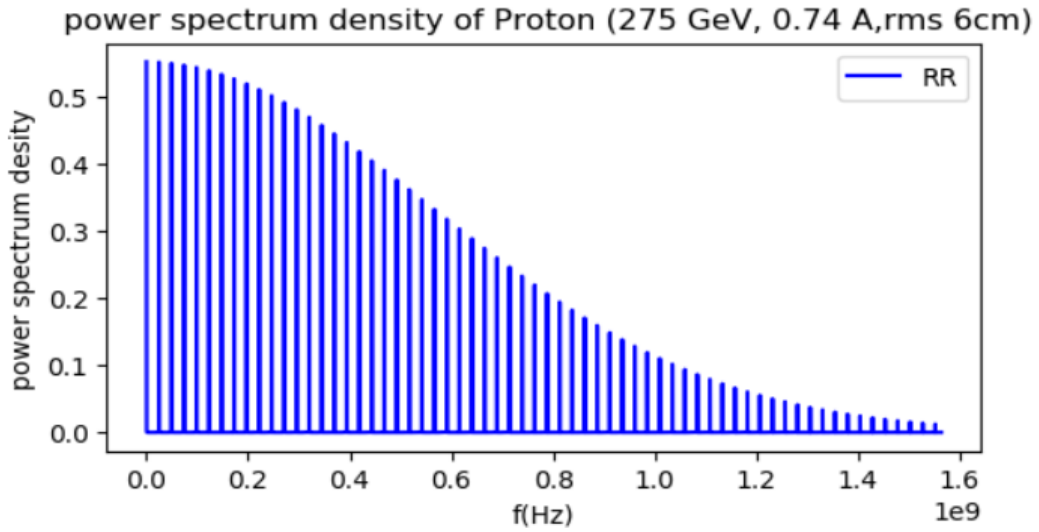

Figure 6.186: Bunch spectrum for highest HOM power case in 591 MHz hadron high frequency storage cavity.

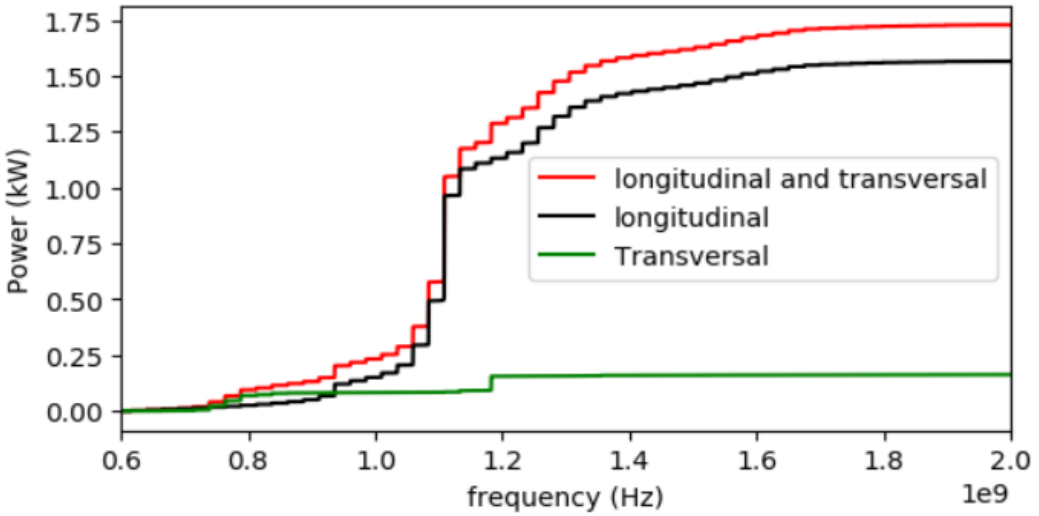

Figure 6.187: Highest HOM power 5-cell 591 MHz hadron storage cavity. Note: beam offset 1 cm for transversal calculation. (±0.1% case).

6.5.5 Crab Cavity RF System Design

Crab Cavity Design Requirements

Based on beam-beam simulations, there are three possible operation scenarios under consideration, hereafter summarized quoting the necessary total crabbing voltage per IP per side: 1, 24 MV deflecting voltage from 197 MHz crab cavity for HSR, and 2.9M V deflecting voltage from 394 MHz crab cavity for ESR. This is the baseline. 2, 33.83M V deflecting voltage from 197 MHz crab cavity, and -4.75 MV from 394 MHz crab cavity for HSR, and 2.9 MV deflecting voltage from 394 MHz crab cavity for ESR. 3, increase the voltages by a factor of 20%.

To meet the requirement, we consider to put two 197 MHz crab cavities in one 197 cryomodule, and put one 394 MHz crab cavity in one 394 cryomodule. For HSR, two 197 cryomodules and two 394 cryomodules are used per IP per side; for ESR, one 394 cryomodule is used per IP per side, with ESR and HSR 394 MHz cryomodules identical.

The design goal is set at 11.5 MV nominal deflecting voltage for the 197 MHz crab cavities, and 3.5 MV nominal deflecting voltage for the 394 MHz crab cavities, with peak electric field $\leq$45 MV/m, and peak magnetic field $\leq$80 mT for all Nb components, the lower the better. During operation, each 197 MHz crab cavity for HSR provides 8.5 MV deflecting voltage, each 394 MHz crab cavity for HSR provides 2.4 MV, and each 394 MHz crab cavity for ESR provides 2.9 MV.

The requirement for aperture is 10 sigma on each side of the beam axis for HSR, corresponding to 10 cm diameter, and 15 sigma for ESR, corresponding to 5.7 cm diameter. Since the same 394 MHz cavity design is used in ESR and HSR, the cavity aperture should be $\geq$10 cm in diameter for both 197 MHz and 394 MHz crab cavities. For simulations, 0.6 mm beam offset is used for the HSR crabbing system, and 0.25 mm is used for the ESR, both numbers contain a safety factor of 2.

The longitudinal space reserved for the crab cavities is 15 m in the HSR, at each side of the IPs, and 4 m in the ESR. Further reducing the crab cavity cryomodule assembly for HSR from 15 m to 12 m is under consideration to provide more space between crab cavities and the next dipole so that chromaticity can be reduced.

During the design of 197 MHz crab cavity, cavity length is limited to 1.5 m, the shorter the better due to limited longitudinal space. A bare cavity equipped with its higher order mode (HOM) dampers and necessary stiffener, without helium vessel, should be able to be fitted into the BNL large vertical test facility, with a diameter constraint of 90 cm.

The fundamental power coupler (FPC) external quality factor (Qext) of 197 MHz crab cavity is set at 3×10^6, with 50 kW power considering 0.6 mm offset and 50 Hz detuning. 70 kW amplifier should be used, and RF window should be able to handle 60 kW power.

The longitudinal and transverse impedance budget (circuit definition) for crab cavities are listed in Table 6.76. HOMs up to 2 GHz should be considered for both 197 MHz and 394 MHz crab cavities. Comparing with the LHC impedance budget requirement, the

longitudinal impedance budget for EIC 197 MHz crab cavity is much tighter. The LHC DQW or RFD HOM damper designs cannot be directly adopted to EIC crab cavities. Our impedance budget is set under the assumption that, at least for those modes with high impedance, the HOMs of all cavities in a ring (either ESR or HSR) do not overlap. This assumption needs to be validated, for all the components in the ESR and the HSR and both broad band and narrow band resonances, after the cavity designs are finalized.

Table 6.76: Impedance budget (in circuit definition) for crab cavities.

HSR	Longitudinal [kΩ]	Transverse [MΩ/m]	Qty of Cavities [a]
per ring	30	10.8	
per 197MHz cavity	3.75	1.35	8
per 394MHz cavity	7.5	2.7	4
ESR	Longitudinal [kΩ-GHz]	Transverse [MΩ/m]	Qty of Cavities [a]
per ring	26	12	
per 394MHz cavity	13	6	2

[a] per ring, considering 1 IP only

Cavities will be made of niobium (Nb), with yield strength at 75 MPa at room temperature. A safety factor of 2/3 should be included in mechanical analysis. The pressure relief valve should be set at 2.2 atmosphere for cryomodules, and for vertical test, it should be lower.

During the energy ramp up of HSR, a combination of tuner and fundamental mode damper (FMD) should be used to avoid beam instability. Beam dynamics simulations are needed to specify these requirements. Currently, the preliminary requirements are $\geq$0.8 MHz tuning range and $\leq$1000 FMD Qext for 197 MHz crab cavity, and $\geq$1.6 MHz tuning range and $\leq$1000 FMD Qext for 394 MHz crab cavity.

The total static and dynamic heat load from all crab cavities should be $\leq$280 W at 2 K operation temperature, based on the input from cryogenic group. The field/power limit of some boundaries are listed in Table 6.77.

Currently, two designs, DQW from BNL and RFD from ODU/JLab are under consideration for 197 MHz crab cavity. In below, both designs are introduced. A final selection will be made and only one design will be prototyped. For 394 MHz crab cavity, the baseline is to scale the 197 MHz design to 394 MHz while keeping the beampipe size the same at 100 mm. This task will start soon after the final selection of 197 MHz design, and it is not included here. We introduce a backup plan that using wide open waveguide (WOW) type [326,327] RFD so that both longitudinal and transverse impedances can be well within the impedance budgets.

Table 6.77: Field or power limit of boundaries.

Location	Limit [a]	Min. Length [m] [b]	Reserve [c]
Cavity helium vessel joint	8 mT	0.674	0.640
Indium seal [d]	2.5 mT	0.948	0.785
Cu gasket [e]	220 A/m	1.469	1.250
Waveguide absorber [f]	10 W	2.000	2.800

[a] Field or power upper limit
[b] Minimum length for DQW. Large HOM waveguide starts from the center of the cavity.
[c] Reserved for RFD
[d] Indium seal for Nb to Nb connection
[e] Cu gasket for Nb to Cu connection
[f] Fundamental power dissipation on rectangular waveguide absorber.

Specifications of key parameters of 197 MHz crab cavity are listed in Table 6.78.

Table 6.78: Key parameters of 197MHz crab cavities.

Property	Specs	DQW	RFD
f0 [MHz]	197.0	197.0	197.0
1st HOM [MHz]		304.2	345.9
Geometry factor [Ω]		68.2	99.0
R/Q [Ω, acc. def.]		1159.7	1148.0
Vt [MV]	11.5	11.5	11.5
Ep [MV/m]	$\leq$45	44.8	44.0
Bp [mT]	$\leq$80	69.5	78.0
Cavity length [mm]	$\leq$1500	821.8	941.0
Cavity height [mm]	<900 ID	452.5	587.0
Cavity width [mm]		584.4	587.0
Tuning range [MHz]	$\geq$0.8	0.8TBD	$\pm$1.3
FPC Qext	3×10^6	3×10^6	3×10^6

197 MHz Double Quarter Wave Crab Cavity

Quarter-Wave Resonators (QWRs) are widely used in accelerators since the concept was first invented by Ben-Zvi and Brennan in 1983 [328]. The QWRs are mainly used as accelerating and storage cavities in various facilities [329–333]. This unique structure, adopted

from coaxial cables, has successfully compiled the electromagnetic field into a one quarter wave length long dimension, which allows it to provide linear high gradient RF field for long bunches within a compact size. Recently QWR structures have been proposed to be used as crab cavities for LHC [334–337]. To mitigate the residual accelerating voltage, the design evolved into a DQW structure with large capacitive center plates providing electrical field for particle deflection. The geometry of a DQW, as well as the EM field in it, is shown in Figure 6.188. The DQW crab cavity design inherited the outstanding features of the QWRs. A 400 MHz DQW was designed for the LHC with a narrowed waist to meet the spacial limit between the existing beam pipes. This design naturally provides vertical deflection with an FPC and all three HOM couplers mounting in the vertical plane, as shown in the left of Figure 6.189. There is no lower order mode or same order mode. The deflecting mode is the fundamental mode of the cavity (the fundamental mode is by definition the lowest frequency mode), while the first HOM has a large separation of more than 150 MHz. Such characteristics simplify the HOM damping to focus on only a Chebyshev high-pass filter, as shown in the right of Figure 6.189 [338]. The HOM filter, consists of a band stop LC structure right above the hook to minimize the RF losses on the Cu gasket that will be used to connect the cavity and the filter, and an L shape structure on the top to form a pass band starting from 570 MHz, the frequency of the first HOM. It provides rejection to the fundamental mode field, while allowing all the HOMs to travel to the outside load. The S21 of this design has a TE11 mode on the hook side and a TEM mode on the port side. The rejection at 400 MHz shows a 34 MHz stop band with S21 $<$ -90 dB, and the rejection for the first HOM at 570 MHz is only -2 dB. There are three HOM filters in each cavity, with one on the FPC side with the pickup port along the beam pipe direction and the other two on the opposite side with the pickup port 60 degrees away from the beam pipe port. This symmetric design is adopted to lower the multipolar components of the fundamental mode field.

While the DQW provides a vertical crabbing kick to the LHC bunches, all EIC DQW crab cavities will be rotated by 90 degrees to provide a horizontal crabbing kick. A first optimization of the EIC 197 MHz DQW cavity focused on maximizing the deflecting voltage V_t while minimizing the magnetic and electric peak surface fields, respectively, E_p and H_p. The cavity is elongated along beampipe direction with an ovaloid profile to maximize V_t. A small angle in the inner conductor wall allowed minimizing H_p further. A sufficiently large radius to blend the capacitive plate edges helped reaching larger V_t/E_p ratio. The corners of the cavity were also rounded to further reduce peak fields. The geometry of the bare DQW cavity is shown in Figure 6.190. Table 6.78 shows the key parameters of 197 MHz DQW.

Due to the tight impedance budget, especially longitudinally, the EIC DQW HOM damper differs from LHC DQW design. Figure 6.191 shows the EIC DQW design with HOM dampers, FPC, FMD and pickup coupler (PU). To damp the first HOM at 304.2 MHz, a large ($>$500mm rectangular width) vertical HOM port is needed, we choose 530 mm $\times$ 75 mm rectangle. 75 mm is chosen to provide enough damping, as well as to suppress the multipacting in this port. To ease the fabrication, this HOM port is designed to replace the cone area of the bare cavity. To keep the symmetry, on the other side of the cavity, the cone area is also replaced by such a large rectangle, with the difference that instead of the HOM

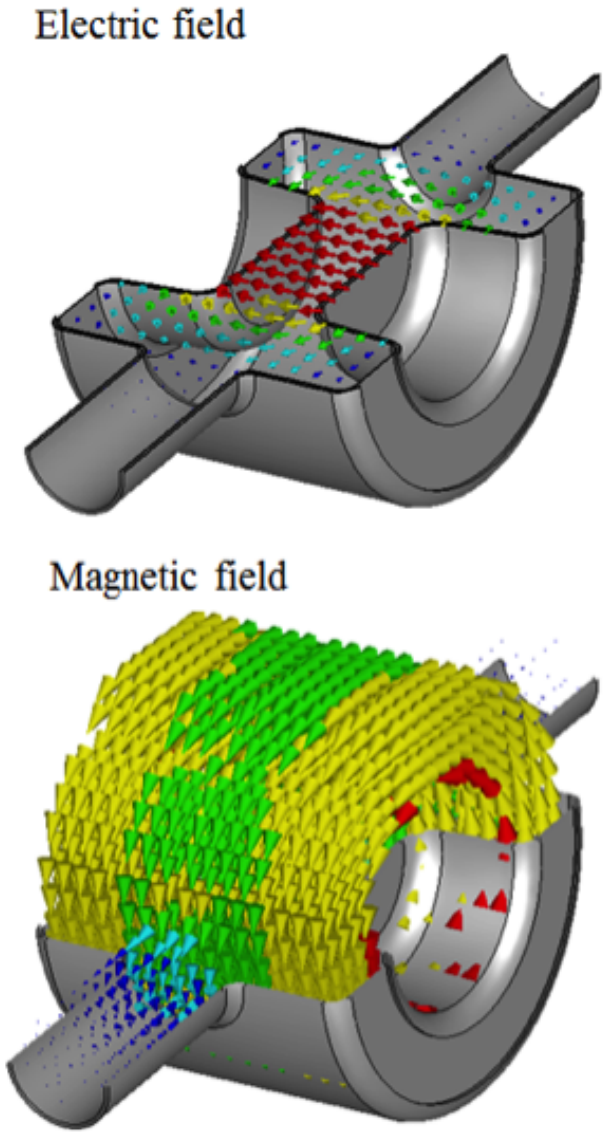

Figure 6.188: Field distribution in a DQW crab cavity without coupler ports.

port, this rectangle is shorted. Two 75 mm ID ports perpendicular to the rectangles are opened, with the one on the HOM port side act as the FPC, and the other one as the FMD. The FPC inner conductor is a 32.6 mm diameter Cu rod, with its tip 75 mm away from the Nb. The FMD inner conductor is a 32.6 mm diameter Nb rod, with its tip 2 mm away from the Nb that provides ∼1000 Qext during HSR energy ramp up, while during normal operation, it will be pulled out of the cavity. The large vertical HOM waveguide damper is used to damp both longitudinal and horizontal modes, and the smaller horizontal waveguide, 240 mm × 50 mm rectangle to coax damper is used to damp both longitudinal and vertical modes. A coaxial PU is designed on the beampipe to provide ∼1 W fundamental mode power at nominal deflecting voltage.

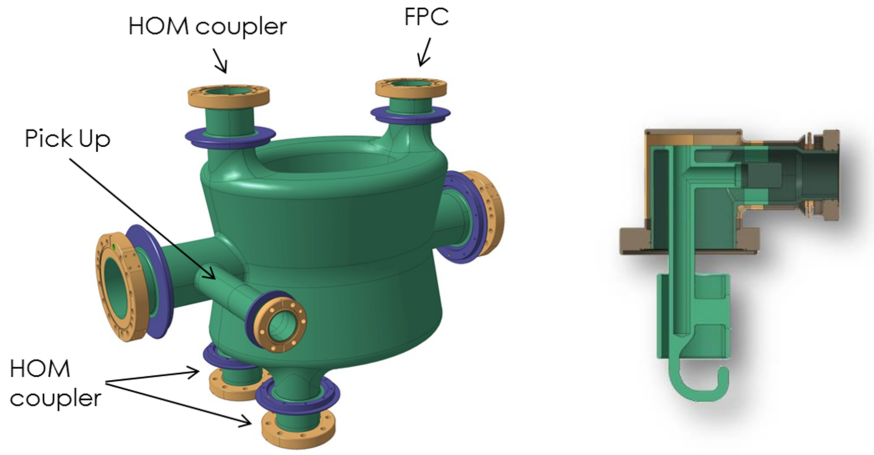

Figure 6.189: Left: LHC DQWCC for vertical crabbing at IP 1. Right: HOM coupler with band-pass filter for LHC DQWCC.

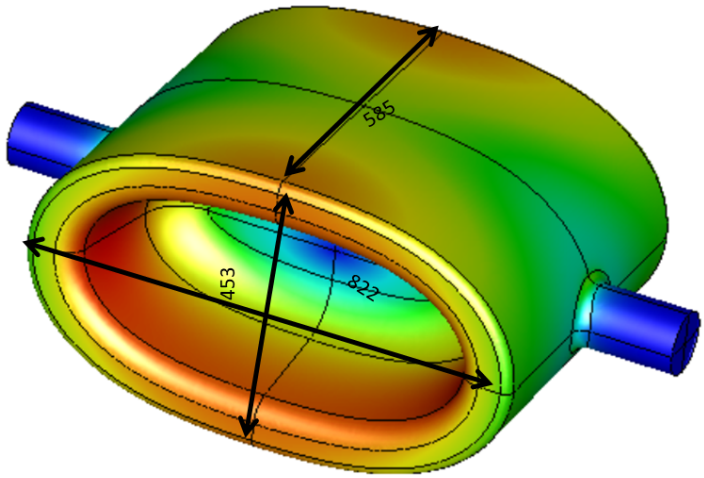

Figure 6.190: EIC DQW bare cavity.

FPC and amplifier The forward power required to reach a crabbing voltage V_t in an SRF deflecting cavity with geometric shunt impedance $(R/Q)_\perp$ and operating at a resonant frequency ω is:

$$P_g = \frac{1}{4(R/Q)_\perp Q_{ext}} \left[V_\perp + y I_b \frac{\omega}{c} (R/Q)_\perp Q_{ext} \right]^2 \tag{6.26}$$

where Q_{ext} is the external Q of the input coupler, I_b is the beam current and y is the beam offset. In a superconducting RF cavity like the EIC crab cavities, the intrinsic Q of the cavity is much larger than the external Q of the Fundamental Power Coupler (FPC), Q_{ext}.

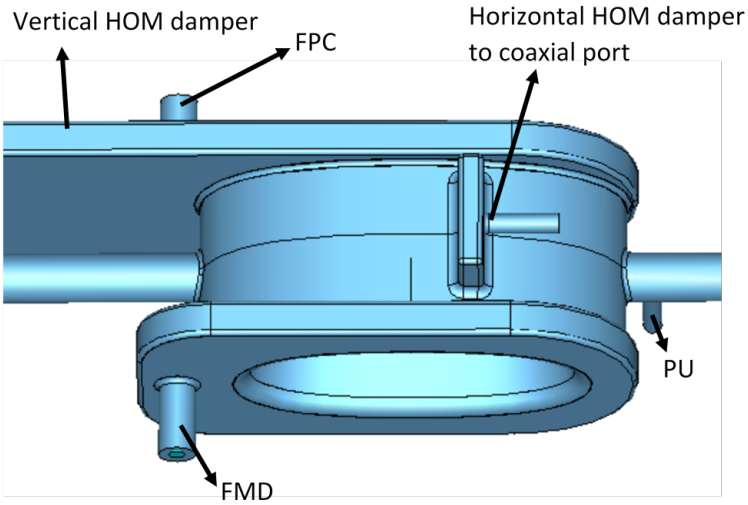

Figure 6.191: EIC 197 MHz DQW cavity with HOM dampers, FPC, FMD and PU.

Therefore the loaded Q of the cavity is dominated by the FPC and $Q_L \sim Q_{ext}$. The highest power demand in the crab cavity system comes when operating with the high-energy, high-current proton beam of the EIC ($E_0 = 275$ GeV, $I_{ave} = 0.74$ A) considering a nominal deflecting kick of 11.5 MV provided by each 197 MHz DQW cavity. The RF power requirement of different loaded Q at different beam offset (top), and at different detuning frequency (bottom) are shown in Figure 6.192. With the FPC loaded Q set at 3×10^6, 10 kW power is needed with beam on-axis and 0 Hz detuning. An additional 15 kW is needed for 0.5 mm offset, and an additional 23 kW is needed for 50 Hz detuning frequency. Each cavity will be powered by its own 70 kW RF amplifier: a tetrode or solid-state amplifier. About 20% of the forward power will be lost in the line connecting the amplifier and the coupler [339]. Effectively, only 56 kW of the forward power provided by the amplifier will be available to feed the cavity, and the FPC RF window should be conditioned to 60 kW. Each EIC crab cavity will be equipped with a single FPC, shown in Figure 6.191. With an external Q of 3×10^6, the FPC dissipates about 100 W when providing the necessary RF power to deliver a 11.5 MV deflecting kick.

HOM impedance and HOM power The EIC 197 MHz DQW crab cavity HOM impedances of all modes up to 2 GHz are shown in Figure 6.193, with the top longitudinal impedances, and the bottom transverse impedances. The solid lines are the impedance budgets shown in Table 6.76. The highest longitudinal impedance is 1.62 kΩ with 105 loaded Q at 0.742 GHz, the highest transverse impedance is 0.22 MΩ/m with 1985 loaded Q at 0.360 GHz, both in circuit definition. The impedance spectrum of this cavity occupies less than 50% of the impedance budget, meaning that in case two IPs are needed for EIC, and assuming the crab cavities will be identical in these two IPs thus the impedance budgets are only 50% of the current values, DQW design can still meet the impedance budgets. For the HOM power calculation, 10 mm off center is used to ensure HOM power from

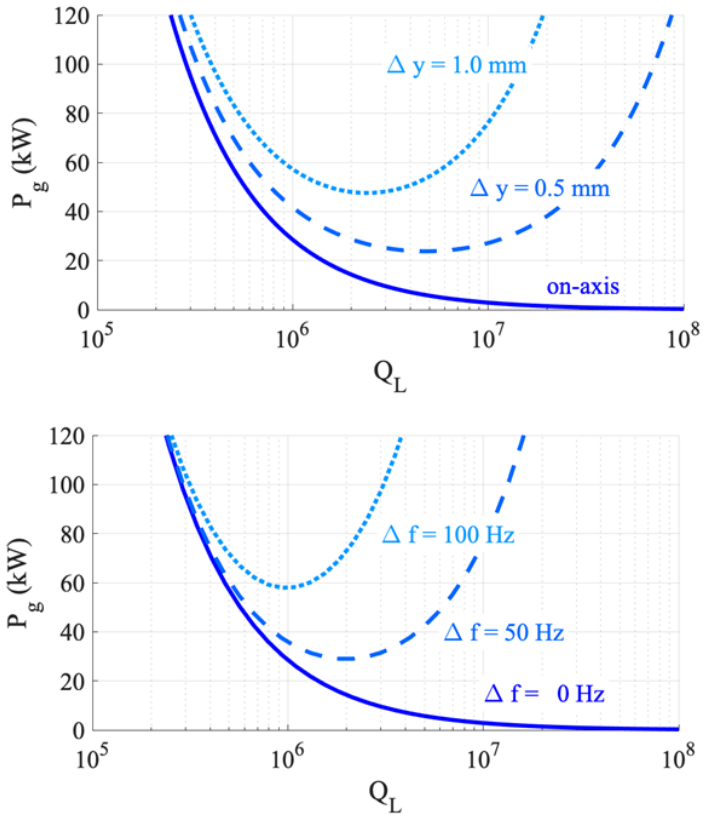

Figure 6.192: Forward power (P_g) required by a 197 MHz DQW crab cavity with $(R/Q)_\perp$ = 1160 Ω to deliver a crabbing kick of 11.5 MV to the high-energy, high-current proton beam of the EIC ($E_0 = 275$ GeV, $I_{ave} = 0.74$ A).

transverse modes are is not under estimated. The frequencies of HOMs are shifted within ±0.2%, and cancellation due to phase difference between different HOMs is not taken into account. All these ensured the worst case scenario estimation. The 290 bunches with 6 cm bunch length and 0.74 A current case produces the highest HOM power at 3.2 kW, with 86% from the longitudinal modes.

Fabrication plan Figure 6.194 shows the fabrication and welding plan for 197 MHz DQW cavity. The fabrication plan is straight forward and all welds are on the line of sight with maximum electron gun-to-work distance at 600 mm. Based on previous welding experience, this is not an issue. Final trimming for frequency adjusting before the last welding is not difficult in this design. Depending on the welding procedure, one could choose one of the following parts for final trimming: the height of the HOM waveguide, the height of the cavity outer wall, or the wall connected to the capacitive plates. Due to the large tuning range, it is possible that the final trimming might not be needed.

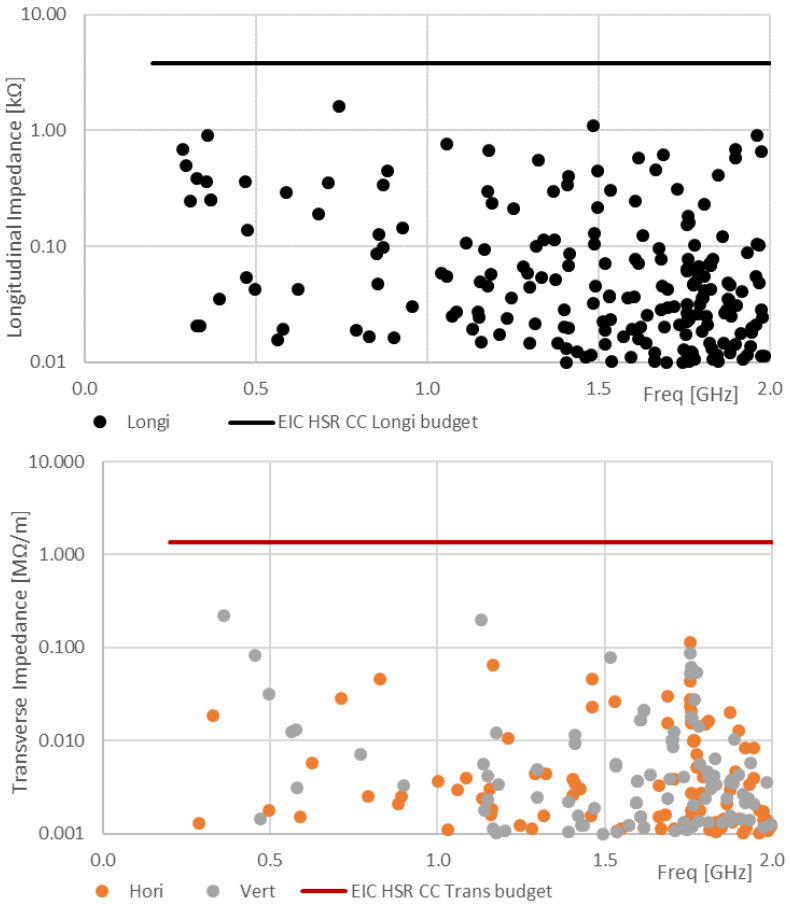

Figure 6.193: EIC 197MHz DQW cavity HOM impedances.

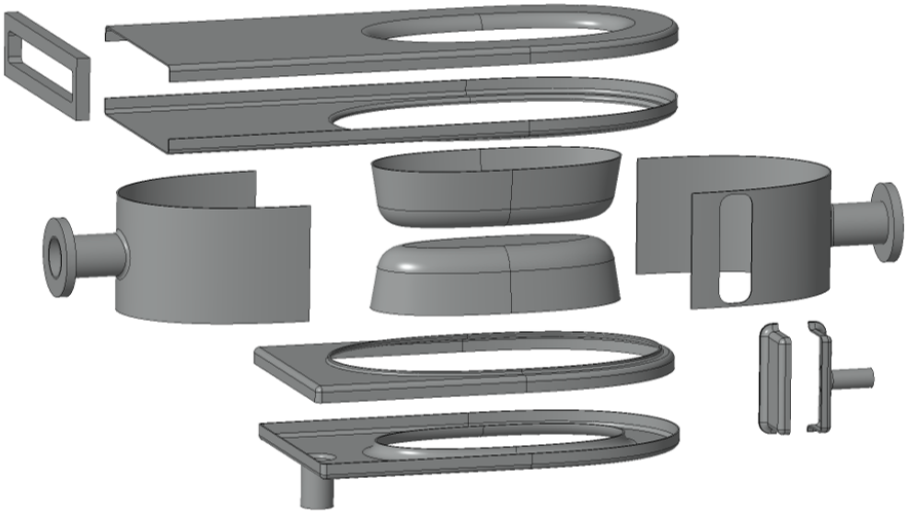

Figure 6.194: The fabrication and welding plan for 197 MHz DQW cavity.

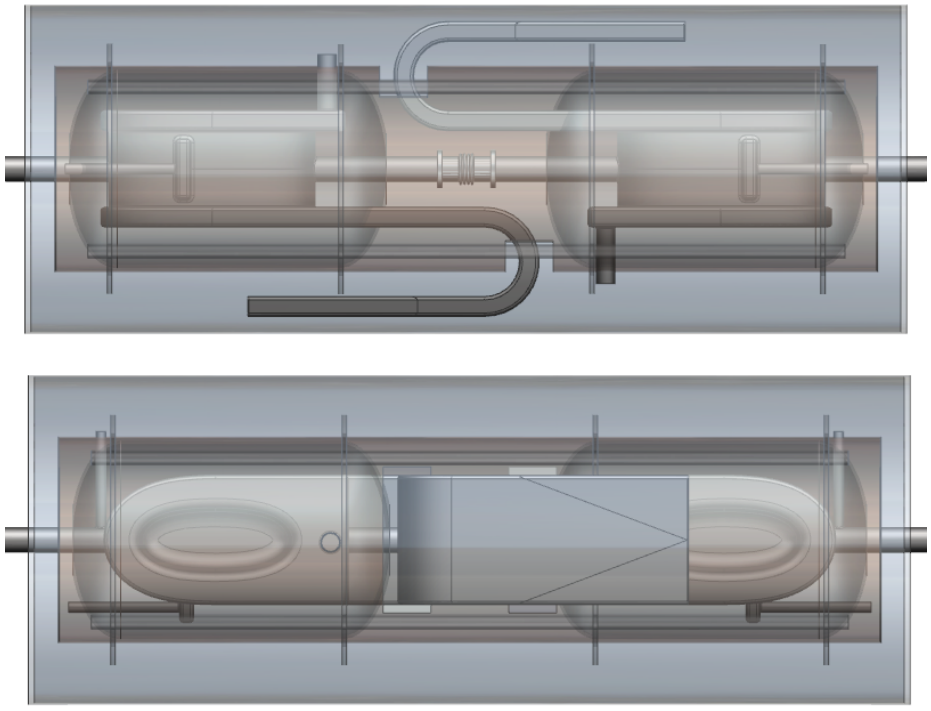

Figure 6.195: Conceptual design of EIC 197 MHz DQW cavity with helium vessel and cryomodule, top: top view; bottom: side view.

Cryomodule Helium vessel and cryomodule similar to ESR 591 MHz cavity can be used for EIC 197 MHz DQW cavity, a conceptual design is shown in Figure 6.195, with the top plot top view and bottom plot side view. The length of this cryomodule is 3.92 m flange to flange, with 2 cavities in 1 cryomodule. In Table 6.77, we listed the minimum distances of the large HOM waveguide starting from the center of the cavity.

197 MHz RF-Dipole Crab Cavity

The RF-dipole (RFD) cavity has been studied as a compact and efficient design for deflecting and crabbing applications. The design has evolved from a parallel-bar geometry to the current design that operates in a TE_{11}-like mode where the primary contribution to the kick is given by the transverse electric field [340]. Unlike TM_{110} type squashed elliptical cavities, the RFD cavities are compact designs that are especially useful at low operational frequencies. Some of the most attractive properties of the RFD cavity design are low balanced surface fields with high net deflection, high shunt impedance, and the absence of lower or same order modes. Several RFD cavities operating at a variety of frequencies ranging from 400 MHz to 750 MHz have been designed, fabricated, and tested, that have demonstrated performances well exceeding specifications [341–343].

One of the key applications of the RFD cavity is the LHC High Luminosity Upgrade at

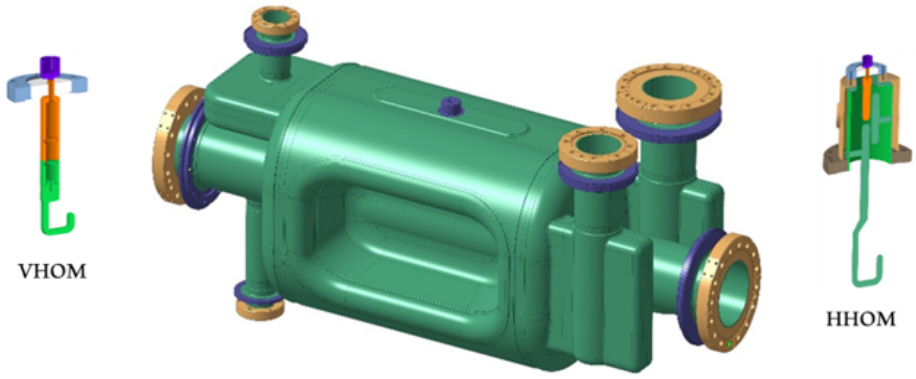

Figure 6.196: 400 MHz RFD crab cavity for LHC Hi-Lumi Upgrade.

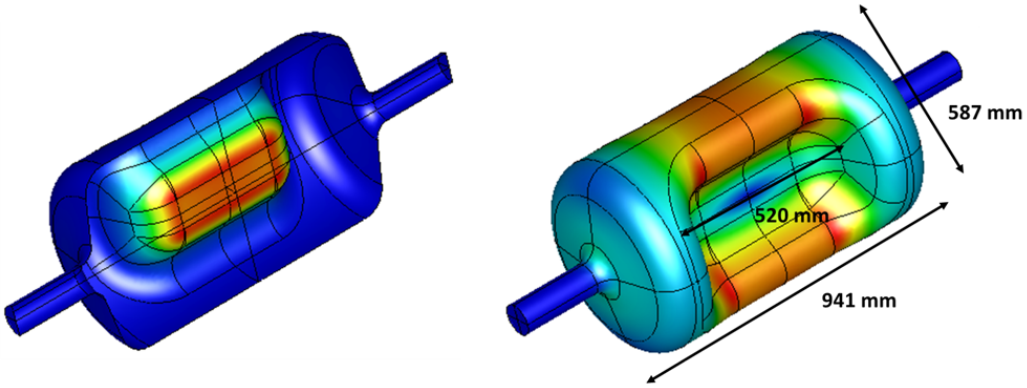

Figure 6.197: 197 MHz RFD crab cavity for EIC. Electric field (left) and magnetic field (right).

CERN [344]. The RFD crab cavity is one of the two crabbing cavities, that will be installed at the LHC enabling head on collision in the horizontal plane, to increase the luminosity of the colliding proton beams [345]. The LHC crab cavity is designed to be a compact square shaped cavity to fit between the two parallel beam pipes with a separation of 194 mm. The cavity has only two HOM couplers named Horizontal HOM (HHOM) and Vertical HOM (VHOM) as shown in Figure 6.196, to damp the modes up to 2 GHz [346]. The HHOM coupler is a high pass filter designed to reject the coupling to the fundamental operating mode and couples to the transverse dipole modes and some accelerating modes, where remaining modes are suppressed by the VHOM coupler. All the ports in the RFD cavity are designed in vertical direction to avoid any obstruction with the parallel beam pipe. The curved pole region allows in reducing the higher order multipole components. Several prototypes of the cavity have been fabricated and successfully tested and a prototype cryomodule with two cavities is planned to be tested at the SPS in 2023 [347, 348].

The EIC RFD crab cavity is designed with a cylindrical outer conductor similar to several proof-of-principle cavities that have been previously designed and prototyped. The EIC crab cavities are designed to provide a transverse kick that crabs the beam in horizontal plane. The EM fields of the 197 MHz RFD cavity are shown in Figure 6.197.

The 197 MHz cavity is designed to deliver low and balanced peak surface field ratios below <45 MV/m and <80 mT for an operational transverse voltage of 11.5 MV. The RFD cavity has peak surface fields of E_p=44 MV/m and B_p=78 mT at a V_t of 11.5 MV with E_p=33 MV/m and B_p=59 mT at operational V_t of 8.5 MV. The high shunt impedance of $(R/Q)_t \times G = 1.14\times10^5\ \Omega^2$ reduces power dissipation per cavity. The dimensions of the bare cavity are 941 mm iris-to-iris length with a diameter of 587 mm. The properties of the RFD cavity are listed in Table 6.78. The operating mode at 197 MHz is the lowest mode with well separated HOMs, where the first HOM is above ∼150 MHz.

The multipacting analysis for the RFD cavity is ongoing. Multipacting resonances in the 197 MHz RFD cavity are expected to be fully processed from the previous experiences on simulation and measurements carried out on several RFD cavity prototypes. The dogbone shaped waveguides are a new design concept on RFD cavities [347]. Therefore, resonant trajectories are being analyzed in detail and design changes will be made to suppress the multipacting resonances.

HOM Couplers The 197 MHz RFD cavity was designed with two higher order mode couplers as shown in Figure 6.198 that suppress the HOM modes up to 2 GHz. The HOM impedances for both longitudinal and transverse modes meet the design specifications of 3750 Ω and 1.35×10^6 Ω/m respectively as shown in Figure 6.199. The baseline RFD cavity is designed with compact dogbone shaped waveguides to reduce the cut-off frequency of the waveguide for improved HOM propagation and to simplify the manufacturability [349]. Four identical waveguide stubs are placed in the endplates of the cavity that simplify the fabrication of the RFD cavity. The dogbone waveguide stubs are tapered to transition into rectangular shaped waveguides to the loads. The waveguides are placed at the end plates in the low field region of the cavity and do not lead to any field enhancement at the edges in the waveguide stubs. Similar to the LHC crab cavity design, the VHOM waveguide coupler doesn't couple to the fundamental mode. The HHOM waveguide couples to the fundamental operating mode therefore made sufficiently long to reduce the fundamental mode fields at the load. The intermediate lengths are listed in Table 6.77.

The baseline RFD cavity includes two waveguide HOM couplers. The cavity will be further optimized in transitioning the waveguides to coaxial couplers that would damp the all the HOMs up to 2 GHz. The RFD cavity with VHOM coupler with waveguide to coaxial transition is shown in Figure 6.200.

Fundamental Power Coupler The FPC is placed on the secondary HHOM waveguide stub as shown in Figure 6.198 and is coupled in horizontal orientation. The RF power coupling required by the 197 MHz RFD cavity is shown in Figure 6.201 for a $(R/Q)_t$ of 1148 Ω at V_t= 11.5 MV with a proton beam energy of 275 GeV with a beam current of 1 A. The required Q_{ext} is 3×10^6 for a transverse beam offset of 0.5 mm. The FPC design is adapted from the 805 MHz SNS coupler, which is a 60 kW horizontally mounted coupler with a coaxial antenna [350]. Therefore, the port size is selected to be 74 mm with an inner

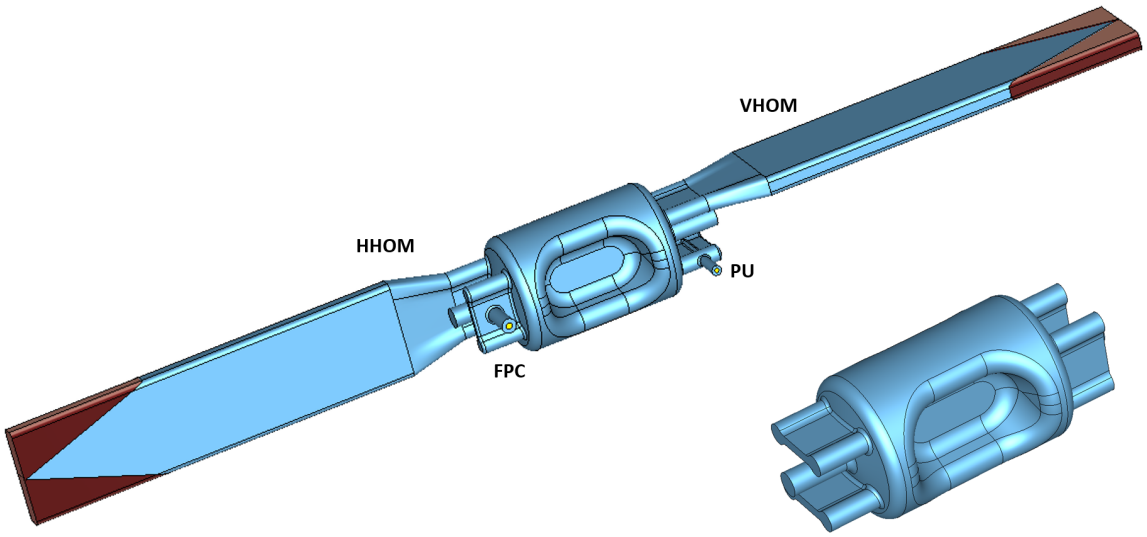

Figure 6.198: 197 MHz RFD cavity with HHOM coupler, VHOM coupler, FPC and PU.

conductor of 32.6 mm. The RF losses at the antenna at V_t= 11.5 MV is 103 W as shown in Figure 6.202 and 56 W at operational V_t of 8.5 MV. Vertical coupling is also a possibility in the RFD cavity and can be used a similar configuration that is used in the LHC RFD cavities, which is a 60 kW coupler coupled to the fundamental mode with a hook [351].

Fundamental Mode Damper The FMD might be needed due to the wide range bunch energy change during beam ramp up. This will require detuning of the fundamental mode by about 1.5 MHz. The requirement can be met with the availability of both tuning range and tuning rate of the RFD cavity. The RFD cavity has a total tuning range of 2.6 MHz. The requirements are not yet specified for FMD and if needed an additional damper can be included in the design.

Field Probe The field probe is designed to be located on the second VHOM waveguide stub (Figure 6.203). The field probe is a coaxial antenna with a coupling of 1.15×10^{11}. The power extracted of the fundamental mode for the coupling of the field probe is listed on Table 6.79. The port diameter of the field probe is currently designed to be 50 mm.

Table 6.79: Power from the field probe for RFD cavity.

Parameter	Operational	Nominal
$V_t[MV]$	8.5	11.5
Stored energy U [J]	51	93
Power P [W]	0.55	1.0

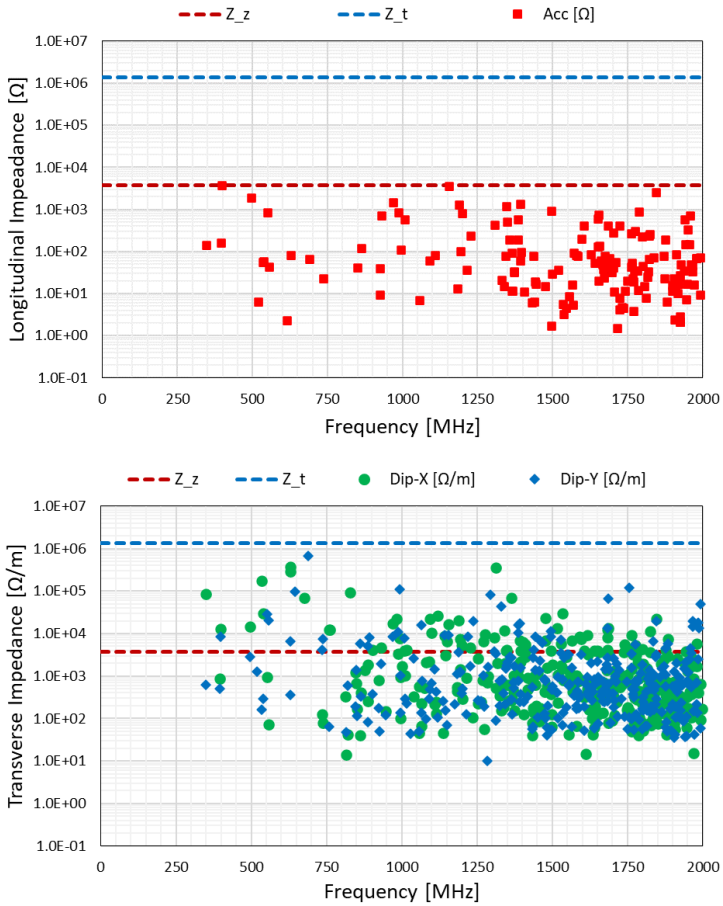

Figure 6.199: Impedances of longitudinal modes (top) and transverse modes (bottom) of the RFD cavity.

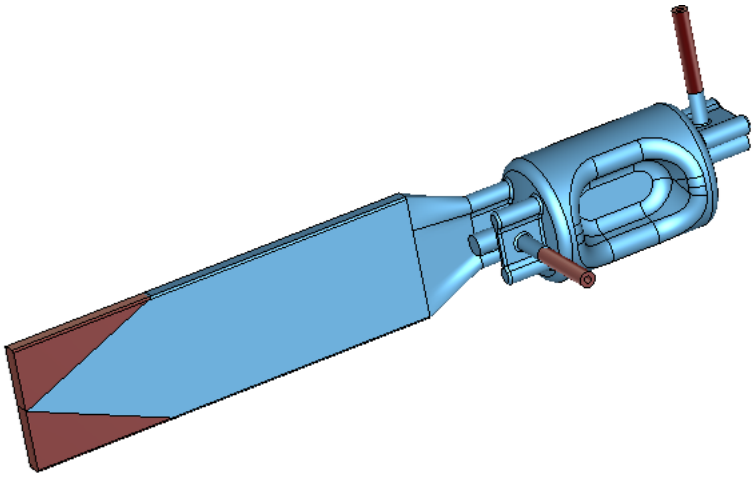

Figure 6.200: RFD cavity with HHOM waveguide coupler and VHOM coupler with coaxial coupler transition.

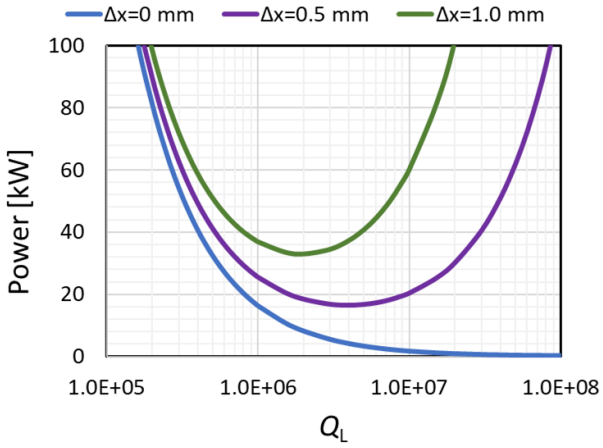

Figure 6.201: Forward RF power required by the 197 MHz RFD cavity with varying beam offsets.

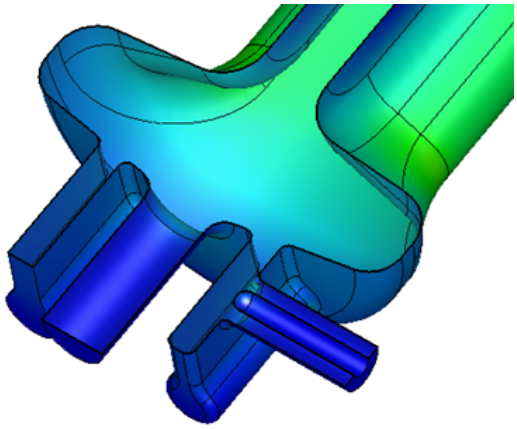

Figure 6.202: RF losses at the coaxial antenna at V_t= 11.5 MV.

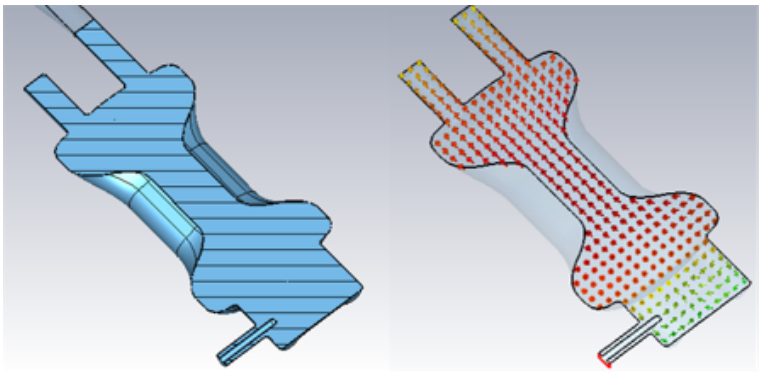

Figure 6.203: Field probe for the RFD cavity.

Higher Order Multipoles Asymmetry in the geometry of a crabbing cavity can lead to nonuniformity in the electromagnetic fields of the fundamental mode and high multipole content. In the RFD design, the introduction of 2 waveguide stubs results in 4 identical waveguide ports that preserve the symmetry and yields low multipole content. Compared to other RFD cavity designs the EIC RFD cavity has negligible shift in electrical center of 6.9 µm. The multipole components of the RFD cavity with 4 identical waveguide ports are shown in Table 6.80 normalized to a V_t of 1 MV. The requirements of the multipole components are not specified yet. However, these components can be further reduced by reshaping the poles if needed.

Table 6.80: Higher order multipole components for the 197 MHz RFD cavity with 4 symmetrical waveguide stubs (Fig 6.198) normalized to V_t of 1 MV.

Parameter	Value
V_t [MV]	1.0
b_1 [mT m]	3.34
b_2 [mT]	1.1×10^{-4}
b_3 [mT/m^1]	52.0
b_4 [mT/m^2]	0.165
b_5 [mT/m^3]	2.6×10^{3}
b_6 [mT/m^4]	143.2
b_7 [mT/m^5]	1.78×10^{5}
V_{acc} [kV]	0.575
Δx [µm]	6.9

Mechanical Design While the RF design satisfies the electromagnetic requirements of the system, the mechanical design has its own requirements such as complying to the pressure vessel code and feasibility of fabrication. The thickness is determined by mechanical stability under various conditions. Stiffeners are used to minimize the thickness of cavity body. the fabrication process and finished cavity are shown in Figure 6.204.

The fabrication plans considered the following aspects:

- Minimum number of forming dies and weld seams
- Avoid weld seams in high field area
- Weld seam 2D lines as opposed to 3D lines for better EBW machine control
- Avoid one sided full penetration weld as much as possible especially on sensitive area

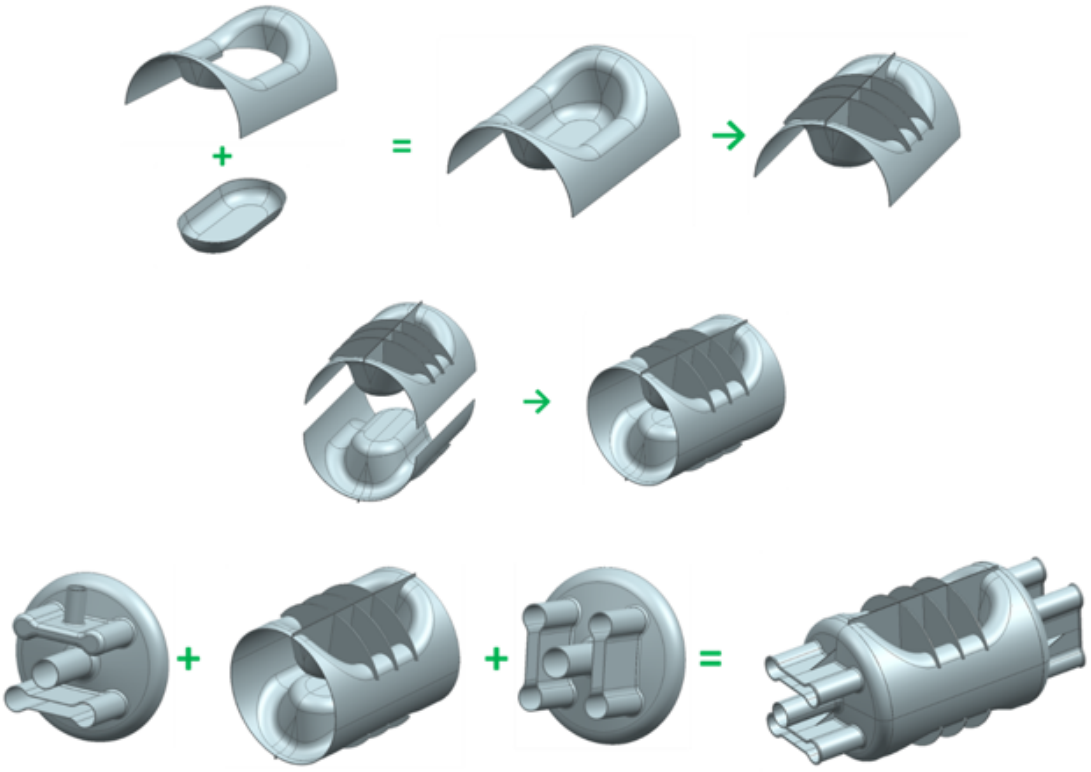

Figure 6.204: Fabrication sequence of the RFD cavity.

- Make all sensitive weld seams available for inspection and polish before moving forward
- Critical operation should be done earlier so it has opportunity to correct and accumulated time and efforts not wasted. For example, establishing pole geometry early on so the most important cavity parameters like frequency and electric center are determined and remained throughout the manufacturing process.

The trimming sensitivity of the 197 MHz RFD cavity is -42.3 kHz/mm (as shown in Figure 6.205). This low sensitivity gives small frequency shift during the final welding of the cavity.

Stress Analysis The cavity was subjected to a number of load cases and each case was analyzed. Typically, the case of over pressurized event during cooldown is the worst case. The case has the possible highest pressure (2.2 atm) in the helium space and the material property at room temperature. Figure 6.206 shows the results of this worst case analyzed for the bare cavity and the stress is below the allowed limit prescribed by pressure vessel code. When the helium vessel is finalized the analysis shall be repeated with more details. The thickness of the cavity determined by the stress analysis is 4 mm throughout the cavity body except the end plate 5 mm thick.

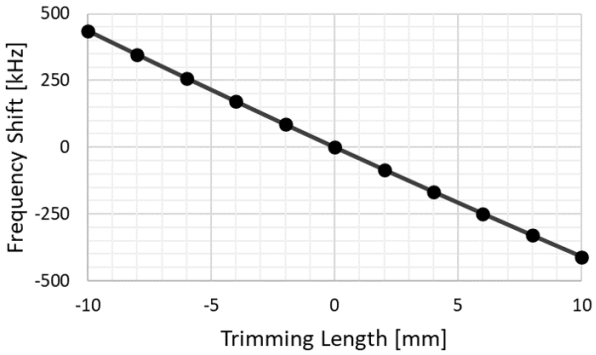

Figure 6.205: Trimming sensitivity of the RFD cavity.

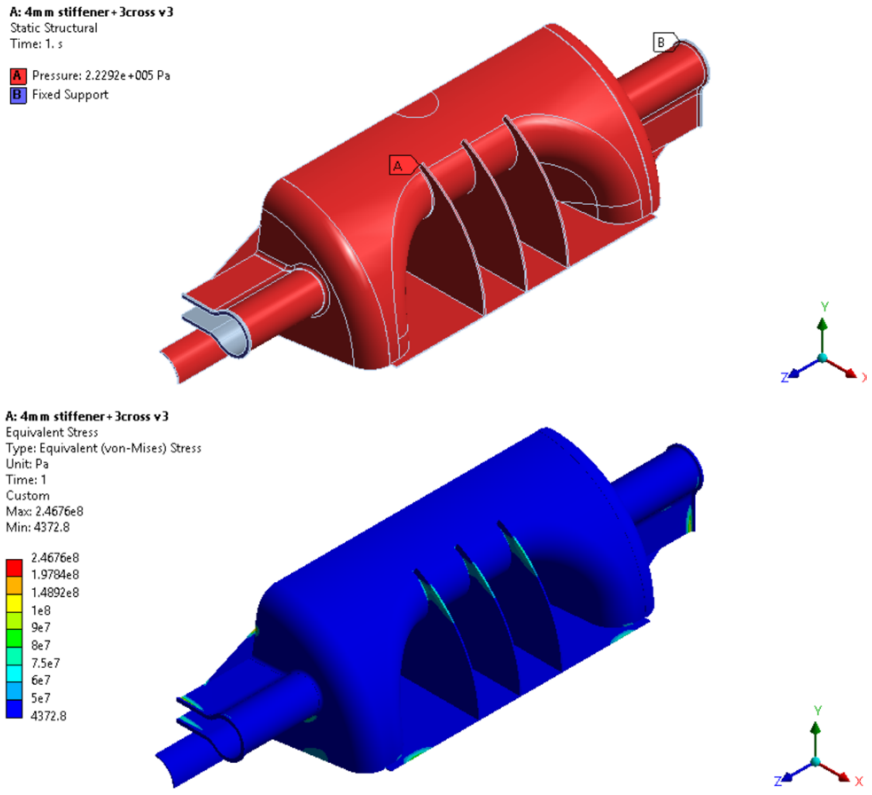

Figure 6.206: Stresses of the RFD cavity.

Tuning The EIC beam operation requires a wide tuning range. The RFD mechanical design allows the range while the stiffeners are not adversely affecting the mechanical flexibility of the cavity. The tuner was already developed for LHC RFD cavity at CERN [352]. The same tuning location and mechanism will be used for EIC as shown in Figure 6.207.

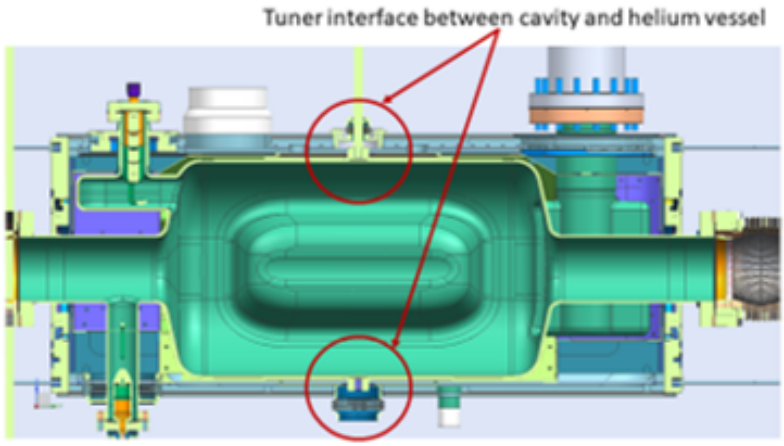

Figure 6.207: Tuner on the 400 MHz RFD cavity for LHC Hi-Lumi upgrade.

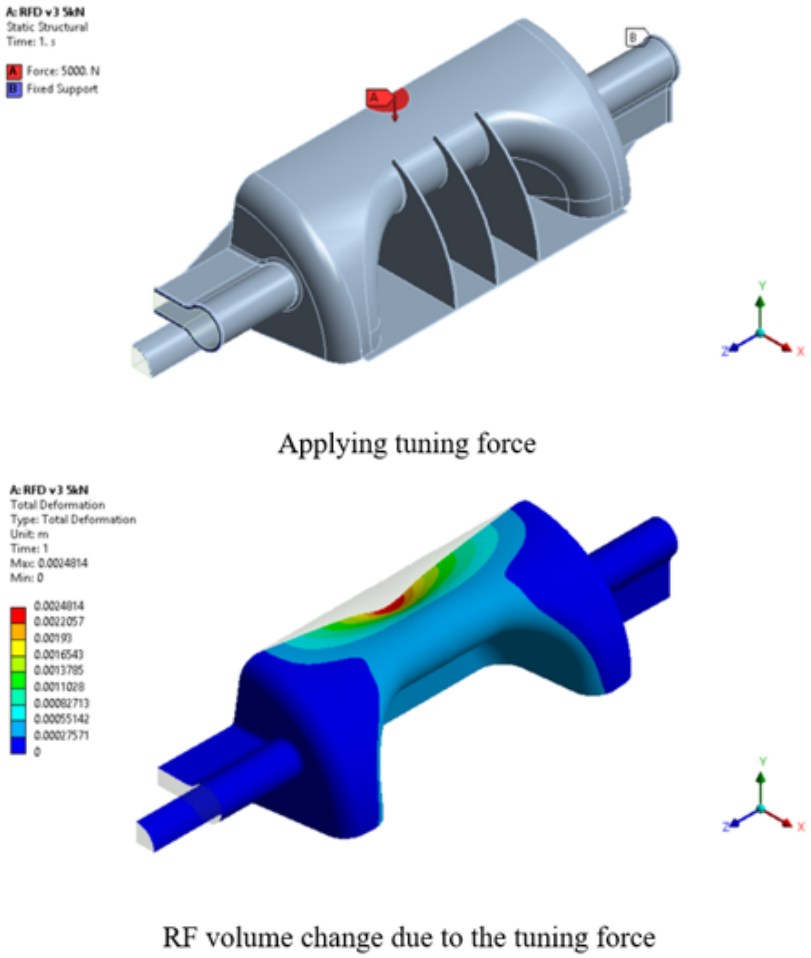

Figure 6.208: Tuning of the RFD cavity.

The tuning range is analyzed through mechanical-electromagnetic coupled finite element analysis. The frequencies are estimated at 2 K by simulating the nominal cavity shape and the deformed cavity after applying the tuning force on the assumed area. The results (see Figure 6.208) shows the tuning range ± 1.3 MHz while cavity maintains deflection about 4.5 mm, below the stress limit at 2 K.

He Vessel and Cryomodule The preliminary cryostat design is shown in Figure 6.209. It shows the orientation of the RFD cavity with HOM couplers and FPC with the He vessel and vacuum vessel. The 197 MHz RFD cavity design with the 394 MHz harmonic crab cavity fits the currently allocated beam line space.

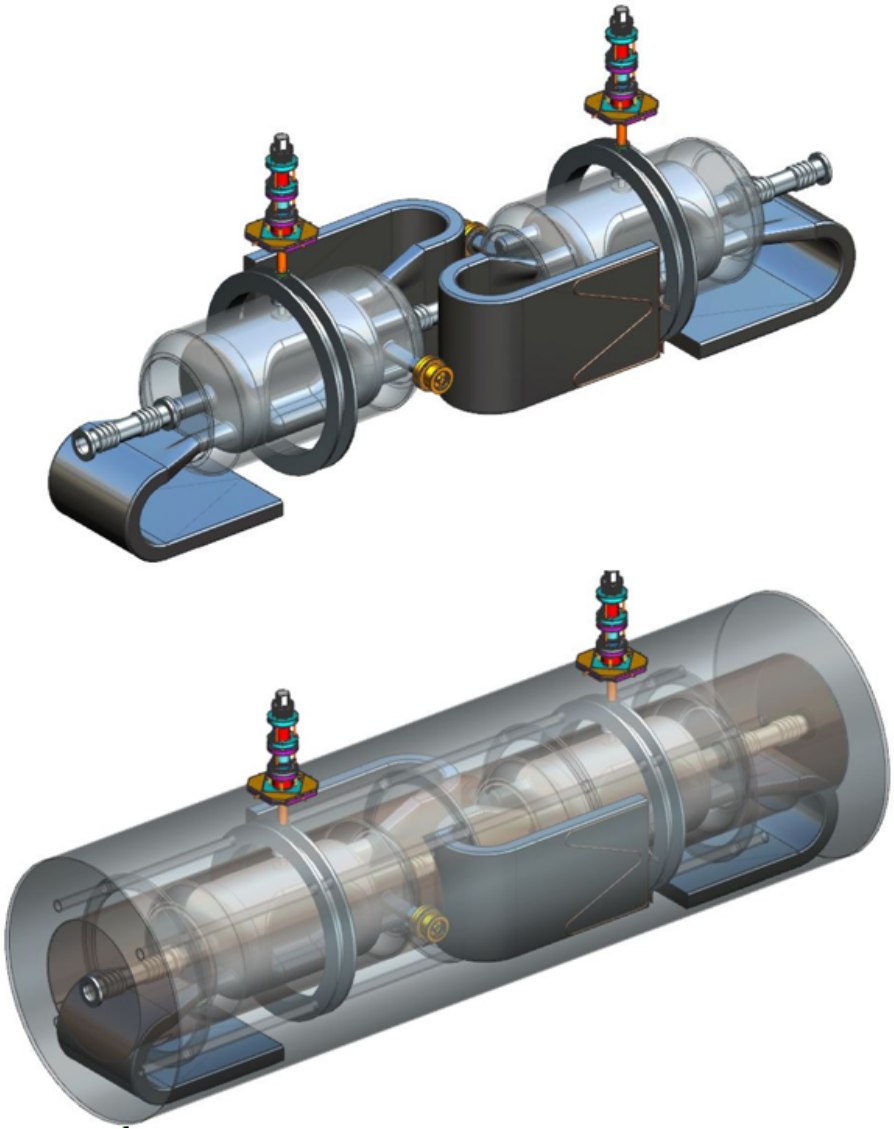

Figure 6.209: Conceptual concept of the RFD cryomodule.

394 MHz Wide Open Waveguide RF-Dipole Crab Cavity

The HSR and ESR will share the same 394 MHz crab cavity design. With this consideration, the cavity is optimized to meet the tighter requirements of the two rings, which is the HSR. The cavity beam aperture is required to be 100 mm. The HOM impedance thresholds are 7.5 kΩ-GHz/cavity for the longitudinal and 2.7 MΩ/m/cavity for transverse respectively, shown in Table 6.76.

Cavity shape An RFD shape with a WOW is considered for the 394 MHz crab cavity as sown in Figure 6.210. For the EIC design, the WOW beam pipe is opened up to the full diameter of the cavity. Such a cavity shape supports a TE11 like mode as the lowest mode which is the crabbing dipole mode. The intrusion of the two poles significantly increases the capacitance of the parallel plates at the gap, thus lowers the cavity frequency well below the cutoff frequency of the WOW waveguide. The deflecting field is well localized around the pole region as shown in Figure 6.210, resulting in a highly efficient RF dipole mode. Table 6.81 summarizes the major RF parameters of the 394 MHz WOW RFD cavity.

Table 6.81: RF Parameters of the 394 MHz WOW RFD cavity.

Parameter	Value
RF frequency f_0 [MHz]	394.0
Cavity dimension in horizontal [m]	0.255
Cavity dimension in vertical [m]	0.340
Beampipe diameter [m]	0.310
R/Q of deflecting mode [Ω, acc. def.]	315
Peak E field at 3.5 MV [MV/m]	42.2
Peak B field at 3.5 MV [mT]	67.0
Lowest dipole HOM freq [MHz]	574
Lowest monopole HOM freq [MHz]	745

HOM damping The WOW RFD cavity shape makes it straight forward to use beam line absorber to achieve strong HOM damping. For the beam line absorbers to be effective, all the HOMs in the cavity need to be propagating in the WOW beam pipe. In this WOW RFD geometry, there are no lower order modes. All the HOMs, except the TM01 like mode, are above the beam pipe cutoff frequency, if the cavity is of a simple circular profile. The design approach for the EIC is to alter the cavity shape such that the lowest TM01 mode will be above the WOW pipe cutoff. This is achieved by incorporating an elliptical cavity profile in the pole region. With this ellipticity, the cavity dimension in the deflecting plane

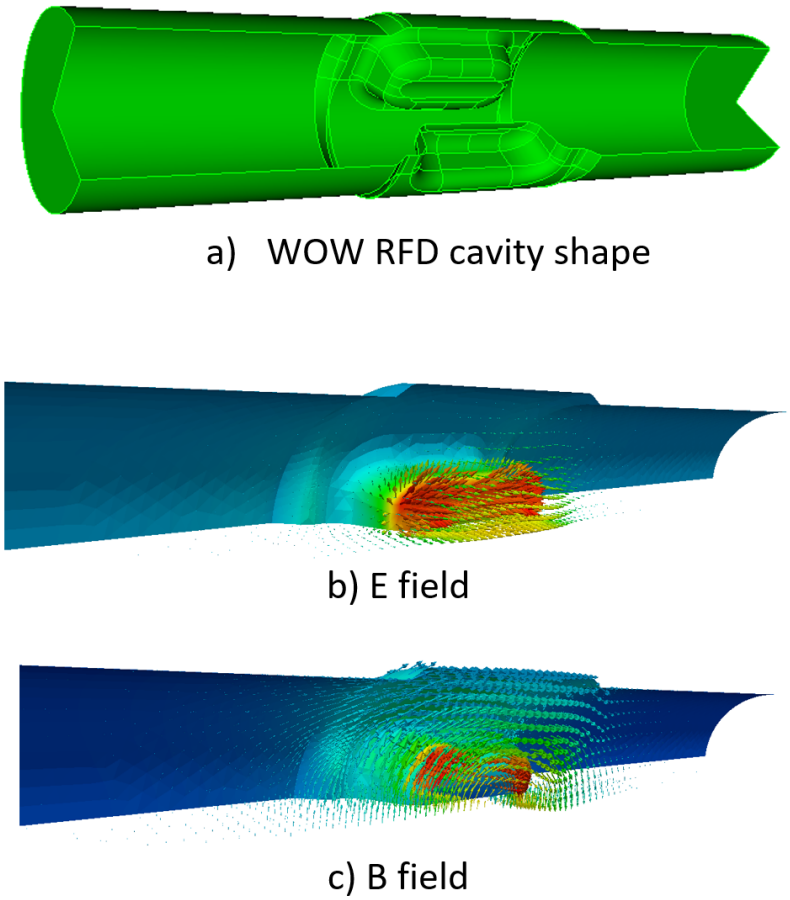

Figure 6.210: The 394 MHz WOW RFD crab cavity for HSR and ESR, from top to bottom: cavity shape; E field distribution; and B field distribution.

is slightly narrower than the beam pipe diameter and slightly larger in the other plane, as shown in Figure 6.210. This cavity shape increases the frequency separation between the deflecting mode and the TM01 accelerating mode. Since the deflecting mode is fixed at 394 MHz, the TM01 is then effectively tuned higher. With all the HOMs tuned propagating in the beam pipe, the HOM absorbers can then be placed further away from the cavity, which minimizes the power loss of the deflecting mode to the absorbers due to a finite attenuation length in the WOW beam pipe.

Beam line absorber There are total 4 beam line absorbers, 2 on each side of the cavity, as shown in Figure 6.211. The closest absorber is at 1 m distance from the cavity center. The absorbers are 220 mm in length. The two absorbers at each side are slightly different in radius (150 mm, 143 mm) and thickness (16 mm, 23 mm) to enhance the HOM absorbing up to 2 GHz frequency range. Because of finite length, the absorbers do not extract the HOM power as a matched load. To achieve the required strong damping, the length of

Figure 6.211: The 394 MHz WOW RFD crab cavity with beam line absorbers, 2 on each side of the cavity.

the WOW beam pipe and the end taper are optimized to enhance the HOM absorbing as well as to minimize the R/Q of HOMs. The end beam pipe of the WOW RFD cavity is 100 mm in aperture. At this diameter, the cutoff frequency is 1.76 GHz for the TE mode and 2.3 GHz for the TM mode. The beam line absorbers need to effectively damp HOMs up to these cutoff frequencies.

The total length of the 394 MHz WOW cavity including the end tapers is about 3.77 m. The Qloss of the fundamental mode due to the evanescent field loss to the absorber is about 2×10^9 and is considered acceptable.

HOM impedance The HOM damping Q_{ext} values are shown in Figure 6.212. The HOM impedances are shown in Figure 6.213. up to 1.8 GHz of frequency. The dashed lines are the threshold of the monopole (red) and dipole (blue) HOMs. The WOW RFD design will meet the EIC impedance requirements for both the HSR and the ESR rings shown in Table 6.76. One notice that the impedances of the dipole HOMs are about two orders of magnitude lower than the threshold of impedance requirement due to the strong damping by the HOM absorbers. An alternative damping scheme is to scale the 197 MHz DQW or RFD design to 394 MHz, which may result in a cavity of much shorter in length, and prototyping of 197 MHz cavity would be enough.

FPC The FPC is consisted of a coaxial transmission line and a magnetic hook antenna. The magnetic hook provides a stronger coupling to the cavity as compared to an electric probe. The hook antenna does not need to be inserted deeper into the strong field region, thus minimizes both the RF heating on the coupler and the field distortion. Figure 6.214 shows the hook position to achieve a Qext of 5×10^5. The surface field enhancement around the coupler is insignificant.

Nb to stainless steel beam pipe transition The location for transitioning from the Nb WOW pipe to the stainless steel (SS) is determined by the power loss level on the SS pipe by the deflecting mode. Figure 6.215 shows the Qloss of the deflecting mode on the SS WOW pipe as a function of the transition position. The room temperature conductivity of 1.16×10^6 for the SS was used in the calculation. The plot indicates that an 800 mm WOW pipe length is needed on either side of the RFD cavity.

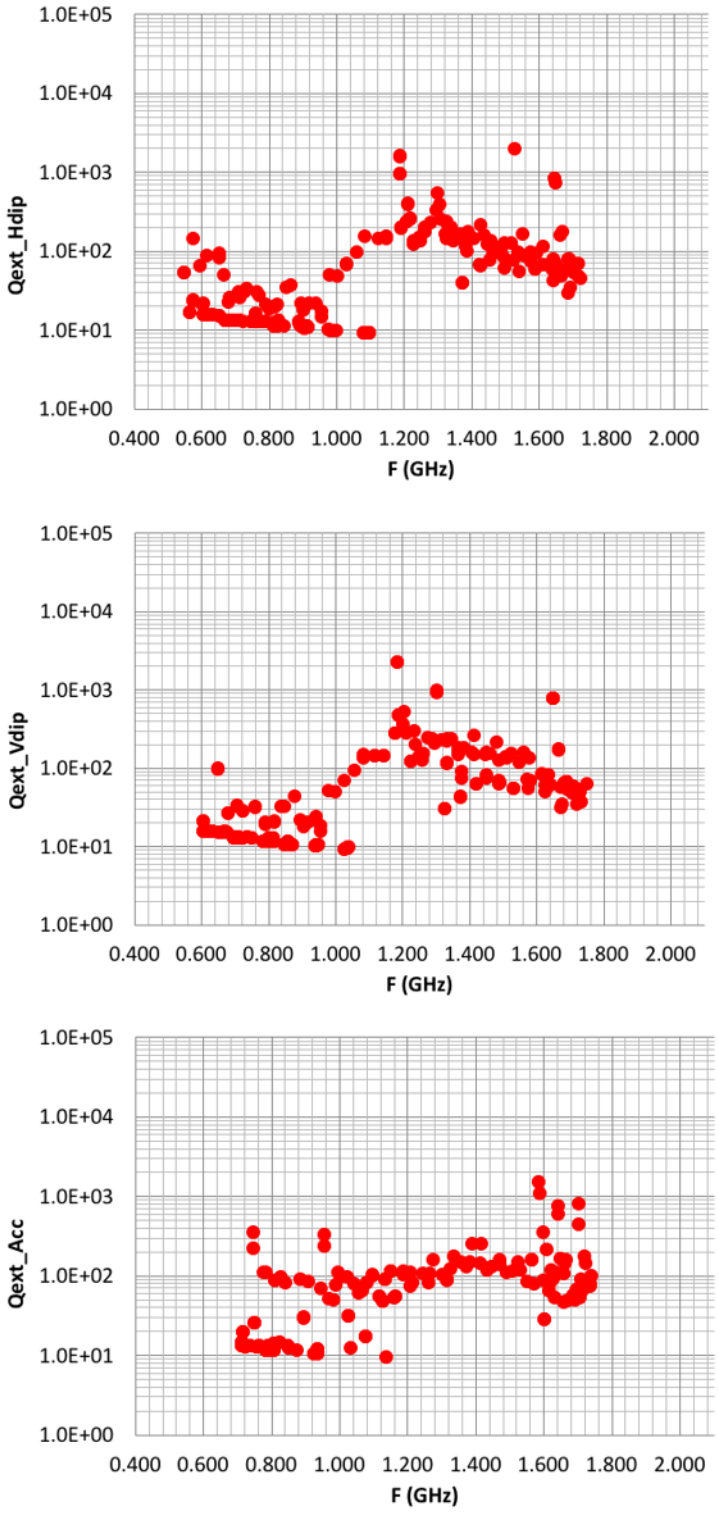

Figure 6.212: Damping Q values of the WOW RFD crab cavity.

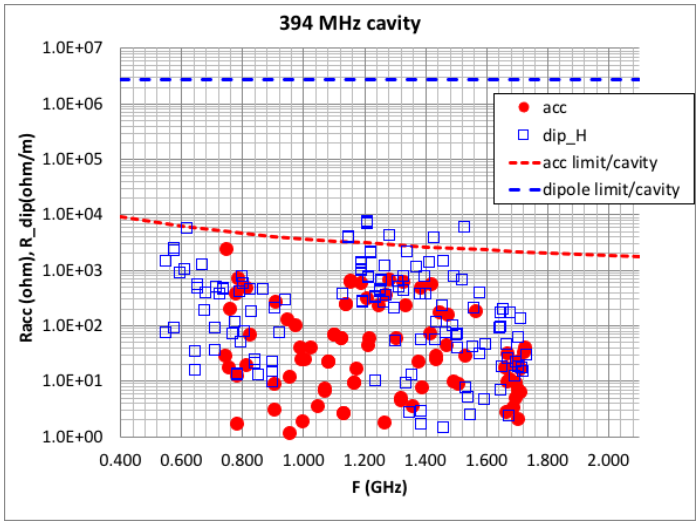

Figure 6.213: HOM impedance of the WOW RFD crab cavity with the beam line absorber damping.

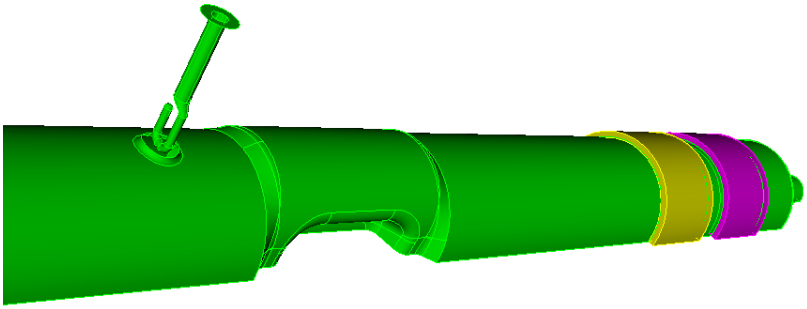

Figure 6.214: FPC for the WOW RFD cavity.

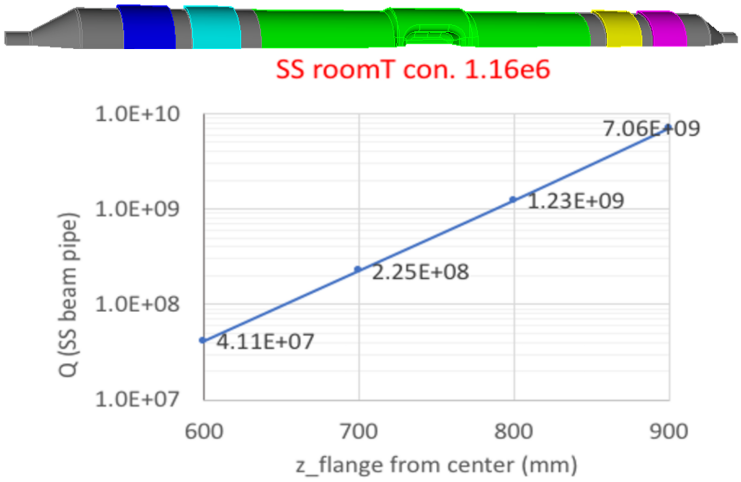

Figure 6.215: RF loss on the SS WOW pipe as a function of transition location. The distance is relative to the center of the cavity.

6.6 Pulsed Systems

6.6.1 Overview of Pulsed Systems

The pulsed systems will use a series of pulse generators and pulsed magnets to accomplish rapid beam transfer during injection and extraction in the EIC chain of accelerators. Solid state technology will be used in all pulsed power systems and utilize laboratory developed systems or commercially available subsystems.

The electron accelerator chain will start with an electron source. The electron bunches generated by the source will be accelerated by a LINAC to 400 MeV and then will be injected into a Rapid Cycling Synchrotron (RCS), which will further accelerate the electron bunches up to 18 GeV. Subsequently the electron bunches will be extracted from the RCS and injected into the electron Storage Ring where they will circulate to collide with the hadron bunches, which will circulate in the hadron ring. The hadron ring will be almost identical to the present RHIC Yellow ring; it will however undergo some upgrades, such as modification of the injection system from the AGS-to-RHIC (AtR) transfer line. Many pulsed systems such as kickers, bumps, and septa will be needed at the injection and extraction areas. The design concepts for these pulsed systems are described in this chapter.

In general, there will be two categories of pulsed systems. One category will be nanosecond fast-pulsed systems, which are at the forefront of accelerator pulsed power technology requiring a substantial research and development effort; the second category will be the advanced systems, which utilize technology that has already been demonstrated but may need further development depending on stability and regulation requirement. The preconceptual design of nanosecond fast kickers for both electron and hadron ring injection will be described in the same section and the rest of the pulsed systems in a separate section.

6.6.2 RCS Beam Injection Pulsed Power Systems

The RCS injection system will include three specialized pulsed systems. additionally it will use three standard RCS corrector magnets to generate a bump to assist in the injection process. The pulsed systems include a pulsed septum, a 10 µs kicker, and a RF 1.69 ns RF kicker system described in section 3.8.4. Two 7 nC pulses spaced by about 2 µs apart will be injected using a 30 mrad septum. A fast kicker will ramp up to to peak deflection in 10 µs and hold its peak value of 1 mrad for 2.5 µs and fall in another 10 µs. This 1.5 m RCS injection kicker will be a window-frame dipole magnet. The magnetic core of each magnet will be made of CMD5005 type ferrites to allow a fast kick to the injected beam without saturating. Two solid copper bus bars will be used to carry the electrical power (Figure 6.216(a)). Due to the low current density in the conductor of each magnet, the kickers only need air cooling. The kicker vacuum chamber will be made of Al_2O_3 (aluminum oxide) with a 4 cm diameter circular hole for the beam. The inner surface of the chamber will be coated with strips of titanium nitride (TiN), about 5 µm thick, to minimize the loss of the deflection

magnetic field due to eddy currents and to enhance field penetration. The pattern of the coating is shown in Figure 6.216(b). The parameters are detailed in Table 6.83.

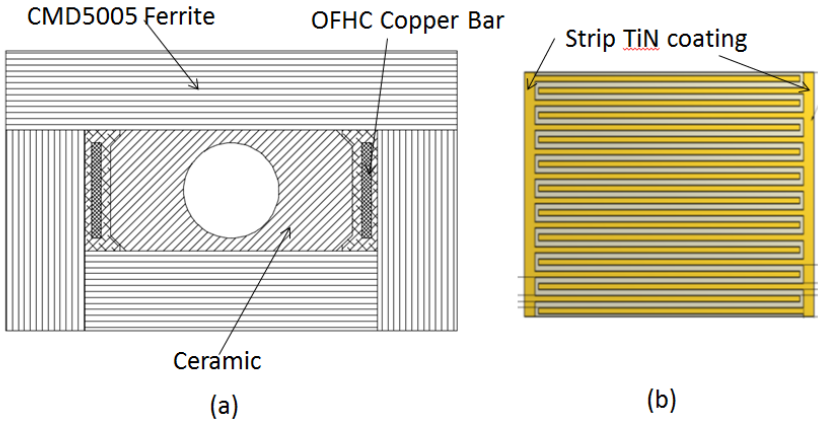

Figure 6.216: Pulsed kicker magnet design: (a) cross section view of the magnet (b) pattern of strip coating on inner surface of ceramic vacuum chamber (courtesy of NSLS-II).

The RCS injection pulsed septum will consist of a C-shape dipole magnet with an insulated, laminated, low carbon iron yoke, and a single-turn excitation coil. The effective thickness of the septum blade is around 5 mm. The parameters are detailed in Table 6.82.

Table 6.82: Design parameters for the RCS injection septum.

Parameter	RCS Injection Septum
Beam energy [GeV]	0.4
Rep. rate [Hz]	1
Def. angle [rad]	0.03
Gap height [cm]	2.5
Gap width [cm]	3
No. of turns	3
Magnetic field [T]	0.08
Magnet length [m]	6.5
Magnet current [A-Turns]	1592
Coil Current [A/Turn]	531
Septum thickness [mm]	5
Base Width [ms]	54
Quantity	1
Style	C-magnet w/t Laminated Yoke

6.6.3 RCS Beam Extraction Pulsed Power Systems

The beam will be extracted using two specialized pulsed systems plus three standard RCS orbit correctors used to create an orbit bump. These pulsed devices include a kicker to deflect the beam by 1.2 mrad. It will need to ramp to its peak value in 2 µs and fall in 10 µs. It will also need to cycle through two kicks in 1000 Hz in order to extract the two RCS bunches at extraction energy. Additionally an extraction septum to deflect the beam by 30 mrad will be needed. The mechanical design of the RCS extraction kicker will be the same as that described for the RCS injection kicker, except for the aperture of the vacuum chamber, see Table 6.82. A half-sine wave pulse generator will power the chain of kicker magnets.

The RCS extraction and ESR injection septa are complementary designs. Each system requires a total of 6.5 m magnetic length. The septa will be divided into several magnets. At least one of magnets in each system will be a pulsed septum. The rest of them can be either DC or pulsed septa.

The RCS extraction pulsed septum will consist of a C-shape dipole magnet with an insulated, laminated, low carbon iron yoke, and a single-turn excitation coil. Figure 6.217(a) shows the cross section of the septum. A copper screen will be placed around the insulated vacuum chamber to limit penetration of the magnetic field into the equilibrium orbit. An additional iron screen will also be used to reduce the stray field. The effective thickness of the septum blade is around 4 mm. Figure 6.217(b) depicts the cross section. An additional

Table 6.83: Design parameters for the RCS injection/extraction kickers.

Parameter	RCS Injection Kicker	RCS Extraction Kicker
Beam Energy [GeV]	0.4	18
Rep. Rate [Hz]	1	1
Def. Angle [rad]	0.001	0.0012
Gap Height [cm]	4	4
Gap Width [cm]	5	4
No. of Turns	1	1
Bending Strength [Tm]	0.00133	0.072
Mag. Field [T]	0.01334	0.072
Mag. Length [m]	1.5	5
Mag. Current [A-Turns]	425	2293
Coil Current [A/Turn]	425	2293
Quantity	1	1
Style	Window Frame w/t Ferrite Core	Window Frame w/t Ferrite

Table 6.84: Design parameters for the RCS extraction septum.

Parameter	RCS Extraction Septum
Beam energy [GeV]	18
Rep. rate [Hz]	1
Def. angle [rad]	0.03
Gap height [cm]	2
Gap width [cm]	3
No. of turns	4
Magnetic field [T]	0.3
Magnet length [m]	6.5
Magnet current [A-Turns]	4777
Coil Current [A/Turn]	1194
Septum thickness [mm]	4
Base Width [ms]	5.5
Quantity	1
Style	C-magnet w/t Laminated Yoke

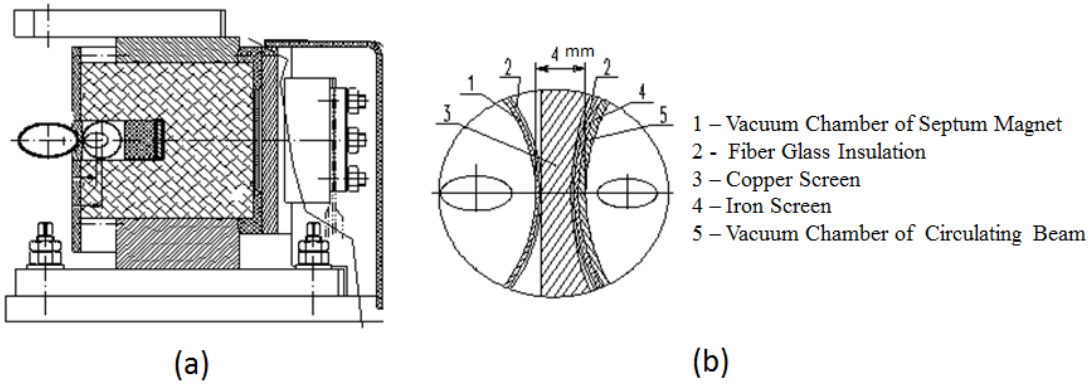

Figure 6.217: Pulsed septum magnet. (a) Cross section view of the magnet. (b) Pulsed septum blade (courtesy of NSLS-II).

iron screen will also be used to reduce the stray field. The 1 m long magnet will be either air- or water-cooled. The vacuum chamber of the RCS extraction pulsed septum will be made of either 316L stainless steel or Inconel 625 with a diameter of 1.5″. The magnetic core will be 1.5 m long. Due to the high magnet current additional consideration will be given to the cooling method in the conceptual design.

The pulse generators for the proposed RCS pulsed systems will be based on demonstrated technologies, such as half-sine wave capacitor discharge pulse generators, pulse-forming network pulse generators, Marx generators, or inductive adder pulse generators. The typical pulse base width will be in the range of 8 µs to 48 µs. These systems are either commercially available or can be made by Brookhaven in collaboration with other institutes or industrial partners.

6.6.4 ESR Beam Injection Pulsed Power Systems

Injection into the ESR will be accomplished using two specialized pulsed systems assisted by three standard ESR corrector magnets. The pulsed systems include an injection septum and an ultra fast strip-line kicker for swap out and swap in injection.

Table 6.85: Design parameters for the ESR injection septum.

Parameter	ESR Injection Septum
Beam energy [GeV]	18
Rep. rate [Hz]	1
Def. angle [rad]	0.015
Gap height [cm]	2
Gap width [cm]	3
No. of turns	4
Magnetic field [T]	0.24
Magnet length [m]	6.5
Magnet current [A-Turns]	3822
Coil Current [A/Turn]	955
Septum thickness [mm]	4
Base Width [ms]	4.5
Quantity	1
Style	C-magnet w/t Laminated Yoke

The ESR injection pulsed septum will be a core-in-vacuum design, which requires a thin 4 mm septum. The core length of the septum is 1.5 m. The cross section of the septum will be as shown in Figure 6.218. The core will be made of insulated, laminated, low carbon steel sheets. A copper septum with thickness of 2 mm will be strengthened by a Mu-metal sheet; and a copper box enclosure around the iron sheets core will contain and dissipate the eddy currents generated by the pulsed field. Due to the high magnet current, additional cooling methods will be investigated in the conceptual design.

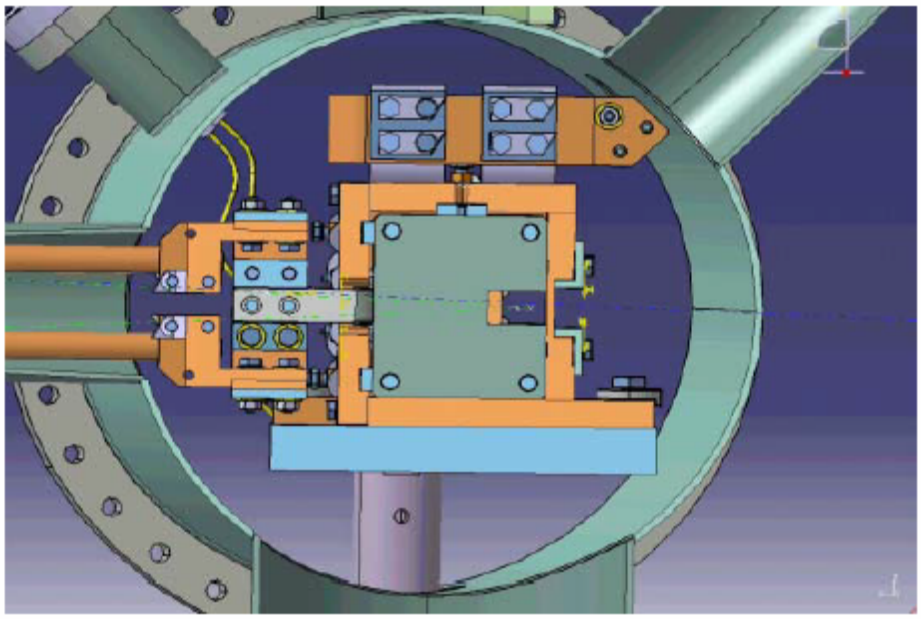

Figure 6.218: Core-in-vacuum pulsed septum with an eddy current screen (courtesy of SOLEIL).

For both the RCS and ESR septa, two options are being considered. One is to have an additional five, sequentially arranged, 1meter long extraction DC septa. The other is to add four more pulsed septa.

If five DC septa are used the magnets will consist of C-shaped low carbon iron yokes with single-turn excitation coils. Figure 6.219 shows the cross section of the septum. The vacuum chamber will be made of solid 316 stainless steel. Water-cooling will be provided for both the coil and the magnet core because of the high magnet current.

For the option of the DC septa, they will be connected in series and powered by a single DC power supply. In case where four additional pulsed septa are used, they will be connected in series and powered by the same half-sine pulse generator in each system. The decision is pending, and a simpler accelerator injection and extraction design layout is being investigated.

The storage ring injection pulse septum and bumps will be similar to the RCS pulsed systems, except they will require higher stability, better waveform regulation, and smaller timing jitter. The pulsed septa will be able to use longer pulse widths while the bump pulse width will be two machine revolutions. To minimize power loss in the cable of the pulsed septa, the use of pulse transformers between the pulse generators and septa will be considered. For the purpose of the pre-conceptual design, the stability and regulation of the kickers will be considered in the $\pm 1\%$ to $\pm 2\%$ range, and the bumps and septa in the $\pm 0.25\%$ range. These parameters will be refined as the design improves. All pulsed systems described in this section will be a few hundred volts to a few kilovolts, well within existing capabilities and experience.

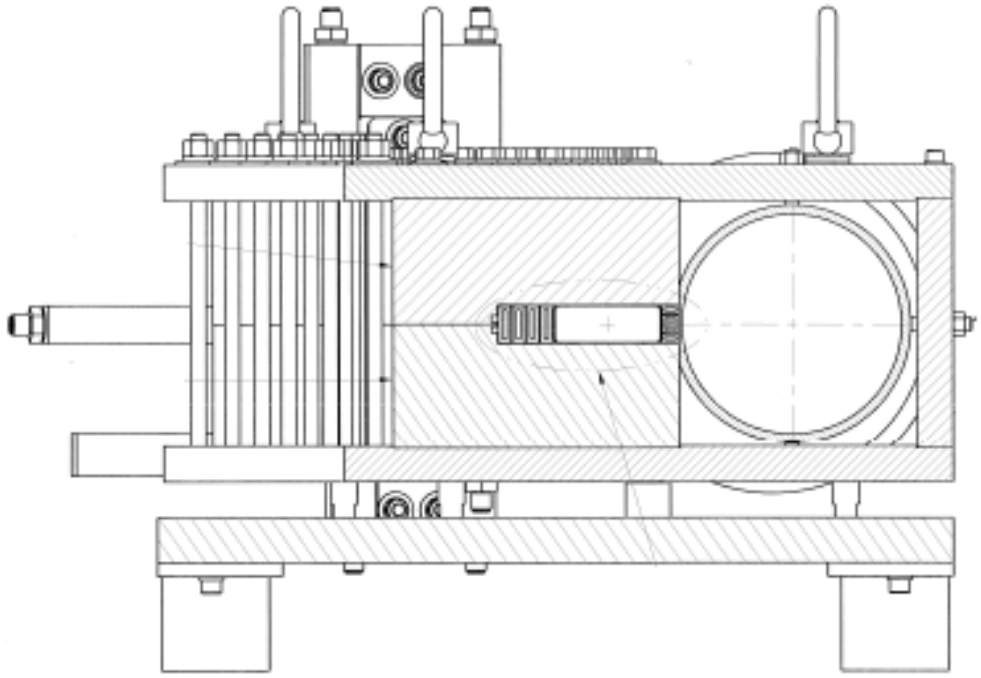

Figure 6.219: RCS extraction and ESR injection DC septum mechanical design (courtesy of NSRL).

ESR Abort Kickers

An electron beam abort system will be needed to dump the entire beam train on demand. This will be accomplished using a kicker system with a rise time of 0.9 µs which will stay up for a full turn or 12.6 µs. It will need to deliver a total of 2.5 mrad kick using 5 kickers each giving 0.5 mrad. The parameters for this kicker are detailed in Table 6.86.

6.6.5 ESR Injection/Extraction and HSR Injection Pulsed Power Systems

Fast kickers are needed for both the hadron ring injection and the electron accelerator complex. For the electron beams fast kickers will be used for extraction from the RCS and injection/extraction into the ESR in a bunch-by-bunch swap-in/swap-out mode. The fast kickers are planned to be strip-line kickers fed by dual channel pulsers in a fashion similar to that being implemented for the Advanced Photon Source Upgrade (APS-U) at Argonne National Laboratory. These kickers have been tested with beam at both the APS and NSLS-II where operation with differential strip-line kicker voltages of ± 15 kV and operation with 200 mA of beam current were demonstrated separately [353]. Here we plan on using similar devices optimized for the EIC which require modifying the strip-line lengths, gap between strip-lines, peak-voltage, feedthroughs, and enhanced damping of

Table 6.86: Design parameters for the ESR abort kickers.

Parameter	ESR Abort Kicker
Beam Energy [GeV]	18
Single Shot Rep. Rate [Hz]	0.0167
Pulse Rise Time [µs]	0.9
Pulse FT [µs]	12.6
Def. Angle [rad]	0.0005
Gap Height [cm]	4
Gap Width [cm]	5
No. of Turns	1
Bending Strength [Tm]	0.0302
Mag. Field [T]	0.0302
Mag. Length [m]	1
Mag. Current [A-Turns]	4816
Coil Current [A/Turn]	4816
Quantity	5

the beam excitation. Due to the similarity in requirements we plan a collaboration with the APS-U in developing and implementing our systems to avoid duplicating development efforts on both the strip-line kicker and pulser.

For the electrons a pulse structure of 10.15 ns is needed with rise/fall times of 3.45 ns and a flat-top of $\pm$40 kV over 3.25 ns. See Section 3.8.5 for pulse details. This pulse structure is achievable with a shortened version of the existing APS-U kickers which are 0.72 m long relative to the 0.4 m long version needed here. This will start as our initial strip-line design and be modified to accommodate the required EIC operating parameters. The APS-U pulser purchased from FID has been demonstrated to be able to operate at 27 kV with a 4.8 ns flat-top. A 40 kV unit is already purchased. This FID pulse generator has the potential to satisfy the design specifications for the electron storage ring extraction nanosecond fast kicker and the hadron ring injection nanosecond fast kicker. Lower voltage FID pulse generators have been tested at Brookhaven and several other institutes and our development effort will build upon the existing test infrastructure already in place.

The hadron ring injection kickers will be upgraded to allow a three-times higher injection bunch number than the existing system. 330 bunches will be injected into 360 buckets with a reserved abort beam gap of 30 buckets. The bunch frequency at injection is approximately 28 MHz. Hence, this kicker system must have timescales of nanoseconds. The typical bunch length will be 15 ns; and the beam center-to-center time will be around 35.7 ns. A series of 20 parallel-plate strip-line push-pull structure kickers is proposed. They will be arranged in series in the hadron injection section. The kicker deflection angle will be

reduced from 1.84 mrad to 1.0 mrad and the kicker aperture will be enlarged from the existing 41.2 mm to 50 mm. These kickers will pulse in a burst mode during injection. The burst mode stability will be a critical parameter in this design.

Each pair of hadron ring injection kickers will be 0.9 m in length and be driven by a pair of nanosecond fast pulse generators in a push-pull fashion. The high voltage pulse generator must have a 10 ns pulse rise time from 2% amplitude to 98% amplitude, a pulse flat top width around 50 ns, and be capable to deliver 500 A into a 50Ω load.

The pulse fall time of the hadron ring injection kicker is not critical, if the pulse falls within the duration of the large abort gap. Almost all nano-second pulse generators will have a much shorter fall time than the 900 ns abort gap. However, the pulse waveform, amplitude repeatability, pulse flat top regulation, and timing stability of the kick are extremely important for the hadron beam injection. The design parameters for the nanosecond fast kickers are listed in Table 6.87.

Table 6.87: Design parameters for the nanosecond fast kicker.

Parallel-Plate Strip Line	Hadron Inj. Kicker
Beam Energy [GeV]	24
Rep. Rate [Hz]	Burst Mode
Total Def. Angle, Rad	0.001
Distance between Plates [cm]	5
Total Deflection Length [m]	18
Voltage per plate $[\pm$ kV]	16.65
Current [A]	333
Number of Sections	20
Deflection length per section [m]	0.9
Style	Push-Pull

Parallel-plate strip line deflectors for nanosecond fast kickers are proposed. They will be used in the single bunch electron beam extraction from the Storage Ring and in the hadron beam injection system. The mechanical design of these strip line kickers will be similar to that as shown in Figure 6.220. The strip line kickers will be made of 316L stainless steel, which includes a surrounding circular chamber, two strip lines, and four HV coaxial feedthroughs rated at 30 kV. Each strip line has a 90° opening angle. The effective deflection length, per section, will be less than a meter. The characteristic impedance of the plate to ground will be around 50Ω.

The FID pulse generator has the potential to satisfy the design specifications for the storage ring extraction nanosecond fast kicker and the hadron ring injection nanosecond fast kicker. An FID pulse generator has been tested at BNL and several other institutes.

Other technologies have been tested at Brookhaven to support our nano-second pulsed

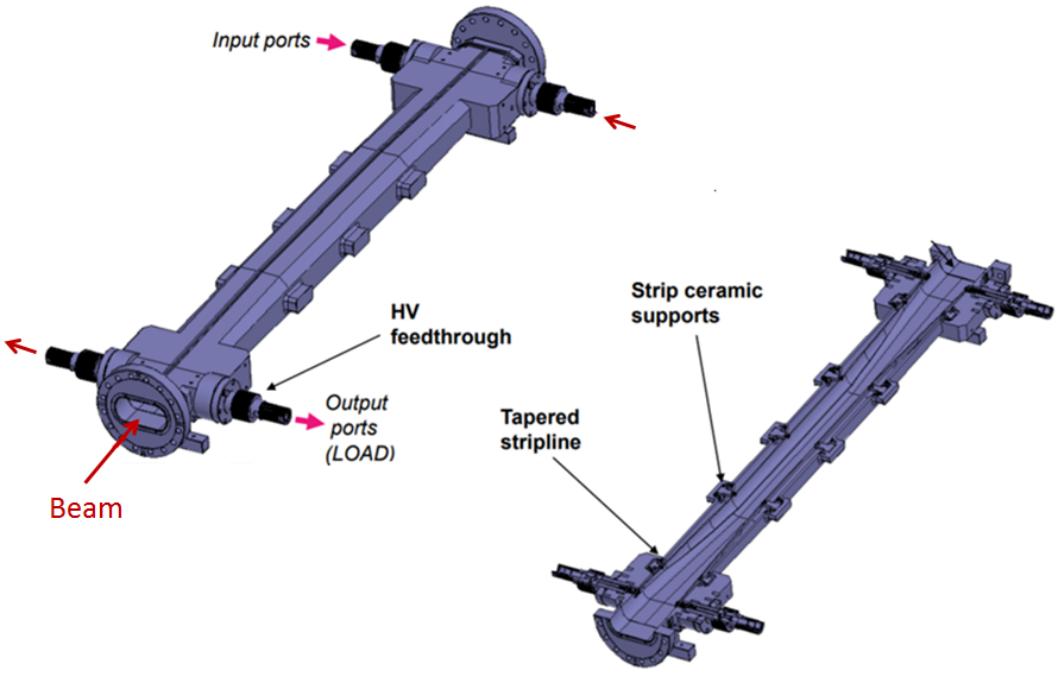

Figure 6.220: Strip-line kicker design (Courtesy of DAFNE).

power technology demand as well. For example, the Blumlein pulse-forming line (PFL) with solid-state switch, the inductive voltage adder (IVA), the parallel-plate with capacitive discharge, etc. Surveying the field of pulsed power technology, the potential of the IVA may one day be fast enough to support the hadron ring injection kicker. Further development of compact Blumlein PFLs or multi-layer PFLs with solid-state switch might offer another technological choice. While the superconducting harmonic RF cavity kicker and the SLAC DSRD kicker may someday be suitable for this application, the DWA kicker and other advanced concepts in the pulsed power field need substantially more design to be practical.

6.7 Beam Polarization Measurement

6.7.1 Mott Polarimeter Design

There are two Mott polarimeters for measuring the electron beam polarization in the pre-injector, one on the cathode preparation system and the other one on the beam line. The cathode preparation polarimeter will be used for checking the beam from the SL-GaAs wafer after activation. Due to the low electron energy, a low-voltage retarding-field Mott polarimeter (compact mini polarimeter) will be used. The pre-injector beam line needs a high energy Mott polarimeter which is similar to the one used in the CEBAF injector.

The spin-coupling inelastic Coulomb scattering, also called Mott scattering, results in a spatial asymmetry by Coulomb-scattering of electrons off heavy atom nuclei. Mott scattering is therefore used for measuring electron polarization. The scattering cross section of electrons with spin polarization $\vec{P}$ is described by the following equation:

$$\sigma(\theta) = I(\theta)[1 + S(\theta)\vec{P} \cdot \vec{n}] \tag{6.27}$$

where θ is the scattering angle, $\vec{n}$ is the unit vector perpendicular to the scattering plane, and $I(\theta)$ is the differential cross section for an unpolarized beam of electrons scattered through the angle θ,

$$I(\theta) = \bar{\lambda}^2\{q^2(1-\beta^2)\frac{|F(\theta)|^2}{\sin^2(\theta)} + \frac{|G(\theta)|^2}{\cos^2(\theta)}\} \tag{6.28}$$

where $2\pi\bar{\lambda}$ is the de Broglie wavelength, $q = \alpha/\beta$, $\alpha = Ze^2/\bar{h}c$, and $\beta = v/c$. $S(\theta)$ is the analyzing power (well-known as the Sherman function) defined by

$$S(\theta) = \frac{2\bar{\lambda}^2 q(1-\beta^2)^{1/2}}{\sin(\theta)I(\theta)}[F(\theta)G^*(\theta) + F^*(\theta)G(\theta)]. \tag{6.29}$$

The complex functions $F(\theta)$ and $G(\theta)$ can be found in Reference [354].

Low Voltage Mott Polarimeter

Before the cathode wafer is inserted into the gun, the polarization of the photo electrons will be checked. Compact polarimeters in the tens of keV range have been investigated at several places like Rice University, BNL, and TJNAF. They have been used for characterizing the cathode material or enabling photocathode pre-qualification for polarized electron sources. The compact polarimeter can be mounted on the cathode preparation chamber. The polarized electron spin direction from GaAs is longitudinal. Multiple electrodes are needed to bend the electron by 90° electrically in order to rotate the electron spins into the transverse direction. Then, the electrons that enter the polarimeter are accelerated to energies of about 20 keV between two hemispherical stainless steel electrodes. Electrons will scatter off a gold target inside of the inner hemisphere. The scattered electrons will

be decelerated and absorbed by channeled electron multipliers (CEM). The CEMs will be mounted 120° left/right due to the maximum Sherman function, as shown in Figure 6.221.

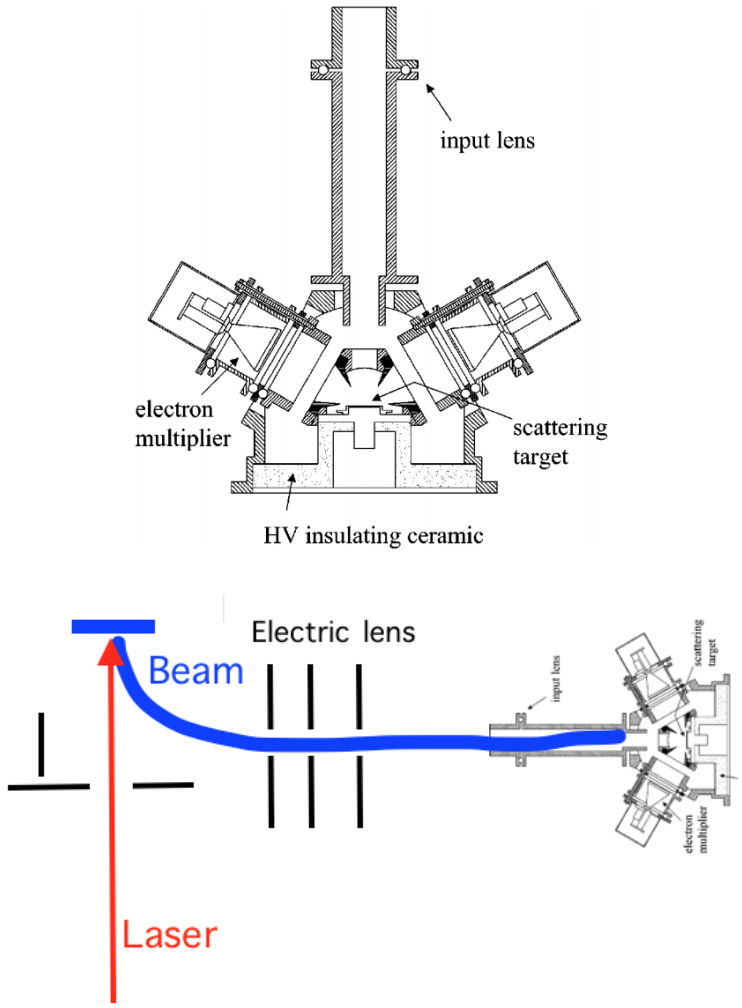

Figure 6.221: Low voltage Mott polarimeter drawing and beam trajectory from cathode to polarimeter.

There are two more CEMs placed up/down to measure out-of-plane polarization that may arise due to physical mechanisms, instrumental asymmetries, or misalignment. The measurement duration to reach 0.5% error is shown in Figure 6.222. As the retarding potential is increased negatively, electrons that have lost energy through inelastic scattering are excluded from the measurement. Once the retarding potential approaches the incident beam kinetic energy, only elastically scattered electron are detected. A 1–5 µm gold film could be plated on a copper cylinder. The two hemispherical electrodes should be rounded and well polished to hold a high surface gradient. All the components inside the Mott chamber should be bakeable to 250° C to achieve XHV.

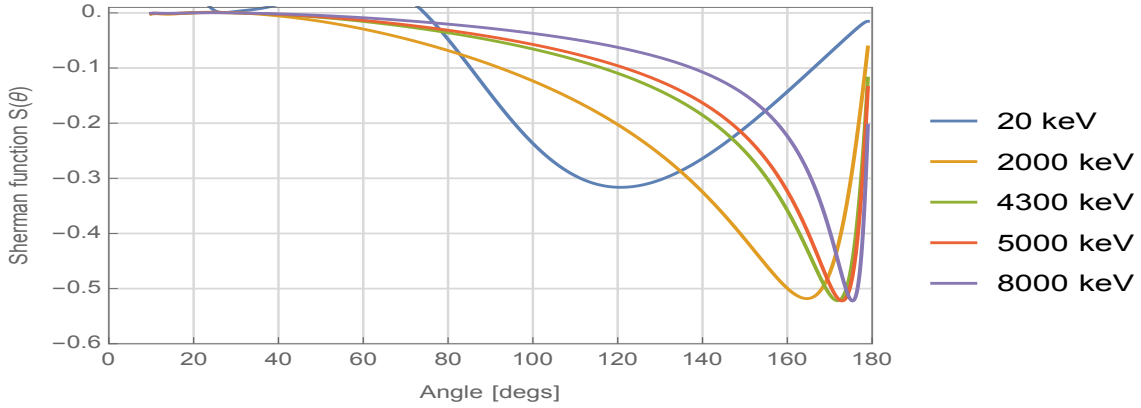

(a) The Sherman function of different electron energy.

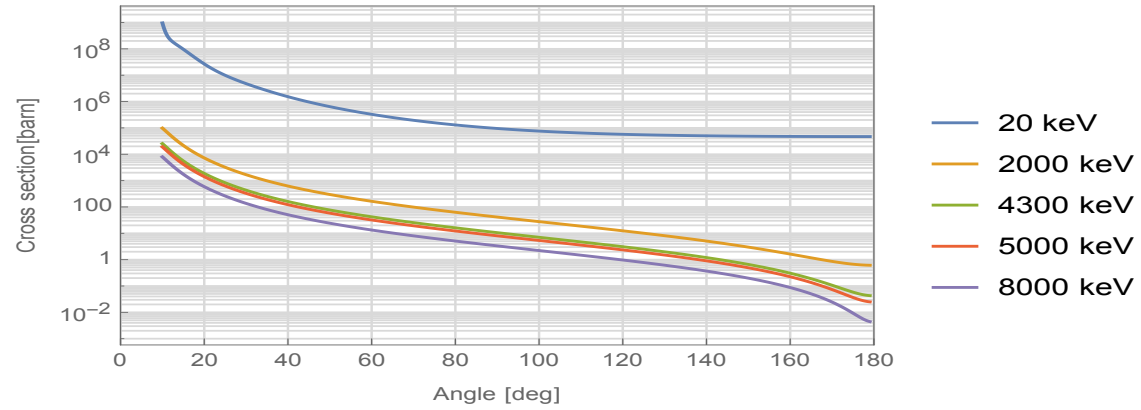

(b) The cross section of an unpolarized beam of electron scattered through an angle θ.

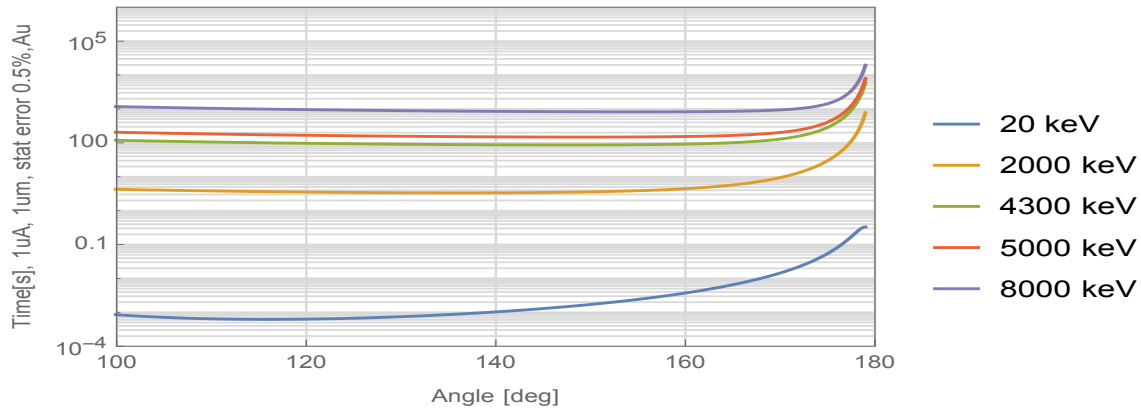

(c) The duration needs for polarization measurement with 0.5% error.

Figure 6.222: Mott polarimeter parameters.

High Voltage Mott Polarimeter

In the baseline design, the Wien filter is not incorporated into the pre-injector. The electron spin direction is parallel to their velocity. In order to measuring the polarization, the beam needs to be kicked out from the pre-injector and passed through a spin rotator to rotate the spin from longitudinal to transverse. The high voltage Mott polarimeter will be placed before the bunching section where the electron beam energy is about 300 keV. At higher energy it would be difficult to rotate the spin by electric fields, and the Sherman function would be lower. Thus, the polarimeter beam line (shown in Figure 6.223) begins at a 12° spectrometer dipole magnet that bends the electron out from the main beam line. A short length of beam pipe transports these electrons from the dipole to the polarimeter. A pair of X/Y steering coils and a vacuum isolation valve are interlocked along this beam pipe.

An adjustable collimator is located at the entrance of the polarimeter, used to define the polarimeter acceptance for the incident electrons. After the spin rotator, the electron beam will scatter off a gold target foil and then pass through a collimator towards the detectors. The detector acceptance for the scattered electrons is defined by the conic apertures in the collimator. At the end of the beam line, a dipole magnet and beam dump are used to suppress background from scattered electrons and gamma radiation.

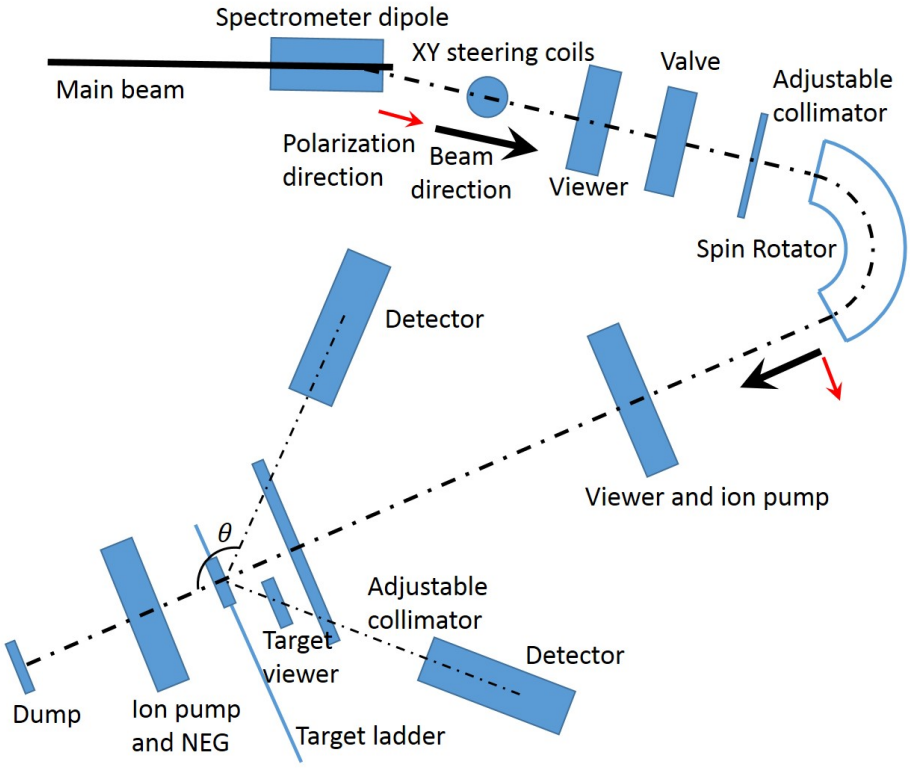

Figure 6.223: Layout of the Mott polarimeter beam line.

Spin Rotator Design

The precession of the spin vector $\vec{s}$ of a particle with mass m, velocity $\vec{v}$ and charge Ze is described by the Thomas-BMT equation. The high energy electron beam requires a dipole to rotate the electron spin direction. For electrons with a few hundred keV, a static electrical field can be used for rotating the electron spin direction.

For an electrical field, the rotation angle φ for the spin direction around the beam axis and the rotation angle ϕ for velocity (or beam axis) are described by

$$\varphi = \frac{Ze(G\gamma^2 - G - 1)}{mc^2(\gamma^2 - 1)} \int E \, \mathrm{d}l \tag{6.30}$$

$$\phi = \frac{Ze\gamma}{mc^2(\gamma^2 - 1)} \int E \, \mathrm{d}l. \tag{6.31}$$

With 300 keV beam, $\gamma = 1.587$. Accomplishing the $\varphi = 90^\circ$ spin rotation requires deflection of the electron beam by $\phi = 143^\circ$, which is produced by $\int E \, \mathrm{d}l = 1.22 \times 10^6 V$.

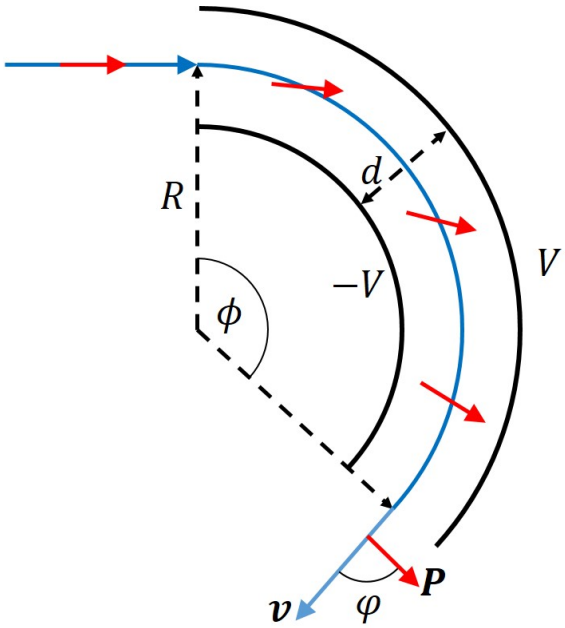

Figure 6.224: Electron beam trajectory and spin precession in electrostatic field of the spin rotator.

The top view of the spin rotator is illustrated in Figure 6.224, which shows the electron beam trajectory and spin precession in the electrostatic field. In the spin rotator, the electrostatic field is $E = 2V/d$, and the electron beam trajectory length is ϕR, thus

$\int E\,\mathrm{d}l = 2V\phi R/d$. The expression for the electrode voltage can be obtained by

$$V = \frac{\gamma^2 - 1}{\gamma}\frac{mc^2}{e}\frac{d}{2R} \tag{6.32}$$

For 300 keV beam energy, $\gamma = 1.587$, thus $V = 244.513\frac{d}{R}[\mathrm{kV}]$. For typical dimensions $d = 10\,\mathrm{cm}$, and $R = 1\,\mathrm{m}$, the voltage applied to the bending plates will be $\pm 24.4\,\mathrm{kV}$.

Design for scattering chamber

The calculated Sherman function and differential cross section for scattering with gold nuclei are shown in Figure 6.221. The detectors are installed at the scattering angle with maximum Sherman function. For a kinetic energy of the electron beam of 300 keV, the scattering angle at the maximum Sherman function is $\theta = 136^\circ$, with the maximum Sherman function being $S(\theta) = 0.4665$.

This Sherman function $S(\theta)$ is only known for single scattering, however the practical Sherman function S_{eff} is always smaller than $S(\theta)$ because of the effects of multiple scattering in the target foil which is sensitive to the thickness of that foil. Thus, the practical effective Sherman function is also a function of the thickness of the target foil.

The effective Sherman function is determined in three steps:

1. Determine the theoretical Sherman function $S(\theta)$ for the single scattering process;
2. Correctly measure the asymmetry for all targets with different thickness by achievement of pure energy spectra;
3. Extrapolate the foil thickness to zero to compare with $S(\theta)$.

The detector count rate R is evaluated by

$$R(\theta) = I(\theta)\rho_{\mathrm{Au}} d_{\mathrm{foil}} \frac{N_A}{M_{\mathrm{Au}}}\frac{I_{\mathrm{beam}}}{e}\Delta\Omega. \tag{6.33}$$

Here ρ_{Au} is the density of gold, d_{foil} is the thickness of gold foil,N_A is Avogadro constant, M_{Au} is the Molar mass and $\Delta\Omega$ is the beam incident solid angle. The time needed to measure beam polarization P to a statistical error of $\Delta P/P$ is evaluated by

$$T = \frac{2N}{R} \approx \frac{1}{2R(\Delta A)^2} = \frac{1}{2R(S(\theta)\Delta P)^2}. \tag{6.34}$$

For $\Delta\Omega = 0.18\,\mathrm{msr}$, $R(136^\circ) = 1.69 \times 10^3\,\mathrm{Hz}/(\mathrm{nA}\cdot\mu\mathrm{m})$, and the corresponding count time $T = 1.36\,\mathrm{s}$ for $\Delta P = 0.1\%$ (msr is mill-steradian).

6.8 Controls System

6.8.1 Controls Overview

The EIC facility is being built as a combination of a large portion of the existing RHIC facility and new construction. The control system for EIC provides integration of all instrumentation as well as the tools required to support all phases of the project. The instrumentation integration must support high speed, tightly synchronized instrumentation, industrial instrumentation, electromechanical systems, and the global systems required to integrate all systems. The tools must provide support for facility wide hardware systems, configuration data management, prototype development, integration, test, commissioning and operations.

Controls provide interfaces with all groups that operate and maintain equipment within the EIC architecture. Controls is directly responsible for the network, synchronized timing and data, and machine protection. Industrial I/O integration, typically PLC or serial devices, may be provided by either the control group or the subsystem groups. The network includes all data transport in the Supervisory Control and Data Acquisition (SCADA) layer, integration of network-based devices into an instrumentation network and point to point networks for communication between FPGA based devices as well as the fiber distribution to support these systems. The control system includes the personnel protection systems will be modified and extended for EIC.

EIC controls must provide software to support construction, installation, integration, commissioning, automation and operations throughout the lifetime of the EIC project and operations. This includes the management of configuration data, integration of commercial and lab developed equipment, transport and aggregation of instrument and computed machine parameters, real time presentation of data, management of archived data and an Application Programming Interface for operations and physicists to develop control and analysis codes for commissioning, operation and machine studies.

The conceptual design for a control system is based on the needs of the project and the available technology. At conceptual design, these needs are not fully formed and thus the design depends heavily on experience. Trends in both hardware and software technology evolve as well. The present plans and cost estimate for the EIC are based on technology that is available today. These designs are based on the use of the RHIC control systems software infrastructure. Consideration will be given to trends throughout the accelerator community that include development of instrumentation, SCADA systems, and data management tools. Final decisions will be made later in the design process and will be based on consideration of requirements, performance, robustness, scalability, flexibility, maintainability, cost efficiency and consistency.

6.8.2 Controls Hardware

Network and Fiber Optic Infrastructure

The EIC will present our current network system with unprecedented bandwidth and speed requirements. This has compelled the consideration of new approaches. We are presently considering a Synchronous Optical NETwork with Synchronous Digital Hierarchy ring topology to meet the needs. This format is well suited to handle the large number of cameras and high-speed orbit feedback systems planned for the EIC. A new Sonet/SDH router will be installed, and multiple packet types will be framed and distributed throughout the EIC. Other technologies will also be considered, to ensure efficient, dependable, and cost-effective networking systems, including implications for long term support and maintenance. A new expanded fiber optic infrastructure will be required for the EIC as well, not only to handle the distributed Sonet/SDH network, but for all our proprietary timing and data links, serial communications of various kinds, timing signals, etc. This necessitates the pulling of new trunk lines, and the installation of fiber patch panels (MIC boxes) as well as new fiber optic transceivers. The new fiber infrastructure will be distributed throughout the EIC infrastructure, including the tunnel, alcoves, and existing as well as new service buildings.

Personnel Protection System

The EIC Personnel Protection System (PPS) will be comprised of the following major components:

1. Allen Bradley Safety PLC Systems, two separate redundant divisions (“A” and “B”)
2. Fiber optic cable network for I/O and auxiliary equipment
3. EIC PPS components and associated cables

The “A” and “B” division PLC systems will each use different PLCs and will be programmed by different engineers to help ensure they will be truly redundant, and without the possibility of common errors. Both systems will run on individual private subnets, and both will be backed up by separate Uninterruptable Power Supplies (UPS). As with all personnel safety systems operated by BNL C-AD, this will be a Q.A. category A-1 system. The Radiation Safety Committee will determine system requirements.

Proprietary Links

Timing and data information is distributed throughout the EIC facility via proprietary data links, such as the Event Link, Real Time Data Link, Reset Link, and Beam Synchronous Link [355–357]. These links are used for purposes such as synchronization of equipment control and data collection, time stamps, real time data processing, and providing beam

position information. New Beam Synchronous links will be required for both the RCS and Storage Ring. Plans call for the use of an off-the-shelf solution built by Micro-Research Finland, currently used with great success at the NSLS-II facility. The timing generator and receiving boards will be housed in VME64X chassis and interconnected with fiber optic cables. The RCS and Storage Ring will also require their own Event Links and Real Time Data Links. These links will be combined into one high speed operations link. This will reduce the associated infrastructure, such as separate fibers and fanout boxes, and will also reduce the number of connections necessary at the various control platforms. All new hardware designs will be compatible with the high-speed link.

SoC Platform

There are multiple areas within the EIC that will require customized hardware that can be configurable to provide unique I/O sets, high speed processing, and fast data throughput. We are developing a stand-alone platform based on a SoC (System on a Chip). The device we are utilizing is a Xilinx part called ZYNQ. The ZYNQ comes with different levels of I/O and processing speeds. This platform will nominally be housed in a 3-U chassis and can be configured with a suite of analog and digital I/O, depending on the requirements. Furthermore, operational firmware can be customized and downloaded remotely to allow for complete flexibility in order to address changing requirements. It will have a high-speed network connection and interface with all Control proprietary links. The plan is to use this platform for complex timing requirements, real-time processing, feedback systems, or anything requiring custom controls. Custom timing needs, small MPS systems, distributed quench detection systems, power supply feedback requirements, and more, are all candidates for this platform.

Power Supply Interface

Current plans call for over two thousand power supplies to be controlled for the EIC. Discussions with the different power supply groups, the need to save space, and economic considerations have led us to the development of several variants of a new Power Supply Interface design (PSI). The new PSI will consist of a master and slave configuration. A PSI master is a derivative of the SoC platform and will control multiple slave units. The slaves provide the actual interface to the power supplies. Many power supplies will have an SFP (Small Form-factor Pluggable) interface, which will be addressed by a type 1 slave. Others will utilize a standard analog reference, calling for a type 2 slave. Working with vendors, some will be able to interface directly to a PSI master using the fiber optic link and its own regulator. Nominally, one PSI master will control up to 32 or more supplies. Resolution and speed requirements have not been finalized, but current PSI plans allow for 18 bits of resolution and update rates of up to 100KHz. The PSIs will return the status and readbacks from each power supply.

Instrumentation Support

Controls hardware provides the conduit for many of the Instrumentation signals into the Controls infrastructure for viewing, processing, and archiving. The BPM electronics used by the Instrumentation group are a VME style design. One board will handle one 4-channel BPM. A 6U Eurocard chassis with a customized VPX type backplane will house up to 15 boards. Each chassis will also house a custom timing board, which will interface to the Beam Synchronous link and distribute the timing signals over the backplane to the electronics boards. All other Instrumentation support will be in the form of standard VME chassis. Each chassis is equipped with a Front-End Computer (FEC), and various in-house designed boards as well as off-the-shelf digital and analog modules. Support is provided for devices such as ICTs, Faraday Cups, FCTs, DCCTs, Profile Monitors, slit scanners, wire scanners, cameras, IR diagnostics, polarimeters, beam loss monitors, etc.

Equipment Protection

The RCS and ESR will have machine protection systems based on the Beam Permit system currently in use in RHIC [358,359]. It is distributed around the entire ring and consists of a master module and multiple slaves. The master initiates a permit by generating a 10 MHz carrier that propagates through each slave, until it finally returns to the master, at which point a permit is established and beam can be established. Each slave and master have multiple inputs that can be used to disrupt the permit upon a fault condition, at which point the beam is aborted.

The laser/gun area and the hadron electron cooling area have been identified as needing machine protection systems. These will be developed for each area using an SoC Platform.

The ESR, IR, and AtR to Blue Transfer Line have been identified as needing a quench detection system. Each will be based on the updated RHIC QDS currently being developed. It consists of a master unit, based on the SoC platform, communicating with a slave unit that resides in a Eurocard chassis. Up to 9 special-purpose ADC cards reside in each chassis, depending on the number of magnets being monitored.

Environmental Monitoring

Environmental monitoring consists primarily of collecting building temperature and humidity data, as well as equipment temperatures. Some of the data will come through deployed VME chassis. Other data will be obtained through proprietary 1-Wire systems, or small devices that interface through Ethernet and are linked to an environmental server with custom software.

6.8.3 Controls Software

Equipment Interface Software

The EIC control system software will support interfaces to a broad range of accelerator equipment with a variety of hardware interfaces. Though we will actively encourage the use of common equipment interfaces, we anticipate the need to support equipment interfaces of many types. Equipment interfaces in the existing RHIC control system, for example, include VME-based interfaces, direct ethernet interfaces, ethernet to GPIB or serial interfaces, and SoC/FPGA interfaces [315, 360, 361]. The equipment interface layer of the control system provides a common interface to control system clients for setting, getting, and continuous monitoring of all controls equipment [362–366]. It may be possible to reuse existing equipment interface software for some systems. New custom equipment interface software will be needed for systems including the new beam sync link and new power supply interfaces. Some special equipment control requirements are presented by the need for synchronized, reproducible control of large numbers of power supplies in the ESR and RCS. We foresee no difficulty in meeting all known equipment control requirements. We anticipate the widespread use of server layer software to manage the control and monitoring of EIC accelerator equipment. The use of "managers" in the RHIC control system has proven effective for coordination of measurement or control processes and for data correlation and distribution. We expect that this server layer software will be particularly important in the EIC environment to automate the synchronized operation of the full EIC complex and to manage the flow of traffic from data intensive systems. Application level software development is also simplified by the implementation of complex data processing and control algorithms at the server level where the results can be made available as a shared resource.

Operator Interfaces

The EIC control system will provide a set of generic application interfaces to allow operators to perform many control system tasks without the need for custom application code. The set of generic operator interfaces provided will, at a minimum, match the functionality provided in the existing RHIC control system. These operator tools include a table-based tool for viewing and editing all control system parameters, a synoptic display tool for monitoring and control of accelerator systems, tools for graphic display of both live and logged data, and tools for the creation and execution of operational sequences. In all cases, configuration of these tools can be managed directly by operations [367, 368].

Custom Application Interfaces

Custom application software will be developed to support selected accelerator subsystems or operational processes. These applications may provide specialized graphic displays of accelerator measurements or user interfaces that guide operators in making decisions

about accelerator control. Custom applications will be built in close collaboration between controls personnel and physicists, operators and support groups. Controls personnel will support an application development environment and a set of application development toolkits (both in-house and 3rd party). These toolkits will support functionality such as communication with control system devices, access to control system services, and the construction of graphical user interfaces. The existing RHIC control system provides extensive toolkits for C++ and Java development but also provides support for applications development in python and Matlab [369]. Support is also provided for mobile and web-based application development. Strategies for application development will be discussed as the EIC project moves forward.

System Services

EIC controls software will be supported by an extensive infrastructure of system services. These will include naming services (to clearly identify control points), database services, alarm and messaging services, general data logging, logging of all changes to control system parameters, system monitoring including automatic recovery from failures, and electronic logbook services. The EIC system service layer is likely to grow from the system service layer of the existing RHIC control system, which supports all of the services identified above. Historically, the RHIC controls service layer software has been written for directly connected C++ and Java desktop clients. More recently, a service layer has been developed that uses the HTTP network protocol and presents a REST (Representational State Transfer) interface to applications [370]. We anticipate the use of this approach in the EIC to allow applications to run on a variety of platforms and to be built using a variety of development tools and languages.

Data Management

A data management plan will be developed for the EIC to ensure that all data necessary to support and document the running of the EIC accelerator complex is reliably stored and made available to EIC operators and engineering and scientific staff in a manner that effectively supports all anticipated uses of the data. We anticipate that different categories of EIC accelerator data will be identified and that requirements for reliability, timeliness of data access, and length of data preservation may differ for these categories of data. Different technical solutions may be employed to satisfy the requirements for different categories of data. Some subset of EIC accelerator data will certainly require high availability data storage with full redundancy and automatic failover for all components. The specific technological choices for data storage will depend on the state of storage technology when the EIC Control System is built. Appropriate disaster recovery plans will be defined for all EIC data management systems. For critical data systems, the goal will be to provide fast, automatic failover to redundant systems. When that is not possible, failover procedures will be well defined with the duration and the impact on EIC operations clearly stated.

Software Quality Assurance

All control system software will be maintained in a revision control system. The history of changes for any software module is available for review. New versions of software will be released using well defined release procedures that capture fallback software versions and capture information about the reason for the release and the testing performed. This is in keeping with standard practices for the existing RHIC control system. The development of software requirements and software designs for EIC controls will be well documented.

6.9 Instrumentation

6.9.1 EIC Instrumentation Overview

The EIC beam instrumentation will be used to ensure expedient commissioning, optimization and performance monitoring. Correction algorithms for optimizing beam parameters and beam-based feedback for guaranteeing reproducibility will use input measurements from the various diagnostics. The diagnostic designs are largely conventional with demonstrated implementation in existing accelerators at BNL and elsewhere. One unique design, described in Section 6.9.2, pertains to a new bunch crabbing angle monitor for the hadron beam.

The stages of accelerator development to be supported by the instrumentation are:

1. Injection and acceleration of electron beams to full energy in the RCS, transfer to and storage in the ESR.
2. Gradual increase in the number of electron bunches stored in the ESR with total current sufficient for establishing collisions.
3. Injection and acceleration of modest-current hadron beams in the HSR.
4. Establishing collisions between electron and hadron beams.
5. Establishing and monitoring collisions of full-intensity electron and hadron beams.
6. Routine monitoring of overall accelerator performance.

The beam instrumentation requirements in all EIC accelerators and transport lines have been designed to ensure the successful execution of these programmatic stages.

6.9.2 Interaction Region Instrumentation

The instrumentation in the IR regions will assist in establishing and maintaining optimum collision configuration, protecting critical devices and monitoring beam parameters. The

electron and hadron beam collide at the interaction point with a 25 mrad crossing angle. The IR is equipped with critical devices including superconducting magnets for final focusing, strong dipole magnets for separating the beams and crab cavities for compensating the crossing angles.

IR Orbit Feedback

To maintain luminosity, a local IR orbit feedback system controlling both beams will be implemented to compensate for ∼10 Hz variations in the hadron ring arising from triplet magnet oscillations and excitations in the range from 2 to 30 Hz in the electron storage ring. Four dual-plane beam position monitors (BPMs), two for each beam, will be installed near the interaction points. For fast correction, 12 air-core steering magnets (8 for the vertical plane and 4 for the horizontal plane) will be used in the electron storage ring. Of the 8 magnets, 4 provide position and angle trajectory control and the remaining 4 magnets cancel the dispersion introduced by the trajectory correction. Four vertical steering magnets, of the same type as the magnets used in the existing RHIC 10 Hz feedback system, will be designed for the hadron ring for each IR. At the colliding beam experiment, the local IR orbit feedback will be designed to optimize luminosity [371] or beam trajectories [372]. Optimizing luminosity is straightforward however it can lead to momentary luminosity reductions as the orbits are varied to determine the trajectories required to maximize luminosity. An advantage of an alternative method of maintaining maximum luminosity by controlling the beam trajectories through the IR is that the small luminosity losses inherent in the first method are avoided.

Loss Monitors

Beam loss detectors will be installed at radiation-sensitive devices and at potential high-loss regions in the IRs to monitor both the hadron and electron beams including at the superconducting crab cavities, the superconducting magnets, the Roman pot detectors and near the experimental detectors.

Crabbing Angle Measurements

The electron and hadron bunches, colliding with a crossing angle of 25 mrad, will be rotated horizontally by superconducting crab cavities to compensate the loss of luminosity due to the crossing angle inherent in the geometry of the IR. The crabbing angle of the bunches will be measured to setup and monitor these crab cavities. Even though the crabbing angle is confined between the cavities on either side of the IR during normal operations, the measurement can be carried out at a place with proper phase advance in other regions of the rings.

Crab cavities placed on one side of the IP will perform the rotation of bunches, and crab cavities on the other side will restore the nominal orientation. To setup the crab cavities,

the crabbing angle will be measured for the following cases: with cavities off as a baseline, with cavities at only one side of the IP turned on, and with cavities on both sides of the IP turned on.

Hadron beam A tilted bunch traversing a button beam profile monitor will produce signals on opposite pickup electrodes that will have different degrees of distortion depending on the tilt angle [373]. In particular, the zero-crossing time difference between the two signals will be approximately proportional to the tilt angle. Simulations were performed to study this effect as a possible diagnostic tool for measuring the crabbing angles of hadron beam for the EIC (see Figure 6.225).

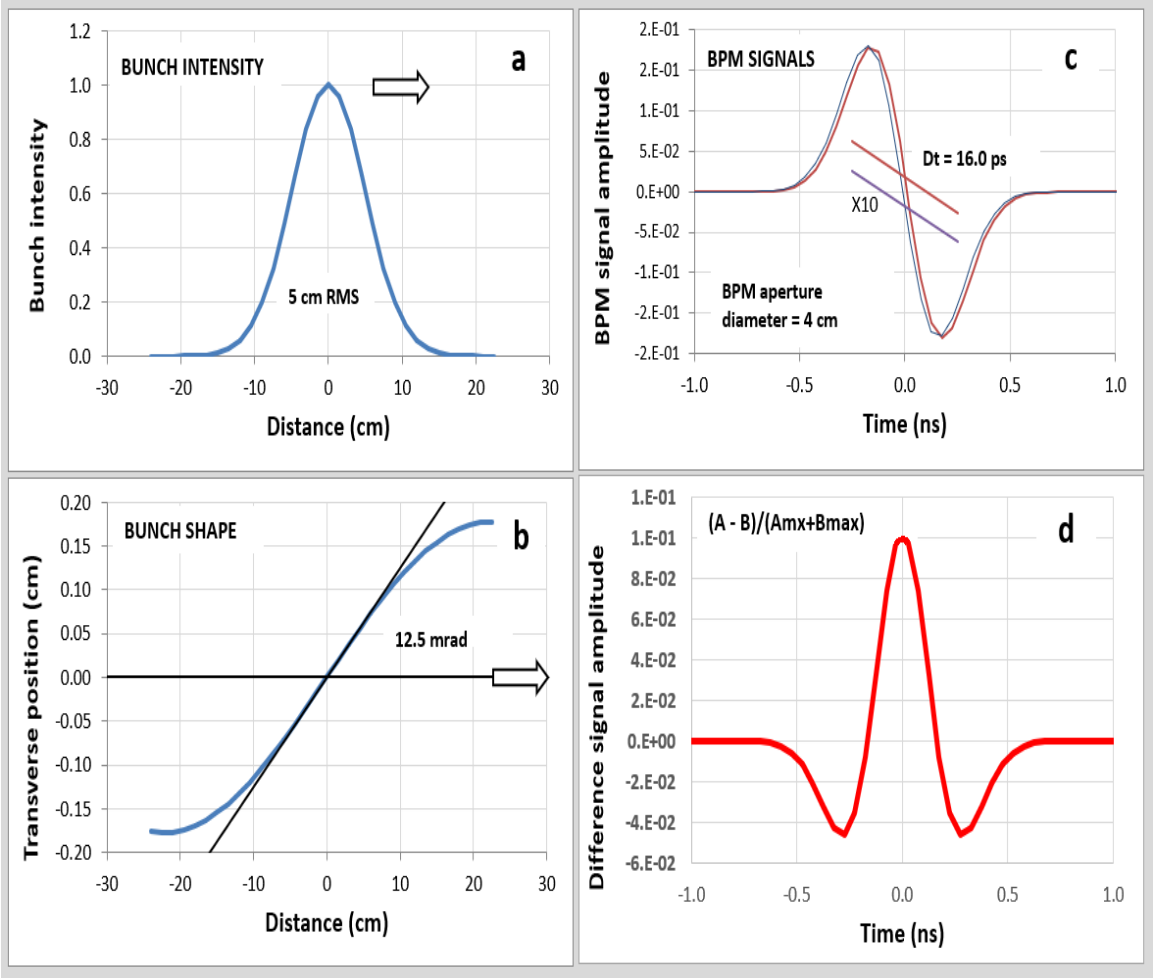

Figure 6.225: (a) Bunch intensity as function of axial position for a 5 cm RMS bunch. (b) Transverse coordinates of the center of a crabbed bunch as function of axial position for a crabbing cavity frequency of 394 MHz. (c) Signals induced on opposite small pickup electrodes of a 4 cm diameter BPM by the bunch described by Figures (a) and (b). (d) Difference signal obtained by subtracting the two signals of Figure (c).

The difference signal shown in Figure 6.225d is approximately proportional to the crabbing angle and can be used for measuring and monitoring that angle. The sensitivity of the method is strongly dependent on the BPM diameter. The diameter assumed in this simulation was 4 cm. A smaller diameter would be preferable.

Electron beam The electron beam crabbing angle will be monitored using a streak camera imaging synchrotron light generated at a location outside of the IR with minimal horizontal dispersion and optimal crabbing angle phase advance. The streak camera detects a horizontal beam profile which is tilted from vertical by an amount proportional to the crabbing angle when only the crab cavities on one side of IP are turned on (see Figure 6.226).

The tilt angle will be tuned to zero using the streak camera as the phase of the crab cavities on the other side of the IP is optimized. The optimal phase advance from IP to the SLM will be a multiple of π for maximum sensitivity to the tilt angle in the x-z profile.

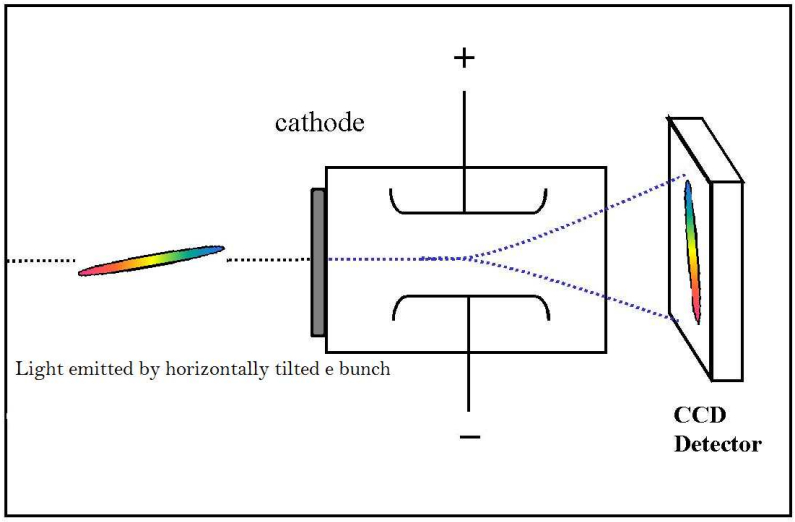

Figure 6.226: Conceptual view of a streak camera measurement of the electron bunch crabbing angle appearing as a tilt of the beam ellipse from the vertical axis.

6.9.3 Electron Storage Ring Instrumentation

A fast current transformer (FCT) will be used to monitor the fill pattern. Redundancy could be provided using the sum signal of a bunch-by-bunch BPM. A DC current transformer (DCCT) will be used to monitor the average current and beam lifetime. Stripline kickers will be installed in both planes for two purposes: to introduce free betatron oscillations of a single bunch for tune measurements with BPMs recording turn-by-turn and to clear ions in the abort gap. To monitor and fine tune injection matching, four BPMs (two each at dispersive and non-dispersive locations) will be used to monitor betatron and synchrotron

oscillations of the first injected bunch. Beam loss monitors that may include Pin diode style BLMs [374] providing high time resolution measurements will be placed at radiation-sensitive devices, such as near the injection kickers, the RF cavities, the collimators, etc and the physics detectors.

Table 6.88: List of electron storage ring diagnostics types and quantities.

Types	Quantity
Beam position monitor	494
Fast current transformer	1
DCCT	1
Synchrotron Light Monitor	2
X-ray Pin-hole	1
Polarimeter	1
Tune meter	1
Longitudinal bunch-by-bunch feedback	1
Transverse bunch-by-bunch feedback	1
Slow orbit feedback	1

Orbit Feedback for the EIC Electron Storage Ring

To maintain luminosity and spin polarization, a slow orbit feedback system is needed in the EIC electron storage ring for controlling beam orbit variations. These orbit variations may occur on time scales ranging from sub-seconds to hours with dominant frequency response in the range of DC to $\sim$10 Hz. The sources of orbit variations [375] include diurnal changes, thermal expansion of machine components, ground vibrations, and noise from power supplies and RF sources. To help preserve polarization and stabilize the beams at the interaction point(s), a slow orbit feedback system will be utilized to ensure an RMS orbit stability of less than 10% of the RMS beam size at all locations in the storage ring. The slow ($<$5 Hz) feedback system consists of three major components: beam position monitors, data processors for collecting data and evaluating the corrections and dipole magnets with associated power supplies for implementing corrections. The components for slow orbit feedback will be discussed in the following.

BPMs The slow orbit feedback system will use the (494) BPMs that are located near every quadrupole magnet in the electron storage ring. For slow orbit feedback or orbit correction, the BPMs will deliver average positions data at a 10 Hz rate with a measurement precision of 10 µm. While commercially available BPM electronics (such as Libera [376], used widely at synchrotron light source facilities) can fulfill these requirements, the in-house design

employing a revised version of the existing BNL-designed V301 BPM electronics [377] is a promising cost-saving option. The BPM electronics will be grouped in ∼30 alcoves and the electronics in each alcove will be connected by fiber-optics links in a global ring structure. This network topology [378–380] has been proven to provide efficient communication at light source facilities.

The planned approach for providing beam position monitor electronics is to use a BNL designed digital sampling system similar to the existing second generation (V301) electronics that has been in use in a variety of ion and electron accelerators for a few years. This system will entail a high-speed four channel analog-to-digital conversion section, with a sampling clock driven by a local phase-locked loop (PLL) capable of phase-locking to the accelerator RF frequency. This will allow for digital down conversion and filtering techniques as well as I/Q demodulation if narrow-band processing is desired. It will also be capable of asynchronous or single-bunch sampling where necessary. The exact cutoff frequencies of the analog filters used in the final design will be determined by the desired sampling approach. A few different versions of the board to suit the multiple applications for the RCS, ESR, HSR, etc. are envisioned.

Using an embedded front-end computer running a Linux operating system will allow a variety of software to process the BPM data. Our current software platform supports data delivery to both the existing BNL Controls system and the EPICS accelerator software framework.

Due to the large number of BPMs throughout the EIC complex, a low-cost approach will be utilized when revising our present electronics design. Using a chassis design which can house multiple BPM boards will also save power and space and allow for a quality clock distribution scheme.

Data processors FPGA-based data processors will receive position data from the BPMs, calculate the required corrector currents and send the corrections to the corrector power supplies. Generic processors in use at select light sources, summarized in [381], will be considered for the ESR fast orbit feedback design.

Correctors and power supplies Approximately 200 DC dipole correctors will be used for slow orbit feedback and orbit correction. These dual-plane correctors will be placed next to defocusing quadrupoles to ensure more precise orbit control in the vertical plane as required for maintaining the beam polarization. The orbit correctors and associated power supplies will provide an angular deflection of ∼0.1 mrad at maximum beam energy of 18 GeV. Correctors used in the IR to separate the beams will also be used by the slow orbit feedback; these power supplies are independently specified to provide angular deflections of up to ∼0.3 mrad at full energy.

Storage Ring Synchrotron Light Monitor (SLM)

An SLM imaging visible radiation [382] will be located near a bending magnet in the injection region. A water-cooled, in-vacuum mirror will be used to transport the light out of the vacuum chamber. Several mirrors with good surface quality ($<1/10\lambda$) will guide the light to a remotely located experimental room containing a CCD/CMOS camera, a gated camera and a streak camera.

A GigE CCD/CMOS camera, externally triggerable with exposure times ranging from 10 µs to 5 s, will be used to image the visible radiation. A commercially available gated camera [383] with gate width of <2 ns (compared to a minimum bunch spacing of 8.9 ns) will be used to detect injection oscillations and for beam studies. A streak camera with ∼1 ps resolution will provide longitudinal profile measurements. The streak camera will be shared with the RCS; an optical beamline from the RCS will be used to transport a beam of synchrotron radiation from the RCS bending magnet to the same experimental room as the main storage ring. A position-sensitive photo-diode (PSD) will be used to measure the synchrotron light photon beam centroid position. The electron beam centroid position can be inferred from the measurement to supplement the electron orbit stability measured by the BPMs.

Storage ring X-ray Diagnostic Beamline (XDB)

The XDB beamline [382] will provide a higher resolution (∼5 µm) beam profile measurement, compared with the visible synchrotron light monitors (∼60 µm) which are limited by diffraction. This beamline will also allow independent measurement of the energy spread and horizontal/vertical emittance. A pinhole assembly including tungsten slits will provide sufficient resolution to precisely measure the beam size. Several different size pinholes will be incorporated to allow easy alignment and measurements at different beam currents and energies. The associated imaging systems consists of a scintillator screen, a large aperture lens and camera to provide large depth of field. The XDB beamline equipped with gated cameras may also be employed to provide high resolution turn-by-turn profile measurements.

Bunch-by-bunch Feedback Systems

Both transverse and longitudinal bunch-by-bunch feedback systems are required in the ESR to damp coupled-bunch instabilities [384]. These instabilities, which can limit the maximum beam currents, are excited by the interaction between the intense electron bunches with the surrounding environment. The resulting "wake field" [385] acts back on the bunches which in turn excites betatron and synchrotron motion. The four main sources [386] of coupled-bunch instabilities are: high-order modes generated by beam passing through resonating cavity structures, interaction with trapped ions, resistive wall impedances produced by the beam interacting with the vacuum surface and the geometric

impedance generated when beam is acted upon by the wakefields generated by discontinuities in the vacuum chambers.

The bunch-by-bunch feedback system consists of three major components [386, 387]: a detector that detects the transverse/longitudinal oscillations of each bunch, a signal processing unit that generates the correction signals and a kicker powered by power amplifiers that applies corrections. The ESR beam position feedback design will be based on experiences at other facilities [388–390]. The design requirements of the components for ESR transverse and longitudinal feedback systems are discussed in the following.

Detectors for transverse bunch-by-bunch feedback A beam position monitor (BPM) with good sensitivity will provide precision measurements of the transverse beam oscillations. A BPM with four 6 mm buttons is under design. The BPM will be placed at a location with large β-function and zero dispersion to ensure large signal amplitudes without dispersion contributions. The detection frequency will be $3f_{\mathrm{RF}}$ for good signal-to-noise ratio. A dynamic range of 50 dB is required for a 1 mm measurement range and 3 µm measurement resolution and low RF front-end noise [391, 392] will be ensured to achieve that. The signal contributions from the average beam position will be removed and the revolution frequency lines will be filtered using notch filters [387].

Detectors for longitudinal bunch-by-bunch feedback Bunch-by-bunch BPM sum signals will be used to provide phase measurements of bunches. The phase error signals will be generated by mixing the BPM response with the local oscillator shifted in phase by $\pi/2$ [386]. Alternatively, a BPM at a dispersive location can be used to measure the energy offset by measuring the horizontal beam offset.

Signal processing unit FPGA-based digital signal processing [387, 391] is being considered for the EIC transverse and longitudinal feedback systems. The options available include both commercial products and in-house design. Three digital processor boxes, Instrumentation Technologies, DimTel and Spring-8's design [393–395], are also being considered.

Transverse kickers Stripline kickers, with high shunt impedance, will be used for each transverse bunch-by-bunch feedback system. A matching of the characteristic impedance with the load impedance (50 Ω) is necessary to avoid reflection of power back to the power amplifier. The beam impedance of the kicker should not be a significant contribution to the impedance budget of the machine. The shunt impedances [391] are shown in Figure 6.227 for kickers of 0.8 and 1 m length. The length of the kicker is chosen as 1 m, which is relatively long for high shunt impedance and less than half of the bunch spacing (2.66 m) so the kicks on bunches are well separated.

The required power to damp the transverse coupled bunch instability is given by [386, 388]

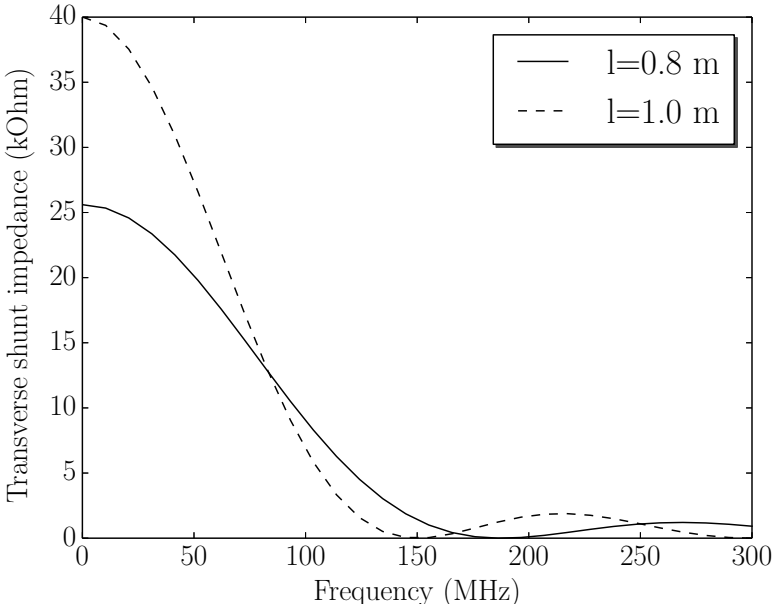

Figure 6.227: Shunt impedance of transverse kickers of 0.8 and 1 m length.

$$P = \frac{2}{R}\left(\frac{T}{\tau}\frac{E_0}{e}\frac{A_{\max}}{\sqrt{\beta_{\mathrm{m}}\beta_{\mathrm{k}}}}\right)^2 \tag{6.35}$$

where R is the shunt impedance of the transverse kicker, T is the revolution time, τ is the growth time of transverse coupled-bunch instability, E_0 is the beam energy, $A_{\max}$ is the maximum position oscillation amplitude and $\beta_{\mathrm{m}}/\beta_{\mathrm{k}}$ is the β-function at the BPM/kicker in the horizontal (h) or vertical (v) plane. With R =15000 Ω, $E_0 = 10\,\mathrm{GeV}$, $\tau = 40 * T$, $T = 12.8 \times 10^{-6}$s, $\beta_{\mathrm{m},h} = 40$, $\beta_{\mathrm{m},v} = 40$, $\beta_{\mathrm{k},h} = 40$ and $\beta_{\mathrm{k},v} = 20$. The required power is shown in Figure 6.228 as a function of the maximum position oscillation amplitude. To damp 0.3 mm beam oscillation, 1 kW power is needed for the vertical feedback system and 500 W for the horizontal system.

Longitudinal kickers A cavity is usually used as a longitudinal kicker [386,396] because of the high shunt impedance and the small size. The longitudinal broadband feedback kicker developed at DAΦNE [397] and used at many other accelerator laboratories will be adopted. The bandwidth of the cavity must be wider than 60 MHz (half of the bunch repetition frequency f_b) to cure all coupled-bunch instability modes. The operating frequency range is usually placed on one side of a multiple of the RF frequency f_{RF}, for example from $2f_{\mathrm{RF}}$ to $2f_{\mathrm{RF}} + 1/2f_{\mathrm{b}}$. The baseband signal from the digital-to-analogue converter (DAC) has to be translated to overlap the kick shunt impedance spectrum [396]. The power re-

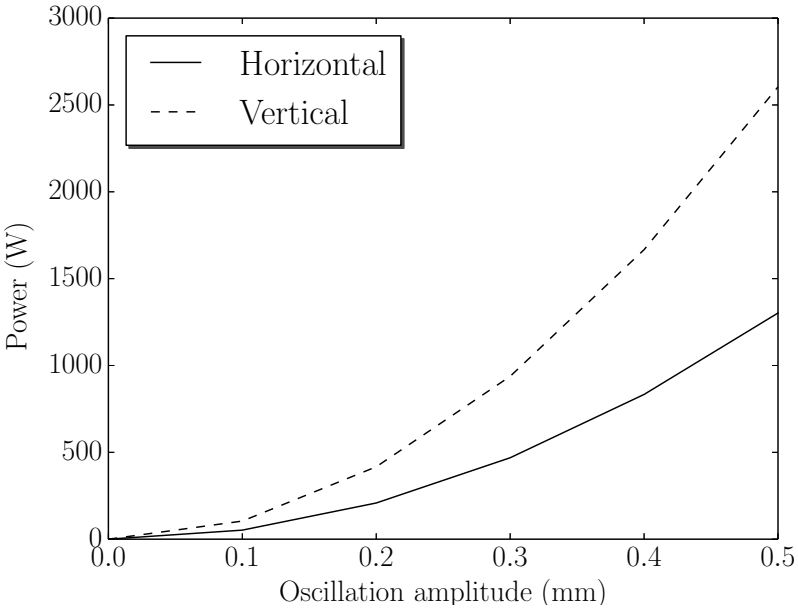

Figure 6.228: The required power for the transverse feedback systems to damp the coupled-bunch instabilities.

quired to damp a longitudinal oscillation [386] is given by

$$P = \frac{2}{R}\left(\frac{\omega_s}{\omega_0}\frac{E_0}{e}\frac{\phi_{\max}}{\alpha f_{\mathrm{RF}}\tau}\right)^2, \tag{6.36}$$

where R is the shunt impedance of the longitudinal kicker, ω_s is the angular synchrotron frequency, ω_0 is the angular revolution frequency, E_0 is the beam energy, α is the momentum compaction factor, f_{RF} is the RF frequency, τ is the instability growth time and $\phi_{\max}$ is the maximum phase oscillation amplitude.

6.9.4 Hadron Ring Instrumentation

Most of the existing RHIC Yellow ring and some of the Blue ring will be used as the HSR for the EIC with some modifications. The existing instrumentation will be upgraded and new diagnostics devices will be included in the new HSR configuration to allow for operation at increased beam intensity and to accommodate the diagnostic requirements including up to 12 times more bunches and up to 8 times shorter bunch length. The increased beam intensity places higher demands on instrumentation used for machine protection. The following upgrades and new additions to beam instrumentation are envisioned for the HSR.

Beam Position Monitors (BPM)

Particle Studio simulations were performed to estimate the signal voltage and power induced on existing Type-2 and Type-3 RHIC stripline BPMs using the parameters for the first two scenarios of strong hadron cooling with the high divergence configuration listed in Table 3.3. To consider a worst-case scenario with some safety margin, the maximum bunch intensity was increased by 10% in each case and a maximum beam-offset of 17 mm instead of the listed 14 mm was used to include uncertainty in absolute orbit and ∼1 mm for chromaticity measurements. Figures 6.229 and 6.230 show the Type-2 BPM model used and the pickup electrode (PUE) signals predicted by the simulation respectively. Table 6.89 lists the parameters used and the resulting power and maximum voltage values obtained.

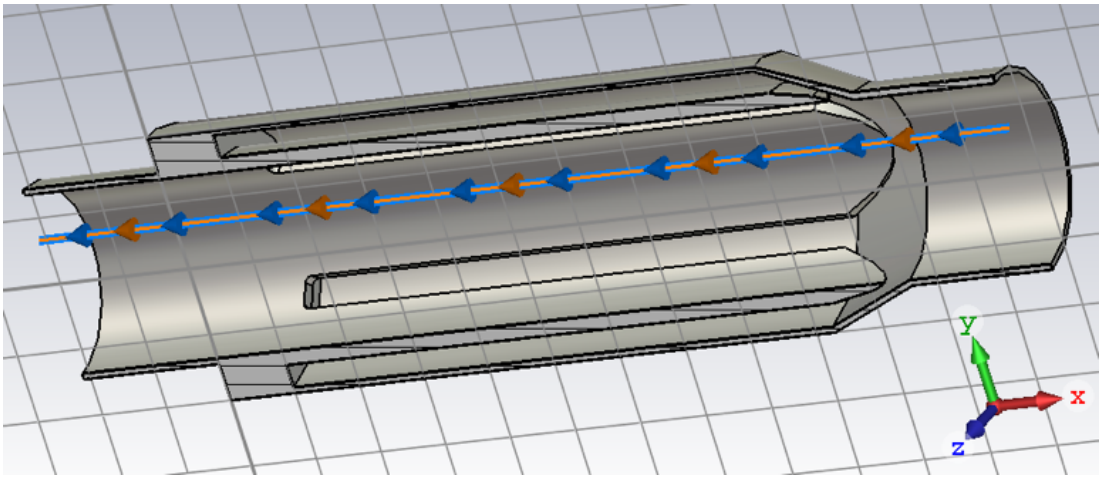

Figure 6.229: Type-2 BPM model used in the PS simulations. The beam is shown at $y = 17\,\text{mm}$.

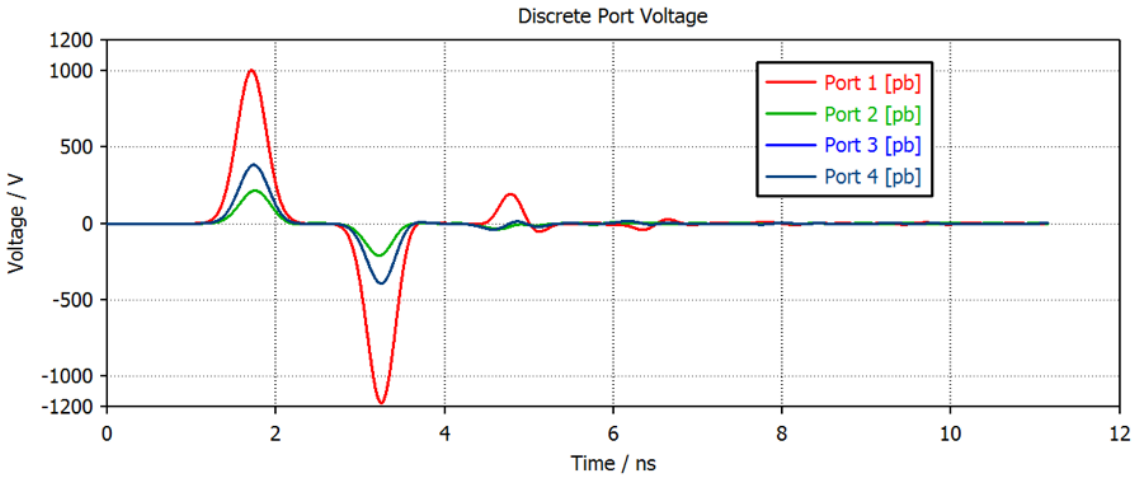

Figure 6.230: Simulated PUE signals for the first case listed in Table 6.89.

For the first case, the maximum voltage exceeds the connector, cable and feedthrough specifications and in all cases the power is too large. In Reference [398], the maximum power into 50 Ω to reach the estimated cable limit was 25 W. While better cables could be used, they will probably not be several times better in terms of reaching a better compromise between low thermal conductivity and low electrical losses. This also excludes the remaining cases. The conclusion is that the two EIC scenarios considered here are not compatible with retaining the original RHIC stripline BPMs.

To overcome these limitations, button BPMs with much smaller surface area will be required to minimize the peak voltages and powers induced by short and intense hadron bunches. Particle Studio simulations were performed using the button BPM design shown in Figure 6.231. The simulated signal voltages for an on-axis beam and a beam with 10 mm transverse offset are shown in Figure 6.232 with beam parameters similar to column 2 of Table 6.89 resulting in acceptable induced voltages (<10 V) and powers (<10 mW).

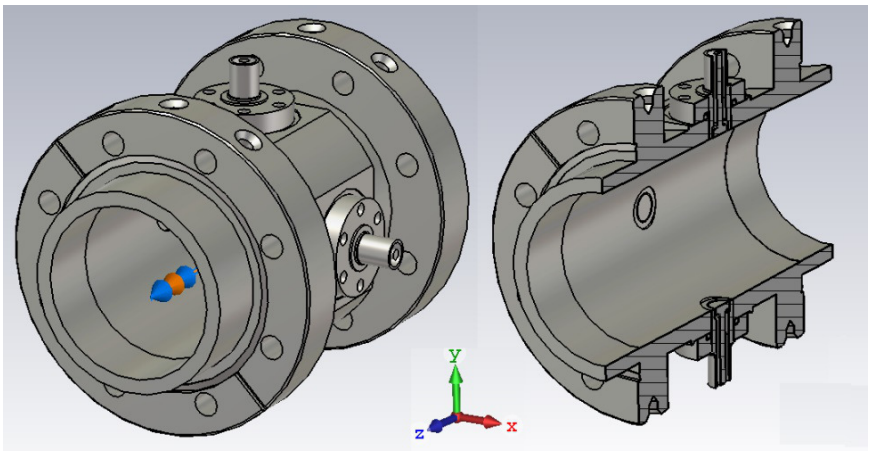

Figure 6.231: Button BPM used in the Particle Studio simulations. The BPM inner diameter is 69 mm and the button diameter is 11 mm. The simulated signals for the case of a 10 mm beam offset are shown in Figure 6.232.

Table 6.89: BPM pickup electrode output voltage and power for different beam parameter sets from Particle Studio simulations with existing Type-2 and Type-3 BPMs.

Parameter	Type-2 BPM		Type-3 BPM	
Bunch intensity [10^{10}]	22	6.6	22	6.6
RMS bunch length [mm]	50	50	50	50
Bunch offset [mm]	17	17	17	17
Number of bunches	330	1320	330	1320
Maximum abs. voltage [V]	1175	353	860	282
Power (into 50 Ω attenuators) [W]	372	134	210	90

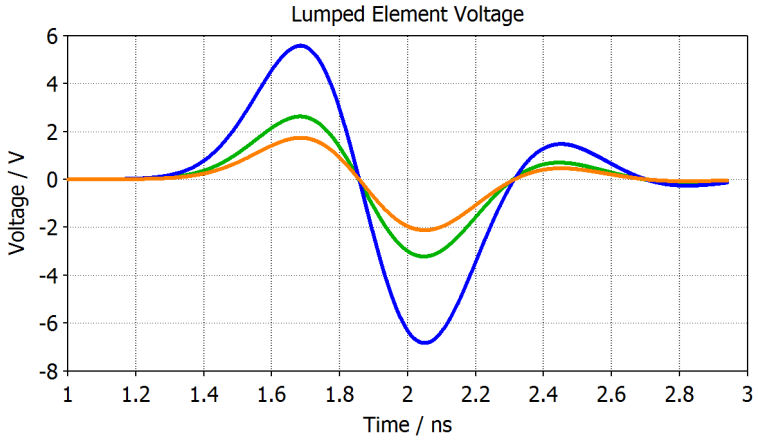

Figure 6.232: Simulated signals from a horizontal BPM button shown in Figure 6.231 for a 5 cm RMS bunch containing 3×10^{11} protons and offset in the x-direction by 10 mm. Green trace middle position, blue +10mm, orange -10mm.

The present proposal is to shield the existing stripline BPMs. The button BPMs will be installed next to the existing stripline BPMs in the HSR. Particle Studio simulations show however that continuous contact to the beampipe at both ends of the BPM shield will be required to avoid beam-induced resonances. Figure 6.233 shows longitudinal impedance curves for various scenarios.

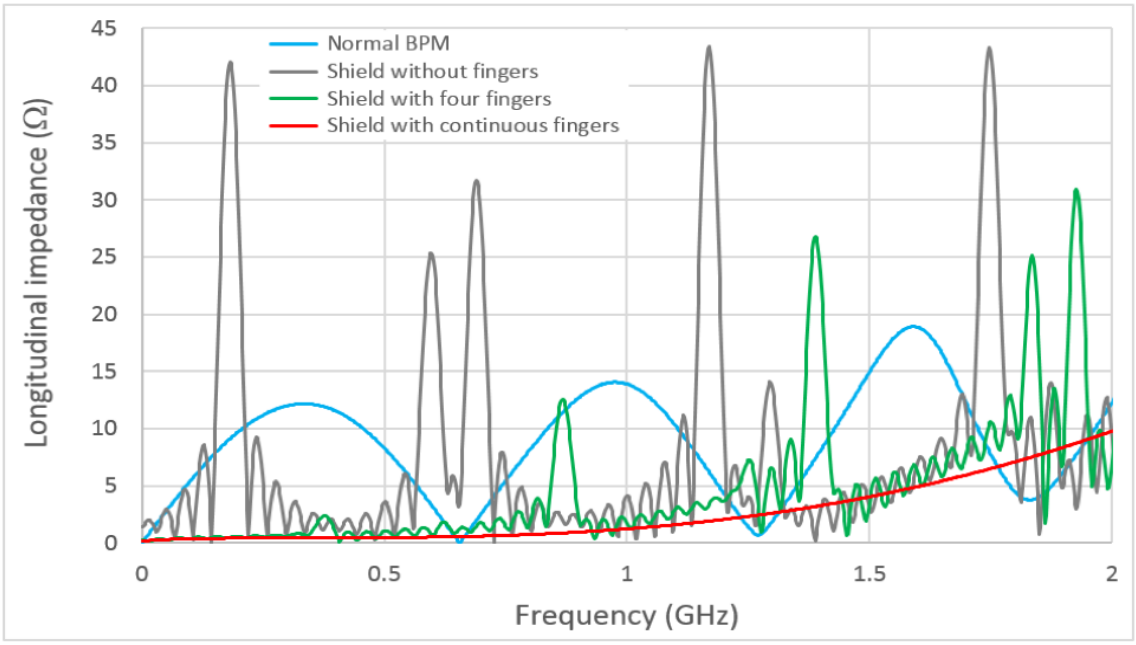

Figure 6.233: Longitudinal impedance of a Type-2 BPM without a shield (Normal BPM) and with various connection scenarios for the end that is not welded. A solid weld (not spot-welding) was assumed at the other end.

BPM Communication Network Upgrade

The BPM communication network will be upgraded using the same techniques developed for the 10 Hz orbit feedback system [399]. The upgraded system integrates a daughter card with the BPM front-end electronics. A 10 GByte copper cable will be used to deliver beam position data from the daughter cards to network switches distributed around the ring and connected with a fiber optic cable. The upgrade will enable fast data delivery and eliminate radiation-sensitive front-end computers (FECs). The bandwidth of the global orbit feedback system using the upgraded BPM communication network will be increased from 1 Hz to 5 Hz.

Ionization Profile Monitors (IPM)

The existing Ionization Profile Monitors (IPMs) [400] will be upgraded and mechanically redesigned to reduce systematic errors. Higher resolution, allowing for measurement of smaller beam emittances, will be achieved with three modifications: the amplitude of the applied sweep voltages will be increased to reduce the transit time of the electrons, the external magnetic fields will be increased to reduce the Larmor radius of the detected electrons and microchannel plate detectors (MCP) with higher spatial resolution will be employed. Contributions arising from space charge effects between the electrons generated by the beam-gas interactions will be reduced as a result of the shorter transit time of the electrons.

Loss Monitors

The existing RHIC argon-filled ion chamber beam loss monitors will not be very sensitive to synchrotron radiation generated by the EIC electron beams. The synchrotron radiation photon critical energy is a typical photon energy such that 50% have lower energy and 50% have higher energy. Calculations show that there are very few photons with 10 times the critical energy. The equation used to calculate the EIC SR photon critical energy is shown below. For the EIC, a beam energy of 10 GeV and the bend radius is 250 m are used. This results in a critical energy of 8.88 keV. This energy is so low that the absorption will be practically 100% in the in the outer radius wall of the vacuum chamber (which is water cooled). Even the tail of the distribution, at $\sim$90 keV will be very strongly attenuated, especially since the radiation is tangential to the orbit.

$$\varepsilon_c\,[\mathrm{keV}] = 2.22\frac{E^3\,[\mathrm{GeV}]^3}{\rho\,[\mathrm{m}]} \tag{6.37}$$

Therefore, the existing RHIC ion chamber beam loss monitors will be re-used to measure hadron beam losses and may be re-positioned and/or the detectors will be protected using lead shielding if needed.

Wall Current Monitor

With more beam intensity and with an RMS bunch length at store reduced from 40 cm to 5 cm, a device with a higher bandwidth than what a traditional wall current monitor (WCM) [401] can typically provide is needed to measure longitudinal bunch profiles and to assist RF cavity configuration and gymnastics. An electro-optic type longitudinal detector is planned for measuring the HSR beams. An associated high bandwidth oscilloscope will be procured as well.

Stripline Kickers and Pickups

There are four two-meter long striplines in the hadron ring used for tune measurements, as an abort-gap kicker and injection damper, and as a longitudinal damper. Due to the high bunch peak intensities and corresponding large induced voltages, these will be replaced by kickers with smaller stripline surface area. The Base-band Tune (BBQ) meter pick-up and kicker, and the head-tail pick-up all use the same style one-meter long pick-up/kicker chambers, these will also be replaced.

Schottky Detector

The low and high frequency Schottky detectors deliver non-invasive tune, chromaticity and energy spread measurements [402]. The low frequency Schottky detector that presently uses stripline BPM pick-ups will be redesigned with smaller surface area detectors to better match the HSR beam parameters. The high frequency cavity will be upgraded to a high shunt-impedance design to maximize the signal to noise ratio of the Schottky signal.

High Bandwidth Detectors for Longitudinal Profile Monitoring

New high bandwidth scopes will be used in conjunction with button BPMs for diagnosis of intra-bunch beam instabilities [403] as potentially driven by electron clouds for example. We also plan to implement the methods developed for the CERN SPS [404] with very similar beam and detector characteristic; using an electro-optical longitudinal profile monitor (upgrade of the existing wall current monitor) to detect with higher time resolution the longitudinal profiles of the hadron bunches and potentially the existence of satellite bunches.

Relocation of Instrumentation

To operate at 41 GeV, the hadron beam will be shifted from the Yellow arc to the Blue arc between IP2 and IP12 to match the revolution frequency of the electron beam. Most of

the instrumentation in these two arcs, including the BLMs and BPMs, will remain in place and be re-used. However, the IPMs in these regions will be relocated to measure beams at all energies. Selected instrumentation from the Blue ring will be relocated to desirable locations in the Yellow ring if needed.

New Hadron Beam Instrumentation

Collimators The collimator system in the hadron ring will be re-designed to better match the HSR beam parameters. Beam position pickups can be installed on the jaws of new collimators for precisely monitoring the relative position of the jaws to the beam [405]. This beam position measurement will facilitate automated control of the collimator positions relative to the beam.

Hadron Injection Instrumentation Since the existing hadron injection location at 6 o'clock in the RHIC tunnel does not allow enough space for the required 25 m long kicker (see section 3.4.5), an alternative ∼650 m path will be taken so the beam can be injected into the Yellow ring at 4 o'clock. The existing Y-arc beam line between the RHIC injector and RHIC (AtR) will be extended to cross over the RHIC Yellow beam line at the location of the existing injection kickers, then continue to allow connection and matching to the superconducting Blue ring arc sextant to transport the beam from the 6 o'clock region to the new 4 o'clock injection area. Another new short beam line will transfer the hadron beam from the end of this Blue arc to the Yellow warm section at 4 o'clock.

In order to ensure efficient hadron beam transport from the end of the existing AtR beam line to Yellow injection at 4 o'clock, new single-pass beam instruments, similar to those in the existing in the AtR will be installed. This includes plunging phosphor screen profile monitors, beam position monitors, current transformers and loss monitors. The hadron beam will be traveling in the opposite direction than usual in this Blue arc, the existing beam position monitors inside the cryostats will be utilized without modification as they will be able to provide quality position signals, with opposite polarity than usual.

6.9.5 Electron Pre-Injector Instrumentation

Instrumentation for the 400 MeV electron LINAC (Figure 3.120) will be designed to measure beam properties at a repetition frequency of 1 Hz with single-bunch charge ranging from 100 pC to the design charge of 10 nC per bunch. A proven configuration of BNL electron beam instrumentation will be implemented, such as those used in the existing LEReC and CeC electron facilities. [406, 407]. Planned instrumentation not yet used routinely at LEReC or CeC but in usage at other accelerator laboratories are included below with corresponding references. The diagnostics in the pre-injector beamline are listed in Table 6.90.

Table 6.90: List of pre-injector diagnostics types and quantities.

Types	Quantity
Faraday cup	4
Beam position monitor	9
Beam position monitor with ion clearing electrodes	1
Integrating current transformer	2
Fast current transformer	1
YAG viewer	9
Single wire scanner	7
Streak camera	1
Mott polarimetry	2
Beam loss monitor (PMT)	4
Optical fiber beam loss monitor	1
Single-slit scanner	1

Beam Position Monitors (BPM)

Beam position monitors each consisting of 4 buttons [408] will be located after the gun, after the first dipole, after the bunching section and between each of the eight S-Band accelerating structures in the LINAC. The BPMs should provide less than 100 µm beam position measurement precision with an acquisition rate of 1 Hz. The first BPMs will also be instrumented for use as ion-clearing electrodes. A pair of BPMs, located downstream of the electron gun, will provide time-of-flight measurements to determine the beam energy. The BPM electronics will be a revised version of the existing BNL designed V301 module.

Current Transformers

Beam current transformers will provide intensity measurements in the pre-injector. Fast current transformers (FCT) will be installed after the gun and before the bunching section to provide measurements of both the bunch charge and bunch length. The bunch length from the gun is about 1.5 ns. After the bunching section, an integrated current transformer (ICT) will be installed between some LINAC accelerating cavity modules. The required measurement accuracy is less than 1%.

Beam Profile Monitors

Profile measurements will be acquired using YAG crystals and wire scanners. Measurements with YAG crystals, being destructive, are foreseen to be performed only during beamline commissioning. The YAG viewers will be placed after the gun, after the first dipole and between bunching cavities. Each diagnostic beamline will also be instrumented with YAG crystals for measurements of the electron beam size, energy and beam energy spread. Wire scanners will be installed between some LINAC accelerating cavity modules.

Longitudinal Profile Monitors

Instrumentation will provide measurements of both absolute and relative electron bunch length. Relative measurements will allow for continuous on-line monitoring; absolute measurements will also be used as input for the relative measurements.

Absolute measurement The bunch length after the bunching section is about 6 ps. Downstream of the bunching section and before the acceleration section, a streak camera will be used to measure the bunch length with an accuracy of less than 10%. After injector commissioning has been completed, the streak camera will be relocated to measure the bunch length in the diagnostic line at the end of the 400 MeV LINAC.

Relative measurement Electrons radiate coherently in a wavelength range comparable with its bunch length. The radiated power, in the said wavelength range, varies with the bunch length. Measurement of the power offers a relative measure of the bunch length. For a 6 ps bunch length, the wavelength of interest is 1.8 mm which corresponds to 150 GHz in frequency. A ceramic gap with waveguide-coupled diodes [409] at frequency of 150 GHz will be installed for relative bunch length measurements after the bunching section. At 400 MeV, diffraction/synchrotron/edge radiation monitor and pyroelectric detectors may be applied.

Emittance Measurements

In the diagnostic line at the end of the 400 MeV LINAC, the electron beam emittances will be measured using a wire scanner and a dedicated upstream quadrupole configured to measure horizontal, vertical and skew profiles. In the pre-injector beamline, downstream of the first dipole, single-slit scanners will be used to measure the transverse emittances of the 350 keV electron beam.

Faraday Cup

Each diagnostic beamline (in the pre-injector downstream of each Mott polarimeter, and at the end of the 400 MeV LINAC) will be instrumented with a Faraday cup to directly measure the beam charge.

Polarization Measurement

Mott polarimeters will be installed at the cathode preparation system and in the first diagnostic beamline close to the LINAC injector. The Mott polarimeters are described in section 6.7.1.

Beam Loss Monitors

Scintillators with multiple photo-multiplier tubes (PMTs), used to detect X-ray and gamma ray, will be placed after the gun, after the first dipole, in the bunching sections and between the acceleration sections to localize beam loss. Additionally, a long optical fiber beam loss monitor will be used between the gun and the entrance of the LINAC.

6.9.6 RCS Instrumentation

The RCS will accelerate two batches of four 7 nC bunches in adjacent RF buckets, they will subsequently be merged into two 28 nC electron bunches. Once per second, new 400 MeV electron bunches are accelerated (in 100 ms or 200 ms) to a beam energy of up to 18 GeV, and injected into the ESR and brought into collisions with the hadron beam. The diagnostics types and quantities in the RCS are listed in Table 6.91.

Table 6.91: List of RCS diagnostics types and quantities.

Types	Quantity
Beam position monitor	576
Fast current transformer	1
DCCT	1
YAG/OTR	7
Synchrotron Light Monitor	1
Tune meter	1

Fast Current Transformer (FCT)

A fast current transformer (FCT) will be used to measure the intensity of single bunches. The FCT should provide $\geq$ 1.25 V/A sensitivity, up to 2 GHz bandwidth, $\leq$ 200 ps rise time with a characteristic impedance of 50 Ω.

YAG/Optical Transition Radiation (OTR)

To facilitate commissioning and reestablishing beam in the RCS, 6 YAG/OTR stations, one in each straight section, and 1 after the injection septum will be installed. Each measurement station will comprise three possible options: a YAG screen (for low bunch charge measurements), an OTR screen (for measurements at higher intensities) and an impedance-matched sleeve connected with RF fingers at both ends for normal beam operations.

Tune Meter

The RCS is designed to accelerate 8 electron bunches from 400 MeV to about 1 GeV, then merge the 8 bunches into 2 that are $\sim$2 µs apart, then accelerate the 2 bunches to the RCS extraction energy. The betatron tunes will be monitored at injection using BPMs to measure injection oscillations and during acceleration using turn-by-turn BPMs with beam excitation applied using fast strip-line kickers.

RCS Synchrotron Light Monitor

A synchrotron light monitor (SLM) [410] will be used for transverse profile measurements in the RCS using synchrotron radiation emitted from an RCS bending magnet. The synchrotron radiation will be extracted through a dedicated optical beamline to a remotely located experimental room. The measured profiles will be used, together with modeled or measured beam optics, to infer the beam emittances and energy spread. Turn-by-turn measurements using gated cameras will provide measurements of injection matching as well as the beam position stability during acceleration. A streak camera will provide measurements of the bunch length and longitudinal profiles.

6.9.7 Transfer Line Instrumentation

Instrumentation in the transfer lines will provide measurements of the following for beam commissioning, regular monitoring and optimization of routine beam operations.

- BPMs

The BPMs in the transfer lines will monitor the single-bunch trajectories at a 1 Hz rate and will be used as input for trajectory correction and/or feedback to optimize beam transmission efficiency. In addition, the BPMs will be used to measure the beam energy and characterize the accelerator lattice. BPMs located in high dispersion regions, will monitor relative changes in the beam energy. The orbit response matrix will be measured and monitored using the BPMs, to localize lattice errors.

- YAG/OTR station

  The transfer lines will include multiple YAG/OTR screens. These will provide position and profile measurements for beams with low (YAG) and high (OTR) bunch charge. A YAG/OTR station at a dispersive location will be used to determine the beam energy spread. Multiple, strategically located YAG/OTR stations will be used in combination for beam emittance measurements.

- ICT/FCT

  An ICT (integrated current transformer) and FCT (fast current transformer) will be installed near the end of the transfer line. The bunch charge, as well as the transmission efficiency, will be measured with high precision using the ICT. The FCT will provide measurements of the beam current and longitudinal profile.

LINAC-to-RCS Transfer Line

In the LINAC-to-RCS transfer line (LtR), the first two dipoles rotate the beam's stable spin direction from longitudinal to horizontal. A solenoid then rotates the stable spin direction from horizontal to vertical. The rest of the beamline elements focus and guide the 400MeV electron beam to the entrance of the RCS. The location of the instrumentation for the LTR is shown in Figure 6.234. The component quantities and their requirements are listed in Table. 6.92.

Both BPMs and YAG/OTR stations will be placed before and after the injection septum, after the kicker for steering the beam during commissioning. A YAG/OTR station in-between the first two dipoles will be used to calibrate beam energy and energy spread. The following three, with possibly a fifth YAG/OTR station, will be used for beam emittance characterization.

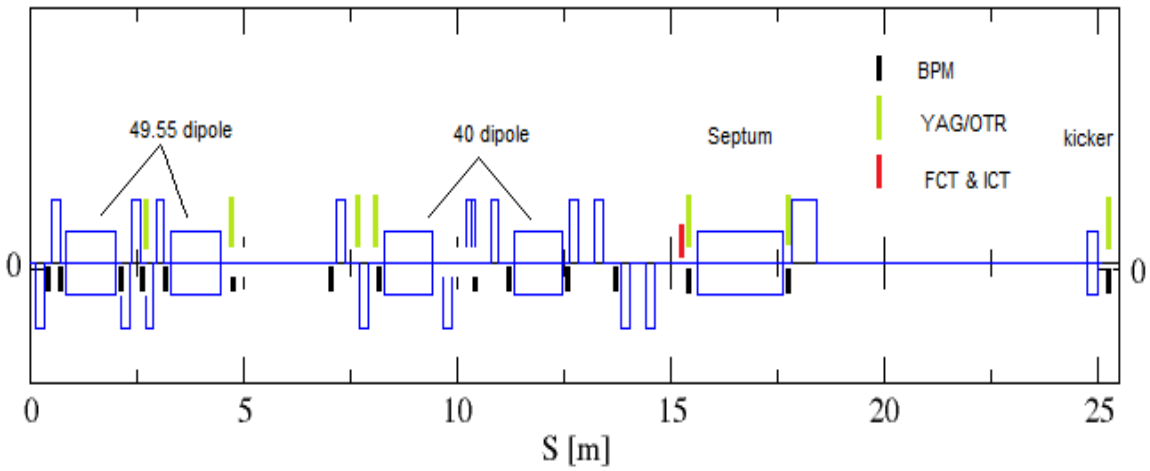

Figure 6.234: Schematics of instrumentation locations in the LINAC to RCS transfer line. The beam travels left to right.

Table 6.92: The number and requirements for the instrumentation in the LINAC to RCS transfer line.

Device	Qty	Requirements
BPMs	15	1 Hz measurement rate, ∼100 µm resolution
YAG/OTR	7	∼50 µm resolution
ICT	1	position insensitive, radiation tolerant, 10 pC accuracy
FCT	1	∼200 ps rise time, upper cutoff frequency ∼2 GHz

RCS to Electron Storage Ring Transfer Line

Each electron bunch extracted from the RCS will pass first through a horizontal septum and a dipole magnet, then through a transport line which includes two vertical dipole magnets towards the end required to steer the beam to the same elevation as the ESR. These electron bunches are accelerated up to 18 GeV once per second, then they are injected into empty buckets in the ESR. The location of instrumentation for the RCS to ESR transfer line is shown in Figure 6.235. The component quantities and the requirements of the diagnostic devices are listed in Table. 6.93.

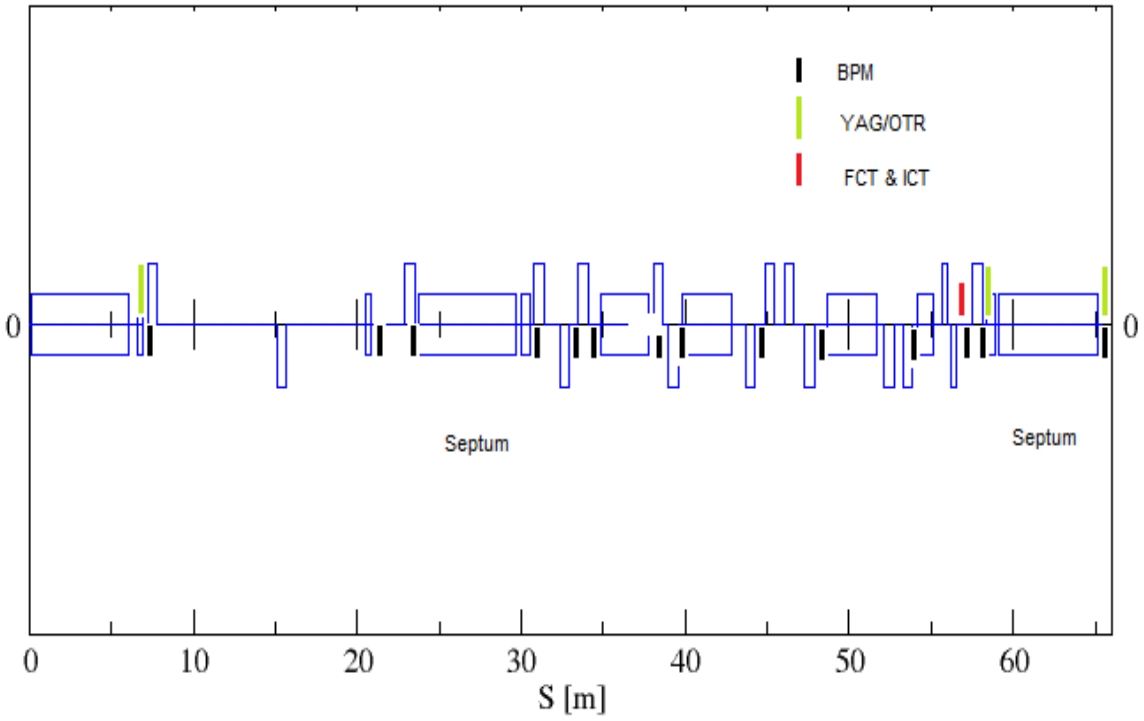

Figure 6.235: Schematics of instrumentation locations in the RCS to ESR transfer line. The beam travels left to right.

Table 6.93: The number and requirements for the instrumentation in the RCS to ESR transfer line.

Device	Qty	Requirements
BPMs	14	1 Hz measurement rate, ∼100 µm resolution
YAG/OTR	3	∼50 µm resolution
ICT	1	position insensitive, radiation tolerant, 10 pC accuracy
FCT	1	∼200 ps rise time, upper cutoff frequency ∼2 GHz

6.10 Cryogenic Systems and Upgrades

The existing central cryogenic plant, sited at the sector 5 location on the Collider, will be used for cooling the hadron storage ring magnets and up to half of the second magnet ring. The central plant will also provide cooling to the new superconducting magnets and superconducting RF systems in the detector IR region, to the superconducting RF systems at IR10, and to the superconducting RF systems at IR02 for the hadron beam electron cooler.

The existing central cryogenic plant will keep its existing oil brake and bearing expanders with renewed oil skids. Due to the existing plant design point, the existing bottom ends exchangers and the ones added for the 2006 upgrade are too small to handle future higher 4.5 K refrigeration loads and require a cold end JT-circuit upgrade (JT-expander and exchangers). Because the plant is a non-LN2 assist plant, without any further expander upgrades the plant working range will be bounded by: the liquefaction capacity which is limited by the original warm expanders sizing (Expander 1 and 2) to around 100 g/s. The heat shield capacity is set by the throughput of expanders 3 and 4, which are expected to be sufficient and can be partly traded to increase liquefaction capacity if required. The 4.5 K refrigeration capacity will be sized by the cold end upgrade to match the new requirements, with adequate margin, to make cold end capacity from the cold ($<$40 K) expanders available for satellite loading over the 4.5 K to 9.6 K range. The cold expander set is still oversized with regard to matching the EIC loads and will run at lower efficiencies. In order to have a hot standby 2nd stage compressor available, the plant capacity has been sized for a cold-box flow of 3200 g/s giving a Carnot work equivalent of around 2400 kW.

Modification of the magnet ring 4.5 K cryogenic distribution system is required for interfacing to the new 2 K superconducting RF systems. Additional local cryogenic equipment required for achieving 2 K cooling will be located in new buildings close to the respective IRs:

- Detector IR region: Modifications will be required to the existing cryogenic distribution system to bring the reconfigured superconducting magnet string and the IR region SC magnets into the forced flow cooling loop of the Hadron Storage Ring magnets. In the IR region there also will be local equipment to provide cooling for the 2 K Superconducting RF (SRF)cavities, 4.5 K spin rotators, and the 1.85 K cooling for the high current high field SC magnets.
- Hadron beam injector transfer line using Blue ring sextant 4/5: Blue ring sextant 4/5 is the magnet sextant used for beam transport from the IR06 hadron beam injector to IR04 where the beam is merged into the hadron storage ring. Modification to the cryo-distribution on the IR06 end and on the IR04 end is required, due to the removal of some superconducting magnets at each end to accommodate the changes. In addition, some modifications of the power circuit for the sextant 4/5 magnets is required to enable separate powering of this sextant at the injection energy current. This requires additional current leads and lead flow cooling.
- Hadron beam low energy mode (41 GeV) using Blue ring sextant 12/1: In the hadron

beam low energy mode the hadron beam will be diverted through this Blue sextant to obtain the correct path length for operations at this energy. Modifications of the power circuit for the sextant 12/1 magnets are also required to allow separately powering of this Blue sextant at the current required to operate at the low energy. Since sextant Blue 4/5 is operational for injection transfer, sextant Blue 2/3 can be used to supply sextant Blue 12/1. Thus, for the Collider low energy mode, two additional sextants of the Blue ring will be operational.

- Hadron cold beam-line cryogenic load: The high bunch density beam will induce additional heat load into the cold-bore of the SC magnets. This will be reduced by installing a copper lined stainless steel beam screen with a thin coating of low SEY material inside the superconducting magnets cold-bore (316 LN stainless steel) beam pipe. Even with a copper beam screen a maximum heat load that will not exceed 0.5 W/m is expected. The heat load would double in each sextant and upgrading the magnet ring re-coolers to larger ones may be necessary. Although the bulk supercritical helium flowing through the magnet string will only rise less than 150 mK, heat transfer performance inside long magnets such as the arc-dipole may result in a magnet coil temperature rise of 0.3 K or more, bringing the coil temperatures close to their quench point. To operate that close to the quench point requires training of the magnets. For practical purposes, it would be too many magnets to train every run, and the conservative approach would be to drop the operating temperature of the entire magnet ring by 0.4 K. This requires adding a cold compressor to handle the Hadron storage ring 4.5 K refrigeration load. This adds a 4.5 K load of around 4000–5000 W (300–370 kW Carnot equivalent) and scales with the 4.5 K refrigeration load.

6.10.1 Central Plant Capacity Distribution and Satellite Locations

Global Cryogenic Systems Requirements

Table 6.94 summarizes the global cryogenic requirements throughout the EIC and total nominal operating loads imposed on the central cryogenic plant for each different load category. The 2 K/1.9K and 4.5 K loads are shown for each location. Because of the existing cryogenic distribution system envelope, the different loads for the satellite locations are returned via the available return options and are grouped under one of the 6 load characteristics. Table 6.95 summarizes the central plant loading with the expected power consumption for each load category, with Table 6.96 showing the operating power draw at each location.

Central Plant Capacity Distribution and Satellite Locations

The existing hadron ring cryogenic distribution system that is part of the superconducting magnet cryostat system will be used for all new cryogenic equipment located throughout

Table 6.94: Overall global cryogenic requirements throughout the Collider and total nominal operational loads imposed on the central cryogenic plant for each different load category, at 275 GeV.

Subsystem	2.0K/1.9K[a] [W]	4.5 Ref [W]	4.5–10K [g/s]	4.5–300K [g/s]	45–80K [g/s]	4.5–80K [g/s]
Hadron storage ring, static		3900		24	66	
Hadron storage ring, beamline		1600				
Blue sector 4-5,12-1,2-3 &VB12		2150		10	35	
Detector IR 4.5 K Magnets		253		3.5	0.3	
Detector IR 1.9 K Magnets	22[a]	136		9.6	0.1	
IR SRF	356	304	20	1.8		3.1
e-rotators		150		1.2		2.4
IR Detector		70		1		1
IR10 Satellite Loads	1134	1248	60	10.7		17.7
IR02 Satellite Loads	594	525	30	3.3		10.3
Plant Cold end, Liq Storage		600				
4.0 K Vapor cold compressor		4500				
Total	2106	15436	100	65	101	35

[a] 1.9 K load only

the collider ring. There are 5 He transfer loops running through each magnet cryostat over the full collider circumference:

- The M-Loop is the main forced flow supercritical cooling loop through the magnets
- The S-Loop supplies 3.5 bar, 4.6 K helium to the re-cooler baths
- The H-Loop is a heat shield loop that takes high pressure 45 K gas from the plant, uses it to cool the heat shields, and returns warmer gas at 80 K back to the plant
- The R-loop is the cold vapor return line which carries 4.5 K, 1.3 bar vapor from the recoolers back to the plant
- The U-Loop has cross-over valves to the S-loop and H-loop, but will be used to return the 10 K gas from the satellites.

Table 6.97 summarizes the existing cryogenic distribution system along the collider along with the interconnects between it and the central cryogenic plant. The existing cryogenic distribution system and its capabilities determine the return options which are noted in Table 6.98. In order to provide cooling capacity for the superconducting components at the various IR locations from the central plant, the distribution system needs to supply 4.5 K liquid and return cold vapor and shield return gas back to the central plant. In the case of the existing hadron ring cryogenic distribution system, the S-header would be used

Table 6.95: Central cryogenic plant loads. The total plant electric power is 10.9 MW.

Parameter	4.5 Ref [W]	4.5 K-10 K [g/s]	4.5 K-300K [g/s]	45 K-80 K [g/s]	4.5-80 K [g/s]
Load [W]	15436	5580	102000	21300	14500
Load [g/s]	822	110	65	102	35
T1 [K]	4.5	4.5	4.5	45	4.5
P1 [bar]	4.2	4.2	4.2	16.0	4.2
H1 [J/g]	12.1	12.1	12.1	250	12.1
Δ H	18.4	50.7	1561	183	420.9
T2 [K]	4.5	10	300	80	80
P2 [bar]	1.26	1.26	1.05	9.0	9.0
H2 [J/g]	30.7	62.9	1573	433	433
Δ Exergy [J/g]	1381	2834	6863	1088	4581
Carnot Work [MW]	1.15	0.31	0.44	0.11	0.16
η_{Carnot}	20%	20%	20%	20%	20%
Plant electric power [MW]	5.74	1.56	2.22	0.55	0.79

Table 6.96: Cryogenic systems electric power.

Location	Power [MW]
Central Plant	10.9
IR Local	0.32
IR10 Local	0.56
IR02 Local	0.35
Operational Total	12.1

to supply 4.5 K liquid helium to the various IR locations. Any 4.5 K loads would return via the R and U headers. 2 K loads would have a local vacuum/cold compressor system and a local refrigeration recovery or 4.5 K cold box with compressor system to handle the local loads and flows from the 2 K loads with 4.5 K capacity assist from the central plant. The U header can also be used to return the warmer 10K flow returning from the IR10 and IR02 cold compressor/recovery cycle back to the central plant cold return header which can be reconfigured to return at a different location on the central plant's cold end heat exchanger stack. Returned thermal shield flows would need to be injected at high pressure back into the hadron ring 45–80 K thermal shield H-header or alternatively return to the warm return header at room temperature and at low pressure.

Table 6.97: Hadron ring cryogenic distribution and plant-to-ring cryogenic distribution. (M, S, H, R and U denote the loops defined in Section 6.10.1).

Ring loop distribution lines	Plant-to-Ring distribution lines
4.5 K magnet cooling loop (M)	4.5 K liquid helium supply (S)
4.5 K liquid supply (S)	4.5 K vapor helium return
4.5 K vapor return (R)	4.5 K helium cool-down return
10 K gas return or utility (U)	45 K heat shield supply
45 K−80 K heat shield loop (H)	80 K heat shield helium return
300 K warm return	300 K warm helium return
	300 K warm helium supply

Table 6.98: Return helium line options.

Cryo distribution line	Return pressure [bar]	Return temperature [K]
4.5 K return	1.25–1.35	4.5
U to CR return	1.5	4.5, 10, 70, 150
Shield return	10–15	50–80
Warm return	1.25–1.5 (CR)	293

Any superconducting devices operating around 4.5 K will operate at slightly different temperatures due to the different boiling point pressures from pressure the drop profile along the 4.5 K vapor return headers. The IR6 devices will see the lowest boiling point pressures because of their location closest to the central plant and thus will be able to operate at a 4.45 K bath temperature. Any specialty high field/high current magnets at the IR region detector area requiring lower operating temperature can be handled by adding capacity to the vacuum pumping system. The cryogenic loads and equipment will be presented for each IR/satellite location in their respective sections. See Table 6.99 for an outline of the required operating temperatures.

Cryogen Circuit Configuration

To cool the Yellow Hadron magnet loop, the current flow scheme is used, with modifications to supply the Blue hadron magnet loop to allow it to operate only one sextant in high energy mode and 3 sextants in low energy mode. The IR region superconducting magnets will be forced flow cooled and will be incorporated into the Yellow hadron cryogenic circuit. Tie-ins at IR10 to the main hadron ring cryogenic distribution are necessary to supply cooling to the superconducting RF systems at IR10. Figure 6.236 outlines a flow scheme for supplying both hadron magnet rings, the IR region, IR02 and IR10 systems.

Table 6.99: Cryogenic system operating temperatures.

Location	Subsystem	Operating temp. [K]
Hadron ring	Yellow ring	4.15[a]/4.55–4.85
Hadron Injection	Blue Sextant 4/5	4.55–4.65
41 GeV sextant	Blue Sextants 12/1&2/3	4.55–4.65
IR region	IR superconducting magnets	4.15[a]/4.55
IR region	High Current superconducting magnets	1.9
IR region	SRF Crab cavities	2.00
IR02	SRF LINAC for Hadron cooler	2.00
IR10	SRF for ESR, RCS, HR	2.00

[a] With 4.2 K Vapor cold compressor to lower the operating temperature

Central Cryogenic System (Sector 5 Position)

The existing cryogenic plant is located at the sector 5 position of the ring. The plant was built in the early 80's for a previous project and will have been in operation for approximately 25 years in 2025. The existing central cryogenic plant will keep its existing oil brake & bearing expanders with renewed oil skids. Due to the existing plant design point, the existing bottom end exchangers and the ones added for 2006 upgrade are too small to handle the higher EIC 4.5 K refrigeration loads and require a cold end JT-circuit upgrade (JT-expander and heat exchangers). Because the plant is a non-LN2 assist plant, without any further expander upgrades the plant working range will be bounded by: the liquefaction capacity which is limited by the original warm expanders sizing [Expander 1 and 2] to around 100 g/s. The cold [<40 K] expanders will be oversized with regard to matching the EIC loads and will run at lower efficiencies. In order to have a hot standby 2nd stage compressor available, the plant capacity has been determined for a cold-box flow of 3200 g/s giving a Carnot work equivalent of around 2400 kW.

The existing compressor system is configured in 2 compression stages, optimized for a compression ratio of 4x per stage with a 16 bar discharge. 1st stage and 2nd stage compressors are all screws compressors with 321 mm rotors with 1.65 L/D. The total mass flow that the compressor system can produce is 4500 g/sec running the spares or 3600 g/sec without running the spare units. Based on skid capacity the cold end upgrade to the existing cold-box would go in increments of 725 kW in Carnot work, translating to 2.9 MW increments. Thus the final plant capacity expressed in compressor power would be either 8.7 or 11.6 MW. The compressors are maintained and rebuilt in accordance with the manufacturer's schedule and are in very good condition. The water-cooled gHe inter-coolers and after-coolers will be due for replacement in the next few years and will be replaced. Various other miscellaneous improvements will also be made throughout the plant system to facilitate emergency operations in case of a power outage or equipment failures.

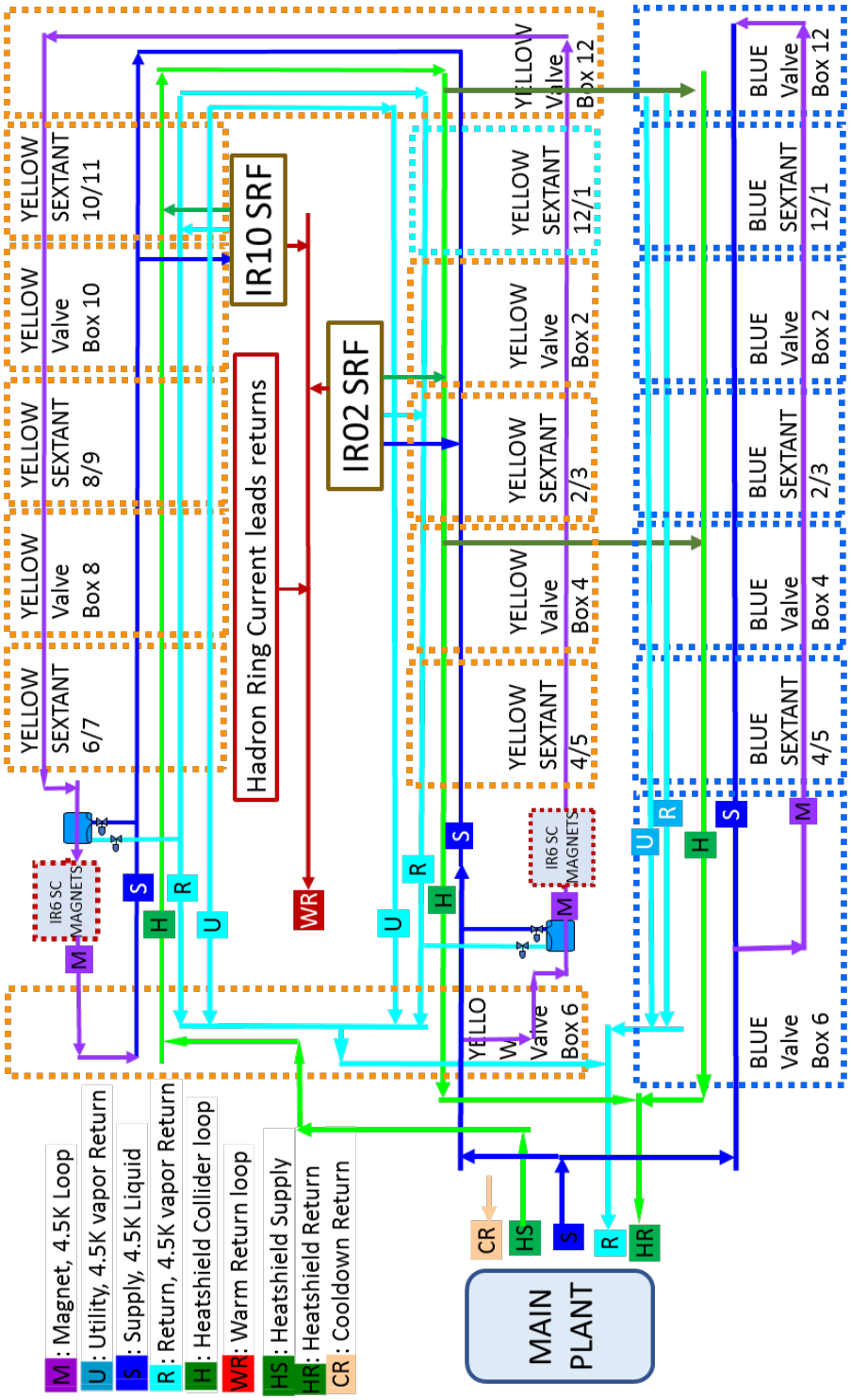

Figure 6.236: Overall cryogenic system distribution schematic.

6.10.2 Hadron Ring Cryogenics Modifications and Upgrades

Hadron Ring

The RHIC cold bore superconducting magnet beamline expects to see an additional dynamic heat load due to the large number of short, high-intensity bunches, and the large beam position offset during the EIC operation. This load will be reduced by inserting beam screens with a copper interior surface into the superconducting magnets cold-bore 316 LN stainless steel beam pipes. With the beam screen, the resistive-wall heat budget has been conservatively set at 0.5 W/m specifically to handle these loads during EIC operation at full energy. As a result, the 4.5 K circuit load will increase by 1600 W.

Magnet Cooling Loop Heat Load Distribution and Temperature Profile

The magnet string is cooled by forced convection super critical flow through the cold-mass with re-coolers spaced at regular intervals to re-cool the supercritical stream that warms up roughly 0.1 K between re-cooling at a nominal mass flow-rate of 150 g/sec with present loading. The loading is fairly uniform along the magnet string, and five (5) nominal 65 W re-coolers are located throughout each ring sextant for re-cooling of the supercritical stream. The last segment of magnets plus the cryogenic distribution line running from the magnet string to the sextant valve-box in each service building, the heat load from the lead pots, and all the cryogenic valves located in the valve-box is removed by a larger nominal 275 W load re-cooler located in each valve-box.

Cooling Within a Magnet

Each magnet has 4 main flow channels along with smaller parallel flow paths including the 2 superconducting bus channels or slots that also flow helium. The heat removal between the cold bore and superconducting coils is accomplished through super critical helium flow inside the annular gaps between the cold bore boundaries and the coils. Figure 6.237 shows a typical cross-section of a dipole and Table 6.100 lists the cooling channel dimensions and helium cooling channel annular gap between beam-line and coil. The beam-line tube is centered vertically with mineral loaded phenolic [RX630] pole pieces and horizontally with G-10 bumpers. The small annular gap between the cold bore beam tube and the superconducting coil insulation provides minimal cooling flow. Analysis of the coil temperature assuming 0.5 W/m beam tube heating and conduction cooling to the outer helium channel with the copper lined screen at cryogenic temperature indicates a 0.3 K temperature rise of the coil section closest to the beam heating peak point.

The additional 1600 W in the SC magnet ring affects the load distribution and temperature profile. Table 6.101 gives the predicted operating temperatures for the present load and high bunch intensity load at a magnet flow of 150 g/sec.

Each sextant magnet string will see an additional 272 W from the beam line. The exist-

Table 6.100: Arc dipole flow channels and beam line dimensions.

Item	Dimension [mm]
Helium channel diameter	30.2
SC bus channel width × height	31.8
Beamline annular channel gap	3.4
Beamline outside diameter	73.0
Coil inside diameter	80.0

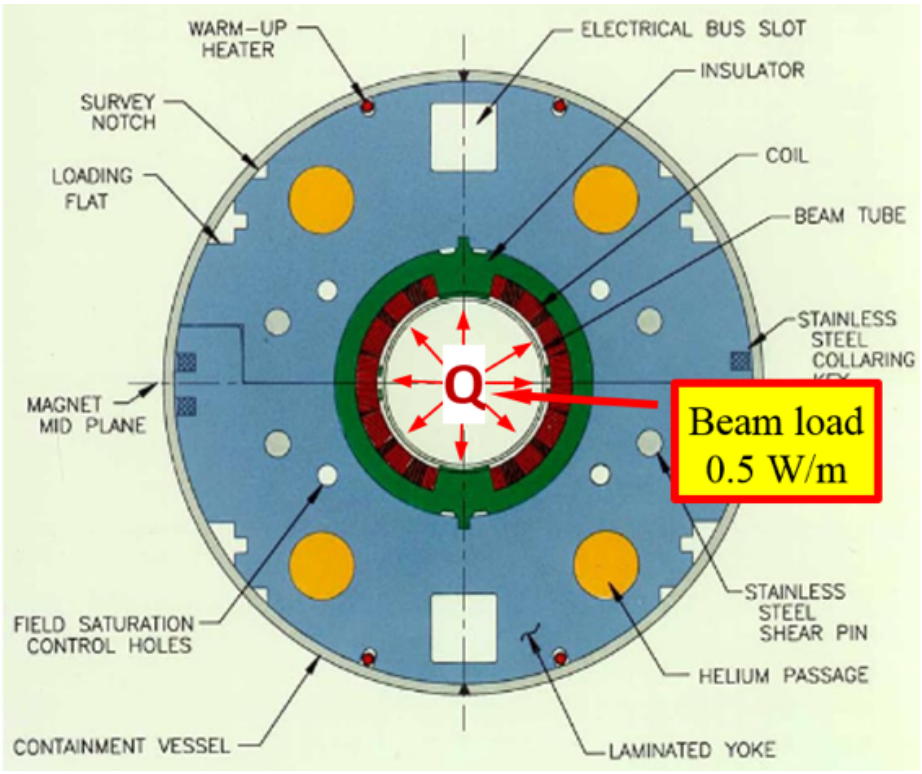

Figure 6.237: Dipole cross section.

ing loads and operating conditions are also tabulated for comparison. Thus, each magnet string section between re-coolers will see the present load of 65 W plus the additional dynamic load of 45 W. The table shows the various heat transfer gradients (nucleate boiling heat transfer gradient and the tube side heat transfer gradient), bulk temperature rises, and the expected boiling pressure increase due to the higher operating pressure on the 4.5 K vapor Return "R" header due to the increased flow. The baseline is done for a 150 g/sec flow rate, but the flow-rate could be increased at the risk of increased flow induced vibration. The enthalpy quench margin will be reduced as a result of the increased load without changing the flow-rate. Operational tests could be done to simulate the warmer operating temperatures by operating only half the re-coolers, however the flow in the annular space

between the cold-bore beam-line and the magnet coils is not known accurately and without a beam-line load, this test is not a final measure of the operational limit. A conservative approach to mitigating magnet operation this close to the quench line, due to this beam line load, is to lower the operating temperature of the magnets. This requires dropping the operating temperature by 0.4 K by adding one stage of cold compressor to lower the boiling point temperature in the re-coolers baths.

Table 6.101: Hadron ring sextant re-cooler loads and temperatures at 150 g/s.

Parameters	Gradients /Rise [K]	He Temp. [K]	Gradients /Rise [K]	He Temp. [K]
Bath Temperature		4.15[a]/ 4.5		4.15[a]/ 4.55
Pool boiling gradient	0.04		0.07	
Tube side heat transfer gradient	0.05		0.9	
Bulk temp. rise between re-coolers	0.10		0.15	
Peak bulk helium temp. (M-line)		4.72		4.86
Peak bulk helium temperature (in cold-bore side channels at the last dipole mag. prior to re-cooler)		4.43[a]/ 4.83		4.9[a]/ 5.30

[a] With 4.0 K Vapor cold compressor to lower the operating temperature

Sextant Blue 4/5 Injection transfer

Modification of sextant Blue 4/5 is required to allow this sextant to be used as the hadron beam transfer line for injection from the AGS ring into the hadron ring. Injection would occur at the start of sector 5 and the required modifications are to remove superconducting magnets starting with the 05DX/05 triplet up to Blue quad B5Q10. As a result the cryogenic distribution system needs to be extended to cover from where the SC magnets are removed all the way to B5Q10. This is a 130 m long RHIC cryogenic distribution spool which includes the superconducting electric bus system starting from the 05 Triplet location. Similarly, at the IR4 end of sector 4, several Blue SC magnets need to be removed to allow warm magnets to divert the injection beam into the fast kickers where the beam merges with the hadron storage ring. Similar to the sector 5 side, a new section of the RHIC cryogenic distribution spool which includes the superconducting electric bus system needs to be added to complete the bypass around the new warm magnets. To allow operation of this sextant by itself, the SC power circuits for the SC magnets need to be modified so they can be powered from the sector 4 and sector 6 lead-pot/valve boxes. Because the cryogenic distribution (for each ring) only has one shield circuit, when this Blue sextant is operated by itself, the shield circuit is completed by taking some shield flow from the Yellow hadron ring circuit and using this Blue shield as the return route back to the sector

6 valve box. This requires a new cryogenic line and control valve to be installed between the Yellow and Blue valve boxes at the sector 4 location.

41 GeV Operating Mode

Sextant Blue 12/1 will be configured to operate with the rest of the Yellow hadron ring in this lower energy mode. Because sextant Blue 4/5 is always used as the injection transfer line, in the low energy mode sextant Blue 2/3 will serve as the cryogen transfer section to cool sextant Blue 12/1, and thus half of the Blue magnet ring will be cold, mainly sextant Blue 4/5, sextant Blue 2/3 and sextant Blue 12/1. The cryogenic distribution (for each ring) only has one shield circuit, the heat shield loop requires cross connect from the Yellow ring to supply heat shield flow into this Blue loop at the sector 12 Blue valve box, along with other modifications to bring this Blue valve box re-cooler into this circuit configuration. In order to power sextant Blue 12/1 independently, modifications will be needed in the sector 2 and sector 12 Blue valve boxes at the current lead pots to split and reconfigure the superconducting bus circuits.

6.10.3 Cryogenics for the IR Region Superconducting Devices

The superconducting equipment and cryogenic subsystems diagram for the IR location is shown in Figure 6.238. The existing hadron magnet ring cryogenic distribution system will be used to supply the new equipment at the various IR locations. Local equipment will be installed to produce 1.9 K cooling for the high field/high current SC magnets, for the 2.0 K cooling of the SRF cavities and to process the shield flow for return into the existing cryogenic distribution system. The IR region will be equipped with superconducting magnets for the electron and hadron beam, and superconducting crab cavities for both the hadron and electron beams. These superconducting cavities will be operated at 2.0 K while most of the superconducting magnets will be operated at 4.5 K, except for 3 high current magnets which will operate at 1.9 K. Table 6.102 lists the cooling method and operating temperatures for each subsystem.

Table 6.102: IR Cryogenic system operating temperatures

Component	Cooling Method	Process Conditions
hadron beam SC magnets	forced flow	4 bar, 4.2–4.6 K
hadron beam HC SC magnets	pressurized bath	1.4 bar, 1.9 K
electron beam IR SC magnets	forced flow	4 bar, 4.2–4.6 K
electron beam SC rotators	saturated bath	1.25 bar, 4.2–4.45 K
hadron beam SC crab cavities	saturated bath	30 mbar, 2.0 K
electron beam SC crab cavities	saturated bath	30 mbar, 2.0 K

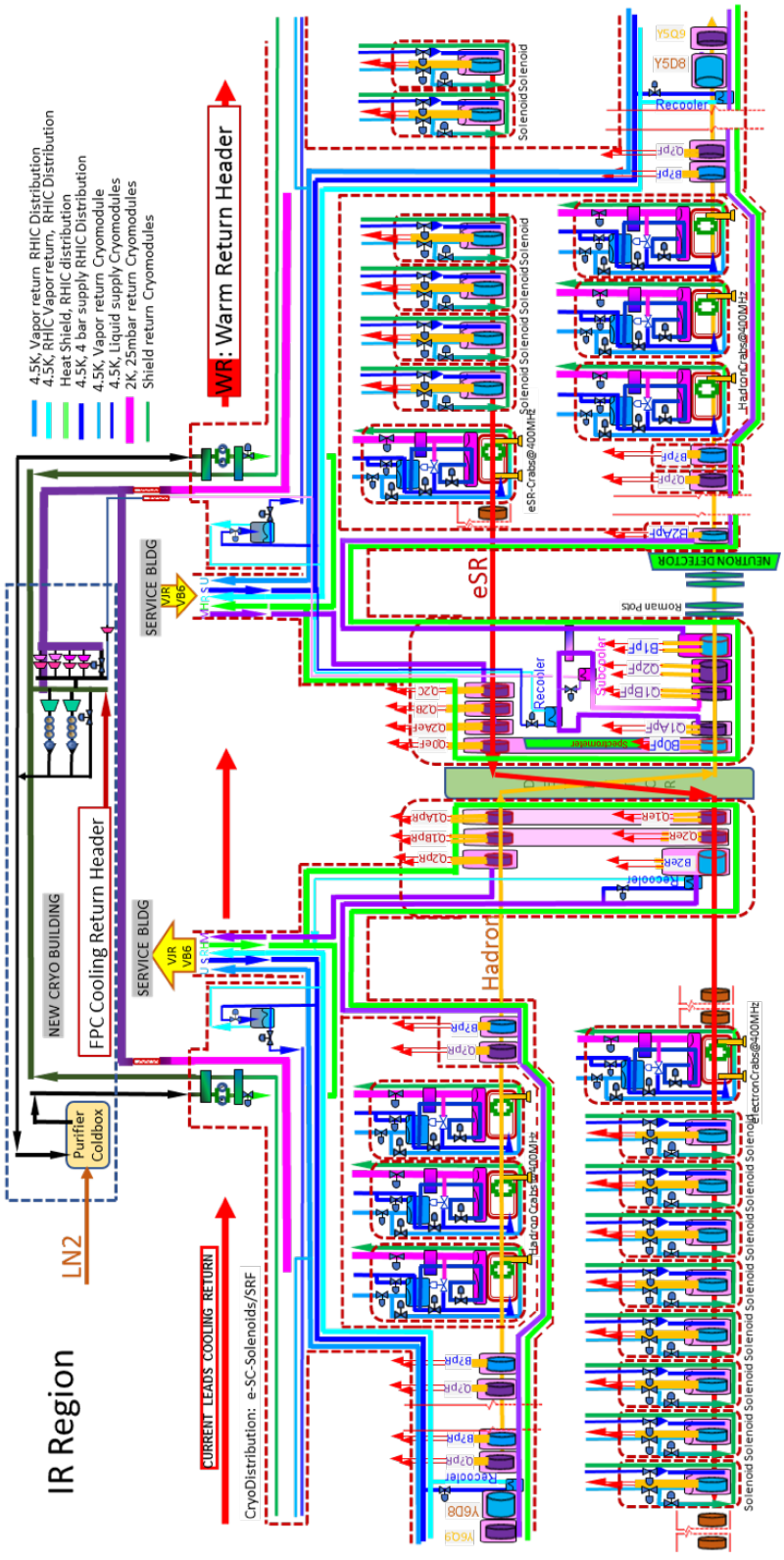

Figure 6.238: IR Region Cryogenics.

Hadron Beam Superconducting Magnets

Because of the expected high intensity hadron beam line heat load, the IR region superconducting magnets will be forced flow cooled instead of boiling bath cooled. The proposed flow circuit scheme is to incorporate the new IR magnets and reconfigured hadron SC magnet string into the Yellow hadron ring cryogenic circuit. This requires some repiping of the cryogenic distribution system on both sides of the IR. The electron beam superconducting magnets that are near the detector because of their proximity to the hadron beam magnets will share cryostat space and will also be forced flow cooled. The IR region magnets will be not be powered via superconducting bus like the hadron ring arc magnets, instead they will be powered via separate warm conductors to each magnet and thus require their own lead cooling. Compared to the hadron ring arc magnets, a large portion of the IR magnets 4.5 K refrigeration load comes from the current lead conduction to the cold end, in addition to the current lead cooling requirements (liquefaction load). Table 6.103 lists the IR superconducting magnets for both the hadron and electron beam on both sides of the detector along with the estimated 4.5 K loads, shield heat loads, and lead cooling flows.

Three IR-region high current/high field superconducting magnets will be cooled to 1.9 K. The 1.9 K He-II volume will be pressurized and cooled via a heat exchanger by a 1.8 K saturated He-II bath. The magnet cryostat will contain a 2 K/4.5 K refrigeration recovery exchanger to allow the 4 bar supply that pressurizes the magnet volume and that also fills the 1.8 K bath to recover against the 1.8 K 16 mbar vapor flow from the bath. Because of the low pressure, the 16 mbar vapor will be heated to room temperature and returned via warm vacuum pumps running with 12 mbar suction.

Electron Beam Superconducting Rotators

The baseline configuration for the electron beam SC magnets further from the IR is bath cooling and will be supplied from the same cryogenic distribution that supplies the SRF crab cavities. Table 6.104 lists the electron beam rotator magnets estimated/budgeted 4.5 K loads, shield heat loads, and lead cooling flows. The configuration assumes each solenoid is in its own independent cryostat and thus jumpers from the main distribution header will be used to connect to each solenoid. The baseline design is to have vapor cooled current leads exiting from the bath volume, but to have sufficient pressure differential for lead flow control, the return flow must be returned to the local compressor. Other cooling configurations are possible such as separating the current lead cooling from the bath volume by supplied 3.5 bar 4.6 K flow to the current leads and returning them directly to the existing hadron ring cryogenic distribution warm return header. The current lead flows will be controlled by individual mass flow controllers and ramped as a function of current.

Table 6.103: IR region 1.9 K and 4.5 K superconducting magnets.

Magnet	Current [A]	Length [m]	1.9 K [W]	4.2 K-4.5 K [W]	Lead Flow [g/s]	Shield Load [W]
Q1A pF	20,000	1.6	6	49	3.1	13
Q1B pF	20,000	1.6	6	49	3.1	13
Q2 pF	15,000	3.8	4.5	38	2.4	17
Valve/Reliefs		5				
Total			16.5	136	8.6	43
B0 pF	500	1.2		2.5	0.08	13
B0A pF	4400	0.6		12	0.7	12
B1 pF	8400	3		22	1.33	16
B1A pF	7670	1.6		20	1.2	16
Q0 eF	500	1.2		2.5	0.12	13
Q1 eF	1000	1.46		3.7	0.24	13
Q1A pR	236	1.8		2	0.0372	14
Q1B pR	265	1.4		2	0.042	13
Q2 pR	215	4.5		2.4	0.034	18
Q1 eR	74	1.8		1.6	0.012	241
Q2 eR	74	1.4		1.5	0.012	12
B2 eR	75	5.5		2.3	0.012	19
Total				74.5	3.8	400

Table 6.104: IR region electron beam superconducting rotators. (Note: lead flow is per lead and not per lead pair).

Solenoid Type	Qty	Current [A]	Load 4.5 K [W]	Lead Flow 4.5 K-300 K [g/s]	Shield Flow 4.5 K-80 K [g/s]
Long	8	500	75	0.036	0.2
Short	8	500	74	0.036	0.1
Total	16		149	1.2	2.4

IR Detector Superconducting Solenoid

It is expected that the detector will have a large diameter superconducting solenoid. The cryogenic cooling capacity allocated for this magnet is shown in Table 6.105.

Table 6.105: The cryogenic cooling capacity allocated for the detector solenoid.

Current [A]	Load (4.5 K) [W]	Load Flow [g/s]	Shield load [g/s]
6500	70	1.0	1

Superconducting RF (SRF) Crab Cavities Cryomodule

Both the hadron and electron beams will be crabbed at the IR region location prior to collision and then de-crabbed using SRF cavities. 4 cryomodules each containing two 197 MHz Crab cavities and the two cryomodules each containing a single 394 MHz Crab cavity will be used for the hadron beam and the two cryomodules each containing a single 394 MHz Crab cavity will be used for the electron beam. The cavities will be operated at 2 K. For the baseline design, each cryomodule will have a local 4.5 K, 1.4 bar phase separator which will feed the 2 K-4 K refrigeration recovery heat exchanger which pre-cools the liquid supply below 3 K before entering the 2 K bath. For each cryomodule, flow has been budgeted for power coupler outer conductor cooling as a liquefaction load (returning at 300 K) and flow has also been budgeted for shield cooling returning below 80 K. Several thermal shield cooling options are possible and similarly, several cooling options are possible for the 5 K intercepts near the cold flanges, the beam line cold to warm transition intercepts, and cooling of the RF power coupler's outer conductors. The final configuration will not be settled until detailed design of the various cryomodules is underway, requirements are known, and preferred configurations are selected for minimizing the risk for microphonics/vibrations and designs are further optimization for cost and efficiency. For the preliminary design the following baseline configuration is used: Power coupler outer-conductor cooling will be supplied as 1.4 bar, 4.6 K liquid and returned at room temperature to local 1.05 bar compressor. 5 K intercepts are assumed to be 4.5 K refrigeration loads and returned to the existing hadron ring's cryo-distribution R-header as cold vapor. Beam lines' cold-to-warm transition heat intercepts and thermal shield will be supplied as 1.4 bar, 4.6 K liquid and returned below 80 K to the local cryogenic subsystem.

Cryogenic Subsystem and Distribution System for Crab Cavities and Electron Beam SC Solenoids

With a total load of 356 W, the 2 K system will consist of at least one stage of cold compressor. The 27 mbar helium flow exiting the cryomodules will return to a return header that is part of the tunnel cryo-distribution system to a cold compressor/refrigeration recovery exchanger cold-box. The helium vacuum compressor discharge along with the room temperature flow from the power coupler/current leads will be compressed by the local compressor to high pressure and onto the refrigeration recovery cold-box. The cold-box will also do refrigeration recovery of the low pressure flow, that is below 80 K, from intercepts and thermal shield flows using the recycled flow from the local compressor and sent back into the existing hadron ring's cryo-distribution high pressure heat shield circuit (H-header). Table 6.106 depicts the loading on the crab cavities with and Table 6.107 shows the local utility demand. Table 6.108 reflects the corresponding IR region loading on the central plant. There will be a cryogenic distribution system in the IR region to supply/return cryogens for the SRF cavities and SC solenoids. It will contain the following:

- 4.5 K, 3.5 bar liquid supply header
- 27 mbar vapor return header
- 16 mbar vapor return header for the high current 1.9 K SC magnets
- 1.3 bar, 4.5 K vapor return header,
- 1.3 bar, 80 K shield/intercept return header.
- 1.15 bar warm gas low pressure return header to local compressor

Table 6.106: Crab cavity (module and system) loads.

Subsystem	Qty	2.0 K Refrig. [W]	4.5 K Refrig. [W]	FPC/Beamline 4.5 K-300 K [g/s]	L.P. Intercept 4.5 K-80 K [g/s]
Hadron Crabs FD	4×2	264	62	1.2	1.0
Hadron Crabs H2	2×1	58	48	0.3	0.6
Electron Crabs	2×1	34	4	0.3	0.6
Cryo-distribution			150		
Margin			40		
Total	8	356	304	1.8	2.2

Table 6.107: IR region local cryogenic system utilities

Local Compressor			Vacuum Pumps		
Flow [g/s]	Power [kW]	Water [GPM]	Flow [g/s]	Power [kW]	Water [GPM]
48	220	76	25	150	52

Table 6.108: IR region cryogenic loading on central plant.

Subsystem	4.5 K Refrig. [W]	C.C. 4.5 -10 K [g/s]	4.5 K-300 K Liquifaction [g/s]	Shield 4.5 K-80 K [g/s]	L.P. Intercept 4.5 K-80 K [g/s]
IR Region Mags.	253		3.5	1.0	
IR Region HC Mags.	136		9.6	0.1	
e Beam Rotators	38		1.2		1.3
SRF Crabs	304	20	1.8		1.0
Detector Solenoid	70	1.0		1.0	
Cryo Distribution	70			1.2	
Total	871		16.1	3.3	2.3

6.10.4 Cryogenics for IR10 Location Superconducting Devices

The superconducting equipment and cryogenic subsystems diagram for the IR10 location is shown in Figure 6.239. There are 3 SRF subsystems located at IR10: The electron storage ring (ESR) SRF subsystem, Rapid Cycling Synchrotron (RCS) SRF subsystem, and the Hadron beam SRF subsystem. All three subsystems will operate at 2.0 K. The electron storage ring system will have eighteen 591 MHz SRF cryomodules. The RCS SRF will use three 591 MHz cryomodules, and the hadron beam SRF will use two 591 MHz cryomodules. Table 6.109 summarizes the cryogenic loads for these subsystems.

SRF Cryomodules

There will be two different 591 MHz cavity designs, a 2-cell version and a 5-cell version. Both will be operated at 2.0 K. The 2-cell version will be used in the Electron Storage Ring (ESR). These cavities will have a large beam pipe diameter (26 cm) to allow the HOM modes energy to propagate to the warm RF absorbers resulting in greater thermal conduction and thermal radiation heat leak. Each cavity is packaged in its own cryomodule.

Table 6.109: IR10 SRF loads.

Subsystem	Modules Qty	2.0 K Refrig.	4.5 K Refrig.	FPC 4.5 K-300 K	L.P. Intercept 4.5 K-80 K
ESR-591 MHz 2-cell	18	900	828	9.0	10.8
RCS-591MHz 5-cell	3	87	138	1.5	0.9
Hadron-591MHz 5-cell	2	100	92	1.0	0.6
Cryo-distribution			100		0.7
Margin		227	200		
Total		1314	1358	11.5	13.0
Carnot Work [kW]		195	101	53	96

For the preliminary baseline design each cryomodule will have a 4.5 K phase separator with a fill valve, a 2 K-4 K refrigeration recovery heat exchanger and cryogenic valves for cavity cool-down, a 2 K J-T bath top fill, 30 mbar vapor return, and thermal shield flow control. The 4.5 K vapor will be returned via the 4.5 K header in the IR10 distribution back to the hadron magnet cryogenic distribution system that takes it back to the central plant. Shield and beam line intercept cooling will be from a 4.5 K source, flow supply can either be 3 bar 4.5 K helium or low pressure liquid from the 4.5 K phase separator. The baseline design for the shield/beam-line cooling [low pressure intercept] is to use a low pressure supply and return this locally to the refrigeration recovery system and local compressor. Each power coupler has been budgeted as a liquefaction load for the outer conductor cooling and the output returns to the local compressor. Connection to the IR10 SRF cryogenic distribution system will be with welded field joints for all SRF cavity cryomodule.

Cryogenic Distribution and Satellite Subsystem

Cryogenic cooling capacity will come from the central plant with supply and return flows routed through the existing hadron rings cryo distribution system's S-line, R-line, U-line, H-line and warm return header. The baseline design consists of a hybrid sub-atmospheric system consisting of 3 stages of cold compressors and warm vacuum compressors, and will have refrigeration recovery heat-exchangers to process the sub-atmospheric cold compressor flow and the 1.1 bar shield/beam line intercept flow. Approximately 62 g/s of 27 mbar flow coming from the 2 K baths are compressed to above 250 mbar in 3 cold-compressor stages before entering a heat exchanger stack with subsequent injection into the warm vacuum compressor that compresses the low pressure helium to 1.1 bar. A local compressor will process the flow from the warm vacuum compressor and the shield/intercept flows to a higher pressure in order to send it back via the refrigeration recovery cold-box for injection back into the hadron ring cryogenic distribution system's shield loop, and the colder, 10 K stream from recovering the sub-atmospheric circuit is injected back into the hadron

ring's cryo-distribution system U-line return circuit. Liquefaction load flow returns to the central plant via the warm return header. Table 6.110 summarizes the operating loads for the local compressor system and Table 6.111 summarizes the loading for each subsystem as well as the expected loading on the central plant.

Table 6.110: IR10 region local cryogenic system utilities.

Local Compressor			Helium Vacuum Compressor		
Flow [g/s]	Power [kW]	Water [GPM]	Flow [g/s]	Power [kW]	Water [GPM]
105	465	178	62	101	38

Table 6.111: IR10 cryogenic loading on central plant.

Subsystem	4.5 K Refrigeration [W]	4.5 K-10 K Non-isothermal [g/s]	4.5 K-80 K Intercept/Shield [g/s]	4.5 K-80 K Liquefaction [g/s]
IR10 Loads	1358	60	11.5	13
R.R. Imbalance			5	
Total	1358	60	16.5	13

Modifications to Hadron Ring Cryogenic Distribution

To accommodate the hadron beam cooling sections on both side of the IR02 location, modification of the hadron ring cryogenic distribution system needs to be made. The 01DX, 01D0, 01Triplet, 02DX, 02D0, and 02Triplet will be removed to make room for the hadron cooler. Two new sections of the hadron ring cryogenic distribution line (which will include the superconducting busses) will need to be installed starting from the incoming lines from the service building at each triplet location, in order to bypass the hadron cooler section back into Q4 magnets. In addition, a tee-off from the hadron ring cryogenic distribution is required to supply and return flows to/from the SRF electron LINAC in the adjacent tunnel.

Cryogenics System for Energy Recovery Superconducting RF LINAC

(To request the content for this section, please contact the EIC Information Services Group Leader, Alyssa Petrone, apetrone@bnl.gov).

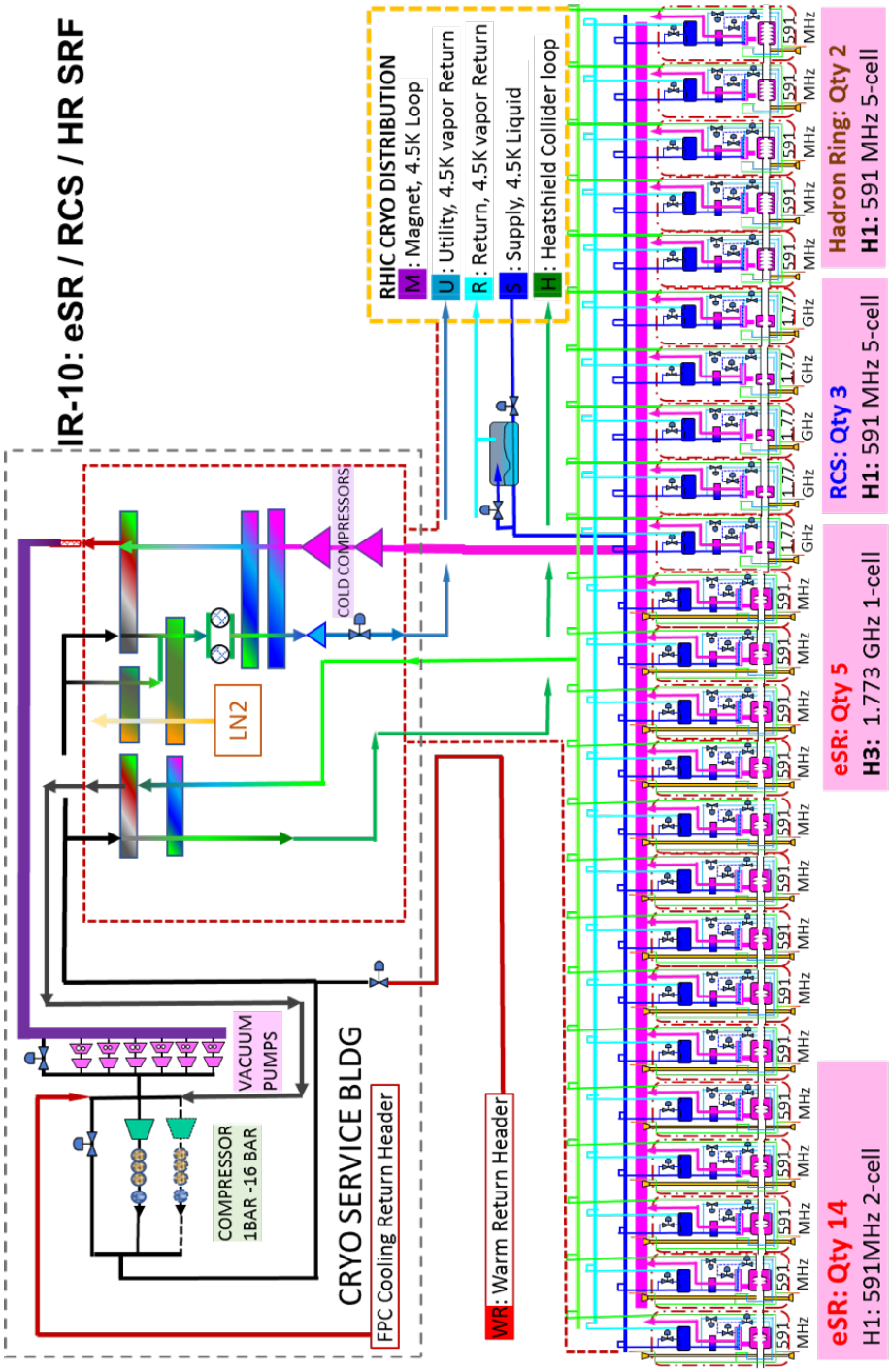

Figure 6.239: IR10 SRF cryogenics system.

Chapter 7

Infrastructure

7.1 Infrastructure Overview

Introduction

The Electron-Ion Collider (EIC) conventional facilities will provide the buildings, utility systems and site infrastructure systems necessary to enable installation and operation of the particle accelerator, storage rings, and target instruments. The conventional facilities must be designed and constructed to enable the performance of the most advanced lepton-hadron collider ever built. Furthermore, the conventional facilities must be constructed on a schedule that enables installation of the accelerator systems in accordance with the overall project schedule.

Project Goals

The conventional facilities must meet the functional goals of creating a stable operating environment for sensitive equipment that is implemented utilizing conventional construction techniques. This section describes the scope and design considerations for the EIC conventional facilities. The anticipated construction costs and currently identified schedule requirements are described in the respective cost and schedule sections of this report.

Project Description

The EIC project leverages the accelerator tunnel and related existing buildings constructed for the Relativistic Heavy Ion Collider (RHIC) built in the late 1970's. Hence, the primary EIC facilities are located adjacent to the existing Interaction Regions (IR), typically reinforced concrete structures, located at the 2 o'clock, 4 o'clock, 10 o'clock, and 12 o'clock positions. Smaller buildings, referred to as alcove buildings, are located outside of the berm and tunnel profile at the 1 o'clock, 3 o'clock, 5 o'clock, 7 o'clock, 9 o'clock, and 11

o'clock positions and house power supplies serving magnet systems within the tunnel. The two largest EIC buildings are located at the 2 o'clock and 10 o'clock locations. Building 1002 houses the electron injection linear accelerator (LINAC), the electron gun and related laser equipment, as well as the Radio Frequency (RF) power supplies to linac RF cavities. Its location has been dictated by the existing spur tunnel originally constructed to house a spectrometer, which provides an opening into the IR region concrete building at 2 o'clock. Similarly, building 1010 is located adjacent to the IR region at the 10 o'clock position and houses the significant quantity of RF equipment with an estimated demand of 30 MW providing RF power to the RF/SRF cavities in the 1010 IR.

Many of the existing structures presently at RHIC and throughout the CAD complex can be re-engineered and adapted to fit requirements of the EIC. These include the service buildings around the exterior of the ring (8 large buildings), the 18 alcoves interior to the RHIC tunnel as well as numerous other structures.

Additionally, major components of the existing electrical systems will be adapted, expanded and upgraded to provide necessary power for the EIC systems. These changes and additions include but not limited to:

- Adding several new buildings
- Increasing the site electrical capacity
- Expanding the site overhead 13.8 kV distribution
- Providing electrical distribution to the new and modified buildings
- Providing network connectivity to each new building

The scope of this effort is limited to the conventional infrastructure upgrades needed to support the science processes. The electrical system will be upgraded from the substation to the point of the processes equipment. It will also include the fitting out of the convention building electrical requirements of each new building. It excludes final connections to the process equipment.

7.2 Mechanical Utilities and Systems Upgrade

7.2.1 Site Buildings and facilities

Table 7.1 shows a list of the new structures and Figures 7.1, 7.2, 7.3, 7.4 and 7.5 show the relative orientation of facilities at Sectors 2, 4, 6, 10 and 12 of the ring respectively.

An example of the the alcove buildings is depicted in Figure 7.6 and a Main Alcove building depicted in Figure 7.7.

Table 7.1: Proposed new buildings.

Building	Designation	Qty	Area	Total Area
Alcove Buildings	ALC-01,03,05,11	4	2,330	9,320
Main Alcove Buildings	ALC-7,9	2	4,320	9,640
Cryogenic Plants 1002,1006	B1002C,B1006C	2	4,320	8,640
Cryogenic Plant 1010	B1010C	1	4,910	4,910
Kicker Power Supplies	B1004	1	4,480	4,480
Kicker Power Supplies	B1012	1	10,630	10,630
Electron Source Building	1002	1	29,560	29,560
RF Building	B1010	1	42,130	42,130
Total Gross Area				119,310

7.2.2 Cooling Systems Upgrade

Facilities such as cooling towers, DI water systems, chillers and air handlers must evolve with the overall complex design. Considerations for foundations, piping controls, ductwork, insulation etc. must also follow design.

EIC Needs

EIC Needs Identified to Date:

- 4 Cooling Tower Systems
- Building, Magnet cooling DI Water for 1002, 1004, 1010 and 1012
- Building, Magnet, RF, and Cavity DI Water for 1010
- Power Supply closed-loop deionized (DI) process chilled water system for Alcove Buildings 1001, 1003, 1005, 1007, 1009, 1011
- Modular, variable capacity air-cooled chiller packages totaling $\approx$ 1000 T for air conditioning loads and, if needed, DI trimming. These modern units reduce O&M costs in this size range.

Air Conditioning

The building airside systems generally consists of fully ducted overhead distribution to ceiling diffusers, registers, and grilles (DRG), supplied via central or distributed variable

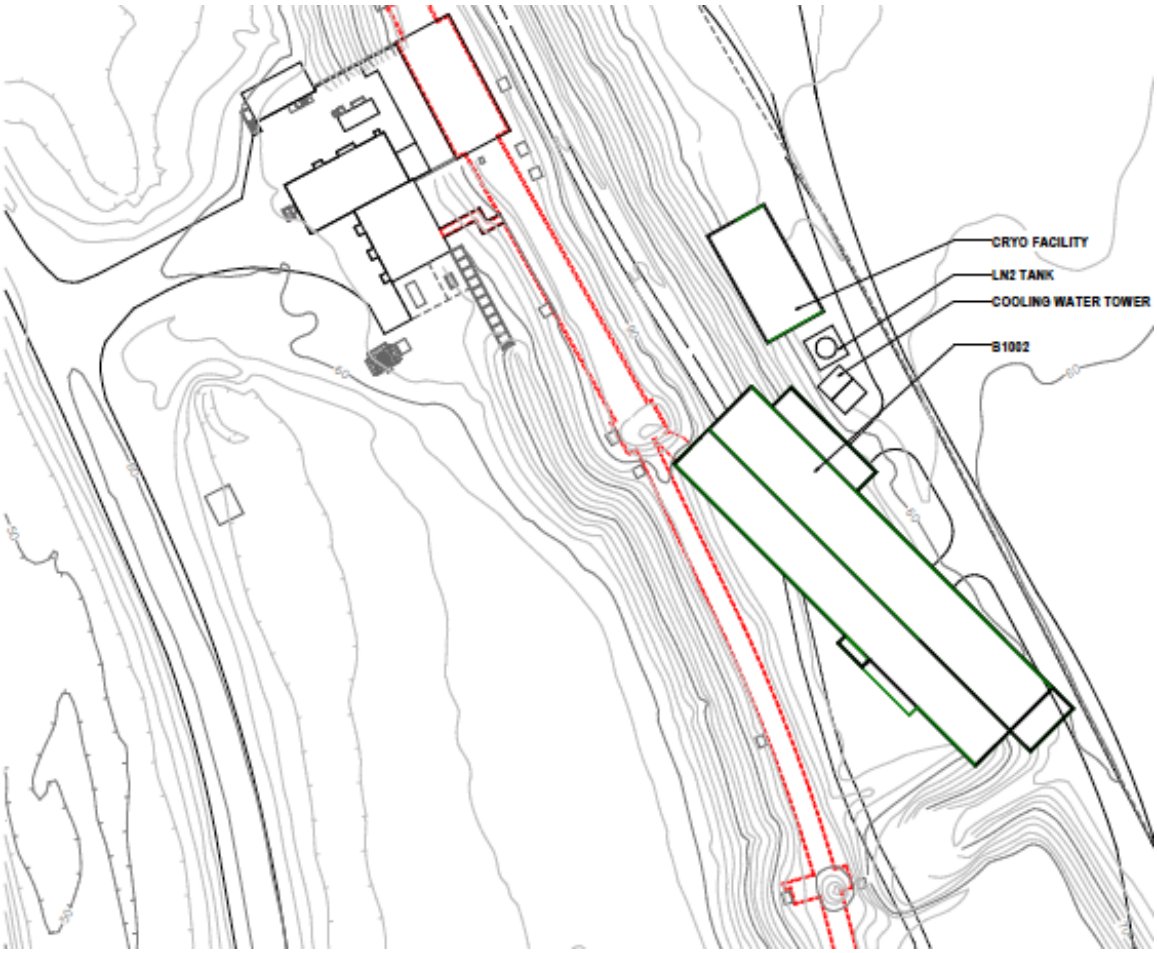

Figure 7.1: Site plan of 1002 facilities section.

air volume (VAV) air handling units (AHU) with chilled water or refrigerant cooling coils. Refer to the following building system description for specific configuration of equipment and distribution.

Building Environment

Equipment and Occupied Rooms: Control, Break, Power Supply and RF Equipment

- Cooling: 75°F DB maximum, with range of +3°F
- Heating: 68°F DB minimum, with range of -3°F

Figure 7.2: Site plan of 1004 facilities section.

- Humidity: 60 indirectly controlled by air handling coil supply air temperature control)

Support Rooms: Pumping, Electrical, Equipment Corridor

- Cooling: 80°F DB maximum, with range of +3°F
- Heating: 60°F DB minimum, with range of -3°F
- Humidity: 60 indirectly controlled by air handling coil supply air temperature control)

Cryogenic Equipment Rooms: Compressor

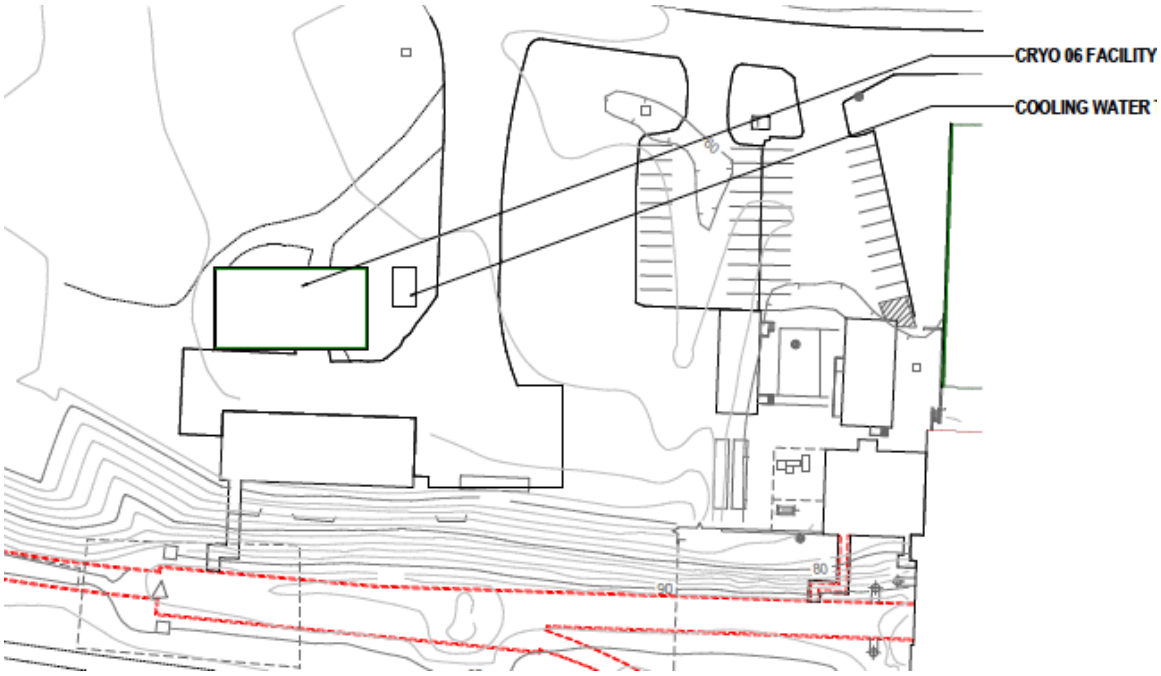

Figure 7.3: Site plan of 1006 facilities section.

- Cooling: Uncontrolled, mechanical ventilation cooling
- Heating: Occupied: 60°F DB minimum, with range of -3°F Unoccupied: 40°F DB minimum, with range of -3°F
- Humidity: Uncontrolled

Data Processing and Server Rooms: Telecommunication Rooms, Controls Room, Rack Rooms

- Cooling: 75°F DB maximum, with range of +3°F
- Heating: 68°F DB minimum, with range of -3°F
- Humidity: 60 indirectly controlled by air handling coil supply air temperature control)

Special Purpose Rooms

1002 Laser Room [1002-N]

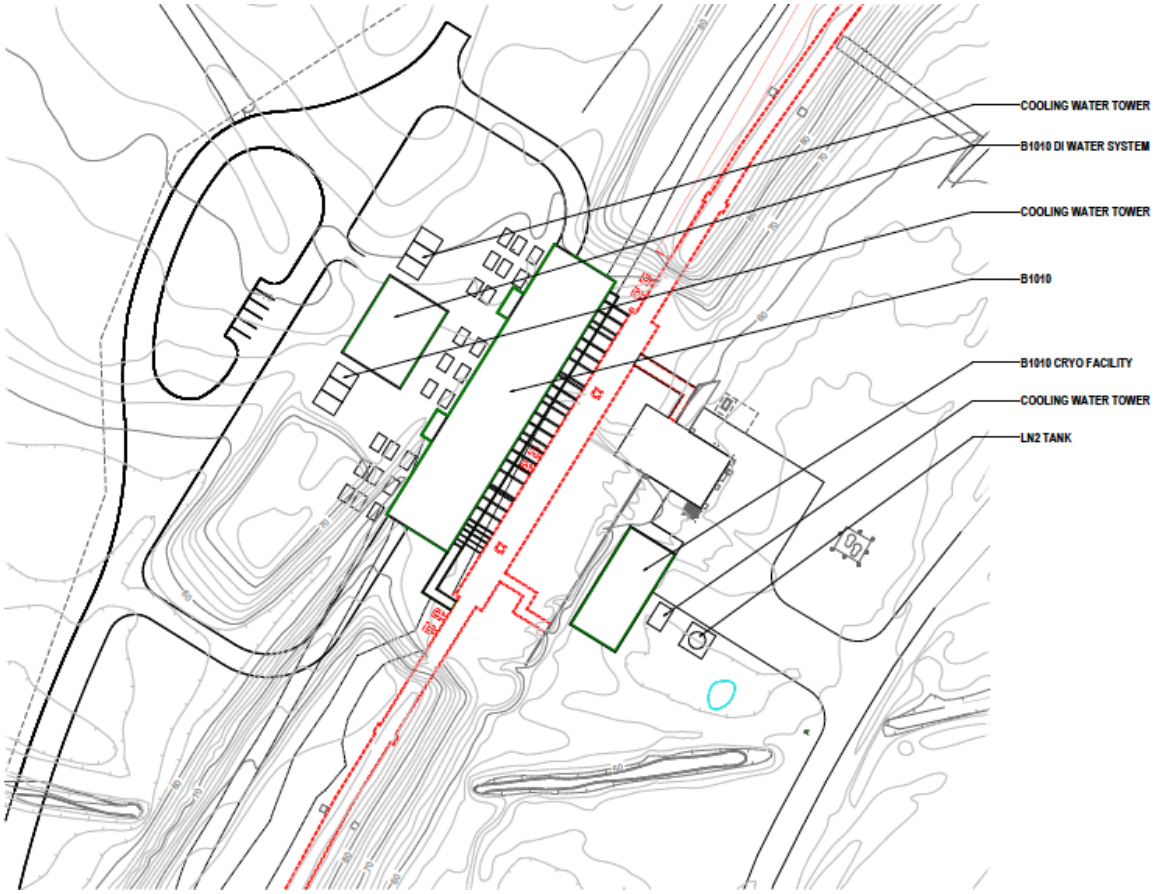

Figure 7.4: Site plan of 1010 facilities section.

- Temperature: 68°F DB set point, with range of ±1°F
- Humidity: 45
- Cleanliness: ISO 7 (FS Class 10,000), 60 air changes per hour, non-unidirectional airflow
- Pressurization: Positive, minimum +0.06" W.C. relative to the adjoining corridor

1002 Gown Room [1002-O]

- Temperature: 68°F DB set point, with range of ±2°F
- Humidity: 45

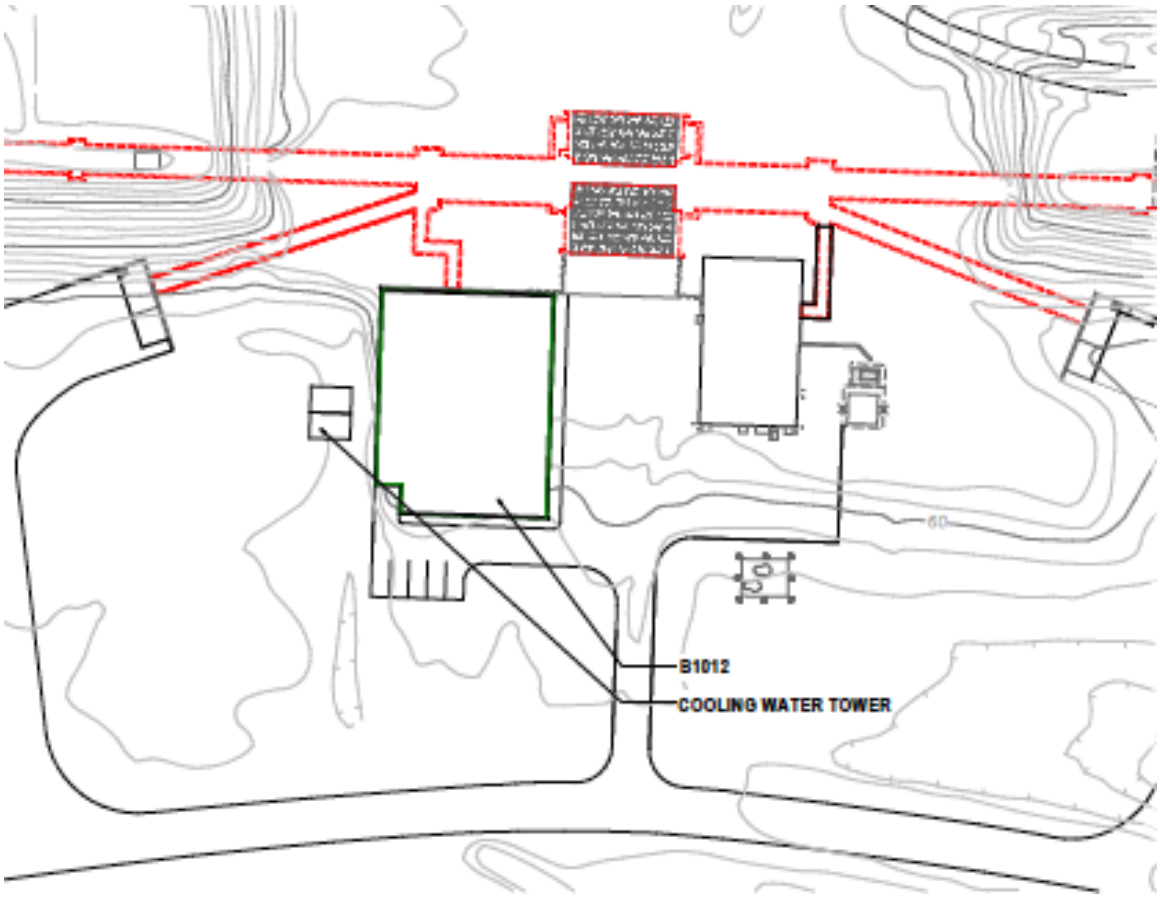

Figure 7.5: Site plan of 1012 facilities section.

- Cleanliness: ISO 8 (FS Class 100,000), 20 air changes per hour, non-unidirectional airflow
- Pressurization: Positive, minimum +0.03" W.C. relative to the adjoining corridor

1012 ESR Power Supplies [1012-B]

- Temperature: 72°F DB set point, with range of ±1°F
- Humidity: 60 indirectly controlled by air handling coil supply air temperature control)

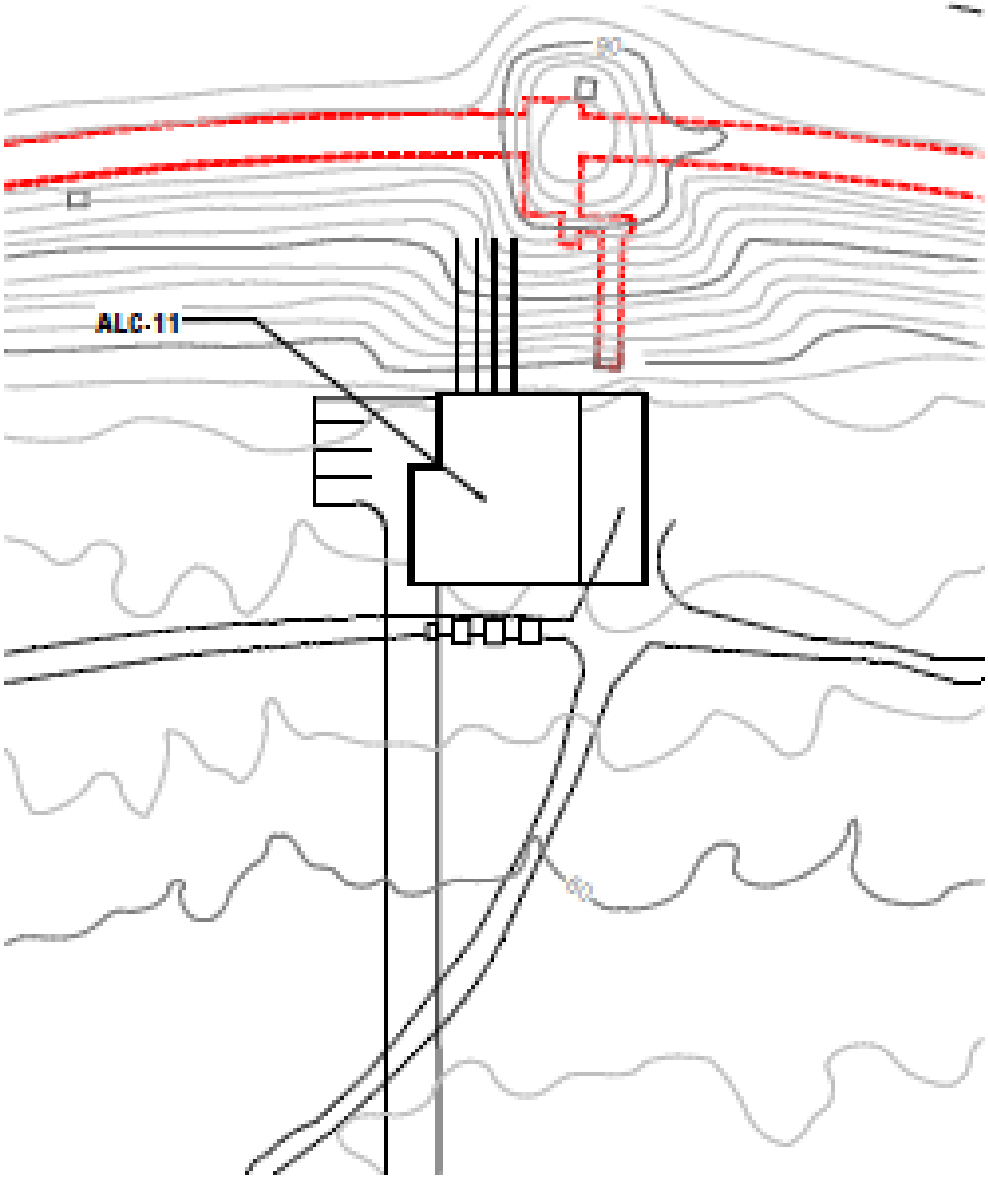

Figure 7.6: Alcove buildings at sectors 1, 3, 5 and 11.

7.2.3 Tunnel and Other Civil Engineering Upgrades

1002 Pre-Injector

The existing spectrometer tunnel may be suitable for all or part of the new beamline.

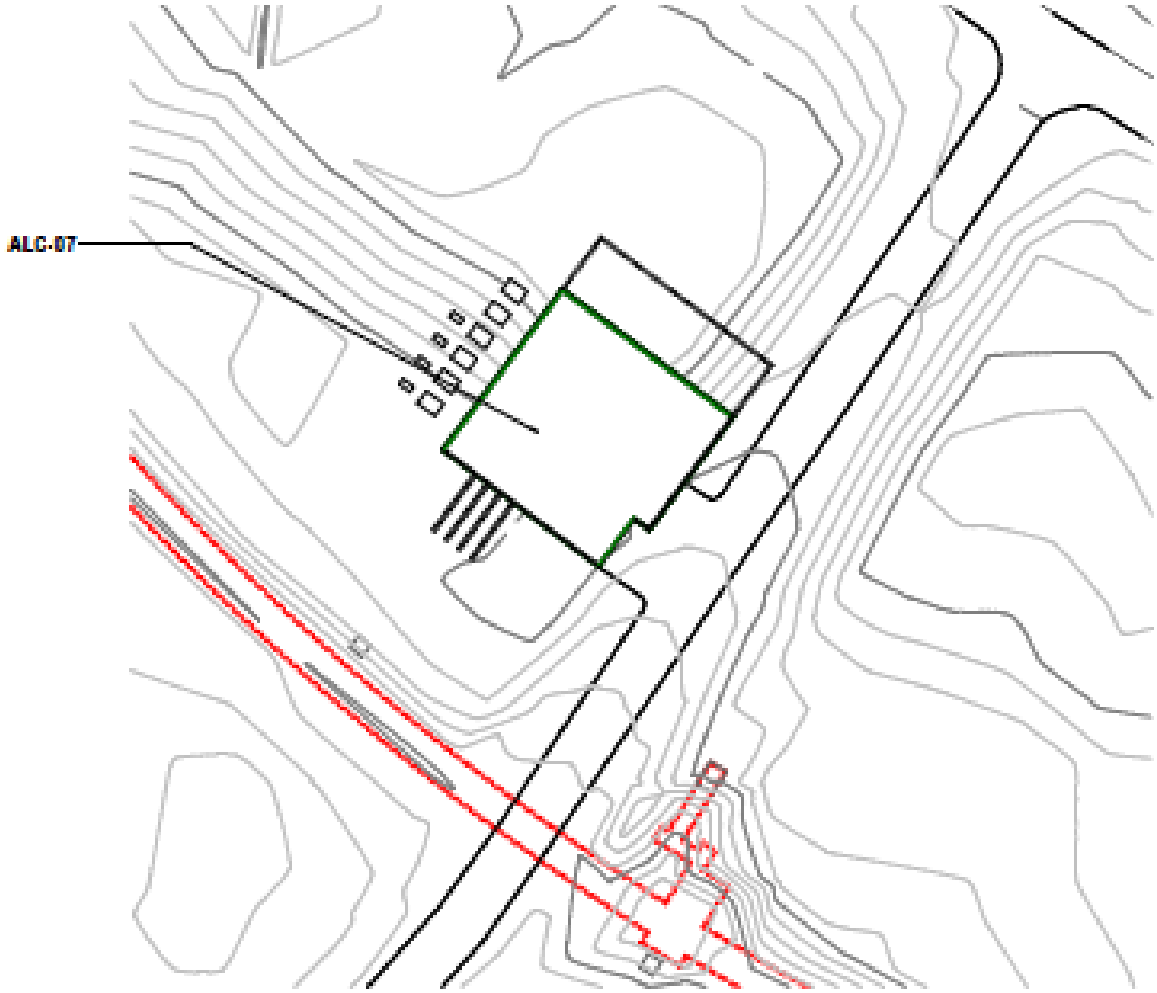

Figure 7.7: Main Alcove buildings at sectors 7 and 9.

- Assumption: Utilize the tunnel and add a new, larger diameter section approximately 100 feet long
- Corrugated arch-plate construction with earth berm covering
- Stabilize existing tunnel with sheet pile during new construction excavation.
- Possible use of poured concrete retaining wall to serve as near wall of building to achieve the shortest possible waveguide run

The existing Spectrometer tunnel is approximately 7 feet tall and 8 feet wide.

Alcoves

The 18 existing in-ring alcoves will be modified to house systems and equipment. Two floor plans will be equally distributed with equipment and are depicted in Figures 7.8 and 7.9 respectively.

7.2.4 Conclusions

RHIC represents an excellent site from a civil and mechanical viewpoint. The ring configuration provides for flexible options for distribution of services and utilities. No insurmountable technological challenges from the civil and mechanical perspective have yet arisen, though there will be significant challenges such as:

- RF waveguide routing will be complex and will most likely require significant invasive construction. Effects on RHIC tunnel stability need to be studied carefully. Structural stability of the arch-plate tunnel is dependent on the integrity of the soil backfill. Soil removal and modification will be done with great care and caution. Additionally, wave-guide routing and installation is subject to the following:
  - Requirement for maximum lengths for RF performance
  - Installation, servicing and removal/replacement concerns
  - Desire for minimum radiation leakage through doglegs, labyrinths or shielding placement
  - Requirements for environmental control and what is needed to deliver this in the RHIC tunnel are largely unknown
  - Extensive A/C ductwork has not as yet been physically accommodated in the design of tunnel sections (upgrades to the IRs can be addressed more readily)
  - Examination of current loads in the tunnel (infiltration, both latent and sensible heat) is in progress.

7.2.5 Path Forward

- Continue to develop the RHIC Infrastructure plan into a fully mature document. The success of the EIC depends, to a large degree, on robust, reliable and up-to date supporting equipment.
- Continue to refine information for the Infrastructure Team regarding specific requirements (and options) for accelerator components. This includes but is not limited to heat loads, flow rates, temperatures, sizes, etc.
- Continue to gather information needed for the NEPA (National Environmental Policy Act) process. Design modifications driven by NEPA outcomes must be identified early on as they can be significant cost drivers.

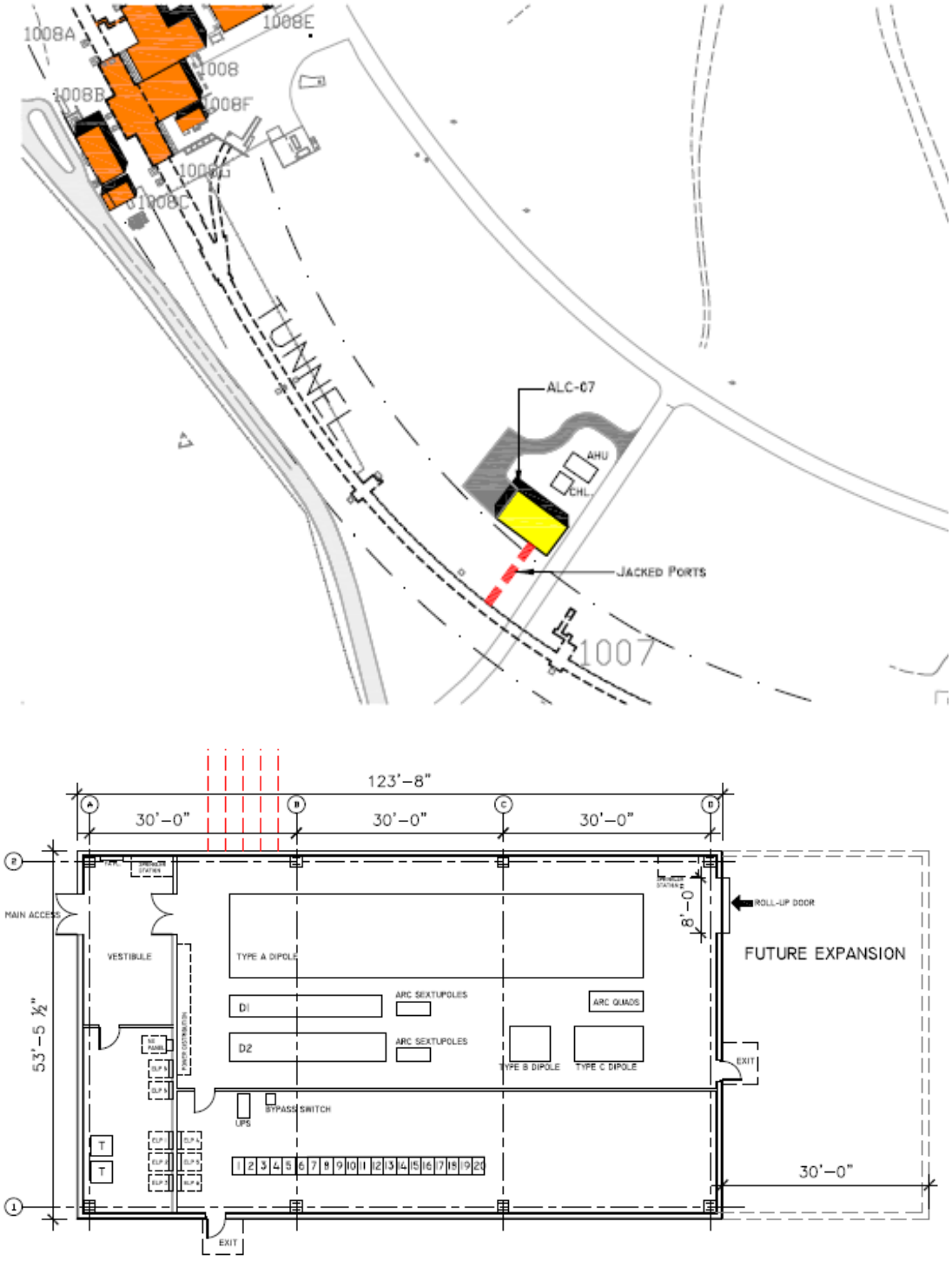

Figure 7.8: Alcove layout Number 1. Top: site plan. Bottom: floor plan.

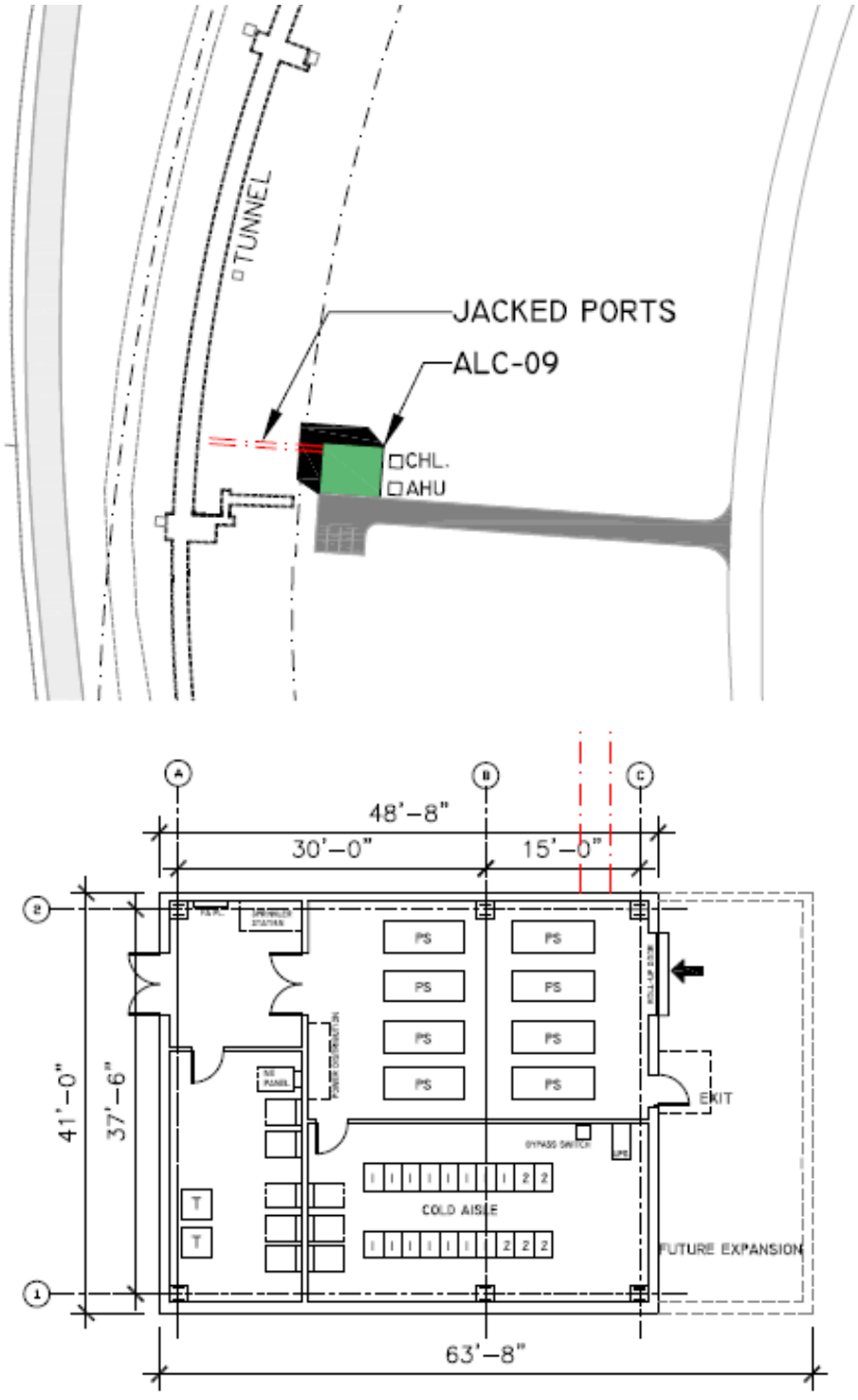

Figure 7.9: Alcove layout Number 2. Top: site plan. Bottom: floor plan.

7.3 Electrical Utilities and Systems Upgrade

Electrical systems at Brookhaven National Laboratory will be upgrading an existing electrical infrastructure at accommodate the needs of the Electron Ion Collider. The section below outlines measures necessary to accomplish this goal.

7.3.1 Site Utilities

Workshops conducted with BNL and information provided by BNL provided the basis for the existing conditions defined herein. The existing RHIC ring and support buildings are served from a 13.8 kV distribution that includes both overhead and underground duct banks originating primarily from switchgear buildings 631 and 638. Busses #8, #6, and #4 primarily feed existing RHIC loads. Bus #7 feeds a 20 MW pulse load and will remain dedicated to that load. The existing distribution will remain continuing to serve the current buildings. The existing buildings located at sectors 1002, 1004, 1006, 1008, 1010, and 1012 have 2500 kVA, 480 V unit-substations that will continue to support those buildings. They also have available reserve capacity that can be used to serve some of the EIC upgrades. Bus # 8 transformer is 69 kV-13.8 kV rated 20/26.7/29.6 MVA and is distributed OverHead (OH) at 13.8 kV with 1192 kCMil conductors. The existing metered demand on bus #8 is 300 amps (7.2 MVA) leaving 12.8 MVA @ base rating available to support the new upgrades. The existing Substation yard for bus #8 was design with provisions for a future transformer #9 and bussing. Building 638 currently houses the 13.8 kV switchgear bus #8 with space dedicated for the future bus #9 switchgear. There is an existing overhead (OH) wood pole distribution that originates at building 638 and is routed to the RHIC near section segment 4. The OH structure was designed to support two separate lines. Currently bus #8 is located on this OH structure with the second supports available for the new bus #9 circuit.

Substation Upgrades

A new 20/26.7/29.6 MVA oil filled 69 kV/13.8 kV transformer #9 will be added to support the increased load supporting the enhanced EIC load. The new transformer #9 will be located in the existing substation yard where existing transformer #8 is located. The switchyard will be expanded to accommodate the additional transformer. The substation yard has provisions for adding the additional transformer #9. These provisions include an OH 69 kV 1200 amp vertical break switch to extend OH 1200 amp air insulating bussing to new transformer #9. The transformer will be protected with a 69 kV, 1200 amp circuit breaker. Existing building 639 has space dedicated for this future installation of #9 bus switchgear. It has duct bank stubbed out of 639 available to extend to the output of the transformer #9. Switchgear #9 will have a nominal rating of 15 kV, 2000 A, 3 wire, 95 kV BIL, 500 MVA symmetrical amp interrupting capacity. It will be equipped with metering, potential transformers, and a feed for a station service transformer. It will have a 2000 amp main breaker, a tie breaker to #8 bus, an equipped space for future breaker, and 1200 amp breaker for the OH feeder to the ring. Protective relaying will be provided in the switchgear for the

transformer and bus protection. BNL has standardized on Schweitzer Engineering Laboratories (SEL) protective relaying, models 751 and 351. Arc flash reduction relaying will be provided including optical arc flash detection. Miscellaneous upgrades to the switchyard include adding a remote annunciator for the new #9 transformer and switchgear, provide a transformer base with oil separation with connection to storm drain and an existing dormant sanitary line will be removed, and switchyard fencing will extended to enclose the new transformer. The existing oil/water separator will also be tied into the storm drain. An existing roadway from 5th Avenue North, located on the east side of the substation, will need to be extended to provide access to the new #9 transformer. The new substation installation will be in compliance with Factory Mutual Insurance Companies requirements for loss prevention. This will include meeting minimum distance requirements between buildings and equipment. It may also require 2 hour fire walls if the distances cannot be met.

Overhead 13.8 kV Distribution

13.8 kV power from the new bus #9 will be distributed to the ring. The existing overhead (OH) wood pole distribution originates at building 638 and is routed to the ring near sector 4. The existing OH structure is designed to support two separate lines. Currently bus #8 is located on this OH structure with the second supports available for the new bus #9 circuit. The #9 bus circuit will be 1192 kCMIL per phase having an of 1140 amps ($\sim$28 MVA). New poles will be required at section 4 to extend the distribution counterclockwise to building 1010. The #9 circuit will transition from the existing poles to the new poles at section 4. The existing #8 OH circuit will be extended from sector 9 to sector 10 to close a loop between the two busses with isolation switches that will be normally open. Fused switches will be provided to where new substations are being provided around the ring. Isolations switches will be installed on adjacent poles to provide the ability to isolate the taped poles. Isolation switches will also be provided for the exiting 13.8 kV distribution to isolate the areas of 1002, 1004, 1006, 1008, 1010, and 1012.

Future Substation and Overhead 13.8 kV Distribution

The reserve capacity on #8 substation and the new # 9 substation will provide sufficient power to support the initial ramp up of the EIC enhancements. At full operation, expected year 2030, it is anticipated that an additional new substation will be required. The current strategy to support this additional power requirement is to add a new 138 kV-69 kV 100 MVA substation that is sourced from the existing 138 kV transmission line. A new 25 MVA 69 kV-13.8 kV #10 transformer and supporting switchgear will be added to the new 138 kV-69 kV 100 MVA substation with overhead distribution to the site. The actual location of the new substation has not been determined. The cost of this infrastructure must be included in current project overall budget.

Building Power Distribution

Buildings will be provided with outdoor unit substations. The quantity of unit substations for each building will be determined from the anticipated load. The loads of each building is included in subsequent paragraphs. Each substation shall include an outdoor metal enclosed switchgear close coupled to a 13,800–480Y/277 volt 2500 kVA oil filled substation type transformer with a secondary air terminal section. The primary switchgear shall consist of a loop switch in series with a fused load interrupter switch. Each transformer shall be triple rated 55° OA, 65° OA, and 65° FA. A duct bank and secondary feeders shall be extended to 480 volt switchgear located in the electrical room of each Building. Additional surface mounted switchboards will be added as required in the experimental equipment rooms will be used to power the equipment.

Emergency Power Distribution

Life Safety Power for some of the existing buildings is provided from six 480 V life safety generators. These six generators are located at buildings, 1004 A, 1006 A, 1008 A, 1012 A, 1010 A and 1002 A. These existing systems will be used to serve the life safety loads of the new buildings being built in the same sector. A single new 150 kW diesel engine driven Life Safety generators in weather proof sound attenuating enclosures will be provided at each Alcoves 1001, 1003, 1007, 1009, and 1011. A single new 400 kW diesel engine driven Life Safety generators in weather proof sound attenuating enclosures will be provided to support the each new Cryogen plants at 1002 1006 and 1010. Fuel oil storage capacity shall provide 12 hour full load operation for each generator and will be stored in a double wall, sub-base fuel tank with remote alarm panel. Each new installation will include an emergency switchboard with two separate transfer switches. One dedicated to life safety loads and the other to serve optional stand-by loads. Emergency power shall be provided to the following loads:

- Egress and exit lighting
- Fire alarm system

Optional stand-by power shall be provided to the following loads:

- Selected exhaust and make-up systems
- Selected HVAC controls
- Mechanical control system
- Telecommunication system
- Security system
- Other Selected equipment

The intent is to prioritize equipment on generator power which is necessary to prevent equipment damage or the loss of an experiment that will takes several days to reproduce.

Uninterruptible Power Systems

Each new building will include a 40 kW UPS with 5 minute runtime lithium ion or valve regulated lead acid batteries. The UPS will be double conversion type with energy saving mode and will be modular to allow expansion to accommodate load growth. The UPS will have maintenance bypass. The UPS will serve rack mounted loads consisting of controls, instrumentation and networking. All building controls and programmable logic controllers will also be on connected UPS. The UPS will be backed up with generator power.

7.3.2 Cable Tray Expansion and Upgrades

Two 24 inch galvanized steel cable trays shall be added to the existing RHIC tunnel tray systems. 24 inch galvanized steel cable tray shall be provided above the scientific equipment and above all racks in each new buildings and alcoves. These peak design loads are based on equipment requirements provided by BNL. Diversity was applied to the connected load as recommended by BNL. The connected load is being refined as additional information is being determined.

7.3.3 Lighting System Expansion and Upgrades

Exterior lighting shall be provided along new roadways, the #9 substation expansion, walkways and building exits. Illumination levels shall be in accordance with DOE and IES standards. Fixtures shall be full cut-off type using LED light sources at a mounting height generally not exceeding 20 feet. Exterior lighting controls shall provide photocell on, photocell off controls with the ability to turn off the lights at a selectable time of day. The exterior lighting system shall comply with LEED Sustainable Site Credit #8 —Light Pollution Reduction and ASHRAE 90.1. The exterior luminaries for egress path lighting shall be connected to life safety power. Interior lighting shall be provided from LED sources. The majority of buildings require the assembly of small color coded components. This requires a high level of visual acuity and the ability to discern colors. Lighting shall be designed as recommended in the IES “The Lighting Handbook, 10th edition”. Lighting will predominately be linear industrial style pendent mounted LED luminaries. Luminaries will have a minimum of 4000k and 90 Color Rendering Index (CRI). Refer to Room data sheets for minimum Lux levels for functional areas. Life safety luminaries will remain on un-switched. Egress lighting will meet NFPA 101 Life Safety Standards. Exit lights shall be LED type. Occupancy sensors shall control lighting in all spaces other than scientific equipment and experimental areas. Offices, storage and similar spaces shall be provided with override off switches at the door. Scientific equipment and experimental areas shall

be provided with a low voltage control system with local on/off override switches. Photo sensors shall be provide in perimeter offices and other spaces with natural lighting. Interior illumination levels shall be in accordance with DOE and IES standards. The interior lighting system power consumption shall comply with ASHRAE 90.1 limitations.

7.3.4 Comments on Electrical Systems Expansions and Upgrades

In this section we outline some comments about the overall scheme for proposed upgrades.

Category of Electrical Power

1. Normal Power: Magnet power supply, water pumps, chillers, HVAC, cryogenic, etc.
2. Normal/Emergency power, Life Safety System: ODH, ACS, fire protection, emergency lights.
3. Normal/Emergency power, Experiment/Cryogenic System, compressed air, heat trace, etc.
4. UPS
5. UPS fed from Normal/Emergency power: Network switches, Cryo control racks, magnet power supply control and communication, access control system.

Features of the New 480 V Substation

- Improved safety utilizing the combination of 13.8 kV load-break switch and medium voltage vacuum circuit breaker for the transformer protection, thus reducing the arc flash potential.
- The current transformers can be installed on the secondary 480 V bus. The protective relays are connected into the primary vacuum circuit breaker. This can effectively provide primary substation transformer protection as well as secondary switchgear bus protection using one device.
- Use of the 13.8 kV circuit breaker can drastically reduce the arc flash energy on the secondary bus for any unit substation.
- Use of dry type transformers negates the need for firewall and transformer oil drain pits.
- New 480 V power circuit breakers would be equipped with remote on/off and remote rack out/in.
- All 480–208/120 V dry type transformers will be installed outdoors to reduce air conditioning heat load and preserve indoor floor space.

- All panel-board molded case circuit breakers have permanent pad lockable hardware for LOTO.
- The 480 V systems are 3 phase/3 wire ungrounded power system. This equipment shall be able to withstand the higher system line to ground voltage when there is a ground fault.

Diesel Generator Power

Emergency power essential for safety to human life (for example, illumination) requires specific features for the generators, installation, maintenance and testing. It is intended to separate the life safety generator (ODH, Ventilation and lighting) from machine operation generator (vacuum system, UPS systems, Network and Phone etc). Option: Separate the Life Safety N/E power panel from Machine N/E power. That will allow for additional diesel generators, as required, to be added later. Figure 7.10 shows an example of an emergency power one-line diagram.

Code Compliance

Use of less flammable transformer oil for RF HVPS will reduce building fire code adherence issues.

In order to meet the electrical code and to pass the electrical inspection program, the system designers should get available fault current values from the Power Distribution Group before ordering magnet power supplies, chillers, VFD, air compressors, motor starters and RF amplifiers. Vendors must meet the short circuit current capacity requirements. The Short Circuit Current Rating (SCCR) must meet NEC Article 409 Industrial Control Panel requirement. Equipment at less than 60 A does not have an SCCR requirement, but still needs to meet available fault current requirements. We plan to specify a 10 kA short circuit current for 208/120 V systems.

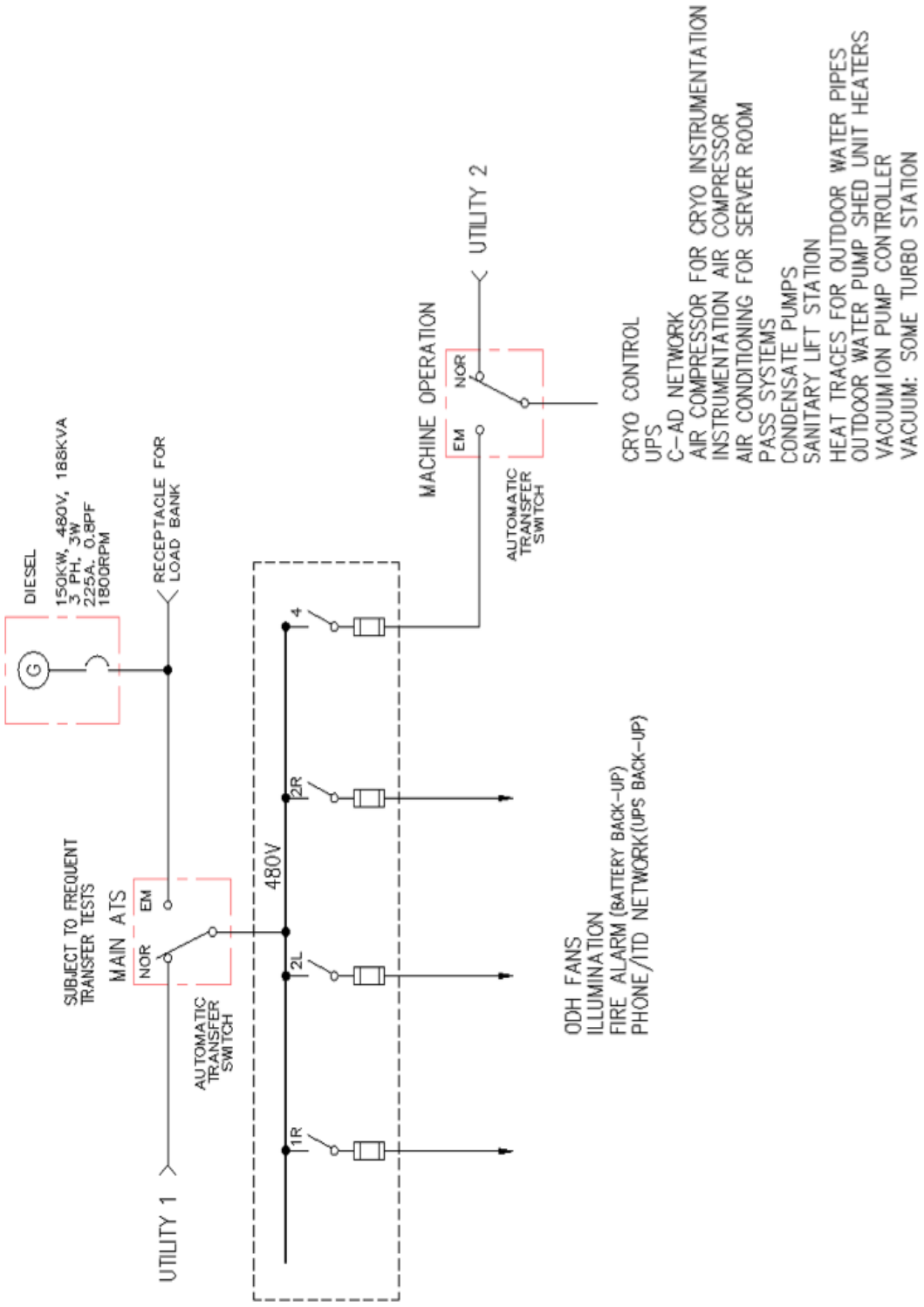

Figure 7.10: Emergency power one-line diagram: Cryogenics.

Chapter 8

EIC Experimental Equipment

8.1 Context of Experimental Equipment Realization

The path chosen for the consideration of the Experimental Equipment scope of the Electron-Ion Collider differs much from the Accelerator scope. Development of the EIC science and the experimental equipment required to successfully implement the science as documented in the NSAC and NAS reports has been driven by an international EIC community. This community formalized itself in 2016 in the EIC User Group (EICUG, see www.eicug.org). The EICUG has in 2020 grown to about 1200 members representing 245 institutions and 33 countries (see www.eigug.org/pnb).

A handful of general-purpose EIC detectors have been conceptualized in the period up to 2019. To bring the state of the EIC experimental equipment definition to a next level, and folding in that the EIC is capable of supporting a science program that includes two detectors, the EICUG put into effect a "Yellow Report" activity[1]. Much documentation on the ongoing Yellow Report activity are given at http://www.eicug.org/web/content/yellow-report-initiative. The main goal of the Yellow Report activity is to advance the state of documented (i) physics studies (White Paper, INT program proceedings) and (ii) detector concepts (Detector and R&D Handbook) in preparation for the EIC. This will provide both the basis for further development of concepts for experimental equipment best suited to the EIC science needs, including complementarity of the two detector/interaction regions, and input towards future Technical Design Reports of the experimental equipment.

The general community strategy for this Yellow Report activity is both to *Quantify physics measurements for existing or new physics topics and implications for detector design*, and alternately to *Study detector concepts based on the requirements defined above, and*

[1]The CERN Yellow Reports series provides a medium for communicating CERN-related work where publication in a journal is not appropriate. Reports include material having a large impact on the future of CERN, as well as reports on new activities which do not yet have a natural platform. The series includes reports on detectors and technical papers, criteria being that the audience should be large and the duration of interest long. The term Yellow Reports is now used frequently for documents with similar purpose in various physics communities unrelated to CERN.

quantify implications for the physics measurements. The Yellow Report will be completed by January 2021, and will present the EIC community consensus on vision towards the general-purpose EIC experimental equipment, and also discuss detector technologies of relevance for two complementary general-purpose detectors. As such, with this community effort ongoing, and with the realization that the detector technologies for the general EIC science program are in general well understood, this section of the CDR describes a "plausible scenario reference EIC detector". This reference detector can execute the EIC science program as documented in the NSAC and NAS reports, but we include also mention of various alternate detector technologies under consideration for one, or even two, of the possible detectors.

We foresee a call for detector proposals to start after the Yellow Report completion. This folds in the result of a "Call for Expressions of Interest (EOI)" (see https://www.bnl.gov/eic/EOI.php). With this call, Brookhaven National Laboratory in association with TJNAF, invited interested groups to submit a (non-binding) Expression of Interest for their potential cooperation on the experimental equipment in support of a broad and successful science program at the EIC. The call also encouraged interested groups to work together within their country, their geographical region, or as a general consortium, to submit such EOIs. Input of these 47 EOIs gives guidance on the detector scope and will also be very influential in determining the trajectory of one or both general-purpose detectors (and their Interaction Regions). We plan to complete the process for selection of final EIC detector proposals by the end of 2021. This will simultaneously serve as stepping stone towards the formation of the detector collaboration(s).

In parallel with a nearly two-decade-long community effort of EIC science development and refinement, and experimental equipment conceptualization, Brookhaven National Laboratory in association with TJNAF and the DOE Office of Nuclear Physics established in 2011 a highly successful and still ongoing generic EIC-related detector R&D program (see wiki.bnl.gov/conferences/index.php/EIC_R%25D). This generic R&D program both built bridges between various domestic and international research groups and scientific communities, and was successful in its own right towards detector R&D. Presently, 281 scientists are engaged in the generic EIC-related R&D program, from 75 institutions in 10 countries. Most of the efforts have been organizationally merged in groups of scientists or consortia, which can provide the seeds for the long-term EIC detector collaboration(s).

In general, much due to the longstanding generic EIC-related detector R&D program, the detector technologies to implement a successful comprehensive Day-One EIC Science program exist. This is the reason that at CD-1 the detector presented in the remainder of the Section will be a plausible scenario reference detector, whereas the EIC User Group continues to consider various technologies for many of the different detector functions to implement, with an eye also to possible detector complementarity for a second detector. Indeed, thanks to the ongoing generic EIC-related detector R&D program, the needs for EIC Project-related detector R&D to address risk also are relatively modest. On the other hand, needs for a generic EIC-related detector R&D program do remain. These are driven both by pursuing alternative detector technologies for a complementary second fully integrated EIC detector and Interaction Region, and to prepare for future cost-effective detec-

tor upgrades to enhance capabilities addressing new nuclear physics opportunities. Furthermore, the EIC science program is expected to span at least two decades, and will in this period likely also require further detector upgrades driven by its science findings.

Thus, we plan a continuation of the successful ongoing EIC-related detector R&D program, but managed in coordination with OPC-supported Project Detector R&D to underscore the strong connection to EIC detectors. The EIC detector R&D plan separates what is project R&D for the reference detector technologies, and what could be risk reduction through alternate technologies or enhance science reach. We intend to use the EIC Detector Advisory Committee to provide advice on questions such as: (i) Are the EIC detector technology choices optimal and feasible on the EIC project time scale? (ii) Does the EIC Project-related detector R&D properly address the risk? (iii) Are there opportunities for generic EIC detector R&D to enhance the day-one and the longer-term EIC science program? and (iv) Is the design of the detector(s) sufficiently sound?

8.2 Experimental Equipment Requirements Summary

The physics program of an EIC imposes several challenges on the design of a general purpose detector, and more globally the extended interaction region, as it spans center-of-mass energies from 29 GeV to 141 GeV, different combinations of both beam energy and particle species, and several distinct physics processes. The various physics processes encompass inclusive measurements $e + p/A \rightarrow e' + X$; semi-inclusive processes $e + p/A \rightarrow e' + h + X$, which require detection of at least one hadron in coincidence with the scattered lepton; and exclusive processes $e + p/A \rightarrow e' + N'A' + \gamma/h$, which require the detection of all particles in the reaction with high precision. Section 2.3 and 2.5 discuss in detail how the requirements on the accelerator, the interaction region and the experimental equipment flow down from the EIC science.

The high level requirements for the EIC general purpose detector are:

- The EIC requires a *h*ermetic detector with *l*ow mass inner tracking.
- The main detector needs to cover the range of $-4 < \eta < 4$ for the measurement of electrons, photons, hadrons, and jets. It will need to be augmented by auxiliary detectors like low-Q^2 tagger in the far backward region and proton (Roman Pots) and neutron (ZDC) detection in the far forward region.
- The components of an EIC detector will have moderate occupancy as the event multiplicities are low. However, depending on the machine background level certain components close to the beamline might see higher occupancies (see Section 8.3.2).
- An EIC detector will have to cope with a data rate of up to $\sim$ 500 kHz at full luminosity.
- Compared to LHC detectors, the various subsystems of an EIC detector have moderate radiation hardness requirements.

The intensive work done in the EIC user group "Yellow Report" initiative has resulted in detailed requirements for the different subdetectors forming the central detector and the individual detectors along the beamline. The current status of these requirements is shown in Table 8.2. The interactive version of the Table at (https://wiki.bnl.gov/eicug/index.php/Yellow_Report_Physics_Common) provides for every requirement a link to all the physics simulations and the study, which sets the most stringent requirement. The main emphasis of the physics simulations was on the EIC science program endorsed be the NAS study (see Chapter 2), but of course also new science ideas have been studied in detail.

The EIC experimental equipment does not stop at the general purpose detector to realize the full science program the design of the IR and the integration of the far forward detectors both along the outgoing lepton and hadron beam are equally critical. The detector performance requirements for these detectors are documented in Table 8.2. The design requirements for the IR are summarized in Table 8.1. Also these requirements are further refined during the continuing "Yellow Report" process. How well the current interaction region design fulfills the requirements is documented in detail in Section 3.2.4.

Table 8.1: Summary of the requirements from the physics program on the overall IR design.

	Hadron	Lepton
Machine element free region	$-4.5\,\text{m}$ to $+5.0\,\text{m}$ main detector beam elements $< 1.5^\circ$ in main detector volume	
Beam Pipe	Low mass material, i.e. Beryllium	
Integration of detectors	Local Polarimeter	
Zero Degree Calorimeter	$60\,\text{cm} \times 60\,\text{cm} \times 2\,\text{m}$ @$s = 30\,\text{m}$	
Scattered proton/neutron acc. all energies for e+p	Proton: $0.18\,\text{GeV/c} < p_T < 1.3\,\text{GeV/c}$ $0.5 < x_L < 1 (x_L = E'_p/E_{Beam})$ Neutron: $p_T < 1.3\,\text{GeV/c}$	
Scattered proton/neutron acc. all energies for e+A	Proton and Neutron: $\theta < 6\,\text{mrad}$ (for $\sqrt{s} = 50\,\text{GeV}$) $\theta < 4\,\text{mrad}$ (for $\sqrt{s} = 100\,\text{GeV}$)	
Luminosity	Relative Luminosity: $R = L^{++/--}/L^{+-/-+} < 10^{-4}$	
		γ acceptance: $\pm 1\,\text{mrad}$ $\rightarrow \delta L/L < 1\%$
Low Q^2-Tagger		Acceptance: $Q^2 < 0.1\,\text{GeV}$

Table 8.2: This matrix summarizes the high level requirements for the detector performance. The interactive version of this matrix can be obtained through the Yellow Report Physics Working Group WIKI page (https://wiki.bnl.gov/eicug/index.php/Yellow_Report_Physics_Common).

η	Nomenclature			Tracking				Electrons and Photons			π/K/p PID		HCAL		Muons
				Min p_T	Resolution	Allowed X/X_0	Si-Vertex	Min E	Resolution σ_E/E	PID	p-Range (GeV/c)	Separation	Min E	Resolution σ_E/E	
-6.9 — -5.8	↓ p/A	Auxiliary Detectors	low-Q^2 tagger		$\delta\theta/\theta$ < 1.5%; 10^{-6} < Q^2 < 10^{-2} GeV^2										
…															
-4.5 — -4.0			Instrumentation to separate charged particles from γ						2%/√E+ (1-3)%						
-4.0 — -3.5														~50%/√E+6%	
-3.5 — -3.0		Central Detector	Backwards Detectors		σ_p/p ~ 0.1%×p+2.0%	~5% or less	σ_{xy}~30μm/p_T+ 40μm	50 MeV		π suppression up to 1:10^4	≤ 7 GeV/c	≥ 3σ	~500 MeV	~45%/√E+6%	Useful for bkg, improve resolution
-3.0 — -2.5															
-2.5 — -2.0					σ_p/p ~ 0.05%×p+1.0%		σ_{xy}~30μm/p_T+ 20μm		7%/√E+ (1-3)%						
-2.0 — -1.5															
-1.5 — -1.0															
-1.0 — -0.5			Barrel	100 MeV π 135 MeV K	σ_p/p ~ 0.05%×p+0.5%		σ_{xyz} ~ 20 μm, $d_0(z)$ ~ $d_0(r\varphi)$ ~ 20/p_T GeV μm + 5 μm		(10-12)%/ √E+(1-3)%		≤ 10 GeV/c			~85%/√E+7%	
-0.5 — 0.0															
0.0 — 0.5															
0.5 — 1.0											≤ 15 GeV/c				
1.0 — 1.5			Forward Detectors		σ_p/p ~ 0.05%×p+1.0%		σ_{xy}~30μm/p_T+ 20μm			3σ e/π	≤ 30 GeV/c			~35%/√E	
1.5 — 2.0															
2.0 — 2.5											≤ 50 GeV/c				
2.5 — 3.0					σ_p/p ~ 0.1%×p+2.0%		σ_{xy}~30μm/p_T+ 40μm				≤ 30 GeV/c				
3.0 — 3.5							σ_{xy}~30μm/p_T+ 60μm				≤ 45 GeV/c				
3.5 — 4.0	↑e	Auxiliary Detectors	Instrumentation to separate charged particles from γ												
4.0 — 4.5															
…															
> 6.2			Proton Spectrometer		$\sigma_{intrinsic}(|t|)/|t|$ < 1%; Acceptance: 0.2< p_T <1.2 GeV/c										

8.3 Operational Requirements for an EIC Detector

EIC is a unique collider with diverse physics topics, which imposes unique requirements on the detector design. Comparing to modern hadron colliders, such as RHIC and LHC, the EIC has much higher crossing frequency ($\sim$ 100 MHz) and high luminosity (10^{34} cm$^{-2}s^{-1}$). However, the EIC cross section ($\sim$ 50 µb) is much smaller than the proton-proton cross section (40–80 mb from RHIC to LHC), making the EIC collision rate ($\sim$ 500 kHz) and particle production rate (4M charged particle per second) a factor 10–1000 lower than that of RHIC and the LHC. Nonetheless, the EIC has a diverse event topology and is sensitive to the machine background and detector noise. All these effects pose challenges to the operational requirements for an EIC Detector. In this section, requirements are studied with integrated detector and IR simulations.

8.3.1 EIC Collision Rates and Multiplicities

The EIC total *e+p* cross-sections is estimated using the PYTHIA6 event generator as listed in Table 8.3.

Table 8.3: Total *e+p* cross-section as a function of electron and proton beam energies. The cross-sections were calculated using PYTHIA6 event generator and might change slightly depending on the settings.

σ_{tot}(µb)		E_e [GeV]		
		5	10	18
E_p [GeV]	41	25.9	30.1	35.0
	100	32.1	37.1	41.6
	275	39.4	44.6	49.3

For each collision Figure 8.1 shows particle production rates for the 20 GeV on 250 GeV beam energy configuration. Events were simulated using PYTHIA6, and the total cross section reported by PYTHIA6 was used to scale event counts to rates. No cuts, for example on event Q^2 or particle momentum, were applied. The η-range spans the expected acceptance of the main EIC detector. "Charged" particles refers to electrons, positrons, and charged long lived hadrons, while "neutrals" refers to photons, neutrons and K^0_L. In response to the collisions, the EIC detector response and data rate is studied using full detector GEANT4 simulations of a generic EIC detector model [411, 412].

The average data rate (Figure 8.2) and the subsystem multiplicity distributions (Figures 8.3) are studied in a simulation combining the EIC tune of PYTHIA6, which samples $\sim$ 50 µb of the *e+p* collision cross section, and the full detector GEANT simulation. At the top instantaneous luminosity of 10^{34} cm^{-1}s^{-1}, the collision-induced zero-suppressed streaming data rate from EIC collisions is around 100 Gbps, which is the minimal amount

of raw data that has to be recorded to disk in order to record all minimum-bias EIC collisions in the central detector without the assumption of online reconstruction and reduction.

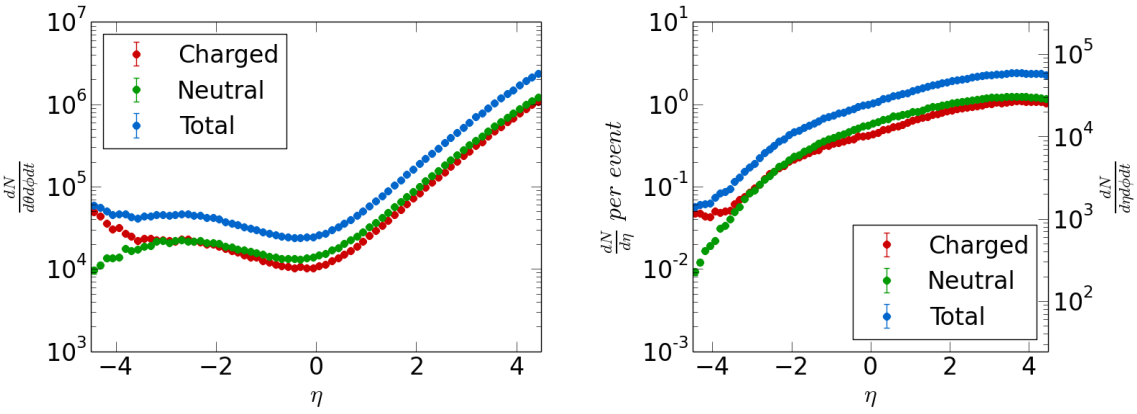

Figure 8.1: Particle production rates as a function of pseudo-rapidity at EIC for 20 GeV on 250 GeV e+p collisions and a luminosity of $10^{33} cm^{-2} s^{-1}$. (a) mean numbers of particles per event (left axis) and particles per second per unit (η, ϕ) (right axis). (b) particles per second per unit (ϕ, θ), i.e., the η-dependent flux at a distance of 1 m from the interaction point.

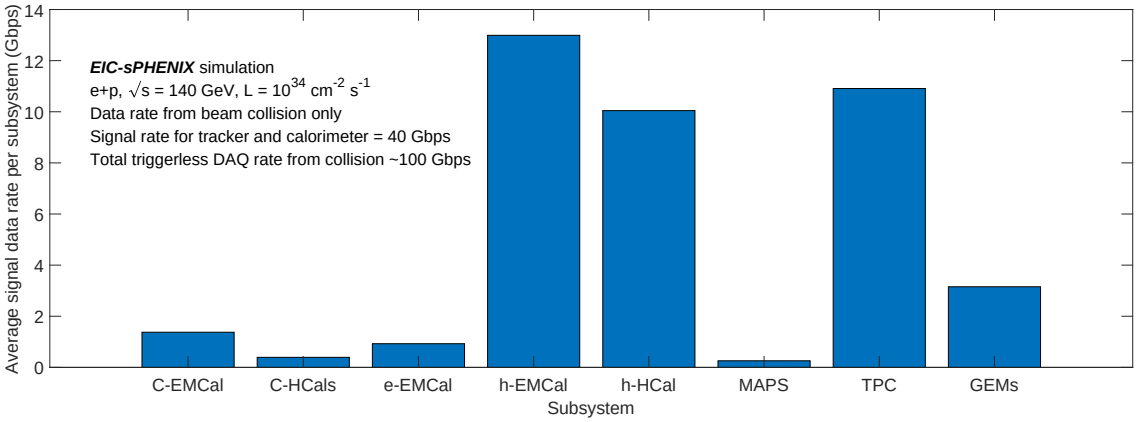

Figure 8.2: Signal data rates from tracking and calorimetric detectors from EIC collisions via full detector GEANT4 simulation of an EIC detector concept based on sPHENIX [411, 412], which also applies to the reference EIC detector as in this report. Zero-suppression and realistic data format based on sPHENIX prototyping are assumed in this estimation. The overall tracker data rate is 40 Gbps. The estimated rate with PID detector and moderate detector noise would reach 100 Gbps for full experiment. Please note that the backgrounds, e.g. beam gas interaction, excessive detector noise, synchrotron photon hit rate, may dramatically increase the data rate in some detectors, but they are not included in this plot and they will be discussed in Section 8.3.2.

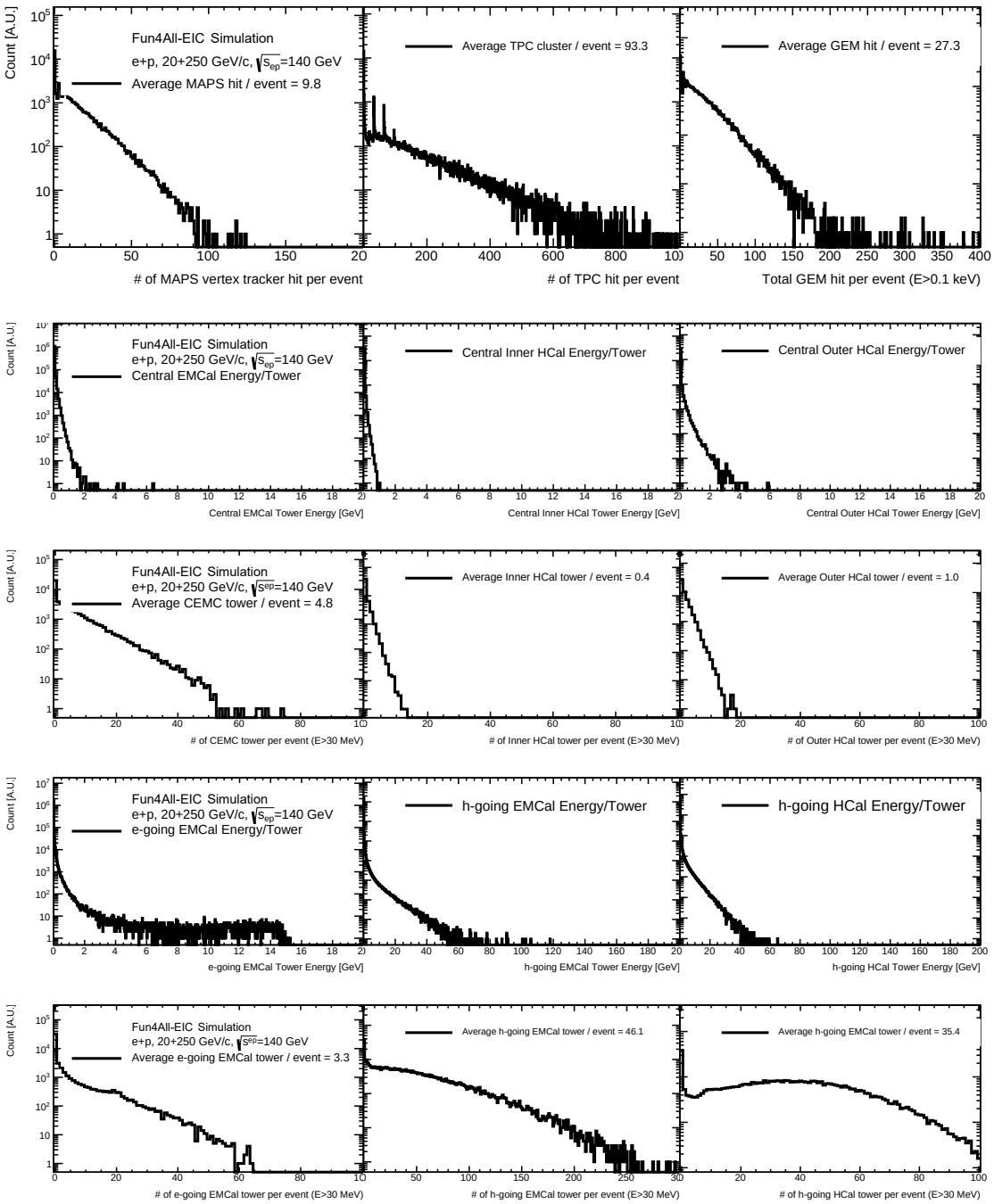

Figure 8.3: First row: Distribution of number of hits in the tracking detectors that originated from a single e+p collision at $\sqrt{s_{ep}} = 140$ GeV. 2nd and 3rd rows: Distribution of per-tower energy and the number of active towers in the central calorimeters that originated from a single e+p collision at $\sqrt{s_{ep}} = 140$ GeV. 4th and 5th rows: Distribution of per-tower energy and the number of active towers in the forward calorimeters that originated from a single e+p collision at $\sqrt{s_{ep}} = 140$ GeV.

8.3.2 IR Integration and Backgrounds

The combination of the relatively low signal rate of the EIC collision and the stringent systematic control for EIC measurements calls for low background and detector noise at an EIC experiment. And in turn, the types and levels of background is one of the main consideration on the detector design and it is a major consideration for IR integration, such as the arrangement of beam magnets and other beam parameters and optics. The experience at earlier accelerator facilities, especially the previous HERA electron-proton collider, indicates the importance of background studies in the early design phase. Primary sources of machine-induced background are discussed in this subsection.

Ionization radiation dose and Neutron flux from the EIC collisions

The ionization radiation dose and neutron flux from the e+p collisions are studied using EICROOT and a generic EIC detector model in the RHIC IP6 experimental hall. The simulation is generated with the EIC tune of PYTHIA6 with 20×250 GeV beam energy and is based on GEANT3 package with the $HADR = 5$ option. As shown in Figure 8.4, the near-beam-line regions experience relatively high ionizing radiation. For example, the e-

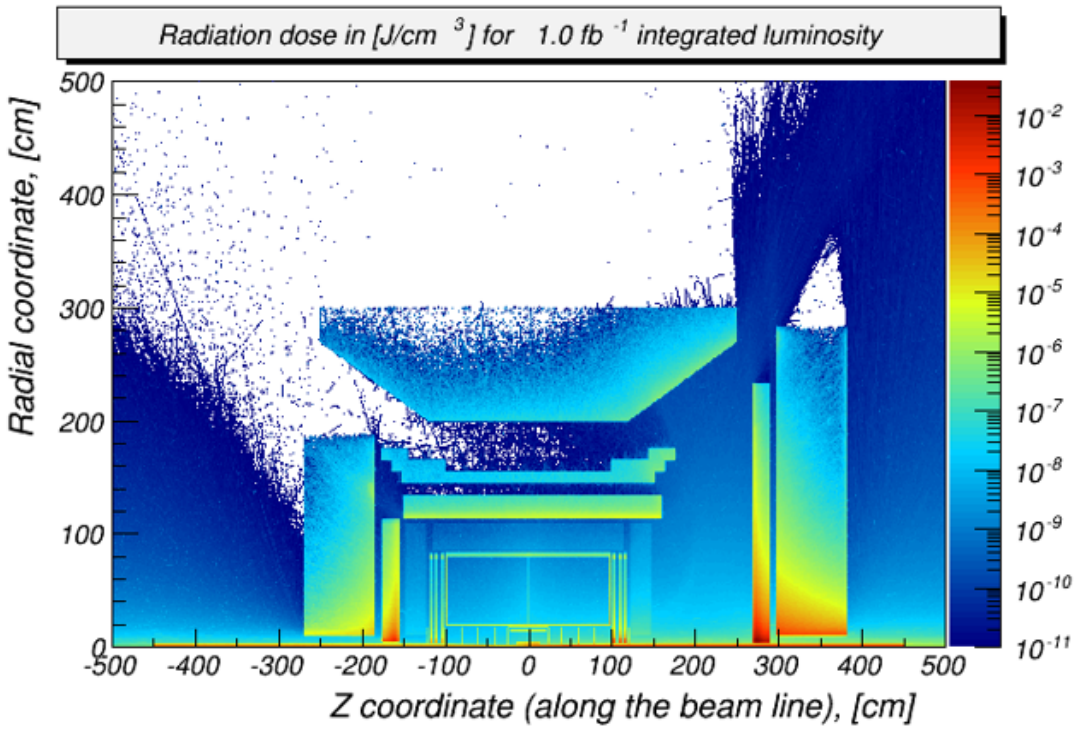

Figure 8.4: Ionizing radiation energy deposition from the e+p collision at $\sqrt{s_{ep}} = 140$ GeV studied using the BeAST detector concept, which also applies to the reference EIC detector as in this report.

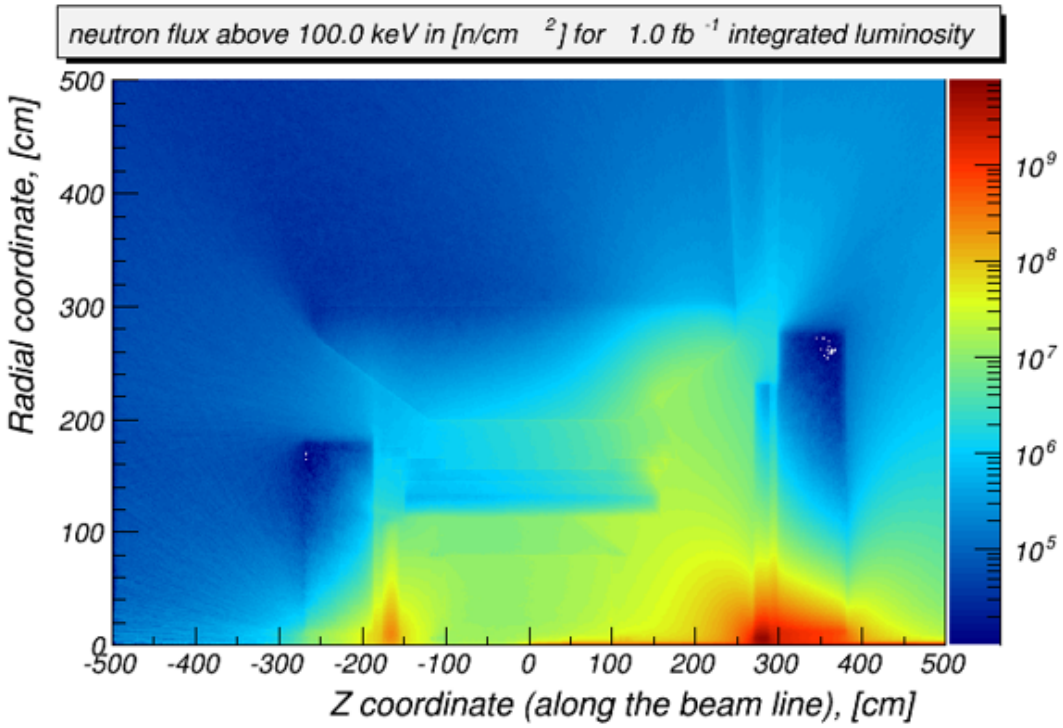

Figure 8.5: Neutron flux from the e+p collision at $\sqrt{s_{ep}} = 140$ GeV studied using the BeAST detector concept placed in the RHIC IP6 experimental hall, which also applies to the reference EIC detector as in this report.

going crystal calorimeters show approximately 2.5 kRad/year max ionizing radiation dose from the e+p collisions at the top luminosity (10^{34} cm^{-2}s^{-1}). The above-100 keV neutron flux is shown in shown in Figure 8.5. The near-beam-line regions, in particular the vertex tracker and the forward-backward calorimeters also experience relatively high neutron flux, exceeding 10^{10} neutrons/cm^2 per year from the e+p collisions at the top luminosity (10^{34} cm^{-2}s^{-1}).

Synchrotron Radiation

Various sources of synchrotron radiation could have an impact on the background level at the IP. When the trajectory of a charged particle is bent, synchrotron photons are emitted that are tangential to the particle's path. Bending and focusing of the electron beam is the main cause of synchrotron radiation within the IR. However, contributions from the upstream electron beam scattering off residual gas must be assessed as well. It is important to place the IP far away from strong bending magnets in the arcs to minimize synchrotron radiation. The tracking detectors in the central detector as well as the calorimeter have to be properly shielded against synchrotron radiation, therefore a number of absorbers and masking must be applied along the electron beam direction. Synchrotron radiation also

deposits several kilowatts of power into the beam pipe in the central detector region, which must then be cooled. Additionally, synchrotron radiation can degrade vacuum quality by causing material desorption from vacuum chamber walls and/or heating residual gas. Synchrotron radiation is also a direct and indirect source of background in the luminosity monitor, and low-Q2 tagger located on the downstream electron side of the IR.

A model of the electron beamline has been used in SynRad [413], where synchrotron radiation at the maximal design value of 0.260 A of 18 GeV electrons, including 26 mA in a broad tail distribution, has been generated. Figure 8.6 shows a view of the upstream electron beamline and IP, with synchrotron radiation generated by the last upstream dipole and FFQ quadrupoles. Electrons enter from the lower left on the figure, at the location of the last dipole, $\approx$ 40 m from the IP. In the background, the IP itself is obscured by the hourglass shape of the central region of the beam pipe.

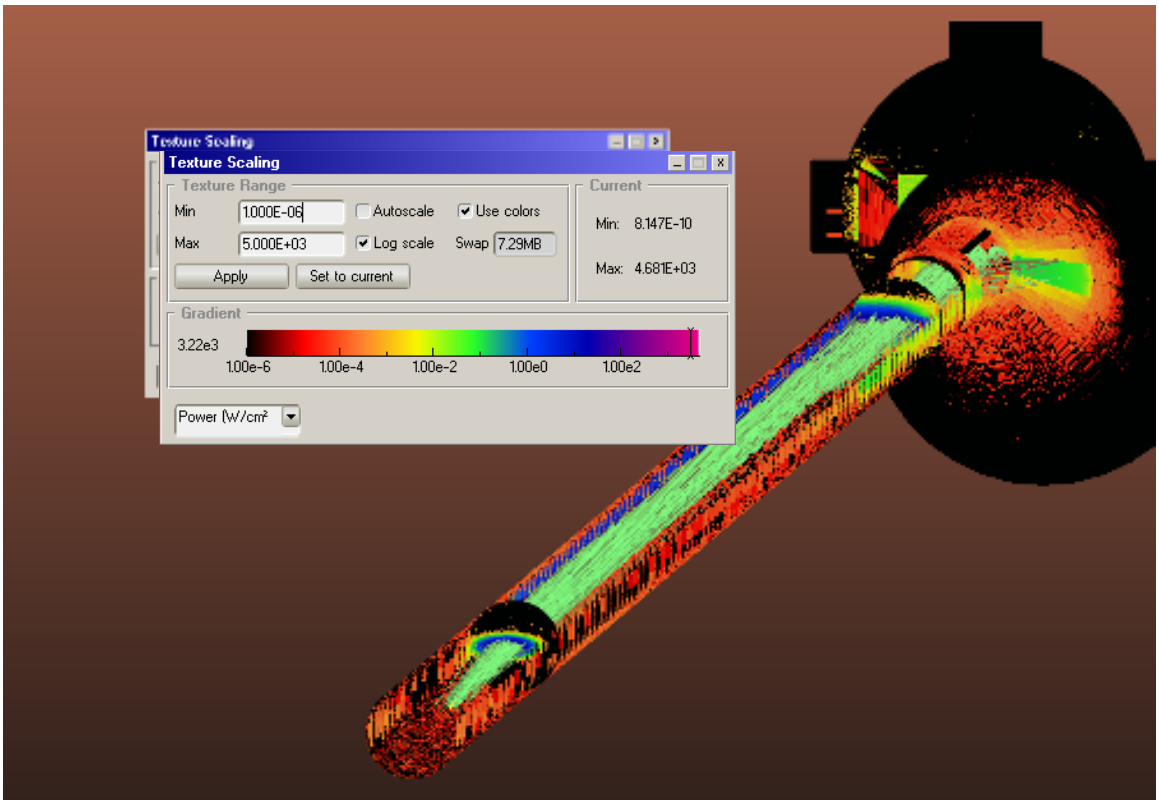

Figure 8.6: SYNRAD generation of synchrotron radiation from 0.260 A of 18 GeV electrons. The color scale is logarithmic, with blue approximately 1 W/cm^2. Electrons enter from the lower left in the figure, the initial radiation fan is generated from the last dipole, at approximately 40 m upstream of the IP. Individual photons are traced by the green lines. The vertical striations on the beam pipe result from the sawtooth inner profile of the pipe, which ensures photons hit the wall locally head-on.

The energy deposition in the Be beam pipe and Si Vertex Tracker layers is illustrated in Figure 8.7. The dose (energy per mass) in the Si layers is plotted in the right panel of

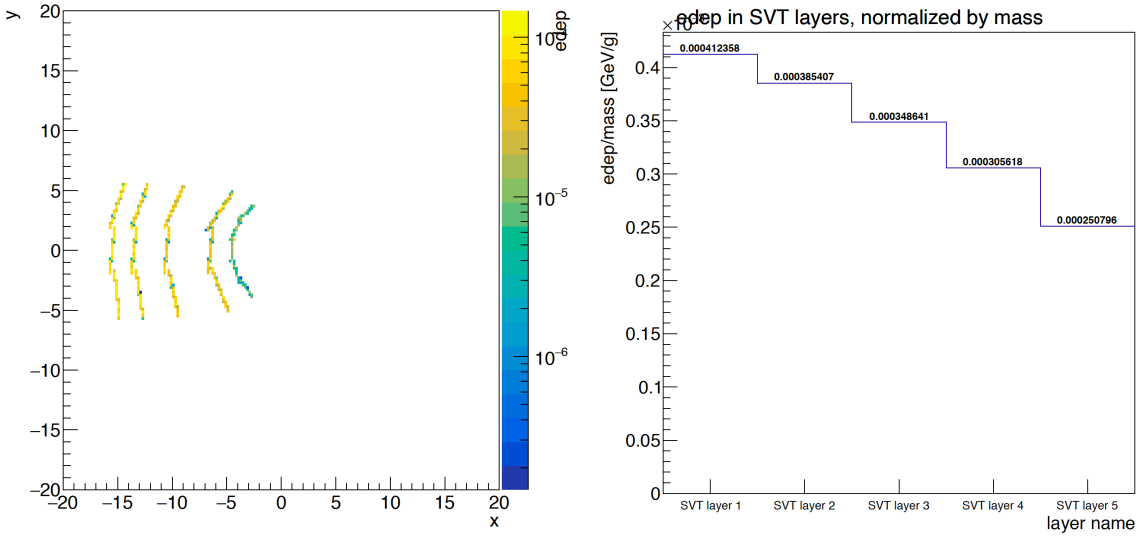

Figure 8.7: Left: synchrotron energy deposition in central Be pipe and 5 layers of SiVT. Energy is integrated over the length of each element. Right: synchrotron radiation dose (GeV/gram) in each of 5 layers of SiVT, which is averaged over the length of each element. The photon flux in these figures is integrated over 0.465 µs of an 18 GeV electron beam at the design current of 0.26 A, including a beam tail.

Figure 8.7. The photon flux in these figures is integrated over 0.465 µs of an 18 GeV electron beam at the design current of 0.26 A, including a beam tail.

Furthermore, a GEANT4-based tool-set is being prepared to examine the hit rate that originates from the synchrotron radiation background in the full experiment apparatus. Figure 8.8 shows the GEANT4 model of IR1 Beam Pipe with Si Vertex Tracker. The SynRad synchrotron radiation simulation [413] as prior discussed is interfaced with the detector response as modeled in full detector GEANT4 simulations and the digitization model of a generic EIC detector model [411, 412], as illustrated in Figure 8.9. The detector hit rate results are pending updated with the July-2020 beam chamber and optics adjustment.

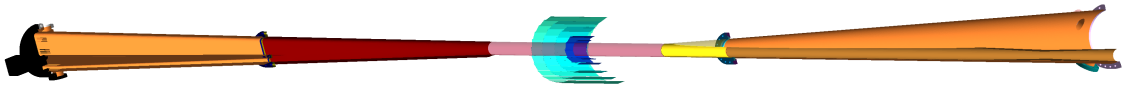

Figure 8.8: GEANT4 model of IR1 Beam Pipe, with Si Vertex Tracker. The electron beam enters horizontally from the right, and exits in the rectangular beam channel to the left. The ion beam enters in the small tube on the lower left, and exits via the large cone on the upper right.

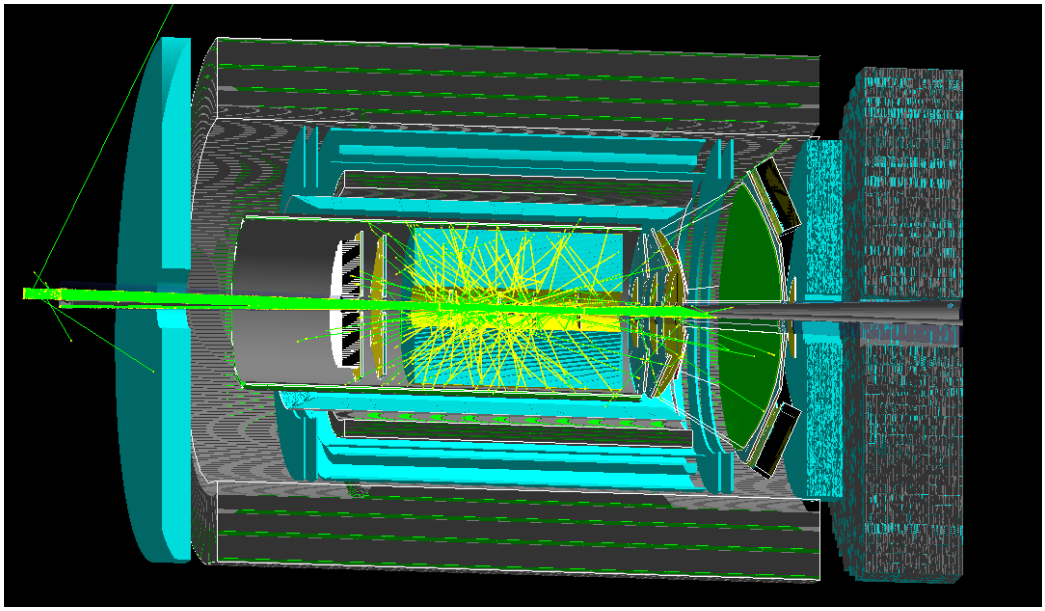

Figure 8.9: GEANT4 simulation of the synchrotron photon background in an EIC detector model [411,412]. The photons (green lines) are generated in SynRad simulation [413] and the photons are interfaced to the GEANT4 simulation after passing the Final Photon Absorber around $z > 3$ m. Although the inner detectors have the highest flux of synchrotron photon background, the background affects tracking and PID detectors in much higher radii too, due to the scattering and secondary interactions.

Beam Gas Interactions

Beam-gas interactions might occur when proton or ion beam particles collide with residual beam gas. Ion beam interactions with gas cause beam loss and halo which may reach detectors. This may be an important source of neutrons that thermalize within the detector hall. The large synchrotron radiation load could heat the beam pipe and residual gas particles from the beam pipe walls could be released, which would lead to a degradation of the vacuum. A crossing angle and short section of shared beam pipe in the EIC design minimize the beam-gas problem.

A model of the interaction region-1 (IR1), $\pm$ 30 m, including all magnets, the tunnel walls, the detector cavern, and a simplified representation of the detector have been created in FLUKA. This is illustrated in Figure 8.10. A more detailed view of the detector model is presented in Figure 8.12.

The studies of the dynamic vacuum in the IR are directly linked to the synchrotron radiation flux impacting the beam pipe. Figure 8.11 illustrates the static vacuum (without synchrotron radiation) in IR1, based on nominal out-gassing rates, the molecular flow conductance of the beam pipe, and the pumping speed of the NEG pumps at $\pm$4.5 m.

In order to efficiently simulate the interactions of the ion beam with the residual gas in the beam-line vacuum, we artificially create a thin "pencil" (diameter 3mm) of air at pressure

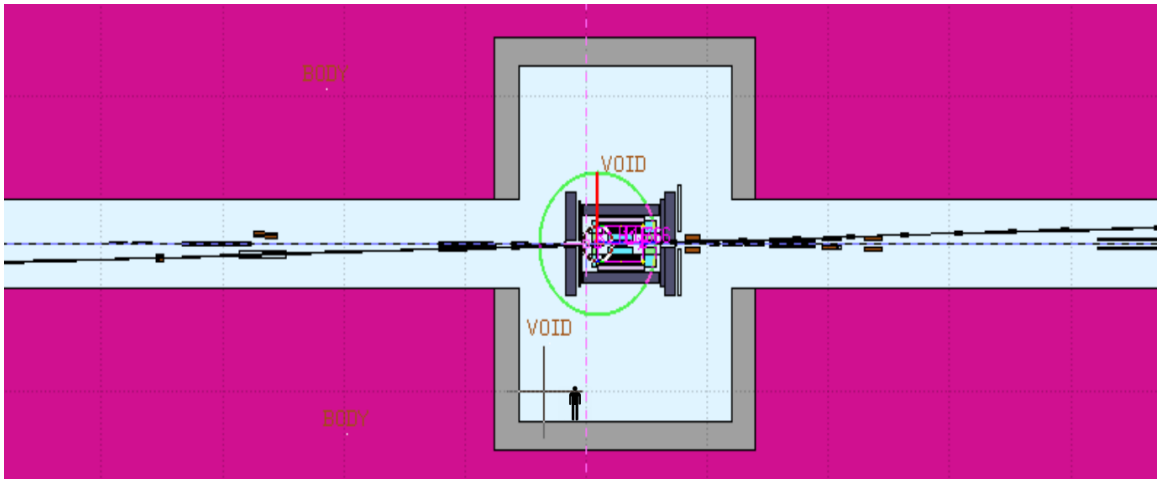

Figure 8.10: Top view of a FLUKA model of the EIC Interaction Region 1 (person for scale comparison is shown at the bottom). Ions enter from lower left, electrons enter on the solenoid axis from the right.

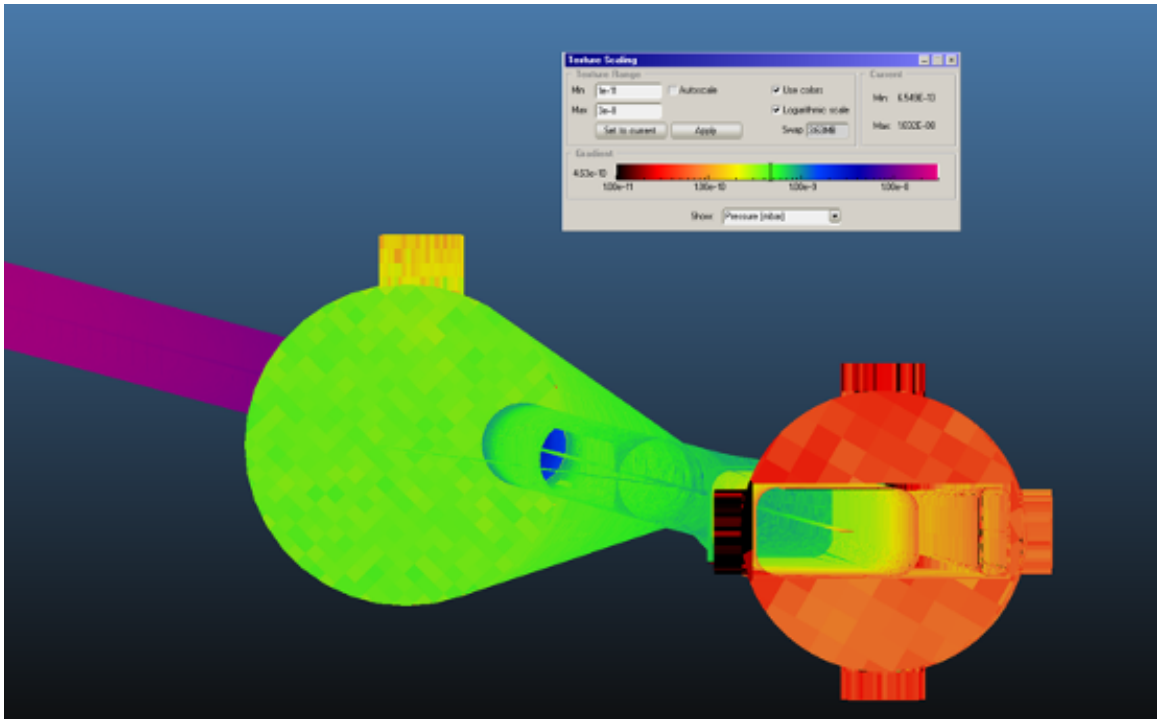

Figure 8.11: MOLFLOW calculation of the static vacuum in the IR. The beam pipe layout is the same as Figure 8.6. In this view, the electron beam enters from the upper left and exits through the large horizontal aperture on the right. The incident ions enter from the right at $z = -4.5$ m via the smaller upright rectangular aperture. The light green color in the central region indicates a vacuum of $\approx 5 \cdot 10^{-9}$ mbar. The downstream ion beam pipe is not shown beyond the flange at $z = 4.5$ m.

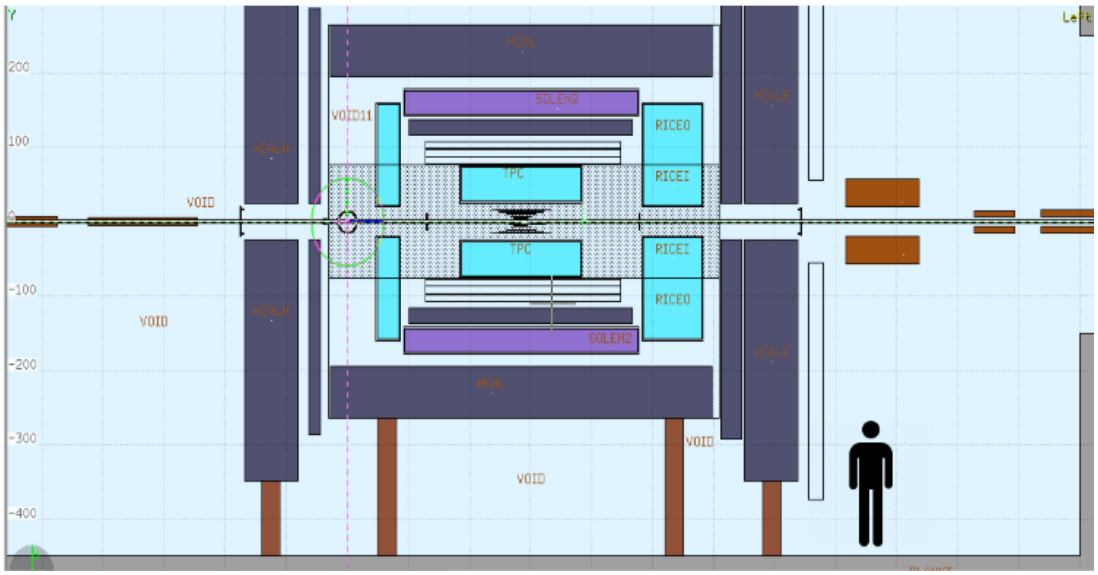

Figure 8.12: Elevation view of the FLUKA model of the EIC Detector. The Si Vertex Tracker (SiVT) in this rendition includes six layers.

$P_F = 100$ mbar along the beam-line. A global view of the neutron fluence is presented in the top panel of Figure 8.13. The simulation includes the full cascading and thermalization of secondaries from the primary beam-gas interactions. The figure illustrates the fact that the detector itself, especially the iron flux return, serves as both a neutron sink and neutron source.

The energy spectrum of beam-gas induced neutron at the central Si Vertex Tracker (SiVT) is illustrated in Figure 8.14. The energy distribution shows a clear peak of fully thermalized neutrons below 1 eV, as well as a knee around 10 MeV from evaporation neutrons. Neutron damage to Si sensors occurs primarily via displacement of nuclei from their ideal lattice positions. This can happen both by direct nSi scattering, and also by recoil from Si(n, γ) reactions. The latter can dislodge nuclei, even for neutron energies well below 1 eV.

The damage induced by neutrons is frequently quantified by an equivalent flux of 1 MeV neutrons. This is computed in the bottom of Figure 8.13. From Figure 8.15, we obtain an annual dose of $6 \cdot 10^{10}\mathrm{n/cm}^2$ (1 MeV equivalent) in the SiVT. This is more than three orders of magnitude less than the suggested tolerance of $10^{14}\mathrm{n/cm}^2$.

Next we we further estimated the data rate across the whole experiment that originated from the beam-gas interactions. The full detector simulation model as described in subsection 8.3.1 is used to simulate the proton beam hydrogen gas interaction generated with PYTHIA8 in the $p + p$ fixed-target configuration. The hydrogen gas pressure is assumed to be a constant 10^{-9} mbar across the experimental region $|z| < 450$ cm, which leads to approximately 10 kHz inelastic beam gas interaction rate. The result collision is propagated through the detector model as illustrated in Figure 8.16. The result data rate is summarized in Figure 8.17.

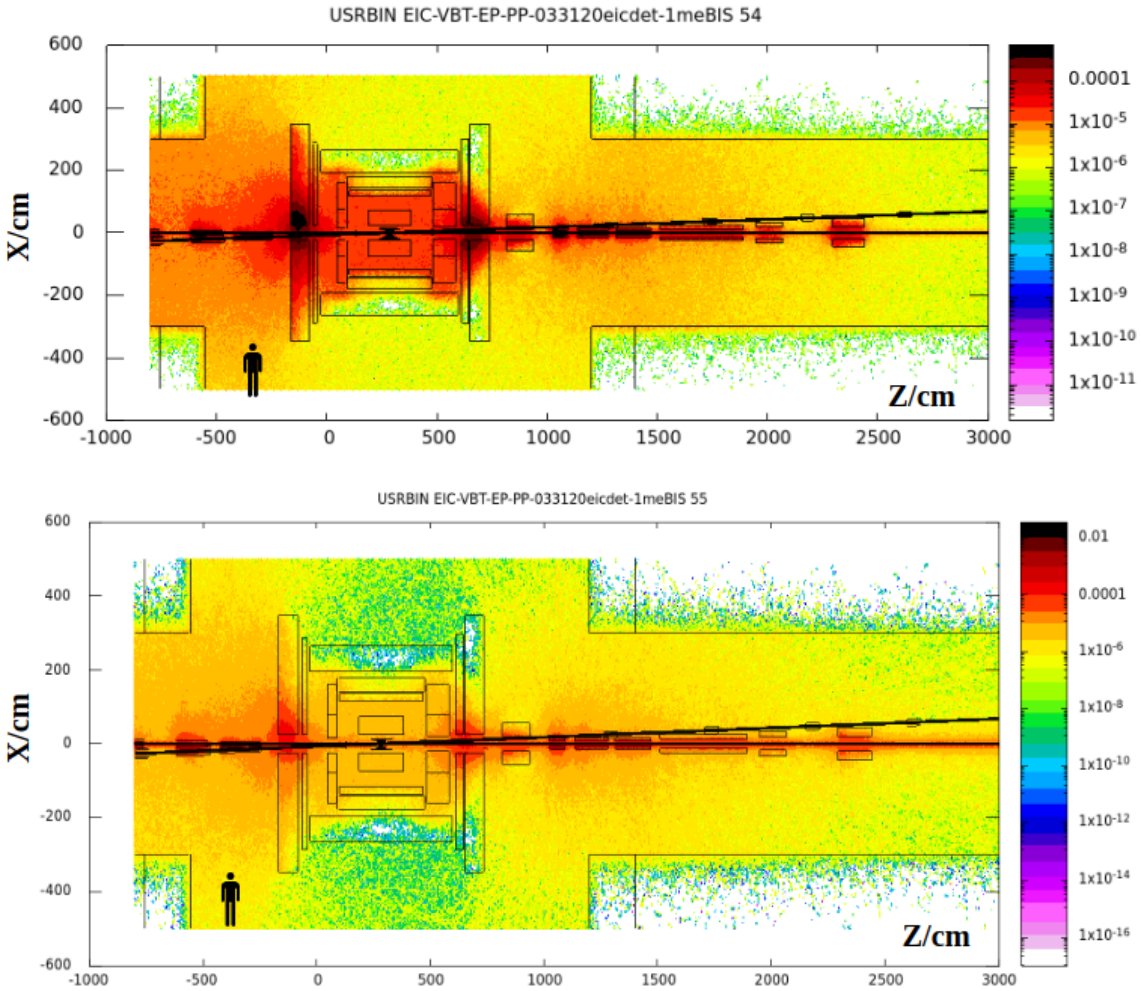

Figure 8.13: Maps for Neutron fluence (top) and 1-MeV-equivalent Neutron fluence (bottom) from $p + Air$ interactions in the beam pipe at proton energy $E_p = 275\,\text{GeV}$ and an artificial pressure P_F ("P-FLUKA") in a thin cylinder along the beam line. The IP is located at $Z = 285$ cm. Neutron fluence is given by the color chart at the right side of the plot in units of neutrons/cm^2/proton at $P_F = 100$ mbar. Normalized rates for current $I = 1$ A and a realistic average beam-line vacuum $P = 10^{-9}$ mbar are obtained by multiplying the color values by $(I/e)(P/P_F) = 6.25 \cdot 10^7$ protons/s. Thus dark red regions (almost yielding to black) correspond to a realistic fluence of $\approx 6 \cdot 10^4$ neutrons/s/cm^2.

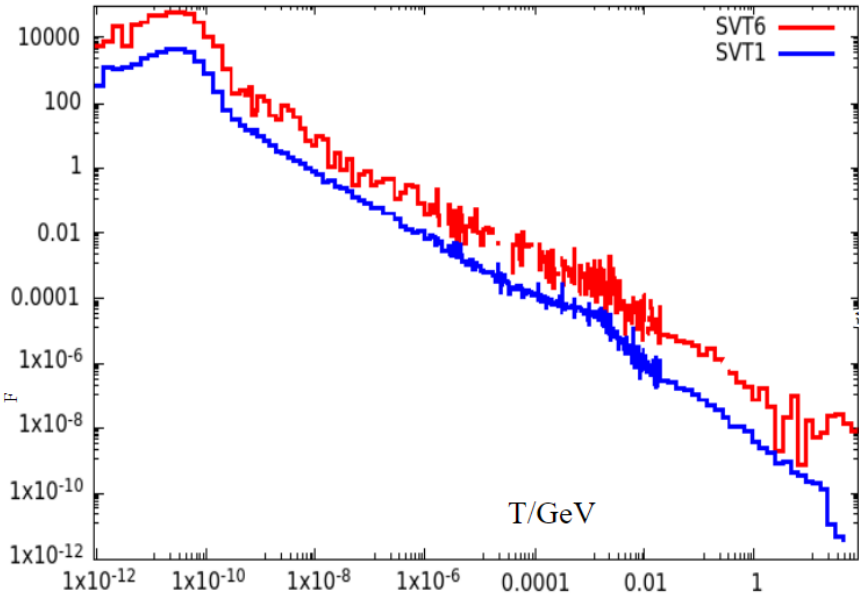

Figure 8.14: Neutron energy spectra from FLUKA simulations in two layers of the SiVT : (1) Outer-most Si layer (SVT1) and (2) Inner-most Si layer (SVT6). The vertical scale is fluence in units of $neutrons/GeV/sr/cm^2/proton$ at pressure $P_F = 100$ mbar. The horizontal scale is neutron energy in GeV. Absolute realistic flux in neutrons/s/sr/cm^2/GeV is obtained by multiplying the vertical axis by $\approx 6.25 \cdot 10^7$ protons/s (see Figure 8.13 caption).

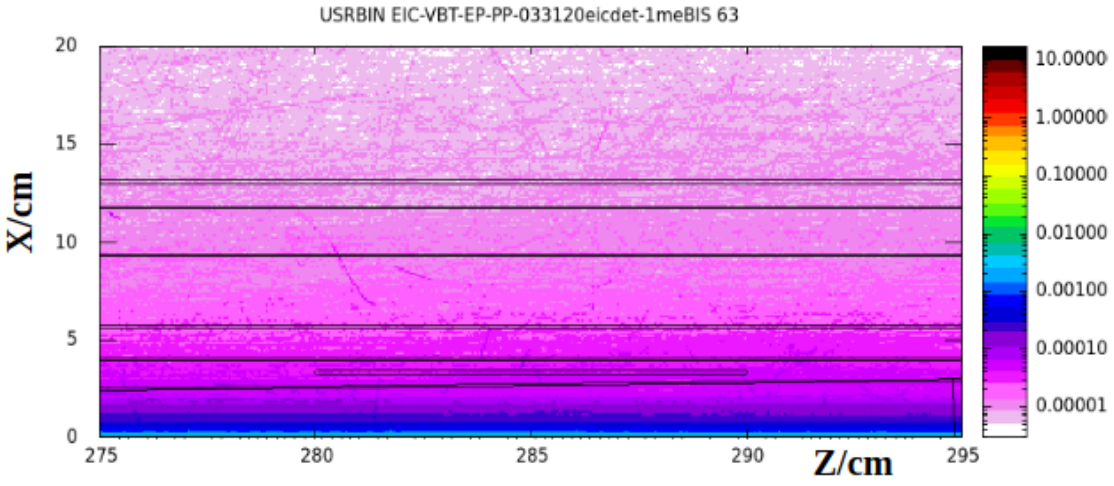

Figure 8.15: One-MeV equivalent neutron fluence map in the area of SiVT; $p + Air$ interactions in the beam pipe at proton energy $E_p = 275$ GeV. IP is located at $Z = 285$ cm. Fluence is given by the color chart at the right side of the plot in units of neutrons/cm^2/proton/P_F, where $P_F = 0.1$ bar is the pressure used in the FLUKA model.

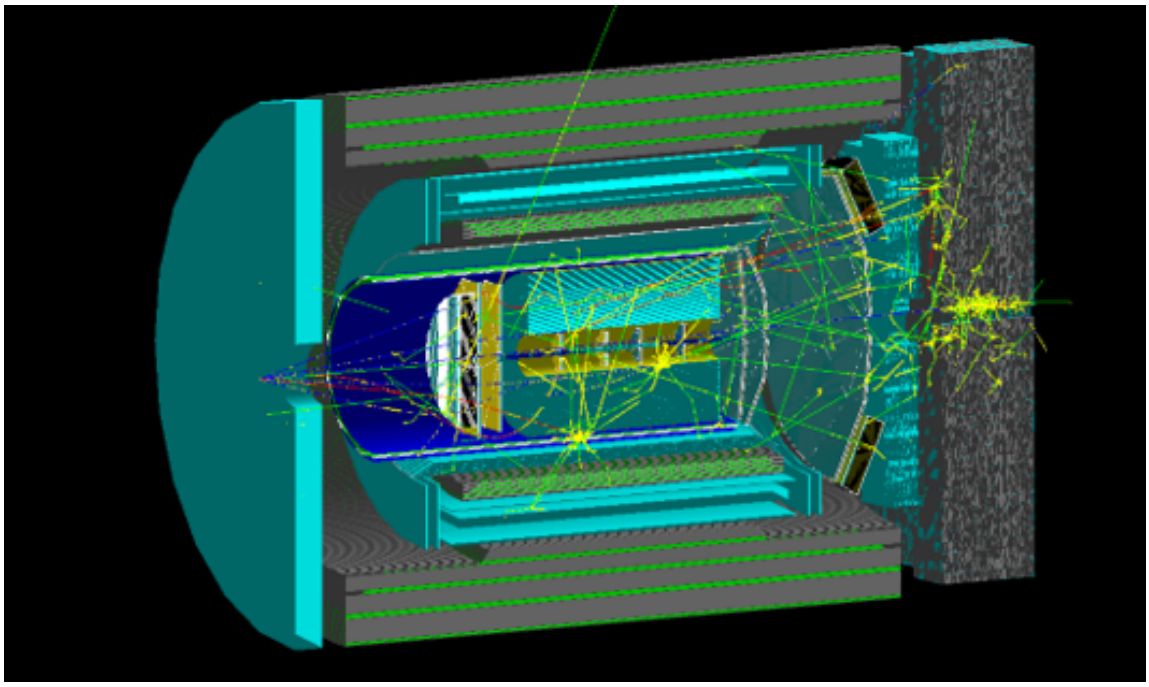

Figure 8.16: GEANT4 simulation of a beam gas interaction background in an EIC detector model [411, 412]. The interaction originate after the last focusing magnet at $z = -4$ m. The produced particle shower will cascade through the central detector stack and induce high multiplicity background throughout the forward and backward spectrometers.

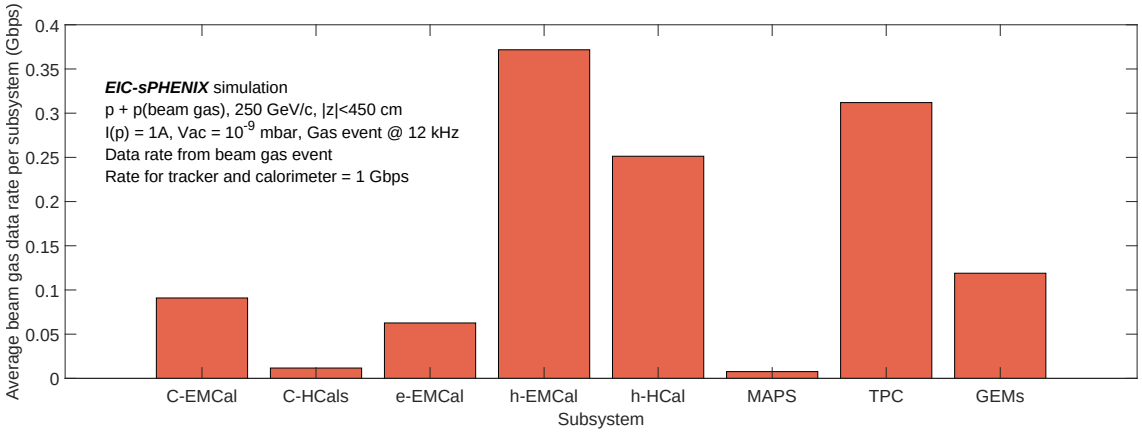

Figure 8.17: Signal data rates from tracking and calorimetric detectors from beam gas collisions via full detector GEANT4 simulation of a detector concept based on sPHENIX [411, 412], which also apply to the reference EIC detector as in this report. This simulation assumes constant 10^{-9} mbar vacuum in the experimental region of $|z| < 450$ cm, which would be modified with a dynamic vacuum profile in the future.

Beam Halo

Particles produced from elastic collisions of both electron and proton beams with residual gas or beam-beam interactions can form a halo distribution around the beam. Often the result is an on-momentum electron or ion with large scattering angle. These particles can then generate additional background by interacting with the beam pipe and can impact the stability of the beam. Beam halos are being studied to determine whether "scraping" the halo with collimators is required, as well as proper placement of those collimators.

Summary and Outlook

Although multiple background sources are discussed in this section, at the time of this report, many aspects of these background estimation can still vary considerably as the accelerator and experiment conceptual design proceeds. Nonetheless, we feel it crucial to point out a few key experimental regions which are susceptible to high background.

- A silicon vertex tracker is expected to be installed with a minimal clearance outside the beam pipe in EIC. The overall collision charged particle flux is relatively low (Section 8.3.1). However, the proximity to the beam pipe exposes this detector to the background such as the synchrotron radiation, beam gas interactions, and beam halo. The current estimation shows an annual neutron fluence reaches $O(10^{11})n/\text{cm}^2$. The synchrotron hit rate ranges from $O(10^8)$ to $O(10^{12})$ pixels per second, depending on the choices of the beam chamber coating. Optimization on the machine and detector design is ongoing to reduce and refine the background rate and to protect this key detector from unexpected beam conditions.
- In addition to the silicon vertex tracker, many tracking and PID detector would observe a considerable hit rate from the scatter synchrotron photons, in particular the main barrel tracker and forward-backward silicon tracker, as illustrated in Figure 8.9. Optimization and detailed estimation are still ongoing.
- Hadronic shower leads to enhanced neutron fluence near the first few hadron interaction lengths of calorimeters at the vicinity of the beam pipe. Current estimations are at the orders of $O(10^{10})n/\text{cm}^2$. Further study and refinement will be carried out.

8.4 Reference EIC Detector

8.4.1 Introduction

The physics opportunities at EIC are intimately connected to the overall design of the experiments and to the performance of the required detectors. From the experimental point of view, the broad physics EIC program can be accomplished by the study of (i) inclusive, (ii) semi-inclusive and (iii) exclusive processes, all of them with initial state of electrons and light or heavy nuclei, with polarized electron and light nuclei beams and spanning a wide range of center of mass energies. The main requirements for the experimental apparatus are based on these processes and the requirements of the wide kinematic coverage, adding more and more complexity moving from reactions (i) to (iii):

- Precise scattered electron identification and extremely fine resolution in the measurement of its angle and energy (Sec. 8.4.2) for all experimental channels; another essential tool for the whole physics scope is the central magnet (Sec. 8.4.3) required for momentum measurements;
- More is needed to access the semi-inclusive processes (ii): excellent hadron identification over a wide momentum and rapidity range, full 2π acceptance for tracking and momentum analysis and excellent vertex resolution by a low-mass vertex detector (Sec. 8.4.2);
- Exclusive reactions (iii) impose the capability to accurately reconstruct all particles in the event using a tracker with excellent space-point resolution, high precision electromagnetic resolution and reasonable precision hadronic calorimetry in the end-caps (Sec. 8.4.2), the complete hermeticity of the setup with the additional requirement of very forward detectors such as Roman pots, and large acceptance zero-degree calorimetry to effectively detect neutrons from the breakup of nuclei or neutral decay products from tagged DIS processes (Sec. 8.4.4);
- The entire experimental program will require the precise control of the luminosity (Sec. 8.6);
- The polarized beams impose the use of electron and light nucleus polarimeters (Sec. 8.6);
- The strategy for detector read-out and data acquisition has to be defined taking into account the data rate of the experiment as well as the rapid developments in the field of digital electronics and computing power, suggesting a global approach to the read-out and data acquisition (Sec. 8.4.5) on the one hand and software and computing on the other hand (Sec. 8.5).

8.4.2 General Purpose EIC Detector

A reference detector design, closely following the physics requirements outlined in chapter 2.3, is shown in Figure 8.35. The general requirements for any detector are similar as they stem from the central goal to cover the entire EIC physics program, the expected event geometries and the constrains coming from the overall collider design. Nevertheless, the detector design and the selected technologies may differ.

We assume the following characteristics for the present discussion. The central detector, discussed in this section, instruments the pseudo-rapidity region $-4 < \eta < 4$. This acceptance range matches the needs of the inclusive, semi-inclusive, jet physics and spectroscopy studies. It is complemented by the very forward and backward detectors (section 8.4.4) ensuring the hermeticity and the forward tagging required by specific items of the physics program; in particular: exclusive reactions and diffractive channels. The main requirements of the central detector dictated by the physics program and the event geometry are related to (1) tracking and momentum measurements, (2) electron identification, (3) hadron identification and (4) jet energy measurements, while (5) the overall detector size is imposed by collider design considerations:

1. very fine vertex resolution, at the 20 μm level for the three coordinates, is needed, while a moderate momentum resolution around 2% matches the physics requirements;

2. the purity requirements for electron/hadron separation are at the 10^{-4} level in the backward and barrel regions and, for this purpose, the figures for the electron energy resolution are very demanding, in particular in the backward region where an r.m.s. of $2\%\sqrt{(E)}$ is needed; in the same direction, the request is for a light detector, where the material budget should not exceed 5% X_0;

3. the identification of the different hadron species in the whole central detector coverage, namely for hadrons with momenta up to 50 GeV/c, is requested with 3σ π/K separation over the whole range as reference figure;

4. the measurement of jet energy in the forward direction is a necessity, while moderate resolution of the order of $50\%\sqrt{(E)}$ can match the needs;

5. the detector extension along the beam lines impacts on the required length around the IP that has to be kept free of machine elements, typically referred to as L^*: the reference figure is ± 4.5 m space around the iteration point.

The required tracking and momentum resolution measurements can be obtained with a $\sim$3 T solenoidal field equipping the internal volume with a set of coaxial trackers with cylindrical symmetry covering the $-1 < \eta < 1$ region and a set of disk-shaped detectors in the forward and backward direction. Different approaches are considered for the set of tracking detectors, respecting the low-mass prescription imposed by the relevance of the electron identification and measurement in DIS studies. The better established is via a vertex barrel formed by 4 layers of high-resolution MAPS sensors with a 20 μm pixel size and

an effective thickness of only $\sim 0.3\%$ radiation length per layer, which offers a fine vertex resolution of 20 µm required for semi-inclusive measurements and spectroscopy. The barrel is surrounded by a TPC, with internal radius of 20 cm and external one of 80 cm, specifically chosen as the main tracking element because of its small overall material budget as it minimizes the rate of photon conversions in detector components. The longitudinal extension of the TPC is longer than the vertex layers: therefore, the TPC provides tracking also in part of the forward and backward regions, while the small angle regions are covered by small-size disk trackers by the same technology used for the vertex barrel. Besides this, the TPC should provide charged particle-identification (PID) information at central rapidities complementing the dedicated PID devices. This setup can be empowered by adding a single layer of a high-resolution tracker with fine spatial and time resolution, for instance by micro-RWELL, external to the TPC to provide better angular information. Such a high-resolution tracker is needed if a DIRC is used for PID in the barrel region as it provides fine angular information at the DIRC entrance. It can also contribute to define the event time.

Alternative options for the tracking are considered. The TPC can be replaced with silicon trackers, namely increasing the number of layers in the vertex. This would result in a faster detector characterized by finer spatial resolution, even if without the PID capabilities provided by the TPC. The whole silicon tracker option has more limited space requirements, therefore making more space available in the barrel for ECal or PID needs. The length along the beam axis of these external layers is shorter than the TPC one: this detector equips the mere barrel region. Therefore, the diameter of the disk trackers has to be increased in order to cover the forward and backward regions. The most external disk detectors, characterized by the largest diameter, can be replaced by light-material MPGDs: low material budget GEM detectors are considered, where the Cu electrodes are reduced to the mere adhesive Cr-film. Another option, also characterized by low material budget, is a set of cylindrical coaxial MPGD layers: microR-WELLs are considered. This option results in a detector faster than the TPC without PID capabilities. A technologically advanced alternative for the vertex sensors is represented by a new-generation of MAPS in 65 nm CMOS imaging technology, being developed within the ALICE ITS3 project. The sensor specifications and the development timescale are largely compatible with those of the EIC. The expected material budget is only about 0.05% radiation length per layer.

The required electron identification as well as measurements of electron kinematic parameters can be obtained with a set of electromagnetic calorimeters of cylindrical symmetry in the barrel region and a set of rectangular shaped detectors in the forward and backward direction. Different approaches are considered for the set of electromagnetic calorimeters as illustrated in Table 8.4.

The EIC high-resolution EM Calorimeters have the following basic requirements:

- Interaction rate capability up to 0.5×10^6 Hz requiring reasonably fast scintillation kinetics
- Sufficient energy resolution and efficiency over a large dynamic range of photon energies, typically from order 50 MeV to 50 GeV

  - In backward region, $\eta <$ -2 or -2.5, energy resolution of order $2.5\%/\sqrt{E}$ to achieve required 10^{-4} π/e rejection (for E $>$ 2 GeV). Or, in other words, to achieve clean electron identification making use of tracking information to determine E/p. For -2 $< \eta <$ -1, an energy resolution of $7\%/\sqrt{E}$ suffices to achieve clean electron identification for E>2.5–3 GeV
  - In backward and especially far-backward region a small constant term, 1% or less, to aid in determination of electron scattering kinematics. Note that to achieve convergence to good energy resolution including constant term typically requires 20 or more radiation lengths (X_0). For PWO, this is $22X_0$ (20 cm), for CsI 27 X_0 (50 cm).
  - Electron energy range from order 1 GeV to order 20 GeV for $\eta <$ -1, and up to $\sim$40 GeV for $|\eta| < 1$.
  - Photon energy range from order 20 MeV to order several tens of GeV

- Adapted geometrical dimensions to contain the major part of the EM shower
  - Sufficient granularity (0.02–0.03) to separate single photons from π^0 decays
  - In the backward region, at a distance of about 3 m, need position resolution of order 2–3 mm to pinpoint electron scattering kinematics, and granularity of order 2 cm.

- Moderate radiation hardness up to $\sim$3 krad/year (30 Gy/year) electromagnetic and 10^{10} n/cm^2 hadronic at the top luminosity.

This rules out most of the well-known scintillator materials. Finally, even a compact geometrical design requires, due to a minimum granularity, a large quantity of crystal modules, which rely on existing technology for mass production to guarantee the necessary homogeneity of the whole calorimeter.

For hadron physics measurements with electromagnetic reactions, such as at multiple setups at Jefferson Lab and also at PANDA/GSI, the most common precision calorimeter of choice has been lead tungstate, $PbWO_4$ (PWO). This is mostly driven by the requirement of good energy resolution and high granularity to detect and identify electrons, photons and pions. Good energy resolution aids in electron-pion separation and to determine the electron scattering kinematics, compactness and high granularity is driven by need for position resolution and separation of single-photons from neutral-pion decays. $PbWO_4$ (PWO) meets the requirements of an extremely fast, compact, and radiation hard scintillator material providing sufficient luminescence yield to achieve good energy resolution at the EIC.

Crystalline scintillators like NaI(Tl), CsI(Tl), and CsI used in detectors at electron-positron colliders like Crystal Ball at SPEAR, Babar at PEPII, or BELLE at KEK have high light output, but cannot provide the required granularity and have relatively slow decay time. These materials also have a relatively low radiation resistance, which makes them not suitable for the EIC operating at top luminosity. BaF2 used at Crystal Barrel/TAPS experiment at ELSA has similar limitations for the granularity and scintillation kinetics. Although

BaF2 has a very fast component its separation from the slow component is nontrivial. BGO and CeF3 are the closest candidate crystalline scintillators to PWO.

Since the highest precision is only needed at very backward rapidities the reference backward endcap electromagnetic calorimeter is a hybrid design with a high-resolution inner part composed of $PbWO_4$ crystals at room temperature and an outer part composed of radiation-hard SciGlass. Due to its larger radiation length, it requires roughly twice the longitudinal length as PWO, for similar energy resolution, but can achieve similar granularity. It also has a high light yield, similar as BGO and CeF_3, that is independent of temperature and high radiation hardness ($>$1000 kRad and $>10^{15}$ n/cm^2). SciGlass is being developed as part of the EIC eRD1 consortium. Successful scaleup has been demonstrated and glass samples of sizes up to $\sim$10 radiation lengths can now be produced reliably. The electron endcap reference hybrid design fulfills the physics requirements and reduces the demand for crystals while keeping the benefits of a homogeneous detector medium.

The reference detector surrounding the barrel is a Pb/Sc Shashlyk sampling calorimeter. This technology consists of a stack of absorber and scintillator plates. The light is collected with the help of WLS fibers passing through the plates. For the absorber lead or tungsten are used. The technology is widely used and allows detectors of various resolutions and sizes. The barrel calorimeter provides and energy resolution of $12\%/\sqrt{E}$ or better to achieve clean electron identification and less than 2–3 cm granularity to separate single photons from π^0 decays. In the forward region, at a distance of 3 m, if only done with the EMcal requires granularity $<$2.5 cm to identify for momenta up to 50 GeV/c. The reference hadron endcap detector is a W powder/ScFi sampling calorimeter. In this technology fibers are embedded into a heavy material like lead or tungsten. In one implementation the fibers are glued between lead sheets. Such SPACAL-type detectors have been used in several experiments. In an alternative implementation, tungsten powder is used for the absorber. This technology has been developed for the EIC as part of the generic EIC detector R&D program and adapted in the sPHENIX experiment.

Alternative options for the electromagnetic calorimeters are provided by replacing the reference with an alternative option studied by the community. The less demanding outer part of the electron endcap electromagnetic calorimeter could be replaced by one of the heterogeneous sampling options listed in Table 8.4. The radiation-hard SciGlass could provide a homogeneous alternative for the large-volume barrel or the hadronic endcap. Another option, characterized by a heterogeneous material approach, is to replace Pb/Sc Shashlyk in the barrel with a different absorber W/Sc Shashlyk or W powder/ScFi, provided that sufficient performance to meet EIC physics requirements can be demonstrated.

The required jet energy measurements can be obtained with a set of hadronic calorimeters in the barrel and forward and backward directions. The hadron calorimeters should be compatible with the requirements:

- Sufficient energy resolution and efficiency over a large dynamic range, typically from order 100 MeV to 100 GeV
  - In the forward direction, $\eta > 1$ high resolution $<40\%/\sqrt{E}$ +5% is desired for

hadron jet measurements

- Sufficiently high granularity to disentangle the different contributions, i.e. proper assignment of signal to the neutral components of the jet
  - currently anticipated granularity 10 cm $\times$ 10 cm
- Adapted geometrical dimensions to contain the major part of the hadron shower
  - In regions $|\eta| < 1$ and backward region 5 λ_{int} are sufficient as particle energies are $<$ 20 GeV/c
  - In the forward region, η >2.5, should be of order 6–7λ_{int}
- Moderate radiation hardness up to $\sim$3 krad/year (30 Gy/year) electromagnetic and 10^{10} n/cm2 hadronic at the top luminosity.
- Compatibility with Particle Flow Approach for jet reconstruction
- Preferably mechanical sturdiness allowing to build self-supporting structures to minimize space required for passive mechanical support structures.

Due to the large size required for hadron calorimeters, these detectors are typically of the sampling type and consist of an EMCal followed by an HCal part. In such a binary system the performance for electromagnetic energy and hadron energy resolution has to be balanced, e.g. for a high resolution EMCal the hadronic resolution is poor and is determined by fluctuations in the energy sharing between the EM and the hadronic calorimeter section, which have very different e/h values. Precision measurements of energy with sampling calorimeters require sufficiently high sampling fraction and sampling frequency to keep sampling fluctuations and fluctuations in the number of signal quanta (EM energy resolution) at the desired level. An increase in sampling fraction leads to significant dilution of the final density of the calorimeters. In addition, calorimeters with large sampling fraction require additional space for mechanical stability, as they are usually not self-supporting.

The best hadronic calorimeters providing hadron energy resolutions of $\sim 35\%/\sqrt{E}$ + (1.3–3.5)% (ZEUS Depleted Uranium, DU/Sc, E864 Pb/ScFi, and the WA80 DU/Sc ZDC) were compensated. Their total hadronic resolution has been dominated by sampling fluctuations. This is a direct consequence of compensation (e/h=1), which requires small sampling fractions, e.g. 2.3% for Pb/Sc detectors and 5.1% for DU/Sc detectors. To give an idea of required space in the detector for high resolution calorimeter systems; the ZEUS calorimeter system took almost 4 m of space, half of space occupied by high resolution DU/Sc calorimeter and the rest by backing calorimeter to control longitudinal leakages. The E864 Pb/ScFi calorimeter system takes about 2 m of space just for Pb/ScFi structure plus an additional 0.7 m of space for readout.

The reference EIC hadron calorimeter for all detector regions is of the binary type composed of W/ScFi for the EM and Fe/Sc sampling for the hadronic part. The steel absorber is preferable over other absorbers like Pb as it allows to serve the dual purpose of magnetic flux return for the overall EIC detector. Steel also generates less neutrons, which can

be advantageous for the envisioned SiPM readout. With exception of the very forward region in the hadron endcap ($\sim \eta > 2.5$), most hadrons will have energies below 10 GeV, and thus compensation (such as using depleted uranium) is not necessary. In the very forward region in the hadron endcap where hadron energies will be mostly above 10 GeV compensation is still relevant. Precise measurement of energy of hadrons with calorimeters requires sufficient containment of hadronic showers. For EIC approximately 5 λ_{int} length are sufficient for most of the detector due to the relatively low hadron energies. For the higher energy hadrons in the forward region in the hadron endcap 6–7λ_{int} are needed. Longitudinal leakage can be controlled with a tail catcher, which will be an integral part of the main calorimeter, where the last few layers of HCal section may have additional independent readout. W/ScFi was chosen for the EM part of the reference detector to simplify the construction of an EM calorimeter with high sampling frequency and small sampling fraction (approximately being compensated). This hadronic calorimeter reference design is expected to achieve a hadronic energy resolution of $50\%/\sqrt{E}$ + 10% and spatial resolution of 30mm. The eRD1 consortium together with the STAR Forward Upgrade recently demonstrated a small prototype of this system and tested it at FNAL in 2019. Accounting for transverse leakages in the test beam prototype energy resolution was found to be close to $60\%/\sqrt{E}$+6%.

Alternative options for the hadronic calorimeters are provided by replacing the reference with an alternative option studied by the community. In regions where the calorimeter material does not play a considerable role in containing the magnetic field a technology based on a different absorber could be used, e.g. Pb/Sc or DU/Sc. An alternate design with Pb/Sc shashlik for the EM part and Fe/Sc for the hadronic part would also be possible. Another option could be an imaging calorimeter based on silicon RPC/DHCAL, which could provide additional particle identification information and possibly improve the jet energy resolution.

There is a desire to have a higher resolution (better than $\sim 40\%/\sqrt{E}$ with a constant term of $\sim$5%) calorimeter system for the forward hadron endcap covering rapidity $>$2.5, i.e. the region where the calorimeter may outperform the tracker. This is similar to the case of electron endcap, where high resolution is required in the inner portion of the endcap and there provided by PWO crystals. Additional R&D efforts will be required to meet the higher resolution requirement in the hadron endcap. One of the most promising methods to achieve better performance for hadronic calorimeters is dual readout. By comparing the signals produced by Scintillation light (S) and Cherenkov light (C) in the same detector, the EM shower fraction, whose fluctuations are the main culprit for problems encountered with hadronic calorimetry, can be determined for individual events. The validity of this principle has been demonstrated with the DREAM fiber calorimeter. However, two factors impacting hadronic resolution remain: sampling fluctuations and fluctuations in the Cherenkov light yield. Homogeneous materials such as crystals and glasses in which both S and C light are generated in the same optical volume have the potential to eliminate these two issues.

Hadron identification with full coverage of the central detector acceptance is critical for flavor and spin structure function studies and nucleon tomography. It requires different

approaches and technologies in the various regions of the central detector in order to cover different momentum ranges and because of different space constraints imposed by the overall setup arrangement.

The reference option for hadron identification in the barrel region is by a high performance DIRC complemented by dE/dx measurements. The DIRC focuses Cherenkov light released and internally reflected in precision quartz bars. The light is channeled away from the central region for detection providing a compact system with photon sensors outside the detector acceptance. High performance is obtained by adding full focalization to the BABAR DIRC concept. It is so possible to obtain 3σ π/K up to 6 GeV/c.

The measurement of dE/dx complementing the particle identification in the barrel is provided by tracking technologies, e.g. TPC. In the forward region, the dRICH (dual RICH) is the reference detector. It includes two radiators, namely a fluoro-carbon gas and aerogel, can cover a wide momentum range with π/K separation at 3σ level or better from 3 GeV/c to 60 GeV/c. An array of mirrors focalizes the light onto an area with limited instrumentation outside the RICH acceptance with reduced constraints on material budget and radiation tolerance. This facilitates the possibility to use SiPMs as photon sensors, able to operate in magnetic field and to detect single photons. The capability of tolerating the foreseen radiation levels requires confirmation.

The reference hadron-PID device in the backward direction is the modular RICH: it uses aerogel radiator in a proximity-focusing arrangement, where the resolution is increased thanks to the use a Fresnel lens as focusing element. The Fresnel lens also filters short wavelength light, which suffers in aerogel by severe Rayleigh scattering dispersion. It can use either SiPMs or Large Area psecPhoton Detectors (LAPPD) as sensors. It provides 3σ π/K separation up to 10 GeV/c. A characterizing aspect of this option is the modular construction, a design that simplifies construction, quality control and assembly of a large system.

Alternative options for hadron-PID are considered for all the various kinematic regions. In the barrel, the BaBar DIRC bars can be reused, even if posing mechanical problems related to the bar length. Moreover, it would result in a 3σ π/K separation up around 4 GeV/c. TOF options in the barrel region are not promising because of the short lever arm available. In the forward direction, an alternative is a windowless gaseous RICH, where the gas radiator also provides the atmosphere of the gaseous MPGD-based sensors. In this case, the use of a single radiator species makes possible the design of a central optics, limiting the effect of the spherical aberration. This gaseous RICH requires to be complemented by a device for lower momenta making use of aerogel, e.g. mRICH modules, or TOF measurements taking advantage of the $\sim$3 m lever arm available. In both dRICH and windowless RICH, an ecofriendly alternative to the C-F gas is represented by pressurized Ar. Varying the pressure up to about 3.5 bar, Ar can mimic C-F gasses providing the same favorable figures for high Cherenkov photon yield and limited chromaticity. In the backward region, similarly to the forward region, the lever arm for a possible TOF system is of a few meters and, therefore, also this option is considered. A proximity focusing aerogel RICH can also be considered in this region. About TOF technologies, two fine time-resolution sensors are considered: LAPPDs, based on the MCP principle, detecting

the Cherenkov light generated in the window by the through-going ionizing particle with 5–10 ps time resolution and Low Gain Avalanche Detectors (LGAD), with 20–35 ps time resolution and also providing an accurate space point for tracking.

The devices for hadron identification, can also contribute to electron/pion separation, where the electromagnetic calorimetry play the major role. Nevertheless, the separation power by calorimeters is optimal only above $\sim$4 GeV/c and it depends on the technology: it can be at the 10^{-4} level for $PbWO_4$ crystals, while it is around 10^{-2} for heterogeneous sampling options. In the backward region, mRICH can provide 3σ e/π separation up around 2 GeV/c, in the forward region dRICH is capable of 3σ e/π separation up around 15 GeV/c. The DIRC can provide separation up to above 1.3 GeV/c only, due to the high refractive index of the quartz radiator. dE/dx measurements in the TPC can contribute at higher momenta, if adequately supported by TOF information. In the barrel, the limited lever arm of approximately 1 m, requires extremely fine TOF resolution to make e/π by dE/dx possible. An alternative option for electron/pion separation in the backward region is the use of a Hadron Blind Detector (HBD) using CF_4 radiator, similar to the one used in the PHENIX experiment, with pion threshold at $\sim$4 GeV/c. Improvements in the MPGD-based photon detectors can be implemented with the addition of more multiplying layers in the gaseous sensor.

Alternative options for e/h separation are by adding a TRD in the forward and backward directions. A TDR concept making use of GEM as sensor is under development and the preliminary indications for the separation power is at the 10^{-1} level. The device can also provide precise tracking information.

Table 8.5 summarizes the subdetector performance parameters obtained by the technologies described above and summarized in table 8.4. The interactive version of this matrix allows to correlated the listed performance with details about the technology and the simulations used to obtain the performance.

Table 8.4: Possible detector technologies for the Main Detector fulfilling the Physics requirements.

System	System Components	Reference Detectors	Detectors, Alternative Options Considered by the Community		
tracking	vertex	MAPS, 20 um pitch	MAPS, 10 um pitch		
	barrel	TPC	TPC [a]	MAPS, 20 um pitch	MICROMEGAS [b]
	forward & backward	MAPS, 20 um pitch & sTGCs [c]	GEMs	GEMs with Cr electrodes	
	very far forward & far backward	MAPS, 20 um pitch & AC-LGAD [d]	TimePix (very far backward)		
ECal	barrel	Pb/Sc Shashlyk	SciGlass	W powder/ScFi	W/Sc Shashlyk
	forward	W powder/ScFi	SciGlass	PbGl	Pb/Sc Shashlyk [e]
	backward, inner	$PbWO_4$	SciGlass		
	backward, outer	SciGlass	$PbWO_4$	PbGl	W powder/ScFi [f]
	very far forward	Si/W	W powder/ScFi	crystals [g]	SciGlass
h-PID	barrel	hpDIRC & dE/dx (TPC)	reuse of BABAR DIRC bars	fine resolution TOF	
	forward, high p	double radiator RICH	fluorocarbon gaseous RICH	high pressure Ar RICH	
	forward, medium p	(fluorocarbon gas, aerogel)	aerogel		
	forward, low p	TOF	dE/dx		
	backward	modular RICH (aerogel)	proximity focusing aerogel		
e/h separation at low p	barrel	hpDIRC & dE/dx (TPC)	very fine resolution TOF		
	forward	TOF & aerogel			
	backward	modular RICH	adding TRD	Hadron Blind Detector	
HCal	barrel	Fe/Sc	RPC/DHCAL	Pb/Sc	
	forward	Fe/Sc	RPC/DHCAL	Pb/Sc	
	backward	Fe/Sc	RPC/DHCAL	Pb/Sc	
	very far forward	quartz fibers/ scintillators			

[a] TPC surrounded by a micro-RWELL tracker
[b] set of coaxial cylindrical MICROMEGAS
[c] Small-Strip Thin Gas Chamber (sTGC)
[d] MAPS for B0 and off-momentum particles, LGAD for Roman Pots
[e] or W/Sc Shashlyk
[f] or W/Sc Shashlyk, also Pb/Sc Shashlyk
[g] alternative options: $PbWO_4$, LYSO, GSO, LSO

Table 8.5: This matrix summarizes the high level performance of the different subdetectors and a 3 T Solenoid. The interactive version of this matrix can be obtained through the Yellow Report Detector Working Group (https://physdiv.jlab.org/DetectorMatrix/).

η	Nomenclature			Tracking						Electrons and Photons			π/K/p		HCAL		Muons
				Resolution	Relative Momentum	Allowed X/X_0	Minimum-pT	Transverse Pointing Res.	Longitudinal Pointing Res.	Resolution σ_E/E	PID	Min E Photon	p-Range (GeV/c)	Separation	Resolution σ_E/E	Energy	
< -4.6	↓ p/A	Far Backward Detectors	low-Q2 tagger														
-4.6 to -4.0				Not Accessible													
-4.0 to -3.5					Reduced Performance												
-3.5 to -3.0		Central Detector	Backward Detector		$\sigma p/p$ ~0.1%×p⊕2%	~5% or less X	150 - 300 MeV/c	dca(xy) ~ 40/pT μm ⊕ 10 μm	dca(z) ~ 100/pT μm ⊕ 20 μm	1%/E ⊕ 2.5%/√E ⊕ 1%	π suppression up to 1:1E-4	20 MeV	≤ 10 GeV/c	≥ 3 σ	50%/√E⊕10%	~500MeV	Muons useful for bkg, improve resolution
-3.0 to -2.5																	
-2.5 to -2.0																	
-2.0 to -1.5					$\sigma p/p$~ 0.02%×p⊕1%					2%/E ⊕(4-8)%/√E ⊕ 2%	π suppression up to 1:(1E-3 - 1E-2)	50 MeV					
-1.5 to -1.0																	
-1.0 to -0.5			Barrel		$\sigma p/p$ ~0.02%×p⊕5%		400 MeV/c	dca(xy) ~ 30/pT μm ⊕ 5 μm	dca(z) ~ 30/pT μm ⊕ 5 μm	2%/E ⊕(12-14)%/√E ⊕ (2-3)%	π suppression up to 1:1E-2	100 MeV	≤ 6 GeV/c		100%/√E+10%		
-0.5 to 0.0																	
0.0 to 0.5																	
0.5 to 1.0																	
1.0 to 1.5			Forward Detectors		$\sigma p/p$ ~0.02%×p⊕1%		150 - 300 MeV/c	dca(xy) ~ 40/pT μm ⊕ 10 μm	dca(z) ~ 100/pT μm ⊕ 20 μm	2%/E ⊕ (4*-12)%/√E ⊕ 2%	3σ e/π up to 15 GeV/c	50 MeV	≤ 50 GeV/c		50%/√E+10%		
1.5 to 2.0																	
2.0 to 2.5																	
2.5 to 3.0					$\sigma p/p$ ~0.1%×p⊕2%												
3.0 to 3.5																	
3.5 to 4.0	↑ e		Instrumentation to separate charged particles from photons		Reduced Performance												
4.0 to 4.5				Not Accessible													
> 4.6		Far Forward Detectors	Proton Spectrometer														
			Zero Degree Neutral Detection														

8.4.3 Central Magnet Consideration

The EIC detector is built around a central solenoid magnet with optional correction trim coils required to meet the solenoid field specification. Tracking resolutions in the central pseudo-rapidity range suggest the nominal field of 3 T, but a range between 1.5 T and 3 T makes physics measurements accessible. A central field as high as 3 T is needed to maximize the effective $|B|\cdot$dl integral for particles scattered at small polar angles, both in forward and backward directions. High magnetic fields come at the cost of reducing the low-pT acceptance of charged tracks. The acceptance for low-pT particles down to the momenta $\sim$100 MeV/c requires that a fraction of physics data are taken at a substantially lower field. Field polarity flip is a standard measure to address systematic effects due to a different acceptance for the positively and negatively charged particles, hence a bipolar magnet operation with a polarity switch is one of the magnet requirements.

Physics studies available to date suggest a solenoid with a bore diameter 2.5–3.5 m in a traditional composition of an EIC detector. Specifications on coil length, presently assumed to be able to provide a $\sim$3.0 m magnetic length as a reference figure, cryostat radial space, and coil configuration require an optimization integrated with the overall detector design. The solenoid design is characterized by three regions, the barrel and backward endcap with the field parallel to the magnet axis and the RICH detector in the forward direction, which extends from +100 cm to +240 cm with respect to the magnet center, where the field lines should be projective with respect to the nominal IP location. A flux return path could be provided through the hadronic calorimeter assemblies in the forward and backward directions. Correction coils in the hadron end-cap may be required to meet the RICH detector readout on field projectivity. The need for these coils should be avoided as they will adversely affect the hadron calorimeter performance, but if needed, should be allowed to occupy a maximum of 10 cm of the available linear space.

Alternative detector integrated designs, where a dipole or toroidal field are superimposed with the solenoid field in the central region of the detector, have been considered to improve the $|B|\cdot$dl integral at small scattering angles. These integrated designs could be an option if an acceptance that meets the physics requirements can be demonstrated.

Re-use of the existing BABAR/sPHENIX magnet is an alternative to the realization of a new solenoid with optimized design. Whereas the new solenoid main specifications are an up-to 3T magnetic field, a 2.5–3.5 m diameter bore, and a magnetic length of $\sim$3 m, the BABAR/sPHENIX magnet provides an up-to 1.5 T field, a 2.8 m diameter bore, and similar magnetic length. The magnet for the BABAR experiment at PEP-II at SLAC, CA was manufactured by Ansaldo, Italy in 1997 and was commissioned in 1998. It was then transferred to BNL, NY in 2015 for use in the sPHENIX experiment where it still resides today. It received a high-field test (up to 1.3 T) in 2018. The prolonged use of the BABAR/sPHENIX magnet requires the implementation of several maintenance and improvement modifications, including new protection circuits such as voltage taps, inspection of and as needed reinforcement of the internal mechanical support, including new strain gauges, and replacement of control instrumentation sensors. Several of these implementations involve the delicate operation of disassembly of the magnet. To repair an existing small leak in the

valve box for the cryogenic cooling system requires a replacement of the valve box or disassembly to inspect cooling pipework and to repair leaks. Moreover, additional changes are required for re-using the magnet, for example those needed to match the requirements of projective field lines in the RICH region.

The main parameters of both a new superconducting solenoid magnet, at the present stage of magnet optimization integrated with the overall detector design, and the existing BABAR/sPHENIX magnet are shown in Table 8.6. For a new magnet, a slightly larger bore of 3.2 m is chosen as compromise between, on one hand, magnet complexity and mechanical Hall space considerations, and on the other hand providing some much-needed space in the bore to ensure more detector technology choices to ensure functionality of tracking, hermetic electromagnetic calorimetry and particle identification (both e/π and $\pi/K/p$) over a large range of particle momenta. The choice of NbTi conductor in a Cu matrix for the new magnet is driven by that for EIC no detection beyond hadronic calorimetry is foreseen beyond the bore, alleviating a material requirement on small radiation lengths and allowing use of Cu facilitating the magnet mechanical design.

Table 8.6: Summary of some of the main requirements of the EIC detector solenoid magnet.

Parameter	New Magnet	BABAR/sPHENIX Magnet
Maximum Central Field [T]	3	1.5
Coil length [mm]	3600	3512
Warm bore diameter [m]	3.2	2.8
Uniformity in tracking region ($z = 0$, $r < 80$ cm) (%)	3	3
Conductor	NbTi in Cu Matrix	Al stabilized NbTi
Operating Temperature [K]	4.5	4.5

The coil length is driven by the present definition of the barrel region as between pseudorapidity of -1 and 1. This corresponds to an angle of $\sim$40 degrees. This means that for a certain bore size, the space for the mechanical length of the magnet cryostat is roughly 20% larger, or 3.84 m for a 3.2 m bore. Folding in an approximate need of 12 cm additional need on each side of the magnet coil for inner vacuum and helium vessels, and multi-layer isolation, determines the coil length requirement to be 3.6 m. A somewhat larger coil length of 3.8 m would not be a major issue, but likely not much more as the edge of the cryostat is one of the regions where detector infrastructure (support, cabling, etc.) will reside, and deliberations between the need for equal coverage of tracking and electromagnetic calorimeter as trade-off with particle identification detector readout will occur.

The main advantage of accessibility of low central solenoid fields (down to $\sim$0.5 T) is towards the low-PT acceptance of charged-particle tracks. A central field of 0.5 T roughly equates to a detection capability of charged particles down to transverse momenta of below $\sim$0.05 GeV/c. This is for example relevant for mapping the decay products of heavy-flavor mesons. The main advantage of a 3 T versus a 1.5 T central solenoid field is for the

momentum resolution of charged particles as function of pseudo-rapidity. The required low p_T detection threshold strongly depends on the fact if one requires particle identification or not and the mass of the particle initiating the track. The achievable lower cut offs for charged pions requiring to reach a PID detector at 1m or only reconstructing the track p_T and its charge with the microvertex tracker are summarized in Table 8.7.

Table 8.7: The achievable lower cut offs for charged pions.

lowest p_T	0.5 Tesla	1 Tesla	3 Tesla
with PID at 1 m	75 MeV	225 MeV	450 MeV
without PID	25 MeV	50 MeV	100 MeV

Doubling the magnetic field can lead to a reduction of the momentum resolution by a factor of ≈2 from a leading order $\sim 1/B$ dependence. This is relevant in the central region, but even more so in the forward pseudo-rapidity regions, η >2, where the momentum resolutions rapidly worsen. For example, for η ∼3, a momentum resolution of ∼2–3% is achievable for pions with momenta up to about 30 GeV/c with a 3 T central field, and only double that resolution for a 1.5 T central field.

8.4.4 Detectors along the Beamline

Far-Forward Detectors

The measurement of exclusive and diffractive e+p and e+A events require careful design considerations for the Far-Forward ($\eta > 4.6$) region of the IR, as well as optimized placement of several detector subsystems, and careful choices of technology. In this section we will describe each detector subsystem in detail and present the physics reach demonstrated by the combined FF detector system.

The overall layout of the Far-Forward (FF) region is shown in Figure 8.18, with a summary of the general acceptances of each current subsystem shown in Table 8.8.

Table 8.8: Summary of far-forward detector locations and angular acceptances for protons, neutrons, and light nuclei or nuclear fragments. In some cases, the angular acceptance is not uniform in ϕ, as noted in the table.

Detector	(x,z) Position [m]	θ [mrad]	Notes
ZDC	(0.96 m, 37.5 m)	θ <5.5	∼4.0 mrad at $\phi = \pi$
Roman Pots (2 stations)	(0.85, 26.0), (0.94, 28.0)	$0.0 < \theta < 5.5$	10σ cut.
Off-Momentum Detector	(0.8, 22.5), (0.85, 24.5)	$0.0 < \theta < 5.0$	$0.4 < x_L < 0.6$
B0 Spectrometer	(x = 0.19, $5.4 < z < 6.4$)	$5.5 < \theta < 13.0$	∼20 mrad at ϕ=0

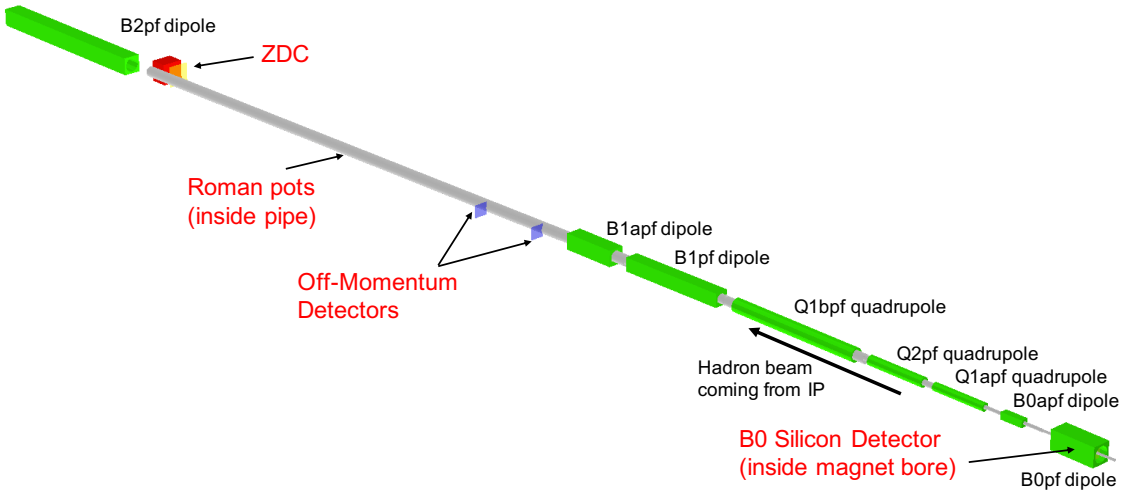

Figure 8.18: GEANT4 rendering of the far-forward hadron beam magnets, a simple sketch of a beam pipe, and the four detector subsystems currently included.

The entire FF detector system consists (currently) of four main components: 1) the Roman Pots system, 2) the B0 spectrometer, 3) the off-momentum detectors, and 4) the zero-degree calorimeter. The main particles which are considered for detection in these subsystems are protons (in 1–3), neutrons (4), and photons (4 and potentially 2). Figure 8.19 shows a top-down sketch of FF hadron and electron lattices and the four detector sys- tems used for the detection of FF charged and neutral particles. In principle, nuclear fragments and charged pions could also be detected in the silicon sensors intended for protons, but PID would need to be considered in the case of proton/pion separation.

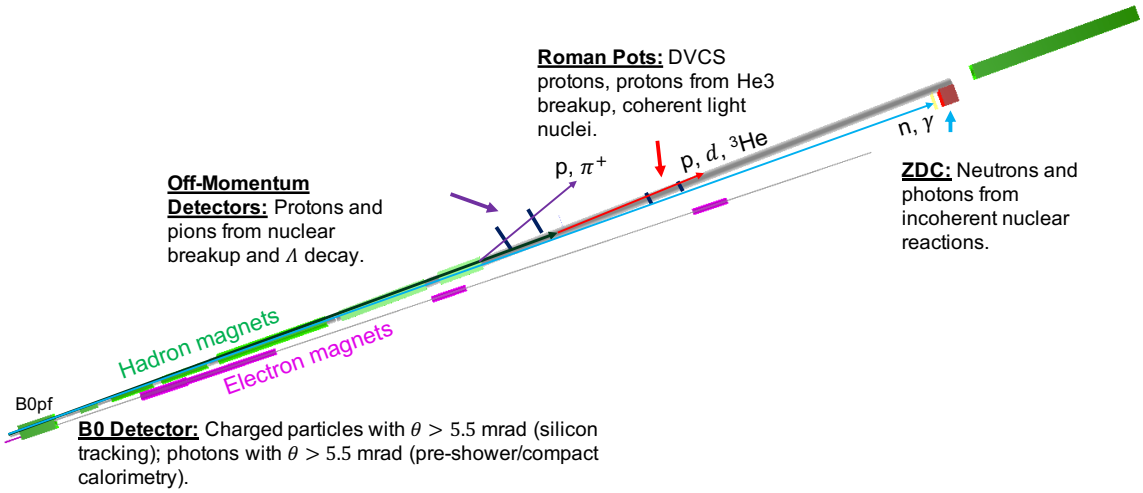

Figure 8.19: Top-down sketch of FF hadron and electron lattices and the four detector systems used for the detection of FF charged and neutral particles.

Section 3.2.4 details numerous studies carried out with MC generators and Geant, and they are summarized in Table 8.9 for convenience.

Table 8.9: Summary of far-forward detector studies used to establish requirements. Full details of the studies are found in Section 3.2.4

Study/Physics Channel	MC Generator	Detectors	Notes
e+p DVCS	MILOU	Roman Pots, B0 Detectors	Baseline requirements for Roman Pots and B0 Detector.
e+d Spectator Tagging	BeAGLE	All	Identified need for off-momentum detectors; tested assumptions for ZDC.
e+^{3}He Spectator Tagging	BeAGLE et al.	All	Reinforced RP requirements.
FF Lambda Decay/ Meson Structure	PYTHIA6	B0 Detectors, Off-Momentum Detectors, ZDC	Established need for silicon detectors before ZDC for tagging π^- from Λ decay.
e+A (Heavy Nuclei)	BeAGLE	All	Preliminary findings for incoherent veto efficiency and low-E photon tagging.

Roman Pots: The Roman Pots consist of two stations with anywhere from 2–5 sensor planes, with the stations spaced 2 m apart. The current straw-man design (see Figure 8.20) assumes an L-shaped sensor with movement only in the y-direction, due to space considerations in the x-directions making additional movement in the x-direction challenging. Other designs are also under consideration to ensure maximal coverage of the acceptance.

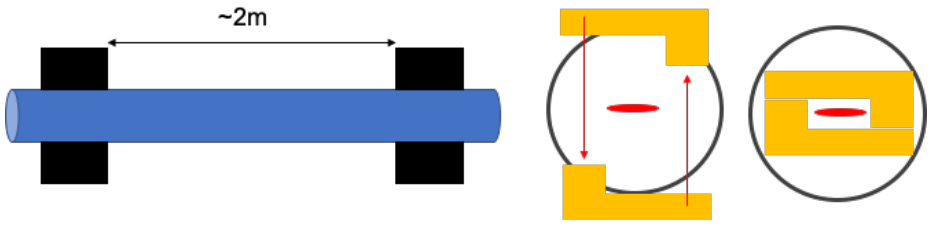

Figure 8.20: Straw-man sketch of a possible Roman Pots detector configuration allowing for only vertical movement, but covering both the horizontal and vertical acceptance. The sensors are situated in the beam pipe, a few centimeters from the beam and generally contained in an aluminum vessel known as a "pot" with a window for proton detection.

A new silicon technology using AC-coupled Low Gain Avalanche Diodes (AC-LGADs) is under consideration to be used to meet the requirements of the Roman Pots. The AC-LGADs provide both timing and spatial information for reconstruction. The Roman Pots system can accept charged particles with a scattering angle of $0.0 < \theta < 5.0$ mrad, and a longitudinal momentum fraction compared to the beam $0.8 < x_L < 1.0$. The lower bound of the angular acceptance is determined by the angular cutoff of the 10σ safe distance of the sensors from the beam, where $\sigma_{x,y}(z) = \sqrt{\beta_{x,y}(z)\epsilon_{x,y}}$ is the transverse size of the beam. This 10σ cut is dependent on both the beam energy, and the optics configuration (so-called "high acceptance" or "high divergence" configurations). Reconstruction of particle tracks is carried out using a linear transfer matrix which is used to calculate the IP coordinates from the local coordinate of the RP hits. This transfer matrix describes the particle transport through the magnetic lattice components from the IP to the RP location.

The contributions to momentum smearing come from the following sources: 1) angular divergence, 2) vertex smearing due to the rotation of the bunch by the crab cavity, 3) finite detector pixel size, 4) beam momentum spread. In general, the angular divergence is the dominant source of momentum smearing, but can be reduced by a different choice of optics (e.g. high acceptance configuration) that will reduce the size of the beam (β-functions) at the Roman Pots location at the expense of reduced overall luminosity.

The contribution from the crab cavity rotation comes from the transverse momentum components imposed on the particles in the bunch by the cavity, with the goal of rotating the bunches such that they overlap at zero degrees at the IP, maximizing the luminosity (see Figure 8.21). When the hadron bunch undergoes crab rotation (rotation in the x-z plane), the x-coordinate of the primary vertex is smeared by approximately half the crossing angle times the bunch length. Assuming a 25 mrad crossing angle with a 10 cm long bunch yields vertex smearing of 1.25 mm.

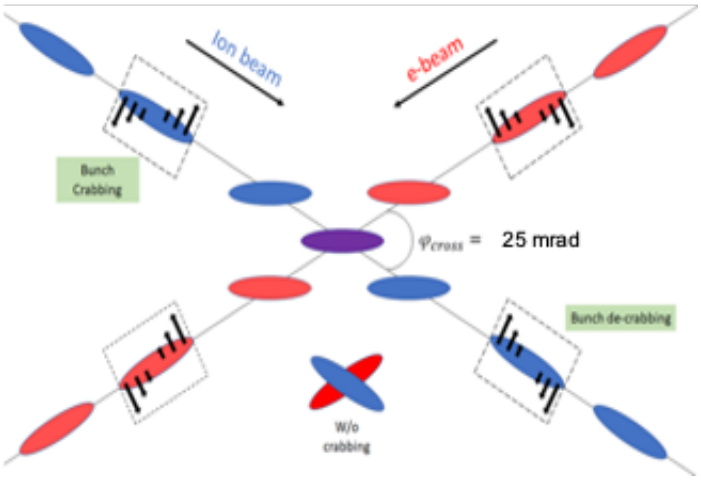

Figure 8.21: Cartoon sketch of the hadron and electron bunches rotated by the crab cavities with a 25 mrad crossing angle. The rotation of these bunches induces a vertex smearing with respect to the FF detectors. This can be removed with timing sufficient to isolate the collision vertex within the bunch.

The crab cavity induced vertex smearing can be fully mitigated by the inclusion of timing ∼30–40 ps, which comes from the reduction of the effective bunch length to 1 cm (yielding a vertex smearing of 125 µm) divided by the speed of light. In addition to mitigating the smearing induced by crab cavity rotation, this fast timing will also be needed to reduce the background associated with high beam currents that will make the beam+machine and beam+gas backgrounds high enough to compete with the DIS rates in the detectors.

Finite pixel size induces smearing by providing uncertainty in the location of a particle hit left by a charged particle. This smearing is best balanced with reasonable channel count by using a (500 µm)×(500 µm) pixel pitch. In order to reduce the potentially large number of required channels in the detector, novel silicon pad patterns (such as zig-zags) are being considered. The beam momentum spread has a negligible contribution to the overall smearing. For the various beam energies + smearing contributions, the integrated p_T-smearing is 15–50 MeV/c. Figure 8.22 shows reconstruction of the momentum transfer, -t, for two different beam energies. Even with the 50 MeV/c total smearing in reconstructed p_T potentially present in the top beam energy configuration, the reconstruction is adequate for extracting a slope — needed for extraction of the impact parameter distribution related to the gluon GPD.

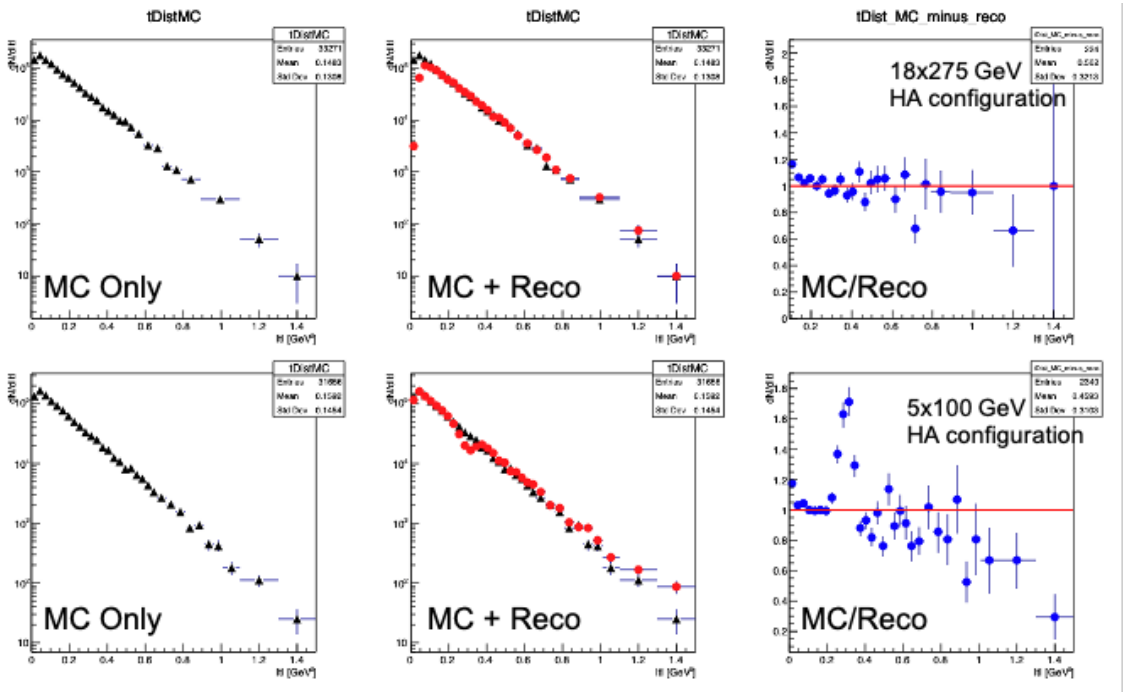

Figure 8.22: Momentum transfer, t, distributions for 18×275 GeV (top row) and 10×100 GeV (bottom row) DVCS events generated with MILOU. The first panel in both rows is the MC generated distribution, the middle panel is the MC (black) plotted with the reconstructed distribution (red), and the third panel is that ratio of the generated distribution over the reconstructed distribution. The acceptance gap between the RP and B0 detectors causes the peak at 0.38 GeV^2, while the residual slope at high-$|t|$ is caused by bin migration due to momentum smearing.

B0 Spectrometer: The B0 spectrometer consists of several planes of silicon placed inside the bore of the B0pf dipole magnet. A GEANT4 rendering of the subsystem is shown in Figure 8.23.

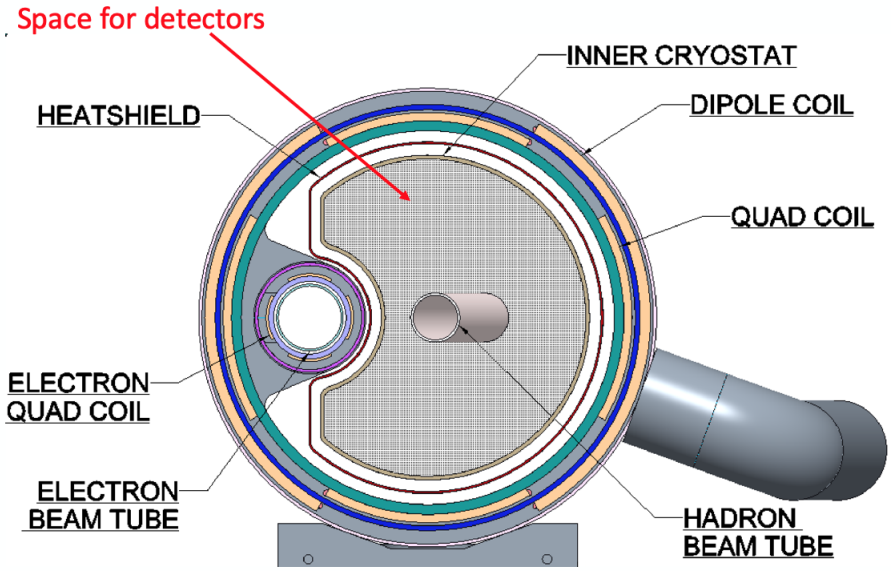

Figure 8.23: Closeup image of the B0pf magnet bore with both hadron and electron beam pipes and warm area for placement of detectors. The detector area allows for up to ∼13 mrad of angular coverage between the two beam pipes, and up to ∼20 mrad of angular coverage between the hadron beam pipe and the inner wall of the bore. Both silicon tracking detectors as well as compact electromagnetic calorimetry are under consideration for integration into the open space in the bore.

The B0 spectrometer can in principle capture charged particles (or potentially photons if an ECAL is included) with scattering angle $5.5 < \theta < 20.0$ mrad, although on the side closest to the IP, the upper bound is closer to 13 mrad due to the electron quadrupole location with respect to the hadron beam pipe. Reconstruction of tracks with the B0 detector is done in the GEANT4 simulations using a conventional Kalman Filtering technique, and is therefore more sensitive to the choice of pixel pitch. This detector will require a minimum of (50 µm)×(50 µm) pixels to achieve the necessary resolution. Access to this detector system will be challenging due to its location in the FF lattice, and the engineering considerations are still under discussion.

Since the sensors will be in a warm portion of the bore, conventional silicon sensors can be employed, but fast (30–40 ps) timing will still be required to reduce smearing and background. A combination of MAPS sensors plus timing layers may be sufficient to supply the necessary spatial and temporal resolution. Additionally, the radiation load in the B0 spectrometer will likely be the highest of any of the FF detectors due to the proximity to the IP, and the amount of machine components which serve as secondary scattering centers for charged particles, which will be directed into the B0 detector.

Off-Momentum Detectors: The Off-Momentum Detectors (OMD) are silicon planes placed just after the B1apf dipole magnet and outside the beam pipe. The silicon sensors will be identical to those used for the Roman Pots subsystem, and have a similar acceptance for charged particles, but with a different range of longitudinal momentum fraction compared to the beam momentum $\frac{p_{part.}}{p_{beam}}$ ($0.4 < \frac{p_{part}}{p_{beam}} < 0.6$), where p_{beam} refers to the equivalent proton momentum setting for the dipole magnets (i.e. 135 GeV/n deuteron beams means p_{beam} =275 GeV/c. This subsystem is required to measure charged particles from nuclear breakup events, where the final state hadrons have a much different rigidity than the nuclear beam, and therefore experience more bending in the dipole magnets, causing them to be deflected outside of the beam pipe before reaching the Roman Pots. Many of these nuclear breakup hadrons will also be captured in the B0 spectrometer, but with a larger scattering angle ($\theta >\sim 5$ mrad).

The OMD system will have overall better acceptance at small scattering angles (< 1 mrad) because these sensors will sit outside the beam pipe and will therefore require no 10σ cut for detector safety. Reconstruction using the normal transfer matrix approach invoked in the Roman Pots will potentially need to be refined due to the non-linear bending experienced in the quadrupole magnets for very off-momentum particles. This imposes additional smearing for especially severely off-momentum protons ($\frac{p_{part.}}{p_{beam}} < 0.3$). Solutions to this non-linear transport are under consideration.

Zero-Degree Calorimeter: As discussed in Section 2.1.2, a zero-degree calorimeter (ZDC) is required both for detection of neutrons in nuclear breakup events, and for veto of heavy-nuclear breakup events. Additionally, the inclusion of a preshower electromagnetic calorimeter will be required for detection of low-energy photons from nuclear excitation, or high-energy photons from forward π^0 decay. In order to achieve the required energy resolution for the hadronic calorimetric portion of the ZDC, a large transverse size (minimum 60 cm $\times$ 60 cm) and longitudinal length (minimum 1 m) will be required to contain the hadronic shower.

Current simulations assume a ZDC with $\frac{\sigma_E}{E} = \frac{50\%}{\sqrt{E}} \oplus 5\%$ and $\frac{\sigma_\theta}{\theta} = \frac{3 \text{ mrad}}{\sqrt{E}}$, but a better resolution may be required to reduce the smearing effects from this assumed resolution on observables. Currently the ALICE Forward Calorimeter (FoCal) [414] ZDC design is being considered as a starting point for the ZDC in the EIC IR, which makes use of tungsten silicon fibers for the hadronic section, and lead-tungstate crystals ($PbWO_4$) for the electromagnetic portion of the calorimeter.

Far-Backward Detectors

The path of the electron beam downstream of the interaction point is shown in Figure 8.24. The horizontal axis is aligned with the direction of the beam at the collision point, along which photons from e+p and e+A interactions will travel. These photons come predominantly from the bremsstrahlung process used for luminosity determination. The lower left of the figure shows possible instrumentation for the luminosity measurement.

Bremsstrahlung also produces electrons with momenta slightly below the beam energy. After being bent out of the beam by lattice dipoles they may be measured by taggers as shown in the top left of the figure.

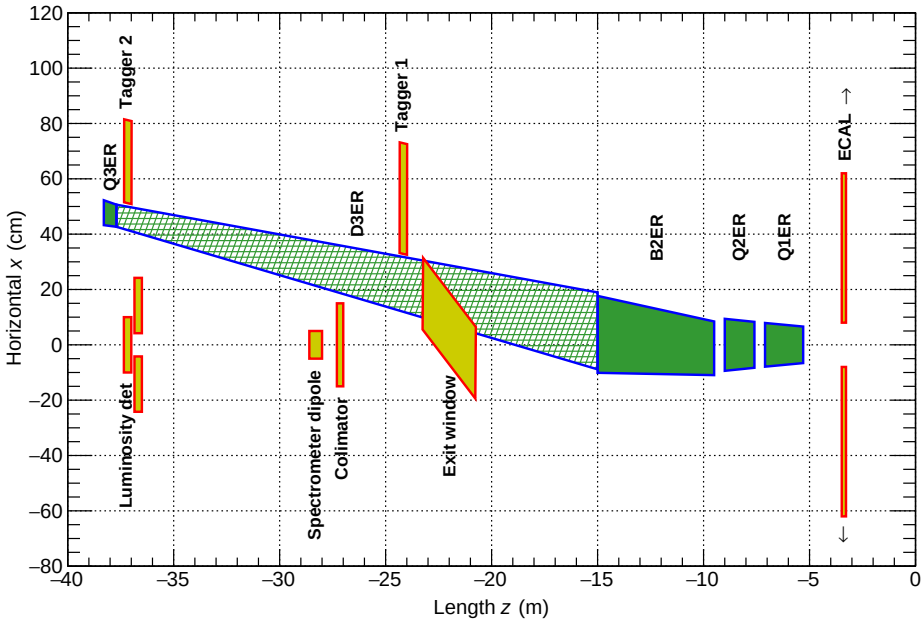

Figure 8.24: The region downstream of the interaction point in the electron direction.

Luminosity Measurement: The luminosity measurement provides the required normalization for all physics studies. At the broadest scale it determines absolute cross sections, such as needed for the structure function F_2 and derived PDFs. On an intermediate scale, it is also required to combine different running periods, such as runs with different beam energies needed to measure F_L, or runs with different beam species to study A dependencies. Asymmetry measurements are conducted using beams with bunches of both spin states. On the finest scale, the relative luminosity of the different bunch crossings is needed to normalize the event rates for the different states; the uncertainty on the relative bunch luminosity is a limiting factor for asymmetry measurements.

The bremsstrahlung process $e + p \longrightarrow e + p + \gamma$ was used successfully for the measurement of luminosity by the HERA collider experiments [76–78]. It has a precisely known QED cross-section which is large, minimizing theoretical uncertainty and providing negligible statistical uncertainty. Thus the scale uncertainty of the luminosity is determined by the systematic uncertainties of the counting of bremsstrahlung events. The ZEUS collaboration at HERA measured luminosity with a 1.7% scale uncertainty; further improvements at the EIC should be able to reduce this to <1% as required by the physics program.

In contrast to HERA, where only the electron beam was polarized, both the electron and proton/light ion beams will be polarized in the EIC. In this case the bremsstrahlung rate is sensitive to the polarization dependent term $a(P_e, P_h)$ in the cross section $\sigma_{\text{brems}} =$

$\sigma_0(1 + a(P_e, P_h))$. Thus, the polarizations P_e, P_h and luminosity measurements are coupled, and the precision of the luminosity measurement is limited by the precision of the polarization measurement. This is especially important for relative luminosities for asymmetry measurements, where the bremsstrahlung process used for normalization has different cross sections for different spin states. The precision needed for the relative luminosity measurement is driven by the magnitude of the physics asymmetries which can be as low as 10^{-4}; the uncertainty on relative bunch luminosities must reach this level of precision.

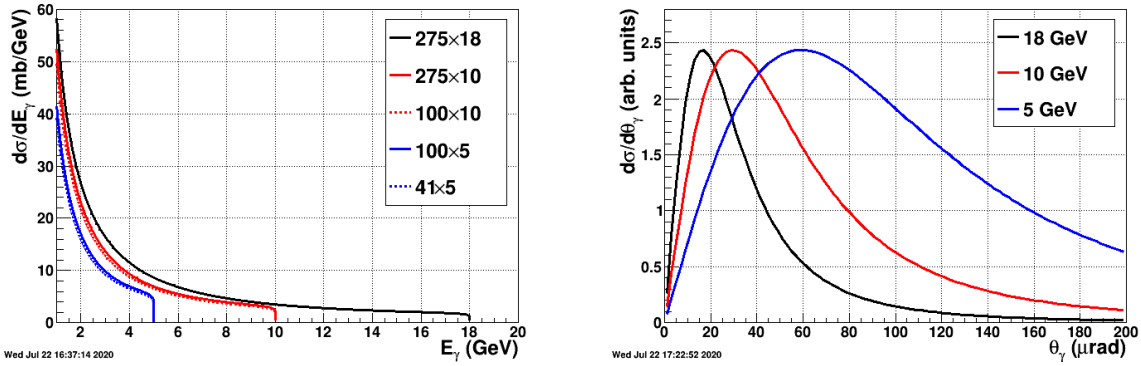

Figure 8.25: Bremsstrahlung photon energy (left) and angular (right) distributions for EIC beam energies.

The bremsstrahlung photon energy E_γ distributions for EIC beam energies are shown in the left of Figure 8.25. They diverge as $E_g \to 0$ and have sharp cutoffs at the electron beam energies. As shown in the right of Figure 8.25, the bremsstrahlung photons are strongly peaked in the forward direction with typical values of $\theta_\gamma \approx m_e/E_e$, with values of 20–60 µrad at the EIC. The RMS angular divergence of the electron beam is significantly larger than these values and will dominate the angular distribution of bremsstrahlung photons.

Bremsstrahlung Photon Detectors: The straightforward method for measuring bremsstrahlung situates a calorimeter at zero degrees in the electron direction counting the resulting photons, as shown lower left of Figure 8.24. The calorimeter is also exposed to the direct synchrotron radiation fan and must be shielded, thus degrading the energy resolution. This also imposes a rough low energy cutoff on photons typically $\approx$ 0.1–1 GeV below which the calorimeter is insensitive. At peak HERA luminosities, the photon calorimeters were sensitive to 1–2 photons per HERA bunch crossing. At an EIC luminosity of $10^{33}\,\mathrm{cm}^{-2}\,\mathrm{s}^{-1}$, the mean number of such photons per bunch crossing is over 20 for electron-proton scattering and increases with Z^2 of the target for nuclear beams. The per bunch energy distributions are broad, with a mean proportional to the number of photons per bunch crossing. The counting of bremsstrahlung photons thus is effectively an energy measurement in the photon calorimeter with all of the related systematic uncertainties (e.g. gain stability) of such a measurement.

An alternative method to counting bremsstrahlung photons, used effectively by the ZEUS collaboration at HERA, employs a pair spectrometer. A small fraction of photons is con-

verted into e^+e^- pairs in the vacuum chamber exit window. A dipole magnet splits the pairs vertically and each particle hits a separate calorimeter adjacent to the unconverted photon path. The relevant components are depicted in the lower left of Figure 8.24. This has several advantages over a zero-degree photon calorimeter:

- The calorimeters are outside of the primary synchrotron radiation fan.
- The exit window conversion fraction reduces the overall rate.
- The spectrometer geometry imposes a low energy cutoff in the photon spectrum, which depends on the magnitude of the dipole field and the location of the calorimeters.

The variable parameters of the last two points (conversion fraction, dipole field and calorimeter locations) may be chosen to reduce the rate to less than or of order one e^+e^- coincidence per bunch crossing even at nominal EIC luminosities. Thus, counting of bremsstrahlung photons is simply counting of e^+e^- coincidences in a pair spectrometer with only small corrections for pileup effects.

The locations of a zero-degree calorimeter and pair spectrometer are shown in the bottom left of Figure 8.24. Careful integration into the machine lattice is required, not only to allow for enough space for the detectors, but also to accommodate the angular distribution of the photons. This is dominated by the angular divergence of the electron beam, with RMS values as high as 0.2 mrad. Thus a clear aperture up to a few mrad is required to measure the angular distribution and minimize the acceptance correction. The spectrometer rate is directly proportional to the fraction of photons which convert into e^+e^- pairs, placing stringent requirements on the photon exit window. It must have a precisely known material composition, and a precisely measured and uniform thickness along the photon direction.

Calorimeters are required for both luminosity devices, for triggering and energy measurements. The high rates dictate a radiation hard design, especially for the zero-degree calorimeter, which must also have shielding against synchrotron radiation. The spectrometer must also have precise position detectors to measure the $e^{\pm}$. Combined with the calorimeter energy measurement this allows reconstruction of the converted photon positions. The distribution of photon positions is required to correct for the lost photons falling outside the photon aperture and detector acceptances.

Bremsstrahlung and Low-Q^2 Electron Detectors: Downstream of the interaction point the electron beam is accompanied by a flux of electrons at small angles with respect to the beam direction and at slightly lower energy. They are predominantly final state electrons from the bremsstrahlung process $e + p \longrightarrow e + p + \gamma$, with an energy distribution the mirror image of the left of Figure 8.25 with $E'_e = E_e - E_\gamma$. Also, a fraction of the electrons in this region are produced in quasi-real photoproduction with $Q^2 \approx 0$.

The final state bremsstrahlung electrons provide a powerful tool for calibrating and verifying the luminosity measurement with photons. Tagging bremsstrahlung electrons and

counting corresponding photons in the photon detectors provides a direct measure of the luminosity detector acceptance in the tagged energy range. This is of paramount importance to precisely determine the pair conversion probability for the luminosity spectrometer, which depends on the exit window composition and thickness.

Tagging of low-Q^2 processes provides an extension of the kinematic range of DIS processes measured with electrons in the central detector. It crosses the transition from DIS to hadronic reactions with quasi-real photons. An example of acceptance as a function of Q^2 for measurements with the central detector and electron taggers as depicted in Figure 8.24 is shown in Figure 8.26 (left). The electrons are generated by a simple model of quasi-real photoproduction [415] and Pythia. The taggers provide useful acceptance in the range $10^{-6} < Q^2 < 10^{-2}\,\mathrm{GeV}^2$. Application of the electron taggers for low-Q^2 physics will face a challenge from the high rate bremsstrahlung electrons, which can be addressed by tagger design and correlation with information from the central detector.

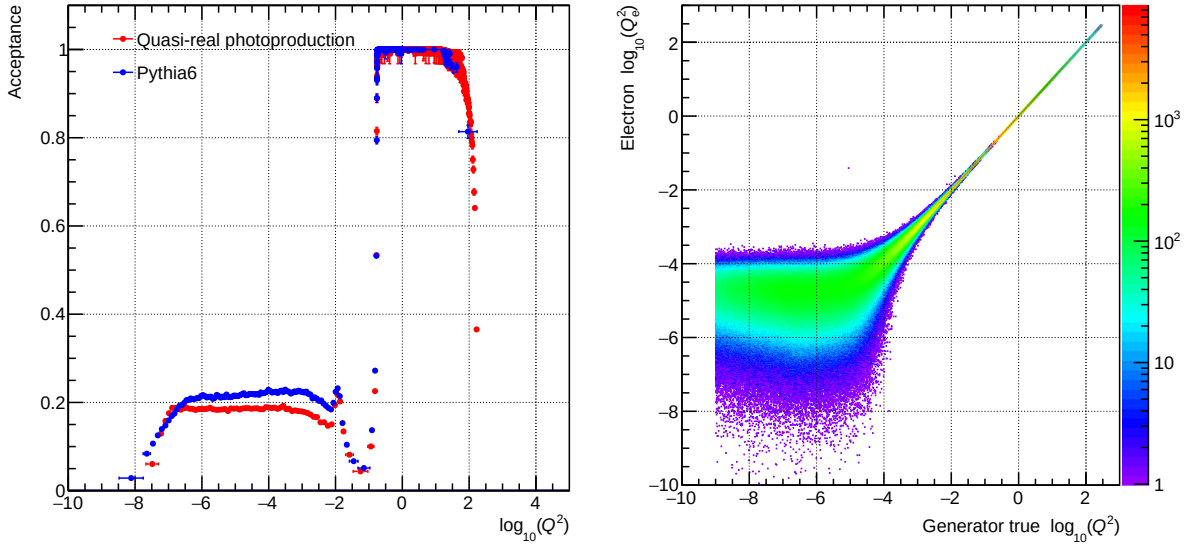

Figure 8.26: left: Acceptance as a function of Q^2 for electrons measured in the central detector (right plateau) and downstream taggers (left plateau). The electrons are generated by a simple model of quasi-real photoproduction and Pythia. right: Comparison of reconstructed and reconstructed electron Q_e^2 with smearing for beam angular divergence.

Possible locations of detectors for these electrons are shown in the top left of Figure 8.24. Electrons with energies slightly below the beam are bent out of the beam by the first lattice dipole after the interaction point. The beam vacuum chamber must include exit windows for these electrons. The windows should be as thin as possible along the electron direction to minimize energy loss and multiple scattering before the detectors.

The taggers should include calorimeters for triggering and energy measurements. They should be finely segmented to disentangle the multiple electron hits per bunch crossing from the high rate bremsstrahlung process. The taggers should also have position sensi-

tive detectors to measure the vertical and horizontal coordinates of electrons. The combined energy and position measurements allow reconstruction of the kinematic variable Q^2 and x_{BJ}. If the position detectors have multiple layers and are able to reconstruct the electron direction this will overconstrain the variable reconstruction and improve their measurement; this may also provide some measure of background rejection. The beam angular divergence will introduce significant errors on the variable reconstruction. The reconstructed versus generated Q^2 is shown in Figure 8.26 (right) with smearing from beam divergence. There is reasonable resolution for Q^2 as low as $10^{-4}\,\mathrm{GeV}^2$; below $10^{-4}\,\mathrm{GeV}^2$ meaningful reconstruction of Q^2 based on the electron is very challenging.

8.4.5 Read-out Electronics Chain and Data Acquisition

Readout Electronics

As shown in Figure 8.27, the on-detector front-end boards (FEB) consist of Application Specific Integrated Circuits (ASIC) for signal processing. For some sub-detectors, the data digitized on FEBs can be transmitted to the DAQ system via fibers. For other sub-detectors, the analog or digital signals can be sent to an intermediate stage front-end processors (FEP); after pre-processing, data is transmitted to the DAQ system. The global timing system fans out system clock, synchronization, and configuration to FEBs and FEPs, to synchronize the whole system.

On the FEBs, ASICs will perform a series of processing tasks on the signals from the detector electrodes. For calorimeters, PID and various gaseous detectors, after the pre-amplifier and shaper, amplitude and fine timing information can be obtained by waveform digitizers, or discriminators and time-to-digital converters. The streaming readout architecture allows the signals to be continuously digitized and streamed out with or without a real-time trigger signal. For the candidate vertex tracker, Monolithic Active Pixel Sensors (MAPS), digital data processing will be integrated into the sensor, in order to process the position and hit count information. We expect that MAPS sensors will output high speed serial data streams to the back-end (relayed and multiplexed by FEPs and finally to the DAQ system). The detailed specifications of front-end ASICs will depend on the requirements of each sub-detector, for instance the dynamic range, detector capacitance, resolution, density and limit of power and cooling. These requirements will determine the gain, peaking time, buffer depth, dead time of the design, and the selection of CMOS technology. Most of the ASIC designs in use by current nuclear physics or high energy physics experiments are based on CMOS technology nodes between 65nm and 250nm.

ASICs will be developed to meet the streaming readout architecture parameters and tailored to the requirements of the various types of EIC sub-detectors, as shown in Figure 8.10. It may be possible to further decrease the number of ASIC variants by combining the specifications of the GEM-type detectors into a single development. It is anticipated that no new designs from scratch will be required as these developments will build on previous ASICs, such as the SAMPA and the VMM chips for example, and these will be adapted to the EIC specifications.

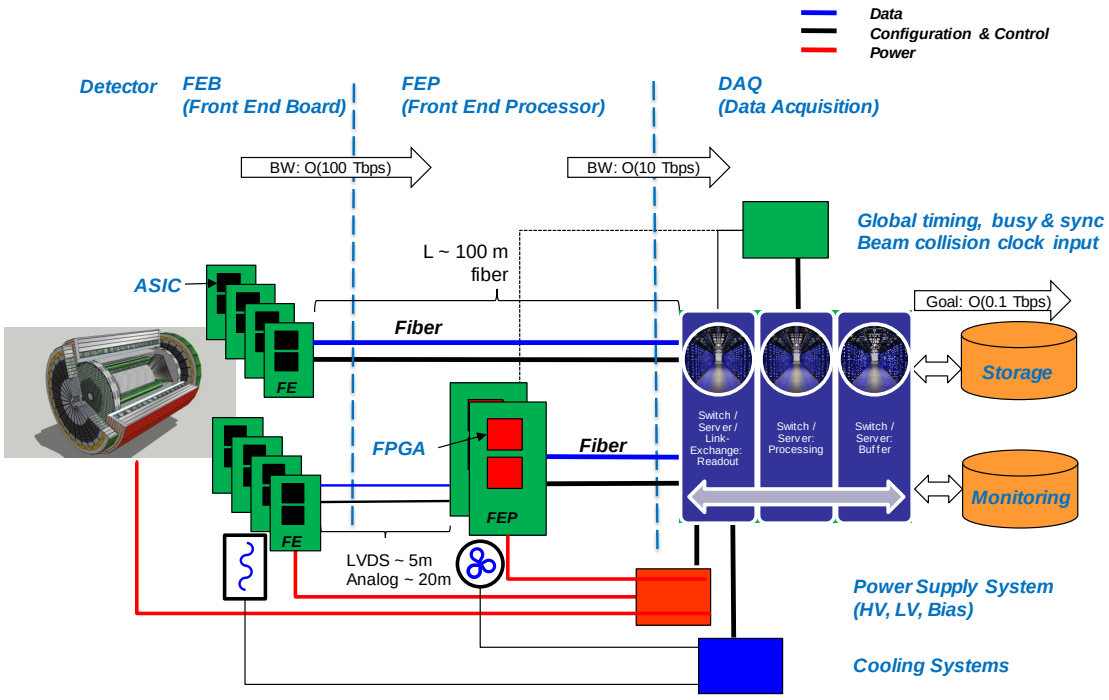

Figure 8.27: Diagram of the detector readout and DAQ system.

Table 8.10: EIC ASIC Development.

Readout Variant	Channels (actual)	Channels (with 10% spare)	Type
V1	200M	220M	Si
V2	220k+	242k+	Stra w/GEM-fADC
V3	377k+	415k+	GEM
V4	461k+	507k+	PMT/SiPM

From the FEBs, digital data from the ASICs can be sent out directly by electrical cable or optical fiber links. Analog signals can be sent out via cables to FEPs for further processing. The front-end ASICs may have integrated serializers, or use standalone serializer and deserializer ASICs for high speed data transmission. Radiation hardened optical links, for example the Versatile Link [416], can be used to convert electric to optical signals. For ASICs with slow digital outputs, devices such as GBT [417], LpGBT can be used to ag-

gregate the data and transmit data at a higher speed, in order to reduce the quantity of fibers.

For the inner detectors, limitations due to available space, power, cooling and integration may prevent their FEBs from digitizing and output data via an optical link. In this case, the FEB output may have a limited range, 1–20 m, such as the case for the analog or LVDS signals. Then, the FEP boards are employed. The FEPs receive these signals from the FEBs, and transmit output data to the DAQ system after further data multiplexing and potential further processing. The main components on the FEPs are the on-board commercial off-the-shelf (COTS) Field Programmable Gate Arrays (FPGA). FPGA selection mainly depends on the its available resources, including high-speed transceivers, differential pins and the logic resources for digital data processing. Standardization of inputs to the FEBs is not easy at an early stage of design; output from the FEBs may also be specific to the ASIC design. The aim is to use a common format (header, timestamp, etc.) for the data stream from the FEPs to the DAQ system. The Printed Circuit Board (PCB) design, fabrication and assembly will be in compliance with standards defined by IPC (Industry Association for Printed Circuit Board and Electronics Manufacturing).

High precision timing distribution is important to synchronize all the front-ends including the FEBs and FEPs. The clock and control commands can be fanned out from the timing system directly to the front-end, or via the custom part of DAQ system, by using the reverse path of the detector data readout. The latest FPGAs support adjusting the phase of clock and data at a resolution of a few picoseconds, which is enough to reduce and compensate for the skew of the timing distribution system. The readout electronics will work together with the DAQ system, handling flow control and busy on and off control and while also meeting the latency and buffering requirements.

The high channel density and power dissipation within the detector volume will require consideration of cooling systems, both liquid and forced convection, as an integral part of the detector package design. We propose to employ readily available equipment (COTS) to support cooling, high voltage, low voltage and bias distribution and these already include the appropriate control infrastructure. Our grounding and shielding plan is based on the use of these COTS equipment, which support floating supplies with grounding referenced at the detector clean ground grid. We also propose to follow the National Electrical Code (NEC) safety standards for wiring and cabling and the FCC standards for minimizing Electro-Magnetic Interference (EMI) to reduce overall noise and maintain good signal integrity.

Data Acquisition System

The data stream from FEB and FEP will be transmitted to the back-end via fibers. We envision a free-streaming DAQ with links going to the DAQ system directly. The DAQ system will mainly consist of COTS components, for instance servers with CPU, GPU or FPGA accelerator cards supporting strong computing capability, high bandwidth network with switches and network-interface-cards (NIC), and devices for permanent data storage.

Both Ethernet and Infiniband are under development towards a terabit per second level of speed. For the EIC, existing technology with 25–100 G bandwidth are expected to be sufficient.

Depending on the detailed design of the FEPs, and if supporting network interfaces, the fibers can go to the switches of the DAQ system directly. To design a common and robust DAQ system for all the front-ends, a common first stage can be developed in the DAQ system. A PCIe based framework, for example, such as FELIX [418], as the first stage of the DAQ system can be a commercial server with custom or commercial PCIe cards. These cards support interfacing the FEBs, FEPs, and global timing system directly. It can receive clock, control, trigger and configuration commands from the timing system, and fan them out to the FEBs and FEPs via fibers. On the reverse direction, it receives data via dedicated optical links and buffering, and monitoring information from the FEBs and FEPs. It will also support handling busy and flow control. The detector data can be processed in the main components FPGAs, or be sent to the network switches through the PCIe bus and COTS NIC cards. Besides PCIe, other technologies can also be used to transfer data to the network switches, for example the 100GbE RDMA over Converged Ethernet, implemented in FPGA with external DDR modules or internal high bandwidth memory (HBM).

As discussed in Section 8.3, the total data rate is still uncertain and evolves with the detector and machine designs. Therefore, in the case of unexpected high background, we envision risk mitigation with possible additional background and noise filtering at the DAQ. One well-established technique is to throttle the detector data stream with calorimeter based trigger signals either in the DAQ FPGA or in the memory of the servers. With advanced real-time algorithms, we envision excessive noise can also be suppressed with signal feature extraction algorithms such as clustering and tracklet building.

Online Computing

If we compare the needs of the EIC with the High Luminosity run of the LHC we see quite striking differences; HL-LHC is planned for a peak luminosity of 7.5×10^{34} cm^{-2} s^{-1}, i.e. 7.5 times larger than the peak luminosity of EIC of 10^{34} cm^{-2} s^{-1}. The p+p cross section at 14 TeV is 1000 times larger than the e+p cross section at the EIC, and the average number of charged hadrons produced in p+p (about 70) is larger by a factor of 10 as compared to e+p.

In order to cope with this the LHC experiments, targeting the study of low cross section reactions, have agreed to limit their collection rate to 10 kHz. Nonetheless the very high hadronic cross section ($\sim$ 80 mb) sided by the high luminosity result in a pile-up of 200 events coming together with the triggered interesting event, a factor of 20 compare to LHC Run2. Present reconstruction time for p+p data is, e.g. for ATLAS [419], 1300HS06 s, or about 100 s at present cores with 13.1 HS06. In 10 years we expect the reconstruction time going down by a factor 10, but while event sizes at the HL-LHC will increase linearly with the pile-up, the reconstruction time will scale exponentially with respect to LHC in Run2.

EIC will collect events at a maximum rate of 500 kHz, 50 times larger than HL-LHC, cor-

responding to the full 30–60 µb cross section as estimated in Table 8.3. Pile-up will not be an issue since for a 1000 times smaller cross section and a factor 10 smaller rates the probability to have a pileup event is around 1%. Nevertheless we expect higher machine background from electrons, as compared to p+p accelerators, an aspect which will have high value in the design of the interaction regions at the EIC as discussed in Section 8.3.

With the machine design not yet frozen, and the detector under development, at the present stage we may only estimate upper bounds for the computing needs on the experiment at the EIC, by using some reasonable assumptions. If we assume as upper bound a 10^{-3} occupancy for the vertex part of the detector, dominated by machine background, and 1% for the rest of the apparatus (5×10^5 Hz times 2×10^8 pixels times 10^{-3} detector occupancy times 4 Bytes address of the hit pixel, with the contribution of the rest of the detector of about 5%) the data flow from the detector will be about 400 GB/s, with an event size of 0.8 MB. Please note this is a conservative estimation assuming vast majority data are background and noise, and the data from the EIC collision signal is only a modest portion of this data flow estimation discussed in Figure 8.2. Nonetheless this estimated flow is within present capabilities.

8.5 Offline Software and Computing

This section will describe the computing needs for the reference detector at the EIC and discuss the foreseen software developments.

Aside from possible contribution of machine backgrounds, the reconstruction of events at the EIC will be easier than the same task at present LHC or RHIC hadron machines, and, in perspective, much easier than for the high luminosity LHC (HL-LHC), which will start operating two years earlier than the EIC, when we may expect a gain in performance for CPUs of about a factor of 10 with respect to now.

Reconstruction time of DIS events at presently running experiments is around 0.35 s (or $\sim$ 5HS06 s) both at COMPASS and at CLAS12, with event sizes of 0.03 MB and 0.02 MB respectively. Filtering out machine background with high efficiency will allow to keep the reconstruction time at 5HS06 s also in 2030. Processing events at the same speed of acquisition, or 500,000 events per second, on today nodes will therefore require 200,000 cores or 1500 nodes, a computing farm well in the size of the EIC project. The expected gain in CPU power in the next 10 years, as well as the possible improvement in the reconstruction software from the use of machine learning techniques give a considerable margin to cope with higher event complexity that may come by higher backgrounds rates.

Software design and development will constitute an important ingredient for the future success of the experimental program at the EIC. Moreover, the cost of the IT related components, from software development to storage systems and to distributed complex e-Infrastructures can be raised considerably if a proper understanding and planning is not taken into account from the beginning in the design of the experiment itself.

A growing group dedicated to this effort already exists. An important step in the clustering

of a core group focusing on computational aspects at an EIC has been the approval by the EIC Generic R&D program of the eRD20 proposal, creating in 2016 the EIC Software Consortium or ESC. ESC has been the backbone to form in 2018 the Software Working Group within the EICUG. The Software Working Group has supported the Yellow Report initiative and provided the tools for simulations and helped in the creation of the infrastructure for storage and documentation.

The Software Working Group is starting in parallel a greenfield development that will focus on different aspects of future needs:

- Simulations for detector optimization, to cover the more immediate needs of the design and integration of the various sub detectors
- Help in the development of state of the art Monte Carlo event generators for the full spectrum of EIC physics. Validation of these generator will be possible by using data from running experiments.
- Development of a full simulation-reconstruction chain allowing to benchmark the performances of the reconstruction software.
- Development of modern "event reconstruction" schemes both using standard approaches but also exploring novel methods based on artificial intelligence machine learning techniques.

The reconstruction software will have to cope with the streaming read-out scheme adopted and will be design to match the chosen solution.

Software tools: While developing the software for simulation and reconstruction of events from a detector which will be up and running in 2030, we need to inquire ourselves about the long term perspective of software used in today HEP experiments and evaluate different options. Leaving aside for the moment both full purpose or dedicated Monte Carlo Event Generator discussed in a separate section, this means that we have to decide on: how to describe the detector; which program to use for particle transportation/interaction; reconstruction tools and the data model.

The choice of LHC experiments for the Run4 and after may guide us in this task.

DD4hep [420] is a toolkit for detector description developed within the AIDA2020 EU program (Advanced European Infrastructures for Detectors at Accelerators). It can be an interesting option for the EIC since recently the CMS collaboration announced that it plans to use it to provide the structure of the experiment to all their data processing applications.

It is worth considering it for the EIC since it is designed to answer a very common need of experiments, i.e. the development of a coherent set of software tools for the description of high-energy physics detectors from a single source of information. Detector description in general includes not only the geometry and the materials used in the apparatus, but all parameters describing, e.g., the detection techniques, constants required by alignment and calibration, description of the readout structures, conditions data and more.

Given it use withing CMS choice, it is expected that DD4hep will be supported over the entire experiment life-time.

DD4hep reuses existing software components, combines the functionalities and thus optimizes the flexibility, minimizing the efforts required by users to leverage the benefits. Reused components include elements of the ROOT geometry package [421] and the GEANT4 simulation toolkit [115].

GEANT4 [115] is the baseline for detector simulation on all LHC experiment and is a natural choice for the EIC. We have developed strong connections with the core developer team of GEANT4 and the improvements in physic list and in non standard geometries which may be needed for the EIC are being discussed with them. About one year ago, the core team of the Software Working Group organized together with the GEANT4 Collaboration a Technical Forum on the EIC. The Forum allowed to discuss both the information on recent updates on GEANT4, but also the physics list for the EIC as maintained by the EIC Software Consortium. The requested improvements on photo-nuclear and electro-nuclear reactions were included in GEANT4version 10.6, and this is under test right now. The study of vectorizing this transportation, as done withing the GEANT4, the vector transport R&D collaboration [422] will offer interesting improving options for GEANT4 itself and we will follow this activity closely.

ROOT [421] is by nowadays standards a fundamental ingredient of virtually all HEP workflows, being used for data persistency, modeling, graphics, and analysis. It is structured to have excellent, active connections with the experiments including, at least for LHC, direct investment by the experiments. The developing team is investing in future developments for HL-LHC, and is also assuming interesting approaches to machine learning tools. It pushes in fact the HEP community to not develop its own machine learning tools but, maybe in a more efficient way, to collaborate with other sciences on improving and growing tool-sets. For that they offer a Toolkit for Multi Variate Analysis TMVA to bridge between ROOT and external machine learning tools such as scikit-learn, XGBoost, TensorFlow, Keras, mxnet, or PyTorch.

ACTS [423] (A Common Tracking Software) is an experiment-independent toolkit for (charged) particle track reconstruction in (high energy) physics experiments, implemented in modern C++, with 2017 standards. It is being developed for the HL-LHC, but is also targeting sPHENIX. Adopts a highly-templated design allowing to avoid virtual lookup, and it is agnostic of detectors and magnetic fields for high portability. Another important aspects with respect to development is the designed rigorous unit tests, an essential aspect for the future EIC software. All these characteristics made this software an interesting option worth evaluation for the reconstruction software for the EIC reference detector.

Many others codes are under evaluation, like GENFIT [424], a generic track-fitting toolkit, GAUDI [425, 426], a software architecture and framework for building HEP data processing applications, JANA2 [427], a multi-threaded event reconstruction and others.

Finally, following the large worldwide spread, we are moving to the use of tools facilitating collaborative analysis and logbook as presently done at CERN with SWAN [428], as a Service for Web-based ANalysis, built upon the widely-used Jupyter notebooks.

Simulations for detector optimization: The tools developed for the Yellow Report initiative will be expanded and used for extensive full simulations of the reference detector. This is a short term goal for software developers in order to support with detailed simulation studies the finalization of the reference detector, thus allowing to move from the CDR stage toward the full technical design.

Monte Carlo event generators for the EIC: The EIC Software Working Group, and before the eRD20 Software Consortium have initiated a project with the Monte Carlo communities in the US and Europe (MCnet) to work on MCEGs for the EIC, requiring MCEG for polarized e+p, e+D, and ^{3}He as well as e+A measurements. The MCEG initiative is connecting the MCEG efforts in NP and HEP and is encouraging a strong interplay between experiment and theory already at an early stage of the EIC. As an initial step, we have started a workshop series on "MCEGs for future e+p and e+A facilities" where the third workshop was held in November 2019 at the Erwin Schrödinger International Institute for Mathematics and Physics in Vienna, Austria. During the workshop, we reviewed the theory for physics with light and heavy ions and discussed the modifications needed on the general-purpose MCEGs to simulate unpolarized observables also for e+A where a precise treatment of the nucleus and its breakup is needed. There were presentations about pioneering MCEG projects for e+A (BeAGLE, spectator tagging in e+D, Sartre), as well as on the ongoing development of the e+A adaptation of JETSCAPE and the Mueller dipole formalism in Pythia8. We also summarized the status of MCEG-data comparisons in HZTool/Rivet that are critical to tune MCEGs to existing DIS and heavy ion data as well on the ongoing work of verifying MCEGs for TMDs with TMD theory/phenomenology. Our current focus is on benchmarks and validation. We are working with the EICUG on benchmark MC productions and the validation of MC results. This will facilitate the adaption of modern MCEGs that have been so far only used by the LHC community.

As a recent development, the DIRE authors [429, 430] introduced radiative effects in the simulation of the DIS. This is an important step, since a full multidimensional analysis will be needed in the study of TMDs and GPDs, given the dependence of the cross section over many kinematic variables. From the experimental point of view, and without entering to much in detail of the analysis, this means that detectors and RC effects will have to be accounted together at simulation level in order to derive matrices transforming from raw counts in the detector to Born cross sections.

The DIRE parton showers is a modern C++ MCEG, usable as a extension of the general purpose event generation frameworks PYTHIA, and will be included as an option from the 8.3 release. This will allow to check the prediction of the Monte Carlo both using the data of running DIS experiments (at TJNAF and COMPASS at CERN) and with the outcome of the simulation of DJANGO [431, 432], the reference tool for the study of RC effects at HERA.

The use of Artificial Intelligence and Machine Learning techniques:

In the world of computing there is growing excitement for what is perceived as the revolution of the new millennium: artificial intelligence (AI). In particular the R&D program of the future EIC could be one of the first programs systematically exploiting AI.

AI is becoming ubiquitous in nuclear physics [433]. According to a standard taxonomy [434], AI encompasses all the concepts related to the integration of human intelligence into machines; a subset of AI is machine learning (ML), which is usually grouped into supervised, unsupervised and reinforcement learning; deep learning (DL) is a particular subset of ML based on deep (*i.e.*, made by many hidden layers) neural networks, which is often considered the evolution of ML since it typically outperforms other methods when there is a large amount of data and features, provided sufficient computing resources. In the most frequent applications in our field, features are selected and a model is trained for classification or regression using signal and background examples.

Experimental particle and nuclear physics is big data [435]: the gigantic data volumes produced in modern experiments are typically handled with "triggers"—a combination of dedicated hardware and software—to decide near-real-time which data to keep for analysis and which to toss out. In this respect, AI plays already an important role in experiments like LHCb [436], where machine learning algorithms (e.g. topological trigger and ghost probability requirements) make almost 70% of these decisions, from triggers to higher level analysis of reconstructed data.

Supported by modern electronics able to continuously convert the analog detector signals, new approaches like Streaming Readout [437] could further the convergence of online and offline analysis: the incorporation of high level AI algorithms in the analysis pipeline can lead to better data quality control during data taking and shorter analysis cycles. Recently the Fast Machine Learning workshop [438] highlighted emerging methods and scientific applications for DL and inference acceleration, with emphasis on ultrafast on-detector inference and real-time systems, hardware platforms, co-processor technologies, and distributed learning. In this context, AI (used here in a broader sense to embrace different approaches) could foster in the next years significant advances in areas like anomaly detection (e.g. [439]) and fast calibration/alignment of detectors.

For tracking detectors, particle tracking is always a computationally challenging step. Several approaches have been developed recently for tracking based on deep learning [440], but there are still open questions about the best way to incorporate such techniques. The problem in Nuclear Physics experiments is typically different, being characterized by most of the computing cycles spent in propagating the particles through inhomogeneous magnetic fields and material maps. Here AI can contribute to determine the optimal initial track parameters allowing to decrease the number of iterations needed by Kalman-Filter.

As for particle identification and event classification, we have witnessed in the last years a growth of applications based on machine learning both for global particle identification (e.g. [441]) as well as custom novel solutions which combine different architectures for specific detectors (e.g. [442] for imaging Cherenkov detectors).

The search for rare signatures in large acceptance detectors at high intensities necessitates advanced techniques to filter those events. The GlueX experiment at Jefferson Lab for example is searching for exotic hadrons and demonstrated the utility of machine learning techniques based on BDTs [443] to achieve the required performance in filtering events with rare reactions [444].

The utilization of jets at the future EIC can be beneficial for a variety of fundamental topics [445], including the gluon Wigner distribution, the gluon Sivers function, the (un)polarized hadronic structure of the photon, the (un)polarized quark and gluon PDFs at moderate to high momentum fraction (x) as well as studies of hadronization and cold nuclear matter properties. Machine Learning is having a major impact in jet physics, empowering powerful taggers for boosted jets as well as flavor tagging, and various deep learning applications like recursive neural network which leverage an analogy to natural language processing [446] have been developed. ML4Jets [447] is a series of workshop dedicated to these topics.

Another area where AI can significantly contribute is that of fast simulations. Simulating the detector response of large scale experiments like EIC is typically slow and requires immense computing power. One of the most computationally expensive step in the simulation pipeline of a typical experiment is the detailed modeling of the high multiplicity physics processes characterizing the evolution of particle showers inside calorimeters. AI, could speed up simulations and potentially complement the traditional approaches. Recent advances with generative networks (e.g. GAN, VAE, Flow-based models [448–450]) look as a compelling alternative to standard methods with orders of magnitude increase in simulation speed [451] but so far usually at the cost of reduced accuracy.

Detector design is another fundamental area of research for EIC. Advanced detector design often implies performing computationally intensive simulations as part of the design optimization process. One of the conclusions from the DOE Town Halls on AI for Science on 2019 [452] was that "*AI techniques that can optimize the design of complex, large-scale experiments have the potential to revolutionize the way experimental nuclear physics is currently done*". There are at present various AI-based optimization strategies based on, e.g. reinforcement learning or evolutionary algorithm [453,454]. Among these, Bayesian Optimization (BO) [455,456] has gained popularity for its ability of performing global optimization of black-box functions that are expensive to evaluate and that can be in addition noisy and non-differentiable. It consists in a surrogate modeling technique where the regression is typically done through Gaussian processes or decision trees depending on the dimensions of the problem, and a cheap acquisition function is used to suggest which design points to query next, overall minimizing the number of evaluations.

Recently, an automated, highly-parallelized, and self-consistent procedure has been developed [457] and tested for the dual-radiator Ring Imaging Cherenkov (dRICH) design, which has been considered as a case study. These studies not only showed a statistically significant improvement in performance compared to the existing baseline design but they also provided hints on the relevance of different features of the detector for the overall performance. This procedure can be applied to any detector R&D, provided that realistic simulations are available. One example is the optimization of detector materials, e.g. the optimization of large size aerogel composites for aerogel-based detectors in [458].

Beyond individual subdetectors AI can be also used to efficiently optimize the design of different sub-detectors combined together, taking into account mechanical and geometrical constraints. An interesting approach consists in a multi-objective optimization (e.g. [459–461]), which allows to encode the performance of the detectors as well as other

aspects like costs in the design process, to determine the Pareto front [462]. Currently ongoing activities within the EIC R&D program which are leveraging AI for optimization include the EM/Hadronic Calorimetry, e.g. optimizing the glass/crystal material selection in "shared rapidity regions" for best performance of the EM calorimeter. Even more, AI has the ability to optimize the collection of all subdetectors of a large detector system, using more efficiently the figures of merit we use to evaluate the performance that drive the detector design. Remarkably, the design optimization of multiple subdetectors operating together has not been explored yet. This is a high dimensional combinatorial problem that can be solved with AI.

This is undoubtedly a strategic moment to discuss how to fully take advantage of the new opportunities offered by AI to advance research, design and operation of the future EIC. The interest of the community has been evidenced by the number of contributions and attendance of workshops dedicated to AI in Nuclear Physics, e.g. at the [433, 463], and the 2021 AI4EIC-exp workshop [464], which bring together the communities directly using AI technologies and provide a venue for discussion and identifying the specific needs and priorities for EIC.

8.6 Lepton and Hadron Polarimetry

Rapid, precise beam polarization measurements will be crucial for meeting the goals of the EIC physics program as the uncertainty in the polarization propagates directly into the uncertainty for relevant observables (asymmetries, etc.). In addition, polarimetry will play an important role in facilitating the setup of the accelerator.

The basic requirements for beam polarimetry are:

- Non-destructive with minimal impact on the beam lifetime
- Systematic uncertainty on the order $\frac{dP}{P} = 1\%$ or better
- Capable of measuring the beam polarization for each bunch in the ring — in particular, the statistical uncertainty of the measurement for a given bunch should be comparable to the systematic uncertainty
- Rapid, quasi-online analysis in order to provide timely feedback for accelerator setup

8.6.1 Electron Polarimetry

The most commonly used technique for measuring electron beam polarization in rings and colliders is Compton polarimetry, in which the polarized electrons scatter from 100% circularly polarized laser photons. The asymmetry from this reaction is measured via the scattered electrons or high energy backscattered photons. A brief review and description of several previous Compton polarimeters can be found in [465]. A particular advantage of Compton polarimetry is that it sensitive to both longitudinal and transverse polarization.

The longitudinal analyzing power depends only on the backscattered photon energy and is given by,

$$A_{\text{long}} = \frac{2\pi r_o^2 a}{(d\sigma/d\rho)}(1-\rho(1+a))\left[1-\frac{1}{(1-\rho(1-a))^2}\right], \tag{8.1}$$

where r_o is the classical electron radius, $a = (1+4\gamma E_{\text{laser}}/m_e)^{-1}$ (with the Lorentz factor $\gamma = E_e/m_e$), ρ is the backscattered photon energy divided by its kinematic maximum, E_γ/E_γ^{max}, and $d\sigma/d\rho$ is the unpolarized Compton cross section. In contrast, the transverse analyzing power depends both on the backscattered photon energy and the azimuthal angle (ϕ) of the photon (with respect to the transverse polarization direction);

$$A_{\text{tran}} = \frac{2\pi r_o^2 a}{(d\sigma/d\rho)}\cos\phi\left[\rho(1-a)\frac{\sqrt{4a\rho(1-\rho)}}{(1-\rho(1-a))}\right]. \tag{8.2}$$

This azimuthal dependence of the asymmetry results in an "up-down" asymmetry (assuming vertically polarized electrons) and requires a detector with spatial sensitivity.

Plans for electron polarimetry at EIC include a Compton polarimeter at IP12 or near IP6. A Compton polarimeter could be easily accommodated at IP12 (where the electron beam is primarily vertically polarized), however this location is far from IP6 where the main physics detector will be located. Although the region near IP6 is crowded, a Compton polarimeter can also be placed in this area with careful attention to integration of the polarimeter with the beamline elements. It is worth noting that a Compton polarimeter at IP6, while closer to the main experiment, would measure a mix of longitudinal and transverse polarization (P_L=70% at 18 GeV and P_L=98% at 5 GeV), rather than the purely longitudinal polarization expected at the detector IP. A schematic of the placement of the Compton polarimeter at IP12 is shown in Figure 8.28 and at IP6 in Figure 8.29.

Nominal electron beam parameters at IP12 are provided in Table 8.11. Beam properties are identical at the IP6 Compton location, with the exception of the beam size, which is about 40% larger horizontally and about a factor of 2 smaller vertically. Of particular note is the relatively short bunch lifetime at 18 GeV. Since measurement of transversely polarized electron beams is generally more time consuming than for longitudinal polarization,

Table 8.11: Beam parameters at IP12 for the EIC nominal electron beam energies.

Parameter	5 GeV	10 GeV	18 GeV
Bunch frequency [MHz]	99	99	24.75
Beam size (x) [μm]	390	470	434
Beam size (y) [μm]	390	250	332
Pulse width (RMS) [ps]	63.3	63.3	30
Intensity (avg.) [A]	2.5	2.5	0.227
Bunch lifetime [min]	>30	>30	6

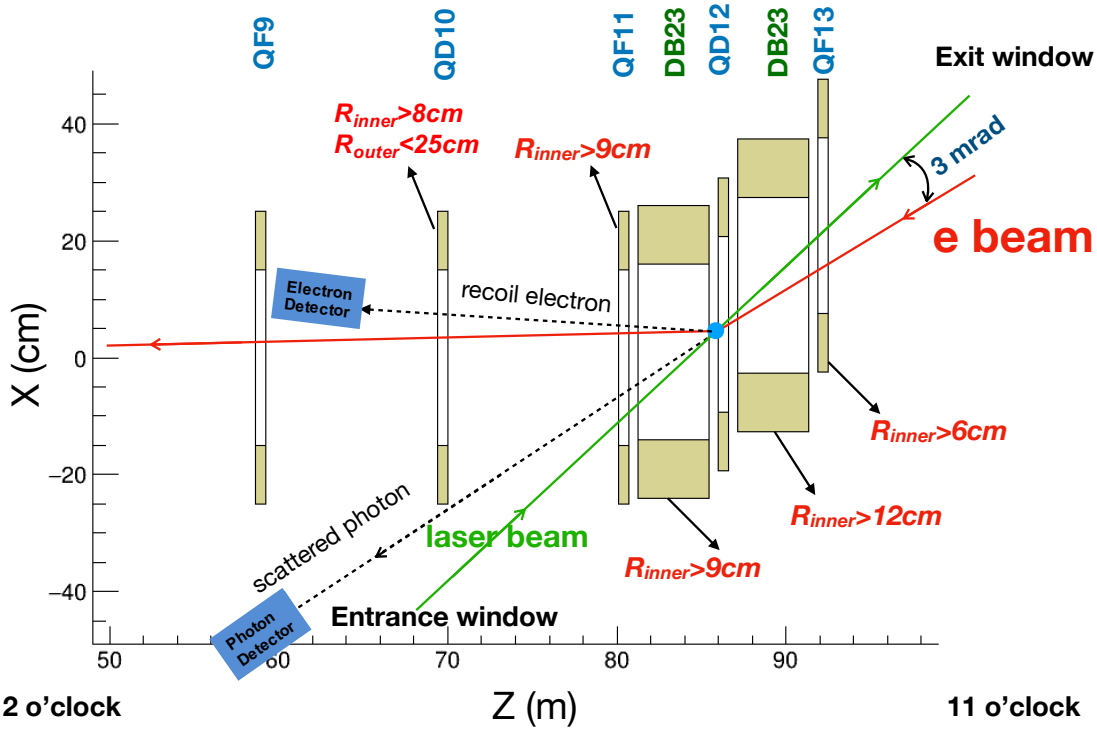

Figure 8.28: Layout of the Compton polarimeter at IP12. In this figure the electron beam travels from right to left — the laser beam collides with the electrons just downstream of QD12. The dipole just downstream of the collision (DB12) steers the unscattered electrons allowing detection of the backscattered photons about 25 m downstream of the collision. DB12 also momentum-analyzes the scattered electrons, facilitating use of a position sensitive electron detector downstream of QD10. Also noted in the figure are constraints on required apertures of the magnets needed to allow transport of the laser beam, backscattered photons, and scattered electrons.

we focus on measurements at IP12 to set a conservative upper limit on the time required for polarization measurements. Table 8.12 shows the average transverse analyzing power, luminosity, and time required to make a 1% (statistics) measurement of the beam polarization for an individual bunch, assuming a single Compton-scattered event per crossing. The constraint of having a single event per crossing is related to the need to make a position sensitive measurement at the photon and electron detectors. Note that even with this constraint, the measurement times are relatively short and, in particular, shorter than the bunch lifetime in the ring.

Even for a single electron bunch (circulating through the ring at a frequency of ≈75 kHz), the luminosities provided in Table 8.12 can be readily achieved using a single-pass, pulsed laser. Since the electron beam frequency varies with energy, it would be useful to have a laser with variable pulse frequency. A laser system based on the gain-switched diode lasers used in the injector at TJNAF [466] would provide both the power and flexible pulse fre-

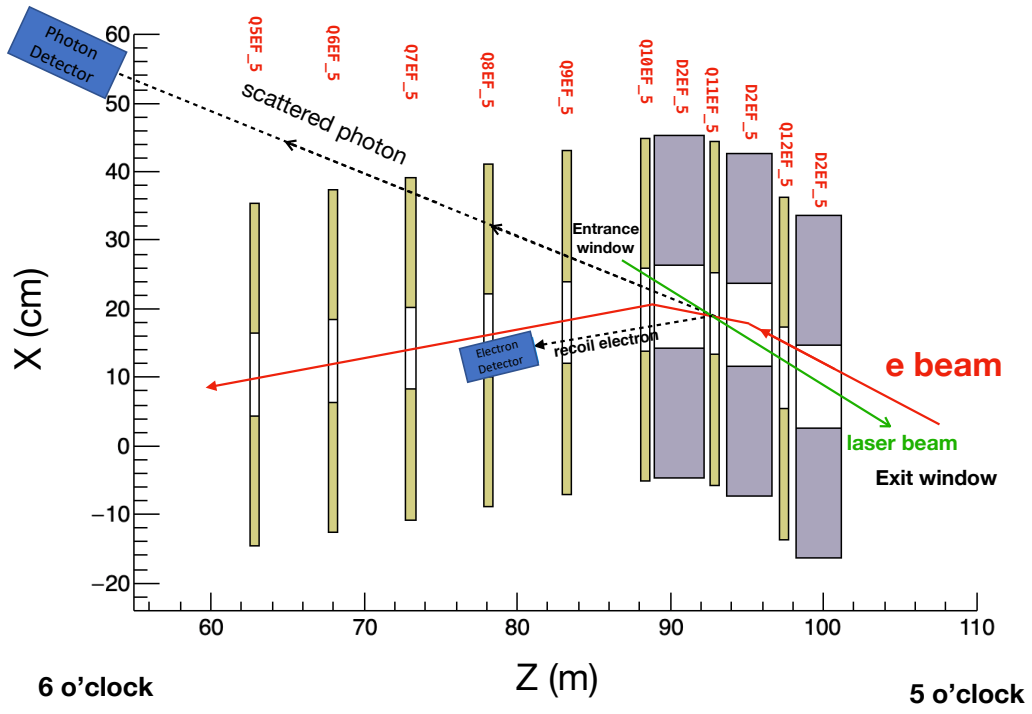

Figure 8.29: Layout of the Compton polarimeter at IP6. The laser-electron collision point is at Q11EF. In contrast to the IP12 layout, the backscattered photons will not clear the outer aperture of the downstream quadrupoles. However, an opening for the photons can be accommodated between the quadrupole coils and by creating a small hole in quadrupole steel where needed.

Table 8.12: Transverse asymmetries, measurement times needed for a 1% statistical measurement for one bunch and needed luminosities for three different beam energies for a 532 nm laser.

E_{beam} [GeV]	σ_{unpol} [barn]	$\langle A_\gamma \rangle$	t_γ[s]	$\langle A_e \rangle$	t_e[s]	L[1/(barn·s)]
5	0.569	0.031	184	0.029	210	1.37E+05
10	0.503	0.051	68	0.050	72	1.55E+05
18	0.432	0.072	34	0.075	31	1.81E+05

quency desired. Such a system would make use of a gain-switched diode laser at 1064 nm, amplified to high average power (10–20 W) via a fiber amplifier, and then frequency doubled to 532 nm using a PPLN or LBO crystal. The repetition rate is set by the applied RF frequency to the gain-switched seed laser.

The detector requirements for the EIC Compton polarimeters are dictated by the requirement to measure the transverse and longitudinal polarization simultaneously. For longitudinal polarization, this means the detectors will require sensitivity to the backscattered photon and scattered electron energy. The photon detector can make use of a fast calorimeter, while the electron detector can take advantage of the dispersion introduced by the dipole after the collision point to infer the scattered electron energy from a detector with position sensitivity in the horizontal direction.

To measure transverse polarization, position sensitive detectors are required to measure the up-down asymmetry. This is particularly challenging given the very small backscattered photon cone at the highest EIC beam energy. At HERA, the vertical position of the backscattered photon was inferred via shower-sharing between the optically isolated segments of a calorimeter [467]. Calibration of the non-linear transformation between the true vertical position and the energy-asymmetry in the calorimeter was a significant source of uncertainty. The detector for the EIC Compton will measure the vertical position directly via segmented strip detectors, avoiding the calibration issues faced at HERA.

The transverse Compton analyzing power vs. position at the detector for the IP12 Compton for the backscattered photons and scattered electrons at 5 and 18 GeV is shown in Figure 8.30. The backscattered photon cone will be largest at the lowest energy (5 GeV) —

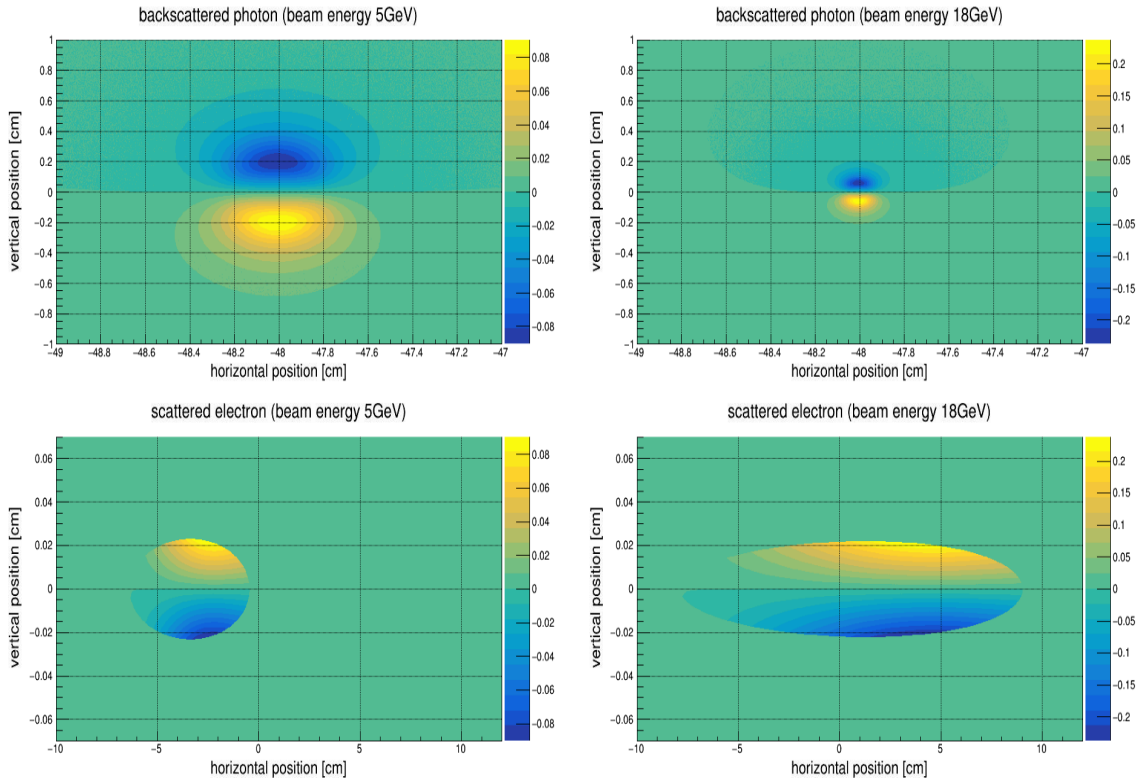

Figure 8.30: Compton (transverse) analyzing power at the nominal photon and electron detector positions for the IP12 polarimeter.

this will determine the required size of the detector. The distribution at 18 GeV, where the cone is the smallest, sets the requirements for the detector segmentation. Note that the scattered electrons are significantly more focused than the photons. Monte Carlo studies indicate that the transverse polarization can be reliably extracted at 18 GeV with a vertical detector segmentation of 100 µm for the photon detector and 25 µm for the electron detector. The detector size should be at least $16 \times 16\,\mathrm{mm}^2$ for the photons and 10 cm $\times$ 1 mm for the scattered electrons. The horizontal segmentation for the electron detector can be much more coarse due to the large horizontal dispersion introduced by the dipole. Note that for the IP6 Compton, the same conclusions apply for the photon detector size and strip-detector segmentation assuming the detector is the same distance from the laser-electron interaction. Initial estimates for the IP6 Compton electron detector suggest that the needed detector size will be similar to the IP12 detector, about 8 cm $\times$ 1 mm, and the same general conclusions with respect to the relative vertical and horizontal strip detector pitch will apply.

Diamond strip detectors are a feasible solution for both the photon and electron detectors. Diamond detectors are extremely radiation hard and are fast enough to have response times sufficient to resolve the minimum bunch spacing (10 ns) at EIC. Tests of CVD diamond with specialized electronics have shown pulse widths on the order of 8 ns [468]. For the photon detector, about 1 radiation length of lead will be placed in front of the strip detectors to convert the backscattered photons. As an alternative to diamond detectors, HVMAPS detectors are also under consideration. The radiation hardness and time response of HVMAPS will need to be assessed to determine their suitability for this application.

As noted earlier, the photon detector will also require a calorimeter to be sensitive to longitudinal components of the electron polarization. Only modest energy resolution is needed; radiation hardness and time response are more important requirements for this detector — a tungsten powder/scintillating fiber calorimeter would meet these requirements.

Backgrounds are an important consideration for Compton polarimetry as well. The primary processes of interest are Bremsstrahlung and synchrotron radiation. Monte Carlo studies have shown that the contribution from Bremsstrahlung should be small for a beamline vacuum of 10^{-9} Torr. Synchrotron radiation, on the other hand, will be a significant concern. Careful design of the exit window for the backscattered photons will be required to mitigate backgrounds due to synchrotron. The electron detector is not in the direct synchrotron fan, but significant power can be deposited in the detector from one-bounce photons. This can be mitigated by incorporating tips or a special antechamber in the beampipe between the Compton IP and the detector [469]. The electron detector will also be subject to power deposited in the planned Roman Pot housing due to the beam Wakefield. Preliminary simulations indicate the Wakefield power should not be large enough to cause problems, but this will need to be considered in the detailed Roman Pot design.

In addition to measurements in the EIC electron ring, it is important to determine the electron beam polarization in or just after the Rapid Cycling Synchrotron (RCS) in order to facilitate machine setup and troubleshoot possible issues with the electron beam polarization. In the RCS, electron bunches of approximately 10 nC are accelerated from 400 MeV

to the nominal beam energy (5, 10, or 18 GeV) in about 100 ms. These bunches are then injected into the EIC electron ring at 1 Hz. The short amount of time each bunch spends in the RCS, combined with the large changes in energy (and hence polarimeter analyzing power and/or acceptance) make non-invasive polarization measurements, in which the the RCS operates in a mode completely transparent to beam operations, essentially impossible. However, there are at least two options for making intermittent, invasive polarization measurements.

The first, and perhaps simplest from a polarimetry perspective, would be to operate the RCS in a so-called "flat-top" mode [470]. In this case, an electron bunch in the RCS is accelerated to its full or some intermediate energy, and then stored in the RCS at that energy while a polarization measurement is made. In this scenario, a Compton polarimeter similar to that described above could be installed in one of the straight sections of the RCS. The measurement times would be equivalent to those noted in Table 8.12 (since those are for a single stored bunch), i.e., on the order of a few minutes.

Another option would be to make polarization measurements in the transfer line from the RCS to the EIC electron ring. In this case, one could only make polarization measurements averaged over several bunches. In addition, the measurement would be much more time consuming due to the low average beam current (≈10 nA) since the 10 nC bunches are extracted at 1 Hz.

The measurement time at 10 nA using a Compton polarimeter similar to the one planned for IP12 would take on the order many days. The IP12 Compton limits the number of interactions to an average of one per crossing to count and resolve the position of the backscattered photons. A position sensitive detector that could be operated in integrating mode, would allow more rapid measurements. However, the required position resolution (25–100 μm) would be very challenging for a detector operating in integrating mode.

An alternative to Compton polarimetry would be the use of Møller polarimetry. Møller polarimeters can be used to measure both longitudinal and transverse polarization and can make measurements quickly at relatively low currents. The longitudinal and transverse Møller analyzing powers are given by,

$$A_{ZZ} = -\frac{\sin^2\theta^*(7+\cos^2\theta^*)}{(3+\cos^2\theta^*)^2}, \tag{8.3}$$

$$A_{XX} = -\frac{\sin^4\theta^*}{(3+\cos^2\theta^*)^2}, \tag{8.4}$$

where A_{ZZ} is the analyzing power for longitudinally polarized beam and target electrons, A_{XX} for horizontally polarized beam and target electrons, and θ^* is the center-of-mass scattering angle. Note that $A_{YY} = -A_{XX}$. The magnitude of the analyzing power is maximized in both cases at $\theta^* = 90$ degrees, where $|A_{ZZ}| = 7/9$ and $|A_{XX}| = 1/9$.

Extrapolating from typical measurement times from the Møller polarimeters at TJNAF (which provide a statistical precision of 1% for the longitudinal polarization in about 15 minutes for a 1 μA beam on a 4 μm iron target), we estimate that a 10% measurement

could be made in about 1.5 hours in the RCS to EIC transfer line. This could perhaps be shorter depending the maximum foil thickness that could be used as the polarimeter target.

A key drawback of Møller polarimetry is that the solid foil targets are destructive to the beam, so cannot be carried out at the same time as normal beam operations. An additional complication is the requirement for a magneto-optical system to steer the Møller electrons to a detector system. In the experimental Hall A at Jefferson Lab, the Møller spectrometer employs several quadrupoles of modest length and aperture, combined with a dipole to deflect the Møller electrons into the detector system. The whole system occupies about 7 m of space along the beamline, but the space used by the quadrupoles can also be used for beam transport during normal operations (i.e., when Møller measurements are not underway).

The preferred choice for polarimetry at the RCS is a Compton polarimeter in the RCS ring, with measurements taking place during "flat-top" mode operation. However, if this "flat-top" mode is not practical, then a Møller polarimeter in the RCS transfer line could serve as a reasonable fallback, albeit with reduced precision and a larger impact on the beamline design.

8.6.2 Hadron Polarimetry

Hadron polarimetry has been successfully performed on RHIC polarized proton beams for nearly two decades. Through continual development a relative systematic uncertainty $< 1.5\%$ was achieved for the most recent RHIC polarized proton run. As the only hadron polarimeter system at a high energy collider it is the natural starting point for hadron polarimetry at the EIC.

Proton Polarimetry at RHIC

Hadron polarization is typically measured via a transverse single spin left right asymmetry: $\epsilon = A_N P$. Unlike for polarized leptons, the proportionality constant is not precisely known from theory. Instead, RHIC employs an absolute polarimeter with a polarized atomic hydrogen jet target (Hjet), illustrated in Figure 8.31. Target recoil protons from the elastic process $pp \to pp$ are measured in detectors in the scattering chamber left and right of the target. The hydrogen polarization vector is alternated between vertically up and down. The RHIC beam also has bunches with up and down polarization states. By averaging over the beam states the asymmetry with respect to the target polarization may be measured, and vice versa:

$$\epsilon_{\text{target}} = A_N P_{\text{target}} \quad \epsilon_{\text{beam}} = A_N P_{\text{beam}} \,. \tag{8.5}$$

The equality of A_N in these two relations relations is a result of time reversal invariance for the purely elastic reaction. The target polarization is precisely measured with a Breit-Rabi polarimeter. Combined with the measured asymmetries the beam polarization is

determined:

$$P_{\text{beam}} = \frac{\epsilon_{\text{beam}}}{\epsilon_{\text{target}}} P_{\text{target}} \,. \tag{8.6}$$

The absolute polarization measurement is independent of the details of A_N.

The recoil protons are detected in silicon detectors which measure kinetic energy and time of flight (TOF); segmentation of the detectors provides the proton scattering angle. The energy-TOF relation allows identification of protons, separating backgrounds from inelastic reactions. The energy-angle measurement of missing mass allows selection of the purely elastic reaction required for the validity of Eq. 8.5. The resolution is sufficient to distinguish between the p and $p\pi$ masses, ~140 MeV difference. The analyzing power A_N is energy dependent; selection of protons in a fixed energy range defines an effective A_N for the measurement.

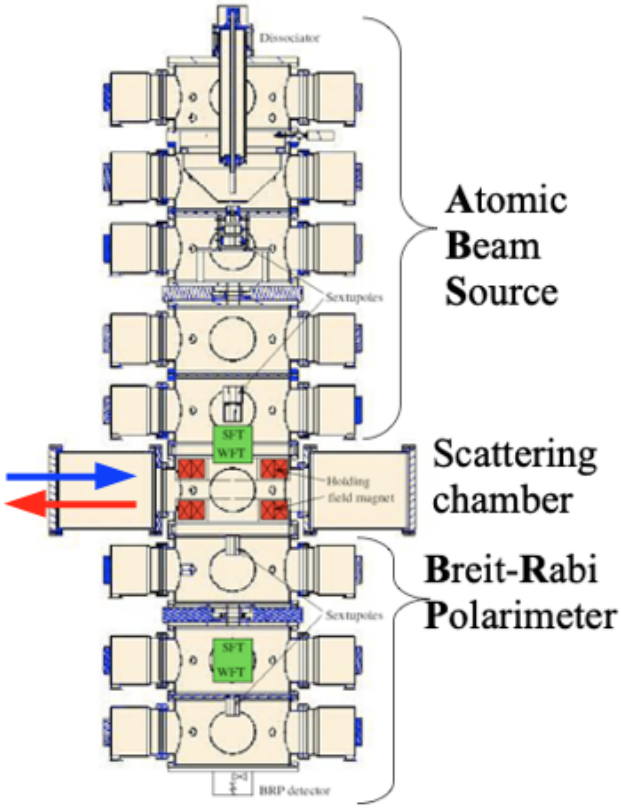

Figure 8.31: The RHIC polarized hydrogen jet polarimeter. The atomic beam source at the top passes polarized hydrogen across the beams (blue and read arrows) in the scattering chamber, with detectors left and right of the beams. The atomic hydrogen polarization is measured by the Breit-Rabi polarimeter at bottom.

The diffuse nature of the polarized jet target provides only a low rate of interactions, resulting in a measurement limited to a relative statistical precision of 5-8% per RHIC fill; it is not sensitive to the inevitable decay of beam polarization throughout a fill. Also, the jet target is wider than the beam and measures only the average polarization across the

beam. The beam polarization is larger at the center than the edges transversely; the polarization of colliding beams differs from the average polarization due to this effect [471]. The polarimeters must measure this transverse polarization profile to provide correct polarizations for use by collider experiments.

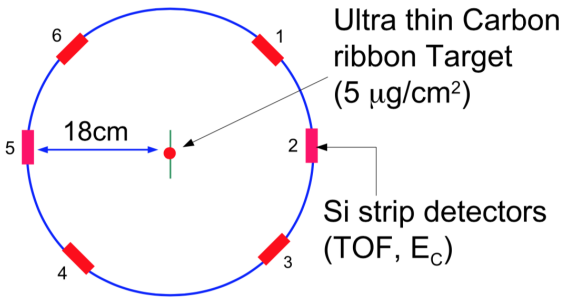

Figure 8.32: Cross section of the RHIC proton-carbon polarimeter. A thin carbon ribbon target is passed across the beam (into page) and scattered carbon nuclei are measured in the six detectors.

At RHIC the required finer grained polarization details are provided by the proton-carbon (pC) relative polarimeter, illustrated in Figure 8.32. A thin carbon ribbon target is passed across the beam and scattered carbon nuclei are measured in detectors arrayed around the beam. The dense target provides a high interaction rate, allowing an asymmetry measurement with a few per cent statistical precision in less than 30 seconds. Such measurements are made periodically throughout a RHIC fill, providing a measurement of the beam polarization decay. The ribbon target is narrower than the beam; thus it is able to measure asymmetry as a function of position across the beam and determine the transverse polarization profile. The absolute polarization scale of the pC polarimeter is set by normalizing an ensemble of pC measurements to the results from the Hjet polarimeter for the corresponding RHIC fills. A pC polarimeter is also installed in the AGS for polarization measurements during injection.

The recoil carbon nuclei are detected in silicon detectors around the target which measure kinetic energy and time of flight (TOF). The energy-TOF relation allows identification of carbon nuclei, reducing backgrounds from other particles. A small background remaining under the signal is calibrated along with the signal in the pC/Hjet normalization. The analyzing power is energy dependent; selection of carbon nuclei in a fixed energy range defines an effective analyzing power for the measurement.

Several effects limit the precision of the polarimetry measurement, including:

- The atomic hydrogen may have a small amount of molecular H_2 contamination not measured by the Breit-Rabi polarimeter, affecting P_{target} in Eq. 8.5.
- Non-proton and inelastic proton backgrounds in the Hjet signal limit the validity of Eq. 8.5.
- The silicon detectors in the pC polarimeter have a dead layer resulting in significant

shifts in deposited energies; this results in instability of the measured energy range and effective analyzing power.

- Scattered carbon nuclei lose a significant fraction of energy exiting the target; mechanical instability of the targets causes this energy loss to vary, resulting in instability of the measured energy range and effective analyzing power.

Efforts continue to reduce these systematic effects in the RHIC polarimeters.

For longitudinal spin runs, polarization measurements near the interaction point and between the spin rotators are required to ensure that the transverse component of the spin direction is zero. At RHIC, the collider experiments use the process $pp \rightarrow Xn$, which has a significant transverse single spin asymmetry for the produced neutrons. The neutrons are detected in the experiments' existing zero degree calorimeters. The asymmetry is zero when the beam spin is fully longitudinal.

Proton Polarimetry at the EIC

Both of the RHIC hadron polarimeters can in principle be used for proton polarimetry at the EIC. Beyond the existing limitations at RHIC, two significant difficulties are presently foreseen, both a consequence of the increased proton beam currents at the EIC.

First, backgrounds in both polarimeters are observed and lie partially beneath the signal events. They are distinguished by energy-TOF distributions different from the signal allowing separation or estimation of a subtraction from the signal. The backgrounds exhibit a small asymmetry with respect to the beam spin state. At the EIC, with higher bunch crossing frequency, the backgrounds will lie under the signal events from adjacent bunches and separation or subtraction based on energy-TOF will not be possible. Also, the adjacent bunches may have the same or opposite beam spin as the central bunch, further convoluting the measurement. Simulations indicate that the backgrounds are from fast particles (pions and protons) which deposit a fraction of their energy in the silicon and pass entirely through the detector. A second detector layer may allow vetoing such punch through events, leaving the signal events which deposit their entire energy in the detector.

Second, materials analysis of the carbon ribbon targets indicates that the higher proton beam currents at the EIC will induce heating to temperatures causing the targets to break after only a few seconds in the beam. A search for alternative target materials has been initiated.

A possible alternative to the pC relative polarimeter has been proposed which would mitigate both of these limitations. It is based on the observation by the PHENIX collaboration of a large azimuthal asymmetry of forward neutrons in the proton direction in p+Au collisions [472]. This effect is well described by an Ultra Peripheral Collision (UPC) process, in which the high Z Au nucleus emits a photon which produces neutrons off of the polarized proton [473]. The produced neutrons have a sizable transverse single spin asymmetry. A polarimeter based on this process would replace the Au beam with a high Z fixed target

as a source of photons. A Xe gas jet may be a suitable target and would not suffer from the heating limitation of the carbon targets. The neutrons would be detected in a zero degree calorimeter. The neutrons arrive at the calorimeter promptly and there is no overlap with adjacent bunches as in the pC polarimeter.

The absolute and relative polarimeters may be situated anywhere in the EIC hadron ring where the spin vector is transverse. The Hjet and pC polarimeters each require 1–2 m space along and transverse to the beam.

The forward neutron process $pp \to Xn$ used at RHIC to ensure longitudinal spin at the interaction points is not available at the EIC. Instead, one relative polarimeter (pC or alternative) should be placed near the experimental interaction point between the spin rotators; a possible location of a pC polarimeter is shown in Figure 3.2 top, it would be located on the rear side between B2APR and Q2PR. The hadron polarimeters are only sensitive to transverse spin polarization. During longitudinal spin runs asymmetry measurements near the interaction point can verify that the transverse component of the spin direction is zero.

^{3}He **Polarimetry at the EIC**

For ^{3}He absolute polarimetry at the EIC, it may be possible to replace the hydrogen jet target with polarized ^{3}He. Such targets have been used in numerous experiments [474–481]. The measurement must select purely elastic scattering events. The lowest lying excitation of ^{3}He is the dissociated deuteron-proton system, with a mass difference of $\sim$5.5 MeV. The missing mass measurement from the energy and angle of the recoil target ^{3}He may have insufficient resolution to distinguish this state. Detectors downstream of the target can aid tagging of breakup of target or beam nuclei.

A polarized ^{3}He target may only be available on a limited basis. In this case it may be used in special runs with an unpolarized proton beam to determine the asymmetry for the elastic ^{3}He$\uparrow$p process. During physics operation with polarized ^{3}He beams, the polarization may be continuously measured with an unpolarized proton target, using the ^{3}He$\uparrow$p asymmetry. To conform with time reversal invariance, the asymmetry calibration with polarized ^{3}He target and unpolarized proton beam must be performed at the same center of mass energy as the operational polarized ^{3}He beam with unpolarized proton target. For both calibration and physics operations, events with breakup of ^{3}He must be excluded to ensure purely elastic scattering.

The pC polarimeter, or an alternative, developed for protons at the EIC should also provide suitable relative polarimetry for light ions. A ^{3}He C polarimeter would require a sufficiently large analyzing power A_N to provide measurable asymmetries. Phenomenological analysis indicates its magnitude is $\sim$70% (and opposite sign) of that for pC; this needs to be tested experimentally.

At some point polarized deuteron beams may be developed for the EIC. The experiences gained from ^{3}He will directly inform deuteron polarimetry.

R&D Studies at RHIC

Polarized proton runs are anticipated for RHIC in 2022 and 2024 before EIC construction begins. The polarimeters will be operational for physics measurements during these runs. They will also be available for studies to guide further development of polarimetry for the EIC.

Some polarimeter developments may be tested during normal polarized proton physics running. These include:

- Some polarimeter detectors, in both the Hjet and pC polarimeters, will have a second layer installed to study tagging of punch through events.
- Any new technologies to replace the carbon targets can be tested in the pC polarimeter.
- A polarimeter based on neutrons from the UPC process could be tested during proton running. It would require addition of a high Z target, such as a Xe gas jet. A zero degree calorimeter would be needed downstream of the target.

Unpolarized ^{3}He beams have previously been operated in RHIC for He-Au collisions at 103 GeV/nucleon. In the next years polarized ^{3}He beams will become available, first at injection energy and later accelerated up to $\sim$58 GeV/nucleon. These beams may be used for ^{3}He polarimetry studies during regularly scheduled accelerator physics experiments. Also, the absolute polarimeter may be equipped with a ^{3}He target, possibly polarized. With various combinations of ^{3}He beams and targets, numerous tests for polarimetry may be conducted. In increasing order of beam and target development, they include:

- Any ^{3}He beam will allow tests of tagging beam nucleus breakup with downstream detectors; this will be possible even with the existing hydrogen target. The energy-TOF relation for carbon nuclei in ^{3}He+C scattering may also be verified in the pC polarimeter; this has already been shown in the AGS pC polarimeter.
- With any ^{3}He beam and ^{3}He target in the absolute polarimeter, the energy-TOF and energy-angle relations for ^{3}He+^{3}He scattering can be tested.
- With any ^{3}He beam and a polarized ^{3}He target in the absolute polarimeter, the target asymmetry in Eq. 8.5 can be measured, establishing the asymmetry for ^{3}He+^{3}He scattering
- With a polarized ^{3}He beam, the beam asymmetry in Eq. 8.5 can be measured with any ^{3}He target in the absolute polarimeter, establishing the asymmetry for ^{3}He+^{3}He scattering, and with the pC polarimeter, establishing the asymmetry for ^{3}He+C scattering.
- With both the ^{3}He beam and target polarized, the beam polarization may be measured as in Eq. 8.6.

8.7 Installation and Maintenance

8.7.1 Infrastructure

The baseline EIC configuration currently includes one fully instrumented Interaction Region (IR) and one general purpose physics detector. It is assumed that the detector will be located in IP6 (the STAR Hall), and that the available infrastructure will either be re-used or will serve as a reference for the future EIC installation. Complementary information about IP8 (the PHENIX Hall) is given where appropriate.

Hall infrastructure

In addition to the beam line area (the Wide Angle Hall), RHIC complex 1006 has an Assembly Building with adequate floor space for detector maintenance work, as well as a control room, counting house, office space, electronic/mechanical workshops, gas shed, online computing room and other service areas, as shown in Figure 8.33.

The general specifications for the IP6 and IP8 experimental halls are provided in Table 8.13.

Table 8.13: IP6 and IP8 experimental hall dimensions and related data. Hall width goes parallel to the beam line in this table, see also the Wide Angle Hall boundaries in Figure 8.33.

	IP6	IP8
Hall length and width ($L \times W$) [cm×cm]	3200×1615	1737×1859
Distance from floor to beam line [cm]	432	523
Door dimensions ($W \times H$) [cm×cm]	823×823	927×1017
Floor load capacity [psi]	5000	4000
Crane capacity [ton]	20	12

The coordinate system of the EIC experiment is oriented as follows. The z-axis is along the beamline toward the outgoing hadron direction, the y-axis points upward, and the x-axis points toward the EIC-accelerator center.

Detector subsystem infrastructure requirements include cooling (HVAC, CW, LCW), power (clean, utility, generator-backed), cryogenics, cabling, service lines, and gas system specifications for gaseous detectors. These requirements cannot be specifically identified at this stage of planning, but will be developed by the Detector Working Groups for a subset of the EIC detector technologies in the future. The new requirements will be reported in the next revision of this document, along with a table containing the existing capacities available in the RHIC IP6 Hall. The following is a list of items which needs to be considered during integration:

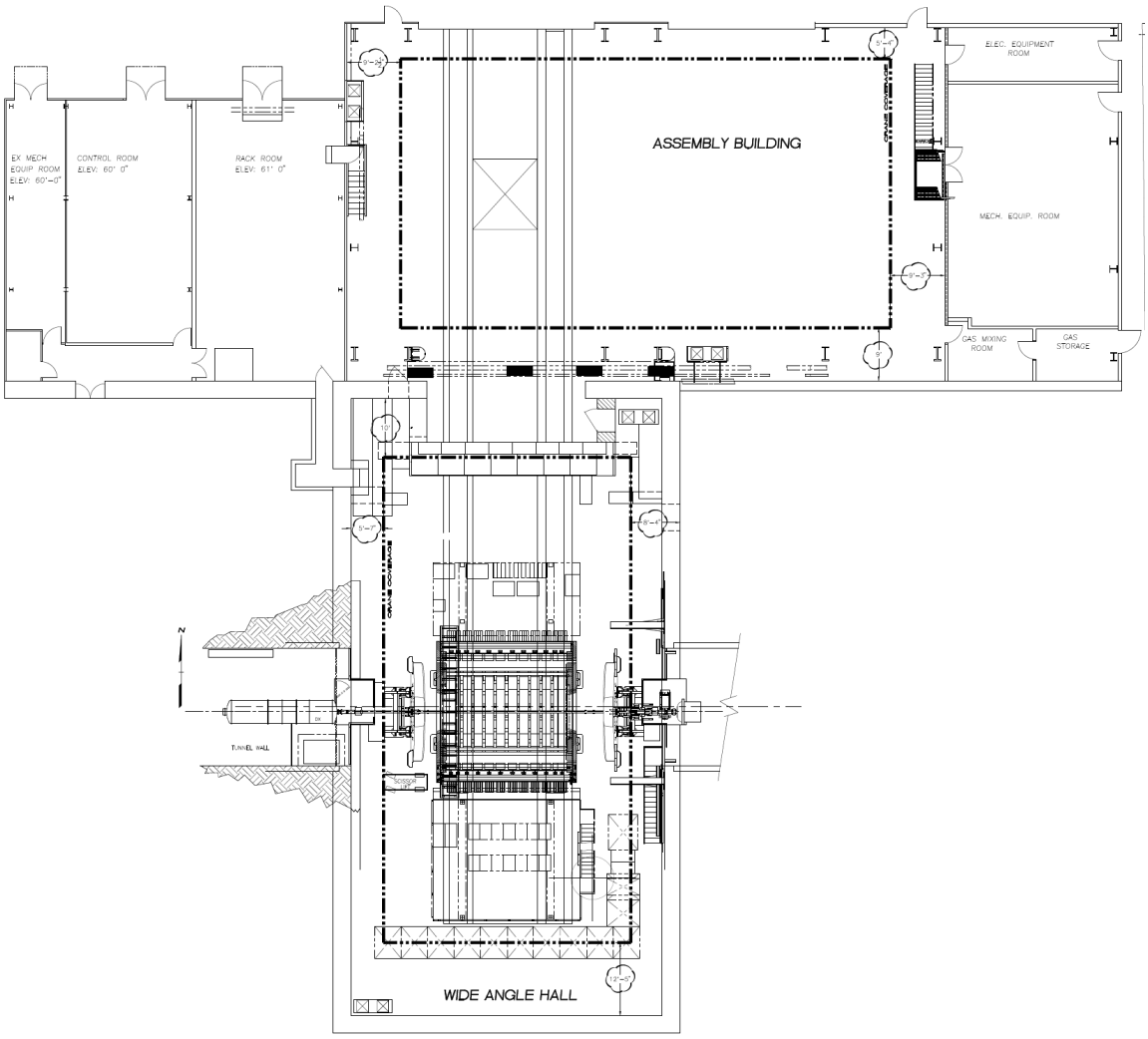

Figure 8.33: RHIC IP6 experimental area layout. STAR detector shown schematically in the beam position.

- *Electronics racks and data cables*

  The bulk of the electronics cables and service lines for the sub-detectors will be routed through gaps which exist between the barrel and endcap regions. As a result, the installation design for these cables must accommodate the removal/repositioning of the endcaps.

- *Power distribution and grounding*

  Electrical requirements for all sub-systems must be defined as part of their func-

tional specification. For power, this includes the voltage and amperage required for each system, as well as any necessary power transformations. Power quality will also need to be identified for each system, e.g. clean power, utility power, generator-backed power, etc.

- *Cooling and gas installation*

  Heat rejection for each system will be identified and quantified. As a best practice, every watt of power that is consumed within or introduced into the experimental hall, must be offset by an equivalent amount of cooling. A cooling assessment will identify which components are cooled by environmental HVAC, which are cooled by LCW, and which are cooled by auxiliary cooling systems. The cumulative load this places on external heat removal systems, such as chilled water plants and cooling towers, will also be assessed.

  The type and volume of gases will be evaluated to determine the best locations for gas storage, the potential risks involved with the various gases, and how gases will be delivered to the sub-systems.

- *Cryogenic capacity*

  The cryogenic demand for each sub-system will be calculated as a collaborative effort between the design engineers and the cryogenic support group. System design will seek to develop a delivery pathway that minimizes losses, and reduces the number of connections and disconnections that are required during normal operations and maintenance.

- *Shielding against penetrating particles from the machine*

  The size and configuration of radiation shielding will be calculated as a collaborative effort between the physicists, design engineers, and the radiation control group.

Safety and Environmental Protection

It is assumed that the experimental hall's safety systems (sprinklers, ODH monitors, smoke alarm) are provided as part of the RHIC infrastructure. The design and operation of the EIC sub-detector components will follow BNL safety regulations governing radiation controls, interlock systems, and hazardous materials or systems such as flammable gases, lasers, cryogenics, etc.

Additionally, the installation area will be equipped with a fast beam dump system which is integrated with the accelerator controls. This system will prevent radiation damage to the detector in the event that unstable beam conditions occur.

Finally, during the collider commissioning phase, an instrumented beam pipe will be installed in place of the actual detector. This device will be equipped with a robust set of apparatus that allows the machine performance to be assessed without exposing the actual EIC detector to potentially damaging beam conditions.

8.7.2 Installation

At this time, the composition of the EIC central detector is not defined to a level of detail that is sufficient to provide a step-by-step installation procedure. However, the overall detector layout, as well as several boundary conditions, are sufficiently understood to make the following assertions:

- In order to maximize luminosity, the beam line final focusing quads must be positioned as close to the IP as possible. The current Interaction Region design provides approximately 9 m of space for the main physics detector, with accelerator beam line elements installed in the adjacent areas. It is assumed that these elements (quads on the incoming hadron side and B0 magnet on the incoming electron side) WILL NOT be moved for installation or maintenance of the central detector.
- Having 4π coverage in tracking, calorimetry and PID, the general purpose EIC detector is likely to consume 100% of the available space.
- The door connecting the assembly area and the installation area is 823 cm wide. Accordingly, the fully assembled, $\sim$9 m long detector cannot be moved intact between the two areas without making structural modifications. To accommodate this, it is assumed that one or more of the calorimetry endcaps will be placed on independent carriages that allow them to be separated from the main detector before moving.
- The space in the installation area is not sufficient to perform any significant assembly or maintenance on the central detector (see Fig.8.33). Consequently, the bulk of assembly and maintenance must be performed in the assembly hall.

Although the following considerations do not represent hard constraints, they will impact system design and operation:

- The solenoid cryostat chimney must be designed such that it does not need to be disconnected whenever the detector is relocated from the installation area to the assembly area, and vice versa. The current expectation is that the cryo-can will be mounted to the interior wall of the assembly area and will be connected to solenoid using a flexible cryogenic line. This line will be sufficiently long to remain connected to the solenoid when the central detector is in either room.
- In order to minimize the amount of silicon detector cabling in the electron endcap acceptance, the pre-assembled silicon tracker modules must be inserted into their nominal position from the hadron endcap side, with all cabling attached and routed through the "service gap" between the barrel and the hadron endcaps. This operation cannot be performed with the high-momentum gaseous RICH detector already installed in the hadron endcap, since it will block access to the central area. Additionally, due to space constraints along the beamline, the $\sim$1.5 m long RICH modules cannot easily be installed into the central detector in the beam position. A possible

solution is to pre-assemble the entire central part of the main detector (the barrel; the silicon forward, vertex, and backward trackers; and all of the endcap acceptance equipment except for the calorimetry), together with the central piece of the beam pipe, in the assembly area.

This set of constraints and supporting considerations provides the foundation for the detector "building block" composition and the installation sequence, described below. A general purpose EIC detector, schematically shown in Figure 8.34, will be used as a reference. Figure 8.35 shows a perspective view of the EIC detector.

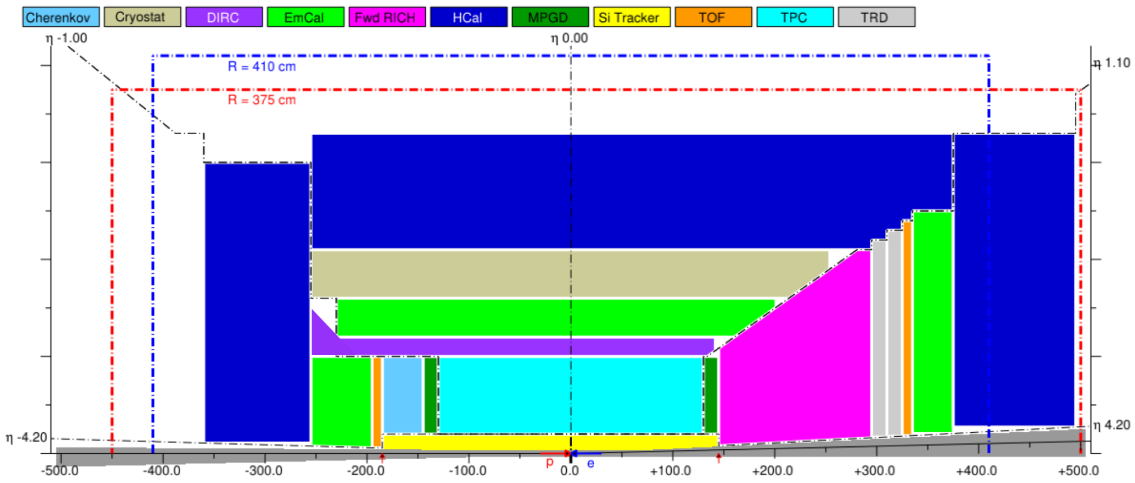

Figure 8.34: A 2D sketch of an EIC detector layout, horizontal cross cut. Only one half of the detector is shown, with the other half being mirror-symmetric in this view, up to the crossing angle. Beam pipe footprint (in dark gray) is to scale. Blue dashed line shows the doorway size between the assembly and the installation halls. Red dashed line shows the realistic central detector envelope with the available [-4.5 ... 5.0] m space along the beam line.

As illustrated in these figures, the detector can be naturally subdivided into three parts: the central barrel, which is built around the solenoid magnet yoke, and the two endcaps. The endcap hadronic calorimeters are expected to be of an Fe/Sc sandwich type, with the magnetic structural steel used as an absorber. By design, they will be self-supporting, serve as a solenoid flux return, and will be able to provide mechanical support to other subsystems. To optimize construction, as well as the access strategy, it may be beneficial to locate not only the hadronic, but also the electromagnetic calorimetry in the endcap assemblies, as shown in Figure 8.36 for the hadronic calorimetry. This will certainly be

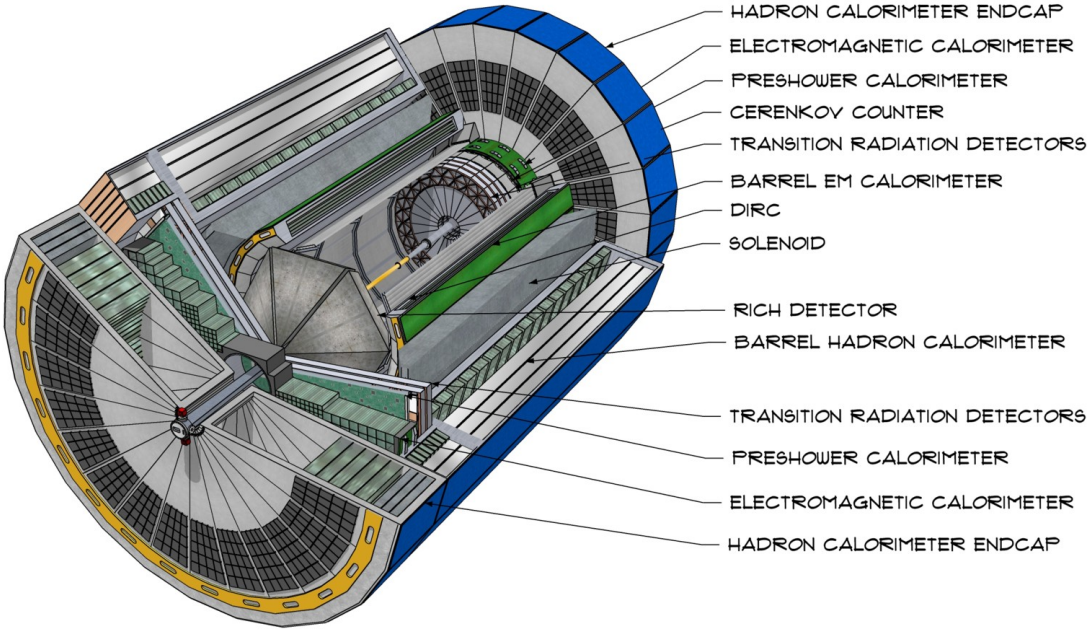

Figure 8.35: CAD model of the EIC detector, with the artistic rendering of the calorimetry subsystems.

true for the hadron endcap should a spaghetti W/SciFi e/m calorimeter technology be used in a configuration with the photo-sensor electronics installed on the upstream end of the towers. In that case, the hadronic and e/m calorimeter assemblies will likely be physically connected to one another face-to-face, with the barrel hadronic calorimeter to hadron endcap split then also needing to be aligned with the front of the e/m calorimeter. Once the endcap halves are rolled out, one will have access to both the e/m calorimetry front end electronics, and to the electronics and services of a substantial fraction of the central (barrel) part of the detector.

In order to meet space constraints, it is expected that the endcap assemblies can be moved laterally relative to the central part of the main detector. This should be achievable with a few cm of clearance, making it unnecessary to move them a substantial distance outward along the beam line. To accommodate this, it will be required that no part of the central detector is installed in the recess of either of the endcaps, and vice versa.

In this approach the support frame and the carriage system consist of five independent parts (one for the central piece and two more for each of the endcaps (see Figure 8.36), each on their own sets of the heavy duty Hilman rollers. Given the size of the endcap calorimeters, and the expected density of the absorber material, the total weight of each of

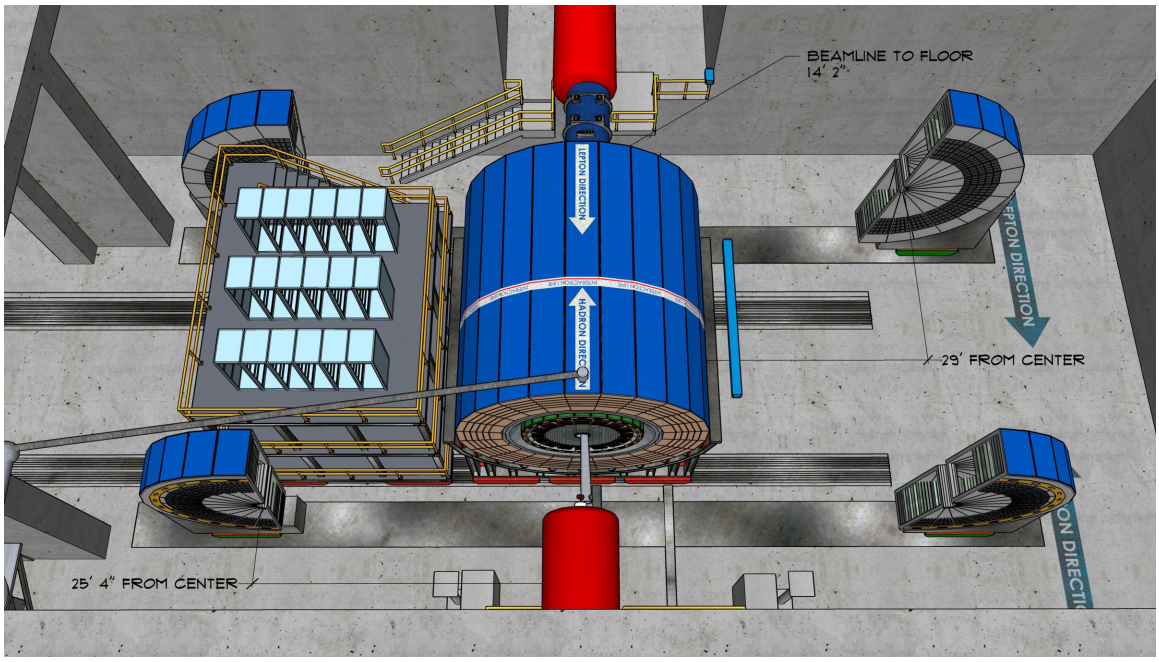

Figure 8.36: Barrel part of the main detector shown in the beam position. The endcaps shown rolled out to provide the space to access the inner parts of the barrel detectors.

the four of the endcap halves is estimated to be between 80–100 tons. The weight of the central part of the detector is estimated to be on the order of 500 tons, similar to the fully assembled sPHENIX detector without endcaps.

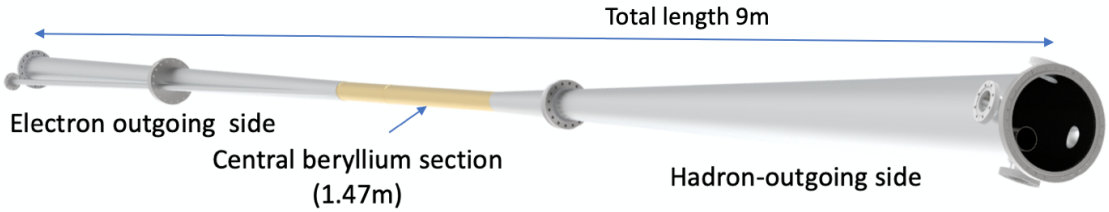

Figure 8.37: Interaction region vacuum chamber layout.

The beam pipe configuration (as shown in Figure 8.37), is expected to roughly follow the

1.5 m + 6.0 m + 1.5 m breakdown scheme, matching the main physics detector and consists of a ∼6.0 m long central part and two ∼1.5 m long endcaps. The central piece may be composed of more than one part. However, the installation procedure described here may be impacted if bulky, permanent flanges are used to interconnect the parts.

As shown in Figure 8.34, it is assumed that a clear ∼40 cm diameter bore is allocated for the forward/vertex/backward silicon detector assembly installation, and it is not obstructed by any other endcap equipment.

The pre-assembly sequence of the endcaps is straightforward, and does not require a detailed description at this stage.

Starting from the outer parts (the hadronic calorimeter, integrated into the solenoid flux return) the central part of the detector will be assembled on its own support structure. The inner barrel components (the solenoid cryostat, e/m calorimeter modules, PID detectors and the central volume tracker) will be added to the assembly one by one, in sequence, as is typically done for this type of detectors (e.g. BaBar and sPHENIX). Next the central piece of the beam pipe, as well as the two pre-assembled halves of the vertex silicon tracker are installed, with the latter ones connected to provide minimal clearance to the beam pipe. The endcap tracker and PID detector modules will be installed afterwards, starting from the inner modules.

The installation sequence of the B0 magnet equipment and the pre-assembled main detector blocks can look like this:

- The silicon tracker and the e/m calorimeter of the B0 magnet spectrometer are installed in its warm bore.
- The approximately 6 m long central part of the main detector, built around the solenoid magnet yoke, is rolled into the beam position, together with the electronics trailer and the pre-installed central piece of the beam pipe. The endcaps are pre-assembled in the experimental hall. When necessary, they can be split in half and moved away from the beamline, allowing access to the beam pipe for installation or removal.
- ∼1.5 m long pieces of the beam pipe are installed, together with the respective pump stands. This operation closes the accelerator UHV volume.
- The endcap halves are rolled towards the beam line and bolted together, as well as connected to the solenoid flux return yoke.

These actions are performed in the reverse sequence to move the detector from the experimental hall to the assembly area for maintenance.

Figure 8.38 shows the final installation of the EIC detector in the IP6 hall.

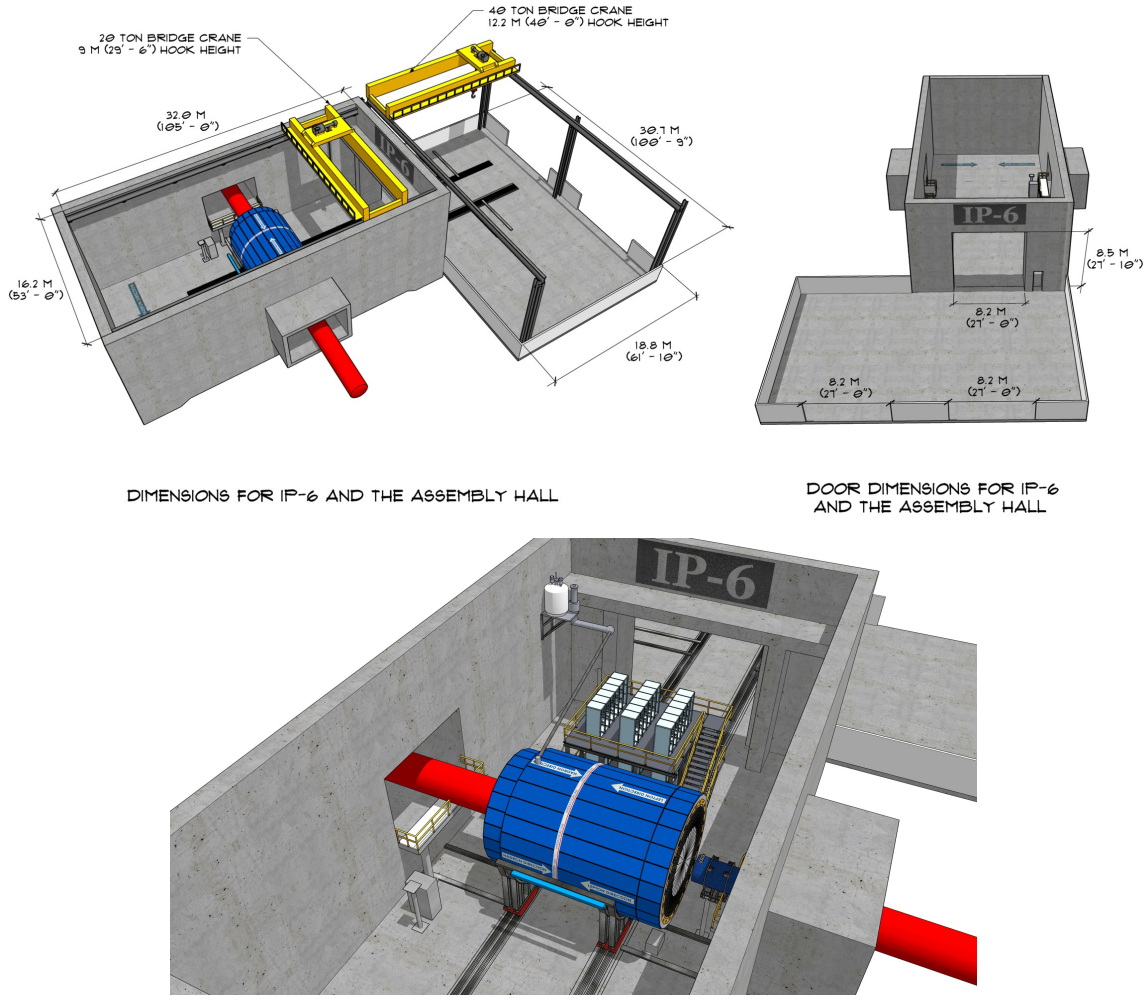

Figure 8.38: A model of the current detector system design in the experimental hall with magnets, cryocan, and rear carriage for the electronics.

Detector Alignment

The internal alignment of the high-precision silicon tracker modules will be done on the bench, prior to installation in the experimental apparatus. It is assumed that the relative alignment of the detector components with respect to one other, to the solenoid magnet and to the beam line elements should be performed to accuracy on the order of $\sim$100 µm. This level of accuracy can be achieved using modern laser tracker survey apparatus, and by providing a redundant set of alignment marks on the detector frames, which are surveyed together with the network of the permanently mounted 3D points (survey mark nests) in the experimental hall. Maintaining visibility of the detector survey marks within the dense EIC installation environment will be a concern though, particularly for the inner tracker modules. Still, it should be noted that the ultimate alignment on the micron level of accuracy will be performed by software using the real particle tracks.

8.7.3 Access and Maintenance

Three different access and/or maintenance scenarios are expected. A short-term (controlled) access to the detector installation area where there will be no (dis)assembly of the equipment. This scenario would allow access to the electronics trailer, as well as the outer part of the sub-detector components, like FEE of the hadronic calorimeters.

A short shutdown (typically an emergency event) would allow the detector endcaps to be rolled out as indicated in Figure 8.36, providing an access to the endcap e/m calorimeters, outer part of the endcap trackers, beam pipe, as well as to a portion of the barrel part of the detector and the B0 silicon tracker for short maintenance. This procedure will be easier in IP-6 (STAR Hall) than in IP-8 (PHENIX Hall) due to the tighter space constraints in IP-8, see Table 8.13, leaving less space to walk or move equipment (Figure 8.39).

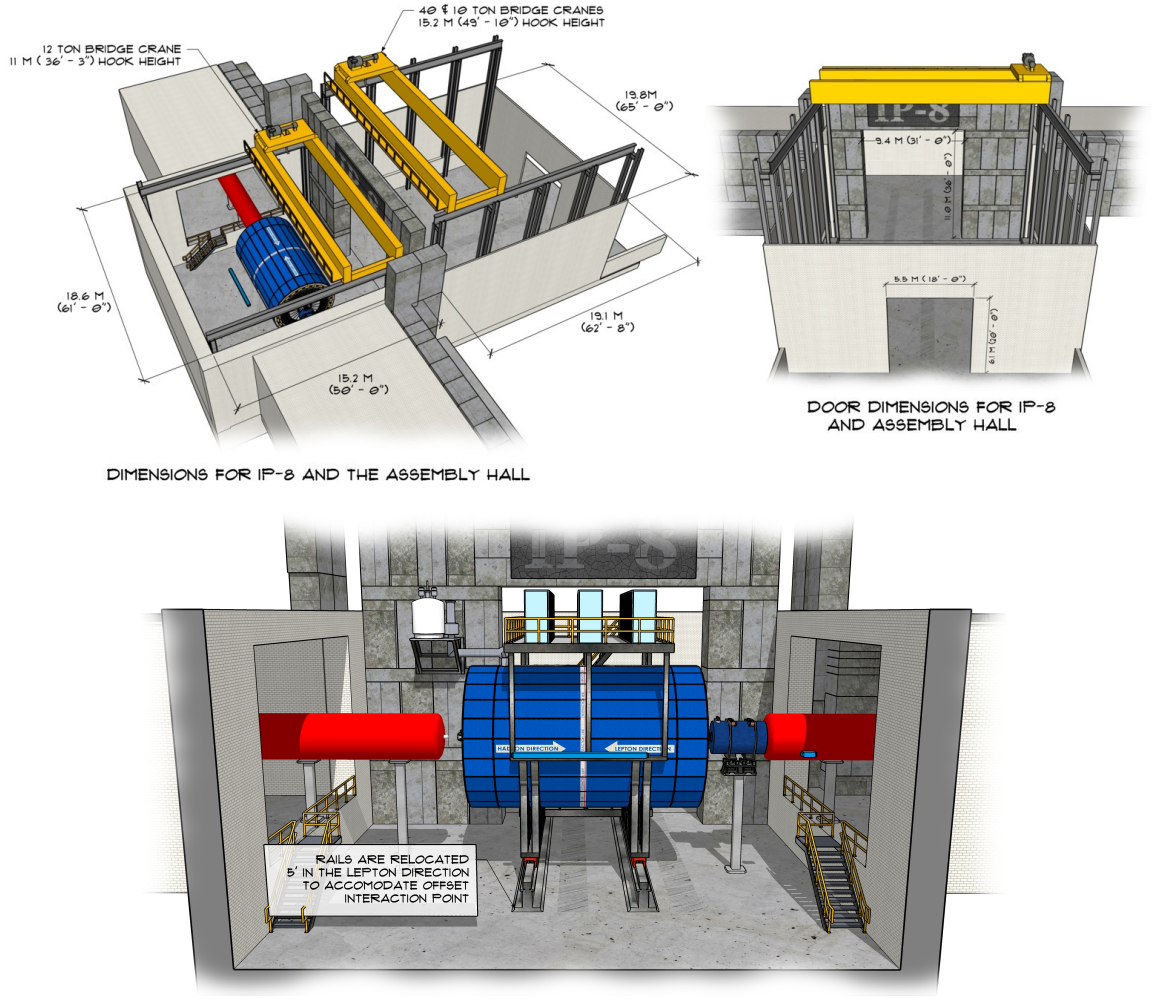

Figure 8.39: IP-8 (PHENIX Hall) installation

During a long shutdown, the barrel part of the EIC detector could be moved out of the hall completely and sub-components could be disassembled safely. Figure 8.40 shows how the barrel part of the detector together with the rear carriage could be rolled into the maintenance area outside of the hall. It is important to keep the readout electronics at the rear carriage next to the detector, to provide an easy way to test sub-components during the shutdown. Such a shutdown involves disassembly of the IP beam pipe section, as well as the beam pipes of RCS, dismantling of the shielding wall between the installation and assembly halls, and would require several weeks of downtime.

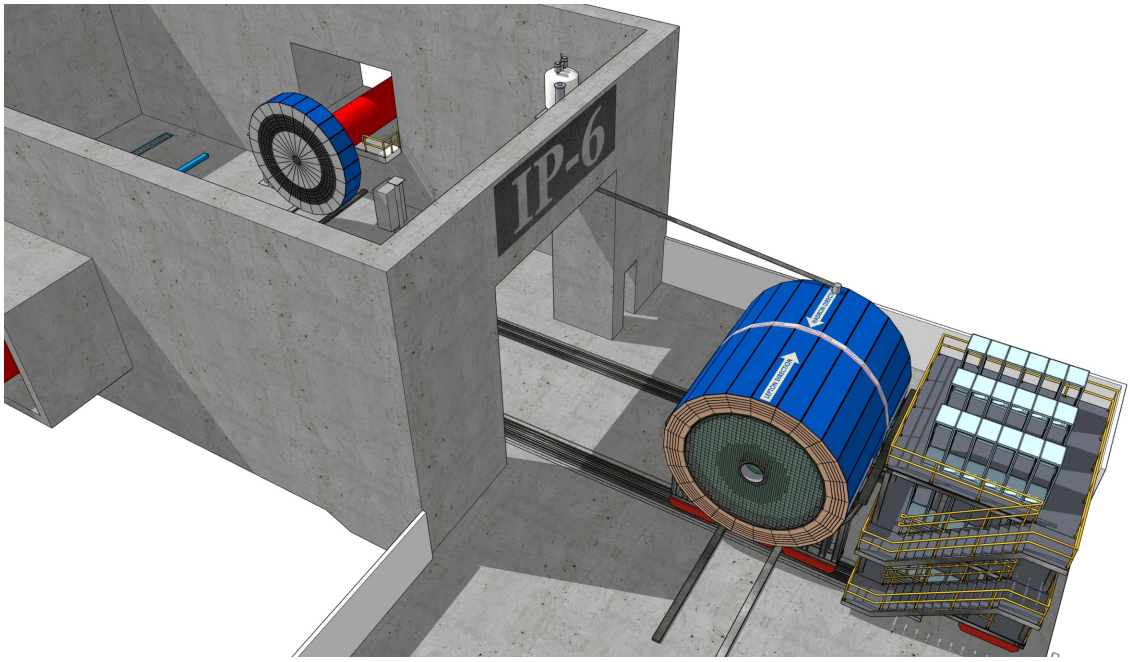

Figure 8.40: The barrel part of the detector and the rear carriage rolled into the maintenance area.

Appendix A

Design Concept of the 2nd Interaction Region

A.1 Introduction

The capability of having two interaction regions (IRs) is one of the specifications of the EIC design. Discussions in the nuclear physics community indicate that there is a significant interest in a complementary 2nd IR. The complementarity in this context means both the energy range where the 2nd IR is optimized to have the highest luminosity and detection capabilities alternative and complementary to the 1st IR. This appendix discusses implementation of the 2nd IR consistent with nuclear physics, accelerator and engineering requirements. These include the operation of both IRs over the entire energy range of $\sim 20\,\text{GeV}$ to $140\,\text{GeV}$ center of mass. Consistently with user demands and the complementarity approach, the 2nd IR is optimized to provide the highest luminosity at a lower CM that the 1st IR, between $\sim 45\,\text{GeV}$ and $\sim 80\,\text{GeV}$. This enables leveling of the EIC luminosity curve over a wider energy range. The 2nd IR can also provide a different acceptance coverage than the 1st IR. This appendix includes consideration of different modes of IR operations and their effect on beam dynamics.

The luminosity and the design of the reference 1st EIC interaction region is optimized emphasizing the discovery potential of the EIC by providing highest luminosity near the upper end of the center-of-mass energy range, that is, from $\sim 80\,\text{GeV}$ to $120\,\text{GeV}$, while covering the entire range of parameters required by the Nuclear Physics Long Range Plan. The large circumference of EIC and the energy reach of the superconducting hadron ring make this solution achievable. The parameter set and design is based on 1160 colliding bunches in each beam:

- Peak luminosity of $L = 10^{34}\,\text{cm}^{-2}\text{s}^{-1}$ at a center-of-mass (CM) energy of $105\,\text{GeV}$;
- Crossing angle $\theta_c = 25\,\text{mrad}$;
- Maximum β-functions in the low-β quadrupole magnets, $\beta_{\text{max}} \leq 1800\,\text{m}$ (for protons

in the vertical direction) and acceptable nonlinear chromaticity resulting in sufficient dynamic aperture;

- IBS growth times in horizontal and longitudinal directions of $\tau_{\mathrm{IBS}} > 2\,\mathrm{hours}$.

The overall EIC layout is sufficiently flexible to allow for alternative optimization. The interaction regions may be optimized at different center-of-mass energies. Moreover, as the EIC will accommodate two interaction regions, the two interaction regions and the colliding beam detectors may be optimized for different parts of the physics program. In this Appendix, the second IR is optimized for operations and luminosity production in the central center-of-mass energy range of EIC.

A.2 Design Requirements

A.2.1 Detection Requirements

To first order, the luminosity at the IP is inversely proportional to the distance between the last upstream and first downstream final focus quadrupoles (FFQs). The statistical uncertainty of measurements in the central detector scales as this distance. However, the closer the beam elements are to the IP, the more they obstruct the acceptance at shallow angles with respect to the beam axis and restrict the acceptance for forward particles. The solenoidal field used in the central detector region to measure the high p_T particles in the central detector is not effective in determining the momenta of particles moving parallel to the beam direction, and additional fields are needed.

From kinematics, the reaction products are biased towards small angles around the original ion beam. In particular, the detection of small-angle products requires acceptance to the recoiling target baryon (3D structure of the nucleon), hadrons produced from its breakup (target fragmentation), or all the possible remnants produced when using nuclear targets (including the tagging of spectator protons in polarized deuterium). The detection has to be done over a wide range of momenta (and charge-to-mass ratios) with respect to the original ion beam. The 2nd IR design must overcome these measurement difficulties posed by the beam elements.

From machine design and luminosity considerations, it is not desirable to leave a very large detector space free of beam focusing elements to allow the small-angle products to accumulate sufficient transverse separation from the incident beams. The solution is to let the small-angle particles pass through the nearest elements of the machine final-focusing system, which simultaneously perform the function of angle and momentum analyzer for the small angle reaction products. A significant challenge of this approach is to balance often contradictory detector and machine optics requirements.

The above detection requirements make the detector and machine designs intertwined and closely integrated. There is no longer a clear separation between the detector and machine components. Several detection parameters directly impact the design choices for the 2nd

IR and vice versa. The major parameters critical to both detector and machine aspects of the design are summarized in Table A.1. Table A.1 also provides a comparison of the 2nd IR parameters to those of the 1st IR.

Table A.1: Summary of 2nd IR design requirements and their comparison to the 1st IR.

#	Parameter	EIC IR #1	EIC IR #2	Impact
1	Energy range electrons [GeV] protons [GeV]	 5–18 41, 100–275	 5–18 41, 100–275	Facility operation
2	CM energy range of optimum luminosity [GeV]	80–120	45–80	Physics priorities
3	Crossing angle [mrad]	25	25–50	p_T resolution, acceptance, geometry
4	Detector space symmetry [m]	-4.5/+4.5	-(3.5–4.5)/ +(5.5–4.5)	Forward/rear acceptance balance
5	Forward angular acceptance [mrad]	20	20–30	Spectrometer dipole aperture
6	Far-forward angular acceptance [mrad]	4.5	5–10	Neutron cone, Max. p_T
7	Minimum $\Delta(B\rho)/(B\rho)$ allowing for detection of $p_T = 0$ fragments	0.1	0.003–0.01	Beam focus with dispersion, reach in x_L and p_T resolution, reach in x_B for exclusive proc.
8	RMS angular beam divergence at IP, h/v [mrad]	0.1/0.2	$<$0.2	Min. p_T, p_T resolution
9	Low Q^2 electron acceptance	$<$0.1	$<$0.1	Not a hard requirement

1. Clearly, the 2nd IR must at least be able to transport both beams over their entire energy ranges for operation of the facility to its entire potential. This first of all means that all dipole magnets in the 2nd IR must have sufficient field integrals to provide the necessary bending angles keeping the IR footprint fixed from the lowest to the highest energy. The quadrupoles must also be strong enough to provide sufficient focusing to properly transport the beam in the entire energy range. This in turn means that none of the 2nd IR magnets can have aperture-edge fields higher than 4.6 T at the top energy. It is of course desirable to operate the 2nd IR in the collision mode. The 2nd IR dipoles and quadrupoles must then have sufficient strengths to focus the beams at the IP while having sufficient large apertures to meet the detection requirements discussed below. Simultaneous operation of the two IR is also subject to the beam dynamics constraints discussed below.

2. Consistently with user demands and the two detector complementarity approach, the 2nd IR is optimized to provide the highest luminosity at a lower CM that the 1st IR, between $\approx$ 45 GeV and $\approx$ 80 GeV. This allows one to level off the luminosity curve of the EIC as a whole at a higher level over a wider energy range. It can also provide a different

acceptance coverage than the 1st IR. The appendix also considers different modes of IR operation and their effect on beam dynamic performance.

3. The ion and electron beams cross at a relatively large angle of 25–50 mrad at the IP. High luminosity is preserved through the use of crab cavities. This angle moves the ion beam away from the electron beam elements and makes room for dipoles located just downstream of the central detector area. The dipoles serve two purposes. First, they shape the beam orbits providing their geometric match, making the IR footprint fit in the available detector hall and tunnel space, and creating room for detectors. Second, the dipole systems allow momentum analysis of the particles with small transverse momentum with respect to the beams. The particles with large transverse momenta are analyzed using the solenoidal field in the central detector.

The crabbing tilt of a bunch at the IP effectively smears the beam spot size seen by the Roman Pot (RP) detectors as illustrated in Figure A.1. The effective beam spot size is one of the sources of uncertainty in a p_T measurement. Ignoring for the moment other sources such as the beam angular spread at the IP, the transverse position of a scattered particle at an RP x_{RP} is related to p_T as

$$x_{RP} = M_{11} x_{IP} + M_{12} p_T / p, \tag{A.1}$$

where x_{IP} is the scattered particle's transverse position at the IP and p is the beam momentum. M_{11} and M_{12} are elements of the linear beam transfer matrix from the IP to the RP known from the magnetic optics design:

$$\begin{aligned} M_{11} &= \sqrt{\beta_{RP}/\beta_{IP}} \cos\Delta\Psi, \\ M_{12} &= \sqrt{\beta_{RP}\beta_{IP}} \sin\Delta\Psi, \end{aligned} \tag{A.2}$$

where β_{RP} and β_{IP} are the Twiss β-functions at the RP and IP, respectively, and $\Delta\Psi$ is the betatron phase advance from the IP to the RP. The measured p_T can be expressed as

$$p_T = p \frac{x_{RP}}{\sqrt{\beta_{RP}\beta_{IP}} \sin\Delta\Psi} - p \frac{1}{\beta_{IP}} \frac{\cos\Delta\Psi}{\sin\Delta\Psi} x_{IP}. \tag{A.3}$$

Since it is challenging to measure x_{IP} precisely, the second term on the right-hand side of the above equation represents a measurement uncertainty

$$\Delta p_T = \left| p \frac{1}{\beta_{IP}} \frac{\cos\Delta\Psi}{\sin\Delta\Psi} x_{IP} \right|. \tag{A.4}$$

x_{IP} consists of a random betatron component x_β and a longitudinal-position-correlated component $z\,\theta/2$:

$$x_{IP} = x_\beta + z\,\theta/2, \tag{A.5}$$

where z is the particles longitudinal position from the center of the bunch and θ is the total beam crossing angle.

The second term in Equation A.5 describes the beam spot size smear. It is typically much

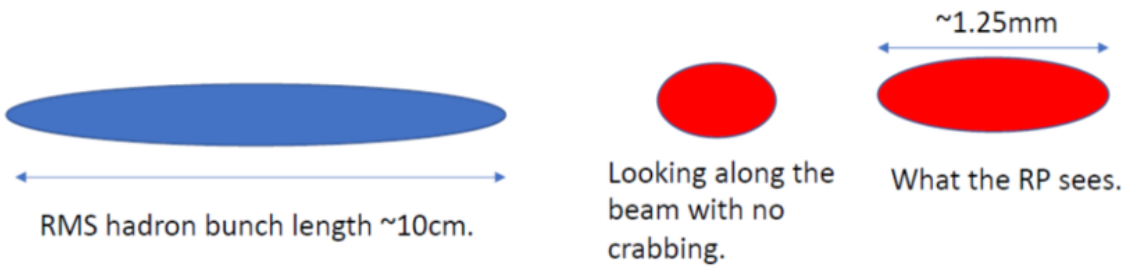

Figure A.1: Apparent smear of the beam spot size at the IP due to the crab tilt.

greater than the first term. Therefore, the uncertainty term in Equation A.4 can be greatly reduced by measuring the event's z position. It has been suggested that, with a feasible RP timing of ~ 35 ps, the z position can be resolved down to ~ 1 cm.

Another factor in the uncertainty term of Equation A.4 is $\cos\Delta\Psi$. By placing the RP at a position with $\Delta\Psi$ close to $\pi/2$, Δp_T in Equation A.4 can in principle be made arbitrarily small. There may be practical considerations limiting the available choice of $\Delta\Psi$ such as the requirement of placing the RP before the crab cavities, which have small apertures and kick the particles. In the presented design of the 2nd IR, $\Delta\Psi$ is adjusted as close to $\pi/2$ at the RP as allowed by other constraints to minimize Δp_T.

Physics simulations set a requirement on the contribution of the crabbing tilt to Δp_T of

$$\Delta p_T < 20 \text{ MeV}. \tag{A.6}$$

Another issue with the size of the crossing angle is that it contributes to the gap in the electron rapidity coverage in the rear direction as illustrated in Figure A.2. There is no full azimuthal coverage within an angle defined by the crossing angle and the size of the ion beam pipe. Assuming 5 cm for the radius of the ion beam pipe at a 2.5 m distance in the rear direction from the IP, the total polar angle of the gap in the rapidity coverage is about 20 mrad$+\theta_{cr}$.

4. The impact of the beam angular spread at the IP $\sigma_{x'}^{IP}$ on the detection properties is two-fold. First, it is another contributor to the uncertainty of the p_T measurement, Δp_T. Second, it sets the limit on the minimum detectable p_T, $p_T^{\min}$.

Due to a finite size of the beam phase space, colliding hadrons have an RMS angular spread of $\sigma_{x'}^{IP}$ at the IP. This results in an additional uncertainty in a measured p_T of

$$\Delta p_T = p\,\sigma_{x'}^{IP}. \tag{A.7}$$

For the optimal case, all independent sources of uncertainties should provide roughly equal contributions, the condition of Equation A.6 applied to Equation A.7 gives

$$\sigma_{x'}^{IP} < 0.2 \text{ mrad}, \tag{A.8}$$

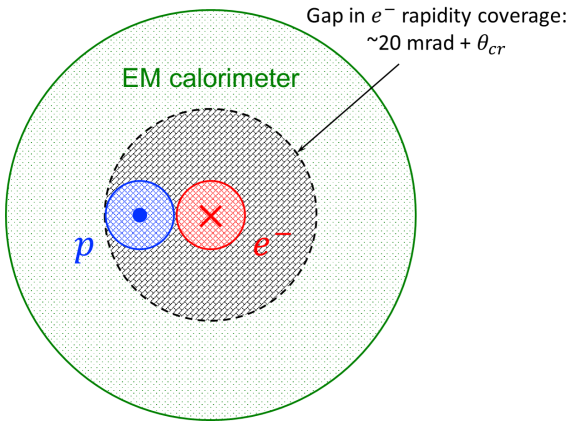

Figure A.2: Gap in the electron rapidity coverage due to the crossing angle and the ion beam pipe. The blue and red circles represent the ion and electron beam pipes at the EM calorimeter location. The black dashed circle outlines the solid angle without full azimuthal detector acceptance.

where we assumed p of 100 GeV/c considering the fact that the 2nd IR is being optimized for operation with maximum luminosity at the lower end of the hadron energy range. Thus, this requirement is somewhat relaxed compared to the 1st IR, which is beneficial to the luminosity as discussed below.

The $p_T^{\min}$ limit has to do with the fact that a particle must come out of the 10σ beam envelope for it to be detected without the beam damaging the detecting element and the detecting element degrading the beam lifetime. The detection occurs occurs downstream of the IP at a location with $\Delta\Psi \sim \pi/2$ where the beam size approaches its maximum. Due to the evolution of the particle's phase space coordinates, the requirement on the transverse offset at the detector translates into a requirement on the particle's angle at the IP:

$$p_T^{\min} > 10\, p\, \sigma_{x'}^{IP} = 10\, p\, \sqrt{\varepsilon/\beta_{IP}}, \tag{A.9}$$

where ε is the beam's geometric emittance. The beam emittance in the hadron collider ring is typically kept at its smallest possible value. Therefore, the only knob available for control of $\sigma_{x'}^{IP}$ and thus of $p_T^{\min}$ is the β_{IP} setting. However, increasing β_{IP} lowers the luminosity. It becomes a matter of balancing the $p_T^{\min}$ value and the luminosity. Collider experiments require

$$p_T^{\min} \simeq 200 \text{ MeV} \tag{A.10}$$

independent of the hadron beam energy. Again, assuming $p = 100$ GeV/c and applying the condition of Equation A.10 to Equation A.9, on gets

$$\sigma_{x'}^{IP} < 0.2 \text{ mrad}, \tag{A.11}$$

The requirements on $\sigma_{x'}^{IP}$ in Equations A.8 and A.11 are consistent with each other even though they originate from the different detection properties.

5. Detector space can be varied between $\pm$4.5 and -3.5 to +6.5 m. The space requirement is correlated with optimization between kinematic requirements for 12–18 GeV electrons and the need for particle tracking and identification of 10–50 GeV hadrons. The 2nd IR should likely be different from the 1st IR.

6. The far-forward acceptance is primarily defined by the apertures of the forward hadron quadrupoles. The relevant parameter is the acceptance solid angle. Therefore, the quadrupole apertures scale linearly with the distance from the IP to keep their opening angles constant. The requirement on the acceptance angle comes from the need to detect the forward neutron cone and charged particles up to a certain p_T, p_T^{max}, which cannot be detected prior to the quadrupoles.

Detection of forward neutrons is critical for example for elastic/diffractive physics. Figure 2.25 shows the angle versus momentum distribution of breakup neutrons in eAu collisions at three different energies. Another example of an important physics process with very forward neutrons is the diffractive reactions with charge exchange $e\,p \rightarrow e' + \pi + n$. The forward neutron parameters are shown in Figure 2.26. These examples demonstrate that the size of the neutron cone is inversely proportional to the collision energy and becomes larger as the energy goes down. Thus, complete neutron detection in the optimum energy range of the 2nd IR requires roughly doubling the angular acceptance and therefore the apertures of the forward hadron quadrupoles. However, combined with the requirements of a full-energy operation, this leads to high aperture-edge fields of the quadrupoles. This in turn contradicts to the limit on the aperture-edge field imposed by engineering considerations. For these reasons, the far-forward acceptance requirement is specified as a range of 5 to 10 mrad.

The study shown in Figure 2.24 demonstrate the impact of the p_T acceptance on the accuracy, with which the physics observable can be extracted from measured data for the DVCS process. The p_T^{min} requirement was discussed earlier. Figure 2.24 illustrates the importance of detecting p_T up to p_T^{max} of about 1.3 GeV. Since the particle angle at the IP is p_T^{max}/p, one arrives at the same conclusions as with the neutron cone that, due to lower optimum energy, the far-forward acceptance angle should be roughly doubled compared to the 1st IR. Thus, the far-forward acceptance requirement from the p_T^{max} point of view is consistent with that from the neutron acceptance point of view. For the reasons discussed above, this requirement is specified as a range of 5 to 10 mrad.

7. The forward angular acceptance is defined by the aperture of the spectrometer dipole located between the IP and forward hadron quadrupoles. It assists in the momentum analysis of the reaction products that are already outside of the far-forward acceptance but are still in the low-resolution area of the detector solenoid. Simulations of the 1st IR indicated that a 20 mrad acceptance should be adequate down to a hadron energy of 100 GeV. Given that the only energy lower than 100 GeV is a single point of 41 GeV, it may not be worth putting too much weight on it in optimization. There is also a balance of the forward acceptance and the solid angle shadowed by the dipole in the forward detector end cap. The dipole is a subject to the constraint of preserving the orbit geometry over the entire energy range, i.e. it must be able to provide a constant bending angle up to 275 GeV with its field not exceeding the NbTi technology limit. It may still be beneficial to

somewhat increase the forward aperture in the 2nd IR if validated by simulations. Thus, the forward acceptance is specified as a range of 20–30 mrad.

8. There are a number of physics drivers for $\Delta(B\rho)/(B\rho)$ at small to zero p_T. This is another dimension of the detector acceptance in addition to p_T.

The $\Delta(B\rho)/(B\rho)$ acceptance is equivalent to $x_L = 1 - \Delta(B\rho)/(B\rho)$ and $x_B = \Delta(B\rho)/(B\rho)$ acceptance in diffraction and imaging studies. Covering the high x_B range in particular at low t requires $x_L < 1$ or equivalently the detection of small $\Delta(B\rho)/(B\rho)$ at small to zero p_T. Figure A.3 shows the distribution of DVCS event in the $x_B - Q^2$ phase space and how the y cuts affect the $x_B - Q^2$ coverage.

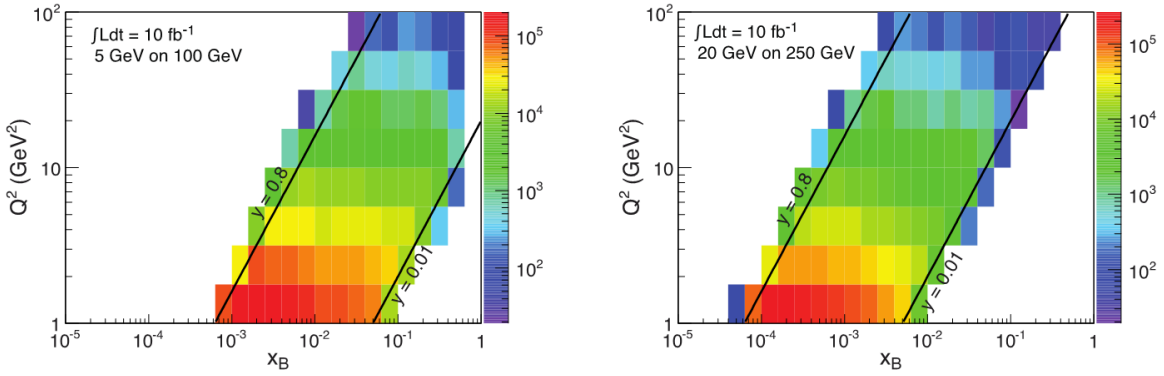

Figure A.3: Distribution of DVCS event in the $x_B - Q^2$ phase space and how the y cuts affect the $x_B - Q^2$ coverage.

Another driver is eA tagging of $(A-1)$ systems including neutron tagging for ed at $p_{RT} <$ Fermi momentum, d tagging for e^3He, ^3H or ^3He tagging for e^4He, and tagging of $(Z,\ A-1)$ and $(Z-1, A-1)$ daughter nuclei for eA in general. Detection of $A-N$ nuclei up to $A-1$ nuclei (although $A-1$ may be rare) improves vetoing efficiency in coherent diffraction studies and enables geometry tagging. Processes requiring high-x_L acceptance at small p_T are summarized in Table A.2.

Precise measurement of $\Delta(B\rho)/(B\rho)$ of the recoil particle allows one to reduce the uncertainty in the spectator momentum, which is dominated by the beam momentum and angular spreads. Figure A.4 illustrates how p_T smear systematically affects the on-shell extrapolation. The resolution $\sigma \sim 0.02$ GeV/c for a 50 GeV/A beam is known to 10%. By measuring $\Delta(B\rho)/(B\rho)$, one can achieve systematic uncertainties for the on-shell extrapolation comparable to the statistical ones.

To become detectable, a fragment with $p_T = 0$ and $\delta \equiv \Delta(B\rho)/(B\rho) \neq 0$ must come out of the $10\sigma_x$ beam envelope:

$$x_{fr} > 10\sigma_x, \tag{A.12}$$

where x_{fr} is the fragments transverse position. This can be achieved by momentum-analyzing the particles using a spectrometer dipole that generates a momentum-position

Table A.2: Schematic classification of processes with estimated coverage and resolution requirements. * is relative to 1/2 deuteron beam momentum.

Processes	Reaction	Relative magnetic rigidity	Coverage	Resolution (charged)	Neutrals	Comments
Exclusive & diffractive scattering on proton	$p \to p,\ n$	1	$p_T = [0,\ \sim 1.3]$ GeV $x_L = [\sim 0.5,\ > 0.99]$ $1 - x_L$ $= [< 10^{-2},\ \sim 0.3]$	$\Delta p_T < 40$ MeV $\Delta x_L / x_L \ll 0.1$ $\Delta(1 - x_L)/(1 - x_L)$ < 0.1	n, Λ, Σ^0	Inelastic diffraction physics & background
Coherent scattering on light nuclei	$A \to A$ $(A = D,\ He)$	1	$p_T = [0,\ \sim 500]$ MeV $1 - x_L$ $= [< 10^{-2},\ \sim 0.1]$	$\Delta p_T < 40$ MeV $\Delta(1 - x_L)/(1 - x_L)$ < 0.1	None	Ion beam divergence (p_T spread) significant
Spectator tagging in deuteron	$D \to p\ (n)$	1/2	$p_T = [0,\ \sim 500]$ MeV $x_L = [\sim 0.25,\ \sim 0.75]^*$	$\Delta p_T < 40$ MeV $\Delta x_L / x_L \ll 0.1$	(n)	Ion beam divergence (p_T spread) significant
Breakup of light and heavy nuclei	$A \to p,\ n,\ A - 1$	Various	$p_T = [0,\ \sim 500]$ MeV x_L various	To be defined	Multiple n	Veto detection for heavy nuclei

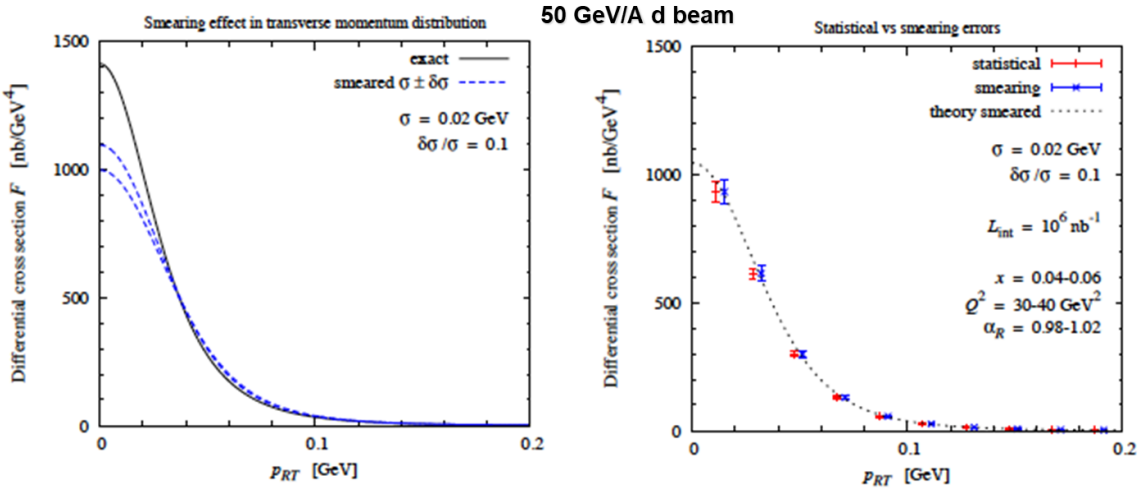

Figure A.4: Systematic impact of the p_T smear on the on-shell extrapolation.

correlation on its downstream side described by the dispersion function D:

$$x_{fr} = D\delta\,. \tag{A.13}$$

The behavior of the beam size depends on the beam emittance ε, an invariant describing the phase-space area occupied by the bunch, the Twiss β function describing the degree, to which the bunch is focused transversely, the dispersion D, the same function as in Equation A.13, and the rms longitudinal momentum spread of the bunch σ_δ:

$$\sigma_x = \sqrt{\varepsilon\beta + D^2\sigma_\delta^2}. \tag{A.14}$$

Combining Equations A.12, A.13, and A.14 gives

$$\delta > 10\sigma/D = 10\sqrt{\varepsilon\beta + D^2\sigma_\delta^2}/D. \tag{A.15}$$

By using a sufficiently strong spectrometer dipole to generate a large D at a Roman pot location and by strongly focusing the beam at the same location, one can attain

$$|D\sigma_\delta| \gg \sqrt{\varepsilon\beta}. \tag{A.16}$$

Equation A.15 then becomes simply

$$|\delta| > 10\sigma_\delta, \tag{A.17}$$

or, equivalently,

$$x_L < 1 - 10\sigma_\delta. \tag{A.18}$$

Equations A.17 and A.18 represent the fundamental limit on the minimum detectable δ at $p_T = 0$ corresponding to the longitudinal analog of the beam stay-clear area.

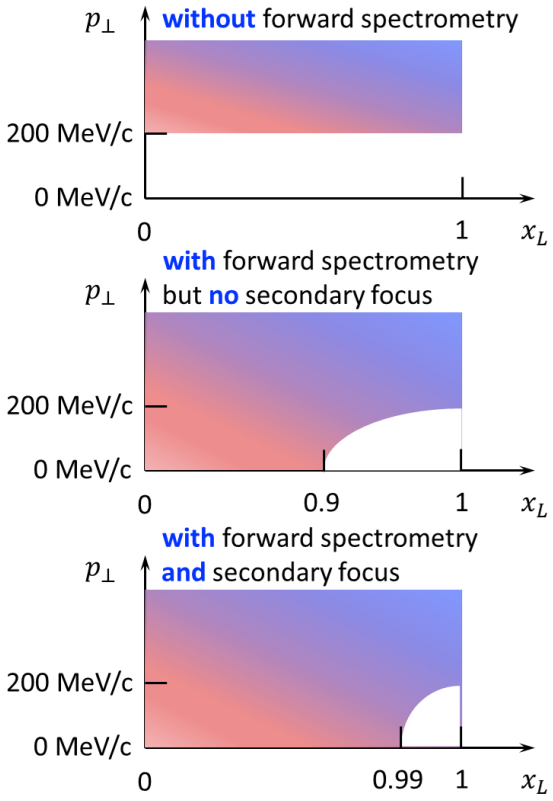

Figure A.5: Illustration of the impact of the forward spectrometry and secondary focus on the detector acceptance in the $x_L - p_T$ space.

Figure A.5 illustrates the impact of the forward spectrometry and secondary focus on the detector acceptance in the $x_L - p_T$ space.

9. The needed acceptance of the low-Q^2 electron tagger is $Q^2 < 0.1$.

10. The synchrotron radiation background generated by the electron beam must not exceed an acceptable limit. One of the criteria setting such a limit is the occupancy of the central tracker. It should typically not be greater than 2%. The main source of the synchrotron radiation in both IRs are the electron final focusing quadrupoles located on the forward side. They bend large-amplitude electrons directing them to the IP but, at the same time, causing them to radiate. Background may originate not only from directly emitted synchrotron radiation but from reflected radiation as well. Besides background problems, synchrotron radiation may deposit heat in the IR components causing out-gassing, pressure rise, cryogenic load, and damage. The IR design must account for and include measures for mitigation of these effects. Such measures include radiation masking, component cooling, and use of appropriate geometry allowing one to dispose of synchrotron radiation in designated locations. For example, the 1st IR combines collimation, cooling, and use of electron final focusing quadrupoles on the rear side with sufficiently large apertures to pass the radiation through.

A.2.2 Machine Requirements

From the lattice design and beam dynamics points of view, the 2nd IR and its impact on the global EIC parameters must meet the following constraints:

- The IR beam lines are able to at least transport electron and ion beams over the entire energy ranges.
- The aperture-edge fields of all magnets are below 4.6 T.
- The IR optics is matched to the regular ring lattice. Modification of the present RHIC straight section can be done up to the D9/Q10 area ($\sim$ 170 m from the collision point).
- With the 2nd IR included, the dynamic apertures and momentum acceptances of the electron and ion collider rings must be sufficiently large.
- The total combined beam-beam tune shift of the two IRs does not exceed 0.03 for ions and 0.1 for electrons.
- The dispersion at the crab cavities satisfies $H_x < 15$ m, or $|D_x| < 0.5$ m and $|D'_x| < 0.1$, in the proton ring and $H_x < 2$ m, or $|D_x| < 0.5$ m and $|D'_x| < 0.1$, in the electron ring as established by beam-beam studies.
- The beam aperture is greater than 10σ of the beam size for protons. For electrons, the beam aperture is greater than $15\sigma_x$ in the horizontal plane and $20\sigma_y$ in the vertical plane to accommodate the non-Gaussian tails building up in the vertical plane due to the beam-beam interaction.
- The synchrotron radiation generated by the electron beam does not affect operation of the IR components.

A.2.3 Geometric Constraints

There are geometric constraints imposed on the 2nd IR design by the existing experimental hall and accelerator tunnel. Figure A.6 shows the layout of RHIC's IP8 area where the 2nd IR can potentially be housed. In addition, the 2nd IR geometry needs to account for positions of certain detector components, provide sufficient space for necessary machine elements, and make room to let other beam lines bypass the detector. The geometric considerations can be summarized as

- The IR footprint fits in the available IP8 area.
- The IR accommodates detector components including a zero-degree calorimeter ($60 \times 60 \times 200$ cm^3), Roman pots, a low Q^2 tagger, and a luminosity monitor.
- Sufficient space is reserved to accommodate two spin rotators and one snake. Each requires $\sim$ 11 m.

- The hadron ring has the inner-to-inner ring configuration (as opposed to the inner-to-outer layout of the present RHIC).
- The collision point can be moved towards the ring center (as compared with the present RHIC) to provide space for the RCS (and the HAR in the on-energy injection scenario) to go around the detector.

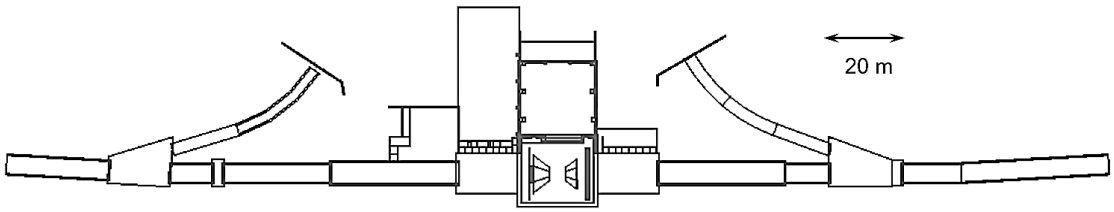

Figure A.6: Layout of RHIC IP8 area.

A.3 Beam Parameter Optimization and Performance Estimate

A.3.1 Single Operation Mode

According to the EIC strategic plan, design of the second interaction region should be optimized for delivering very high luminosity, up to 10^{34} cm^{-2}sec^{-1}, in a low to medium center-of-mass energy range up to $\sim$ 63 GeV. There are several significant changes from the primary detector parameters in choosing key machine and beam parameters to reach this luminosity goal.

1. The total numbers of bunches stored in the two collider rings are increased to 2320. As a result, the bunch repetition rate is doubled.
2. With a higher bunch repetition rate, the bunch populations are a factor of two smaller with the same average beam current.
3. Smaller bunch population permits preparation of a colliding ion beam with a shorter bunch length and smaller transverse emittance with help of strong cooling, thus allowing one to employ a small β^* to boost the luminosity.
4. The crab crossing angle is increased to 50 mrad to mitigate a much short bunch spacing for the colliding beams, they can be compensated by crab cavities to restore head-on collisions. Lower beam energy requires less crabbing RF voltage.
5. Low energy collisions utilizing low lepton beam energies allows installation of electron final focusing magnets inside the main detector as the scattering angles, especially for the scattered lepton corresponding to $Q^2 \approx 1$ GeV^2, are larger and the reduction of the effective acceptance due to the magnets can be neglected.

6. The smaller emittance for a low energy electron beam makes it easier to manage the synchrotron radiation fan emitted by the electron beam in the low-β quadrupole magnets.

On the other hand, ranges of several other key parameters such as total lepton beam synchrotron radiation power, maximum values of lepton and hadron beam-beam parameters, maximum hadron beam space charge tune-shift and highest proton/ion beam current remain the same as for the primary detector. Electron beam current at 5 GeV is increased to 3.2 A since the bunch repetition rate is doubled so the bunch current is decreased accordingly. Such current has already been achieved in PEP-II b-factory at a similar energy.

Summarizing optimization of the luminosity for the second detector, we find that utilizing more bunches is beneficial at lower beam energies. The IR chromaticity for protons will increase naturally due to use of a smaller β^*, thus achieving sufficient dynamic aperture is more challenging. It should also be mentioned that some mandatory measurements such as a bunch-by-bunch polarization measurement for hadrons will become more demanding

Table A.3: EIC beam parameters for different center-of-mass energy with strong hadron cooling.

Species	proton	electron	proton	electron	proton	electron
Energy [GeV]	100	10	100	5	41	5
CM energy [GeV]	63.2		44.7		28.6	
Bunch Intensity [10^{10}]	3.4	9.5	3.44	11.0	3	11
Number of bunches	2320		2320		2320	
Beam current [A]	1	2.75	1	3.2	0.874	3.2
RMS norm. emit, h/v [µm]	2.75/0.25	391/25	2.75/0.25	196/20	2/0.5	196/32
RMS emittance, h/v [nm]	25.6/2.3	20/1.3	25.6/2.3	20/2.0	44.8/11.2	20.0/3.3
β^*, h/v [cm]	15/2	19.2/3.6	15/2	19.2/2.27	15/4	31.9/12.3
IP RMS beam size, h/v [µm]	61.9/6.8		61.9/6.8		81.9/21.2	
K_x	9.1		9.1		3.9	
RMS $\Delta\theta$, h/v [µrad]	413/341	323/187	413/341	323/300	546/529	244/144
BB parameter, h/v [10^{-3}]	7.6/9.2	36/61	9/11	71/76	10.7/11	55/87
RMS emit. ϵ_{long} [10^{-3}eV·sec]	21		21		16.1	
RMS bunch length [cm]	4	2	4	2	7.5	2
RMS $\Delta p/p$ [10^{-4}]	10	6.6	10	6.6	8.8	6.8
Maximum space charge	0.026		0.026	neglig.	0.05	neglig.
Piwinski angle [rad]	6.6	2.6	16.2	8.1	22.7	6.1
Longitudinal IBS time [h]	2.7		2.7		2.0	
Transverse IBS time [h]	1.7/3.3		1.7/3.3		2.8/2.1	
Hourglass factor, H	0.81		0.77		0.84	
Luminosity [10^{33} cm^{-2}sec^{-1}]	9.01		10.01		2.33	

with the higher bunch frequency because events originating from different bunches could overlap in the polarimeter. Table A.3 shows the main design parameters for the second IR/detector at the $100\times10\,\mathrm{GeV}^2$, $100\times5\,\mathrm{GeV}^2$ and $41\times5\,\mathrm{GeV}^2$ energy points.

A.3.2 Operation in Parallel with the 1st IR

The 2nd IR is designed to operate in the entire energy range of the EIC. Some of the questions concerning simultaneous operation of the two IRs include their total chromatic effect, beam-beam tune shift, and the crabbing voltage required for operation of the 2nd IR at high energies due to its larger crossing angle. The chromatic compensation is briefly discussed in Section A.6.

The beam-beam tune shift is indeed cumulative between the two IRs. However, when one IR operates at its optimum, the other IR is away from its and is probably not running near the beam-beam tune shift limit. Simultaneous operation may even be somewhat complementary rather than competing from this point of view.

The required crabbing voltage V_{crab} is given by

$$V_{crab} = \frac{cE_b}{e2\pi f\sqrt{\beta_x^{crab}\beta_x^*}}\tan\left(\frac{\phi_{cross}}{2}\right), \tag{A.19}$$

where E_b is the beam energy, ϕ_{cross} is the beam crossing angle, f is the cavity frequency, β_x^{crab} is the horizontal beta function at the crab cavity location and β_x^* is the horizontal beta function at the IP. One can avoid increase in V_{crab} at high energies due to the larger crossing angle of the 2nd IR by adjusting the parameter $\sqrt{\beta_x^{crab}\beta_x^*}$. This results in luminosity reduction. However, the luminosity at high energy is dominated by the 1st IR.

A.4 Geometric Layout

Layout of the 2nd IR is shown in Figure A.7. It also indicates locations of the main forward and auxiliary detector components. This particular layout implements the most aggressive crossing angle under consideration of 50 mrad. The ion beam enters on the rear side and exits on the forward side. On the forward side, the ion beam first goes through a large-aperture spectrometer dipole. Its aperture is instrumented with trackers. It is used to momentum analyze and detect forward scattered particles. Particles at angles below a few mrad are detected in the far-forward section. The pass through the apertures of the final focusing ion quads and then momentum-analyzed by a subsequent set of spectrometer dipole. The dipoles are followed by several stages of Roman pots for detection of particles near the beam envelope. The dipoles also separate charged particles from neutrons and photons, which continue moving in straight paths from the IP and are detected in a Zero-Degree Calorimeter (ZDC). The dipoles bend the ion beam towards the electron beam to reduce the beam separation and allow both beam lines to fit in the available space. The far-forward acceptance angle pictured in Figure A.7 has the most aggressive size being

explored of ± 10 mrad. Figure A.7 also illustrates integration of the low Q^2 and luminosity monitor on the rear side

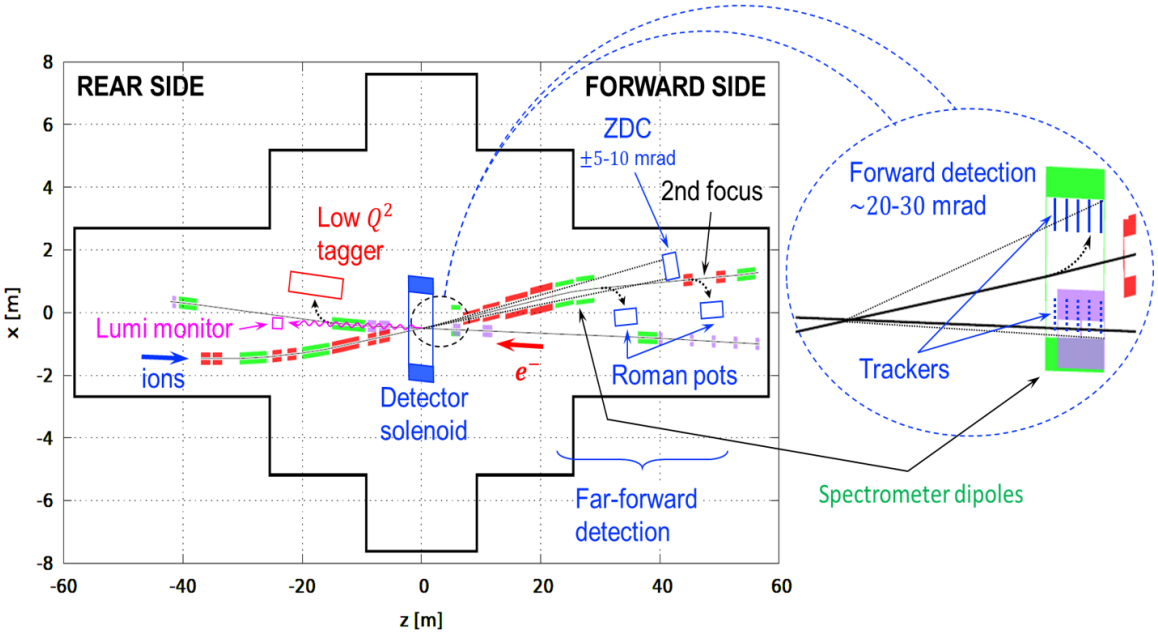

Figure A.7: Layout of the 2nd IR with a 50 mrad crossing angle indicating locations of the main forward and auxiliary detector components. The black solid line outlines the size of the IP8 experimental hall and adjacent tunnel.

Figure A.8 is a larger-scale of the 2nd IR. It illustrates integration of the necessary machine components including crab cavities and spin rotators. To allow for seamless geometric and optical match of the 2nd IR into the collider rings, we extracted the necessary end-point parameters from the 1st IR. We selected points just after the upstream and just before the downstream spin rotators and then used their coordinates and optical functions as the boundary conditions for the 2nd IR design. Note that the direction of the beam crossing in the 2nd IR is opposite to that in the 1st IR. Therefore, we first flipped the 1st IR layout about the axis going through the IP perpendicular to the axis of the experimental hall and then used this flipped version to find the end point coordinates for the 2nd IR. This procedure was only used to determine the start and end coordinates of the 2nd IR beamlines. The sequence of the beam line elements along each beam preserved the logic of the 1st IR.

The requirements on electron polarization control impose strict constraints on the orbital bending angles between the IP and the upstream and downstream electron spin rotators. This limits the flexibility in the geometry of the electron beam line. Therefore, the optics and geometry of the electron beam line of the 2nd IR are nearly identical to those of the 1st IR. We only made minor modifications to the 1st IR electron beam line design to account for the change in the beam crossing direction. Any change in the crossing angle must be accommodated by the ion IR beam line. Thus, we included several dipoles before the final focusing quads on the rear side and after the far-forward detection region on the forward side. These sections house crab cavities and provide optical match to the ion collider ring.

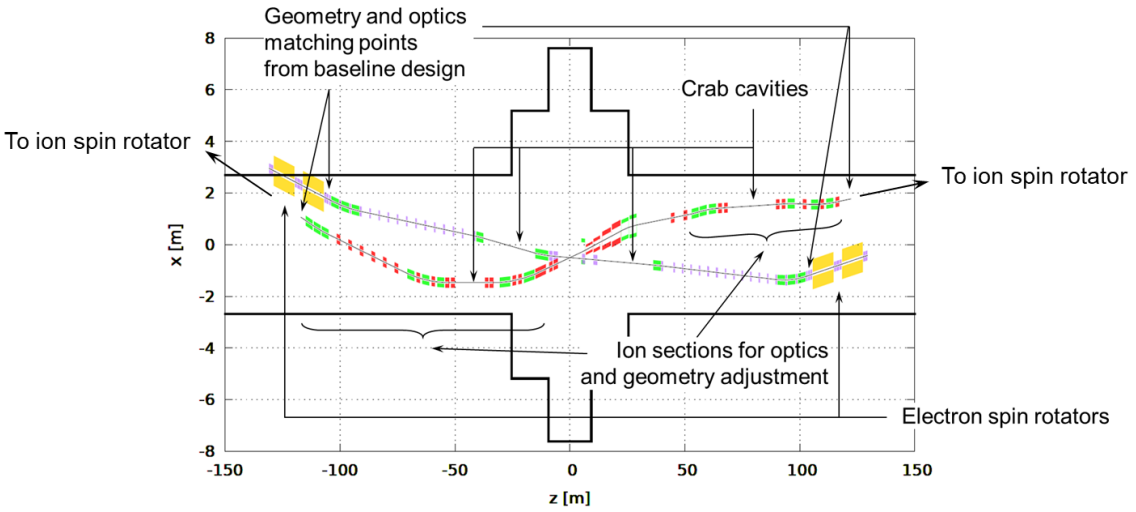

Figure A.8: Zoomed out view of the 2nd IR layout illustrating integration of machine components including crab cavities and spin rotators and indicating locations of the optics and geometry matching points derived from the 1st IR.

The positions and bending angles of the dipoles on the forward side were optimized to simultaneously provide a geometric match and allow for a good control of the $\mathcal{H}$ function necessary for optical match.

A.5 Linear Optics Design Concept

A.5.1 Hadron Beam Optics

The optics of the 2nd IR must be flexible enough to allow for optimization of the luminosity and detection in different collider configurations, including different beam energies, ion species, and detector solenoid strengths. Figure A.9 shows a concept of the ion IR optics designed to support these and other detection and machine requirements described in Section A.2. There are three physical quads upstream and four physical quads downstream of the IP. Their lengths and apertures have been optimized so that the 2nd IR can operate all the way to the top energy of 275 GeV while not exceeding the aperture edge field of 4.6 T. The apertures of the downstream quads increase proportionally to their distance from the IP to form a clear line of sight with an angular acceptance of ± 10 mrad.

Up to about 135 GeV ion energy, the maximum integrated field gradients of the two adjacent quadrupoles on each side of the IP are sufficient to focus the beam at the IP by running them with opposite polarities as doublets as shown in Figure A.9. In the 135 GeV to 275 GeV energy range, the integrated gradient requirements exceed what the first two quadrupoles only can provide. They are then configured to run with the same polarities, thus together forming the first quadrupole of an effective doublet. The third upstream physical quad and the third and fourth downstream physical quads are switched on as

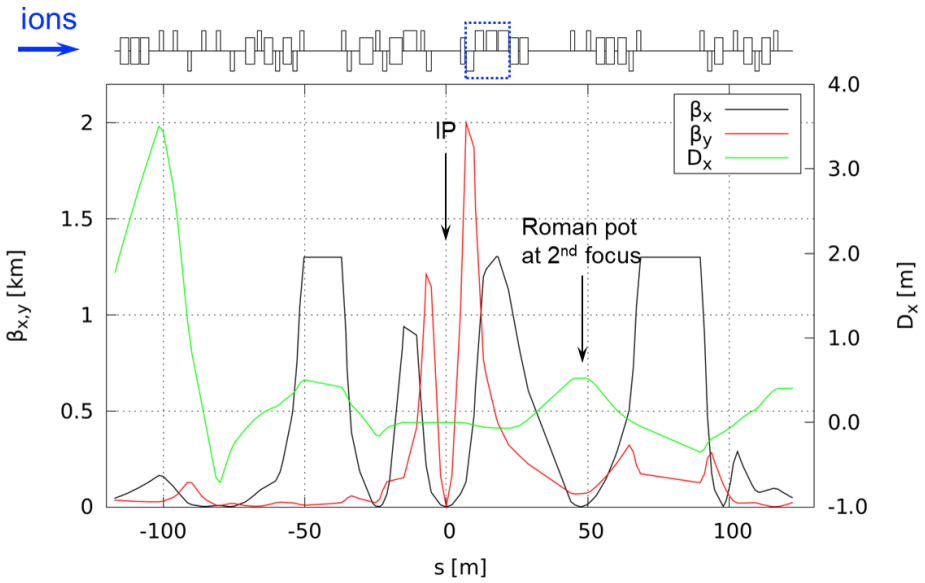

Figure A.9: Horizontal and vertical β functions $\beta_{x,y}$ (left vertical scale) and horizontal dispersion D_x (right vertical scale) are plotted versus the distance along the beam s for ion energies of up to 135 GeV. Positions of the IP and of the Roman Pot at the secondary focus are indicated.

the second quadrupoles of the effective doublets as shown in Figure A.10. Thus, the focal length of the doublet—and therefore the β^* values—can be adjusted in the two energy ranges while keeping the same maximum β values in the IR. The maximum values of both β_x and β_y are limited to about 2 and 1.2 km, respectively. This limit follows that of the 1st IR and may be further optimized. The $\beta^*_{x/y}$ values under this limitation are 37/2.5 cm and 96/3.3 cm in the energy ranges of up to 135 and 275 GeV, respectively. Such an optimization enhances the luminosity at the lower end of the overall energy range, where it tends to suffer more from collective effects. The resulting parameters of the detector region magnets at 135 and 275 GeV are listed in Table A.4.

The upstream FFB has a shorter effective focal length than the downstream one to minimize its chromatic contribution while satisfying the detector requirements. As shown in Figures A.9 and A.10, there is a set of spectrometer dipoles in the downstream part of the IR. The first -6 mrad spectrometer dipole is in front of the downstream FFB. It is used for momentum analysis of the forward scattered particles in the low-momentum-resolution region of the solenoid near its axis. Two additional spectrometer dipoles with bending angles of 15 mrad each are located after the downstream FFB. They momentum-analyze small-momentum-offset particles that are moving very close to or within the ion beam. The dipoles are followed by a 15 m long machine-element-free straight section instrumented with several stages of Roman pots and high-p_T detectors. A quadrupole at the end of the straight section adjusts the dispersion slope zero in the straight section after it. Tracks of the off-momentum particles inside the detectors in that straight section are then parallel to the beam and perpendicular to the detector plane, which simplifies

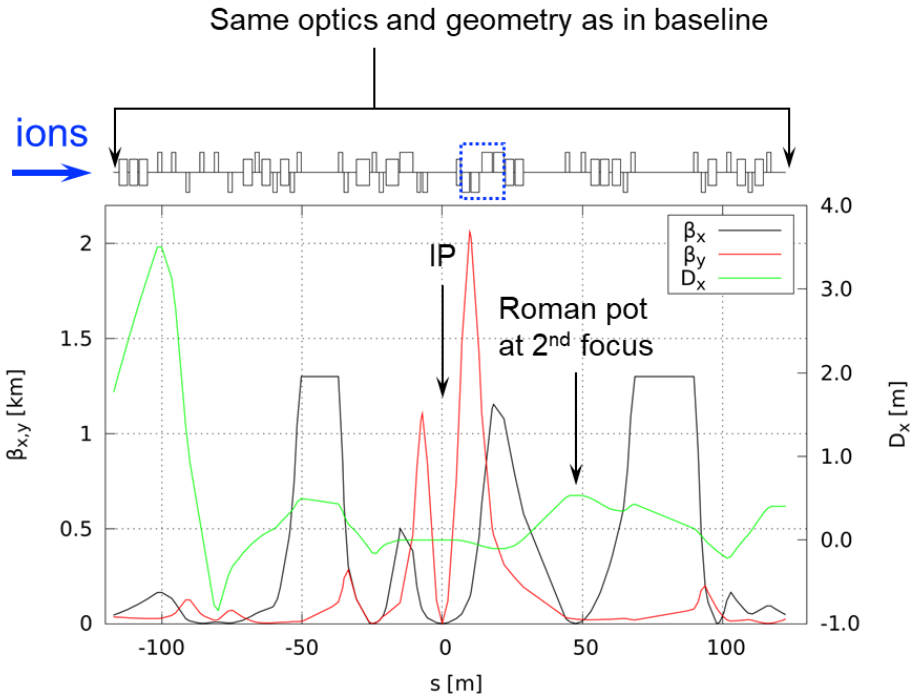

Figure A.10: Horizontal and vertical β functions $\beta_{x,y}$ (left vertical scale) and horizontal dispersion D_x (right vertical scale) are plotted versus the distance along the beam s for ion energies from 135 to 275 GeV. Positions of the IP and the Roman Pot at the secondary focus are indicated.

their reconstruction. The horizontal dispersion in the straight section reaches about 0.5 m. Note that the maximum fields of all spectrometer dipoles and aperture-edge fields of all quadrupoles do not exceed 4.6 T at 275 GeV allowing for operation of the 2nd IR in the entire energy range.

The beam is focused again in both planes in the middle of the straight section with zero dispersion slope and maximum dispersion value as shown in Figures A.9 and A.10. The horizontal β function is of the order of 0.5 m at the secondary focal point. The vertical β function can be adjusted in a range form $<$1 m to tens of meters. This region with a large $\sim$0.5 m zero-slope dispersion and a strong beam focus has been designed for placement of a Roman pot as discussed in Section A.2. A combination of the small beam size and large dispersion allow for the placement of a Roman Pot detector closer to the beam and therefore detect smaller momentum offsets than without the secondary focus. This makes particles with a relative magnetic rigidity offset of greater than 1% come out of the beam core. Implementation of the secondary focus leads to additional chromatic contribution, but it is necessary for forward detection. Performance of this design from the forward detection point of view is quantified below.

The beam parameters at the IP and secondary focus are determined by the lattice optical functions, transverse beam emittances, and beam momentum spread. At the points where the derivatives of the β function (β) and dispersion (D) are zero, the rms transverse beam

Table A.4: Parameters of the 2nd IR magnets for ions at 135 and 275 GeV.

Magnet Name	Magnet Type	Length [m]	Aperture Radius [cm]	135 GeV Field [T] or [T/m]	275 GeV Field [T] or [T/m]
iQUS2	Quad	4.5	4	23.5	55.5
iQUS1b	Quad	1.4	4	18.9	-76.6
iQUS1a	Quad	1.8	4	-81.5	-103.8
iBDS0	Dipole	1.5	34.5	-1.8	-3.7
iQDS1a	Quad	2.8	9.8	-46.8	-46.8
iQDS1b	Quad	2.8	13.1	29.2	-28.9
iQDS2a	Quad	3.7	17.8	2	25.8
iQDS2b	Quad	3.7	22	4.3	13.9
iBDS1	Dipole	3	25.5	2.3	4.6
iBDS2	Dipole	3	29	2.3	4.6
iQDS3	Quad	1.5	4	18	38.3
iQDS4	Quad	1.5	4	19.6	14.1

size $\sigma_{x,y}$ and angular spread $\sigma_{x',y'}$ are given by:

$$\begin{aligned} \sigma_{x,y} &= \sqrt{\beta_{x,y}\varepsilon_{x,y} + (D_x \Delta p/p)^2}, \\ \sigma_{x',y'} &= \sqrt{\varepsilon_{x,y}/\beta_{x,y}}, \end{aligned} \tag{A.20}$$

where $\beta_{x,y}$ are the horizontal/vertical β functions, $\varepsilon_{x,y}$ are the horizontal/vertical geometric beam emittances, D_x is the horizontal dispersion, and $\Delta p/p$ is the relative beam momentum spread. The geometric beam emittances can be expressed in terms of the invariant normalized beam emittances $\varepsilon^N_{x,y}$ as:

$$\varepsilon_{x,y} = \varepsilon^N_{x,y}/(\beta\gamma), \tag{A.21}$$

where $\beta\gamma = p/mc$ is the relativistic parameter.

Since the collision products originate with a small offset from the IP and the optics provides point-to-point focusing from the IP to the secondary focus, the transverse offset of a collision fragment at the secondary focus is determined primarily by a combination of the dispersion at that location and the fragment's relative magnetic rigidity offset:

$$\Delta x_{fr} = D_x \Delta(B\rho)/(B\rho), \tag{A.22}$$

where $B\rho = p/(Ze)$ is the magnetic rigidity. A fragment can be detected if it comes out of the beam stay-clear area: $\Delta x_{\rm fr} > 10\sigma_{\rm x}$. Reducing $\beta_{\rm x}$ by focusing the beam a second time and maximizing $D_{\rm x}$ at the secondary focus improves the detector's momentum acceptance. We ignore for the moment the beam size smear at the secondary focus due to the crabbing tilt. Assuming $p = 275\,\mathrm{GeV/c}$, $\varepsilon^N_{\rm x/y} = 3.3/0.3$ µm, and $\Delta p/p$ =6.8×10^{-4} and using the optics parameters of Figure A.10, Equation A.22 gives $\Delta(B\rho)/(B\rho) > 0.7\%$. Large dispersion also provides a high resolution in $\Delta(B\rho)$. Note that, as soon as the $|D_{\rm x}\sigma_\delta| \gg \sqrt{\beta_{\rm x}\varepsilon_{\rm x}}$ is reached, further increase of $D_{\rm x}$ or reduction of $\beta_{\rm x}$ does not improve the $\Delta(B\rho)/(B\rho)$ because the beam size is already dominated by the dispersive contribution.

The secondary focus section is followed by a section housing crab cavities and providing optical and geometric match to the ion collider ring. This section includes dipoles for geometry and dispersion control. The positions and bending angles of these dipoles were optimized to simultaneously provide a geometric match and allow for a good control of the $\mathcal{H}$ function necessary for optical match. The optical functions at the end of the 2nd IR are matched to the optics of the ion collider ring extracted from the 1st IR design as described in Section A.4. Similarly, on the rear side, there is a section of dipoles and quadrupoles for geometric and optical match to the collier ring upstream of the IP. The geometric and optical matching conditions are again obtained from the 1st IR design. The optics of this section is also optimized for placement of crab cavities. The 2nd IR was designed in such a way that the dipoles and quadrupoles in the rear and forward matching sections serve as knobs allowing one to accommodate variations in the design parameters such as the crossing angle, β^* values, and end-point optics and geometry.

A.5.2 Electron Beam Optics

The electron optics of the 2nd IR is shown in Figure A.11. As discussed in Section A.4, the 2nd IR electron optics is largely based on the 1st IR design due to the geometric constraints imposed by the electron spin rotators. For crossing angles larger than 25 mrad, there is room for further optimization of the electron design due to a larger transverse spacing of the electron and ion beams than in the 1st IR.

Quad doublets are used as both the upstream and downstream The electron IR meets the detection requirements described in Section A.2. In particular, measurements of particles down to zero angle with respect to the electron-beam direction are needed. The rear side of the electron IR integrates a luminosity monitor and a low-Q^2 tagger. Low-Q^2 tagging is done using a spectrometer dipole placed on the rear side right after the electron FFQs. The optics before the FFQs on the forward side and after the FFQs on the rear side is optimized for placement of crab cavities. Parameters of the electron detector region elements at 18 GeV are listed in Table A.5.

The minimum relative momentum offset, which makes particles come out of the beam stay clear, can be calculated using the following formula.

$$\left(\frac{\Delta p}{p}\right)_{\rm min} = \frac{10\sigma_{\rm x}}{D_{\rm x}}. \tag{A.23}$$

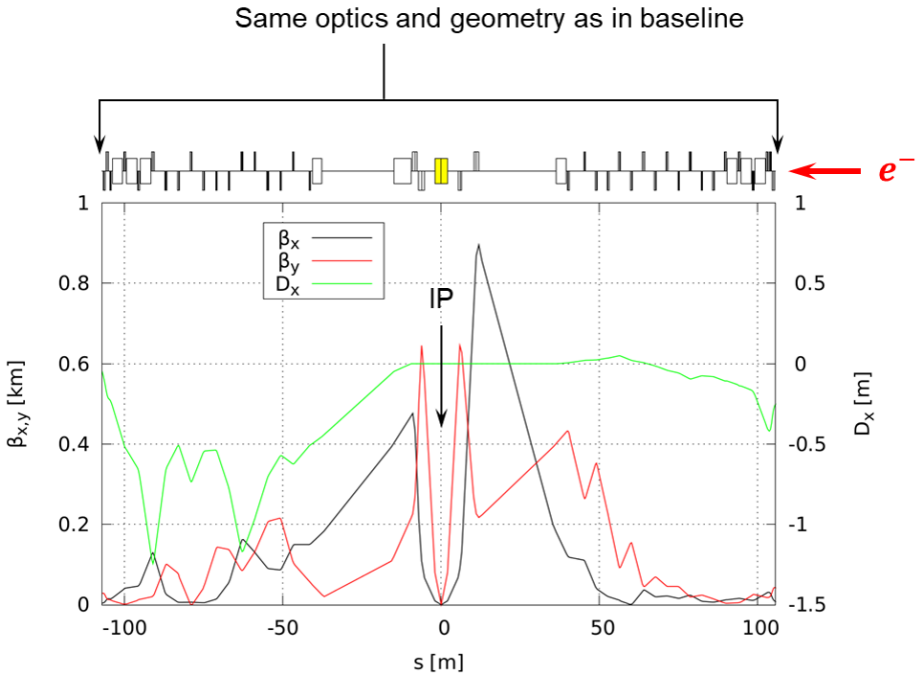

Figure A.11: Horizontal and vertical β functions $\beta_{x,y}$ (left vertical scale) and horizontal dispersion D_x (right vertical scale) of the 2nd electron IR are plotted versus the distance along the beam s.

Table A.5: Parameters of the 2nd IR magnets for electrons at 18 GeV.

Magnet Name	Magnet Type	Length [m]	Aperture Radius [cm]	Field [T] or [T/m]
eBDS1	Dipole	5.5	4	-0.2
eQDS2	Quad	1.4	4	13.3
eQDS1	Quad	1.8	4	-14
eQUS1	Quad	1.2	4	-13.5
eQUS2	Quad	1.6	4	6.2

Here $\sigma_x = \sqrt{\beta_x \epsilon_x + (D_x \Delta p/p)^2}$ is the rms value of the beam size, and D_x is the horizontal dispersion. Assuming $p = 10\,\mathrm{GeV/c}$, $\varepsilon_x = 20$ nm, and $\Delta p/p$ =5.8×10^{-4} and using the optics parameters of Figure A.11, the minimum relative rigidity offset is 0.1 in the middle of the straight after the low-Q^2 spectrometer dipole where $\beta_x \simeq 286$ m and $D_x \simeq 26$ cm.

The geometric and optical matching constraints at the end points of the electron 2nd IR in Figure A.11 were obtained from the 1st IR design as discussed in Section A.4. The geometry

of the electron 2nd IR was adjusted to account for the change in the beam crossing direction compared to the first IR. The optics was rematched accordingly.

A.6 Nonlinear Dynamics Considerations

The horizontal/vertical chromatic contributions ξ_x/ξ_y of the ion IR designs shown in Figures A.9 and A.10 are -79/-67 and -65/-56 in the low- and high-energy configurations, respectively. The ξ_x/ξ_y contribution of the electron IR shown in Figure A.11 is -14/-42. These are significant but reasonable chromaticity values and they can also be further optimized. Due to the $\sim \pi$ phase advance between the upstream and downstream FFBs, their chromatic contributions add up. Moreover, the downstream sides of the electron and ion IRs include a secondary focus, which further increases their chromatic contributions.

The chromaticities generated by the IRs require dedicated correction schemes. If not locally canceled, the chromatic β perturbation propagates around the ring, giving rise to large non-linear momentum dependencies of the betatron tune. A conventional design is to use local sextupoles generating a chromatic β wave opposite to the one from each FFB, so they cancel each other out. A separate local correction is necessary on each side of the IP to avoid the chromatic beam smear at the IP. The desired conditions at the sextupoles for an efficient correction are:

1. Large dispersion and β function to achieve compensation with a reasonable sextupole field;
2. Large β_x/β_y and β_y/β_x ratios at the x and y sextupoles, respectively, for orthogonal correction;
3. The β wave generated by the sextupoles must be opposite in phase to the chromatic kick of the FFBs, which, in case of local correction, means $\sim n\pi$ phase advance between the FFQ and the sextupoles;
4. The phase and amplitude of the sextupole β wave must account for chromatic contributions of the quadrupoles located between the sextupoles and the FFBs.

The non-linear fields of sextupoles also generate second and higher-order geometric (amplitude-dependent) aberrations, resulting in non-linear tune shift and excitation of third and higher-order resonances. These effects can significantly limit the dynamic aperture (DA). A common way to compensate for these aberrations is to use non-interleaved pairs of identical sextupoles with $-I$ separation between them. As demonstrated at KEKB, a pseudo $-I$ separation can also be used, which differs from $-I$ in that the matrix terms M_{21} and M_{43} are not zero. The latter adds flexibility to the sextupole optics.

Periodically placed sextupoles in a regular FODO lattice can also be used for local chromatic compensation. One can use them to build up a β wave while canceling the sextupole kicks over several FODO cells. The number of cells necessary for this cancellation depends

on the cell phase advance. In the EIC, the two arc sections adjacent to each IR can be used for local chromatic compensation. The sextupoles located around the rest of the ring can be used for correction of the remaining chromaticity.

In case of a simultaneous operation of the two IRs, one can use the chromatic β wave generated by one IR to cancel the chromatic kick of the other. This requires a certain betatron phase advance between the IRs. The phase advance can be adjusted in the arc section separating the two IRs. If the IRs are not identical the size of the β wave can be adjusted using sextupoles between the IRs.

A.7 Engineering Feasibility Considerations

Engineering feasibility of all of the 2nd IR magnetic elements needs a detailed evaluation. All of the 2nd IR magnets meet the nominal requirement of their fields being less than 4.6 T at the maximum beam energy of 275 GeV. However, some of the quadrupoles and magnets may still present engineering challenges due to their large apertures. Preliminary designs have been done for the largest-aperture quadrupole and dipole magnets in Table A.4, iQDS2b and iBDS2. The magnetic design of the quadrupole is shown in Figure A.12. Analysis of this preliminary design shows that the quadrupole is in a safe range of operation. Its peak coil field is expected to be at about 4.2 T. Optimization of the dipole design is in progress.

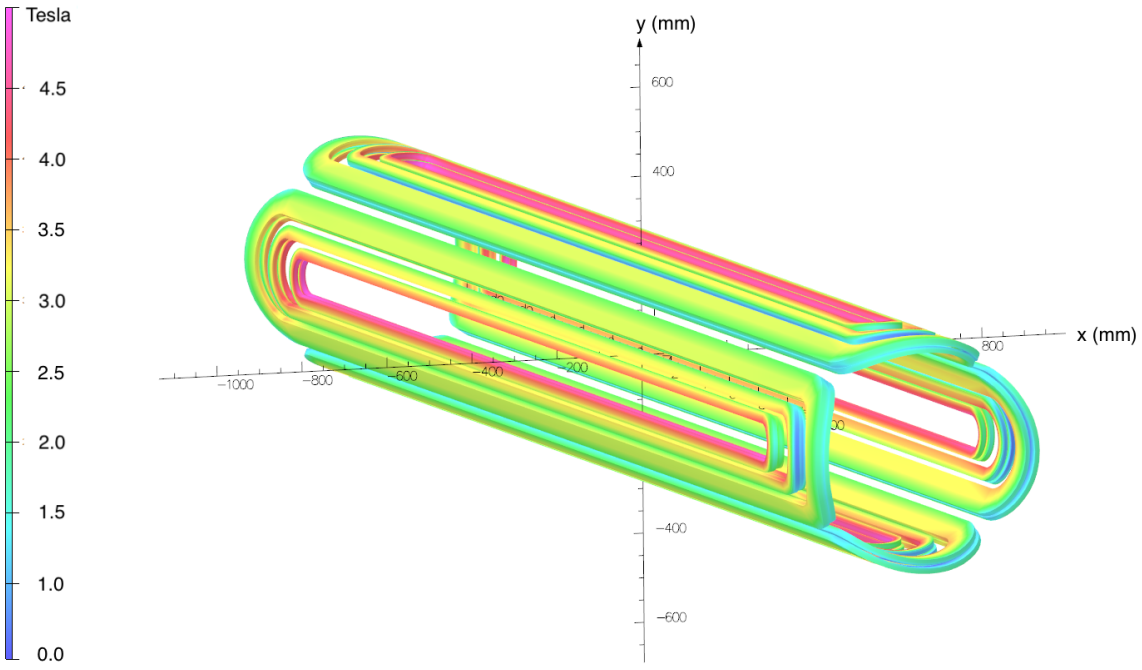

Figure A.12: Magnetic design of the largest-aperture ion quadrupole, iQDS2b.

Appendix B

Available Hadron Beams and Reliability of the RHIC Complex

The EIC uses the existing RHIC hadron complex. In this appendix we compare the EIC required hadron beams with (i) what the injector complex has already demonstrated, (ii) what beam parameters have been demonstrated in RHIC after acceleration, and (iii) document the reliability of the AGS and RHIC after decades of operation. We limit the comparison here to the EIC operations cases with polarized proton and gold beams of the highest bunch intensities as these are generally the most demanding.

RHIC has also accelerated and stored beams of d (deuteron), h (helion), Al (aluminum), Cu (copper), Ru (ruthenium), Zr (zirconium), and U (uranium) ion beams. Polarized proton beam operation extended from 31.2 to 255 GeV and Au beam operation from 3.85 to 100 GeV/nucleon. A full listing of all past hadron operating parameters in RHIC is in Ref. [482].

B.1 Hadron Beams from the Injector Complex

The RHIC injectors have accelerated a wide variety of beams for RHIC and for the NASA Space Radiation Laboratory (NSRL). In addition, most of the protons from the 200 MeV H^- LINAC are delivered to the Brookhaven LINAC Isotope Producer (BLIP), primarily for the production of medical isotopes.

Table B.1 shows the beam parameters required for polarized proton and gold beams in the EIC, and the demonstrated beam parameters from the injector complex. From the various EIC operating modes the case for highest bunch intensity is selected for both polarized proton and gold beams. A hadron bunch injected into the EIC is either not split longitudinally, split once, or split twice. To define the required parameters at injection we make the following assumptions for the parameter evolution from the AGS extraction to EIC storage energy:

1. Up to 10% intensity loss (transfer and ramp)
2. Up to 10% transverse emittance increase (transfer and ramp)
3. Up to 10% longitudinal emittance increase (transfer, ramp and bunch splits)
4. No polarization loss

For the highest bunch intensity cases the hadron beams required for EIC injection have already been demonstrated in the RHIC injectors.

Table B.1: Comparison of required EIC hadron beam parameters at AGS extraction, and demonstrated beam parameters. Shown are the EIC cases with the highest bunch intensity demand from the AGS. The proton case (left) is for 275 GeV protons on 10 GeV electrons with strong hadron cooling. The Au ion case (right) is for 110 GeV/nucleon gold on 10 GeV electrons with either stochastic or strong hadron cooling.

Parameter	proton		Au ion	
	EIC design	RHIC demonstrated	EIC design	RHIC demonstrated
Energy [GeV/nucleon]	23.8	23.8	9.80	9.80
Particle per bunch [10^{10}]	30	30	0.22	0.22
RMS norm. emittance, h/v [µm]	3.0/3.0	2.3/3.0	1.8/1.8	1.8/1.8
RMS long. emittance [10^{-3}eV·s]	130	75	670	120
RMS bunch length [cm]	63	48	172	140
RMS $\Delta p/p$ [10^{-4}]	8	6	9.8	8.5
Polarization [%]	70	65	—	—

For all other cases of e+p or e+A collisions the required p or Au beam parameters have also been demonstrated in the injectors with the exception of polarized d or polarized h beams. For the e+p cases without cooling smaller emittances than shown in Table B.1 are needed, but at reduced bunch intensities. For the reduced intensity the needed small emittance has been demonstrated. For the asymmetric normalized emittances in the uncooled e+p cases, the smaller emittance has also been demonstrated.

B.2 Hadron Beams in RHIC

RHIC has accelerated and stored beams of polarized protons, d (deuteron), h (helion), Al (aluminum) Cu (copper), Ru (ruthenium), Zr (zirconium) and U (uranium) ions. The differences of hadron beams in RHIC and the EIC are:

1. The larger number of bunches in the EIC

2. The shorter bunch length and larger momentum spread in the EIC
3. The asymmetric transverse emittances in the EIC
4. The beam-beam interaction with crab crossing and a different sign

For EIC Table B.2 shows the beam parameters required for polarized proton and gold beams, and the demonstrated beam parameters at RHIC store. From the various EIC operating modes the case for highest bunch intensity is selected for both polarized proton and gold beams.

Table B.2: Comparison of required EIC hadron beam parameters at store, and demonstrated beam parameters at full energy in RHIC. Shown are the EIC cases with the highest bunch intensities. The proton case (left) is for 275 GeV protons on 18 GeV electrons with strong hadron cooling. The Au ion case (right) is for 110 GeV/nucleon gold on 10 GeV electrons with stochastic cooling.

Parameter	proton		Au ion	
	EIC design	RHIC demonstrated	EIC design	RHIC demonstrated
Energy [GeV/nucleon]	275	255	110	100
Particle per bunch [10^{10}]	20	22.5	0.1	0.22
RMS norm. emit., h/v [µm]]	5.9/2.5	3.1/3.1	2.0/2.0	2.0/2.0
BB parameter, h/v [10^{-3}]	$+15/+10^{\dagger}$	$-18/-18^{\dagger}$	+11/+4	−4/−4
RMS long. emittance [10^{-3}eV·s]	110	55	0.2	0.27
RMS bunch length [cm]	6	55	18	35
RMS $\Delta p/p$ [10^{-4}]	6.8	1.7	10	7.7
Polarization [%]	70	55	—	—

† For 1 crab collision in EIC, and 2 collisions in RHIC.

For the proton case the EIC required bunch intensity has been accelerated and stored with the transverse sum emittance smaller than the required sum emittance. The demonstrated beam-beam parameter in RHIC (with 2 head-on collisions) exceeds the required beam-beam parameter in the EIC (with 1 crab collision).

For the Au ion case more than the required bunch intensity and emittances also have been demonstrated at store. The reduction in the bunch intensity will also satisfy the longitudinal beam parameters.

B.3 AGS and RHIC Reliability

RHIC and its 4 injector accelerators have been operated very reliably for a long time with an ongoing program of maintenance and upgrades. Below we show the AGS reliability in its 4th decade of operation and the RHIC reliability in its 1st and 2nd decade of operation. After 2001 the AGS only served as RHIC injector. Reliability here is defined as time when beam is available as a fraction of scheduled time with beam. The difference between delivered and scheduled time is failure time.

The AGS began operation in 1960 and Figure B.1 shows an operating period starting 29 years after its commissioning and lasting for more than a decade. During this period the machine was running with high-intensity beams, which is particularly challenging for high reliability. RHIC operations with the AGS as injector started in FY 2000 and Figure B.1 shows the last 17 operating years. In most years, the AGS and RHIC meet or exceeded the target of 80% reliability.

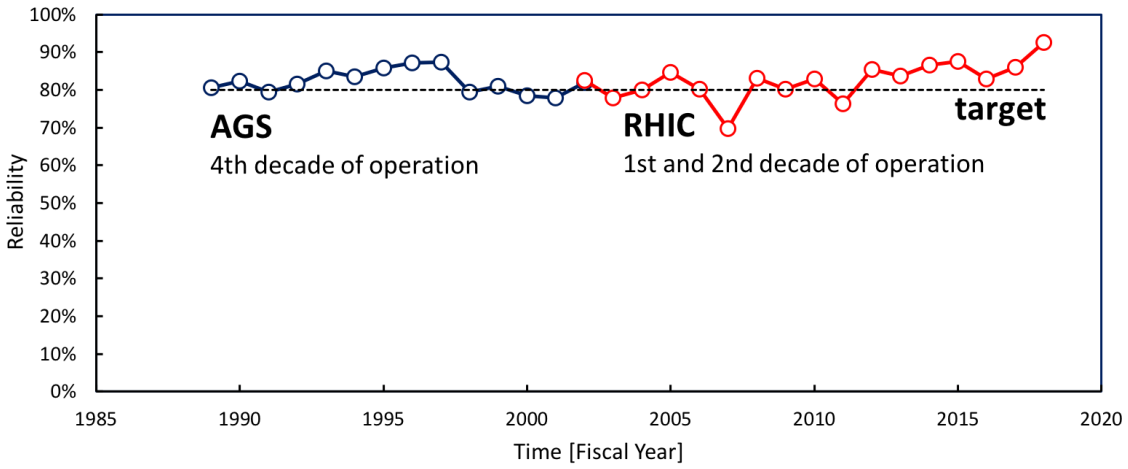

Figure B.1: AGS reliability in its 4th decade of operation (with high intensity beam), and RHIC reliability in its 1st and 2nd decade of operation.

A program of preventive maintenance, monitoring of system failure rates, upgrades of systems with high failure rates, and replacement of anticipated obsolete systems has allowed maintaining high reliability in the AGS after decades of operation, and the RHIC hadron complex over the first two decades of operation.

Systems need replacements on different time scales. For example, electronics rarely exceeds 20 years, and power electric installation 40 years. Physical structures such as halls and tunnels can be maintained indefinitely. The RHIC complex presently does not operate with high-intensity beams, and the upgrade and replacement programs allow maintaining the complex without a time limit.

Appendix C

EIC Project Summary

The Conceptual Design Report is one of several documents prepared as a basis for the EIC project Critical Decision 1 milestone (CD-1). Together they define the Project. Here we briefly summarize some of the project-defining elements that are not explicitly discussed in the CDR but are detailed elsewhere in the CD-1 documentation.

C.1 Project Description

The EIC Project will design, build, and install the accelerator hardware for a new electron storage ring, an electron injector, and modifications to the hadron ring required to produce an electron ion collider and infrastructure. It will include one interaction region, with allowance for a second interaction region, and one detector. The facility is designed to meet requirements to ensure high reliability and availability for the user program. To meet the mission need, an Acquisition Strategy is being developed that includes a list of Key Performance Parameters for the facility that ensure the science requirements described in Chapter 2 can be met, as well as a management and business plan that meets DOE guidelines for a project of this scale, and a detailed risk analysis.

C.2 Schedule and Cost Range

The EIC project will be delivered within 10-15 years. Initial critical decision milestones, as shown in Table C.1, have been developed and are being used to guide the conceptual cost and schedule determination.

Following the approval of CD-0, based on a preliminary conceptual design, an Independent Cost Review determined a cost range for the project between a low value of $1.6B to a high value of $2.6B. A final cost, and a funding profile, will be determined as the project advances through the CD-2 and CD-3 milestones.

Table C.1: EIC project high level schedule.

Key Milestones	Schedule
CD-0, Approve Mission Need	12/19/2019 (actual)
CD-1, Approve Alternative Selection and Cost Range	3Q FY2021
CD-2, Approve Performance Baseline	4Q FY2022
CD-3, Start of Construction	4Q FY2023
CD-4a, Approve Start of Operations	4Q FY2030
CD-4, Project Completion (defined as delivery of all RF power)	4Q FY2032

Glossary of Acronyms

Name	Description
aC	amorphous Carbon
ACS	Access Control Systems
ADC	Analog to Digital Converter
ADO	Accelerator Device Object, device software manager in C++ programming
AGS	Alternating Gradient Synchrotron: an accelerator at Brookhaven National Laboratory that serves as injector to RHIC
ANL	Argonne National Laboratory
API	Application (Program) Interface
APS	Argonne Photon Source: a light source facility at Argonne National Laboratory
ARR	Accelerator Readiness Review
ATLAS	A colliding beams detector at the CERN Large Hadron Collider
AtR	AGS to RHIC beam transfer line: a part of RHIC accelerator complex
AWG	American Wire Gauge
B-factory	A particle collider designed to produce large numbers of B mesons
B-field	Magnetic field
BLA	Beam Line Absorbers
BLM	Beam Loss Monitor
BNL	Brookhaven National Laboratory
BPM	Beam Position Monitor
CAD	Computer Aided Design
C-AD	Collider-Accelerator Department, Brookhaven National Laboratory
CBI	Coupled bunch instability
CBM	Coupled bunch modes
CC	Crab Cavity
CCD	Charged Coupled Device: a silicon chip for capturing and manipulating digital data
CCG	Cold cathode ion gauge
CDEV	Common Device interface
CDR	Conceptual Design Report
CDS	Computers, Devices, and Software
CEBAF	Continuous Electron Beam Accelerator Facility at TJNAF, Virginia

CEC	Coherent Electron Cooling
CEM	Channeled Electron Multiplier
CERN	European Organization for Nuclear Research: accelerator laboratory in Switzerland
CESR	Cornell Electron Storage Ring facility
CM or c.m.	Center of mass
CME	Center of mass energy
CMOS	Complementary Metal-Oxide-Semiconductor: a silicon chip for manipulating digital data
CNS	Controls Name Server
COMPASS	An experiment at CERN utilizing muon and proton beams
COTS	Commercial off-the-shelf
CSR	Coherent synchrotron radiation
CVD	Chemical Vapor Deposition
DAC	Digital to Analog Converter
DAFNE	An accelerator facility in Frascati, Italy
DCCT	Direct Current Current Transformer: a precision DC current transducer
DESY	Deutsche Electronen Synchrotron Laboratory: an accelerator facility in Hamburg, Germany
DOE	U.S. Department of Energy
DoS	Density of State
DQW	Double Quarter Wave
DQWCC	Double Quarter Wave Crab Cavity
DVCS	Deeply Virtual Compton Scattering
DVVM	Deeply Virtual Vector Meson
EBIS	Electron Beam Ion Source
EBW	Electron Beam Welding
EH&S	Environment Health and Safety
EHS&Q	Environment Health Safety and Quality
EIC	Electron Ion Collider
EIS	Environmental Impact Statement
EMC	European Muon Collaboration experiment at CERN
EOM	Electro-Optic Modulator
EPS	Equipment control and Protection System at RHIC
ERL	Energy Recovery LINAC
ESR	Electron Storage Ring: a part of EIC accelerator complex
eSTAR	A proposed EIC detector based on the existing STAR detector at RHIC
FCT	Fast Current Transformer
FEC	Front End Controller/Computer
FEL	Free Electron Laser
FHA	Fire Hazard Analysis
FMD	Fundamental Mode Damper

FODO	A particular grouping of focusing and defocusing magnets used in accelerator beams
FONSI	Finding of No Significant Impact
FPC	Fundamental Power Coupler
FPGA	Field-Programmable Gate Array
FRIB	Facility for Rare Isotope Beams under construction at Michigan State University
FSAD	Final Safety Analysis Document
FY	Fiscal Year
GEMA	planar multi-electrode array used to measure particle trajectories in gas-filled detectors
GPIB	General Purpose Interface Bus, IEEE-488
GPM	General Purpose Monitor
HAR	Hadron Accelerator Ring: a part of EIC accelerator complex
HEBT	High Energy Beam Transport
HERA	Hadron-Electron Ring Accelerator at DESY in Hamburg, Germany
HERMES	A fixed-target experiment at HERA facility
HHOM	Horizontal Higher Order Modes
HOM	Higher Order Modes
HSR	Hadron Storage Ring: a part of EIC accelerator complex
HTTP	Hypertext Transfer Protocol
IBS	Intrabeam Scattering
ICR	Independent Cost Review
ICT	Integrating Current Transformer
IEEE	Institute of Electrical and Electronics Engineers
ILC	International Linear Collider
INT	Institute for Nuclear Theory at the University of Washington, Seattle
IOT	Inductive Output Tube: a vacuum tube used as a high power RF amplifier
IP	Interaction Point
IAD	Ion Assisted Deposition
IPM	Ionization Profile Monitor
IR	Interaction Region
ISO	Optical isolator, or International Standards Organization
IVA	Inductive Voltage Adder
JFT	A Japanese tokamak fusion research facility
TJNAF	Thomas Jefferson National Accelerator Facility, Newport News, Virginia
KEK	High Energy Accelerator Research Laboratory, Tsukuba, Japan
KEKB	A particle accelerator operating as a B-factory at KEK
KPP	Key Performance Parameter
LARP	Large Hadron Collider (LHC) Accelerator Research Program
LBNL	Lawrence Berkeley National Laboratory in California
LDRD	Laboratory Directed Research and Development
LEP	Large Electron Positron collider, predecessor to the LHC at CERN
LEReC	Low Energy RHIC electron Cooling

LHC	Large Hadron Collider at CERN in Geneva, Switzerland
LINAC	Linear Accelerator
LLRF	Low Level Radio Frequency
LPOL	Longitudinal polarization measurement of the electron beam at HERA
LtR	LINAC to RCS transfer line: a part of EIC accelerator complex
MAPS	A planar multi-electrode array on a microchip, used to measure charged particle trajectories in compact gas-filled detectors
MBEC	Micro-bunched electron beams
MCP	Micro Channel Plate detector
MPS	Machine Protection System
NAS	National Academy of Science and Network Attached Storage system
NCRF	Normal Conducting Radio Frequency
NEA	Negative Electron Affinity
NEG	Non-Evaporation Getter
NEPA	National Environmental Policy Act
NPCT	New Parametric Current Transformer
NSAC	Nuclear Science Advisory Committee for U.S. Department of Energy
NSLS-II	National Synchrotron Light Source-II at Brookhaven National Laboratory
NSRL	NASA Space Radiation Laboratory at Brookhaven National Laboratory
ODH	Oxygen Deficiency Hazard
OFHC	Oxygen-Free High Conductivity copper
OPPIS	A polarized ion source used for injection of polarized protons into RHIC
OTR	Optical Transition Radiation
PASS	Personnel Access Safety System
PDF	Particle Distribution Function
PED	Project Engineering and Design
PEP-II	Positron-Electron Project, a colliding beams facility at SLAC
PETRA	A high energy electron-positron accelerator facility at DESY, now operating as a light source
PFL	Pulse Forming Line
PHENIX	A large colliding-beams detector at RHIC
PID	Particle Identification
PLC	Programmable Logic Controller
PLL	Phase-Locked Loop
PoP	Proof of Principle
PPM	Office of Project Management
PPS	Personnel Protection System
PSAD	Preliminary Safety Assessment Document
PSD	Photon Stimulated Desorption, or Power Spectrum Density
PSEG	A local utility company providing electrical power to Brookhaven National Laboratory
PSI	Power Supply Interface
PVD	Physical Vapor Deposition

PWO	Lead Tungstate crystal
QCD	Quantum Chromodynamics
QE	Quantum Efficiency
QWR	Quarter-Wave Resonator
RACF	RHIC and ATLAS Computing Facility at Brookhaven National Laboratory
R&D	Research and Development
RCS	Rapid Cycling Synchrotron: a part of EIC accelerator complex
RCStSR	The beam transfer line from RCS to the EIC Storage Ring
REST	Representational State Transfer protocol
RF	Radio Frequency
RFD	RF-Dipole
RGA	Residual Gas Analyzer
RHIC	Relativistic Heavy Ion Collider at Brookhaven National Laboratory
RICH	Ring Imaging Cherenkov detector
RMS	Root Mean Square
RRR	Residual Resistivity Ratio
RTD	Resistance Temperature Detector
RTDL	Real Time Data Link
RtS	RCS to electron Storage Ring transfer line, a part of EIC accelerator complex
SAD	Safety Assessment Document
SBEND	Sector Bend in RCS ring lattice
SBMS	Standards-Based Management System
SCCR	Short Circuit Current Rating
SEY	Secondary Emission Yield
SIDIS	Semi-Inclusive Deep Inelastic Scattering (of high energy electrons)
SIL	Safety Integrated Level
Sindi	Synoptic Display tool
SIP	Sputtering Ion Pump
SLAC	Stanford Linear Accelerator Center in California SLC SLAC Linear Collider
SLM	Synchrotron Light Monitor
SM	Standard Model of particle physics
sPHENIX	A proposed new RHIC detector to replace PHENIX
SPS	Super Proton Synchrotron, and accelerator at CERN
SR	Synchrotron Radiation
SRF	Superconducting Radio-Frequency
SRP/CS	Safety Related Parts of Control Systems
SRS	Spin Rotator Solenoid
SW	Standing Wave
SOC	System on a Chip
Tape	Tool for Automated Procedure Execution
T-BMT	Thomas-BMT equation, named after Thomas, Bargmann-Michel-Telegdi
TAL	Triplet Achromat Lattice

TBA	Triple Bend Achromat
TEC	Total Estimated Cost
TIG	Tungsten Inert Gas (a specialized form of welding)
TMCI	Transverse Mode Coupling Instability
TMD	Transverse Momentum Distribution
TMP	Turbomolecular Pump
TPC	Time Projection Chamber
TPOL	Transverse Polarization measured for the electron beam at HERA
TSP	Titanium Sublimation Pumps
TWP	Traveling Wave Plates
UHV	Ultra-High Vacuum
UPC	Ultra-Peripheral Collisions
UPS	Uninterruptable Power Supply
VCO	Voltage Controlled Oscillator
VCXO	Voltage Controlled Crystal Oscillator
VHOM	Vertical Higher Order Modes
VME	VERSAModule Europa, IEEE-1014-1987, chassis for electronic control modules
WCM	Wall Current Monitor
WOW	Wide Open Waveguide
XDB	Xray Diagnostic Beamline
XHV	Extremely High Vacuum
YAG	A type of laser using a Yttrium-Aluminum-Garnet crystal
ZDC	Zero Degree Calorimeter
ZEUS	A large detector at the HERA collider
ZFCT	Zero Flux Current Transformer, a type of DCCT

References

[1] Harrison, M. and Ludlam, T. and Ozaki, S., "RHIC Project Overview," *Nucl. Instr. Meth. A*, vol. 499 (2-3), p. 235, 2003.

[2] O. S. Bruning, P. Collier, P. Lebrun, S. Myers, R. Ostojic, J. Poole, and P. Proudlock, "LHC Design Report Vol.1: The LHC Main Ring," 2004.

[3] W. Busza, K. Rajagopal, and W. van der Schee, "Heavy Ion Collisions: The Big Picture, and the Big Questions," *Annual Review of Nuclear and Particle Science*, vol. 68, pp. 1 – 49, 2018.

[4] P. Schmüser and F. Willeke, *The Electron-Proton Collider HERA, Accelerators and Colliders, Landolt-Börnstein - Group I Elementary Particles, Nuclei and Atoms*, vol. 21. Springer-Verlag, Berlin Heidelberg, 2013.

[5] A. Lung, "Future plans at Jefferson Lab: 12-GeV CEBAF upgrade and electron-ion collider (ELIC)," in *Proceedings, 16th International Workshop on Deep Inelastic Scattering and Related Subjects (DIS 2008): London, UK, April 7-11, 2008*, p. 230, 2008.

[6] F. Bradamante, "The COMPASS experiment at CERN," *Nucl. Phys.*, vol. A622, pp. 50C–65C, 1997.

[7] A. Accardi *et al.*, "Electron Ion Collider: The Next QCD Frontier," *Eur. Phys. J.*, vol. A52, no. 9, p. 268, 2016.

[8] A. Aprahamian *et al.*, "Reaching for the horizon: The 2015 long range plan for nuclear science." DOE/NSF Nuclear Science Advisory Panel (NSAC) Report, 2015.

[9] National Academies of Sciences, Engineering, and Medicine, "An Assessment of U.S.-Based Electron-Ion Collider Science." The National Academies Press, Washington DC, 2018. `https://doi.org/10.17226/25171`.

[10] K. H. Ackermann *et al.*, "STAR detector overview," *Nucl. Instrum. Meth.*, vol. A499, pp. 624–632, 2003.

[11] M. Connors, "Design, status and schedule of the sPHENIX experiment at RHIC," *Nucl. Phys.*, vol. A967, pp. 548–551, 2017.

[12] F. Willeke, "Overcoming performance limitations due to synchro-betatron resonances in the HERA electron ring," in *9th European Particle Accelerator Conference (EPAC 2004) Lucerne, Switzerland, July 5-9, 2004*, 2004.

[13] A. Piwinski, "Intra-beam-Scattering," in *Proceedings, 9th International Conference on the High-Energy Accelerators (HEACC 1974): Stanford, California, May 2-7, 1974*, pp. 405–409, 1974.

[14] D. Kayran *et al.*, "Proof-of-principle experiment for FEL-based coherent electron cooling," *Conf. Proc.*, vol. C110328, pp. 2064–2066, 2011.

[15] A. Sokolov and I. Ternov, "Polarization and Spin Effects in the Theory of Synchrotron Radiation," *Doklady Akademii Nauk SSSR (USSR)*, vol. 153, 1963.

[16] Ya. S. Derbenev and A. M. Kondratenko, "Diffusion of particle spins in storage elements," *Sov. Phys. JETP*, vol. 35, p. 230, 1972.

[17] D. Sagan, "Beam-beam effects with errors in the crab compensation," *Conf. Proc.*, vol. C930517, pp. 3470–3472, 1993.

[18] R. B. Palmer, "Energy Scaling, Crab Crossing, and the Pair Problem," in *High energy physics in the 1990's: Proceedings*, vol. C8806271, pp. 613–619, 1988.

[19] KEK, "KEKB B factory design report," 1995.

[20] "PEP-II: An Asymmetric B Factory. Conceptual Design Report.," 1994.

[21] Ya. S. Derbenev and A. M. Kondratenko, "Acceleration of Polarized Particles to High-Energies in Synchrotrons," in *Proceedings: 10th International Conference on High-Energy Accelerators, Protvino, Jul 1977. 1.*, vol. 2, pp. 70–75, 1977.

[22] "Low-Energy Cooling for the Electron Ion Collider," Tech. Rep. BNL-220686-2020-TECH, JLAB-TN-20-043, 2020.

[23] "Frequent On-Energy Injection Design Option of Electron-Ion Collider," Tech. Rep. BNL-220687-2020-TECH, Brookhaven National Laboratory, 2020.

[24] V. N. Litvinenko and Y. S. Derbenev, "Coherent Electron Cooling," *Phys. Rev. Lett.*, vol. 102, p. 114801, 2009.

[25] K. Ohmi, "Simulation of beam-beam effects in a circular e+ e- collider," *Phys. Rev.*, vol. E62, pp. 7287–7294, 2000.

[26] J. Qiang, M. A. Furman, and R. D. Ryne, "A parallel particle-in-cell model for beam-beam interaction in high energy ring colliders," *J. Comput. Phys.*, vol. 198, pp. 278–294, 2004.

[27] D. P. Barber, F. Brinker, W. Decking, E. Gianfelice-Wendt, J. Keil, M. Vogt, and F. J. Willeke, "Longitudinal Positron Polarisation in HERA-II," in *9th European Particle Accelerator Conference (EPAC 2004) Lucerne, Switzerland, July 5-9, 2004*.

[28] R. Assmann, A. Blondel, B. Dehning, P. Grosse-Wiesmann, R. Jacobsen, J. P. Koutchouck, J. Miles, M. Placidi, R. Schmidt, and J. Wenninger, "Deterministic harmonic spin matching in LEP," in *4th European Particle Accelerator Conference (EPAC 94) London, England, June 27-July 1, 1994*, vol. C940627, pp. 932–934, 1994.

[29] M. Blaskiewicz, "A multipurpose coherent instability simulation code," in *Particle Accelerator Conference, 2007. PAC. IEEE*, pp. 3690–3692, IEEE, 2007.

[30] B. Podobedov and M. Blaskiewicz, "Limiting Coherent Longitudinal Beam Oscillations in the EIC Electron Storage Ring," Tech. Rep. BNL-215885-2020-TECH, 2020, BNL, 2020.

[31] N. Biancacci, M. Blaskiewicz, Y. Dutheil, C. Liu, K. Mernick, M. Minty, and S. White, "Transverse Impedance Measurement in RHIC and the AGS," in *Proceedings, 5th International Particle Accelerator Conference (IPAC 2014): Dresden, Germany, June 15-20, 2014*, p. TUPRI071, 2014.

[32] M. Blaskiewicz, J. Brennan, and K. Mernick, "Longitudinal Impedance of RHIC," in *Proceedings, 6th International Particle Accelerator Conference (IPAC 2015): Richmond, Virginia, USA, May 3-8, 2015*, p. MOPMN020, 2015.

[33] M. Blaskiewicz, J. M. Brennan, and F. Severino, "Operational Stochastic Cooling in the Relativistic Heavy-Ion Collider," *Phys. Rev. Lett.*, vol. 100, p. 174802, 2008.

[34] A. Fedotov *et al.*, "Experimental Demonstration of Hadron Beam Cooling Using Radio-Frequency Accelerated Electron Bunches," *Phys. Rev. Lett.*, vol. 124, no. 8, p. 084801, 2020.

[35] D. Ratner, "Microbunched Electron Cooling for High-Energy Hadron Beams," *Phys. Rev. Lett.*, vol. 111, no. 8, p. 084802, 2013.

[36] M. Woods, J. Clendenin, J. Frisch, A. Kulikov, P. Saez, D. Schultz, J. Turner, K. Witte, and M. Zolotorev, "Observation of a charge limit for semiconductor photocathodes," *J. Appl. Phys.*, vol. 73, pp. 8531–8535, 1993.

[37] T. Abe, K. Akai, N. Akasaka, K. Ebihara, E. Ezura, T. Furuya, K. Hara, T. Honma, K. Hosoyama, S. Isagawa, A. Kabe, T. Kageyama, T. Kobayashi, Y. Kojima, K. Marutsuka, S. Mitsunobu, H. Mizuno, Y. Morita, F. Naito, H. Nakai, H. Nakanishi, K. Nakanishi, S. Ninomiya, M. Nishiwaki, M. Ono, H. Sakai, M. Suetake, T. Tajima, T. Takahashi, S. Takano, Y. Takeuchi, Y. Yamamoto, Y. Yamazaki, M. Yoshida, S.-i. Yoshimoto, and K. Yoshino, "Performance and Operation Results of the RF Systems for the KEK B-Factory," *Progress of Theoretical and Experimental Physics*, vol. 2013, 03 2013. 03A006.

[38] D. Boer *et al.*, "Gluons and the quark sea at high energies: Distributions, polarization, tomography," *arXiv preprint arXiv:1108.1713*, 2011.

[39] E. C. Aschenauer, S. Fazio, J. H. Lee, H. Mantysaari, B. S. Page, B. Schenke, T. Ullrich, R. Venugopalan, and P. Zurita, "The Electron-Ion Collider: Assessing the Energy Dependence of Key Measurements," *arXiv preprint arXiv:1708.01527*, 2017.

[40] "Generic Detector R&D for an Electron Ion Collider," 2011 - 2018. `https://wiki.bnl.gov/conferences/index.php/EIC_R%25D`.

[41] R. L. Jaffe and A. Manohar, "The G(1) Problem: Fact and Fantasy on the Spin of the Proton," *Nucl. Phys.*, vol. B337, pp. 509–546, 1990.

[42] E.-C. Aschenauer *et al.*, "The RHIC SPIN Program: Achievements and Future Opportunities," *arXive preprint arXive:1501.01220*, 2015.

[43] E. C. Aschenauer, R. Sassot, and M. Stratmann, "Unveiling the Proton Spin Decomposition at a Future Electron-Ion Collider," *Phys. Rev.*, vol. D92, no. 9, p. 094030, 2015.

[44] E. C. Aschenauer, I. Borsa, G. Lucero, A. S. Nunes, and R. Sassot, "Revisiting Helicity Parton Distributions at a Future Electron-Ion Collider," 7 2020.

[45] E. C. Aschenauer, R. Sassot, and M. Stratmann, "Helicity Parton Distributions at a Future Electron-Ion Collider: A Quantitative Appraisal," *Phys. Rev.*, vol. D86, p. 054020, 2012.

[46] D. Boer and P. J. Mulders, "Time reversal odd distribution functions in leptoproduction," *Phys. Rev.*, vol. D57, pp. 5780–5786, 1998.

[47] L. Zheng, E. C. Aschenauer, J. H. Lee, B.-W. Xiao, and Z.-B. Yin, "Accessing the Gluon Sivers Function at a future Electron-Ion Collider," *arXive preprint arXive:1805.05290*, 2018.

[48] D. W. Sivers, "Hard scattering scaling laws for single spin production asymmetries," *Phys. Rev.*, vol. D43, pp. 261–263, 1991.

[49] D. W. Sivers, "Single Spin Production Asymmetries from the Hard Scattering of Point-Like Constituents," *Phys. Rev.*, vol. D41, p. 83, 1990.

[50] J. Cammarota, L. Gamberg, Z.-B. Kang, J. A. Miller, D. Pitonyak, A. Prokudin, T. C. Rogers, and N. Sato, "Origin of single transverse-spin asymmetries in high-energy collisions," *Phys. Rev. D*, vol. 102, no. 5, p. 054002, 2020.

[51] D. Boer, C. Lorcé, C. Pisano, and J. Zhou, "The gluon Sivers distribution: status and future prospects," *Adv. High Energy Phys.*, vol. 2015, p. 371396, 2015.

[52] D. Müller, D. Robaschik, B. Geyer, F. M. Dittes, and J. Hořejši, "Wave functions, evolution equations and evolution kernels from light ray operators of QCD," *Fortsch. Phys.*, vol. 42, pp. 101–141, 1994.

[53] A. V. Radyushkin, "Scaling limit of deeply virtual Compton scattering," *Phys. Lett.*, vol. B380, pp. 417–425, 1996.

[54] X.-D. Ji, "Deeply virtual Compton scattering," *Phys. Rev.*, vol. D55, pp. 7114–7125, 1997.

[55] X.-D. Ji, "Gauge invariant decomposition of nucleon spin," *Phys. Rev. Lett.*, vol. 78, pp. 610–613, 1997.

[56] E.-C. Aschenauer, S. Fazio, K. Kumericki, and D. Mueller, "Deeply Virtual Compton Scattering at a Proposed High-Luminosity Electron-Ion Collider," *JHEP*, vol. 09, p. 093, 2013.

[57] P. Barry, N. Sato, W. Melnitchouk, and C.-R. Ji, "First Monte Carlo Global QCD Analysis of Pion Parton Distributions," *Phys. Rev. Lett.*, vol. 121, no. 15, p. 152001, 2018.

[58] J. Sullivan, "One pion exchange and deep inelastic electron - nucleon scattering," *Phys. Rev. D*, vol. 5, pp. 1732–1737, 1972.

[59] A. C. Aguilar *et al.*, "Pion and Kaon Structure at the Electron-Ion Collider," *Eur. Phys. J. A*, vol. 55, no. 10, p. 190, 2019.

[60] F. Gelis, E. Iancu, J. Jalilian-Marian, and R. Venugopalan, "The Color Glass Condensate," *Ann. Rev. Nucl. Part. Sci.*, vol. 60, pp. 463–489, 2010.

[61] L. Zheng, E. C. Aschenauer, J. H. Lee, and B.-W. Xiao, "Probing Gluon Saturation through Dihadron Correlations at an Electron-Ion Collider," *Phys. Rev.*, vol. D89, no. 7, p. 074037, 2014.

[62] K. J. Eskola, P. Paakkinen, H. Paukkunen, and C. A. Salgado, "EPPS16: Nuclear parton distributions with LHC data," *Eur. Phys. J.*, vol. C77, no. 3, p. 163, 2017.

[63] A. H. Mueller and J.-W. Qiu, "Gluon Recombination and Shadowing at Small Values of x," *Nucl. Phys.*, vol. B268, p. 427, 1986.

[64] E. C. Aschenauer, S. Fazio, M. A. C. Lamont, H. Paukkunen, and P. Zurita, "Nuclear Structure Functions at a Future Electron-Ion Collider," *Phys. Rev.*, vol. D96, no. 11, p. 114005, 2017.

[65] X. Chu, E.-C. Aschenauer, J.-H. Lee, and L. Zheng, "Photon structure studied at an Electron Ion Collider," *arXive preprint arXive:1705.08831*, 2017.

[66] B. Page, X. Chu, and E. Aschenauer, "Experimental Aspects of Jet Physics at a Future EIC," *Phys. Rev. D*, vol. 101, no. 7, p. 072003, 2020.

[67] M. Arratia, Y. Song, F. Ringer, and B. Jacak, "Jets as precision probes in electron-nucleus collisions at the Electron-Ion Collider," *Phys. Rev. C*, vol. 101, no. 6, p. 065204, 2020.

[68] X. Liu, F. Ringer, W. Vogelsang, and F. Yuan, "Lepton-jet Correlations in Deep Inelastic Scattering at the Electron-Ion Collider," *Phys. Rev. Lett.*, vol. 122, no. 19, p. 192003, 2019.

[69] I. Vitev, "Radiative processes and jet modification at the EIC," in *Probing Nucleons and Nuclei in High Energy Collisions: Dedicated to the Physics of the Electron Ion Collider*, pp. 244–247, 2020.

[70] J. Blumlein, "The Theory of Deeply Inelastic Scattering," *Prog. Part. Nucl. Phys.*, vol. 69, pp. 28–84, 2013.

[71] S. Chekanov *et al.*, "Leading proton production in deep inelastic scattering at HERA," *JHEP*, vol. 06, p. 074, 2009.

[72] S. Roesler, R. Engel, and J. Ranft, "The Monte Carlo event generator DPMJET-III," in *Advanced Monte Carlo for radiation physics, particle transport simulation and applications. Proceedings, Conference, MC2000, Lisbon, Portugal, October 23-26, 2000*, pp. 1033–1038, 2000.

[73] L. Zheng, E. C. Aschenauer, and J. H. Lee, "Determination of electron-nucleus collision geometry with forward neutrons," *Eur. Phys. J.*, vol. A50, no. 12, p. 189, 2014.

[74] G. R. Young *et al.*, "The 0-degree calorimeter for the relativistic heavy ion experiment WA80 at CERN," *Nucl. Instrum. Meth.*, vol. A279, pp. 503–517, 1989.

[75] Zero-degree High-Precision Hadronic Calorimetry, `https://wiki.bnl.gov/conferences/images/9/97/ZDC-2014-EIC-RD_2.pdf`.

[76] F. D. Aaron *et al.*, "Determination of the Integrated Luminosity at HERA using Elastic QED Compton Events," *Eur. Phys. J.*, vol. C72, p. 2163, 2012. [Erratum: Eur. Phys. J.C74,2733(2012)].

[77] H1 Luminosity Monitor, `http://www-h1.desy.de/h1/www/h1det/lumi/`.

[78] Zeus Luminosity Monitor, `http://www-zeus.desy.de/zeus_det_papers/zeus_det_papers.html`.

[79] `http://www.desy.de/~pol2000/Welcome.html`.

[80] `https://wiki.bnl.gov/rhicspin/Polarimetry`.

[81] Workshop on Opportunities for Polarized He-3 in RHIC and EIC, `https://indico.bnl.gov/conferenceDisplay.py?ovw=True&confId=405`.

[82] "CESR operating parameters." `https://www.classe.cornell.edu/Research/CESR/OperatingParameters.html`.

[83] E. D. Bloom *et al.*, "The PEP-II asymmetric B factory: Design details and R & D results," in *4th European Particle Accelerator Conference (EPAC 94) London, England, June 27-July 1, 1994*, vol. C940627, pp. 464–466, 1994.

[84] J. Seeman *et al.*, "Performance of the PEP-II B-Factory collider at SLAC," in *Proceedings, Particle Accelerator Conference, PAC'05, Knoxville, USA, May 16-20, 2005*, vol. C0505161, p. 2369, 2005.

[85] K. Oide, "KEKB B-factory, the luminosity frontier," *Prog. Theor. Phys.*, vol. 122, pp. 69–80, 2009.

[86] S. Peggs, "Vertical emittance control," *CESR CBN-81-26*, 1981.

[87] T. Roser *et al.*, "Configuration manual polarized proton collider at RHIC." `https://www.bnl.gov/cad/accelerator/docs/pdf/RHICPPCMan.pdf`, 2006.

[88] G. Wei *et al.*, "Evaluation and compensation of detector solenoid effects in the JLEIC," *IPAC 16*, 2016.

[89] J. Beebe-Wang, ed., *Electron Ion Collider eRHIC Pre-Conceptual Design Report*. No. BNL-211943-2019-FORE, Brookhaven National Laboratory, 2019.

[90] D. Sagan and D. Rubin, "Linear analysis of coupled lattices," *PRAB*, vol. 2, no. 074001, 1999.

[91] S. Peggs, "The projection approach to solenoid compensation," *CERN/SPS/82-2*, 1982.

[92] A. Kondratenko *et al.*, "Impact of the tilted detector solenoid on the ion polarization at JLEIC," *J. Phys.: Conf. Ser. 938 012021*, 2017.

[93] G. Wei *et al.*, "Integration of the full-acceptance detector into JLEIC," *IPAC 17*, 2017.

[94] V. Morozov *et al.*, "Full acceptance interaction region design of JLEIC," *IPAC 19*, 2019.

[95] G. Wei *et al.*, "Complete beam dynamics of the JLEIC ion collider ring including imperfections, corrections, and detector solenoid effects," *NAPAC 16*, 2016.

[96] S. Peggs and S. Tepikian, "Roll misalignments and skew errors of IR triplet quads," *RHIC/AP/11*, 1993.

[97] M. Bassetti, M. Biagini, and C. Biscari, "Solenoidal field compensation," *ICFA beam dynamics workshop 14*, 1997.

[98] S. Peggs, "Coupling and decoupling in storage rings," *PAC 83*, 1983.

[99] E. Achenauer and H. Witte, "EIC detector solenoid parameters." Private communication.

[100] R. Brown *et al.*, "The STAR detector magnet subsystem," *PAC 97*, 1997.

[101] S. Peggs, "Skew quad compensation in a mini-beta lumionstiy lattice," *CESR CBN-81-17*, 1981.

[102] S. Peggs, "Practical details of CLEO solenoid compensation," *CESR CBN-81-24*, 1981.

[103] "SynRad+ is part of the MolFlow+ code from CERN, which traces photons to calculate flux and power distribution on a surface caused by synchrotron radiation."

[104] EicRoot simulation framework, `http://svn.racf.bnl.gov/svn/eic/eicroot`.

[105] Z. Tu, A. Jentsch, M. Baker, L. Zheng, J.-H. Lee, R. Venugopalan, O. Hen, D. Higinbotham, E.-C. Aschenauer, and T. Ullrich, "Probing short-range correlations in the deuteron via incoherent diffractive J/ψ production with spectator tagging at the EIC," 5 2020.

[106] T. Abe *et al.*, "Beam operation with crab cavities at KEKB," in *Proceedings, 22nd Particle Accelerator Conference, PAC'07, Albuquerque, USA, June 25-29, 2007*, vol. C070625, p. 1487, 2007.

[107] K. Akai *et al.*, "Commissioning and Beam Operation of KEKB Crab RF System," in *RF superconductivity. Proceedings, 13th International Workshop, SRF 2007, Beijing, China, October 14-19, 2007*, 2007.

[108] P. Baudrenghien, A. Macpherson, R. Calaga, V. Parma, E. Jensen, E. Montesinos, O. Capatina, and K. Brodzinski, "Functional Specifications of the LHC Prototype Crab Cavity System," Tech. Rep. CERN-ACC-NOTE-2013-003, 2013.

[109] G. Bassi, A. Blednykh, and V. Smaluk, "Self-consistent simulations and analysis of the coupled-bunch instability for arbitrary multibunch configurations," *Phys. Rev. Accel. Beams*, vol. 19, no. 2, p. 024401, 2016.

[110] W. Bruns, `http://www.gdfidl.de`.

[111] K. L. F. Bane and M. Sands, "The Short-Range Resistive Wall Wakefields," *AIP Conf. Proc.*, vol. 367, pp. 131–149, 1996.

[112] Piwinski, A, "Beam losses and lifetime," in *CERN Accelerator School*, CERN, 1985.

[113] C. Montag *et al.*, "Overview of the eRHIC Ring-Ring Design," in *Proceedings, 8th International Particle Accelerator Conference (IPAC 2017): Copenhagen, Denmark, May 14-19, 2017*, p. WEPIK049, 2017.

[114] S. Khan, unpublished.

[115] S. Agostinelli *et al.*, "GEANT4: A Simulation toolkit," *Nucl. Instrum. Meth.*, vol. A506, pp. 250–303, 2003.

[116] G. Voutsinas *et al.*, "FCC-ee interaction region backgrounds," *Int. J. Mod. Phys. A*, vol. 35, no. 15n16, p. 2041009, 2020.

[117] A. Abada *et al.*, "FCC-ee: The Lepton Collider: Future Circular Collider Conceptual Design Report Volume 2," *Eur. Phys. J. ST*, vol. 228, no. 2, pp. 261–623, 2019.

[118] P. Lewis *et al.*, "First Measurements of Beam Backgrounds at SuperKEKB," *Nucl. Instrum. Meth. A*, vol. 914, pp. 69–144, 2019.

[119] S. Peggs *et al.*, "Preparing optics for dual-rigidity tracking and simulation in the HSR." Unpublished memo, October 2020.

[120] F. Meot and G. Robert-Demolaize, "Radial-Offset Optics in EIC Hadron Lattices. Trajectory Lengthening," Tech. Rep. EIC-ADD-TN-006, BNL, 2020.

[121] H. Lovelace *et al.*, "Radial shift lattice design using bmad toolkit," Tech. Rep. EIC-ESR-TN-010, BNL, 2020.

[122] D. Bruno, "RHIC dipole corrector power supply performance limits." Private communication, November 2020.

[123] F. Meot, "The ray-tracing code Zgoubi - status," *NIM Physics Research A*, vol. 767, pp. 112–125, 2014.

[124] X. Gu *et al.*, "RHIC Au-Au Operation at 100 GeV in Run 16," in *Proceedings, NAPAC'16, 2016*, 2016.

[125] Y. Luo *et al.*, "Calculation of particle loss maps for 2016 RHIC gold-gold run," in *Proceedings, IPAC'17, 2017*, 2017.

[126] Y. Luo *et al.*, "Symplectic and exact tracking of low energy 197Au178+ ions in RHIC," in *Proceedings, IPAC'19, 2019*, 2019.

[127] G. Robert-Demolaize *et al.*, "Off-momentum optics correction in RHIC," in *Proceedings, NAPAC'19, 2019*, 2019.

[128] T. Satogata, K. Brown, E Pilat, A. Alai Tafti, S. Tepikian, J. van Zeijts, "The RHIC/AGS Online Model Environment: Design and Overview," *Proceedings of the 1999 Particle Accelerator Conference*, March 1999.

[129] D. Sagan, "Bmad: A relativistic charged particle simulation library," *Nucl. Instrum. Meth.*, vol. A558, no. 1, pp. 356–359, 2006. Proceedings of the 8th International Computational Accelerator Physics Conference.

[130] Accelerator Division, *RHIC:relativistic hadron ion collider configuration manual*. Collider-Accelerator Department, Upton,NY, 4 ed., November 2006.

[131] Y. Luo, S.Tepikian, W.Fischer, G.Robert-Demolaize, D.Trbojevic, "Sorting Chromatic Sextupoles for Easily and Effectively Correcting Second Order Chromaticity in the Relativistic Heavy Ion Collider," Tech. Rep. 248, Brookhaven National Laboratory, Upton,NY, January 2009. BNL-81976-2009-IR.

[132] M. Harrison, S. Peggs, and T. Roser, "The RHIC Accelerator," *Annu. Rev. Nucl. Part. Sci.*, 2002.

[133] H. Hahn, E. Forsyth, H. Foelsche, M. Harrison, J. Kewisch, G. Parzen, S. Peggs, E. Raka, A. Ruggiero, A. Stevens, S. Tepikian, P. Thieberger, D. Trbojevic, J. Wei, E. Willen, S. Ozaki, S.Y. Lee, "The RHIC design overview," *Nuclear Instruments and Methods in Physics Research*, vol. A, no. 499, pp. 245–263, 2003.

[134] J. Bengtsson, "The Sextupole Scheme for the Swiss Light Source (SLS): An Analytic Approach," Tech. Rep. 9, Paul Scherrer Institut (PSI), Villegen, Switzerland, March 1997.

[135] H. Huang *et al.*, "Overcoming depolarizing resonances with dual helical partial siberian snakes," *Phys. Rev. Lett.*, vol. 99, p. 154801, 2007.

[136] H. Huang *et al.*, "Overcoming horizontal depolarizing resonances with multiple tune jumps," *Phys. Rev. ST Accel. Beams*, vol. 17, no. 8, p. 081001, 2014.

[137] C. Gardner *et al.*, "Increasing the AGS Beam Polarization with 80 Tune Jumps," *Conf. Proc. C*, vol. 1205201, pp. 1015–1019, 2012.

[138] H. Huang *et al.*, "Overcoming depolarizing resonances in the AGS with two helical partial Siberian snakes," pp. 748–750, 2007.

[139] N. Tsoupas, H. Huang, W. MacKay, F. Méot, T. Roser, and D. Trbojevic, "BNL alternating gradient synchrotron with four helical magnets to minimize the losses of the polarized proton beam," *Phys. Rev. ST Accel. Beams*, vol. 16, no. 4, p. 043501, 2013.

[140] N. T. A. U. Luccio, N. Malitksy, "Focusing of the AGS Cold Snake," Tech. Rep. C-A/AP/248, BNL, 2006.

[141] H. Huang *et al.*, "AGS Polarized Proton Operation Experience in RHIC Run17," in *8th International Particle Accelerator Conference*, p. TUPVA149, 2017.

[142] C. Gardner *et al.*, "Operation of the RHIC Injector Chain with Ions from EBIS," in *6th International Particle Accelerator Conference*, p. THPF046, 2015.

[143] N. Tsoupas *et al.*, "Lowering the RHIC-Injection Lambertson Septum magnet to reduce the strength of the RHIC Injection Kickers," Tech. Rep. EIC Technical Note, EIC.

[144] J. Alessi, D. Barton, E. Beebe, D. Gassner, *et al.*, "Electron Beam Ion Source Preinjector Project (EBIS) Conceptual Design Report," Tech. Rep. BNL-73700-2005-IR, Brookhaven National Laboratory, 2005.

[145] A. Nikiel-Osuchowska, G. Collier, B. Głowacz, T. Pałasz, Z. Olejniczak, W. P. Węglarz, G. Tastevin, P.-J. Nacher, and T. Dohnalik, "Metastability exchange optical pumping of ^{3}He gas up to hundreds of millibars at 4.7 Tesla," *The European Physical Journal D*, vol. 67, no. 9, p. 200, 2013.

[146] D. M. Hardy, R. J. Spiger, S. D. Baker, Y. S. Chen, and T. A. Tombrello, "Polarization in ^{3}He+^{4}He elastic scattering," *Phys. Lett.*, vol. 31B, pp. 355–357, 1970.

[147] D. M. Hardy, R. J. Spiger, S. D. Baker, Y. S. Chen, and T. A. Tomberllo, "Scattering of ^{3}He and ^{4}He from polarized ^{3}He between 7 and 18 MeV," *Nucl. Phys.*, vol. A195, pp. 250–256, 1972.

[148] V. I. Ptitsyn, Yu. M. Shatunov, and S. R. Mane, "Spin response formalism in circular accelerators," *Nucl. Instrum. Meth.*, vol. A608, pp. 225–233, 2009.

[149] A. Ropert, "Low emittance lattices," in *Advanced accelerator physics. Proceedings, 5th Course of the CERN Accelerator School, Rhodos, Greece, September 20-October 1, 1993. Vol. 1, 2*, pp. 147–166, 1993.

[150] S.-Y. Lee, *Accelerator physics*. World Scientific Publishing Company, 2011.

[151] V. Ptitsyn and T. Satogata, "RHIC orbit control," *MOPLE073*, 2002.

[152] A. Latina, J. Pfingstner, D. Schulte, E. Adli, F. Decker, and N. Lipkowitz, "Experimental demonstration of a global dispersion-free steering correction at the new linac test facility at SLAC," *Physical Review Special Topics-Accelerators and Beams*, vol. 17, no. 4, p. 042803, 2014.

[153] R. Assmann, P. Raimondi, G. Roy, and J. Wenninger, "Emittance optimization with dispersion free steering at LEP," *Physical Review Special Topics-Accelerators and Beams*, vol. 3, no. 12, p. 121001, 2000.

[154] S. R. Mane, Yu. M. Shatunov, and K. Yokoya, "Spin-polarized charged particle beams in high-energy accelerators," *Rept. Prog. Phys.*, vol. 68, pp. 1997–2265, 2005.

[155] C. Bernardini, G. F. Corraza, G. Di Giugno, G. Ghigo, R. Querzoli, J. Haissinski, P. Marin, and B. Touschek, "Lifetime and beam size in a storage ring," *Phys. Rev. Lett.*, vol. 10, pp. 407–409, 1963.

[156] S. Seletskiy and A. Drees, "Electron Ion Collider Machine Protection System: requirements for an Electron Storage Ring abort system," Tech. Rep. unpublished, BNL, 2020.

[157] S. Seletskiy, A. Drees, A. Blednykh, G. Robert-Demolaize, T. Shrey, and M. Valette, "Electron Ion Collider Machine Protection System: on the necessity of the MPS abort system for Rapid Cycling Synchrotron," Tech. Rep. unpublished, BNL, 2020.

[158] V. Ranjbar, M. Blaskiewicz, F. Méot, C. Montag, S. Tepikian, S. Brooks, H. Witte, I. Marneris, V. Ptitsyn, and F. Willeke, "Spin resonance free electron ring injector," *Phys. Rev. Accel. Beams*, vol. 21, no. 11, p. 111003, 2018.

[159] P. A. Adderley, J. Clark, J. Grames, J. Hansknecht, K. Surles-Law, D. MacHie, M. Poelker, M. L. Stutzman, and R. Suleiman, "Load-locked dc high voltage GaAs photogun with an inverted-geometry ceramic insulator," *Physical Review Special Topics - Accelerators and Beams*, vol. 13, no. 1, 2010.

[160] D. Schultz, R. Alley, H. Aoyagi, J. Clendenin, J. Frisch, C. Garden, E. Hoyt, R. Kirby, L. Klaisner, A. Kulikov, G. Mulhollan, C. Prescott, P. Saez, H. Tang, J. Turner, M. Woods, D. Yeremian, and M. Zolotorev, "The high peak current polarized electron source of the Stanford Linear Collider," *Nuclear Inst. and Methods in Physics Research, A*, vol. 340, pp. 127–132, feb 1994.

[161] J. Grames, P. Adderley, J. Brittian, J. Clark, J. Hansknecht, D. Machie, M. Poelker, M. Stutzman, K. Surles-Law, and E. Pozdeyev, "A biased anode to suppress ion back-bombardment in a DC high voltage photoelectron gun," *AIP Conf. Proc.*, vol. 980, pp. 110–117, 2008.

[162] C. Hernandez-Garcia, M. Poelker, and J. Hansknecht, "High voltage studies of inverted-geometry ceramic insulators for a 350 kV DC polarized electron gun," *IEEE Transactions on Dielectrics and Electrical Insulation*, vol. 23, pp. 418–427, February 2016.

[163] J. Clendenin, R. Alley, H. Aoyagi, J. Frisch, C. Garden, E. Hoyt, R. Kirby, L. Klaisner, A. Kulikov, C. Prescott, P. Saez, D. Schultz, H. Tang, J. Turner, M. Woods, A. Yeremian, and M. Zolotorev, "Performance of the SLC polarized electron source with high polarization," in *Proceedings of International Conference on Particle Accelerators*, (Washington, DC), pp. 2973–2975, IEEE, 1993.

[164] B. Bacha and others, "NSLS-II injector commissioning and initial operation," in *6th International Particle Accelerator Conference, IPAC 2015*, 2015.

[165] J. Y. Choi, O. Yujiro, E. Atsushi, S. I., O. Satoshi, and K. Takuya, "Bunching system of the KEKB linac," 1996.

[166] "Parmela." `http://www.pulsar.nl/gpt/`.

[167] S. Liu, M. Fukuda, S. Araki, N. Terunuma, J. Urakawa, K. Hirano, and N. Sasao, "Beam loading compensation for acceleration of multi-bunch electron beam train," *Nuclear Instruments and Methods in Physics Research Section A: Accelerators, Spectrometers, Detectors and Associated Equipment*, vol. 584, no. 1, pp. 1 – 8, 2008.

[168] N. Tsoupas, J. Glenn, H. Huang, W. MacKay, D. Raparia, and K. Zeno, "Matching the BtA line to the bare-AGS (Part 1)," Tech. Rep. BNL-99484-2013-IR, Brookhaven National Laboratory, 2008.

[169] N. Tsoupas, H. Foelsche, J. Claus, and R. Thern, "Closed orbit calculations at AGS and extraction beam parameters at H13," Tech. Rep. BNL-101857-2013-IR, Brookhaven National Laboratory, 1994.

[170] N. Tsoupas, W. Fischer, J. Kewisch, W. W. MacKay, S. G. Peggs, F. Pilat, S. Tepikian, and J. Wei, "Focusing and matching properties of the ATR transfer line," in *17th IEEE Particle Accelerator Conference (PAC 97): Accelerator Science, Technology and Applications Vancouver, British Columbia, Canada, May 12-16, 1997*, vol. C970512, pp. 222–224, 1997.

[171] V. Bargmann, L. Michel, and V. L. Telegdi, "Precession of the polarization of particles moving in a homogeneous electromagnetic field," *Phys. Rev. Lett.*, vol. 2, pp. 435–436, 1959.

[172] Y. Huang, H. Wang, R. A. Rimmer, S. Wang, and J. Guo, "Multiple harmonic frequencies resonant cavity design and half-scale prototype measurements for a fast kicker," *Phys. Rev. Accel. Beams*, vol. 19, no. 12, p. 122001, 2016.

[173] Y. Huang, H. Wang, R. A. Rimmer, S. Wang, and J. Guo, "Ultrafast harmonic rf kicker design and beam dynamics analysis for an energy recovery linac based electron circulator cooler ring," *Phys. Rev. Accel. Beams*, vol. 19, no. 8, p. 084201, 2016.

[174] G.-T. Park, J. Guo, J. Henry, M. Marchlik, F. Marhauser, R. Rimmer, H. Wang, and S. Wang, "Status Update of a Harmonic Kicker Development for JLEIC," in *10th International Particle Accelerator Conference*, p. WEPRB099, 2019.

[175] G. Park, H. Wang, J. Guo, F. Marhauser, S. Wang, and R. Rimmer, "The design of an ultra-fast harmonic kicker," tech. rep., Jefferson Lab, 2019.

[176] G. Park, J. Guo, S. Wang, R. Rimmer, and H. Wang, "The Beam Exchange of a Circulator Cooler Ring with an Ultrafast Harmonic Kicker," tech. rep., Jefferson Lab.

[177] H. Zhao, J. Kewisch, M. Blaskiewicz, and A. Fedotov, "Ring-based Electron Cooler for EIC," Tech. Rep. BNL-220731-2020-TECH, Brookhaven National Laboratory, 2020.

[178] J. Kewisch, H. Zhao, M. Blaskiewicz, and A. Fedotov, "Design of Electron Storage Ring for High-Energy EIC Cooling," Tech. Rep. BNL-220732-2020-TECH, Brookhaven National Laboratory, 2020.

[179] Ya. S. Derbenev, "Coherent electron cooling. 1. Physics of the method in general," Tech. Rep. UM-HE-91-28, U. Mich., 1991.

[180] Y. Derbenev and V. Litvinenko, "FELs and high-energy electron cooling," in *Proceedings of the 2007 FEL Conference, Novosibirsk, Russia*, p. TUCAU01, 2007.

[181] G. Stupakov, "Microbunched electron cooling (MBEC) for future electron-ion colliders," in *Proceedings, 61st ICFA Advanced Beam Dynamics Workshop on High-Intensity and High-Brightness Hadron Beams (HB2018): Daejeon, Korea, 17-22 June, 2018*, p. WEA2WA02, 2018.

[182] G. Stupakov, "Cooling rate for microbunched electron cooling without amplification," *Phys. Rev. Accel. Beams*, vol. 21, p. 114402, Nov 2018.

[183] P. Baxevanis and G. Stupakov, "Diffusion and nonlinear plasma effects in microbunched electron cooling," in *Proceedings of the 2019 North American Particle Accelerator Conference (NAPAC19)*, (Lansing, Michigan), p. WEPLH17, 2019.

[184] P. Baxevanis and G. Stupakov, "Tolerances on energy deviation in microbunched electron cooling," in *Proceedings of the 2019 North American Particle Accelerator Conference (NAPAC19)*, (Lansing, Michigan), p. WEPLH16, 2019.

[185] G. Stupakov and P. Baxevanis, "Microbunched electron cooling with amplification cascades," *Phys. Rev. Accel. Beams*, vol. 22, p. 034401, Mar 2019.

[186] P. Baxevanis and G. Stupakov, "Transverse dynamics considerations for microbunched electron cooling," *Phys. Rev. Accel. Beams*, vol. 22, p. 081003, Aug 2019.

[187] G. Stupakov and P. Baxevanis, "3D Theory of Microbunched Electron Cooling for Electron-Ion Colliders," in *Proceedings, 10th International Particle Accelerator Conference: Melbourne, Australia, May 19-24, 2019*, p. 814, 2019.

[188] V. Litvinenko and G. Wang, "Relativistic effects in micro-bunching," in *Proceedings of the 2014 FEL Conference, Basel, Switzerland*, p. THP035, 2014.

[189] G. Stupakov, "Cooling Rate for Microbunched Electron Cooling without Amplification," Tech. Rep. SLAC-PUB-17208, SLAC, 2017.

[190] D. Ratner, "Microbunched Electron Cooling for Hadrons," in *ICFA Beam Dynamics Newsletter No. 65*, 2014.

[191] E. A. Schneidmiller and M. V. Yurkov, "Using the longitudinal space charge instability for generation of vacuum ultraviolet and x-ray radiation," *Phys. Rev. ST Accel. Beams*, vol. 13, p. 110701, 2010.

[192] M. Dohlus, E. A. Schneidmiller, and M. V. Yurkov, "Generation of attosecond soft x-ray pulses in a longitudinal space charge amplifier," *Phys. Rev. ST Accel. Beams*, vol. 14, p. 090702, 2011.

[193] A. Marinelli, E. Hemsing, and J. B. Rosenzweig, "Using the relativistic two-stream instability for the generation of soft-x-ray attosecond radiation pulses," *Phys. Rev. Lett.*, vol. 110, no. 6, p. 064804, 2013.

[194] V. Lebedev, "Optical Stochastic Cooling," *ICFA Beam Dyn. Newslett.*, vol. 65, pp. 100–116, 2014.

[195] K. Yokoya, "Resistive wall impedance of beam pipes of general cross-section," *Part. Accel.*, vol. 41, pp. 221–248, 1993.

[196] T. O. Raubenheimer and F. Zimmermann, "A fast beam-ion instability in linear accelerators and storage rings," *Phys. Rev.*, vol. E52, pp. 5487–5497, 1995.

[197] G. V. Stupakov, T. O. Raubenheimer, and F. Zimmermann, "Fast beam ion instability. 2. Effect of ion decoherence," *Phys. Rev.*, vol. E52, pp. 5499–5504, 1996.

[198] R. Nagaoka *et al.*, "Observations and analysis of fast beam-ion instabilities at SOLEIL," in *Proceedings, International Workshop on Linear Colliders 2010:(ECFA-CLIC-ILC Joint Meeting)*, 2010.

[199] R. Nagaoka, "Fast beam-ion instability." `https://www-bd.fnal.gov/icfabd/Newsletter62.pdf`, 2016.

[200] K. Ohmi, "Ion Instability in SuperKEKB Phase I Commissioning," in *Proc. IPAC 2017*, 2018. p. 3741, THPAB002.

[201] M. Blaskiewicz, "Beam-Beam Damping of the Ion Instability," in *Proc. NAPAC'19*, no. 4 in 3rd North American Particle Accelerator Conference, pp. 391–394, JACoW Publishing, Geneva, Switzerland, 10 2019. https://doi.org/10.18429/JACoW-NAPAC2019-TUPLM11.

[202] L. Wang, Y. Cai, T. O. Raubenheimer, and H. Fukuma, "Suppression of beam-ion instability in electron rings with multi-bunch train beam fillings," *Phys. Rev. ST Accel. Beams*, vol. 14, p. 084401, 2011.

[203] J.-M. Wang, "Modes of storage ring coherent instabilities," *AIP Conf. Proc.*, vol. 153, pp. 697–788, 1987.

[204] A. V. Burov and V. Lebedev, "Transverse Resistive Wall Impedance for Multi-Layer Round Chambers," in *8th European Particle Accelerator Conference (EPAC 2002)*, pp. 1452–1454, 6 2002.

[205] P. Zenkevich, O. Boine-Frankenheim, and A. Bolshakov, "A new algorithm for the kinetic analysis of intra-beam scattering in storage rings," *Nuclear Instruments and Methods in Physics Research Section A: Accelerators, Spectrometers, Detectors and Associated Equipment*, vol. 561, no. 2, pp. 284–288, 2006.

[206] Y. Cai, "Single-particle dynamics in electron storage rings with extremely low emittance," *Nucl. Instr. Meth. A*, vol. 645, p. 168, 2011.

[207] Y. Cai, "Symplectic Maps and Chromatic Optics in Particle Accelerators," *Nucl. Instr. Meth. A*, vol. 797, p. 172, 2015.

[208] Y. Cai, M. Donald, J. Irwin, and Y. Yan, "LEGO: A Modular Accelerator Design Code," tech. rep., Stanford Linear Accelerator Center, 1997.

[209] Y. Luo, "SimTrack: A compact C++ code for particle orbit and spin tracking in accelerators," *Nucl. Instrum. Meth.*, vol. A801, pp. 95–103, 2015.

[210] P. Baudrenghien and T. Mastoridis, "Transverse emittance growth due to rf noise in the high-luminosity lhc crab cavities," *Phys. Rev. ST Accel. Beams*, vol. 18, p. 101001, Oct 2015.

[211] E. D. Courant and R. D. Ruth, "The Acceleration of Polarized Protons in Circular Accelerators," Tech. Rep. BNL-51270, BNL, 1980.

[212] M. Froissart and R. Stora, "Depolarization of a polarized proton beam in a synchrotron," Tech. Rep. ANL-TRANS-570, ANL, 1968.

[213] L. H. Thomas, "The Kinematics of an electron with an axis," *Phil. Mag. Ser.7*, vol. 3, pp. 1–21, 1927.

[214] F. Méot, "The ray-tracing code zgoubi–status," *Nuclear Instruments and Methods in Physics Research Section A: Accelerators, Spectrometers, Detectors and Associated Equipment*, vol. 767, pp. 112–125, 2014.

[215] M. Bai, H. Huang, A. Marusic, M. G. Minty, V. Ptitsyn, and V. H. Ranjbar, "Experimental Effects of Orbit on Polarization Loss in RHIC," in *Proceedings, 3rd International Conference on Particle Accelerators (IPAC 2012): New Orleans, USA, May 2-25, 2012*, vol. C1205201, pp. 3788–3790, 2012.

[216] D. P. Barber, J. Kewisch, G. Ripken, R. Rossmanith, and R. Schmidt, "A Solenoid Spin Rotator for Large Electron Storage Rings," *Part. Accel.*, vol. 17, p. 243, 1985.

[217] J. Buon and K. Steffen, "HERA variable-energy "mini" spin rotator and head-on ep collision scheme with choice of electron helicity," *Nucl. Instrum. Meth.*, vol. A245, p. 248, 1986.

[218] V. Baier, V. Katkov, and V. Strakhovenko, "Kinetics of radiative polarization," *Sov. Phys. JETP*, vol. 31, p. 908, 1970.

[219] Ya. S. Derbenev and A. M. Kondratenko, "Polarization kinematics of particles in storage rings," *Sov. Phys. JETP*, vol. 37, pp. 968–973, 1973. [Zh. Eksp. Teor. Fiz.64,1918(1973)].

[220] J. Kewisch, *Depolarisation der Elektronenspins in Speicherringen durch nichtlineare Spin-Bahn-Kopplung*. PhD thesis, Hamburg Univ., 1985.

[221] F. Schmidt, E. Forest, and E. McIntosh, "Introduction to the polymorphic tracking code: Fibre bundles, polymorphic taylor types and exact tracking," 2002.

[222] Z. Duan. , Private communication, 2018.

[223] Y. Alexahin and E. Gianfelice-Wendt, "Determination of linear optics functions from TBT data," *JINST*, vol. 6, p. P10006, 2011.

[224] M. Bai *et al.*, "Polarized proton collisions at 205-GeV at RHIC," *Phys. Rev. Lett.*, vol. 96, p. 174801, 2006.

[225] L. A. Ahrens, Y. Dutheil, J. W. Glenn, H. Huang, F. Méot, T. Roser, V. Schoefer, and N. Tsoupas, "Modelling of the AGS Using Zgoubi — Status," *Conf. Proc.*, vol. C1205201, pp. 181–183, 2012.

[226] V. Ranjbar, "Calculating the polarization lifetime from the Thomas-Bargmann-Michel-Telegdi equation," *Phys. Rev. Accel. Beams*, vol. 22, no. 9, p. 091001, 2019.

[227] A. Zelenski, "Polarization measurements and absolute polarization values evolution during proton beam acceleration in the RHIC accelerator complex," *PoS*, vol. PSTP2013, p. 056, 2013.

[228] K. Hock *et al.*, "Intrinsic Resonances and AC-Dipole simulations of ^{3}He in the AGS-Booster," Tech. Rep. C-AD Tech Note 597, BNL, 2017.

[229] K. Hock *et al.*, "Overcoming proton and ^{3}He Intrinsic Resonances in the AGS Booster with an AC-dipole," Tech. Rep. C-AD Tech Note 601, BNL, 2018. `www.osti.gov/servlets/purl/1469789`.

[230] M. Bai, *Overcoming the He Intrinsic Spin Resonance by Using an RF Dipole*. PhD thesis, Indiana University, 1999.

[231] K. Hock, H. Huang, F. Méot, P. Oddo, N. Tsoupas, J. Tuozzolo, and K. Zeno, "Status of AC-Dipole Project at RHIC Injectors for Polarized Helions," in *9th International Particle Accelerator Conference*, p. TUPAF005, 2018.

[232] K. Hock *et al.*, "Status of AC Dipole Project at RHIC Injectors for Polarized ^{3}He, Update," in *10th International Particle Accelerator Conference*, p. TUPTS109, 2019.

[233] K. Hock, H. Huang, F. Méot, P. Oddo, and N. Tsoupas, "Scanning the AC Dipole Resonance Proximity Parameter in the AGS Booster," in *10th International Particle Accelerator Conference*, p. TUPTS110, 2019.

[234] R. Thern, "Booster Ring Correction Magnets," Tech. Rep. Booster Tech Note 226, BNL, 1994.

[235] V. H. Ranjbar, "Approximations for crossing two nearby spin resonances," *Phys. Rev. Accel. Beams*, vol. 18, no. 1, p. 014001, 2015.

[236] S. Y. Lee and L. G. Ratner, "Feasibility of a polarized deuteron beam in the AGS and RHIC," *Nucl. Instrum. Meth.*, vol. A306, pp. 51–55, 1991.

[237] E. D. Courant, "Possibilities of accelerating polarized D, ^{3}He and other ions in RHIC," Tech. Rep. AGS/RHIC/SN report 066, Brookhaven National Laboratory, 1997.

[238] H. Huang, F. Méot, V. Ptitsyn, V. Ranjbar, and T. Roser, "Polarization preservation of polarized deuteron beams in the electron ion collider at Brookhaven National Laboratory," *Phys. Rev. Accel. Beams*, vol. 23, no. 2, p. 021001, 2020.

[239] F. Méot, "An ergodic approach to polarization in eRHIC electron storage ring," tech. rep., Brookhaven National Laboratory, 2018.

[240] B. Parker, M. Anerella, J. Escallier, A. Ghosh, A. Jain, A. Marone, J. Muratore, and P. Wanderer, "Bnl direct wind superconducting magnets," *IEEE Transactions on Applied Superconductivity*, vol. 22, pp. 4101604–4101604, June 2012.

[241] B. Parker and J. Escallier, "Serpentine coil topology for bnl direct wind superconducting magnets," in *Proceedings of the 2005 Particle Accelerator Conference*, pp. 737–739, May 2005.

[242] B. Parker and Others, "Superconducting Corrector IR Magnet Production for SuperKEKB," in *1st North American Particle Accelerator Conference (NAPAC2013) Pasadena, CA, USA, September 29-October 4, 2013*, 2013.

[243] H. Witte, B. Parker, and R. Palmer, "Design of a Tapered Final Focusing Magnet for eRHIC," *IEEE Transactions on Applied Superconductivity*, vol. 29, pp. 1–5, aug 2019.

[244] D. Meyer and R. Flasck, "A new configuration for a dipole magnet for use in high energy physics applications," *Nuclear Instruments and Methods*, vol. 80, pp. 339–341, apr 1970.

[245] R. Meinke, C. Goodzeit, and M. Ball, "Modulated double-helix quadrupole magnets," *IEEE Transactions on Appiled Superconductivity*, vol. 13, pp. 1369–1372, jun 2003.

[246] H. Witte, T. Yokoi, S. L. Sheehy, K. Peach, S. Pattalwar, T. Jones, J. Strachan, and N. Bliss, "The Advantages and Challenges of Helical Coils for Small Accelerators – A Case Study," *IEEE Transactions on Applied Superconductivity*, vol. 22, pp. 4100110–4100110, apr 2012.

[247] S. Caspi, D. Arbelaez, L. Brouwer, S. Gourlay, S. Prestemon, and B. Auchmann, "Design of a Canted-Cosine-Theta Superconducting Dipole Magnet for Future Colliders," *IEEE Transactions on Applied Superconductivity*, vol. 27, pp. 1–5, jun 2017.

[248] B. Auchmann, L. Brouwer, S. Caspi, J. Gao, G. Montenero, M. Negrazus, G. Rolando, and S. Sanfilippo, "Electromechanical Design of a 16-T CCT Twin-Aperture Dipole for FCC," *IEEE Transactions on Applied Superconductivity*, vol. 28, pp. 1–5, apr 2018.

[249] L. Lalitha, "Conceptual Electromagnetic Design of the EIC Electron Spin Rotator Solenoid," Tech. Rep. JLab Internal Report, JLab, 2020.

[250] M. Wiseman *et al.*, "EIC SRS Solenoid Preliminary Cryostat Report," Tech. Rep. JLAB-EIC-)))))SRS-CRY-A001, JLab, 2020.

[251] W. Crahen *et al.*, "SRS Solenoid magnet magnetic and structural analysis," Tech. Rep. MEG0002020-A003 Rev -, LHC, 2020.

[252] R. Dixon, W. Markiewicz, and C. Swenson, "Mechanical properties of epoxy impregnated superconducting solenoids," July 1996.

[253] W. Rogowski, "Die Electrische Festigkeit am Rande des Plattenkondensators," *Archiv fur Elektrotechnik*, vol. XII. Band, no. 1. Heft, pp. 1–15, 1923.

[254] A. W. Chao and M. Tigner, eds., *Handbook of Accelerator Physics and Engineering*. World Scientific, 1999.

[255] "ANSYS is an engineering simulation and 3-D design software, that calculates the thermal and mechanical conditions."

[256] C. Foerster, C. Lanni, and K. Kanazawa, "Measurements of photon stimulated desorption from thick and thin oxide of kekb collider copper beam chambers and a stainless steel beam chamber," *Journal of Vacuum Science & Technology A: Vacuum, Surfaces, and Films*, vol. 19, no. 4, pp. 1652–1656, 2001.

[257] "MolFlow+ is a Monte-Carlo simulation code for ultrahigh vacuum systems with complex geometries and surface conditions." `www.molflow.web.cern.ch`.

[258] J. Jones, S. Sharma, D. Bromberek, and J. Howell, "APS SR flexible bellows shield performance," in *Proceedings, 1999 Particle Accelerator Conference (PAC'99): New York, New York, March 29-April 2, 1999*, pp. 3095–3097, 1999.

[259] N. R. Kurita, A. Kulikov, and J. Corlett, "Final Design and Manufacturing of the PEP II High Energy Ring Arc Bellows Module," *Conf. Proc.*, vol. C970512, p. 3639, 1997.

[260] H.-C. Hseuh, C. Hetzel, S. Leng, K. Wilson, H. Xu, and D. Zigrosser, "National synchrotron light source ii storage ring vacuum systems," *Journal of Vacuum Science & Technology A: Vacuum, Surfaces, and Films*, vol. 34, no. 3, p. 031603, 2016.

[261] Y. Suetsugu, K.-i. Kanazawa, K. Shibata, M. Shirai, A. E. Bondar, V. S. Kuzminykh, A. I. Gorbovsky, K. Sonderegger, M. Morii, and K. Kawada, "Development of bellows and gate valves with a comb-type rf shield for high-current accelerators: Four-year beam test at KEK B-factory," *Rev. Sci. Instrum.*, vol. 78, p. 043302, 2007.

[262] C. Herrera, "Eddy current effect in the AGS vacuum chamber," tech. rep., BNL, 1966. AGSCD Technical Note No. 49.

[263] A. Hershcovitch *et al.*, "Enhancing RHIC luminosity capabilities with in-situ beam pipe coating," in *Proceedings, Particle Accelerator Conference (PAC 2009): Vancouver, BC, Canada, 2009*, p. MO6RFP001, 2009.

[264] P. Cruikshank *et al.*, "Mechanical Design Aspects of the LHC Beam Screen," Tech. Rep. LHC Project Report 128, LHC, 1997.

[265] V. Baglin, "HL-LHC Vacuum System: Base line, layout & aperture, material, RF bridges," in *HL-LHC Vacuum System, WP2 meeting, CERN, 27 June 2017*, 2017.

[266] A.W. Chao, *Physics of collective beam instabilities in high-energy accelerators*. John Wiley & Sons, 1993.

[267] R. T. Avery, A. Faltens, and E. C. Hartwig, "Non-Intercepting Monitor of Beam Current and Position," in *Proc. of the 4th Particle Accelerator Conference, Chicago, IL (IEEE, Piscataway, NJ, 1971*, 1971.

[268] A. Piwinski, "Wakefields and ohmic losses in round vacuum chambers," Tech. Rep. DESY HERA 92-11, HERA, 1992.

[269] N. J. Simon, E. S. Drexler, and R. P. Reed, "Properties of Copper and Copper Alloys at Cryogenic Temperatures," *NIST Monograph 177*, 1992.

[270] N. Wang and Q. Qin, "Resistive-wall impedance of two-layer tube," *Phys. Rev. ST Accel. Beams 10, 111003*, 2007.

[271] F. Bloch, "Zum elektrischen Widerstandsgesetz bei tiefen Temperaturen [Electrical resistance law for low temperatures]," *Zeitschrift fur Physik (in German) 59 (3-4)*, 1930.

[272] E. Gruneisen, "Die Abhangigkeit des elektrischen Widerstandes reiner Metalle von der Temperatur [The temperature dependence of electrical resistance in pure metals]," *Annalen der Physik (in German), 408 (5)*, 1933.

[273] M. Deutsch, "An accurate analytic representation for the Bloch-Gruneisen integral," *Journal of Physics A: Mathematical and General, 20 (13)*, 1987.

[274] U. Iriso and S. G. Peggs, "Maps for electron clouds," *Phys. Rev. ST Accel. Beams, vol. 8, p. 024403*, 2005.

[275] U. Iriso and S. G. Peggs, "Maps for coupled electron and ion clouds in accelerators," *Phys. Rev. ST Accel. Beams, vol. 9, p. 071002*, 2006.

[276] W. Fischer *et al.*, "Electron cloud observations and cures in the Relativistic Heavy Ion Collider," *Phys. Rev. ST Accel. Beams, vol. 11, p. 041002*, 2008.

[277] C. Benvenuti, P. Chiggiato, F. Cicoira, and Y. L'Aminot, "Nonevaporable getter films for ultrahigh vacuum applications," *Journal of Vacuum Science & Technology A: Vacuum, Surfaces, and Films*, vol. 16, no. 1, pp. 148–154, 1998.

[278] G. Iadarola, *Electron cloud studies for CERN particle accelerators and simulation code development*. PhD thesis, Universita degli Studi di Napoli Federico I, 2014.

[279] A. Romano, *Electron cloud formation in CERN particle accelerators and its impact on the beam dynamics*. PhD thesis, TU Damstadt and Universitat Rostock, 2018.

[280] G. Iadarola *et al.*, "Electron cloud studies for the upgrade of the CERN PS," Tech. Rep. CERN-ACC-2013-0095, CERN, 2013.

[281] Y. Ji *et al.*, "Secondary electron yield measurement and electron cloud simulation at Fermilab," in *Proc. of IPAC2015, Richmond, VA, USA, MOPMA039*, 2015.

[282] V. Petit *et al.*, "In-situ SEY measurements at the SPS." `https://indico.cern.ch/event/772318/contributions/3209167`.

[283] R. Salemme *et al.*, "Vacuum Performance of Amorphous Carbon Coating at Cryogenic Temperature with Presence of Proton Beams," in *Proc. of IPAC2016, Busan, Korea, 2016*, 2016.

[284] J. Beebe-Wang, ed., *Electron Ion Collider eRHIC Pre-Conceptual Design Report*. Brookhaven National Laboratory Formal Report, BNL-211943-2019-FORE, 2019.

[285] B. Henrist *et al.*, "The secondary electron yield of TiZr and TiZrV non-evaporable getter thin film coatings," *Appl. Surf. Sci. 172, 1-2, pp. 95 –102*, 2001. `https://doi.org/10.1016/S0169-4332(00)00838-2`.

[286] G. Lopez, "Temperature rise in the beam tube during quench due to eddy currents and related effects," Tech. Rep. SSCL-295, CERN, 1990. `https://lss.fnal.gov/archive/other/ssc/sscl-295.pdf`.

[287] R. Salemme, V. Baglin, G. Bregliozzi, P. Chiggiato, and R. Kersevan, "Amorphous Carbon Coatings at Cryogenic Temperatures with LHC Type Beams: First Results with the COLDEX Experiment," in *6th International Particle Accelerator Conference*, p. WEPHA007, 2015.

[288] M. Taborelli, "E-cloud: where are we?." LIU Day, CERN, Geneva, Switzerland, 2010. `https://indico.cern.ch/event/112934/`.

[289] C. Yin Vallgren *et al.*, "Amorphous carbon coatings for the mitigation of electron cloud in the CERN Super Proton Synchrotron," *Phys. Rev. ST Accel. Beams*, vol. 14, p. 071001, 2011.

[290] M. Van Gompel, P. Chiggiato, P. Costa Pinto, P. Cruikshank, C. Pasquino, J. Perez Espinos, A. Sapountzis, M. Taborelli, and W. Vollenberg, "Amorphous Carbon Thin Film Coating of the SPS Beamline: Evaluation of the First Coating Implementation," in *Proceedings, 8th International Particle Accelerator Conference (IPAC 2017): Copenhagen, Denmark, May 14-19, 2017*, p. MOOCA3, 2017.

[291] Y. Ji, *Electron Cloud Studies at Fermilab*. PhD thesis, Illinois Institute of Technology, Dec. 2019.

[292] M. Angelucci, A. Novelli, L. Spallino, A. Liedl, R. Larciprete, and R. Cimino, "Minimum thickness of carbon coating for multipacting suppression," *Phys. Rev. Res.*, vol. 2, no. 3, p. 032030, 2020.

[293] P. C.-P. others, "Carbon coatings with low secondary electron yield," *Vacuum*, vol. 98, pp. 29–36, 2013.

[294] M. Rhoades-Brown and M. Harrison, "Vacuum requirements for RHIC," 12 1991.

[295] A. K. V.V. Anashin, R.V. Dostovalov, "The vacuum studies for LHC beam screen with carbon fiber cryosorber," in *Proc. of APAC 2004, Gyeongju, Korea (2004)*, 2004. `https://accelconf.web.cern.ch/a04/PAPERS/TUP13004.PDF`.

[296] M. Taborelli *et al.*, "Nine years of carbon coating development for the SPS upgrade: achievements and heritage," Tech. Rep. CERN-ACC-2016-0010, CERN, 2016.

[297] P. Costa-Pinto. Private Communication, May 15, 2020, 2020.

[298] P. Costa Pinto, S. Calatroni, P. Chiggiato, P. Edwards, M. Mensi, H. Neupert, M. Taborelli, and C. Yin-Vallgren, "Carbon coating of the SPS dipole chambers," *Conf. Proc. C*, vol. 1206051, pp. 141–148, 2013.

[299] N. Bundaleski, S. Candeias, A. Santos, O. Teodoro, and A. Silva, "Study of SEY degradation of amorphous carbon coatings," *Conf. Proc. C*, vol. 1206051, pp. 149–152, 2013.

[300] S.-H. Kim, J. Carwardine, Z. Conway, G. Decker, M. Kelly, B. Mustapha, P. Ostroumov, and G. Waldschmidt, "Higher Order Mode Damping in a Higher Harmonic Cavity for the Advanced Photon Source Upgrade," in *Proceedings, 17th International Conference on RF Superconductivity (SRF2015): Whistler, Canada, September 13-18, 2015*, p. THPB072, 2015.

[301] W. Xu, Z. Altinbas, S. Belomestnykh, I. Ben-Zvi, M. Cole, S. Deonarine, M. Falletta, J. Jamilkowski, D. Gassner, P. Kankiya, *et al.*, "Design, simulations, and conditioning of 500 kw fundamental power couplers for a superconducting rf gun," *Physical Review Special Topics-Accelerators and Beams*, vol. 15, no. 7, p. 072001, 2012.

[302] H. P. Kindermann and M. Stirbet, "The variable power coupler for the LHC superconducting cavity," in *Accelerator Technology for the 21st Century: Proceedings, 9th Workshop on RF Superconductivity (SRF 1999): Santa Fe, New Mexico, November 1-5, 1999*, 2000.

[303] J. Brennan, A. Campbell, S. Kwiatkowski, J. Rose, W. Pirkl, and A. Ratti, "RHIC 28 MHz Accelerating Cavity System," in *Proceedings Particle Accelerator Conference, PAC 2001, Chicago, USA, June 18-22, 2001*, vol. C0106181, pp. 840–842, 2001.

[304] M. Blaskiewicz, J. M. Brennan, J. Butler, J. DeLong, W. Fischer, and T. Hayes, "RF Techniques for Improved Luminosity at RHIC," in *9th European Particle Accelerator Conference (EPAC 2004) Lucerne, Switzerland, July 5-9, 2004*, 2004.

[305] R. Garoby, "RF Gymnastics in Synchrotrons," in *Proceedings, CAS - CERN Accelerator School: RF for Accelerators, Ebeltoft, Denmark, 8 - 17 Jun 2010*, 2011.

[306] L. A. Ahrens *et al.*, "High intensity performance of the Brookhaven AGS," in *Proceedings, 1999 Particle Accelerator Conference (PAC'99): New York, New York, March 29-April 2, 1999*, vol. C990329, pp. 614–616, 1999.

[307] C. Gardner, "Simulation of 6 to 2 to 1 merge and squeeze of Au77+ bunches in AGS," Tech. Rep. BNL-112197-2016-IR, Brookhaven National Laboratory, 2016.

[308] K. Zeno, "Overview and analysis of the 2016 gold run in the booster and ags," Tech. Rep. BNL-112663-2016-IR, Brookhaven National Laboratory, 2016.

[309] T. Hayes, F. Severino, and K. S. Smith, "Concept and Architecture of the RHIC LLRF Upgrade Platform," in *Proceedings, 24th Particle Accelerator Conference, PAC'11, New York, USA, March 28-April 1, 2011*, vol. C110328, pp. 1410–1412, 2011.

[310] T. Hayes and K. S. Smith, "A Hardware Overview of the RHIC LLRF Platform," in *Proceedings, 24th Particle Accelerator Conference, PAC'11, New York, USA, March 28-April 1, 2011*, vol. C110328, pp. 645–647, 2011.

[311] M. Harvey, T. Hayes, F. Severino, K. S. Smith, L. T. Hoff, R. C. Lee, A. Marusic, P. Oddo, and K. L. Unger, "Embedded System Architecture and Capabilities of the RHIC LLRF Platform," in *Proceedings, 24th Particle Accelerator Conference, PAC'11, New York, USA, March 28-April 1, 2011*, vol. C110328, pp. 672–674, 2011.

[312] T. Hayes, F. Severino, and K. S. Smith, "A Deterministic, Gigabit Serial Timing, Synchronization and Data Link for the RHIC LLRF," in *Proceedings, 24th Particle Accelerator Conference, PAC'11, New York, USA, March 28-April 1, 2011*, vol. C110328, pp. 642–644, 2011.

[313] K. S. Smith *et al.*, "Overview of LLRF Developments at the BNL Collider-Accelerator Complex 2011-2013." Low Level RF Workshop 2013, Lake Tahoe, California, USA., 2011.

[314] K. S. Smith, "BNL Status and New Projects, LLRF Developments at the BNL Collider-Accelerator Department." Low Level RF Workshop 2017, Barcelona, Spain., 2017.

[315] F. Severino *et al.*, "Distributed Feedback Loop Implementation in the RHIC Low Level Platform." Proceeding of ICALEPCS2013, FRCOBAB05, San Francisco, California, USA., 2013.

[316] C. Schmidt *et al.*, "Recent Developments of the European XFEL LLRF System," in *Proceedings, 4th International Particle Accelerator Conference (IPAC 2013): Shanghai, China, May 12-17, 2013*, p. WEPME009, 2013.

[317] C. Hovater *et al.*, "The LCLS-II LLRF System," in *Proceedings, 6th International Particle Accelerator Conference (IPAC 2015): Richmond, Virginia, USA, May 3-8, 2015*, p. MOPWI021, 2015.

[318] F. Qiu, D. Arakawa, Y. Honda, H. Katagiri, T. Matsumoto, S. Michizono, T. Miura, T. Obina, H. Sakai, and S. Wibowo, "Performance of the Digital LLRF Systems at KEK cERL," in *Proceedings, 6th ICFA Advanced Beam Dynamics Workshop on Energy Recovery Linacs (ERL 2015): Stony Brook, NY, USA, June 7-12, 2015*, p. WEIDLH2066, 2015.

[319] C. Serrano *et al.*, "Design and Implementation of the LLRF System for LCLS-II," in *Proceedings, 16th International Conference on Accelerator and Large Experimental Physics Control Systems (ICALEPCS 2017): Barcelona, Spain, October 8-13, 2017*, p. THSH202, 2018.

[320] P. Marchand, "Review and Prospects of RF Solid State Amplifiers for Particle Accelerators," in *8th International Particle Accelerator Conference*, p. WEZB1, 2017.

[321] E. Montesinos, "High Power Solid State Power Amplifers for the CERN LHC Injector Upgrade for SPS Programme." https://indico.cern.ch/event/472685/contributions/2196909/, 2016.

[322] S.-H. Kim, Z. Conway, P. Ostroumov, G. Waldschmidt, B. Mustapha, M. Kelly, G. Decker, and J. Carwardine, "Higher order mode damping in a higher harmonic cavity for the advanced photon source upgrade," 2015.

[323] R. Connolly, J. Aspenleiter, and S. Kwiatkowski, "Modifying CERN SPS Cavities and Amplifiers for use in RHIC," in *Particle Accelerator Conference, 1997. Proceedings of the 1997*, vol. 3, pp. 2947–2949, IEEE, 1997.

[324] A. Andersson, E. Elafiffi, M. Eriksson, D. Kumbaro, P. Lilja, L. Malmgren, R. Nilsson, H. Svensson, P. Tavares, *et al.*, "The 100 MHz RF System for the MAX IV Storage Rings," in *Particle Acelerator. Proceedings, 2nd International Conference, IPAC 2011, San Sebastian, Spain, September 4-9, 2011*, vol. C110904, pp. 193–195, 2011.

[325] S. Bellavia, I. Ben-Zvi, M. C. Grau, C. Pai, Q. Wu, and G. Miglionico, "Fundamental Damper Power Calculation of the 56MHz SRF Cavity for RHIC," in *Proceedings, 24th Particle Accelerator Conference, PAC'11, New York, USA, March 28-April 1, 2011*, vol. C110328, pp. 919–921, 2011.

[326] A. Lunin, I. Gonin, T. Khabiboulline, V. Yakovlev, and A. Zholents, "Design of a Quasi-Waveguide Multicell Deflecting Cavity for the Advanced Photon Source," *Phys. Procedia*, vol. 79, pp. 54–62, 2015.

[327] K. Papke, A. A. Carvalho, C. Zanoni, and A. Grudiev, "Design studies of a compact superconducting rf crab cavity for future colliders using nb/cu technology," *Phys. Rev. Accel. Beams*, vol. 22, p. 072001, Jul 2019.

[328] I. Ben-Zvi and J. Brennan, "The quarter wave resonator as a superconducting linac element," *Nuclear Instruments and Methods in Physics Research*, vol. 212, no. 1-3, pp. 73–79, 1983.

[329] W. Hartung, J. Bierwagen, S. Bricker, C. Compton, J. DeLauter, P. Glennon, M. Hodek, M. Johnson, F. Marti, P. Miller, *et al.*, "Superconducting quarter-wave resonator cavity and cryomodule development for a heavy ion re-accelerator," in *XXIV International Linear Accelerator Conference, Victoria, BC*, 2008.

[330] R. Laxdal, K. Fong, M. Laverty, A. Mitra, R. Poirier, I. Sekachev, and V. Zvyagintsev, "Recent progress in the superconducting rf program at triumf/isac," *Physica C: Superconductivity*, vol. 441, no. 1-2, pp. 13–20, 2006.

[331] M. Kelly, J. Fuerst, S. Gerbick, M. Kedzie, K. Shepard, G. Zinkann, and P. Ostroumov, "Superconducting quarter-wave resonators for the ATLAS energy upgrade," *Proceedings of LINAC08, Victoria, BC, Canada*, 2008.

[332] Q. Wu, S. Belomestnykh, I. Ben-Zvi, G. McIntyre, R. Porqueddu, S. Seberg, and T. Xin, "Superconducting test of the 56 MHz SRF quarter wave resonator for RHIC," in *Proceedings of the 16th International Conference on RF Superconductivity, (SRF2013):Cite Internationale Universitaire, Paris, France, 2013*, p. THP031, 2013.

[333] S. Miller *et al.*, "Construction and Performance of FRIB Quarter Wave Prototype Cryomodule," in *Proceedings, 17th International Conference on RF Superconductivity (SRF2015): Whistler, Canada, September 13-18, 2015*, p. FRAA06, 2015.

[334] I. Ben-Zvi, "4th LHC Crab Cavity Workshop; December 15-17, 2010; CERN, Geneva, Switzerland 2010 (unpublished)."

[335] I. Ben-Zvi in *Proceedings of 15th International Conference on RF Superconductivity, Chicago, IL, 2011, p. 637*, 2011.

[336] Q. Wu, I. Ben-Zvi, S. Belomestnykh, and R. Calaga, "Quarter Wave Crab Cavity Design and Status, Fermilab, IL, CM18/HiLumi Collaboration Meeting, May 7-9, 2012. https://indico.fnal.gov/event/6859/contribution/4/material/slides/."

[337] R. Calaga, B. Xiao, S. Belomestnykh, Q. Wu, I. Ben-Zvi, and J. Skaritka, "A double quarter-wave deflecting cavity for the LHC," 2013.

[338] B. Xiao, "Overview of Recent HOM Coupler Development," in *Proceedings, 17th International Conference on RF Superconductivity (SRF2015): Whistler, Canada, September 13-18, 2015*, p. THBA04, 2015.

[339] K. Smith, "priv.communication (6 february 2018)."

[340] S. U. De Silva and J. R. Delayen, "Design evolution and properties of superconducting parallel-bar rf-dipole deflecting and crabbing cavities," *Phys. Rev. ST Accel. Beams*, vol. 16, p. 012004, January 2013.

[341] S. U. De Silva and J. R. Delayen, "Cryogenic test of a proof-of-principle superconducting rf-dipole deflecting and crabbing cavity," *Phys. Rev. ST Accel. Beams*, vol. 16, p. 082001, Aug 2013.

[342] S. U. De Silva and J. R. Delayen, "Superconducting rf-dipole deflecting and crabbing cavities," in *Proceedings of the 2013 Conference on RF Superconductivity, Paris, France*, p. 1176, September 2013.

[343] A. Castilla and J. R. Delayen, "Analysis of a 750 mhz srf dipole cavity," in *Proceedings of the 2015 Conference on RF Superconductivity, Whistler, BC, Canada*, p. 1200, September 2015.

[344] A. G., B. A. I., B. O., F. P., L. M., R. L., and T. L., *High-Luminosity Large Hadron Collider (HL-LHC): Technical Design Report V. 0.1*. CERN Yellow Reports: Monographs, Geneva: CERN, 2017.

[345] O. Bruning, "Hl-lhc project status." 10^{th} HL-LHC Collaboration Meeting, CERN, 2020.

[346] Z. Li, S. De Silva, J. Delayen, R. Olave, and H. Park, "Fpc and hi-pass filter hom coupler design for the rf dipole crab cavity for the lhc hilumi upgrade," in *6th International Particle Accelerator Conference*, p. 3492, 2015.

[347] S. D. Silva, J. Delayen, Z. Li, and H. Park, "Cryogenic test results of the sps prototype rf-dipole crabbing cavity with higher order mode couplers," in *Proc. 29th Linear Accelerator Conference (LINAC'18), Beijing, China*, p. 402, September 2018.

[348] R. Calaga, "Update on the rfd crab cavity prototype development and test plans." 10^{th} HL-LHC Collaboration Meeting, CERN, 2020.

[349] F. Marhauser, "Next generation HOM-damping," *Superconductor Science and Technology*, vol. 30, p. 063002, may 2017.

[350] I. E. Campisi, E. F. Daly, J. E. Henry, P. Kneisel, W. J. Schneider, M. Stirbet, and K. M. Wilson, "The fundamental power coupler prototype for the spallation neutron source (sns) superconducting cavities," in *PACS2001. Proceedings of the 2001 Particle Accelerator Conference (Cat. No.01CH37268)*, vol. 2, pp. 1140–1142 vol.2, 2001.

[351] E. Montesinos, "High power rf and couplers status." 8^{th} HL-LHC Collaboration Meeting, CERN, 2020.

[352] K. Artoos, L. Arnaudon, R. Calaga, E. Cano-Pleite, O. Capatina, T. Capelli, D. Cartaxo dos Santos, M. Garlasché, D. Glenat, A. Krawczyk, R. Leuxe, P. Minginette, J. Mitchell, B. Prochal, J. Swieszek, S. Verdú-Andrés, and T. J. Jones, "Status of the HL-LHC Crab Cavity Tuner," no. SRF2019, pp. 648–653. 6 p, 2019.

[353] C. Yao *et al.*, "Preliminary Test Results of a Prototype Fast Kicker for APS MBA Upgrade," in *Proc. of North American Particle Accelerator Conference (NAPAC'16), Chicago, IL, USA, October 9-14, 2016*, no. 3 in North American Particle Accelerator Conference, (Geneva, Switzerland), pp. 950–952, JACoW, Jan. 2017. https://doi.org/10.18429/JACoW-NAPAC2016-WEPOB24.

[354] N. Sherman, "Coulomb scattering of relativistic electrons by point nuclei," *Physical Review*, vol. 103, no. 6, pp. 1601–1607, 1956.

[355] B. R. Oerter, "Accelerator timing at the Relativistic Heavy Ion Collider," in *Accelerator and large experimental physics control systems. Proceedings, 7th International Conference, ICALEPCS'99, Trieste, Italy, October 4-8, 1999*, vol. C991004, pp. 191–192, 1999.

[356] H. Hartmann, "RHIC Real Time Data Link System," in *17th IEEE Particle Accelerator Conference (PAC 97): Accelerator Science, Technology and Applications Vancouver, British Columbia, Canada, May 12-16, 1997*, vol. C970512, p. 2499, 1997.

[357] T. Kerner, C. R. Conkling, and B. Oerter, "V123 beam synchronous encoder module," in *Proceedings, 1999 Particle Accelerator Conference (PAC'99): New York, New York, March 29-April 2, 1999*, pp. 699–701, 1999.

[358] C. R. Conkling, Jr., "RHIC Beam Permit and Quench Detection Communications System," in *17th IEEE Particle Accelerator Conference (PAC 97): Accelerator Science, Technology and Applications Vancouver, British Columbia, Canada, May 12-16, 1997*, vol. C970512, p. 2496, 1997.

[359] D. Kayran, Z. Altinbas, J. P. Jamilkowski, R. C. Lee, and B. Oerter, "The Machine Protection System for the & Energy Recovery LINAC," in *Proceedings, 24th Particle Accelerator Conference, PAC'11, New York, USA, March 28-April 1, 2011*, vol. C110328, pp. 630–632, 2011.

[360] M. Harvey, T. Hayes, L. Hoff, R. C. Lee, P. Oddo, K. Smith, and F. Severino, "Realization of a Custom Designed FPGA Based Embedded Controller," in *Proceedings of ICALEPCS07, Knoxville, Tennessee, USA*, vol. WPPB25, pp. 451–453, 2007.

[361] R. Hulsart, P. Cerniglia, N. Day, R. Michnoff, and Z. Sorrell, "A Versatile BPM Signal Processing System Based on the Xilinx Zynq SoC," in *Proceedings, 5th International Beam Instrumentation Conference (IBIC 2016): Barcelona, Spain, September 11-15, 2016*, p. WEPG12, 2017.

[362] L. T. Hoff and J. F. Skelly, "Accelerator devices at persistent software objects," *Nucl. Instrum. Meth.*, vol. A352, pp. 185–188, 1994.

[363] R. H. Olsen, L. T. Hoff, and T. Clifford, "Code Generation Of RHIC Accelerator Device Object," in *Proceedings of ICALEPCS 1995*, 1995.

[364] J. Chen, G. Heyes, W. Akers, D. Wu, and W. Watson, "CDEV: An Object-Oriented Class Library for Developing Device Control Applications," in *Proceedings of ICALEPCS*, 1995.

[365] P. Kankiya, L. T. Hoff, and J. P. Jamilkowski, "Hardware Interface Independent Serial Communication (IISC) ," in *Proceedings of ICALEPCS*, vol. MOPPC039, 2013.

[366] A. Sukhanov, J. Jamilkowski, and A. Marusic, "Interface Between EPICS and ADO," in *Proceedings, 16th International Conference on Accelerator and Large Experimental Physics Control Systems (ICALEPCS 2017): Barcelona, Spain, October 8-13, 2017*, p. TUPHA146, 2018.

[367] T. D'Ottavio, P. Dyer, G. Marr, and S. Nemesure, "Creating Interactive Web Pages for Non-Programmers," in *Proceedings, 16th International Conference on Accelerator and Large Experimental Physics Control Systems (ICALEPCS 2017): Barcelona, Spain, October 8-13, 2017*, p. TUSH101, 2018.

[368] B. Frak, K. A. Brown, T. D'Ottavio, M. Harvey, and S. Nemesure, "Synoptic Displays and Rapid Visual Application Development," in *Proceedings of ICALEPCS*, vol. TUPPC131, 2013.

[369] T. D'Ottavio, K. Brown, A. Fernando, and S. Nemesure, "Building Controls Applications Using HTTP Services," in *Proceedings, 16th International Conference on Accelerator and Large Experimental Physics Control Systems (ICALEPCS 2017): Barcelona, Spain, October 8-13, 2017*, p. THMPA06, 2018.

[370] B. Frak, T. D'Ottavio, M. Harvey, J. P. Jamilkowski, and J. Morris, "Application of Transparent Proxy Servers in Control System ," in *Proceedings of ICALEPCS*, vol. MOPPC157, 2013.

[371] L. Hendrickson, M. Sullivan, T. Himel, *et al.*, "Slow feedback systems for PEP-II," Tech. Rep. SLAC-PUB-8480, SLAC, 2000.

[372] Y. Funakoshi, M. Masuzawa, K. Oide, *et al.*, "Orbit feedback system for maintaining an optimum beam collision," *Physical Review Special Topics-Accelerators and Beams*, vol. 10, no. 10, p. 101001, 2007.

[373] P. Thieberger, M. Minty, and C. Montag, "Proposed BPM-Based Bunch Crabbing Angle Monitor," in *9th International Particle Accelerator Conference*, p. WEPAF018, 2018.

[374] K. Wittenburg, "The PIN-diode beam loss monitor system at HERA," in *AIP Conference Proceedings*, vol. 546, pp. 3–22, AIP, 2000.

[375] N. Hubert, L. Cassinari, J. Denard, A. Nadji, and L. Nadolski, "Global orbit feedback systems down to DC using fast and slow correctors," *DIPAC09, Basel, Switzerland*, 2009.

[376] "Instrumentation Technologies." `www.i-tech.si/accelerators-instrumentation/`.

[377] Z. Sorrell, P. Cerniglia, R. Hulsart, K. Mernick, and R. Michnoff, "Beam Position Monitors for LEReC," in *5th International Beam Instrumentation Conference*, p. MOPG08, 2017.

[378] C. Steier, A. Biocca, E. Domning, S. Jacobson, G. Portmann, and Y. Wu, "Design of a fast global orbit feedback system for the Advanced Light Source," in *Particle Accelerator Conference, 2001. PAC 2001. Proceedings of the 2001*, vol. 2, pp. 1252–1254, IEEE, 2001.

[379] N. Hubert, L. Cassinari, J. Denard, A. Nadji, L. Nadolski, and D. Pédeau, "Design of a fast orbit feedback for SOLEIL,"

[380] Y. Tian, L. Dalesio, K. Ha, W. Cheng, J. De Long, W. Levine, and L. Yu, "NSLS-II fast orbit feedback system," *ICALEPCS2015, MOX3O05*, 2015.

[381] Y. Tan, "Fast orbit feedback conceptual design report," *Australian Synchrotron Technical Note AS-201107-01*, 2011.

[382] W. Cheng, "Synchrotron light monitor system for NSLS-II," 2010.

[383] "Princeton Instruments." `https://www.princetoninstruments.com/products/PI-MAX4-emICCD/`.

[384] D. Boussard, "Coupled bunch instabilities," in *Fermilab III Instabilities Workshop*, p. 53.

[385] A. Chao, *Physics of collective beam instabilities in high energy accelerators*. Wiley, 1993.

[386] M. Lonza and H. Schmickler, "Multi-bunch feedback systems," *arXiv preprint arXiv:1601.05258*, 2016.

[387] D. Teytelman, *Architectures and algorithms for control and diagnostics of coupled bunch instabilities in circular accelerators*. PhD thesis, Stanford U., 2003.

[388] W. Barry, J. Byrd, J. Corlett, *et al.*, "Design of the PEP-II transverse coupled-bunch feedback system," in *Particle Accelerator Conference, 1995., Proceedings of the 1995*, vol. 4, pp. 2681–2683, IEEE, 1995.

[389] A. Drago, "Feedback systems for FCC-ee," *arXiv preprint arXiv:1704.06162*, 2017.

[390] M. Tobiyama, E. Kikutani, J. Flanagan, and S. Hiramatsu, "Bunch by bunch feedback systems for the KEKB rings," in *Particle Accelerator Conference, 2001. PAC 2001. Proceedings of the 2001*, vol. 2, pp. 1246–1248, IEEE, 2001.

[391] W. Cheng, "NSLS2 transverse feedback system design," *Proc. of BIW*, vol. 10, p. 473, 2010.

[392] W. Cheng, B. Bacha, D. Teytelman, *et al.*, "Commissioning of bunch-by-bunch feedback system for NSLS2 storage ring," *Proceeding of IBIC2014 (Monterey, CA, USA, 2014)*, p. 707, 2014.

[393] "Instrumentation Technologies d.o.o.." `http://www.i-tech.si`.

[394] "Dimtel Inc.." `http://www.dimtel.com`.

[395] T. Nakamura and K. Kobayashi, "FPGA based bunch-by-bunch feedback signal processor," *Proceedings of ICALEPCA*, 2005.

[396] W. Wu, Y. Kim, J. Li, *et al.*, "Development of a bunch-by-bunch longitudinal feedback system with a wide dynamic range for the HIGS facility," *Nuclear Instruments and Methods in Physics Research Section A: Accelerators, Spectrometers, Detectors and Associated Equipment*, vol. 632, no. 1, pp. 32–42, 2011.

[397] R. Boni, F. Marcellini, M. Serio, *et al.*, "A waveguide overloaded cavity as longitudinal kicker for the DAPHNE bunch-by-bunch feedback system," *Part. Accel.*, vol. 52, pp. 95–113, 1996.

[398] P. Thieberger, C. Pai, K. Mernick, *et al.*, "High intensity RHIC limitations due to signal heating of the cryogenic BPM cables," in *Proceedings of PAC1013, Pasadena, CA USA*, p. THPHO09, 2013.

[399] J. Piacentino *et al.*, "RHIC 10 Hz Global Orbit Feedback System," *Conf. Proc.*, vol. C110328, pp. 609–611, 2011.

[400] R. Connolly, R. Michnoff, and S. Tepikian, "Residual-gas-ionization beam profile monitors in RHIC," in *Particle Accelerator Conference, 2005. PAC 2005. Proceedings of the*, pp. 230–234, IEEE, 2005.

[401] A. D'Elia, R. Fandos, and L. Soby, "High Bandwidth Wall Current Monitor for CTF3," *Conf. Proc.*, vol. C0806233, p. TUPC021, 2008.

[402] W. Barry, J. N. Corlett, D. A. Goldberg, and D. Li, "Design of a Schottky signal detector for use at the Relativistic Heavy Ion Collider (RHIC)," in *Particle accelerator. Proceedings, 6th European conference, EPAC'98, Stockholm, Sweden, June 22-26, 1998. Vol. 1-3*, pp. 1514–1516, 1998.

[403] V. Ptitsyn, M. Blaskiewicz, W. Fischer, R. Lee, and S. Y. Zhang, "Measurements of Fast Transition Instability in RHIC," *Conf. Proc.*, vol. C100523, p. TUPEB053, 2010.

[404] R. Steinhagen, M. Boland, and T. Lucas, "A multiband-instability-monitor for high-frequency intra-bunch beam diagnostics," in *Proceedings of IBIC2013, Oxford, UK*, p. TUBL3, 2013.

[405] R. Assmann *et al.*, "The final collimation system for the LHC," *Conf. Proc.*, vol. C060626, pp. 986–988, 2006.

[406] D. Gassner, J. Brutus, R. Hulsart, *et al.*, "Coherent electron cooling proof of principle phase 1 instrumentation status," Tech. Rep. BNL-105994-2014-CP, Brookhaven National Laboratory, 2014.

[407] T. Miller, M. Blaskiewicz, K. Drees, *et al.*, "LEReC instrumentation design & construction," *IBIC 2016*, 2016.

[408] Z. Sorrell, P. Cerniglia, R. Hulsart, K. Mernick, and R. Michnoff, "Beam Position Monitors for LEReC," in *Proceedings, 5th International Beam Instrumentation Conference (IBIC 2016): Barcelona, Spain, September 11-15, 2016*, p. MOPG08, 2017.

[409] J. Frisch *et al.*, "Beam measurements at LCLS," in *Beam Instrumentation Workshop 2008, proceedings of the 13th Beam Instrumentation Workshop, Tahoe City, California, USA, 4-8 May 2008*, pp. 49–58, 2008.

[410] W. Cheng, B. Bacha, D. Padrazo, *et al.*, "NSLS2 Diagnostic Systems Commissioning and Measurements," *IBIC2014, Monterey, CA, USA*, 2014.

[411] A. Adare *et al.*, "Concept for an Electron Ion Collider (EIC) detector built around the BaBar solenoid," 2 2014.

[412] "An EIC Detector Built Around The sPHENIX Solenoid - A Detector Design Study," 10 2018.

[413] R. Kersevan and M. Ady, "Recent developments of Monte-Carlo codes Molflow+ and Synrad+," in *10th International Particle Accelerator Conference*, p. TUPMP037, 2019.

[414] A. P. de Hass *et al.*, "The FoCal prototype – an extremely fine-grained electromagnetic calorimeter using CMOS pixel sensors," *Journal of Instrumentation*, 2018.

[415] U. Amaldi, ed., *Study of an ep Facility for Europe DESY, Hamburg, April 2-3, 1979.*, vol. 790402, (Hamburg, Germany), Deutsches Electron Synchrotron / European Committee for Future Accelerators, 1979.

[416] S. D. C. Soós *et al.*, "Versatile Link PLUS transceiver development," *Journal of Instrumentation*, 2017.

[417] CERN GBT Project: GBTX Manual, `https://espace.cern.ch/GBT-Project/GBTX/Manuals/gbtxManual.pdf`.

[418] K. Chen, H. Chen, J. Huang, F. Lanni, S. Tang, and W. Wu, "A Generic High Bandwidth Data Acquisition Card for Physics Experiments," *IEEE Trans. Instrum. Measur.*, vol. 69, no. 7, pp. 4569–4577, 2019.

[419] S. Campana and T. Wenaus, "An ATLAS distributed computing architecture for HL-LHC," *J. Phys. Conf. Ser.*, vol. 1085, no. 3, p. 032029, 2018.

[420] M. Frank, F. Gaede, C. Grefe, and P. Mato, "DD4hep: A Detector Description Toolkit for High Energy Physics Experiments," *J. Phys. Conf. Ser.*, vol. 513, p. 022010, 2014.

[421] R. Brun, A. Gheata, and M. Gheata, "The ROOT geometry package," *Nucl. Instrum. Meth. A*, vol. 502, pp. 676–680, 2003.

[422] G. Amadio *et al.*, "GeantV Alpha Release," *J. Phys. Conf. Ser.*, vol. 1085, no. 3, p. 032037, 2018.

[423] X. Ai, "Acts: A common tracking software," *arXiv: Instrumentation and Detectors*, 2019.

[424] J. Rauch and T. Schlüter, "GENFIT — a Generic Track-Fitting Toolkit," *J. Phys. Conf. Ser.*, vol. 608, no. 1, p. 012042, 2015.

[425] G. Barrand *et al.*, "GAUDI - A software architecture and framework for building HEP data processing applications," *Comput. Phys. Commun.*, vol. 140, pp. 45–55, 2001.

[426] M. Clemencic, H. Degaudenzi, P. Mato, S. Binet, W. Lavrijsen, C. Leggett, and I. Belyaev, "Recent developments in the LHCb software framework Gaudi," *J. Phys. Conf. Ser.*, vol. 219, p. 042006, 2010.

[427] D. Lawrence, A. Boehnlein, N. Brei, and D. Romanov, "JANA2: Multithreaded Event Reconstruction," *J. Phys. Conf. Ser.*, vol. 1525, no. 1, p. 012032, 2020.

[428] E. Tejedor, E. Bocchi, D. Castro, H. Gonzalez, M. Lamanna, P. Mato, J. Moscicki, and D. Piparo, "Facilitating collaborative analysis in SWAN," *EPJ Web Conf.*, vol. 214, p. 07022, 2019.

[429] S. Höche and S. Prestel, "The midpoint between dipole and parton showers," *Eur. Phys. J. C*, vol. 75, no. 9, p. 461, 2015.

[430] F. Dulat, S. Höche, and S. Prestel, "Leading-Color Fully Differential Two-Loop Soft Corrections to QCD Dipole Showers," *Phys. Rev. D*, vol. 98, no. 7, p. 074013, 2018.

[431] G. Schuler and H. Spiesberger, "DJANGO: The Interface for the event generators HERACLES and LEPTO," in *Workshop on Physics at HERA*, pp. 1419–1432, 1991.

[432] E. C. Aschenauer, T. Burton, T. Martini, H. Spiesberger, and M. Stratmann, "Prospects for Charged Current Deep-Inelastic Scattering off Polarized Nucleons at a Future Electron-Ion Collider," *Phys. Rev.*, vol. D88, p. 114025, 2013.

[433] P. Bedaque, A. Boehnlein, M. Cromaz, M. Diefenthaler, L. Elouadrhiri, T. Horn, M. Kuchera, D. Lawrence, D. Lee, S. Lidia, *et al.*, "Report from the AI For Nuclear Physics Workshop," *arXiv preprint arXiv:2006.05422*, 2020.

[434] P. Mehta, M. Bukov, C.-H. Wang, A. G. Day, C. Richardson, C. K. Fisher, and D. J. Schwab, "A high-bias, low-variance introduction to machine learning for physicists," *Physics reports*, vol. 810, pp. 1–124, 2019.

[435] C. Lynch, "Big data: How do your data grow?," *Nature*, vol. 455, no. 7209, p. 28, 2008.

[436] Alves Jr, A Augusto and Andrade Filho, LM and Barbosa, AF and Bediaga, I and Cernicchiaro, G and Guerrer, G and Lima Jr, HP and Machado, AA and Magnin, J and Marujo, F and others, "The LHCb detector at the LHC," *Journal of Instrumentation*, vol. 3, no. 08, p. S08005, 2008.

[437] "Streaming Readout Workshop," 2020. https://www.bnl.gov/srvii2020/.

[438] "Fast Machine Learning Workshop," 2020. https://indico.cern.ch/event/924283/.

[439] R. Chalapathy and S. Chawla, "Deep learning for anomaly detection: A survey," *arXiv preprint arXiv:1901.03407*, 2019.

[440] S. Farrell, P. Calafiura, M. Mudigonda, D. Anderson, J.-R. Vlimant, S. Zheng, J. Bendavid, M. Spiropulu, G. Cerati, L. Gray, *et al.*, "Novel deep learning methods for track reconstruction," *arXiv preprint arXiv:1810.06111*, 2018.

[441] D. Derkach, M. Hushchyn, T. Likhomanenko, A. Rogozhnikov, N. Kazeev, V. Chekalina, R. Neychev, S. Kirillov, F. Ratnikov, L. collaboration, *et al.*, "Machine-Learning-based global particle-identification algorithms at the LHCb experiment," in *Journal of Physics: Conference Series*, vol. 1085, p. 042038, IOP Publishing, 2018.

[442] C. Fanelli and J. Pomponi, "DeepRICH: learning deeply Cherenkov detectors," *Machine Learning: Science and Technology*, vol. 1, no. 1, p. 015010, 2020.

[443] H. Drucker and C. Cortes, "Boosting decision trees," in *Advances in neural information processing systems*, pp. 479–485, 1996.

[444] M. Dugger, B. Ritchie, I. Senderovich, E. Anassontzis, P. Ioannou, C. Kourkoumeli, G. Vasileiadis, G. Voulgaris, N. Jarvis, W. Levine, *et al.*, "A study of decays to strange final states with GlueX in Hall D using components of the BaBar DIRC," *arXiv preprint arXiv:1408.0215*, 2014.

[445] B. Page, X. Chu, and E. Aschenauer, "Experimental aspects of jet physics at a future EIC," *Physical Review D*, vol. 101, no. 7, p. 072003, 2020.

[446] G. Louppe, K. Cho, C. Becot, and K. Cranmer, "QCD-aware recursive neural networks for jet physics," *Journal of High Energy Physics*, vol. 2019, no. 1, p. 57, 2019.

[447] "Ml4jets workshop," 2020. https://iris-hep.org/projects/ml4jets.html.

[448] I. Goodfellow, J. Pouget-Abadie, M. Mirza, B. Xu, D. Warde-Farley, S. Ozair, A. Courville, and Y. Bengio, "Generative adversarial nets," in *Advances in neural information processing systems*, pp. 2672–2680, 2014.

[449] C. Doersch, "Tutorial on variational autoencoders," *arXiv preprint arXiv:1606.05908*, 2016.

[450] D. J. Rezende and S. Mohamed, "Variational inference with normalizing flows," *arXiv preprint arXiv:1505.05770*, 2015.

[451] M. Paganini, L. de Oliveira, and B. Nachman, "Accelerating science with generative adversarial networks: an application to 3D particle showers in multilayer calorimeters," *Physical review letters*, vol. 120, no. 4, p. 042003, 2018.

[452] R. Stevens, V. Taylor, J. Nichols, A. B. Maccabe, K. Yelick, and D. Brown, "AI for Science," tech. rep., Argonne National Lab.(ANL), Argonne, IL (United States), 2020.

[453] K. Li and J. Malik, "Learning to optimize," *arXiv preprint arXiv:1606.01885*, 2016.

[454] D. Whitley, "A genetic algorithm tutorial," *Statistics and computing*, vol. 4, no. 2, pp. 65–85, 1994.

[455] J. Snoek, H. Larochelle, and R. P. Adams, "Practical bayesian optimization of machine learning algorithms," in *Advances in neural information processing systems*, pp. 2951–2959, 2012.

[456] D. R. Jones, M. Schonlau, and W. J. Welch, "Efficient global optimization of expensive black-box functions," *Journal of Global optimization*, vol. 13, no. 4, pp. 455–492, 1998.

[457] E. Cisbani, A. Del Dotto, C. Fanelli, M. Williams, M. Alfred, F. Barbosa, L. Barion, V. Berdnikov, W. Brooks, T. Cao, *et al.*, "AI-optimized detector design for the future Electron-Ion Collider: the dual-radiator RICH case," *Journal of Instrumentation*, vol. 15, no. 05, p. P05009, 2020.

[458] "Town Hall on A.I. Projects in the Experimental Physics Program," 2020. https://wiki.jlab.org/epsciwiki/index.php/Aug˙28,_ENP_%2B_CST_AI/ML_Town_Hall.

[459] K. Deb, S. Agrawal, A. Pratap, and T. Meyarivan, "A fast elitist non-dominated sorting genetic algorithm for multi-objective optimization: NSGA-II," in *International conference on parallel problem solving from nature*, pp. 849–858, Springer, 2000.

[460] K. Deb, *Multi-objective optimization using evolutionary algorithms*, vol. 16. John Wiley & Sons, 2001.

[461] P. Feliot, J. Bect, and E. Vazquez, "A Bayesian approach to constrained single-and multi-objective optimization," *Journal of Global Optimization*, vol. 67, no. 1-2, pp. 97–133, 2017.

[462] Y. Jin and B. Sendhoff, "Pareto-based multiobjective machine learning: An overview and case studies," *IEEE Transactions on Systems, Man, and Cybernetics, Part C (Applications and Reviews)*, vol. 38, no. 3, pp. 397–415, 2008.

[463] "Joint Machine Learning Workshop, GlueX Panda EIC," 2020. https://indico.gsi.de/event/9244/.

[464] "AI4EIC-exp Workshop." Center for Frontiers in Nuclear Science, Stony Brook, 2021. https://indico.bnl.gov/category/218/.

[465] K. Aulenbacher, E. Chudakov, D. Gaskell, J. Grames, and K. D. Paschke, "Precision electron beam polarimetry for next generation nuclear physics experiments," *Int. J. Mod. Phys. E*, vol. 27, no. 07, p. 1830004, 2018.

[466] J. Hansknecht and M. Poelker, "Synchronous photoinjection using a frequency-doubled gain-switched fiber-coupled seed laser and ErYb-doped fiber amplifier," *Phys. Rev. ST Accel. Beams*, vol. 9, p. 063501, 2006.

[467] B. Sobloher, R. Fabbri, T. Behnke, J. Olsson, D. Pitzl, S. Schmitt, and J. Tomaszewska, "Polarisation at HERA - Reanalysis of the HERA II Polarimeter Data -," *HERA Internal Note*, 1 2012.

[468] A. Camsonne, J. Hoskins, *et al.*, "eRD15: R&D for a Compton Electron Detector," *EIC R&D Progress Report*, June 2017.

[469] A. Camsonne, J. Hoskins, *et al.*, "eRD15: R&D for a Compton Electron Detector," *EIC R&D Progress Report*, January 2016.

[470] F. Méot *et al.*, "eRHIC EIC: Plans for Rapid Acceleration of Polarized Electron Bunch at Cornell Synchrotron," in *9th International Particle Accelerator Conference*, p. MOPMF013, 2018.

[471] W. Fischer and A. Bazilevsky *Phys. Rev. ST Accel. Beams*, vol. 15, p. 041001, 2012.

[472] C. Aidala *et al. Phys. Rev. Lett.*, vol. 120, p. 022001, 2018.

[473] G. Mitsuka *Phys. Rev.*, vol. C95, p. 044908, 2017.

[474] P. Anthony *et al.*, "Deep inelastic scattering of polarized electrons by polarized He-3 and the study of the neutron spin structure," *Phys. Rev.*, vol. D54, pp. 6620–6650, 1996.

[475] K. Ackerstaff *et al.*, "Measurement of the neutron spin structure function g1(n) with a polarized He-3 internal target," *Phys. Lett.*, vol. B404, pp. 383–389, 1997.

[476] D. DeSchepper *et al. Nucl. Instrum. Meth. A*, vol. 419, pp. 16–44, 1998.

[477] M. Amarian *et al. Phys. Rev. Lett.*, vol. 89, p. 242301, 2002.

[478] J. Krimmer, M. Distler, W. Heil, S. Karpuk, D. Kiselev, Z. Salhi, and E. Otten *Nucl. Instrum. Meth. A*, vol. 611, pp. 18–24, 2009.

[479] J. Krimmer *et al. Nucl. Instrum. Meth. A*, vol. 648, pp. 35–40, 2011.

[480] E. Long *et al. Phys. Lett. B*, vol. 797, p. 134875, 2019.

[481] T. Okudaira *et al. Nucl. Instrum. Meth. A*, vol. 977, p. 164301, 2020.

[482] "Run overview of the relativistic heavy ion collider." https://www.agsrhichome.bnl.gov/RHIC/Runs/.